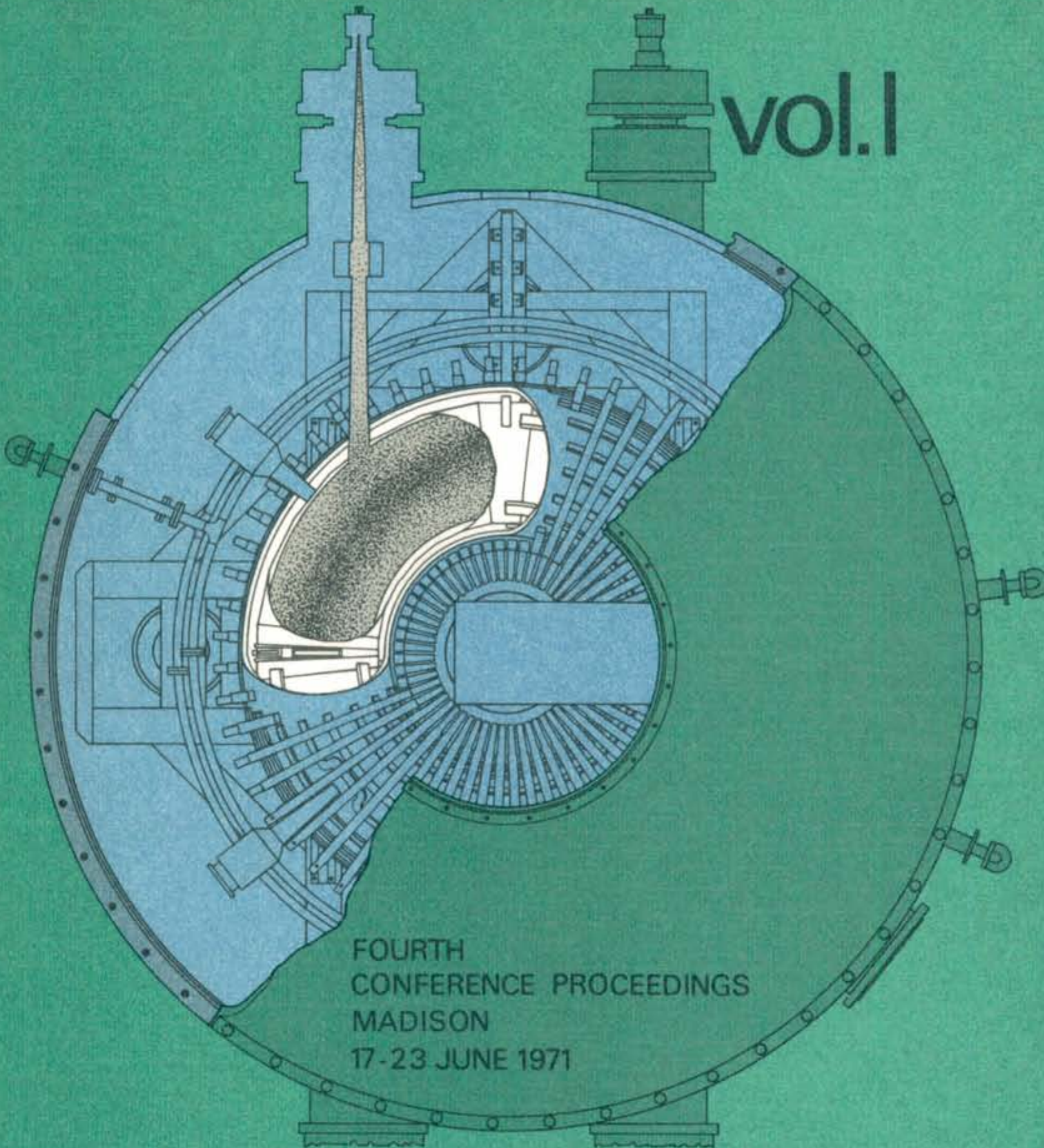

vol. I

FOURTH
CONFERENCE PROCEEDINGS
MADISON
17-23 JUNE 1971

plasma physics and controlled nuclear fusion research 1971

INTERNATIONAL ATOMIC ENERGY AGENCY, VIENNA 1971

PLASMA PHYSICS AND CONTROLLED NUCLEAR FUSION RESEARCH 1971

The following States are Members of the International Atomic Energy Agency:

AFGHANISTAN
ALBANIA
ALGERIA
ARGENTINA
AUSTRALIA
AUSTRIA
BELGIUM
BOLIVIA
BRAZIL
BULGARIA
BURMA
BYELORUSSIAN SOVIET SOCIALIST REPUBLIC
CAMEROON
CANADA
CEYLON
CHILE
CHINA
COLOMBIA
CONGO, DEMOCRATIC REPUBLIC OF
COSTA RICA
CUBA
CYPRUS
CZECHOSLOVAK SOCIALIST REPUBLIC
DENMARK
DOMINICAN REPUBLIC
ECUADOR
EL SALVADOR
ETHIOPIA
FINLAND
FRANCE
GABON
GERMANY, FEDERAL REPUBLIC OF
GHANA
GREECE
GUATEMALA
HAITI
HOLY SEE
HUNGARY
ICELAND
INDIA
INDONESIA
IRAN
IRAQ
IRELAND
ISRAEL
ITALY
IVORY COAST
JAMAICA
JAPAN
JORDAN
KENYA
KHMER REPUBLIC
KOREA, REPUBLIC OF
KUWAIT
LEBANON
LIBERIA
LIBYAN ARAB REPUBLIC
LIECHTENSTEIN
LUXEMBOURG
MADAGASCAR
MALAYSIA
MALI
MEXICO
MONACO
MOROCCO
NETHERLANDS
NEW ZEALAND
NIGER
NIGERIA
NORWAY
PAKISTAN
PANAMA
PARAGUAY
PERU
PHILIPPINES
POLAND
PORTUGAL
ROMANIA
SAUDI ARABIA
SENEGAL
SIERRA LEONE
SINGAPORE
SOUTH AFRICA
SPAIN
SUDAN
SWEDEN
SWITZERLAND
SYRIAN ARAB REPUBLIC
THAILAND
TUNISIA
TURKEY
UGANDA
UKRAINIAN SOVIET SOCIALIST REPUBLIC
UNION OF SOVIET SOCIALIST REPUBLICS
UNITED ARAB REPUBLIC
UNITED KINGDOM OF GREAT BRITAIN AND NORTHERN IRELAND
UNITED STATES OF AMERICA
URUGUAY
VENEZUELA
VIET-NAM
YUGOSLAVIA
ZAMBIA

The Agency's Statute was approved on 23 October 1956 by the Conference on the Statute of the IAEA held at United Nations Headquarters, New York; it entered into force on 29 July 1957. The Headquarters of the Agency are situated in Vienna. Its principal objective is "to accelerate and enlarge the contribution of atomic energy to peace, health and prosperity throughout the world".

Printed by the IAEA in Austria
October 1971

PROCEEDINGS SERIES

PLASMA PHYSICS AND CONTROLLED NUCLEAR FUSION RESEARCH 1971

PROCEEDINGS OF THE
FOURTH INTERNATIONAL CONFERENCE ON PLASMA PHYSICS
AND CONTROLLED NUCLEAR FUSION RESEARCH
HELD BY THE
INTERNATIONAL ATOMIC ENERGY AGENCY
AT MADISON, USA, 17-23 JUNE 1971

In three volumes

VOL. I

INTERNATIONAL ATOMIC ENERGY AGENCY
VIENNA, 1971

PLASMA PHYSICS AND CONTROLLED NUCLEAR FUSION RESEARCH 1971
IAEA, VIENNA, 1971
STI/PUB/288

FOREWORD

The ultimate goal of controlled nuclear fusion research is to make a new energy source available to mankind, a source that will be virtually unlimited and that gives promise of being environmentally cleaner than the sources currently exploited. This goal has stimulated research in plasma physics over the past two decades, leading to significant advances in the understanding of matter in its most common state as well as to progress in the confinement and heating of plasma. An indication of this progress is that in several countries considerable effort is being devoted to design studies of fusion reactors and to the technological problems that will be encountered in realizing these reactors.

This range of research, from plasma physics to fusion reactor engineering, is shown in the present three-volume publication of the Proceedings of the Fourth Conference on Plasma Physics and Controlled Nuclear Fusion Research. The Conference was sponsored by the International Atomic Energy Agency and was held in Madison, Wisconsin, USA from 17 to 23 June 1971. The enthusiastic co-operation of the University of Wisconsin and of the United States Atomic Energy Commission in the organization of the Conference is gratefully acknowledged. The Conference was attended by over 500 scientists from 24 countries and 3 international organizations, and 143 papers were presented. These papers are published here in the original language; English translations of the Russian papers will be published in a Special Supplement to the journal Nuclear Fusion.

The series of conferences on Plasma Physics and Controlled Nuclear Fusion Research has become a major international forum for the presentation and discussion of results in this important and challenging field. In addition to sponsoring these conferences, the International Atomic Energy Agency supports controlled nuclear fusion research by publishing the journal Nuclear Fusion, and has recently established an International Fusion Research Council. The primary aim of this Council, which had its first meeting in conjunction with the Madison Conference, is to promote international co-operation in controlled nuclear fusion research and its application. By these activities the International Atomic Energy Agency hopes to contribute significantly to the attainment of controlled fusion power.

EDITORIAL NOTE

The papers and discussions incorporated in the proceedings published by the International Atomic Energy Agency are edited by the Agency's editorial staff to the extent considered necessary for the reader's assistance. The views expressed and the general style adopted remain, however, the responsibility of the named authors or participants.

For the sake of speed of publication the present Proceedings have been printed by composition typing and photo-offset lithography. Within the limitations imposed by this method, every effort has been made to maintain a high editorial standard; in particular, the units and symbols employed are to the fullest practicable extent those standardized or recommended by the competent international scientific bodies.

The affiliations of authors are those given at the time of nomination.

The use in these Proceedings of particular designations of countries or territories does not imply any judgement by the Agency as to the legal status of such countries or territories, of their authorities and institutions or of the delimitation of their boundaries.

The mention of specific companies or of their products or brand-names does not imply any endorsement or recommendation on the part of the International Atomic Energy Agency.

CONTENTS OF VOL. I

TOKAMAKS I (Session C)

PLASMA FOCUS; LASER- AND ELECTRON-BEAM-PRODUCED PLASMAS (Session D)

INTERNAL RING DEVICES
ASTRON

(Session A)

Chairman: M. GOTTLIEB

Papers A-4 to A-8 were presented by
B. LEHNERT as Rapporteur

Papers A-9 and A-10 were presented by
N. C. CHRISTOFILOS as Rapporteur

PLASMA INJECTION, HEATING, CONFINEMENT, AND LOSSES IN MULTIPOLE STRUCTURES†

D.W. KERST, H.K. FORSEN, D.M. MEADE,
D.E. LENCIONI*, J.C. SPROTT**, H.V. De la FUENTE***,
A.W. MOLVIK, R.A. BREUN, A.J. CAVALLO,
J.R. DRAKE, J.R. GREENWOOD, T.C. JERNIGAN,
R. PRATER, J.W. RUDMIN
University of Wisconsin
Madison, Wisconsin,
United States of America

Abstract

PLASMA INJECTION, HEATING, CONFINEMENT, AND LOSSES IN MULTIPOLE STRUCTURES.

Plasma behaviour and losses to the walls and to the surfaces of the isolated levitated hoops in a toroidal octupole have been examined for gun-injected and for microwave-produced plasmas with densities of 10^9 to 10^{11} cm^{-3} in the volume of 8×10^6 cm^3. Methods of plasma focusing by a magnetic lens which increase the gun plasma stream density by a factor of 40 are being applied to the octupole to raise the density. It has been discovered that electron cyclotron resonance heating (ECRH) also generates hot ions in the levitated octupole. The energy and density of these ions is comparable to that of gun-injected plasma (10 eV to 200 eV).

Thin striped multi-electrode plasma collectors measure losses to surfaces with minimum mechanical or electrical disturbance to the body of the plasma, and a modulated light beam has been used to transmit signals outward from an isolated hoop. Losses to the hoop are sensitive to the time variation of B. A three-dimensional search of plasma structure with thin probes revealed some fluctuations during plasma motion caused by B more noticeable in the larger levitated octupole than in a small one-third scale supported hoop octupole. Correction of port-hole-field disturbances in the small octupole have been successful in reducing losses by 30% in the vicinity of the hole.

Injection inside the confinement region of the small octupole has been used with small plasma sources to produce densities of 10^{13} cm^{-3}. These studies have shown that stability and trapping efficiency are dependent on the location and orientation of the injector but not on the density.

A toroidal magnetic field of 1000 G is being added to the levitated octupole.

The transport of plasma (T_e = 2 eV, n = 10^9 cm^{-3}) to the internal ring of a d.c. multipole-like device was increased by over a factor of 10 by the addition of a 1% magnetic perturbation which caused field lines to spiral across the confinement region. The plasma transport was reduced by a factor of 30 to 50 with the application of a toroidal magnetic field which was larger than the error field.

Introduction

The experiments to be described were performed on a large support-free octupole,[1] and on the older small one-third size supported conductor octupole, both inductively excited, and on a single ring steady current device to simulate a multipole hoop. Miniature stripe detectors were developed to collect plasma loss arriving at selected surface areas without perturbing the plasma. Measurements on the surface of a completely isolated hoop surrounded by plasma were telemetered out by a modulated light beam. For non-destructive monitoring of the confined plasma a microwave Fabry-Perot interferometer with its mirrors outside of the stable plasma region was used.

---

† This work was supported by the U.S. Atomic Energy Commission.

* Now at Lincoln Laboratory, Massachusetts Institute of Technology, Lexington, Massachusetts.

** Now at Oak Ridge National Laboratory, Oak Ridge, Tennessee.

*** Now at the Instituto Politécnico Nacional, Mexico City, Mexico.

Characteristics of the Inductively Excited Support-Free (Levitated) Octupole

Figure 1 shows the essential dimensions with the diagnostic equipment in place.

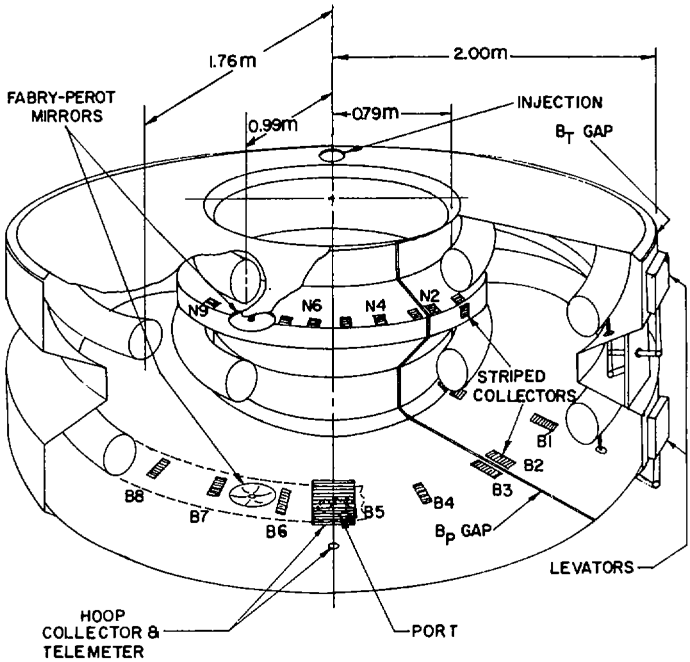

FIG. 1. Levitated octupole showing striped collectors B on the bottom and N on the nose, and the isolated-hoop striped collector with telemeter. Poloidal field lines enter at B_P gap and toroidal lines enter at B_T gap.

The hoop supports are removed for 0.020 sec near peak field when plasma is formed. This eliminates loss from thermal flow of plasma directly to the supports, and it also eliminates the electric fields caused by supports which can drive convection.

Inductive half sine wave excitation causes the flux plot to be confined by the conducting surfaces of the walls and hoops with the magnetic field diffusing into the skin layer. Moving field lines carry plasma to and from the wall at times when the lines are diffusing into and out of the walls respectively. The field lines cease to diffuse into the conducting wall and start to come back out at $\omega t = 3\pi/2$ which is at 0.031 sec for the large octupole. At this time there should be no plasma motion at surfaces to or from the walls or hoops, and the structure should behave as though it had superconducting wall and hoop surfaces. However, the strength of the magnetic field is decreasing with time at $\omega t = 3\pi/2$ as flux lines with plasma on them leave the chamber at the B_p voltage gap. The half sine wave pulse ends at 0.043 sec.

With a clamp or crowbar short circuit switched across the voltage gap at peak field the exponential decay has a time constant of 0.08 sec. This clamp results in symmetry of losses to the wall since field lines continually soak into the skin at all surfaces and azimuths after clamping; whereas for sine excitation there is a rush of plasma at late times toward the voltage gap as shown in Fig. 2 (left).

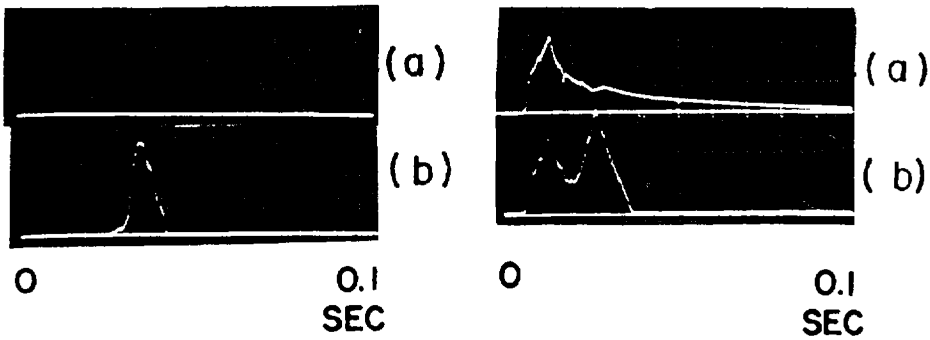

FIG.2. (Left, a). Striped loss collector current at voltage gap while clamped shows no excessive plasma loss there. (Left, b) sine excitation plasma loss at voltage gap as field goes to zero. (Right, a) Langmuir probe monitor on the separatrix with 0.08 s clamped field decay. (Right, b) same with sine excitation.

For sine excitation the peak plasma density moves inward away from a probe on the separatrix at early times and outward past the probe at late times when it is destined for the outer wall and the voltage gap, Fig. 2(b) (right). Figure 2(a) (right) shows the result of the exponential clamped field decay with the continual decrease in plasma density as plasma moves away toward wall surfaces. Although supports return at 0.05 sec some plasma is still contained past 0.2 sec (Fig. 3).

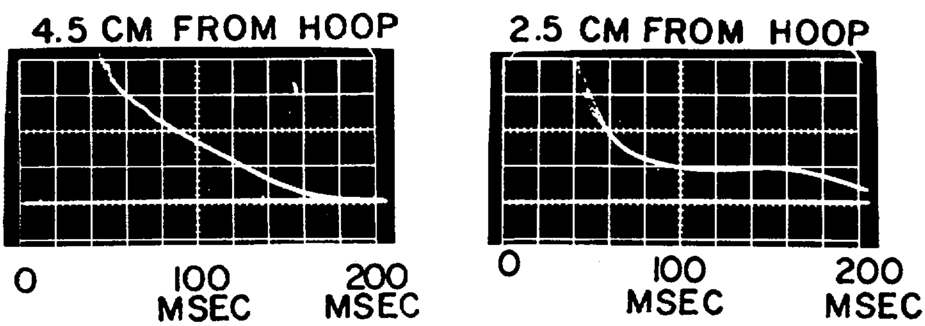

FIG.3. Langmuir-probe monitor ion-saturation current after supports have returned. Clamped-field intensity decay life is 0.08 s. Sensitivity is 10 times that of Fig.2 (a, right). Separatrix is 5.0 cm from hoop.

Because of these effects of dB/dt it is appropriate to measure the rate of plasma loss to walls instead of measuring lifetimes. An equivalent life, τ, is then calculated from $dN/dt = -N/\tau$.

The following methods of determining losses are employed. (1) Any hoop left on its support can be biased to read plasma loss current collected on it. (2) Small insulated flexible wires can be connected to hoops to collect plasma loss current. After levitation these are the only obstructions in the plasma. (3) All obstructions are eliminated with the modulated light beam telemeter buried in a large hoop. Its signal received outside the plasma indicates how much plasma has fallen onto a striped collector flush with the hoop surface. Striped collectors[4] are made by printed circuit techniques on thin insulating sheets with adjacent conducting stripes alternating in collecting potential and spaced by a distance preferably less than the Debye distance. (4) Striped collectors are also placed on the vacuum tank wall. (5) A Fabry-Perot interferometer determines the quantity of plasma in its sampling volume as a function of time. (6) Langmuir probe determinations of the spatial density distribution as a function of time provide a measurement of total particle loss. (7) Ion detectors are used to observe decay of hot ions.

In both (6) and (7) the detector adds to the loss.

Gun injection produces densities of $n > 10^9$ cm^{-3} with $T_i \sim 20$ eV to 50 eV. Electron-cyclotron resonance heating at 2.45 GHz produces $n > 10^9$ cm^{-3} at 100 watts preionization up to 0.018 sec. and $n \sim 10^{11}$ cm^{-3} with 100 KW at 2.9 GHz for 144 microseconds. Background pressure can be 10^{-7} Torr with 3×10^{-7} to 1.5×10^{-6} Torr for the microwave plasmas. Swept probes gave 8 ± 1 eV electron temperature for the supported case with gun plasma 0.0005 sec after injection and 16 ± 2 eV with levitation. By 0.005 sec. after injection these temperatures had cooled to 5 eV and 6 eV respectively. For microwave plasma produced by C. W. preionization followed by the high power heating pulse the temperatures were strongly dependent on background pressure as well as on the supported or levitated condition of the hoops. Temperatures ranged from 7 to 15 eV for the levitated case and from 5 to 8 eV for the supported case 0.001 sec after the heating pulse. It is evident that with levitation higher initial temperatures are achieved. There is, in addition, a hot component of electrons formed by ECRH that has been observed by scintillation probes. The lifetime of the hot component is very sensitive to the presence of the supports or small obstacles like the wires sometimes used to connect to the hoops.

The maximum field B_P at a hoop surface is 14 kg with 14 gyroradii on each side of the separatrix for 50 eV protons. A toroidal field, B_T, of up to 100 G is possible at present, but the measurements described are usually at half this magnitude for B_P and B_T.

Loss Measurements

1) Plasma density distributions taken by a Langmuir probe at 0.020, 0.025, and 0.030 seconds for gun plasma injected at 0.014 sec. give the total number of contained particles as a function of time. Azimuthal symmetry is assumed and the integration is done in flux space taking into account the time dependence of the computer-determined flux plots. For the supported case observed losses indicated a lifetime of $\tau_{GS} = 0.025 \pm .005$ sec. For the levitated case the loss rate varied over the intervals of observation. The loss rate between 0.020 and 0.025 sec., when dB/dt is near zero gave a lifetime $\tau_{GL} = 0.1$ sec. This is the most

conservative estimate of lifetime within the spread of the data points and taking cooling into account. Later in the 0.025 to 0.030 sec interval losses were again evident at a rate corresponding to a lifetime of τ_{GL} = 0.030 ± 0.005 sec.

2) The Fabry-Perot interferometer, which is a non-destructive shot to shot monitor, can give information on decay of the total number of particles by weighting its volume sensitivity distribution with the Langmuir probe density distribution shapes mentioned above. Near peak field with gun plasma it gives $\tau_{GL} \sim 0.020$ sec.

3) Connection to a hoop by the supports or by the fine wires allows biasing and measurement of plasma loss coming to that hoop. There are experimental difficulties with the whole plasma potential then being moved and the time dependence and quantity of the loss collected on one hoop being influenced by the bias of another hoop. The lifetime given by this method for gun plasma is τ_{GW} = 0.08 sec assuming all loss to be to hoops.

4) Striped loss collectors, 40 cm^2 and 122 cm^2 in area, were located on the wall and one collector of 350 cm^2 area was wrapped around the lower outer hoop as shown in Fig. 1. These collectors had 8 stripes per centimeter which seemed adequately fine compared with 4 and 16 stripes per centimeter collectors on the wall of the small octupole. At peak field the loss density collected at the inward bulge, or nose, on the wall where ψ_c is very close to the wall, is usually a factor of three greater than the loss density in the middle of the lid where ψ_c is about 10 cm from the wall, but in one case it is an order of magnitude greater. At late times the nose acts as a limiter and collects a still greater proportion of the plasma. Fig. 4 shows wall losses.

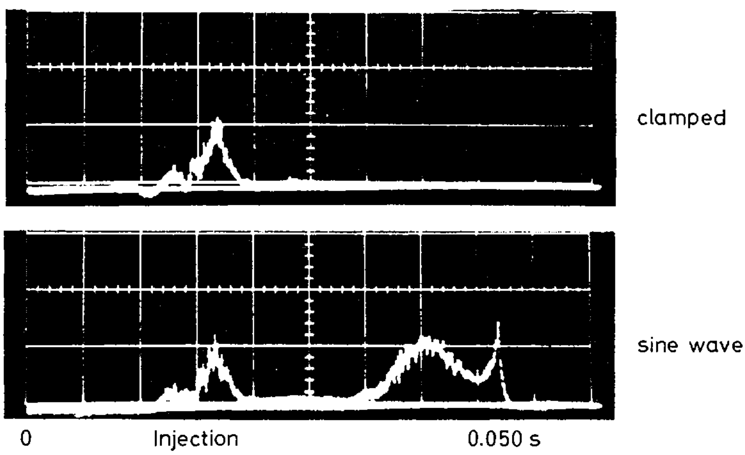

FIG.4. (Top) loss collected on a nose or bulge collector with the clamped magnetic field decaying exponentially with life 0.08 s. (Bottom) the same with half sine excitation terminating at 0.043 s. 6.5×10^{11} particles per cm^2 and sec division. $N \sim 10^{16}$.

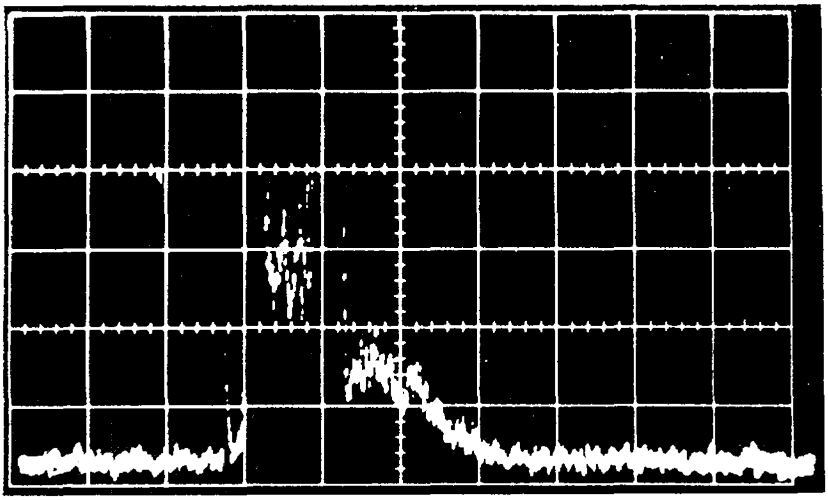

FIG.5. Loss telemetered by light beam from the levitated lower outer hoop at 0.022 s where 60 μA show 2×10^{17} particles per second. Loss to the hoops assuming uniformity. $N \sim 10^{16}$. Outer-wall surface loss is less than 0.2 of hoop surface loss.

Losses to the lower outer hoop telemetered to the laboratory are shown in Fig. 5. Characteristic of loss signals from the hoop collector for different conditions is the vanishing trend of the loss at 0.030 sec. This is about the time at which the tangential electric field on the conductor goes through zero and reverses for half sine wave excitation. Some tests show a subsequent rise in loss collection.

Most of the loss has been found to be on the high field side of the hoop in tests on the small octupole with four striped collectors on the minor hoop circumference.

On the support-free octupole the total hoop surface is half as great as the total wall surface and it collects an order of magnitude more loss than the wall does at 0.022 seconds. At later times, 0.030 sec, the hoop loss approaches the wall value except for sine excitation which sends plasma toward the outer wall as the field decreases.

Summarizing the measurements with method 4), the collectors, we note that measurement 1) is self sufficient since it measures densities on all flux lines (except those inside ψ_s around the inner hoops). Density uniformity in azimuth and along field lines is assumed. The supported case gave $\tau = 0.025$ sec which is the same life found by a measurement with method 4), the hoop loss collector, using the radial density distributions taken from method 1) to evaluate N. For the levitated case method 1) gave $\tau = 0.10$ sec with the density distribution shown in Fig. 6. With a radically different density distribution sharply peaked midway between the hoop surface and ψ_s method 1) gave $\tau = 0.030$ sec and under the same circumstances of this inverted density gradient near the hoop method 4) gave large collector loss on the hoop and $\tau = 0.014$ sec. In the latter case the test had to be made with fine wires to the hoop collector because the telemeter had been damaged by high power microwaves.

With 100 watt microwaves without a toroidal field method 4) gave $\tau_{supported}$ = 0.1 sec, $\tau_{levitated}$ = 0.05 sec while with $B_T \sim 35$ Gauss $\tau_{supported}$ = 0.054 sec, $\tau_{levitated}$ = 0.007 sec. The greater losses to the hoop collector with levitation are the result of a large density of plasma formed very closs to the hoop surface and its collector by microwaves. The density profiles show this with an unstably inverted density gradient extending closer to the hoop than it is safe to put the Langmuir probe which determines the profile. Supports tend to eliminate this excessive microwave plasma close to the hoop surface.

Evidently the plasma density distribution influences the losses in a way which is especially noticeable if the variation is local near a collector. Another way in which the distribution influences the calculated τ is in the determination of N. A monitor of N such as a fixed small Langmuir probe or the Fabry-Perot interferometer requires the distribution throughout to be known if the monitor is to give N. However the density distribution is a function of the state of support or levitation, the existence of obstacles, the magnitude of B_P and B_T, and the time of plasma formation.

For comparison the Bohm time is 0.005 sec for our plasmas, and the loss to support lifetime for 50 eV ions is greater than 0.01 sec.

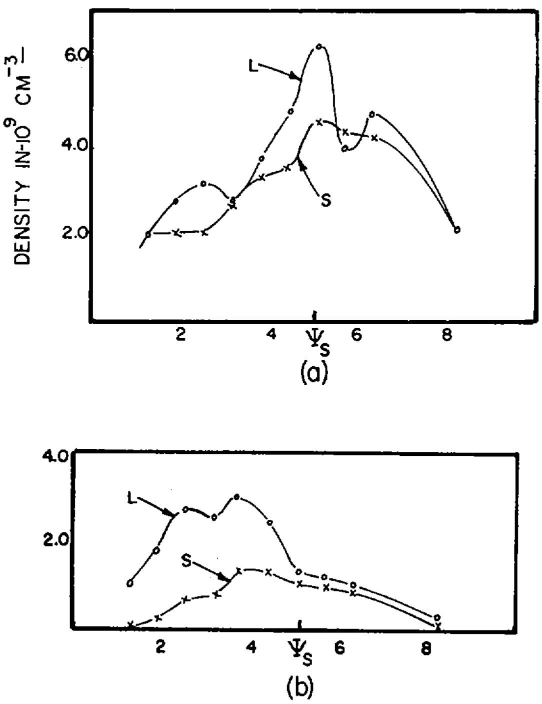

FIG.6a. Density distribution 0.0001 s after gun injection;
6b. Density distribution 0.0005 s after gun injection.

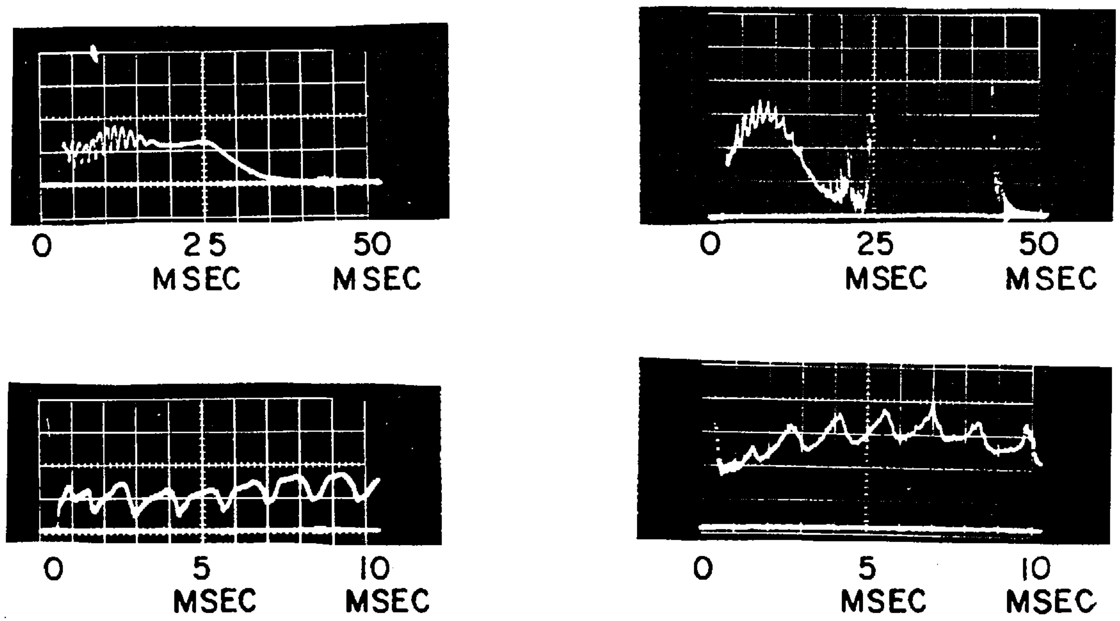

FIG.7. (Left) Langmuir density probe on minor axis of toroid. (Right) Striped-loss-collector current near voltage gap (B3).

Plasma Formation

Gun plasma density profiles for supported and levitated cases are shown in Fig. 6. At 0.0005 sec. the density inside the separatrix is a factor of three greater for the levitated case than for the supported case. The supports significantly decrease the plasma capture efficiency inside the separatrix but thermal flow to supports does not account for the difference.

Plasma injection at 0.002 sec, while the magnetic field is rising rapidly causes a large slow density oscillation from 400 Hz up to 800 Hz at the best background pressure. It is seen by Langmuir probes, by the Fabry-Perot interferometer, and by wall collectors closest to the gap, Fig. 7. The oscillation is in phase throughout a plane at one azimuth, but differing azimuths are out of phase. The propagation is opposite to the direction of the induced hoop current.

Filling experiments were performed in the small octupole using a miniature coaxial gun of 1.5 cm O.D. and 4.5 cm length.[5] With a central cathode of lithium, a 25 eV lithium plasma of 10^{13} cm^{-3} density could be trapped. Trapping efficiency was measured by collecting the saturated ion current to a biased, vertical wire across the plasma volume. The relative efficiencies for three different modes are shown in Fig. 8 as a function of gun position in the mid-plane. In the θ-mode the gun is aimed in the toroidal direction and in the R-mode it is aimed along the major radius toward the inner wall. In the Z-mode injection is vertical and except at the symmetry point, ψ_s, it is parallel to field lines in the poloidal direction. The relative trapping efficiencies are strongly dependent on the gun's radial location as well as the mode.

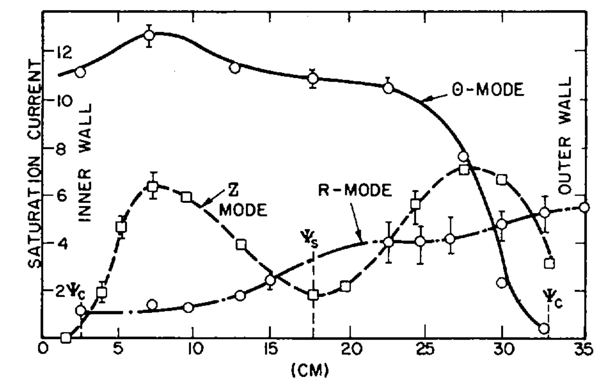

FIG. 8. Trapped-particle monitor current as a function of miniature coaxial gun distance across the mid-plane from the inner wall of the small octupole.

Z-mode injection fills regions of common flux which quickly sets up an octupole polarization field dominated by inward E x B drifts till the density peaks on ψ_s. R-mode injection exhibits some trapping even when the plasma is injected toward ψ_c and only a few centimeters from it. Injecting in the θ-mode at ψ_s produces a plasma with angular momentum. For this case the density remains peaked outside ψ_s and it is not constant along field lines and the field lines are not equipotentials.

A search for hot ions generated secondarily by ECRH is under way in the large octupole. A small gridded probe and ion extraction for analysis are being tried. Ions above 200 eV are sought since that is the energy above which they appeared in the small octupole. The violent floating potential fluctuations during ECRH after high power heating must subside before hot ion analysis is attempted by an extraction technique.

Field Errors

The large octupole was machined for symmetry. Wedge porthole plugs are used to conduct the wall current across the holes, and the voltage gap is trimmed to appear to widen proportional to radius at all times. The pulsed field has the conducting boundary condition that perpendicular components of the field are suppressed. Thus, elimination of dimensional errors eliminates pulsed errors, but steady currents or permanent magnets can send their field lines through the wall to cause field perturbations. These can be trimmed down to the size of the earth's field by magnetic shielding and by correcting coils on the large octupole. As plasma observations are refined, several corrections and structural perturbations which are not yet fully trimmed can be examined. For example, the gun porthole was open for these tests. It can be closed by its copper bar plug having the same overall resistance as the missing aluminum wall. On the small octupole it has been possible to reduce local loss to a hoop by 30 percent by partially correcting an existing porthole perturbation. The floating potential cell-like pattern around this hoop is very similar to that found near ψ_c,[6], Fig. 9, but the density distribution was essentially uniform while that near ψ_c varied greatly.

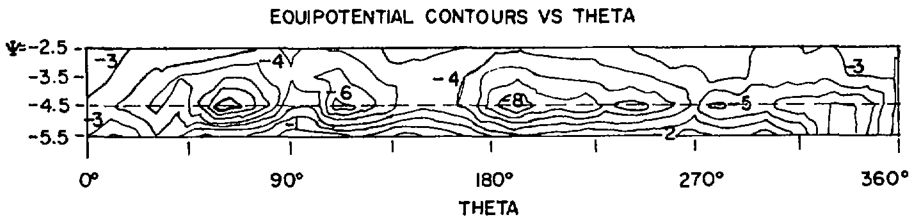

FIG. 9. Floating potentials near hoop surface on the small octupole. Contours below the dashed line are not necessarily closed as shown because the potentials near ψ = -5.5 were taken on lines of force on the weak field side of the hoop which penetrate the conducting surface.

Some artificial error tests have been made on the large octupole directly at a wall collector. The most noticeable effect was during the R.F. plasma heating period when the resonance zones were moved to give a larger loss for one polarity of error.

Anomalous loss of plasma to the internal rings of multipole and single ring devices has been observed to be a substantial fraction of the total loss. This anomalous loss can find explanations in terms of plasma confinement in a perturbed magnetic field. In a shearless multipole an infinitesimal magnetic perturbation can cause a field line to move a finite distance across the confinement region to the internal ring. Plasma can now be lost to the internal ring by simply flowing along the magnetic

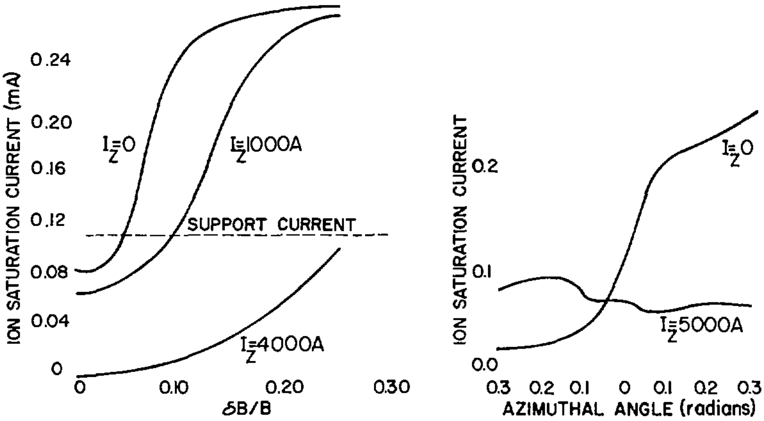

FIG.10. Ion flux to the internal hoop as a function of the ratio of the peak dipole field error at the separatrix near the hoop to the poloidal field at that point for various toroidal magnetic fields is shown on the left. The field error averaged over the entire machine is roughly two orders of magnitude smaller. The azimuthal density profile for a 10% peak error for various toroidal fields. An I_z = 5000 A corresponds to a toroidal field ≈ 2% of the poloidal field near the hoop.

field lines. A steady state device with a single mechanically supported internal ring was used to study the transport of collisional plasma to the ring under the influence of controlled field errors. In particular a one percent field error was observed to increase the plasma loss to the internal ring by over a factor of 10 to a level ≈20 percent of the Bohm diffusion rate. Furthermore, the addition of a small (5 percent) toroidal magnetic field to the perturbed system reduced the plasma getting to the internal hoop by a factor of 50 to the level of ion-neutral cross field diffusion (Fig. 10).

The azimuthal density gradients generated by the magnetic perturbation were reduced by a factor of 10 by the toroidal field. The experimental results for this collisional plasma were in semiquantitative agreement with a theoretical model in which plasma is lost to the internal ring by diffusing along magnetic field lines. The results on the small device and the parallel flow model suggest that the anomalous losses to rings in other devices may be due to small magnetic field errors. If so, this anomalous loss can be drastically reduced by the addition of a sufficiently large toroidal field, roughly the order of the peak error field. The familiar stellarator field topology then results with its characteristic responses to field perturbations. For the purpose of topology it should always be possible to escape from the problem of compensating for field perturbations in a pure poloidal field device by switching to the more familiar stellarator perturbation problem by the addition of a toroidal field.

Acknowledgements

We are greatly indebted to Paul D. Nonn for the development of the modulated light beam telemetering system for the support-free octupole. Time dependent flux plots for sine excitation were made by R. L. Willig with aid from H. K. Meier and J. D. Steben and Delmar Marshall. The computer work and flux plotting for design determination were carried out by J. D. Steben.[7]

References

[1]. H. K. Forsen, D. W. Kerst, R. A. Breun, A. J. Cavallo, J. R. Drake, and J. C. Sprott, in Proceedings of the Fourth European Conference on Controlled Fusion and Plasma Physics, Rome, Italy, August 1970, page 24.

[2]. J. A. Schmidt and G. L. Schmidt, Phys. Fluids 13, 1351 (1970).

[3]. J. C. Sprott, Bull. Amer. Phys. Soc. 15, 1449 (1970).

[4]. D. E. Lencioni and D. W. Kerst, Bull. Amer. Phys. Soc. 15, 1466 (1970).

[5]. H. V. De la Fuente and H. K. Forsen, to be published in Rev. Sci. Instr.

[6]. J. A. Schmidt, Phys. Rev. Letters 24, 13, 721 (1970).

[7]. J. D. Steben, to be published.

DISCUSSION

J.R. ROTH: The frequency and cusped nature of the losses shown in Fig.7 of your paper remind one of classical moving striations. If this propagating density wave were a striation, one might expect circumferential electric fields of about 1 volt/cm, propagation in the direction of the electric field, and a frequency that is independent of the magnetic field but dependent on both electron and neutral number densities. Are your measurements consistent with the identification of this density wave as a classical moving striation?

D.W. KERST: The frequency depends on the background gas density but the direction of propagation is opposite to the toroidal electric field, which is less than 0.02 V/cm.

PLASMA CONFINEMENT IN THE dc OCTOPOLE*

T. OHKAWA, M. YOSHIKAWA,†
J.R. GILLELAND, T. TAMANO
Gulf General Atomic Company, San Diego, Calif.,
United States of America

Abstract

PLASMA CONFINEMENT IN THE dc OCTOPOLE.

The plasma in the dc octopole decays in two successive stages: the collisional regime and then the collisionless regime. In the collisional regime the density decays in inverse proportion to the time from the density of 10^{11} cm^{-3} to about 2×10^9 cm^{-3}. The measured diffusion coefficient varies linearly with the density and as -2 power of the octopole field. The values of the coefficient are within a factor of three of the theoretical values for the classical diffusion. In the collisionless regime the density decays exponentially. The confinement time is 0.4 s for the hydrogen plasma with the electron temperature of 0.5 eV. The plasma losses to the supports and to the walls are comparable. The confinement time is affected by the following parameters: (1) impurity gas pressure, (2) ion mass M_i, (3) electron temperature T_e, (4) field errors, and (5) voltages applied to the particle loss collectors. The confinement time is shortened by the presence of the oxygen-containing gas such as O_2, H_2O, and CO_2 above the pressure of 10^{-8} Torr. At the normal background pressure of these gases (below 2×10^{-9} Torr) the effect is negligible. The confinement time scales as $\sqrt{M_i/T_e}$, T_e is increased by the electron cyclotron heating and M_i is varied from hydrogen to neon mass. The confinement time is independent of the magnetic field strength. An error field applied externally shortens the confinement time. The scaling law of the confinement time is the same with and without the external error field. The single particle confinement experiment using filament-produced electrons also shows the similar scaling. These observations indicate that the plasma reaches the walls by flowing along the magnetic flux lines. A large voltage on the particle collector reduces the confinement time. The confinement time becomes dependent on the magnetic field suggesting a cross-field loss. In summary, the plasma loss at high densities is due to the collisional diffusion. In the collisionless regime, there are two loss processes, namely a trivial loss to the supports and a loss to the walls due to the field errors in the magnetic field.

I. INTRODUCTION

The preliminary experiments[1] have shown that the plasma in the dc octopole device decays in two stages, namely the high density regime and the low density regime. In the high density regime ($n > 2 \times 10^9$ cm^{-3}) the plasma density decays in inverse proportion to time. The measured diffusion coefficient is proportional to the density and to the -2nd power of the octopole field. This behavior agrees with that of the classical diffusion. The numerical agreement is within a factor of three. In the low density regime ($n < 2 \times 10^9$ cm^{-3}) the density decay is exponential. The loss process in this regime was not clearly understood.

The experiments described in this paper concern the loss processes in the low density regime. The method of approach is to find the plasma and machine parameters which affect the plasma confinement and then to evaluate the extent to which the parameters limit the confinement time. Three major parameters which change the confinement properties are (a) the residual gases in the vacuum chamber, (b) the bias voltages applied to the particle collectors, and (c) the magnetic field errors superposed on the octopole field.

* Work supported by the U.S. Atomic Energy Commission, Contract No. AT(04-3)-167, Project Agreement No.38.

† Present address: Japan Atomic Energy Research Establishment, Japan.

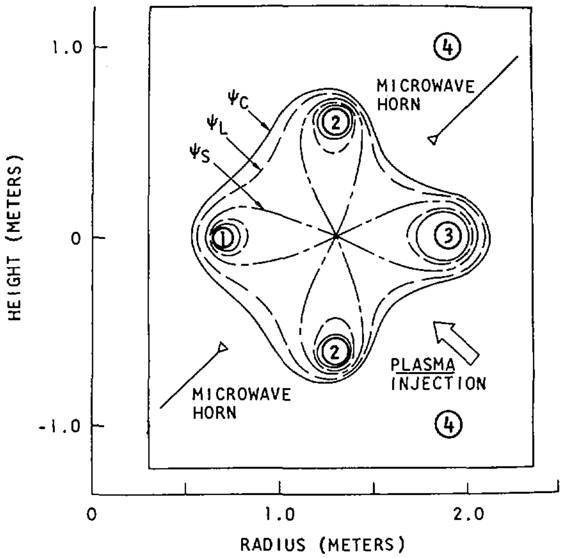

FIG.1. Octopole flux configuration showing location of the six current rings and main flux surfaces. ψ_S is the separatrix, ψ_L is the surface with a minimum $\oint d\ell$, and ψ_C is the surface with minimum $\oint d\ell/B$. The horns for the microwave interferometer and the path of the injected plasma are also shown.

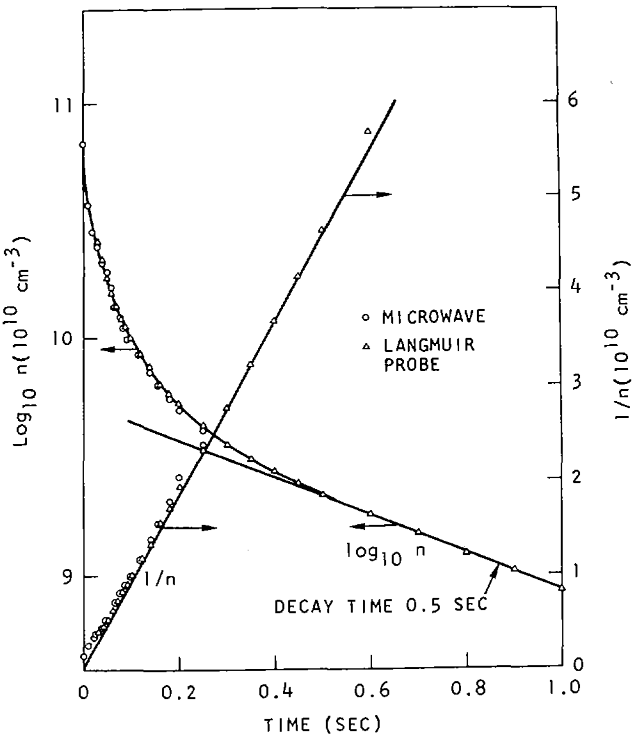

FIG.2. Time dependence of the plasma density n. Both 1/n and ln n are shown.

II. LOW DENSITY PLASMA IN THE dc OCTOPOLE

The dc octopole device at Gulf General Atomic has been described in Ref. 1. Figure 1 shows the configuration of the device and the flux lines. The internal rings are each held in position by three mechanical supports, one of which serves as a coaxial electrical feed. The plasma volume is approximately 10^7 cm^3 and the support area is roughly 10^2 cm^2. For most of the experiments the average magnetic field on the stability limit is $B_{OCT} = (\oint d\ell)/(\oint d\ell/B) = 260$ G, which corresponds to an average of 18 gyroradii between the separatrix and the stability limit for 1-eV protons. The hydrogen plasma is produced by a coaxial gun and is injected between the current rings as shown in Fig. 1. The end of the gun is located just outside of the stability limit. The hydrogen plasma is used for most of the experiments. The helium and neon plasmas are also used to investigate the dependence of the plasma confinement on the ion mass. The base pressure is about 5×10^{-8} Torr. When the gun is fired, the pressure increases to about 1×10^{-5} Torr because of the released gas from the plasma gun. Microwave interferometers (3 cm and 8 mm) measure the plasma density integrated over the diagonal path through the magnetic axis shown in Fig. 1. Langmuir probes are used to measure the electron temperature and plasma density. Ion energies are measured using a gridded electrostatic probe. Plasma losses toward the wall are measured by limiters or particle collectors which are located at the stability limit. Losses to the current rings are measured by limiters located near the rings on the magnetic-field lines which are separated from the separatrix by the same amount of flux as the stability-limit line. Particle collectors are also mounted on all supports to measure the support losses.

The plasma density measured by the 3 cm microwave interferometer and the Langmuir probe positioned on the octopole axis is shown as a function of time in Fig. 2. Initially, the plasma density varies in inverse proportion to the time as seen from the 1/n vs time plot. The plasma loss in the high density regime is consistent with the classical diffusion as mentioned in Section I. After 0.5 sec from the injection time, the plasma decays exponentially with a time constant of 0.4-0.5 sec. The transition density is around 2×10^9 cm^{-3}. The electron temperature is about 0.5 eV for hydrogen, helium, and neon plasmas. The plasma loss to the support is about one-half of the total loss. The rest is equally divided between the ring limiters and the outside limiters.

III. RESIDUAL GAS EFFECT ON PLASMA CONFINEMENT

The confinement time is reduced when a gas is deliberately introduced into the vacuum chamber. The effect of the residual gas on the plasma confinement is evaluated by (a) measuring the partial pressures of the residual gas composition and (b) measuring the effectiveness of each gas species in reducing the confinement time.

(a) Measurement of Partial Pressures in the Vacuum Chamber

There is an indication that the composition of the residual gas changes during the process of pump down. The confinement time depends more on the pumping time than on the ionization gauge reading during the course of the initial pump down. It usually takes two days pumping and a pressure of 10^{-7} Torr before the confinement time settles down. However, after that the pressure may be allowed to rise again to 2×10^{-7} Torr with very little effect on the confinement time. A possible explanation is that the gas composition has changed during the process of outgassing.

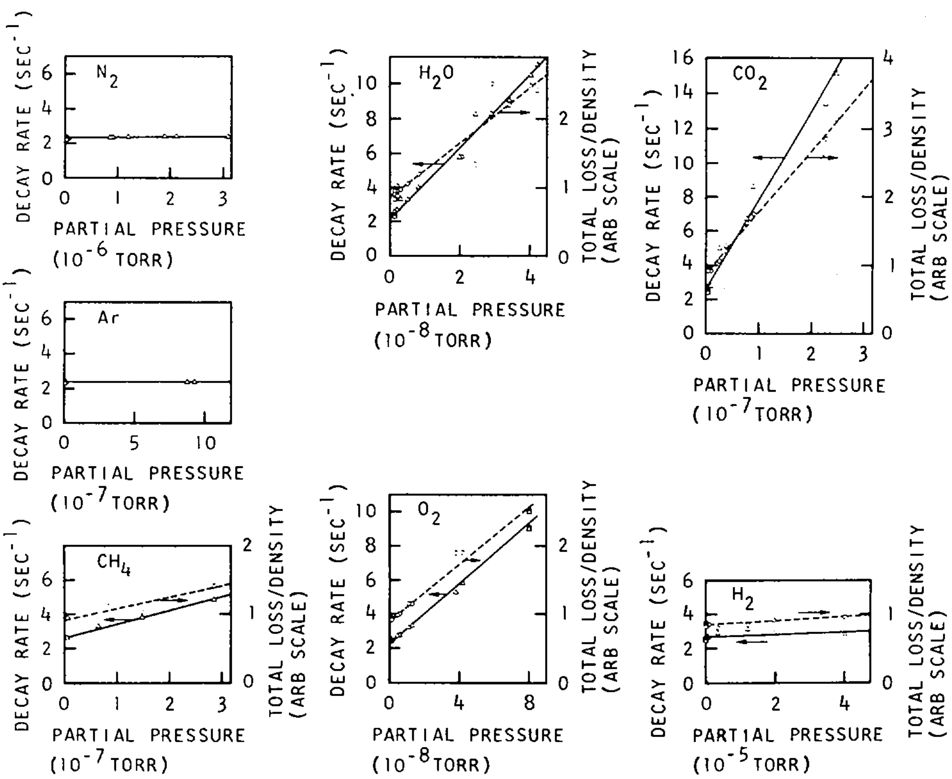

FIG.3. The decay rate and the normalized plasma loss of hydrogen plasma are shown as a function of the partial pressure of various gases. The gases are introduced externally into the vacuum chamber.

A bakeable mass spectrometer (Consolidated Electrodynamic 21-615) is installed on the vacuum chamber. Table I lists the detected gases in the first column, their possible sources in the second column, and their partial pressures in the third column. The measurement is made after two weeks of continuous pumping. The vacuum pressure measured by the ionization gauge is 7×10^{-8} Torr.

The dominant gases are nitrogen, argon, methane, and water. The hydrogen gas is from the plasma gun. The partial pressure rises almost linearly to the peak value of 1×10^{-5} Torr at 0.2 sec and then decays with a time constant of 1 sec. The hydrocarbon peaks between M = 30 and 50 do not fit any known pattern for diffusion pump oils and solvents. It suggests the conversion of hydrocarbons into hydrocarbons of lower mass on the clean titanium surfaces.

(b) Measurement of the Effect of Various Gases on the Plasma Confinement

The density decay rate and the total plasma loss are measured as a function of the partial pressure of each gas species. The density decay rate is measured at the density of about 2×10^{8} cm^{-3} by a Langmuir probe

TABLE I. RESIDUAL GASES FOUND IN THE dc OCTOPOLE DEVICE

Gas	Source(s)	Residual Partial Pressure (Torr)	Partial Pressure to reduce the confinement time by 2 (Torr)
N_2	Air leak, outgassing	2×10^{-8}	$\gg 3 \times 10^{-6}$
Ar	Air leak, not pumped by Ti surface	5×10^{-9}	$\gg 1 \times 10^{-6}$
CH_4(Methane)	Outgassing of epoxy, conversion of other hydrocarbons by Ti surface	5×10^{-9}	3×10^{-7}
H_2O	Outgassing of walls	2×10^{-9}	1×10^{-8}
C_2H_6(Ethane)	Outgassing of epoxy, mechanical pump oil fragment	1.5×10^{-9}	---
Other Hydrocarbons	Outgassing of epoxy, backstreaming of diffusion pump oil, mechanical pump oil fragments, cleaning solvents	$< 5 \times 10^{-10}$	---
O_2	Air leak, outgassing	2×10^{-10}	2×10^{-8}
CO_2	Air leak	$< 1 \times 10^{-10}$	5×10^{-8}
CO		$< 1 \times 10^{-9}$	---
H_2	Influx from the plasma gun	(peaks at 0.2 sec after the injection)	$\gg 4 \times 10^{-5}$

placed on the octopole axis. The total loss is measured by the ring and the outside limiter and the supports. Figure 3 shows the result for nitrogen, argon, methane, water, oxygen, carbon dioxide, and hydrogen. The decay rate is shown by full lines and the total loss by broken lines.

Table I lists in the fourth column the partial pressure at which the confinement time is reduced to one-half of the confinement time under normal conditions. By comparing the third column with the fourth it is seen that none of the residual gas species has a partial pressure high enough to account for the observed decay rate.

Figure 3 and also the fourth column of Table I show that the gases with oxygen in the molecular structure such as oxygen, carbon dioxide, and water are much more effective than nitrogen, hydrogen, argon, and methane. It should be noted that the presence of the gases increases the loss to the wall as well as the loss due to atomic processes.

The data available on the interactions between ions, electrons, and molecules are not extensive enough to evaluate all the processes which may be involved in the plasma loss processes. The molecular oxygen ions may be produced during the early stage of confinement by charge exchange $H^+ + O_2 \rightarrow H + O_2^+$. The cross section is large ($\sim 2 \times 10^{-15}$ cm^2) even at low energies [2]. The negative ions may also be produced at early time of the confinement $e + O_2 \rightarrow O^- + O$. The reaction rate[3] $\overline{\sigma v}$ is about 10^{-11} cm^3/sec at the electron temperature of a few eV. The recombination cross section of the oxygen ions is not well known. If however, the recombination rate of hydrogen ions[3] could be used as an indication, the reaction rate is small (10^{-12}-10^{-13} cm^3/sec). The mutual neutralization process $O^- + X^+ \rightarrow O + X$ is not known, although the reaction rate as high as 10^{-8} cm^3/sec is given as a rough theoretical estimate at the room temperature [3].

We have not been able to find a combination of these processes which may explain the experimental observations. The increase of the loss to the wall also remains unexplained.

IV. EFFECT OF THE ELECTROSTATIC POTENTIAL APPLIED TO THE PARTICLE COLLECTORS

The plasma confinement time is independent of the bias voltages on the limiters provided they are below 10 V. When the bias voltage is increased to above 50 V the confinement time is substantially reduced and the plasma loss to the limiters and the supports increases.

Figure 4 shows the confinement time as a function of the octopole field. The full line shows the case with small bias voltages (- 8V) and the broken line shows the case with large bias voltages (about - 50 V). In the latter case the confinement time τ is roughly proportional to the octopole field. It is observed that the boundary defined by the limiters becomes sharper with the larger bias voltage. As a result the density profile becomes narrower which may contribute to the reduction of the confinement time.

An azimuthal distribution of the density is measured near the supports. It showed the density has a step near the support. When the supports are positively biased, the density is higher on the upstream side in the direction of the electron ∇B drift. The step can be reversed or eliminated by changing the polarity of the bias voltage [4]. The plasma confinement is independent of the size or the polarity of the step. Since the elimination of the density step near the supports is not accompanied by the improvement in the plasma confinement, the plasma convection near the supports does not seem to be a major cause of plasma loss.

The loss process responsible for shortening the confinement time has not been identified. It could be either due to a large scale convection induced by the voltages on the limiters or due to the acceleration of the plasma loss by the magnetic field errors described in the following section.

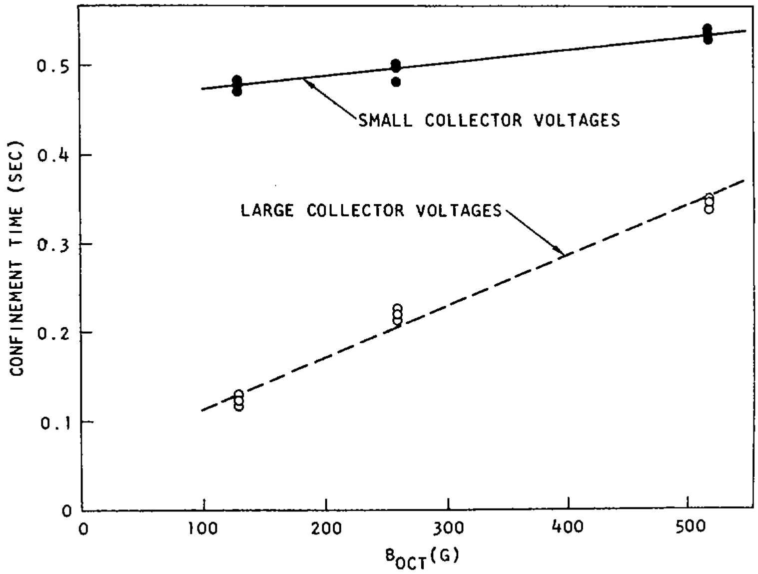

FIG.4. Confinement time of hydrogen plasma shown as a function of the octopole field. The full line is with large bias voltages on the particle collectors and the broken line is with small bias voltages on the particle collectors.

V. EFFECT OF THE FIELD ERRORS ON THE PLASMA CONFINEMENT

The experiment on the present effect is described in detail in a separate paper [5]. The experimental results are summarized and briefly discussed in this section.

(a) Scaling Law of the Plasma Confinement

The plasma confinement time τ in the dc octopole is studied as a function of the ion mass m_i, the electron temperature T_e, and the octopole field B_{OCT}. The experimental scaling law of the confinement time is $\tau \sim \sqrt{m_i/2kT_e}$ and is independent of the octopole field. The ion mass is varied by changing the species of gas supplied to the plasma gun. The electron temperature is raised by the electron cyclotron heating. This scaling suggests that the plasma loss is due to the plasma flow along the flux lines. Each flux line in the ideal toroidal octopole is closed on itself, however the presence of the field error makes them escape out of the confinement volume.

(b) Addition of External Error Field

In order to study the plasma behavior in the octopole field with field errors, the error field is applied externally. Two kinds of error field are used. One is the axisymmetric error field which is applied by varying the current of each internal ring from its preset value. The other is the axially asymmetric error field. It is produced by ten current loops placed on the median plane on the side wall of the vacuum chamber [6]. The direction of the axis of the current loops is radial and alternated from one loop to the next.

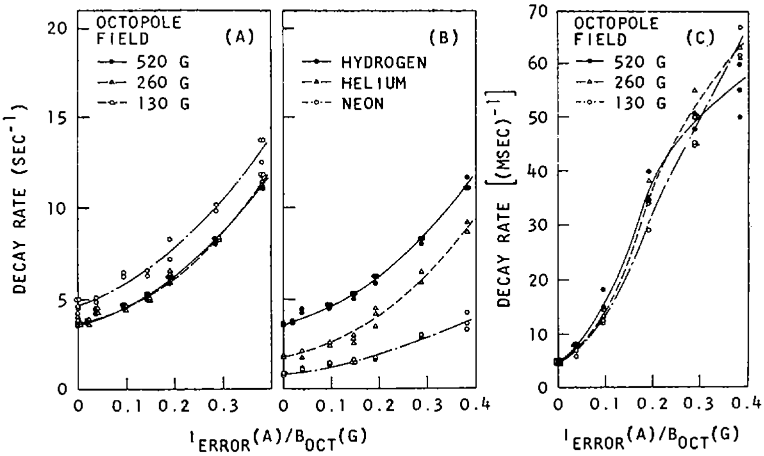

FIG.5. The decay rate shown as a function of I_{ERROR}/B_{OCT} (a) for hydrogen plasma with various values of the octopole field, (b) for various kinds of the plasma with the octopole field of 130 G, and (c) for the electrons with various values of the octopole field. I_{ERROR}/B_{OCT} = 0.4 A/G corresponds to about 1/4% of the error field.

It is observed that the axisymmetric error field is orders of magnitude less effective than the axially asymmetric error field in reducing the confinement time. This is quite reasonable since the axisymmetric error field still maintains the closure of the flux lines. In the following, experimental results are presented and discussed only for the effect of the axially asymmetric error field. The plasma confinement is studied by varying the aforementioned parameters m_i, T_e, B_{OCT}, and the error field B_{ERROR}. The behavior of electrons emitted from a hot filament is also studied and compared with the plasma behavior. The electron confinement experiment is designed so that the electron density is low enough to insure that an individual electron will trace the magnetic flux lines without plasma effects.

(c) Experimental Result

The density decay rate $1/\tau$ of the plasma shows the scaling given by

$$1/\tau = \sqrt{2kT_e m_i}\; f(I_{ERROR}/B_{OCT}) \qquad (1)$$

where f is a function determined by the magnetic configuration and independent of the magnetic field strength. The decay rates for various cases are shown in Fig. 5. In Fig. 5a, B_{OCT} is varied for the hydrogen plasma. In Fig. 5b the ion mass is varied for a fixed value of B_{OCT}. The relative size of the error field is varied in Fig. 5-c. The value of I_{ERROR}/B_{OCT} = 0.4 A/G corresponds to the rms spatial average error field $\langle B^2_{ERROR}\rangle^{\frac{1}{2}}$ of about 1/4% of B_{OCT}.

The decay rate $1/\tau$ for the electron confinement is shown as a function of I_{ERROR}/B_{OCT} in Fig. 5c. $1/\tau$ rises faster with I_{ERROR}/B_{OCT} than in the plasma case. However, the scaling law suggested by Eq. (1) holds approximately for both the plasma and the electron confinement. This

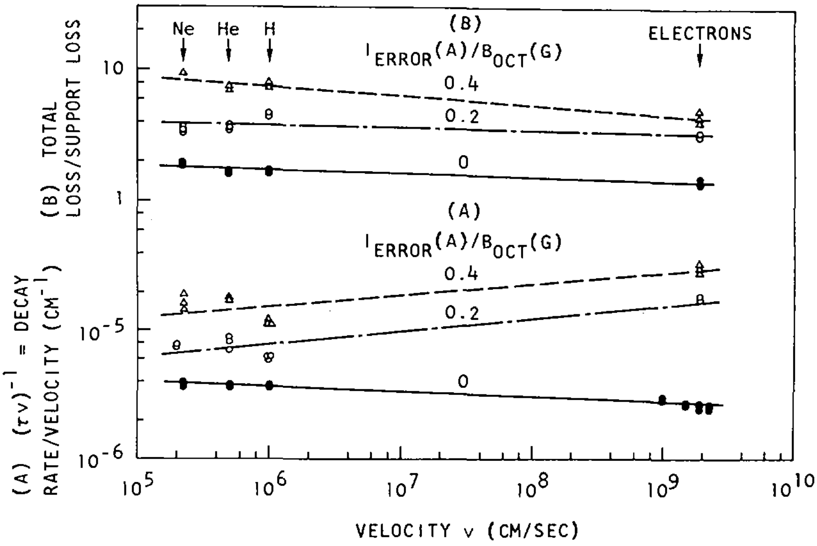

FIG.6. The characteristic length $(\tau v)^{-1}$ is shown as a function of v. v is the acoustic velocity for plasma and the kinetic velocity for electrons. τ is the confinement time.

is shown in Fig. 6. The reciprocal of the characteristic length $(\tau v)^{-1}$ is plotted as a function of v, where v is the acoustic velocity $\sqrt{2kT_e/m_i}$ for the plasma and $\sqrt{2E_e/m_e}$ for the electron experiments. The characteristic length is independent of v for over four orders of magnitude, both with and without the externally-applied error field.

The increase in the decay rate with I_{ERROR}/B_{OCT} is accompanied by an increase in the loss to the ring limiters and the outside limiter. The functional dependence on I_{ERROR}/B_{OCT} is quite similar to $f(I_{ERROR}/B_{OCT})$ shown in Fig. 5. In Fig. 6 the total loss flux normalized to the support loss is shown as a function of v. The dependence on v is very weak both with and without the externally-applied error field.

(d) Interpretation of the Experimental Result

Equation (1) suggests that the plasma and the electrons are lost by a flow along the flux lines. The characteristic length $1/f(I_{ERROR}/B_{OCT})$ is the average length of the flux lines, until they hit the walls or the supports. Since the field configuration is determined by the ratio of B_{ERROR} to B_{OCT}, the line length depends only on I_{ERROR}/B_{OCT}. The loss to the supports is proportional to nv. Therefore, the fact that the ratio of the loss to the wall and to the supports is independent of v with a given magnetic configuration supports the above interpretation.

A quantitative comparison is made by calculating the confined length of flux lines. The calculation is based on a simplified model assuming a single internal ring instead of four. The calculation shows that when the error field is applied by external current loops the flux line length is approximately 4×10^4 cm for $I_{ERROR}/B_{OCT} = 0.4$ A/G. The experimental value is about 10^5 cm. The agreement is good when we consider the crudeness of the model used in the calculation.

The length of flux lines in the absence of the externally-applied field errors is also estimated from the magnetic field measurement. There are two possible sources of the residual field errors. One is the imperfection in the winding of the internal rings, and the other is the magnetization of the building structures. The center of the ampere turns of the ring may deviate from the perfect circle. If the deviation is a helical displacement or a sinusoidal displacement, the flux line does not spiral out. This is because the radial component of the error field averages out on a zero-th order flux line. One of the simplest deviations which lead to the spiralling flux lines is a composite helix which winds and unwinds periodically. We write the trace of the center of the ampere turns as $r = r_s$ and $\theta = \theta_0 \cos kz$, where r_s is the radius of the helix and z is taken in the direction of the ring current. The calculation shows that the line length is about $2\,|\,r_2-r_1\,|\,/\theta_0 k^2 r_s^2$, where r_1 and r_2 are the r-coordinates of the ends of the flux lines. The values for r_s, θ_0, and k may be found from the measurements of the magnetic field. The length is 10^5 cm for a typical set of parameters. This value is somewhat smaller than the experimental value of 8×10^5 cm calculated from the confinement time. The agreement is fair when we consider the crude model used in the calculation.

The decay rate $1/\tau$ increases linearly with I_{ERROR}/B_{OCT} at large values as expected from the simple calculation. At the low values however, the decay rate $1/\tau$ increases slowly with the error field. This can be interpreted as an interference effect between two modes with different values of k.

VI. SUMMARY

The plasma confinement at a low plasma density in the dc octopole device is studied by varying the plasma and the machine parameters.

The measurement of the plasma confinement in the presence of various gases shows that the oxygen-containing gas in the range of 10^{-8} Torr in the partial pressure affects the plasma confinement by increasing the loss to the walls and possibly through recombination process. However, this type of loss is too small to account for the observed plasma loss under the standard operating conditions. The existence of the support does not affect the plasma confinement any more than by collecting particles on their surface. The convective motion near the supports is not the main cause of the plasma loss.

The dependence of the confinement time on the ion mass, the electron temperature, the octopole field, and the error field indicates that the plasma is lost by a flow along the flux lines. The flux lines connect the plasma region and the wall because of the presence of inherent or applied error fields. The confinement time estimated from the magnetic field measurement is consistent with the experimentally observed value.

REFERENCES

[1] OHKAWA, T., et al., Phys. Rev. Letters 24 3 (1970) 95.

[2] FLEISCHMANN, H. H., YOUNG, R. A., and McGOWAN, W., Phys. Rev. 153 (1967) 19.

[3] McDANIEL, E. W., "Collision Phenomena in Ionized Gases" (John Wiley and Sons, Inc., New York 1964).

[4] SCHMIDT, J. A. and SCHMIDT, G. L., Bull. Am. Phys. Soc. 13 11 (1968) 1526.

[5] YOSHIKAWA, M., et al., "Effect on Field Errors on the Plasma Confinement in the dc Octopole," to be published.

[6] YOSHIKAWA, M., et al., Bull. Am. Phys. Soc. 15 11 (1970) 1454.

DISCUSSION

A.N. DELLIS: During the initial classical decay regime, is the observed density gradient sufficiently strong to predict classical diffusion at the observed time scale?

T. OHKAWA: The diffusion coefficients are calculated from the measured density gradients at every point on the density profile. Their values agree with the classical formula within the limits of experimental error.

B. COPPI: How do you interpret the apparent absence of bounce frequency effects on transport in your experiments?

T. OHKAWA: The anomalous diffusion in the average well region is regarded as collisional diffusion due to orbit spread caused by a slight asymmetry. The normal part, in the absence of a toroidal magnetic field, fits the classical formula within the limits of experimental error. The addition of toroidal fields does not change the diffusion rate. We have not been able to explain the fact that the plasma does not recognize the presence of a toroidal field or the bounce frequency.

CONFINEMENT OF PLASMAS IN THE SPHERATOR

R. FREEMAN*, M. OKABAYASHI, G. PACHER, B. RIPIN,
J.A. SCHMIDT, J. SINNIS, S. YOSHIKAWA
Princeton University Plasma Physics Laboratory,
Princeton, New Jersey, United States of America

Abstract

CONFINEMENT OF PLASMAS IN THE SPHERATOR.

A spherator with levitated superconducting ring (LSP) went into operation in 1970. The ring has a current of 85 kA and can be levitated for periods up to two hours by means of magnetic feedback stabilization. Plasmas were formed by application of several resonant and non-resonant microwave heating methods as well as ohmic heating. Gases used were H_2, D_2, He, and A with filling pressures 1×10^{-6} - 2×10^{-5} Torr.

The electron temperature decays from 10 eV to 0.2 in the afterglow produced by electron cyclotron heating due to charge exchange and ion-electron coupling. Plasma confinement times of 100 - 300 ms were obtained under the best conditions in the density range 10^{10} - 10^{11} cm^{-3}. The observed confinement times are approximately 1/4 to 1/6 of classical confinement times calculated numerically, which indicates that an additional loss mechanism may still persist. This additional loss may be due to magnetic field errors or residual plasma density inhomogeneities in the form of fluctuations and convective cells. The good plasma confinement can be spoiled by the application of magnetic field perturbations of several per cent of the confining field strength. It was also found that the plasma confinement times are very sensitively dependent on impurity concentration. The impurity effect is attributed to ion-impurity molecule charge exchange followed by dissociative electron recombination.

High-energy electrons in the energy range of 5 keV to 300 keV can be produced by electron cyclotron heating (ECH) and trapped for several seconds at low background neutral pressures. Ionization by runaway electrons, if any, does not affect the confinement measurement in normal afterglows.

Plasma can also be ohmically heated by electric fields in the poloidal direction. The resulting plasma has a density of $2 - 5 \times 10^{12}$ cm^{-3} with an initial electron temperature of 30 - 100 eV. The plasma density decay time measured immediately after the ohmic heating pulse is approximately 25 ms. The current penetration indicates that a mild anomalous skin effect exists.

Evidence is also presented which indicates that a trapped-particle instability can be present when the magnetic fields are adjusted so that trapped particles are located in bad curvature regions.

I. INTRODUCTION

The original multipole[1] experiments [1, 2, 3, 4] demonstrated that a quiescent plasma could be contained in an internal ring device. However, due to the ring supports [5, 6] and magnetic field inhomogeneities [7] a sizeable anomalous loss was observed. In some multipole experiments [8] this anomalous loss was shown to scale with magnetic field (B) and electron temperature (T_e) like the well-known Bohm loss [9] ($\Gamma \propto T_e/B$) even though the magnitude was the order of ten less than Bohm's prediction. Improved multipoles with smaller supports and greater magnetic symmetry showed confinement that was greatly improved ($\tau \sim 300\ \tau_B$) as well as plasma parameters under which the confinement had a classical behavior [10].

---

* Present address: Culham Laboratory, Abingdon, Berks, United Kingdom.

1 Including levitrons and spherators.

A series of experiments conducted in the supported spherator have shown that the anomalous particle loss across the magnetic field exists. It is inferred that this loss is produced by the convective cells generated by supports. The results of these experiments will be discussed in Section 3.

The experiments in the levitated spherator were designed to eliminate this cause of anomalous loss mechanism, thereby increasing the confinement time to find the next limiting factor in plasma confinement. The results of these experiments at low electron temperatures ($0.1 < T_e < 10$ eV) will be discussed in Section 4. The effect of adding magnetic field errors to the spherator has been measured and will be discussed in Section 5. The results of experiments employing ohmic heating to reach moderate electron temperatures ($10 < T_e < 100$ eV) will be discussed in Section 6. The production and containment of high energy electrons (1 keV $< T_e <$ 300 keV) will be described in Section 7. Fluctuations are observed with certain magnetic field configurations. These fluctuations are associated with mirror trapping of particles and will be described in Section 8.

2. EXPERIMENTAL ARRANGEMENT

2.1 Description of device

The final version of the supported spherator (SP-3) and the levitated spherator (LSP) are quite similar. Both have a superconducting ring of 46 cm major radius and 9 cm minor radius. In the supported version the ring is supported with three 4mm upper supports and three 1mm lower supports. In the levitated version the ring is filled with liquid helium and vented through two spears which are withdrawn from the plasma volume before the experiment. The ring is levitated by a force from a coil which is situated under the vacuum vessel as shown in Fig. 1.

A toroidal field (TF) is produced by currents passing down the vertical axis of the vacuum vessel. A vertical externally-produced magnetic field (EF) is generated by a set of coils with their axes aligned vertically. The levitated ring is unstable in the external fields and must be stabilized by a set of coils situated near the wall of the vacuum vessel. The current in these coils is controlled by sensing heads which emit and detect light beams passing over the surface of the ring to determine the ring position. [11] Two stabilization systems have been employed in the LSP. The stabilizing magnetic fields of the first were excited by 3-phase, 60-cycle ac power, causing magnetic perturbations as high as 100 gauss (10% of the main confining field). To avoid these excessive perturbations during the experiment, a gating (blanking) period, to cut off this stabilizing field for up to 40 milliseconds, is used during the plasma production and the study of the subsequent plasma afterglow. The first stabilization system was replaced by one using dc power to excite the stabilization coils. The magnetic perturbations due to the second stabilization system are typically less than 0.5% of the confining field.

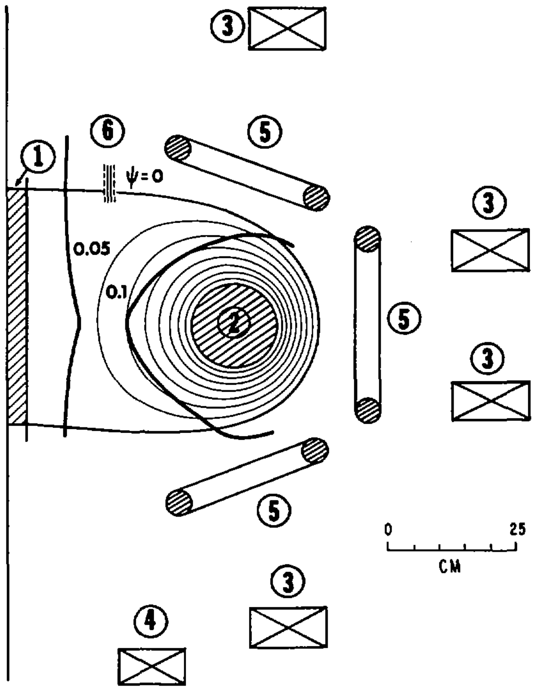

FIG.1. Cross-sectional view of the levitated spherator: (1) TF coil, (2) levitated superconducting ring, (3) external coils, (4) coil for levitating the ring, (5) stabilizing field coils, and (6) limiter. The poloidal flux surfaces (ψ) are shown along with the surfaces of electron cyclotron resonance at 2.45 GHz.

TABLE I. PARAMETERS

Magnetic field strength (B)	~ 1 kG
Ring current I_P	85 kAt
I_T/I_P	0.5 - 0.6
Background pressure	1×10^{-7} Torr
Neutral gas density	$0.5 - 2 \times 10^{11}$ cc^{-1}
Filling gases	H_2, D_2, He, A
Plasma density	$(1\text{-}30) \times 10^{11}$ cc^{-1}
Electron temperature (T_e)	(0.1 - 100) eV
Plasma volume	2×10^5 cc
$\tau_B(T_e = 1$ eV)(Bohm time)	2.9 msec
$\tau_c(T_e = 1$ eV, $n = 2 \times 10^{11}$)	600 msec

2.2 Plasma production and heating

The parameters typical of the spherator experiments to be described are shown in Table I. Plasma production was accomplished with Electron Cyclotron Heating (ECH) to reach temperatures of 10 eV and densities of $2 \times 10^{11} cc^{-1}$. Frequencies at which resonance occurs in the plasma volume fall roughly between 2 - 4 GHz. The afterglow of the ECH produced plasma cooled rapidly ($\tau_E \sim$ 10 msec) due to electron ion coupling and ion neutral charge exchange. Electron Nonresonant Heating (NRH) was used ($f \sim$ 5 GHz) to maintain a uniform electron temperature across the plasma. A list of the microwave power sources is given in Table II. Ohmic heating (OH) was used to increase the electron temperatures and densities above the level obtained with microwave heating. The power available for OH was very much greater than for ECH although the OH efficiency was poor. The OH power sources are also listed in Table II.

TABLE II. PLASMA HEATING

Type	Frequency	Mode	Power
ECH	2.45 GHz	Pulsed	100-1000 W
NRH	5.6 GHz	Pulsed, CW	50-400 W
ECH	3.5 GHz	Pulsed, CW	5 - 70 W
NRH	18 GHz	Pulsed	1 - 5 kW
OH	200 KHz	Pulsed	1 kW
OH	10 kHz	Pulsed	2 kW
OH	1 kHz	Pulsed	~ 1 MW

2.3 Diagnostics

In Table III are listed the most important diagnostics used during the experiments. Two 4 mm microwave interferometers were used, one with a beam path passing outside the levitated ring, the other passing inside the ring. A 24 segment axisymmetric limiter was used in the supported spherator and an 18 segment limiter in the levitated spherator. Each segment was a pair of plates which could be biased independently. A single metal screen was placed on each side of the set of segments and biased independently. The loss to the supported ring was measured and found to be small compared to the outward loss. The loss to the levitated ring was not measured.

TABLE III. DIAGNOSTICS

(i)	Interferometer: density and decay rate.
(ii)	Probes: temperature, density distribution, floating potential and fluctuations.
(iii)	Loss detectors: decay rate.
(iv)	Spectroscopy: temperature, recombination, and impurities.
(v)	For high energy electron diagnostics, see Table IV.

3. CONVECTIVE CELLS IN THE SUPPORTED SPHERATOR

The spherator has strong magnetic field properties for stabilizing the plasma and, as previously reported, low frequency fluctuations were successfully stabilized. However, in the supported spherator even after the elimination of low frequency fluctuations an anomalous plasma loss across the magnetic field still exists. [4, 12]

The parametric investigation of the confinement time in the supported version revealed two distinct properties of plasma confinement. First, as shown in Fig. 2a the ratio of the flux of particle loss across the magnetic field, $\Gamma_\perp$, to the flux of particle-loss to the supports, Γ_s, decreased with a decrease of the neutral pressure [5, 13]. Second, the confinement time is increased proportional to the inverse of the sound velocity as shown in Fig. 2b [4].

To explain these results the following hypothesis was introduced: the ion-neutral collisions cause a density gradient to develop along the magnetic field lines which pass through the supports, resulting in density inhomogeneities which lead to particle transport across the magnetic surfaces. Following this model the particle loss across the magnetic field $\Gamma_\perp$ and the confinement time were calculated. The result of the theoretical calculation of $\Gamma_\perp/\Gamma_s$ is shown by solid line in Fig. 2a. In Fig. 2b, the estimate for the plasma confinement time was plotted for two extreme cases due to the ambiguity of the inhomogeneity caused by the supports. The results of the calculation are in good agreement with the anomalous loss rate observed in the supported version of the spherator.

In order to study experimentally the nonuniformity due to the presence of the supports, the azimuthal distribution of plasma loss across the magnetic field was measured by using an axially-symmetric, 24-segmented limiter [14]. Figure 3a shows the azimuthal loss distribution plotted in polar coordinates. The three large peaks in the loss distribution are separated by approximately 120°, the same periodicity as the upper and lower mechanical supports. The maxima appear between the supports due

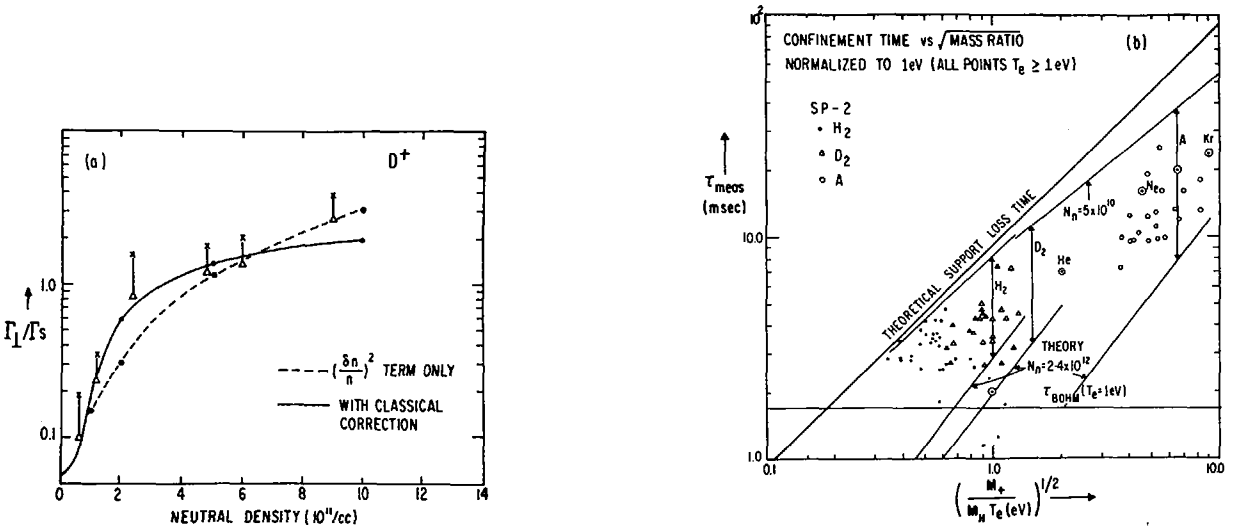

FIG. 2. (a) $\Gamma_\perp/\Gamma_s$ versus neutral density for a deuterium microwave-discharge plasma. (b) Confinement time, τ_{meas} versus $(M_+/M_H T_e)^{1/2}$ for the supported spherator (M_+ is the ion mass and M_H is the hydrogen mass). The plasma confinement times were estimated assuming that convective cells were present due to the supports.

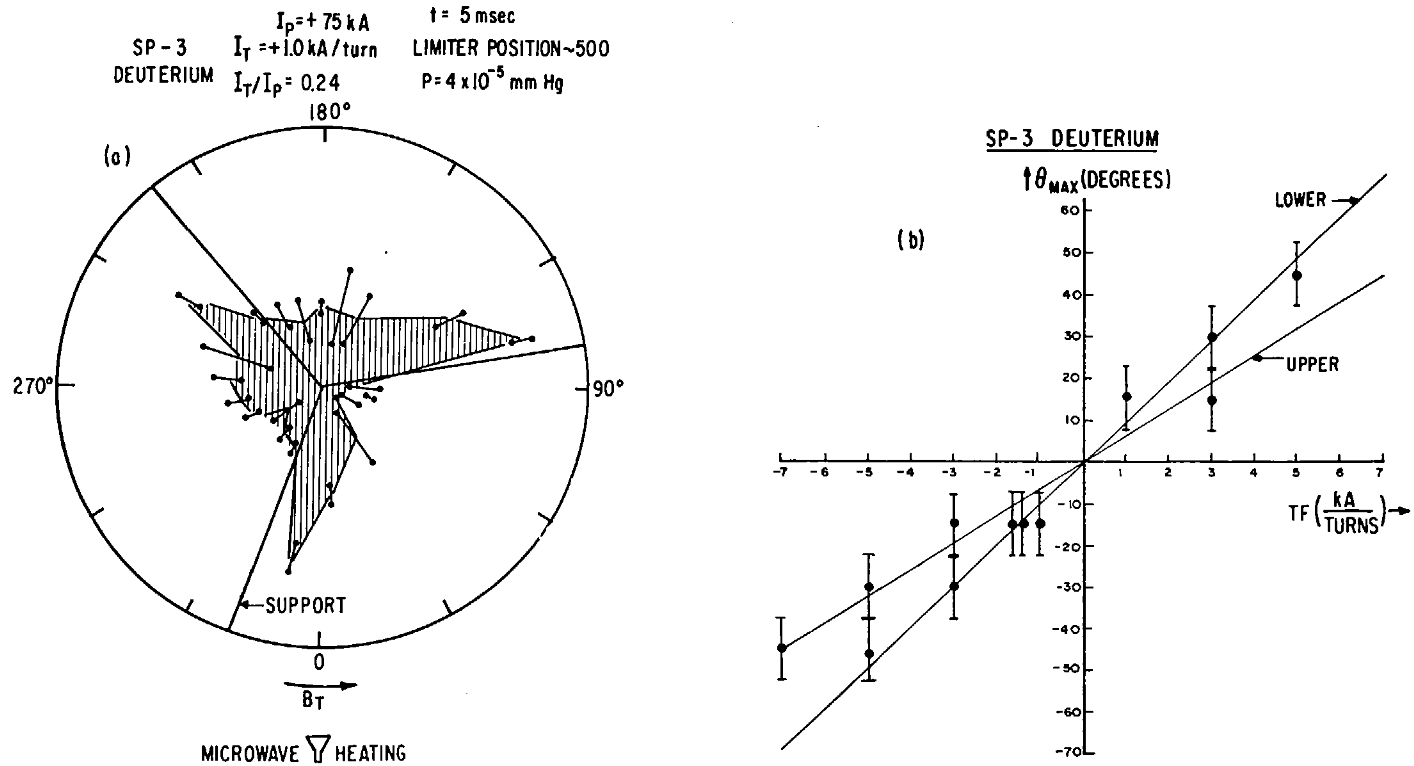

FIG.3. (a) Azimuthal distribution of plasma loss. The azimuthal locations of the mechanical supports for the ring are shown by the solid lines. The upper and lower supports are located at the same azimuth. The shift of maxima is due to the rotational transform. (b) Position of plasma loss maxima versus toroidal field strength. The solid lines are the theoretical projection of the supports (upper and lower) along a magnetic field line to the limiter position.

to the relatively high rotational transform for this toroidal field strength. The angle, Θ_{max} which is the angle between a maximum of plasma loss and the closest support, is plotted versus the toroidal field coil current in Fig. 3 b. The solid lines, labeled upper and lower, indicate the shift expected by following along a field line from the upper and lower support locations to the limiter position. The results are in a good agreement with the calculated line within the 15° resolution of the measurement.

4. CONFINEMENT PROPERTIES IN THE LEVITATED SPHERATOR (T_e < 10 eV)

As discussed in the previous section an hypothesis (convective cells due to the existence of supports) was introduced to explain the observed anomalous loss mechanism. The levitated ring experiments are of great interest due to the elimination of the convective cells as well as the direct loss to the supports.

Since the levitated version has a magnetic field configuration similar to that of the supported version, the comparison of the experimental results between the supported version and the levitated version should demonstrate the effect of the obstacles located in the plasma confinement regime on the confinement time. The drastic difference between the plasma confinement properties for both versions is shown in Fig. 4. These experiments were performed using approximately the same parameters: magnetic field strength, deuterium gas filling pressure and 500 W of electron cyclotron heating. The plasma confinement time is increased from 20 msec in the supported version to 100-150 msec in the levitated version. It should also be

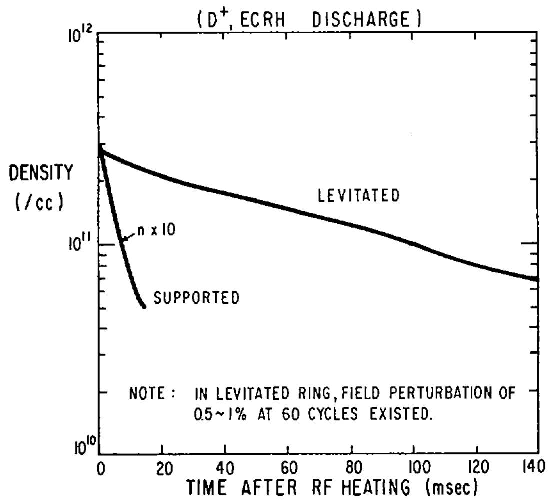

FIG.4. Comparison of confinement times between the supported version and the levitated version. Both experiments were performed with approximately the same parameters.

noticed that the initial plasma density for the levitated version was increased by a factor of 10 compared with that of the supported version due to the longer energy confinement time during the microwave heating.

In order to investigate whether there still exists any anomalous plasma loss mechanism after the elimination of the cause of the convective cells, the confinement properties were studied by varying the plasma density and the electron temperature. The combination of several methods of plasma heating, listed in Table II, especially nonresonant heating, provides the relatively wide range of plasma density, n_e, (2×10^{12} - $5 \times 10^{10}\,cc^{-1}$) and electron temperature, T_e, (10 - 0.1 eV) with a long temperature decay time. Figure 5 shows the reduction of plasma loss produced by increasing the electron temperature with nonresonant heating. Without nonresonant heating the electron temperature decays quickly from 7 eV to 0.6 eV and the loss rate increased within 10 - 20 msec. On the other hand with nonresonant heating the electron temperature stays at 1.0 - 0.8 eV and the loss rate is slower. The plasma loss rate increases 3 - 5 msec after the termination of nonresonant heating. One possible explanation for the reduced loss at higher electron temperature is the stabilization of

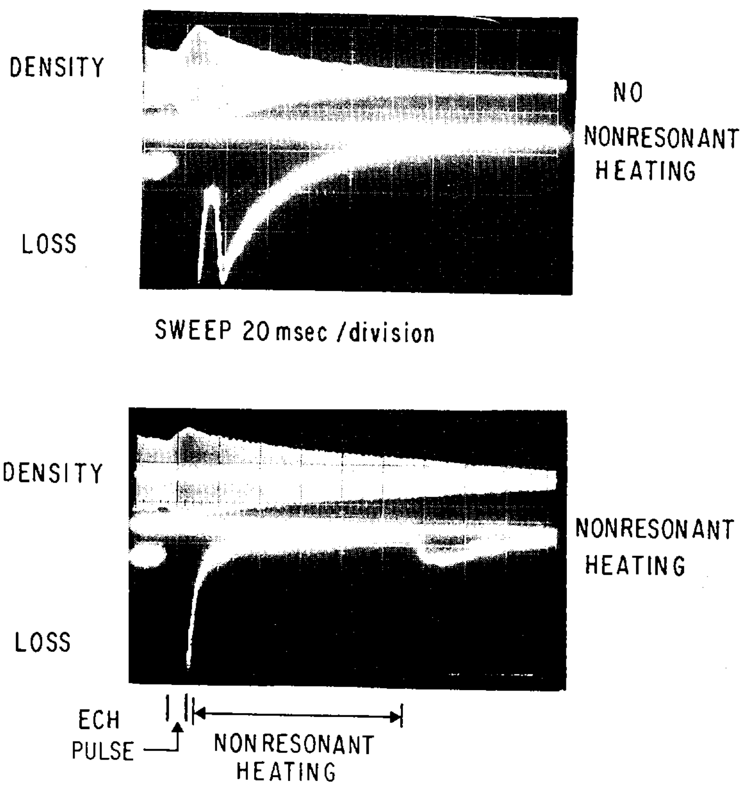

FIG.5. The effect of heating on plasma loss. The non-resonant heating reduces the measured plasma decay time and loss. The loss increases shortly after the heating is removed.

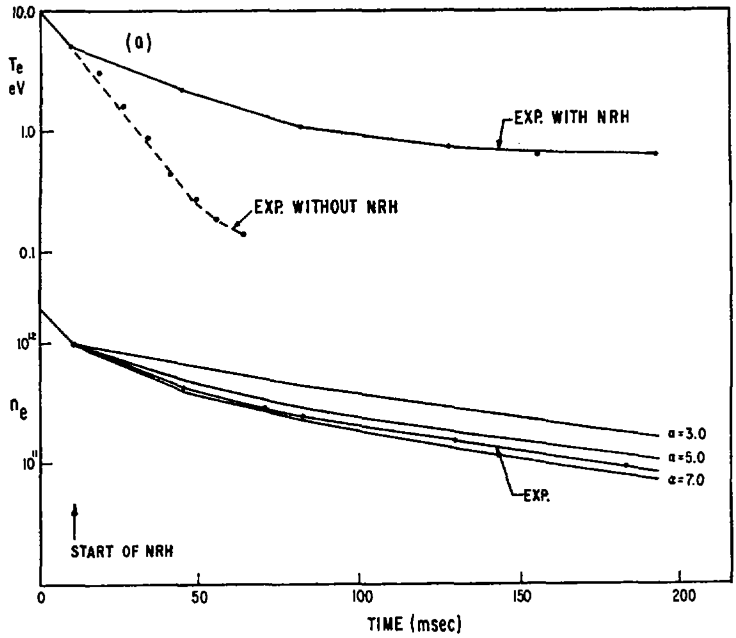

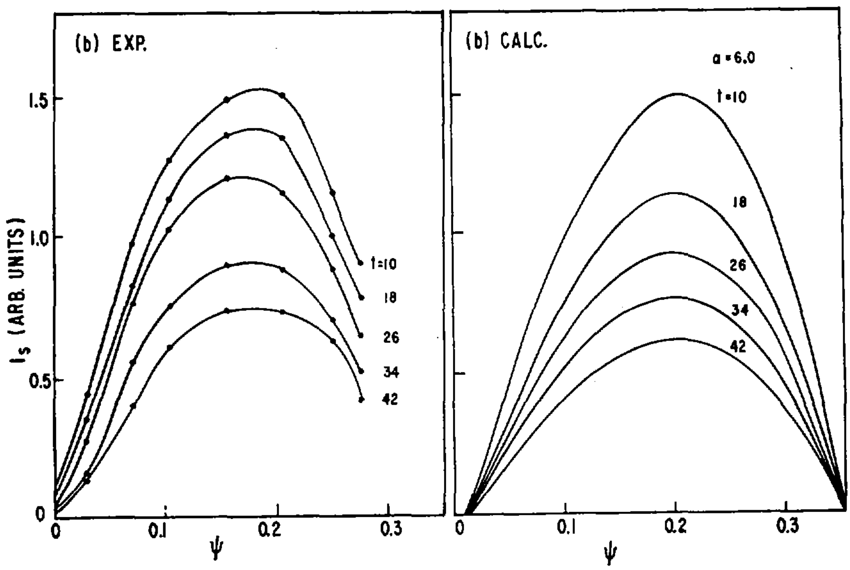

FIG. 6. (a) The comparison of measured density decay and the density decay calculated assuming electron-ion collisions. (b) The comparison of the time sequence of the measured ion saturation current profile, I_s, with that calculated, time in milliseconds is the parameter.

resistive drift instability [15]. Alternatively, if the loss is determined by a diffusion process which decreases as the electron temperature increases, as in the classical diffusion, this behavior is to be expected. More discussions on this will be given later.

Figure 6 shows the experimental results obtained with the combination of ohmic heating discharge (1 kHz and 20 kA) and nonresonant heating (5.6 GHz and 200 W). Nonresonant heating increased the electron temperature decay time from 20 msec to 70-100 msec. The ion saturation current profile decays uniformly during the nonresonant heating, which indicates that the density profile is close to the fundamental mode. The confinement time is 100-120 msec at $n_e = 2 \times 10^{11} cc^{-1}$ and $T_e \sim 1$ eV. It is also possible to estimate the confinement time from the measured loss rates by the formula

$$\tau_\perp = \frac{\int n dV}{\Gamma_\perp}$$

where $\int dV$ is the integral over the plasma volume. The density decay time calculated from the loss rate is 100-150 msec, which is in good agreement with those measured with the microwave interferometer. Ionization due to the nonresonant heating was monitored by measuring the neutral helium excitation line (5876 Å). The absolute intensity of this line showed the electron temperature, the same as that measured by a Langmuir probe within a factor of 1.5. These results eliminate the possible effect of ionization due to the nonresonant heating.

The confinement times at various electron temperatures at the fixed plasma density ($n_e \sim 2 \times 10^{11} cc^{-1}$) were obtained by several methods of heating:

(1) In the afterglow plasma produced by ohmic heating (1 kHz and 20 kA) the confinement time is 50-60 msec at $n_e \sim 2 \times 10^{11} cc^{-1}$ and $T_e \sim 0.1$ eV.

(2) Ohmic heating with 100W at 10 kHz gives a confinement time of 70-80 msec at $T_e = 0.5$ eV and $n_e \sim 1 - 2 \times 10^{11} cc^{-1}$.

(3) Low power microwave resonant heating with 3.5 GHz ($\sim$ 100 W) yields a 100-120 msec confinement time at $T_e \sim$ 1-2 eV and $n_e \sim 2 \times 10^{11} cc^{-1}$.

(4) A nonresonantly heated steady state discharge shows 130-170 msec at $n_e \sim 2 \times 10^{11} cc^{-1}$ and T_e = 4-5 eV.

(5) The afterglow plasma produced by ECH (500 W and 2.5 GHz) decays with a time constant of 100-150 msec at $n \sim 2 \times 10^{11} cc^{-1}$ and $T_e \sim 1$ eV.

It is necessary to be cautious about the possibility of ionization due to the presence of high-energy electrons in the case of an ECH produced plasma with 500 W. The electron temperature decay is somewhat slower than would be expected from the electron-ion cooling and the subsequent ion-neutral cooling via charge exchange, which indicates that the high-energy (runaway) electrons were feeding energy to the plasma electrons. The estimate of the energy and density of the hot electrons in the confinement region was performed by measuring the soft x-rays, hard x-rays and synchrotron radiation. As will be discussed in Section 7 the correction for the confinement time is less than 10%.

In Fig. 7 the observed confinement times as a function of electron temperature are summarized at $n_e \sim 1\text{-}2 \times 10^{11} cc^{-1}$. The plasma confinement time appears to be increased proportional to the square root of the electron temperature, which is the same dependence as the classical collisional process. However, the observed decay times are smaller by a factor of 5-6 than that calculated for the classical decay process.

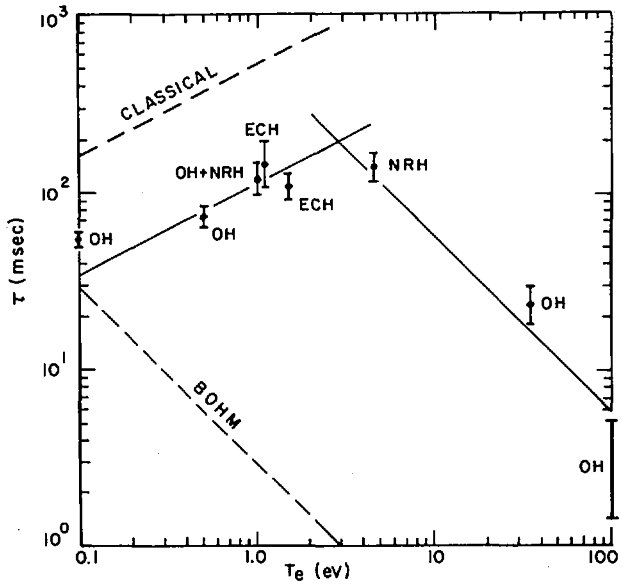

FIG. 7. Measured confinement time versus electron temperature ($n_e \sim 2 \times 10^{11}$ cm^{-1}). The dashed lines are the Bohm (τ_B) and classical (τ_{cl}) containment times. The solid lines are 200 τ_B and $\tau_{cl}/5$. The confinement times for electron temperatures above 5 eV were obtained during (100 eV) and slightly after (at 30 - 40 eV) ohmic heating. The loss during ohmic heating appeared to be increased owing to turbulence and ohmic-heating-produced field errors.

Since the observed confinement time shows a square root dependence on the electron temperature, it is of interest to compare the experimental time sequence of density decay and density profile with those for classical decay process. The calculation was performed using the measured electron temperature decay, the real magnetic field configuration and the diffusion coefficient given in Ref. [16]. The numerical calculation was done for the fundamental mode with the assumption that the electron temperature and plasma density have the same spatial dependence. The classical confinement time, τ_{cl}, including the Pfirsch-Schlüter factor is about 600 msec at T_e = 1 eV and $n_e = 2 \times 10^{11} cc^{-1}$. The neoclassical diffusion process would not change this value more than 8%, since the calculated value, τ_p, with the poloidal field only is 0.92 τ_{cl}. (The neoclassical confinement time would be between τ_p and τ_{cl}.) Without the Pfirsch-Schlüter factor the confinement time is 1.02 τ_{cl}. The reason for the minor differences between the confinement time with different diffusion coefficients is due to the small ratio of the toroidal current to the poloidal current (0.54). The comparison of the measured density decay with these calculations are shown in Fig. 6. α is the anomalous factor compared with the classical diffusion coefficient. The observed density decay agrees reasonably well with that calculated with an anomalous factor of 5-6. Also, the change of the observed ion saturation current profile agrees well with that calculated for an anomalous factor of 6.

The magnetic field strength dependence was not investigated due to the technical difficulty of stabilizing the levitated ring for various magnetic field configurations. However, from the above results, the empirical diffusion coefficient may be given by

$$D = \alpha D_{cl} , \qquad \alpha \sim 6$$

This expression is consistent with the pseudoclassical diffusion coefficient [17], $D = 5\ D_{pcl}$ (D_{pcl} is the classical diffusion coefficient determined only by the poloidal field strength), since as discussed above, D_{cl} is approximately D_{pcl}.

Radiation and three body recombinations were ruled out as a possible cause of the anomalous plasma loss by measuring the absolute intensity of several neutral excitation lines. The measurement showed these recombination rates slower than the plasma decay rate by at least a factor of 10. However, the confinement time has a dependence on the background pressure (mainly H_2O) in the range of 10^{-7} - 5×10^{-6}Torr, indicating that some atomic or molecular process (e.g., molecular recombinations) may be responsible for the remaining nonclassical behavior. The presence of convective cells as observed in the supported version is unlikely since the confinement times did not show any noticeable dependence on the ion mass for a change by a factor of 40. The asymmetric field caused by the misalignment of coils or the excitation of the ring stabilizing field can cause another type of loss mechanism, which will be discussed in Section 5.

Another possible cause is that in our experimental parameter range, the Debye length is comparable to the electron Larmor radius so that the simple binary collisional analysis may no longer be justified. Thus, some enhancement factor proportional to ω_{ce}/ω_{pe} might be necessary.

5. EFFECT OF MAGNETIC FIELD ERROR

The investigation of magnetic field errors was carried out in both the supported and the levitated spherator. Figure 8 shows numerical calculations of the distorted magnetic surfaces caused by the existence of an additional horizontal magnetic field with a strength of 2 gauss ($\sim$ 0.2% of the main magnetic field). In the immediate vicinity of the separatrix; i.e., ψ = 0, field lines become ergodic, that is, there no longer exists magnetic surfaces and field lines fill three dimensional space. This domain widens with the increasing horizontal field. However, away from the separatrix closed surfaces exist. In this region magnetic islands appear as in Fig. 8 and field lines do not spiral out.

An additional horizontal magnetic field with appropriate strength and direction can compensate some types of field errors; for example, those due to the relative tilt of the external field coil and the poloidal center ring. As shown in Fig. 9 the initial asymmetry of the plasma loss caused by a misalignment of the magnetic field coils disappeared when cancelled by a 5 gauss horizontal magnetic field (done in the supported spherator SP-2) however, the total particle loss,

$$\Gamma_{\perp} = \int_{0}^{2\pi} \gamma d\theta$$

was not changed, which indicates that the confinement time was insensitive to 0.2-0.5% field errors in the afterglow plasma [18].

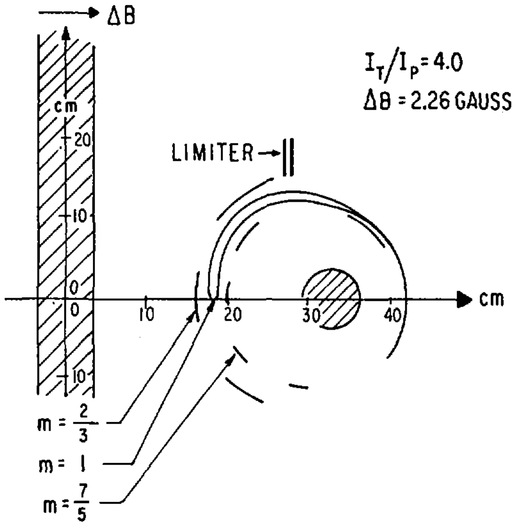

FIG.8. The distortion of magnetic surface due to an additional horizontal magnetic field of 2 G. The magnetic field islands appear at m = 2/3, 1, 7/5 (m is the rotational transform divided by 2π) for the SP-2 spherator.

In the levitated spherator an ac stabilizing magnetic field error was produced by exciting current in the ring stabilizing coils, 40 msec after the plasma production. The loss produced by this magnetic field error increased as shown in Fig. 10.

In the levitated spherator with a dc stabilizing field a magnetic field error was introduced purposely by superimposing a pulsed current on the stabilizing currents. The confinement time appears to decrease by 20-30% with a 0.5-1.0% magnetic field error in the case of a steady state discharge ($T_e >$ 5 eV). In the afterglow plasma ($T_e <$ 3 eV) the confinement time was insensitive to the existence of the magnetic field perturbations.

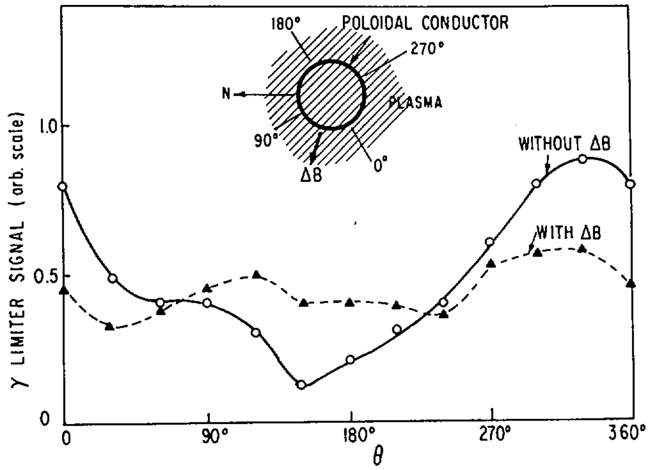

FIG. 9. The azimuthal loss distribution γ with and without an additional horizontal magnetic field.

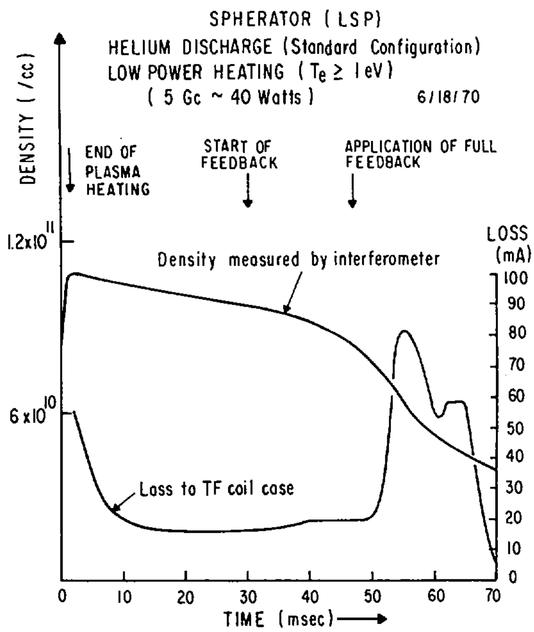

FIG. 10. The density and loss rate versus time with 5 ~ 10% magnetic field perturbations for the levitated spherator. The perturbing magnetic field was introduced 40 ms after the main heating was turned off. The density decay time was reduced from 120 ~ 150 ms to 40 ~ 50 ms owing to the magnetic field error.

From these results it may be concluded that higher temperature and larger magnetic field errors increase the plasma loss rate, although we need more data to determine whether this dependence is due to destruction of the outer magnetic surfaces or change of the diffusion coefficient. The confinement measurements discussed in Section 4 are not effected since the electron temperature is relatively low and the magnetic field perturbation is less than 0.5%.

6. OHMIC HEATING

The power absorbed in the plasma during microwave heating was found insufficient to raise the bulk of the electrons to a temperature greater than 10 eV. Ohmic heating was employed in the spherator because of its simplicity and proven capability of delivering high power to the electrons. The objectives of the ohmic heating experiments were threefold. The first objective was the production of higher electron temperature and the containment studies associated with these temperatures. The second objective was the determination of the effect of turbulence on the magnetic field penetration into the plasma. The third objective was to determine whether the plasma can be contained during a rather violent heating process, such as the application of turbulent heating.

A poloidal ohmic heating electric field was produced by a three turn coil concentric with the toroidal field (TF) windings. The three turns passed through the central TF bundle and closed 120° apart outside of the vacuum vessel. The vacuum vessel had an electrical brake to eliminate poloidal currents in the vessel. The OH coil was energized by a capacitor bank (200 μF) which could be charged to a maximum of 10 kV, giving a maximum current in the OH coil (I_{OH}) of 45 kA turns. For the maximum OH current the typical vacuum electric field averaged over a flux shell in the plasma volume was 4 V/m. The ringing frequency of the OH system is 1.2 kHz with a decay time of 3 msec. The OH current could be crowbarred at any time during the pulse.

The ohmic heating current was passed through an ECH-produced plasma of density $\sim 10^{11} cc^{-1}$. For moderate ohmic heating currents ($I_{OH} \sim$ 13 kAt.) the density (Fig. 13) remained relatively constant during the first half cycle rising during subsequent cycles with a time constant given by the inverse of the maximum ionization rate coefficient times the neutral density ($\tau = 1/n_o < \sigma v_e >$). After the density increased by about an order of magnitude its rate of increase was reduced. Ion gauge measurements showed a decrease in the neutral pressure during the first few half cycles then a large increase in background pressure arising several milliseconds after the initiation of the ohmic heating current. This indicated initial neutral ionization, then large impurity impingement from the vacuum walls.

6.1 Flux penetration

The flux penetration into the plasma was measured with a single loop enclosing the plasma similar to one turn of the OH coil. This loop was compensated with several smaller turns not enclosing the plasma so that the vacuum field gave a null signal. The compensated loop signal was then a measure of the magnetic flux rejected from the plasma by the plasma currents.

By varying the ohmic heating current the magnetic field penetration into the plasma could be measured for two conditions; the electron drift velocity (v_d) much greater than the ion acoustic velocity [$C_s = (T_e/M_i)^{1/2}$] but less than the electron thermal velocity (v_{th}); i.e., ($C_s << v_d < v_{th}$), and for the electron drift velocity greater than the electron thermal velocity; i.e., ($v_{th} < v_d$). Figure 11 shows an integrated compensated loop measurement during which both conditions are present, along with a signal proportional to the ohmic heating current for reference. During the first half cycle the electron drift velocity approaches or slightly exceeds the electron thermal velocity, while during the second half cycle the reduction in OH current and the increase in electron density have combined to reduce the electron drift velocity below the electron thermal velocity. At the peak of the first half cycle a slight flattening of the flux penetration can be noted. The second half cycle shows a larger flux rejection by the plasma even though the OH current has decayed, indicating a larger plasma conductivity during this half cycle. This effect is further demonstrated in Fig. 12 where the plasma current as measured by the flux rejection of the plasma is plotted as a function of the OH current for two initial plasma densities. For an initial density of $0.8 \times 10^{11} cc^{-1}$ the electron drift velocity approaches the electron thermal velocity at a plasma current of approximately 7 kA, at this point there is a sharp reduction in the plasma conductivity and increase in flux penetration. If the current is increased above this level by a large amount the plasma density is reduced from its initial value due to large losses and the flux penetration is further increased as illustrated by the plasma current at 33 kAt OH current. If the initial plasma density is increased the electron drift velocity is reduced for the same plasma current; a higher current is then required to bring the electron drift velocity up to the electron thermal velocity as illustrated by the curve for an initial density of $1.6 \times 10^{11} cc^{-1}$.

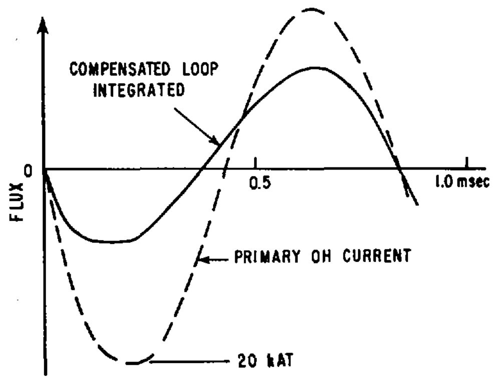

FIG.11. Time variation of the integral of the compensated loop voltage is a measure of the magnetic flux rejected by the plasma along with the time variation of the ohmic-heating (OH) current.

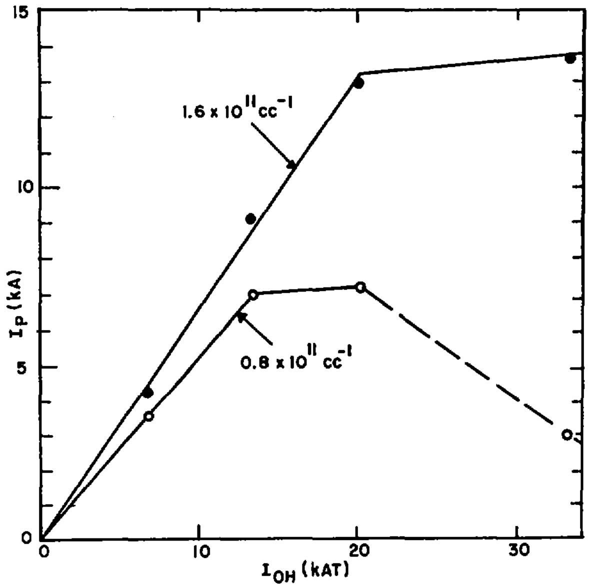

FIG. 12. Plasma current as determined by the plasma magnetic field rejection versus ohmic-heating coil current for two initial plasma densities. A saturation in plasma current is seen when the electron drift velocity is comparable to the electron thermal velocity. For drift velocities much in excess of the thermal velocity the plasma density decreases rapidly along with the plasma current (dashed line).

It is seen in Fig. 12 that a sharp increase in plasma resistivity occurs when $v_d \sim v_{th}$ for the electrons. To determine the plasma resistivity for $v_d < v_{th}$ the potential measured with the compensated loop can be calculated using assumed resistivities and these values can be compared to the measured value to determine the correct resistivity.

Langmuir probes were used to measure T_e. Also the energy content of the plasma was determined from the increase in density when the OH was crowbarred. Using these methods for the I_{OH} = 15 kAt condition ($v_d \sim 20C_s$) the electron temperature was found to be about 60 eV near peak current. The compensated loop measurement indicated an effective electron temperature of 23 eV. The measured resistivity is found to be about four times the classical value. Comparing this to the measured value of 60 eV gives an anomalous electron ion collision frequency which is four times the classical collision frequency at this temperature or related to the ion plasma frequency:

$$\nu_{eff} \sim \frac{\omega_{pi}}{4 \times 10^3}$$

6.2 Containment

The most important objectives of the OH experiments were the determination of the effect of the plasma turbulence produced by high electron drift velocities on the plasma containment, as well as the effect on containment of the increased electron temperature produced by the ohmic heating.

Voltage fluctuations were observed on the compensated loop signal during certain phases of the OH current. These fluctuations can be seen on the first trace of Fig. 13. These fluctuations are high frequency (~ 1 MHz) but have been filtered in the Fig. 13 so that they will be visible on the oscillograph. Correlated with these voltage spikes are x-ray emissions and μwave emissions in the region of 1.8 GHz. Voltages fluctuations occur at the time when the electric field produced by the ohmic heating is near maximum.

The effect of the fluctuations on containment can be illustrated by a plot of the inverse of the containment time as shown in Fig. 13. The inverse containment time was determined by dividing the loss, as measured at the surface of the plasma with the limiter, by the total electrons in the plasma. As seen in Fig. 13 the loss shows a large variation during one cycle of the OH current which is correlated with the voltage fluctuations.

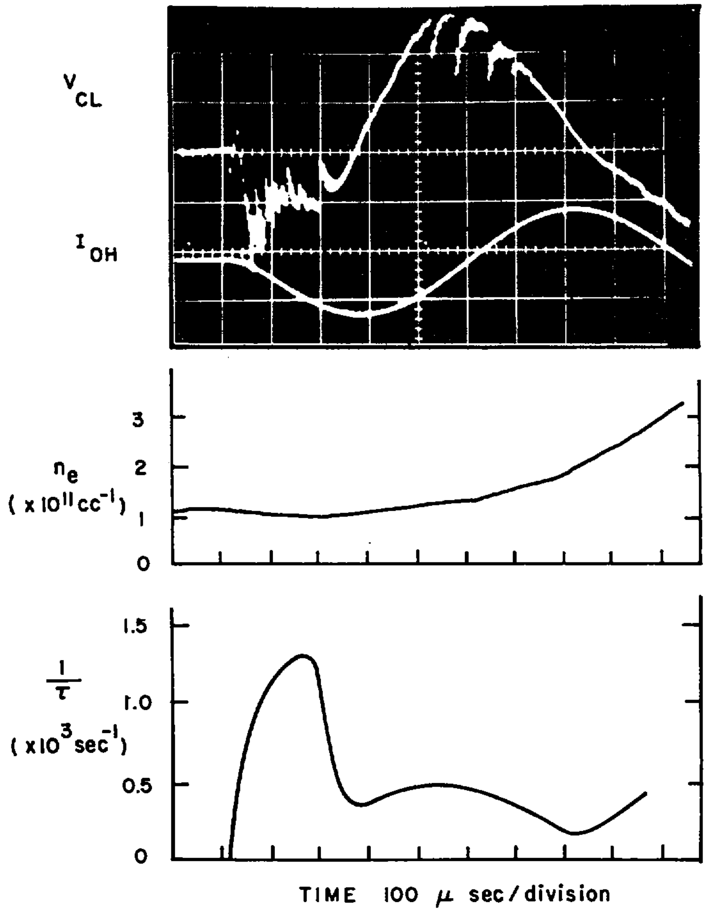

FIG. 13. Characteristics of the OH-discharges shown is the compensated voltage (V_{cl}); a low pass filter was used to make the voltage fluctuations more visible on the oscillograph. I_{OH} is the ohmic heating primary current. The electron density (n_e) shows a slight decrease during the first half cycle then a substantial increase. The inverse containment time, τ^{-1}, shows a loss correlated with the voltage fluctuations.

Presumably if the OH current was stopped while the electron temperature was maintained the confinement would be improved. It is likely that the confinement time is also affected by magnetic field errors produced by the azimuthal nonuniformity of the OH current which is carried by only three turns.

It has been shown in Fig. 12 that when the OH current is increased beyond a factor of two of the current at which the resistivity increases sharply ($v_d \sim v_{th}$), the loss increases. This loss exceeds the ionization rate so that the plasma density drops to near zero in about 100 microseconds. This occurs during the first quarter cycle. The best confinement times obtained during and directly after the ohmic heating (for $v_d < v_{th}$) are shown in Fig. 7. The confinement time at 60 eV was obtained during heating while the points for lower temperatures (30-40 eV) were obtained after the OH was crowbarred. In Fig. 7, the confinement times above 10 eV can be compared to the solid line which represents two-hundred times the Bohm confinement time.

7. HIGH ENERGY ELECTRON DISCHARGE

If the background neutral pressure is reduced and an electron cyclotron heating (ECH) pulse is applied (~ 10 msec, 1 kW, 2.45 GHz), it is possible to reach the mode shown in Fig. 14. The plasma density increases only after the microwave heating has terminated, a phenomenon observed previously in a similar device [3]. This plasma is found to be produced by ionization of the background gas by high energy (runaway) electrons.

The presence of high energy electrons is inferred by the various diagnostics summarized in Table IV. The insertion of a probe into the magnetic mirror region of the spherator extinguishes the runaway condition, but an obstable inserted radially into the horizontal plane does not affect the discharge. It is concluded then that the high energy electrons appear to be confined to the mirror region. Spatial measurements of the high energy electrons scattered into the mirror loss cone were obtained with scintilation probe measurements and hard x-rays ($\geq$ 100 keV) emanating from a movable carbon target in the horizontal plane. These data indicate that the electrons mirror near the electron cyclotron resonant surface indicated on Fig. 1. Standard pulse height and absorber analysis of the x-ray measurements indicate that there are both soft and hard energy electron components (~ 5 keV and 150 keV or more) present. The soft x-ray count rate is seen to decay with a time constant of approximately 6 msec in Fig. 15a. Receiver power detected near the cyclotron frequency (2 GHz) initially exhibits a similar decay time whereas the second harmonic power (4 GHz) does not. This is consistent with the soft electron component emitting cyclotron radiation primarily at the fundamental. The hard x-ray count rate together with synchrotron radiation for the same case, shown in Fig. 15b persists for long times and have nearly the same decay rate. Since the synchrotron radiation is approximately proportional to the number of hot electrons present and their perpendicular energy whereas the x-ray count rate is proportional to the number of hot electrons only, it appears that the temperature decay time is much longer than the containment time of the hot component. The initial total synchrotron radiation emitted, assuming a temperature of

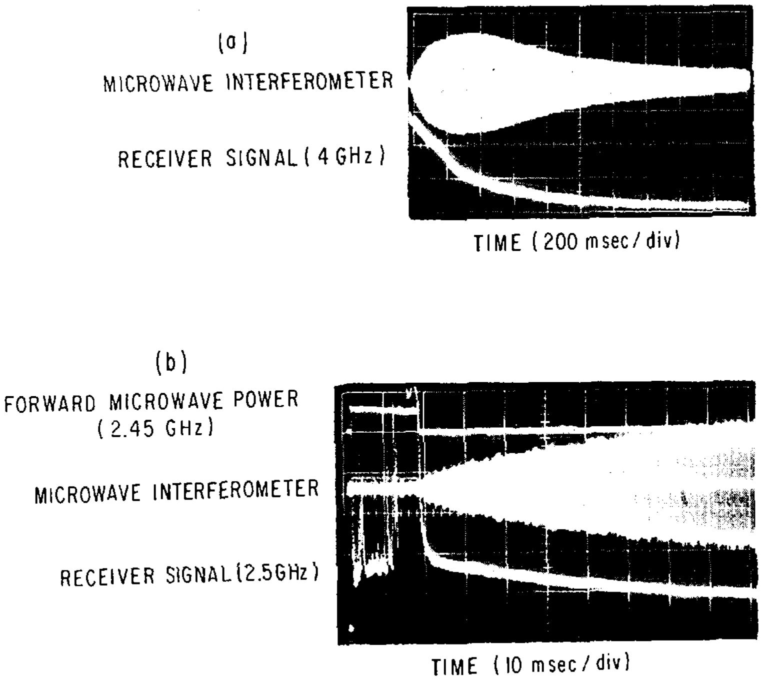

FIG. 14. Runaway electron discharges in helium gas at a gauge pressure of 10^{-6} Torr. (a) Microwave interferometer (70 GHz) signal showing the growth of the plasma density with time following the ECH-pulse. Peak density in this case is 4×10^{10} cm^{-1}. The receiver signal (tuned near the second harmonic of the cyclotron frequency) is also shown. (b) A shorter time interval showing that the plasma density increases only after the microwave heating has ended.

150 keV, is consistent with an average density of approximately 5×10^8 electrons cc^{-1}. The ratio of the synchrotron power radiated at the fundamental to second harmonic ($\sim$ 2:1) is also consistent with 150 keV energy. The decay time of the synchrotron radiation is nearly proportional to the neutral particle density below 10^{-6}Torr; reaching 4 seconds at 2×10^{-7} Torr in the case of helium. This is in agreement with a loss mechanism explained by atomic collisions.

The mechanism by which the electrons are accelerated to high energy proceeds much too slowly to be a resonant electron cyclotron interaction. The initial rate of energy gain E of the hot electrons, obtained from x-ray data, shown in Fig. 16a, as a function of the applied ECH power is linear below 500 watts. The insert in Fig. 16a shows that the energy gain is nearly linear in time up to energies of $\sim$ 200 keV with some saturation above this point. These data are in qualitative agreement with the upper off-resonance heating theory of Eldridge [19] which predicts that

$$E \propto P_a t/\gamma$$

TABLE IV. HIGH-ENERGY ELECTRON DIAGNOSTICS AND PRINCIPAL RESULTS

Diagnostic	Description	Results
Microwave interferometer	70 GHz system	Gives an upper limit of 10^9 hot electrons cc^{-1}.
Hard X-ray	2" NaI crystal with light pipe and PMT	Typical X-ray temperatures of 150 keV are obtained.
X-ray target	Movable carbon target (5mm dia, 5mm long) in horizontal plane	Localizes hot electrons to flux surfaces with deep magnetic mirrors and exterior to electron cyclotron resonant surfaces.
Soft X-ray	2-30 keV sensitivity. Si drift detector	Typical soft X-ray temperatures of 5 keV and e-folding times of 6 msec.
Target insertion		
Mirror region	Probe	A probe inserted into the mirror region eliminates all indication of runaway electrons.
Horizontal plane	Probe, carbon target	No effect noted.
Synchrotron emission	In frequency range of 2-4 GHz with a superhet receiver	Fundamental and second harmonic detected. Indicates an electron temperature of 150 keV and hot electron density of $5 \times 10^8 cc^{-1}$. The two energy component decay is noticeable.

where P_a is the applied power and $\gamma = (1 - (v/c)^2)^{-1/2}$. The synchrotron spectra shown in Fig. 16b are also consistent with this interpretation. A short ECH pulse yields electrons which radiate primarily at the applied cyclotron frequency. However, longer applied pulses cause the fundamental synchrotron radiation to peak at lower frequencies (presumably due to the relativistic mass increase) and exhibit increased harmonic content due to increased electron energies. These results are similar to the experiments of Shohet et al. [20] and Ard et al. [21] on ECH plasmas in mirror machines.

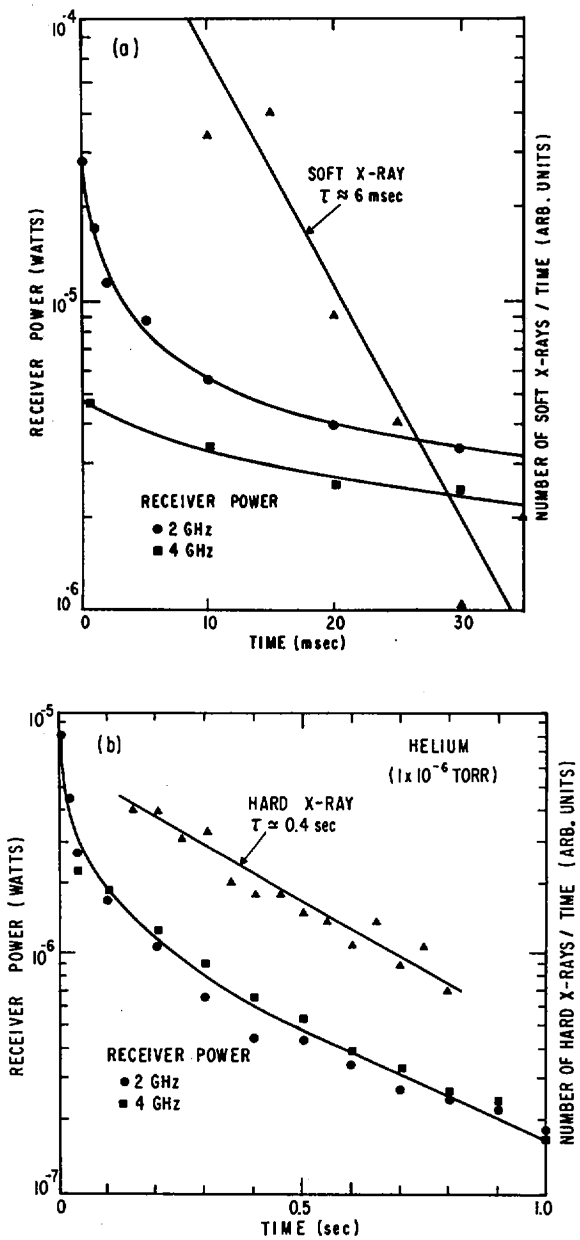

FIG. 15. X-ray count rates and receiver power versus time. (a) Soft X-ray (5 keV) count rate has a decay time of 6 ms. Synchrotron power near the fundamental (2 GHz) has a similar initial decay whereas the power near the second harmonic (4 GHz) does not exhibit an initial rapid decay. (b) Hard X-ray (~ 150 keV) count rate and synchrotron power have a similar decay time indicating the energy loss time is much longer than the containment time for high energy electrons.

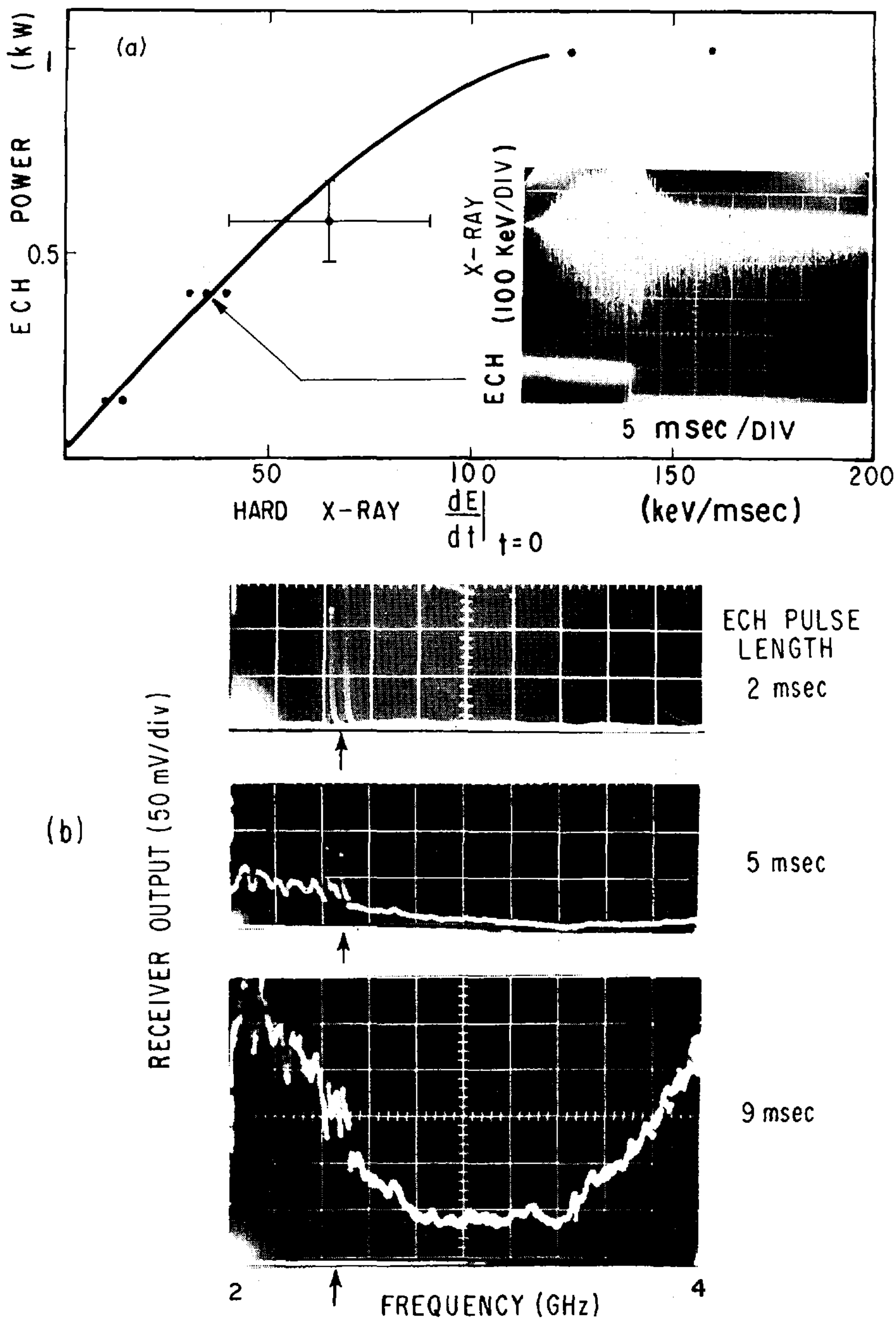

FIG.16. (a) ECH power applied versus initial rate of X-ray energy gain. (b) Microwave emission spectra taken 20 - 30 ms after termination of the ECH-pulse for several pulse widths. The electron energy gain with increasing pulse width is reflected in the increased broadening and harmonic content of the spectra. (Double peaks arising in the spectra are due to the two sidebands of the receiver.)

The ionization rate due to the hot electrons may be estimated by measuring the loss rate Γ of cold plasma across the magnetic field with the limiter and using the relation

$$\left(\frac{dn}{dt}\right)_{ioni} = \frac{\Gamma}{V} + \left(\frac{dn}{dt}\right)_{obs}$$

where V is the plasma volume and $(dn/dt)_{obs}$ is the density increase (decrease) observed by the microwave interferometer. The result in Fig. 17 shows that the ionization rate is consistent with the amount of runaway electrons present. A cold plasma decay time of up to 400 msec is indicated in this case. The electron temperature of the plasma resulting from the ionization of the neutral background gas is typically less than 5 eV.

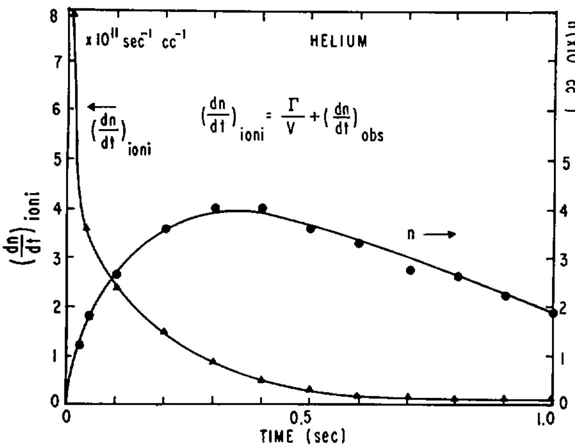

FIG. 17. Ionization rate versus time deduced from the measured cold plasma decay rate and the plasma loss across the magnetic field.

Above a pressure of 1.5×10^{-6} Torr the discharge loses the characteristics of a runaway condition. Namely, the plasma density maximizes during the ECH pulse at a value ($\sim 5 \times 10^{11} cc^{-1}$) much greater than that possibly produced by runaway ionization alone, the synchrotron power emission is substantially reduced and its decay is a more rapidly decreasing function of pressure, and the observed x-ray fluxes are reduced. In addition, the insertion of a probe into the magnetic mirror region, which destroys the runaway condition, has little effect on the discharge density or confinement time. The possible error in the determination of the plasma confinement time due to ionization by runaway electrons is estimated to be below 10% for neutral pressures above 2×10^{-6} Torr.

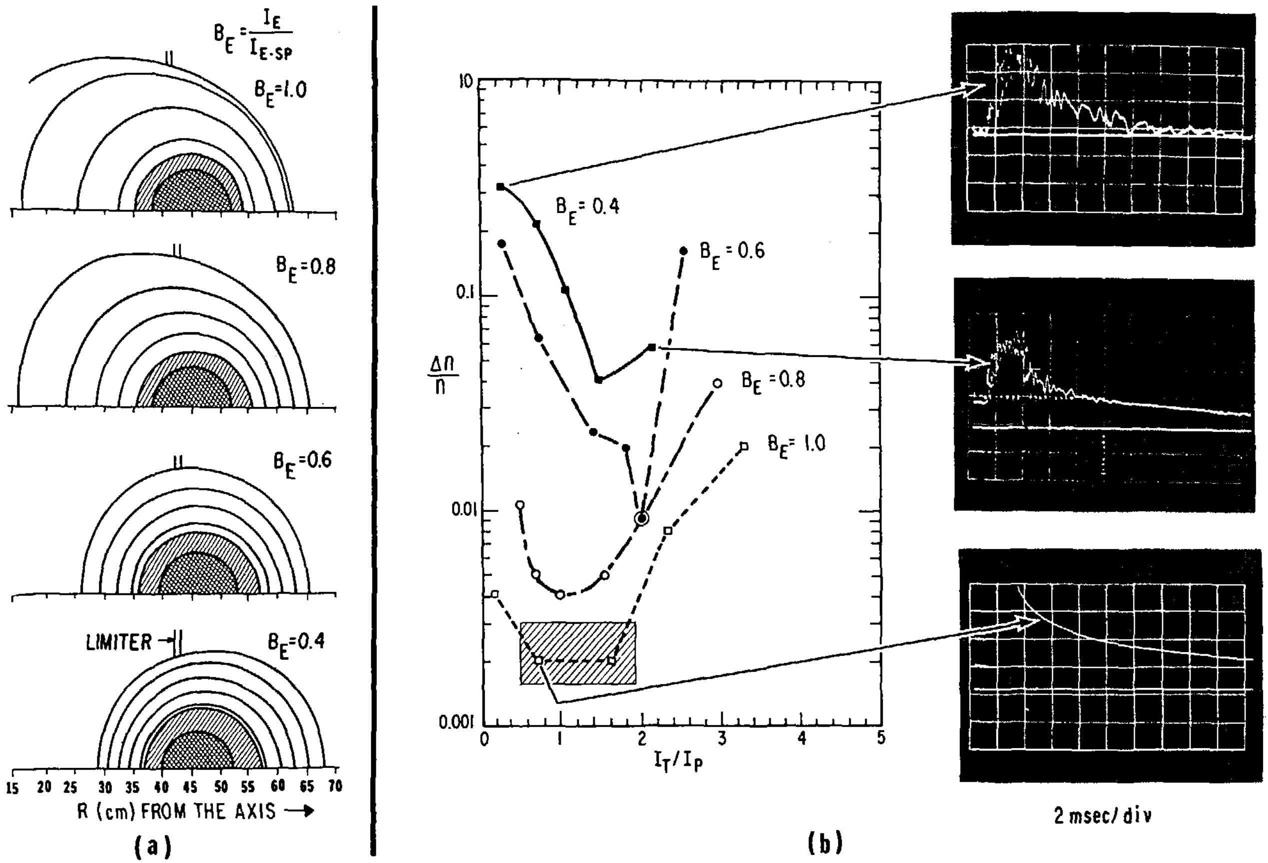

FIG. 18. (a) Magnetic field configurations for different strengths of poloidal external field. B_E is the poloidal external field strength normalized by that of the standard experimental configuration. (b) The observed fluctuation level versus I_T/I_P.

8. INSTABILITIES RELATED TO MIRROR TRAPPING

A question arises as to what magnetic parameters determine the plasma stability. A number of theoretical papers [22-25] have predicted that high shear and average minimum-B properties should stabilize low frequency oscillations.

Experiments were performed in the supported spherator to test various magnetic field configurations. As shown in Fig. 18a in the normal spherator configuration ($B_E = 1.0$) the external field pushes the magnetic surfaces toward the toroidal field coil; which tends to produce an average minimum B. As the external field is decreased, the ψ = constant surfaces do not extend to the region near the axis of symmetry, causing the good curvature region to decrease. Consequently for $B_E = 1.0$ an average magnetic well ($V^{**} < 0$) does not exist at the lower ratio of the toroidal to poloidal field (I_T/I_P). For the cases of $B_E = 0.6$ and 0.4, there is no average well in our experimental range.

The dependence of the fluctuation level on the magnetic configuration and the toroidal field is shown in Fig. 18b. The cross-hatched region shows the standard experimental conditions. The influence of the fluctuation level on the density decay time is illustrated by Fig. 19a, where the fluctuation level is replotted as a function of the measured confinement time. This plot shows that the confinement time increases significantly as the fluctuation level is reduced. If V^{**} is the relevant parameter to describe the stability properties, the higher toroidal field should produce a more stable plasma. Experimentally, however, higher toroidal field causes the plasma to become unstable. If shear is the important parameter the fluctuation amplitude versus the shear angle $< \kappa L_s >$ should reflect the stability properties. (κ is the inverse density gradient.) However, Fig. 19b shows a factor of 100 difference in the fluctuation level for approximately the same value of $< \kappa L_s >$. Thus, it is clear that some factor other than shear and V^{**} is responsible for the change in the fluctuation level.

A possible important property of the magnetic field configuration is the location of the mirror trapping, since this location can be changed by changing the magnetic field configuration. In the case of $B_E = 1.0$ with lower toroidal field (when the fluctuations are small), the trapped particles are located in a good curvature region near the toroidal field conductor and with an increase in the toroidal field (when the fluctuations increase) the trapping region moves towards the outside horizontal plane, where the curvature is bad. Thus, the observed instability may be related to the trapped particle instability.

The growth rate for the trapped particle instability was calculated numerically using the dispersion relation. [26, 27] In Fig. 19c the fluctuation level was plotted versus the integrated growth rate, Γ. The theoretical description not only qualitatively gives the instability properties observed, but it also predicts reasonably well the real part of the frequency and the direction of wave propagation. The detailed analysis is presented in Ref. [28].

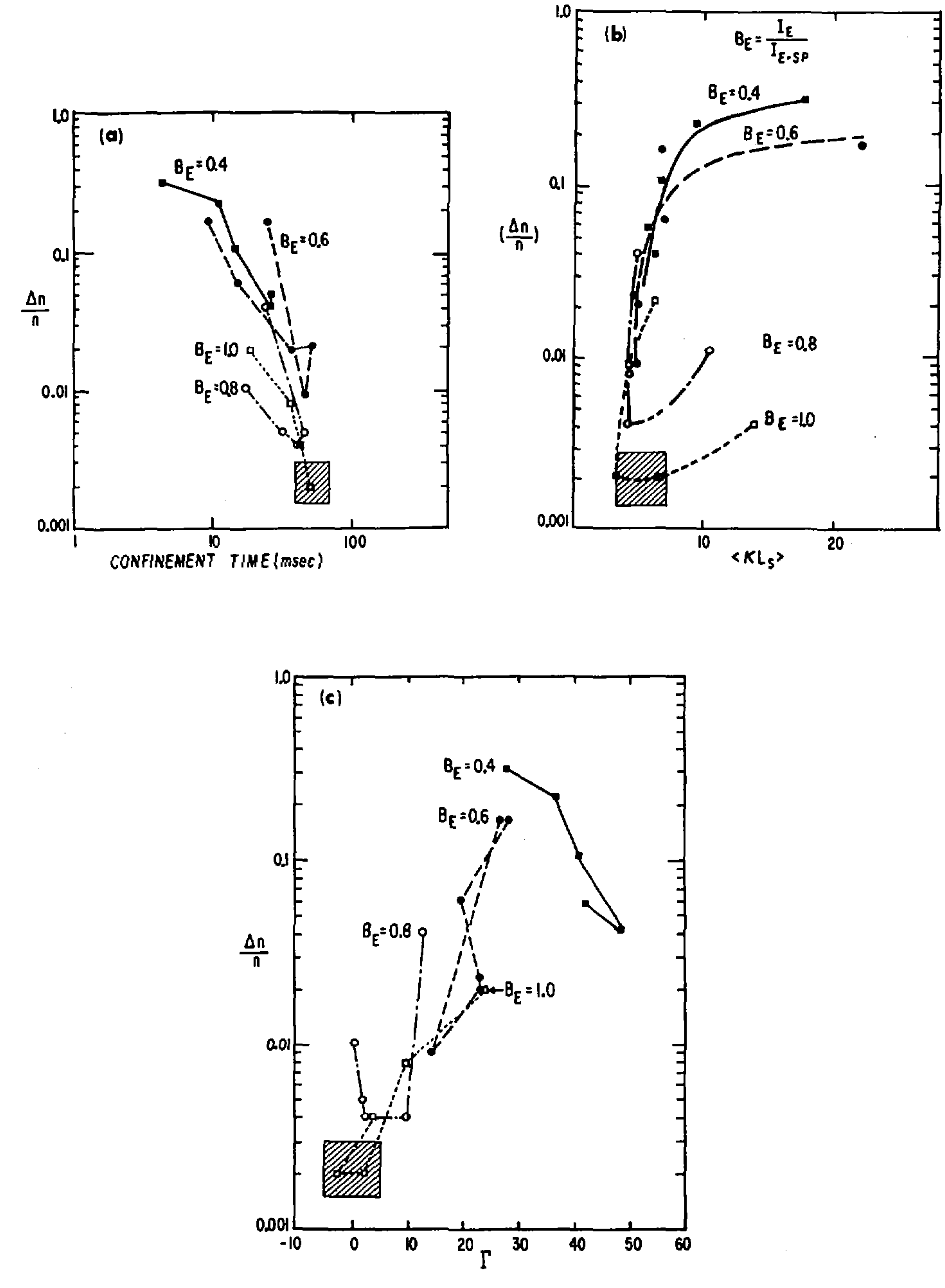

FIG. 19. (a) Fluctuation level versus observed confinement time. (b) Fluctuation level versus $\langle \kappa L_s \rangle$ (κ is the inverse of the density gradient length and L_s is the shear length). (c) Fluctuation level versus the calculated integrated growth rate over time Γ.

9. SUMMARY AND CONCLUSION

The experiments in the supported spherator have indicated that the plasma loss across the magnetic field is dominantly caused by the convective cells produced by the supports. The experiments with the levitated spherator have shown that this is indeed the case. Plasma confinement times up to 200 msec have been obtained in the afterglow of the levitated device. However, the best available numerical calculation using the classical transport coefficients shows that this observed plasma confinement time still is, at best, a factor of 4 shorter than the calculated classical value. The fact that a $\omega_c > \omega_{pe}$ region exists in the wing of the density profile may increase the classical collision frequency by a factor of ~ 1.5. This still leaves a discrepancy of at least a factor 2.5 - 3 between observed and calculated confinement times.

A series of measurements to determine quantitatively the concentration of high energy electrons have shown that (1) the high energy electrons can be generated and trapped for several seconds, (2) the energy range is 5 keV to 200 keV, and (3) under normal operating conditions, the effect of ionization by high energy electrons would alter the observed confinement in the afterglow at most by 10%.

High power ohmic heating has produced electron temperature in the range of 30-100 eV. The current penetration indicates a mild anomalous skin effect exists. If v_d/v_{th} is less than 1, it is found that a major fraction of the plasma can be contained. Thus, turbulent heating may be applied with a tolerable plasma loss rate to a toroidal confinement device. The plasma confinement times in the high power OH phase, are estimated from the loss collectors. Since the time for which the electron temperature remains high is short (less than 1 msec), the plasma confinement time ($\sim$ 10 msec or more) obtained from the loss detector may not reflect the true confinement time, as the density profiles cannot relax to the fundamental mode in a time considerably shorter than the confinement time. Nonetheless the fact that a finite amount of the plasma reaches the collector indicates that a mechanism exists whereby the plasma is lost across the magnetic field. The preliminary confinement results during ohmic heating are shown in Fig. 7. The results suggest that the plasma confinement may behave as $1/T_e^n$ $(1/2 \leq n \leq 1)$, deviating at higher electron temperature from pseudoclassical diffusion. The mechanism for this loss may be field errors or MHD instabilities. Large field errors ($\delta B/B > 2\%$) had a highly detrimental effect on plasma confinement for temperatures greater than 1 eV. Preliminary results indicate that magnetic field errors of about 0.5% give an increase in plasma loss during ECH heating.

An improved spherator (FM-1) which is nearing completion will employ a divertor with the objective of reducing the background neutral pressure. The divertor is provided to capture plasma which is lost from the confining region. Assuming that 50% of plasma particles which are lost are captured by the divertor, it is possible to numerically calculate the behavior of plasma parameters if electron heating power of 100 watts is applied. The result is shown in Fig. 20. We note that there is rapid decrease of neutral density to 1/50th of the base pressure. At this level, the plasma cooling would be very small.

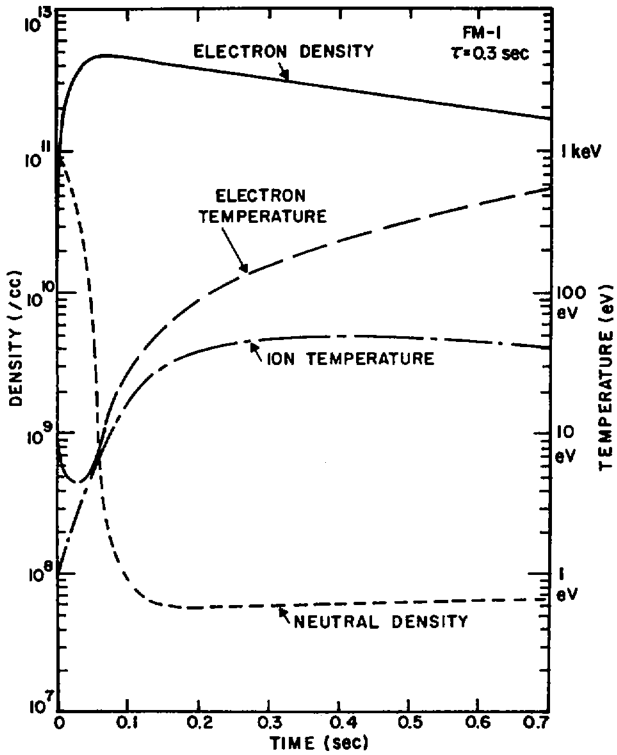

FIG. 20. Electron and ion temperatures, neutral and electron densities versus time determined numerically for the FM-1 device. A continuous electron heating power of 100 W was assumed.

The main conclusion may be summarized briefly as follows: the plasma confinement time up to 5 eV in the afterglow can follow the pseudo-classical diffusion time, while confinement times over 10 eV during the heating are considerably lower than the pseudoclassical diffusion time and have a $1/T_e$ (pseudo-Bohm) or $1/T_e^{1/2}$ dependence. Afterglow experiments with electron temperatures over 10 eV may show confinement time improvement over the present experiments carried out during heating.

ACKNOWLEDGMENT

This work was supported by USAEC Contract AT(30-1)-1238.

REFERENCES

[1] DORY, R. A., KERST, D. W., MEADE, D. M., WILSON, W. E., ERICKSON, C. W., Phys. Fluids 9, 997 (1966).
[2] OHKAWA, T., SCHUPP, JR., YOSHIKAWA, M., VOORHEES, H. G., Plasma Physics and Controlled Nuclear Fusion Research (IAEA, Vienna, 1966), Vol. II, p. 531.

[3] BIRDSALL, D. H., BRIGGS, R. J., COLGATE, S. A., FURTH, H. P., HARTMAN, C. W., Plasma Physics and Controlled Nuclear Fusion Research (IAEA, Vienna, 1966) Vol. II, p. 291.

[4] YOSHIKAWA, S., BARRAULT, M., HARRIES, W., MEADE, D., PALLADINO, R., VON GOELER, S., Plasma Physics and Controlled Nuclear Fusion Research (IAEA, Vienna, 1969) Vol. I, p. 403.

[5] FREEMAN, R., OKABAYASHI, M., PACHER, H., PACHER, G., YOSHIKAWA, S., Phys. Rev. Letters, 23, 756 (1969).

[6] SCHMIDT, J. A., SCHMIDT, G. L., Phys. Fluids 13, 1351 (1970).

[7] SCHMIDT, J. A., Phys. Rev. Letters 24, 721 (1970).

[8] MEADE, D. M., MOLVIK, A. W., RUDMAN, J. W., SCHMIDT, J. A., Phys. Rev. Letters, 22, 1354 (1969).

[9] SPITZER, L., Jr., Phys. Fluids 3, 659 (1960).

[10] OHKAWA, T., YOSHIKAWA, M., KRIBEL, R. E., SCHUPP, A. A., JENSEN, T. H., Phys. Rev. Letters 24, 95 (1970).

[11] FILE, J., MARTIN, G., MILLS, R., WAKEFIELD, K., J. Appl. Physics 42, 6(1971).

[12] VON GOELER, S., SADOWSKI, M., PACHER, H., YOSHIKAWA, A., Phys. Fluids 13, 790 (1970).

[13] YOSHIKAWA, S., FREEMAN, R., OKABAYASHI, M., Princeton University Plasma Physics Laboratory Report MATT-7-6 (1969).

[14] FREEMAN, R., OKABAYASHI, M., PACHER, G., YOSHIKAWA, S., Princeton University Plasma Physics Laboratory Annual Report MATT-Q-27, 1 (1970).

[15] PACHER, H., PACHER, G., YOSHIKAWA, S., Phys. Rev. Letters 25, 1559 (1970).

[16] JOHNSON, J., VON GOELER, S., Phys. Fluids 12, 255 (1969).

[17] YOSHIKAWA, S., Phys. Rev. Letters, 25, 353 (1970).

[18] OKABAYASHI, M., FREEMAN, R., YOSHIKAWA, S., Princeton University Plasma Physics Laboratory Annual Report MATT-Q-26, 24 (1969).

[19] ELDRIDGE, O., Oak Ridge Nat. Lab. Report ORNL-4545, 32 (1970).

[20] SHOHET, J. L, et al., University of Wisconsin Dept. of Elec. Eng. Report C00-1695-32 (1970).

[21] ARD, W. B., DANDL, R. A., EASON, H. O., EDMONDS, P. A., ENGLUNC, A. D., LIVESEY, R. L., McGUFFIN, M. W., NOLAN, S. T., Oak Ridge Nat. Lab. Report ORNL-4545, 59 (1970).

[22] KERST, D. W., and OHKAWA, T., Phys. Rev. Letters 7, 41 (1961).

[23] YOSHIKAWA, S. and CHRISTENSEN, Phys. Fluids 9, 2295 (1966).

[24] JOHNSON, J. and GREENE, J., Plasma Phys. 9, 611 (1967).

[25] KRALL, N. and ROSENBLUTH, M., Phys. Fluids 8,. 1488 (1965).

[26] KADOMTSEV, B. B., and POGUTSE, O. P., Sov. Phys.-JETP 24; 1172 (1967).

[27] POGUTSE, O. P., Nuclear Fusion 9, 157 (1969).

[28] OKABAYASHI, M., FREEMAN, R., Princeton University Plasma Physics Laboratory Report MATT-783 (1970).

DISCUSSION

M. YOSHIKAWA: One of the slides you projected showed that the confinement deteriorates when Ohmic heating is applied. Do you think the reduction in confinement time is due to the field error produced by the heating coil? Or is it possible that the electron drift velocity is greater than the sound velocity of the plasma?

J.A. SCHMIDT: The reduced confinement time may very well be due partly to field errors caused by the three-fold symmetry of the Ohmic heating coil. The electron drift velocity due to the Ohmic heating current is much greater than the ion sound velocity, and ion sound turbulence is observed. This turbulence may enhance the plasma diffusion.

G.O.J. von GIERKE: In your paper you give certain variables as functions of the ratio I_T/I_P. How did you vary I_T/I_P in the experiments?

J.A. SCHMIDT: We varied it by changing the current I_T, which determined the toroidal field.

A. GIBSON: How are you able to exclude the possibility that ionization effects due to thermal electrons might invalidate the measurements of confinement time and, secondly, what errors appear in the estimation of ionization effects owing to uncertainties in the measured electron temperature?

J.A. SCHMIDT: Ionization is important above 2 eV and for this reason the confinement time is determined from the external loss measurement. When this method is used, the errors in electron temperature measurements are not important in the confinement measurements.

A. GIBSON: How reliable are estimates of confinement time obtained from the escaping flux, bearing in mind that the flux to the inner ring is not measured?

J.A. SCHMIDT: The loss to the internal ring was measured in the supported spherator and was only small; the loss was then assumed small in the levitated spherator. In the afterglow, where the ionization rate for thermal electrons is negligible and runaway electrons are absent, the confinement times obtained from the loss measurement compare well with those determined from interferometer-measured density decays.

H. DREICER: You said that your plasma cools rapidly owing to electron-ion energy exchange and ion-neutral charge exchange. Apart from cooling the ions, charge exchange also causes the diffusion of ions across magnetic field lines with an r.m.s. diffusion step equal to the ion gyration radius. When the corresponding electron flow across field lines is inhibited, the space charge electric fields which are produced may set the plasma into macroscopic motion. Do you think it possible that the plasma confinement time you have reported is affected by this cross-field diffusion induced by charge-exchange?

J.A. SCHMIDT: At electron and ion temperatures below a few eV, under our standard experimental conditions, the momentum transfer rate coefficient for charge-exchange is negligible compared with the electron-ion momentum transfer coefficient. Above 5 eV the ion diffusion due to charge-exchange would become important if an anomalous electron diffusion mechanism were present.

PLASMA CONFINEMENT AND HEATING IN THE INTERNAL RING DEVICE F IV

B. LEHNERT, J. BERGSTRÖM, M. BUREŠ, E. TENNFORS, B. WILNER
Royal Institute of Technology,
Stockholm, Sweden

Abstract

PLASMA CONFINEMENT AND HEATING IN THE INTERNAL RING DEVICE F IV.

A closed magnetic confinement region of nearly spherical shape is produced in device F IV by a ring-shaped internal conductor and a pair of external coils. The internal ring is suspended by magnetically shielded supports. To secure good confinement, theory predicts that the guiding-centre drifts of the plasma particles across the magnetic field must be small compared to the thermal velocity, and that the separation distance of a pair of supports should be small compared to the length of the supports.

In the F IV device a fully ionized plasma of density 10^{21} m^{-3} is created by means of crossed electric and magnetic fields. The plasma is surrounded by a neutral gas blanket. The azimuthal fluid motions are limited after reaching the fully ionized state, and the plasma is sustained by high-frequency heating, tuned to the lowest magneto-acoustical resonance frequency, at about 1.2 MHz. The power absorption by the plasma is then of the order of 0.5 MW. In some experiments the supports have been magnetized by currents up to 23 kA, at a mean strength of 0.43 Vs/m^2 of the main magnetic field at the supports.

So far, the experiments indicate that magnetic line-tying effects at the outer plasma boundary are essential to the stability of the plasma, that plasma equilibrium becomes possible also in the presence of magnetized supports, and that magnetic shielding of the latter reduces the total power losses of the plasma.

1. INTRODUCTION

According to earlier suggestions [1,2], a closed magnetic bottle can be produced by a ring-shaped coil placed inside a confined plasma and being suspended by magnetically shielded supports. Theory requires two necessary conditions to be fulfilled for internal ring systems to provide an effective confinement in a stable state [3-5]:

(A) The electric field should produce a slow guiding centre drift of the plasma particles across the magnetic field, as compared to their thermal velocity. Thus, the particles can only be prevented from reaching the shielded supports when the "plasma wind" by the transverse electric field is subsonic.

(B) For dipole-shaped supports, which can be made force-free, the ratio $R_s = d_t/2d_1$, between their length d_t inside the plasma confinement region and their separation distance $2d_1$ is of vital importance. To make an equilibrium possible, it should be chosen large enough for the surfaces of the average magnetic gradient drift to generate a closed confinement region.

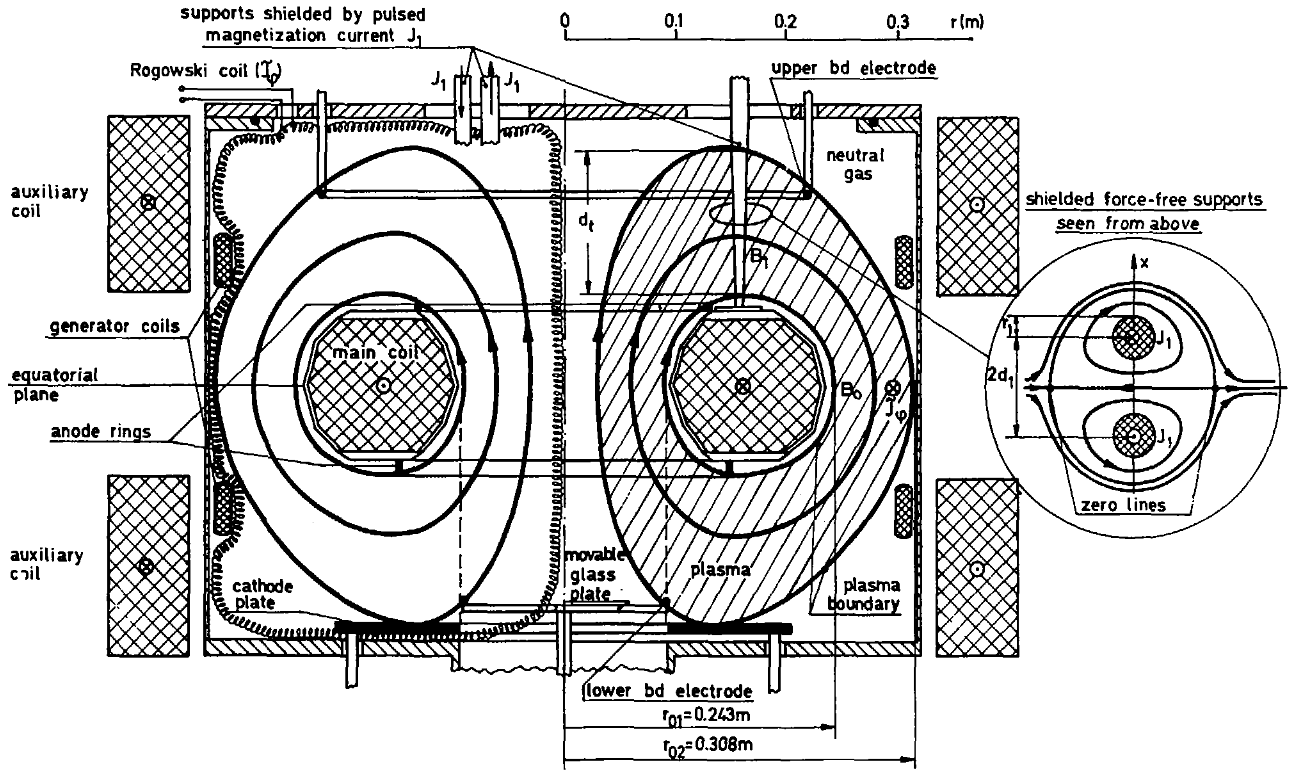

FIG. 1. Outline of device F IV. Shaded area represents confinement region. Main coil is suspended by three pairs of shielded, divergent supports.

During the last five years many experiments have been performed with internal ring systems under various conditions. For the "Spherator" having a levitated unsupported internal ring, very encouraging results were recently reported on a stable state with 0.2 sec. confinement time [6]. With unshielded supports there are several indications that the main loss mechanism is due to the flux of plasma and heat to the supports [7-9]. Magnetic shielding is expected to change the support loss as well as the geometry of the magnetic bottle. Certain experiments indicate that such shielding prevents the plasma from reaching the supports [10,11]. From the investigations reported so far it is not clear, however, whether the magnetic disturbance from the supports will affect the plasma equilibrium and stability. Several theoretical and experimental results might appear to be in contradiction on this point [3-5, 11-17]. Part of these discrepancies can probably be traced to the difference in experimental conditions, in particular with respect to the support ratio R_t and the plasma density.

In the present experiments with device F IV a confinement region of nearly spherical shape is produced by an internal ring system [2] as outlined in Fig. 1. These experiments are characterized by several important features, the combination of which is unique as compared to other similar projects:

(i) A fully ionized plasma of density as high as about $10^{21}m^{-3}$ is created by the crossed field technique of rotating plasmas.

(ii) The confinement region is surrounded by a neutral gas blanket.

(iii) To satisfy condition (A) the rotation is stopped after reaching a fully ionized state, and the plasma is then sustained by high-frequency heating.

(iv) To satisfy condition (B) the support ratio has been chosen as large as $R_s \simeq 5$.

2. SUMMARY OF THEORETICAL INVESTIGATIONS

2.1. The effects of shielded supports

2.1.1. Magnetic reduction of support loss

To estimate the current J_1 required for shielding the supports of Fig. 1, we consider a simplified two-dimensional case in which the effects of the transverse electric field are neglected [see also refs. 2,3]. We introduce the support radius r_1, the ratio $f = d_1/r_1 > 1$, the local strength B_1 of the main magnetic field, and the ratio $F = \mu_0 J_1/2\pi r_1 B_1 = b_1/B_1$ between the field b_1 due to the magnetization current J_1 and the main field B_1 at the support surface. Further $\xi = x/r_1$ where x is a local linear coordinate defined inside the circle in the right hand part of Fig. 1, and $\xi = \xi_i$ refers to the magnetic field line which touches the support surface from the outside. A particle with Larmor radius a_1 in the field B_1 is then prevented from reaching the same surface when

$$\theta_1 = a_1/r_1 \leqslant \theta_{1c} = \frac{1}{2} \mid F \ln \mid (\xi_i + f)/(\xi_i - f)\mid - \xi_i \mid \quad (1)$$

Two zero lines of vanishing magnetic field strength arise in the plasma region of this plane model when $F > 1 - 1/2f$. The leads become force-free when $F = 2f$.

The real magnetic configuration of Fig. 1 differs somewhat from this two-dimensional model. It includes a small field along the support direction, near the zero-lines of the part of the magnetic field which is perpendicular to the supports [2].

The shielding conditions for the central parts of the confinement region are demonstrated by Fig. 2 for hydrogen ions at the equivalent temperature T_0 and with an average magnetic field strength $\bar{B}_1 = 0.43$ Vs/m^2 at the supports of F IV.

2.1.2. Plasma equilibrium

Magnetic shielding introduces a local disturbance on the magnetic field, and the question arises whether this permits a closed magnetic bottle to be established. An analysis of the average particle drifts from field line to field line does in fact show than an equilibrium is possible when the average magnetic gradient drift forms closed nested contours in the $\alpha\beta$-space defined by the magnetic field lines [3,17]. Such equilibria should exist at sufficiently large support ratios R_s. On the other hand, for systems with R_s close to unity, such as multipole devices with shielded supports in the strongest field region, magnetic shielding should strongly perturb the local field geometry and destroy the equilibrium [13,4].

The plasma losses from the zero lines in the very narrow weak-field regions are expected to become strongly reduced, because the plasma becomes anisotropic in these regions [2,17]. However, there are certain mechanisms which may increase these losses, such as those from trapped particles [5] and instabilities [3], and which require special attention.

2.2. Stability

Internal ring systems of the present type can be stabilized by strong magnetic shear from a superimposed toroidal field [2,6,18] or by a field with minimum average B-properties [18]. These possibilities have not yet been used in F IV and similar devices [19], because the dominating losses are so far of classical origin only. That such devices should still become flute stable can be explained by the joint action of the finite Larmor radius and magnetic line-tying effects, in combination with an appropriate density distribution of the plasma [20]. Thus, the short connection length of the field lines and the contact between the outermost plasma layers and the cathode plate in Fig. 1 puts a strong constraint on the plasma boundary layers.

If this type of flute stabilization also works at extremely high temperatures, it may provide an alternative to the methods of shear and minimum average B-stabilization. It introduces less restrictions on the field geometry than these latter methods which are limited to specific classes of magnetic bottles.

It has finally been suggested by one of us (B.L.) to introduce a separate "boundary (bd) discharge" along the magnetic field to improve the electrical contact between the plasma and a limiter like the cathode plate, whenever this becomes necessary.

2.3. The plasma balance

2.3.1. The fully ionized state of a non-rotating plasma

In a stable quasi-stationary state the total energy losses $\Lambda = \Lambda_{\parallel} + \Lambda_{\perp}$ of the plasma in a configuration of the type given by Fig. 1 consist of one part $\Lambda_{\parallel}$ due to heat, ionization and excitation radiation losses from plasma escaping along the field lines, and one part $\Lambda_{\perp}$ due to losses across the magnetic field. Thin partially ionized wall layers are formed from plasma particles escaping along the field lines. At the present temperatures the layer thickness becomes several ion mean free paths [21,22]. The heat losses of a hydrogen plasma are then roughly given by [21-23]

$$\Lambda_{\parallel} = \kappa_w \Lambda_s \ (1 + f_{we}) \tag{2}$$

$$\Lambda_{\perp} = 4\pi k_2 (\ln\Lambda_D) k_B^2 c_1 N_0^2 T_0^{1/2} \ (r_{02} + r_{01}) L/(r_{02} - r_{01}) \tag{3}$$

where

$$\Lambda_s = (25\pi/2m_p)^{1/2} c_2 k_B (\overline{B_0/B_1}) \ (r_{02}^2 - r_{01}^2)(kT_0)^{3/2} \bar{B}_0 N_0 \tag{4}$$

$$f_{we} = f_{en}\sigma_{en} \left[(72c_1/25m_e \xi_w \sigma_{inw})(\pi m_p k T_0/2)^{1/2} \right]^{1/2} \tag{5}$$

$$k_B = \left[T_b/129 \ (\ln\Lambda_D) \ \sigma_{inb} \ (8m_p k/\pi)^{1/2} \right]^{1/2} \tag{6}$$

In eq. (2) κ_w is the longitudinal loss factor, being equal to 1 when plasma and heat escapes to a wall surface along the field lines, all around the perimeter of the device. With the unmagnetized supports of F IV the same factor becomes $\kappa_w = 0.060$, and in the case of vanishing support loss $\kappa_w = 0$. Further, k_2 represents the transverse heat conductivity which in MKS units has the values 1.50×10^{-42} and 1.87×10^{-43} according to Spitzer [24] and Thompson [25], Λ_D is the ratio between the Debye distance and the impact parameter, $c_1 \approx 0.76$ and $c_2 \approx 0.62$ are dimensionless constants, $N_o = \bar{n}_o/k_B\bar{B}_o$ and $N_{no} = n_{no}/k_B\bar{B}_o$ where n_o and n_{no} are the average densities of the fully ionized plasma and the neutral gas blanket and the relation between N_o and N_{no} is given elsewhere [22,23], T_o is the temperature in the central region of the plasma, r_{01} and r_{02} are the radial extensions of the confinement region in the equatorial plane of Fig. 1, $L = V/\pi(r_{02}^2 - r_{01}^2)$ and V are the effective length and volume of the same region, m_p and m_e are the masses of a proton and an electron, σ_{en} and σ_{in} the cross sections for electron-neutral and ion-neutral collisions with subscripts ($_w$) and ($_b$) denoting values at a wall and in the boundary region, ξ is the ionization rate, and a bar indicates meanvalue formation over the plasma.

If an azimuthal high-frequency current of peak value $\tilde{J}_\varphi$ is induced in the plasma, the Ohmic heating power becomes

$$P_\varphi = 64.5\pi\ (\ln\Lambda_D)\ (r_{02} + r_{01})\tilde{J}_\varphi^2/\delta_\varphi\ (r_{02} - r_{01})T_o^{3/2}\ L \tag{7}$$

The coefficient δ_φ depends on the distribution of the heating power over the plasma volume.

The results of eqs. (2) - (7) are illustrated by Fig. 3 for k_2 given by Spitzer and parameter values roughly corresponding to the present experiments.

2.3.2. The minimum-P effect

The plasma cannot be sustained in a fully ionized state unless the power input is kept above a certain sharply defined minimum level and a corresponding minimum temperature T_{om} which are determined by the plasma balance [21,22]. As

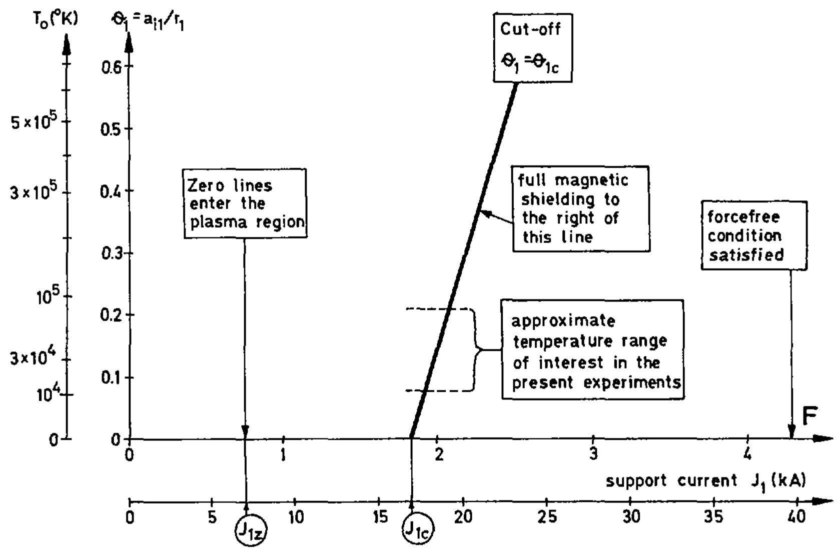

FIG. 2. Calculated conditions for support shielding of hydrogen ions of equivalent temperature T_0 at an average magnetic field strength $\bar{B}_1 = 0.43$ Vs/m in F IV.

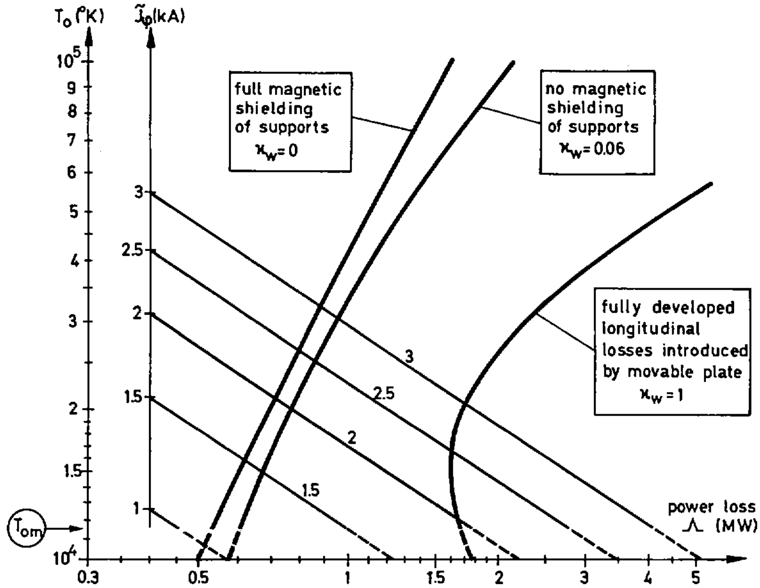

FIG.3. Calculated total power loss Λ as a function of the central plasma temperature T_0 under conditions corresponding to F IV. Hf heating by current $\tilde{J}_\varphi$ at $\delta_\varphi = 0.1$ given by oblique lines.

soon as T_o becomes less than T_{om} there is a sudden transition to a lowly ionized state, as demonstrated earlier [26,27]. This level has been indicated on the temperature axis of Fig. 3.

3. EXPERIMENTAL ARRANGEMENT

The confinement region is denoted by the shaded area in Fig. 1, as given by earlier calculations [28,22]. The plasma boundaries are defined by the field lines which graze the anode rings and the cathode plate. In the equatorial plane the average magnetic field strength is $\bar{B}_o = 0.32$ Vs/m^2, and at the supports $\bar{B}_1 = 0.43$ Vs/m^2.

Three pairs of divergent supports having a mean ratio $R_s \simeq 5$ suspend the main coil. The supports can be magnetized by a pulsed current J_1 which varies in time as shown by Fig. 6, so far with the peak values up to $J_{1max} = 23$ kA. The pulses are generated by a condenser bank connected to the primary winding of a pulse transformer having three secondary windings.

A movable glass plate shown in Fig. 1 can be raised such as to cover the internal area of the main coil. With the plate in this position the longitudinal loss factor becomes $\kappa_w = 1$. With the plate removed, the same factor is reduced to $\kappa_w = 0.060$ for unshielded supports, and is expected to decrease further to zero when full magnetic shielding can be performed.

All discharges have been run with hydrogen at a density n_{no} of the neutral gas corresponding to about 30×10^{-3} mm Hg pressure and a mean density $n_o \approx 10^{21} m^{-3}$ of the fully ionized plasma.

High-frequency power tuned to the lowest magneto-acoustical plasma resonance [2], at about 1.2 MHz, is fed into the plasma by means of a pair of generator coils, with currents being in the same phase. The hf power source consists of a pulsed class-C oscillator connected to a tank circuit formed by the generator coils and an external assembly of hf condensers.

One example of the different types of operation of the device is given by Figs. 4 and 5. A rotating plasma is created by a first condenser bank connected at time t = 0 between the anode rings and the cathode plate. A fully ionized plasma is then generated, and is further accelerated and heated by switching on a second condenser bank at time t_2. Later at t_o, hf heating is superimposed on the shear heating of the rotating plasma. At this moment the plasma is hot enough for a good coupling and matching to the hf source. The rotation is then allowed to decay slowly, the plasma heating being gradually taken over by the oscillator. Finally, at time t_s , the rotation is stopped by a short circuit. The plasma is then sustained by hf heating only.

To investigate the influence of line-tying effects on the flute-stability of the plasma, the device of Fig. 1 has also been equipped with electrodes for discharges along the boundary. Only one of the bd-electrodes in Fig. 1 is used at a time in combination with the cathode plate. As far as can be seen from the present experiments, such bd-discharges are necessary only within a restricted range of the plasma parameters. They are only used in the experiments of Section 4.2, to obtain a better understanding of the way in which the boundary conditions affect the plasma stability.

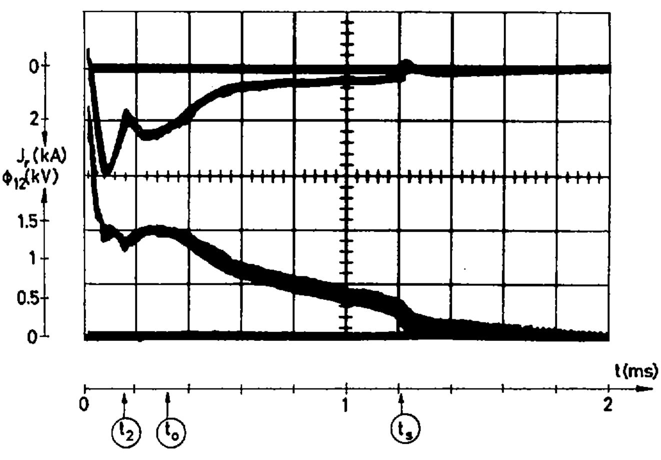

FIG.4. Current J_r and voltage Φ_{12} between anode rings and cathode plate of a rotating plasma mode being stopped by a short-circuit at t_s.

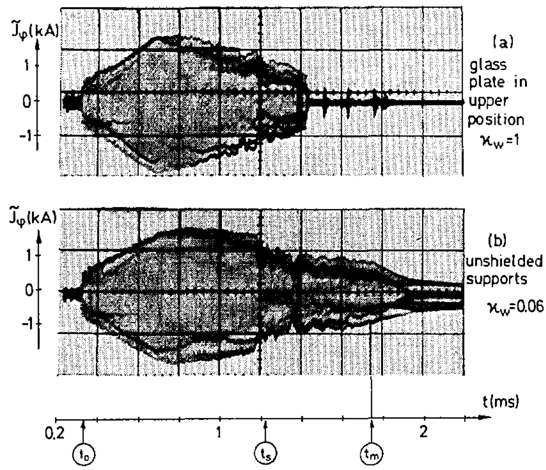

FIG.5. Azimuthal hf plasma current $\tilde{J}_\varphi$ as a function of time. Unshielded supports. (a) Movable plate introduced, $\kappa_W = 1$; (b) Plate removed, $\kappa_W = 0.060$.

The diagnostical methods reported here are limited to measurements of the voltage ϕ_{12} and the current J_r between the anode rings and the cathode plate, and of the azimuthal high-frequency current $\tilde{J}_\varphi$ as recorded by the Rogowski coil placed around the plasma in Fig. 1. However, the present investigations are also intimately connected with an extensive analysis including spectroscopic, microwave, and probe measurements earlier made with devices closely related to F IV [19,22,27,29,30].

4. EXPERIMENTAL RESULTS

4.1. High-frequency power absorption

We first turn to the power balance of the plasma in absence of magnetic shielding. At an initial d.c. voltage ϕ_0=18 kV of the oscillator power source, Fig. 5b shows that it is possible to keep the plasma in a fully ionized state, somewhat above the minimum power level P_m and minimum temperature T_{om}. This is the case both during the period $t < t_s$ of plasma rotation, and during times $t_s < t < t_m$ where the plasma is sustained by hf heating only. The plasma balance breaks down at $t = t_m$ where the azimuthal current $\tilde{J}_\varphi$ drops rapidly to a low level. The reason for this is that the voltage ϕ_0 of the oscillator is limited in time and decreases for times $t > 1.6$ msec. As a consequence, the minimum power is passed near $t = t_m$.

The heating power can be estimated from a comparison with earlier experimental investigations on the minimum-P effect [22,27], from Spitzers formula of the plasma resistivity [24] and the induced current $\tilde{J}_\varphi$, and from the calculations demonstrated by Fig. 3. In all these cases the power absorbed by the plasma comes out to be a little more than 0.5 MW during the non-rotating mode.

That power is actually fed into a resonant mode at about 1.2 MHz has been further demonstrated by slightly changing the experimental parameters. Thus, when the oscillator is no longer tuned to the plasma resonance, the current $\tilde{J}_\varphi$ is much smaller than that of Fig. 5b and the power absorption becomes quite small.

4.2. The effect of boundary discharges

To investigate the influence of line-tying effects at the outer plasma boundary special experiments have been made with the bd discharges described in Section 2.2, to separate the power balance from the line-tying mechanism. The supports of the main coil in Fig. 1 were then replaced by three unshielded rods having the longitudinal loss factor $\kappa_W = 0.061$. Hf power was fed into a plasma with gradually decreasing rotation velocity, at an oscillator voltage as low as $\emptyset_0 = 14$ kV to limit the power input and plasma temperature. Under such conditions one should expect line-tying to become less effective, especially when the current to the cathode plate becomes small.

The effect of a discharge between the upper bd electrode of Fig. 1 and the cathode plate is demonstrated by Fig. 7. The results are essentially the same when using the lower bd electrode. Fig. 7a shows the behaviour of the current $\tilde{J}_\varphi$ in absence of the bd discharge. Here the current drops partly on account of the gradually decreasing total power input, but ineffective

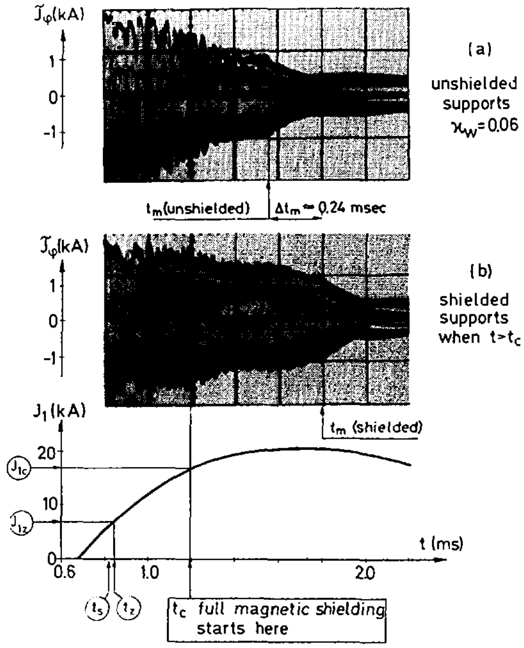

FIG. 6. Non-rotating hf heated mode. (a) Unshielded supports; (b) Supports shielded by current J_1 as seen from curve at bottom of figure.

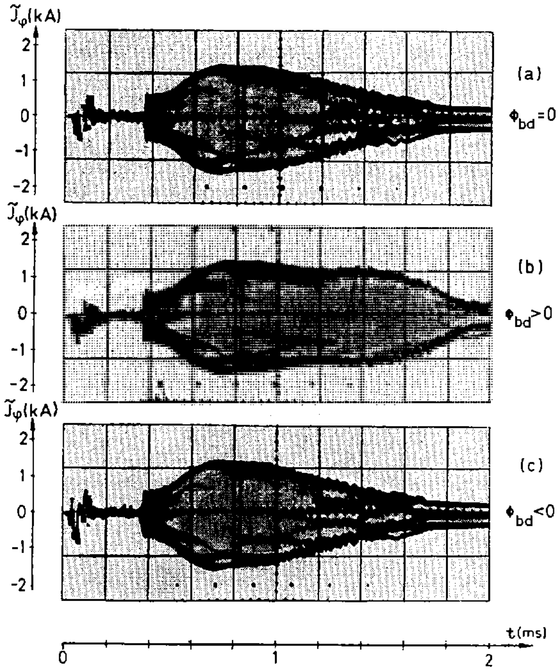

FIG.7. The influence of a boundary discharge by the upper bd electrode. No short-circuit of plasma rotation. (a) No bd discharge; (b) Bd-discharge with positive polarity; (c) Negative polarity.

line-tying and a gradually growing flute instability may also account for the decrease of $\tilde{J}_\varphi$ at the later stages of the discharge.

The latter statement is supported by the fact that a bd discharge of positive polarity ($\emptyset_{bd} > 0$) with respect to the cathode plate allows the plasma to be kept in a fully ionized mode for a much longer time, as shown in Fig. 7b. The current of the bd discharge is in this case $J_{bd} = 300$ A and the corresponding power $P_{bd} \simeq 30$ kW, i.e. only about 5% of the total power input.

Finally, with negative polarity ($\emptyset_{bd} < 0$) and fixed values of J_{bd} and P_{bd}, there is no essential change in the plasma balance compared to $\emptyset_{bd} = 0$, as shown by Fig. 7c.

These results can be interpreted as follows:

(i) The bd discharge should not directly affect the energy balance of the plasma, because P_{bd} is small compared to the total power input, the bd discharge does not feed power into the central parts of the plasma, and entirely different results are obtained with the same P_{bd} but reversed polarity.

(ii) The bd discharge may on the other hand affect the boundary conditions.

(iii) At a decreasing driving current J_r of the rotating plasma, the electrical contact with the cathode plate may become insufficient, in a way which cannot be compensated by the hf power in the present temperature range.

(iv) With positive bd polarity the currents J_{bd} and J_r are added at the cathode plate. This is expected to improve the line-tying conditions at the plate and may account for the increased duration of the plasma in Fig. 7b. With negative bd polarity, on the other hand, the bd electrode partly takes over the role of the cathode and the local current arriving at the negative electrodes should be essentially the same as without a bd discharge. Therefore Figs. 7a and 7c are expected to have similar properties.

4.3. Magnetic shielding of supports

4.3.1. The effect of the zero lines on a rotating plasma

If the support current J_1 is switched on during the rotating plasma mode, without an applied hf power, the electrode voltage ϕ_{12} and the current J_r behave as shown in Fig. 8. At time t_z there is a sudden and steep decrease in the voltage. This occurs almost exactly at the point where the support current passes the value J_{1z} and the zero lines enter the plasma region.

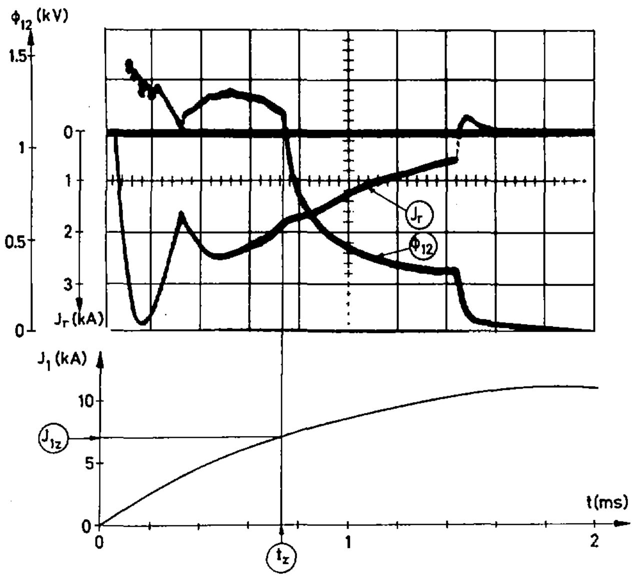

FIG.8. Zero line effect on rotating plasma. The abrupt change in the derivative of the voltage Φ_{12} at t_z occurs at $J_1 \cong J_{1z}$ where the zero lines should appear in the plasma.

By taking the size of the weak-field region [3] into consideration, the thermal resistance due to the zero lines can be estimated to about 1 ohm at $T_o = 3\times10^4$ °K, and it should vary as $1/T_o^{13/6}$. This agrees rather well with the experimental observations. Further, the applied electric field at $t=t_z$ in Fig. 8 is not far from that required for run-away phenomena, but these are less likely to arise in the present type of magnetic field.

4.3.2. The high-frequency heated non-rotating plasma

We now turn to the behaviour of the hf heated plasma in Figs. 5 and 6 at times $t > t_s$ where the rotation has been stopped:

(i) In Fig. 5a where fully developed longitudinal losses are caused by the glass plate, the hf power is insufficient to sustain the plasma and the balance of the latter breaks down at an early stage. Further, the oscillator stops at t = 1.24 msec., on account of an overvoltage produced by a strongly decreased loading. This is consistent with the results of Fig. 3 for κ_w = 1 and 0.06. Thus, Figs 5 a and 5b indicate that the transverse power loss, which may possibly arise from instabilities, is in any case small compared to the longitudinal losses in the present range of κ_w.

(ii) When proceeding from Fig. 5a to 5b and from 6a to 6b there is a gradual increase in the duration of the fully ionized state, which is characterized by large currents $\tilde{J}_\varphi$ and strong power absorption. Irrespective of the experimental details, this is in itself an indication that the losses of the system should decrease when passing from $\kappa_w = 1$ to a system with unshielded supports having $\kappa_w = 0.06$, and further to one with magnetically screened supports where we expect $\kappa_w \simeq 0$.

(iii) At support currents $J_1 < J_{1c}$ and times $t < t_c$ no effective shielding should arise according to Fig. 2. Further, when a plasma equilibrium becomes possible, some of the external parts of the confinement region may still get lost on account of the introduced magnetic field perturbations [3,4,17]. A slight increase in the losses should then be expected to occur from support magnetization in the range $0 < J_1 < J_{1c}$. During the time interval $t_z < t < t_c$ a comparison between Figs. 6a and 6b shows that there is no detectable change in the plasma behaviour when the magnetic shielding is switched on, even if the local field at the supports becomes strongly perturbed and 6 zero lines arise inside the plasma confinement region. Similar results have been obtained also for maximum support currents in the range $J_{1z} < J_{1max} < J_{1c}$.

(iv) At support currents $J_1 > J_{1c}$ and times $t > t_c$ an effective shielding should take place according to Fig. 2. This condition is satisfied only during the later part of Fig. 6b, i.e. when $t > t_c$. From Figs 6a and 6b is seen that there is an elongation $\Delta t_m \simeq 0.24$ msec. in the duration of the fully ionized plasma state when magnetic shielding is expected to take place. Further, the amplitude of $\tilde{J}_\varphi$ is clearly seen to be larger in the shielded than in the unshielded case.

(v) With a power input having the initial value $P_{\varphi 0} = 0.8$ MW and decreasing linearly at the rate $dP/dt = -0.4$ MW/msec., Fig. 3 yields a time delay $\Delta t_m = 0.15$ msec. and about a 15% increase in the amplitude $\tilde{J}_\varphi$ when the transition is made from unshielded ($\kappa_W = 0.06$) to fully shielded ($\kappa_W = 0$) supports. Thus, the obtained and estimated time delays and current amplitudes are of the same order of magnitude. It is further obvious from Fig. 3 that the transverse losses $\Lambda_\perp$ dominate the heat balance at the present small values of κ_W, low temperatures, and weak magnetic fields in device F IV. The present results can therefore only be taken as a first indication that magnetic shielding of the supports improves the plasma confinement.

5. CONCLUSIONS

From the present results, which are partly on a preliminary stage and should be extended to wider ranges of the parameters involved, the following conclusions can be drawn:

(i) A fully ionized non-rotating plasma of density 10^{21} m^{-3} can be sustained above the minimum power level by hf heating. The absorbed power is about 0.5 MW, during times being long compared to the plasma relaxation times and to the growth rates of a flute instability.

(ii) The present and earlier experiments suggest that magnetic line-tying is essential to the stability of the outer plasma boundary. This is supported by the fact that weak discharges, running along the field lines in the boundary region and having negligible direct influence on the absorbed power, strongly affect the plasma balance under special conditions.

(iii) The zero lines of the shielded supports produce a rather strong brake on a rotating plasma, as expected from theory.

(iv) There are two important ranges of the support current J_1 in a non-rotating plasma. The first is given by $J_{1z} < J_1 < J_{1c}$ and the second by $J_{1c} < J_1$, with the zero lines entering the plasma at J_{1z}, and cold ions being shielded from the support surfaces at J_{1c}. For systems having large support ratios R_s, theory predicts a slight increase in the plasma losses in the first range, whereas the plasma confinement should become improved in the second range.

(v) In the experiments there is no detectable change in the plasma confinement and balance when $J_{1z} < J_1 < J_{1c}$, even if the zero lines should then appear in the plasma and the local magnetic field near the supports becomes strongly perturbed.

(vi) When $J_1 > J_{1c}$ the experiments yield a small but detectable reduction in the power loss, on account of magnetic shielding. This reduction is too small for far-reaching conclusions to be drawn about the efficiency of magnetic shielding, but it is on the other hand, of the magnitude expected from theory.

To investigate the problem of magnetic shielding further, the experiments have to be extended to higher temperatures, larger dimensions and stronger magnetic fields.

ACKNOWLEDGEMENTS

The authors are indebted to Messrs S. Holmberg, D. Haslbrunner, R. Ekman, P. Mattson, G. Hägerström, G. Kindberg, L. Westerberg and S. Hillberger for valuable help with the construction and building of the experimental equipment, and for valuable assistance in the experimental work. This investigation has been supported financially by the Swedish Atomic Research Council and the Bank of Sweden Tercentenary Fund.

REFERENCES

[1] LEHNERT, B., Nature, Lond. 181 (1958) 331.

[2] LEHNERT, B., J. Nucl. Energy C 1 (1959) 40.

[3] LEHNERT, B., Plasma Physics 10 (1968) 263 and 281.

[4] LEHNERT, B., Physics Fluids 12 (1969) 2710.

[5] RUSBRIDGE, M.G., Plasma Physics 13 (1971) 33.

[6] FREEMAN, L., JOHNSON, M., OKABAYASHI, M., PACHER, G., SCHMIDT, J. and YOSHIKAWA, S., Fourth European Conf. on Controlled Fusion and Plasma Physics, C.N.E.N., Rome, Aug. 31-Sept. 4 (1970).

[7] OHKAWA, T., SCHUPP, A.A., VOORHIES, H.G., and YOSHIKAWA, M., Proc. Int. Conf. on Plasma Phys. and Controlled Nucl. Fusion Res. Culham 1965, Vol 2, p. 531, IAEA, Vienna.

[8] DORY, R.A., KERST, D.W., MEADE, D.M., WILSON, W.E., and ERICKSON, C.W., Physics Fluids 9 (1966) 997.

[9] DELLIS, A.N., ALLEN, T.K., HARDCASTLE, R.A., PRENTICE, R. and REYNOLDS, D.A., Bull.Am.Phys.Soc. 13 (1968) 1527.

[10] BURKHART, L.C., DiMARCO, J.N., HAMMEL, J.E., HENSON, R.M., and KARR, H.J., Physics Fluids 11 (1968) 1562.

[11] FORSEN, H.K., KERST, D., LENCIONI, D., MEADE, D., MILLS, F., MOLVIK, A., SCHMIDT, J., SPROTT, J., and SYMON, K., Plasma Physics and Controlled Nuclear Fusion Research, IAEA, Vienna, Vol. I (1969) 313.

[12] FORSEN, H.K., MOLVIK, A.W., and SPROTT, J.C., Bull.Am. Phys. Soc. 13 (1968) 266.

[13] MEADE, D.M., Physics Fluids 11 (1968) 2497.

[14] YOSHIKAWA, S., Physics Fluids 11 (1968) 2777.

[15] OHKAWA, T. and ROSTOKER, N., Physics Today 20(1967)48.

[16] YOSHIKAWA, M., OKHAWA, T., and SCHUPP, A.A., Physics Fluids 11(1968)2265.

[17] LEHNERT, B., Nuclear Fusion 10(1970)283.

[18] YOSHIKAWA, S., and CHRISTENSEN, U. Physics Fluids 9(1966)2295.

[19] BERGSTRÖM, J., HOLMBERG, S., and LEHNERT, B., Proc.Int.Conf. on Plasma Phys. and Controlled Nucl. Fusion Res. Culham 1965, Vol. 1, p. 341, IAEA, Vienna.

[20] LEHNERT, B., Physics Fluids 9 (1966)1367.

[21] LEHNERT, B., Arkiv Fysik 38(1968)499.

[22] LEHNERT, B., BERGSTRÖM, J., HOLMBERG, S., and TENNFORS, E., Electron and Plasma Physics, Roy.Inst. of Technology, Stockholm, Rep.69-34(1969).

[23] LEHNERT, B., Nuclear Fusion 8(1968)173.

[24] SPITZER, L., "Physics of Fully Ionized Gases", Interscience Publ., New York(1962).

[25] THOMPSON, W.B., "An Introduction to Plasma Physics", Pergamon Press, Oxford-London-New York-Paris (1962).

[26] LEHNERT, B., BERGSTRÖM, J., and HOLMBERG, S., Third European Conf. on Controlled Fusion and Plasma Physics, Utrecht, p. 57, Wolters-Noordhoff Publ., Utrecht(1969).

[27] LEHNERT, B., BERGSTRÖM, J., BUREŠ, M., and TENNFORS,E., Fourth European Conf. on Controlled Fusion and Plasma Physics, C.N.E.N.,p.102, Rome(1970).

[28] BONNEVIER, B., Private communication(1968).

[29] VINOGRADOV, N.I., and TENNFORS, E., Third European Conf. on Controlled Fusion and Plasma Physics, Utrecht, p. 56, Wolters-Noordhoff Publ., Utrecht (1969).

[30] LEHNERT, B., BERGSTRÖM, J., HOLMBERG, S., and WILNER, B., Physica Scripta 1(1970)39.

PLASMA CONFINEMENT IN THE JAERI HEXAPOLE WITH HIGH TOROIDAL FIELD

S. TAMURA, H. YAMATO*, T. NAGASHIMA, M. YOSHIKAWA,
H. OHTSUKA, T. SUGAWARA*, T. SHIINA, S. MATSUDA, S. MORI,
Japan Atomic Energy Research Institute,
Toaki, Ibaraki-ken, Japan

Abstract

PLASMA CONFINEMENT IN THE JAERI HEXAPOLE WITH HIGH TOROIDAL FIELD.

The behaviour of a plasma confined in a toroidal hexapole configuration (JFT-1) is studied with and without superposition of a toroidal magnetic field (B_θ). The quasi-stationary hexapole field is produced by three current-carrying hoops which are held in place by supports. The average hexapole field strength on the stability limit line is up to 2800 G, which corresponds to an average of 8 gyroradii between the separatrix and the stability limit line for 20 eV hydrogen ions.

Plasmas, produced either by microwave heating at the electron cyclotron frequency ($kT_i < kT_e \sim 1$ eV, $n \sim 3 \times 10^{10}$ cm^{-3}) or by a coaxial gun ($kT_e < kT_i \sim 20$ eV, $n \sim 10^{11}$ cm^{-3}), are stably confined in the hexapole without noticeable fluctuations in the interior of the the plasma. Measurement of particle loss shows that most of the plasma is lost across the magnetic field to the hoops and walls for microwave-produced plasmas. The particle life-time is typically 1.2 ms and is consistent with the result of particle loss measurements. The life-time of the gun-injected plasma at higher magnetic fields is limited by the particle loss to the supports. At lower magnetic fields, the life-time agrees with the virtual confinement time calculated from the perpendicular loss rate. It approaches to the support loss time as the magnetic field is increased. This feature is also consistent with the observed diffusion coefficients.

The application of a high toroidal magnetic field of up to 920 G near the separatrix has no marked effect on the overall confinement properties of plasmas.

I INTRODUCTION

In recent years important contributions to toroidal confinement research of low-β plasmas have been made by a number of confinement experiments in the multipole configurations [1~5]. The influence of a toroidal magnetic field on plasma confinement in the multipole systems has also been discussed in several papers [4,6].

Experiments with a toroidal hexapole device have been carried out at JAERI since 1969 [7]. A toroidal magnetic field (B_θ) of up to 920 G near the separatrix has been superimposed on the hexapole field to investigate how the added B_θ field influences the behavior of confined plasmas.

In this paper are described the overall confinement properties of plasmas, produced either by microwave heating or by a coaxial gun, in the hexapole configuration both with and without toroidal magnetic field.

* On leave from The Research and Development Center, Tokyo Shibaura Electric Co., Ltd., Kawasaki, Japan.

II APPARATUS

A cross-sectional view of the hexapole device is shown in Fig.1. The machine parameters are summarized in Table I. The hexapole field is produced by three concentric current-carrying hoops (HC-1 and HC-2's in Fig.1) which are held in position by 4-mm-diam rod supports. The hoops consist of multi-turns of copper wire and are energized by a condenser bank of 28400 μF charged up to 3 kV. The quarter period of the current is about 8 msec.

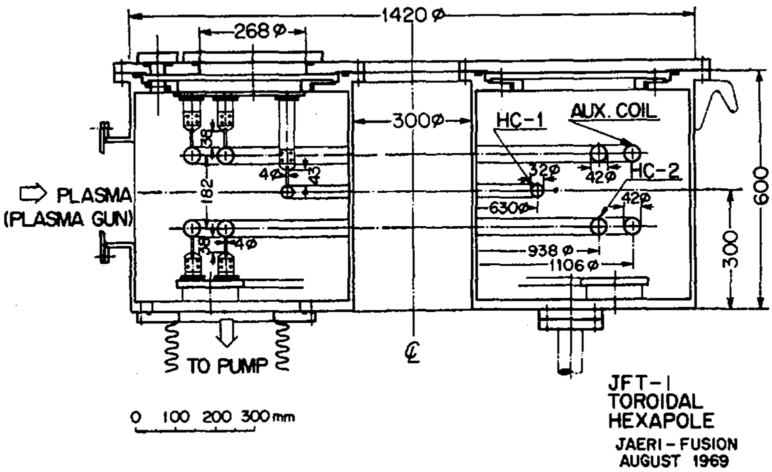

FIG.1. Cross-sectional view of the hexapole device (JFT-1).

The field pattern of the hexapole is shown in Fig.2 (a) together with the location of limiters used as particle loss detectors. In calculating the field pattern, circumferential currents in the walls of the vacuum chamber due to time-varying hexapole field are included and the field parameters (flux function, etc.) are obtained as a function of time. The field configuration changes in general with time as the wall currents decay, but it remains almost stationary for several milliseconds near the field maximum.

A toroidal field of up to 1.4 kG at the minor axis and the duration of about 5 sec can be applied to the plasma by energizing a 400 kAT toroidal winding (not shown in Fig.1). With the addition of a B_θ the magnetic configuration becomes a stellarator-like field with a large rotational transform and large shear. In Fig.2 (b) the rotational transform $\iota/2\pi = 2\pi/\oint(B_\theta/RB_P)dl$, where B_P is a poloidal field is plotted against flux function (ψ).

Plasmas have been produced either by microwave electron resonance heating at 12 cm wavelength or by a coaxial plasma gun.

TABLE I. MACHINE PARAMETERS

1.	Major radius	43.5 cm
2.	Position of ψ_C and the field strength at the point	28.5 cm, 13 kG and 52.0 cm, 1.14 kG on the median plane from the major axis 6.3 cm vertical from the median plane where the field is the local minimum, 1.98 kG
3.	Average magnetic field strength on ψ_C	$\langle B\rangle = (\oint dl)/(\oint dl/B) = 2.76$ kG
4.	Distance between ψ_S and ψ_C in units of gyroradius of 20 eV hydrogen ions	7.6
5.	Plasma volume inside of ψ_C	6.8×10^4 cm^3
6.	Total surface area of the hoop supports and the current feeds	69 cm^2
7.	Toroidal magnetic field	400 kAT pulsed with duration of 5 sec B_θ at outer ψ_C on the median plane (52.0 cm) = 1.18 kG

Microwave power at frequency of 2.45 GHz is injected into the chamber filled with working gas (usually hydrogen) at pressures around 10^{-5} Torr with no preionization. The incident power is up to 3 kW with pulse length of 0.5 msec. The gas is ionized and heated to produce a cold ion plasma ($kT_i < kT_e \sim 1$ eV) with densities of $10^{10} \sim 10^{11}$ cm^{-3} and electron temperatures of typically $0.2 \sim 2$ eV in the afterglow. Plasmas can also be injected by a coaxial gun which produces about 10^{18} particles with a mean energy of 50 eV. The plasma is guided through an expansion chamber by a pulsed linear octopole guide field. Usually the plasma is injected after the peak of the hexapole field (~9 msec). The initial plasma density in the hexapole can be varied from 10^8 to 10^{12} cm^{-3} by varying the guide field. The ion and electron temperatures are approximately 10 and 3 eV, respectively, at 0.6 msec after the injection.

Electron temperatures are determined by Langmuir probe characteristics, and plasma densities are determined both by probes and by a microwave interferometer. Ion temperatures

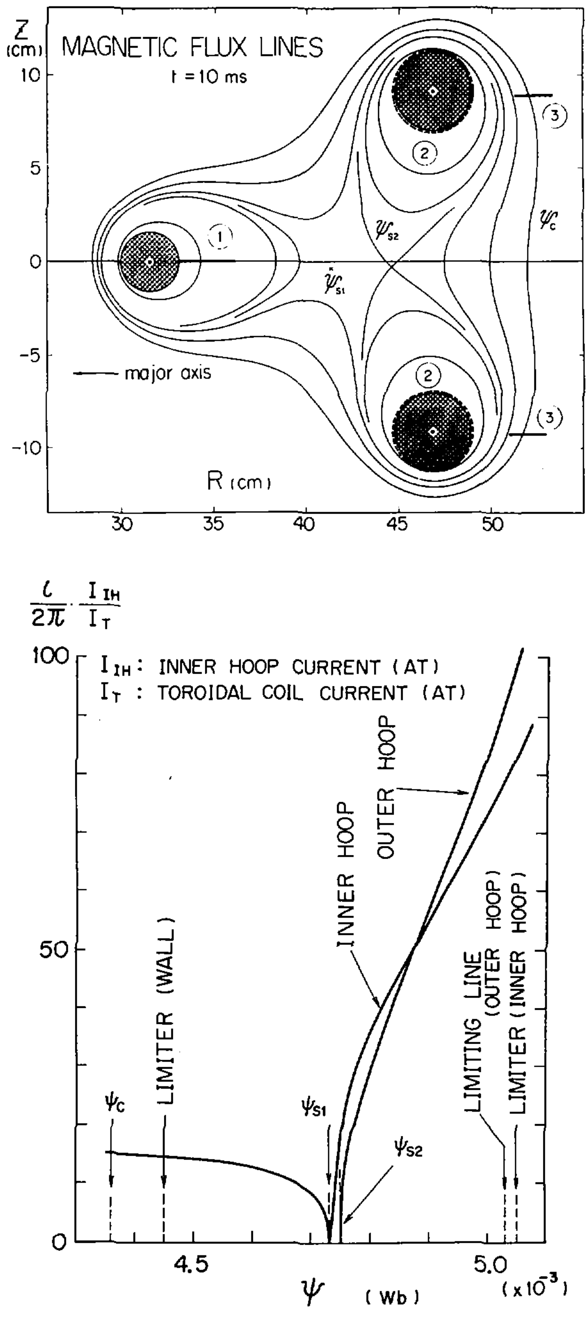

FIG.2. (a) Hexapole flux configuration. Also shown are the limiters used as particle loss detectors: ① inner hoop limiter detectors, ② outer hoop loss detectors, and ③ wall limiter detectors. (b) Rotational transform versus flux function. Differentiation of $\iota/2\pi$ with respect to ψ gives shear.

are measured using a gridded electrostatic probe. Various types of particle loss detectors are used to estimate the plasma loss fluxes (Fig.2 (a)).

III EXPERIMENTAL RESULTS

MICROWAVE-PRODUCED PLASMAS

The microwave pulse is applied typically at 8.5 msec after the initiation of the hexapole field. Within the range of typical experimental parameters used, high-energy electrons do not influence the experiments. The average magnetic field on ψ_c ($\langle B \rangle$) is typically 1.38 kG and this corresponds to an average of 18 gyroradii between ψ_s and ψ_c for 1 eV protons.

As is usually done in confinement experiments with internal conductor systems [2,3,4], confinement is evaluated by measuring particle loss fluxes in different directions. At the densities in the present experiment, recombination loss is negligible. The results are summarized in Figs.3 and 4. In Fig.3 the relative ratios of the integrated loss fluxes in different directions to the total loss are shown for various

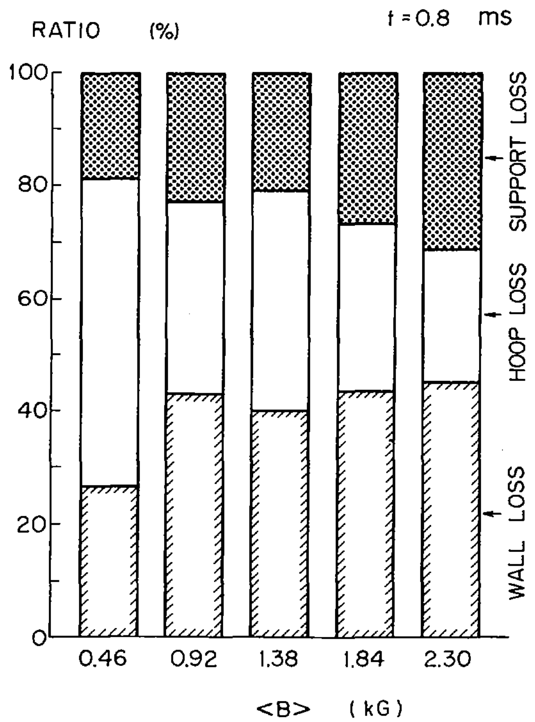

FIG.3. Particle losses in different directions divided by the total loss flux obtained from loss flux measurements for microwave-produced plasmas. Time is measured after the microwave power is switched off. Relatively large hoop loss at $\langle B \rangle$ = 0.46 kG is due to resonance zones localized in regions very close to the hoops.

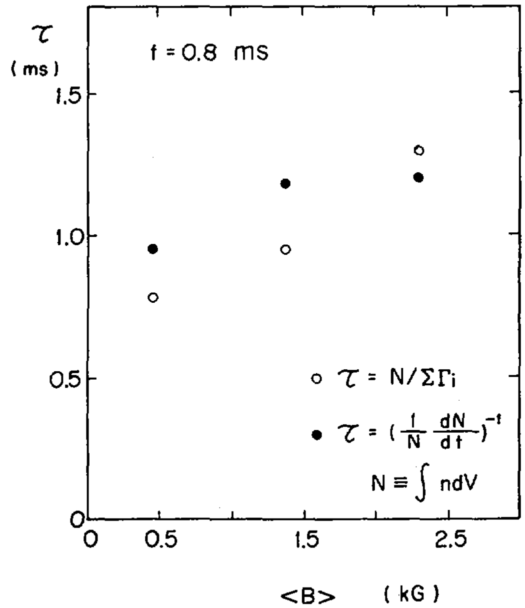

FIG.4. Confinement times of microwave-produced plasmas estimated from loss flux measurements and the decay of the total number of particles versus average hexapole field strength.

average magnetic fields at 0.8 msec after the microwave is turned off. The plasma is lost largely across the magnetic field. The fractional losses of plasma in different directins are almost independent of the hexapole field over the range of $\langle B \rangle$ greater than about 1 kG. In the hoop loss the outer hoop loss is dominant. As the density decays, these fractional losses remain almost unchanged.

Confinement times are estimated in two different ways:
(1) The number of particles confined in the hexapole field at time t is determined by integrating the density distribution over the plasma volume as $N(t) = \int n(\psi,t)V'(\psi)d\psi$, where n is the density obtained from Langmuir probe measurements, and the confinement time is calculated from $\tau = N/(dN/dt)$.
(2) Using the total loss rate $\Gamma(t)$ at a given time obtained from loss flux measurements, the confinement time is calculated from $\tau = N(t)/\Gamma(t)$. Confinement times estimated from these two methods are in good agreement as shown in Fig.4. Similar agreement between them is also obtained as the density decays. The accuracy of measurements of particle loss fluxes is examined by comparing the decrease in the total number of particles (ΔN) in time Δt with the total particle loss during this time ($\Gamma \cdot \Delta t$) at t = 0.8 msec. It is found that the relation $\Delta N = \Gamma \cdot \Delta t$ holds within 20 %.

A B_θ field of up to 380 G on the median plane at outer ψ_c is added to the hexapole. This B_θ field produces rotational transform $\iota/2\pi$ of about 7 at ψ_c. The density profile on the median plane shifts outwards as the B_θ is increased because resonance zones shift towards the walls due to increase in the resultant magnetic field. The confinement time is estimated as before and found to be slightly longer than without B_θ, but no marked effect on the overall confinement properties (loss fluxes and their relative ratios, etc.) has been observed by the application of B_θ.

GUN-INJECTED PLASMAS

The plasma from a coaxial gun is injected into the hexapole and the subsequent behavior of the plasma has been investigated. The azimuthal motion of the plasma subsequent to the injection vanishes, in most cases, in about 0.3 msec for hydrogen plasmas with ion energies of approximately 20 eV. The plasma density in the hexapole thereafter becomes almost uniform in the azimuthal direction. The electron temperature and the ion temperature are plotted in Fig.5 as a function of time. Also shown is the plasma density obtained from the probes near ψ_s.

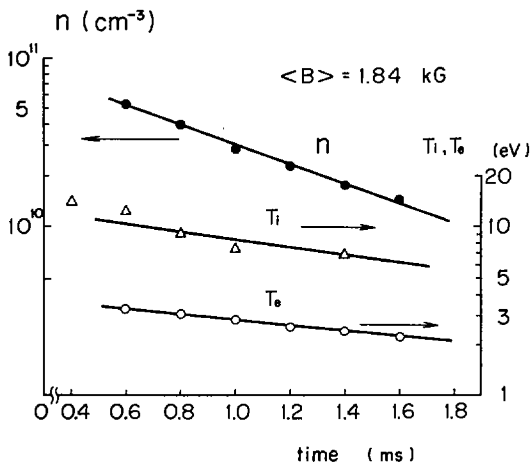

FIG. 5. Plasma density, ion temperature, and electron temperature measured near ψ_s for gun-injected plasmas. Time is measured from the firing of the gun.

The confinement time is estimated in the same way as described previously. The confinement time is typically 1 msec and is only weakly dependent on the hexapole field. It is almost independent of the superimposed toroidal field. The relative ratios of particle losses in different directions are shown in Fig.6. The ratio of the support loss increases with the average hexapole field; the support loss is the dominant loss at higher magnetic fields. This is confirmed by introducing extra supports in the plasma. The confinement time is found to scale with the surface area of the supports to a good approximation.

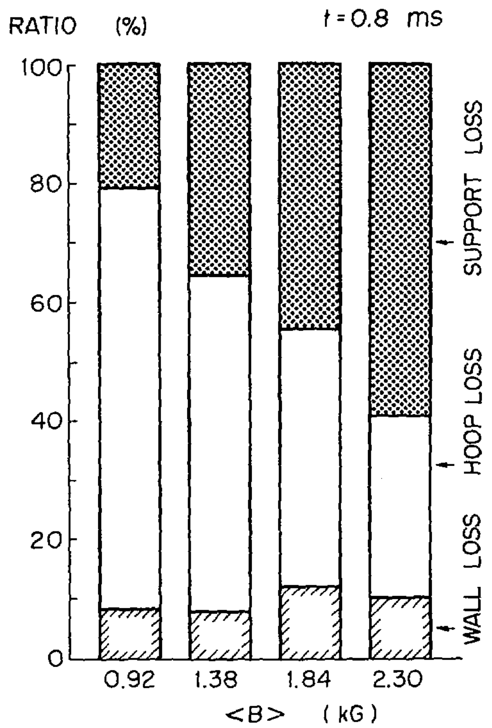

FIG.6. Particle losses in different directions divided by the total loss flux for gun-injected plasmas. Time is measured from the firing of the gun.

An estimate of diffusion coefficients is made by measuring the loss fluxes of particles across flux surfaces and the density profiles. If the density is assumed to be constant on flux lines ψ = const, the following equation is obtained: $\Gamma = \langle D\rangle (\partial n/\partial \psi) \oint 2\pi R^2 B_p dl$, where Γ is the particle flux across a given flux surface and $\langle D\rangle$ is defined by $\langle D\rangle = \oint D R^2 B_p dl / \oint R^2 B_p dl$. The results are summarized in Fig.7. The measured diffusion coefficients $\langle D\rangle$ are shown as a function of average hexapole field on the flux surface where $\langle D\rangle$'s are evaluated. In calculating $\langle D\rangle$ the density gradients $\partial n/\partial \psi$ are evaluated at positions one gyro-orbit of 10 eV protons inside of the limiting flux surfaces. The observed $\langle D\rangle$'s are almost linearly dependent on magnetic field and are at least an order of magnitude less than the Bohm diffusion coefficient defined by $\langle D_B\rangle = (T_e/16) \times (\oint R^2 dl / \oint R^2 B_p dl)$. The observed diffusion coefficient near the outer hoops is approximately an order of magnitude larger than those observed near the inner hoop and the wall. This in fact causes large particle loss to the outer hoops, but underlying physical mechanisms are still unexplained. Superimposed toroidal fields have no significant effect on the diffusion coefficients as shown in Fig.7.

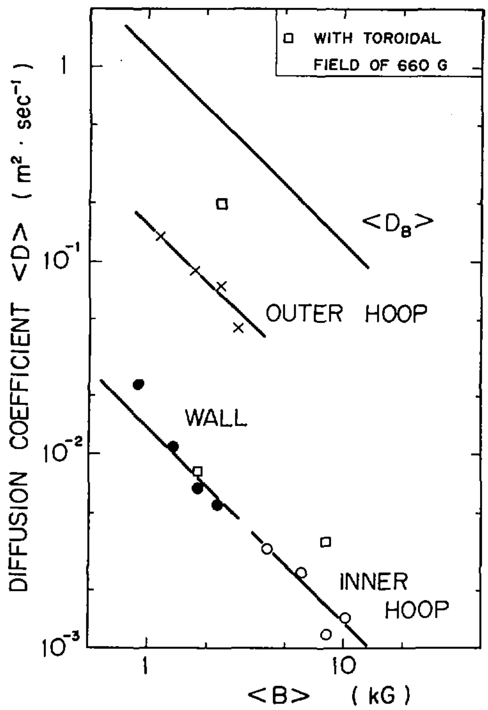

FIG.7. Diffusion coefficients < D > determined by the measurements of loss fluxes and the density profiles for gun-injected plasmas when the hexapole field is varied. Note that here < B > is the hexapole field averaged on the flux surface where diffusion coefficients are evaluated (not on ψ_c). The squares represent the case where B_θ of 660 G at ψ_s is added to the hexapole field of < B > = 1.84 kG on ψ_c.

IV DISCUSSION

Measurements of the confinement time show that apparently it is limited by the particle loss to the supports at higher magnetic fields for gun-injected plasmas. The experiment with extra supports indicates that the confinement time scales with the surface area of the supports and also that no local enhancement of the particle loss to the hoops and walls is caused by the presence of the supports. These results are consistent with the picture that the loss is to the supports but not due to the presence of the supports. If a virtual confinement time is defined by $\tau_\perp = N(t)/\Gamma_\perp(t)$, where $\Gamma_\perp(t)$ is the perpendicular loss rate, it is dependent on < B > as expected from the observed diffusion coefficients. The observed confinement time agrees well with $\tau_\perp$ at lower < B > and approaches to τ_s at higher < B >, where τ_s is the support loss time calculated from the measured loss flux.

Since the dominant loss for microwave-produced plasmas is apparently the loss across the magnetic field, the virtual confinement time $\tau_\perp$ is much the same as the observed confinement time which is almost independent of $\langle B \rangle$. It seems unlikely that the life time of the microwave-produced plasmas is limited by particle loss due to such field errors as to make particles escape along the field lines away from the confinement region, because the confinement times of almost the same magnitude are obtained with the gun-injected plasmas which have much higher ion and electron temperatures than microwave-produced plasmas. In contrast with the gun-injected plasmas, large density and potential fluctuations with frequencies of up to 100 kHz have been observed near ψ_c, especially in unfavorable regions. These fluctuations are possibly responsible for plasma transport across the magnetic field near the walls. Quantitative studies on the fluctuation-induced loss are now in progress.

The application of a high toroidal field has no significant effect on the overall confinement properties of both the gun-injected and the microwave-produced plasmas. Fluctuations which appear near ψ_c seem to penetrate to the separatrix as the toroidal field is increased. An investigation of these fluctuations is now under way with emphasis on their effects on plasma confinement.

REFERENCES

[1] OHKAWA, T., SCHUPP, A.A., YOSHIKAWA, M., VOORHIES, H.G., Plasma Physics and Controlled Nuclear Fusion Research (IAEA, Vienna, 1966), Vol. II, p. 531.

[2] FORSEN, H., KERST, D., LENCIONI, D., MEADE, D., MILLS, F., MOLVIK, A., SCHMIDT, J., SPROTT, J., SYMON, K., Plasma Physics and Controlled Nuclear Fusion Research (IAEA, Vienna, 1969), Vol. I, p. 313.

[3] YOSHIKAWA, S., BARRAULT, M., HARRIES, W., MEADE, D., PALLADINO, R., VON GOELER, S., Plasma Physics and Controlled Nuclear Fusion Research (IAEA, Vienna, 1969), Vol. I, p. 403.

[4] YOSHIKAWA, M., OHKAWA, T., SCHUPP, A.A., Phys. Fluids 12 (1969) 1926.

[5] OHKAWA, T., YOSHIKAWA, M., KRIBEL, R.E., SCHUPP, A.A., JENSEN, T.H., Phys. Rev. Letters 24 (1970) 95.

[6] LENCIONI, D.E., POUKEY, J.W., SCHMIDT, J.A., SPROTT, J.C., ERICKSON, C.W., Phys. Fluids 11 (1968) 1115.

[7] MORI, S., TANAKA, M., INOUE, K., YAMATO, H., TAMURA, S., KAWASHIMA, N., KUNIEDA, S., International Symposium on Closed Confinement Systems, 1969, Dubna, USSR.

CONVECTIVE MOTION IN THE CLIMAX TOROIDAL QUADRUPOLE DEVICE

A.N. DELLIS, J.H.P.C. MEGAW, R. PRENTICE, C.D. KING
UKAEA Culham Laboratory,
Abingdon, Berks, United Kingdom

Abstract

CONVECTIVE MOTION IN THE CLIMAX TOROIDAL QUADRUPOLE DEVICE.

Plasma confinement in the CLIMAX induced-current toroidal quadrupole has been measured during a period of slow field decay giving ~ 15 ms of experimental time. Hydrogen plasma, peak density $n \sim 10^{12}$ cm^{-3}, $T_i \sim 50$ eV, $T_e \sim 5$ eV, fills the MHD-stable region inside the minimum $U = \oint d\ell/B$ critical surface, ψ_c, in about 100 μs after cross-field injection from a 40 kV conical theta pinch with solenoid guide field. At the maximum ring current used (400 kA total) there are >5 ion gyro-radii between ψ_c and the separatrix ψ_s, and the calculated Bohm time for $T_e = 5$ eV is ~ 220 μs.

The measured potential distribution shows a convective flow of plasma at ~ 10^5 - 10^6 cm/s, around the major azimuth φ, which reverses sign on crossing the separatrix ψ_s. Superimposed on this is a flow across the constant-U flux surfaces, as shown by azimuthal variations in the potential, which produces large-scale convective cells.

The major cause of this flow is localized plasma cooling by neutral gas entering from the plasma gun. Charge neutrality in the presence of ∇B drifts requires that $\partial(nT)/\partial\varphi = 0$ at all times, where $T = T_e + T_i$, and T_i is the mean local ion temperature. A steady-state variation of potential V is produced and satisfies $(\partial V/\partial\varphi) = -(\partial V/\partial\psi)\,[(1/T)(\partial T/\partial\varphi)]/[(1/nU)(\partial(nU)/\partial\psi)]$. The local outward flux of plasma $\Delta\Gamma = nU(\partial V/\partial\varphi)\Delta\varphi$ is positive when $\partial T/\partial\varphi$ is negative.

The original plasma gun, producing > 10^{-4} torr locally, gave density decay times ~ 2 ms independent of B. A modified gun producing much lower neutral gas pressure inside ψ_c has increased this time to ~ 4 ms with ~ B^1 dependence. Where probe current measurements previously showed a similar decay rate both inside and outside ψ_s, the plasma from the modified gun exhibits a decay time for $(nT_i^{\frac{1}{2}})$ which is slower inside ψ_s and exceeds 10 ms near the rings, with $T_e > 3$ eV. Simultaneous injection of neutral gas from a replica of the original gun causes the faster decay to reappear and probe measurements near it show a modification of the plasma flow agreeing with the theoretical model.

Calculation of the total outward plasma flux $\Gamma = \int_0^{2\pi} nU\,(\partial V/\partial\varphi)\,d\varphi$ from the measured values of n and V shows, however, that the convective motion cannot by itself account for the observed plasma loss rate, but is rather a mechanism by which plasma is redistributed inside the trap.

INTRODUCTION

The presence of low frequency electric fields in multipole devices, causing E x B convective motion of the plasma, has been reported by several authors. Some measurements on a toroidal octupole [1,2] have identified this convection as a major source of plasma loss, whilst those on a linear quadrupole [3] showed convection to make little contribution to the losses. The results of a study of plasma convection in the CLIMAX toroidal quadrupole are presented here and show that the convection itself is not directly responsible for the main plasma loss. Preliminary observations of the phenomena have been previously reported elsewhere[4].

APPARATUS

The engineering design of the CLIMAX toroidal quadrupole has been previously described [5]. A schematic cut-away diagram

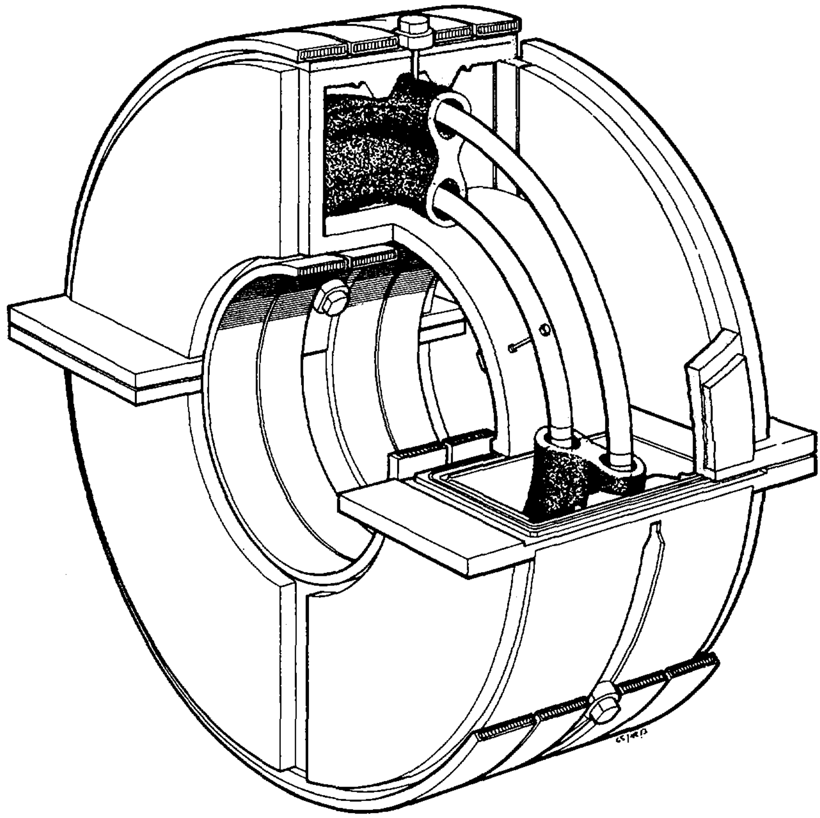

FIG. 1. Simplified diagram of CLIMAX.

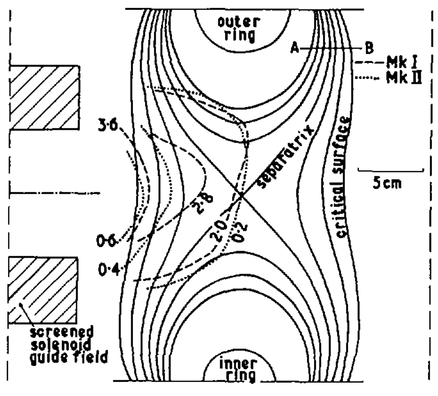

FIG. 2. Partial *minor* cross-section of the CLIMAX tank showing contours of neutral-gas pressure (in units of 10^{-4} torr) superimposed on the computed magnetic field pattern.

of the device is given in Fig. 1. The two coplanar solid copper rings of major diameters 130 and 190 cm are each held in place in the vertical plane by three slender supports. The induced currents of up to 400 kA per ring decay by only 25 per cent in 10 ms.

Toroidal magnetic flux surfaces of constant $U = \oint d\ell/B$ are referred to by the parameter ψ representing, in arbitrary units, the total flux between the surface and the separatrix ψ_s (cf. Fig.2). The minimum U critical surface ψ_c has $\psi = +3$ and negative ψ values are used to label the private flux surfaces encircling only one of the rings. At a current of 200 kA per ring each ψ unit corresponds to a magnetic flux of 1.13×10^{-2} Wb.

The major toroidal azimuthal angle is called ϕ. Hydrogen plasma is injected at $\phi = 0$ through a guide field solenoid (screened from the poloidal field) from a conical theta pinch gun of the type described by Allen et al.[6]. The hydrogen gas is stored at 5 psi above atmospheric pressure in a plenum of volume 6×10^{-2} cm^3 and released by a fast acting gas valve. Measurements on the gun plasma show < 10 per cent of the gas to be ionized so that neutral hydrogen gas flows into the quadrupole region. The distribution of this gas is indicated in Fig. 2 as contours of equal pressure labelled in units of 10^{-4} torr. They were measured with a fast acting ionization gauge whilst operating the gas valve, but not the thetatron, and are shown superimposed on part of a minor cross-section of the torus at $\phi = 0$. The flux surfaces and the position of the end of the guide field solenoid and its screen are also indicated. These pressures were found to change slowly over several milliseconds. The broken line contours in Fig. 2 represent pressures from the Mk I gun which was used in all previously reported work [4,7]; the dotted contours show those obtained from the Mk II gun which has a longer guide field solenoid and which was used in most of the results reported here.

In some experiments, additional neutral gas was injected from a 'gas injector' giving the same pressure distribution as the Mk I gun.

The base pressure in the CLIMAX vacuum tank was held below 10^{-7} torr (normally 3×10^{-8} torr) by evaporating titanium inside the tank every few hours.

METHOD OF MEASUREMENT

Spatially resolved measurement of probe ion saturation current i_p and floating potential V_f were made by simultaneously recording the time resolved signals from eight single Langmuir probes, taking the form of 1 mm diameter glass insulated stalks with tips of tungsten or platinum of diameter 0.5 mm and exposed length 0.5 mm. The probes are mounted in pairs, 45° apart in the major toroidal azimuth ϕ, on four carriages which enable adjacent probes to be moved successively to a common point for purposes of normalizing their readings. In this way the whole circumference of the tank is covered. The line AB in Fig. 2 represents the motion of the probe tip as it is preset on any value of ψ. The magnetic field at the probe tip varies over its travel by ± 10 per cent from 2500 G. The signals were fed to oscilloscopes and to an on-line data acquisition system.

An 8.6 mm microwave interferoemter [8] is used to measure the integrated line density through the central field zero between the rings at azimuth $\phi = 117°$.

RESULTS

Previously reported experiments [7] using the Mk I plasma gun found the probe ion current to decay with a time constant $\tau_p \sim 1$ ms on both negative and positive ψ surfaces. The density decay time τ_m, measured with the microwave interferometer, was ~2 ms and that for the ion temperature T_i (deduced from these figures as ~1 ms) was confirmed by subsequent measurements with a gridded probe which showed $T_i = 30$ eV at t = 1 ms after injection.

The dependence of τ_m on ring current for the Mk II gun is shown in Fig. 3. All the results which now follow were taken at a current of 135 kA per ring for which $\tau_m = 3.7$ ms. The decay of probe ion current at $\phi = 180°$ is shown for several ψ values in Fig. 4. At $T_i = 30$ eV the density is $n \approx 10^{11}\,cm^{-3}$ for $300 \mu A/mm^2$. Measuring the probe ion current along the interferometer path and comparing the microwave phase shift yields a value T_i of 20-30 eV at t = 1.6 ms after plasma injection.

Fig. 5 shows contours, in the ψ,ϕ plane, joining points of equal floating potential (continuous lines labelled in volts) and joining points of equal ion saturation current (broken lines labelled in arbitrary units) for time t = 1.6 ms. Fig. 6 shows the ion current contours in the same units at t = 5.5 ms.

Injecting gas from the 'gas injector', described above, causes the decay time τ_m to reduce from 3.7 to 2.3 ms and probe measurements show marked differences to occur in the equipotential and ion current contours close to the injector. The effect is demonstrated in Figs. 7 and 8 which show equipotential contours (labelled here in half volts) for a low density plasma injected from a gun retracted by 10 cm from the normal position. The effect when gas is injected at $\phi = 155°$ is seen in Fig. 8. Although injecting the gas accelerates the decay of probe ion current at most places, the decay on negative ψ close to the azimuth ϕ where gas is injected is reduced. For $\psi \leq -2$ it is converted into a growth of probe current with time, following time t ~ 1 ms.

Application of a toroidal magnetic field B_ϕ changes the form of the potential contours. Fig. 9 shows the equipotential contour plot at t = 1.6 ms for the case when $B_\phi = 275$ G at the mean major toroidal radius. Compared with Fig. 5, where $B_\phi = 0$, the polarity of the contours has reversed, the centre of the plasma now being

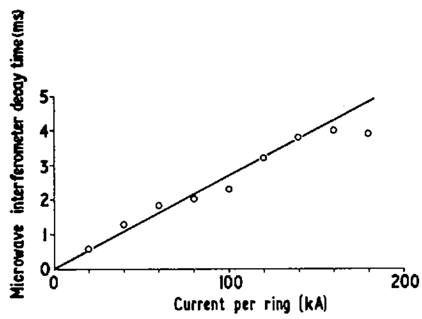

FIG.3. Dependence of density decay time, measured with the interferometer, on ring current.

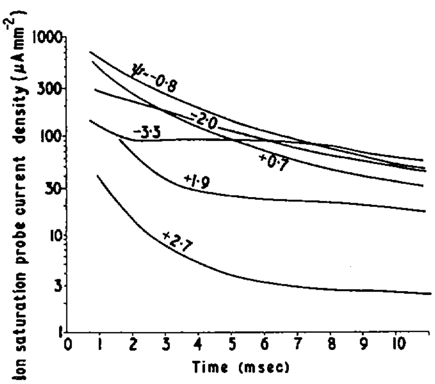

FIG.4. Measured time dependence of probe current at φ = 180° and different values of ψ.

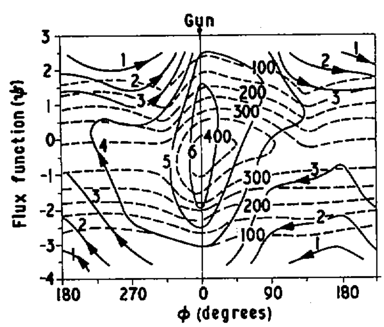

FIG.5. Contours in the (ψ, φ) plane of equal floating potential (continuous lines marked in volts) and of equal ion saturation current (broken lines marked in arbitrary units) at t = 1.6 ms.

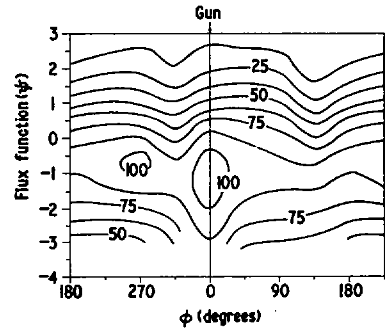

FIG. 6. Ion saturation contours at t = 5.5 ms.

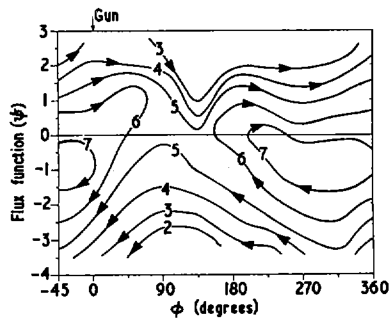

FIG. 7. Equipotential contours (marked in half volts) for a low-density plasma at t = 1.6 ms.

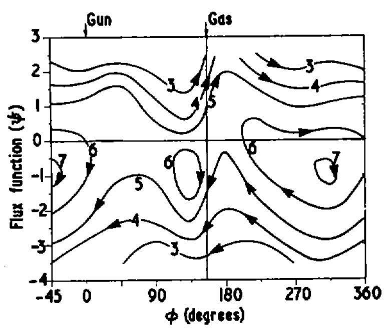

FIG. 8. As Fig. 7 but with neutral gas injected at $\varphi = 155°$.

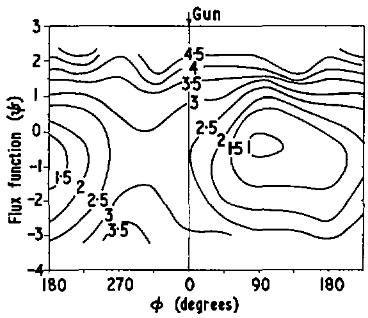

FIG. 9. Equipotential contours (marked in volts) at t = 1.6 ms in the presence of toroidal field B_{φ} = 275 G. Normal density of plasma.

negative. There is a progressive change of potential distribution as B_{ϕ} is increased but $B_{\phi} \sim 50$ G is sufficient to cause the polarity change. The value of τ_m increases from 3.7 to 6.0 ms when B_{ϕ} is increased from 0 to 275 G.

The direct plasma flux to the six ring-supports has been estimated by biasing a retractable dummy support and measuring the ion saturation current collected. For the Mk II gun plasma the calculated plasma density decay time corresponding to this flux exceeds 30 ms.

In experiments using the Mk I gun plasma [7] floating potential steps $\Delta V \sim 1$ volt, reversing in sign either side of ψ_s, were observed on crossing the azimuth of a ring support. Similar steps have been reported by others [1]. They have not been detected in the Mk II gun plasma and so certainly have $\Delta V \ll 1$ volt.

The electron temperature is found from single probe characteristics to be $T_e \sim 3$eV at t = 1.6 ms.

As in the previous work [7] fluctuations $\sim$ 20 kHz are observed in V_f and i_p for $\psi > +1$, although no successful correlation measurements have yet been made on them.

INTERPRETATION

The equipotential and constant probe current contours in Fig. 5 show V and n to be functions of ψ and ϕ. Arrows on the equipotentials indicate the E x B drift directions, flow across the constant U surfaces being produced by the ϕ components of the electric field, E_{ϕ}.

Assuming perfectly toroidal constant U surfaces (i.e., $\partial U/\partial\phi = 0$) the net particle flux of electrons towards increasing ψ crossing such a surface is:

$$\Gamma(\psi) = 10^8 \int_0^{2\pi} nU \frac{\partial V}{\partial \phi} \, d\phi \tag{1}$$

where V is in volts, n is in cm^{-3} and U is in $cm\ G^{-1}$. Consideration of the variation of canonical angular momentum in the presence of E_ϕ leads to the same expression for the guiding centres of the ions.

The physical distance corresponding to $\delta\psi = 3$ flux units is $\sim 10^3$ times less than that corresponding to $\delta\phi = 2\pi$, so that the true E x B velocities are almost entirely along the $\pm\phi$ direction. However, the times taken to cross one ψ flux unit and one radian of ϕ are comparable and given respectively in milliseconds by $t_\psi = 1.2/(\partial V/_{\partial\phi})$ and $t_\phi = 1.2/(\partial V/_{\partial\psi})$ for the ring current used.

Continuity of particle flux predicts a local rate of electron density decay:

$$-\left(\frac{\partial n}{\partial t}\right)_E = \frac{2\pi . 10^8}{\psi_o U}\left\{\left[\frac{\partial V}{\partial \phi}\frac{\partial (nU)}{\partial \psi} - \frac{\partial V}{\partial \psi}\frac{\partial (nU)}{\partial \phi}\right] - \frac{\partial (nTe)}{\partial \phi}\frac{\partial U}{\partial \psi}\right\} \tag{2}$$

where ψ_o is the flux in Maxwells corresponding to one flux unit, viz. 7.7×10^5 for these results and V and T_e are in volts. To maintain charge quasi-neutrality requires that $\partial(nT)/\partial\phi = 0$, where $T \equiv T_e + T_i$, this defining the MHD stable state inside ψ_c. If the ion velocity distribution is not Maxwellian, T_i refers to the average ion energy. The term in square brackets in equation (2) is usually dominant and certainly so near ψ_c where $\partial U/_{\partial\psi} \to 0$. The sign of $(^{\partial n}/_{\partial t})_E$ then depends on the sense of the angle between contours of constant V and nU, being zero if these contours coincide. Because V and nU are periodic in ϕ the presence of any negative $(\partial n/\partial t)_E$ must be accompanied by regions of positive $(\partial n/\partial t)_E$ at some other place on the same constant U surface, a situation which is inconsistent with keeping $\partial(nT)/\partial\phi = 0$ unless there is local plasma cooling or local particle loss by some other mechanism.

Consider the voltage step ΔV observed in the Mk I gun experiments on crossing the azimuth of the dummy ring-support. The experimental observation that $\partial n/\partial\phi = 0$ means that the local contribution of ΔV to Γ (equation 1) is zero. But the sense of ΔV predicts $(\partial n/\partial t)_E$ from equation (2) to be positive at the support and negative elsewhere. This local surplus of plasma must be removed, in this case by loss along the lines of force to the support. Integration of (2) shows the loss flux required to be $10^8 \int \partial(nU)/_{\partial\psi} . \Delta V(\psi) d\psi$ which predicts an equivalent current at t = 1 ms of approximately 100 mA. Biasing the support to -50 V relative to the wall drew an ion current of 70 mA, which is within the experimental error of the same value.

Comparing Figs. 7 and 8 shows that a strong local $\partial V/\partial\phi$ is induced by injecting cold gas. Charge exchange will produce a cold ion density n_c at a rate $(n-n_c)\nu_x$ where ν_x (s^{-1}) is the effective charge exchange collision frequency. To produce the strong effect observed, on a millisecond time scale, requires $\nu_x \geqslant 10^3\, s^{-1}$ in the perturbed region. Taking the relevant cross sections as $10^{-17}\, cm^2$ and $2.10^{-15}\, cm^2$ respectively for 30 eV protons in H_2 and in atomic hydrogen yields $\nu_x = 3 \times 10^3 p_o$ for H_2 and $\nu_x = 1 \times 10^6 p_o$ for H_1, where p_o is the original hydrogen pressure in millitorr. Inspection of Fig. 2 shows that ν_x due to H_2 can be $\sim 10^3$ within about 10 cm of the gas injector. However atomic hydrogen, formed by dissociation in the plasma, needs only a pressure $\sim 10^{-3}$ mtorr to give $\nu_x \sim 10^3$.

The local mixture of cold and hot ions, thermalizing with a time constant of the order of milliseconds can be assigned an average temperature T_i which will have a minimum in regions occupied by cold gas. Provided the shape of each constant U surface is completely independent of ϕ, as has been assumed, the condition $\partial(nT)/\partial\phi = 0$ means that the probe ion saturation current, which can be written: $i_p \propto n^{\frac{1}{2}}(nT)^{\frac{1}{2}}$, is proportional to $n^{\frac{1}{2}}$ on each surface. The enhancement of i_p near $\phi = 0$ in Figure 5 corresponds to the presence of cold gas from the plasma gun.

Inspection of Fig. 6 suggests, however, that the strict independence of the constant surfaces from ϕ is removed by a perturbation near the insulating gaps of the vacuum tank (at ϕ = 135 and 315°). The $n^{\frac{1}{2}}$ variation of i_p then applies strictly along a constant U surface rather than at constant ψ co-ordinate. Despite this uncertainty the contours of constant nU are qualitatively similar to those of constant i_p. The logarithmic infinity in U at ψ_s affects only a region much smaller than the ion gyro radius.

If T_i is constant in time the V and nU contours should coincide to give $(\partial n/\partial t)_E = 0$ in equation (2). In this case

$$\frac{\partial V}{\partial \phi} = -\frac{\partial V}{\partial \psi}\left[\frac{1}{T}\,\frac{\partial T}{\partial \phi}\right]\Big/\left[\frac{1}{nU}\,\frac{\partial (nU)}{\partial \psi}\right]$$

and $\partial V/\partial\phi$ has the opposite sign to $\partial T/\partial\phi$, a situation clearly seen near the cold regions in Figs. 5 and 8. The final term in equation (2) may be significant for negative ψ values where $|\partial U/\partial\psi|$ is largest. However, in places where cold ions are still being produced, a positive $(\partial n/\partial t)_E$ is necessary to keep $\partial(nT)/\partial\phi = 0$. In Fig. 5 the angle between the V and i_p contours shows this effect where the E x B flow approaches the $\phi = 0$ azimuth, with negative $(\partial n/\partial t)_E$ elsewhere, the time scales being roughly of the order of a millisecond.

As distinct from this rearrangement of plasma within the trap the net amount of plasma leaving the trap due to this convection is determined from equation (1). Even taking the most pessimistic assumptions in estimating n from i_p, the calculated value of Γ is too low by between one and two orders of magnitude to account for the $\tau_m = 3.7$ ms density decay time observed with the microwave interferometer. Considering the local regions of outward flow alone, there is insufficient particle flux to account for the observed loss rate, because n is too low in the outer regions. The continuous increase in n near $\phi = 0$, which should accompany the continuous cooling, is not observed and so there must be another mechanism for removing plasma from this region.

For $\psi > +1$ the fluctuations observed in V and n may be sufficient to cause this plasma loss provided they are strongly correlated and have a wavelength $\leqslant 1$ cm. Neither of these conditions has been experimentally confirmed. For negative ψ where fluctuations are not detected, the ion current decay rate, τ_p, (Fig.4) is in fact slower than that for positive ψ.

Errors in the measurement of electric fields will arise if the electron temperature is not uniform, since it is the probe floating potential which is measured. No gradients of T_e have been detected, but if the electrons are cooler near the cold gas the outward particle convection flux (equation 1) will be even less than that already assumed. Operation of the probe tips in a nearly uniform magnetic field avoids changes of floating potential due to changes of this field.

The growing density at $\psi \leq -2$, in the vicinity of injected gas, is consistent with the application of equation (2) to the potential contours in Fig. 8.

When $B_\phi = 275$ G is applied the equipotential contours, Fig. 9, show the potential to be almost independent of ϕ for $\psi > +1$. In this case the particles flux from equation (1) is zero. Even at $\tau_m = 6.0$ ms, the density decay time is anomalously short, so that further evidence that convection is not the primary cause of plasma loss is provided. The change in potential distribution with increasing B_ϕ is probably associated with the influence of B_ϕ on imperfections of the poloidal field. Such effects have been discussed by Williamson [9].

CONCLUSION

Large scale convective motion in CLIMAX has been observed and associated with the presence of cold neutral gas. Calculations from accurate measurements of the floating potential and ion saturation current of eight movable probes show that this convection is not directly responsible for loss of plasma from the trap, but rather for the rearrangement of plasma inside the trap required to keep the plasma pressure constant on the magnetic flux surfaces.

ACKNOWLEDGEMENTS

The authors particularly wish to thank Dr. T. K. Allen who pioneered the whole experiment and who has provided constant stimulating advice, and Drs. R. J. Bickerton and R. S. Pease for their continuing interest and guidance. We also gratefully acknowledge the assistance of Messrs. J. Coultas, A. G. Delph and S. R. C. Green and of Mr. T. E. James' engineering team including Messrs. K. Harries, P. M. Barnes, J. Phillpott and J. L. Browning. The neutral gas pressure measurements were made by Mr. D. A. Boyd. We also thank Professor M. G. Rusbridge for his interest and advice.

REFERENCES

1. FORSEN, H., et al. Plasma Physics and Controlled Nuclear Fusion Research (Proc. Conf. Novosibirsk, 1968) 1, IAEA, Vienna (1969) 313.

2. SCHMIDT, J. A., Phys. Rev. Letters 24, (1970), 721

3. HARRIES, W. L., Physics Fluids 13 (1970) 1751

4. MEGAW, J. H. P. C., et al. Proc. 4th European Conference on Controlled Fusion and Plasma Physics, (Rome), CNEN, Rome (1970) 23.

5. PHILLPOTT, J. et al. UKAEA Culham Report CR68/132 (Paper 3, 5th Symposium on Fusion Technology, Oxford, 1968).

6. ALLEN, T. K., COX, A. J., and SPALDING, I. J., Plasma Physics and Controlled Nuclear Fusion Research (Proc. Conf. Culham, 1965) 2, IAEA, Vienna (1966) 427.

7. ALLEN, T. K., et al. Proc. 3rd European Conference on Controlled Fusion and Plasma Physics (Utrecht) Wolters-Noordhoff, Groningen (1969) 8.

8. HOTSTON, E.S., and SEIDL, M. J.Sci.Instrum., 42 (1965) 225.

9. WILLIAMSON, J. H., J. Plasma Physics 5 (1971) 229.

HIGH-ENERGY GUN-INJECTED TOROIDAL QUADRUPOLE*

J.E. HAMMEL, I. HENINS, R.W. KEWISH, Jr., J. MARSHALL, A.R. SHERWOOD
Los Alamos Scientific Laboratory, University of California,
Los Alamos, New Mexico,
United States of America

Abstract

HIGH-ENERGY GUN-INJECTED TOROIDAL QUADRUPOLE.

A quadrupole device is being used to investigate the trapping and containment of an energetic gun plasma. The quadrupole is designed to contain a peak density of 5×10^{13} cm^{-3} at 2.5 keV within the MHD-stable region. At design field there are 5 gyro-radii for 2.5-keV protons from the separatrix to the ψ_{crit}.

The interior conductors are directly driven with a 0.8-MJ capacitor bank. The current to the coils is fed through a single pair of dipole-guarded conductors to each coil. The coils are also supported from the current feed. The dipole guard is in a force-free configuration with 5 gyro-radii for 2.5-keV protons from the separatrix (between the dipole and quadrupole fields) to the dipole surface. The dipole is designed so that loss of plasma from the dipole region will be directed away from the interior conductors. This feature is necessary for the prevention of contamination by secondary gas produced by plasma lost at the dipole guard.

Experiments at one-half design value of magnetic field have shown that the kilovolt energy gun plasma is trapped by depolarization currents around the coils, and that a very high percentage (>50%) of the gun output can be trapped. The plasma density is measured by a unique Michelson interferometer using CO_2 laser light. The energy of the plasma is derived from magnetic pickup loops placed outside the containment region.

The leak caused by the dipole guard field has been examined by double electric probe measurements. The plasma drift thus inferred is an order of magnitude less than that predicted by a model of Meade's or by calculations by us. This casts doubt upon the validity of any such simple model and emphasizes the necessity of further experimental investigation of the matter.

New coils which are being built to operate at full design magnetic field strength will allow a check on the containment time of the device for kilovolt energy plasma.

This experiment differs markedly from other multipole experiments in that it is primarily an injection experiment with the objective being to study the process and efficiency of trapping a gun plasma having CTR temperature and density in a closed confinement geometry. A second objective is to investigate the possibility of direct access to the interior conductors by means of employing magnetic dipole guarding of the electrical feeds and mechanical supports. Only after the achievement of favorable results for these objectives will the usual confinement and stability studies be made.

The experiment is designed to contain a peak density of 5×10^{13} cm^{-3} at 2.5 keV within the MHD stable region. The quadrupole field is chosen partially because it can be tailored to reject the slow component of the plasma gun while it has a short connection length for trapping the fast plasma component of the gun. At full field strength there are five gyroradii between ψ_{crit} (the last MHD stable flux surface) and the quadrupole separatrix for 2.5-keV protons. Current experiments are at half magnetic field strength. Experiments at full field strength await new coils presently under construction.

* Work performed under the auspices of the US Atomic Energy Commission.

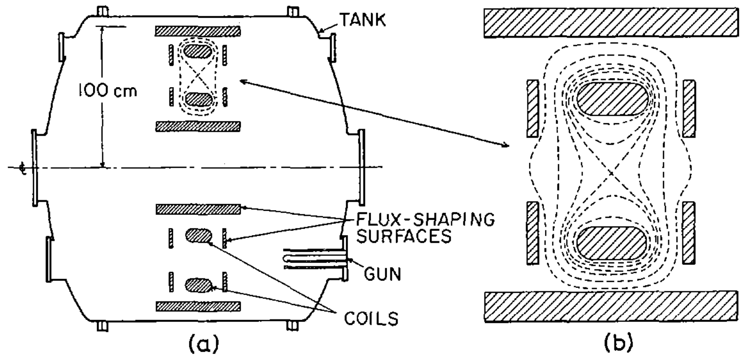

FIG. 1. (a) Schematic of the experimental apparatus.
(b) Typical magnetic field lines.

A schematic diagram of the apparatus is shown in Fig. 1. Each coil is supported by a single pair of dipole-guarded current feeds which are not shown. The plasma is injected parallel to the axis of the coils and directly at the null of the quadrupole field. The azimuthal position of this injection can be varied, but for all measurements so far it has been 165° from the azimuth of the coil supports. The four flux-shaping rings increase the amount of MHD stable flux, increase the height of the magnetic barrier that must be crossed by the injected plasma, and provide an azimuthally continuous slot through which the plasma may be injected into the containment region. Thus the quadrupole field is not perturbed by an injection port.

Figure 1b shows the magnetic field shape. The design value for the field between the inner coil and its cylindrical flux-shaping surface is 40 kG. The corresponding figure for the outer coil is about 27 kG.

From previous experiments it is known that the plasma coming from our coaxial gun has most of its energy in streaming motion and very little in thermal motion. Although the physical processes involved are not yet completely understood, it is believed that this highly directional plasma penetrates the magnetic barrier by means of $\vec{v} \times \vec{B}$ polarization electric fields. These electric fields have been measured in the present experiment and are found to be equal to $\vec{v} \times \vec{B}$ within experimental error. Furthermore it is believed that the trapping occurs primarily because of depolarization currents that flow along magnetic field lines when the plasma stream crosses the quadrupole null. These depolarization currents have been measured by means of Rogowski loops and are found to be about right to provide the proper impulse to cancel the momentum of the incoming plasma stream.

Area density measurements of the plasma in the region of the quadrupole null have been made at an azimuthal position 75° from the injection region and 90° from the dipole-guarded coil supports. These measurements were made by means of a CO_2 laser interferometer shown in Fig. 2. The reason for using the "misaligned" Michelson configuration (the two displaced beam splitters) was to avoid difficulties that were encountered if any reflected beams were allowed to reenter the laser cavity. This instrument was used to make area density measurements in a range corresponding to 1/600 to 1/3 of a fringe. A typical result for the area density as a function of time is shown in Fig. 3. Although most of the density measurements were taken along a line passing through the quadrupole null, some measurements were taken along other lines parallel to the axis but displaced towards either coil.

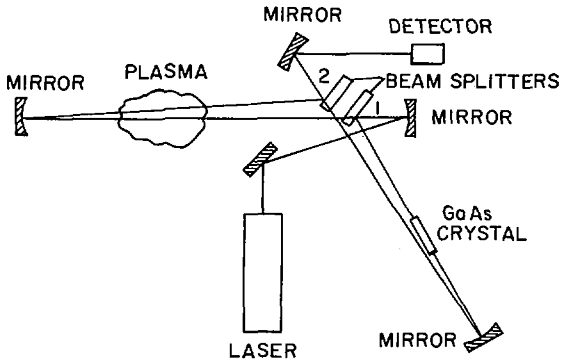

FIG. 2. CO_2 laser interferometer (λ = 10.6 μ).

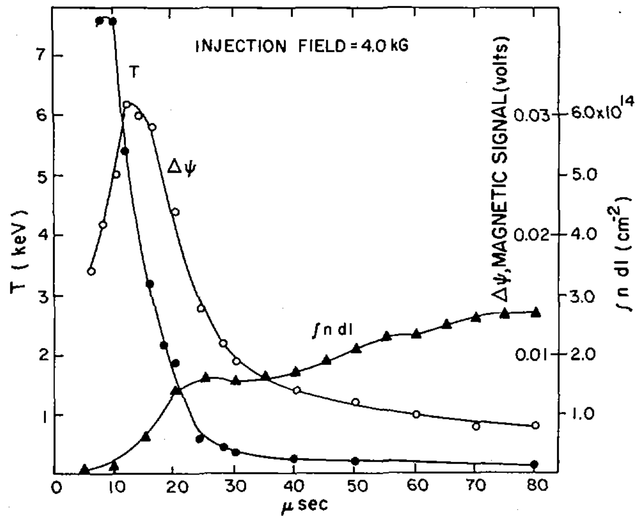

FIG. 3. Typical experimental results. Temperature, area density, and diamagnetic signal plotted as functions of time.

The observed flat profile can be compared to the predictions of various models for the plasma distribution. For example, comparison with a cosine distribution (see below) suggests that the plasma is centered on the separatrix or perhaps displaced slightly outward.

Plasma diamagnetism has been measured by magnetic pickup loops placed at various azimuthal and axial positions (but always outside ψ_{crit}). If the magnetic loops are placed inside of ψ_{crit} they are bombarded by plasma and become very luminous. When placed outside of ψ_{crit} the loops are usually untouched by plasma, however, during certain shots for unknown reasons the plasma will leave the confinement volume. This is observed by the sudden bombardment of the magnetic loops and by a reversal of the loop signal beginning 30 to 40 μsec after injection. The usual behavior gives a loop signal which remains positive and smooth for more than 100 μsec, as is shown in Fig. 3.

Plasma energies have been inferred from the flux change in these magnetic pickup loops. To do so a model for the plasma distribution must be employed and the perturbed magnetic field calculated [1]. We used the model of an azimuthally symmetric isotropic plasma pressure given by

$$p = \frac{p_o}{2}\left[1 + \cos \pi \frac{\psi - \psi_o}{\psi_1 - \psi_o}\right]$$

where ψ is the flux function, ψ_o is the flux surface for the quadrupole separatrix and ψ_1 corresponds to the edge of the plasma distribution. The plasma energies inferred in this way can be combined with the area densities given by the interferometer to yield a value for the plasma temperature. Furthermore, the total amount of kilovolt energy plasma deduced in this manner is very close to the total output of energetic plasma from the gun. Figure 3 shows a typical result for the deduced plasma temperature plotted as a function of time. The observed rapid drop in the plasma temperature may be due primarily to the fact that present magnetic field strength is much too small for effective containment of this energetic gun plasma.

The dipole-guarded feed to the inner coils is a part of the experiment 1) because it allows the quadrupole to operate with high energy plasma without the difficulty and cost of a levitated system, and 2) it gives experimental evidence on the possibility of direct access to an interior conductor through guarding. The dipoles are placed in the high field region of each interior coil and are designed for force-free operation. The nulls produced by this configuration are closed by a suitable cross current before they can reach the coil in order to prevent plasma bombardment of its surface.

The dipole guard produces an inevitable leak from the containment volume; however, such a leak would be acceptable if it were small enough. A direct measure of the leak associated with the dipole has not been made to date; however, a leak rate can be derived from electric field measurements made in the vicinity of the dipole. Potential differences are measured between magnetic field lines which pass near the dipole by means of a set of five double probes. The maximum signal is less than 50 V/cm and generally occurs on the probe spanning the dipole separatrix (the line going through the dipole null). The signals become very small or negative about 2 cm on either side of the dipole separatrix. For the electric field at the separatrix, the $\vec{E} \times \vec{B}$ drift velocity is such as to transport the plasma out of the machine. The equivalent area of the leak will be defined by

$$A = \frac{4\int\oint \frac{E}{B}\, d\ell\, d\eta}{v_{therm}}$$

where ℓ is the coordinate along $\vec{B}$ and η is the coordinate normal to $\vec{B}$ and to the dipole axis. Since experimentally the measured electric field remained essentially unchanged when the probes were moved along the magnetic field lines in the vicinity of the dipole, E can be taken out of the integral. Thus the area is evaluated by using the calculated value of $\oint \frac{d\ell}{B}$ around the quadrupole and the electric field as measured by the probes. The resultant equivalent leak area found is just under 4 cm^2.

This area can be compared with the leak area found with a simplified theoretical model given by Meade [2]. This model applied to this experiment would predict an equivalent leak area of 90 cm^2, or about 25 times greater than the area found from electric field measurements.

Further investigation by us and by D. Baker indicates inadequacies in the model that could account for this discrepancy; for example, in application to our geometry the two-dimensional nature of this model is not sufficient. In addition, no account is taken of density gradients created by the flow. If this very small leak area is further confirmed by direct measurements, dipole-guarded supports would be useful for interior access both in experiment and in CTR systems.

In summary, the experiment has been operated only up to half design magnetic field to date but two important results have emerged. First, the efficiency of trapping of the energetic component of the gun plasma is very high. Second is the apparent low loss area introduced by the dipole guard. Installation of the new coils for operation at higher magnetic fields will hopefully answer questions about confinement and loss mechanisms.

REFERENCES

[1] BAKER, D. A., MANN, L. W., Bull. Am. Phys. Soc. 14, 1051 (1969).
[2] MEADE, D. M., Phys. Fluids 11, 2497 (1968).

PLASMA PRODUCTION AND HEATING IN THE SUPERCONDUCTING LEVITRON*

O.A. ANDERSON, D.H. BIRDSALL, C.W. HARTMAN,
E.B. HOOPER, Jr., R.H. MUNGER, C.E. TAYLOR
Lawrence Radiation Laboratory, University of California,
Livermore, Calif.,
United States of America

Abstract

PLASMA PRODUCTION AND HEATING IN THE SUPERCONDUCTING LEVITRON.

Plasma production and heating in the Superconducting Levitron are described. The device has a floating superconducting ring with 40-cm major radius and 5-cm minor radius, which carries up to 600 kA current. Toroidal field is provided by a current of up to 1 MA. Six poloidal field coils are used to shape the magnetic surfaces to obtain field configurations with strong shear and with minimum average B, a local minimum-B well, or minimum $\partial B/\partial s$ ($\delta B/B \lesssim 0.005 - 0.05$). Large area surfaces at liquid helium temperature which are not directly exposed to the plasma provide ultrahigh vacuum. Methods of production and heating of dense plasma with appreciable β have been studied using a classical diffusion and thermal conduction model, which includes trapped-particle effects. Computations have been made both for heating by an initial hot electron plasma and for energetic neutral injection. The latter technique yields $n \approx 10^{13}$ cm^{-3}, $T_e \approx T_i \approx 0.3$ to 0.8 keV with existing sources (200 mA equivalent current at 2 keV). Production and heating by energetic electrons proceeds in two steps: First, a hot electron plasma with $n \approx 10^{11}$ to 10^{13} cm^{-3}, $T_{e,\,hot} \approx 100$ to 500 keV is established by electron cyclotron resonance heating (ECRH). Second, dense plasma is formed by injection of a short pulse (50 μs) of neutral gas. The inherent cutoff limit of direct ECRH is thereby overcome. Numerical computations of the subsequent in situ heating by energetic electrons predict $T_i = 0.14$ to 2.0 keV, $n = 5 \times 10^{13}$ to 10^{14} cm^{-3} for $B_{poloidal} = 1.5$ to 6 kG. Thus, heating and ion temperatures comparable to or greater than obtained in the Tokamak T-3 device are predicted. This technique allows scaling to ignition temperature for a D-T plasma using available microwave power sources and a somewhat larger device.

INTRODUCTION

The investigation of plasma confinement and heating in closed vacuum magnetic field configurations is considerably simplified if the configuration has axisymmetry. For this reason, and also because strong shear and deep average B wells can be obtained, floating ring devices have been the subject of considerable study during the past decade. Experiments were initiated in 1960 with the levitron device employing a copper floating ring [1]. Resistive decay of the ring current imposed the requirement that the experiments be pulsed, with consequent electric field component along B and limited available confinement time.

The realization, in recent years, of practical superconducting magnets has allowed the replacement of the normal-conductor floating ring with a superconducting ring, thereby achieving essentially steady confinement fields. This development has been incorporated in a recently constructed device, the Superconducting Levitron (SCL). In this paper we describe the SCL and discuss plasma formation and heating techniques for obtaining isotropic plasmas with density and temperature of thermonuclear interest. The two techniques discussed, energetic neutral atom injection and heating by low-density hot electrons, may also be used in other toroidal fusion devices.

* Work performed under the auspices of the US Atomic Energy Commission.

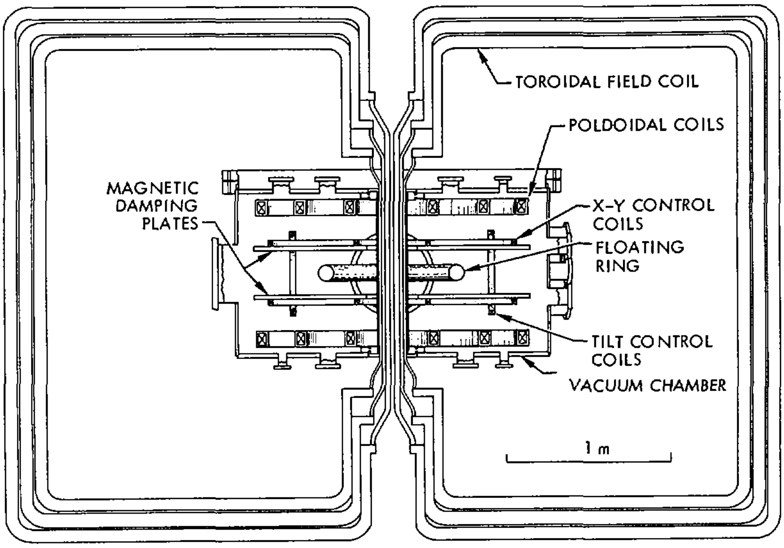

FIG. 1. Cross-sectional view of the SCL. The magnetic field is generated as follows: (a) Floating ring, 40-cm major radius, 4.5-cm minor radius, 600 kA-turns maximum; (b) 6 superconducting poloidal field coils in pairs above and below the ring with major radii 26 cm, 56 cm, and 80 cm, and with maximum currents I_1 = 660 kA-turns, I_2 = 260 kA-turns, and I_3 = 420 kA-turns, respectively; (c) 12 superconducting ring position control coils; (d) toroidal field winding 600 kA-turns maximum continuous, 1 MA for 10-s pulse.

DESCRIPTION OF THE SCL

The SCL is shown schematically in Fig. 1. Three sets of windings [2] provide the magnetic fields: (a) poloidal field windings—the floating ring and six poloidal field coils located above and below the ring, (b) eight ring displacement (x-y) control coils and four ring tilt control coils, and (c) a conventional water-cooled toroidal field winding. The floating ring, poloidal field coils, position control coils, and magnetic damping plates are all cooled to liquid helium temperature, and the assembly is surrounded by a liquid nitrogen-cooled heat shield.

The maximum ring current is limited by hoop stress to the design value of 600 kA-turns. At present the ring has been tested to 308 kA-turns. At this current, the ring remains superconducting up to about 12°K. Twenty-five g of helium sealed within the ring provide a heat capacity of about 2 kJ. The ring is inductively excited and remains superconducting and levitated without cooling or added heat load for a period of 4 to 6 h. Re-cooling by heat conduction through indium-copper contacts, using the four retractable cooling probes, requires about 15 min.

In the static field of the toroidal and poloidal windings, the ring is unstable to tilt and transverse displacement. High-purity aluminum eddy current plates are located 14 cm above and below the ring, as shown. The plates stabilize the ring for frequencies $\gtrsim$10 Hz, but because of resistive decay of eddy currents, position control coils are needed for lower frequencies. The ring position is detected optically and correction signals are amplified [3] and applied to the position coils. Under typical field conditions at $I_{Ring} \cong 300$ kA-turns, the ring position is held constant to within ±0.01 cm of magnetic center with correction fields of ~5 G.

Ring current is established after the desired initial flux is created with the ring in a normal state, by inductive coupling with the poloidal field coils (Fig. 1). The magnetic field configuration is established by adjusting the current in the poloidal field coils. In the following discussion three field configurations [1,4] are considered: (a) the minimum average B (Min $\overline{B}$) configuration, (b) the minimum B (Min B) configuration, and (c) the field configuration having B nearly constant on flux surfaces (Min $\partial B/\partial s$). Configurations (a), (b), and (c) are shown in Fig. 2.

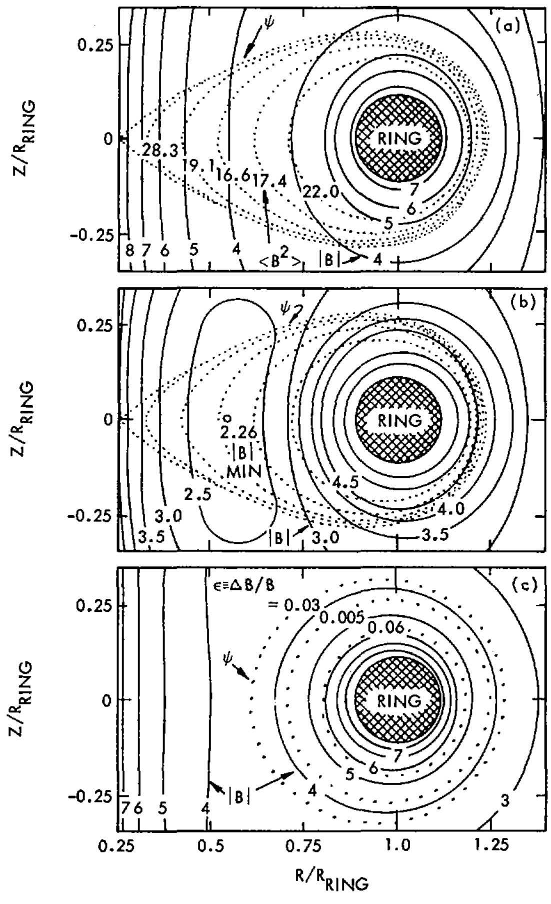

FIG. 2. SCL field configurations, showing flux surfaces (dotted) and constant-B contours (solid lines); B is in kilogauss for ring current I_r = 200 kA. Trim currents I_1, I_2, I_3 arranged in pairs at $Z/R_{ring} = \pm 1$, R/R_{ring} = 0.6, 1.4, and 2.0. (a) Min-B configuration, with $\langle B^2 \rangle$ labelled on each flux surface. Toroidal-field current $I_T = 2I_r$; $I_1 = -0.9\, I_r$, $I_2 = -0.43\, I_r$, $I_3 = -0.47\, I_r$. (b) Min B configuration, showing absolute well. $I_T = I_r$; I_1, I_2, and I_3 same as above. (c) Min $\partial B/\partial s$ configuration, with $\Delta B/B$ labelled on each flux surface. $I_T = 1.8\, I_r$; $I_1 = -0.9176\, I_r$, $I_2 = +0.0812\, I_r$, $I_3 = -0.6775\, I_r$.

ENERGETIC NEUTRAL INJECTION

Energetic neutral injection can provide an effective means of forming a hot, dense plasma in steady state provided anomalous plasma loss is not too large. The retention of cold plasma in a toroidal system relaxes considerably the vacuum requirements to achieve buildup [5]. To assess neutral injection in the SCL, a neutral beam in the range $I_b \simeq 0.1$ to 1 A (equivalent) and 1 to 5 keV energy is considered [6]. A possible beam line is shown in Fig. 3.

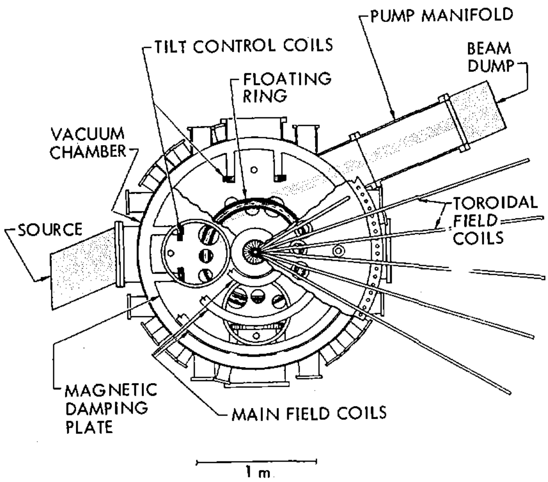

FIG. 3. Top view of the SCL, showing a tentative neutral beam layout.

As a model for plasma formation by energetic neutral injection and by hot electron heating discussed later, we consider plasma losses to occur as the result of "neoclassical" particle diffusion and ion thermal conduction [7]. This model, which includes the effects of particle excursions from magnetic surfaces, is observed to be in reasonable agreement with experiments in devices similar to the SCL [1,8]. To relate to field configuration the loss rates τ_n^{-1} and τ_T^{-1} given in the appendix, we consider the upper bound to neoclassical diffusion and thermal conduction losses by evaluating the diffusion coefficients using only the poloidal field component, when appropriate.

We consider two limiting cases: (a) when the plasma is a thin target for the neutral beam and (b) when it is thick. For the thin case, the density equation is

$$\frac{I_b}{V}\,\frac{\langle\sigma_I v_e\rangle}{v_b}\,n\ell = \frac{n}{\tau_n} \tag{1}$$

and the energy equation is

$$\frac{I_b}{V}\left[\frac{2}{3}\,E\left(\frac{\langle\sigma_I v_e\rangle}{v_b}\,\ell\right) + \left(\frac{2}{3}\,E - T\right)\sigma_{cx}\,\ell\right] = nT\left(\frac{1}{\tau_T} + \frac{2}{\tau_n}\right) \tag{2}$$

where I_o is the equivalent neutral beam current, V is the plasma volume (5×10^4 cm^3), $\langle\sigma_I v_e\rangle/v_b$ is the effective electron ionization cross section,

ℓ is the path length in the plasma (40 cm along the path shown in Fig. 3), E is the beam energy in volts, and σ_{cx} is the charge exchange cross section. If the plasma is thick, Eqs. (1) and (2) become

$$\frac{I_b}{V} = \frac{n}{\tau_n} \tag{3}$$

and

$$\frac{I_b}{V}\frac{2}{3}E = nT\left(\frac{1}{\tau_T} + \frac{2}{\tau_n}\right) \tag{4}$$

Equations (1) through (4) have been solved for a plasma half-width a = 4 cm (see Appendix). The results are summarized in Table I and Fig. 4 for a hydrogen plasma. In Fig. 4, the maximum plasma density limit is assumed to occur when the beam penetration length is about 4 cm. Since $B_p \simeq$ 5 to 10 kG, and neutral beams having $I_b \simeq 0.1$ A (equivalent) at 1 to 5 kV can be obtained from available sources, $I_b B_p^2 \simeq$ 2.5 to 10; thus n ≃ 1 to 5×10^{13} cm^{-3}, and T ≃ 0.2 to 2.4 keV is predicted.

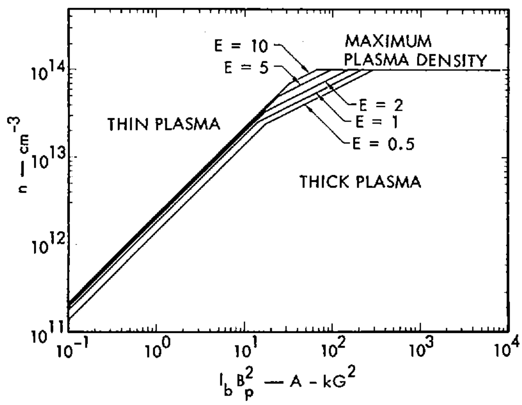

FIG. 4. Plasma densities attainable by neutral injection.

TABLE I. PLASMA TEMPERATURE USING NEUTRAL INJECTION

Beam energy E(keV)	Temperature (keV)	
	Thin plasma	Thick plasma
0.5	0.16	0.09
1.0	0.37	0.19
2.0	0.83	0.38
5.0	2.4	0.95
10.0	5.1	1.9

We have considered the effects of cold neutral molecules streaming into the plasma region either from the source or because of ambient pressure in the range 10^{-7} to 10^{-6} torr H_2 (room temperature). Dissociation at the plasma surface produces Franck-Condon [9] neutrals that penetrate the plasma. For a comparatively high flux $I_{FC}/I_b \simeq 1$, the density and temperature change only slightly (≈50%) if $6 < I_b B_p^2 < 10^2$ A-kG^2.

It is anticipated that, in an experiment, the neutral beam will be injected into an initiating microwave discharge. Since a few time constants, τ_n, are required to reach steady plasma, beam duration greater than 1 sec is required.

PLASMA HEATING BY ENERGETIC ELECTRONS

A second method of plasma production, which is particularly useful for the SCL because of the absence of a loss cone, employs collisional heating by energetic electrons [10]. This method proceeds in two stages, as shown in Fig. 5. First, a hot electron plasma is produced in the confinement region by electron-cyclotron-resonance (ECR) heating at 10.6 GHz and, possibly, additional power at a higher frequency [11]. Typically, plasma can be produced by this technique which has an energy density stored in hot electrons approaching that required for ignition of a D-T plasma, but because of the microwave cutoff limitation, density is limited to 10^{11} to 10^{12} cm^{-3}. At this density, cold neutrals are able to penetrate the plasma and thus the ions are expected to remain relatively cold by charge exchange. To overcome the cutoff limitation and enter a burnout regime, a second stage is employed (Fig. 5). A pulse of gas is injected, then ionized and heated by the hot electron plasma, forming a dense isotropic plasma.

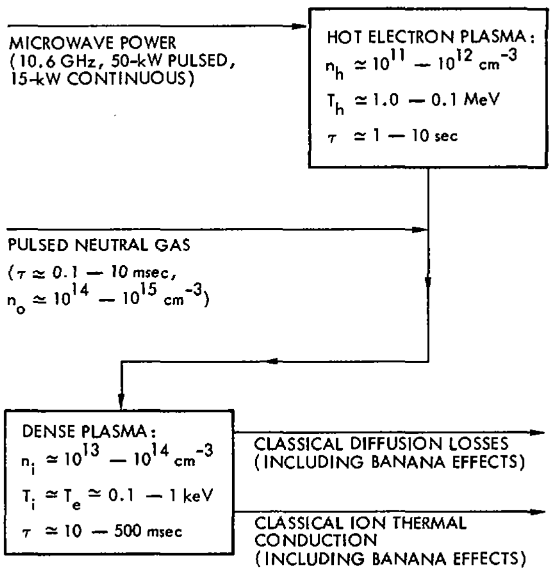

FIG. 5. The generation of a dense, hot ion plasma using hot electrons.

The production of hot electron plasma by ECR heating has been studied in magnetic mirror devices [11] and in the copper ring levitron [1]. Mirror experiments have shown that plasma can be produced with parameters $n_h \simeq 10^{11}$ to 10^{12} cm^{-3}, $T_h = 0.1$ to 1 MeV, and $\beta \simeq 0.2$ to 0.8. Three significant differences exist between continuous ECR heating in mirrors and in the SCL where: (a) cold plasma is retained and continues to be heated, (b) loss-cone instabilities do not necessarily cause the loss of hot electrons, and (c) nonadiabatic electrons are not necessarily lost.

Since the heating microwaves must propagate across the confining field, the cold plasma component may effect considerably ECR heating in the SCL compared with mirrors, where propagation along B is allowed. A strong limitation on the production of energetic electrons was observed in the copper ring levitron when appreciable cold plasma was present. This limitation, if important for continuous heating in the SCL, can be avoided in two ways: (a) by careful control of the gas pressure at the discharge so that the total plasma density is limited, or (b) by performing the initial heating cycle (1 to 10 sec) with cold plasma interceptors placed in the region $B \simeq B_{max}$ and withdrawn before pulse gas injection. Heating with interceptors should be very similar to that observed in open ended systems; consequently, a similar plasma should be formed. Control of the gas pressure will be accomplished by having freshly gettered liquid nitrogen-cooled surfaces adjacent to the plasma and by utilizing the diverter field shape provided by the separatrix in the Min $\overline{B}$ and Min B configurations.

If it is assumed that the above techniques produce a hot electron plasma with $n_h \simeq 10^{11}$ to $10^{12}/cm^3$ and $T_h \simeq 0.1$ to 1 MeV, dense plasma is then formed by injection of a pulse of room temperature hydrogen gas for a period $\tau \gtrsim 50$ μsec. The gas pulse enters the plasma confinement region as molecular hydrogen, which is dissociated and ionized. As the dense plasma forms and is heated, further penetration of molecules is prevented and dissociation occurs at the plasma surface. The resulting Franck-Condon neutrals continue to penetrate the plasma volume until burnout conditions are approached.

The buildup of dense plasma is given approximately by

$$\frac{dn_e}{dt} = \langle\sigma_I v\rangle_h n_h n_o + \langle\sigma_I v\rangle_e n_e n_o \quad (5)$$

Here, spatial variations have been neglected and n_h and T_h are assumed constant. The second term in Eq. (5) is limited by the rate of collisional energy transfer from the hot electrons. Thus, "clamping" of T_e by excitation and ionization losses reduces the contribution of the second term in Eq. (5) to a value less than that provided by the hot electrons initially.

For hot electron parameters $n_h = 10^{11}$ to 10^{12} cm^{-3} and $T_h = 1$ to 0.1 MeV, it appears that the 50-μsec pulse of gas should be able to penetrate the confinement region. In addition to ionization, n_e may also be augmented by inward diffusion while T_e is low.

Following the initial ionization phase, the dense plasma ($n_e \simeq 10^{13}$ to 10^{14} cm^{-3}) is heated by the hot electron component and loses energy by diffusion and ion thermal conduction. To estimate the heating, we have used the dense model discussed earlier for dense plasma losses and have numerically solved the rate equations:

Hot Electrons:

$$n_h = \text{constant} \quad (6)$$

$$\frac{dT_h}{dt} = \frac{T_e - T_h}{\tau_{he}} + \frac{T_i - T_h}{\tau_{hi}} \tag{7}$$

Dense Electrons:

$$n_e(t) = n_i(t) - n_h \tag{8}$$

$$\frac{dT_e}{dt} = \frac{T_h - T_e}{\tau_{eh}} + \frac{T_i - T_e}{\tau_{ei}} \tag{9}$$

and

Dense Ions:

$$\frac{dn_i}{dt} = -\frac{n_i}{\tau_n} \tag{10}$$

$$\frac{dT_i}{dt} = \frac{T_h - T_i}{\tau_{ih}} + \frac{T_e - T_i}{\tau_{ie}} - \frac{T_i}{\tau_T} \tag{11}$$

where

$$\frac{1}{\tau_{jk}} = \frac{2n_k}{m_j m_k}\left(\frac{kT_j}{m_j} + \frac{kT_k}{m_k}\right)^{-3/2}\left(\frac{4}{3}(2\pi)^{1/2} e^4 \ell n \Lambda\right)$$

The times τ_n and τ_T, are given in the appendix, except that D must be multiplied by the factor

$$\frac{T^{1/2}}{2n}\left(\frac{T_i + T_e}{T_e^{3/2}} n_e + \frac{T_i + T_h}{T_h^{3/2}} n_h\right)$$

and in X, n and T refer to the ion species. In solving the above equations, n_h = constant until $T_h \simeq T_e$, after which n_h is added to n_e.

Figure 6 and Table II give some results of the numerical solutions obtained for the SCL parameters given earlier. In Table II at $t = t_p$, the ion temperature is at its maximum ($T_i = T_{ip}$) and at $t = t_1, t_2$, $T_i = T_{ip}/2$. To establish a correspondence with the magnetic field shown, B is taken as the

TABLE II. PREDICTED PLASMA PARAMETERS USING ECR HEATING

B (kG)	$n_e(0)$ (10^{13}/cm^3)	$T_h(0)$ ($n_h = 10^{12}$) (keV)	t_p (msec)	$T_i(t_p)$ (keV)	$n_e(t_p)$ (10^{13}/cm^3)	t_1 (msec)	t_2 (msec)	$u_{dp}(t_p)/u_{ho}(0)$
1.5	10	100	40	0.14	1.3	0.7	70	0.008
3	10	250	70	0.56	3.1	6	150	0.22
6	5	400	290	2.0	3.0	40	800	0.41
12	5	1600	2200	8.0	3.1	300	~4000	0.46

mean poloidal field strength $\langle B_p \rangle = \psi_p/a$ for the Min $\overline{B}$ and Min B configurations (Figs. 2-a and 2-b), thus establishing a rough upper bound for classical losses. For the Min $\partial B/\partial s$ configuration (Fig. 2-c) the average value of the total field $\langle B \rangle = \int B\, d\rho/a$ is taken since banana effects are small. For the configurations shown in Fig. 2:

(a) Min $\overline{B}$, $\langle B_p \rangle$ = 1.9 kG, I_R = 200 kA-turns,

(b) Min B, $\langle B_p \rangle$ = 3.9 kG, I_R = 200 kA-turns,

(c) Min $\partial B/\partial s$, $\langle B \rangle$ = 4.2 kG, I_R = 152 kA-turns.

In evaluating $\langle B_p \rangle$ for (a), ψ_p was evaluated between the surface of Min $\overline{B}$ and the separatrix, assuming that n peaks at the Min $\overline{B}$ surface. In (b), ψ_p was calculated between the surface of peak density (Fig. A-1) and the separatrix surface, assuming that shear stabilization obtains. For both (a) and (b), ECR zones for 10.6 GHz heating correspond to the B = 3.8 kG contours in Figs. 2-a and 2-b. In (c) I_R and B_T have been reduced so that the ECR zone is at the contour labeled B = 5 kG, where diffusion established n_{peak} for the dense plasma.

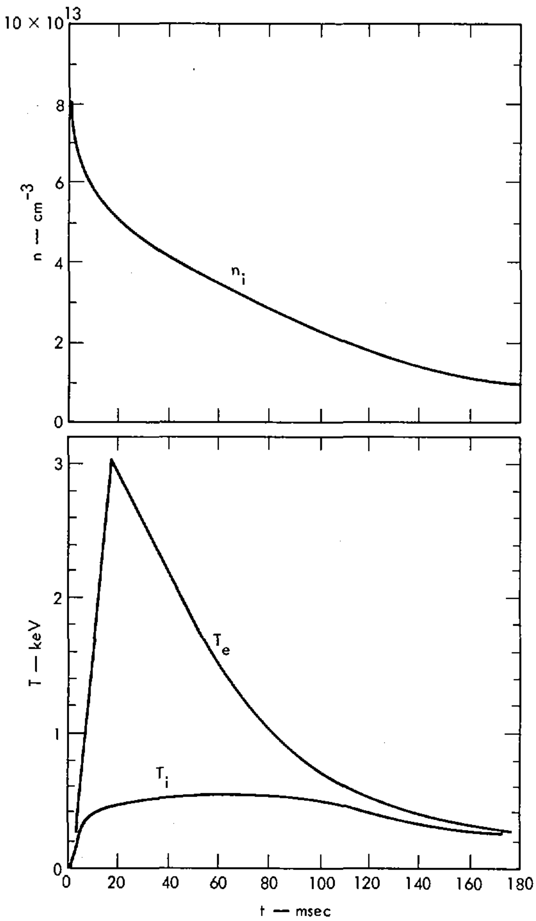

FIG. 6. Evolution of the plasma for B = 3 kG, $n_e(0) = 10^{14}$ cm^{-3}, $n_h = 10^{12}$ cm^{-3}, and $T_h(0)$ = 250 keV.

Ion temperatures in the range T_{ip} = 0.2 to 0.6 kV are predicted. For ECR heating at 18 GHz, T_{ip} = 1 to 2 keV is predicted and, for heating at the magnetic field produced at maximum ring current (600 kA-turns), T_{ip} is in the range for ignition of a D-T plasma.

Because of the approach to burnout conditions, charge exchange losses are small when T_i is appreciable. Energy is transferred from hot electrons to dense isotropic plasma at substantial β and at a rate comparable to strong ohmic heating. As the ratio

$$\frac{u_{dp}}{u_{ho}} = \frac{n(t_p)\left(T_e(t_p) + T_i(t_p)\right)}{n_h(0)\, T_h(0)}$$

in Table II shows, the energy transfer becomes more efficient as B is increased.

SUMMARY AND PRESENT STATUS

Two methods have been described for producing a dense, hot plasma in the range $n \simeq 10^{13}$ to 10^{14} cm^{-3}, $T_i \simeq 0.2$ to 2 keV. The first method requires intense neutral beams in the range $I_b \simeq 0.1$ to 1.0 A equivalent, E = 1 to 10 keV, and plasma losses that are nearly classical. The neutral beam requirements appear to be well within the present state of source development.

The second method, using hot electron heating, has the advantage that the rate of energy transfer to the dense plasma can be several orders of magnitude greater than with neutral injection. Consequently, a greater anomalous increase in dense plasma losses can be overcome. Since ECR heating can be scaled to higher fields than achievable in the SCL, an approach to the Lawson criterion could be made with available microwave sources.

At present the SCL is undergoing engineering shakedown tests; the ring has been successfully levitated in several poloidal field configurations [12]. Plasma experiments using ECR heating are now in preparation.

APPENDIX: TRANSPORT RATES

To obtain the approximate density and temperature transport rates, τ_n^{-1}, τ_T^{-1}, an equivalent cylindrical system was considered with the axis aligned in the direction of the ring current. The magnetic field was taken as $B = B_p \sim 1/\rho$, and the plasma components were all assumed to have a single temperature since, typically, thermalization takes place more rapidly than transport.

The diffusion equations [13],

$$\frac{\partial n}{\partial t} = \frac{1}{\rho}\frac{\partial}{\partial \rho}\left(\rho D \frac{\partial n}{\partial \rho}\right) + \frac{1}{4}\frac{1}{\rho}\frac{\partial}{\partial \rho}\left(\rho D \frac{n}{T}\frac{\partial T}{\partial \rho}\right) \tag{A-1}$$

$$\frac{\partial T}{\partial t} = \frac{7}{6}\frac{D}{n}\frac{\partial n}{\partial \rho}\frac{\partial T}{\partial \rho} + \frac{7}{6}\frac{D}{4T}\left(\frac{\partial T}{\partial \rho}\right)^2 + \frac{1}{6}\frac{T}{n\rho}\frac{\partial}{\partial \rho}\left(\rho D \frac{\partial n}{\partial \rho}\right) + \frac{1}{6}\frac{T}{n\rho}\frac{\partial}{\partial \rho}\left(\frac{nD\rho}{4T}\frac{\partial T}{\partial \rho}\right) + \frac{1}{n\rho}\frac{\partial}{\partial \rho}\left(n\rho\chi \frac{\partial T}{\partial \rho}\right) \tag{A-2}$$

were integrated numerically[1] subject to the boundary conditions $n = n_o << n_{peak}$, $T = T_o << T_{peak}$ at $\rho = \rho_i = 6$ cm and at $\rho = \rho_o = 14$ cm. In Eqs. (A-1) and (A-2)

$$D = \left[\frac{8}{3}(2\pi)^{1/2} e^2 c^2 \left(\frac{m_e}{k}\right)^{1/2} \ell n\Lambda\right] \frac{n}{B^2 T^{1/2}}$$

$$\chi = \frac{1}{6}\left(\frac{2m_i}{m_e}\right)^{1/2} \left[\frac{8}{3}(2\pi)^{1/2} e^2 c^2 \left(\frac{m_e}{k}\right)^{1/2} \ell n\Lambda\right] \frac{n}{B^2 T^{1/2}}$$

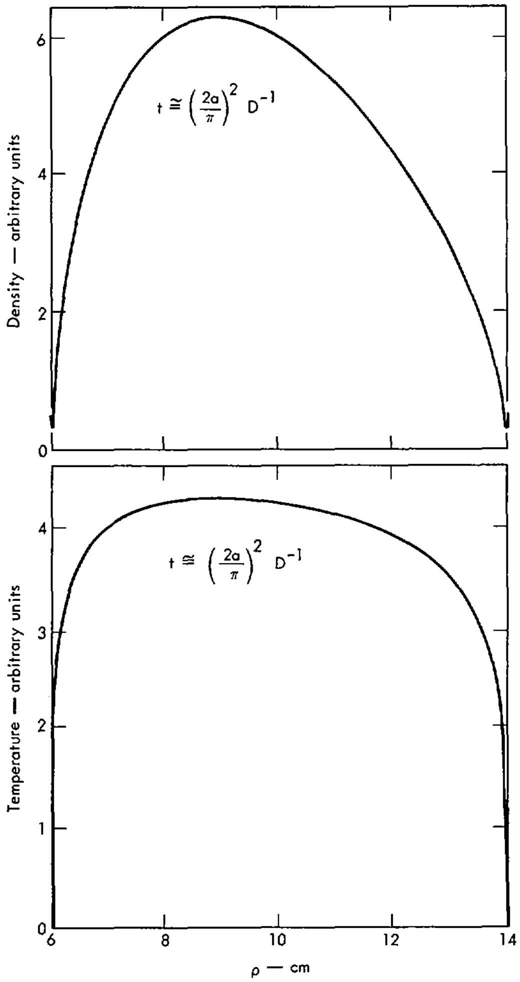

FIG. A-1. Solution of Eqs. (A-1) and (A-2). (a) Density profile after reaching steady shape; $t \simeq (2a/\pi)^2 D^{-1}$. Initial profile was formed from cosine shapes which peaked at 8.8 cm and fell to 5% of peak value at $r_i = 6$ cm and $r_o = 14$ cm. (b) Temperature profile at same t; initial profile was trapezoidal, going to 0.1% of central value at boundaries.

[1] We thank Dr. John Killeen for the numerical integration of these equations.

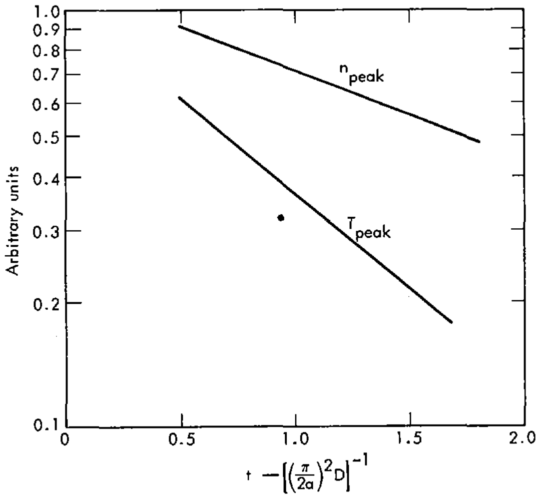

FIG. A-2. Decay of $n_{peak}(t)$ and $T_{peak}(t)$ for the case shown in Fig. A-1. The time scale is normalized to $(2a/\pi)^2\ D^{-1}$, the slab-model density decay time.

$n = n_e = n_i$, and $T = T_e = T_i$. After initial transients die out, the n and T profiles assume a steady shape. Such profiles and the corresponding decay rates of n and T are shown in Figs. A-1 and A-2 for a typical case. The decay rates may be written as

$$\tau_n^{-1} = q_1\ D\left(\frac{\pi}{2a}\right)^2 \tag{A-3}$$

and

$$\tau_T^{-1} = q_1\ q_2\ X\left(\frac{\pi}{2a}\right)^2 \tag{A-4}$$

where $2a = \rho_0 - \rho_i$. The factors $(\pi/2a)^2$ are obtained from a slab diffusion model. The correction factors q_1 and q_2, obtained by comparison with the numerical results, were found to be fairly constant over the range of interest and insensitive to the boundary conditions. Typically, $q_1 = 0.5$ and $q_2 = 0.25$.

ACKNOWLEDGMENTS

The authors wish to thank Dr. T. K. Fowler for his continued support of this project. We also wish to express our thanks to the SCL operator crew under direction of R. E. Riley, the electronics crew under direction of D. Branum, members of the mechanical engineering staff, and Mrs. S. Hawley for typing of the rough drafts.

REFERENCES

[1] ANDERSON, O. A., BIRDSALL, D. H., HARTMAN, C. W., LAUER, E. J., FURTH, H. P., Plasma Physics and Controlled Nuclear Fusion I (Proc. Conf. Novosibirsk, 1968) IAEA, Vienna (1969) 443.
[2] TAYLOR, C. E., DUFFY, T. J., Engineering Problems of Fusion Research (Proc. Sym. Los Alamos, April 1969) paper A-5.

[3] ROSSOW, T. L., Engineering Problems of Fusion Research (Proc. Sym. Washington, April 1971) paper E-3.
[4] HALBACH, K., ANDERSON, O. A., FUSS, D., Plasma Physics 12 (1970) 207.
[5] FUTCH, A. H. Jr., DAMM, C. C., Plasma Physics 9 (1967) 423.
[6] HARTMAN, C. W., HOOPER, E. B. Jr., "Assessment of Neutral Injection for the Superconducting Levitron," Lawrence Radiation Laboratory, Livermore, Calif., Rep. UCRL-50976 (1970).
[7] RUTHERFORD, P. H., Phys. Fluids 13 (1970) 482.
[8] FREEMAN, R. OKABAYASHI, M., PACHER, G., RIPIN, B., SCHMIDT, J., SINNIS, J., YOSHIKAWA, S., These proceedings, paper CN-28/A-3 (1971).
[9] MASSEY, H. S. W., Electronic and Ionic Impact Phenomena, Vol. II, Clarendon, Oxford (1969) 881.
[10] ANDERSON, O. A., HARTMAN, C. W., "Plasma Heating in the Superconducting Levitron by Energetic Electrons," Lawrence Radiation Laboratory, Livermore, Calif., Rep. UCRL-50824 (1970).
[11] DANDL, R. A., DUNLAP, J. L., EASON, H. O., EDMONDS, P. H., ENGLAND, A. C., HERRMANN, W. J., LAZAR, N. H., Plasma Physics and Controlled Nuclear Fusion Research II (Proc. Conf. Novosibirsk, 1968) IAEA, Vienna (1969) 435.
[12] TAYLOR, C. E., DUFFY, T. J., ROSSOW, T. L., BRANUM, D. R., SEXTON, J. H., LEBER, R. L., Engineering Problems of Fusion Research (Proc. Sym. Washington, 1971) paper A-6.
[13] ROSENBLUTH, M. N., KAUFMAN, A. N., Phys. Rev. 109 (1958) 1.

DISCUSSION

TO PAPERS IAEA-CN-28/A-4, A-5, A-6, A-7, A-8

D.M. MEADE: You state in your paper (CN-28/A-4) that the application of magnetic screening improved confinement, as had been predicted by theory. How much was the confinement improved in the experiments? How much improvement was predicted by theory?

B. LEHNERT: The improvement predicted by theory is shown in Fig.3 of the paper, which indicates the temperature T and the required H.F. heating current $\widetilde{J}_\varphi$ as functions of power loss for shielded and unshielded supports. The predicted and observed plasma behaviours agree within the limits of experimental error. In these experiments we have been working with comparatively weak magnetic fields ($B_0 \approx 0.3$ Vs/m^2) and low temperatures ($T \approx 5 \times 10^4$ to 10^5 °K), where the classical heat losses across the magnetic field and along the field lines to the unshielded supports are comparable. In future experiments the ratio of these losses should be decreased by using larger values of B and T, and it should then become easier to detect even the very small residual losses which may exist in the presence of support shielding.

D.M. MEADE: Have you made probe measurements in the plasma with a view to direct determination of the plasma fluctuations and hence the stability?

B. LEHNERT: In earlier experiments, not reported here, we conducted extensive investigations of the plasma and its boundary region by means of probes, microwaves, high-speed photography; in addition, we studied the overall plasma balance, during a decaying mode with the energy source removed. In all these cases the plasma was found to be flute stable. In experiments with rotating plasmas we reached "centrifugal" β-values - ratios between "centrifugal" and magnetic pressures - as high as 15 per cent during a free-wheeling mode.

TRAPPING EXPERIMENTS IN THE ASTRON*

N.C. CHRISTOFILOS, W.C. CONDIT, Jr., T.J. FESSENDEN,
R.E. HESTER, S. HUMPHRIES, G.D. PORTER, B.W. STALLARD,
P.B. WEISS
Lawrence Radiation Laboratory, University of California,
Livermore, Calif.,
United States of America

Abstract

TRAPPING EXPERIMENTS IN THE ASTRON.

The results of trapping experiments in Astron are presented. The location of the trapping region was moved 9.5 m from the injection point to prepare for experiments in which pulses are overlapped to build up an E-layer with field reversal. This was made possible by increasing the energy of the injected electrons to 6 MeV. By trapping this far from the inflector, it is possible to use a vacuum field which has a 10% deep well with small radial gradients. Thus the E-layers formed are unlikely to be ejected by a second pulse. However, because of the small radial gradients, the threshold for the precessional instability is small, and the E-layers that are formed are stable.

Single pulse trapping experiments with these deep, symmetric traps have produced E-layers with 5% field reversal (diamagnetic strength 5% of the vacuum field). The injected currents were in excess of 600 A.

Electronic equipment which will shortly provide a burst of 100 electron pulses at a rate of 960 pps is now available for a burst of three pulses. The first electron pulse is always lost to generate a thin plasma, while the second and third pulses have been stacked. The total circulating current in each of the stacked pulses is 1500 A thus the circulating current of the E-layer formed with two overlapped pulses is 3000 A. The diamagentic strength is 7%. No additional losses or reduction of the trapping efficiency was observed in stacking the second pulse.

A new feature of the Astron facility is the addition of a toroidal field generated by a pulsed axial current along the axis of the Astron solenoid. The presence of a weak toroidal field during the electron injection provides enough focusing to remove the threshold of stable precessional oscillations. Since in the presence of toroidal field the precessional oscillations are always stable it is possible to trap the E-layer in deeper mirror field (e.g. 14% instead of 8 to 10%). A stronger toroidal field during injection ($B_\theta \approx B_z$) provides axial focusing of the injected electron bunch resulting in improved trapping efficiency by about three-fold. In single pulse injection trapped E-layers of circulating current of 4000 A and diamagnetic strength of 15% have been observed. Finally, a strong toroidal field increasing in time applied after the E-layer trapping compresses the length of the E-layer. A toroidal field equal to 60% of the poloidal guiding field compresses the E-layer length by approximately a factor of two.

1. INTRODUCTION

The key feature of the Astron concept is a layer of relativistic electrons which provides both the magnetic confinement and heating of the plasma to fusion temperature. The currents of rotating relativistic particles at a sufficient level can create a magnetic field configuration with a unique property, namely, a magnetic well with closed magnetic lines. The closed lines provide confinement of plasmas with isotropic pressure while, for properly designed configurations, the destabilizing curvature drifts inherent in line closure tend to be overcome at every point along the lines by the favorable magnetic gradient drift prevailing within the closed magnetic well.

Since 1964 when experiments to trap and study the E-layer properties started, the goal of the Astron program has been to demonstrate an E-layer with closed magnetic lines as a first step, then plasma confinement at fusion temperature as the second step.

* Work performed under the auspices of the US Atomic Energy Commission.

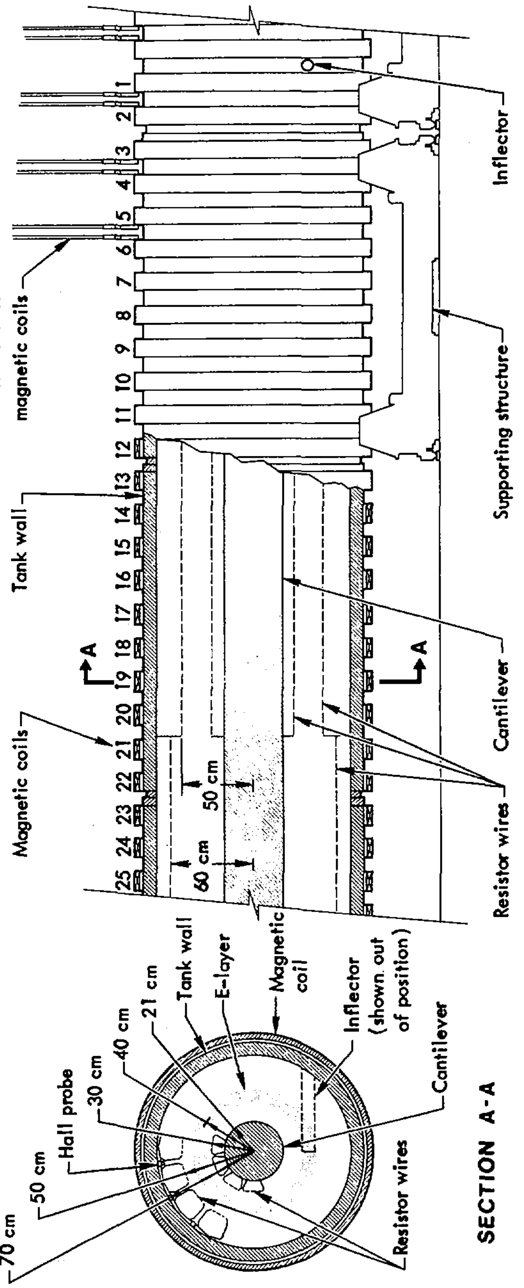

FIG. 1. Cross-section of the Astron tank.

Trapping of single electron pulses results in forming E-layers of diamagnetic strength from 5 to 15%. Therefore, stacking of many electron pulses is required in order to achieve an E-layer with diamagnetic strength higher than 100% and thus form the closed magnetic well required for plasma confinement. It has been recognized since 1965 that a fast modulator which can pulse the Astron electron accelerator at a rate of approximately 1000 pps is required to inject the electron pulses at a rate high enough to form an E-layer with field reversal. At that time the electron energy of the Astron accelerator was 3.5 MeV and the beam current 200 A. In 1967 a large scale improvement of the Astron facility was initiated. The first step was the construction and installation of a new evacuated chamber and new solenoid which was completed early in 1968. Since the last meeting of IAEA held in Novosibirsk, USSR, two major improvements of the Astron facility have been completed:

1) Increasing the electron energy to 6 MeV at a beam current of 600 A.
2) The addition of electronic equipment to pulse the accelerator in bursts of 100 pulses at a rate 960 pps. This equipment is now in the final testing stage providing at this time a burst of three pulses at a rate of 960 pps every 0.60 seconds.

Electrons are injected in the Astron solenoid in a poloidal field constant in time. Therefore, trapping of the electrons and formation of the E-layer is possible by employing a mechanism of energy loss of the electrons as they are falling in the mirror field. The energy loss is provided by resistive wires which are located near the outer wall of the tank (Fig. 1). The wires are carried in thin stainless steel containers at a radius of 50 cm. The radius of the outer wall of the evacuated chamber is 70 cm. Solenoidal coils are located in the cantilevers (Fig. 1) which also carry resistive wires. The inside coils are required to provide a magnetic field configuration which satisfies the so-called "betatron condition" allowing the injected electron bunch to maintain constant radius although it is falling in the mirror well.

The injected electron bunch travels at a radius of approximately 40 cm between the inner and outer resistive wires. The magnetic field of the electron bunch traveling between the resistor wires penetrates the spaces between the wires and the outer wall and the inner wires and the cantilever. Since the magnetic field of the electron bunch is varying with time generates currents in the wires thus energy losses resulting in slowing down the axial velocity of the electrons [1].

Trapping efficiency over 50% has been observed under certain conditions. The trapping with the resistors is discussed in more detail in the following Section.

An important question raised in the past was whether or not it is possible to stack electron pulses. What was under question was whether there is adequate momentum-space and whether or not the incoming electrons will displace the already trapped electrons. In the stacking of pulses electron losses can be created by the electromagnetic interaction of the already trapped electrons with the newly injected electrons. From momentum conservation one can observe that the larger the number of trapped electrons is, the smaller the momentum transfer per trapped electron should be. Therefore, the greatest difficulty in stacking pulses from the aspect of electron interaction is the stacking of the second over the first pulse which already has been successfully demonstrated.

Experiments of stacking electron pulses are discussed in Section 3 of this report.

A new feature of the Astron facility added very recently is a pulsed toroidal field generated by a pulsed current flowing in the cantilever section of the evacuated chamber. The toroidal field is generated along an 18 meter section of the Astron evacuated chamber.

Initially a 400 kJ capacitor bank was used to provide 200 kA of axial current every 60 seconds. In addition two small pulse generators were installed, one providing 10,000 A every second and the other 80,000 A of axial current every three seconds. Experiments to date indicate that the toroidal field can be very useful in many ways to the Astron facility. The presence of a weak toroidal field, approximately 5% of the guiding poloidal field during electron injection provides adequate focusing to remove the threshold to the stable regime of the precessional oscillations of the E-layer [2]. As a result it is possible now to increase the field index of the external poloidal field thus increasing the depth of the mirror trap from 8 or 10 to 14% or more. A stronger toroidal field during the injection ($B_\theta \approx B_z$) of the electrons appears to provide axial focusing of the injected electron bunch resulting in improved trapping efficiency. A time varying toroidal magnetic field applied shortly after formation of the E-layer is observed to compress the length of the E-layer. The experimental results to date with the toroidal field are discussed in Section 3 of this report.

In a theoretical paper [3] presented at the Novosibirsk meeting it was suggested that the addition of shear would stabilize the plasma with less total circulating current in the E-layer. Recently, since last December, the effect of the toroidal field in the E-layer orbits and equilibrium have been investigated theoretically [4,5,6,7,8,9]. The theoretical studies lead to the conclusion that by compressing the E-layer by a time varying toroidal field it is possible to increase the transverse momentum; hence, the total electron energy of the relativistic electrons. Thus by compressing an E-layer with an initial energy of 6 MeV it is possible to accelerate the electrons up to 15 or 20 MeV while at the same time the electron current density will become high enough to provide rapid heating of the confined plasma. The most important consequence of the addition of the toroidal capability in the Astron facility is that it appears that it is not impossible with the present Astron facility with some minor modifications to prove feasibility of the Astron concept by demonstrating plasma in the keV range in the next two years.

2. TRAPPING AND LIFETIME OF THE E-LAYER

The interactions of the injected electron bunch with the resistors has been extensively studied since 1968 when the new evacuated chamber and solenoid were made available. Previously, imperfections of the magnetic field precluded trapping in high vacuum, thus the question had been raised whether the resistors or the gas required for prompt neutralization of the E-layer were responsible for the trapping. Therefore, the injection and trapping of the E-layer were investigated experimentally by measuring the fields of the electron bunch with fast time response (10 nsec) magnetic probes. The probes were placed at a number of axial locations along the Astron tank. At injection the signal outputs of the probes were simultaneously recorded on photographic film. The traces were then digitized at 10 nsec time intervals and stored on punched cards for computer analysis. The computer was used to generate displays of the E-layer as it moved in the axial direction in Astron.

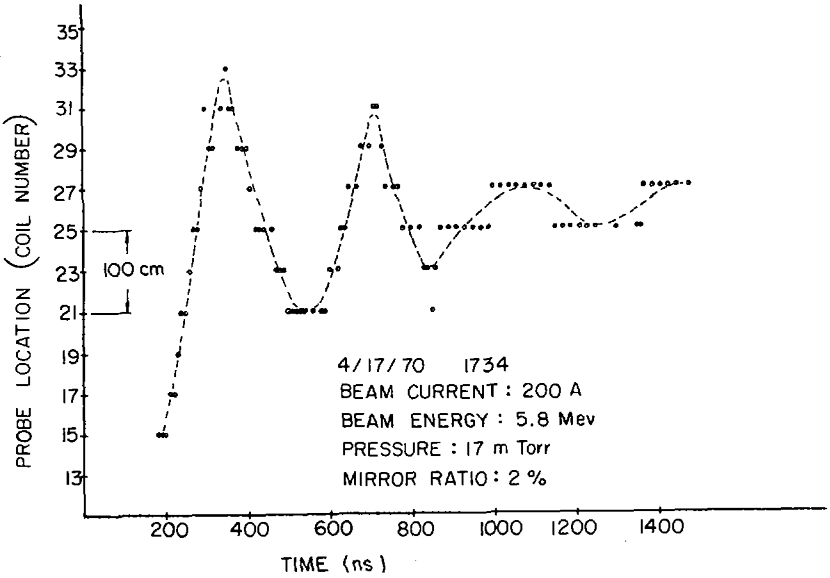

FIG. 2. Position of peak E-layer density versus time.

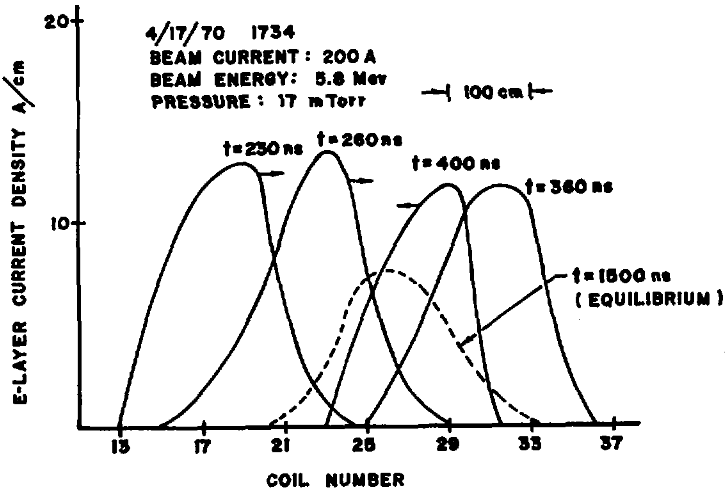

FIG. 3. Measured E-layer current profiles during trapping.

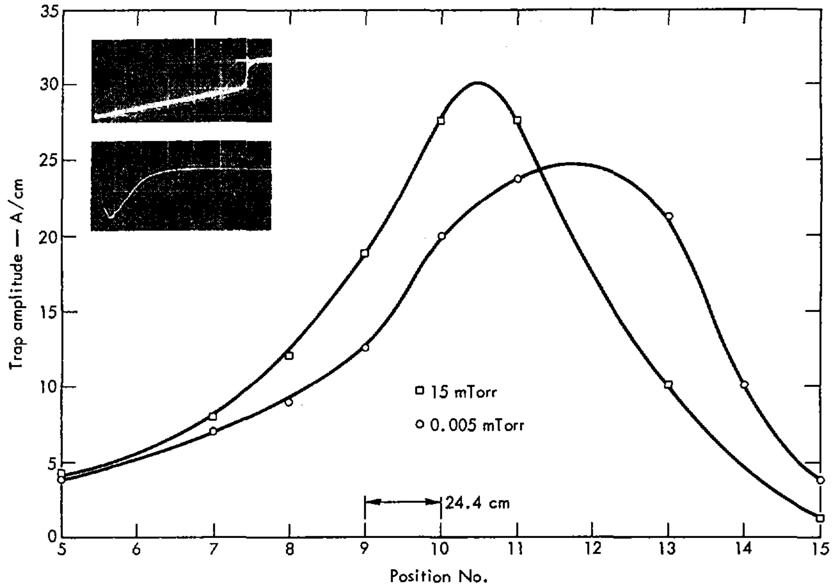

FIG. 4. Distribution of the E-layer along the Astron tank at H_2 pressures of 15 and 0.005 mTorr (date of measurement = March 4, 1970, beam current 1 m before injection point = 400 A, current trapped = 3330 A at 15 mTorr and 3170 A at 0.005 mTorr, E-layer diamagnetic strength = 7.9% at 15 mTorr and 6.6% at 0.005 mTorr). The oscillograms show two outputs from the diamagnetic probe located at coil 11. The top oscillogram (vertical scale = 12.5 A/cm/div, horizontal scale = 0.2 msec/div) was obtained at 15 mTorr, and the bottom oscillogram (vertical scale = 12.5 A/cm/div, horizontal scale = 5 μs/div) was obtained at 0.005 mTorr.

The results of an experiment with a 200 A beam of 5.8 MeV energy are shown in Figs. 2 and 3. Figure 2 shows the position of peak E-layer current density as a function of time as the E-layer oscillates in the magnetic well. Note the damped motion of the E-layer showing a loss of axial energy. Figure 3 shows the E-layer at various times in the magnetic trap as well as the final distribution of charge after the transients at injection were damped. Distribution of the E-layer current at small increments of time have been assembled to make a motion picture which shows the injection process. Several examples are shown in the oral presentation.

In order to elucidate the question raised on the contribution of the resistors and the background gas in the electron trapping an experiment was done which proves that the residual gas plays no role in the trapping of the E-layer as shown in Fig. 4. During one day's run, trapping experiments were conducted at two pressures -- 15 and 0.005 mTorr. The latter is the base pressure in the tank. Clearly, the total trapped charge is almost the same for both pressures. The high-vacuum trap is somewhat longer because of the self-fields of the E-layer. At 15 mTorr, the E-layer is neutralized in about 0.27 μsec whereas 800 μsec are required for neutralization at 0.005 mTorr. Thus, at higher pressures, the magnetic field of the E-layer tends to hold the E-layer together, making a narrower distribution. It is clear from the oscillograms in Fig. 4 that the lifetime of the E-layer in a high vacuum is much less than it is at 15 mTorr. This can be explained

TABLE I. COMPARISON OF ENERGY LOSS RATES

Time (nsec)	v_z/c	K_θ(A/cm)	P_E(mW)	P_T(mW)
275	0.10	16	1.6	1.8
430	0.057	9	0.49	0.32
650	0.065	7.3	0.17	0.25
780	0.047	7.8	0.13	0.21

v_z = axial velocity of electron bunch

K_θ = current density at peak of bunch

P_E = resistor loss rate calculated from probe measurements

P_T = resistor loss rate calculated from energy

by the neutralization phenomenon. In a high vacuum the stabilizing forces that arise from the image currents in the walls are cancelled by the electric field of the E-layer. Hence, the precessional instability grows rapidly and the E-layer dumps in the first cycle. It is thus very clear that the gas has a strong effect on both the shape and the lifetime of the E-layer, but it has very little effect on the trapping of the E-layer.

An analysis of the resistor interaction with the E-layer was performed in cylindrical geometry which considered the effects of resistors on the cantilever and on the wall. In this analysis the long-thin E-layer approximation was used [10]. This allows the currents flowing in the resistors to be easily calculated. From these currents the Ohmic energy loss per unit length is found and identified as the energy lost by the layer as it moves towards the trap. The results of this analysis compare favorably with the original analysis by Christofilos [1]. One finds that the energy dissipated depends primarily on the distance traveled by the layer and is a rather weak function of the E-layer velocity. This is a simple statement of the fact that the energy dissipated depends on the number of wires cut by the fields of the layer. For comparison of the above resistor energy loss theory with experiment we present the results of the experiment with a 200 A beam of 5.8 MeV energy. The energy dissipated by the resistors was measured experimentally through the use of the fast magnetic probes. For this experiment there were no resistors on the cantilever near the center of the trap so that the probe measurements yield the total energy loss. A comparison of the energy loss rate determined experimentally (P_E) with those calculated theoretically (P_T) is presented in Table I. As can be seen the two results agree within a factor of two.

The E-layer lifetime has been studied as a function of the background gas pressure. In these experiments the pressure was changed and the coils around the inflector were individually tuned to optimize trapping. Thus, the trapping amplitude achieved depended on how much time was spent on "fine tuning". A great deal of time was spent on tuning at 15 mTorr, somewhat less at 2 mTorr, and relatively little at points in between.

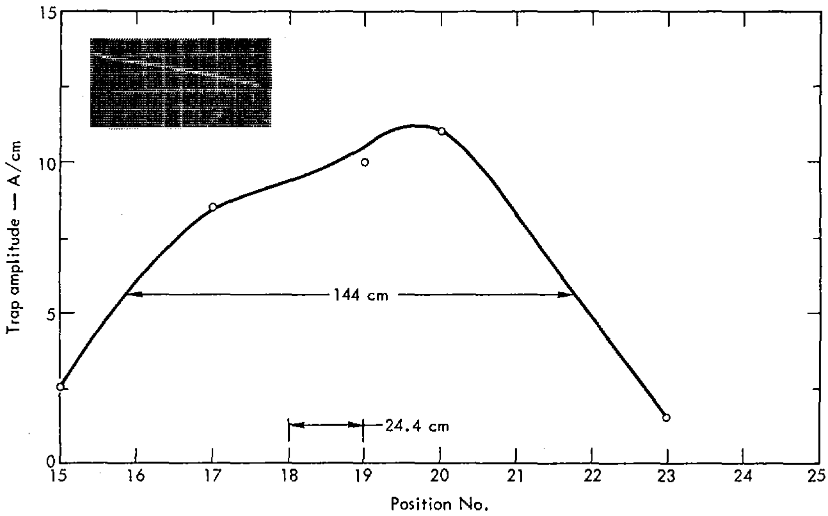

FIG. 5. Distribution of the E-layer along the Astron tank (date of measurement = April 6, 1970, beam energy = 5.9 MeV, beam current 1 m before injection point = 400 A, pulse width = 120 ns, energy window = ±1%, H_2 pressure = 2 mTorr, current trapped = 1280 A, trapping efficiency = 22%, E-layer diamagnetic strength = 2.7%, E-layer half-life = 18 ms). The oscillogram (vertical scale = 2.5 A/cm/div, horizontal scale = 2 ms/div) shows the output from the diamagnetic probe located at coil 21.

Even with the dependence on tuning time, the trapping amplitude at 2 mTorr was only about 20% less than that at 15 mTorr. Thus, the trapping mechanism was not dependent on the pressure in traps located 6 to 9 meters from the inflector. As before, the E-layer was slightly longer at lower pressures. An interesting feature in Fig. 5 is the long half-life of the E-layer -- 18 msec. This is the longest half-life measured to date. At higher pressures the E-layer lifetime is observed to be inversely proportional to the gas pressure e.g., $\tau_{1/2} = (36/p)$ where p is expressed in mTorr.

At injection two distinct instabilities are present at frequencies of several hundred megahertz to 40 gigahertz. As previously reported the first instability to be observed is called the negative mass instability and is responsible for most of the rf noise at injection. This instability results from a strong azimuthal bunching of the relativistic electrons and has been the subject of considerable investigation [11]. Theory has clearly shown that the instability is quenched by spreading of the injected electrons by the strong electric fields of this mode. Observation has shown that this instability is quenched in a few hundred nanoseconds during the trapping phase.

The second instability occurring just after injection involves an interaction of the relativistic electrons with the cold plasma electrons and is called the hybrid mode. This instability is delayed until the E-layer is charge neutralized by primary ionization whereupon its presence is signified by a burst of light and a jump in plasma density indicating an rf breakdown. We studied the relationship between the plasma density, the emission frequency, and time via the following procedure. A signal proportional to the transmission frequency of a YIG* filter was used to drive the x axis

*Yttrium, iron and garnet.

of an oscilloscope. The y axis was driven by the output of a k-band interferometer that measured the cold-electron density. The output of the YIG filter, which was blocked during the negative-mass mode, was used to modulate the intensity of the oscilloscope beam. Thus, when the hybrid mode occurred, the emission frequency and the plasma density at which the emission occurred were simultaneously recorded as shown in Fig. 6. The hybrid mode instability is observed to be quenched in a couple of microseconds as soon as the plasma density reaches a value of approximately 100 times the E-layer electron density. The quenching of the instability could be attributed to plasma collisions or combination of spreading the E-layer electron transverse velocity and plasma collisions.

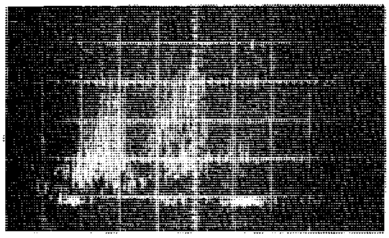

FIG. 6. Oscillogram showing the relationship between the plasma density and the emission frequency of the hybrid mode (vertical scale = 1.2×10^{10} particles/cm^3/div, horizontal scale = 40 MHz/div, centre frequency 1200 MHz). The recording equipment was turned off until 1 μs after injection in order to suppress the rf-generated by the negative-mass mode; it was then turned on for 2 ms.

The multiple pulse stacking experiments have shown that each pulse excites the hybrid mode for a few microseconds. This indicates that this instability is not quenched merely by the existence of cold plasma and that it is most probably quenched by spreading of the E-layer electrons transverse velocity in combination with the presence of cold plasma.

Following the quenching of the two instabilities observed during injection and plasma formation no other instability has been observed during the long lifetime of the E-layer. The precessional oscillations are always stable when the E-layer current per cm is above a certain threshold level by the image currents generated in the walls of the evacuated chamber by the self-field of the E-layer [2].

3. PULSE STACKING

In this section we discuss experiments that have been done to demonstrate the feasibility of building up the E-layer by trapping-successive pulses, i.e., pulse stacking. In order to do this it has been necessary to develop electronic equipment which fires the accelerator at a rate of 960 pulses per second. This then allows a pulse to arrive in the trapping region before the previously formed E-layer has decayed appreciably. Hence the pulse can be added to the E-layer. Unfortunately, to date we are limited by a lack of some necessary electronic components to an accelerator burst of three pulses. The first pulse has different energy, current, and injection angle, so it is not trapped. Hence, we have been able to stack only two pulses.

There was no toroidal field used during these experiments. The E-layer is therefore subject to the precessional instability. To overcome this instability during its formation, it is necessary to neutralize the

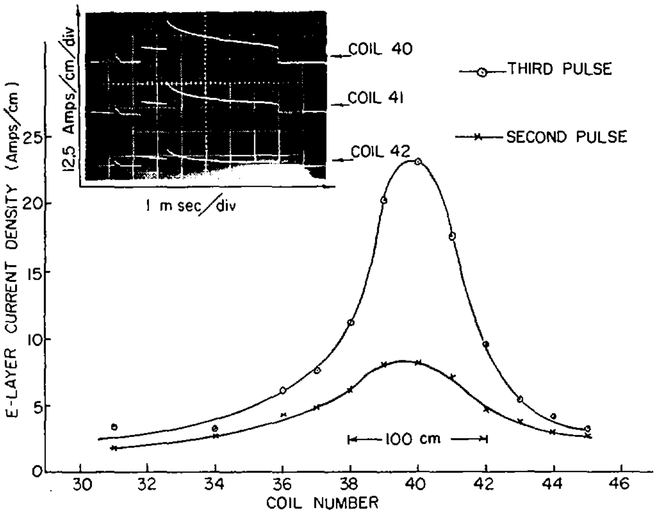

FIG. 7. Typical results of pulse stacking experiments. The total circulating current after the second pulse is 1500 A and the total current after the third pulse is 3000 A. The injected current is 600 A at 5.8 MeV.

E-layer very early in time so that the field of image currents in the walls generated by the self-field of the E-layer stabilize the precessional oscillations [2]. In the past, this has been done by using a static pressure of several microns of hydrogen in the Astron tank. The plasma produced by the 6 MeV electrons ionizing this neutral gas then neutralizes the E-layer. The use of the neutral gas also means that the electron "beam" is neutralized during the transport to the trapping region, a distance of 9.8 m. This creates a radially thick beam during the transport. Because of this it has been necessary to use shallow (2-3%) mirror fields. However, due to the interaction between the previously formed E-layer and an incoming pulse, it is not possible to stack pulses in a shallow mirror. Hence, it is desirable to have a pressure of a few microns in the trapping region and high vacuum in the transport region.

To achieve this, a set of 8 fast-acting needle valves [12] were arranged symmetrically around the tank at the trap center. These valves are each capable of introducing up to 15,000 micron-liters of hydrogen in slightly under one millisecond. During the first millisecond after the valves are fired, the gas is redistributed in the vicinity of the fast valves and it then expands freely at slightly over the sonic velocity. Thus, for a period of several milliseconds after the valves are fired, the pressure in the tank satisfies the conditions set forth in the previous paragraph.

Typical results of the pulse stacking experiments using the fast gas valves, are shown in Fig. 7. The oscillogram shows the signals from 3 of 11 magnetic probes which measure the self-magnetic field of the E-layer at eleven positions along the Astron tank. Note that the first pulse is not trapped well as previously explained. The second pulse is trapped with a peak current density of about 8A/cm and a total circulating current of 1500 A. The total current is then doubled by the addition of the third pulse. Hence the trapping efficiency is not altered by the presence of

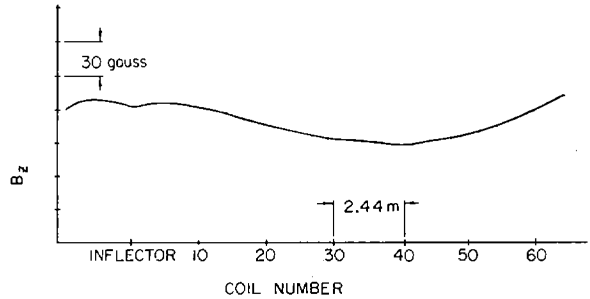

FIG. 8. External field profile for pulse stacking experiments.

the E-layer. The peak current density is more than doubled, to about 23 A/cm, because the larger self-forces cause the E-layer to compress axially. The external field profile is shown in Fig. 8. Note that the mirror depth is about 8% rather than the 2%-3% mirror depth used when trapping in a static gas pressure.

4. TOROIDAL MAGNETIC FIELD INTERACTIONS WITH THE E-LAYER

Experiments with toroidal field interacting with the E-layer have been in progress during the last two months. There are two applications of the toroidal magnetic field in the Astron.

1) To employ toroidal magnetic field during the injection of the electrons.
2) To employ a strong toroidal field of intensity which is several times the intensity of the poloidal guiding field, to compress the transverse dimensions of the E-layer.

The first class of experiments can be divided in two categories. A relatively weak toroidal field ($B_\theta \approx .05\ B_z$) removes the threshold for precessional stability, [2] thus allowing trapping of the E-layer in magnetic traps much deeper than is possible without the toroidal field. According to Ref.13 the frequency of radial and axial betatron oscillations of the E-layer as modified by the toroidal field are

$$\nu_r = (1 - n + n_e + \mu_i)^{1/2}\ \omega_0 \tag{1}$$

$$\nu_z = [n + n_e + \mu_i\ (a^2/b^2)]^{1/2}\ \omega_0 \tag{2}$$

where $n = (R\partial B_z/B_z\partial r)$ is the field index of the external mirror field, n_e is the field index of the field of image currents in the walls generated by the self-field of the E-layer, $\omega_0 = v_\theta/R$ is the rotation frequency of the E-layer electrons, R is the equilibrium radius and

$$\mu_i = \alpha_1\ (B_\theta^2/B_z^2) \tag{3}$$

and a, b are the radial and axial half-thickness of the E-layer respectively. According to Ref.13 the coefficient μ_i is due to a focusing force generated by a term ($v_\perp \times B_\theta$) where $v_\perp$ is an internal collective motion of the E-layer

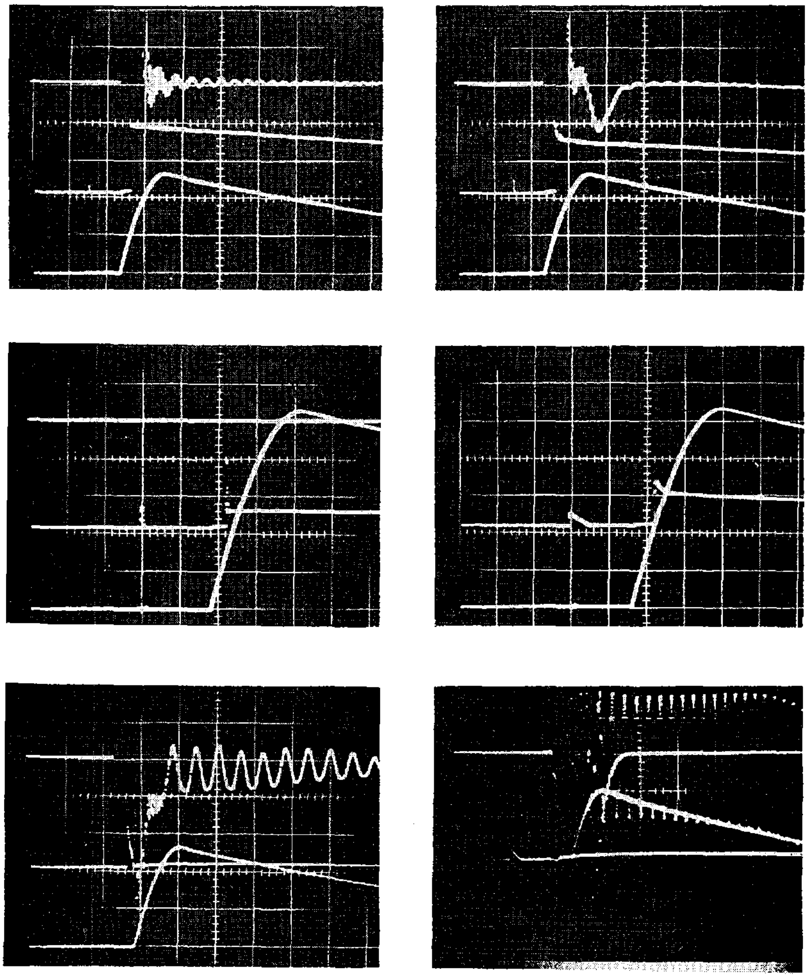

FIG. 9. Effect of toroidal field in precessional oscillations.

Precession frequency
83 kHz
$n = 1.3 \times 10^{-3}$

Precession frequency
175 kHz
$n = 2.9 \times 10^{-3}$

Lower trace: Axial current in the Astron solenoid, 1 ms/div., 3700 A/div. in top and bottom pictures, 1850 A/div. in the middle pictures; middle trace: E-layer current/cm, 1 ms/div., 2.5 A/cm/div.; upper trace: $\dot{B}_e$, time derivative of the E-layer self-field, time 20 μs/div.

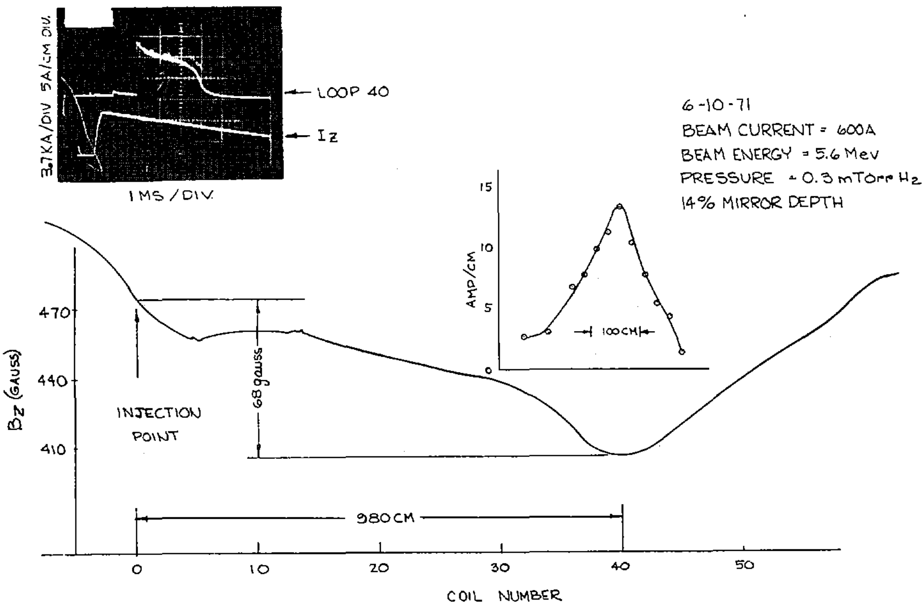

FIG. 10. Trapping in deep mirror in the presence of a weak toroidal field during injection.

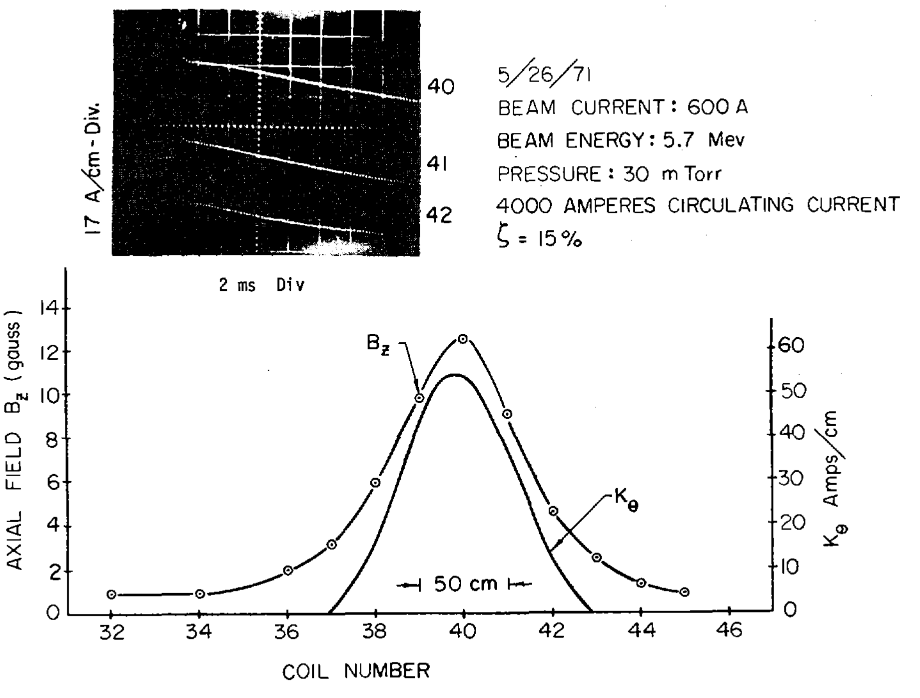

FIG. 11. Trapping in the presence of strong toroidal field at injection ($B_\theta \approx B_z$).

electrons generated by the presence of the toroidal field. In the absence of toroidal field electrons oscillate in the axial direction with a spectrum of axial velocity v_z but no net axial current exists. In the presence of the toroidal field the axial motion is polarized and a net current exists in one direction in the E-layer region located at $r > R$ and in the other direction in the E-layer region located at $r < R$. In this way a $(j_\perp \times B_\theta)$ force is generated where the current $j_\perp$ is in the r, z plane and parallel to the surface of the E-layer. The resulting force is always directed inwards thus it is a focusing force expressed in the dimensionless unit μ_i.

In order to determine the value of the unknown coefficient (α_1) the following experiment was done. A weak E-layer was trapped in the presence of a toroidal field. The value of μ_i was larger than $(n - n_e)$ as it is evidenced in the oscillogram at the top of Fig. 9 where it is shown that precessional oscillations are damped out promptly upon formation of the E-layer. The E-layer lifetime is very long. In the next step the pulsed axial current which generates the toroidal field was delayed so that the value of the toroidal field at electron injection was reduced to a value where $n - \mu_i \approx 0$. Sporadic trapping at very low level occurred occasionally as shown in the oscillograms at the middle of Fig. 9. Then the axial current was further delayed until no toroidal field was present during injection. The trapped E-layer current was at low level below the threshold for precessional stability and small enough to obtain $n_e << n$. Thus the frequency of the precessional oscillations was measured, hence the value of n^* was determined in two cases. This experiment allowed the measurement of the value of the coefficient (α_1) which was found to be of the order of unity. The value of the field required at injection for good trapping is such that $\mu_i \approx 2n$ which requires an axial current of the order of 10,000 A. The current profile of the E-layer and the external field with 14% deep mirror are shown in Fig. 10. Note that when the axial current I_z decays to a level where $(\mu_i + n_e - n = 0)$ an integral resonance occurs resulting in dumping the E-layer as shown in the oscillogram at the top left of Fig. 10.

The second application at injection is to increase the value of the toroidal field to several hundred oersteds, requiring an axial current of 100,000 A to achieve axial focusing of the injected electron bunch. The required field value to achieve axial focusing as a function of the injected electron current and energy is calculated in Ref. 13. Injection into a strong toroidal field resulted in single pulse trapping of E-layers having over 4,000 A of circulating current with peak diamagnetic strength ζ of 15%. The current profile of the E-layer is shown in Fig. 11.

The most important application of the toroidal field, however, is the compression of the transverse dimensions of the E-layer by a strong toroidal field. According to Ref. 14 the application of a toroidal field $B_\theta >> B_z$ where B_z is the poloidal guiding field should compress the E-layer to a ring of circular cross-section and minor radius (r_θ) where

$$r_\theta = \left(\frac{B_z}{B_\theta}\right)^{1/2} \cdot \psi^{1/2} \cdot R \qquad (4)$$

where

$$\psi = (a\, b\, v_r\, v_z/c^2R^2)^{1/2}$$

*The frequency of the precessional oscillation $\omega_p = \frac{n}{2}\omega_o$.

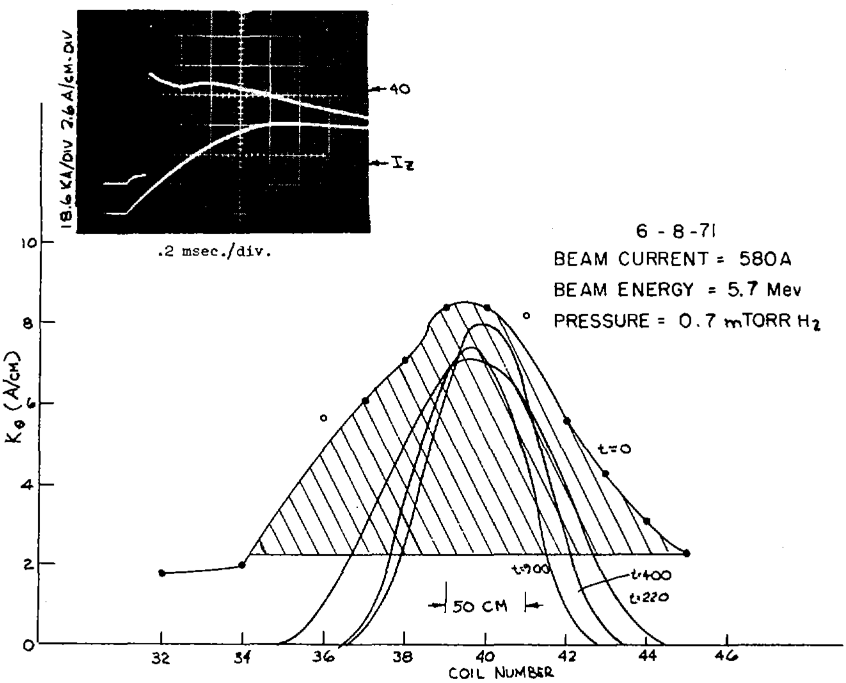

FIG. 12. E-layer current profiles during compression by a time-varying toroidal field.

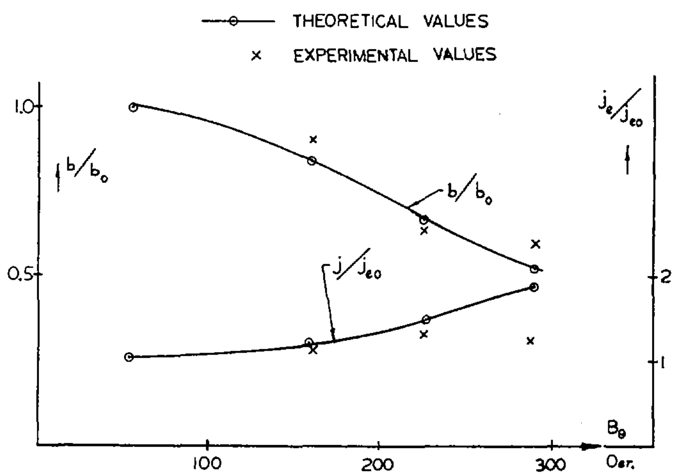

FIG. 13. Current per cm and length of the E-layer during compression by a time-varying toroidal field.

and v_r, v_z are the peak values of the initial r, z velocity components of the E-layer electrons. During the compression phase when $B_\theta < B_z$ and in the case $\nu_z < \nu_r$ the axial length b of the E-layer is given in Ref. 15 by the following equation

$$b = \left(\frac{\nu_{zo}}{\nu_z}\right)^{1/2}\left(\frac{B_z^2}{B_z^2 + B_\theta^2}\right)^{1/4} b_o \tag{5}$$

where b_o is the initial length of the E-layer at the beginning of the compression. For $B_e < B_z$ Eqs. 2, 3 and 6 yield

$$b = b_o \frac{n^{1/2}(b_o/a)}{\left(1 + \frac{B_z^2}{B_\theta^2}\frac{b^2}{a^2} n\right)^{1/2}}\left(\frac{B_z^2}{B_\theta^2 + B_z^2}\right)^{1/2}\left(\frac{B_z}{B_\theta}\right) \tag{6}$$

During the compression phase the transverse velocity of the E-layer increases as the transverse dimensions decrease in accordance with momentum-space conservation. As long as B_θ is smaller than B_z and $\mu_i < 1$ the radial thickness changes only slightly for the frequency of radial betatron oscillations remains practically constant. All the compression is initially in the axial dimension because the frequency of the axial betatron oscillations change very fast as μ_i becomes larger than n.

The initial distribution of the transverse velocity of the E-layer electrons is nearly gaussian. Consequently particles with initial large value of transverse velocity are lost during the compression process. Under the assumption that the electrons with higher axial velocity are lost first and by measuring the axial distribution of the current of the E-layer at the end of the compression phase it is possible to determine the current distribution in the E-layer - before it is compressed - of the electrons which survive the compression by the simple procedure of finding in the initial current distribution an area representing the circulating current of the compressed E-layer and chop-off the area containing the electrons with the highest axial velocity. The current profile of an E-layer before and after three stages of compression is shown in Fig. 12. The area representing the surviving circulating current is the shaded area shown in the current profile before it is compressed. Then the full width at half-maximum in the shaded area is considered the initial width (b_o) of the E-layer. The width (b) and peak current j_e^* are plotted in Fig. 13 as a function of the time varying field B_θ. Theoretical values calculated from Eq. 6 for $n = 1.3 \cdot 10^{-3}$, $(b_o/a_o) = 10$ and $B_z = 500$ oersteds are also shown in Fig. 13. It appears that the experimental values are consistent with the theoretical calculations.

REFERENCES

[1] CHRISTOFILOS, N. C., "Astron Electron Injection", Lawrence Radiation Laboratory, Livermore, Report UCRL-5617-T, (1959).

[2] CHRISTOFILOS, N. C., et al., Proc. 3rd Int. Conf. on Plasma Phys. and Controlled Nucl. Fusion Res., Novosibirsk, 1968, Vol. I, IAEA, Vienna (1969) 967.

[3] FOWLER, T. K., et al., Proc. 3rd Int. Conf. on Plasma Phys. and Controlled Nucl. Fusion Res., Novosibirsk, 1968, Vol. I, IAEA, Vienna (1969) 981.

[4] YOSHIKAWA, S., Physical Review Letters, 26 (1971) 295.

[5] CHRISTOFILOS, N. C., "E-Layer Equilibrium in the Presence of Toroidal Magnetic Field", Lawrence Radiation Laboratory, Livermore, Report UCID-15770, (1970).

[6] CHRISTOFILOS, N. C., "Plasma Confinement in a Toroidal Field Modified by the E-Layer Field", Lawrence Radiation Laboratory, Livermore, Report UCID-15774 (1970).

[7] CHRISTOFILOS, N. C., "Better Approximations to E-Layer Equilibria in the Presence of a Toroidal Field", Lawrence Radiation Laboratory, Livermore, Report UCID-15781 (1971).

[8] YOSHIKAWA, S. and CHRISTOFILOS, N. C., These Proceedings, Paper No. CN-28/F-1 (1971).

[9] CHRISTOFILOS, N. C., "Acceleration of Relativistic Electrons by Compression with a Pulsed Toroidal Magnetic Field", Lawrence Radiation Laboratory, Livermore, Abstract UCRL-73171 (1971)(Submitted to the 8th Int. Conf. on High Energy Accelerators, CERN, Geneva, September 20-24, 1971).

[10] PORTER, G. D., and WEISS, P. B., "Calculation of an Enclosed, Cylindrically-Symmetric Green's Function and Its Comparison to Field Measurements", Lawrence Radiation Laboratory, Livermore, Report UCRL-72936 (1971).

[11] BRIGGS, R. J., and NEIL, V. K., Plasma Physics 9 (1967) 209.

[12] BIRDSALL, D. H. and PING, D. E. Rev. Sci. Inst. 36 (1965) 1777.

[13] CHRISTOFILOS, N. C., "Focusing E-Layers and Electron Rings with Toroidal Magnetic Field", Lawrence Radiation Laboratory, Livermore, Report UCRL-73227 (1971) (Submitted to Physical Review Letters).

[14] CHRISTOFILOS, N. C., "Compressing the E-Layer With a Pulsed Toroidal Magnetic Field", Lawrence Radiation Laboratory, Livermore, Report UCRL-73214 (1971) (Submitted to Physical Review Letters).

[15] RENSINK, M. E., "E-Layer Compression by a Toroidal Field", Lawrence Radiation Laboratory, Livermore, Report UCIR-563 (1971).

THEORETICAL STUDY OF E-LAYER AND PLASMA BEHAVIOUR IN ASTRON*

D.V. ANDERSON, G.A. BENFORD, M. BRETTSCHNEIDER, J. KILLEEN,
W.A. NEWCOMB, A.A. MIRIN, M.E. RENSINK
Lawrence Radiation Laboratory, University of California
Livermore, Calif.,
United States of America

Abstract

THEORETICAL STUDY OF E-LAYER AND PLASMA BEHAVIOUR IN ASTRON.

The injection, equilibrium, and stability of the E-layer and confined plasma in Astron are investigated. Self-consistent equilibrium configurations for a collisionless E-layer and an ideal plasma fluid have been obtained from a numerical solution of Ampere's law, using various models for both the E-layer and the plasma pressure profiles. The degree of field reversal and the shape of the magnetic well can be varied so as to obtain equilibria with favourable stability properties.

The stability of an E-layer, alone or in conjunction with a cold background plasma, has been analysed for modes with wavelengths less than or comparable to E-layer dimensions. The results are in good qualitative agreement with experimental observations on the precession, negative-mass, and plasma hybrid modes. The most important stabilizing mechanism is seen to be energy spread in the E-layer.

The stability of the confined plasma is investigated using the magnetohydrodynamic (MHD) energy principle. A numerical solution of the eigenvalue problem, which arises from minimization of the potential energy, allows the MHD-stability of any of the equilibrium models used to be tested. The limiting plasma pressure is determined, and specific numerical examples of stable equilibria are given.

A time-dependent numerical model of the Astron, with which injection and trapping can be studied in detail, has also been developed. The effects due to the resistors, neutralization, and the ambient plasma have been included. The model is axially symmetric. The E-layer electrons are simulated by many thousands of finite-size super-particles, which move in the r-z domain and have velocity components v_r, v_θ, and v_z. The model is relativistic and the electromagnetic fields are obtained by solving four wave equations — three for the vector potential and one for the scalar potential. The E-layer and plasma currents and the current induced in the resistor wires are included in the above field equations. The computed self-fields are added to the external field to give the field configuration as a function of time. Numerical results indicate that resistive trapping behaviour of one pulse is similar to that experimentally observed. Results of multiple pulse injection will be presented.

1. INTRODUCTION

In this paper we review progress in four areas of theoretical study related to the Astron experiment. These areas include the injection and trapping of the electron layer, the calculation of E-layer and plasma equilibrium, the stability of the confined plasma equilibrium, and the stability of the E-layer itself.

To consider the stability of the confined plasma we briefly review our computational studies [1] of E-layer and plasma equilibria. This work has recently been reported [2] in considerable detail. Self-consistent equilibrium configurations for a collisionless E-layer and an ideal plasma fluid have been obtained from a numerical solution of Ampere's law. In section 2 we describe models of the E-layer and plasma and give results corresponding to these models.

* This work was performed under the auspices of the US Atomic Energy Commission.

In section 3 we consider the hydromagnetic stability of these confined configurations. We do this by using the MHD energy principle. A numerical solution of the eigenvalue problem, which arises from minimization of the potential energy, allows us to test the stability of the equilibrium solutions that we have obtained in section 2. We illustrate this procedure for several E-layer and plasma models and for a range of values of β.

In section 4 the stability of the E-layer is considered using a linearized Vlasov equation for the layer and a fluid description for the plasma. Several modes are identified and analyzed using perturbation theory. Stabilizing mechanisms are examined and evaluated.

In the final section we describe our efforts in the numerical simulation of the Astron experiment. This work at present has been concentrated on the injection phase. We describe a two-dimensional simulation code capable of modeling many aspects of the experiment, including the effect of the resistors, neutralization of the E-layer, the shape of the vacuum field, and the mode of injection. We show results for the trapping of two pulses.

2. E-LAYER AND PLASMA EQUILIBRIA

The equilibrium magnetic field for Astron configurations is obtained by solving Ampere's law,

$$\nabla \times \vec{B} = 4\pi \vec{j} \tag{1}$$

We include a given vacuum magnetic field and the fields due to the E-layer and confined plasma. The E-layer current density is obtained from the definition

$$\vec{j}_E = q_E \int d^3p \, \vec{v} \, f_E \tag{2}$$

where f_E is a given phase space distribution function that satisfies the time-independent Vlasov equation. The plasma current density is obtained from the equilibrium equation for an ideal conducting fluid

$$\vec{j}_p \times \vec{B} = \nabla p \tag{3}$$

where p is a given scalar pressure function. We use cylindrical coordinates (r,θ,z) and assume current only in the θ direction. Then, the magnetic field is derivable from the flux function $\psi(r,z)$ via

$$\vec{B} = r^{-1} \nabla\psi \times \hat{\theta} \tag{4}$$

where $\hat{\theta}$ is a unit vector. The distribution function f_E can be an arbitrary positive functional of the constants of the motion, energy H, and canonical angular momentum P_θ. We have used three such models in our calculations:

$$f_1 = \Lambda e^{-\beta(H+\alpha P_\theta)} \tag{5a}$$

$$f_2 = \Lambda e^{-\beta H} \delta(P_\theta - P_0) \tag{5b}$$

$$f_3 = \Lambda \delta(H - E_0) \delta(P_\theta - P_0) \tag{5c}$$

where Λ, β, α, P_0, E_0 are constant parameters. The plasma pressure is constant on a flux surface, so p can be an arbitrary positive functional of the flux $\psi(r,z)$. In our system, the closed flux surfaces have $\psi \leq 0$ and we have chosen a model,

$$p_1 = K(\psi_0 - \psi)^m \, \theta(\psi_0 - \psi) \tag{6}$$

where ψ_0 is a negative constant which defines the boundary of the plasma. We have also used a cosine model of the form

$$p_2 = K \cos^m \left[\frac{\pi}{2}\left(\frac{\psi - \psi_V}{\psi_0 - \psi_V}\right)\right] \theta(\psi_0 - \psi) \tag{7}$$

where ψ_V is the value of the flux at the bottom of the magnetic well. For these models, Ampere's law becomes a nonlinear partial differential equation for $\psi(r,z)$. For example, using the f_3 model for an E-layer with no plasma present, the dimensionless form of this equation is [2]

$$R \frac{\partial}{\partial R}\left(\frac{1}{R}\frac{\partial \psi}{\partial R}\right) + \frac{\partial^2 \psi}{\partial Z^2} = AR^{-1}(P - Q\psi)\theta(E - R^{-1}\,|P - Q\psi|) \tag{8}$$

where A, P, Q, and E are constants. It is solved numerically on a rectangular domain in the R-Z plane, with perfectly conducting boundaries at R_W and at $\pm Z_W$. The given vacuum magnetic field is not affected by these boundary conditions.

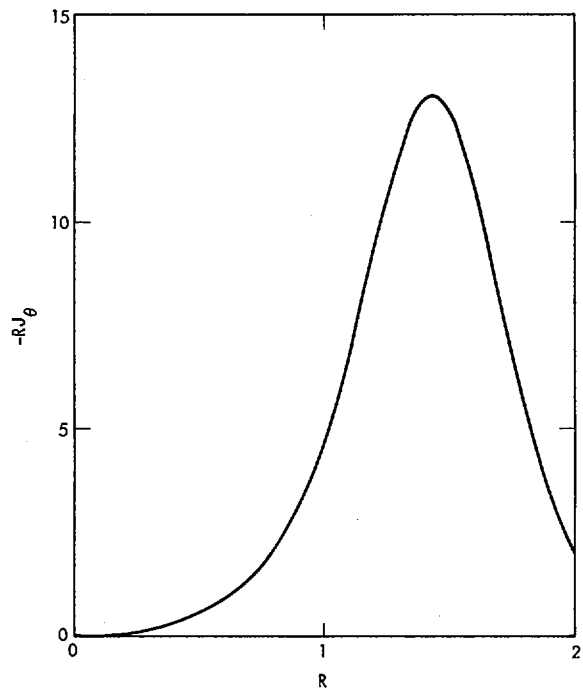

FIG. 1. E-layer current profile at the midplane for the "rigid rotor" model, Eq. (5a). There is a perfectly conducting wall at R = 2.

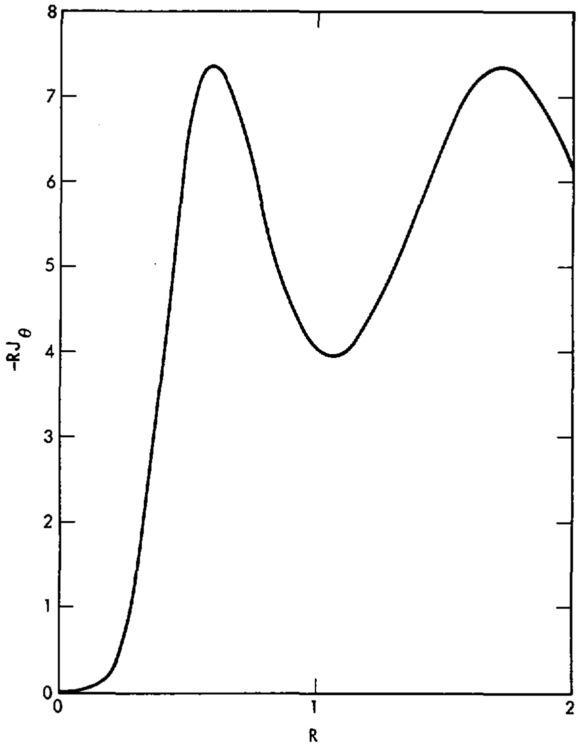

FIG. 2. E-layer current profile at the midplane for the "relativistic Maxwellian" model, Eq. (5b). There is a perfectly conducting wall at R = 2.

Using the three E-layer models given by Eq. (5), one typically gets the current distribution shown in Figs. 1 through 3. Models 1 and 2 have the undesirable feature of finite current density at the conducting outer wall. Thus, we have concentrated on model 3, which has sharp current boundaries. This model also has the advantage that the current density is hollowed out. For stable plasma confinement, this hollow E-layer configuration is a desirable feature. In Table I the dimensionless quantities used to describe the E-layer shown in Fig. 3 have been converted to cgs units. Results are given for an electron layer and a proton layer. Flux surfaces for a reversed-field situation are shown in Fig. 4. The position of the E-layer current boundary is indicated in the figure. The addition of plasma does not significantly change this picture. The plasma is embedded inside the E-layer within the region of closed field lines, as indicated in Fig. 5. Plasma pressure profiles for the two models given by Eqs. (6) and (7) are shown in Fig. 6.

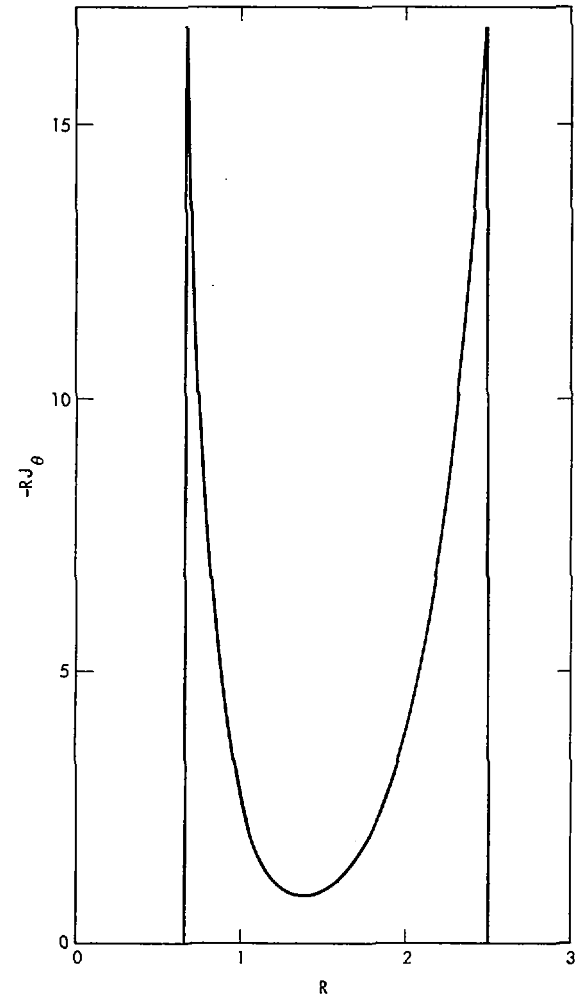

FIG. 3. E-layer current profile at the midplane for the "delta-function" model, Eq. (5c). There is a perfectly conducting wall at R = 3.5.

TABLE I. E-LAYER PARAMETER VALUES

	Electron layer	Proton layer
Vacuum magnetic field	500 G	100,000 G
Mean layer radius	50 cm	85 cm
Particle number density	3×10^{10} cm^{-3}	4×10^{12} cm^{-3}
Particle kinetic energy	5 MeV	1.2 GeV

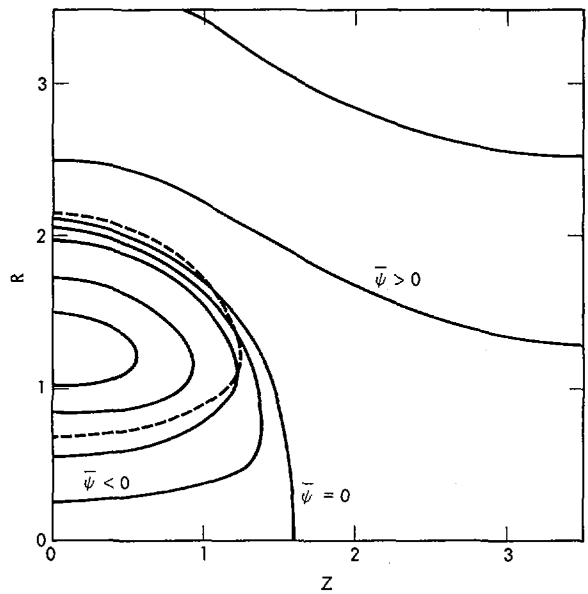

FIG. 4. Flux surfaces for reversed-field Astron equilibria. The last closed flux surface is denoted by $\bar{\psi} = 0$. The E-layer current boundary is indicated by the dashed line.

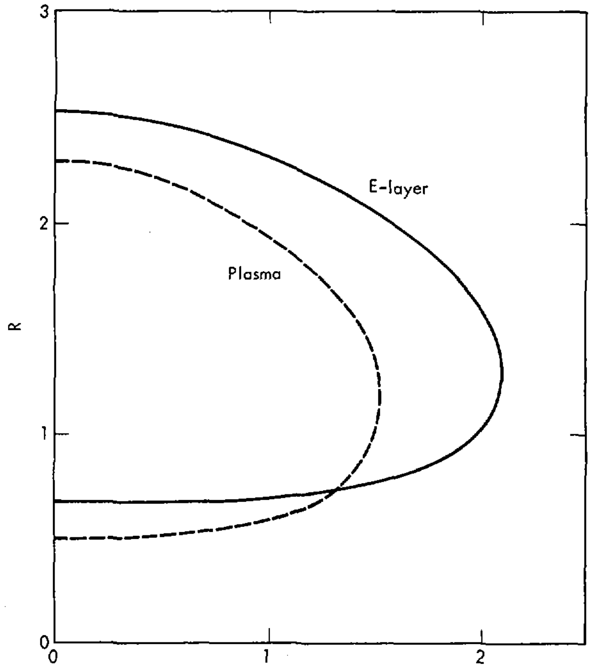

FIG. 5. The relative position of the E-layer and plasma in the R-Z-plane. The midplane is at Z = 0. There are conducting boundaries at R = 3.5 and Z = ±2.5.

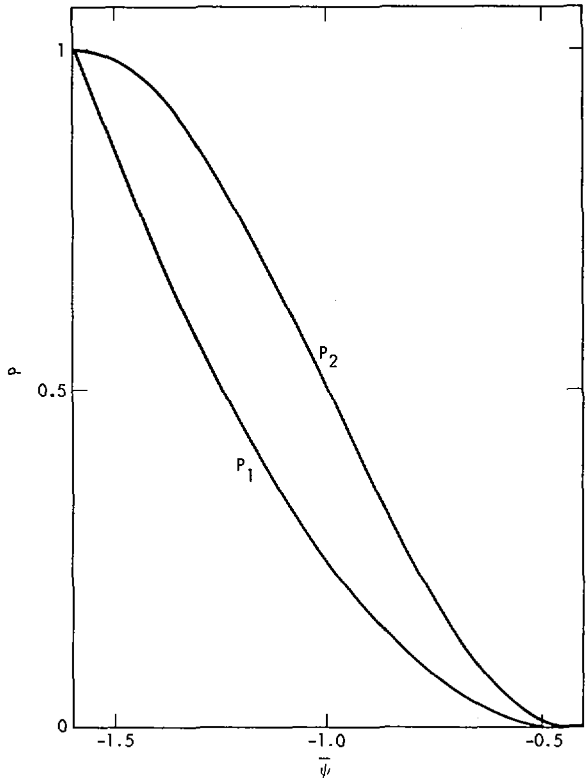

FIG. 6. Plasma pressure profiles for the two models given in Eqs (6) and (7) with m = 2. The centre of the plasma is at $\bar{\psi}_V = -1.6$ and the outer surface is at $\bar{\psi}_0 = -0.4$.

3. PLASMA STABILITY

To analyze the stability of Astron configurations it is convenient to identify three possible roles for the confined plasma [3]: (1) it supports high-frequency oscillations, possibly driven by the E-layer; (2) at lower frequencies it maintains charge neutrality; and (3) if the plasma is hot, the plasma energy might itself drive instability. In its role as an oscillator and a neutralizer, the plasma can be treated in the zero temperature approximation. This is done in section 4. Here, we consider the third possibility. We regard the E-layer as rigid and consider the MHD stability of the confined plasma in the given self-consistent magnetic field (see section 2). We use the energy principle [4], modified [5] to take account of the E-layer current. Minimizing the energy with respect to all possible plasma displacements, one obtains an eigenvalue equation for the fastest growing mode,

$$\frac{d}{d\ell}\left(\frac{1}{r^2 B}\frac{dX}{d\ell}\right) + \frac{\Lambda - p'D}{B} X = \frac{D}{B} f \tag{9}$$

where X is the component of the plasma displacement perpendicular to the flux surface, ℓ is the distance measured along a field line, and Λ is the

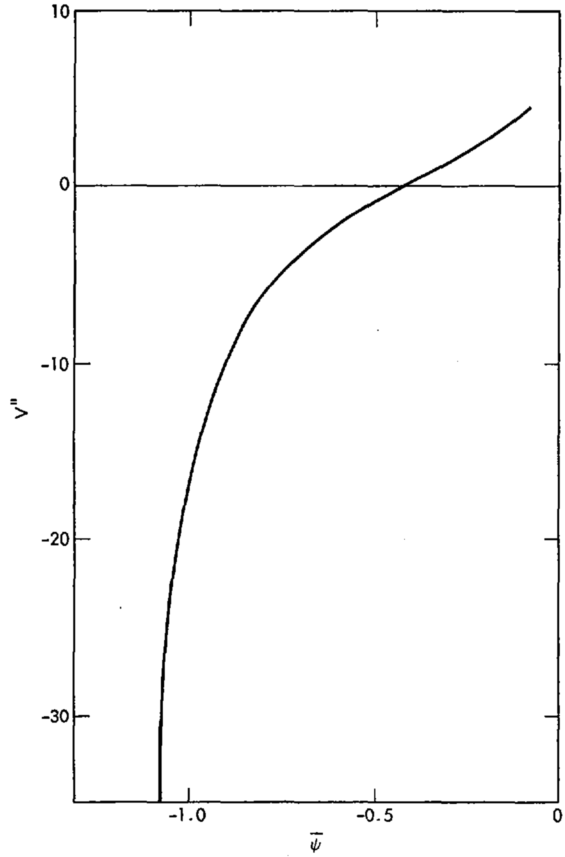

FIG. 7. The $\beta = 0$ stability criterion, V''. The E-layer model is that shown in Fig. 3. The centre of the E-layer is at $\bar{\psi} = -1.25$ and the outer surface of the E-layer is near $\bar{\psi} = -0.40$.

energy eigenvalue associated with this mode. A sufficient condition for stability is $\Lambda > 0$ on all flux surfaces. We have solved this eigenvalue problem numerically for some of the equilibria given in the previous section.

A necessary condition for stability is obtained by taking $X(\ell)$ constant on a flux surface, and this leads to the "interchange" criterion,

$$\Lambda_{I-c} \equiv \gamma p\left(\frac{V'' - p'L'}{V' + \gamma p L'}\right)\left(\frac{V''}{V'} + \frac{p'}{\gamma p}\right) > 0 \tag{10}$$

where V', V'', and L' are line integrals defined in reference [5]. In the limit of small plasma pressure this becomes a necessary and sufficient condition,

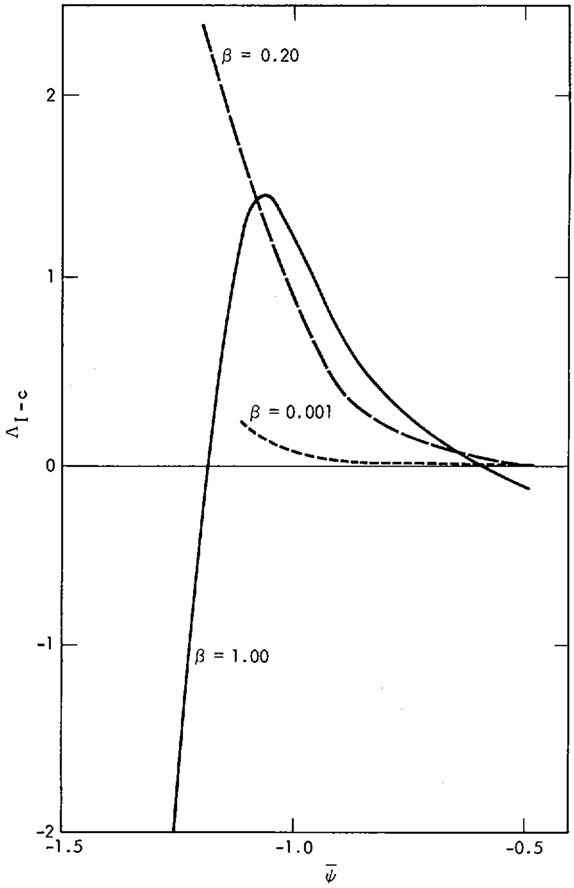

FIG. 8. The "interchange" energy eigenvalue, Λ_{I-c}, for various plasma pressures. Flux surfaces for which $\Lambda_{I-c} < 0$ are unstable. The outer surface of the plasma is at $\bar{\psi} = -0.40$.

$$\Lambda^{(1)}_{I-c} \equiv \gamma p \frac{V''}{V'}\left(\frac{V''}{V'} + \frac{p'}{\gamma p}\right) > 0 \tag{11}$$

and, since p' is negative, one obtains

$$V'' \equiv \frac{d}{d\psi}\left[\oint \frac{d\ell}{B}\right] < 0 \tag{12}$$

for stability.

To illustrate these remarks we give results for a typical case in which the delta function model, Eq. (5c), was used for the E-layer and the quadratic model, Eq. (6) with m = 2, was used for the plasma. In Fig. 7 we plot V'' vs $\bar{\psi}$ for $\beta = 0$. The flux surfaces with $\bar{\psi} > -0.4$ lie outside the E-layer

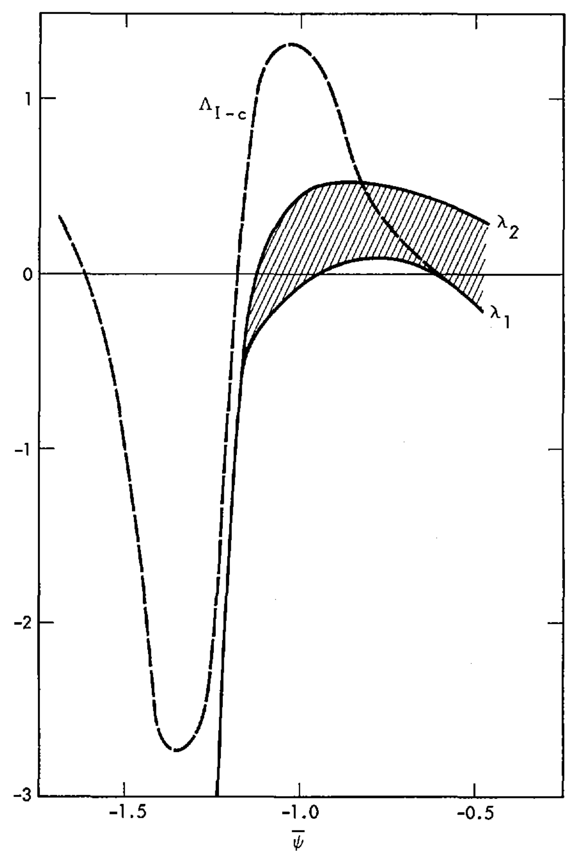

FIG. 9. The first and second eigenvalues of the homogeneous form of Eq. (9). The plasma β in this case was 1.20. The "interchange" eigenvalue is seen to bear little relation to the true eigenvalue for high-β plasmas.

and are unstable in the low β limit. Thus, we restrict the plasma to closed flux surfaces within the E-layer itself, choosing $\bar{\psi}_0 = -0.4$ in Eq. (6). The "interchange" energy eigenvalue Λ_{I-c} is shown in Fig. 8 for $\beta = 0.001$, 0.20, and 1.00. We see that for $\beta = 1.00$, the inner flux surfaces are "interchange" unstable in this model. This is caused by large pressure gradients near the center of the plasma and can be avoided by proper shaping of the model pressure profile. For example, the model given by Eq. (7) has weaker gradients and yields better stability results on these inner flux surfaces. To obtain the optimum marginally stable pressure profile one should use the procedure suggested in reference [5] whereby the maximum p' is computed on each flux surface by setting $\Lambda = 0$ in Eq. (9). To ensure self-consistency, the equilibrium magnetic field must then be recomputed. The entire process is repeated several times and should converge to give the maximum plasma pressure consistent with MHD stability.

For high β plasma, a numerical solution of the eigenvalue problem is necessary and yields the results shown in Figs. 9 and 10. The true energy eigenvalue Λ lies in the interval between λ_1 and λ_2, where these are the first

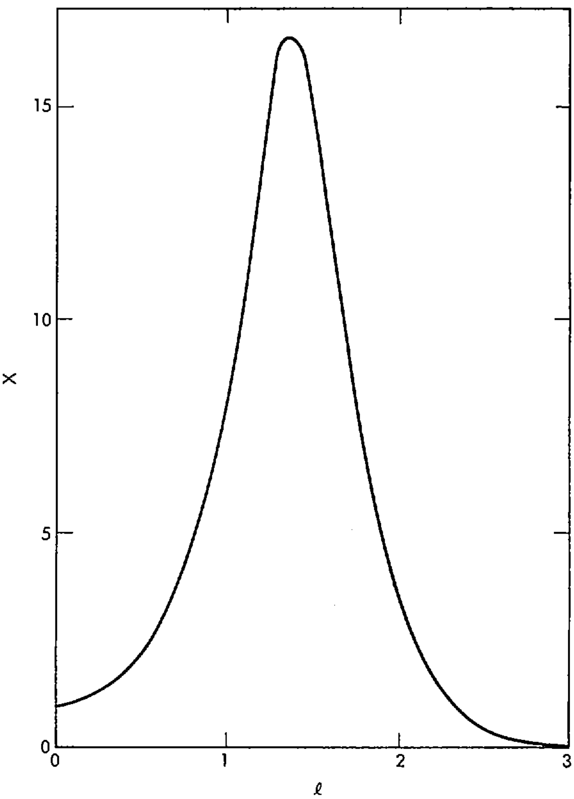

FIG. 10. The symmetric "ballooning" eigenfunction for the unstable flux surface at Ψ = -1.25 in Fig. 9. ℓ is the distance along a field line, starting at the midplane near R = 2.5 and returning to the midplane near R = 1.0.

and second eigenvalues associated with the left-hand side of Eq. (9). (See reference [4].) In this particular case, the outermost flux surface was unstable because the plasma extended beyond the E-layer boundary and V'' became positive. Some of the innermost flux surfaces are also found to be unstable for this plasma model. The instability is apparent from Fig. 9 in terms of both Λ and Λ_{I-C}. The more stringent condition is imposed by Λ, and the eigenfunction differs considerably from the assumed "interchange" eigenfunction as shown in Fig. 10. One might call this a "ballooning" instability since X represents the plasma displacement normal to a flux surface and has a maximum where the curvature of the field line is greatest. An indication of why this plasma model is unstable at high β can be seen in Fig. 11. The plasma produces a current spike that is comparable in magnitude to the current density in the E-layer itself. Thus, the stabilizing hollowed-out current profile is locally destroyed. Other plasma models which do not have this feature are being studied, and preliminary results show improved stability.

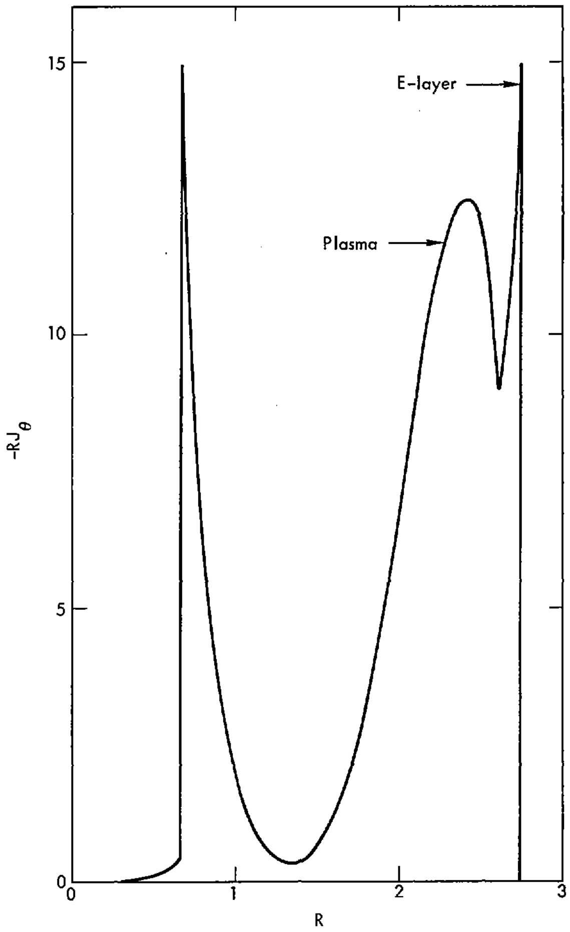

FIG. 11. The total current profile at the midplane for an E-layer containing a high β plasma. The E-layer model is given by Eq. (5c) and the plasma model by Eq. (6).

4. E-LAYER STABILITY

In this section we examine the stability of the E-layer in the presence of a background plasma and a self-consistent equilibrium magnetic field. We use a linearized time-dependent Vlasov description for the E-layer, and zero temperature fluid equations for the plasma. Together with Maxwell's equations and a set of boundary conditions, this defines the normal modes of the system. To avoid the complications due to the finite size of the system we introduce two simplifying assumptions: (1) the equilibrium E-layer particle orbits in the r-z plane are a superposition of simple harmonic motion in both r and z, i.e.

$$r(t) = R + \rho_r \sin(\beta t + \alpha_r)$$

$$z(t) = \rho_z \sin(\xi t + \alpha_z) \tag{13}$$

where R is the mean gyro-radius of the particle, ρ is the amplitude of the oscillatory motion, β and ξ are the radial and axial betatron frequencies, and α is a phase factor; (2) the perturbing electromagnetic field is a "local plane wave" in the r-z plane with a wavelength that is small compared to the thickness and length of the E-layer, i.e.,

$$\vec{E}(\vec{r},t) \approx \vec{\epsilon}\, e^{+i\vec{k}\cdot\vec{r}-i\omega t}$$

where $k_r\rho_r$ and $k_z\rho_z$ are large. With these two assumptions we can use the Fourier-Laplace transform method to analyze the perturbed system (as in the theory for an infinite homogeneous medium). For convenience we also assume an equilibrium distribution function of the form,

$$f_E = e^{-\beta H} G(P_\theta) \tag{14}$$

and, later we specialize to

$$G(P_\theta) = \Lambda\delta(P_\theta - P_0) \tag{15}$$

The dispersion relation giving the frequency ω in terms of the wave vector $\vec{k}$ is derived from the linearized wave equation,

$$\vec{k}\times(\vec{k}\times\vec{\epsilon}) + \frac{\omega^2}{c^2}\vec{\epsilon} = -\frac{4\pi i\omega}{c^2}\left[\vec{j}_E + \vec{j}_p\right] \tag{16}$$

Here the E-layer current perturbation is given by

$$-\frac{4\pi i\omega}{c^2}\vec{j}_E = \frac{\omega_{pE}^2}{c^2}\sum_n\sum_m g_{nm}\frac{\vec{u}_{nm}}{\omega_{nm}+\ell\Omega_c}\left\{\frac{m_E n\beta}{k_r T}\omega\epsilon_r - \frac{\ell}{\nu^2 R}\left(\frac{1-\nu^2/\gamma^2}{\omega_{nm}+\ell\Omega_c}\right)\omega\epsilon_\theta\right.$$
$$\left. + \frac{m_E m\xi}{k_z T}\omega\epsilon_z + \frac{m_E R\Omega_c}{T}\left[\frac{m\xi}{k_z}\left(\frac{\ell}{R}\epsilon_z - k_z\epsilon_\theta\right) + \frac{n\beta}{k_r}\left(\frac{\ell}{R}\epsilon_r - k_r\epsilon_\theta\right)\right]\right\} \tag{17}$$

and the plasma current (we consider only the electrons) is given by

$$-\frac{4\pi i\omega}{c^2}\vec{j}_e = \frac{\omega_{pe}^2\omega}{c^2}\,\frac{\left[\tilde{\omega}\vec{\epsilon} + i\vec{\omega}_{ce}\times\vec{\epsilon} - \vec{\omega}_{ce}(\vec{\omega}_{ce}\cdot\vec{\epsilon})/\tilde{\omega}\right]}{\tilde{\omega}^2 - \omega_{ce}^2} \tag{18}$$

where $m_E = \gamma m_e$ is the relativistic mass, $T = \beta^{-1}$ is the E-layer temperature, $\Omega_c = \omega_{ce}/\gamma$ is the E-layer gyrofrequency, $\tilde{\omega} = \omega + i\nu_c$ with ν_c the electron-neutral collision frequency, and ℓ, m, and n are integers. We also have used $\vec{u}_{nm} \equiv (n\beta/k_r)\hat{r} + (-R\Omega_c)\hat{\theta} + (m\xi/k_z)\hat{z}$ and $\omega_{nm} \equiv \omega - n\beta - m\xi$. The g_{nm} are constants of order unity for small values of n and m. It should be noted that the particle orbit frequencies (Ω_c, β, ξ), which appear in the dispersion relation, actually depend on the energy and canonical angular momentum of the particles. Thus, a spread in particle energies leads to a spread in Ω_c, β, and ξ, and Eq. (17) should really be integrated over a probability distribution for these frequencies.

On the basis of Eqs. (16) through (18) we can examine several possible modes in Astron by identifying the dominant contributions in $\vec{j}_E$. Although our dispersion relation has been derived for short wavelength perturbations ($k_r\Delta$, $k_zL \gg 1$), it also gives qualitative information about modes whose wavelengths may be comparable to E-layer dimensions ($k_r\Delta$, $k_zL \sim 1$).

Three types of instabilities have been observed in Astron experiments and these are contained in our theory. The negative-mass instability [6] at harmonics of the E-layer gyro-frequency ($\omega \sim \ell\Omega_c$) can be derived by considering just the n = m = 0 term in Eq. (17). This leads to the usual stability condition $\nu^2 > \gamma^2$ for constant Ω_c. With a spread in gyro-frequencies one gets a damping contribution proportional to $\ell\delta\Omega_c$ and the mode may be stabilized. A rigid-body azimuthal precession of the E-layer in Astron is observed to be unstable for very weak E-layers. [7] The single-particle precession frequency is given by $\omega - \beta + \Omega_c \approx 0$ so the appropriate term in Eq. (17) is easily identified and leads to the E-layer precession frequency,

$$\omega = \frac{1}{2}\left(\frac{R}{B_z}\,\frac{dB_z^{\text{external}}}{dR}\right)\Omega_c,$$

where R is the layer radius and B_z^{external} is the magnetic field due to sources outside the E-layer. If the background plasma is resistive, or if the finite conductivity of the tank walls is taken into account, the frequency has an imaginary part,

$$\text{Im}\,\omega = -\sigma\left(\frac{1}{2}\,\frac{R}{B_z}\,\frac{dB_z^{\text{self}}}{dR}\right)\left(\frac{1}{2}\,\frac{R}{B_z}\,\frac{dB_z^{\text{external}}}{dR}\right)\Omega_c$$

where σ is proportional to the conductivity. For very weak E-layers, the gradient in B_z^{external} is negative due to the applied mirror field; for stronger E-layers it becomes positive due to image currents in the tank walls. Thus, the precession mode stabilizes as observed experimentally. A third instability, which has been seen in Astron, is the hybrid mode [8]—the excitation of background plasma oscillations by the E-layer. In our model the electrons in the background plasma can support oscillations at the upper hybrid frequency $\omega_H = \sqrt{\omega_{pe}^2 + \omega_{ce}^2}$. When a harmonic of the E-layer gyro-frequency coincides with ω_H, we may expect unstable oscillations at $\omega \sim \omega_H \sim \ell\Omega_c$. We obtain the dispersion relation for this mode from the n = m = 0 term in $\vec{j}_E$ with $\vec{k} \perp \vec{B}$ in the background plasma. Since this mode involves a resonant interaction between $\ell\Omega_c$ and ω_H, it is clear that any spread in Ω_c will tend to stabilize the mode and collisions in the background plasma might quench it completely.

We have also used this theory to consider instabilities, which have not been observed in Astron, but, which might be present in some instances. One such mode is the tearing [9] of a long E-layer into a series of shorter E-layers or electron rings. One can show that this does not occur if the equilibrium E-layer is self-pinched; i.e., its length is determined by a balance between the axial kinetic pressure of the E-layer particles and the axial magnetic pressure of the E-layer self-field. During the early stages of E-layer formation, when the axial kinetic pressure is not sufficient to balance the magnetic forces, there is some evidence for a tearing mode in both the experiment and the simulation results. However, the nonlinear development of this instability leads to a single self-pinched E-layer which is stable. Another mode which might exist in Astron is the kink-type "firehose" instability [10]. The self-pinched E-layer can be regarded as a relativistic beam (bent into a circle to form a ring or torus) and, in a resistive background plasma, it may be subject to a kink instability. Following Rosenbluth's beam analysis, one can derive a dispersion relation for this mode from Eqs. (16) through (18). Thus, we find

$$\omega + \ell\Omega_c = \pm\sqrt{4\pi i\sigma_\theta \ell\Omega_c v_\perp^2/c^2}$$

where $v_\perp$ is the thermal velocity associated with the beam. The applied magnetic field in Astron is in the z-direction, so the plasma conductivity σ_θ across field lines is small. This leads to a very weak instability which might be suppressed by image currents in the conducting tank walls.

5. NUMERICAL SIMULATION OF INJECTION AND TRAPPING

5.1. Description of the problem

In Astron, a beam of relativistic electrons is injected into an evacuated cylindrical region in which an externally applied magnetic field has been established. The cylindrical region is bounded by two concentric aluminum shells. The outer shell is 12 cm thick and its inner radius is 74 cm. The thin inner shell has a radius of 20 cm. The velocity of the injected electrons makes an angle of 85 deg with the axis of the region. To facilitate trapping, a cylinder of resistor wires, aximuthally oriented, has been installed at a radius of 52 cm. The electrons that are trapped form a cylindrical layer (shell) known as the E-layer. The mean radius of the E-layer is 40 cm; its length varies from 1 to 4 meters, depending on the initial conditions.

The E-layer consists of about 10^{15} electrons. It is, of course, impractical to follow each electron individually. Furthermore, we are not interested in the position and velocity of each electron; we are only interested in the electron density. We approximate the E-layer by a large number of super-particles and follow each particle individually. The electron density is, then, obtained from the super-particle density. The force on a particle is obtained from the full electromagnetic field and its trajectory is determined from the solution of the relativistic equations of motion. The number of super-particles used must be sufficiently large to give an accurate statistical representation of the E-layer and yet small enough to be practical. In practice we use between 10^4 and 3×10^4 particles.

The computation proceeds as follows: First the charge and current densities are determined from the known positions and velocities of the particles. These charge and current densities are then used to determine the vector and scalar potentials by solving the respective wave equations. The new values of the vector and scalar potentials are used to calculate the force on each particle. These forces are used to move each particle in accordance with the relativistic equations of motion. The above process is then repeated.

5.2. Mathematical model

5.2.1. Field equations

If we employ the relations $\vec{B} = \nabla \times \vec{A}$, $\vec{E} = -\nabla\phi - (1/c)(\partial\vec{A}/\partial t)$, and $\nabla \cdot \vec{A} + (1/c)(\partial\phi/\partial t) = 0$ with Maxwell's equations, we obtain the following wave equations

$$\nabla^2\vec{A} - \frac{1}{c^2}\frac{\partial^2\vec{A}}{\partial t^2} = -\frac{4\pi}{c}(\vec{j} + \vec{j}_{res}) \tag{19}$$

and

$$\nabla^2\phi - \frac{1}{c^2}\frac{\partial^2\phi}{\partial t^2} = -4\pi\rho \tag{20}$$

where $\vec{A}$ and ϕ are the vector and scalar potentials, respectively, and $\vec{j}$, j_{res}, and ρ are the E-layer current density, resistor current density, and the charge density.

The walls of the cylinders are assumed to be perfect conductors. The boundary conditions at a perfect conductor are $B_\perp = 0$ and $E_\parallel = 0$. These conditions are satisfied by $A_{\theta int}(r,z) = 0$, at all boundaries; $\phi(r,z) = 0$, at all boundaries; $A_z(r,z) = 0$, at $r = r_1, r_2$ for all z; and $A_r(r,z) = 0$, at $z = z_1, z_2$ for all r, where $A_{\theta int}$ is that part of A_θ which is generated by internal sources, i.e., currents in the E-layer and in the resistors. The rest of A_θ, henceforth designated $A_{\theta coil}$, is generated by current in the external coils. The remaining boundary conditions are $(\partial/\partial r)[rA_r(r,z)]|_{r=r_1,r_2} = 0$ for all z, and $(\partial/\partial z)[A_z(r,z)]|_{z=z_1,z_2} = 0$ for all r.

5.2.2. Superparticle model

The superparticles in this model are finite-sized and composed of a large number of electrons uniformly distributed throughout their volume. The shape of each superparticle is that of a ring of rectangular cross section.

The velocity of a superparticle has three components, v_r, v_θ, and v_z. Since the superparticle is ring shaped, v_r refers to the speed with which it is expanding (contracting) and v_θ to the speed with which it rotates about the axis. v_z is the usual axial component of velocity.

The charge density ρ of a superparticle is given by $\rho = n_e(e/2\pi r\Delta r\Delta z)$, where n_e is the number of electrons per superparticle, e the electronic charge, r the radius of the superparticle, Δr its radial thickness, and Δz its axial thickness.

The three components of the current density of a superparticle are given by

$$J_r = n_e\frac{ev_r}{2\pi r\Delta r\Delta z}, \quad J_\theta = n_e\frac{ev_\theta}{2\pi r\Delta r\Delta z}, \quad J_z = n_e\frac{ev_z}{2\pi r\Delta r\Delta z} \tag{21}$$

The field equations are solved in a domain that is subdivided by a finite difference mesh. The charge and current densities must be known on the mesh points. The equations of motion yield the positions of the centers of the superparticles. These positions, usually, do not coincide with any mesh point. Therefore some method must be devised whereby we can obtain the charge and current densities at the mesh points from the known positions and velocities of the superparticles. In the method that we use, the charge and current of a superparticle is shared among each of the four neighboring grid points in accordance with a standard [11] area weighting procedure.

5.2.3. Equations of motion

We assume that the canonical angular momentum is a constant of the motion

$$m_0\gamma r^2\dot{\theta} + \frac{e}{c} rA_\theta = P_\theta = \text{const.} \tag{22}$$

It is convenient to introduce the function $\psi = (\gamma/c)r^2\dot{\theta}$ so that

$$\psi = \frac{P_\theta}{m_0 c} - \frac{e}{m_0 c^2} rA_\theta \tag{23}$$

and, since we are assuming that all the particles have the same P_θ, we can use ψ in place of A_θ. The rationale for introducing ψ is that it obviates the necessity of calculating v_θ.

We now introduce the dimensionless velocity $\underline{u}$ defined by

$$\underline{u} = \frac{\gamma}{c}\underline{v} \tag{24}$$

where $\gamma = (1 - v^2/c^2)^{-1/2}$. Substituting Eq. (24) into the expression for γ we get $\gamma = (1 + u_r^2 + u_\theta^2 + u_z^2)^{1/2}$. From Eq. (23) we have $\psi = ru_\theta$, hence $\gamma = (1 + u_r^2 + u_z^2 + \psi^2/r^2)^{1/2}$. If we differentiate Eq. (24) with respect to time and rearrange the terms, we get

$$\begin{aligned} \ddot{r} &= \frac{c}{\gamma}\dot{u}_r - \frac{c}{\gamma^2}\dot{\gamma}u_r \\ \ddot{z} &= \frac{c}{\gamma}\dot{u}_z - \frac{c}{\gamma^2}\dot{\gamma}u_z \end{aligned} \tag{25}$$

Assuming axial symmetry, we have the following equations of motion:

$$m_0(\gamma\ddot{r} + \dot{\gamma}\dot{r} - \gamma r\dot{\theta}^2) = -e\frac{\partial\phi}{\partial r} - \frac{e}{c}\frac{\partial A_r}{\partial t} + \frac{e}{c}\left[r\dot{\theta}\frac{1}{r}\frac{\partial}{\partial r}(rA_\theta) - \dot{z}\left(\frac{\partial A_r}{\partial z} - \frac{\partial A_z}{\partial r}\right)\right] \tag{26}$$

$$m_0(\gamma\ddot{z} + \dot{\gamma}\dot{z}) = -e\frac{\partial\phi}{\partial z} - \frac{e}{c}\frac{\partial A_z}{\partial t} + \frac{e}{c}\left[\dot{r}\left(\frac{\partial A_r}{\partial z} - \frac{\partial A_z}{\partial r}\right) + r\dot{\theta}\frac{\partial A_\theta}{\partial z}\right] \tag{27}$$

Substitution of Eqs. (24) and (25) into Eqs. (26) and (27) yields for the radial equation of motion,

$$\frac{du_r}{dt} = -\frac{c}{\gamma}\frac{\partial}{\partial r}\left(\frac{\psi^2}{2r^2}\right) - \frac{e}{m_0 c}\frac{\partial\phi}{\partial r} - \frac{e}{m_0 c^2}\left[\frac{\partial A_r}{\partial t} - \frac{c}{\gamma}u_z\left(\frac{\partial A_r}{\partial z} - \frac{\partial A_z}{\partial r}\right)\right] \tag{28}$$

Similarly the axial equation of motion becomes

$$\frac{du_z}{dt} = -\frac{c}{\gamma}\frac{\partial}{\partial z}\left(\frac{\psi^2}{2r^2}\right) - \frac{e}{m_0 c}\frac{\partial\phi}{\partial z} - \frac{e}{m_0 c^2}\left[\frac{\partial A_z}{\partial t} + \frac{c}{\gamma}u_r\left(\frac{\partial A_r}{\partial z} - \frac{\partial A_z}{\partial r}\right)\right] \tag{29}$$

5.3. Special features of the Astron model

5.3.1. Current in the resistors

The function of the resistors is to extract energy from the E-layer electrons. The resistors consist of a large number of very fine (1.5 mil) wires. They are wound on a cylindrical frame of fixed radius such that the current in them flows in the θ direction only. It is convenient to replace the individual resistor wires with a resistor sheet.

The current density in the resistors is given by $j_{\theta res} = \sigma_\theta E_\theta$, where σ_θ is the conductivity of the resistor sheet and E_θ the θ component of the electric field at the resistors. E_θ is calculated from $E_\theta = -(1/c)(\partial A_\theta/\partial t)$, where A_θ is the θ component of the vector potential.

5.3.2. Neutralization scheme

Consider a small region of neutral gas into which a bunch of electrons has entered. The electrons remain in this region for a time δt. By the time they leave they will have undergone n_i ionizing collisions. Since the incident electron bunch has a high electric field associated with it, the cold electrons that are freed by the ionizing collisions are accelerated out of the region. When the electron bunch leaves, the region contains n_i positive ions. If we now imagine similar bunches entering the region in succession, the number of positive ions in the region will build up until the number of ions equals the number of electrons in the incident beam.

Let us consider a beam of M electrons circulating in one zone. The number of ionizing collisions made by this beam of electrons in a distance $c\delta t$ is given by $n_i = NQMc\delta t$, where N is the number of gas atoms per cm^3, Q is the ionization cross section, M is the number of beam electrons, and c is the velocity of light. Note that the ratio $n_i/M = NQc\delta t$ is independent of electron density. This ratio can also be interpreted as the fraction of the beam neutralized in time δt. Replacing electrons with superparticles, we can say that $NQc\delta t$ is the fraction of the superparticle charge that is neutralized in time δt. If we give the pressure in microns and use $Q \approx 2.5 \times 10^{-19}$ cm^2, we have $NQc\delta t = 2.7 \times 10^{-4}\ p\delta t$. After one time step, $\Delta\tau$, they contribute $n_i = 2.7 \times 10^{-4}\ Mp\Delta\tau$ positive ions to that space.

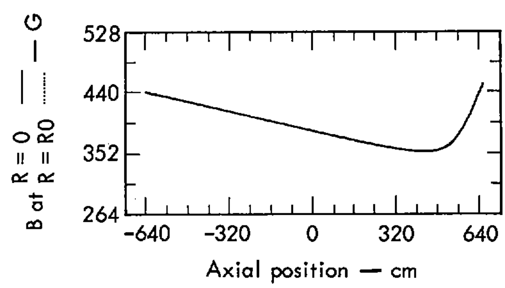

FIG. 12. B_z as a function of z at the injection radius. This field is computed from the program COILS.

5.4. Results

We have made provision for varying a large number of parameters. A large number of graphs are also provided. At present, we can vary the injection current, the pulse length, the number of pulses, and the number of particles used. The applied magnetic field can be evaluated through the use of either of two analytical models or from a computer program called COILS, which calculates the field at any desired point in space due to a set of coils whose centers are on the axis. In addition, we can include an arbitrary toroidal field (Fig. 12).

In a typical Astron run, the beam current varies from 100 to 800 A. Similarly the pulse length varies from 100 to 300 nsec. The average electron energy is, generally, about 5.5 MeV. The background pressure varies from near vacuum to about 50 μm. Generally it is about 10 μm. The shape of the applied field depends on the experiment. When the object is to optimize trapping (as it usually is), the shape of the field near the injection point is that of a shallow mirror, whereas the field at the far end of the intended trapping region is, generally, a steep mirror.

We shall discuss the results of one case where we have injected a pulse of 200 nsec duration at 800 A. We followed the motion of this pulse for a microsecond—by this time it had essentially reached a steady state. We then injected a second pulse of 100 nsec duration, also at 800 A. The second pulse is trapped and we follow the motion of both pulses until steady state is reached.

We use parameters similar to those used by the Astron group when they study injection and trapping. The physical parameters for the first pulse are:

Injection current	800 A
Pulse length	200 nsec
Background pressure	10 microns
Axial injection velocity	0.1 C
Radial injection velocity	0
Magnetic field	Fig. 12
Resistance	7 ohms/square
Resistor radius	52 cm
Tank radius (inner)	72 cm
Injection radius	50 cm
Injection energy	5.28 MeV

The mesh parameters are:

Number of axial zones	100
Number of radial zones	18
Axial space step ΔZ	13 cm
Radial space step ΔR	4 cm
Time step	0.133 nsec
Total number of particles injected	21,000

Injection occurs in the second zone from the left end boundary. Fourteen particles are injected per time step. They are spread uniformly over the zone. All the particles are given the same initial axial velocity. Injection begins at t = 0 and ends at t = 200.

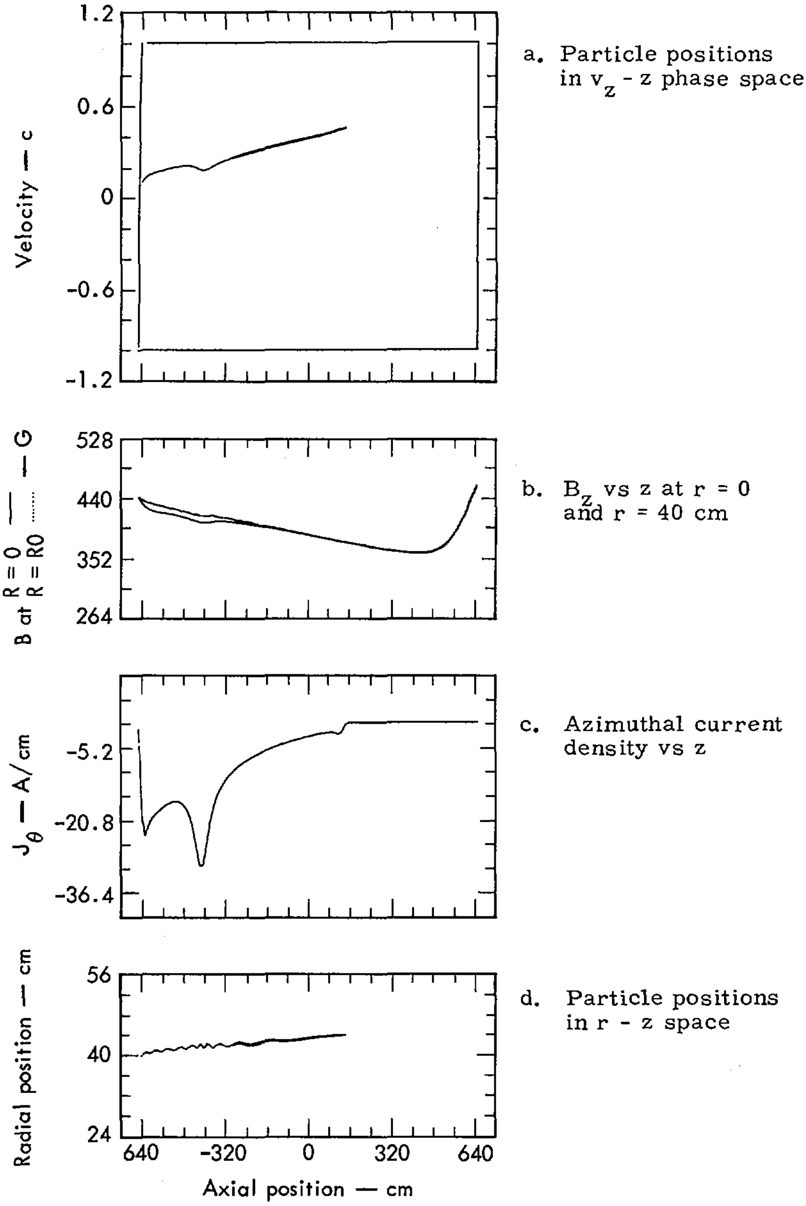

FIG. 13. State of the system at 96 nsec.

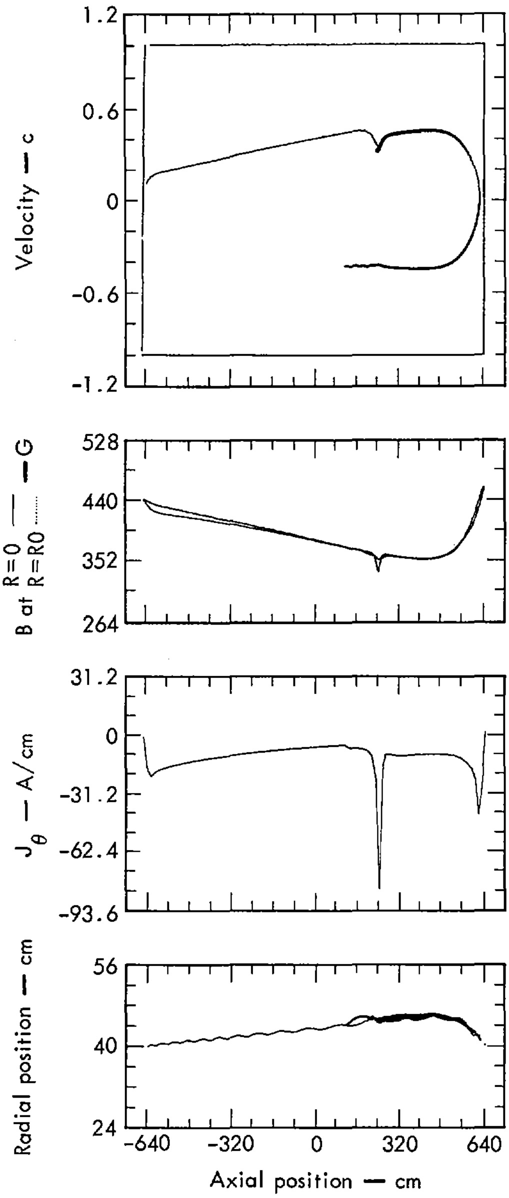

a. Particle positions in v_z - z phase space

b. B_z vs z at r = 0 and r = 40 cm

c. Azimuthal current density vs z

d. Particle positions in r - z space

FIG. 14. State of the system at 192 nsec.

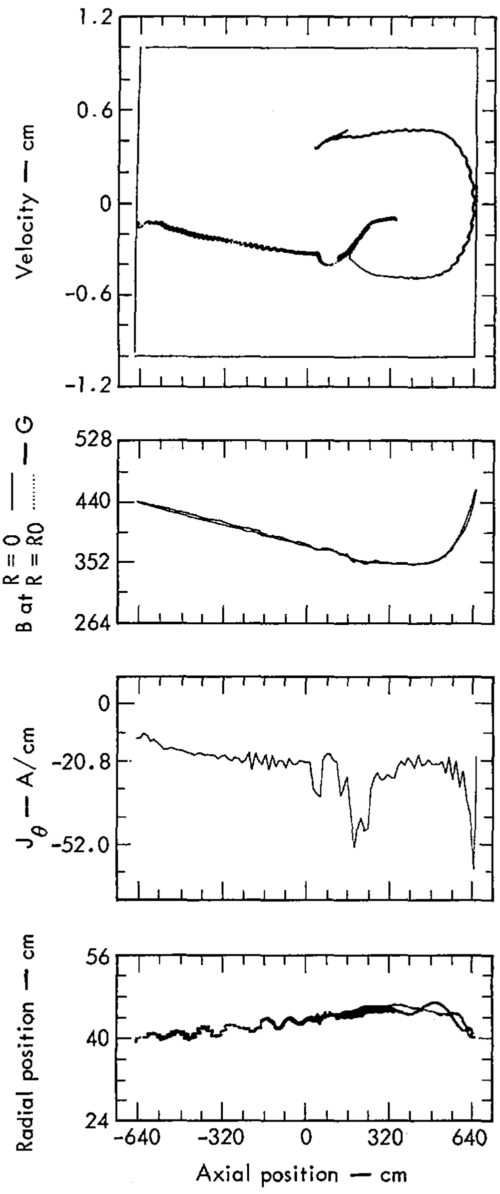

a. Particle positions in v_z - z phase space

b. B_z vs z at r = 0 and r = 40 cm

c. Azimuthal current density vs z

d. Particle positions in r - z space

FIG. 15. State of the system at 284 nsec.

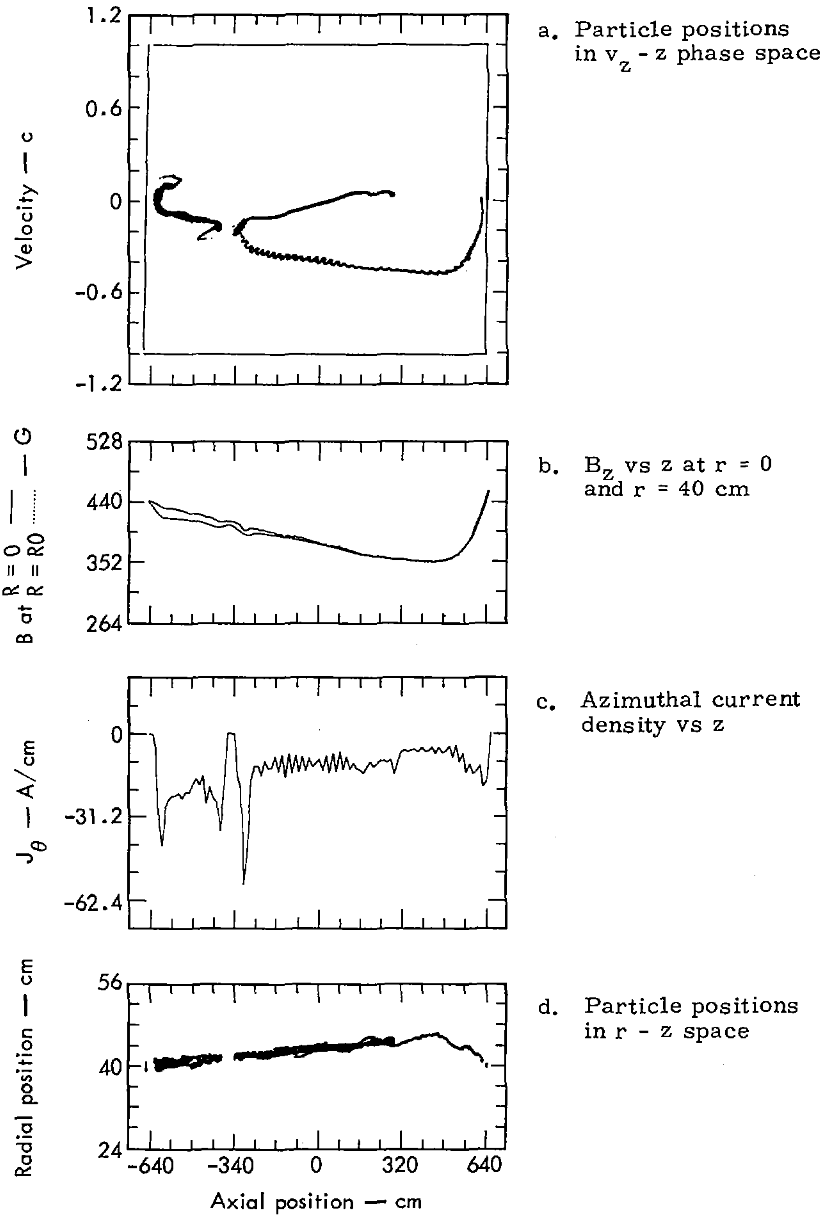

FIG.16. State of the system at 340 nsec. (The thickening at the left and right boundaries is caused by the particles leaving through that boundary. Once a particle strikes a boundary it is removed from the calculation; however, its last position is plotted on the phase space and configuration space plots.)

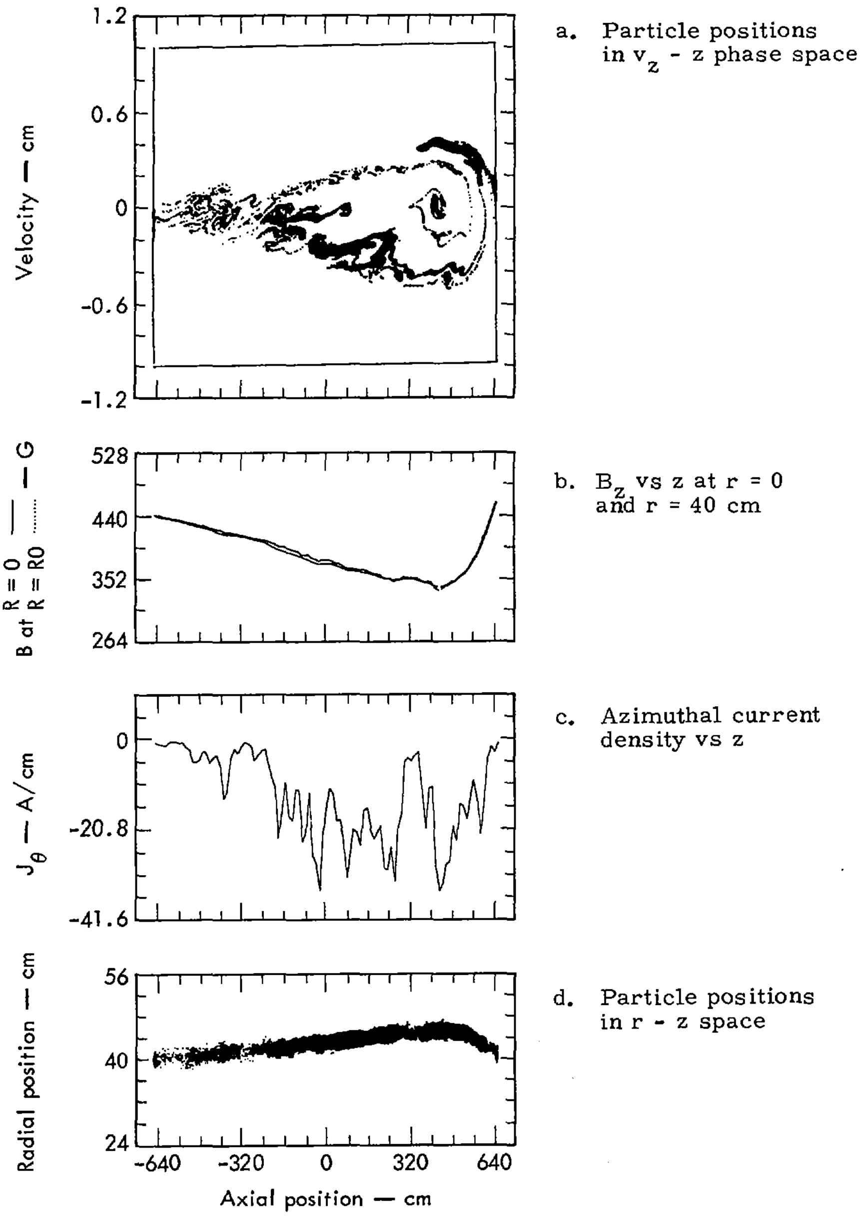

FIG. 17. State of the system at 648 nsec.

As the particles are injected they decrease the field in the injection region. The particles injected later in the pulse are not trapped in this well; they are merely slowed by it. As soon as the particles leave the well they accelerate rapidly (Fig. 13a, b). As the particles proceed down the ramp they carry their well with them, thus extending it. Furthermore, the ramp in the injection region has been considerably steepened by this well (Fig. 13b).

The particles injected still later in the pulse see this steeper ramp and are accelerated by it into the well. When they reach the bottom of the well their acceleration decreases, since the ramp is much shallower there (Fig. 13a, b). Because of this acceleration the particles injected later in the pulse have a greater axial velocity than the particles injected earlier in the pulse. As a result they overtake the earlier injected particles, which are forming the well at the forward end. Upon reaching the forward end of the well they climb the rim and in the process are slowed somewhat. The dip in Fig. 13a shows those particles that are climbing out of the well.

Since the particles to the left of the dip move faster than those in the dip, particles tend to accumulate there (Fig. 14c). This accumulation results in the formation of another well at the dip (Fig. 14b). The average axial velocity of the particles in the new well is positive so they travel together down the ramp carrying the well with them. In subsequent usage the term "well" refers to this well. Comparison of Figs. 13a, 14a, 15a shows that the dip becomes progressively deeper with time.

The particles injected first (leading particles) reach the far end of the mirror at t = 144 nsec. A few of them collide with the right-end boundary and leave the system (Fig. 14a). By t = 192 nsec the leading particles have been reflected at the far mirror and have begun to encounter the well (Fig. 14a). Note that the well is quite deep (Fig. 14b). This interaction of the reflected particles with the well results in modulation of their axial velocity (Fig. 15a).

The well reaches the far mirror at t = 226 nsec. Since the velocity of the particles in the well is not as high as that of the particles preceding or following the well, they do not climb as high up the mirror (Fig. 15a). For this reason, and because of the enhanced interaction with the resistors, they do not climb as far back up the ramp (Fig. 15a). The modulation of the upper curve in Fig. 15a is due to the interaction of those particles with the well.

By t = 284 nsec the particles have returned to the injection region, completing one round trip. Some of these particles collide with the left-end boundary and leave the system (Fig. 15a). The particles injected last (trailing particles) reach the end of the far mirror at t = 347 nsec. Meanwhile the leading particles have begun going down the ramp for the second time (Fig. 16a). Note that the particles in the well do not go very far up the ramp. By t = 488 nsec the trailing particles have completed one round trip. Some of the particles strike the left-end boundary and leave the system. At this time the leading particles have reached the end of the far mirror and have been reflected by it for the second time.

In Fig. 17a note that the particles are beginning to form clumps. The leading particles complete the second round trip by t = 581 nsec (Fig. 17a). The particles continue to slosh back and forth, losing energy to the resistors and exchanging energy and linear momentum among themselves. Clumping, which is evidence of thermalization, is seen to increase with time (Figs. 17a, 18a, and 19a). The problem ran 9450 cycles, which is equivalent to

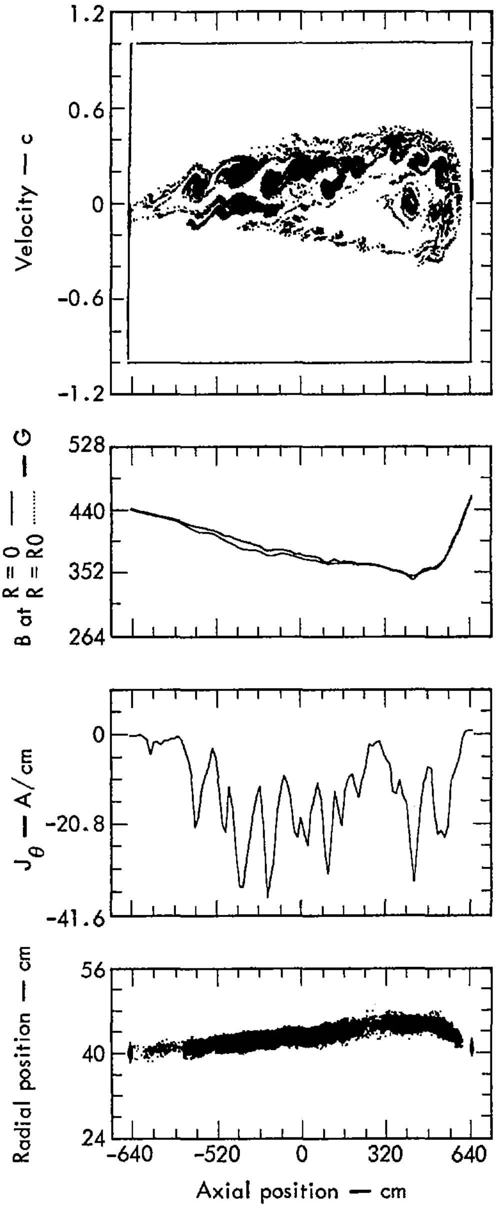

a. Particle positions in v_z - z phase space

b. B_z vs z at r = 0 and r = 40 cm

c. Azimuthal current density vs z

d. Particle positions in r - z space

FIG. 18. State of the system at 788 nsec.

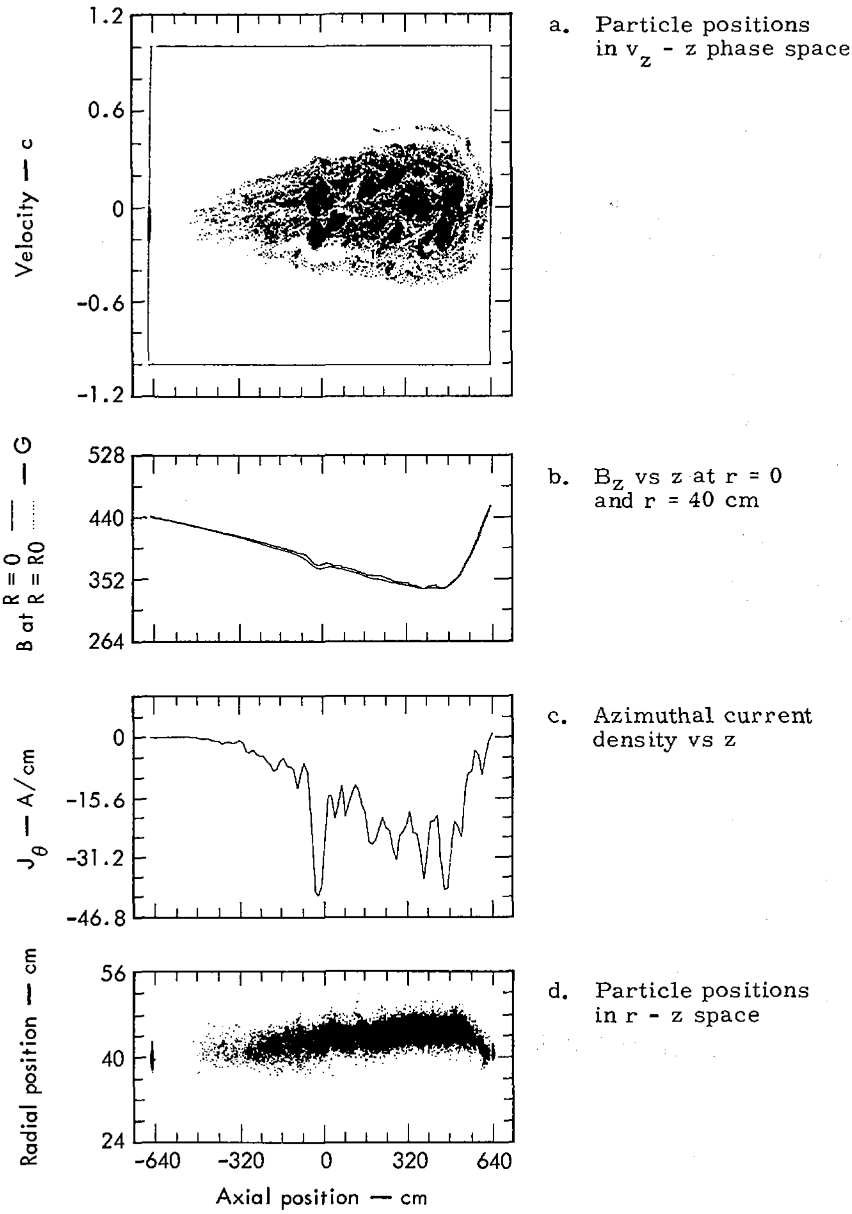

FIG. 19. State of the system at 1260 nsec.

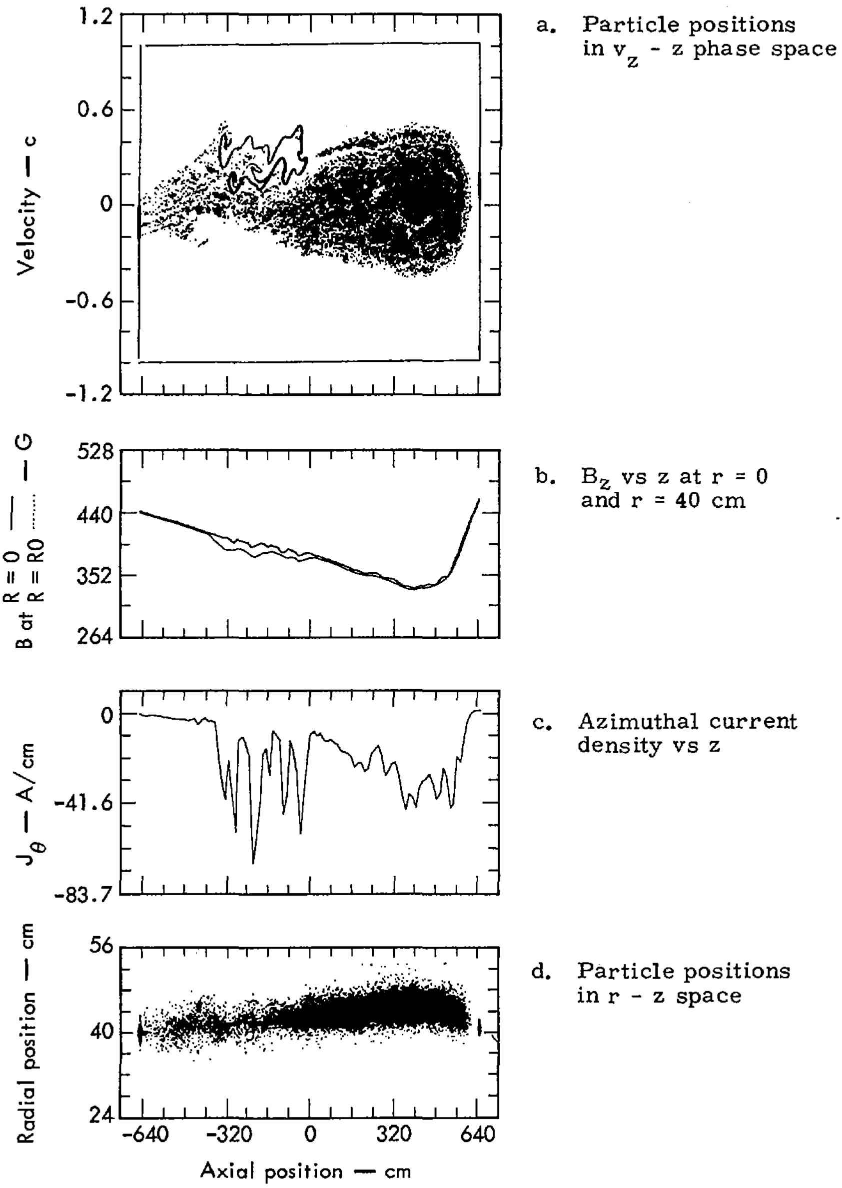

FIG. 20. State of the system at 1396 nsec.

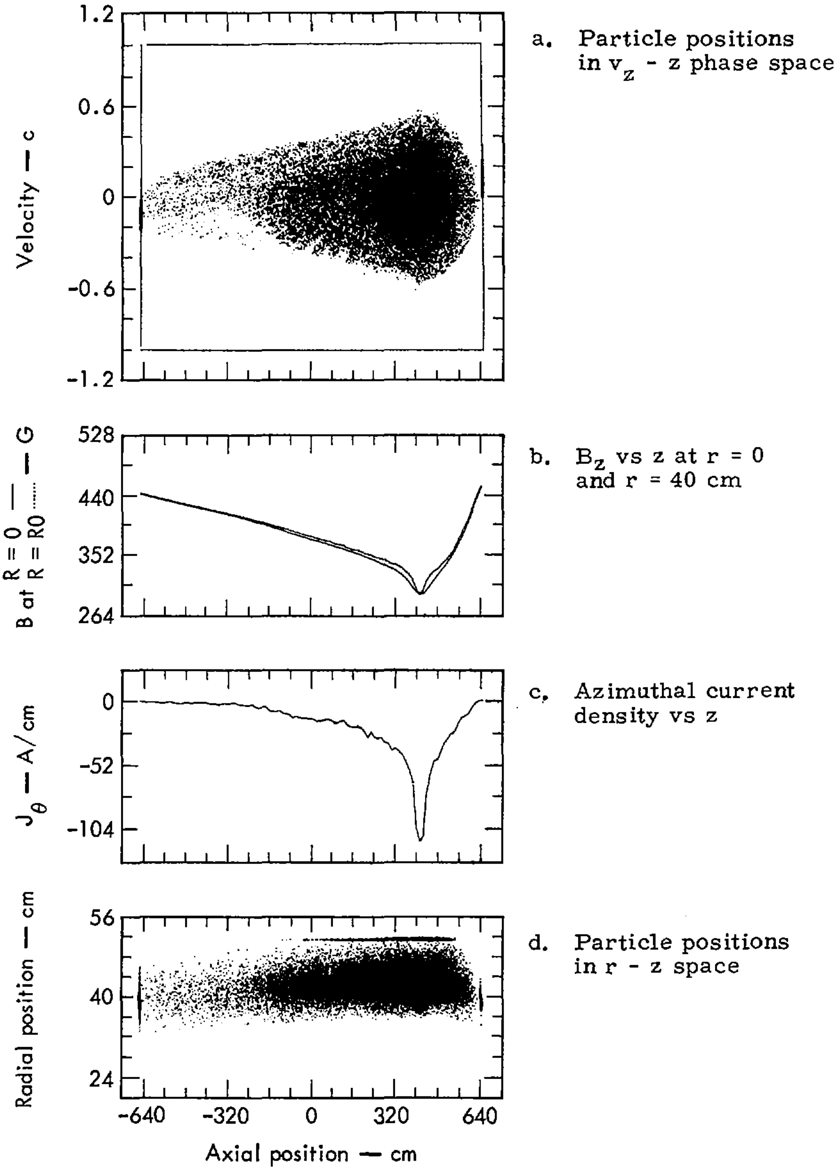

FIG. 21. State of the system at 2044 nsec.

1260 nsec. All told, 1193 particles were lost, all due to collision with either the left or right end boundaries. Throughout the calculation the energy was conserved to better than one part in 500.

To study the effect of overlapping one pulse with another, we injected a second pulse. The parameters of the second pulse are:

Injection current	800 A
Pulse length	100 nsec
Axial injection velocity	0.1 C
Radial injection velocity	0
Injection radius	40 cm
Injection energy	5.28 MeV
Number of superparticles	10,500
Background pressure	10 microns (partially ionized due to the first pulse)

Injection begins at t = 1260 nsec. By this time the particles from the first pulse have substantially thermalized. The newly injected particles begin to exhibit collective behavior very early in the second pulse. This is due to the fact that they were injected into a medium that is sufficiently ionized that the magnetic attraction between the particles outweighs their mutual electrostatic repulsion. This results in the slowing down of the leading particles and in the formation of a clump (Figs. 20a, b, c) as the later particles overtake.

The particles move as a unit down the ramp (Figs. 20a, c). Their average axial velocity is much smaller than the particles of the first pulse. Injection stops at t = 1360 nsec. Note that in contrast to the particles of the first pulse the particles of the second pulse form into clumps while they are still on the upper portion of the ramp (Fig. 20c). By t = 1444 nsec, the leading particles have reached the far mirror. They have formed into distinct clumps, and inside each clump significant thermalization has taken place (Figs. 20a, c). The trailing particles reach the end of the far mirror by t = 1508 nsec.

By t = 2044 nsec, they have coalesced and the particles have reached steady state (Figs. 21a, b, c, d).

There is a current of 24,649 A circulating in the system. The E-layer extends over 80 cm. The maximum current density is 115 A/cm. The maximum field reduction is 16 percent at R = 40 cm and 16 percent at R = 0.

REFERENCES

[1] ANDERSON, D. V., KILLEEN, J., Bull. Am. Phys. Soc. 14 (1969) 1030; Bull. Am. Phys. Soc. 15 (1970) 1456.

[2] ANDERSON, D. V., KILLEEN, J., RENSINK, M. E., "The Computation of E-Layer and Plasma Equilibria in Astron," Lawrence Radiation Laboratory, Livermore, Rept. UCRL-72730 (1971) (submitted to the Physics of Fluids).

[3] BENFORD, G., et al., 3rd Int. Conf. Controlled Nuclear Fusion and Plasma Physics (Proc. Conf. Novosibirsk) 1 IAEA, Vienna (1969) 981.

[4] BERNSTEIN, I. B., et al., Proc. Roy. Soc. (London) A244 (1958) 17.

[5] JOHNSON, J. L., KULSRUD, R. M., WEIMER, K. E., Plasma Phys. 11 (1969) 463.

[6] BRIGGS, R. J., NEIL, V. K., Plasma Phys. 9 (1967) 209.

[7] BEAL, J.W., et al., 3rd Int. Conf. Controlled Nuclear Fusion and Plasma Physics (Proc. Conf. Novosibirsk) 1 IAEA, Vienna (1969) 967.
[8] FESSENDEN, T.J., STALLARD, B.W., "Observation of the hydrid mode," in Controlled Thermonuclear Research Annual Report, July 1969 Through June 1970, Lawrence Radiation Laboratory, Livermore, Rept. UCRL-50002-70 (1970).
[9] NEIL, V.K., Phys. Fluids 5 (1962) 14.
[10] ROSENBLUTH, M.N., Phys. Fluids 3 (1960) 932.
[11] BIRDSALL, C.K., LANGDON, A.B., OKUDA, H., in Methods in Computational Physics (Academic Press, New York, 1970), Vol. 9, pp. 241-257.

APPLICATION OF INTENSE RELATIVISTIC ELECTRON BEAMS TO ASTRON-TYPE EXPERIMENTS

M.L. ANDREWS†, H. DAVITIAN, H.H. FLEISCHMANN,
R.E. KRIBEL††, B.R. KUSSE, J.A. NATION
Department of Applied Physics and Laboratory for Plasma Studies,
Cornell University, Ithaca, N.Y.
R. LEE, R.V. LOVELACE†††, R.N. SUDAN†††
US Naval Research Laboratory, Washington, D.C.
United States of America

Abstract

APPLICATION OF INTENSE RELATIVISTIC ELECTRON BEAMS TO ASTRON-TYPE EXPERIMENTS.

Owing to recent advances in high-voltage pulse technology, high-current electron beams of several hundred kA and up to a few MeV became available for fusion research over the last few years. In addition to possible applications to plasma heating, these beams may be useful for production of relativistic-electron current layers. Typical beams contain considerably more electrons than needed for an astron experiment. The relatively poor angular beam divergence can be balanced by the focusing magnetic self-fields of the beam. Small-scale experiments were performed using the pulsed high-voltage facility at Cornell. Electron beams of 10-30 kA having energies of 300-400 keV and an angular divergence of a few degrees were injected into magnetic fields of 200-300 gauss, the injection angle ranging from 75 to 85 degrees. To provide space-charge neutralization, air pressures in the range 0.2-1 Torr were maintained in the field region. When injecting into a homogeneous magnetic field, optical observation shows the beam to remain self-focused and to propagate in spirals along the field lines approximately corresponding to the average electron energy and injection angle. Also, reflection from a mirror and partial trapping between two mirrors bracketing the injector is observed. Well-shielded magnetic probes on the field axis indicate diamagnetic field changes of up to 40% of the original field when injecting into a homogeneous field. In the double-mirror arrangement, field changes of up to 140%, i.e. actual field reversal, are observed. The radial distribution of the magnetic field indicates a thickness of the current layer of the same order as the radius. Because of the presence of the injector, the relativistic electrons were lost rapidly. Experiments on the trapping in regions separate from the injector and on the influence of pre-ionization on the beam behaviour will be discussed.

1. INTRODUCTION

Present day high-voltage pulse technology makes available relativistic electron beam pulses having currents of several hundred kA, electron energies of a few MeV and pulse durations of up to 100 ns. In fusion research, these beams may be used to heat sizable amounts of plasma to fusion temperature. Equally important, applications may be expected to all confinement schemes in which currents flowing in the plasma are used to control equilibrium and/or stability of a fusion plasma, thus,

† Present address: Physics Department, The Wright State University, Colonel Glenn Highway, Dayton, Ohio 45433.

†† Present address: Physics Department, Drake University, Des Moines, Iowa 50318.

††† Permanent address: Laboratory of Plasma Studies, Cornell University, Ithaca, New York 14850.

including schemes like astron, tokomak, spherator, etc. In this paper, first results of experimental and theoretical investigations regarding the applicability to Astron-type schemes are reported.

As suggested in 1958 by Christifilos [1], stable confinement of a fusion plasma may be attainable by injecting a cylindrical layer of highly relativistic electrons into a magnetic mirror field. If this "E-layer" is sufficiently strong to reverse the direction of the magnetic field on the cylinder axis, the magnetic field in the vicinity of the layer constitutes an absolute-minimum-B configuration with closed field lines. In the resulting well-known ASTRON-experiment at Livermore it is attempted to create such current layers by injection of a low-divergence electron beam from an induction accelerator. After considerable technological developments, presently single-pulse trapping of an 800-amp-6-MeV electron beam leads to E-layers with axial field changes ranging up to 13% and stable confinement times of up to 12 ms [2]. The stacking of a sequence of pulses, which is presently being investigated, is expected to lead to full field reversal.

On the other hand, single pulses of the mentioned high-current beam generators often contain easily more than 10 times the number of electrons necessary to attain field reversal in a sizable container. Generally, these beams are expected to have more angular divergence than the 800-A beam at Livermore which may create some difficulties at injection. However, as in straight-tube propagation [3-5], this divergence may be compensated by magnetic self-focusing of the beam and if sufficient trapping can be accomplished, this increased spread in perpendicular energy is expected to result in a more stable E-layer of large volume. In the first part of this paper, first results of a small-scale experiment are reported in which field reversal was achieved for a short time by single pulse injection of a high-current beam pulse. In these experiments, sizable effects on trapping and build up of these E-layers and on heating of this plasma may result from return currents induced in the plasma and flowing opposite to the flow of the relativistic electrons. Results of a theoretical analysis of this problem are reported in the second section.

2. EXPERIMENTS ON E-LAYER GENERATION

In the experimental investigations, electron beams, generally having currents of 30-60 kA, energies of 300-500 keV and a pulse duration of 60 ns were generated in the Cornell electron beam facility [6]. After guidance through a magnetically shielded injector tube, having 4 cm inner diameter and 1.10 m length, the beam was injected into a lucite tank, 25 cm in diameter and 1.80 m in length. Usually an injection angle of 83 degrees with respect to the tank axis and an injection radius of about 8 cm was used. To provide a return path for the beam current, the tank was lined with a copper screen electrically connected to the injector and to a metal flange at the downstream end of the tank. Upstream, the tank was sealed with a transparent lucite flange. Homogeneous windings around the tank and additional movable mirror coils provided the basic mirror field for trapping of the electrons. These coils were energized from a capacitor bank having a quarter-cycle rise time of 3.4 ms. To allow space charge neutralization, gas pressures from 0.1 - several Torr were maintained in the tank (Fig. 1).

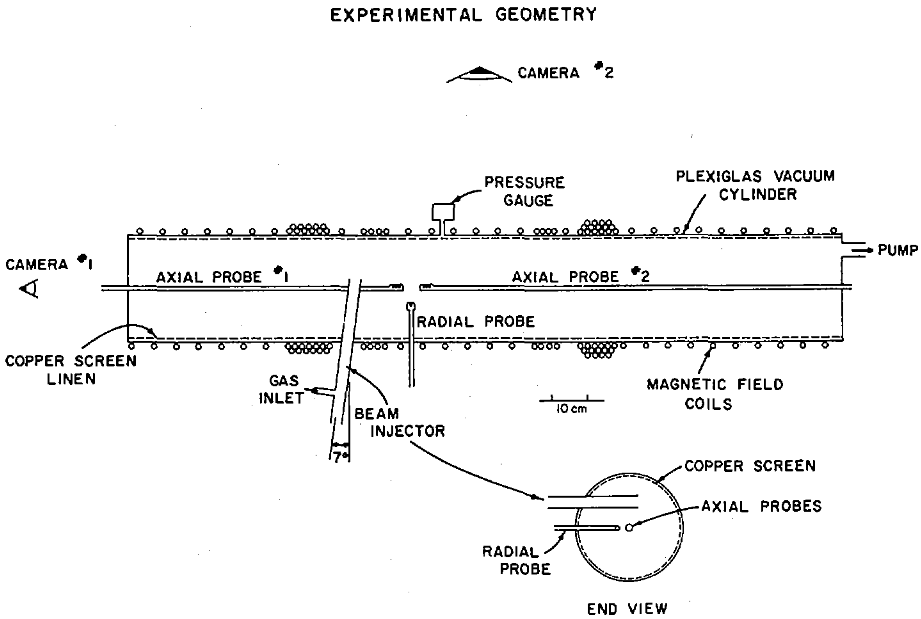

FIG. 1. Experimental arrangement.

For diagnostic purposes, open-shutter cameras viewed the tank from the side and through the lucite flange at the upstream end. Fast changes of the axial magnetic field were measured by three magnetic pick-up coils. Two of these coils could be moved along the tank axis entering from opposite ends while the third could probe the field at various radial positions. All probes were electrostatically shielded and their signals integrated electrically. The effectiveness of the electrostatic shielding and the general noise level were tested by placing all three probes in adjacent positions on axis. The two identically wound axial probes showed signals of opposite polarity, otherwise identical within 10%. The radial probe exhibited the expected signal amplitude and polarity depending upon orientation. Also, other polarities and calibrations were carefully tested.

Experiments were performed for a number of combinations of pressure, injection currents, beam energies, injection angles and applied magnetic field strengths and configurations. Good propagation was found for pressures above 150 microns with improving reproducibility at higher pressures.

Using a uniform magnetic field, the beam was observed to propagate along a spiral path down the tank, pitch and diameter being in rough agreement with the injection angle and corresponding single electron Larmor radius. When a single mirror of sufficient strength was applied along the path, reflection of the beam was observed. Since the mirror was short, a mirror ratio of almost 2, i.e. far above the adiabatic threshold, had to be applied to produce this reflection. Insertion of a second mirror on the upstream end resulted in a similar reduction of the number of electrons escaping to the upstream flange. An example of the camera recordings taken when two mirrors were used is shown in Fig. 2. The end camera clearly

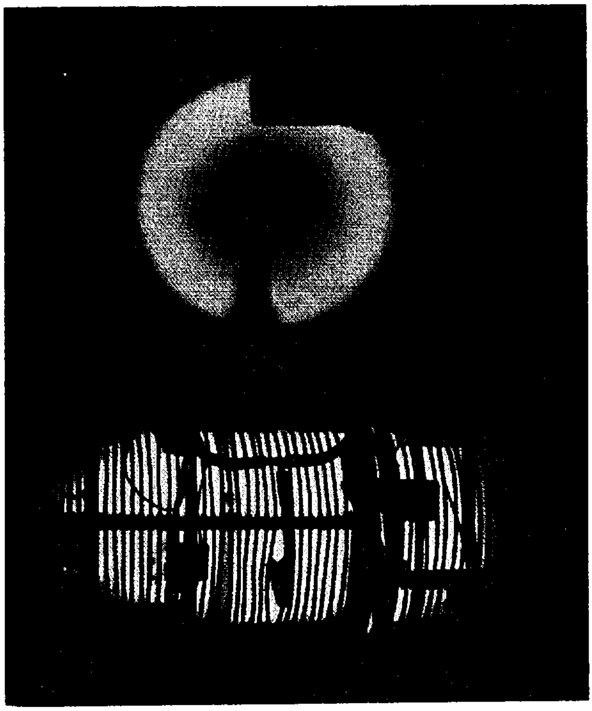

FIG. 2. Optical recording from double-mirror arrangements.

showed the ring of light produced by the beam. The side camera showed the "cigar"-shaped region of light. The dark vertical strips were produced by the field coils. The mirror peaks were located just outside either end of the cigar.

Magnetic field changes on axis were measured about 17 cm downstream from the injector. As to be expected, the observed field changes were all directed opposite to the applied field. Under otherwise comparable conditions, the beam produced field increased from 30% of the applied field for the uniform configuration to 40-50% with a single mirror to 100-140% in the double-mirror arrangement. In this latter configuration actual field reversal on axis and a minimum-B geometry were produced.

This double mirror arrangement was investigated in more detail for a particular set of experimental parameters (beam energy ≈ 340 keV, beam current ≈ 60 kA, pressure 800 microns). Radial and axial profiles of the magnetic field changes were determined. For each measurement one axial probe was kept at a fixed position and used as a reference while the other probes were moved in steps from shot to shot. Examples of the scope traces are displayed in Fig. 3. During this sequence axial probe number 1 was kept fixed and signals from it are shown in the right hand column of this figure. The signals on the radial probe at various radial positions are shown in the left hand column. For both probes, negative

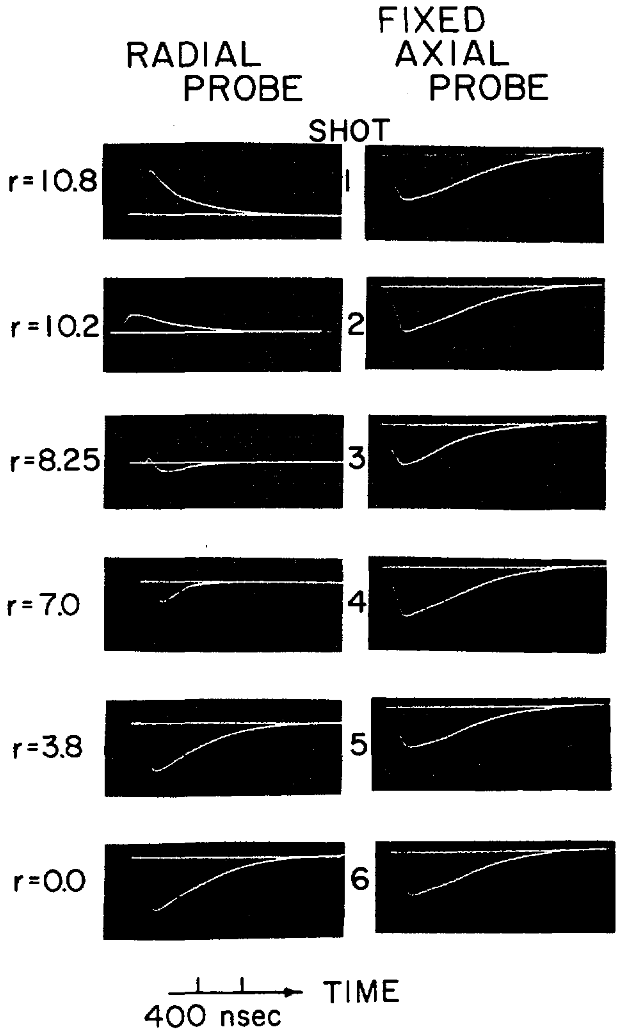

FIG.3. Examples of ΔB_z probe traces.

signals represent field changes opposite to the applied field. On axis, signals generally rose for about 90-120 ns and then decayed with a half-time of 400-600 ns. The RMS scatter of their amplitude was somewhat less than 10%. Figure 4 shows a plot of the radial dependence of the peak field changes ΔB_z normalized to the corresponding signal observed on the fixed axial probe. From the slope of this curve, it can be seen that while some current existed for small radial position, most flowed in a strip a few centimetres wide centred around 9 cm. As to be expected, the total magnetic flux inside the copper screen was conserved.

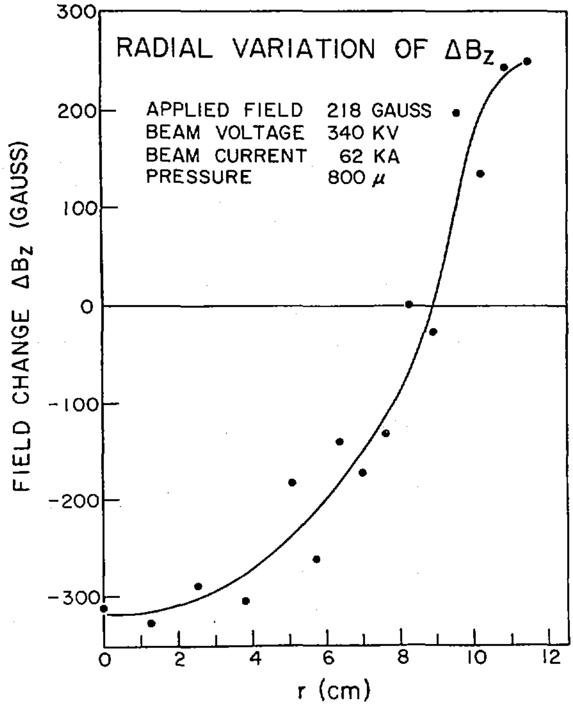

FIG.4. Radial dependence of ΔB_z.

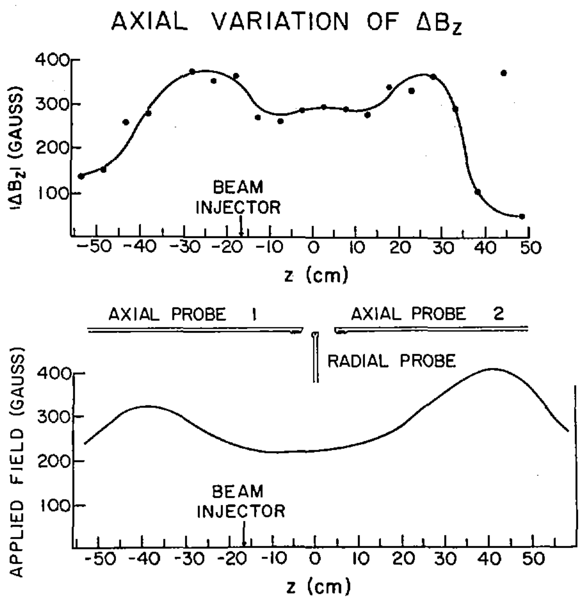

FIG.5. Axial field distributions.

The axial profile along with the applied magnetic field is shown in Fig. 5. Around z = 0 the ΔB_z signal appeared relatively constant reversing the total field from around +220 G to -70 G. The ΔB_z signals increased slightly at positions just inside the mirrors. At the mirror peaks the ΔB_z signal decreased substantially. However, as can be seen from the figure (and also from side photographs) more complete confinement was provided by the large downstream mirror than by the weaker upstream one. Between the mirror peaks the time dependence of ΔB_z was essentially as shown in the traces of Fig. 3. Outside of the mirrors the ΔB_z signals were much shorter lasting for only approximately 100 ns.

Thus, in the double-mirror arrangement, a compact current sheet with closed field lines and a minimum-B geometry was created. However, the confinement time of the fast electrons cannot necessarily be equated with the decay time to the magnetic probe signals. In straight-beam propagation experiments, it is known [3, 5, 7] that the net-current in the beam, consisting of the beam current minus induced counterstreaming currents in the created plasma, may be considerably smaller than the beam current itself. Also, owing to a relatively high conductivity of the final plasma, these net currents may persist considerably longer than the original electron beam. Similar effects can be expected also in the presence of an external magnetic field. A direct measurement of the fast-electron life-time could not yet be performed. However, in the present arrangement, relatively short life-times are expected. At injection, the average pitch distance for the electron trajectories was only about 6 cm compared with the injector diameter of 4.5 cm. Thus, the probability for the electrons to hit the injector or the surrounding highly perturbed field region was large and certainly limited the electron life-time to a few oscillations between the mirrors, each taking approximately 40 ns. In addition, the life-time may have been shortened by symmetries from imprecise positioning of the field coils and from stray fields.

The existence of induced counterstreaming currents in the plasma may be of considerable importance not only for the decay of the magnetic probe signals but also for the trapping of the electrons, both in our case and also in the stacking process in Livermore. Therefore, a theoretical analysis of this question was performed which is described in the next section.

3. MAGNETIC NEUTRALIZATION BY PLASMA CURRENTS

The injection of an electron beam into a cold dense plasma ($N_p >> N_b$, where N_p is the plasma, and N_b is the beam electron density) is accompanied by a return current [7] which acts to neutralize the magnetic field of the beam if $a/\lambda_E >> 1$, where a is the beam radius, $\lambda_E = c/\omega_p$ is the electromagnetic skin depth, and $\omega_p = (4\pi e^2 N_p/m_e)^{\frac{1}{2}}$ is the plasma frequency. This result may be understood most simply as follows: Assume that the plasma may be described by the generalized Ohm's law

$$\frac{\partial}{\partial t} + \frac{1}{\tau} J_p = (\omega_p^2/4\pi)\vec{E} + (e/mc)\vec{J}_p \times \vec{B} \tag{1}$$

where τ^{-1} is the effective collision frequency, and $J_p(x, t)$ is the plasma current density. For the sake of simplicity, let us, for the moment, neglect external magnetic fields, B_0, and in addition the self-magnetic field due to the beam and plasma current densities. Thus, the Hall contribution in Eq. (1) is neglected. Then by operating on Eq. (1) with $\nabla \times \nabla \times$ and using Faraday's and Ampere's laws (assuming overall charge neutrality and neglecting the displacement current) we obtain

$$\lambda_E^2 \frac{\partial}{\partial t} + \frac{1}{\tau} \vec{\nabla} \times \vec{\nabla} \times \vec{J}_p = - \frac{\partial}{\partial t} (\vec{J}_p + \vec{J}_b) \tag{2}$$

where the total current density $\vec{J}(\vec{x}, t) - \vec{J}_p(\vec{x}, t) + \vec{J}_b(\vec{x}, t)$ is written as the sum of the plasma and beam contribution. Estimating the scale of the gradient operator in Eq. (2) to be of the order of the beam radius a, it is clear that for $a/\lambda_E >> 1$ and short times we have $\vec{J}_p = -\vec{J}_b$. The theory of the induced "return" current $\vec{J}_p$ has been discussed in detail by a number of authors [7]; the current $\vec{J}_p$ is produced by the plasma electrons streaming in the direction opposite that of the beam with the small velocity $V_p = -(N_b/N_p) V_b << V_b$, where $V_b \simeq c$ is the beam velocity. Observations of the return current are described in Ref. [8]. Note that the near cancellation of the beam and plasma currents lends support to the neglect of the self-magnetic field in Eq. (1).

For slow time variations of the return current, $(\partial/\partial t)\, j_p << J_p/\tau$ Eq. (2) may be rewritten as

$$\left(\frac{\partial}{\partial t} + \frac{\lambda E^2}{\tau} \nabla^2\right) \vec{J}_p = -\frac{\partial}{\partial t} \vec{J}_b \tag{3}$$

where we have assumed $\vec{\nabla} \cdot \vec{J}_p = 0$ as is compatible with neglect of the displacement current. For the case of a beam with a sharp front propagating in the +z direction, for example, of the form $\vec{J}_b(\vec{x}, t) = \vec{J}(\vec{x}, t)\, U(V_b t - z)$, (where U(x) is the unit step function, $U(x > 0) = 1$, $U(x < 0) = 0$), the right hand side of Eq. (3) is non-zero only at the beam front. Behind the front the plasma current $\vec{J}_p(\vec{x}, t)$ obeys a diffusion equation. The characteristic decay time of the return current is: $T_d = \tau (a/\tau_E)^2$, a result originally obtained by Lee and Sudan [9]. The corresponding decay length is $L_n = T_d V_b$.

Although the energy density of the return current is much smaller than that of the beam, the plasma response may nevertheless have a strong effect on the beam dynamics in certain situations. For the case of an intense linear beam, it has been pointed out [10] that the electric field, which sustains the return current at the same time exerts a substantial drag on the beam. This drag converts most of the energy of a high ν/γ beam to plasma thermal energy in a distance much less than the above-mentioned decay length L_n.

Propagation across a magnetic field

In the above discussion, effects due to an external magnetic field were not considered. In general, the problem of the injection of a beam into a magnetized plasma has been discussed in considerable detail by Lee and Sudan [9] and one finds that for injection along the magnetic field lines the field has little direct effect on the generation of a return current. However, for injection across the magnetic lines of force, such as the injection of a beam of electrons into a magnetic mirror field, as in the experiment described in the previous section, the magnetic field introduces new complications in the physics of the return current flow. This problem was first considered by Lee and Sudan for the case where ion motion was neglected. We have now included the dynamics of the ions and these results are presented here.

If the beam is to be current neutralized the return current must be induced to flow across the magnetic field. The mechanism which allows the electrons to flow across the magnetic field is provided by a space charge electric field which builds up when the beam expels excess electrons in the process of becoming charge neutral. This electric field provides the proper $\vec{E} \times \vec{B}_0/|B_0|^2$ drift velocity for the plasma electrons. In this connection it should be noted that even in the absence of any external magnetic field this situation obtains whenever the return current has decayed a significant amount to generate an azimuthal field B_θ. The return current flows across B_θ only by generating a radial electric field sufficient for force free motion.

Assuming for the moment that the characteristics of the polarization field do not change as the ions begin to react to this field we would then expect the ions to respond in one of two ways: either they are accelerated directly into the region of space charge separation and neutralize the electric field, or they begin to drift with the same $c(\vec{E} \times \vec{B}_0)/|B_0|^2$ drift velocity as the electrons. In either case, the resulting plasma return current will go to zero.

To determine the exact time scale, and the correct physical mechanism for the decay of the return current, the cold plasma fluid equations are used to calculate the dynamics of both the plasma electrons and ions. To simplify the calculations, but not alter the basic physical phenomena, we will treat the case of a slab beam of thickness 2a with its head at $Z = 0$. In this configuration there will be no variation in the x-direction, the direction parallel to the magnetic lines of force, but all components of the electromagnetic fields and currents will be taken into account. Using the method described in Ref. [9], one then has the following expression for the component of the plasma current density in the direction of beam propagation,

$$\vec{J}_p\,(t \to \infty, \vec{X}) = (1/\pi) \int_{-\infty}^{+\infty} dK\, K^{-1} \sin(KA) \exp(-iKY)$$

$$\int_{-\infty}^{0} d\vec{Z} \int_{-\infty}^{+\infty} dX \exp[-i(Z + Z)X] \cdot X^2 [X(X + i\nu) + 1 + \mu\zeta^2/\alpha^2$$

$$- i\zeta K(1-\mu)/\beta_0] \times \Big\{ X \big\{ [(X^2 + K^2)(X + i\nu) + X]$$

$$\times [X(X + i\nu) - 1/\alpha^2] - \zeta^2 X (X^2 + K^2)/\alpha^2 \big\} + \mu\zeta^2 (1 + \mu\zeta^2)$$

$$\times (X^2 + K^2)/\alpha^4 - \mu\zeta^2 X [\mu X (X^2 + K^2)/\alpha + X/\alpha^2 + i2\nu (X^2 + K^2)/\alpha^2] \Big\}^{-1}$$

where $\zeta = \omega_c/\omega_p$, $\mu = m_e/m_i$, $\alpha = \beta_0\gamma_0$, $\alpha\nu = \nu_c/\omega_p$, ν_c is the electron collision frequency, and the two position variables have been normalized to λ_E such that $x = X\lambda_E$ and $y = Y\lambda_E$; and $A = a/\lambda_E$. Performing a contour integration in X and then the Z-integration, the expression for the return current is now

$$J_p(\eta, Z) = -\pi^{-1}\int_0^\infty d\vec{X}\,\vec{X}^{-1}\left\{\sin[(1+\eta)\vec{X}] + \sin[(1-\eta)\vec{X}]\right\}$$

$$\times\left\{A^2/[\vec{X}^2(1+\xi^2) + A^2]\right\} H(\vec{X}) \tag{5}$$

where we have defined the new variables as $\vec{X} = KA$, and $\eta = Y/A$. The function $H(\vec{X})$ is given by

$$H(\vec{X}) = [V_1 \exp(-iV_1 Z) - V_2 \exp(-iV_2 Z)]/(V_1 - V_2)$$

where

$$V_{1,2} = \frac{-i\nu\vec{X}^2/2 \pm (1/2)\{4\mu\xi^2\vec{X}^2[\vec{X}^2(1+\xi^2) + A^2] - \nu^2\vec{X}^4\}^{\frac{1}{2}}}{\vec{X}^2(1+\xi^2) + A^2}$$

The integral in Eq. (5) can only be done, for arbitrary values of μ, ξ, ν, η, and A, by numerical methods. For large A, that is $A \gg \nu/\mu^{\frac{1}{2}}\xi$, the function $H(\vec{X})$ then becomes

$$H(\vec{X}) \approx \cos(\mu^{\frac{1}{2}}\xi\vec{X}Z/A)$$

For $\eta = 0$, i.e., $R = 0$, the return current is

$$J_p(0, Z) = -(2/\pi)\int_0^\infty d\vec{X}\,\vec{X}^{-1}\sin(X)\cos(\mu^{\frac{1}{2}}\xi\vec{X}Z/Z)$$

$$= U(1 - \mu^{\frac{1}{2}}\xi Z/A)$$

where U(x) is a unit step function as before. Thus we see that the return current is unity until $Z \sim A/(\mu^{\frac{1}{2}}\xi)$, and then it is zero. The new current neutralization length is given by

$$L_n = A/\mu^{\frac{1}{2}}\xi$$

This corresponds to a diffusion time in the laboratory frame given by

$$\tau_d = \omega_{ci}^{-1}\mu^{\frac{1}{2}}a/(\lambda_E\alpha)$$

As we see, this time could be less than, greater than, or equal to the ion cyclotron period depending on the magnitude of the parameters within the brackets. The general integration of Eq. (5) has been carried out numerically and the results are shown in Fig. 6 for a fixed value of A. For values of $\xi > 0.1$, the length over which the return current will flow is significantly degraded by the magnetic field. In all the data shown the normalized

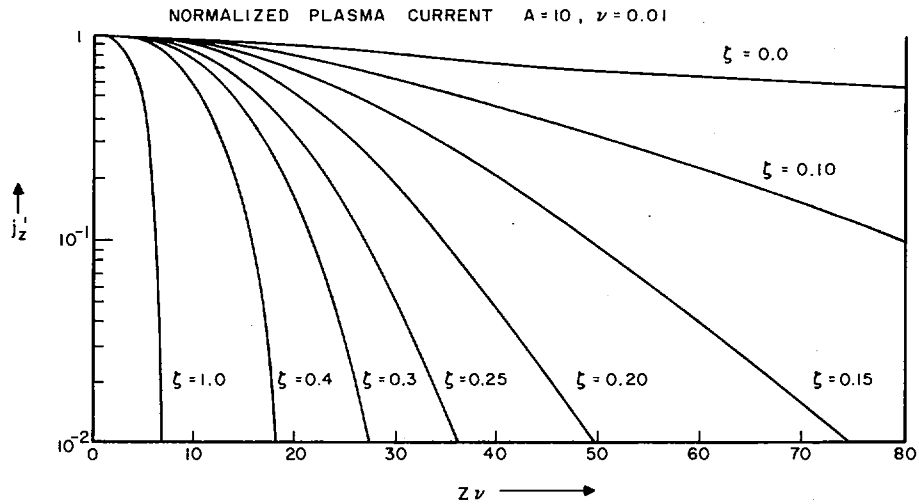

FIG.6. Normalized plasma current, A = 10, ν = 0.01.

collision frequency was taken to be 0.01. However, it should be noted that in the limit A → ∞, the neutralization length is independent of ν and only depends on A, μ, and ζ.

We can estimate the decay time of the plasma return current for the conditions of the experiment. In the E-layer $B_z \sim 200$ G, a ~ 2 cm, ω_{ci} for nitrogen ions = $2\pi\ 10^4$ and estimating the plasma density to be 10^{14} cm^{-3} we obtain $\tau d \sim 1 - 1.5\ \mu$s which is in rough agreement with the experimental decay times of 600 s.

It must be noted that in these calculations the beam electrons are held rigid. In the light of the remarks [10] made earlier the response of the beam electrons to the drag of the return current may be significant, and the decay time of the plasma current may be altered.

4. CONCLUSIONS

In the present arrangement with the injector between the mirrors, sufficient trapping of beam electrons occurs to produce an E-layer with full field reversal. However, very little can be said at present on the stability of such electron layers. The decay of the magnetic probe signals appears mostly determined by the decay of induced currents in the plasma itself. In addition to the acceptable agreement between the observed times and the estimates of section 3, also the additional rise of the magnetic probe signals after the termination of the injection pulse is an indication of the presence of such plasma current. As mentioned, the present injector geometry can be expected to be the main limit of the fast-electron life time. To remove this limitation, trapping away from the injector has to be accomplished. For this purpose lower gas pressures and higher beam energies have to be employed. To provide sufficiently fast space-charge neutralization, pre-ionization may have to be used. In this case, the question of plasma currents may become even more important: they may influence both the trapping of the beam and the behaviour of the resulting E-layer. At high plasma densities, where a strong initial quenching of the beam currents occurs, sizable portions of the beam energy may be transferred directly to the plasma. Corresponding experiments are in preparation.

ACKNOWLEDGEMENTS

The experimental work was supported by the US Office of Naval Research under contract N00014-67-A-0077-0003. Part of the theoretical work was supported by the US Atomic Energy Commission under contract AT-30-1-4077.

REFERENCES

[1] CHRISTOFILOS, N.C., 2nd Int. Conf. Peaceful Uses Atom. Energy (Proc. Conf. Geneva) 32 (1958) 279.
[2] LAWRENCE RADIATION LABORATORY, Report UCRL-50002-69.
[3] GRAYBILL, S.E., NABLO, S.V., Appl. Phys. Letts 8 (1966) 18.
[4] YONAS, G., SPENCE, P., in 10th Symposium on Electron, Ion and Laser Technology, (MARTON, G., Ed.) San Francisco Press, San Francisco (1969) 143.
[5] ANDREWS, M.L., DAVITIAN, H., FLEISCHMANN, H.H., HAMMER, D.A., NATION, J.A., Appl. Phys. Letts 16 (1970) 98.
[6] CLARKE, J.J., URY, M., ANDREWS, M.L., HAMMER, D.A., LINKE, S., 10th Symposium on Electron, Ion and LaserBeam Technology, (MARTON, G., Ed.) San Francisco Press, San Francisco (1969) 145.
[7] HAMMER, D.A., ROSTOKER, N., Physics Fluids 13 (1970) 1831; LEE, R.E., SUDAN, R.N., Lab. of Plasma Studies, Cornell Univ., LPS Report No. 42 (1970), to appear in Physics Fluids, June 1971; COX, J.L., BENNETT, W.H., Physics Fluids 13 (1970) 182.
[8] GRAYBILL, S.E., UGLAM, J., NABLO, S.V., Bull. Am. Phys. Soc. 13 (1968) 56.
[9] LEE, R.E., SUDAN, R.N., Physics Fluids 14 (1971) 1213.
[10] LOVELACE, R.V., SUDAN, R.N., submitted to Phys. Rev. Letts May (1971) (Cornell University, LPS Report No. 75 (1971)).

PINCHES
STABILIZATION METHODS

(Session B)

Chairman: C. M. BRAAMS

Papers B-6 and B-7 were presented by
H. ZWICKER as Rapporteur

Papers B-8 to B-12 were presented by
E.S. WEIBEL as Rapporteur

Papers B-13 to B-15 were presented by
P.E. STOTT as Rapporteur

НАГРЕВ И УСТОЙЧИВОСТЬ ПЛАЗМЫ В КОМБИНИРОВАННОМ ПИНЧЕ

И.Ф.КВАРЦХАВА, Г.Г.ЗУКАКИШВИЛИ,
Ю.В.МАТВЕЕВ, Ю.С.ГВАЛАДЗЕ,
Н.А.РАЗМАДЗЕ, А.А.БЕСШАПОШНИКОВ,
Э.К.ТИХАНОВ, З.Д.ЧКУАСЕЛИ,
Э.Ю.ХАУТИЕВ, И.Я.БУТОВ
Физико-технический институт
Государственного комитета по
использованию атомной энергии СССР,
Сухуми,
Союз Советских Социалистических Республик

Abstract — Аннотация

PLASMA HEATING AND STABILITY IN A COMBINED PINCH.

In earlier papers the authors considered the results of experiments involving discharges in chambers of large diameter (d = 36 cm), when the plasma sheath acquires a developed filament-like structure. It was shown that a combined pinch has a number of advantages over Z and theta pinches: there are no repeated discharge breakdowns, which are characteristic of Z pinches, and no cumulative streams from the plasma surface, as observed in theta pinches. Thanks to its filament-like structure, the combined pinch has greater stability with respect to the Kruskal-Shafranov criterion. These experiments were carried out with heavy gases (helium, neon) at a relatively low temperature ($T_e \approx 15$ eV). In the present paper the authors consider the results of experiments with a discharge chamber of small diameter (d = 6.5 cm), when there are no filaments in the plasma. The length of the theta pinch magnetic coil L = 21 cm. The axial magnetic field $H_z \simeq 65$ kOe. The longitudinal current of the Z pinch varied within the range 5-50 kA. The half-period of the discharge was the same for both pinches ($T/2$ = 9.5 μs); the two discharges were triggered simultaneously in an already existing plasma with electron temperature ~5 eV. The measurements showed that for currents not exceeding the Kruskal-Shafranov value (~10 kA) a plasma is stable throughout the half-period of the discharge; the electron temperature (determined by measuring the absorption of soft X-rays by aluminium foils) rises with increasing H_z and reaches 150 eV when H_z is at its maximum. Neutron emission is also greatest at maximum H_z. Investigation of the axial and radial distributions of the neutron yield showed that neutrons are emitted from a plasma column with a diameter ~1.5 cm and length ~15 cm, which coincides with the region of soft X-ray emission. The total neutron yield is of the order of 10^6 per discharge and corresponds to an ion temperature ~1 keV. The electron concentration gradients along the radius of the plasma column and the electron concentration profiles were determined by means of the laser schlieren method with time resolution. In the absence of a filament-like structure, when the currents exceed the Kruskal-Shafranov value, a magnetohydrodynamic instability of the m = 1 mode with wavelength $\lambda = 2L$ develops. The variations in the instability growth rate as a function of the current I_z agree qualitatively with MHD theory; however, the measured values are approximately an order of magnitude less than theoretical. Some data are also presented on the influence of a high-frequency (~0.7 Mc/s) longitudinal current on the stability of a combined pinch.

НАГРЕВ И УСТОЙЧИВОСТЬ ПЛАЗМЫ В КОМБИНИРОВАННОМ ПИНЧЕ.

В предыдущих наших работах рассматривались результаты экспериментов, проводившихся с разрядами в камерах большого диаметра (d = 36 см), когда сжимающаяся плазменная оболочка обладает развитой волокнистой структурой. Эти результаты свидетельствуют о том, что комбинированный пинч обладает рядом преимуществ по сравнению с зет- и тета-пинчами. В нем отсутствуют повторные пробои вдоль стенок разрядной камеры, характерные для зет-пинча; кумулятивные струи с поверхности плазмы, наблюдаемые в тета-пинчах. Кроме того, комбинированный разряд обладает повышенной устойчивостью по отношению к критерию Крускала-Шафранова, связанной с наличием волокнистой структуры. Эти опыты проводились на тяжелых газах (гелий, неон) при сравнительно низкой температуре ($T_e \simeq 15$ эВ). В докладе рассматриваются результаты опытов с разрядной камерой

малого диаметра (d = 6,5 см), когда в плазме отсутствуют волокна. Длина магнитной катушки тета-пинча L = 21 см. Аксиальное магнитное поле H_z = 65 кэрст. Продольный ток зет-пинча варьировался в диапазоне 5 ÷ 50 кА. Измерения показали, что при токах, не превышающих значение Крускала-Шафранова (~10 кА), плазма устойчива в течение всего полупериода разрядного тока. При этом электронная температура, измеренная по поглощению мягкого рентгеновского излучения в алюминиевых фольгах, нарастает с увеличением H_z и в максимуме H_z достигает 150 эВ. Эмиссия нейтронов также достигает наибольшей величины в максимуме H_z. Исследование аксиального и радиального распределения выхода нейтронов показало, что они излучаются из плазменного шнура диаметром ⩽ 1,5 см и длиной ~15 см, что совпадает с областью излучения мягкого рентгена. Полный выход нейтронов составляет ~10^6 н/разряд и соответствует ионной температуре 1 кэВ. Градиенты электронной концентрации вдоль радиуса плазменного шнура, а также профили электронной концентрации определялись с помощью шлирен-метода, разрешенного во времени (многолучевой шлирен-осциллограф на основе гелий-неонового лазера). В условиях многоволоконной структуры плазменного шнура при токах, превышающих значение Крускала-Шафранова, развивается МГД-неустойчивость моды m = 1 с длиной волны λ = 2L. Изменение инкремента неустойчивости в зависимости от тока качественно согласуется с МГД-теорией, однако, измеренные значения примерно на порядок меньше теоретических. Рассматриваются также некоторые новые виды МГД-нестабильностей, обусловленные процессами на границе плазмы с магнитным полем и в приэлектродных областях разряда. Они приводят к нестабильностям в зет-пинче моды m = 1 и к выбросу тонких плазменных оболочек поперек удерживающего поля в зет- и тета-пинчах. Показано, что в комбинированном пинче с развитой волокнистой структурой могут быть подавлены и эти нестабильности.

ВВЕДЕНИЕ

В нашем новосибирском докладе [1] было показано, что с точки зрения нагрева и удержания плазмы комбинированный пинч обладает определенными преимуществами по сравнению с обычными зет- и тета-пинчами. Эти преимущества обусловлены, главным образом, наличием развитой волокнистой структуры зет-компоненты пинча. Скручивание волокон, происходящее под действием поля тета-пинча, приводит к парамагнитному эффекту (усилению аксиального магнитного поля внутри жгута волокон), что и обеспечивает возможность превышения критического тока Крускала-Шафранова. Нетрудно видеть, что комбинированный пинч может обладать хорошей устойчивостью лишь при достаточно большом числе волокон и высокой симметрии их пространственного распределения. В экспериментах [1] это достигалось, в основном, выбором диаметра и геометрической формы камеры (правильный шестигранник с диаметром вписанной окружности ~36 см).

В данном докладе приводятся экспериментальные результаты по нагреву и устойчивости плазмы в комбинированном пинче для случая, когда зетовая компонента тока формируется в виде одиночного волокна. Как показали исследования, при этом комбинированный пинч сохраняет устойчивость лишь для токов в зет-пинче, не превышающих предел Крускала-Шафранова. Обсуждаются также некоторые новые данные, являющиеся дальнейшим подтверждением преимуществ комбинированного пинча с развитой волокнистой структурой. Опыты показывают, что в зет-пинчах со сплошными электродами всегда возникают довольно сильные МГД-нестабильности, обусловленные приэлектродными процессами; в зет- и тета-пинчах наблюдаются нестабильности, связанные с явлением так называемого "обратного скина" [2,3] и проявляющиеся в выбросе поверхностного слоя плазмы поперек удерживающего магнитного поля. Из характера указанных нестабильностей следует, что в условиях комбинированного пинча с высокой симметрией токовых волокон они могут быть подавлены или существенно ослаблены.

1. КОМБИНИРОВАННЫЙ ПИНЧ В ОТСУТСТВИИ МНОГОВОЛОКНИСТОЙ СТРУКТУРЫ ЗЕТ-КОМПОНЕНТЫ

Экспериментальная установка описана в работе [1], поэтому здесь мы перечислим только основные ее параметры. Диаметр разрядной камеры — 6,5 см. Длина магнитной катушки тета-пинча L = 21 см, напряженность аксиального магнитного поля H_z = 65 кэ. Продольный ток зет-пинча, зажигаемого между кольцевыми электродами, изменялся в диапазоне 5 ÷ 50 кА. Полупериоды разрядных токов в обоих пинчах одинаковы (T/2 = 9,5 мксек); разряды включаются одновременно в предварительно созданной дейтериевой плазме с электронной температурой ~5 эВ и степенью ионизации 60%. В некоторых режимах основной разряд включался в максимуме квазипостоянного антипараллельного магнитного поля H_{z0} напряженностью до 5 кэ. Регистрация во времени спектральных линий в видимой области спектра производилась монохроматором, за выходной щелью которого располагался блок фотоэлектронного умножителя (ФЭУ). С помощью этой методики были измерены температура и концентрация электронов в форплазме, а также показано, что примеси с электродов и стенок камеры в течение первого полупериода не попадают в разряд.

Для регистрации тормозного рентгеновского излучения использовалась камера-обскура. При записи изменения интенсивности мягкого рентгеновского излучения во времени детектором служил тонкий (0,3 мм) полистироловый сцинтиллятор и ФЭУ. Интегральные за время разряда фотографии плазмы с торца разрядной камеры в тормозном излучении получены на рентгеновской фотопленке. Электронная температура плазмы оценивалась по поглощению тормозного излучения в алюминиевых фольгах разной толщины. Нейтроны регистрировались полистироловым сцинтиллятором и ФЭУ. Полный выход нейтронов измерялся методом радиоактивного индикатора. Исследование пространственного распределения нейтронного выхода из разрядного объема производилось щелевым коллиматором.

Для измерения градиентов электронной концентрации по радиусу плазменного шнура использовался метод шлирен-фотографии. Как известно [4], угол отклонения светового луча связан с параметрами плазмы соотношением:

$$\alpha = 4{,}45\,10^{-14}\lambda^2\,\nabla\bar{N}_e l \qquad (1)$$

где λ — длина волны падающего излучения, см;
$\nabla\bar{N}_e$ — среднее значение перпендикулярной лучу компоненты градиента плотности электронов вдоль луча в плазме, см$^{-4}$;
l — длина пути в плазме, см.

Поскольку это соотношение справедливо при малых углах отклонения, то линейное смещение луча в плоскости регистрации прямо пропорционально $\nabla\bar{N}_e$. Таким образом, записывая движение луча, прошедшего через плазму, можно получить изменение градиента плотности электронов в данной области плазмы в течение разряда.

В качестве источников света использовался гелий-неоновый лазер (λ = 6328 Å) мощностью 25 мВт. Свет от лазера соответствующей оптикой формировался в узкую полоску, разделялся щелевой диафрагмой на семь лучей и фокусировался в центральную часть разрядной камеры. При этом ширина луча составляла 0,4 мм, а высота – 3 мм. Выходящий из плазмы световой пучок проходил путь длиной 17 м и собирался объективом в фокальной плоскости сверхскоростного фоторегистратора. Лазер включался на время одного оборота зеркала фоторегистратора. Без плазмы запись световых лучей на пленке имеет вид параллельных прямолинейных полосок, число которых равно числу щелей в диафрагме [5]. Как видно из рис. 4, такие шлирен-осциллограммы позволяют проследить за динамикой развития разряда, измерить усредненное по длине плазменного столба распределение радиальных градиентов электронной концентрации, а также оценить распределение плотности по диаметру разрядной камеры в различные моменты времени в предположении, что величиной концентрации в пристеночной области можно пренебречь.

Как указывалось выше, в отличие от работы [1], в рассматриваемых здесь экспериментах зетовая компонента пинча состоит из одного волокна. Поскольку волокна представляют собой элементарные зет-пинчи и диаметр волокна сравним с толщиной скина [6], то для их возникновения в начальной стадии разряда должны быть выполнены следующие условия:

$$1)\ I_z^2 \gg 200\ N\kappa(T_e + T_i) \qquad 2)\ \delta \ll R \qquad (2)$$

где I_z – полный ток зет-пинча;
N – число частиц на единицу длины плазменного шнура;
T_e и T_i – электронная и ионная температуры;
δ – толщина скин-слоя;
R – радиус разрядной камеры.

Первое условие легко реализуется в том случае, когда скорость нарастания тока велика, а начальная температура плазмы мала (плазма не нагрета предварительно), второе – в разрядных камерах большого диаметра. Оба эти условия были выполнены в опытах, описанных в работе [1].

В рассматриваемых ниже опытах величина зетового тока была ограничена устойчивостью плазменного шнура ($I_{z\,крит} \simeq 10$ кА), плазма предварительно нагревалась до температуры 5 эВ. Легко видеть, что в этом случае первое условие не выполнено. Кроме того, толщина скин-слоя в начальной стадии разряда была сравнима с радиусом разрядной камеры ($R \simeq 3{,}2$ см). Следует отметить, что большинство экспериментов в последнее время проводится именно в таких условиях, и, естественно, в них не наблюдаются токовые структуры. С точки зрения влияния волокнистой структуры на устойчивость комбинированного пинча, представляло интерес исследование предельного случая, когда зетовая компонента пинча состоит из одного волокна. Кроме того, уменьшение разрядного объема (при той же энергоемкости конденсаторной батареи) позволило существенно увеличить температуру плазмы.

В данных экспериментах мощность тета-пинча существенно больше мощности зет-пинча, поэтому такие параметры разряда, как скорость сжатия плазменной оболочки, концентрация и ионная температура, определяются, главным образом, тета-пинчем. Зет-пинч вызывает лишь небольшой дополнительный джоулев нагрев электронной компоненты, который не меняет в целом качественной картины разряда. Основная роль продольного тока состоит в том, что он определяет МГД-устойчивость плазменного шнура.

Качественное представление об эмиссионных характеристиках разряда в зависимости от начальных условий опыта можно получить из табл.I.

На рис. 1 и 2 приведены осциллограммы тока в катушке тета-пинча, нейтронного и мягкого рентгеновского излучений и линии D_β для начальных условий, приведенных во второй и третьей графах табл. I. На этих же рисунках справа показаны фотографии плазмы с торца в мягких рентгеновских лучах. Рис. 1(а) и 2(а) соответствуют тета-пинчу, 1(б) и 2(б) – комбинированному пинчу в устойчивом режиме, 1(в) и 2(в) – комбинированному пинчу в неустойчивом режиме. Эти рисунки позволяют проследить за развитием разряда во времени. Сначала рассмотрим рисунки 1(а),(б) и 2(а),(б).

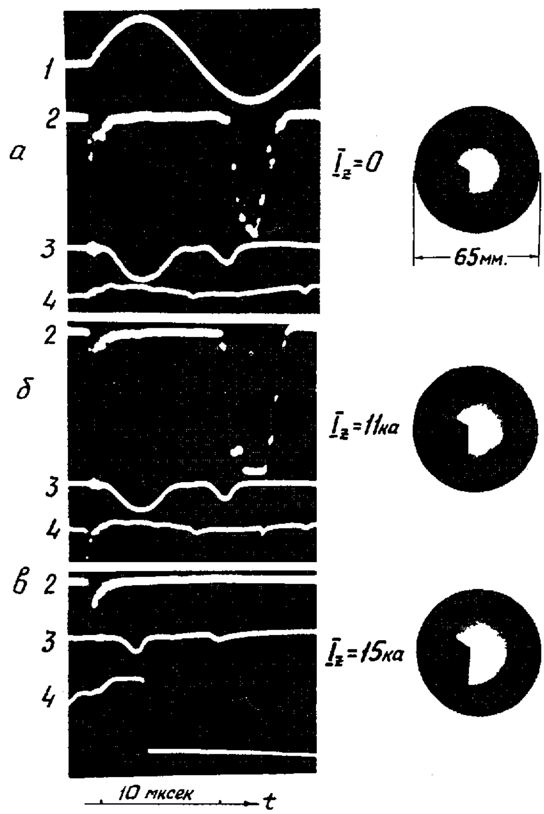

Рис. 1. Осциллограммы: 1 – тока, 2 – нейтронного импульса, 3 – мягкого рентгеновского излучения, 4 – линии D_β .

(а) – Тета-пинч, (б) – комбинированный пинч в устойчивом режиме, (в) – комбинированный пинч в неустойчивом режиме.

Справа: фотографии плазмы в мягких рентгеновских лучах. $P = 10^{-1}$ мм рт. ст., H_z = 65 кэ, H_{z0} = -5 кэ.

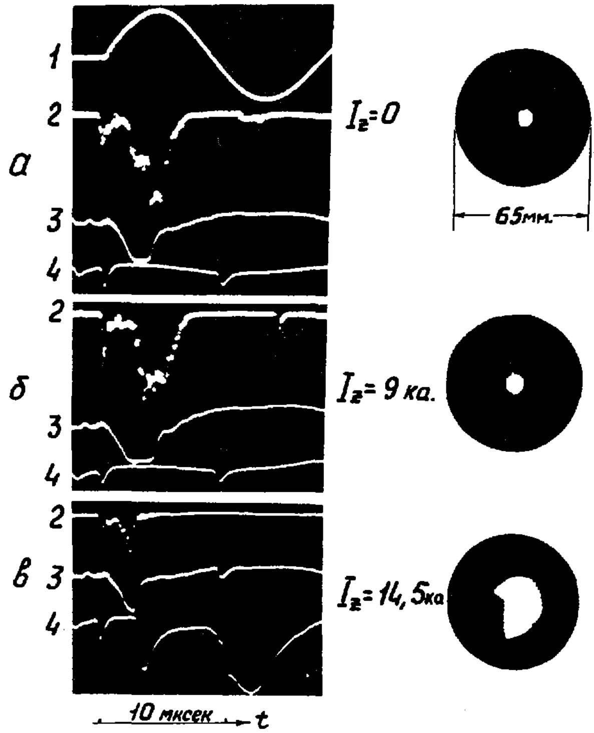

Рис. 2. Осциллограммы: 1 – тока, 2 – нейтронного импульса, 3 – мягкого рентгеновского излучения, 4 – линии D_β.

(а) – Тета-пинч, (б) – комбинированный пинч в устойчивом режиме, (в) – комбинированный пинч в неустойчивом режиме.

Справа: фотографии плазмы в мягких рентгеновских лучах. $P \approx 10^{-2}$ мм рт. ст., H_z = 65 кэ, H_{zo} = 0.

К концу фазы быстрого радиального сжатия плазмы, которая в зависимости от начальных условий может длиться 0,3-0,9 мксек, интенсивность линии D_β резко уменьшается. Некоторое увеличение интенсивности D_β наблюдается только в начале второго полупериода, когда плазменная оболочка вновь формируется у стенок камеры. Этот факт свидетельствует о том, что плазма полностью ионизована в течение всего первого полупериода разряда. После быстрого сжатия следует медленное адиабатическое дожатие, которое длится вплоть до максимума магнитного поля. В этой стадии появляются тормозное и нейтронное излучения. При начальном давлении 10^{-1} мм рт. ст. длительность тормозного излучения в первом полупериоде достигает 6 мксек; форма импульса – симметричная, и его максимум совпадает с максимумом магнитного поля, рис. 1(а),(б). Нейтронное излучение при этом не регистрируется, так как ионная температура не превышает 500 эВ. В результате потерь плазмы через концы пинча оставшиеся частицы приобретают более высокую температуру, что приводит к появлению нейтронного излучения. Сравнение рис. 1(а) и

2(б) показывает, что при начальном давлении 10^{-1} мм рт. ст. во втором полупериоде реализуются примерно такие же условия, как и при давлении 10^{-2} мм рт. ст. в первом полупериоде. Это означает, что в результате концевых потерь полное число частиц за время T/2 = 9,5 мксек уменьшается примерно на порядок. В последующих полупериодах (см. табл. I) за счет дальнейшего снижения концентрации плазмы возникают условия, благоприятные для перехода электронов в режим "убегания", и появляется жесткое рентгеновское излучение с энергией до 100 кэВ.

Эмиссия нейтронов достигает наибольшей величины в максимуме магнитного поля и всегда сопровождается мягким рентгеновским излучением. Однако следует отметить, что импульс тормозного излучения, как правило, несколько опережает по времени нейтронный импульс, рис. 2(а),(б). Это связано с различием механизмов нагрева ионов и электронов. Ионы в основном греются за счет быстрого радиального сжатия и последующего адиабатического дожатия, в то время как нагрев электронов осуществляется за счет джоулевых потерь и поступления энергии от ионов. Как показывают оценки, при начальном давлении 10^{-1} мм рт. ст. в нагреве электронов оба эти фактора играют примерно одинаковую роль. На рис. 3 показано изменение электронной температуры плазмы со временем для указанного режима. С уменьшением плотности плазмы роль джоулева нагрева возрастает, а эффективность передачи энергии от ионов к электронам падает. Поскольку джоулев нагрев приводит к температуре электронов значительно меньшей, чем имеют ионы, а времена релаксации между ионной и электронной компонентами больше времени формирования пинча, то легко объясняется наблюдаемая на опыте разница электронной и ионной температур. (Ионная температура в 2-4 раза превышает электронную температуру).

Фотографии плазмы в мягких рентгеновских лучах, приведенные на рис. 1(а),(б) и 2(а),(б) показывают, что, по крайней мере, за время тормозного излучения плазменный шнур сохраняет аксиальную симметрию и оторван от стенок камеры.

ТАБЛИЦА I. ЭМИССИОННЫЕ ХАРАКТЕРИСТИКИ РАЗРЯДА В ЗАВИСИМОСТИ ОТ НАЧАЛЬНЫХ УСЛОВИЙ ОПЫТА

Условия опытов	Мягкое рентгеновское излучение	Выход нейтронов	Жесткое рентгеновское излучение
1. $P = 10^{-1}$ мм рт. ст. $H_{zo} = 0$	II полупериод	Нет	III полупериод
2. $P = 10^{-1}$ мм рт. ст. $H_{zo} = -5$ кэ	I и II полупериоды	II полупериод	III полупериод
3. $P = 10^{-2}$ мм рт. ст. $H_{zo} = 0$	I полупериод	I полупериод	II полупериод
4. $P = 10^{-2}$ мм рт. ст. $H_{zo} = -5$ кэ	I полупериод Эмиссия больше чем при $H_{zo} = 0$	I полупериод Эмиссия больше чем при $H_{zo} = 0$	II полупериод

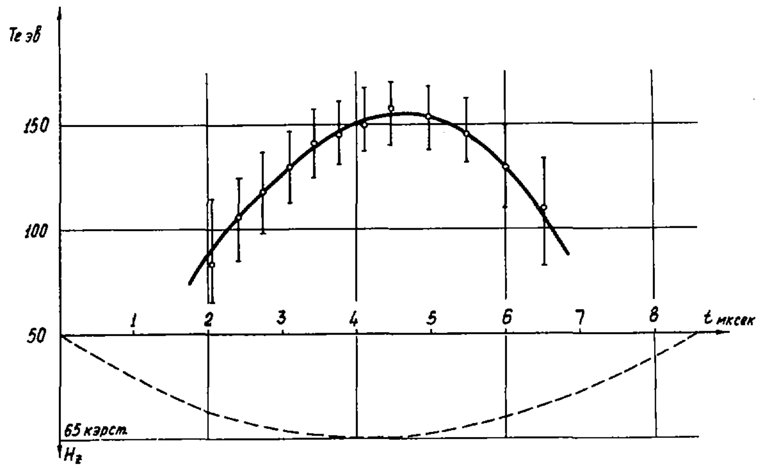

Рис. 3. График зависимости электронной температуры от времени. Пунктиром обозначено изменение магнитного поля. $P = 10^{-1}$ мм рт. ст., $H_{zo} = -5$ кэ.

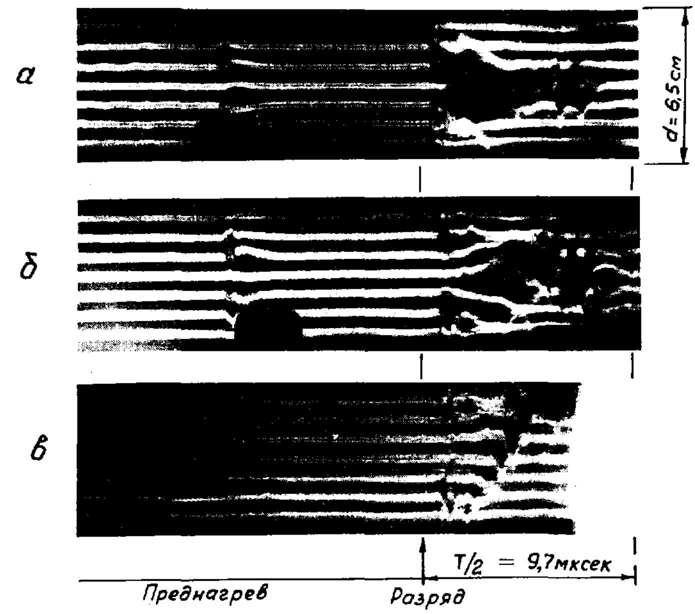

Рис. 4. Шлирен-осциллограммы плазмы в комбинированном пинче.
(а) – устойчивый режим, I_z = 10 ка, H_{zo} = 0, (б) – устойчивый режим, I_z = 10 ка, H_{zo} = -5 кэ, (в) – неустойчивый режим, I_z = 15 ка, H_{zo} = -5 кэ. $P = 10^{-1}$ мм рт. ст., H_z = 65 кэ.

На рис. 4(а),(б) приведены шлирен-осциллограммы для начальных условий, указанных в графах 1 и 2 табл. I. По этим фотографиям удается проследить за развитием разряда (перед основным разрядом видна фаза преднагрева). В том случае, когда $H_{zo} = 0$, рис. 4(а), сжатие плазменной оболочки начинается практически сразу же после включения тета-пинча. Когда $H_{zo} \neq 0$, рис. 4(б), начало сжатия задерживается на время:

$$\Delta t = \frac{2\,H_{zo}}{H_z\,\omega}$$

где ω – частота поля H_z.

После фазы быстрого сжатия периферийные лучи в течение всего полупериода остаются невозмущенными, т.е. плазменный шнур сохраняет макроскопическую устойчивость. Отклонение центральных лучей со временем уменьшается, что связано с потерями плазмы через концы системы.

На рис. 5(а) представлены результаты обработки шлирен-осциллограмм для комбинированного пинча в устойчивом режиме при $P = 10^{-1}$ мм рт. ст. и $H_{zo} = -5$ кэ. Градиенты плотности в направлении к оси разрядной камеры считаются положительными, к стенке – отрицательными.

Верхние кривые плотности построены интегрированием градиентов (вычисленных по формуле 1) по шагу диафрагмы, нижние – только по ширине луча. Непосредственно после первого сжатия распределение плотности по диаметру имеет двугорбый профиль с минимумом концентрации на оси. Оно соответствует плазменной оболочке с захваченным обратным магнитным полем. После одного слабого радиального колебания распределение плотности перестраивается, принимая профиль с максимумом концентрации в центре. Этому моменту по зондовым измерениям магнитного поля на оси разрядной камеры соответствует быстрая диффузия антипараллельного поля через плазменную оболочку. Здесь следует обратить внимание на два обстоятельства. Первое заключается в том, что диффузия обратного поля происходит значительно быстрее (за 0,3-0,5 мксек), чем следовало бы ожидать, исходя из проводимости плазмы. Это явление часто наблюдается в быстрых тета-пинчах. По-видимому, в зависимости от конкретных условий, исчезновение антипараллельного поля может происходить по-разному: в коротких пинчах это может происходить в результате "опрокидывания" плазменного кольца [7]; в длинных пинчах быстрая диффузия обратного поля, скорее всего, связана с аномальным увеличением сопротивления плазмы в скин-слое.

Второе обстоятельство связано с тем, что, несмотря на быстрое исчезновение обратного магнитного поля (через 1,5 ÷ 2 мксек от начала разряда), плазменный шнур испытывает радиальные колебания в течение всего полупериода, в то время как без начального поля эти колебания намного слабее и проявляются лишь в конце полупериода, рис. 4(а),(б).

Как видно из рис. 5(а), концентрация электронов при начальном давлении 10^{-1} мм рт. ст. достигает 10^{17} $см^{-3}$ и со временем меняется слабо, в то время как число частиц на единицу длины плазменного шнура существенно уменьшается. Постоянная времени концевых потерь

$$\tau = \frac{N}{dN/dt} \tag{3}$$

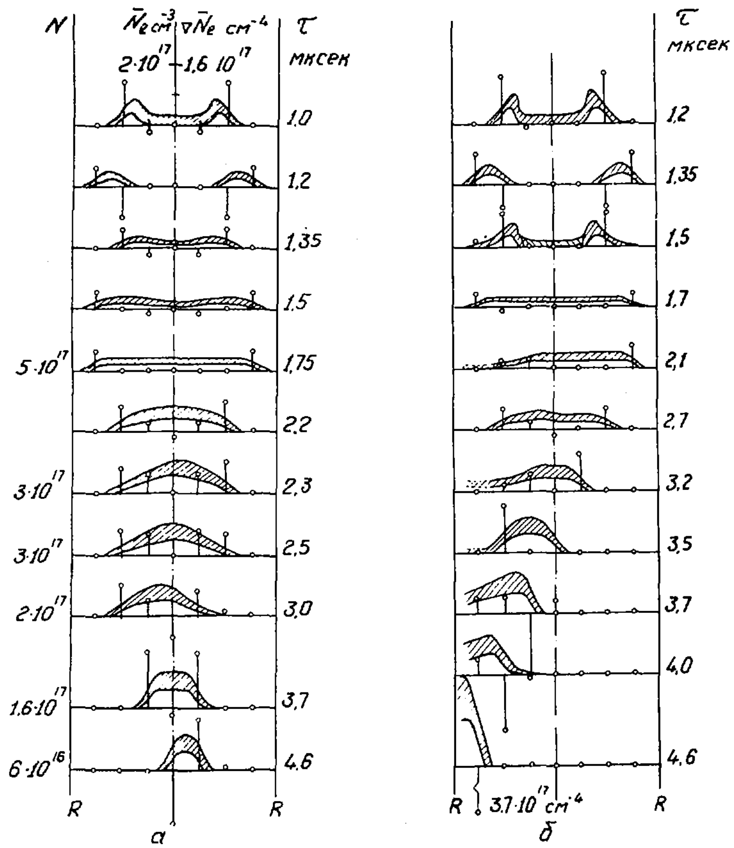

Рис. 5. Распределение градиентов плотности $\nabla\bar{N}_e$ (вертикальные линии) и плотности $\bar{N}_e$ по диаметру разрядной камеры для разных моментов времени. N – полное число частиц на единицу длины плазменного шнура.

(а) – устойчивый режим, $I_z = 9$ ка, $H_{zo} = -5$ кэ, (б) – неустойчивый режим, $I_z = 18$ ка, $H_{zo} = -5$ кэ. $P = 10^{-1}$ мм рт. ст., $H_z = 65$ кэ.

в этом режиме составляет ~ 2 мксек. При давлении 10^{-2} мм рт. ст. концентрация составляет $2\cdot10^{16}$ см$^{-3}$, а постоянная времени концевых потерь уменьшается.

На рис. 6 и 7 приведены кривые распределения нейтронного выхода по радиусу и вдоль оси разрядной камеры, соответственно. Эти кривые показывают, что нейтроны излучаются, в основном, из приосевой области диаметром $\leqslant 1{,}7$ см (1,7 см – пространственное разрешение коллиматора). При этом, эмиссия максимальна в средней части пинча и уменьшается к его краям. Как показывают торцевые фотографии плазмы, мягкий рентген также излучается из приосевой области, диаметр которой для условий, указанных на рис. 2(а) и (б), не превышает 1 см.

Таким образом, нейтроны и мягкий рентген излучаются из одной и той же области и наблюдаются одновременно. Полный выход нейтронов достигает $\sim 10^6$ н/разряд и при концентрации плазмы $\sim 2\cdot10^{16}$ см$^{-3}$ соответствует ионной температуре ~ 1 кэВ.

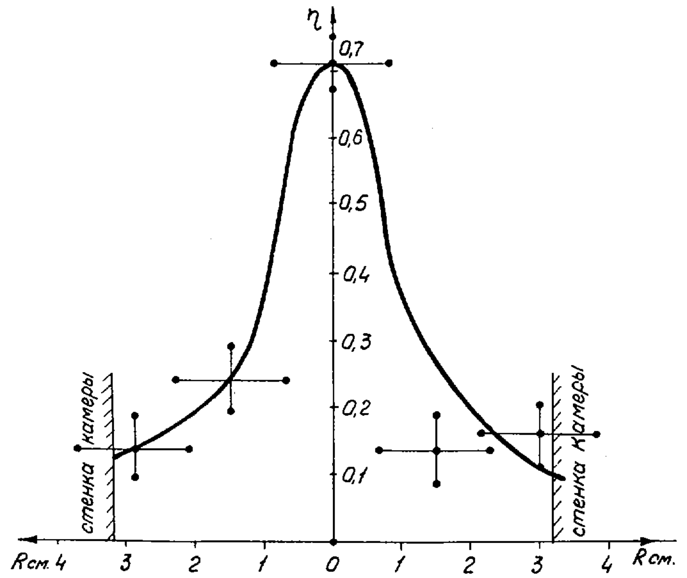

Рис. 6. Распределение нейтронного выхода по радиусу разрядной камеры в относительных единицах. Горизонтальные черточки на экспериментальных значениях означают пространственное разрешение коллиматора. P = 10^{-2} мм рт. ст., H_z = 65 кэ, H_{zo} = -5 кэ.

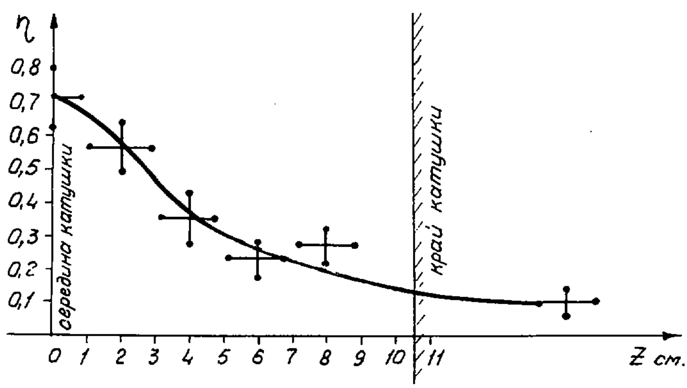

Рис. 7. Распределение нейтронного выхода вдоль оси разрядной камеры в относительных единицах. P = 10^{-2} мм рт. ст., H_z = 65 кэ, H_{zo} = -5 кэ.

При токах в зет-пинче, превышающих критическое значение (10 кА), в комбинированном пинче развивается неустойчивость, проявляющаяся в том, что импульсы нейтронного и тормозного излучений обрываются, и в момент касания плазмой стенки камеры вспыхивает интенсивное излучение D_β, обусловленное рекомбинацией дейтерия, рис. 1(в) и 2(в). Между вспышкой D_β и срывом нейтронного и тормозного излучений наблюдается четкая корреляция. На фотографиях рис. 1(в) и 2(в) видна граница сектора, образованного плазменным шнуром, смещенным относительно оси.

(На этих фотографиях просматривается не весь диаметр разрядной камеры; изображение ограничено кольцевой диафрагмой и клином из более толстой алюминиевой фольги). Наблюдаемая форма сектора соответствует спиральной деформации плазменного шнура с модой $m = 1$ и длиной волны $\lambda = 2L$. Измерения D_β коллимированным приемником вдоль оси разрядной камеры показывают, что плазменный шнур касается стенки разрядной камеры только в центральной области под магнитной катушкой и подтверждают вывод о длине волны неустойчивости.

Для режима низкого начального давления (10^{-2}мм рт. ст. и $H_{zo} = 0$) было проведено сравнение экспериментальных результатов с теорией Крускала-Шафранова [8], согласно которой величина критического тока равна:

$$I_{z\,\text{крит}} = \frac{10\pi(2-\beta)r_o^2 H_z}{2\lambda} \tag{4}$$

где r_o – радиус плазменного шнура,

β – среднее значение $8\pi nkT/H_z^2$ по радиусу плазмы.

Оценка критического тока по формуле дает величину ~ 10 кА, что удовлетворительно согласуется с данными наших опытов.

На рис. 8 показано изменение инкрементов МГД-неустойчивости γ в зависимости от тока в зет-пинче I_z. Первая кривая – экспериментальная. Инкременты измерялись по набору осциллограмм, подобных осциллограммам, показанным на рис. 1(в) и 2(в), и по шлирен-осциллограммам, см. рис. 4(в) и 5(б). Вторая кривая построена на основе теоретического выражения инкремента, полученного из МГД-теории [9]:

$$\gamma = [-(2-\beta)\kappa^2 + 2m\kappa]^{1/2} V_A \tag{5}$$

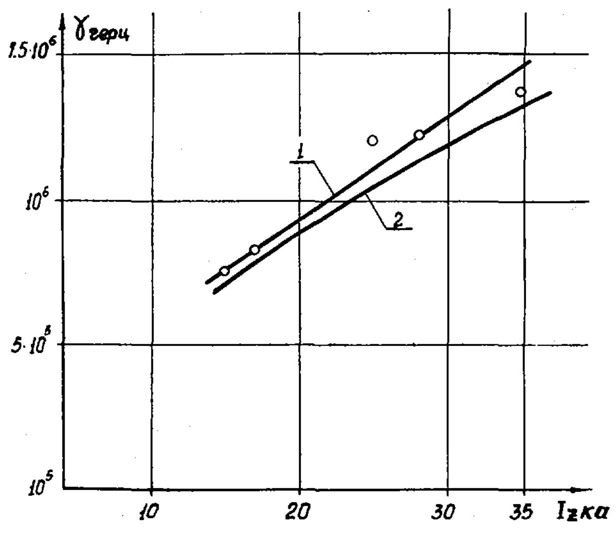

Рис. 8. Изменение инкремента γ в зависимости от тока в зет-пинче I_z. Первая кривая – экспериментальная. Вторая – построена на основе МГД-теории; для удобства значения вычисленных инкрементов уменьшены в семь раз.

где $м = 2I_z/10r_0^2 H_z$ — шаг магнитной спирали,
$к = 2\pi/\lambda$ — волновое число,
V_A — альфвеновская скорость.

Измеренная скорость нарастания нестабильности в зависимости от величины тока в зет-пинче качественно согласуется с линейной МГД-теорией. Однако экспериментальные значения инкрементов примерно в семь раз меньше теоретических. Подобный факт отмечался и в работе [10]. Он, по-видимому, связан с концевыми эффектами.

Следует отметить, что величина критического тока практически не зависит от амплитуды начального обратного поля. Это связано с тем, что неустойчивость начинает развиваться только после того, как это поле диффундирует из плазмы и профиль плотности принимает вид с максимумом концентрации на оси (см. рис. 5). Подобная картина сохраняется при токах зет-пинча, не превышающих ~60 кА. Если ток I_z выше указанной величины, неустойчивость развивается уже до исчезновения обратного захваченного поля. В этом случае плазменный шнур, отклоняясь от равновесного положения и скручиваясь в спираль, несет с собой антипараллельное магнитное поле.

Влияние временного сдвига между разрядами сводится к следующему: когда зет-пинч включается раньше тета-пинча, неустойчивость развивается при меньших токах I_z, чем при одновременном их включении; если зет-пинч включается позже тета-пинча, то развитие неустойчивости задерживается. В этих опытах с помощью временной задержки между включением зет- и тета-пинчей фактически варьировалось амплитудное значение тока I_z. Как нетрудно видеть, эти результаты находятся в согласии с описанными выше данными.

2. КОНЦЕВЫЕ НЕСТАБИЛЬНОСТИ ЗЕТ-ПИНЧА

На рис. 9 приведена типичная кадровая СФР-грамма простого зет-пинча (скорость съемки $2\cdot10^6$ кадров в секунду), горящего между сплошными электродами. Кадры этой СФР-граммы, охватывающие и приэлектродные области, отчетливо демонстрируют зарождение и дальнейшее развитие специфических нестабильностей, возникающих на концах пинча. В анодной области наблюдается сильное пережатие, приводящее к обрыву пинча. Место обрыва сразу же шунтируется током, текущим в окружающей плазме. В катодной области, напротив, происходит отщепление поверхностного слоя плазмы, расширяющегося в виде конической оболочки, основание которой вскоре охватывает почти всю поверхность катода. Возникающие при этом концевые возмущения плазмы распространяются вдоль пинча и приводят к возбуждению нестабильности типа $m = 1$.

В этих опытах изучалось также распределение разрядного тока по поверхности электродов в зависимости от их полярности. С этой целью использовался электрод, составленный из пяти концентрических цилиндров, обладающих малой и почти одинаковой индуктивностью. У торца электрода эти цилиндры изолированы друг от друга тонким слоем фторопласта. На рис. 10 приведены соответствующие осциллограммы токов. Датчиками токовых сигналов служили пояса Роговского, последовательно охватывающие составные цилиндры. Для непрерывных кривых составной электрод является анодом, а для пунктирных — катодом.

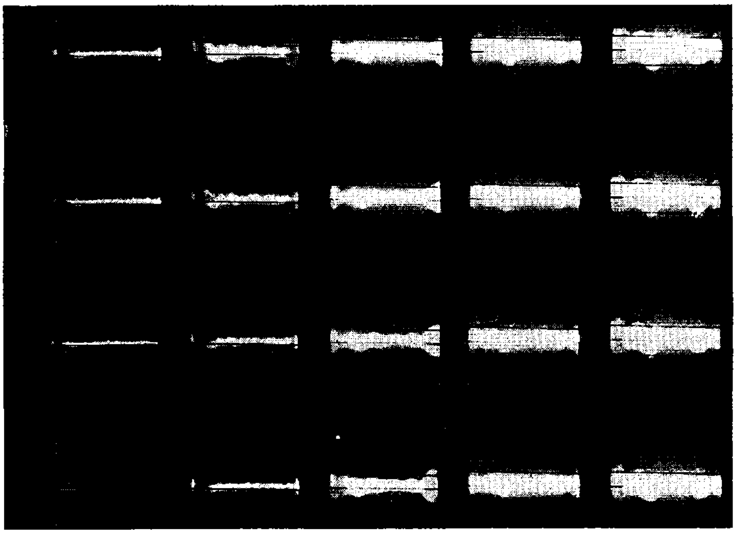

Рис. 9. Зет-пинч (фотография сбоку). Электроды – сплошные. Газ: Не, $P = 10^{-1}$ мм рт. ст., $I_z = 650$ ка, $T/2 = 13{,}5$ мксек. Экспозиция каждого кадра – 0,5 мксек. Временной интервал между кадрами – 0,5 мксек.

Эти осциллограммы показывают, что различному поведению плазмы на концах пинча (см. рис. 9) соответствует различное распределение тока по поверхности электродов. Когда составной электрод является анодом, ток на торец центрального стержня течет почти с момента зажигания разряда и круто нарастает. Аналогичная ситуация наблюдается на торцах двух последующих цилиндров. В случае же катода, ток на торец центрального стержня начинает течь с задержкой в 2,5 мксек. При этом, и на последующих цилиндрах токи удерживаются на уровнях, более низких, чем в случае анода. Отсюда следует однозначный вывод, что прикатодные процессы препятствуют эффективному сжатию тока (плазмы) под действием силы $j \times H$, в то время как прианодные процессы, напротив, способствуют этому.

Из приведенных осциллограмм следует также, что полупериоды токов, текущих на торцы внутренних цилиндров, заметно превышают полупериод общего разрядного тока (кривая 5), что указывает на наличие в разрядном объеме замкнутых индукционных токов, возникающих в результате сохранения магнитного потока. Это подтверждается и осциллограммами сигналов от магнитных зондов, расположенных внутри разрядного объема.

Следует отметить, что по данным наших опытов, проводящихся с коаксиальным ускорителем плазмы, аналогичные эффекты наблюдаются у конца центрального электрода в зависимости от его полярности. При этом, в широких пределах разрядного тока (от 10^4 до 10^6 А) они приводят к снижению (при центральном катоде) или к усилению (при центральном аноде) степени сжатия плазменной струи, являющейся пинчевым продолжением центрального электрода. В этом, по-видимому, состоит одна из

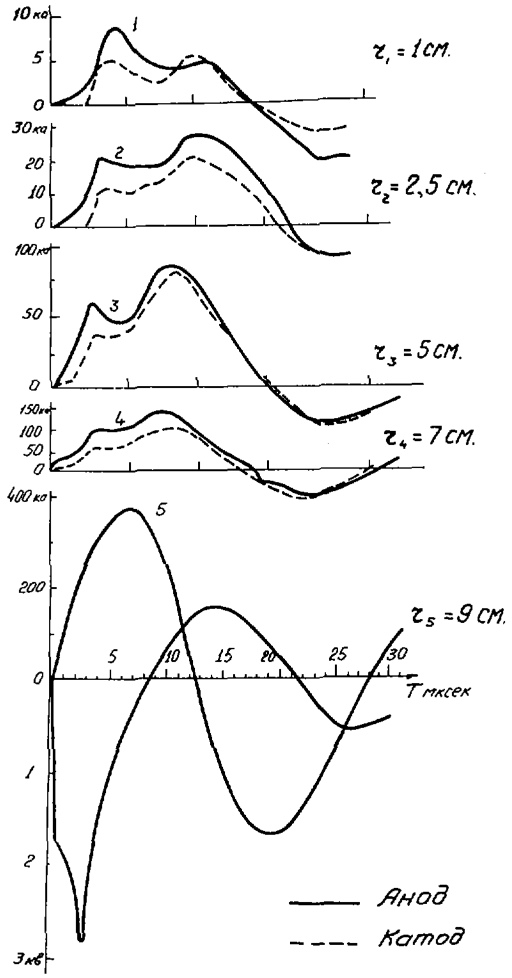

Рис. 10. Зет-пинч. Осциллограммы, характеризующие распределение тока по радиусу электродов в зависимости от их полярности. Газ: Ar, Р = 10^{-1} мм рт. ст., I_z = 380 ка, T/2 = 14 мксек.

возможных причин наблюдаемой на опыте зависимости нейтронного выхода из "плазменного фокуса" от полярности приложенного к ускорителю напряжения. Мы полагаем, что наиболее вероятной причиной рассматриваемых влияний приэлектродных процессов на поведение сильноточной плазмы является взаимодействие быстрых локальных плазменных струй катодных и анодных "пятен" с магнитным полем тока и разрядной плазмой. Это согласуется с наблюдаемыми следами эрозии электродов разряда. Очевидно, эти струи, обладающие скоростями ~10^6 см/сек [11], обогащают приэлектродные области плазмы быстрыми ионами. В магнитном поле разрядного тока ионные компоненты анодных струй отклоняются к оси пинча и усиливают степень сжатия плазмы, в то время как ионные компоненты катодных струй, отклоняясь в противоположную сторону, препятствуют такому сжатию. Опыт показывает, что в условиях комбинированного пинча отсутствуют рассмотренные выше концевые нестабильности. Это и понятно, так как использование кольцевых электродов для зет-пинча существенно снижает влияние приэлектродных процессов.

4. СКИНОВЫЕ НЕСТАБИЛЬНОСТИ ПИНЧЕВЫХ РАЗРЯДОВ

Наши ранние эксперименты показали, что в определенных стадиях развития разряда в зет- и тета-пинчах возбуждаются МГД-нестабильности, проявляющиеся в выбросе поверхностного слоя плазмы поперек удерживающего поля. В последующих исследованиях было установлено, что выброс поверхностного слоя плазмы связан с возбуждением в нем тока обратного направления.

На рис. 11 и 12 приведены типичные СФР-граммы зет- и тета-пинчей, иллюстрирующие эффект расслоения плазмы. Рис. 11 относится к зет-пинчам, зажигаемым в отсутствии продольного магнитного поля H_{zo}, рис. 11(а), и при $H_{zo} = 3{\cdot}10^3$ Гс, рис. 11(б). В обоих случаях сжатие происходит еще до максимума тока в первом полупериоде и выброс наружной оболочки плазмы с центрального пинча начинается с момента формирования шунтирующего разряда в пристеночной области. При этом, по данным зондовых измерений, на поверхности пинча возбуждается ток обратного направления (рис. 13). Ситуация в некотором смысле аналогична той, с которой мы встречаемся при образовании плазмы в тета-пинчах.

Наложение продольного магнитного поля не препятствует расслоению пинча, а лишь ограничивает скорость начавшегося перемещения плазмы.

Расслоение плазменной оболочки и движение поверхностного слоя к периферии наблюдалось нами и в медленных зет-пинчах в области за максимумом тока, протекающего в цепи [12]. В этом случае обратный ток возникал в поверхностном слое пинча вследствие эффекта "обратного скина" [2,3] или вследствие уменьшения проникшего в проводник магнитного потока.

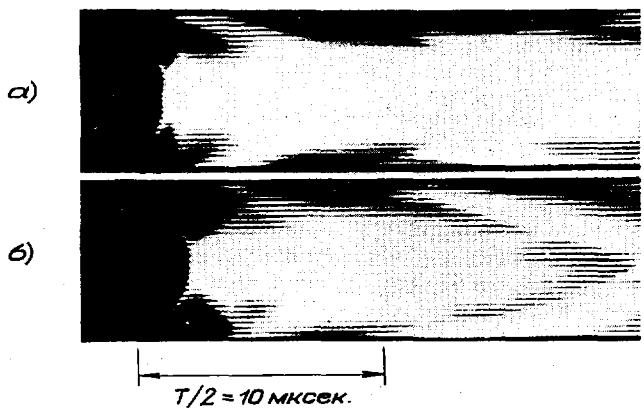

Рис. 11. СФР-граммы динамических зет-пинчей, полученные при ориентации щели на диаметральный ряд отверстий в одном из электродов. Диаметр камеры – 30 см; расстояние между электродами – 20 см; $I_{max} \approx 5{\cdot}10^5$ а; $T/2 = 10$ мксек; давление воздуха $P_0 = 10^{-1}$ мм рт. ст. В случае (а) $H_{zo} = 0$; в случае (б) $H_{zo} = 3{\cdot}10^3$ гс.

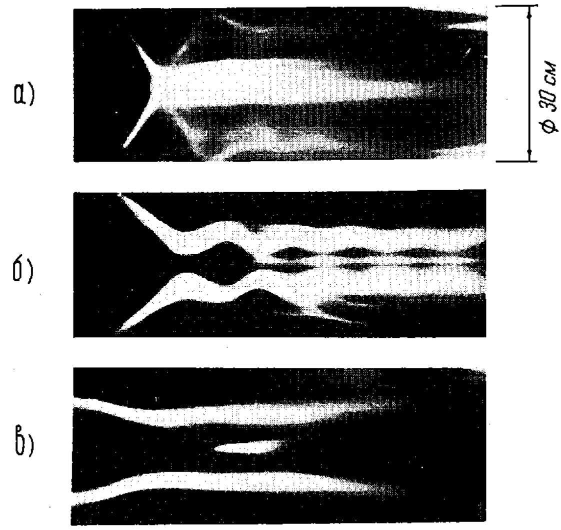

Рис. 12. СФР-граммы тета-пинчей в водороде, иллюстрирующие расслоения оболочки плазмы (скиновые нестабильности):

(а) $P_0 = 5 \cdot 10^{-2}$ мм рт. ст.; $I_{max} \simeq 4 \cdot 10^5$ а;

(б) $P_0 = 10^{-1}$ мм рт. ст.; $I_{max} \simeq 7 \cdot 10^5$ а;

(в) $P_0 = 5 \cdot 10^{-1}$ мм рт. ст.; $I_{max} \simeq 7 \cdot 10^5$ а;

Во всех случаях период колебаний тока в катушке T = 30 мксек. Длительность фоторазверток – 15 мксек.

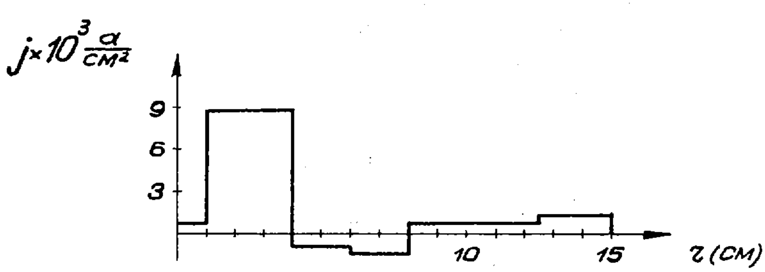

Рис. 13. Гистограмма распределения плотности разрядного тока по сечению камеры для момента времени, соответствующего повторному зажиганию разряда. Соответствующая СФР-грамма приведена на рис. 11(а).

Из результатов расчета, выполненного нами для недеформируемого проводника, когда $R/\delta \simeq 2 \div 3$ (R – радиус проводника, δ – глубина скина), следовало, что отношение максимальной величины обратного тока к максимальному значению тока прямого направления в соответствующем полупериоде составляет $\sim 1/4$. Поскольку для зет-пинчей R/δ, как правило, больше единицы, то в поверхностном слое плазмы к концу полупериода возникал значительный по величине ток обратного направления. Взаимодействие его с магнитным полем основного тока приводит к расслоению пинча и выбросу поверхностного слоя к стенке камеры. При этом ядро пинча получает соответствующий обратный импульс.

Проведенные нами эксперименты с тета-пинчами также показали наличие подобного типа нестабильностей. Причем, как видно из рис. 12, отщепления плазмы возникают как с наружной (в стадиях сжатия), так и с внутренней (в стадиях расширения) сторон плазменной оболочки. Наблюдаемые нестабильности и в этом случае удается объяснить на основе представлений об "обратном скине".

Как известно, в тета-пинчах без предыонизации газа (нами исследовались такие режимы) оболочка плазмы образуется в разрядном объеме спустя некоторое время после начала протекания тока в возбуждающей катушке. При этом существующее в разрядном объеме магнитное поле захватывается полой плазменной оболочкой. В дальнейшем, по мере сжатия плазмы, это поле нарастает. Ускоренное движение плазмы к оси и сохранение внутри оболочки магнитного потока свидетельствует о наличии в толще этой оболочки сложной структуры токов [13]. По наружной поверхности оболочки протекает скинированный ток, противоположный по направлению току в катушке (ток из-за взаимоиндукции). Направление тока, текущего по внутренней поверхности оболочки, совпадает с током в катушке, рис. 14(б).

Проведенные эксперименты показали, что распределение тока может еще более усложниться, если поток, пронизывающий сжимающуюся оболочку плазмы, начинает уменьшаться (ток в катушке может нарастать). При этом на внешней поверхности плазмы возбуждается дополнительный ток, совпадающий по направлению с током в катушке.

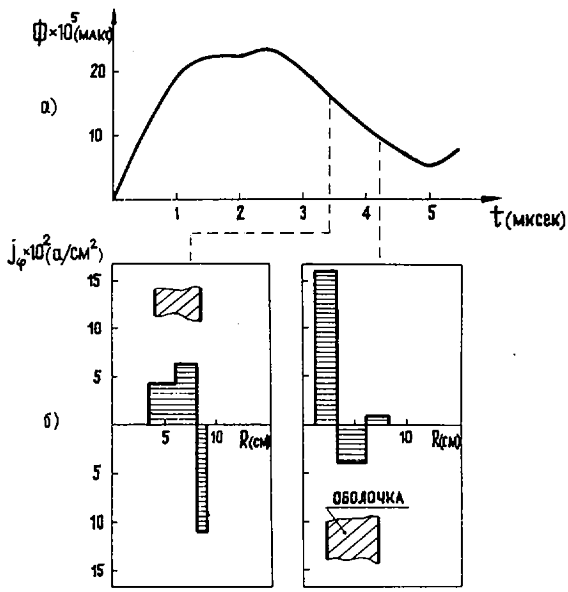

Рис. 14. Характер изменения потока Ф в быстрых тета-пинчах через площадь, ограниченную наружным контуром плазмы (а), и соответствующие различным моментам времени распределения азимутального тока j_φ по ширине плазменной оболочки (б). Внутренний диаметр разрядной камеры – 30 см. Период колебаний тока в катушке T = 36 мксек. Максимальное сжатие плазмы наступает при t = 5 мксек.

На соответствующих фотографиях динамических тета-пинчей наблюдаются расслоения сжимающейся плазмы и выбросы коаксиальных пинчам поверхностных слоев на периферию. В некоторых случаях скорость слета близка к скорости сжатия плазмы, рис. 12(а).

В условиях тета-пинчей сжатая к оси плазма часто сохраняет трубчатую форму, рис. 12(б),(в) и совершает радиальные пульсации около равновесного радиуса, рис. 12(б). Опыты показали, что в этом случае наблюдается несколько отщеплений тонких цилиндрических слоев плазмы, имеющих место как с наружной, так и с внутренней сторон пульсирующей оболочки. Отщепления слоев с внутренней поверхности оболочки также удается объяснить на основе представлений об "обратном скинировании" тока. Для этого необходимо учесть, что ток, протекающий по внутренней поверхности трубчатого тета-пинча, колеблется при радиальных пульсациях в соответствии с изменением напряженности захваченного в начальной стадии разряда магнитного поля. При расширении оболочки ток будет уменьшаться, что и приведет к появлению индукционного тока обратного направления. Взаимодействие этого тока с захваченным магнитным полем обуславливает выброс плазмы с внутренней поверхности оболочки.

Таким образом, в отличие от недеформируемых проводников с жесткими внутренними связями, в плазме возникает новый вид МГД-нестабильности, обусловленный индукционными токами обратного направления. В ряде случаев эти нестабильности могут вносить существенный вклад в так называемую "аномальную" диффузию плазмы.

Следует отметить, что в комбинированном пинче с развитой волокнистой структурой зетовой компоненты скиновые нестабильности не могут развиться, так как плазма состоит из тонких волокон, разделенных друг от друга магнитным полем и возбуждение поверхностных токов затруднено.

ВЫВОДЫ

1) В разрядных камерах малого диаметра комбинированный пинч имеет гладкую структуру плазменной оболочки. В этом случае плазменный шнур устойчив при токах в зет-пинче, не превышающих предел Крускала-Шафранова. Величина критического тока практически не зависит от амплитуды начального антипараллельного магнитного поля, так как оно аномально быстро диффундирует из плазменной оболочки.

2) В устойчивых режимах плазма является источником мягкого рентгеновского и нейтронного излучений. Эмиссия нейтронов достигает наибольшей величины в максимуме магнитного поля и наблюдается из приосевой области диаметром $\leqslant 1{,}7$ см, что совпадает с областью излучения мягкого рентгена. Полный выход нейтронов составляет $\sim 10^6$ н/разряд и при концентрации плазмы $2 \cdot 10^{16}$ см$^{-3}$ соответствует ионной температуре ~ 1 кэВ. Электронная температура в несколько раз ниже ионной температуры.

3) Плазма теряется, в основном, через концы системы; скорость концевых потерь возрастает с увеличением ионной температуры.

4) При значениях зетового тока, превышающих предел Крускала-Шафранова, развивается МГД-неустойчивость с модой $m = 1$ и длиной волны $\lambda = 2L$. Измеренные инкременты почти на порядок ниже теоретических.

5) Стабильность комбинированного пинча улучшается с увеличением числа волокон зетовой компоненты тока. При этом необходима высокая симметрия пространственного распределения системы волокон.

6) Комбинированный пинч с развитой волокнистой структурой устойчив не только в отношении обычных МГД-нестабильностей, но и в отношении рассмотренных выше нестабильностей зет-пинча, а также скиновых нестабильностей зет- и тета-пинчей.

ЛИТЕРАТУРА

[1] КВАРЦХАВА, И.Ф., ЗУКАКИШВИЛИ, Г.Г., ГВАЛАДЗЕ, Ю.С., МАТВЕЕВ, Ю.В., РАЗМАДЗЕ, Н.А., ЧКУАСЕЛИ, З.Д., ОРЕШКИН, В.К., БУТОВ, И.Я., III Конференция по исследованиям в области физики плазмы и управляемых термоядерных реакций, Новосибирск, CN-24/B-6, 1968.
[2] ЛИБИН, З., Журнал прикладной физики 4 3 (1927) 45.
[3] HAINES, M.G., Proc. phys. Soc. 74 part 5, (1959) 479.
[4] ASCOLI-BARTOLI, V., MARTELLUCCI, S., MAZZUCATO, E., Nuovo Cimento 2 32 (1964) 298.
[5] БЕСШАПОШНИКОВ, А.А., ЗУКАКИШВИЛИ, Г.Г., КУЧУБЕРИЯ, И.Х., СИМОНОВА, Н.В., ПТЭ 2 (1971) 151-153.
[6] КВАРЦХАВА, И.Ф., КЕРВАЛИДЗЕ, К.Н., ГВАЛАДЗЕ, Ю.С., ЗУКАКИШВИЛИ, Г.Г., Ядерный синтез 5 (1965) 181.
[7] CLARK, G.L., WUERKER, R.F., Phys. Fluids 5 12 (1962) 1503-1506.
[8] ШАФРАНОВ, В.Д., Физика плазмы и проблемы управляемых термоядерных реакций. АН СССР 4 (1958) 61.
[9] КАДОМЦЕВ, Б.Б., Вопросы теории плазмы. Госатомиздат (1963) 132.
[10] LITTLE, E.M., NEWTON, A.A., QUINN, W.E., RIBE, E.L., SAWYER, G.A., THOMAS, K.S., III Конференция по исследованиям в области физики плазмы и управляемых термоядерных реакций, Новосибирск, CN-24/K-2, 1968.
[11] КЕСАЕВ, И.Г., Катодные процессы электрических дуг. Изд-во "Наука", 1968.
[12] КВАРЦХАВА, И.Ф., МАТВЕЕВ, Ю.В., ХАУТИЕВ, Э.Ю., Ядерный синтез 3 (1971).
[13] NIBLETT, G.B.F., GREEN, T.S., Proc. phys. Soc. 74 (1959) 737.

Z-PINCH EXPERIMENTS WITH SHOCK HEATING*

D.A. BAKER, L.C. BURKHARDT, J.N. DIMARCO,
P.R. FORMAN, A. HABERSTICH, H.J. KARR,
L.W. MANN, J.A. PHILLIPS, A.E. SCHOFIELD
University of California, Los Alamos Scientific Laboratory,
Los Alamos, New Mexico,
United States of America

Abstract

Z-PINCH EXPERIMENTS WITH SHOCK HEATING.

Two z-pinch experiments are reported. The first is a linear pinch whose results have encouraged the authors to construct the second, a toroidal system. In these experiments, a shock produces plasma temperatures higher than have been produced by ohmic heating. Theory predicts that with the higher temperatures the drift instabilities can be avoided resulting in a reduction of the anomalous field diffusion. MHD calculations predict stable configurations for some diffuse z-pinch profiles with a reversed B_z field external to the pinch, and a conducting wall.

The linear z-pinch experiment has a length of 30 cm, a diameter of 10 cm and the discharge current is ~ 200 kA. Initial values of $\dot{B}_\theta$ of 80 kG/μs produce the shock. A magnetic energy storage system generates the necessary high voltage $\lesssim$ 80 kV. Probes measure the initial shock structure and plasma pressure profiles. Together with holographic interferometric density measurements, they yield temperatures ($T_i + T_e$) of 750 eV and peak densities of $10^{16}/cm^3$ with initial pressure of 30 mTorr of deuterium. The limit of sensitivity of the holographic technique prevents data from being obtained at a lower filling pressure where higher plasma temperatures should be obtained. The plasma column exhibits gross stability for times of the order of the time scale of the experiment (~8 μs). One-dimensional MHD calculations are performed both with classical and anomalous resistivities. The results, including density and magnetic field profiles, are compared with experiment.

The toroidal experiment has a major diameter of 76 cm and a minor diameter of 10.25 cm. A 500 kJ inductive energy storage system develops a peak voltage of ≤ 320 kV around the circumference of the torus with maximum plasma currents of about 200 kA. Iron cores couple the primary to the plasma secondary circuit.

Toroidal equilibrium calculations have been made for diffuse plasma profiles. A numerical stability analysis of these toroidal equilibria, free from previous limitations on aspect ratio, plasma and magnetic field profiles, and beta, is in progress.

The toroidal z-pinch has the advantage of having azimuthal symmetry, stable equilibria and the possibility of exceeding the Kruskal-Shafranov limit.

I Introduction

The shock heated z-pinch program at LASL investigates the production and confinement of plasmas by the magnetic field of an axial current. The plasma is initially heated by a shock driven by the magnetic field of a rapidly rising z-current followed by adiabatic compression. Significantly higher temperatures are reached by this method than have been achieved by ohmic heating in our earlier investigations.

* Work performed under the auspices of the US Atomic Energy Commission.

In our experiments, initial values of $\dot{B}_\theta$ of $\geq 8 \times 10^{10}$ G/sec produce the shock. Magnetic energy storage with fuse switching into a low inductance system is used to obtain the fast rise time of the current.[1] After the rise of current the voltage across the pinch is small and the current remains nearly constant during the confinement period.

At the higher temperatures obtained in these z-pinch experiments the containment properties are improved over those obtained in our earlier experiments. In addition, there should be a reduction in the energy loss rates by radiation from partially ionized impurities,[2] and anomalous field diffusion associated with current driven instabilities.[3]

A longitudinal B_z field internal to the pinch gives m = 0 stability while the B_z field external to the pinch remains small. Thus, the current limit of other devices such as Tokamaks can be exceeded by orders of magnitude.

In section II, MHD theory in linear geometry predicts complete stability for a specific field and current distribution, with wall and plasma dimensions characteristic to these experiments. Further MHD calculations described in section III predict ion temperatures, field and plasma density distributions for the z-pinch. The equilibrium and stability of z-pinches in toroidal geometry are discussed in section IV. Experimental results for the linear shock heated z-pinch are given in section V and preliminary results and a physical description of the toroidal pinch are included in section VI.

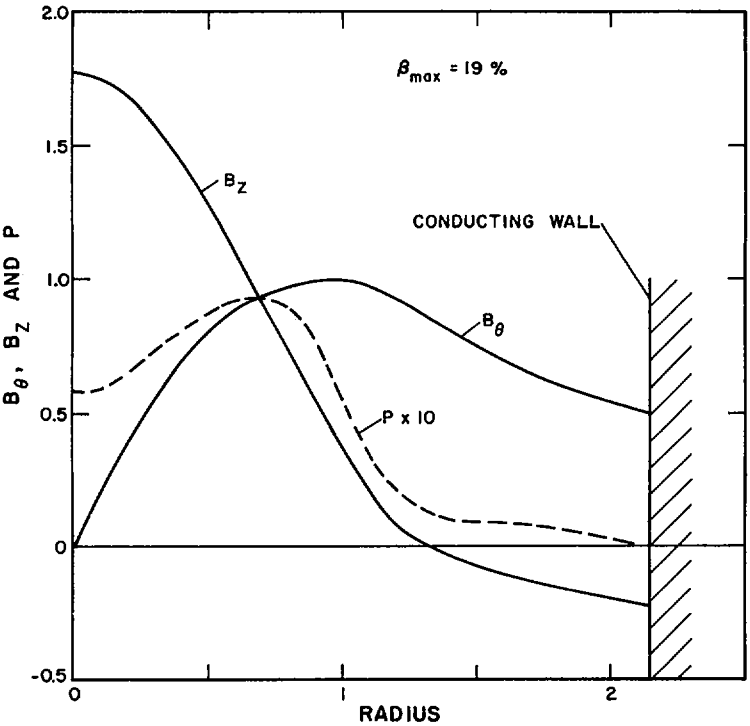

FIG. 1. Pressure and magnetic field profiles for an MHD-stable linear z-pinch.

II MHD Stability of the Z-Pinch

The stability in the linear geometry of the diffuse z-pinch profiles has been studied[4,5] using ideal MHD. Completely MHD stable profiles can be found whose z-current far exceeds the Kruskal-Shafranov limit. These profiles are usually characterized by some combination of: a) small reversal in B_z; b) B_θ falling faster than 1/r in some region; c) and β not too large. β is defined as the ratio of peak plasma pressure to peak B_θ field pressure. Such a profile is illustrated in Fig. 1. The magnetic field and pressure profiles shown in the figure approximate those measured[6] with a small reversal of B_z near the wall and β limited to ~ 19%. Higher β's[5] can be obtained if larger B_z reversals can experimentally be produced in the plasma.

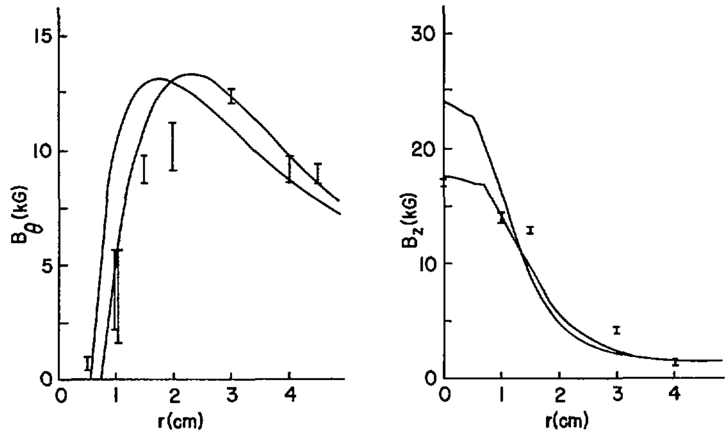

FIG. 2. Calculated and measured B_θ and B_z magnetic fields as functions of radius, r.

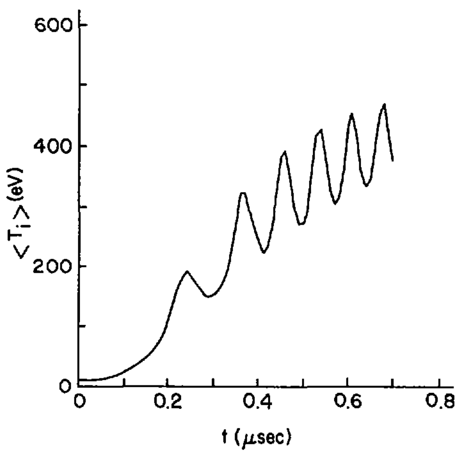

FIG. 3. Average ion temperature per particle $<T_i>$ as function of time, t.

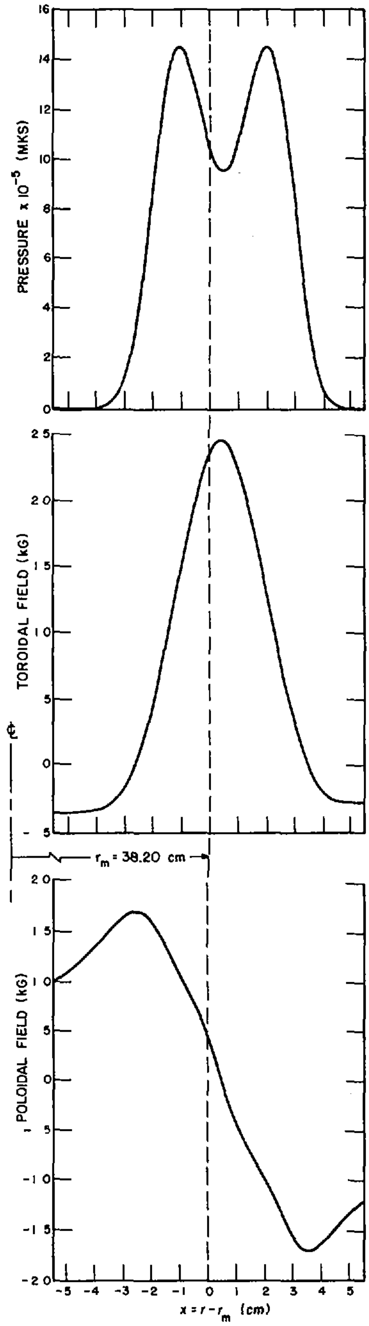

FIG. 4. Toroidal z-pinch equilibrium: radial profiles of magnetic field and pressure in the symmetry plane of a 300 kA toroidal z-pinch.

III MHD Dynamics of the Z-Pinch

One-dimensional numerical calculations of the linear and toroidal z-pinches have been performed.[7] The pinches are driven by a circuit equivalent to the inductive energy storage systems used in the experiments. To account for the enhanced diffusion observed during the early stages of the linear pinch, a local Bohm type resistivity is switched on in the plasma whenever the electron drift velocity exceeds the ion acoustic velocity.[8]

Figure 2 shows radial distributions of B_θ and B_z at 1 μsec in the linear discharge. The vertical bars indicate the spread in the measurement.[9] The solid curves correspond to the extreme positions of the z-pinch which is still experiencing some bouncing. The anomalous resistivity amounts to 5 times the Bohm value.

Figure 3 shows predicted average ion temperatures for the toroidal experiment. The transfer voltage is 60 kV, the filling pressure 10 μHg and the resistivity 1 times Bohm. The calculated peak z-current is 210 kA and the peak z-voltage 110 kV. To include possible trapped particle effects, a Galeev-Sagdeev resistivity has been used in some of the calculations.[10] The effect on the final temperature is not unfavorable.

IV MHD Toroidal Equilibrium and Stability

A. Equilibrium

The results of the shock heated linear experiment and the above MHD stability computations on the linear hollow z-pinch have led to an examination of the corresponding toroidal case. Numerical calculations[11] are used in order to be free from the limitations of large aspect ratio and small ratios of poloidal to toroidal fields inherent in the Tokamak expansions.

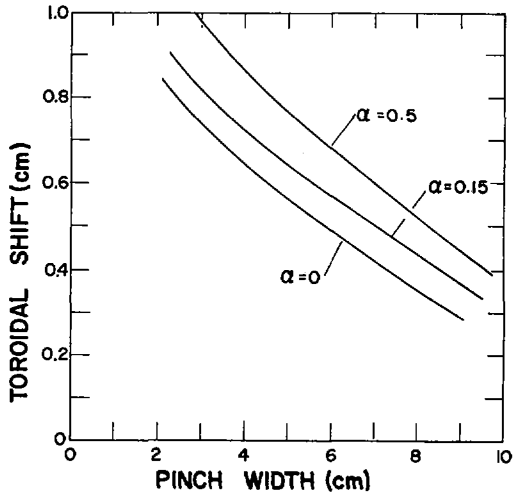

FIG. 5. Absolute shift of the magnetic axis versus width of the hollow pressure profile for the geometry specified in section VI. The width is measured where the pressure drops to 1% of its peak value. The parameter α gives the ratio of the value of reversed toroidal field (measured at minimum major radius of the discharge vessel) to the maximum value of toroidal field inside the plasma.

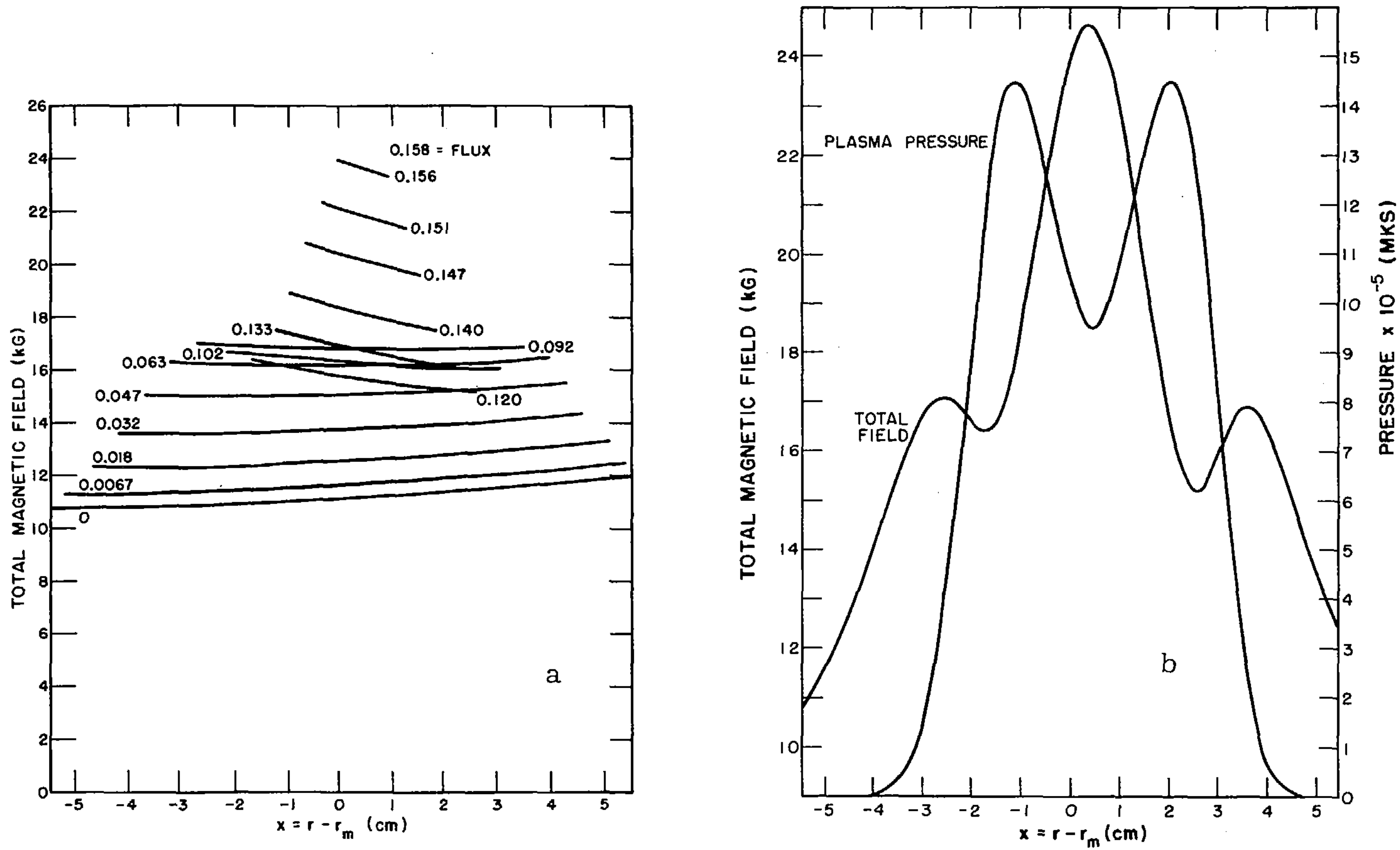

FIG. 6. a) Plots of the total field magnitude along the field lines for a hollow z-pinch equilibrium as a function of major radius. The curves are numbered according to the amount of flux in webers between each flux surface and the outer wall; b) Radial distribution of total magnetic field and pressure in the equitorial plane for a toroidal z-pinch equilibrium.

Pressure and field distributions representing a hollow 300 kA pinch with 25 kG compressed longitudinal field inside and 15% reversed field outside calculated for the geometry of our toroidal fast z-pinch are shown in Fig. 4. The variation of the toroidal outward shift of the magnetic axis for the same values of pressure and peak B_z field for hollow equilibria are shown in Fig. 5. Each curve represents a given value of reversed field outside the pinch.

The toroidal shift of the flux surfaces is compared with the result of Shafranov[12] obtained by aspect ratio expansions. The expected agreement is obtained at large aspect ratios.[13]

Some interesting properties of this type of equilibrium shown in Fig. 5 can be seen in Fig. 6a. Here is shown the total magnitude of the magnetic field on flux surfaces as functions of the major radius from the symmetry axis. The values of flux are indicated starting with zero at the outer conducting boundary. These plots have their maximum length, at the outer wall, and become shorter for flux surfaces approaching the magnetic axis. In Tokamaks the toroidal 1/R field dominates and the strongest fields, which are at the smaller radii, will mirror particles toward the region of unfavorable toroidal curvature (large major radii). This is also true in the z-pinch equilibrium for the region well inside the pinch where the poloidal field is small. But, as can be seen from Fig. 6a at outer flux surfaces, where the poloidal field dominates, the field becomes maximum at the outermost radii. This means that particles will be mirrored toward the smaller major radii producing marked differences in the trapped particle effects. The maximum mirror ratio is 1.1; the corresponding maximum mirror ratio for the Tokamak with this aspect ratio is 1.3. The distribution of the plasma pressure relative to the total magnetic field is also shown in Fig. 6b.

-4-

B. Stability

Since the toroidal equilibria were obtained numerically it is evident that any stability analysis will also involve numerical techniques. Previous work has been done with numerically obtained toroidal multipole equilibria having poloidal field only. In that case an application of the energy principle[14,15] allows the problem of stability to be answered by numerically integrating an ordinary differential equation along the field lines. We found that the critical beta values for MHD stability for the multipole geometries were an order of magnitude lower than previous estimates.[16]

The stability problem for the azimuthally symmetric toroidal equilibria with mixed poloidal and toroidal fields is a much more difficult problem since the Fourier modes the short way around the torus are coupled and the Euler-Lagrange equations corresponding to a minimization of δW are second order partial differential equations, which have singularities. To minimize these difficulties the energy integral is worked with directly. Earlier investigations of Suydam[17] and computer studies by Sykes[18] on one-dimensional equilibria indicate that this approach may be able to determine stability with a mesh resolution about five times larger than the singularity separation in the corresponding variational equations. This earlier ground work has been extended to our two dimensional toroidal equilibria. These calculations are as yet incomplete.

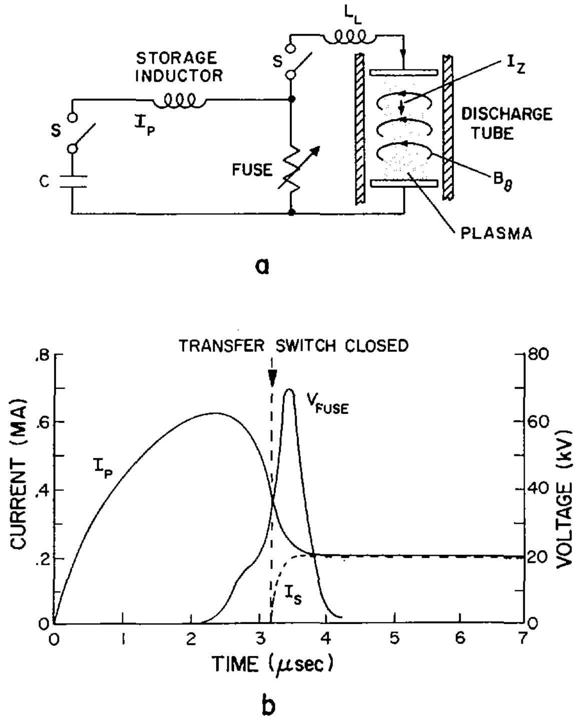

FIG. 7. a) Schematic of magnetic energy storage circuit; b) Time behaviour of currents and voltage in the above circuit.

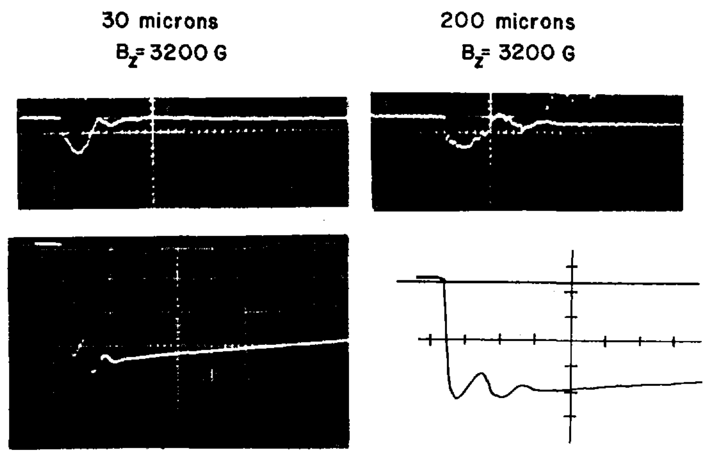

FIG. 8. Linear z-pinch voltage and current for different filling pressures. Voltage and current: 49 kV/div; 60 kA/div; (sweep time 0.5 μs/div).

V Linear Z-Pinch Experiment

A schematic of the linear experiment is shown in Fig. 7. Deuterium gas is preionized with a 25 kA axial current pulse in a 30 cm long 10 cm diameter discharge tube. The primary energy storage is a 450 μF capacitor bank, charged to 12.5 kV. The energy is then transferred into the storage inductance of 35 nH. Joule heating of the fuse causes its resistance to increase. The resulting voltage fires the air gap transfer switch and diverts the current to the z-pinch. Initial current rise time of 2×10^{12} A/sec is achieved by this method resulting in a $\dot{B}_\theta$ of 8×10^{10} G/sec.

Z-pinch voltage and current are displayed in Fig. 8. Voltages of 40-60 kV are developed along the pinch. A B_θ probe signal determines that the current sheath moves off the wall. Assuming a symmetrical current distribution, at least 90% of the current is inside the probe radius of 2.5 cm. In previous fast z-pinch experiments[19] a secondary breakdown is observed along the wall of the discharge tube at the time of maximum compression of the plasma. Examination of streak photographs, the current inventory, and the observed oscillations of the pinch voltage indicate that a secondary breakdown is not taking place. A breakdown is inhibited by the

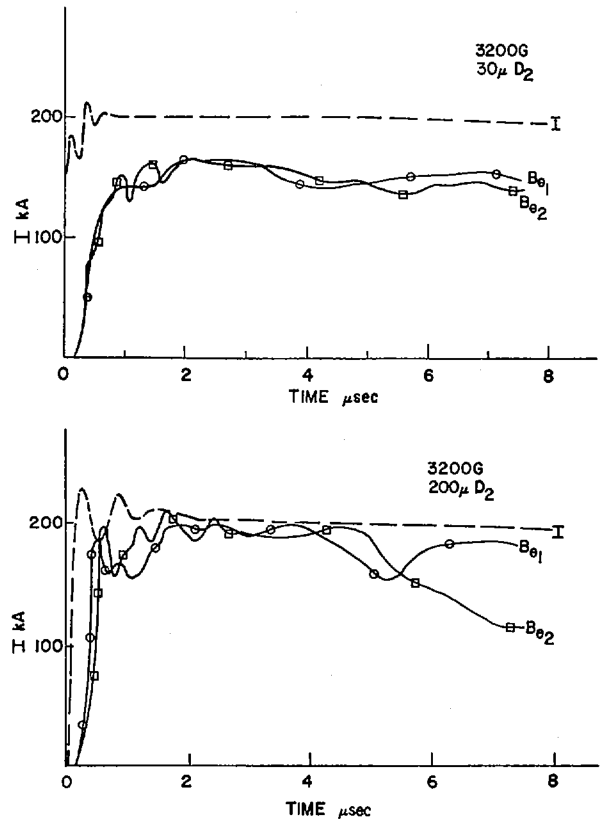

FIG. 9. Comparisons of I_z determined from magnetic probes, with total pinch current, for two different filling pressures.

magnetic energy storage system which tends to maintain a constant current and a low voltage across the discharge at the time of peak compression when $\dot{L} = 0$.

Shock generation is indicated by streak photographs which show luminous fronts propagating with velocities as high as 4.2×10^7 cm/sec at 20 mTorr filling pressure. The shock structure is obtained from the B_z and B_θ probes. These probes are also used to deduce the total plasma pressure which combined with holographic interferometric density measurements yield peak plasma temperatures ($T_i + T_e$) of 750 eV and peak electron densities of $\lesssim 10^{16}/\text{cm}^3$.

Figure 9 presents the currents deduced from the B_θ signals of two diametrically opposed probes equidistant from the axis. Also plotted is the total current in the z-pinch. Current symmetry is maintained for ~ 8 μsec for a filling pressure of 30 mTorr D_2 and 3.2 kG bias field. When the filling pressure is increased by a factor of 6.6 to 200 mTorr with an implied reduction of the plasma temperature, it can be seen from Fig. 9 that the current symmetry is lost in ~ 5 μsec. In both cases at 900 G bias field the symmetry is lost within 1 μsec of the pinch formation.

From these results it has been determined that shock heating with a constant current source can result in the formation of a high temperature z-pinch. In addition, the pinch exhibits gross stability for times that scale differently with density from expected MHD growth rates. It is inferred that a higher plasma temperature is necessary to maintain the gross stability of the plasma.

VI Toroidal Z-Pinch Experiment

The toroidal z-pinch experiment, ZT-1, eliminates the end effects inherent in the linear system. As described in section IV above, the toroidal z-pinch with symmetry about the major axis has an equilibrium. A drawing of the apparatus is shown in Fig. 10 and a list of parameters is summarized in Table I.

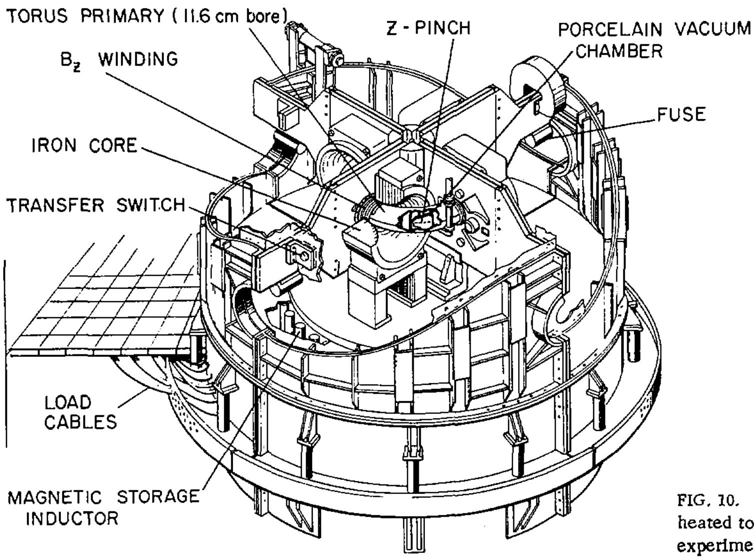

FIG. 10. Schematic of shock heated toroidal z-pinch experiment.

TABLE I. LIST OF PARAMETERS

Discharge tube bore	10.25 cm
Major radius of discharge tube	38 cm
Aluminium primary bore	11.4 cm
Iron core/quadrant (biased)	~0.10 Vsec
Discharge current	$\lesssim$ 300 kA
Capacitor bank energy (at 40 kV)	~0.5 MJ
B_z bias field	0 to 6 kG
Magnetic energy storage drum diameter	244 cm

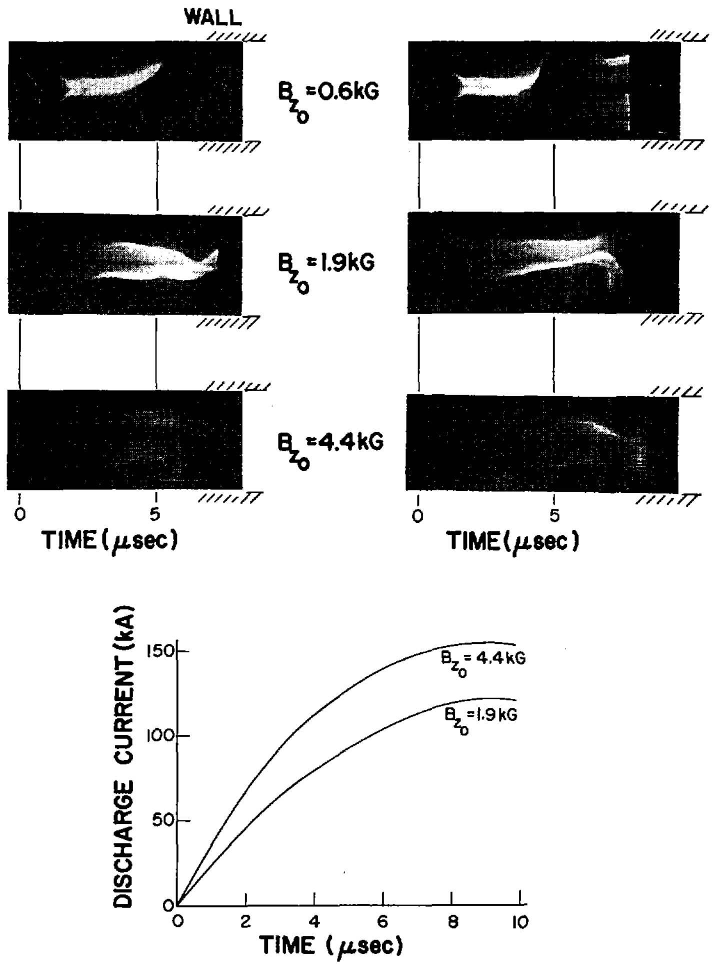

FIG. 11. Two examples of streak photographs for three values of B_z bias field, and time behaviour of the discharge currents.

The discharge is produced in a ceramic torus which is inside a close fitting aluminum shell that serves as the transformer primary. The primary is divided into quadrants with low inductance parallel plate transmission lines connecting each quadrant to the magnetic storage circuit. The iron cores couple the primary and gas discharge currents and limit the magnetization current. The B_z field winding is on the outside of the aluminum primary. The primary is split along its major circumference to allow the B_z field to enter the discharge region.

The main bank supplies a peak current of ~ 5 MA to the magnetic energy storage drum. The magnitude of the storage inductance can be varied from 8 to 35 nH. The upper part of the coaxial structure directs the current flow to the fuses, transfer switches, and torus. The contoured upper section is designed to minimize the inductance between the fuses. The voltages developed across the fuses are equal within ~ 10%.

Initial tests of the ZT-1 experiment have been made without fuses. Direct connections to the main capacitor bank are made by shorting the transfer switches. The quarter period of the sinusoidal current is ~ 10 μsec and in these preliminary tests the discharge current is limited to 180 kA. Under these conditions of relatively slow rising currents and B_θ fields, shock heating is negligible and only ohmic and compressional heating occur.

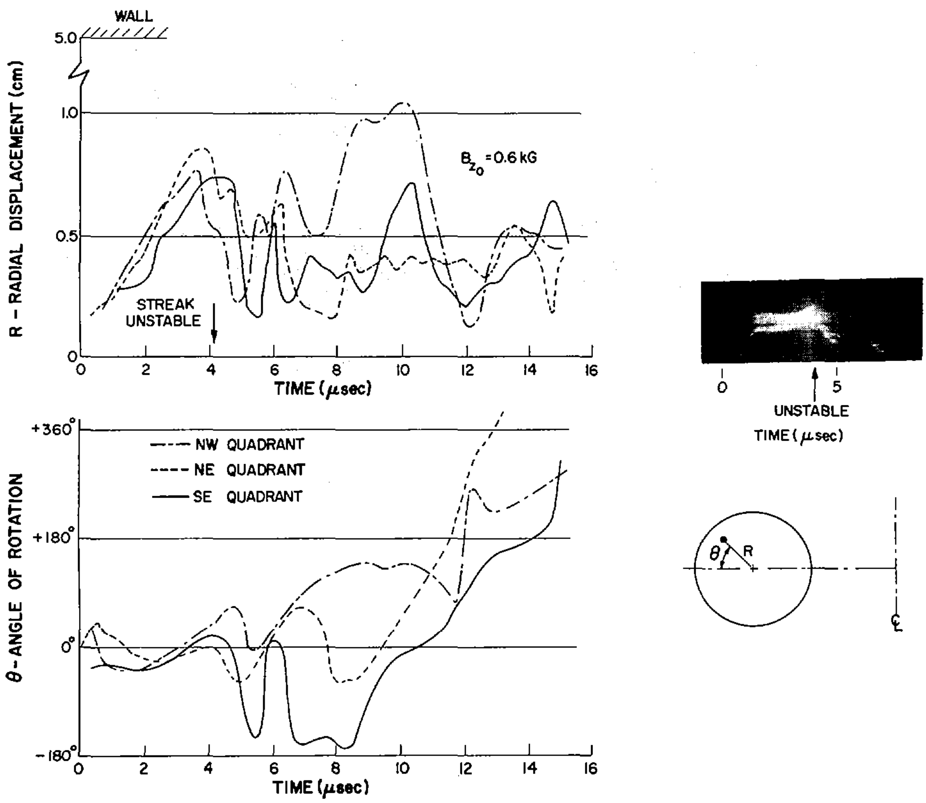

FIG. 12. The radial and angular displacement of the current centroid as measured in three quadrants of the toroidal pinch. The streak photographs taken on the same discharge are shown.

Streak photographs taken along a major radius through a quartz window in the ceramic torus are shown in Fig. 11. Two examples are shown at three values of bias field with a deuterium gas pressure of ~ 50 mTorr. They show the formation of a pinch which lasts from 3 to 6 μsec, depending on the B_{zo} bias field. The column then moves toward the wall. Within 1 μsec after the onset of the gross displacement a filamentary structure appears. The B_z field as measured at the tube wall drops to low values and reverses with low B_{zo} fields.

The centroid of the current distribution is determined by a system of B_θ coils[20] located about the minor circumference of the torus at 3 azimuthal positions along the major circumference. The measured radial and angular displacement of the current centroid as a function of time for one discharge is shown in Fig. 12. Initially the discharge moves outward along a major radius to its equilibrium position. At ~ 4 μsec, when the displacement has reached ~ 0.8 cm, the current center moves irregularly about the axis with amplitude $\lesssim$ 1 cm. Examination of the streak photograph for the same discharge, Fig. 12, shows that at ~ 4 μsec the small vertical motion of the pinch ceases and the pinch column appears as streamers which fill the tube.

With ohmic heating the toroidal discharge has many of the characteristics of the earlier Perhapsatrons.[2,5] Operation at high voltages with the fuses and transfer switches is in progress.

ACKNOWLEDGEMENTS

We acknowledge with pleasure the support of H. T. Motz, R. F. Taschek, and J. L. Tuck for the z-pinch program; the theoretical support of J. P. Freidberg and R. L. Morse; the technical assistance of W. Bowman, R. Holm, D. Jardine, G. Roybal and N. Salazar; and the engineering support of R. Dike and C. Charlton.

REFERENCES

[1] J. N. DiMarco and L. C. Burkhardt, Los Alamos Report LA-4075-MS, p. 3 (1968)

[2] H. J. Karr, E. A. Knapp and J. E. Osher, Phys. Fluids, 4, 424 (1961)

[3] W. E. Drummond and M. N. Rosenbluth, Phys. Fluids, 5, 1507 (1962)

[4] J. P. Freidberg, Private Communication

[5] D. C. Robinson, Fourth European Conference on Controlled Fusion and Plasma Physics, Rome, 1970, p. 38

[6] J. P. Conner, D. C. Hagerman, J. L. Honsaker, H. J. Karr, J. P. Mize, J. E. Osher, J. A. Phillips and E. J. Stovall, Jr., Proceedings of the 2nd United Nations International Conference on the Peaceful Uses of Atomic Energy, Geneva, 1958, Vol. 32, p. 297

[7] A. Haberstich, Los Alamos Report LA-4585-MS, p. 37 (1971)

[8] H. A. B. Bodin, J. McCartan and G. H. Wolf, Third European Conference on Controlled Fusion and Plasma Physics, Utrecht, 1969, p. 74

[9] J. N. DiMarco and L. C. Burkhardt, Bull. Am. Phys. Soc. II, 14, 1015 (1970)

[10] A. A. Galeev and R. Z. Sagdeev, Zh, Eksp. Teor. Fiz., 53, 348 (1967), Sov. Phys. JETP, 26, 233 (1968)

[11] D. A. Baker and L. W. Mann, Los Alamos Report LA-4585-MS, p. 46 (1970)

[12] V. D. Shafranov, J. of Nuclear Energy, Part C, 5, 251 (1963)

[13] D. A. Baker and L. W. Mann, Bull. Am. Phys. Soc., II, 15, 1448 (1970)

[14] I. B. Bernstein, M. D. Kruskal and R. Kulsrud, Proc. Roy. Soc. (London), 244A, 17 (1958)

[15] J.M. Greene and J. L. Johnson, Advances in Theoretical Physics, Vol. 1, Academic Press, New York (1965)

[16] D. A. Baker and L. W. Mann, Bull. Am. Phys. Soc., II, 14, 1051 (1969)

[17] B. R. Suydam, Private Communication

[18] A. Sykes, Unpublished

[19] H. A. B. Bodin, A. A. Newton and N. J. Peacock, Nuclear Fusion, 1, 54 (1960)

[20] A. Haberstich and P. R. Forman, Bull. Am. Phys. Soc. II, 13, 1489 (1968)

DISCUSSION

H.A.B. BODIN: I have two questions. First of all, can you say whether or not the characteristics of the instability in the linear shock-heated device - onset time, mode type, etc. - were similar to the instability characteristics observed in your preliminary, resistively heated toroidal experiments?

J.A. PHILLIPS: It is difficult to compare the stabilities of the Ohmic and shock-heated Z-pinches since the former have a slow-rising current and the latter a constant current. As stated in the paper, however, the data from the shock-heated linear experiment indicate that as the temperature is raised the duration of gross stability is increased.

H.A.B. BODIN: Can you enlarge on your remark that the stability is expected to be better in the high-temperature shock-heated system?

J.A. PHILLIPS: As stated in our paper, the purpose of our shock-heated Z-pinch program is to produce a high-temperature pinch in an attempt to avoid the serious difficulties previously experienced in low-temperature experiments. It is my opinion that the role of impurities in loss of plasma confinement with low-temperature Z-pinches has not been adequately studied. In the work of Karr, Osher and Knapp, Ref. 2 in our paper, the onset of strong line radiation from impurities was correlated with the loss of magnetic field energy. The onset could be delayed by reducing the impurity level in the initial gas filling. It is suggested, among other possibilities, that radiation cooling reduces plasma thermal velocities below the electron drift velocity and that current-driven drift instabilities are excited. At the high temperatures sought in our experiment, impurities will be completely ionized and cooling by line radiation will be negligible.

ON THE DECAY OF THE LONGITUDINAL CURRENT IN TOROIDAL SCREW PINCHES

P. C. T. VAN DER LAAN, W. SCHUURMAN, J. W. A. ZWART,
J. P. GOEDBLOED
Association Euratom-FOM,
FOM-Instituut voor Plasma-Fysica,
Rijnhuizen, Jutphaas, The Netherlands

Abstract

ON THE DECAY OF THE LONGITUDINAL CURRENT IN TOROIDAL SCREW PINCHES.

In toroidal screw pinch experiments in Garching and in Jutphaas the longitudinal plasma current is observed to decay rapidly, which leads to a loss of equilibrium or to instability. Several causes for this decay are listed. The problem of the matching of a decaying pinch to the external circuits is discussed. External losses in the z-circuit give rise to currents in the plasma near the wall and thereby to an enhanced decay of the net longitudinal plasma current. Losses in the θ-circuit, however, tend to increase the longitudinal current.

Also the volume currents flowing in a combined pinch lead to a transfer of energy from one field component to the other; calculations are given for a uniform-pitch screw pinch.

A toroidal screw pinch will oscillate around its eccentric equilibrium position. The oscillation may force field lines into the wall and decrease thereby the plasma current. This effect diminishes when the external inductances in the z-circuit are small.

At this stage it is not possible to conclude what cause or causes are responsible for the decay of the plasma current; further experimental and theoretical studies are therefore needed.

1. Introduction

Outside a plasma formed by implosion a low-density plasma is observed, probably originating from the ionization of neutral gas left behind by the snow plough. The low-density plasma has a high conductivity so that the magnetic flux in any moving contour is conserved. In a cylindrical system this results in the conservation of the pitch of each individual helical field line, provided end effects play no role. Analogously, in a torus the rotational transform of a field line is conserved. These conservation properties lead to field distributions determined by the history of the fields at the wall. In general, the field distribution is such that currents must flow; in the low-density plasma the inertia and pressure gradients are negligible and therefore these currents are force-free.

In a pinch where B_z and B_θ at the wall have the same wave-form a uniform-pitch region is formed. In this situation the conditions for equilibrium and stability are much more easily satisfied than in the case where the same central column is surrounded by a vacuum field [1], [2]. In a torus the currents in the outside region increase the Kruskal-Shafranov current, I_{KS}. Stability is predicted below and above I_{KS}; fairly large values of β are allowed when q, which is the ratio of I_{KS} to the plasma current equals approximately 3/4, 5/12, 7/24, ... [3].

Stability tests in the region below and at 1.3 I_{KS} have been only partly successful. Firstly, it is difficult to lower the β-value of the central pinch and secondly, in our experiments the lifetime of the plasma is relatively short. This effect is related to the main subject of the paper: the decay of the longitudinal plasma current. This decay has also been observed in Garching [4].
In Section 3 a number of possible causes of this decay are discussed, in particular the processes in the plasma layer stagnating against the wall because of an expansion of the plasma. Another effect already important during the implosion is the interaction of the two field components in a combined pinch which leads to a flow of energy from the B_θ-field, to the B_z-field, or vice versa (Section 2).

2. Energy flow in a combined pinch

In a combined pinch two energy sources provide the magnetic energy flowing in during the build-up of the configuration. This influx of energy per second is given by $\mu_o^{-1} \iint (\vec{E} \times \vec{B}).d\vec{S}$. In a torus surrounded by a copper shell the E-field is introduced as voltages V_z and V_θ across the gaps encircling the tube axis and the major axis, respectively. The rate of energy input can then be written as

$$dW/dt = V_z I_{zp} + V_\theta I_\theta \tag{1}$$

where the two terms represent the energy coming form the z-bank and the θ-bank; I_{zp} is the longitudinal plasma current and I_θ the primary θ-current. The energy input leads to the build-up of magnetic energies $W(B_z)$, $W(B_\theta)$, to heating of the plasma and to radiation. If the last two effects are small, the rate of rise of $W(B_z) + W(B_\theta)$ is given by Eq.(1). However, the energy in one field component is not exclusively supplied by the corresponding capacitor bank; currents flowing in the plasma result in an interaction between the two field components. This effect often resembles a magnetic coupling, but is better described in terms of the motion of plasma shells which act as moving weightless pistons transferring mechanical energy from one field region to the other.

In a simplified constant pitch cylindrical screw pinch of radius b and length ℓ in which inertia and plasma pressure are neglected calculations yield the following expressions:

$$\begin{aligned}
W(B_z) &= A(1+\alpha) \\
W(B_\theta) &= A\,\alpha^{-1}(1+\alpha)^2\left\{\ln(1+\alpha) - \frac{\alpha}{1+\alpha}\right\} &&= A(\tfrac{1}{2}\alpha + \tfrac{1}{3}\alpha^2 + \ldots) \\
\int V_\theta I_\theta dt &= A\,\alpha^{-1}(1+\alpha)\ln(1+\alpha) &&= A(1 + \tfrac{1}{2}\alpha - \tfrac{1}{6}\alpha^2 + \ldots) \\
\int V_z I_{zp} dt &= A(1+\alpha)\ln(1+\alpha) &&= A(\alpha + \tfrac{1}{2}\alpha^2 - \ldots.)
\end{aligned} \tag{2}$$

where $A = \pi b^2 \ell\, B_z^2(b)/2\mu_o$, $\alpha = \mu^2 b^2$ and $\mu = B_\theta / rB_z$.

An energy flow diagram for small μb is given in Fig. 1.

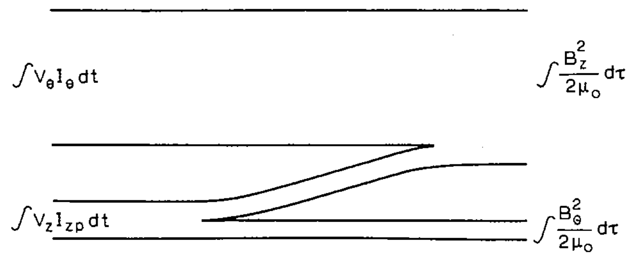

FIG. 1. Energy flow diagram for a screw pinch ($\mu b \ll 1$).

In this limit half the energy of the z-bank is deposited in the B_θ-field, whereas the other half enlarges the B_z-field. This means that the B_z-field is compressed by the B_θ-field, which also explains why in the B_z-circuit the plasma behaves paramagnetically. Coupling effects are also to be expected for the general case; the calculations are then more complicated. In principle, these calculations are contained in MHD-codes, like the Hain-Roberts code.

3. Possible causes for the decay of the plasma currents

In an actual experiment many causes may act simultaneously, for simplicity we describe the effects separately.

a) Volume dissipation. If the primary circuits are ideally clamped, only the resistivity η of the plasma causes interdiffusion of field and plasma. For a screw pinch even the case of uniform η is difficult to treat because the two field components are interacting and also because the fields may not remain force-free during the evolution [5], [6]. If μr is small j_z is approximately uniform; the inductance is then $\mu_o \ell/8\pi$, which gives a decay time for j_z

$$\tau = \mu_o b^2/8\eta \qquad (3)$$

Here external inductances are assumed zero, if these are present τ is lengthened because more magnetic energy is available.

b) Resistive plasma layer near the wall. A disadvantage of the fast circuits used in pinch experiments is that the field lines often escape easily, because of either imperfect clamping or resistance.

This escaping field should match the boundary conditions imposed at the wall. By-passing the circuit equations we replace the external circuits by voltage sources and suppose further that the voltages at the gaps produce homogeneous fields E_z and E_θ at the inner surface of the quartz wall.

An E_θ-field applied to a theta-pinch after the current maximum has to penetrate a stationary resistive plasma layer next to the quartz before it can act on the mobile low-density plasma outside the pinch. The latter acquires a velocity $v_r = E_\theta/B_z$ which cancels the E-field seen by the plasma and on the other hand allows the E-field in the laboratory frame to penetrate easily. The outflow of field lines is only hindered by the opposing currents in the layer next to the wall.

If the resistivity is small these currents would effectively stop the E-field and thereby "clamp" the tube internally. Stated otherwise, an ideally conducting plasma immobilized by an insulating wall is equivalent to a perfectly conducting wall. Although such clamping has been observed in some θ-pinches shortly before current reversal, experiments at higher fields suggest that the layer next to the wall has a high resistivity and therefore has little influence on the energy flow. Apparently, this layer, separating the highly conducting plasma from the outside world is strongly cooled when $\vec{j} \times \vec{B}$ forces push it against the wall.

In a combined pinch the situation is more complicated. The E-vector applied at the inner surface of the quartz wall may lie in any of the quadrants of the tangent plane (Fig. 2).

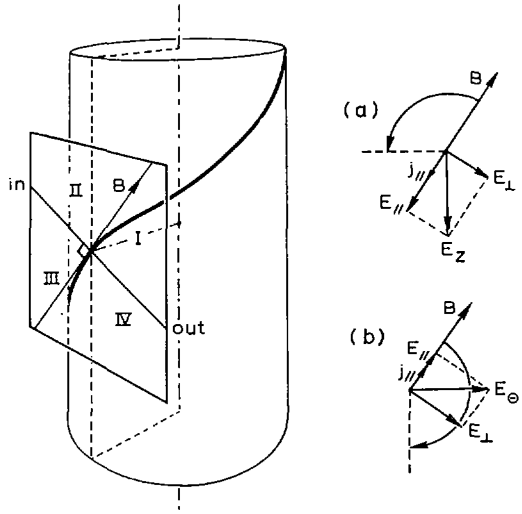

FIG. 2. The applied E-vector at the inner surface of the quartz wall can be parallel or perpendicular to the local B-field. In the insets the orientation of the fields is shown in plane view for a pinch with external losses in the z-circuit only (a) or in the θ-circuit only (b).

If E is applied perpendicular to B it causes an in- or outward motion. For the inward motion currents $j_\perp$ start to flow in the resistive plasma but die out again when the plasma velocity is such that $\vec{E} + \vec{v} \times \vec{B} = 0$. If in addition an $E_{\shortparallel}$ component is present (quadrant II or III) a current $j_{\shortparallel}$ is set up which causes a rotation of the B-field at the wall making it perpendicular to E again (clockwise for j parallel to B, anticlockwise for j antiparallel to B). Whether this really happens depends on the resistivity of the plasma; the inward motion is helpful because it allows the plasma to become hot and it also widens the current layer. For E-fields in the quadrants I and IV the induced motion of the field lines is outward. Perpendicular currents in the plasma stagnating against the wall probably remain small, allowing the field to escape with little dissipation. The currents $j_{\shortparallel}$ set up by $E_{\shortparallel}$ rotate the B-field. The outward motion limits these currents by narrowing the penetration depth and by pressing the plasma against the wall. Nevertheless, currents will continue to flow until either the B-field at the wall has rotated or the external circuit can no longer maintain the E-field.

As a first example we take a screw pinch with a perfectly clamped θ-coil and with external losses in the z-circuit. The E_z-field thus applied (see Fig. 2a) causes the plasma to move outward and in addition produces parallel currents causing an anticlockwise rotation of the B-field at the wall towards the θ-direction. These currents near the wall reverse the net I_{zp} and produce a strong oppositely directed B_θ-field. The energy in the z-circuit may be exhausted long before this process has come to an end.

A second example is a screw pinch in which only the θ-circuit has losses. The E_θ-field causes an outward velocity and currents parallel to $\vec{B}$. The B-field rotates clockwise to the z-direction (Fig. 2b), which means that B_z at the wall has to change sign. During the first stage of this rotation I_{zp} is increased.

These examples show that wall effects cannot explain the decay of I_{zp} in all cases. To avoid the complications caused by wall effects it is advisable to clamp both circuits ideally or at least such that the remaining E-field is perpendicular to B.

c) Oscillation around equilibrium position. The implosion of the screw pinch is fairly symmetric in the tube, whereas the equilibrium position is eccentric. Therefore an oscillation of the m=1, k=0 type in the median plane of the torus is excited. Although this oscillation is stable it may give rise to a motion of field lines into the wall, to a decay of I_{zp}, to a corresponding outward shift of the equilibrium position until finally the pinch reaches the wall. To limit this effect the E_z-field at the inside of the tube must be kept small, in other words the B_θ-flux within the tube should be constant during the oscillation. To achieve this the external inductance L_{ext} in the primary z-circuit (see Fig. 3) should be small compared to L_i, the plasma inductance associated with the B_θ-flux in the tube. Secondly, to minimize the stray inductance between coil and plasma, L_{cp}, the quartz wall should be thin and the metal wall should fit the tube closely. Of course, field errors, especially those near the outer wall should be reduced.

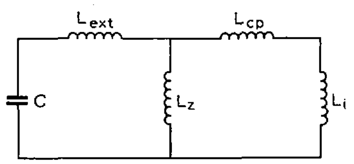

FIG. 3. Equivalent circuit for the primary and the secondary z-circuit, coupled by the inductance L_z of the toroidal coil.

d) Instabilities. If the central column develops a kink instability, a strong coupling between the two banks is to be expected. Experimental results on the decay of field components are therefore only useful during the stable period.

Interchange-like instabilities in the low-density plasma may lead to a loss of plasma and thereby to a loss of plasma currents.
Numerical and analytical calculations for the uniform-pitch outside region of a linear screw pinch [7] show that the growth rates are small when $\mu b \ll 1$. This growth rate is enhanced when pressure gradients are present. These instabilities may for example arise at the transition between force-free fields and the vacuum field in the quartz [8].

4. Acknowledgements

We thank Professor C.M. Braams and Dr. M.P.H. Weenink for stimulating and helpful discussions. We are indebted to our colleagues in the group, especially to Dr. R.J.J. van Heijningen and Dr. A.J. Postma for their vigorous efforts to confirm by experiments our too rapidly changing viewpoints. Dr. C. Bobeldijk contributed during an earlier stage of this study.

This work was performed under the association agreement of Euratom and FOM with financial support from ZWO and Euratom.

5. References

[1] Bobeldijk, C., et al., Proc. 3rd Conf. on Plasma Physics and Contr. Nucl. Fusion Res., Novosibirsk (1968) vol. 1, 287.

[2] Schuurman, W., Bobeldijk, C., de Vries, R.F., Plasma Physics 11 (1969) 495.

[3] de Vries, R.F., et al., Proc. 3rd Eur. Conf. on Contr. Fusion and Plasma Physics, Utrecht (1969) 88.

[4] Grossmann, P., et al., 4th Eur. Conf. on Contr. Fusion and Plasma Physics, Rome (1970) 49.

[5] Jette, A.D., and Sreenivasan, S.R., Physics of Fluids 12 (1969) 2544.

[6] Goedbloed, J.P., Rijnhuizen Report 70-64.

[7] Hagebeuk, H.J.L., and Goedbloed, J.P., to be published.

[8] Robinson, D.C., 4th Eur. Conf. on Contr. Fusion and Plasma Physics, Rome (1970) 38.

DISCUSSION

G.H. WOLF: You stated that anomalous resistivity is not required to explain the current damping in the outer plasma region. In view of the high current density and low plasma density in this region, however, couldn't the electron drift velocity exceed one of the other characteristic velocities, e.g. the sound speed?

P.C.T. VAN DER LAAN: One cannot, at present, exclude anomalous resistivity or instabilities as a cause of the current damping. The threshold for the electron drift velocity may be higher for velocities parallel to the B-field than for perpendicular velocities. In experiments at lower plasma currents, e.g. less than the Kruskal-Shafranov current, the current densities in the outside region are of course smaller.

H. ZWICKER: In this same connection, I should like to add that our measurements on a toroidal screw pinch, reported in paper B-6, also show that one cannot ignore the possibility of anomalous resistivity as a cause of z-current damping. The z-current densities measured in the outer plasma, and the electron temperatures, seem to indicate that the electron drift velocity may exceed the thermal velocity at densities of about 10^{14} cm^{-3} or less.

EXPERIMENTAL AND THEORETICAL STUDIES OF A HIGH-BETA TOROIDAL PINCH

H.A.B. BODIN, E.P. BUTT, J.E. CROW, F.E. IRONS,
J. JUNKER*, A.A. NEWTON, D.C. ROBINSON
UKAEA Research Group, Culham Laboratory,
Abingdon, Berks,
United Kingdom

Abstract

EXPERIMENTAL AND THEORETICAL STUDIES OF A HIGH-BETA TOROIDAL PINCH.

Observations on various axisymmetric pinch systems operating above the Kruskal-Shafranov limit are in broad agreement with predictions.

The experiment has five capacitor banks (2 MJ in all) which can be programmed in any sequence. Longitudinal currents and fields (B_z) up to 250 kA and 12 kG were used, with rise-times about 10 μs. The quartz torus, major diameter 2 m and bore 12 cm, was filled with deuterium between 10 and 50 mtorr pressure.

Theoretically, unless the pressure gradient is positive, a pitch (rB_z/B_θ) minimum is sufficient for instability. Stability is possible with total β up to 0.3-0.4 when the external B_z reverses. The inclusion of compressibility increases instability growth rates, and three characteristic eigenfunctions are computed, two of which are identified in the experiment. Estimates show that energy losses which can be neglected for power inputs of $\gtrsim$25 eV/particle/μs, obtainable by compression, can become important at power inputs typical of resistive heating.

In screw pinches temperatures up to 200 eV are obtained in the central core, which can remain grossly stable for 20 μs. The outer regions where most of the axial current flows are relatively cold, with a resistivity temperature of 5 eV, and always show radial magnetic field fluctuations. Stabilized z-pinches have resistivity and pressure balance temperatures about 10 eV with $\beta_\theta = 0.3$. In well-compressed plasmas a stable phase of up to 15 μs precedes non-localized pressure-driven instability which appears when the pressure gradient near the axis changes from positive to negative. Weakly compressed pinches become unstable in $\lesssim$ 1 μs to a localized mode expected from an outer pitch minimum. Applying reversed external B_z to weakly compressed pinches increases the stable time from $\lesssim$ 1 μs to 6 or 7 μs, while with compressed pinches the reversed field configuration lasts up to 15 μs, being limited by the same pressure-driven mode as before.

1. INTRODUCTION

This paper describes a study of the diffuse pinch system, which is an axisymmetric configuration operating above the Kruskal-Shafranov limit. Its important feature is that stability can be obtained with $\beta > 0.1$[1], values which can, in principle, be reached at reactor temperatures by joule heating from the longitudinal current. When B_z reverses outside the plasma (Fig.1(d)) M.H.D. stability is possible for β up

---

* On attachment from the Institut für Plasma-Physik, Garching bei München, Germany.

[1] The total beta is defined as $\beta = 8\pi p/(B_z^2 + B_\theta^2)$ and β_θ, the value with respect to B_θ is defined by $\beta_\theta I^2 = 2\,Nk\,(\overline{T}_e + \overline{T}_i)$, where N is the line density and $\overline{T}_e$, $\overline{T}_i$ are the average temperatures; I is the axial current.

to 0.3-0.4. In the diffuse pinch $B_z \sim B_\theta$, $\beta \sim \beta_\theta$ and the shear parameter is of order unity. Both shear and conducting walls are necessary for stability, rather than a magnetic well.

The diffuse pinch was investigated on Zeta, where configuration 1(d) set itself up, following instabilities and wall contact, with $T_e = 200$ eV and $\beta = 0.1\text{-}0.2$[1]. A reversed electric field E_z was required for stability. The stable phase lasted until classical field diffusion caused the decay of the reversed B_z in about 3 msec and this natural occurrence of a stable configuration supports expectations that stability is not sensitive to the detailed field configuration for type 1(d). In the screw pinch 1(c) the plasma is heated and compressed by means of fast rising B_θ and B_z applied together. In screw pinch experiments carried out elsewhere[2,3] stability for 10 or 20 μsec has been reported, often limited by an m = 1 instability because beta exceeds the stability limit of about 0.1; values of $n_e \sim 10^{16}\,\mathrm{cm}^{-3}$ and ion temperatures up to 1000 eV have been obtained[3].

The principle objectives of the present investigations, a preliminary account of which is given in this paper, are: to study ways of setting up stable high-β distributions which minimise wall contact by means of field programming[4] and to compare the properties of different pinch configurations. An investigation of the setting up phase requires a study of the growth of instabilities, as well as marginal stability. Theoretical predictions on the growth rates, wave numbers and eigenfunctions of unstable configurations are presented in Section 2 and compared with experimental results in Sections 6 and 7. The configurations studied include the "stabilised" pinch with a vacuum region surrounding the plasma (Fig.1(a)) and with currents extending out to the wall 1(b), the screw pinch 1(c) and the reversed pinch 1(d). In cases 1(a), 1(b) and 1(d) the plasma is heated by the axial current, while in the case 1(c) fast compression heating is used. In Section 5 heating and energy losses in compression and resistively heated systems are discussed.

The experiment utilises a two megajoule capacitor bank with five separate units, and the current, I_z, and B_z can be programmed in any sequence. A quartz torus of major diameter and bore of 200 cm and 12 cm was used. The plasma temperatures and densities obtained are in the range 10-200 eV and $0.2\text{-}2 \times 10^{16}\,\text{cm}^{-3}$ with $\beta \simeq 0.05\text{-}0.9$.

2. THEORY

2.1 Marginal Stability

Numerical methods(5) based on Newcomb's analysis provide a rigorous test for the M.H.D. stability of any distribution but recently analytic criteria for kink stability have been obtained(6). Marginal stability analysis alone is insufficient to assess fully the confinement capability of a system particularly during the setting up phase. For example, configurations can be unstable to slow-growing or highly localised modes which are easily suppressed by non-ideal M.H.D. effects.

Instabilities can be driven by pressure gradients or currents ($j_{\parallel}$) and both types can be localised or non-localised in the radial direction. All four types are relevant to the experiments described here. The Suydam criterion applies to localised pressure driven modes.

It has been shown(6) that the sign of the variation of the potential energy depends only on two terms, of the form

$$F_1\ (k,\ r,\ dp/dr) + F_2\ (k,\ r,\ P,\ B_\theta)$$

where $P = rB_z/B_\theta$ is the pitch, k the wave number and the other symbols are as usual. The two terms represent the energy sources leading to pressure and current driven modes respectively. Except in the case of a positive pressure gradient, which is stabilising, the first term is always destabilising and the marginal stability is determined by the radial variation of the pitch. When $dp/dr < 0$ a pitch minimum is a sufficient condition for instability. It follows that the stabilised pinch with a vacuum outside as in Fig.1(a) is unstable; with distributed currents (case 1(b)) and the screw pinch, case 1(c) stability is possible with $\beta = 0.05\text{-}0.1$ (exceptionally $\beta > 0.1$ in the screw pinch); in both these cases an insulating wall gives a local minimum in P. All configurations with a vacuum outside are unstable unless the pitch minimum coincides with a positive pressure gradient, which can only exist within a magnetically

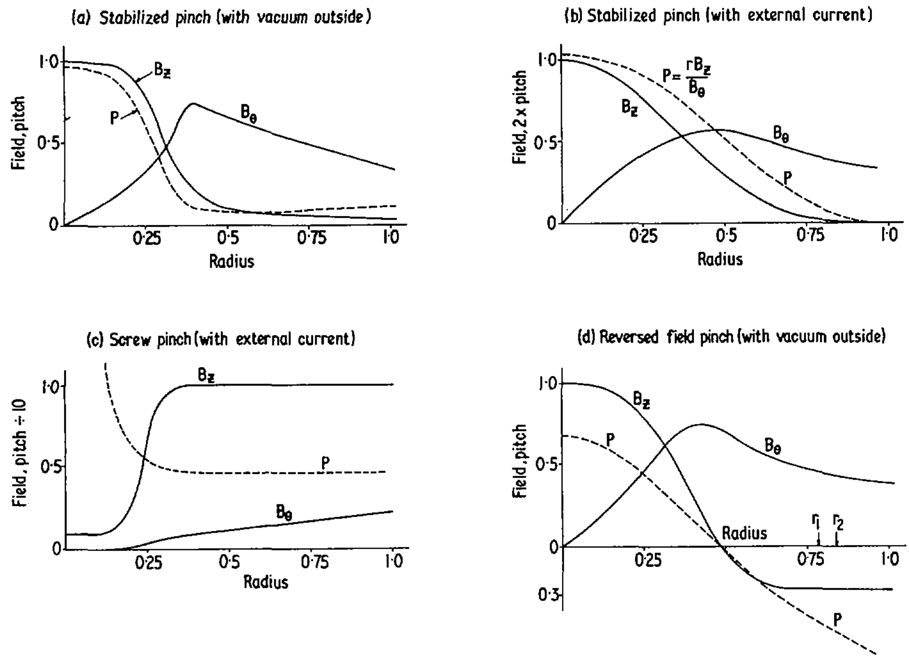

FIG. 1. Examples of typical field configurations studied in the experiment. The radial variation of the pitch P is also shown. (a) stabilized pinch with vacuum region between plasma and conducting wall; (b) stabilized pinch with external current; (c) screw pinch with external current; (d) reversed field pinch, with the wall positions for stability according to Newcomb (r_1) from the flux condition (r_2) shown.

confined plasma, or is removed by reversing the external B_z, as in case 1(d), for which necessary stability conditions are given in Table 1. Theoretically this configuration can also be stable to resistive and micro-instabilities[7,8].

2.2 Growth Rates and Eigenfunctions

Growth rates and eigenfunctions of a cylindrical plasma have been calculated including compressibility which, although not required in a marginal analysis, is necessary because the most important types of instability have the wave vector of the perturbation along a field line and a correct description of the motion then requires compressibility.

The equation[9] for the radial displacement, ξ_r, has been solved numerically and an example of computed growth rates as a function of wave number, k, and ratio of specific heats, γ, is shown in Fig.2. It is seen that the growth rate is larger

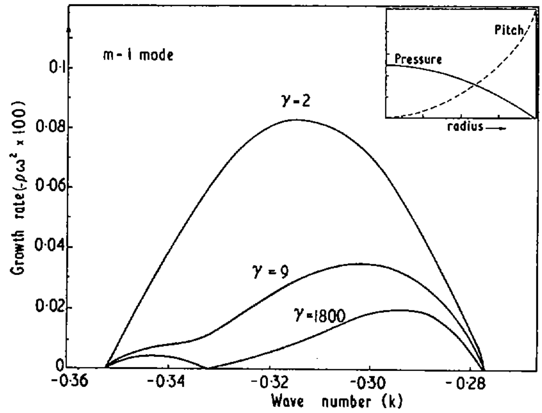

FIG. 2. Computed values of growth rate as a function of wave number showing the effect of compressibility. Inset is the radial variation of pitch and pressure for the model field configuration used. The incompressible case is shown for $\gamma = 1800$.

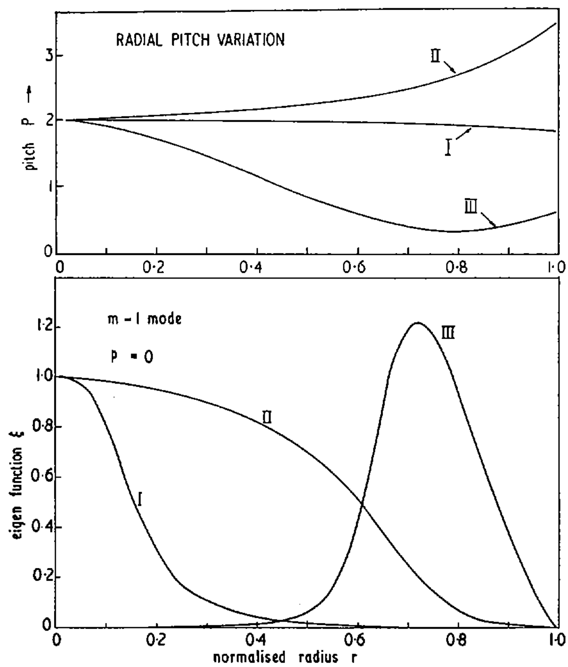

FIG. 3. Computed eigenfunctions for various configurations, with zero pressure and full compressibility. The pitch distributions used are shown above.

with compressibility ($\gamma = 2$) and $\rho\omega^2$ has a maximum near the wave number given by $\underline{k}.\underline{B} = 0$, while for incompressibility ($\gamma \to \infty$) $\rho\omega^2$ peaks on either side of this wave number. In this example the pressure gradient and pitch, which determine the behaviour, are negative and increasing outwards from the axis respectively (see insert in Fig.2), both characteristics leading to instability. Examples can be solved analytically; in particular for $kb << 1$ where pressure driven modes predominate, the growth rate is given by

$$\omega^2 = - \frac{2\ k^2 b^2}{\rho(3.83)^2} \left(\frac{1}{r} \frac{dp}{dr} \right)_{r \to 0} \qquad (1)$$

where b is the conducting wall radius.

Three basic types of eigenfunctions are illustrated in Fig.3 corresponding to the three forms of radial pitch variation shown. The examples chosen are for current driven modes, assuming $dp/dr = 0$. In case I, with a weak pitch maximum at the axis (small shear) which is close to the marginal stability limit, there is a localised mode near the axis. A pitch minimum on the axis gives a non-localised mode (case II) while a pitch minimum in the outer regions gives a mode localised there (case III). The growth rate for case I is given by

$$\omega^2 = \frac{5(k\ b)^4}{\rho\ b^2} \cdot B_\theta^2\ (b) \cdot \alpha^2\ e^{4\pi/\varepsilon} \qquad (2)$$

$$\varepsilon = \sqrt{\frac{4 + 9\alpha}{-\alpha}} \quad , \qquad -\frac{4}{9} < \alpha < 0$$

where

$$\alpha = \frac{P}{2}\left(\frac{d^2 P}{dr^2} \right)_{r \to 0}$$

is the curvature of the pitch on axis[10]. Except when $kb << 1$, as in a Tokamak, ω is large. Strongly localised modes near the axis are only obtained for pressure or current driven instabilities when the mode number is close to that for marginal stability.

In general the existence of a negative pressure gradient near the axis leads to a non-localised mode of the form shown in case II, Fig.3 which will destroy the plasma rapidly. A localised mode associated with an outer pitch minimum, although it can have a faster growth rate, will take several growth times before it leads to a significant reduction in the plasma energy.

TABLE I. NECESSARY STABILITY CONDITIONS FOR REVERSED FIELD PINCH (Fig. 1(d))

Basic conditions	In practical terms
$\frac{\lvert P_r \rvert}{P_{r=0}} < 3$	$\frac{\lvert B_{z(r=b)} \rvert}{B_{z(r=0)}} \lesssim 30\%$
$\beta_\theta < 1 \quad (m = 1)$ $\beta_\theta < 0.5 \ (m = 0)$	$\beta_{r=0} \lesssim 40\%$
$\phi_z = 2\pi \int_0^b B_z \, r dr > 0$	$\frac{a}{b} \gtrsim 0.5$

b = radius of conducting wall

3. EXPERIMENTAL DETAILS

The parameters of the five capacitor banks, which can be fired in any sequence, were measured simulating the plasma by a 6 cm diameter copper toroid and are given in Table II. Usually peak I_z in the plasma was between 50 and 150 kA (maximum value used was 250 kA) with peak fast B_z up to 12 kG. Deuterium at filling pressures p_o between 10 and 50 mtorr were used.

Diagnostics included measurements of current, voltage and flux from which the paramagnetism was obtained. The radial magnetic field was measured with small coils on the outside and at the top and bottom of the quartz torus (major axis vertical) which gives the equilibrium position and is a sensitive guide to the gross or outer region stability. Helically wound coils with a sine or cosine variation in the turns/cm which encircle the quartz torus give the position of the plasma within the minor cross-section. Optical and radiation measurements have been made with calibrated image converter cameras and the time history of spectral lines and the continuum have been studied using filters and a monochromator. Magnetic probes, consisting of six pairs of coils of approximate dimensions 2mm, each pair measuring B_θ and B_z were introduced into the plasma from above.

TABLE II. PARAMETERS OF EXPERIMENT

CLEAR QUARTZ TORUS	BORE	12 cms
	MAJOR DIAMETER	2 metres
METAL SHELL	BORE	15 cms

ELECTRICAL PARAMETERS * OF CAPACITOR BANK

	ENERGY MJ	VOLTAGE KV	Peak B_z OR I_z	RISETIME μsec	DECAY TIME μsec
1. Preionization	0.0035	60	60 kA	1.2	10
2. Slow B_z	1	8	6 kG	160	1500
3. Fast B_z	0.54	± 40	± 18 kG	7.5	270
4. Fast I_z	0.27	40	380 kA	13.5	470
5. Fast I_z	0.27	± 40	± 380 kA	13.5	470

* measured simulating plasma by copper toroid 6 cm diameter.

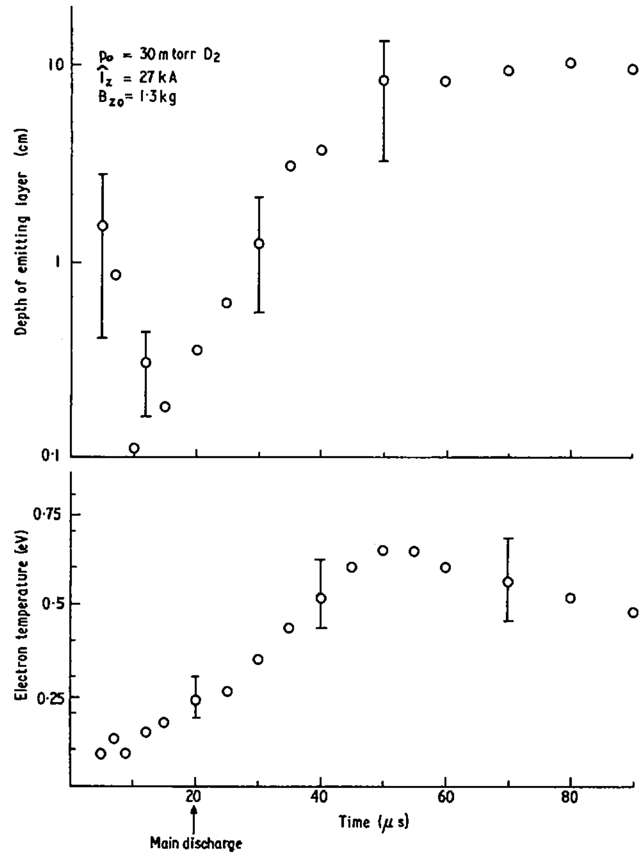

FIG. 4. Time variation of the temperature and depth of the line emitting region during the preionization discharge.

4. PREIONIZATION PLASMA

The gas was preionized by an axial current whose peak value varied from 10 to 30 kA depending on bias field and filling pressure; current trapping[11] results in a unidirectional oscillatory current of period 5 μsec which ionized 30-50% of the filling gas at pressures between 10 and 50 mtorr. The electron temperature peaked on the axis, reached its maximum value of 2 eV at 5 μsec and decayed slowly thereafter, falling to 1.5 eV at 20 μsec when the main discharge was fired.

In addition to highly ionized gas at 1.5-2 eV there is a strong line emitting region close to the walls,[12] whose temperature and density were measured from the Balmer decrement and from Stark broadening and whose depth was then obtained from the absolute line intensity. In this region $n_e = 5\text{-}10 \times 10^{13}\ \text{cm}^{-3}$ compared with an average value in the main column of $10^{15}\ \text{cm}^{-3}$ and an initial atom density of $2 \times 10^{15}\ \text{cm}^{-3}$ ($p_o = 30$ mtorr). The time variation of the temperature and depth of the line emitting region are shown in Fig.4 and are about 0.25 eV and 1 cm at 20 μsec. Heat loss, mainly by atom thermal transport(12) from this relatively cold layer, causes almost all the joule heat from the preionization current corresponding to 200 eV per particle over 50 μsec, to be lost.

5. HEATING AND ENERGY LOSSES

5.1 Experimental Observations

The average pressure of the central luminous column of compression heated screw pinches, whose area was obtained optically, was estimated from the diamagnetism correcting for the paramagnetic effect of the axial current (see Section 6.2). The average density was obtained from the mass oscillation frequency which, in the screw (and toroidal theta) pinches studied corresponds to a compression of half the filling gas, compared with 80-100% previously reported from linear theta pinches(13). At $p_o = 15$ mtorr and $B_z = 12.5$ kG, $\frac{1}{2}(T_e + T_i) = 210 \pm 40$ eV, average $n_e = 8 \pm 2 \,.\, 10^{15}$ cm at 7 μsec, values consistent with those obtained from the M.H.D. code(14); a direct comparison is not possible until the inefficient gas sweep up is understood. However, in Fig.5 the observed heating rate as a function of the initial rate of rise of B_z is seen to be in reasonable agreement with the theoretical curve, raised by a factor of two to simulate 50% sweep up.

Plasma resistance measurements and probe data, from which it is deduced that most of the longitudinal current is uniformly distributed outside the central column, show that the resistivity temperature is about 5 eV in screw pinches. This suggests that the temperature in the outer regions is of the same order.

In resistively heated stabilised pinches the power input is relatively small. The temperature has been measured in stable conditions, observed at currents below about 100 kA (see Section 6.2). For example, at $I_z = 60$ kA, $p_o = 30$ mtorr, magnetic probe data gives

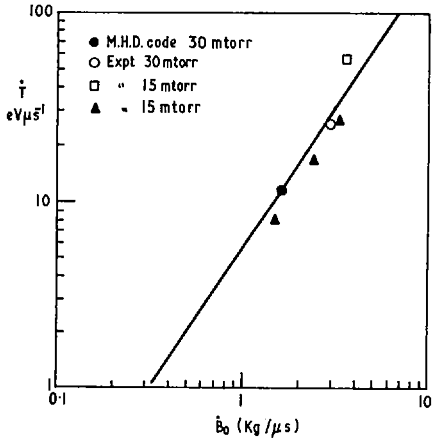

FIG. 5. Rate of rise of spatially averaged temperature $\frac{1}{2}(T_e + T_i)$ as a function of initial value of B_z for compression heated pinches, theory and experiment. The line, obtained from a number of computations (one point shown) is raised by a factor of two to simulate 50% gas sweep up. Solid points are theta pinches and open points screw pinches.

$\frac{1}{2}(T_e + T_i) = 9 \pm 2$ eV in agreement with pressure balance for $\beta_\theta = 0.4$ and in approximate agreement with average values from M.H.D. computations.

5.2 Energy Losses in Compression and Resistively Heated Pinches

Data from several experiments shows that energy losses which are small at input powers above 25 eV/particle/μsec (at the densities used) can become important at lower input powers, sometimes leading to temperature limitation. Since such powers are only obtainable in the present experiment by B_z compression, which (except for the screw pinch) is usually incompatible with stability requirements, estimates have been made of energy losses which could become important at lower input powers typical of resistive heating. These include radiation(15), ionization, neutral atom transport by free flight or thermal conduction(12,16) and electron conduction, particularly from turbulence(17).

Using a coronal model(15) the estimated line radiation losses from oxygen are 10 eV per μsec at 15 eV and 1% concentration. Incomplete ionization of the filling gas can lead to neutral atom transport or ionization losses. Numerical simulation of the preionization decay(16) shows an atom layer near the wall (see Section 4) from which energy is lost through electron-atom transfer followed by

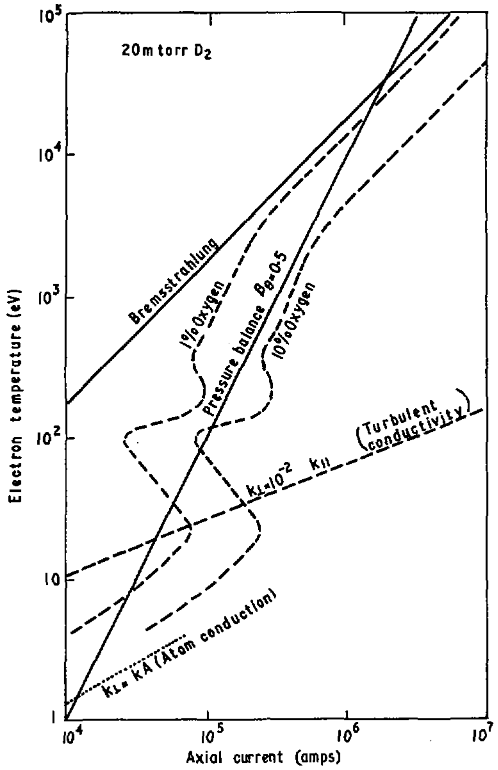

FIG. 6. Calculated values of the equilibrium electron temperature (for $T_e \gg T_i$) as a function of current assuming various loss mechanisms. Also shown is the pressure balance temperature with $\beta_\theta = 0.5$.

atom thermal conduction, which explains the temperature limitation of 1-2 eV. Ionization losses were studied for a theta pinch by computing the heating rate for 100% and 10% (uniform) initial ionization as a function of the initial rate of rise of B_z. When $\dot{B}_o$ = 10 kG/μse there is rapid ionization and little difference in the heating rate (~ 80 eV/μsec) whereas at 2 kG/μsec the heating rate falls from 7 to 0.7 eV/μsec when the initial ionization is reduced from 100% to 10%. Experimentally in both theta and screw pinches the heating rate is sensitive to preionization timing when $\dot{B}_o \lesssim 5$ kG/μsec.

Calculated equilibrium electron temperatures for the experiment at p_o = 20 mtorr, obtained by balancing the classical joule heating against losses, are shown in Fig.6 with the pressure balance value for β_θ = 0.5 and $T_e >> T_i$. Curves for radiation due to hydrogenic bremsstrahlung and lines plus bremsstrahlung for 1% and 10% oxygen impurity are shown, together with electron thermal conduction assuming $k_\perp = 10^{-2}\, k_\parallel$, a value observed in turbulent conditions[18] and an empirical curve for atom thermal conduction[12].

It is deduced from these calculations that there are several sources of heat loss which must be reduced before pressure balance temperatures $\tilde{>}$ 100 eV can be obtained with power inputs in the 10 eV/μsec range. Evidently from results on Zeta and Tokamaks, metal walls and operation at lower densities are important in these respects. In contrast, for fast compression heating with high energy input rates and rapid wall isolation the processes described above are relatively unimportant in quartz systems at least for time scales in the 10 μsec range[19].

6. EXPERIMENTAL RESULTS ON VARIOUS CONFIGURATIONS

6.1 Screw Pinches (p_o = 10-40 mtorr, $\hat{B}_z$ = 3-12 kG, $\hat{I}_z$ = 30-100 kA)

Screw pinches were obtained by firing I_z (risetime 7-10 μsec) and B_z (risetime 4-7 μsec) simultaneously. The electrical behaviour is characterised by $\theta = B_\theta/B_z$ at the metal walls, radius b. The field distribution can be calculated at any time, assuming models, from a knowledge of θ at that time. Discharges with θ down to 0.1 were studied (maximum $q_{r=b} \sim 0.6$). The paramagnetism is plotted against θ in Fig.7, together with theory for distributions described by the force-free paramagnetic model[20] (FFPM) surrounding a uniform core radius a,[2]

$$\text{i.e.} \qquad \frac{\varphi_f}{\phi_o} = 1 + \frac{\theta^2}{2} - \frac{a^2}{b^2}(1 + \theta^2)(1 - \sqrt{1 - \beta}) \qquad (3)$$

In this model a uniform axial electric field is assumed together with the relation $j_\parallel = \sigma_\parallel E_\parallel$; the radial variation of B_z and B_θ is calculated for different values of θ. The FFPM describes pinches with distributed currents (e.g. Fig.1(b)) and when $\theta \leqslant 1$ it gives the same distributions as the constant pitch model[21]. It is seen from Fig.7 that the data agrees with theory within the experimental error, indicating distributed currents in the

[2] Average beta, defined with respect to the external B_z field, is used for screw pinches.

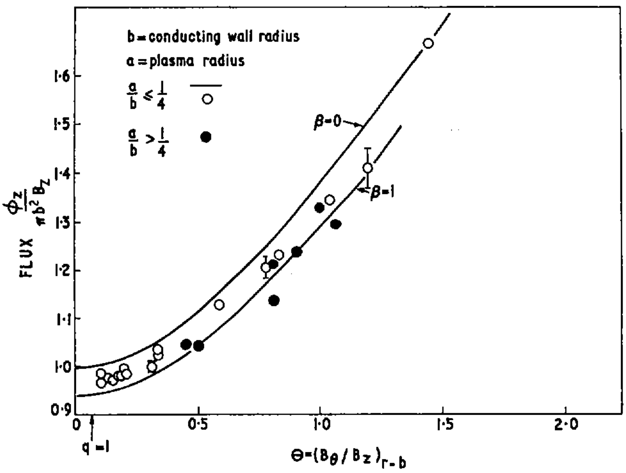

FIG. 7. Paramagnetism/diamagnetism in a screw pinch as a function of θ. Curves from a model in which a uniform central core, radius a, is surrounded by a force-free paramagnetic field distribution are shown.

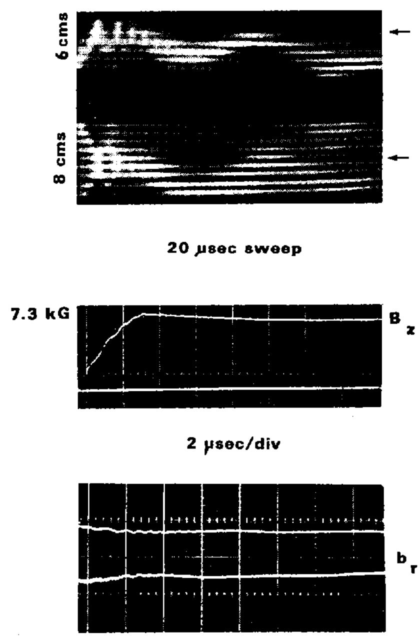

FIG. 8. Streak photograph of a screw pinch with oscillograms showing the axial magnetic field, B_z (with crowbar) and the radial magnetic field component at the walls, b_r.

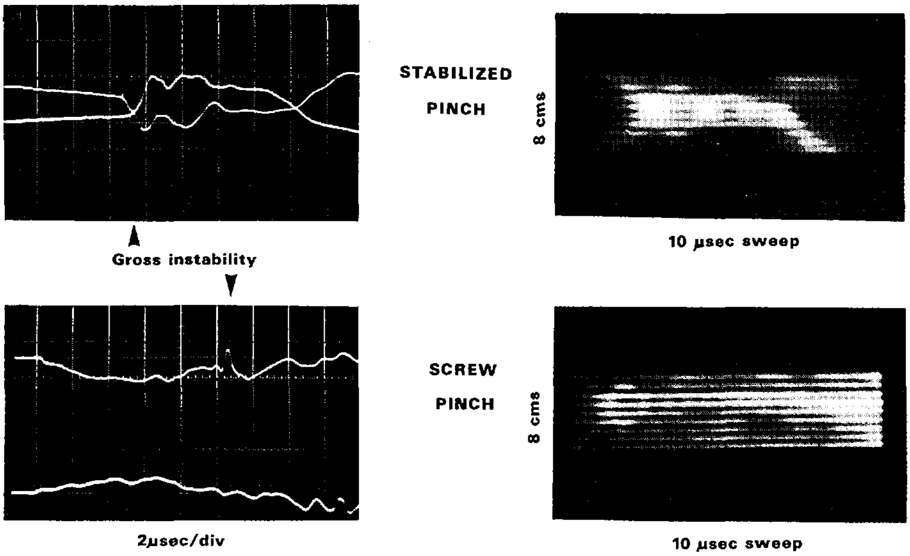

FIG. 9. A comparison between a screw pinch and well compressed "stabilized" pinch. Streak photographs and radial magnetic field oscillograms are shown.

experiment. For $\theta \lesssim 0.4$ the plasma becomes diamagnetic as in a theta pinch and the data indicates $\beta \sim 0.5$-1; note that the theoretical curves become insensitive to β for $\theta \gtrsim 0.8$.

The toroidal displacement, measured optically and by helical coils, agrees to better than 15% with theory(22) for circular magnetic surfaces when $0.3 < \theta < 1$; the expression for Δ approximates to $\Delta = \frac{b^2}{2R}\frac{\beta}{\theta^2}$ when $\theta < 0.5$. When $\Delta \sim b/2$ the observed value of Δ is less than theory by factors of two or more e.g. at $\theta = 0.15$ the values are 3.5 and 7.5 cms respectively; this suggests that for highly distorted magnetic surfaces the equilibrium values of β_θ become larger.

The stability has been studied optically and from the radial magnetic field component, b_r. In the example in Fig.8 the central luminous column is grossly stable for 15-20 μsec. Although there is sometimes evidence for the expected (Section 1) non-localised pressure driven $m = 1$ instability, more often including crowbarred discharges, the central column progressively becomes diffuse and its luminosity decays. The diamagnetism and

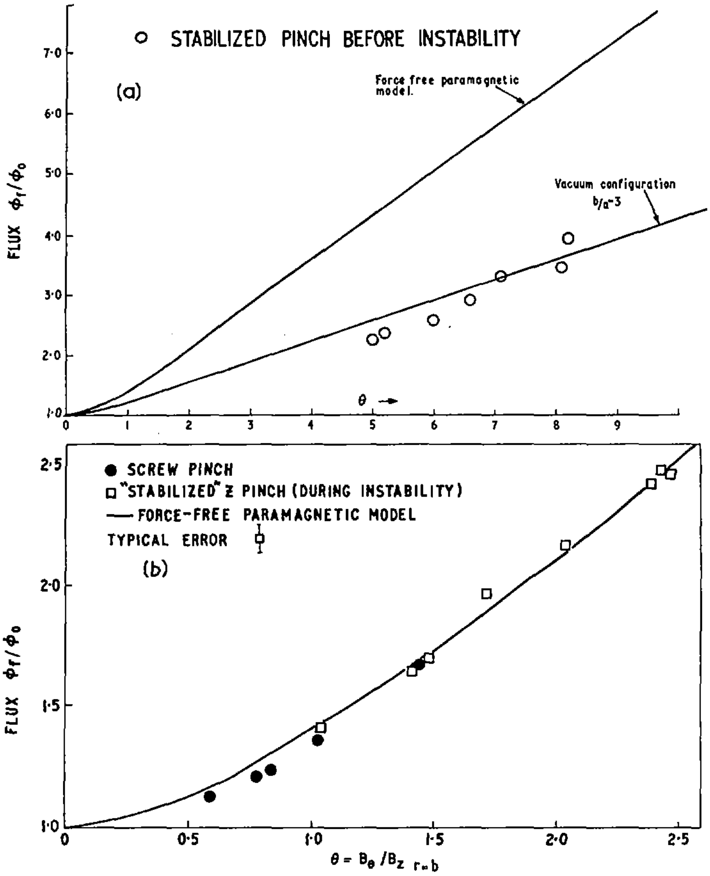

FIG. 10. Paramagnetism as a function of θ (a) above - "stabilized" z-pinch before the onset of instability with theory for a distribution with a vacuum outside the plasma; (b) below - "stabilized" z-pinch during an m ≈ 1 instability with theory for the force-free paramagnetic model. Some data from the screw pinch is also shown in the lower figure.

magnetic probe data at earlier times tentatively indicate energy losses or diffusion from the main column. Throughout this grossly stable phase the b_r signal showed fluctuations at frequencies above 1 MHz, indicating outer region instabilities, probably from the pitch minimum at the quartz walls, an example of case III, Fig.3. In Fig.9 photographs and b_r oscillograms of the grossly stable phase in examples of screw and stabilised pinches are compared. Although the central column lasts longer in the screw pinch no b_r fluctuations are seen in the stabilised pinch, indicating outer region and gross stability occur together in this case.

6.2 "Stabilised" Pinches
(p_o = 30-60 mtorr, B_{zo} = 0.2-5 kG, $\hat{I}_z$ = 50-150 kA)

"Stabilised" pinches are obtained by applying an initial slow B_z field followed by a rapidly rising axial current, and include configurations shown in Figs. 1(a) and 1(b).

The axial flux, increased by the paramagnetic effect[23], was measured before the onset of instability and is plotted against θ (usually measured at peak current) in Fig. 10(a). The data agrees with theory assuming a vacuum distribution (cf. Fig. 1(a)). When the discharge becomes unstable the paramagnetism increases rapidly to the value for the fully diffuse configuration of the FFPM (c.f. Fig. 1(b)), as seen in Fig. 10(b).

During the stable phase the displacement of the equilibrium position, which varied between 1 and 6 mm, was compared with theory,

$$\Delta = \frac{b^2}{2R}\left[\log b/a + \left(1 - \frac{a^2}{b^2}\right)\left(\frac{\ell_i}{2} + \beta_\theta - \frac{1}{2}\right)\right]$$

where ℓ_i is the plasma inductance per unit length, for values of b/a from 1.5-7. Best agreement, within about 15%, was found assuming a vacuum distribution with ℓ_i = 1 and β_θ = 0.5, but a fit could also be obtained with β_θ = 0.25. Probe data indicated β_θ = 0.3 and ℓ_i = 0.8.

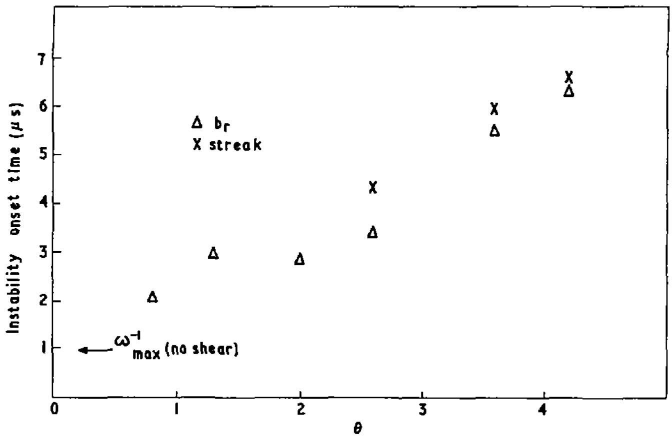

FIG. 11. The onset time of an m = 1 instability in the "stabilized" pinch obtained from streak photographs and from the radial magnetic field component as a function of θ. The maximum growth time of an instability calculated without shear is shown. p_0 = 30 mtorr.

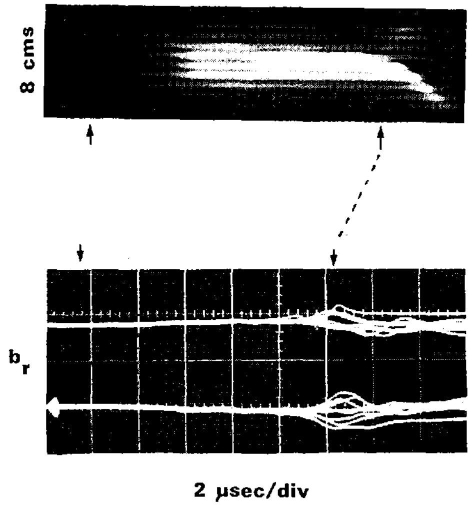

FIG. 12. Streak photograph of a well compressed "stabilized" pinch showing the onset time and growth of an m = 1 instability. Also shown are overlaid oscillograms of the radial magnetic field b_r in the same conditions.

The instability onset time is shown as a function of θ in Fig.11. The onset time increases with θ and reaches 7 μsec when $\theta = 5$, a value exceeding the growth time in an approximately shear free field (eq.1) by a factor of 7. It should be noted that at still larger θ (not shown) the compression ratio exceeds the value for wall stabilisation of gross current driven kinks and the curve turns over as expected.

A streak photograph of a compressed plasma is shown in Fig.12 together with overlaid oscillograms of b_r. Stability for about 8 μsec is followed by a non-localised m = 1 mode growing in about 1 μsec with a wavelength estimated from the helical coils of about 3 cm, i.e. $k \sim \theta/a$. The b_r signal and optical data show a reproducible onset time followed by random, unstable behaviour during which the paramagnetic effect reverses the longitudinal field in the outer region[1]. The instability has the characteristics of a non-localised pressure driven mode (Section 2.2), and it appears just after the pressure gradient near the axis, initially positive, becomes negative, presumably due to diffusion. This change in sign is deduced from probes and, indirectly, from Abel inverted light intensity profiles. These plasmas, which have been

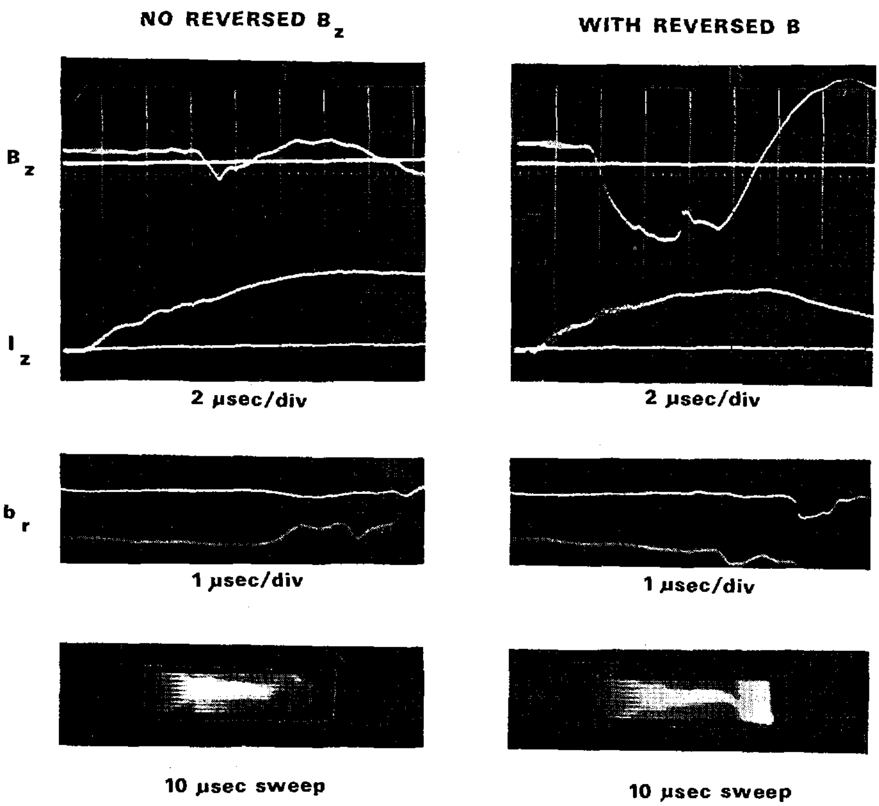

FIG. 13. Streak photographs and oscillograms of the axial magnetic field and the radial magnetic field component b_r for a compressed stabilized pinch with (on the right) and without (on the left) an applied reversed axial field on the outside. (*Note that the time-scale for the b_r oscillogram is 1 μs per division and that for the B_z and I_z 2 μs per division*).

observed to remain stable for up to 15 μsec, show no evidence for modes due to an outer pitch minimum.

Weakly compressed plasmas with $\theta \simeq 0.5$-2 become unstable in 1-2 μsec or less to a wavelength of 30 cm corresponding to the pitch in the outer region, in a manner consistent with expectations for configurations with an outer pitch minimum (case III, Fig.3).

6.3 Reversed Field Configurations

Theoretically a reversed B_z removes the outer pitch minimum and associated instability in configurations with a vacuum between the plasma and conducting wall such as Fig.1(a), to form distributionsof the type shown in Fig.1(d). The effect of

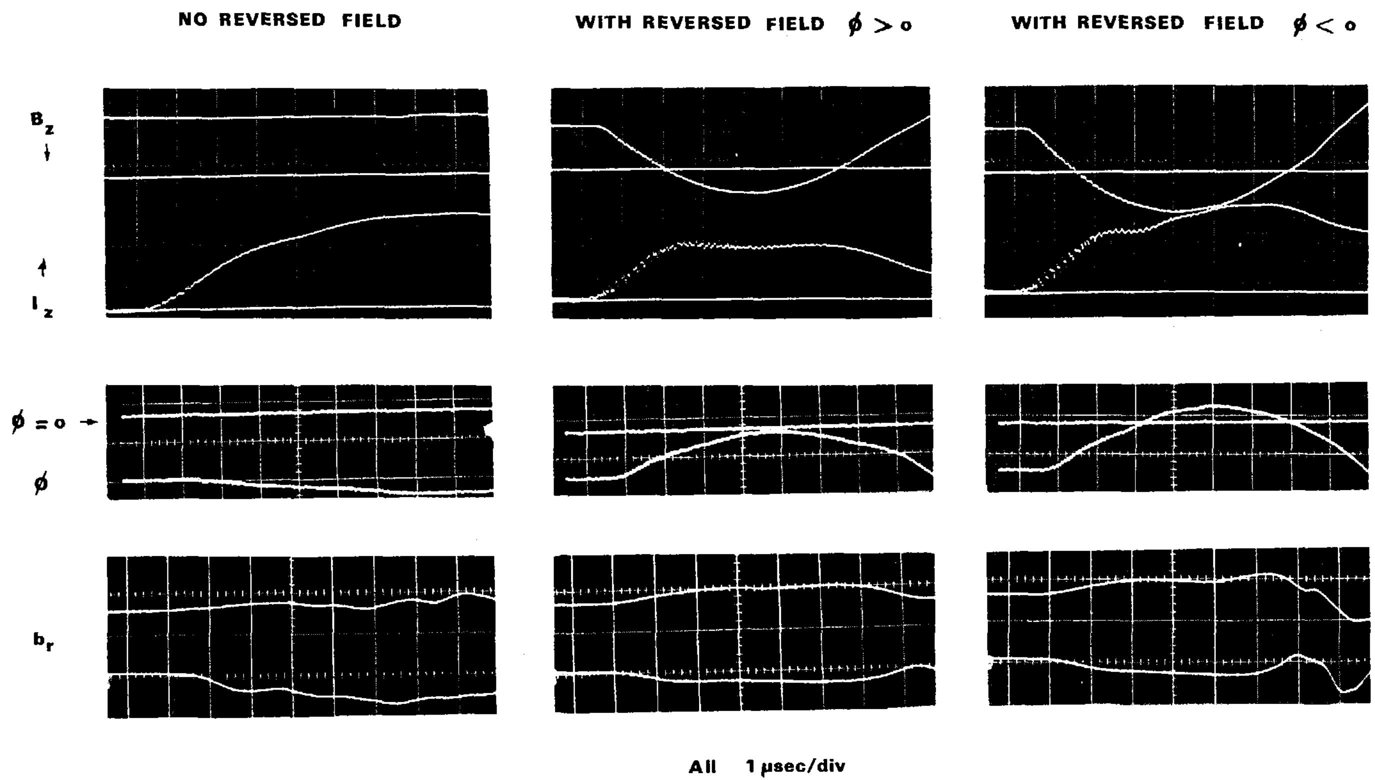

FIG. 14. Oscillograms of current, axial field and flux and b_r showing the effect of applying a reversed B_z to a weakly compressed "stabilized" pinch. Examples without reversed field (left), with reversed field (centre) and with sufficient reversed field to change the sign of the total axial flux, ϕ, (left) are shown. p_0 = 40 mtorr.

applying negative B_z at times varying from $\Delta t = 0$-$4\ \mu$sec after the start of the axial current to the two stabilised pinch configurations described above was studied.

Reversed field configurations obtained by applying a negative external B_z to the well compressed plasmas ($\theta > 3$) described above can remain stable with $\beta_\theta = 0.3$-0.4 for up to 15 μsec; they are destroyed by the same non-localised pressure driven instability as without reversed B_z. This is shown in Fig.13, where it is seen both optically and from b_r that the onset time and growth of the instability are unaffected by the reversed field. This result is in accord with expectations, since compressed pinches do not show outer region instabilities and modes driven by a negative pressure gradient near the axis are not expected to be strongly influenced by a reversed external B_z. Note that no tearing mode was seen.

The application of reversed field to weakly compressed pinches ($\theta < 2$) which become unstable in the outer regions in $\lesssim$ 1-2 μsec is complicated. The plasma tends to expand outwards, interact with the walls and lose trapped flux, an effect well known in theta pinches(23) and only modestly reduced by the B_θ at the values of $\dot{I}_z$ available. When $\Delta t = 4\ \mu$sec relatively little flux is lost, but the instability is already well developed when B_z at the plasma surface changes sign and only a marginal improvement is obtained(24).

A marked improvement was found when $0 < \Delta t < 0.5\ \mu$sec, but in this range more than half the initial trapped flux was lost, although no other effects such as enhanced luminosity at the walls were noted. This is seen in Fig.14 where oscillograms of I_z, B_z, the axial flux ϕ_z and b_r are shown for an example with no reversed field (on the left) and two examples with reversed field. Note that 1-2 μsec elapse before the field changes sign at the plasma surface. In Fig.15 overlaid b_r oscillograms for three examples with and without reversed field are shown. In all cases the onset time of the instability increased from about 1 μsec to 6 or 7 μsec, and the b_r signals (Fig.15) are smooth and reproducible for this time. In Case A there is almost no compression and b_r shows large irreproducible fluctuations in less than 1 μsec without reversed field, which are

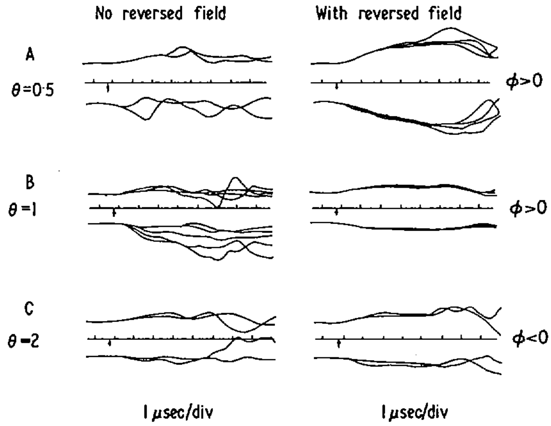

FIG. 15. Tracings of overlaid b_r oscillograms showing the effect of applying a reversed B_z to "stabilized" pinches with different compression ratios. Other conditions correspond to Fig. 14. Examples with reversed field are on the right. In case A with almost no compression instabilities appear in less than 1 μs without reversed field; in case B there is stability with reversed field for 7 μs while in case C the compression ratio is increased so that the total axial flux φ changes sign with applied reversed field.

suppressed with negative B_z; this shows the importance of firing the reversed B_z close to $\Delta t = 0$. In the second example in Fig. 14 and case B in Fig. 15 the negative I_z bank was used (note the flat-topped current pulse). In the example on the right hand side of Fig. 14 (and case C in Fig. 15) the reversed B_z is increased so that the total axial flux becomes negative (see ϕ_z oscillogram in Fig. 14) thus violating the third stability condition in Table I; in these conditions the plasma becomes less reproducible.

Although when negative external B_z was applied to weakly compressed pinches there was a 6 or 7-fold increase in the stable period and the outer region instability was removed, the use of the crowbar gave little further improvement, probably because field diffusion causes the configuration to change into an unstable one. Processes which take place during the setting up phase such as the outward expansion and associated loss of flux, and factors governing the stability in the interval between applying the reversed B_z and the field changing sign at the plasma surface are complex. Until they are understood it is not possible to explain other observations, such as the fact that the improvements in stability shown in Figs. 14 and 15 could not be reproduced at higher power and/or lower filling pressures.

Detailed magnetic probe data is required to make further progress in understanding the reversed field configuration.

7. DISCUSSION AND CONCLUSION

A range of field configurations, including reversed field pinches which were stable with β_θ = 0.3-0.4, has been set up experimentally using programming in a controlled way. Their behaviour agrees in general with expectations.

The screw pinch, in which compression heating need not be incompatible with stability requirements, has temperatures in the central column of up to 200 eV (β = 0.9) and gross stability for up to 20 μsec. However, the outer region, where probe data show most of the axial current flows, is relatively cold with a resistivity temperature of 5 eV, and always shows external radial magnetic field fluctuations, as expected from instabilities due to the outer pitch minimum. Further measurements are required to determine the extent to which the energy balance in the hot core is influenced by the outer regions.

In stabilised pinches the power input is low and the maximum temperatures obtainable in stable conditions are typically 10 eV with β_θ = 0.3-0.4 at currents of 50-100 kA and filling pressures about 40 mtorr. Weakly compressed plasmas ($\theta < 2$) become unstable in times of the order of 1 μsec or less to localised modes, probably from the outer pitch minimum. These outer region modes were removed when the external B_z was reversed as expected and the stable phase was increased to 6 or 7 μsec. In these conditions the setting up of the reversed field configurations was found to be complex, particularly because outer region instabilities can grow before the field at the plasma boundary reverses. Well compressed pinches ($\theta > 3$) remain stable for up to 15 μsec and reversed field configurations with β_θ = 0.3-0.4 were obtained which lasted for the same time by applying a negative external B_z. In both cases the plasma lifetime was limited by a non-localised mode driven by a negative pressure gradient near the axis which was not expected to be strongly influenced by the reversed field.

It is concluded from experiments and theoretical estimates that radiation, ionization, atom transport and turbulent conductivity can limit the temperature obtainable in quartz systems for power inputs in the 10 eV/particle/μsec range typical of resistive heating. These losses are less important, at least for times in the 10 μsec range, in compression heated systems with rapid wall isolation and power inputs $\tilde{>}$ 25 eV/particle/μsec.

Theoretical analysis of the growth of instabilities, important during the setting up phase, shows that compressibility has to be taken into account and its effect is to increase the growth rate. Eigenfunctions were computed for three characteristic forms of unstable displacement - non-localised, localised near the axis and localised in the outer regions. A negative pressure gradient near the axis gives rise to a non-localised mode. Many of the experimental observations have been explained theoretically: for example, localised modes in the outer regions have been seen in both stabilised and screw pinches when there were pitch minima, and the non-localised pressure driven mode limiting compressed stabilised pinches appeared when the pressure gradient near the axis changed from positive to negative. Experimental estimates of growth rates and wave numbers are consistent with theoretical predictions where direct comparisons have been made.

ACKNOWLEDGEMENTS

The authors with to thank their many colleagues, engineers for building the machine and keeping it operational and others for carrying out the measurements and for discussions.

REFERENCES

[1] ROBINSON, D.C., KING, R.E., (1968) 3rd I.A.E.A. Conf. on Controlled Fusion, Novosibirsk, Paper B-8, Proc.1 (263).

[2] BOBELDIJK, C., et al. (1968) 3rd I.A.E.A. Conf. on Controlled Fusion, Novosibirsk, Paper B-10, Proc. 1 (287).

[3] WILHELM, R., ZWICKER, H., (1970) Z. Physik 240 (295).

[4] OHKAWA, T., et al., (1963) Phys. of Fluids 6 (46).

[5] ROBINSON, D.C., (1970) Culham Report CLM-P 247 and Plasma Physics (in press).

[6] GIBSON, R.D., WHITEMAN, K.J. (1968) Plasma Physics 10 (110).

[7] STRINGER, T.E., Private communication.

[8] HAIN, K., LÜST, R., (1958) Z. Naturforshg 13a (986).

[9] ROBINSON, D.C., (1969), Symp. on Closed Configs, Dubna.
[10] ELLIS, W.R., (1970) Bull. Am. Phys. Soc. Ser II, 11 (1448).
[11] IRONS, F.E., ELLIS, W.R., NEWTON, A.A. (1971) to be published.
[12] BEACH, A.D., et al. (1969) Nuclear Fusion 9 (215).
[13] HAIN, K., et al. (1960) Z. Naturfschg. 15a (1039).
[14] KARR, H.J., et al. (1961) Phys of Fluids 4 (424).
[15] VASILEV, A.P., et al. (1960) Nuclear Fusion Suppl. 2 (655).
[16] LONG, J.W., NEWTON, A.A. (1971) Submitted to 10th Int. Conf. on Ionization Phen. Oxford.
[17] RUSBRIDGE, M.J., (1969) Plasma Physics 11 (35).
[18] BODIN, H.A.B., et al. (1968) 3rd I.A.E.A. Conf. on Controlled Fusion, Novosibirsk, Proc. 2 (533).
[19] RUSBRIDGE, M.J., et al. (1962) Nuclear Fusion Suppl. 3 (895).
[20] SCHUURMAN, W., et al. (1968) Plasma Physics 11 (495).
[21] SHAFRANOV, V.D., (1963), Nuclear Fusion 3 (183).
[22] BICKERTON, R.J., (1958), Proc. Phys. Soc., 72 (466).
[23] GREEN, T.S., NEWTON, A.A. (1966) Phys. of Fluids 9 (1386).
[24] BODIN, H.A.B. et al. (1970) Bull. Am. Phys. Soc. Ser II, 11 (1423).

DISCUSSION

T. OHKAWA: Is the current density in the discharge below or above the sound-wave instability threshold?

H.A.B. BODIN: In general, at our currents and filling densities, the electron drift velocity is well below the sound speed. During some phases of the discharge, however, particularly if a classical sheath tries to form, the threshold can be exceeded locally.

F.L. RIBE: In the case of the low-compression, stabilized pinch with a reversed outer longitudinal field, you say that the onset of the stabilized mode is delayed and that the plasma goes unstable. Is this a non-localized m = 1 mode with the plasma moving as a whole to the wall?

H.A.B. BODIN: In weakly-compressed reversed field pinches the fields decay by resistive diffusion. We have not studied the ultimate fate of such plasmas in detail, but the column shrinks until, presumably, the wall stabilization condition is violated. We have not attempted to identify the unstable modes in this phase.

G.J. YEVICK: The use of B_z and B_θ appears to be a powerful tool for controlling plasmas. The problem is to ascertain the proper time-dependence of B_z and B_θ and their absolute and relative magnitudes. For example, should one have a fast θ-pinch followed by a declining B_z field, while in the meantime B_θ is growing?

H.A.B. BODIN: I agree with you that the use of B_z and B_θ is a powerful tool. We have studied a wide range of different configurations, but have only reported experiments on those which appear to be of most interest.

Unless B_θ is fired close to or before B_z, the "theta pinch" plasma will quickly hit the wall owing to lack of equilibrium. When the two are fired closer together we have the screw pinch, which gives effective heating from fast B_z compression but is not expected to be stable - with a circular cross-section - for β much above 10%. With β up to 40%, stability and equilibrium are predicted theoretically and observed in our experiments in the reversed-field mode, but in this case heating is by resistive dissipation from the axial current and is relatively inefficient. Effective heating and stability at high values of β are difficult to achieve together.

M. LEVINE: In our TORMAC experiment, in which we start with a stabilized pinch, we observe turbulence at the plasma frequency. Could this have any bearing on your stability considerations?

H.A.B. BODIN: I do not know enough about your experiment to comment on whether the phenomenon you mention is likely to occur in the experiment I have described. We have not studied high-frequency turbulence and have not observed any unexplained phenomena which seem likely to be due to such effects. In general I do, of course, agree with you that high-frequency turbulence can be important.

EXPERIMENTS ON A TOROIDAL SCREW PINCH WITH VARIOUS FIELD PROGRAMMING

H. ZWICKER, R. WILHELM, H. KRAUSE
Max-Planck-Institut für Plasmaphysik, Euratom-Association,
Garching, Munich,
Federal Republic of Germany

Abstract

EXPERIMENTS ON A TOROIDAL SCREW PINCH WITH VARIOUS FIELD PROGRAMMING

In the toroidal screw pinch ISAR-IV (large diameter 60 cm, aspect ratio 5, maximum storage, energy 140 kJ) attempts were made to get an improved stability of the plasma by different kinds of field programming.

The best results were obtained with positive trapped B_z-fields and simultaneous switching of main B_z-field and I_z-current. In this case the dense plasma column ($n_e \approx 2\text{-}3 \times 10^{16}$, $kT \approx 50\text{-}100$ eV, $\beta \approx 15\text{-}20\%$) is surrounded by a force-free plasma (β=1%) with weak shear and it behaves stably for, at least, 25 μs. The resulting containment time $n\tau$ of near 10^{12} s cm^{-3} remains a factor of 2-3 below the upper limit given by the classical diffusion. The following loss of the equilibrium position near the coil axis ($\Delta \approx 1\text{-}2$ cm) is connected to a strong damping of the axial plasma current which starts near the end of the containment. It may be assumed that the increase of the effective plasma resistance mainly results from a contact of the force-free regions with the tube wall. Attempts were made to improve the containment by suitable programming of a plasma z-current. The results are presented.

Experiments with one quartz limiter inside the torus improved the equilibrium but introduced instabilities at the new surface of the dilute plasma.

To obtain more information about the outer region, the dilute plasma was produced without a dense core and separated from the tube walls by weak adiabatic compression. Under these Tokamak-like conditions the q-value was varied. In the region of $q \approx 1$ there appeared instabilities which seem to haver higher m-modes and rather short wavelengths.

In a different kind of field programming the field distribution of the "diffuse pinch" was realized within an accuracy of 5-10% ($kT \approx 100$ eV, $\beta \approx 30\%$).

In contrast to the predictions of MHD-theory, stability was observed only for about 3 μs. Then the plasma is totally destroyed, presumably by resistive instabilities.

1. INTRODUCTION

It is well known that the simple screw-pinch equilibrium is MHD-unstable. This difficulty might be overcome by some kind of dynamic stabilization provided that the observed growth rates of the most dangerous m = 1 modes [1] can be reduced.

For this reason, the investigations on the toroidal screw-pinch device ISAR-IV were continued with various additional field programming. Figure 1 shows schematically the experimental arrangement and some technical parameters. The main bank is fed into the collector by 96 single circuits. Each of them has its own combined trigger and crowbar spark gap system. Two of these circuits are drawn in the figure. An additional circuit for the production of a slowly rising toroidal field B_{z0} has been omitted in the drawing. The filling gas was deuterium at an initial pressure between 15 mTorr and 50 mTorr.

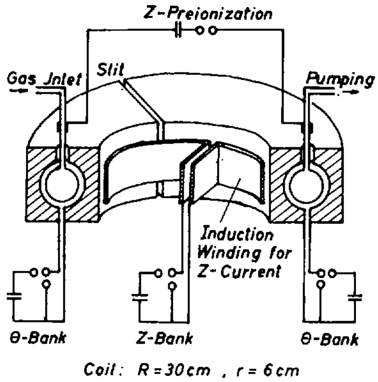

	Θ	Z	B_{z0}
W	125 kJ	20kJ	40kJ
B_{max}	33kG	—	21kG
J_{plasma}	—	100... 150kA	—
U	40kV	80kV	18kV
T/4	1.9μs	1.9μs	25μs
τ_{crowb}	~100μs	~100μs	—
L	~2nH	~50nH	—

FIG. 1 Schematic of the experimental arrangement of screw pinch ISAR-IV.

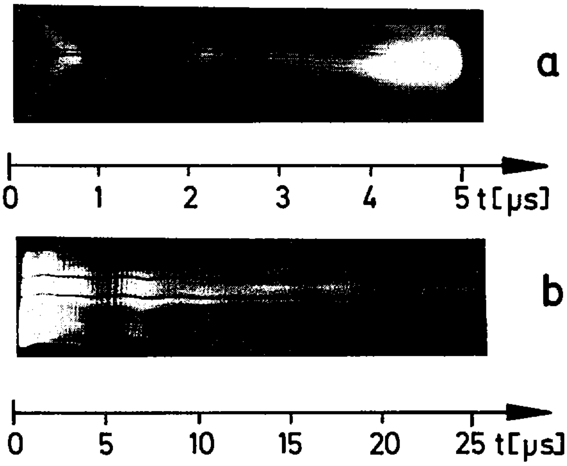

FIG. 2 Influence of positive bias field B_{z0} on stability of the screw pinch. a) B_{z0} = 0; b) B_{z0} = 1.5 kG. p_0 = 50 mTorr D_2. Outer wall on top.

2. STABILITY BEHAVIOUR WITH POSITIVE BIAS FIELD

The first step was the superposition of an additional field B_{z0} parallel to the main B_z-field and simultaneous switching of main field B_z and current I_z. In this case, the m = 1 growth rates were clearly reduced compared to the case without bias field. The plasma was stable for at least 25 μs at temperatures $T_e = T_i \approx 50 - 100$ eV and densities $n_e \approx 2\text{-}4 \times 10^{16}\ cm^{-3}$. As an example, Fig. 2 gives streak pictures at a filling pressure p_0 = 50 mTorr a) without and b) with positive bias field of B_{z0} = 1.5 kG for all other initial parameters unchanged. The strong reduction of the m = 1 growth rates is mainly the consequence of the reduced β-value which was decreased from about 0.75 to 0.15 - 0.2 with bias field. This is in agreement with

MHD-calculations by W. Grossmann which, under the assumptions of diffuse density profile and constant pitch for our experimental conditions at β = 0.2, predict an m = 1 growth time at typically 50 μs.

The experiments showed, however, that in spite of the absence at m = 1 modes the plasma life-time is limited to about 25 μs. This is because during the stable stage the equilibrium position is lost and the plasma shifts slowly towards the outer wall of the discharge tube, as seen in Fig. 2b. The observed loss of equilibrium is associated with a damping of the axial plasma current I_z.

3. LOSS OF EQUILIBRIUM

To test whether or not the slow drift is due to the decreasing plasma Z-current, additional Z-currents were induced by a second Z-bank in such a way that the damping of the measured Z-currents in the plasma was strongly reduced. Figure 3 shows the time behaviour of the radial position of the dense plasma column as it was evaluated from several shots a) with normal and b) with additional induced Z-currents. The corresponding Z-currents are given in Fig. 4. A reduction of the plasma drift in case b) can be seen clearly. However, full equilibrium cannot be obtained during the stable phase of the plasma, even if the Z-current is held essentially constant.

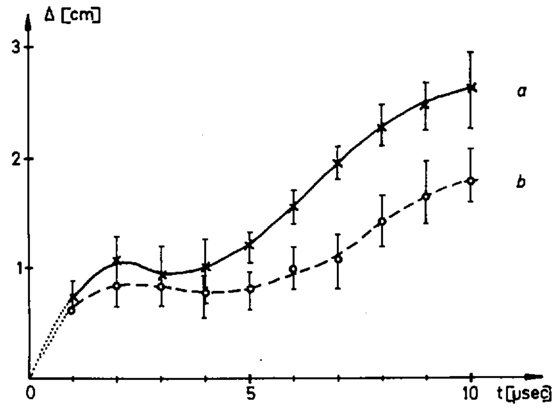

FIG. 3 Radial position of the plasma column as a function of time. a) normal; b) with reduced Z-current damping.

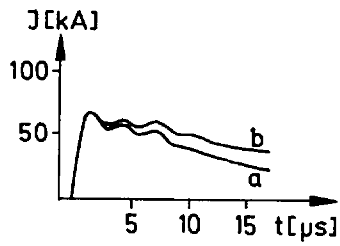

FIG. 4 Measured plasma Z-current for discharges of Fig. 3. a) normal; b) with additional induced current.

This result implies that the loss of equilibrium is not only due to the current damping in the thin, pressureless plasma which surrounds the dense core and which carries the main part of the Z-currents, as has been shown earlier. The main reason seems to be a change in the radial current-density distribution resulting from field diffusion in the plasma column. This must be taken into account because the classical field diffusion time for the measured electron temperature of T_e = 40 - 50 eV is comparable with our time scale of about 25 μs.

In order to reduce the possible influence of field diffusion on the equilibrium the plasma temperature was increased by a reduction of the filling pressure from p_0 = 50 mTorr ($T_e \approx$ 45 eV) to p_0 = 20 mTorr where $T_e + T_i \approx$ 180 eV was measured. In these cases, however, the damping of the plasma Z-current is stronger than in the case with p_0 = 50 mTorr. Stereoscopic streak pictures showed further that the plasma surface is destroyed at a very early stage by strong local instabilities arising in the pressureless plasma.

4. POSITION OF EQUILIBRIUM

A further question in the experiments with p_0 = 50 mTorr concerned the quantitative position of the equilibrium during the stable stages which depends critically on β. A β of about 0.2 was roughly evaluated from magnetic probe measurements during the first five microseconds. The observed equilibrium at 1,2 cm off the axis could be understood neither by the constant pitch model nor by direct equilibrium calculations based on the measured field distribution (Fig. 5). The mean β-value had to be smaller by a factor of 3. Therefore the β-value in the plasma column was determined more precisely from spectroscopic measurements of the electron temperature and the radial density distribution. Combined with the measured

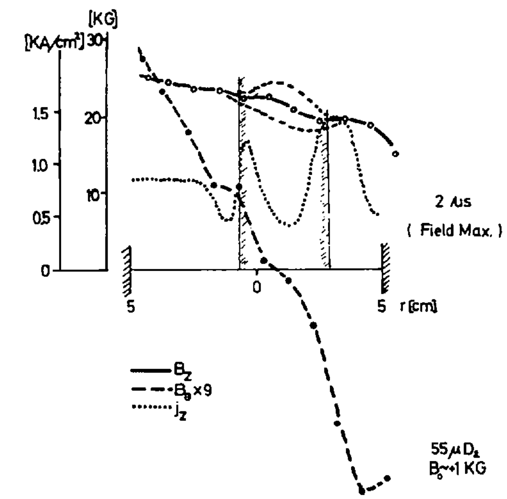

FIG. 5 Radial distribution B_z(r) and B_θ(r) for screw pinch with B_{z0} = 1 kG, measured at peak field B_z.

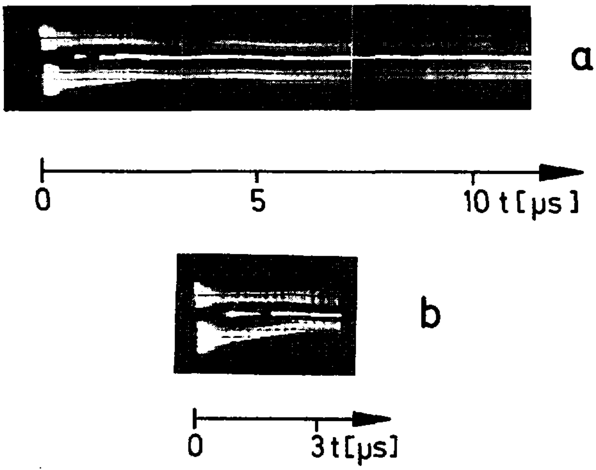

FIG. 6 Stereoscopic streak pictures of screw pinch discharges with a) diffuse; b) more rectangular density distribution. In case b) Z-discharge started 50 ns before Θ-discharge. All other parameters unchanged.

B_z at the coil surface there resulted a value of β = 20 % at the plasma centre, in good agreement with the result of the direct probe measurements. The measured radial density distribution, however, showed a relatively diffuse profile with a continuous transition to the pressureless plasma. This was confirmed by additional measurements of the field gradient with special probes. These results imply that the mean β-value of the plasma, $\bar{\beta}$, is much less than 0.2. In this way the observed equilibrium position can be understood in spite of the high β near the plasma centre.

A certain experimental confirmation of the importance of the mean β for the screw-pinch equilibrium is shown in the streak pictures of Fig. 6. They show two discharges under the same conditions (I_z, B_z, B_{z0}, p_0). In the lower case (b), only the Z-current is started 5×10^{-8}s before the main bank. This results in a more rectangular density distribution than in the upper case (a). Consequently, for the same β-value of about 0.2 at the centre, the mean value $\bar{\beta}$ is much smaller in case (a) than in case (b). The equilibrium position in (b) is therefore far off the axis and the plasma hits the wall after about 4 μs, whereas in (a), with the same Z-current, the column stays near the axis for more than 12 μs.

5. REDUCTION OF WALL CONTACT

One of the reasons for the observed loss of equilibrium (Fig. 2b) is the increasing damping of the Z-currents. Presumably the corresponding increase in plasma resistance results mainly from an enhanced wall contact of the pressureless plasma due to the increasing deviation from axial symmetry. This might be related to the results of spectroscopic measurements of the radial intensity distribution of the continuum. They indicate the existence of a distinguished layer near the wall with a width of about 0.5 cm. Further measurements of intensity and of the half widths of the D_α, D_β and D_γ

lines in this region showed that the layer has only $T_e \approx 0.3$ - 0,5 eV at a density of 2 - 4 $\times 10^{14}$ cm^{-3}. It could be possible that this cold region causes the damping of the Z-currents and starts the loss of equilibrium.

An attempt was made to reduce the possible damping of the Z-currents from wall contact by inserting a quartz limiter (free diameter 8 cm, centre 1 cm off the axis) into the torus.

Magnetic probe measurements of the radial field distribution at the opposite side of the limiter showed that the limiter influences the poloidal field B_θ and therefore the I_z-distribution all over the circumference of the torus.

Compared with the case without limiter, the B_θ-field decreased in the region blocked by the limiter. The Z-currents were mainly concentrated in the cross-section determined by the limiter. Streak pictures obtained nearby and opposite to the limiter showed that the equilibrium position stayed near the axis. The plasma is destroyed, however, after 10 - 15 μs, mainly by instabilities in the outer regions.

A further attempt at reducing the wall contact of the Z-currents was made by an additional compression. This was obtained by a B_z-field which continued to rise after the I_z-maximum. The result was a very strong decrease of the total Z-current and a loss of equilibrium after a few microseconds. The observed behaviour of the plasma Z-current is a result of negative Z-currents in the outer regions. They arise as a consequence of flux conservation for B_θ during the compression of the still rising B_z-field.

6. STABILITY OF THE DILUTE PLASMA

To obtain information on the stability behaviour of the thin current carrying plasma which surrounds the dense column, a dilute plasma was produced without a central core. It was separated from the tube wall by a weak adiabatic compression with a compression ratio of about 1.2.

For this purpose, the Z-discharge was started shortly before the B_z-field had reached its maximum. For these Tokomak-like conditions the q-value was varied by variation of the Z-current. Stereoscopic streak pictures indicated that for $q \lesssim 1$ - 2 there appeared instabilities which seem to have higher m-modes and rather short wavelengths. This shows that the instabilities obtained for comparable conditions in the outer regions of the screw pinch are essentially independent of the behaviour of the dense central plasma column.

7. STABILITY WITH NEGATIVE BIAS FIELDS

Earlier investigations had shown that the superposition of negative bias fields to the simple screw pinch increases the m = 1 growth rates considerably [2]. However, a similar configuration with trapped antiparallel field, proposed by Bodin et al. [3], should be MHD-stable. The stability behaviour of this reversed field-pinch configuration was therefore investigated.

The necessary field programming started with a quasi-stationary field B_{z0} of 1.5 kG. After pre-ionization the main Z-current of about 150 kA was induced and crowbarred after 2 μs. At this stage the bias field was reversed by switching on a positive B_z-field. During the rise of this B_z-field

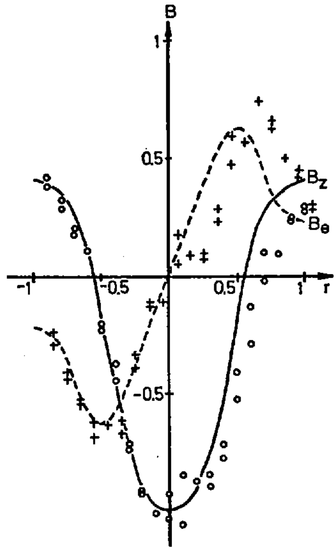

FIG.7 Relative field distribution of reversed field pinch configuration. Measured values (o) B_z and (+) B_θ near the end of the stable phase. The curves give the theoretical distributions according to Ref. [4]. Tube wall at r = 1.

to 11 kG the plasma Z-current was automatically reversed in the outer plasma region due to the conservation of the B_θ-flux. In this way the theoretically proposed field distribution could be realized with fairly good accuracy. Figure 7 shows the measured radial distribution of B_z and B_θ 2.5 μs after the ignition of B_z. The full and the dotted curves give the theoretical distribution [4] which should be MHD-stable. The small deviations from the theoretical curves are due to the toroidal geometry. Assuming pressure equilibrium, the field measurements and the filling pressure of p_0 = 20 mTorr give a maximal β-value of about 0.3. The temperature is on the order of 100 eV at this stage. Streak pictures and diamagnetic probe measurements showed that this configuration remains stable only for about 3 μs. Then the plasma is destroyed by an instability with a growth time of typically 0.2 μs. Type and cause of this instability are not yet clear.

8. CONCLUSION

So far, the investigations have shown that the strongest reduction of the m = 1 modes is obtained for the screw pinch with positive bias field. If the slow loss of equilibrium can be overcome, the application of dynamic stabilization, already studied in a linear screw pinch [5], seems to be reasonable. However, the necessary operation at β-values of 0.1 - 0.2 reduces the efficiency of the heating by fast implosion and adiabatic compression. Operation in the keV-regime, therefore, seems to be difficult.

For this reason, it might be desirable to produce a screw-pinch equilibrium which is at least m = 1 stable at higher β-values too. This might be possible for screw pinches with non-circular plasma cross-sections [6, 7].

REFERENCES

[1] WILHELM, R., ZWICKER, H., Z. Physik 240 (1970) 295.
[2] GROSSMANN, P., WILHELM, R., ZWICKER, H., in Controlled Fusion and Plasma Physics (Proc. 4th. Europ. Conf., Rome) Rome (1970) 49.
[3] BODIN, H.A.B., McCARTAN, I., in Closed Confinement Systems, (Proc. Int. Symp., Dubna 1969).
[4] Culham Report CLM-PR 12 (1969).
[5] BECKER, G., GRUBER, O., HEROLD, H., these Proceedings.
[6] LAVAL, G., MASCHKE, E.K., PELLAT, R., ROSENBLUTH, M.N., Internal Report IC/70/35.
[7] WILHELM, R., ZWICKER, H., these Proceedings.

A TOROIDAL SCREW PINCH WITH NON-CIRCULAR PLASMA CROSS-SECTION

R. WILHELM, H. ZWICKER,
Max-Planck-Institut für Plasmaphysik, Euratom Association,
Garching bei München,
Federal Republic of Germany

Abstract

A TOROIDAL SCREW PINCH WITH NON-CIRCULAR PLASMA CROSS-SECTION.

Application of MHD-theory to a screw pinch or Tokamak with circular cross-section shows that equilibrium and stability are obtainable only at β-values of the order of several per cent.

Simple equilibrium and stability considerations for a screw pinch with flat plasma cross-section, however, showed that in this case β-values in the region $\beta \approx 1$ should be allowed.

Using the low inductive capacitor bank ISAR-IV, in a toroidal discharge chamber with a volume of 220 litres in flat geometry (50 cm mean diameter, 100 cm height) the plasma is produced by a fast rising magnetic field (rise time 6 μs, e-folding time $\approx$ 1 ms, peak field 10 kG). The results concerning equilibrium and stability of this flat plasma in the temperature regime of 100-200 eV are reported.

1. INTRODUCTION

It has been shown that a toroidal screw-pinch plasma can be m = 1 stable for β-values up to 10% [1]. At these low β-values, however, adequate heating is apparently not produced by the shock wave, which is the usual heating mechanism in high-β plasmas. Moreover, local instabilities and a lack of equilibrium were observed in the experiments mentioned above, even under conditions of m = 1 stability.

To overcome these difficulties, a new experiment was started in which the toroidal plasma is distorted into a belt-shaped plasma so that the formerly circular cross-section becomes long and thin. Simple considerations involving the Shafranov-Kruskal limit [2] show that with such a geometry it should be possible to obtain a m = 1 stable plasma with a small radial displacement even for high β-values. In addition, growth times of other unstable modes should become much longer in comparison with those observed in the circular high-β case [3].

2. EQUILIBRIUM AND STABILITY

With the notations defined in Fig. 1, the conditions for a toroidal equilibrium can be roughly estimated by using the pressure balance between the two points A and B:

$$\beta\,(B_\Phi^2\,(B) - B_\Phi^2(A)) \approx B_x^2(A) - B_x^2\,(A) \tag{1}$$

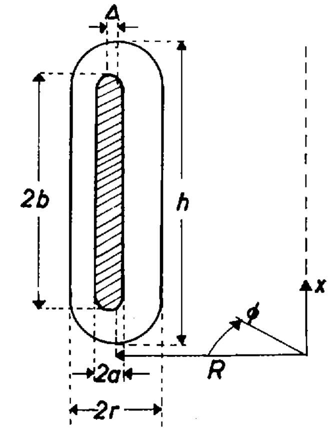

FIG. 1. Geometry and notations for belt-shaped screw-pinch.

Introducing the Kruskal-condition modified to

$$B_x/B_\Phi \approx \frac{2\,b}{\pi\cdot R}\,\frac{1}{q} \quad (q = \text{safety factor}) \tag{2}$$

and assuming a compression of the field component $B_x(A)$ corresponding to the toroidal displacement Δ, we obtain a critical value of β for m = 1 stability:

$$\beta \leqq \frac{4\,b^2\,\Delta}{q^2\cdot \pi^2\cdot a^2\cdot R}\,;\quad \Delta \ll 2\,r \tag{3}$$

This implies that the stability condition (3) can be fulfilled also for $\beta \approxeq 1$, if the ratio b/a is large enough.

In spite of this positive result, localized instabilities could be more dangerous in the belt-shaped geometry than in the case of a circular cross-section. This is confirmed by Laval et al. [4], who give a formula for the energy variation on the basis of the Mercier criterion [5]. For a screw pinch with circular cross-section, δW can be approximated by

$$\delta W_0 \propto \left\{1 - \frac{1}{q_0^2}\right\} \tag{4}$$

which, in principle, can be positive. In the belt-shaped geometry, however, δW becomes

$$\delta W_1 \propto -\left\{\frac{1}{q_1^2}\right\} \tag{5}$$

and is always negative.

On the other hand, to obtain a toroidal equilibrium at higher β-values, the necessary limitation of the q-values becomes significant. The limits can be derived from Ref. [6] and roughly have the following form:

$$q_0^2 < \frac{a}{R\langle\beta\rangle} \qquad \text{(circular)} \qquad (6)$$

$$q_1^2 < \frac{3\,b^2}{4\alpha\,R\langle\beta\rangle} \qquad \text{(elliptical, } b \gg a) \qquad (7)$$

$\langle\beta\rangle$: averaged β-value.

In the regime of higher $\langle\beta\rangle$-values, q_0^2 becomes much less than unity, and the known instabilities for the circular cross-section will occur. In the same approximation for the belt-shaped case q_1^2 can be greater than unity. Then, corresponding to the decrease in $|\delta W_1|$ by a factor $4a^2/3b^2$, the growth rates of the unstable modes might be smaller by a factor of the order of a/b.

3. EXPERIMENTAL ARRANGEMENT

An extremely flat configuration similar to a screw pinch was first studied in modified θ-pinches [7, 8]. The decisive disadvantages of these systems arose from the open-ended geometry. The experiment described here, however, is a modification of a circular toroidal screw pinch. By an enlargement of the dimension perpendicular to the torus plane the stability condition (3) is fulfilled for $\beta \approx 1$ and $\Delta \approx a$.

To obtain the necessary high Φ-current with the same time behaviour as the main $B_{\bar{\Phi}}$ field, the two fields are produced by a single fast capacitor bank of 120 kJ stored energy. This was done by a screwed arrangement of the current-carrying conductors, as seen in Fig. 2. The overlapping of the 16 copper ribbons shown in detail in the figure avoids the appearance of stray fields. The outer ring also shown in Fig. 2 can be crow-barred, which provides the flux compression during the toroidal shift. Furthermore, a 20 kJ capacitor bank can be fed into the same ring. This gives the possibility of influencing either the radial distribution of j_Φ or the shear.

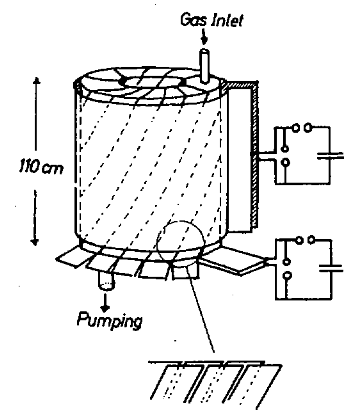

FIG. 2. Schematic of the experimental arrangement for the belt-shaped screw-pinch.

The pre-ionization (not shown in the figure) is realized by a pulsed capacitively coupled RF-discharge and a subsequent weak screw-pinch discharge. The technical data of the device are summarized as follows

$R \approx 23$ cm	$U = 40$ kV
$h \approx 100$ cm	$\lvert B_{max}\rvert = 12$ kG
$r \approx 8$ cm	$\lvert \dot{B}\rvert = 2.6 \times 10^9$ G/s (vacuum)
	$\tau/4 = 4\,\mu s$
	$\tau_{crowbar} = 0.5$ ms
	$I_\Phi = 0.5 - 1$ MA.

Owing to the nearly plane geometry, the surface of the magnetic piston remains practically constant during the implosion. According to a rough calculation using the snow-plow model, this implies an effective ion heating by the compression wave. Therefore, in spite of the relatively small values of peak field and rise time, plasma temperatures up to 300 eV can be expected at the time of field maximum of the belt pinch.

4. RESULTS

The first results concerning formation, equilibrium, and stability of the produced plasma seem to be promising. This is demonstrated in Fig. 3 at one of the first few streak pictures taken parallel to the torus axis in a time scale of 50 μs. The filling pressure is 50 mTorr D_2. The corresponding time behaviour of the main field (B_Φ-component) is shown for the same time in Fig. 4. The streak picture shows that the shock forms a plasma belt which is very plane along the total line of sight of about 1 m. This exact hollow cylinder moves into the toroidal equilibrium and remains completely stable for a first phase of 20-30 μs. After this time small motions of the plasma

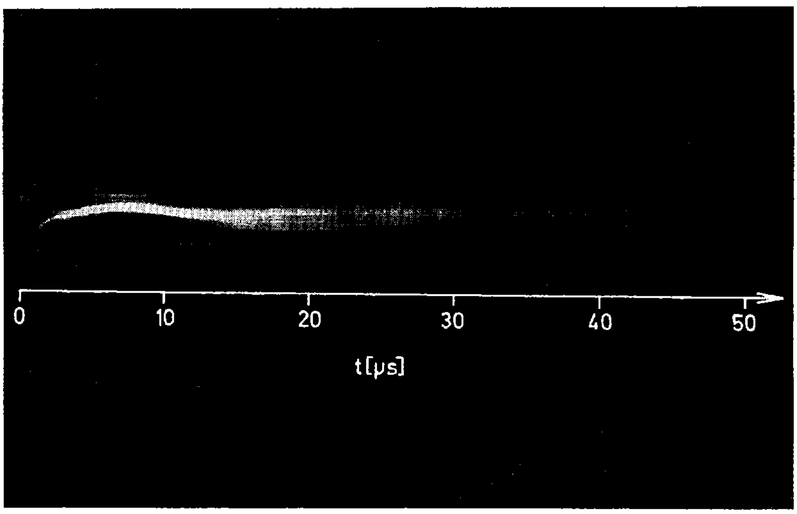

FIG. 3. Streak picture of the belt pinch (U = 25 kV, p = 50 mTorr D_2).

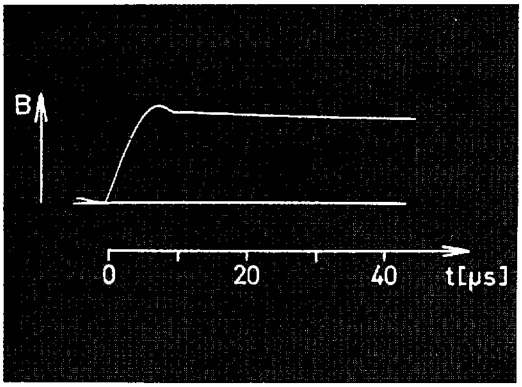

FIG.4. Time behaviour of magnetic field (B_Φ-component).

surface appear, which, however, are exactly reproducible. Therefore, it might be assumed that these effects are due to the still insufficient homogeneity of the magnetic fields.

A rough estimation of the plasma parameters gives a temperature of 50-100 eV (at reduced bank energy), a density of about 10^{16}, and a β-value near to one.

These very first experiments indicate the following main results:

1) A toroidal high-β plasma is formed and heated by the well known combination of shock and adiabatic compression. This allows an increase of the obtainable temperatures into the keV-region by a relative simple and possible enlargement of the presently used bank.
2) The very low efficiency of shock heating which results from the high compression ratio in high-β pinches with circular cross-section is avoided in the belt geometry. In the present experiment, this energy transfer was increased by more than one order of magnitude compared to the circular toroidal screw pinch investigated before. This good energy transfer makes the shock heating in the belt geometry very attractive compared to other known heating mechanisms for low-density plasmas.
3) The large plasma hollow cylinder is stable for an encouragingly long time. First discharges using nearly full bank energy and lower filling densities indicate an enhanced plasma containment for a time of about 75 μs at temperatures above 100 eV.

REFERENCES

[1] ZWICKER et al., these Proceedings.
[2] SHAFRANOV, V.D., in Plasma Physics and the Problem of Controlled Thermonuclear Reactions 2 London, Pergamon Press (1959) 187.
[3] WILHELM, R., ZWICKER, H., Z. Physik 240 (1970) 295.
[4] LAVAL, G., MASCHKE, E.K., POLLAT, R., International Centre for Theoretical Physics, Trieste, Report IC/70/110.

[5] ADAM, J.C., MERCIER, C., in Plasma Physics and Controlled Nuclear Fusion Research (Proc. Conf. Novosibirsk, 1968), Vol.1 (Vienna, 1969) 199.

[6] LAVAL, G., MASCHKE, E.K., PELLAT, R., ROSENBLUTH, M.N., International Centre for Theoretical Physics, Trieste, Report IC/70/35.

[7] KOLB, A.C., DIXON, P.H., DÜCHS, D., ELTON, R.C., YOUNG, M.P., in Plasma Physics and Controlled Nuclear Fusion Research (Proc. Conf. Novosibirsk, 1968) 2 (Vienna, 1969) 567.

[8] PLANTIKOW, U., SCHLÜTER, J., Verhandlungen der Deutschen Physikalischen Gesellschaft 7 (1971) 453.

DISCUSSION

TO PAPERS IAEA-CN-28/B-6, B-7

J.L. TUCK: Many laboratories are re-examining the Z-pinch. Its properties are such that only a moderate amount of success in stabilization would immediately promote it to an important position, technically. Your time of 25 μs is the longest time I have heard reported. You state that the loss of stability occurs for unknown reasons, and occurs even when the z-current is kept up by external programming. Have you considered that the instability may have been precipitated by the pinch having moved outside the stable region as a result of Joule heating?

H. ZWICKER: The discharge which I discussed is not a Z-pinch, as the implosion and the confinement are due to the θ-pinch field. The Z-pinch field is a factor of 5 less and produces the toroidal equilibrium. As regards the second part of your question, the loss of equilibrium after about 25-30 μs seems to be not so much the result of an instability of the dense core as the consequence of field diffusion disrupting the current distribution which is necessary for equilibrium. Ohmic heating is certainly present. We know from probe measurements, however, that only about 5-10% of the z-current flows into the dense plasma column. The main fraction is in the thin pressureless plasma.

J.L. TUCK: I have a second question. In spite of the apparent prolonged stability of the "belt-shaped" pinch, which you have shown as a wide belt of small uniform thickness, such a configuration could not be stable against a contraction of the width dimension and a swelling of the thickness, i.e. into the form of an ellipsoid of dimensions determined by wall effects. Do you not agree?

H. ZWICKER: Yes, I do. However, this axial contraction is limited by the poloidal field flux conservation due to the conducting walls. The equilibrium shape still gives a plasma cross-section whose height is much greater than its width.

F.G. WAELBROECK: I should like to add in this connection that at Jülich we have been working for over two years on the confinement of plasma in essentially this "belt-shaped" geometry (see paper J-2). Numerical computations by Dr. Janicke have shown that the equilibrium cross-section can be strongly elongated, especially when the total plasma energy is high. This is also confirmed experimentally. Axial compression due to field curvature effects, if it occurs, does not necessarily lead to a circular cross-section. Field-shaping effects due to the external conductors play a dominant role for large plasma volumes.

H.A.B. BODIN: I have a comment and a question. You reported results relating to a reversed field pinch in which the plasma became unstable in a few microseconds. As far as I understand your experiment, our findings under similar conditions would support this. In our experiments with weakly-compressed pinches, described in Paper B-5, it was necessary to fire the reversed B_z in less than 0.5 μs from the start of the I_z current in order to suppress instabilities, probably because in such conditions without reversed B_z unstable modes grow in ~ 1 μs. If we fire the fast B_z after more than 0.5 μs, and I think this corresponds to your experiments, we obtain little improvement and our results are comparable to yours. My question relates to the important point of whether the cold unstable outer region affects the energy content of the hot central core. In the Culham experiment there was some preliminary evidence that this might be so. In the case of the ISAR-IV toroidal screw pinch do you know if the energy content of the hot core is maintained after peak field?

H. ZWICKER: For the conditions under which macroscopic instabilities are observed in the outer plasma regions we have no measurements from which we can deduce the energy content of the hot core during the later stages of the discharge.

F.G. WAELBROECK: In your screw-pinch experiments with positive-bias field, not only the β changes, but also the rotational transform angle ι. What are the values of ι for the cases discussed here, and could you comment on the role of ι?

H. ZWICKER: There is no simple answer to your question. One must take into account that the rotational transform changes with the radial distance from the axis. It is also a function of time as a consequence of the drift into the asymmetric equilibrium position. Speaking in terms of q, near the dense core, we have typical values of about 0.8 for q in the trapped parallel field case. This is about 20% greater than in the cases without trapped field.

T. OHKAWA: Is there any indication of the presence of several magnetic axes?

H. ZWICKER: We have not yet made measurements of field distributions. The experimental data are, however, chosen in such a manner that there should not be several magnetic axes.

ANOMALOUS RESISTIVITY IN AN R.F. CONFINED PLASMA
Theory and experiment

F. HOFMANN
Centre de Recherches en Physique des Plasmas, Lausanne, Switzerland

Abstract

ANOMALOUS RESISTIVITY IN AN R.F. CONFINED PLASMA: THEORY AND EXPERIMENT.

In this paper, MHD calculations are compared with measurements made on an r.f. confined, high-β plasma. It is shown that the electrical resistivity in the current-carrying skin layer considerably exceeds the classical value. Several theoretical formulae for anomalous resistivity, multiplied by arbitrary scaling factors, are used in the calculations. Optimum values for the scaling factors are found by comparison with measurements.

1. INTRODUCTION

Anomalous plasma resistivity has been investigated, both experimentally and theoretically, by a large number of authors (see, for example, Refs [1-7]. Here, we wish to consider a particular experiment, i.e. the confinement of a cylindrical, high-β plasma column by rapidly oscillating azimuthal and axial magnetic fields [8, 9]. In this experiment, the magnetic field and plasma are separated by a relatively thin skin layer which carries very high currents. Within the skin layer, electron drift velocities are high and the electron temperature considerably exceeds the ion temperature. Both of these conditions may lead to microinstabilities and plasma turbulence and thus enhance the electrical resistivity. Measurements [9] have shown that the resistivity in the skin is indeed higher than that predicted by classical theory.

In this paper, we investigate several theoretical models for anomalous resistivity by comparing measurements with numerical calculations based on the magneto-hydrodynamic approximation. The calculations were performed using a one-dimensional MHD computer program [11, 12] which has been developed at this laboratory during the past several years.

2. ANOMALOUS RESISTIVITY

We shall consider three different theoretical predictions for the anomalous resistivity, i.e. the "Bohm resistivity" [13]:

$$\eta_{Bo} = \frac{B}{16\ e\ n_e} \tag{1}$$

Buneman's two-stream resistivity [4]:

$$\eta_{Bu} = \frac{1}{200\pi\ \epsilon_0 \omega_{pe}} \tag{2}$$

and Sagdeev's resistivity [14] of a weakly turbulent plasma:

$$\eta_{Sa} = 10^{-2} \frac{m_e}{n_e e^2} \omega_{pi} \frac{v_D}{v_i} \frac{T_e}{T_i} = \frac{1}{100\, \epsilon_0\, \omega_{pe}} \frac{v_D}{v_e} \frac{T_e}{T_i} \tag{3}$$

Here, v_D is the electron drift velocity ($v_D = j/en_e$), v_i and v_e are defined as $(kT_e/m_i)^{\frac{1}{2}}$ and $(kT_e/m_e)^{\frac{1}{2}}$, respectively, and the rest of the symbols have their usual meaning. MKS units are used throughout.

It should be noted that the "plasma-clump" model of Dupree [6] leads to an anomalous resistivity which is formally identical with Eq. (2), except that it is larger by a factor of five. All of these theoretical predictions must, of course, be regarded as very rough estimates.

Assuming that it is primarily the high electron drift velocity which is responsible for anomalous resistivity, we multiply Eqs (1) and (2) by the ratio (v_D/v_e):

$$\eta_{Bo}' = \frac{B}{16\, e\, n_e} \frac{v_D}{v_e} \tag{1'}$$

$$\eta_{Bu}' = \frac{1}{200\pi\, \epsilon_0\, \omega_{pe}} \frac{v_D}{v_e} \tag{2'}$$

This procedure is very similar to that which has been used at Culham [15] for calculations on the initial phase of a θ-pinch [16]. The Sagdeev resistivity, Eq. (3), already includes the electron drift velocity as a factor and, therefore, does not need to be multiplied by (v_D/v_e). We also note that $(\eta_{Sa}/\eta_{Bu}') = 2\pi\,(T_e/T_i)$.

We now make the assumption that the total electrical resistivity is simply the sum of classical and anomalous resistivities:

$$\eta = \eta_{cl} + \eta_{an} \tag{4}$$

The classical resistivity is given by

$$\begin{aligned} \eta_{cl_{\parallel}} &= \eta_{Sp} + \frac{\nu_{e0} m_e}{n_e e^2} \\ \eta_{cl_{\perp}} &= 1.97\, \eta_{cl_{\parallel}} \end{aligned} \tag{5}$$

where η_{Sp} is the Spitzer resistivity [10], ν_{e0} is the collision frequency for electrons with neutral atoms, and the subscripts $\parallel$ and $\perp$ indicate whether the current vector is parallel or perpendicular to the magnetic field vector.

The anomalous resistivity, as given by Eqs (1'), (2') and (3), is assumed to be isotropic. This assumption is based on measurements [9] which indicate that the parallel and perpendicular resistivities are roughly equal, for those cases where the anomalous part dominates.

3. MHD MODEL

In this section, we shall present a brief summary of the magneto-hydrodynamic model which we are using. A more complete description of the computer code may be found in Ref. [12]. The model is basically a one-dimensional, four-fluid representation of a partially ionized plasma. Electrons, neutral atoms, and two different kinds of ions make up the four fluids. In the particular case considered here, the two ion species represent singly and doubly charged helium ions. The temperatures as well as the fluid velocities of all ions are assumed to be equal. A one-dimensional treatment of the problem is justified by the fact that the duration of the experiment is short compared to the time it takes for a sound wave to travel from one end of the discharge tube to its midplane.

Cylindrical symmetry, quasi-neutrality and ideal gases are assumed. Momentum and energy transfer between electrons, ions and neutral atoms, due to ionization, recombination, charge exchange and elastic collisions are taken into account. Viscosity terms are included in the momentum and energy equations for all fluids except for the electrons. Ion currents in the azimuthal and axial directions are neglected. The various transport and reaction rate coefficients are expressed as functions of the local plasma parameters.

The basic equations are:

$$\frac{\partial n}{\partial t} + \nabla \cdot (n\vec{v}) = S \tag{6}$$

$$\rho\left[\frac{\partial \vec{v}}{\partial t} + (\vec{v}\cdot\nabla)\vec{v}\right] = -\nabla\left[p + \frac{2}{3}\mu(\nabla\cdot\vec{v})\right] + \nabla\cdot[\mu(\nabla\vec{v} + \vec{v}\nabla)] + \vec{F} \tag{7}$$

$$\frac{3}{2}n\left[\frac{\partial T}{\partial t} + (\vec{v}\cdot\nabla)T\right] = -p(\nabla\cdot\vec{v}) + \nabla\cdot[Q\nabla T] + W \tag{8}$$

$$\nabla \times \vec{E} = -\frac{\partial \vec{B}}{\partial t} \tag{9}$$

$$\nabla \times \vec{B} = \mu_0 \vec{j} \tag{10}$$

Equations (6), (7) and (8) are written for electrons, ions and neutral atoms. In Eq.(6), the quantity S describes creation and destruction of particles as a result of ionization and recombination. ρ and μ, in Eq.(7), designate the mass density and the viscosity, respectively. $\vec{F}$ includes the Lorentz force and all forces arising from friction between the various fluids (including resistivity). A "generalized" version of Ohm's law is obtained from the electron momentum equation, Eq.(7), by putting the viscosity equal to zero. The "temperature", T, in Eq.(8), is defined as p/n, and Q is the thermal conductivity divided by the Boltzmann constant. W is an energy source (or sink) which describes the following phenomena: (a) energy equipartition, (b) heating due to dynamical friction, including "Joule heating", (c) ionization and recombination, and (d) viscous heating of ions and neutral atoms. The remaining symbols in Eqs (6) - (10) are defined as usual. The MHD equations are written in finite difference form and solved by an implicit Lagrangian method [12].

The physical model outlined above is basically the same as the standard MHD model [17] with the important exception that, here, we have included electron inertia. This is essential for a realistic treatment of high-frequency magnetic fields and currents.

4. COMPARISON BETWEEN MHD CALCULATION AND EXPERIMENT

Let us first summarize the main parameters of the experiment [8, 9] (Table I).

A complete set of measurements on this apparatus has been reported elsewhere [9]. Here we wish to consider the magnetic-field and electron-density distributions.

TABLE I. MAIN EXPERIMENTAL PARAMETERS

Internal diameter of discharge tube	4.9 cm
Length of tube (distance between z-electrodes)	48.8 cm
Maximum amplitude of B_z (B_θ) at inner wall of discharge tube	2.1 (2.3) kG
Frequency of oscillation of B_z and B_θ	3.1 MHz
Phase difference between B_z and B_θ, at the wall	90°
Duration of oscillating B_z and B_θ fields	2.3 μs
Filling gas	He
Initial gas pressure	60 mTorr

MHD calculations, using the model described in the previous section, have been performed with the aim of simulating experimental conditions as realistically as possible. In addition to the parameters listed above, certain assumptions had to be made concerning the initial and boundary conditions to be used in the calculations. As an initial condition, we have taken a uniformly distributed, 30% preionized gas, at a temperature of 1 eV. Furthermore, a constant flux of particles (10^{20} cm^{-2} s^{-1}) from the wall into the discharge tube has been assumed. This assumption is deduced from and consistent with measurements [9]. It is not necessary for the operation of the code.

The comparison between measurements and calculations is shown in Figs 1, 2 and 3, for the three resistivity models (see section 2). As a typical example, we have chosen the results at 1.5 μs after the start of the experiment. Similar graphs are obtained at other times. The parameter α is an arbitrary factor by which the anomalous part of the resistivity has been multiplied. For α = 1, the anomalous resistivity is as given by Eqs (1'), (2') and (3), and for α = 0, the resistivity is purely classical. It is evident that, as we add more and more anomalous resistivity, the differences between theoretical curves and experimental points first decrease and then increase again. This suggests that there is, for each case, some optimum value of α. To find these optimum α's, we have computed the quantity

$$\overline{(\Delta B_\theta)^2} = \frac{1}{t_2 - t_1} \frac{1}{R^2} \int_{t_1}^{t_2} \int_0^R (B_{\theta_{meas}} - B_{\theta_{calc}})^2 \, 2\, r\, dr\, dt \tag{11}$$

$$(t_1 = 1\ \mu s,\ t_2 = 2\ \mu s,\ R = 2.45\ cm)$$

which is a space-time average of the square of the difference between measured and calculated azimuthal magnetic fields. This quantity is plotted in Fig. 4, as a function of α, for the various resistivity models. Each curve possesses a well defined minimum. The co-ordinates of the minima are listed in Table II.

It should be pointed out that $\alpha_{min,\,Bohm} = 1.0$, for example, does not imply that we are actually observing "Bohm resistivity", because we have introduced the factor (v_D/v_e), a quantity which is always less than unity.

The mean squared difference between measured and calculated electron densities, $\overline{(\Delta n_e)^2}$, is not being considered here. As can be seen from Figs 1, 2 and 3, this quantity is quite small and its dependence on α is weak. However, it should be noted that the minimum $\overline{(\Delta B_\theta)^2}$ roughly coincides with the minimum $\overline{(\Delta n_e)^2}$.

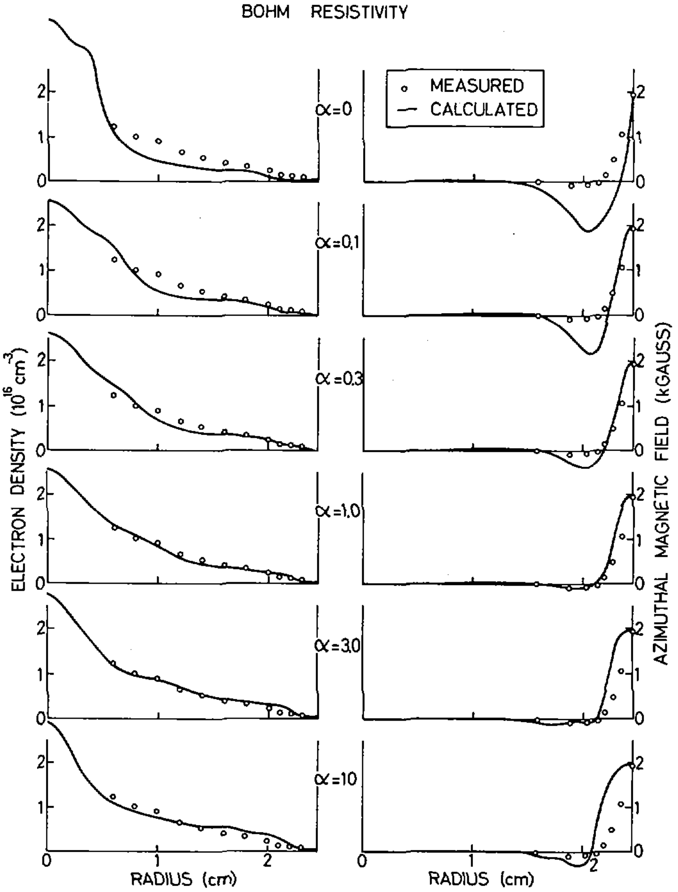

FIG. 1. Measured and calculated electron density and magnetic field distributions at 1.5 μs (classical + Bohm resistivity).

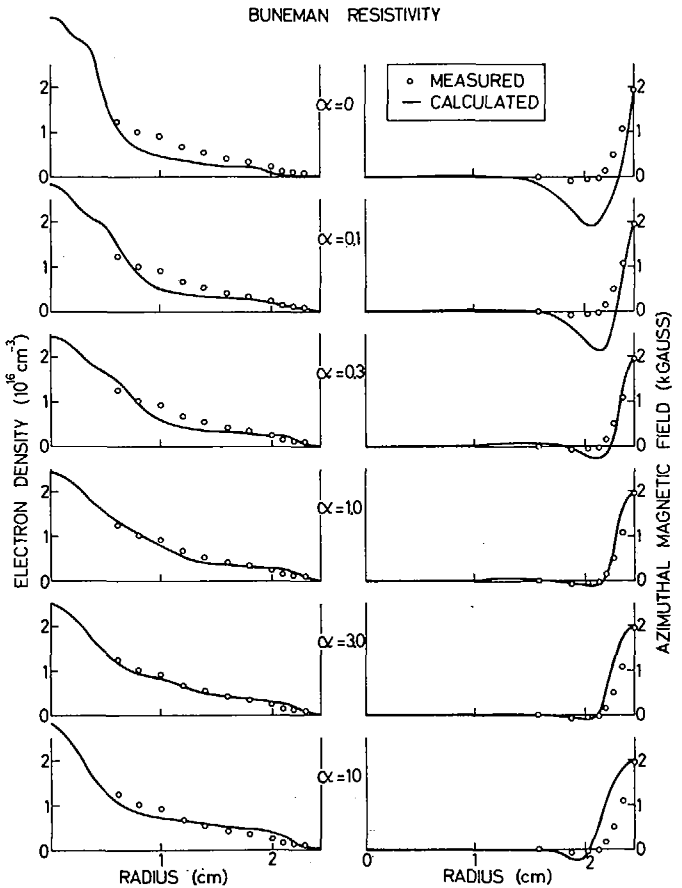

FIG. 2. Measured and calculated electron density and magnetic field distributions at 1.5 μs (classical + Buneman resistivity).

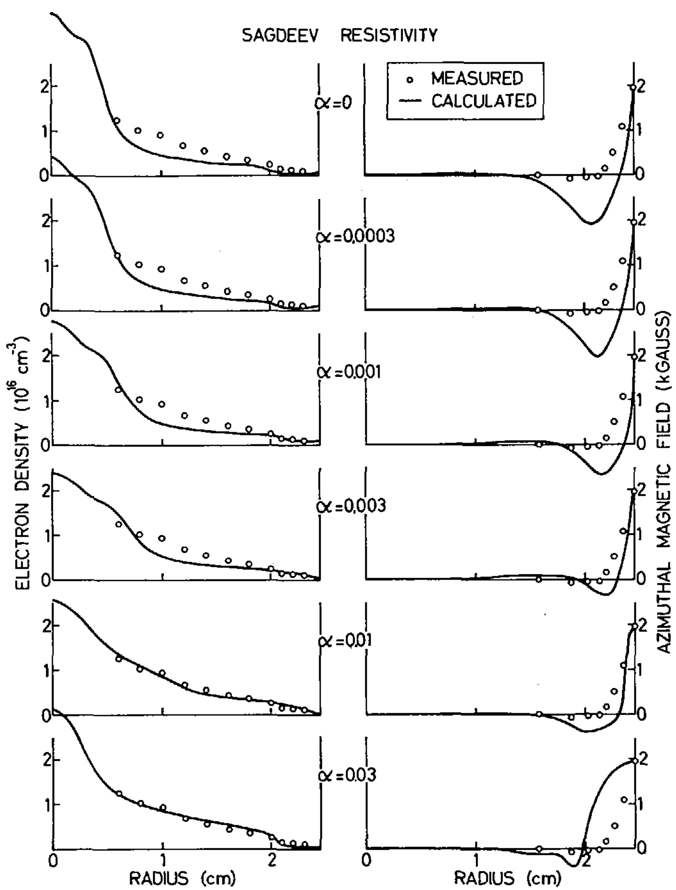

FIG. 3. Measured and calculated electron density and magnetic field distributions at 1.5 μs (classical + Sagdeev resistivity).

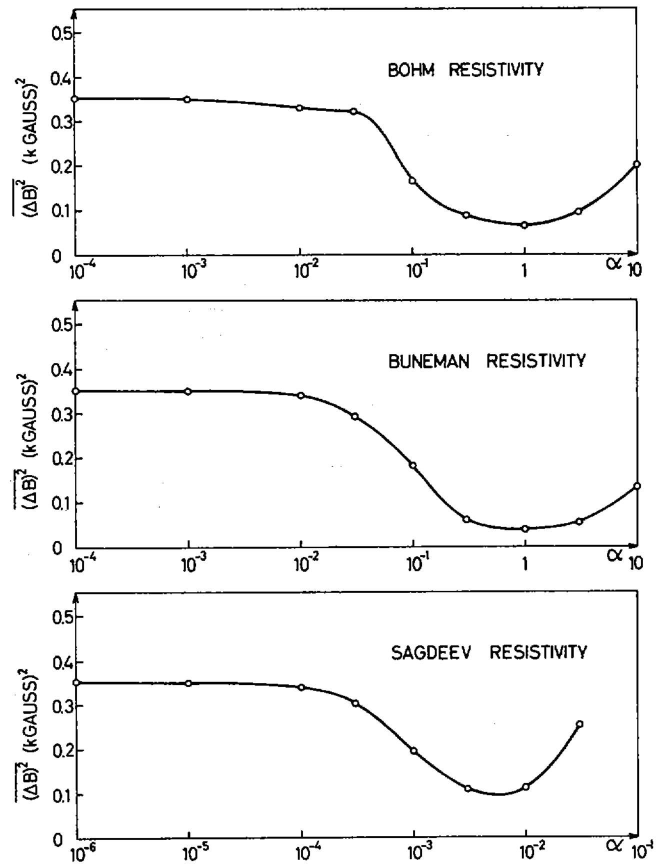

FIG.4. Mean squared difference between measured and calculated azimuthal magnetic fields, $\overline{(\Delta B_\theta)^2}$, for three resistivity models.

TABLE II. CO-ORDINATES OF MINIMA

	α_{min}	$(\Delta B_\theta)^2_{min}\,(kG)^2$
Bohm	1.0	0.0065
Buneman	1.0	0.04
Sagdeev	6×10^{-3}	0.10

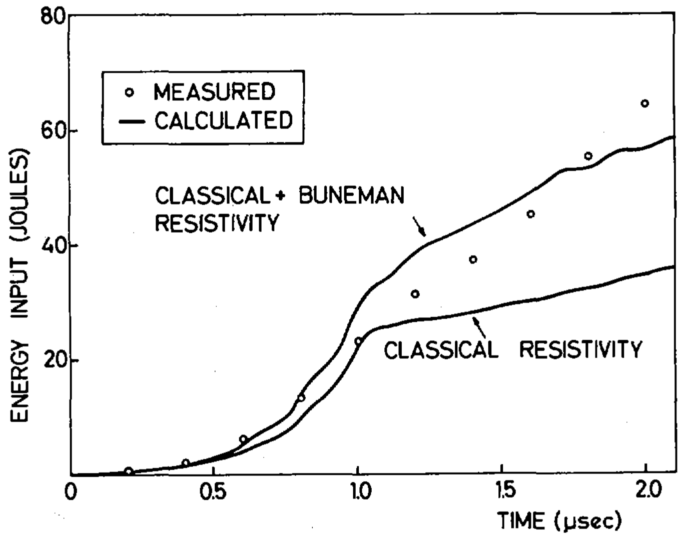

FIG.5. Measured and calculated energy input as a function of time.

Figure 5 shows a comparison between the measured and calculated energy inputs, as a function of time. Again, it is evident that the calculation using anomalous resistivity (Buneman, α = 1.0) agrees much better with the measurements than does the classical calculation.

The ratio between anomalous and classical resistivity, of course, varies considerably with position and time. Within the current-carrying skin layer, this ratio is usually between 10 and 20.

5. CONCLUSIONS

For the particular experiment that we are considering, we have shown that MHD calculations using an anomalously large electrical resistivity reproduce the measurements much more accurately than do those using classical resistivity only. The Bohm and Buneman formulae (multiplied by the ratio of the electron drift velocity to the electron thermal speed, as indicated in Eqs (1') and (2')), lead to very similar results, the Buneman model producing a slightly better fit to the measurements than the Bohm model. The Sagdeev resistivity does *not* give as good agreement as do the other two; it must be multiplied by a small number ($\sim 10^{-2}$) if the results are to be meaningful at all.

ACKNOWLEDGMENTS

The author wishes to thank Professor E.S. Weibel, Drs A. Heym, I.R. Jones and F.S. Troyon for many fruitful discussions. He appreciates the help and cooperation of the staff of the "Centre de Calcul de l'Ecole

Polytechnique Fédérale, Lausanne" and the staff of the "Rechenzentrum der Eidgenössischen Technischen Hochschule, Zürich".

This work was supported by the "Fonds National Suisse de la Recherche Scientifique".

REFERENCES

[1] COPPI, B., MAZZUCATO, E., Physics Fluids 14 (1971) 134.
[2] SANTINI, F., COPPI, B., DOBROWOLNY, M., in Controlled Fusion and Plasma Physics (Proc. 4th Europ. Conf. Rome, 1970).
[3] SIZONENKO, V.L., STEPANOV, K.N., Nucl. Fusion 10 (1970) 155.
[4] BUNEMAN, O., Phys. Rev. 115 (1959) 503.
[5] HAMBERGER, S.M., JANCARIK, J., Phys. Rev. Letts 25 (1970) 999.
[6] DUPREE, T.H., Phys. Rev. Letts 25 (1970) 789.
[7] BORIS, J.P., DAWSON, J.M., ORENS, J.H., ROBERTS, K.V., Phys. Rev. Letts 25 (1970) 706.
[8] JONES, I.R., LIETTI, A., PEIRY, J.-M., Plasma Physics 10 (1968) 213.
[9] BERNEY, A., HEYM, A., HOFMANN, F., JONES, I.R., Plasma Physics (to be published).
[10] SPITZER, L., Jr., Physics of Fully Ionized Gases, John Wiley, New York (1962).
[11] HOFMANN, F., in Controlled Fusion and Plasma Physics, (Proc. Conf. Rome, 1970).
[12] HOFMANN, F., Lausanne Report LRP 46/71 (1971).
[13] BODIN, H.A.B., NEWTON, A.A., Physics Fluids 12 (1969) 2175.
[14] SAGDEEV, R.Z., Proc. Symp. Appl. Math., 18 (1967) 281.
[15] McCARTAN, J., private communication (1970).
[16] BEACH, A.D., et al., Nucl. Fusion 9 (1969) 215.
[17] HAIN, K., HAIN, G., ROBERTS, K.V., ROBERTS, S.J., KÖPPENDÖRFER, W., Z. Naturforsch. 15a (1960) 1039.

DYNAMIC STABILIZATION OF THE m = 1 MODE ON A SCREW PINCH

G. BECKER, O. GRUBER, H. HEROLD
Max-Planck-Institut für Plasmaphysik,
Euratom Association, Garching, Munich
Federal Republic of Germany

Abstract

DYNAMIC STABILIZATION OF THE m = 1 MODE ON A SCREW PINCH

Dynamic stabilization of the helical m = 1 instability characteristic for the high-β screw pinch was studied in the linear device Isar-III (T_i = 50 to 200 eV; $\beta \approx 0.5$). The growth rates ω_i and wave-lengths of these modes were found to be very similar in the toroidal and linear "Isar" screw pinches for adequate plasma parameters. Mainly two methods of dynamic stabilization were investigated: 1. Superimposing an axially uniform h.f. B_z-field $\tilde{B}_z$ on the quasi-steady B_{z0}; 2. Superimposing an h.f. axial current $\tilde{I}_z$ on the screw pinch. Preliminary experiments were done with the magnetic field configuration of a standing wave.

The stabilizing effect of the axially uniform $\tilde{B}_z$ is very probably caused by inertial forces in the oscillating plasma column. If one works with two stabilizing frequencies ω_s, a stabilizing condition $\epsilon > C\omega_i/\omega_s$ holds ($\epsilon = \tilde{B}_{z0}/B_{z0}$). The experimentally determined C values were about 1.5 to 2.5. It is further demonstrated that the fulfilment of this condition is facilitated when working in resonance with the natural plasma oscillation. The application of the $\tilde{B}_z$-method is limited by wall breakdown.

Oscillating currents $\tilde{I}_z = \tilde{I}_{z0} \sin \omega_s t$ with ω_s = 4.8 and 8 × 10^6 s^{-1} were added to the quasi-stationary I_{z0} to study the stabilization by dynamic shear. Magnetic-probe measurements revealed that for both ω_s the $\tilde{I}_z$ (after initial transients) do not penetrate into the dense plasma column. Nevertheless, a reduction of the m = 1 growth rate occurred for $\tilde{I}_{z0} \approx I_{z0}$ which was the higher the greater the $\tilde{I}_z$-flow close to the plasma core. The skin depths observed for the $\tilde{I}_z$ were larger than those expected from classical theory in accordance with a measured high anomalous resistivity.

1. INTRODUCTION

Experimental evidence indicates that most of the configurations presently under consideration for high-β toroidal plasma containment predominantly exhibit m = 1 instabilities. Thus, dynamic control of these modes is an interesting prospect. This paper describes experiments on dynamic stabilization of the helical m = 1 modes characteristic of hot high-β screw pinches. The experiments were carried out in a linear screw pinch. This is advantageous because the m = 1 modes are well isolated there from other instabilities and their growth rate can easily be controlled by variation of the axial current. Furthermore, the growth rate and the wave-length of the m = 1 instability were found to be about the same in a linear and a toroidal (aspect ratio 5) high-β screw pinch for adequate plasma parameters [1, 2]. Obviously, neither the end effects nor the effects of toroidal curvature strongly affect m = 1 growth. Thus, the stabilization experiments may have some relevance for the toroidal screw pinch, too, although more complicating side effects are to be expected.

Mainly two basic methods of dynamic control were studied. Firstly, the plasma surface was made to oscillate by an axially uniform high-frequency component of the B_z-field. Special attention was given to the possibility of working in resonance with natural plasma oscillation (m = 0, k = 0) to save h.f. energy. In a second approach, an oscillating component was superimposed on the longitudinal current to study the effects of dynamic shear. Preliminary experiments were also carried out with the magnetic field configuration of a standing wave. First results on the $\tilde{B}_z$-stabilization were reported in Ref. [3]. Related experimental work to the $\tilde{I}_z$-stabilization is given in Refs [4, 5], theory in Refs [8 - 10].

2. EXPERIMENTS

2.1. Apparatus and plasma properties

The plasmas used in the stabilization experiments were produced in the linear Isar-III screw pinch. Figure 1 gives a schematic of the basic screw-pinch circuits and the circuits for the h.f. stabilization. The coil length was 100 cm, the electrode distance 120 cm and the free diameter of the quartz tube 10.5 cm. In most of the experiments the basic pinch plasma had a $k(T_e + T_i)$ of 50 to 300 eV, β on the axis ≥ 0.5, a density on the axis of about 5×10^{16} cm^{-3} and a radius of 1.5 cm. All values are taken at maximum compression (4 μs). The plasma life-time characterized by the 1/e drop in line mass caused by end loss was about 8 μs. The z-and θ-currents were adjusted to be strictly in phase (see Fig. 4) in most of the experiments. $B_z^2 \gg (B_\theta)^2_{rp}$ was always fulfilled. Thus plasma containment was achieved by the B_z-field.

2.2. Stability of the basic screw pinch

Helical m = 1 instabilities develop after the dynamic phase of the screw pinch and cause a destruction of the pinch by wall contact. The growth rates vary approximately linearly with the total I_z as shown in Fig. 2 and are well in agreement with those predicted by theory [6, 7]. Also a comparison with the ω_i of a toroidal screw pinch with almost identical plasma parameters for the same k-mode is given in Fig. 2. In most experiments

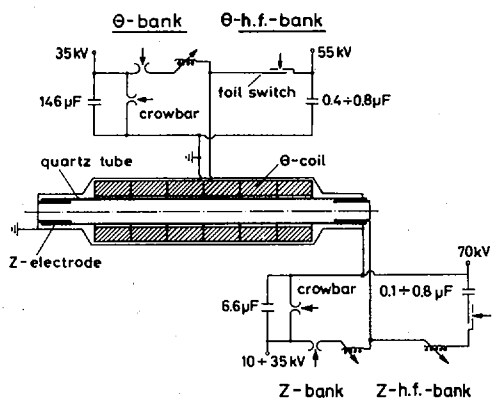

FIG. 1 Schematic of linear screw pinch and circuit diagram.

the wave length of the unstable helix was about 1 m, roughly in accordance with numerical stability calculations (similar to those in Ref. [7]) using typical experimental B_z, B_θ and density distributions (Fig. 3). As can be seen in Fig. 3, a considerable fraction of I_z flows outside the dense plasma column in a dilute plasma with $n_e \lesssim 2 \times 10^{14} cm^{-3}$. The width of the current profile can easily be changed by short delays of the onset of the z and θ-discharge. A more peaked B_θ profile (higher current density in the dense plasma) gives an appreciable enhancement, and a broader profile gives a reduction of ω_i if stability is compared for constant total I_z current, in agreement with theory [7].

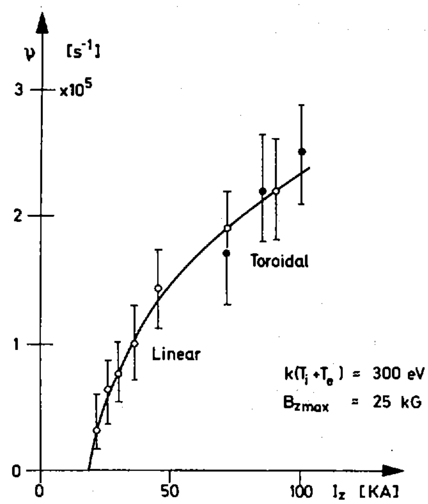

FIG. 2 Growth rates $\nu = \omega_i/2\pi$ for the m = 1 instabilities in a linear (circles) and toroidal screw pinch (dots) as a function of total I_z-current

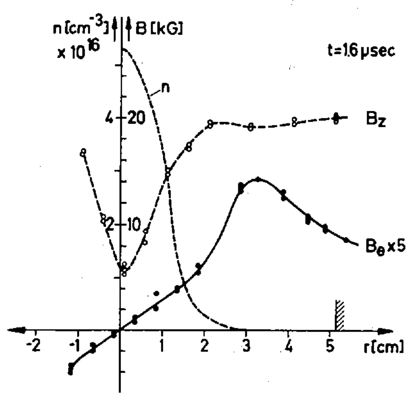

FIG. 3 Radial distribution of B_θ, B_z and density for a linear screw pinch (t = 1,6 μs; P_0 = 40 mTorr; T_i = 150 eV)

2.3. Oscillating B_z-field

2.3.1 Experiments

High-Q capacitors and foil switches with low jitter (30 ns) and low inductance (2 nHy) were used in both of the h.f. circuits. The oscillating B_z-field component was produced and superimposed on the main B_{z0}-field in one common coil ($B_z = B_{z0} + \tilde{B}_{z0} \sin \omega_s t$) (see Fig. 1). The amplitude ratio $\epsilon = \tilde{B}_{z0}/B_{z0}$ could be varied between 0.05 and 0.2. The stabilizing frequencies ω_s were 7×10^6 and 10.5×10^6 s^{-1}. Normally, $\tilde{B}_z$ was switched on when a well compressed pinch plasma had developed but with still some oscillatory motion present, as indicated in Fig. 4. $\tilde{B}_z$ caused an oscillatory axisymmetric motion of the plasma, well observable in streak pictures and density profiles. Provided that ϵ was chosen high enough for a fixed ω_i and with $\omega_s > \omega_i$, normally an appreciable reduction of the m = 1 instability growth could be observed. This is demonstrated in typical stereoscopic streak pictures of the screw pinch taken side-on with and without $\tilde{B}_z$ (Fig. 5a). A lengthening of 5 to 6 μs of the plasma life-time (until wall contact) could be achieved, at most. The residual instability may be related to the drop in the stabilizing amplitude. The 1/e time of the $\tilde{B}_z$-amplitude was about 8 μs for the lower ω_s.

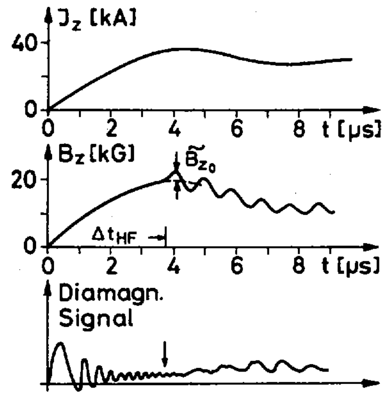

FIG.4 Longitudinal current, B_z-field and diamagnetic signal in a $\tilde{B}_z$-stabilized screw pinch.

Experiments with many different ω_i, adjusted by variation of I_z, and with the two stabilizing frequencies gave a condition $\epsilon > C\ \omega_i/\omega_s$ which had to be fulfilled to observe the above mentioned stabilizing effect on the m = 1 modes. The values of C in the present experiments were found to be 2 ± 0.5. The relative amplitude of the plasma radius motion $\Delta r_p/r_{p0}$ was correlated to ϵ approximately like $\Delta r_p/r_{p0} = \epsilon$. Thus, the stabilizing effect observed shows qualitatively the dependence on frequency and amplitude characteristic for the inverted pendulum. From this it can be concluded that it is likely caused by inertial forces. It should be mentioned that also a slight time variation of the shear $(\mu'/\mu)r_p$ was observed during the B_z-oscillation as is demonstrated in Fig. 6.

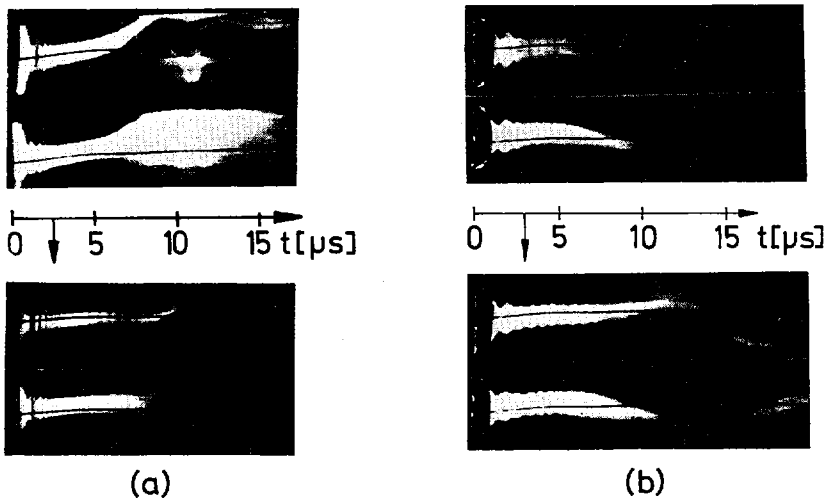

FIG. 5 Stereoscopic streak pictures of screw pinches without (top) and with (bottom) $\tilde{B}_z$-stabilization. Arrow indicates onset of the h.f. discharge. (a: 40 mTorr, deuterium, $\omega_s \neq \omega_0$; b: 320 mTorr, deuterium, $\omega_s = \omega_0$).

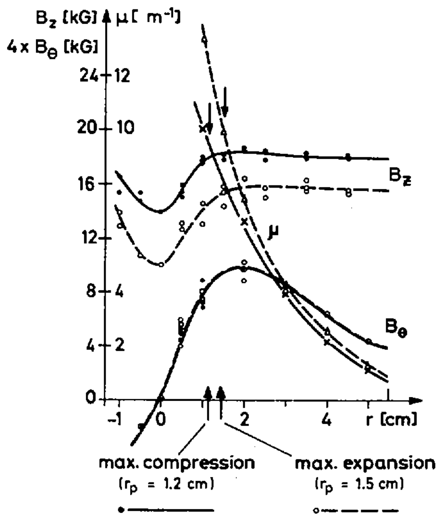

FIG. 6 Radial B_z and B_θ magnetic field distribution and pitch wave number μ, taken at times of successive $\tilde{B}_z$ maxima and minima. Arrows indicate position of plasma radius.

When we attempted to apply higher $\epsilon\,\omega_s$, breakdown in the plasma sheath adjacent to the tube wall occurred. This caused strong damping of the oscillating current. A breakdown condition inferred from theoretical treatment of θ-pinch breakdown [8], $r_g\,\epsilon\,\omega_s \geq 7.5$, ($r_g$ radius of tube wall in cm; ω_s in MHz) holds almost exactly.

A higher $\Delta r_p/r_{p0}$ for a given ϵ should in principle be achievable if the enforced plasma motion is in resonance with the natural radial plasma oscillation ($m = 0$; $k = 0$) of a frequency given by $\omega_0 \approx B_z/\sqrt{M_i}$. ($M_i$ is the line mass). This would save h.f. energy and help to avoid breakdown. Unfortunately, ω_0 is rather high for hot pinches. ω_0/ω_s was between 2 and 5 in the experiments reported up to now. To work in resonance ($\omega_0 = \omega_s$) we increased the line mass in the pinch without changing the B_{z0}-field. The plasma temperature was reduced to 15 eV. Typical resonance phenomena could be observed in these experiments first carried out on a θ-pinch ($I_z = 0$). Phase shifts of about 90° between driving field and radial motion of the plasma occurred. The resonance amplitudes built up within a few radial oscillations and could be driven to "overstability". But the damping factors were found to be sufficient to control the plasma oscillations simply by an appropriate choice of ϵ. When the h.f. fields were applied to the screw pinch a pronounced stabilizing effect occurred as can be seen in Fig. 5b. Under such conditions a reduction of C by about a factor of two was achieved.

2.3.2 Comparison with theory

The $\tilde{B}_z$-field generates cylindrical plasma oscillations. The enforced motion is axially symmetric and a direct stabilization of $m = 1$ by $\tilde{B}_z$ is impossible. An effective mode coupling for $m = 0$ (radial oscillations) and $m = 1$ (instability) is needed. This problem was treated theoretically by several authors. Berge [13] calculated the dynamic effect due to a standing wave magnetic field on $m = 1$ instability. A sharp pressure profile and a rigid displacement of the plasma ($m = 1$; $\nabla\vec{\xi} = 0$) is assumed. There is no dynamic effect in the limiting case of infinite periodicity length (B_z axially uniform), and mode coupling for $m = 0$ and $m = 1$ does not exist. A normal-mode analysis by Wobig and Tasso [14] for a diffuse profile and inertial dominating forces yields a coupling between $m = 0$ and $m = 1$ motion. But the coupling force calculated for a Gaussian profile is about one order of magnitude smaller than the experimentally determined value. A similar result can be derived from a paper by Freidberg and Wesson [15]. They calculated the coupling of an axially symmetric force (centrifugal force) with the $m = 1$ instability for all k-values, assuming a diffuse profile and $\nabla\vec{\xi} = 0$.

The models for a diffuse profile are more realistic but they also cannot explain the experimental effect quantitatively. One possible explanation for this is that the plasma oscillations are always symmetric with respect to the plasma axis when rigid displacement ($\nabla\vec{\xi} = 0$) for the $m = 1$ motion is assumed. A considerably more effective mode coupling is expected and confirmed by estimates for a compressible model. Here, the plasma profile is no longer axially symmetric, for example, because the destabilizing $m = 1$ force does not accelerate all plasma elements equally. Such a compressible model, including inertial forces, may better explain the experimental results.

2.4. Oscillating axial current

H.f. currents $\tilde{I}_z$ with amplitudes of 15 to 50 kA were fed into the screw pinch using the same electrodes for $\tilde{I}_z$ and the quasi steady current I_{z0} (Fig. 1). $\tilde{I}_z$ and I_{z0} usually had comparable amplitudes. ω_s was 1.6×10^6; 4.8×10^6 and $8 \times 10^6\ s^{-1}$.

In part of the experiments, B_{z0} was increased from the normally used 18.5 kG to 47 kG by reduction of the coil length from 100 cm to 50 cm. Measurements of the B_θ-field distributions with probes revealed that the h.f. current does not penetrate into the dense plasma core, but flows in the dilute plasma between a radius of about 3 cm (plasma radius $\approx$ 1.5 cm) and the tube wall as shown in Fig. 7 for $\omega_s = 4.8 \times 10^6\ s^{-1}$. I_{z0} in the dense plasma was only slightly affected. The penetration depth of $\tilde{I}_z$ into the dilute plasma was by far higher than the classical skin depth. It decreased with ω_s and was higher in discharges with elevated B_{z0} for a given ω_s. Variation of the pre-ionization and of the electrode geometry and distance did not change the current distribution. Quartz limiters (free diameter 5 cm) shifted the current distribution only slightly inward. The average specific resistivity

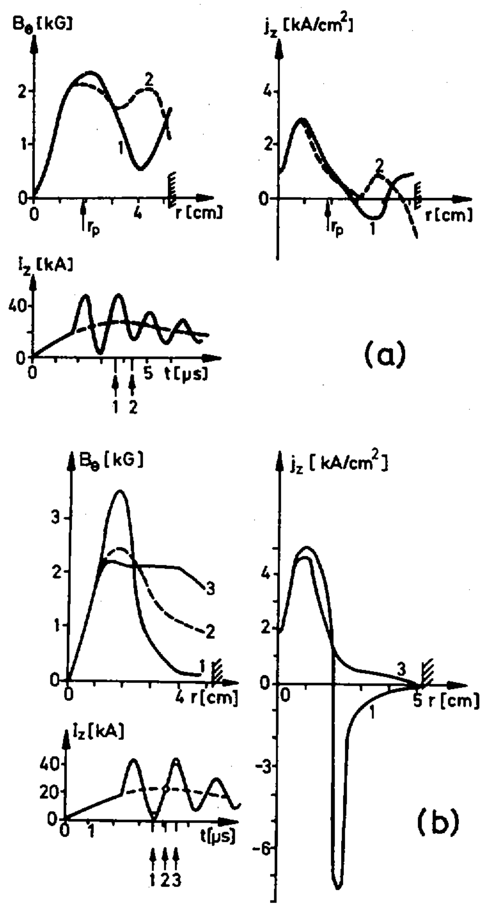

FIG. 7 Radial B_θ and current density distribution in an $\tilde{I}_z$-stabilized screw pinch taken at the indicated times:

a) I_{z0} = 27 kA; $\tilde{I}_{z0}$ = 23 kA; B_{z0} = 18.5 kG

b) I_{z0} = 25 kA; $\tilde{I}_{z0}$ = 23 kA; B_{z0} = 47 kG of the h.f. current carrying plasma was determined by measurements of the $\tilde{I}_z$-damping. The losses in the outer circuit and in the plasma between coil end and electrodes were considered. ρ_{ex} averaged over the width of the current profile was found to be 6×10^{-2} Ωcm (13×10^{-2} Ωcm) at a B_{z0} of 18.5 kG, (47 kG) for $\omega_s = 4.8\times10^6$ s^{-1} (3.7×10^6 s^{-1}). The classical resistivity is calculated to be at least a factor 10^2 to 2×10^2 lower if $T_e \geq 20$ eV is assumed. The contribution of neutrals (ionization by I_{z0}) and impurities is considered to be small. Anomalous high resistivity under similar conditions was reported in Scylla-IV and Tokomak TM-3 experiments [11, 12]. In the present experiment, the applied electric field was considerably higher than the critical field. But no fast electrons (detection limited to E ≥ 15 keV) could be found by means of soft X-ray measurements. This points to mechanism suppressing runaways. Ion sound instability cannot be excluded since $V_D > \sqrt{(T_e/m_i)}$ is fulfilled and, reasonably, $T_e > T_i$, owing to I_{z0} current heating (electron drift velocity $V_D = 2\times10^7$ cm/s; $V_{the} = 2.5\times10^8$ cm/s; $\omega_{pe} \approx \omega_{ge}$; electron plasma and gyro frequency).

Application of $\tilde{I}_z$ to the θ-pinch ($I_{z0} = 0$) did not affect its stability in agreement with Refs [4, 5]. This is expected because $\tilde{I}_z$ does not penetrate into the dense plasma column.

When $\tilde{I}_z$ was superimposed on the screw pinch a reduction of the m = 1 growth rates was observed even when $\tilde{I}_z$ flows in the dilute plasma, only. The stabilizing effect for a given j_z-distribution scales roughly with $\tilde{I}_{z0}$ (the amplitude of $\tilde{I}_z$) but contrary to the $\tilde{B}_z$-stabilization with ω_i/ω_s provided $\omega_s > \omega_i$. Better stabilization occurs when more h.f. current flows close to the dense plasma core (in accordance with the statements of section 2.2 on the influence of radial current distribution on stability). Under typical conditions ($\omega_s = 3.7\times10^6$ s^{-1}; $\tilde{I}_{z0} = 35$ kA) a reduction of ω_i by a factor 2.5 could be achieved. A rough theoretical model that starts with the equations of motion of the m = 1 mode (sharp plasma profile) and that introduces a dynamic shear by means of $\tilde{I}_z$ (Mathieu's formalism) qualitatively describes the observed dynamic effect with respect to ω_i, ω_s and $\tilde{I}_{z0}/I_{z0}$.

Experimental side effects complicate the interpretation. They have to do (compare field profiles of Fig. 7a and 7b) with initial transients (at $t_{h.f.}$) of time scale 1 μs leaving "frozen-in" B_θ-distortions and possibly with strong heating by the h.f. currents. Also luminous wall effects appeared which may be caused by part of $\tilde{I}_z$ flowing at the wall (< 10 - 20%).

2.5. Magnetic field configuration of a standing wave

In preliminary experiments 6 loops positioned inside the θ-coil (axial distance 16 cm) were made to oscillate ($\omega_s = 4.5\times10^6$ s^{-1}) to give a $\tilde{B}_z$-amplitude at r_p of ± 0.8 kG. No stabilizing effect could be observed. The stabilization condition given by Berge [16] was not fulfilled. Wall breakdown occurred in the strongly inhomogeneous loop fields.

3. CONCLUSIONS

Appreciable stabilizing effects on a non-localized m = 1 instability could be achieved by the method of enforced plasma oscillation. Relative field amplitudes ϵ of 0.1 to 0.2 are necessary for $\omega_s \gg \omega_i$. The effect is higher than expected from idealized theories. Dynamic shear caused by oscillating axial currents flowing outside the dense plasma column reduces m = 1 growth, too.

Side effects govern the methods of dynamic stabilization. In the $\tilde{B}_z$-method $\omega_s \epsilon$ is limited by wall breakdown. For $\tilde{I}_z$-stabilization, the existence of a dilute plasma outside the core is important. Anomalous resistivity occurs therewhich determines the skin depth and causes excessive h.f. energy loss.

REFERENCES

[1] WILHELM, R., ZWICKER, H., Z. Physik 240 (1970) 295.
[2] GRUBER, O., HEROLD, H., to be published in Z. Physik.
[3] GRUBER, O., BECKER, G., HEROLD, H., API Conference Proceedings No. 1, (1970) 286.
[4] GRIBBLE, R.F., LITTLE, E.M., QUINN, W.E., RIBE, F.L., SAWYER, G.A., THOMAS, K.S., WELDON, D.M., in Controlled Fusion and Plasma Physics (Third Europ. Conf. Utrecht) (1969) 79.
[5] GORDIENKO, V.P., DUBOVOI, L.V., ROIFE, I.M., Plasma Physics 10 (1968) 499.
[6] SCHUURMANN, W., BOBELDIJK, C., DEVRIES, R.F., Plasma Physics 11 (1969) 495.
[7] FREIDBERG, J.P., Physics Fluids 13 (1970) 1812.
[8] WEIBEL, E.S., Physics Fluids 3 (1960) 946.
[9] TROYON, F., LRP 10-63, Lausanne (1963).
[10] BOBYREV, N.A., FEDYANIN, O.I., Zh. tekh. Fiz. 33, (1963) 1187 [Sov. Phys. Tech. Phys. 8, 887 (1964)]
[11] LITTLE, E.M., NEWTON, A.A., QUINN, W.E., RIBE, F.L., Plasma Physics and Controlled Nuclear Fusion Research, Vol II. (1969) 555.
[12] ARTSIMOVICH, L.A., et al., in Plasma Physics and Controlled Nuclear Fusion Research (Proc. Conf. Novosibirsk, 1968) 1 (1969) 157.
[13] BERGE, G., Physics Fluids 13 (1970) 103.
[14] WOBIG, H., TASSO, H., API Conf. Proceedings No. 1, (1970) 239.
[15] FREIDBERG, J.P., WESSON, J.A., Physics Fluids 13 (1970) 1117.
[16] BERGE, G., FREIDBERG, J.P., Los Alamos Report LA-DC 11969 (1970).

ПРОХОЖДЕНИЕ ИОННО-ЗВУКОВОГО БАРЬЕРА И УСТОЙЧИВОСТЬ ЗАМАГНИЧЕННОЙ ТОРОИДАЛЬНОЙ ПЛАЗМЫ ПРИ ПРОТЕКАНИИ ВЧ-ТОКА

Р.А.ДЕМИРХАНОВ, Д.Г.БАРАТОВ, А.Г.КИРОВ, В.Г.МЕРЕЖКИН, В.Н.ЖАРИКОВ, Н.И.МАЛЫХ, В.А.ЖДАНОВ
Физико-технический институт Государственного комитета по использованию атомной энергии СССР, Сухуми,
Союз Советских Социалистических Республик

Abstract — Аннотация

PENETRATION OF THE ION-ACOUSTIC BARRIER AND STABILITY OF A MAGNETIZED TOROIDAL PLASMA UNDER CONDITIONS OF HIGH-FREQUENCY CURRENT FLOW.

In this paper the results are reported of experimental investigations into the phenomena which occur when a longitudinal high-frequency current flows along a magnetized plasma column, $\tilde{\beta}$ being greater than unity. The skin effect of the HF field is investigated as a function of plasma density and temperature and of ion mass. In addition, the conditions of the build-up and stabilization of magnetohydrodynamic instabilities are determined as a function of the parameters of the plasma and the magnetic fields. Experiments were carried out on the R-0 and RT-2 toroidal devices under the following conditions: plasma density $1 \times 10^{13} - 5 \times 10^{14}\ \mathrm{cm^{-3}}$, temperature 5-70 eV, strength of the quasi-constant toroidal magnetic field up to 12 kOe and HF current in the plasma up to 2.5 kA with a frequency of 0.2-1.9 Mc/s. The experimental investigations showed the following: (1) Over a wide range of plasma densities and temperatures and of ion mass (A = 1-131) the skin effect of the HF field is determined by Coulomb collisions. The role of ion-acoustic turbulence in the broadening of the skin layer and in the attainment of the effective frequency of electron collisions is negligible. The skin-layer depth is practically independent of the ion mass. The current velocity of the electrons in the skin layer is much greater than the ion-sound velocity; (2) When an HF current flows in a plasma a resonance build-up a helical magnetohydrodynamic instability may occur under certain circumstances. It is shown that a high level of macroscopic stability is achieved when the frequency of the HF field is of an order greater than the magnetohydrodynamic instability increment. Under these conditions the energy lifetime is close to that obtained by the classical diffusion formula, where the depth of the collisional skin layer is taken as the characteristic diffusion dimension.

ПРОХОЖДЕНИЕ ИОННО-ЗВУКОВОГО БАРЬЕРА И УСТОЙЧИВОСТЬ ЗАМАГНИЧЕННОЙ ТОРОИДАЛЬНОЙ ПЛАЗМЫ ПРИ ПРОТЕКАНИИ ВЧ-ТОКА.

В докладе приводятся результаты экспериментальных исследований явлений, происходящих при протекании по замагниченному плазменному шнуру продольного высокочастотного тока при $\tilde{\beta} > 1$. Исследовано скинирование ВЧ-поля в зависимости от плотности плазмы, ее температуры и массы ионов, а также определены условия раскачки и стабилизации МГД-неустойчивости в зависимости от параметров плазмы и магнитных полей. Эксперименты проводились на тороидальных установках Р-0 и РТ-2 в условиях: плотность плазмы – $1 \cdot 10^{13} \div 5 \cdot 10^{14}\ \mathrm{см^{-3}}$, температура – $5 \div 70$ эВ, напряженность квазипостоянного тороидального магнитного поля – до 12 кэ, ВЧ-ток в плазме – до 2,5 кА при частоте $0{,}2 \div 1{,}9$ МГц. В результате экспериментальных исследований показано: (1) В широком диапазоне плотности плазмы, температуры и массы ионов ($A = 1 \div 131$) скинирование ВЧ-поля определяется кулоновскими столкновениями. Вклад ионно-звуковой турбулентности в уширение скин-слоя и в эффективную частоту столкновений электронов незначителен. Глубина скин-слоя практически не зависит от массы ионов. Токовая скорость электронов в скин-слое много больше скорости ионного звука. (2) При протекании ВЧ-тока в плазме при определенных условиях возможна резонансная раскачка винтовой МГД-неустойчивости. Показано, что высокий уровень макроскопической устойчивости достигается, когда частота ВЧ-поля на порядок превышает инкремент МГД-неустойчивости. В этих условиях энергетическое время жизни близко к величине, полученной по формуле классической диффузии, в которой в качестве характерного диффузионного размера взята глубина столкновительного скин-слоя.

ВВЕДЕНИЕ

При использовании ВЧ-полей мегагерцового диапазона частот типа Е-волны[1] для динамической стабилизации и нагрева замагниченных плазменных шнуров возникает ряд физических проблем. К ним, в частности, относится вопрос о скорости диссипации энергии ВЧ-поля в области скин-слоя, т.е. о величине эффективной частоты столкновений электронов ν_{eff}. При ν_{eff}, значительно превышающей кулоновскую частоту столкновений ν_{ei}, использование ВЧ-полей для динамической стабилизации плазмы может оказаться энергетически невыгодным. Такие высокие значения ν_{eff}, как показывает теория, могут возникать при достижении токовой скоростью электронов $\tilde{v}_e$ ионно-звукового барьера C_s. Увеличение ν_{eff} должно привести к уширению скин-слоя относительно его классического значения. Поэтому получение информации о реальном значении ν_{eff} путем изучения глубины скин-слоя в условиях, близких режиму динамической стабилизации ($\tilde{\beta} > 1$, квазинепрерывный режим действия ВЧ-поля), представляет определенный интерес.

Другая проблема связана с тем, что при конечной глубине скин-слоя область гидродинамической неустойчивости типа Шафранова-Крускала и ее инкременты могут существенно измениться по сравнению с результатами существующих теорий, в основе которых лежит предположение о бесконечно тонком скин-слое. Кроме того, вследствие переменности тока возможна дополнительная параметрическая раскачка МГД-неустойчивости.

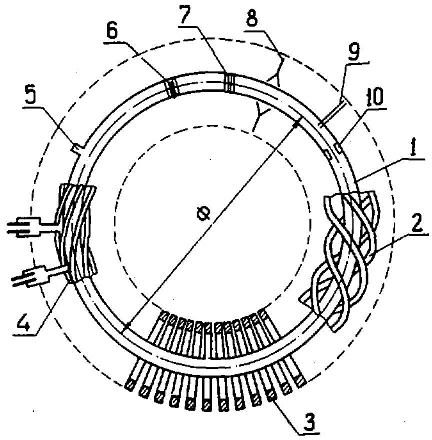

Рис. 1. Принципиальная схема установок Р-0 и РТ-2:
1 – кварцевая разрядная камера, 2 – винтовая стеллараторная обмотка, 3 – катушки квазипостоянного тороидального магнитного поля, 4 – витки винтового ВЧ-контура, 5 – патрубок для оптических измерений, 6 – пояс Роговского, 7 – диамагнитный датчик, 8 – антенны микроволнового интерферометра, 9 – магнитные и двойные электрические зонды, 10 – болометрический датчик.

[1] Электрическое поле направлено вдоль разрядной камеры.

ТАБЛИЦА I. ОСНОВНЫЕ ПАРАМЕТРЫ ЭКСПЕРИМЕНТАЛЬНЫХ УСТАНОВОК Р-0 и РТ-2

Параметры установок	Р-0	РТ-2
1. Большой диаметр тороидальной кварцевой камеры (см)	100	130
2. Диаметр сечения камеры (см)	10	8
3. Напряженность тороидального магнитного поля (кэ)	10	20
4. Длительность полупериода магнитного поля (мсек)	15	15
5. Число заходов винтовой обмотки стеллараторного поля	3	2
6. Число шагов винтового поля	12	12
7. Радиус стеллараторной обмотки (см)	9,2	10
8. Максимальное расчетное значение угла вращательного преобразования	3π	$3{,}5\pi$
9. Максимальное значение среднего шира	0,08	0,02
10. Максимальный ток в винтовой обмотке (кА)	70	100
11. Напряженность ВЧ-поля нулевой моды (э) Частота поля (МГц)	200 0,2	200 1,6 ÷ 1,9
12. Напряженность ВЧ-поля "вращающийся квадруполь" (э) Частота поля (МГц)	600 0,5	– –
13. Число винтовых витков ВЧ-контура	8	8
14. Число оборотов винтового ВЧ-контура	1	3
15. Длительность импульса ВЧ-поля (мсек)	0,5 ÷ 1,5	1

В данном докладе приводятся результаты экспериментальных исследований глубины скин-слоя (часть I) и МГД-устойчивости (часть II) замагниченного плазменного шнура при $\tilde{\beta} > 1$ в широком диапазоне изменения плотности плазмы, ее температуры, массы ионов и напряженностей ВЧ- и квазипостоянных магнитных полей. Эксперименты были проведены на идентичных установках Р-0 и РТ-2, схемы и основные параметры которых приведены на рис. 1 и в табл. I.

ЧАСТЬ I. СКИНИРОВАНИЕ ВЧ-ПОЛЯ В ЗАМАГНИЧЕННОМ ПЛАЗМЕННОМ ШНУРЕ

1. Вопрос о том, вносят ли мелкомасштабные турбулентности существенный вклад в эффективную частоту столкновений электронов при протекании ВЧ-токов в скин-слое при $\tilde{\beta} > 1$ является важным для метода ВЧ-динамической стабилизации. В бесстолкновительном режиме ($\nu_{ei} < \omega$) токовая скорость электронов в скин-слое $\tilde{v}_e$ при $\tilde{\beta} \gg 1$ удовлетворяет условию $C_s < \tilde{v}_e < v_{Te}$. Поэтому можно ожидать развития в скин-слое интенсивных ионно-звуковых неустойчивостей и его соответствующего уширения.

В этом смысле, с физической точки зрения, задача о ВЧ-скин-слое примыкает к проблеме турбулентного нагрева плазмы сильным импульсом тока и возникновению большого аномального сопротивления [1]. Так, расчет глубины скин-слоя в предположении высокого уровня ионно-звуковых неустойчивостей и "замораживания" токовой скорости электронов в районе ионно-звукового барьера C_s приводит к значению $\delta_T = (C/\omega p i)(1/\sqrt{\beta})$ [2], что соответствует очень высокой эффективной частоте столкновений электронов.

Насколько сильно эффекты, характерные для турбулентного нагрева, будут проявляться в режимах динамической стабилизации, т.е. "заморозится" ли токовая скорость электронов в скин-слое в районе ионно-звукового барьера и будет ли глубина скин-слоя близка δ_T ?

В теоретических работах [3] содержится указание на возможность прохождения ионно-звукового барьера в определенных условиях (в частности, тогда, когда отношение Te/Ti не очень велико). В теоретической работе [4] прямо показано практически непрерывное ускорение электронов вплоть до v_{Te} при достаточно высоком энергетическом времени жизни плазмы. Эти соображения оставляют надежду на возможность проскока ионно-звукового барьера в типичных для ВЧ-динамической стабилизации экспериментальных условиях.

2. Как видно из формулы для δ_T, глубина турбулентного скин-слоя зависит от плотности плазмы, массы ионов и напряженности ВЧ-поля. В данной работе в качестве основной меры, характеризующей вклад ионно-звуковой неустойчивости в эффективную частоту столкновений, принято отношение экспериментальной величины скин-слоя $\delta_{экс}$ к классическому значению $\delta_{\nu_{ei}}$, рассчитанному по экспериментально измеренной электронной температуре плазмы, а также отношение токовой скорости электронов $\tilde{v}_e$ к скорости ионного звука C_s. Обе эти величины исследуются в зависимости от плотности плазмы и массы ионов (H_2, He, Ar, Xe). Измерение глубины скин-слоя при разряде в тяжелых газах (Ar, Xe) позволяет сделать отношение $\delta_{экс}/\delta_T$ и $\tilde{v}_e/C_s$ более контрастным и выяснить зависимость глубины скин-слоя и эффективной частоты столкновений от массы ионов.

В нашей работе [5] при измерении распространения винтового ВЧ-квадрупольного поля в замагниченный плазменный шнур было показано, что в сильно столкновительном режиме ($\nu_{ei} \gg \omega$) величина $\delta_{экс}$ слабо отличается от значения, даваемого классической формулой $\delta_{\nu ei} = C/\omega pe \sqrt{2\nu_{ei}/\omega}$, хотя токовая скорость электронов, особенно для тяжелых газов, превосходит C_s. Однако в экспериментах [5] присутствовали эффекты аномального проникновения ВЧ-квадрупольного поля в плазму, связанные с его винтовым характером. Кроме того, область экспериментальных значений n_e и T_e была относительно узкой. В данной работе, являющейся продолжением работы [5], эксперименты проводятся с ВЧ-полем типа "нулевая мода" (однонаправленные ВЧ-токи в плазме), когда эффекты проникновения, связанные с винтообразностью ВЧ-контура, отсутствуют.

Эксперименты были проведены на установке Р-0, параметры которой приведены в табл. I. Квазипостоянное поле H_0 было стеллараторным трехзаходным магнитным полем с $I/H = 9{,}3$, что соответствовало углу вращательного преобразования $i \simeq 25°$ на период поля и позволяло при $H_0 \simeq 5$ кэ обеспечивать равновесие плазменного шнура до $nT \leq 2\cdot 10^{15}$ эВ/см^3. Частота ВЧ-тока была $f = 0{,}2$ МГц, его величина в плазме составляла $\sim 2{,}2$ кА, напряженность ВЧ-магнитного поля на границе плазменного столба составляла $\tilde{H}_\varphi \sim 150$ э. Длительность импульса ВЧ-поля равнялась $\tau \simeq 1$ мсек. Рабочими газами служили водород, гелий, аргон, ксенон при начальных давлениях от $1 \cdot 10^{-4}$ до $1 \cdot 10^{-2}$ тор.

Плотность плазмы измерялась микроволновым интерферометром с $\lambda = 2{,}3$ мм. Распределение плотности плазмы по сечению определялось с помощью локального микроволнового зонда, состоящего из двух тонких волноводов, вводимых в плазменный столб.

Электронная температура, в случае разряда в гелии, определялась по относительной интенсивности линий нейтрального гелия $(J_\lambda = 5048\,\text{Å})/(J_\lambda = 4713\,\text{Å})$, ионная температура плазмы, усредненная по длительности импульса ВЧ-поля, измерялась с помощью спектрографа по допплеровскому уширению спектральных линий атомов соответствующих газов.

Полная энергия плазмы $\langle nT \rangle$ измерялась с помощью диамагнитных датчиков, расположенных на поверхности разрядной камеры.

Распределение ВЧ-магнитного поля в плазме измерялось пятикатушечным магнитным зондом.

В процессе экспериментов квазипостоянное магнитное поле практически не менялось: $H_0 \simeq 4$-5 кэ. При ВЧ-токе в плазме $J_p \simeq 2{,}2$ кА запас устойчивости Шафранова-Крускала q для плазменного шнура, ограниченного конечной магнитной поверхностью, вписанной в разрядную камеру, был равен $q = (H_0 a)/(H_\varphi R) \simeq 2{,}5$. Эффективный радиус плазмы составлял около 3 см. Распределение плотности, измеренное локальным микроволновым зондом, показало, что плазма сосредоточена в пределах магнитной поверхности. Из интерферометрических микроволновых измерений следует, что степень ионизации ~ 100% и средняя по сечению плотность плазмы пропорциональна начальному давлению p_0.

Результаты измерений электронной температуры по относительной интенсивности линий гелия (рабочий газ – гелий) приведены на рис. 2. Электронная температура гелиевой плазмы, рассчитанная из измерений диамагнетизма плазмы и распределения плотности по сечению, с точностью до фактора $\alpha = 1 \div 2$ совпадает с данными рис. 2. Это позволяет вычислять электронную температуру для H_2, Ar и Xe из диамагнитных измерений полной энергии плазмы и микроволновых измерений распределения

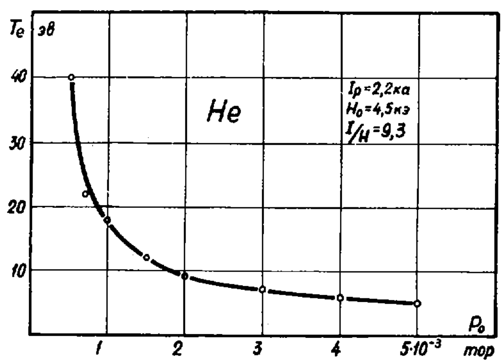

Рис. 2. Зависимость электронной температуры, измеренной спектроскопически, от начального давления p_0 (плотности плазмы).

плотности по сечению шнура. Завышенная "диамагнитная температура" при низких начальных давлениях может быть объяснена вкладом ионной температуры, что подтверждается спектроскопическими измерениями доплеровского уширения спектральных линий. Полученные таким образом значения электронной температуры использовались для расчета классического столкновительного скин-слоя $\delta_{\nu ei}$ в зависимости от начального давления и сорта газа.

Из измеренных магнитными зондами распределений ВЧ-магнитного поля $\tilde{H}_\varphi(r)$ рассчитывалось распределение плотности ВЧ-тока по сечению плазменного столба $j_z(r)$. Из совокупности кривых $j_z(r)$ определялся параметр $\delta_{экс}$ и токовая скорость электронов в скин-слое в зависимости от плотности плазмы. Результаты такой обработки – отношения экспериментального параметра $\delta_{экс}$ к рассчитанному по классической формуле значению глубины скин-слоя $\delta_{\nu ei}$ в зависимости от начального давления, т.е. плотности плазмы, и для двух масс ионов ($m_{He} = 4$, $m_{Xe} = 131$) представлены на рис. 3. Аналогичным образом ведет себя функция $(\delta_{экс}/\delta_{\nu ei})(P_0)$ и для H_2 и Ar. Характерной особенностью кривых на рис. 3 является то, что в широком диапазоне плотностей плазмы и температур (см. рис. 2) экспериментальное значение параметра $\delta_{экс}$ практически не отличается от расчетного значения $\delta_{\nu ei}$. Однако в области малых плотностей это отношение начинает увеличиваться, но за счет уменьшения величины $\delta_{\nu ei}$, которое происходит вследствие увеличения температуры плазмы. Абсолютная величина $\delta_{экс}$ в этой области начальных давлений не увеличивается.

На рис. 4(б) показано изменение токовой скорости электронов в скин-слое при уменьшении плотности плазмы и при сопровождающей это уменьшение плотности увеличении температуры в плазменном шнуре. Из рис. 4(б) видно, что абсолютная величина токовой скорости электронов $\tilde{v}_e$ при разряде в гелии непрерывно нарастает. При уменьшении плотности аналогичные зависимости имеют место и для других газов. На рис. 4(а) построено отношение токовой скорости электронов к скорости ионного звука для тех же условий. Видно, что это отношение также монотонно растет, выходя на насыщение в области малых плотностей. Аналогичные эффекты наблюдаются и при разряде в Xe, рис. 5.

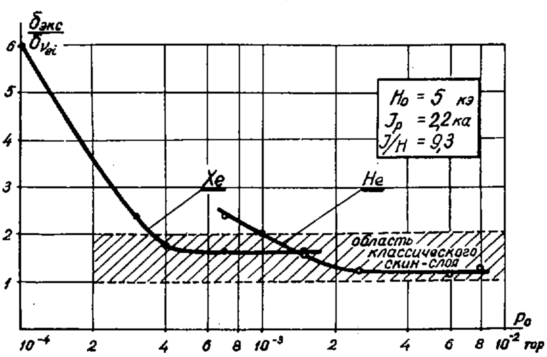

Рис. 3. Зависимость от начального давления p_0 (плотности плазмы) отношения $\delta_{экс}/\delta_{\nu ei}$. Рабочие газы – He и Xe.

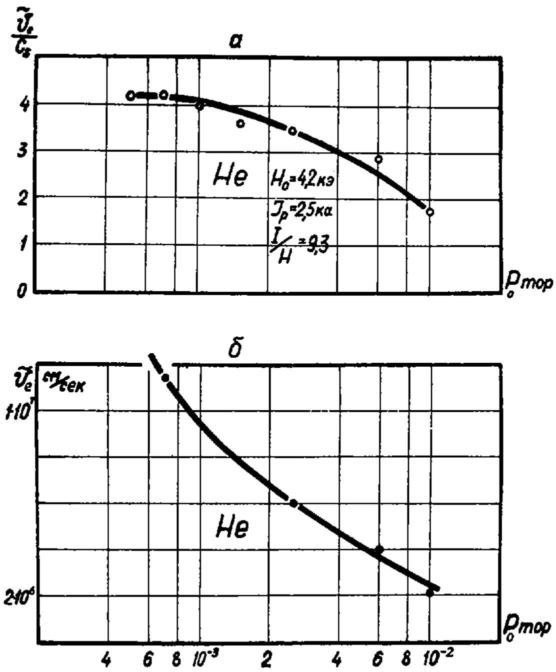

Рис. 4. Зависимость от начального давления ρ_0 (плотности плазмы) токовой скорости электронов $\tilde{v}_e$(б) и ее отношения к скорости ионного звука ($\tilde{v}_e / C_s$)(а). Рабочий газ — He.

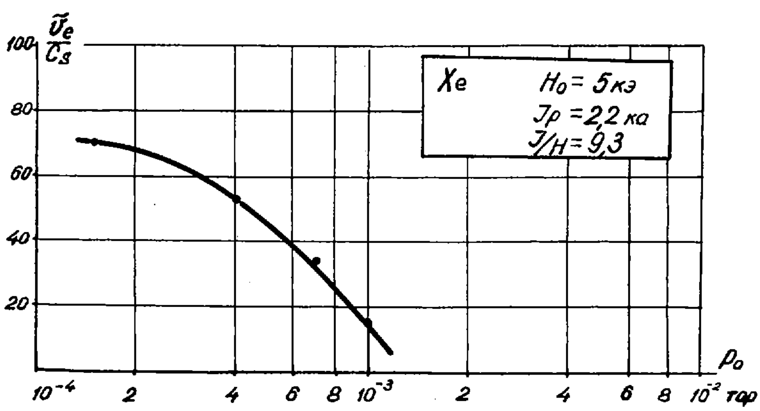

Рис. 5. Зависимость от начального давления ρ_0 (плотности плазмы) отношения токовой скорости электронов к скорости ионного звука $\tilde{v}_e / C_s$. Рабочий газ — Xe.

С целью обнаружения собственно ионно-звуковых колебаний электрического поля и их динамики в течение импульса ВЧ-поля были проведены измерения СВЧ-шумов в диапазоне частот от $2\cdot10^8 \div 6\cdot10^8$ Гц в гелиевой плазме в области скин-слоя с помощью двойного коаксиального электрического зонда, соединенного с перестраиваемым резонансным волномером. Измерения показали, что интенсивные колебания с максимумом спектральной плотности в районе $f_0 = 4\cdot10^8$ Гц ($f_0 = \omega pi/2\pi$ при $n \simeq 10^{13}$ см$^{-3}$) возникают только на начальной, неустановившейся стадии разряда. При переходе в установившуюся стадию разряда, когда произведены измерения глубины скин-слоя, уровень этих колебаний падает примерно на порядок.

Из спектроскопических измерений следует, что ионная температура аргоновой и ксеноновой плазмы может достигать величины порядка нескольких десятков электронвольт, т.е. приближаться к электронной. Такая относительно высокая ионная температура не может быть объяснена кулоновским механизмом передачи энергии от электронов к ионам для Ar и Xe и, вероятно, является результатом какого-то типа коллективных процессов. Вообще, как показал эксперимент на установках Р-0 и РТ-2, отношение T_e/T_i в основных режимах не очень велико, $T_e/T_i \simeq 2 \div 3$, хотя всегда больше единицы.

3. В процессе измерения газокинетической энергии плазмы $\langle nT \rangle$ на сигналах диамагнетизма были обнаружены интенсивные низкочастотные (порядка нескольких десятков кГц) колебания, резко возрастающие при уменьшении плотности плазмы. Порог возрастания этих колебаний зависел от массы ионов так, что произведение пороговой плотности плазмы на массу ионов, $n_e m_i$, оставалось с точностью до фактора 2 постоянным для всех газов (H_2, He, Ar, Xe). Изменение амплитуды колебаний $\Delta \langle nT \rangle$ (в относительных единицах) в зависимости от плотности плазмы для разных рабочих газов показано на рис. 6.

В режимах с интенсивными колебаниями полной энергии плазмы локальный микроволновый зонд регистрировал сильные колебания плотности в той же области частот, причем эти колебания плотности захватывали почти все сечение плазменного шнура. Как будет видно из части II, в этих режимах в плазменном шнуре возникают токовые винтовые структуры, вращающиеся вокруг оси разряда. Совокупность экспериментальных данных позволяет связать эти колебания с раскачкой МГД-неустойчивости типа Шафранова-Крускала.

Область существования этих неустойчивостей совпадает с областью начальных давлений на рис. 3, когда отношение $\delta_{\text{экс}}/\delta_{\nu ei}$ начинает возрастать. Эти макроскопические колебания плазмы могут привести к эффективному размазыванию плотности тока по сечению плазменного столба, так как временная неопределенность момента измерения напряженности ВЧ-магнитного поля магнитным зондом от разряда к разряду, пока зонд перемещается по сечению разрядной камеры, в наших экспериментах была не меньше нескольких десятков микросекунд, т.е. сравнима с периодом низкочастотных колебаний основных параметров плазменного шнура (плотности плазмы, ее температуры, геометрии токовой оболочки).

Таким образом, эффективное уширение скин-слоя, как для гелия, так и для ксенона, в области относительно малых плотностей плазмы может быть объяснено этими макроскопическими неустойчивостями. Это же, вероятно, объясняет выход на насыщение отношения $\tilde{v}_e/C_s$ при малых плотностях плазмы, рис. 4 и 5.

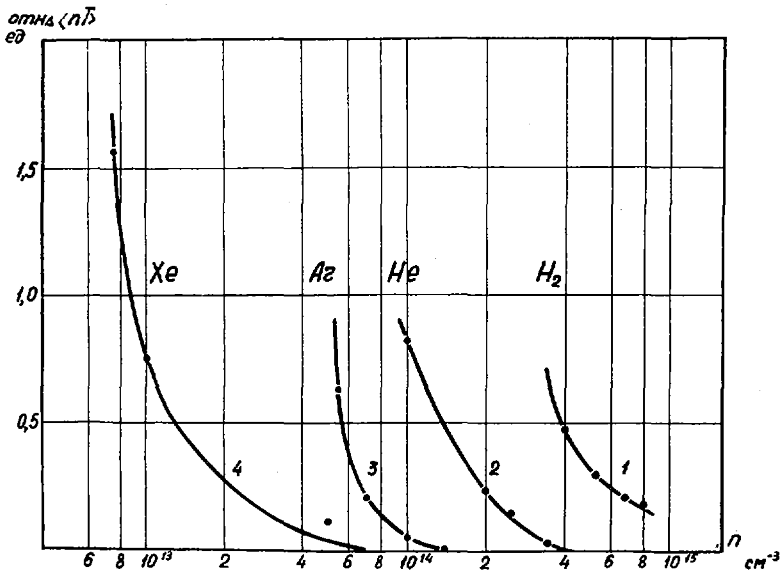

Рис. 6. Зависимость амплитуды низкочастотных колебаний диамагнетизма плазмы $\Delta\langle nT \rangle$ (относительно единицы) от плотности плазмы и массы ионов $H_0 = 4 \div 5$ кэ, $J_p = 2{,}2$ кА.

4. Вся совокупность приведенных экспериментальных результатов позволяет сделать следующие выводы:

а) В режимах, близких режимам динамической стабилизации замагниченной плазмы: $\tilde{\beta} > 1$ (в наших экспериментах обычно $\tilde{\beta} \geqslant 2$), при плотностях плазмы $n_e \simeq 10^{13} \div 5 \cdot 10^{14} см^{-3}$, $T_e \simeq 5 \div 50$ эВ, $T_e/T_i \lesssim 2 \div 3$ ионно-звуковая турбулентность не оказывает определяющего влияния на характер скинирования ВЧ-поля в плазменном шнуре.

б) Глубина скин-слоя в этих условиях слабо отличается от значения, даваемого формулой для кулоновского столкновительного скин-слоя $\delta_{\nu ei} = (C/\omega pe)\sqrt{2\nu_{ei}/\omega}$ вплоть до $\nu_{ei} \simeq \omega$ (газ Xe, $n_e \simeq 10^{13}$ $см^{-3}$, $T_e \simeq 50$ эВ) и всегда меньше величины $\delta_T = (C/\omega pi)(1/\sqrt{\tilde{\beta}})$.

в) Глубина скин-слоя, а следовательно, и эффективная частота столкновений электронов, практически не зависит от массы ионов. Эффективная частота столкновений электронов в основной области экспериментальных параметров плазмы незначительно превышает ν_{ei}. Эффективное экспериментально измеренное уширение скин-слоя в области малых плотностей может быть объяснено раскачкой макроскопических МГД-неустойчивостей.

г) Токовая скорость электронов $\tilde{v}_e$ в скин-слое в этих условиях всегда значительно превышает скорость ионного звука C_s.

ЧАСТЬ II. МГД-УСТОЙЧИВОСТЬ ПЛАЗМЕННОГО ШНУРА С ПРОДОЛЬНЫМ ВЧ-ТОКОМ В СИЛЬНОМ МАГНИТНОМ ПОЛЕ

Теоретические исследования о возможности использования ВЧ-полей для динамической стабилизации кинетических неустойчивостей плазмы [6] предполагают существование макроскопической устойчивости плазмы в

ВЧ-поле. Однако, это предположение нуждается в детальном экспериментальном изучении. Значительный интерес представляет исследование устойчивости при $\tilde{\beta} \equiv (nT)/(\tilde{H}^2/16\pi) \gg 1$ и $\tilde{\beta} \equiv (nT)/(\tilde{H}^2/8\pi) \ll 1$. В случае продольного ВЧ-тока эти условия эквивалентны $\tilde{H} \ll H_0$, и при $a/R < 1$ величина запаса устойчивости $q = (H_0 a)/\tilde{H} R)$ может превышать единицу.

Известно [7,8], что в замагниченном плазменном шнуре с током могут развиваться винтовые конвективные возмущения с инкрементом $\gamma = (H\varphi)/(a\sqrt{8\pi n_i m_i})$, структура которых определяется условием $m/n > q(a) > (m-1)/n$ (m и n – поперечный и продольный номера мод возмущений), а глубина локализации возмущения $\Delta \simeq a/2m$. В условиях плазмы со скинированным ВЧ-током, когда глубина скин-слоя δ много меньше радиуса плазмы a, возмущение может охватить всю глубину токового слоя δ даже при достаточно большом $m \simeq a/2\delta$. Поэтому следует ожидать, что высокие моды винтовых возмущений плазмы с ВЧ-током могут представлять столь же большую опасность, как и мода $m = 1$ в случае плазмы с плавным распределением квазипостоянного тока по сечению шнура.

Устойчивость шнура по отношению к винтовым возмущениям зависит от скорости изменения шага силовой линии магнитного поля. В работе [9] на примере возмущения с $m = 1$ теоретически показано, что при частоте изменения поля $\omega \gg \gamma$ возмущение не успевает перестраиваться и неустойчивость подавляется даже при $q < 1$. Однако при $\omega/\gamma \gtrsim 1$ возможна параметрическая раскачка возмущения с $m = 1$ [10]. По-видимому, не исключена также параметрическая раскачка возмущений с $m > 1$.

Цель предпринятых нами исследований состояла в экспериментальном изучении характера устойчивости плазмы с ВЧ-током и в отыскании режимов устойчивого протекания токов. Сведения об устойчивости получены на основе изучения зависимостей от параметров плазмы и поля следующих характеристик: структура возмущений токовой границы плазменного шнура; низкочастотные колебания энергии и плотности плазмы; энергетическое время жизни плазмы.

1. Условия экспериментов и методы исследований

Эксперименты проводились на установке РТ-2 [11], схематически представленной на рис. 1 (см. также табл. I). Индукционный квазистационарный ВЧ-разряд в гелии или водороде с длительностью 1 мсек создавался ВЧ-генераторами с самовозбуждением, питающими синфазными токами тороидальную систему винтовых проводников. Частота изменения плазменного тока ω составляла 1,65 или 1,9 МГц. Диапазон условий экспериментов: плотность плазмы – $2\cdot10^{13} \div 4\cdot10^{14}$ см$^{-3}$, "диамагнитная" температура плазмы – $3 \div 70$ эВ, напряженность тороидального магнитного поля $H_0 = 1 \div 12$ кэ, амплитуда продольного ВЧ-тока $\tilde{J}_m = 0{,}8 \div 1{,}6$ кА, радиус плазмы $a \simeq 3$ см, $\tilde{\beta} > 10$. Эксперименты проводились в условиях квазистационарности основных параметров плазмы (плотность, энергосодержание, мощность, вводимая в плазму, амплитуда ВЧ-тока) в течение длительности ВЧ-импульса.

Измерения диамагнетизма плазмы и болометрические измерения мощности, вводимой в разряд ВЧ-током, использовались для расчета среднего энергетического времени жизни плазмы τ_E, глубины скин-слоя и эффективной частоты соударений. Изменением энергии на длительности ВЧ-импульса, а также потерями энергии на излучение можно пренебречь. С помощью диамагнитной методики измерялась также величина энергетического времени жизни плазмы в режиме распада ($\tau_{пТ}$) после быстрого выключения ВЧ-тока. В типичных условиях экспериментов $\tau_E < \tau_{пТ}$ (что указывало на активную роль тока в потерях плазмы), и это соотношение не зависело от конфигурации квазипостоянного магнитного поля. Кроме того, τ_E меньше оценки времени тороидального дрейфа плазмы. В связи с этим исследование устойчивости и удержания плазмы проведено, в основном, в чисто тороидальном магнитном поле.

Структура поперечных возмущений границы плазменного шнура изучалась с помощью фоторазвертки свечения поперечного сечения плазмы. В качестве усилителя света использовался электронно-оптический преобразователь. Структура поперечных и продольных возмущений токовой границы плазмы исследовалась также по сдвигу фазы сигналов восьми магнитных зондов, установленных на поверхности кварцевого тора.

Для изучения скорости нарастания низкочастотных возмущений плазмы использовались данные о колебаниях стационарного уровня плотности и энергии плазмы. Сведения о колебаниях средней плотности плазмы в диапазоне частот $10^4 \div 10^7$ Гц были получены из спектрального анализа колебаний фазы микроволнового луча (длина волны 0,8 мм), прошедшего сечение плазмы. Информация о средней скорости нарастания возмущений энергии плазмы $(1/\bar{E})(d\tilde{E}/dt)$ на частотах до 1 МГц была получена из диамагнитных измерений величин $\bar{\bar{E}}$ и $(d\bar{\bar{E}})/(dt)$.

2. Структура возмущений в плазменном шнуре

Практически во всех исследованных режимах существует заметная пространственно-временная модуляция свечения плазмы. На фоторазвертках свечения, рис. 7(а), видны контрастные изменения в макроскопической устойчивости границы плазменного шнура при изменении плотности плазмы. При увеличении плотности плазмы в несколько раз относительно критического значения $\bar{n}_{кр}$(при котором наблюдались самопроизвольные обрывы стационарного ВЧ-разряда) подавлялись крупномасштабные возмущения границы плазменного витка, но возникали быстрые и относительно неглубокие возмущения. Существовали переходные режимы, в которых эти возмущения возникали одновременно. Пространственная структура возмущенной границы оказывается, как правило, достаточно сложной. Наиболее часто наблюдается результат наложения двух "вращающихся" возмущений с различным номером m и периодом вращения T_m. Причем, одна из мод часто бывает более яркой, но ее период всегда кратен периоду второй моды возмущения. Как видно из рис. 7а (1а), ярко светящимся линиям соответствует возмущение шнура с $m = 1$ и периодом вращения T_1 = 20 мксек. На этой же фотографии достаточно четко видны следы более медленных возмущений, соответствующие моде $m = 3$ с периодом T_3 = 60 мксек. Поэтому возмущение границы плазмы в этом режиме характеризуем сложной модой m^* с номером 4.

При увеличении плотности, наряду со стабилизацией границы плазменного шнура, происходило увеличение макроскопической стабильности ВЧ-разряда, наблюдаемое по диамагнетизму плазмы. Корреляция между частотами вращения возмущений шнура и частотами модуляции диамагнитного сигнала свидетельствовала о развитии возмущений границы шнура и их заметном вкладе в потери плазмы в неустойчивых режимах. Аналогичные изменения в характере возмущений границы плазменного шнура и макроскопической стабильности разряда при изменении плотности плаз-

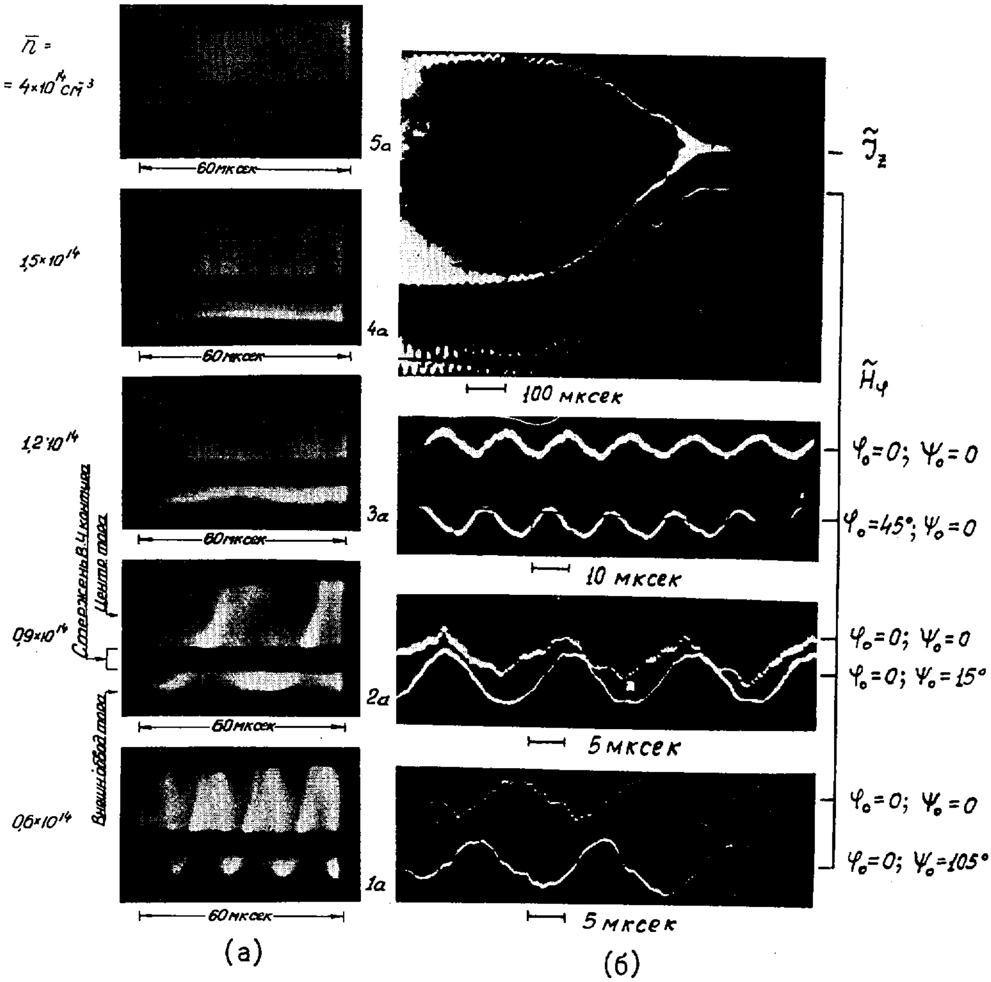

Рис. 7. (а) – фоторазвертки свечения плазмы, $H_0 = 4$ кэ, $\tilde{J}_m = 1,6$ кА. (б) – осциллограммы тока в плазме $\tilde{J}_z$ и напряженности ВЧ-поля $\tilde{H}_\varphi$ на границе шнура, $H_0 = 4,8$ кэ, $\tilde{J}_m = 1,6$ кА, $\bar{n} = 4 \cdot 10^{13}$ см$^{-3}$.

мы наблюдались и при больших напряженностях поля, однако, структура возмущений была более высокомодной. Результаты оптических измерений структуры поперечных возмущений границы плазменного шнура позволили предположить, что при формировании моды возмущения определяющую роль играет наклон силовой линии магнитного поля на границе шнура в максимуме плазменного тока. На это указывала близость расчетной величины параметра $q = (H_0 a)/(\tilde{H}_\varphi R)$ с номерами мод возмущений при $H_0 = 4$ кэ и $H_0 = 8$ кэ. При изменении плотности плазмы и тока происходило изменение номера моды m и радиуса a плазмы, но так, что $q \simeq m$.

Зондовые измерения показали, что в режимах с заметным уровнем возмущений плазмы, видимых на фоторазвертках, существует значительная ($\sim$20%) модуляция ВЧ-поля $\tilde{H}_\varphi$ вблизи границы плазменного шнура. Сдвиг фазы колебаний сигналов от двух магнитных зондов, разнесенных на угол $\varphi_0 = 45°$, в малом сечении тора (рис. 7б), также изменялся при варьировании поля H_0 и соответствовал номерам мод, наблюдаемых на фоторазвертках. Измерения сдвига фазы колебаний амплитуды поля $\tilde{H}_\varphi$ магнитными зондами, установленными в экваториальной плоскости тора на его внешнем обводе в точках $\psi_0 = 0°, 5°, 15°, 75°, 105°, 135°$ и $190°$, показали, что возмущения шнура сильно вытянуты вдоль его оси, но их угол наклона не остается строго постоянным. В экспериментах с $H_0 = 4{,}8$; 7; 9,5 кэ, при фиксированном токе в шнуре и $\tilde{J}_m = 1{,}6$ кА, период продольных возмущений шнура соответствовал значению $n = 2$.

На рис. 8 приведены результаты измерений, из которых следует, что соотношение между модами возмущений шнура и величиной q удовлетворяет неравенству $m/n \lessapprox q$ при изменении q в широких пределах. На основании близости величин m/n и q можно заключить, что в неустойчивом плазменном шнуре с ВЧ-током развиваются возмущения, шаг которых равен или несколько меньше шага силовой линии на границе плазмы при амплитудном значении тока в шнуре и выделенном направлении его протекания.

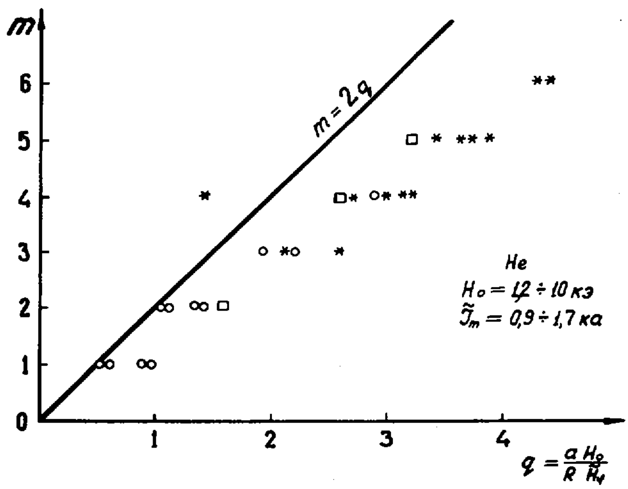

Рис. 8. Зависимость моды поперечных возмущений m от параметра q. о и * – оптические измерения (о – регулярные возмущения, * – сложные возмущения). □ – зондовые измерения.

3. Низкочастотные колебания энергии и плотности плазмы

Характерным является то, что при уменьшении плотности плазмы происходит раскачка низкочастотных колебаний интегральных параметров плазмы. В диапазоне частот 50 кГц ÷ 1 МГц амплитуда нерегулярных колебаний линейно уменьшается с ростом частоты. В спектре колебаний плотности четко выделены колебания на частоте тока. В качестве характеристики средней скорости потерь энергии взята величина $(1/E)(d\tilde{E}/dt)$, которую можно рассматривать как экспериментальный инкремент неустойчивости, приводящей к потерям энергии плазмы. На рис. 9 приведены зависимости величины $(1/\tilde{E})(d\tilde{E}/dt)$ от плотности плазмы при различных ВЧ-токах и массах ионов. Особенностью зависимостей является их пороговый характер. При изменении амплитуды тока от 1,2 до 1,6 кА кривая в случае гелия сдвигается в область больших плотностей на величину, пропорциональную квадрату отношения токов. Из сравнения кривых, полученных на гелиевой и водородной плазмах, следует, что при неизменной величине $(1/\tilde{E})(d\tilde{E}/dt)$ сохраняется неизменной величина альфвеновской скорости, вычисленной для амплитудного значения ВЧ-поля на границе плазмы. Для отмеченных на рис. 9 трех значений плотности альфвеновская скорость практически постоянна – 2,6; 2,4; $2{,}6 \cdot 10^6$ см·сек$^{-1}$. Изменение массы ионов в широком диапазоне показало, что на порогах раскачки низкочастотных колебаний с точностью фактора 2 сохраняется величина $n_e m_i$ (рис. 6). Порог раскачки колебаний не зависит от напряженности квазипостоянного магнитного поля. На основании приведенных результатов можно заключить, что низкочастотные колебания, так же как и наблюдаемые возмущения границы плазмы, являются следствием гидромагнитной неустойчивости плазменного тока.

Измерения, проведенные с помощью микроволнового интерферометра на длине волны 0,8 мм показали, что при увеличении плотности выше критической $\bar{n}_{кр}$(соответствующей порогу раскачки низкочастотных колебаний и самопроизвольному обрыву ВЧ-разряда), происходит трансформация спектра колебаний. При $\bar{n} > 1{,}5\,\bar{n}_{кр}$ в колебаниях плотности изменяется лишь частота тока. Модуляция плотности на частоте тока практически

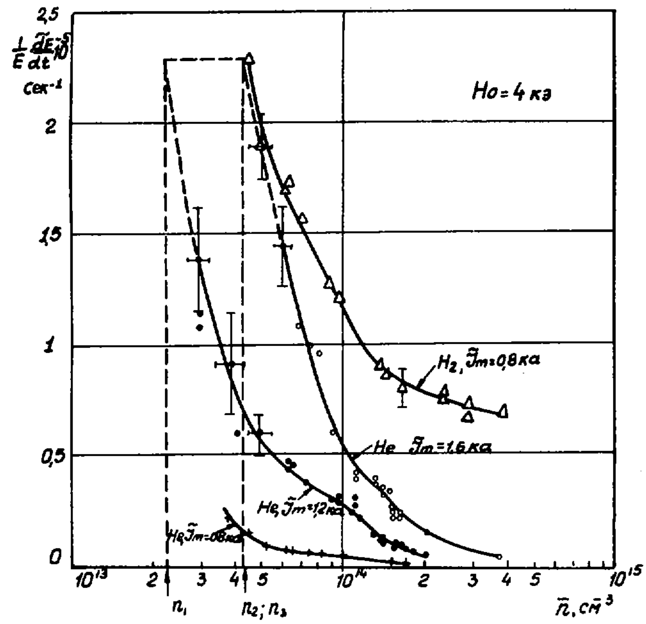

Рис. 9. Сдвиг порогов раскачки низкочастотных колебаний энергии плазмы при изменении массы ионов и плазменного тока.

не изменялась при изменении плотности в пределах $(1{,}5 \div 3)\,\bar{n}_{кр}$ и пороговым образом уменьшалась при $\bar{n} > 3\bar{n}_{кр}$. Зависимость модуляции от напряженности поля H_0 и тока в плазме $\tilde{J}_m$ близка к виду: $\tilde{N}/\bar{N}\ \alpha\,(\tilde{J}_m/H_0)$.

Оценки времени жизни плазмы по нерегулярным возмущениям ее энергии на частотах до 1 МГц и колебаниям плотности плазмы на частоте тока 1,65 МГц, полученные из выражений $\tau_g = \bar{E}/(d\tilde{E})/(dt)$ и $\tau_N = \bar{N}/\tilde{N}\omega$, свидетельствуют о заметной роли этих возмущений в энергетических потерях плазмы в неустойчивых режимах. Из сравнения зависимостей от плотности величин τ_E , τ_N и τ_g , приведенных на рис. 10, можно видеть, что только при предельно малых плотностях, близких к критическим, нерегулярные возмущения шнура на частотах до 1 МГц могли играть определяющую роль в энергетических потерях плазмы. В области больших плотностей потери плазмы обусловлены регулярными возмущениями шнура на частоте тока, а при дальнейшем увеличении плотности происходит отключение и этого вида потерь.

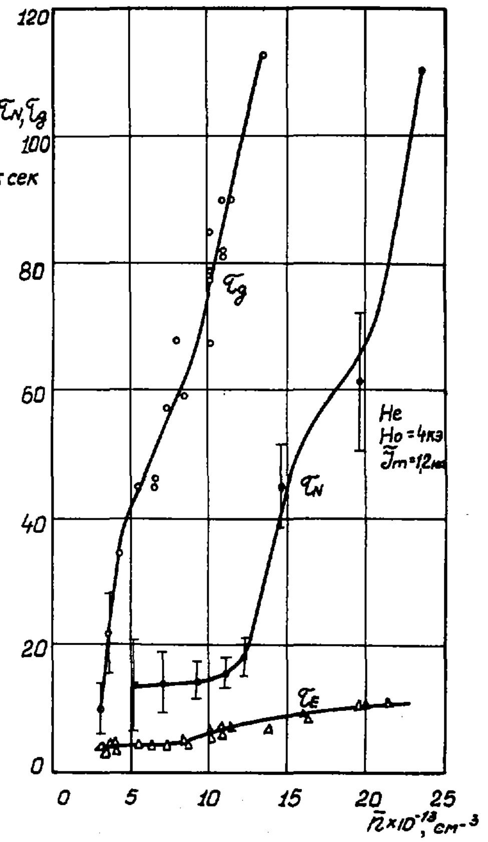

Рис. 10. Зависимости от плотности плазмы характерных времен потерь. τ_g — время, рассчитанное по нерегулярным колебаниям энергии плазмы на частотах до 1 МГц. τ_N — время, рассчитанное по регулярным колебаниям плотности на частоте тока. τ_E — энергетическое время жизни плазмы, H_0 = 4 кэ, $\tilde{J}_m$ = 1,2 кА.

4. Энергетическое время жизни плазмы

На рис. 11 приведены зависимости энергетического времени жизни τ_E от средней плотности плазмы в разрядной камере, полученные при различных величинах тороидального магнитного поля. Минимальные значения плотности на кривых соответствуют порогу раскачки сильной МГД-токовой неустойчивости, приводящей к выбросу шнура на стенки и обрыву стационарного ВЧ-разряда. Функционально зависимость времени жизни от напряженности магнитного поля и ВЧ-тока близка к виду $\tau_E \propto (H_0/\tilde{J}_m)$. В области магнитных полей ~ 12 кэ наблюдается отклонение от линейного характера зависимости τ_E (H_0) при величине $\tau_E \simeq 15$ мксек, связанное с тороидальным дрейфом плазмы. Это подтвердили измерения в равновесных условиях (при включении стеллараторного поля), которые показали отсутствие отклонений от линейного характера при $H_0 = 12$ кэ.

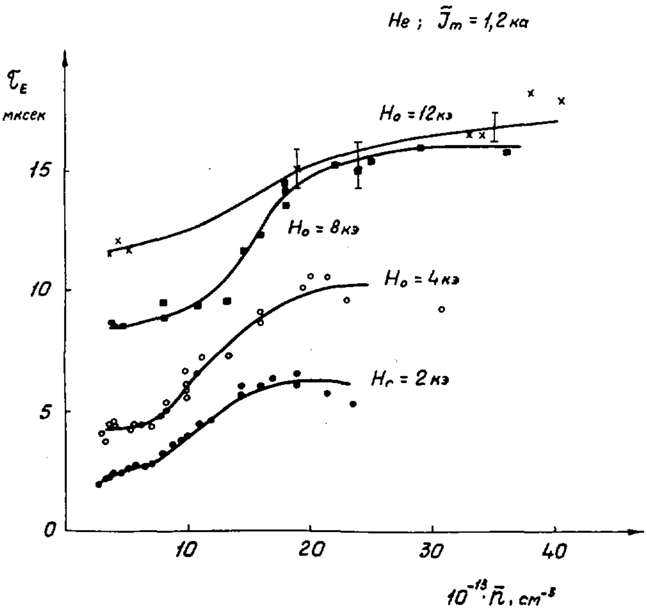

Рис. 11. Зависимости энергетического времени от плотности плазмы.

На рис. 12 представлены зависимости усредненной по размеру шнура "диамагнитной" температуры плазмы $\bar{T}_p$ от усредненной плотности плазмы $\bar{n}_p$, полученные при различных напряженностях магнитного поля. При неизменных магнитном поле и токе произведение $\bar{n}_p \bar{T}_p$ остается примерно постоянным (сплошные кривые на рис. 12 — расчетные кривые $\bar{T}_p \propto \bar{n}_p^{-1}$). Функциональная зависимость нагрева от напряженности магнитного поля и тока плазмы соответствует виду $\bar{n}_p \bar{T}_p \propto H_0 \tilde{J}_m$. Кроме того, нагрев, по-видимому, не зависит от массы ионов и частоты изменения тока (эксперименты проведены на водороде и гелии при частотах тока 1,65 МГц и 1,9 МГц, см. рис. 12).

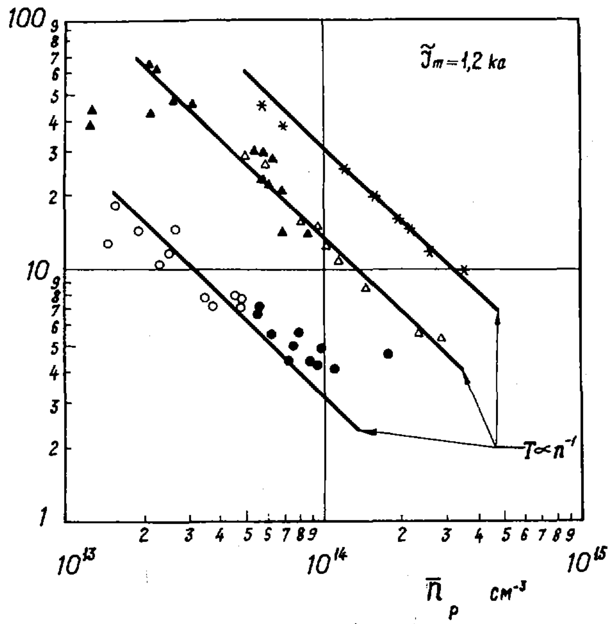

Рис. 12. Зависимости усредненной по шнуру "диамагнитной" температуры от плотности плазмы. о и • – $H_0 = 1{,}2$ кэ (о – He, • – H_2; f = 1,9 МГц) △ и ▲ – $H_0 = 4$ кэ (△ – He, f = 1,65 МГц; ▲ – H_2, f = 1,9 МГц). * – $H_0 = 8$ кэ (He, f = 1,65 МГц).

Предполагая классический характер потерь энергии электронами из скин-слоя ($\tau \simeq (\delta^2/D)$, $D = \rho_e^2 \nu_{eff}$, $\delta = C/\omega pe \sqrt{2\nu_{eff}/\omega}$ при $\nu_{eff} > \omega$), можно получить оценочные выражения для эффективности нагрева плазмы ВЧ-током [12] и времени жизни:

$$nkT = \frac{H_0 \tilde{J}_m}{2\sqrt{2}\,aC} \qquad \text{и} \qquad \tau = \frac{\sqrt{2}\,aC}{\omega} \frac{H_0}{\tilde{J}_m}$$

Эти оценки правильно описывают полученные зависимости удержания и нагрева плазмы от напряженности магнитного поля и амплитуды тока. Расчетное энергетическое время жизни превышает измеренное в 1,5 раза, расчетное энергосодержание в скин-слое в шесть раз превышает измеренное для шнура радиуса a или в 1,5 раза, если предположить, что энергия плазмы сосредоточена в основном в скин-слое ($a/2\delta \simeq 4$). На основании приведенных данных можно заключить, что в области плотностей плазмы $\geqslant 1 \cdot 10^{14}$ см$^{-3}$, где МГД-неустойчивость отсутствует, потери плазмы происходят по законам классического переноса на диффузионном размере масштаба глубины столкновительного скин-слоя.

ЗАКЛЮЧЕНИЕ

Таким образом, экспериментальное исследование явлений, происходящих при протекании по замагниченному тороидальному плазменному шнуру продольного ВЧ-тока с $\tilde{\beta} > 1$, показало:

1. В широком диапазоне плотности плазмы, температуры и массы ионов скинирование ВЧ-поля определяется кулоновскими столкновениями. Вклад ионно-звуковой турбулентности в уширение скин-слоя и в эффективную частоту столкновений электронов незначителен. Глубина скин-слоя практически не зависит от массы ионов. Токовая скорость электронов в скин-слое много больше скорости ионного звука.

2. При протекании ВЧ-тока в плазме при определенных условиях возможна раскачка винтовой МГД-неустойчивости с номером моды m, удовлетворяющим условию резонанса $m/n \simeq q$, где $q = (H_0 a)/(\tilde{H}_\varphi R)$. Показано, что высокий уровень макроскопической устойчивости достигается, когда частота высокочастотного поля на порядок превышает инкремент МГД-неустойчивости. В этих условиях энергетическое время жизни близко к величине, полученной по формуле классической диффузии, в которой в качестве характерного диффузионного размера взята глубина столкновительного скин-слоя.

ЛИТЕРАТУРА

[1] ЗАВОЙСКИЙ, Е.К., Атомная энергия 14 (1963) 56; ФАНЧЕНКО, С.Д. и др., ЖЭТФ 46 (1964) 493; ДЕМИРХАНОВ, Р.А. и др., Труды конференции в Калэме. Вена 2 1966, стр. 327.

[2] РЮТОВ, Д.Д., ЖТФ 39 (1969) 10; СОЛДАТЕНКОВ, Т.Р., Ядерный синтез 10 (1970) 69.

[3] РУДАКОВ, Л.И., КОРАБЛЕВ, Л.В., ЖЭТФ 50 (1966) 220; КОВРИЖНЫХ, Л.В., ЖЭТФ 52 (1967) 1406.

[4] ВЕКШТЕЙН, Г.Е., РЮТОВ, Д.Д., САГДЕЕВ, Р.З., Письма в ЖЭТФ 12 (1970) 419.

[5] ДЕМИРХАНОВ, Р.А. и др., Труды конференции в Утрехте, 1969.

[6] ДЕМИРХАНОВ, Р.А., Труды симпозиума по взаимодействию ВЧ-полей с плазмой. Сакле, 3 1968, стр. 809.

[7] ШАФРАНОВ, В.Д., ЖТФ 40 2 (1970) 241.

[8] ВИНОГРАДОВ, Н.Д., РАЗУМОВА, К.А., Труды конференции в Калэме. Вена 2 1966, стр. 617.

[9] БОБЫРЕВ, Н.А., ФЕДЯНИН, О.И., ЖТФ 33 10 (1963) 1187.

[10] НИКУЛИН, М.Г., ЖТФ 39 12 (1969) 2144.

[11] ДЕМИРХАНОВ, Р.А., БАРАТОВ, Д.Г., МАЛЫХ, Н.И., МЕРЕЖКИН, В.Г., СТОТЛАНД, М.А., ТЕН, Ю., ХИЛЬ, Ш.В., ЖЭТФ 60 2 (1971) 569.

[12] ДУБОВОЙ, Л.В., ФЕДЯКОВА, В.П., ЖЭТФ 58 4 (1970) 1168.

К ВОПРОСУ О ВЫСОКОЧАСТОТНОЙ СТАБИЛИЗАЦИИ ТОРОИДАЛЬНОГО ПЛАЗМЕННОГО ШНУРА С ТОКОМ В ПРОДОЛЬНОМ МАГНИТНОМ ПОЛЕ

М.А.ВАСИЛЕВСКИЙ, И.М.РОЙФЕ,
Е.В.СЕРЕДЕНКО
Научно-исследовательский институт
электрофизической аппаратуры им. Д.В.Ефремова,
Ленинград,
Союз Советских Социалистических Республик

Abstract — Аннотация

HIGH-FREQUENCY STABILIZATION OF A CURRENT-CARRYING TOROIDAL PLASMA COLUMN IN A LONGITUDINAL MAGNETIC FIELD.

The authors present results obtained with the "Toloskop" device in investigations of a stabilized current-carrying toroidal plasma column in a longitudinal magnetic field for a stability margin coefficient $q \le 1$. The boundaries of the stability regions determined in the experiment for various quasi-constant and high-frequency (stabilizing) current ratios are compared with estimates based on the model of a plasma column with a boundary in the region of the high-frequency current skin effect.

К ВОПРОСУ О ВЫСОКОЧАСТОТНОЙ СТАБИЛИЗАЦИИ ТОРОИДАЛЬНОГО ПЛАЗМЕННОГО ШНУРА С ТОКОМ В ПРОДОЛЬНОМ МАГНИТНОМ ПОЛЕ.

Приводятся результаты исследования на установке "Толоскоп" стабилизированного тороидального плазменного шнура с током в продольном магнитном поле при значениях коэффициента запаса устойчивости $q \leqslant 1$. Определенные в эксперименте границы областей устойчивости, полученные при различных соотношениях квазипостоянного и высокочастотного (стабилизирующего) токов, сравниваются с оценками, полученными для модели плазменного шнура с границей в области скинирования высокочастотного тока.

Как уже отмечалось [1], в экспериментах на установке "Толоскоп" был обнаружен эффект стабилизации тороидального квазипостоянного разряда в продольном магнитном поле в условиях нарушенного критерия Шафранова-Крускала. Этот эффект возникал при наложении на квазипостоянный ток высокочастотного (ВЧ) тока с частотой порядка 10^6 Гц и с амплитудой, сравнимой с величиной квазипостоянного тока.

В дальнейшем мы более подробно исследовали случай тороидального разряда с одним ВЧ-током [2,3]. В широком диапазоне амплитуд ВЧ-тока, величины магнитного поля и начальных давлений рабочего газа в экспериментах с одним ВЧ-током тороидальный плазменный шнур был неустойчив. Эта неустойчивость носила характер МГД-параметрической неустойчивости, предсказываемой теорией [4,5], основанной на идеальной МГД-модели.

В последнее время на установке "Толоскоп" ведутся исследования режимов, где наблюдается стабилизация квазипостоянного разряда ВЧ-током. Следует отметить, что обнаруженный эффект стабилизации не находит объяснения в рамках указанной идеальной МГД-модели. Поэтому представляют интерес исследования, связанные с выяснением механизма стабилизации.

(а)

(б)

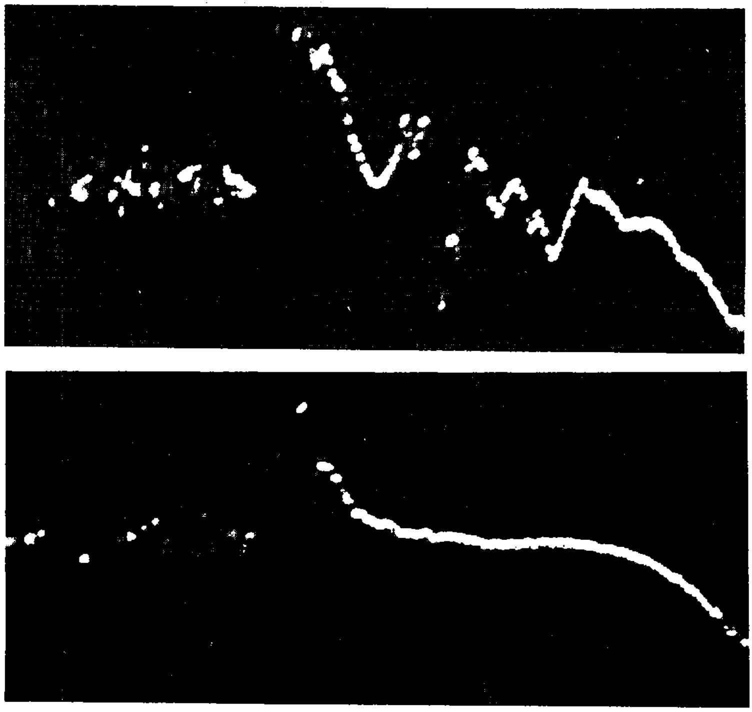

Рис. 1. Типовые осциллограммы сигналов внешнего магнитного зонда: (а) – неустойчивый режим; (б) – устойчивый режим.

Основные данные установки были приведены в работах [1-3]. Отметим лишь, что разрядная тороидальная кварцевая камера, с внутренним малым диаметром – 62 мм и большим диаметром – 600 мм, в большинстве последних экспериментов не имела диафрагм. Для регулирования положения центра токового шнура использовались управляющие обмотки по типовой схеме, применяемой на установках "Токамак". Эти обмотки уложены на проводящий кожух, окружающий камеру. Кожух имеет по одному продольному и поперечному разрезу для создания в камере продольного магнитного поля и ВЧ-тока.

При проведении исследований использовались следующие диагностики: магнитные и диамагнитные зонды, 2,26 мм – интерферометр, спектрометрия. Рассмотрим некоторые режимы работы установки. На рис. 1 приведены типичные осциллограммы неинтегрированных сигналов магнитных зондов, установленных снаружи кварцевой камеры. Продольное магнитное поле $H_z < 1$ кэ; квазипостоянный ток I_{-} – около 3 кА; амплитуда ВЧ-тока $I_{\sim}$ на рис. 1(а) – менее 3 кА, на рис. 1(б) – около 3 кА. Начальное давление рабочего газа – водорода – $2 \cdot 10^{-3}$ торр. Рис. 1 иллюстрирует стабилизирующее действие ВЧ-тока по мере увеличения его амплитуды. Дифференцированный сигнал магнитного поля позволяет одновременно фиксировать как быстрые, но сравнительно небольшие, так и медленные, но большие по величине смещения центра шнура. ВЧ-составляющая сигнала с рабочей частотой 1,1 МГц отфильтрована. Интересно отметить,

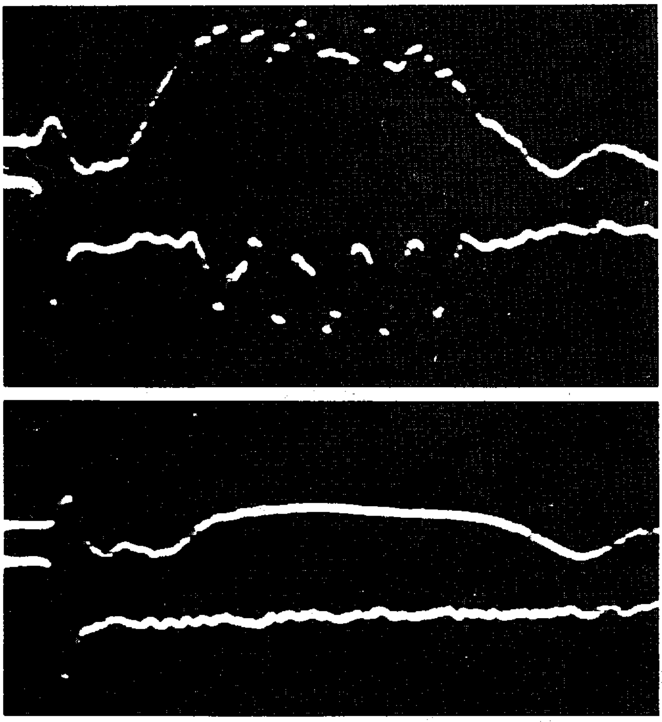

Рис. 2. Осциллограммы сигналов диамагнитного зонда (верхний луч) и свечения линии H_β (нижний луч) при H_z = 600 э, начальном давлении водорода – $2 \cdot 10^{-3}$ торр. Цена деления – 20 мксек:
(а) – $I_\sim$ = 6 кА, I_- = 9 кА;
(б) – $I_\sim$ = 6 кА, I_- = 7 кА.

что при включении квазипостоянного тока заметно уменьшаются колебания, определяемые параметрической неустойчивостью ВЧ-тока. На осциллограммах (рис. 1) время включения квазипостоянного тока сдвинуто относительно времени включения ВЧ-тока, и в этом промежутке видны колебания, характерные для параметрической неустойчивости.

Приведем некоторые спектрометрические характеристики исследуемых режимов установки. На рис. 2 приведены осциллограммы свечения линии H_β (нижний луч) и сигнала диамагнитного зонда (верхний луч). В неустойчивом режиме, рис. 2(а), видно, что при периодических охлаждениях плазменного шнура (выбросы вверх на сигнале диамагнитного зонда) имеет место периодическое вспыхивание линии H_β (выбросы вниз на нижнем луче). На рис. 3 приведены осциллограммы сигналов ФЭУ, линии примеси OII (верхний луч) и линии H_β (нижний луч). В неустойчивом режиме, рис. 3(а), при вспышках линии H_β линия OII соответственно притухает, т.е. плазменный шнур в эти моменты времени охлаждается. Соответствующие осциллограммы для устойчивого режима приведены на рис. 3(б).

(а)

(б)

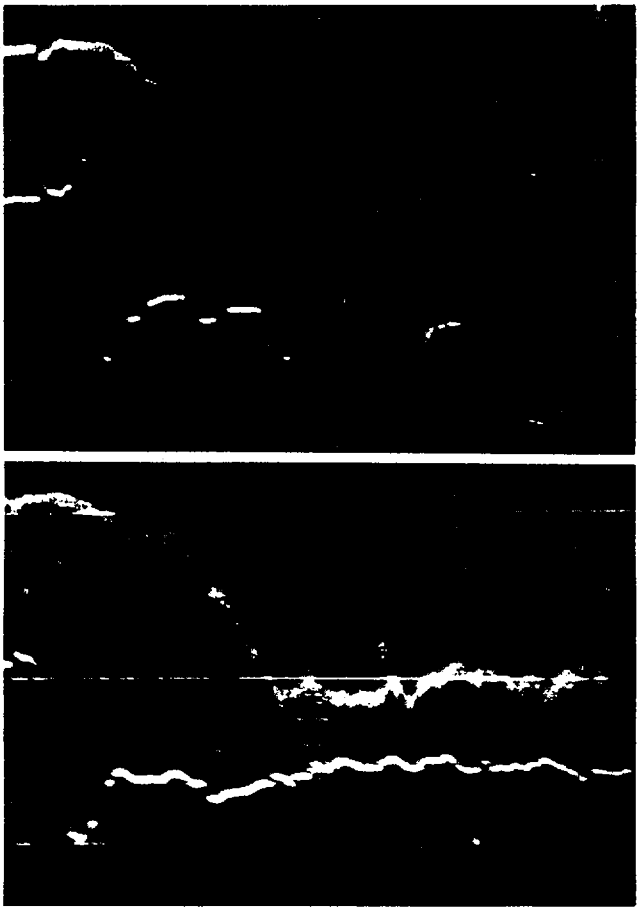

Рис. 3. Осциллограммы свечения линии OII (верхний луч), H_β (нижний луч) при $H_z = 400$ э, начальное давление водорода $2 \cdot 10^{-3}$ торр. Цена деления – 20 мксек:
(а) – $I_\sim = 3{,}5$ кА, $I_- = 8$ кА;
(б) – $I_\sim = 3{,}5$ кА, $I_- = 5$ кА.

Исследование нагрева и удержания тепла плазменным шнуром в этих режимах, очевидно, представляет существенный интерес. Такие исследования ведутся в настоящее время. Однако уже теперь можно отметить, что в стабильных режимах имеет место заметное повышение температуры ионной и электронной компонент плазмы и увеличение энергетического времени жизни.

Исследования устойчивости проводились в широком диапазоне магнитных полей, квазипостоянного и ВЧ-токов. Наличие устойчивого состояния фиксировалось по исчезновению колебаний в сигналах дифференциальных магнитных зондов, в сигналах диамагнитных зондов и в спектрометрических характеристиках. В неустойчивом состоянии колебания

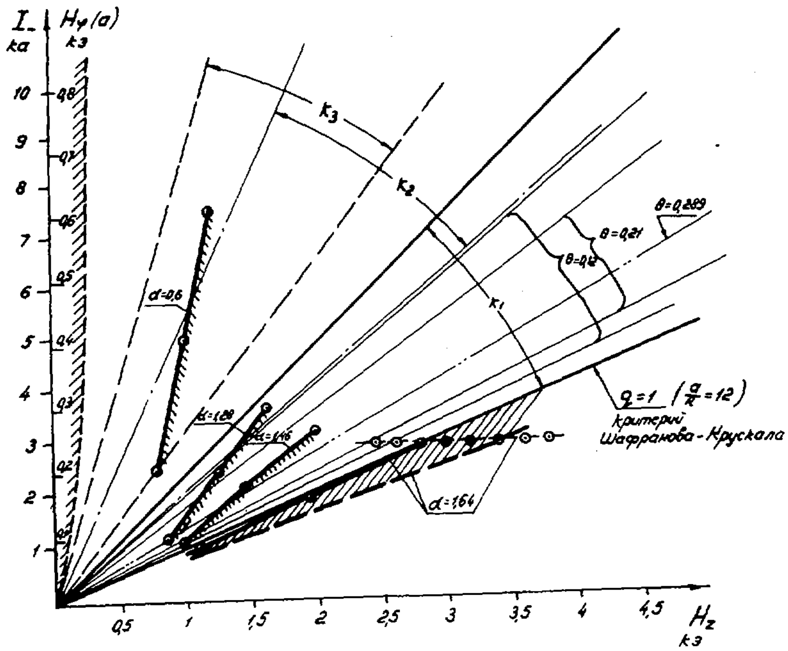

Рис. 4. Диаграмма областей устойчивости.

этих сигналов хорошо коррелировались. Проведенные исследования позволяют сделать вывод о наличии областей устойчивого состояния шнура в координатах $I_- - H_z$, принимая $\alpha = I_\sim / I_-$ = Const в качестве параметра.

Рассмотрим более подробно результаты, связанные с исследованием обнаруженных областей устойчивости. На рис. 4 приведены области устойчивости. Эти области расположены между пунктирной линией со штриховкой, находящейся вблизи оси ординат при $H_z < 0{,}2$ кэ, и соответствующей сплошной линией для ряда значений α. Штриховка нанесена со стороны области неустойчивости. При $\alpha \geqslant 1{,}64$ найдена вторая область устойчивости для сильных магнитных полей. На рис. 4 приведены также некоторые расчетные зависимости, определенные для параметров установки "Толоскоп". Так, линия q = 1 соответствует нижней границе устойчивости для k_1 в соответствии с критерием Шафранова-Крускала. Области k_1, k_2, k_3 – расчетные, соответственно, k_1 – для самого длинноволнового возмущения вдоль большой окружности тора, k_2 – второй и k_3 – третьей гармоник. Обрабатывая данные, приведенные на рис. 4, можно построить зависимость $\alpha(H_z)$ при I_- = Const и $\alpha(I_-)$ при H_z = Const для границ областей устойчивости. Эти зависимости приведены на рис. 5. Рассматривая эти кривые, можно ввести некоторое значение $\alpha_{кр}$, к которому асимптотически стремятся кривые $\alpha(H_z)$ или сходятся кривые $\alpha(I_-)$.

Измерения распределения магнитных полей токов внутри разрядной камеры проводились при помощи магнитных зондов. Зонды перемещались внутри стеклянной трубки, вставленной горизонтально поперек разрядной

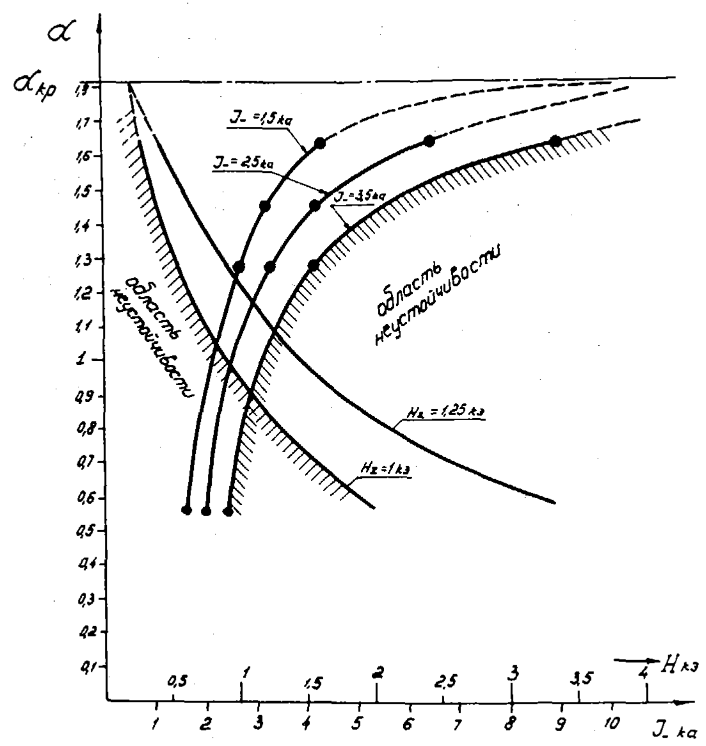

Рис. 5. Зависимости $\alpha(H_z)$ при $I_- = \text{const}$; $\alpha(I_-)$ при $H_z = \text{const}$.

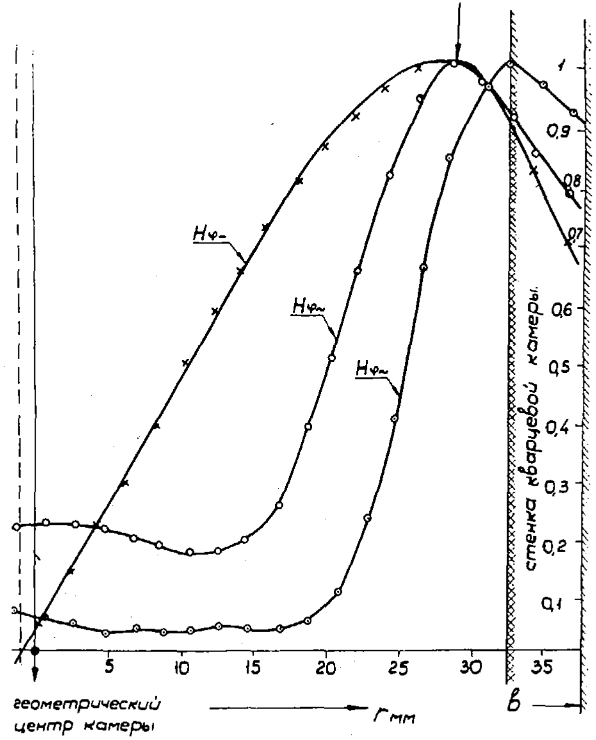

Рис. 6. Распределение полей токов в разрядной камере при H_z = 600 э, I_- = 5 кА;
$I_\sim$ = 3,5 кА, начальном давлении водорода – $2 \cdot 10^{-3}$ торр.

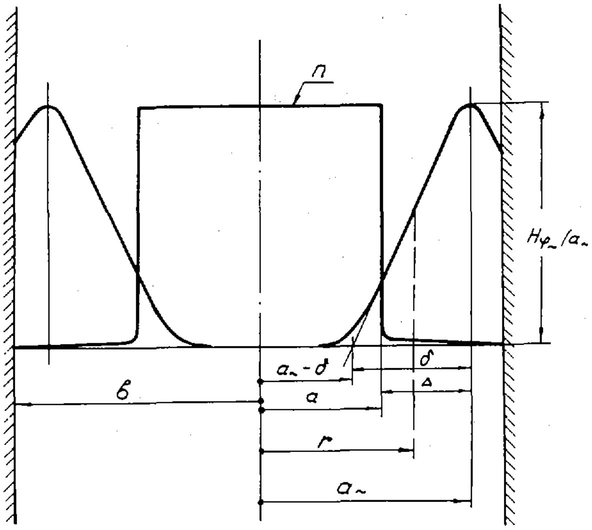

Рис. 7. Идеализированная модель распределения полей ВЧ-тока, концентрации n и квазипостоянного тока внутри разрядной камеры.

камеры. На рис. 6 приведены результаты измерений полей для одного из стабильных режимов. На рис. 6 приведены также две кривые $H_{\varphi\sim}$-поля ВЧ-тока. Кривая $H_{\varphi\sim}$, имеющая максимум на стенке камеры, соответствует моменту времени, предшествующему включению квазипостоянного тока. Из рассмотрения рис. 6 можно сделать вывод, что граница квазипостоянного тока расположена в области скинирования ВЧ-тока. Кроме того, при включении квазипостоянного тока заметен отход границы протекания ВЧ-тока внутрь разрядной камеры. Этот результат может играть определяющую роль в уменьшении амплитуды колебаний, вызванных параметрической неустойчивостью, в связи с тем что при включении квазипостоянного тока плазменный шнур выводится в значительной мере из области протекания ВЧ-тока. В целом, полученные результаты позволяют сделать предположение об определяющей роли в наблюдаемых эффектах стабилизации низкочастотных колебаний скинирующих полей ВЧ-тока. Оценку стабилизирующего действия этих полей можно провести следующим образом. Допустим, что в исследуемых режимах координаты протекания ВЧ-тока фиксированы и определяются радиусом — $a_\sim$. При этом $H_{\varphi\sim} = H^0_{\varphi\sim}\, e^{-[(a_\sim - r)/\delta]} \sin \omega t$. Радиус основной части плазменного шнура квазипостоянного разряда — a и меньше $a_\sim$. Принятая модель представлена на рис. 7. Пользуясь этой моделью и принятыми допущениями, можно записать дополнительную стабилизирующую силу, воздействующую на плазменный шнур, выведенный из состояния равновесия, как:

$$\frac{\partial}{\partial r}\left(\frac{H^2_{\varphi\sim}}{4\pi}\right)\partial r\Big|_{r=a} = \alpha^2\,\frac{H^2_{\varphi\sim}}{4\pi}\cdot\frac{e^{-\frac{2\Delta}{\delta}}}{\delta}\,\xi$$

где $\xi = \partial r$ — элементарное смещение.

В работе [6] приведены выражения для сил, действующих на плазменный шнур, образованный квазипостоянным током в продольном магнитном поле. Сравнивая их с вводимой дополнительной силой, можно определить, что для стабилизации длинноволновых возмущений (изображенная на рис. 4 область k_1 в этом случае вырождается в линию) достаточно, чтобы она была в ~3 раза меньше, например, стабилизирующих сил, действующих на шнур со стороны проводящего кожуха (отношение этих сил – коэффициент $\theta = 0{,}289$). Для коротковолновых возмущений при $q < 1$ эта дополнительная стабилизирующая сила должна играть основную роль. Следует отметить, что эффект стабилизации может быть обязан и другим механизмам, связанным с воздействием на плазменный шнур скинированного ВЧ-тока. Дальнейшие исследования позволят, мы надеемся, точно определить природу этого эффекта.

В заключение авторы считают своим долгом поблагодарить А. Б. Березина за постановку, а Б. В. Люблина – за проведение спектрометрических измерений. Авторы выражают благодарность В. Д. Шафранову, Л. В. Дубовому и М. Л. Левину за плодотворные обсуждения результатов работы.

ЛИТЕРАТУРА

[1] РОЙФЕ, И.М., ВАСИЛЕВСКИЙ, М.А., Plasma Physics and Controlled Nuclear Fusion Research II IAEA, Vienna, 1969, p.477.

[2] ВАСИЛЕВСКИЙ, М.А., РОЙФЕ, И.М., СЕРЕДЕНКО, Е.В., Доклад на II конференции по замкнутым системам. Дубна, 1969.

[3] ВАСИЛЕВСКИЙ, М.А., РОЙФЕ, И.М., РОДИЧКИН, В.А., СЕРЕБРЕНЫЙ, Г.А., ТИМОНИН, А.М., Доклад А-4 на III совещании по диагностике плазмы. Сухуми, 1970.

[4] БОБЫРЕВ, Н.А., ФЕДЯНИН, О.И., ЖТФ 33 (1963) 1187.

[5] НИКУЛИН, М.Г., ЖТФ 39 (1969) 2144.

[6] ШАФРАНОВ, В.Д., Атомная энергия 5 (1956) 38.

DISCUSSION

TO PAPERS IAEA-CN-28/B-8, B-9, B-10, B-12

M.K. KEILHACKER: I have a question concerning paper B-8 by F. Hofmann. Did I understand you correctly that, in the experiment which is compared with the computed magnetic-field and density profiles for different types of anomalous resistivity, the ratio of drift velocity to electron thermal velocity is about 1: 10. If that is so, it does not make sense to use a Buneman type of resistivity to fit the experimental data.

E.S. WEIBEL: Many different experiments on anomalous resistivity for conditions similar to ours have shown that the effective collision frequency was roughly equal to the ion plasma frequency times a numerical factor, i.e. the resistivity was proportional to $1/\sqrt{n_e}$. The Buneman resistivity is also proportional to $1/\sqrt{n_e}$, as is the Dupree plasma clump resistivity, and that is why we used it in our study.

EXPERIMENTAL STUDY OF DRIFT WAVE STABILIZATION

B.E. KEEN, P.E. STOTT
UKAEA Research Group, Culham Laboratory,
Abingdon, Berks,
United Kingdom

Abstract

EXPERIMENTAL STUDY OF DRIFT WAVE STABILIZATION.

The stability and containment of a magnetically confined low-β plasma may be seriously weakened by drift waves. These are driven unstable by a plasma density gradient in both collisionless and collisional plasmas. We have studied various a.c. and d.c. stabilization techniques including magnetic shear, feedback and dynamic methods.

The d.c. shear stabilization has been studied in a 4-metre-long column of thermally ionized alkali-metal plasma. At densities of 10^8-10^9 cm^{-3} and with $T_e = T_i = 0.2$ eV, the electron mean free path is longer than the length of the column and the plasma is collisionless. A strongly sheared magnetic field is produced by means of an $\ell = 3$ helical winding surrounding the plasma. As the shear is increased from zero the amplitude of the unstable drift waves is reduced until stability is reached for values of the shear parameter $\theta \sim 0.1$.

Successful experiments have been performed on the feedback stabilization of collisional drift waves in various gaseous arc plasmas ($n \sim 10^{11}$-10^{12} cm^{-3}; $T_e \sim 5$ eV). The results have been interpreted in terms of non-linear theory of the Van-der-Pol type which predicts a variation of the instability amplitude and its frequency as a function of the gain and phase angle in the feedback loop. Comparison between these predictions and experimental results shows good agreement.

Dynamic stabilization of collisional drift instabilities has been demonstrated in helium and hydrogen afterglow plasmas ($n \sim 10^{10}$ cm^{-3}, $T_e \sim 0.1$ eV), in which an oscillating azimuthal magnetic field, B_θ at a frequency ω is applied to the plasma, perpendicular to the main confining field, B_z. The B_θ field was generated by passing an a.c. current at frequency ω either through a central conductor immersed in the plasma, or through a series of peripheral conductors external to the plasma in a "Picket-Fence" arrangement. The mechanism for stabilization, in this case, is that the azimuthal field, B_θ, provides a path for electrons to cross the d.c. field lines, thus 'short-circuiting' the instability. The instability has been stabilized with moderate values of B_θ/B_z ($\sim$1%), the applied frequencies being in the range 0.1-10 MHz.

In each case, the stabilization technique has been successful in reducing the instability amplitude, and the cross-field diffusion has been decreased.

1. INTRODUCTION

Recently there has been much interest in the low frequency drift instabilities present in a plasma. These micro-instabilities are driven unstable by the plasma density gradient in both collisionless and collisional plasmas. Their importance derives from the possible connection between the anomalously high diffusion of plasma across a containing magnetic field and the presence of these finite amplitude waves in the plasma. Therefore, any method which stabilizes or suppresses drift waves is a desirable feature in a containment device. This paper reports experiments which have been performed in order to suppress drift waves by d.c. shear stabilization, feedback stabilization and a.c. dynamic stabilization. The relevant experimental details are shown in Table I.

TABLE I. EXPERIMENTAL DETAILS

Instability / Plasma		SHEAR: Collisionless drift wave [1] Q-machine (Li or Na)	FEEDBACK: Collisional drift wave [7] hollow cathode arc (Ar)	DYNAMIC: Drift dissipative [16] afterglow (H_2, He)
Peak density	cm^{-3}	10^8	5×10^{12}	$10^{10} - 10^8$
T_e	eV	0.2	5	0.1
T_i	eV	0.2	$\ll T_e$	$\ll T_e$
Axial field B_z	G	700 - 2000	1000	100 - 250
Plasma diameter	cm	7.5	7.0	5.0
$K = (\partial \ell n\, n_o / \partial r)^{-1}$	cm	0.4 - 1.0	1.4	1 - 1.4
Column length L	cm	40 - 400	200	50 - 180
Parallel wavelength - λ_z	cm	2L	200 cm	L

2. SHEAR STABILIZATION

The magnetic shear was generated by an external stellarator-type $\ell = 3$ helical winding (axial periodicity $L_\omega = 80$ cm, maximum current 48 kA, 10 s pulse). Computation of the helical fields were in good agreement with measurements using an electron beam to trace out the field lines which lay on a nested set of trefoil shaped cylindrical surfaces. The rotational transform $\iota \propto r^2$ (approximately) and was close to 2π at the separatrix. The shear length $L_s = [(1/L_\omega)\ r\ \partial\iota/\partial r]^{-1} \propto r^{-2}$ and was about 7 cm at the separatrix. The separatrix was kept within the radius of the ionizing endplates in order to avoid confusion between the 'edge noise' (driven by the large temperature discontinuity at the edge of the endplate) and the true drift waves (driven by a density gradient within the column).

The plasma density profile $n_o(r)$ and the density fluctuation amplitude $n_1(r)$ were measured with single spherical Langmuir probes biased to collect ion saturation current (Fig.1a). The same probes were used with a high impedance 'boot-strap' amplifier to measure the potential fluctuations $\varphi_1(r)$. The peak relative amplitude of the density and potential oscillations occurred close to the steepest part of the density gradient and $n_1/n_o \simeq e\varphi_1/kT_e \leq 20\%$. Similar oscillations had been identified previously as collisionless drift waves [1]. Collisions of electrons with ions ($\lambda_{ei} \approx 10^3$ cm) or with neutrals ($\lambda_{en} \gg 10^3$ cm for a typical base pressure of 10^{-7} Torr) were too infrequent in this plasma to generate collisional drift waves. Clearly defined azimuthal modes were identified with mode numbers m in good agreement with the fastest growing modes predicted by linear theory, i.e. $k_\perp \rho_i \simeq m\rho_i/r = 1$. For the stabilization experiments, the plasma radius and magnetic field were increased so that $\rho_i/r \ll 1$ and the frequency spectrum of the instability revealed a mixture of many modes with large values of m.

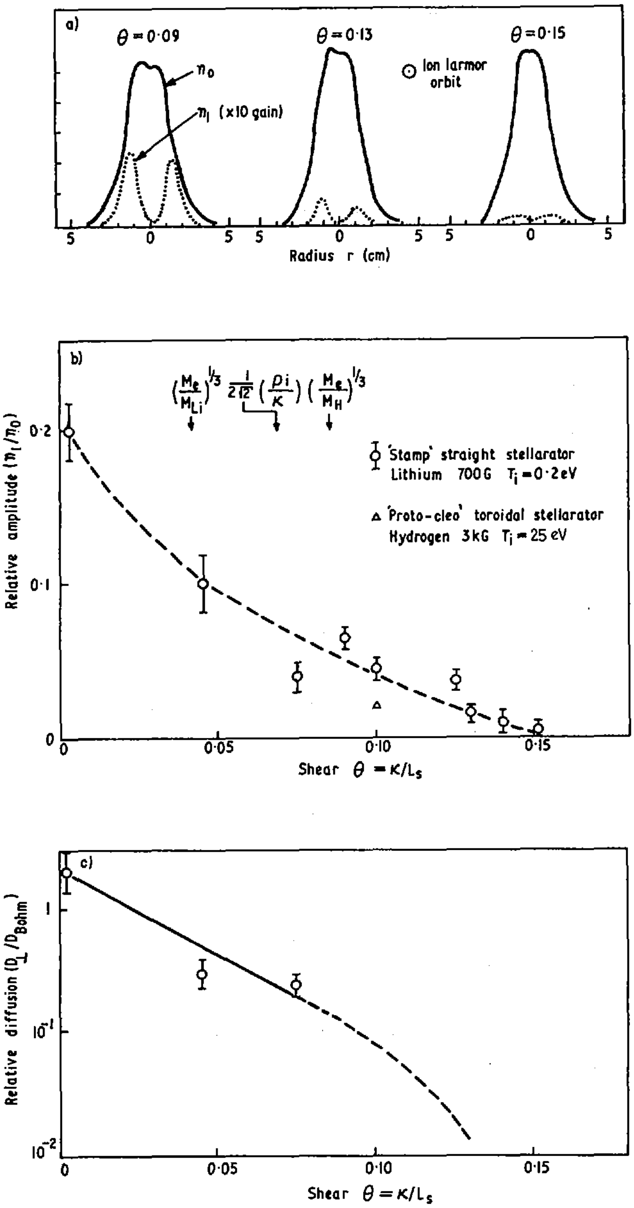

FIG. 1. a) Profiles of density n_0 and fluctuation amplitude n_1 for various values of shear;
b) Variation of reduced instability amplitude n_1/n_0 with shear. The theoretical stability criteria are indicated together with a measurement in a hydrogen plasma in the Proto-Cleo toroidal stellarator [19];
c) Variation of normalized diffusion coefficient $D_\perp/D_{Bohm}$ with shear. The broken line is taken from Fig. 1 b) assuming $D_\perp/_{Bohm} \propto (n_1/n_0)^2$.

Several theoretical estimates of the critical shear needed to stabilize the collisionless drift waves have been published. Krall and Rosenbluth [2] considered a slab model with a localized density gradient producing a potential well which was examined for stability of the normal modes. The stability criterion $\theta = \kappa/L_s \geq (1/2\sqrt{2})\rho_i/\kappa$ was obtained. With increasing shear the radial extent of the region of instability may shrink to such a small extent that these normal modes are not localized. Rutherford and Frieman [3] considered a wave packet of the normal modes which grew initially as a local perturbation before convecting into a stable region where it was ultimately damped. Since the critical amplitude of such a wave packet was undefined, the choice of stability criterion was somewhat arbitrary but to restrict the growth to a single e-folding factor required $\theta \geq (m_e/m_i)^{\frac{1}{3}}$. A more recent analysis by Pearlstein and Berk [4] has shown that normal modes may occur even in the limit of high shear $\theta \geq (1/2\sqrt{2})\rho_i/\kappa$ and these modes are stable only if $\theta \geq (m_e/m_i)^{\frac{1}{3}}$.

Experimentally as the shear was increased, the relative amplitude n_1/n_o fell and became effectively zero for $\theta \geq 0.15$ (Fig.1b). This value exceeds the theoretical estimate of Krall and Rosenbluth by a factor of 2, which is surprisingly close agreement in view of the theoretical approximations. The theory assumed a slab model with uniform shear whilst the experiment was cylindrical and the shear was non-uniform both radially and azimuthally. In addition the linear growth rate of the drift waves may have been enhanced due to finite length effects [5]. The experimental results were all in the regime $(1/2\sqrt{2})\rho_i/\kappa > (m_e/m_i)^{\frac{1}{3}}$, and the wave packet regime was not tested. Machine developments are in hand to extend the range of measurements.

The most important manifestation of the drift instability is the effect on the plasma containment. The radial particle flux transported by the wave is: $j_\perp = (1/rB) \quad \partial\langle n_1\varphi_1\rangle/\partial\psi$ where the correlation function $\langle n_1\varphi_1\rangle$ was measured using two probes as a function of the azimuthal angle ψ. An outwardly directed plasma flux was measured with a maximum close to the radius where κ was a minimum. Good agreement was obtained with the total flux measured on a particle collector surrounding the outside of the column [6]. The collected flux fell sharply when the shear was increased. In a uniform field, (i.e. $\theta = 0$) the radial diffusion coefficient $D_\perp$ was nearly inversely proportional to the field strength B and was of the order of $D_{Bohm} = ckT_e/16\ eB$. This was roughly two orders of magnitude larger than the diffusion coefficient for binary collisions. An accurate calculation of $D_\perp$ in the sheared field was complicated by the presence of convective cells in this particular instance, but values calculated from the mean density gradient showed a clear improvement as θ was increased (Fig.1c). Further measurements to extend the results to larger values of θ and to eliminate the convective cells are proceeding.

3. FEEDBACK STABILIZATION

In these experiments, density perturbations ($n_1/n_0 \approx 15\%$) were detected on an ion-biased probe, and this signal was returned through a wideband amplifier, a phase shifter and a power amplifier, to a plate in the plasma. This plate was in the same axial plane as the detecting probe and could be moved radially across the plasma. Feedback effects were observed from a further ion-biassed probe, which could be moved axially and radially, whose output was displayed on a spectrum analyzer.

The stability theory of the situation has been considered by adopting a non-linear equation of the Van der Pol [8] type to describe the temporal variation of the density perturbations, n_1, in the plasma. Recent work [9-13] has shown that this equation gives a good description of non-linear phenomena occurring with certain instabilities, and,as a consequence, the equation has been adopted on a phenomenological basis. The equation in its simplest form including a feedback term is:

$$\frac{d^2 n_1}{dt^2} - (\alpha - 3\beta n_1^2)\frac{dn_1}{dt} + \omega_0^2 n_1 + g\,\omega_0^2 n_1(\tau) = 0 \qquad (1)$$

where $\alpha/2$ is the initial growth rate ($\alpha/\omega_0 \ll 1$), β a non-linear saturation coefficient, g is an absolute gain factor, and $n_1(\tau)$ represents a density perturbation delayed in time τ from the undelayed value n_1, ($\omega_0\tau = \delta$, the phase delay) [14].

This difference differential equation, Eq.(1), has been solved and the following relationships are obtained:

$$a^2/a_0^2 = \left[1 + g\frac{\omega_0^2}{\alpha\omega}\ \sin\delta\right] \qquad (2)$$

$$2\,\Delta\omega/\omega_0 = [\ 1 + g\ \cos\delta\ ] \qquad (3)$$

where $\Delta\omega = \omega - \omega_0 \ll \omega_0$, and $a_0 = (4\alpha/3\beta)^{\frac{1}{2}}$ is the amplitude without feedback. Eq.(2) shows that the amplitude a increases or decreases according to the sign of $\sin\delta$, and that optimum suppression is achieved with:

$$\sin\delta = -1 \quad (\text{i.e.}\quad \delta = -90^\circ \quad \text{or} \quad 270^\circ) \qquad (4)$$

and then suppression occurs when $g = \alpha/\omega_0$.

Experiments were performed to check this theory. Initially, the phase δ in the feedback loop was set for minimum amplitude a, which then was measured as a function of the gain G ($\propto g$) in the wide-band amplifier. The variation of $(a/a_0)^2$ as a function of G, for the suppressor plate set at different radii, was checked, and a good linear relationship was obeyed, as predicted by Eq.(2).

At optimum gain, ($G_0 = 25.2$), a was measured as δ, was varied. These results are shown in Fig.2, of $(a/a_0)^2$ versus phase δ, and show that optimum suppression is achieved when $\delta = -90^\circ$, or $+270^\circ$ as predicted by Eq.(4). Other gain values of $G = 12.6$ and 7.9 are shown plotted in Fig.2.

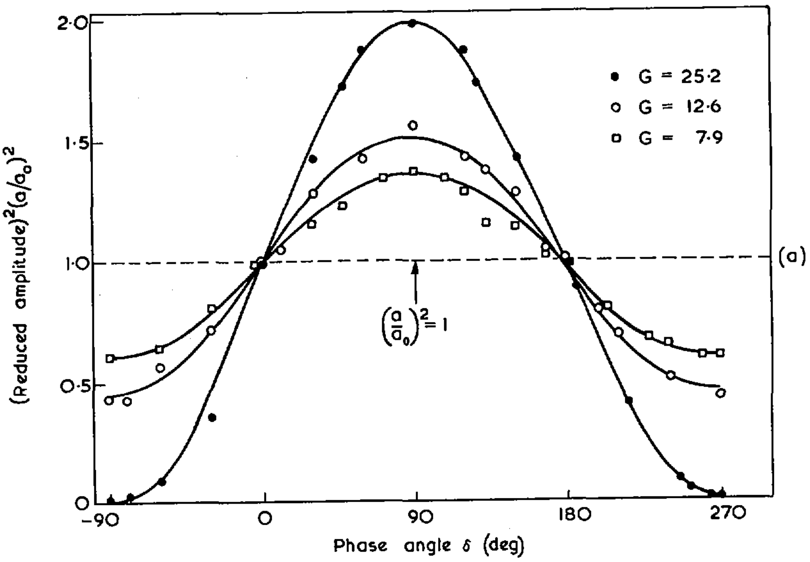

FIG. 2. The square of the reduced amplitude $(a/a_0)^2$ plotted versus the phase change δ, in the feedback loop.

The absolute gain g of the system was calibrated by using Eq. (3). The frequency shift $\Delta\omega = \omega - \omega_0$ was measured as a function of $\cos\delta$, a linear relationship resulted with a slope proportional to g. At optimum suppression ($G_0 = 25.2$) $g = \alpha/\omega_0$, from which a value of $\alpha/\omega_0 = 0.12 \pm 0.02$ was obtained.

From this calibration the theoretical variation of $(a/a_0)^2$ as a function of δ for each value of G, was calculated (Eq. (7)) and is shown as the solid lines in Fig. 2a. Finally, a further check on theory was made by a direct measure of the growth rate $\alpha/2$. By gating the feedback signal at periodic intervals, and analyzing the instability signal a value of $\alpha/\omega_0 = 0.14 \pm 0.03$ was obtained, in good agreement with the previous value.

Under the conditions for optimum suppression, the peak density was found to increase above that value when the instability was present. Analysis [15] of the density profiles in the two cases showed that the cross-field diffusion constant was reduced by a factor ~ 2 upon suppression of the instability.

4. DYNAMIC STABILIZATION

Dynamic stabilization was achieved by either applying an a.c. azimuthal magnetic field H_ψ, or by an a.c. axial electric field E_z at a frequency W. The field H_ψ was induced by an a.c. current flowing in a central insulated conductor, as shown in Fig. 2b, Case A), or alternatively from currents in four parallel conductors external to the glass plasma tube, as shown in Fig.2b, Case B. The axial electric field was applied by imposing an a.c. potential between the cathode and anode plate.

The effect of these electric and magnetic fields has been considered theoretically [17,18], in the linearized kinetic equation approach. These equations were taken in the 'slab model' approximation, in which both electron-neutral (ν_e) and ion neutral (ν_i), collision frequencies were taken into account. Density n_1 and potential φ_1 perturbations were assumed of the form $\exp-i(\omega t - \vec{k}\cdot\vec{r})$, averaged over a time interval $\sim 1/W$, were eliminated by using the continuity equations. The following complex dispersion relationship was obtained.

$$\omega^2\{1 + \Delta A\omega_s/\Omega\} + \omega\{(g - \omega^*\omega_s\Delta A/\Omega) + i(\nu_i + K^2 D_e + K^2\ \omega_s/k_z^2)\}$$
$$- \{(K^2 D_e\nu_i + g\ \omega^*\omega_s/\Omega) + i(K^2\omega_s\omega^*/k_z^2 - g\ \nu_i)\} = 0 \qquad (5)$$

where: $\Omega = k_z^2 D_e$, $\omega_s = k_z^2\Omega_e\Omega_i/k_\perp^2\nu_e$ and $k_\perp^2\nu_e = k_x^2 + k_y^2$.

Here: $\Delta A = \frac{1}{2}(p^2 - q^2 - S^2)$, $g = k_y\{e^2/4m^2(W^2 + \nu_e^2)\Omega_e\}(\partial E_z^2/\partial x)$,

$\omega^* = -k_y cT_e/eH_O\kappa$, $K^2 = k_z^2 + k_y^2 h^2/2$, $h = H_\psi/H_O$, $D_e = T_e/m\ \nu_e$,

$p = k_z cE_z/m\nu_e W$, $q = k_y^2 D_e h^2/4W$ and $S = 2k_x k_y D_e h/W$.

This equation has been obtained in the following approximations: (1), $\omega \ll \Omega_i$; (2), $\nu_e \ll \Omega_e$; (3), $\nu_i \ll \Omega_i$; (4), $\omega \ll W$, and (5), $T_e \gg T_i$

Solution of the equation shows that $\Re e(\omega) = \omega$ is relatively unaffected by the introduction of the a.c. fields, whereas the growth rate $\gamma = \Im m(\omega)$ is given by:

$$\gamma = \gamma_O\ \{1 - \{LX - Mg + N\Delta A\}\omega^3/\omega_s\omega^*\gamma_O\} \qquad (6)$$

where:

$$L = (\omega_s + \Omega - \nu_i)/(\omega_s + \Omega + \nu_i)$$
$$M = 2\{\omega_s + \Omega - (\omega^*\omega_s)^2/2\Omega^2\nu_i\}/\omega^*\omega_s$$
$$N = 2\{\omega_s + 2\Omega + 2\nu_i\}/\Omega\ ,\quad X = k_y^2 h^2/2k_z^2$$

and γ_O is the growth rate when H_ψ and E_z are zero. Stabilization results when: $LX - Mg + N\Delta A \geq \gamma_O\omega_s\omega^*/\omega^3$. (7)

The resulting theoretical stability threshold values for the reduced magnetic field amplitude $h = H_\psi/H_O$ as a function of frequency, W, are shown in Fig.3a. The experimental values for comparison are shown in Fig.3b. In Case A, some agreement is obtained although the absolute magnitude is about a factor of 3-4 too high. For Case B, the results indicate that the field h is smaller than in Case A, as predicted, but is a factor of 10 smaller, whereas theory would only predict a factor of 2, at most.

The experimental results corresponding to the case of an applied a.c. electric field, E_z , are shown in Fig.3c, and the theoretical predictions are shown by the full curve in the same figure. At higher frequencies (> 10 MHz), it is seen that both

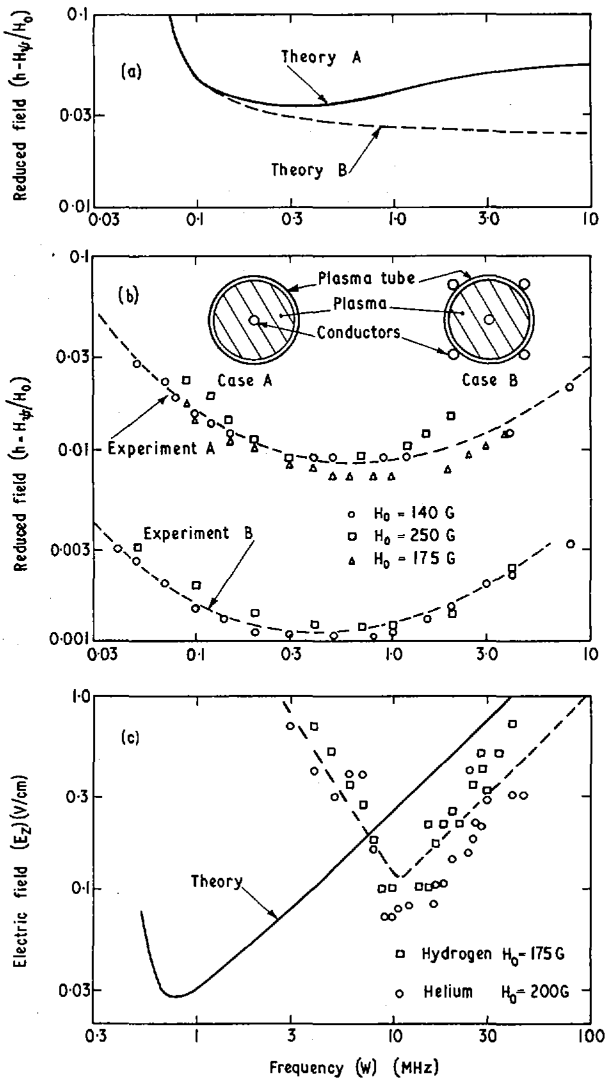

FIG. 3. The reduced magnetic field, $h = H_\psi/H_0$, plotted against frequency, W, for (a) theoretical predictions; (b) experimental results, for cases A and B, and (c) the threshold electric field plotted versus frequency.

theory and experiment show a linearly increasing threshold electric field ($E_z \propto W$) as a function of W, but the theoretical magnitude is again high by a factor $\sim$2-3. At low frequencies the disagreement is quite marked, and is probably related to the assumption in the theory that the ion motion is uninfluenced by the a.c. fields, which is invalid at these frequencies.

An oscillating magnetic field, B_z, applied in the axial direction was used to check that the suppression was not due to possible local heating or plasma production effects caused by the r.f. source. No suppression effects were observed even with oscillating fields an order of magnitude higher in amplitude. Therefore, it is inferred that the mechanism of suppression, in this case, is the method suggested by theory.

Hence, it has been shown that the drift-dissipative instability can be stabilized by moderate a.c. magnetic fields, $h = H_\psi/H_0 (\lesssim 3\%)$ and by small electric fields, E_z, $(\lesssim 1$ V/cm). Comparison with theory shows that the general feature of the frequency variation can be predicted, although predicted magnitudes are not too good.

5. CONCLUSIONS

These experiments have shown that drift waves can be stabilized by several methods. Strong magnetic shear was effective in stabilizing the collisionless drift waves and all modes appeared to be suppressed. In a stellarator reactor values of shear not too much in excess of $(1/2\sqrt{2})\rho_i/\kappa$ should suffice to stabilize the normal modes, but the more stringent condition $\theta \geq (m_e/m_i)^{\frac{1}{3}}$ was not tested.

Feedback stabilization was shown to be effective in stabilizing the collisional drift wave. It appears to be a promising method for stabilizing single modes but may be more difficult to apply to a system with many degrees of freedom. Effective remote feedback methods must be developed for reactor plasmas.

Dynamic stabilization was shown to be effective in suppressing the drift dissipative instability. In principle it should be equally effective on the collisionless drift-wave in both the single-and multi-mode case. However, in order to apply this method in a reactor, the problem of penetrating the plasma with the a.c. fields must be solved.

ACKNOWLEDGEMENT

It is a pleasure to acknowledge the valuable experimental contributions made by M.W. Alcock, J. Burt and W.H.W. Fletcher.

REFERENCES

[1] STOTT, P.E., LITTLE, P.F. and BURT, J., In Proc. of the 3rd European Conf. on Controlled Fusion and Plasma Physics, Utrecht, The Netherlands, June, 1969, Wolters-Noordhoff Publishing, Groningen, The Netherlands. (1969)

[2] KRALL, N.A. and ROSENBLUTH, M.N., Phys. Fluids, 8 (1965) 1488.

[3] RUTHERFORD, P.H. and FRIEMAN, E.A., Phys. Fluids, 10 (1967) 1007.

[4] PEARLSTEIN, L.D. and BERK, H.L., Phys. Rev. Letters, 23 (1969) 220.

[5] BERTOTTI, B. and NOCENTINI, A., Plasma Physics, 12 (1970) 39.

[6] STOTT, P.E., LITTLE, P.F. and BURT, J. Phys. Rev. Letters, 25 (1970) 996.

[7] ALDRIDGE, R.V. and KEEN, B.E., Plasma Physics, 12 (1970) 1.

[8] Van der POL, B. Phil. Mag., 43 (1922) 700.

[9] LASHINSKY, H., Proc. of Conf. on Plasma Physics and Controlled Nuclear Fusion Research, Culham Laboratory, England, (1965), IAEA, Vienna, Austria, (1966) 499.

[10] ABRAMS, R.H., YADLOWSKY, E.J. and LASHINSKY, H., Phys. Rev. Letters, 23 (1969) 275.

[11] KEEN, B.E. and FLETCHER, W.H.W., Phys. Rev. Letters, 23 (1969) 760.

[12] KEEN, B.E. and FLETCHER, W.H.W., Phys. Rev. Letters, 24 (1970) 130.

[13] STIX, T.H., Phys. Fluids, 12 (1969) 617.

[14] KEEN, B.E., Phys. Rev. Letters, 24 (1970) 259.

[15] KEEN, B.E. and ALDRIDGE, R.V., J. Phys. (A), 4 (1971) 120.

[16] ALCOCK, M.W. and KEEN, B.E., J. Phys. (A), 3 (1970) 121.

[17] IVANOV, A.A. and TEICHMANN, J., Czech. J. Phys., 19 (1969) 941.

[18] TEICHMANN, J., Phys. Letters, 32A (1970) 47.

[19] BOLTON, R.A.E. et al., (Submitted for publication in Phys. Fluids).

FEEDBACK AND DYNAMIC STABILIZATION METHODS AND THEIR POWER REQUIREMENTS
A comparative evaluation

H.W. HENDEL*, T.K. CHU
Princeton University Plasma Physics Laboratory
Princeton, New Jersey,
United States of America

Abstract

FEEDBACK AND DYNAMIC STABILIZATION METHODS AND THEIR POWER REQUIREMENTS: A COMPARATIVE EVALUATION.

Experiments on linear and non-linear feedback and on dynamic stabilization of drift and transverse Kelvin-Helmholtz instabilities are described and compared with theory. Experimental results on number of models stabilized, growth-rate ranges affected, and power required are used to evaluate these non-static methods for applications in fusion plasmas.

Linear feedback ($f_{fb} = f_{inst}$; specific phase required) reduces the instability amplitude by two orders of magnitude. It is frequency- and mode-selective and most easily used near-marginal instability; stabilization of many oscillatory modes simultaneously is difficult. Remote feedback has been demonstrated. Non-linear feedback (repetition rate $\leq f_{inst}$; specific phase required), uses constant corrective signal whenever the instability amplitude grows above a present level. It may be applied at repetition rates below the instability frequency. Results are comparable to those of linear feedback. However, harmonics or higher modes are easily destabilized.

Dynamic methods ($f_{dyn} \gg f_{inst}$; no phase requirement) are observed to stabilize not only many modes of one instability, but also broad-band turbulence and different instabilities simultaneously, in agreement with the interpretation based on generation of a new dynamic equilibrium stable against a class of instabilities.

Power requirements may determine feasibility of non-static stabilization in fusion plasmas. For linear feedback, since the suppressing signal is proportional to the instability amplitude, the power necessary for stabilization is relatively small. For dynamic stabilization, or equivalently, for the generation of a stable dynamic equilibrium, the required energy per growth time ($1/\gamma$) is independent of instability amplitude and comparable to a fraction of the plasma internal energy. Feasibility, therefore, is determined by dissipation. The required power for feedback stabilization is $P_{fb} \approx \omega\eta^2(bn_0kT) \sim \eta^2 \gamma^3$, while for dynamic stabilization $P_{ds} \approx 10\,\omega\,(bn_0kT) \sim 10\,\gamma^3$, where ω and η are instability frequency and normalized amplitude, and bn_0kT is a fraction of the internal energy. Calculated power levels are in agreement with experiments. These considerations indicate that for high-growth-rate instabilities the power required for dynamic stabilization may be excessive.

INTRODUCTION

Suppression of plasma instabilities by the time-varying methods of feedback and dynamic control has been recently employed in a variety of experiments [1]. In this paper we summarize and compare results on suppression of low-frequency drift [2] and transverse Kelvin-Helmholtz instabilities [3] to elucidate the relative merits of the different methods by comparing mode selectivities, feedback repetition rates, and power requirements. These power considerations are applicable to instabilities in general.

---

* On leave from RCA Laboratories, Princeton, New Jersey.

Feedback stabilization interacts only with the unstable mode, is therefore mode selective and most easily used near marginal instability where few modes exist and mode interaction is negligible. The stabilization of many modes simultaneously is difficult, at least with a limited number of suppressor stations per mode. In nonlinear feedback, a constant corrective signal is applied whenever the instability amplitude grows above a predetermined level. Results are comparable to those of linear feedback, but harmonics or higher modes are more easily destabilized. Repetition rates can be below the instability frequency, depending on the growth rate. In dynamic stabilization the stabilizing frequency is much higher than the instability frequency and no phase requirement need be met. Many modes, different instabilities, and turbulence may be stabilized simultaneously. However, interpretation is generally more difficult, since the plasma equilibrium is no longer the initial one (as in the feedback case, where upon stabilization, i.e., reduction of the instability amplitude towards zero, the feedback signal also goes towards zero), but is determined by the high frequency dynamic signal. Effects of plasma parameter changes on the instability therefore must be separated from those of the dynamic equilibrium generated. In addition, the remaining large-amplitude dynamic stabilizing signal may produce plasma losses.

Finally, we address ourselves to the power levels necessary. In dynamic stabilization, the plasma must remain in the new dynamic, stable equilibrium and the power cannot be reduced after stabilization. However, in feedback stabilization, when the amplitude of the instability is reduced, the feedback amplitude reduces accordingly, indicating lower power requirement for stabilization. Qualitative agreement between results of experiments and calculation on the (reactive) power requirement for feedback and dynamic stabilization is obtained. Using estimated dissipation, we compare the power density necessary for stabilization with expected reactor power output. It is concluded that, for high-growth-rate instabilities, excessive power is required for dynamic stabilization.

FEEDBACK EXPERIMENTS

The experimental work was performed on the Princeton Q-1 device [2]. In this thermally ionized plasma both the drift and Kelvin-Helmholtz instabilities can be destabilized by variation of the plasma parameters so that a marginally unstable plasma can be produced. By further increasing the destabilizing parameter, multi-mode and turbulent regimes are accessible. The instabilities used are the density gradient-driven drift instabilities in the collisionless [4] and collision dominated [2] regimes and the transverse Kelvin-Helmholtz instability [3]. They have been identified in considerable detail and their theory is well understood and verified by experiments. Thus possible effects of the stabilizing method on the instabilities through changes of plasma parameters (e.g., a density reduction due to insertion of feedback probes) may be taken into account. The collisional drift and the Kelvin-Helmholtz instabilities can be made marginally unstable by adjustments of the magnetic field so that only one oscillatory mode is present, in agreement with theory. Thus, phase, amplitude and growth rates can be determined accurately and compared with linear-theory predictions.

In general, in the experiments a single detector and a single suppressor were used, i.e., no attempt was made to employ a many-station, distributed system. In the case of feedback suppression of a number of modes, several one-detector, one-suppressor systems were used.

The main results on feedback stabilization of collisional drift waves by modulated parallel-electron-current sink [5] using Langmuir probes, on remote stabilization by modulated heat source [6] using resonance absorption at the upper hybrid frequency, and on stabilization of the transverse Kelvin-Helmholtz instability [7] by electron sink using Langmuir probes have been reported elsewhere. Results on nonlinear feedback of the collisional drift wave and on linear feedback of the collisionless drift wave will be given.

In all feedback experiments performed on the first destabilized coherent mode, the instability amplitude could be reduced by approximately a factor of 100, with gain and phase of the suppression signal agreeing with linear theory results. Simultaneously, plasma confinement increased by an amount known to be due to the wave induced loss (up to ~ 30% for the collisional drift wave). Typical results of the growth rate with electron-sink feedback measured for varied feedback phase relations between wave and feedback signal are given in Fig. 1a. Figure 1b shows theoretical linear growth rate, obtained from the dispersion relation [5]

$$b\omega^2 + [b(\omega_e + i\sigma_e) + i\frac{1+2b}{t_\parallel} + \frac{i}{t_\perp}]\omega - \frac{1}{t_\parallel t_\perp}[2 + t_\parallel\sigma_e + t_\perp\sigma_i]$$
$$+ i\omega_e[\frac{1}{t_\perp} - \frac{1}{t_\parallel} + \sigma_i - \sigma_e] = 0$$

where $\omega_e = k_y v_d$, $v_d = -(cKT/eBn_o)(dn_o/dx)$, $b = \frac{1}{2}k_\perp^2 r_L^2$, $r_L = (2KT/M)^{1/2}/\Omega_i$, $1/t_\parallel = k_\parallel^2 KT/m_e\nu_{ei}$, $\sigma = |\sigma| \exp(i\theta)$, and $1/t_\perp = \frac{1}{4}b^2\nu_{ii}$. To show that

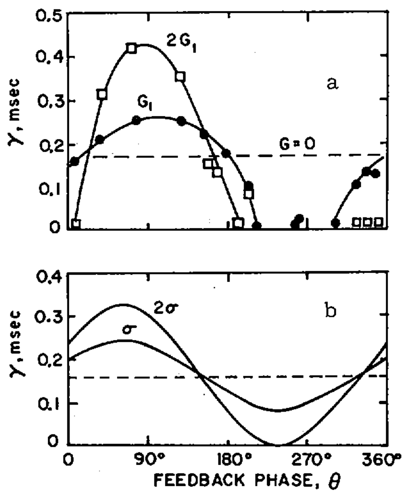

FIG. 1. Growth rate versus feedback phase delay for two different feedback gains: a) Experiment; b) Theory. Growth rate is measured from time variation of instability amplitude after feedback is turned on or off.

this feedback interaction with the plasma is through particle sinks $S = \sigma\tilde{n}$, the suppressor probe size (and therefore the collecting area) and its location (with respect to the instability-amplitude spatial distribution) was extensively varied so that the required bias voltage on the probe changed by several orders of magnitude. Figure 2 shows that the current necessary for stabilization is approximately constant, indicating that the number of charges removed is responsible for stabilization.

It has been shown [8], that linear feedback cannot stabilize pure MHD interchange modes, whose perturbation amplitude is constant along the confining field, and that in these cases nonlinear feedback, i.e., the application of a constant corrective signal for the duration of the unwanted plasma displacement, may be effective in suppressing the perturbation. We have studied nonlinear feedback in the case of the collisional drift wave, applying a constant corrective signal whenever the instability amplitude is positive. Langmuir probes acting as current sinks are used as detectors and suppressors; duration, phase, and amplitude of the rectangular suppressor signal are varied. Figure 3 shows a stabilization characteristic similar to that of linear feedback, Fig. 1. Note that good suppression can

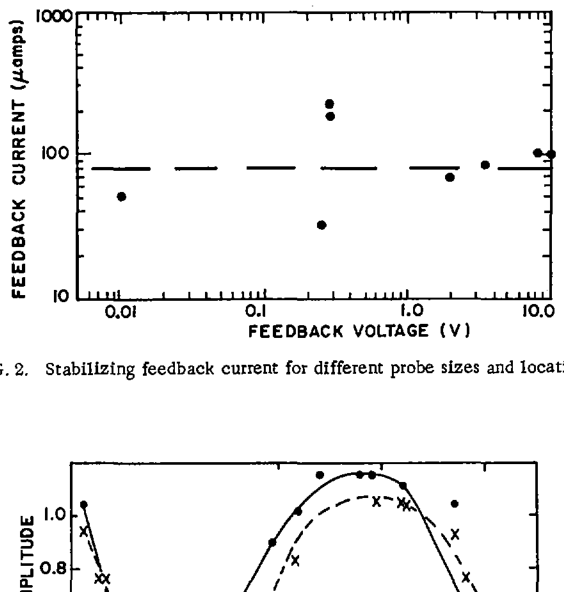

FIG. 2. Stabilizing feedback current for different probe sizes and locations.

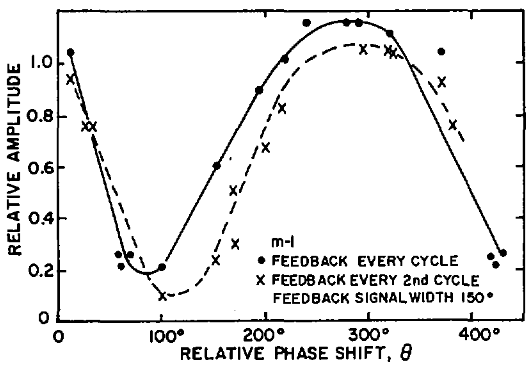

FIG. 3. Instability amplitude versus non-linear feedback phase shift, at optimized gain.

be achieved with one pulse every second cycle. Figure 4 indicates that, as might be expected, a higher gain is necessary when the suppressor signal is applied only every second cycle. Figure 5 shows the effect of suppressor-signal duration at optimum phase. The optimum pulse duration is slightly less than the duration of the plasma excursion, i.e., less than half a period. However, nonlinear suppression can excite harmonic frequencies and higher modes.

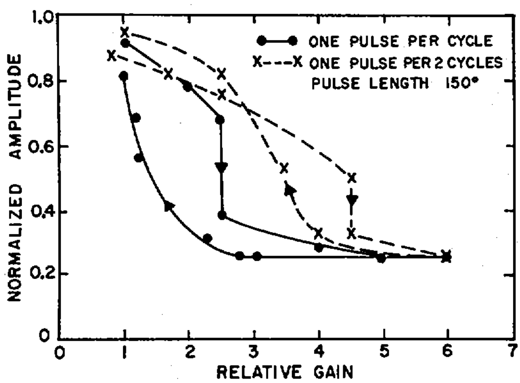

FIG. 4. Instability amplitude versus non-linear feedback gain, at optimized phase.

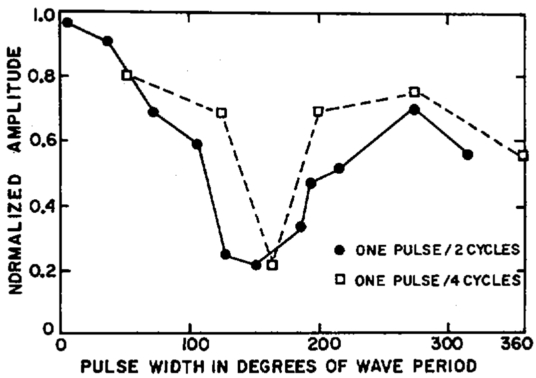

FIG. 5. Non-linear feedback pulse-width versus instability amplitude, at optimized phase shift.

In the simultaneous presence of a number of modes (collisionless drift wave), or when a number of modes (multi-mode regime of collisional drift wave) is predicted to be linearly unstable but suppressed by nonlinear effects due to one dominant mode, stabilization with the simple one-detector, one-suppressor systems tends to increase the amplitudes of modes which experience correct phase for positive feedback. In Fig. 6a, a single mode of the collisional drift wave is present without feedback. Upon suppression (~ 40 db), no new mode is excited. In the case of the collisionless drift wave, Fig. 6b, at least three modes are present without

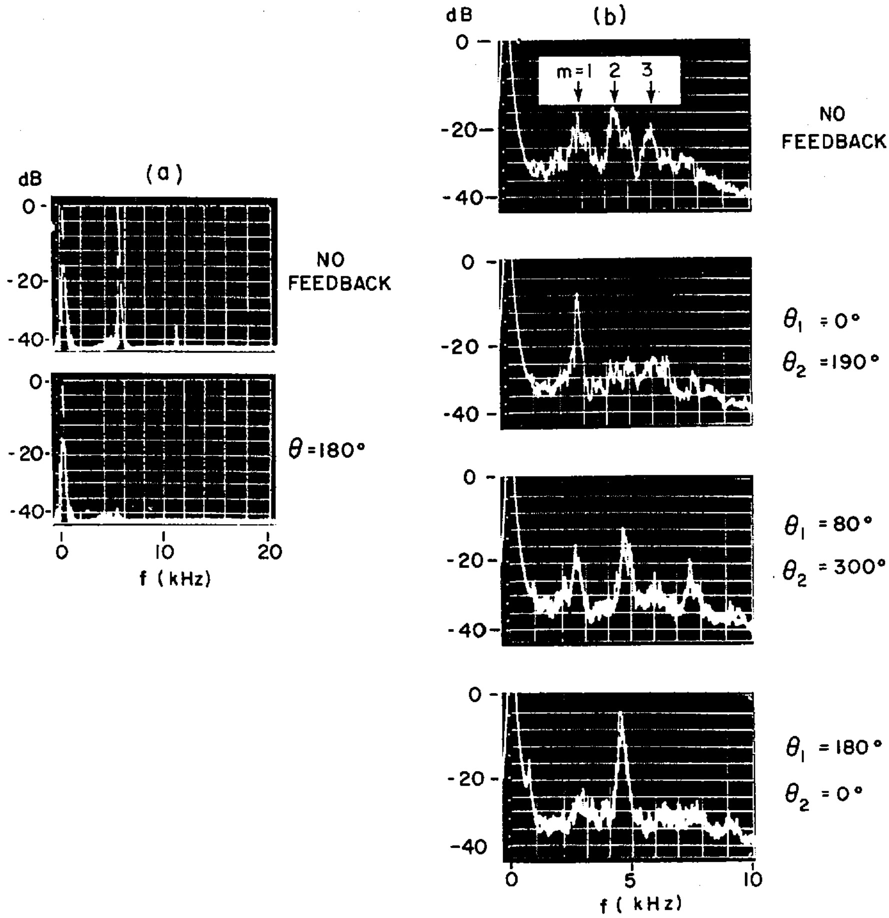

FIG. 6. Instability frequency spectra without and with feedback. (a) Collisional, (b) collisionless drift instability. In (a) one, in (b) two feedback circuits are applied.

stabilization and feedback adjusted to be negative for one mode may be positive for another mode, enhancing its amplitude. A more complex, distributed arrangement of probes may be able to differentiate different modes.

DYNAMIC STABILIZATION

Dynamic stabilization experiments have been carried out using the following methods: (1) an ac field along the plasma column applied through the ionizer plates, (2) irradiation of the plasma with microwaves at the electron cyclotron or upper hybrid frequencies, and (3) application of axial or radial electric fields by one or two electron-emitting ring probes.

In all experiments, amplitude reduction or complete disappearance of the low-frequency drift wave or transverse Kelvin-Helmholtz mode was observed, and dependences on magnetic field, density, temperature, and rf intensity and frequency were measured.

Two fundamental and mutually dependent difficulties, however, are present in the interpretation of these results:

1. Theoretically, any self-consistent calculation must include plasma dissipative effects when rf is applied.

2. Experimentally, application of rf results in plasma parameter changes, i.e., variations of density, temperature, potential, and their gradients.

The experiments are especially complicated by the density reduction which accompanies rf application. Therefore, in general, it cannot be conclusively concluded that the disappearance of low-frequency instabilities is attributable to a stable equilibrium configuration generated by the dynamic frequency since changes of plasma parameters and the rf-induced plasma losses are not known.

In the experiment carried out with a hot, electron-emitting ring probe located in the midplane of the plasma column and radially near the density gradient maximum, by applying axial ac fields ($\omega_d \leq \omega \leq 100\,\omega_d$) between ring and end plates or radial fields to a nearby hot ring, stabilization was observed for the drift instability in the entire unstable regime for single-modes, multi-modes and turbulence. In these experiments, upon stabilization in the marginal regime, the plasma density increases, by an amount equal to the instability-induced loss. At the flux tube of the ring probe, large radial electric fields at the driving rf are measured ($\partial\phi(z)/\partial r \sim 1$ V/cm). Figure 7 shows the variation of drift-wave amplitude as a function of rf intensity for B = 4000 gauss (single-mode regime) and 6000 gauss (turbulent regime). The transverse Kelvin-Helmholtz instability has also been stabilized by similar methods.

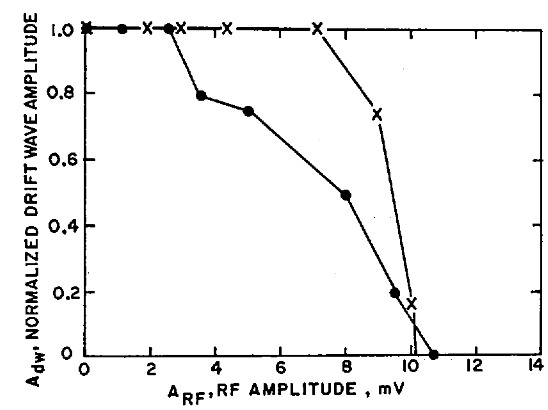

FIG. 7. Drift wave amplitude versus rf amplitude. •: B = 4000 G, single-mode regime. ×: B = 6000 G, turbulent regime. f_{rf} = 100 kHz, f_{dw} = 4 kHz.

POWER REQUIREMENT

The required power to feedback stabilize the drift instability by parallel electron current is

$$P_{fb} = \tilde{E} \cdot \tilde{J} = \frac{\tilde{\phi}}{\lambda_{\|}} \frac{e\tilde{n}\lambda_{\|}}{t_{\|}} = \frac{e\tilde{\phi}}{KT} \frac{\tilde{n}}{n_o} n_o KT \frac{1}{t_{\|}} \tag{1}$$

where $\tilde{\phi}$ and $\tilde{n}$ are the instability potential and density amplitude, $\lambda_{\|}$ the parallel wavelength. Noting $1/t_{\|} \approx b\omega_d \approx (0.1\,\omega_d)$, we obtain

$$P_{fb} \approx (\eta^2)\ (bn_o KT)(\omega_d) \tag{2}$$

where $\eta = e\tilde{\phi}/KT \approx \tilde{n}/n_o$. The stabilizing power is thus proportional to the plasma internal energy, the growth rate, and the square of the (relative) amplitude. Alternatively, the required power can be expressed as

$$P_{fb} = M\eta^2\gamma^3 \tag{3}$$

where M is the plasma mass per unit volume.

For dynamic stabilization with $E_z^{rf}(x)$ at frequency Ω, the stability criterion is [9,10] $v_y^{rf} \gtrsim bv_d$, where $v_y^{rf} = \langle v_z^{rf} \times B_y^{rf} \rangle = \frac{1}{2}(1/\omega_{ce})$. $[e^2(E_z^{rf})^2/m_e^2\Omega^2]\,\kappa_E$, $\kappa_E = (1/E_z^{rf})\,\partial E_z^{rf}/\partial x)$. The required power is

$$P_{ds} \doteq E^{rf} \cdot J^{rf} = v_y^{rf} \frac{2\omega_{ce} m_e \Omega}{\kappa_E} n_o \tag{4}$$

Using $-\nabla n_o/n_o \approx \kappa_E/2$, we obtain [11]

$$P_{ds} = bn_o\, kT\, \Omega \tag{5}$$

For $\Omega \approx 10\,\omega_d$, a reasonable lower limit of Ω to avoid possible parametric excitation, the ratio of required feedback to dynamic stabilization powers is

$$\frac{P_{fb}}{P_{ds}} \approx \frac{\omega_d}{\Omega} \eta^2 \tag{6}$$

TABLE I. POWER REQUIREMENT FOR FEEDBACK AND DYNAMIC STABILIZATION

$\tilde{n}/n_o$ (normalized amplitude)	$n_o kT$ (joules/cm^3)	Power Required (μW)			
		Feedback Stabilization		Dynamic Stabilization	
		Experiment	Calculation	Experiment	Calculation
0.1	4×10^{-9}	0.75×10^2	1.0×10^2	2.5×10^5	1.6×10^5

A comparison of calculated and measured power for the collisional drift instability is shown in Table 1. Qualitative agreement exists.

To estimate the dissipated power associated with feedback and dynamic stabilization for reactor purposes, it is necessary to know the dissipation factor 1/Q, (Q = total field energy/energy dissipated per rf cycle) of the plasma-feedback or plasma-dynamic stabilization system:

$$P_{\text{dissipative}} = P_{\text{reactive}}/Q \tag{7}$$

Q depends on the dissipation in plasma and circuit. An upper limit can be obtained by estimating only the plasma dissipation, in a longitudinal or transverse rf electric field:

$$\frac{1}{Q_{\parallel}} \approx \frac{\nu}{\Omega}\,\frac{\omega_p^2}{\Omega^2+\nu^2} \tag{8}$$

$$\frac{1}{Q_{\perp}} \approx \frac{\nu}{\Omega}\,\frac{\omega_p^2}{(\Omega^2+\omega_{ce}^2)+\nu^2} \tag{9}$$

For dynamic stabilization with high Ω so that $\Omega \gg \nu$, $\omega_p/\Omega \sim \omega_p/\omega_{ce} \sim 1$,

$$P_{\perp\,\text{dissipative}} \approx P_{\parallel\,\text{dissipative}} \approx (n_o KT)(\epsilon\nu) \tag{10}$$

The estimated power requirement, according to Eq. (10), for a variety of MHD and electrostatic modes, is found to be a large fraction of a fusion reactor output.

CONCLUSION

A fundamental difference exists between feedback and dynamic stabilization: for feedback control, the plasma equilibrium remains unchanged and the time-varying suppression signal interacts, efficiently, only with the unstable part of the plasma—the instability mode of amplitude $\tilde{n}$; for dynamic stabilization, the high-frequency field interacts with the entire plasma (in the region of localization of the instability) of density n_o, and this interaction may be regarded as the generation of a new, time-averaged equilibrium which is stable against a class of perturbations.

Feedback, therefore, depends on frequency (growth rate) and instability amplitude, is highly mode selective and difficult to apply in regions of strong mode interactions (including turbulence), can be successful at a repetition rate lower than the instability frequency, requires relatively low power and leaves the plasma in its original equilibrium. Dynamic stabilization is independent of instability amplitude, can be used in the single-mode, multi-mode and turbulent regimes, but requires excessive power since a new (dynamic) equilibrium must be maintained. The application of rf power may affect the plasma in such a way as to stabilize the instability by changing the zero order plasma parameters, thus complicating the understanding of dynamic stabilization experiments.

The power level necessary for stabilization is high and may seriously limit applicability of dynamic stabilization. However, by proper choice of rf advantages may be derived from the simultaneous heating and stabilization effects of rf fields.

ACKNOWLEDGMENT

This work was supported by USAEC Contract AT(30-1)-1238.

REFERENCES

[1] For a review of recent work and a bibliography see Feedback and Dynamic Control of Plasmas, CHU, T. K. and HENDEL, H. W., Eds. AIP Conference Proceedings, Vol. 1, American Institute of Physics, New York, 1970.

[2] HENDEL, H. W., CHU, T. K., and POLITZER, P. A., Phys. Fluids 11 (1968) 2426; HENDEL, H. W. and CHU, T. K. "Collisional Drift Instability," Chapter 9, in Methods of Experimental Physics, Vol. 9A, GRIEM, H. and LOVBERG, R. H., Eds. Academic Press, New York, 1970.

[3] JASSBY, D. L. and PERKINS, F. W., Phys. Rev. Letters 24 (1970) 256; JASSBY, D. L., Ph.D. Thesis, Princeton University, 1970.

[4] POLITZER, P. A., Ph.D. Thesis, Princeton University, 1969.

[5] SIMONEN, T. C., CHU, T. K., and HENDEL, H. W., Phys. Rev. Letters 23 (1969) 568.

[6] HENDEL, H. W., CHU, T. K., PERKINS, F. W., and SIMONEN, T. C., Phys. Rev. Letters 24 (1970) 90; CHU, T. K., HENDEL, H. W., PERKINS, F. W., and SIMONEN, T. C., Ref. 1, page 94.

[7] CHU, T. K., HENDEL, H. W., JASSBY, D. L., and SIMONEN, T. C., Ref. 1, page 142.

[8] MELCHER, J. R., Ref. 1, page 38; MILLNER, A. R. and PARKER, R. R., Ref. 1, page 54.

[9] DEMIRKHANOV, R. A., GUTKIN, T. I., and LOZOVSKII, S. N., JETP 28 (1969) 1164.

[10] LEPECHINSKY, D., ROLLAND, P., and TEICHMANN, J., Ref. 1, page 214.

[11] Power requirements for different dynamic stabilization schemes (e.g., rf electron short-circuit of transversely propagating modes [A. A. Ivanov and S. Teichmann, Czech. J. Phys. 19B, 941 (1969)], are found nearly the same as those for inhomogeneous rf fields used in the present calculation. Equations (2), (3), and (5) are general and hold for MHD-type instabilities as well. For instance, for linear momentum feedback, the feedback force and work done are $M\eta\gamma^2$ and $M\eta^2\gamma^3$, respectively. Feedback power is, therefore, $M\eta^2\gamma^3$. Expressing growth rate $\gamma(r^2 \sim g/\lambda)$ in terms of an accelerating field $g(\sim v_{th}^2/R)$ and using a wavelength λ comparable to the device dimension R, we obtain $P_{fb} \approx M\eta^2\gamma^3 \approx \epsilon\eta^2 n_o KT\gamma$, where ϵ represents effectively the fraction of particles participating in the instability. A similar result can be derived for dynamic stabilization of MHD modes.

REMOTE PLASMA CONTROL, HEATING AND MEASUREMENTS OF ELECTRON DISTRIBUTION AND TRAPPED PARTICLES BY NON-LINEAR ELECTROMAGNETIC INTERACTIONS*

A.Y. WONG, F.F. CHEN, N. BOOTH, D.L. JASSBY,
R. STENZEL, D. BAKER, C.S. LIU
University of California, Los Angeles, Calif.
United States of America

Abstract

REMOTE PLASMA CONTROL, HEATING AND MEASUREMENTS OF ELECTRON DISTRIBUTION AND TRAPPED PARTICLES BY NON-LINEAR ELECTROMAGNETIC INTERACTIONS.

Non-linear electromagnetic interactions with plasmas are generalized to include excitations at both cut-offs and resonances for extraordinary and ordinary modes of propagation. Experimental confirmations are presented. The collisionless and efficient nature of a "double-resonance" scheme in which high-frequency electron resonant modes couple to low-frequency resonant ion modes is exploited for plasma control and heating of plasma ions when a direct coupling to ion modes is not feasible. A new method of measuring electron velocity distribution functions at various radii of a fusion plasma is presented in which the cross-sections of laser scattering are dramatically increased. Finally, the electromagnetic excitation and detection of magnetically trapped particles via the echo technique are examined.

We wish to present a generalized view on the remote interaction [1] of, and study of fusion plasmas by, electromagnetic radiation at the electron characteristic frequencies—cut-offs and resonances. The central idea is that electromagnetic fields incident on the plasma are enhanced at these frequencies and the electron orbits are significantly perturbed to produce, through nonlinear mixing, new plasma modes. If these new modes are also resonant, such an interaction scheme is called the "Double Resonance Method". The "double resonance" interaction can be summarized as follows and in Table I.

1. Parametric Excitation [2] (Unmodulated Carrier).

Here one large amplitude, high frequency wave drives a low frequency "signal" wave and an "idler" wave, whose frequency matches the difference of the driver and signal frequencies. A low frequency wave present initially (as part of the fluctuation spectrum) is amplified. This interaction occurs only if the pump wave power exceeds an absolute threshold which depends not only on the damping and other energy loss mechanisms but, more importantly, on the initial amplitude of the fluctuations. Another type of excitation with an unmodulated carrier occurs when the RF can induce zeroth-order changes in plasma parameters (e.g., density gradient) which then trigger instabilities (e.g., drift waves).

2. Mode-Coupling Excitation (Modulated Carrier).

Here two large amplitude, high frequency waves drive a low frequency wave at their difference frequency. This will amplify fluctuations present initially and also produce low frequency waves even if they are not favored

* Research supported by AEC and AFOSR.

TABLE I. CLASSIFICATION OF TYPES OF INTERACTION AND EXPERIMENTAL VERIFICATION.

Characteristic Frequencies / Types of Interaction		Cut-off			Resonances	
	Modes	Experimental Verification	Application	Modes	Experimental Verification	Appli-
Parametric Coupling	X		(ii)	X	this paper	(i)
	0	ref. 3,4 & this paper	(iii)	0*		
Mode Coupling	X	ref. 1	(i), (ii)	X	ref. 1	(i), (iii)
	0	this paper	(i), (ii)	0*		

* Although the cold plasma theory predicts only a cut-off for the 0-mode, inclusion of the plasma pressure shows that electrostatic plasma waves (resonance) and ion waves can be excited. Rigorously speaking, the cut-off of the EM wave and the resonance of the electrostatic modes can occur simultaneously.

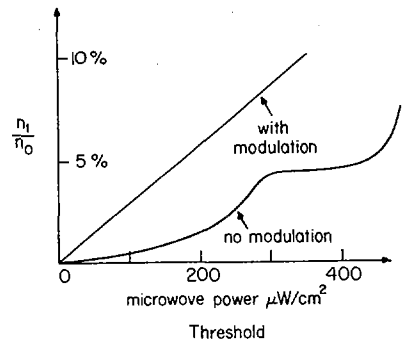

FIG. 1. Comparison between threshold behaviour of parametric and mode-coupling excitations. The amplitude of the excited electrostatic ion cyclotron mode is plotted versus the power of the high-frequency extraordinary mode. Parametric excitation is effective only after a certain threshold is reached.

in the natural spectrum. As shown in our experimental results (Fig. 1) there is no real "threshold" for mode-coupling excitation, although the loss mechanisms will partially determine the final saturated amplitude of the low frequency wave and, therefore, the input power required to produce detectable effects. Finally, the nonlinear couplings will peak where the RF electric field is large; for the X-mode ($\underline{E} \perp \underline{B}_o$) this will occur near the right hand cut-off and upper hybrid resonance; and for the 0-mode ($\underline{E} \parallel \underline{B}_o$) at the plasma cut-off.

As experimental results on the excitation at upper hybrid resonances have already appeared in literature [1], we shall present new experimental data involving the characteristic frequency at cut-off for the parametric and mode coupling cases. Although the fields are not as strongly enhanced as at resonance, the cut-off has the distinct advantage that it is always accessible.

Recent Experimental Results on Interactions at Cut-off.

1. Mode Coupling at the Cut-off Frequency of X Mode

A microwave beam in the extraordinary mode at frequency ω_μ modulated at the electrostatic ion cyclotron frequency ω_i is irradiated on a Q-device (f_{pe} = electron plasma frequency = 1.2 GHz, f_{ce} = electron cyclotron frequency = 3.7 GHz, $T_e = T_i = 0.2$ eV). As the magnetic field is decreased (Fig. 2) there reaches a point where only an interaction at cut-off is possible; i.e., $\omega_\mu = \omega_R > \omega_{h\ max}$ where $\omega_R \approx (\omega_{ce}^2 + 2\omega_{pe}^2)^{1/2}$ and $\omega_{h\ max} = (\omega_c^{\ 2} + \omega_p^{\ 2})^{1/2}$.

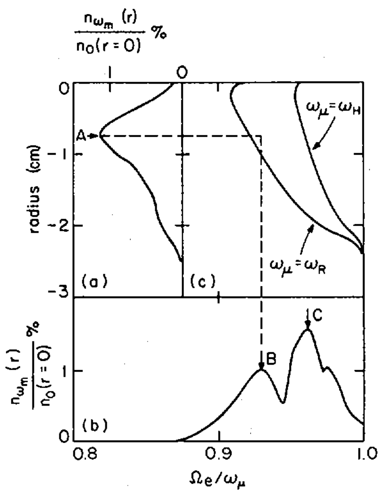

FIG. 2. Experimental verification of excitation at cut-off of extraordinary mode.
a) Radial amplitude profile of excited electrostatic ion cyclotron waves at a B field (Ω_e/ω_μ = 0. 923) denoted by the arrow B.
b) Amplitude of excited electrostatic ion cyclotron waves versus variation in B field Ω_e/ω_μ measured with probe at radius A. Arrow B indicates the cut-off excitation, while arrow C the upper hybrid excitation.
c) Loci of $\omega_\mu = \omega_h$ and $\omega_\mu = \omega_R$ versus Ω_e/ω_μ. The radial density variation is included. The interaction at cut-off is confirmed when $\omega_\mu = \omega_R > \omega_{h\ max}$. Coincident enhancements of excited ion oscillations are observed at a radial location and B field that correspond to the locus $\omega_\mu = \omega_R$.

The amplitude of the excited ion oscillations $n_i/n_o(\omega_{ci})$ is monitored as function of radius and magnetic field. Coincident enhancements of $n_i/n_o(\omega_{ci})$ are observed at peaks A, B at the radius where $\omega_\mu = \omega_R$, indicating the occurrence of the cut-off interaction. The power required is approximately 3.0 mW/cm.

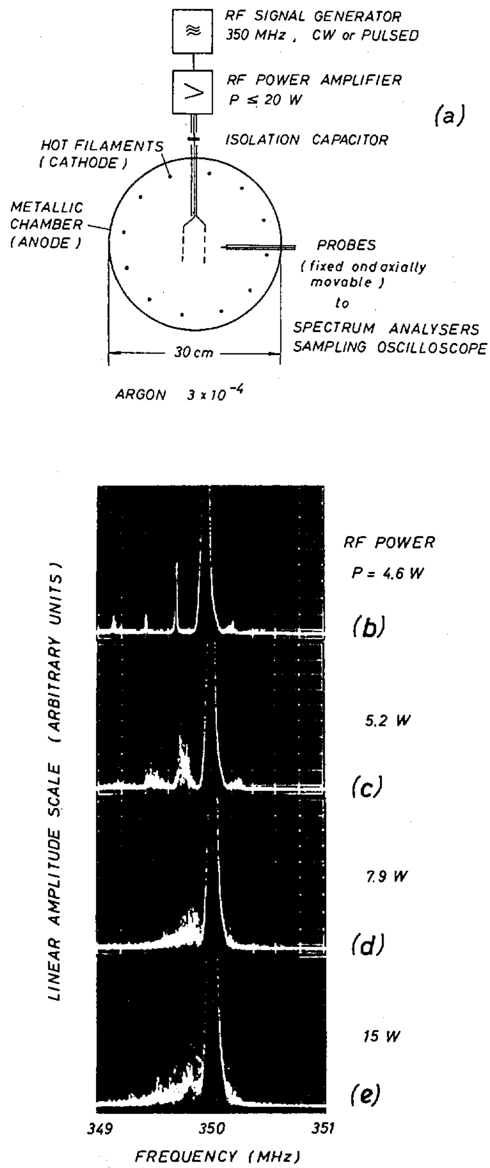

FIG. 3. Parametric excitation near $\omega_{\mu} = \omega_{pe}$.
a) Experimental arrangement in the UCLA DP device. Typical parameters of the plasma generated by a dc discharge in argon at 3×10^{-4} Torr are: $T_e \cong 2$ eV, $T_i \cong 0.2$ eV, $n_0 \cong 10^9$ cm^{-3}, $\delta n/n_i \approx 10^{-3}$. The pump rf electric field with frequency $f_0 = 350$ MHz is provided by a parallel-plate capacitor (4 cm × 4 cm wire grids, 3 cm spacing) immersed into the center of the plasma. The electrodes are coupled capacitively to the rf generator in order to avoid dc currents flowing into the plasma.
b), c), d), e) Spectra of the pump and the electrostatic plasma waves versus input pump power; the signals were detected by a shielded probe inside the plasma.

2. Mode Coupling at the Cut-off Frequency of O-mode.

Similar interactions between the high frequency electromagnetic waves in the ordinary mode and the electrostatic ion cyclotron modes are observed. The O-mode excitation is confirmed by noting that $\omega_\mu \cong \omega_p(r_o)$, where r_o = the radius of interaction, and that the interaction is insensitive to changes in the B field. The threshold power for the excitation of electrostatic ion cyclotron modes ($n_o \simeq 10^{11}$ cm^{-3}, $T_e = T_i = 0.2$ eV) is 3.0 mW/cm .

3. Parametric Coupling Between an Electromagnetic Pump ω_o, an Electron Plasma Wave ω_e, and an Ion Acoustic Wave ω_i; $\omega_o = \omega_e + \omega_i$.

The experiment [3] is performed in a uniform, quiescent, collisionless magnetic-field-free plasma as produced by the UCLA double-plasma devices. The pump electromagnetic field with frequency f_o = 350 MHz is provided by a parallel-plate capacitor immersed in the center of the plasma. The rf spectrum of a signal picked up by a shielded probe inside the plasma is shown in Fig. 3b-d. The incident rf signal is tuned to the electron plasma frequency as determined from Langmuir probe measurements. As the rf pump power is raised beyond a sharp threshold ($P_t \simeq 4.5$ watts) a nearly monochromatic sideband appears at $\omega_e = \omega_o - \omega_i$ below the pump frequency ω_o. With increasing pump power the sideband grows, smaller sidebands appear at $\omega_o + \omega_i$, $\omega_o - 2\omega_i$ (Fig. 3b), the lines broaden (Fig. 3c,d) and finally approach a continuous noise spectrum (Fig. 3e).

The asymmetric line shape is a result of the downward decay of the pump into electron and ion modes. The threshold field of E_{th} = 7V/cm and the measured wave number of the electron and ion modes k = 5.3 cm^{-1} are in good agreement with the theoretical predictions E_{th} = 5.1 V/cm and k = 6.3 cm^{-1}. The concept of parametric coupling was also demonstrated recently in an ionospheric experiment [4].

Applications to Fusion Plasmas

1. Plasma Control.

Control of low-frequency instabilities in toroidal devices can be achieved by feedback stabilization if localized signals can be injected into the interior of a thermonuclear plasma. A complete remote detection and feedback stabilization using microwaves have been demonstrated. Since it operates directly on the internal electric field in a plasma, the double resonance method is intrinsically more efficient than the method of neutral beams [5]. If the density is between 10^{15} and 10^{16} cm^{-3}, the wavelength of the incident beam with $\omega = \omega_h$ lies in the range 300-750 μm. This is the range covered by recently developed far-infrared lasers, such as HCN, which can provide much higher power than submillimeter microwave generators. There is, however, a problem of accessibility. The thickness d of the evanescent layer between the $\omega = \omega_r$ and $\omega = \omega_h$ radii is easily found to be

$$d = \omega_c \Lambda(\omega_o - \omega_c)/\omega_p^2$$

where Λ is the density scale length. In the experiments described above, $k_o d$ is approximately $3(\Lambda/\lambda_o) \simeq 0.5$, where $k_o = \omega_o/c$, and the Budden tunneling factor $\exp-(1/2)\pi k_o d) \simeq 0.5$ is not significant. In a reactor, however, $k_o d$ will be larger than 10^3, and no tunneling to the resonance layer can be expected. There are three ways around this problem.

a) The interaction at the cut-off can be used. For an O-mode, Ginzburg [6] has shown that the electric field near the cut-off reaches an amplitude $1.9\ (k_o\Lambda)^{1/6}$ times the incident amplitude. Thus the cut-off interaction would be expected to be relatively stronger in a fusion plasma than in the present experiments.

b) For $\omega_p < \omega_c$, the evanescent layer can be avoided by making use of the magnetic field inhomogeneity [7] in a torus. The laser beam must then be injected, by means of a mirror, from the strong field side of a torus near the major axis.

c) The radiation at $\omega = \omega_h$ can be generated at the resonant layer by a second nonlinear process in which two CO_2 lasers operating on different lines produce a difference frequency equal to ω_h. One of the lasers is then modulated at the feedback frequency. The efficiency has been calculated by Etievant et al. [8] and depends critically on the width of the resonance. It is probable, however, that a weakly nonlinear theory such as this will not describe the results adequately. Even if the down-conversion is efficient, the efficiency will still be limited by the Manley-Rowe relation to the ratio of wavelengths ($\sim$ 3%). This should not be a hardship, since currently available dc power from CO_2 lasers is more than 10^7 times that available from HCN lasers.

2. Ion Heating at the Electrostatic Ion Cyclotron Frequencies and Lower Hybrid Frequency.

We wish to point out an rf heating method which is external to the plasma and does not suffer from the coupling problems of most ion cyclotron heating schemes [9].

Rf power is coupled with high efficiency into the plasma at electron resonances such as the electron cyclotron and the upper hybrid resonance or with lower efficiency at the electron plasma frequency. Due to gradients and/or parametric effects electron normal modes couple to ion normal modes such as drift waves, ion cyclotron and acoustic waves [1]. For low damping ion waves easily become unstable and build up to significant amplitudes. For single-frequency heating a minimum threshold field is required to excite ion oscillations. However, with two heating frequencies separated in frequency by an ion resonance such as the lower hybrid resonance, forced ion oscillations are obtained for any heating power.

The driven electrostatic ion oscillations lead to an ion temperature increase when the phase between field and particle velocity is randomized. In a collisionless plasma this is accomplished by modulating the frequency difference stochastically with correlation time approximately equal to the ion oscillation period. With the results of Fig. 1 and an ion heating model developed in [10] we estimate a required X-mode heating power $P_{absorbed} \simeq 4$ W/cm^2 to raise the ion temperature from 0.2 eV to 1 eV on a Q-machine plasma at B = 800 G.

3. Measurement of the Electron Velocity Distribution.

In fusion plasmas it is of interest to measure the electron distribution at various radii. Since laser scattering by electron plasma waves has a much larger cross section (NL^3, the number of electrons participating in the collective motion) than scattering by incoherent electrons, we propose a method which involves the parametric excitation of electron plasma waves by an electromagnetic wave in the ordinary mode, matched to the plasma wave frequency at the desired radius.

As suggested by our experimental findings [scattering wavelength $\lambda \ll$ density gradient length, $n_o/(dn_o/dx)$] the parametric excitation of electron plasma waves can be enhanced by the high energy tail in the electron distribution. The overall enhancement can be estimated as

$$\frac{S_{par}(\omega_e,k_e)}{S_{eq}(\omega_e,k_e)} \propto \frac{f_o(v=\omega_e/k_e)}{\frac{\partial f_o}{\partial v}(v=\omega_e/k_e)} \; \frac{1}{[1 - E^2/E^2_{thres}]}$$

where $S_{par}(\omega_e)$ is the power spectrum of plasma fluctuations under parametric excitation which are enhanced by the high energy tail, and $S_{eq}(\omega_e)$ is the power spectrum for a Maxwellian plasma without parametric excitation and high energy tail. The factor $f_o(v)/f_o'(v)$ represents the Cerenkov emission of plasma waves by non-thermal electrons. Our experimental results have shown that an enhancement by several orders of magnitude can be expected. An excitation source of 1 watt at ω_e should be sufficient. The detection of the plasma waves (ω_e, k_e) is accomplished by the scattering of another pulsed laser beam of much higher frequency and power. The angle of the scattering determines $\underline{k}_e$, and the upper and lower sidebands of the high frequency beam can yield amplitude of plasma waves propagating along or opposite to the direction of current flow on Tokamaks or spherators. By measuring a range of k_e's through variation of the detection angle θ, the amplitudes of plasma waves at different phase velocities ω_e/k_e and $f_o(v=\omega_e/k_e)$ can be estimated.

4. Measurement of Trapped Particle Behavior.

Recently the excitation and detection of magnetically trapped particle echoes have been proposed [11] to study the lifetime, orbits, and diffusion rate of such particles. The spatially selective nature of the electromagnetic excitation at either the cyclotron frequency or the upper hybrid frequency which resonantly changes $V_\perp$ is particularly suited to this task. The bounce frequency

$$\omega_b^{-1} = \frac{1}{2\pi} \oint ds \left[\frac{2}{m} (W - \mu B - q\Phi) \right]^{-1/2}$$

and hence the phase of the magnetically trapped particle, is altered if $\mu = 1/2\ MV^2/B$ is changed by two successive electromagnetic impulses separated by τ. Depending on their phase $\theta = \omega_b \tau$ with respect to these pulses some trapped particles acquire higher or lower energy and their bounce frequencies are correspondingly increased or reduced. These accelerations and decelerations of various groups of trapped particles in phase space permit a regrouping of the trapped particles at time τ after the second impulse; echoes can be observed as collective radiation from the trapped particles.

By following the procedure of ref. 11 we derive an expression for the number of trapped particles that regroup to form echoes as:

$$|n^{(2)}/N_o|_{echo} = (\delta W/\overline{W})^2\ (\overline{\omega}_b T_o)^2$$

where
$\underline{T}_o$ = the duration of the excitation electromagnetic pulse
$\overline{\omega}_b$ = the average bounce frequenccy,
$\delta\overline{W} = \delta(1/2\ mV^2)$ = change in perpendicular energy as a result of resonant acceleration by the pulse of electromagnetic waves at ω_b of duration T_o,
$\overline{W}$ = average energy of trapped particle.

An estimate of the magnitude and duration of the applied perturbation pulses can be made, based on our experience with electrostatic trapped particles [3] that an echo $n^{(2)}/N_o \gtrsim 10^{-2}$ can be detected. The precise time of occurrence of echoes makes it possible to devise detection schemes with the above sensitivity. We found that $q\phi/W \simeq 0.1$ and $\omega_b T_o \simeq 0.5$ can be sufficient to generate observable echoes. Under present parameters of fusion devices, $\overline{W} = 500$ eV and $(\overline{\omega}_b)_{el} \simeq 10^9$ rad/sec, electromagnetic pulses of 10 W and duration 10 nsec can be employed to generate trapped particle echoes.

REFERENCES

[1] WONG, A.Y., BAKER, D. R., BOOTH, N., Phys. Rev. Letters 24 (1970) 804; BOOTH, N., WONG, A. Y., UCLA Plasma Physics Group Report R-83, Dec. 1970.

[2] DUBOIS, D. F., GOLDMAN, M. V., Phys. Rev. 164 (1967) 207; WONG, A. Y., GOLDMAN, M. V., HAI, F., ROWBERG, R., Phys. Rev. Letters 21 (1968) 518;

NISHIKAWA, K., J. Phys. Soc. Japan 24 (1968) 916, 1152;
WONG, A. Y., ARNUSH, D., FRIED, B. D., KENNEL, C. F., TAYLOR, R. J., BOOTH, N., TRW Systems Group Report, Dec. 1970.
[3] STENZEL, R., UCLA Plasma Physics Group Report R-84, March 1971.
[4] WONG, A. Y., TAYLOR, R. J., TRW Systems Internal Report #I-I, March 1971.
[5] CHEN, F. F., FURTH, H. P., Nuclear Fusion 9 (1969) 364.
[6] GINZBURG, V. L., The Propagation of Electromagnetic Waves in Plasmas (Pergamon Press, 1964), p. 366.
[7] WONG, A. Y., KUCKES, A. F., Phys. Rev. Letters 13 (1964) 306.
[8] ETIEVANT, C., OSSAKOW, S., OZIZMIR, E., SU, C. H., FIDONE, I., Phys. Fluids 11 (1968) 1778.
[9] STIX, T. H., PALLADINO, W. R., Phys. Fluids 1 (1958) 466;
CATO, J. E., KRISTIANSEN, HAGLER, M. V., Bull. Am. Phys. Soc. 15 (1970) 1431.
[10] ASTRELIN, V. T., BUCHELNIKOVA, N. S., KUDRYAVTSEV, A. M., Sov. Phys.-Tech. Phys. 15 (1970) 915.
[11] LIU, C. S., WONG, A. Y., Phys. Rev. Letters 25 (1970) 1702.

DISCUSSION

TO PAPERS IAEA-CN-28/B-13, B-14, B-15

F.L. RIBE: You said that MHD-modes are not subject to linear feedback stabilization. I think it is more accurate to say that MHD interchange modes cannot be so stabilized. At Los Alamos we intend to do an experiment using feedback to stabilize the MHD m = 1 mode on a high-β stellarator. These MHD-modes are not interchange modes.

E.S. WEIBEL: The power required for dynamic stabilization must depend on the resistivity of the plasma. What resistivity was used?

P.E. STOTT: Perhaps the authors of papers B-14 or B-15 will answer this.

H.W. HENDEL: We used classical plasma resistivity with no dissipation in the circuit.

F.F. CHEN: In answer to Mr. Weibel's question, I should like to add that the feedback amplitude needed to stabilize resistive drift does not depend on the resistivity. The feedback signal has only to cancel the charge separation caused by the difference between the ion and electron perpendicular drifts.

P.K. KAW: In the Culham experiment (paper B-13) there seemed to be a critical frequency at which the dynamic stabilization was most efficient - as seen by a minimum in the electric field required. Was this frequency related to some natural plasma oscillation frequency?

P.E. STOTT: No. Equation 7 gives the theoretical condition for marginal stability; the frequency at which the optimum threshold electric field E_z occurs can be found from this expression. In the present case the minimum occurred for a frequency $\omega \simeq \nu_e$ the electron collision frequency.

K.I. THOMASSEN: You stated that attempts to feedback-stabilize several azimuthal modes simultaneously have been unsuccessful. I should like to mention, however, that in an experiment carried out by Lindgren and Birdsall at Berkeley a year ago m = 1, 2 and 3 drift modes were simultaneously stabilized with three separated amplifier and feedback systems using frequency-selective filters.

TOKAMAKS I

(Session C)

Chairman: B. B. KADOMTSEV

Paper C-3 was presented by
V. D. SHAFRANOV as Rapporteur

Papers C-5 and C-6 were presented by
L. M. KOVRIZHNYKH as Rapporteur

Papers C-9 and C-10 were presented by
E. MESERVEY as Rapporteur

OAK RIDGE TOKAMAK RESEARCH*

C.F. BARNETT, J.F. CLARKE, R.C. DAVIS, R.A. DORY,
P.H. EDMONDS, H.K. FORSEN**, J.T. HOGAN, G.G. KELLEY,
M.J. LUBIN†, J.R. McNALLY, O.B. MORGAN, M. MURAKAMI,
M. ROBERTS, J.M. SOURES†, L.D. STEWART, W.L. STIRLING,
M.M. WIDNER
Oak Ridge National Laboratory,
Oak Ridge, Tenn., United States of America

Abstract

OAK RIDGE TOKAMAK RESEARCH.

Research related to the ORMAK experiment is described.

1. Theory: To aid interpretation of experimental data, detailed behaviour of Tokamak discharges has been calculated, using two-fluid MHD theory augmented where necessary and possible by specific experimental features (banana orbits, impurities, external circuits, etc.). Time-dependent spatially-resolved integration of the ion and electron heat flow equations and Maxwell equations (as in work by Dnestrovsky et al.) has given data for experimental comparison, for determination of poorly known parameters (resistivity and electron thermal conductivity anomalies, etc.), and for study of sensitivity to parameters normally not adjustable in experiments (scaling laws). The pressure balance equation is used with these results to determine overall plasma diamagnetism.

Because ohmic heating becomes ineffective in the keV régime, we have studied supplementary heating by injection of energetic neutrals. We find factors of 2-3 gain in ion temperature with feasible injectors.

2. Experiment: The ORMAK experiment is designed to go well into the collisionless (banana) régime where a reactor would operate. In this régime, the effect of asymmetries could be quite harmful so they have been minimized by careful design. Parameters are R = 80 cm, r_p = 23.5 cm, and A = R/r_p = 3.4. Total currents of 400 kA (programmable) will eventually be available to give q (safety factor) = 1.5 at the maximum toroidal field of 25 kG. A programmable vertical field is provided for positioning the plasma. At 400 kA, theory predicts $T_e \sim 2$ keV and $T_i \sim 1$ keV at $n = 5 \times 10^{13}$ cm^{-3}. The authors describe the initial results from this device, including space- and time-resolved laser measurements of electron temperature and density, and charge-exchange measurements of ion temperature. These measurements will be correlated with computed values to determine transport coefficients. Magnetic probes will be used to study mode patterns of instabilities and movement of the plasma column.

1. INTRODUCTION

The experimental device ORMAK-I was designed on the basis of predicted neo-classical behavior to push far into the collisionless (banana) regime[1]. Specifically, it has a low aspect ratio (major diameter/minor diameter = A = 3.4) and a large minor radius (23.5 cm) and can be pulsed at constant current for several expected energy containment times. The toroidal magnetic field is 25 kG. This paper will describe the experimental program and some of the theoretical work which has been done in support of this program.

---

* Research sponsored by the US Atomic Energy Commission under contract with the Union Carbide Corporation.

** University of Wisconsin, Madison, Wisconsin.

† University of Rochester, Rochester, New York.

2. DESIGN AND CONSTRUCTION OF THE ORMAK FACILITY

The design was begun in May, 1969 and construction was completed in January, 1971. Troubleshooting and final electrical work continued until the beginning of plasma operation in May, 1971.

2.1. General Description of the Device

The ORMAK device uses a symmetric, low aspect ratio magnetic field structure to confine the plasma. All three magnetic (toroidal, poloidal or plasma current, and vertical) coil systems are cooled by liquid nitrogen and each is driven by a programmable current supply. A gold-plated, separately pumped, conducting liner surrounds the plasma providing a clean environment for minimum impurity levels. The entire device, including the voltage inducing ferromagnetic core, and the support structure, is enclosed in a vacuum tank for thermal insulation, reduction of pressure on the plasma liner and ease of maintaining high vacuum in that liner. Figure 1 indicates all the major components of the present device.

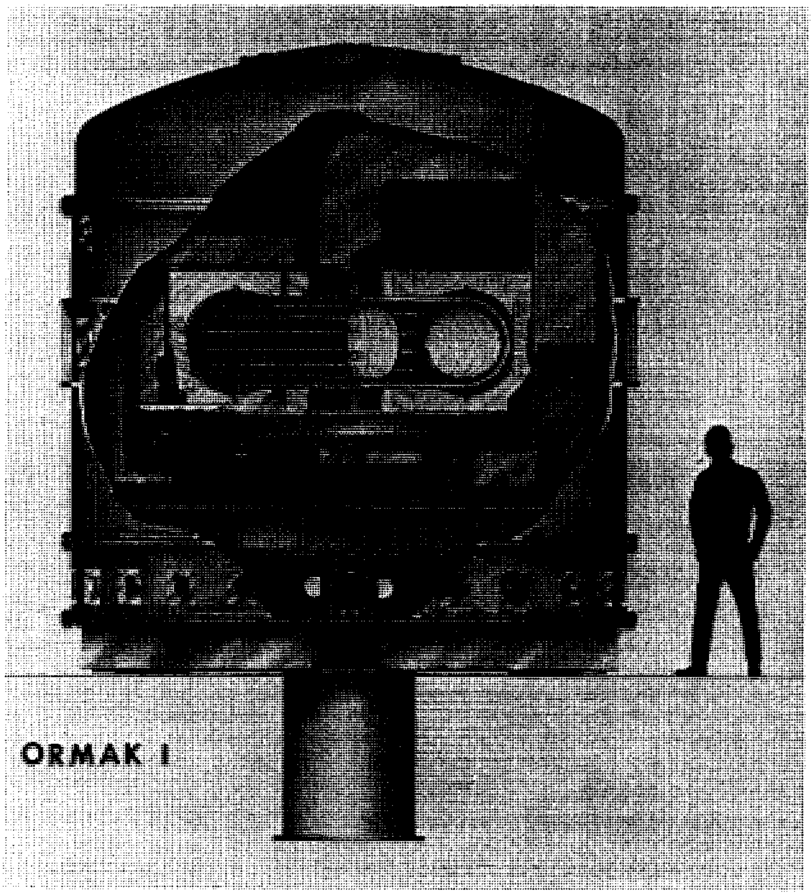

FIG.1. ORMAK-I. A cut-away view of the device taken from the detailed design drawings. The plasma is contained in the toroidal magnetic field produced by the coils located in the centre of the vacuum tank.

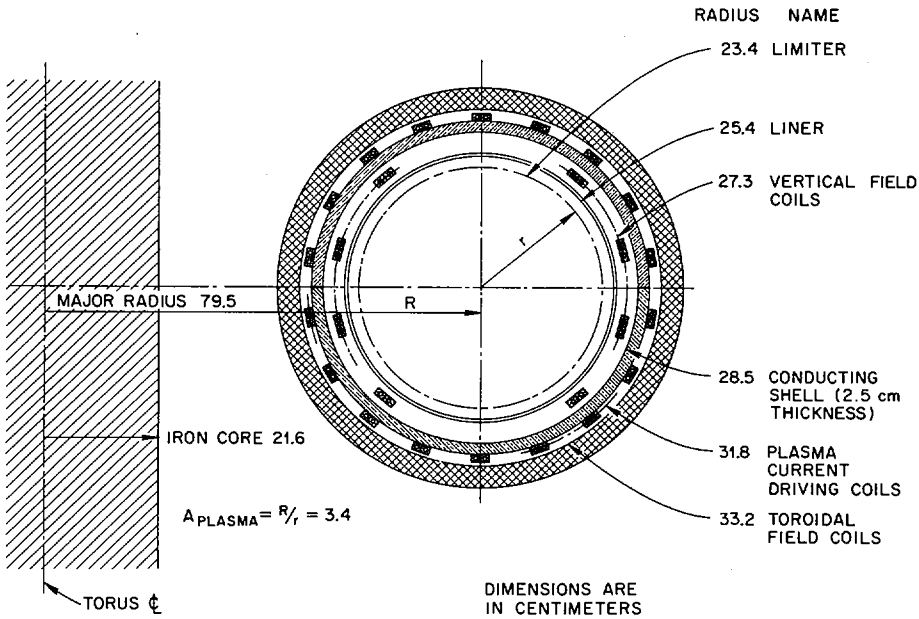

FIG. 2. Cross-sectional elevation of ORMAK.

2.2. Magnetic Field Structure

Figure 2 illustrates the dimensions and relative positions of the three magnetic field coil systems and the passive conducting shell as well as the limiter and liner.

2.2.1. Toroidal Field

The toroidal field, B_T, is produced by a set of 56, equally spaced, cryogenically cooled, copper coils. The maximum design field strength is 25 kG on the center line and maintained flat (~ .1% ripple) for about .3 sec. The geometric ripple at the outer edge of the plasma is .05% and the tracking among the four 3 MW dc generators (which each feed 15 kA through 14 coils equally spread in azimuth) is .05% resulting in a net .1% ripple.

2.2.2. Plasma Current

The plasma current is driven by a coil made of eighteen turns symmetrically arranged in the minor cross section. The design maximum current is about 400 kA, maintained for the experimental flat-field time of ~ .3 sec. The eighteen turn coil is arranged in two nine-turn halves, top and bottom, and can be connected either in series or parallel. Calculations show that over a wide range of plasma conditions the equilibrium poloidal magnetic field would be uniform in the minor cross section thereby determining the uniform spacing of the coils. As with the toroidal field, the poloidal field coils are fed by parallel lines closely coupled together to reduce field errors, eliminate any net orthogonal flux and reduce inductance. Because the machine is broken into two halves along a vertical plane through a major diameter, each poloidal winding has two pieces that must be joined as the machine halves are rolled together. Demountable pressure joints using an annealed silver shim were used to make these 30 kA connections.

A .72 volt-sec ferromagnetic core (made of .012" grain oriented, 4% silicon steel) is used to minimize the energy necessary to induce the azimuthal electric field. With a back-bias winding, the core should provide sufficient volt-sec to drive the plasma current at $q = 2.5$ and $B_T = 25$ kG for the anticipated duration of the experiment.

The poloidal field power supply provides either 40 or 80 volts/turn from a 20 kJ capacitor bank and a programmable current from a battery bank capable of millisecond response times.

2.2.3. Vertical Field

The plasma current ring is acted upon radially by the J x B force exerted by the vertical field, $B_{\perp}$. Eight conductors are located inside the conducting shell, each carrying up to 30 kA, producing a programmable field of up to 150 G. The vertical field is azimuthally symmetric as are the other magnetic fields.

2.2.4. Conducting Shell

The aluminum conducting shell has appeared necessary in Tokamak experiments, thus far, and is used here both as a passive feedback system for current and also as a mechanical support for the plasma current and vertical field coils. This shell is a 2.5 cm thick toroid split into four quarters. One cut in the horizontal plane along the outer major circumference is necessary to prevent induction current while the generator current is rising. The cut in the vertical plane (in practice, 10 cm wide permitting access for laser scattering and limiter replacement) is necessary to prevent shorting of the plasma driving voltage.

2.3. Cooling

All three sets of copper current conductors are hollow for the passage of liquid nitrogen coolant; the aluminum shell is indirectly cooled by the poloidal and vertical field coils.

2.4. Liner

The liner is electrically conducting and continuous in all directions, in order to provide protection against non-symmetric electric fields. As a compromise between the requirements of mechanical rigidity and the passage of high frequency electromagnetic signals, the liner is made of .010" non-magnetic stainless steel sheet. To reduce the adherence of impurities on the wall and to reduce the radiation cooling from the outside to the cooled surfaces, the liner is gold plated on both surfaces with about 1 micron of vacuum deposited gold applied to each baked segment of the liner. Mechanical clamps form the closures between the two halves of the liner.

2.4.1. Limiter

The limiter determines the cross sectional size of the plasma. Since most of the pulse power will be dissipated on it, it is made of 1/2" sq. tungsten formed in a four segment circle. Each quadrant (up, down, in, out) is electrically insulated and reasonably well isolated thermally. Temperature is measured by platinum temperature transducers. The outer segment is removable allowing replacement of this most vulnerable element.

2.5. Diagnostics

Figure 3 is a plan view of the machine indicating the diagnostic devices. The Thomson-scattering Laser apparatus, a four-pulse ruby laser, provides pulses spaced as close together as 500 μsec, each with an energy > 10 joules. The scattered signals are examined at seven radial points for spatial and temporal resolution of n and T_e. The input laser beam is directed inward along a radius in the equatorial plane and the scattered

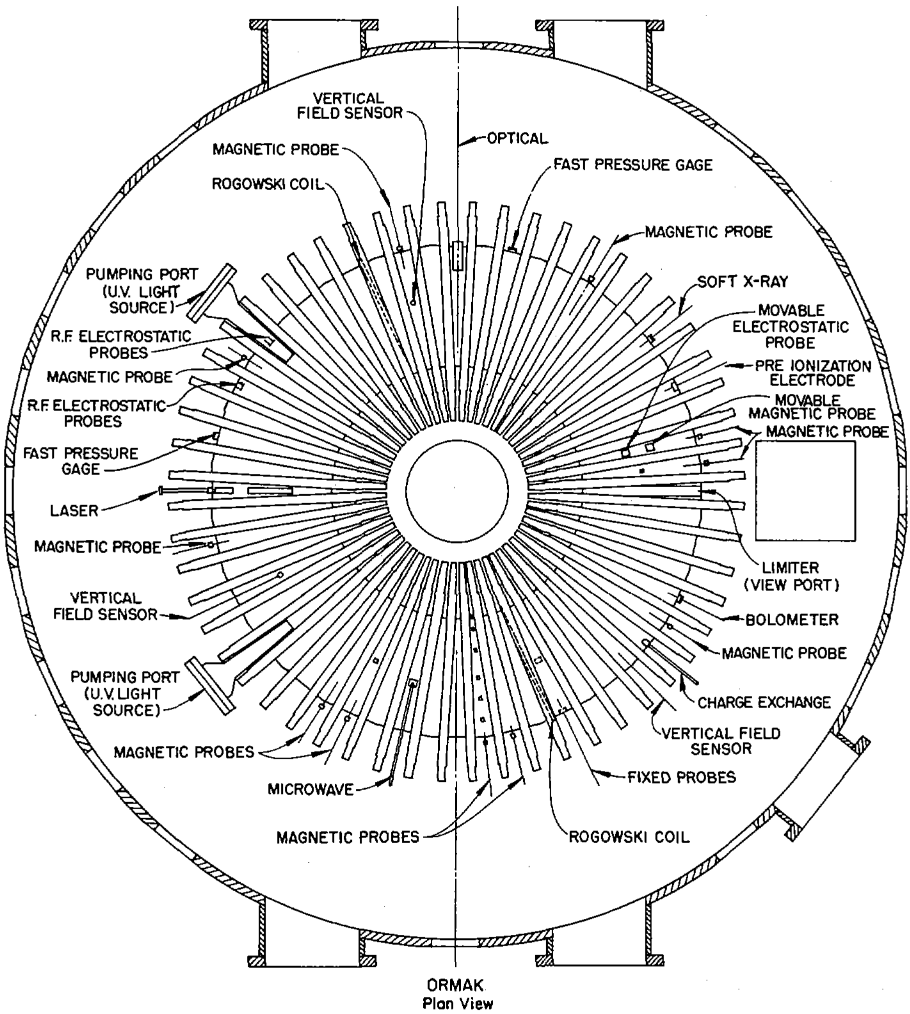

FIG.3. Plan view of ORMAK.

light is examined by 22 photomultipliers. Ten channels record the complete energy spectrum at any one predetermined radial point in the plasma. The remaining 12 channels are used in pairs with interference filters at six other radial points to get electron temperature and density.

3. THEORY

We have used the MHD thermal transport equations[2], Maxwell's equations and neo-classical thermal conductivity coefficients[3] with suitable numerical techniques to simulate Tokamak discharges. The work is similar to that done by French[4] and Russian[5] groups. In agreement with the earlier work, we find large discrepancies between the numerical results and the experimental data[6] unless the plasma resistivity and electron thermal conductivity are enhanced by anomaly factors $\gamma_R \sim 4$ and $\gamma_T \sim 10$ over the classical values. The resistivity anomaly factor γ_R is consistent with independent measurements[7] of the ratio of plasma resistivity to Spitzer's value. With such anomaly factors, it is possible to obtain, over a broad range of experimental conditions, a reasonable fit to the T-3 data[6] giving T_e profiles as functions of time and the energy containment time τ_E.

Using the same anomaly factors, similar calculations for the parameters of ORMAK suggest $T_e \sim 400$ eV, $T_i \sim 200$ eV at $n = 1.5 \times 10^{13}$ cm^{-3} under the initial operating conditions $B_T = 8$ kG and $I_T = 80$ kA, while $T_e \sim 1000$ eV, $T_i \sim 600$ eV at $n = 5 \times 10^{13}$ cm^{-3} at full operating conditions with $q = aB_T/RB_P = 2.5$ at $B_T = 25$ kG and $I_T = 344$ kA.

The full details of the simulation work are being prepared for publication elsewhere, but for completeness here, we mention that the calculation treats a one dimension discharge but uses transport coefficients corrected for toroidal curvature effects. The ion and electron temperatures, toroidal current density j_T and poloidal magnetic field B_P are treated dynamically, while the plasma density profile is held static as suggested by experiment: $n = n_o(1 - r^2/2a^2)$ where $r = a$ is the radius where the plasma pressure becomes negligibly small.

Two features of the T-3 results were striking: 1) Plasma heating occurs predominately during periods of rising toroidal current I_T, decaying in times ~ 5 msec after I_T is regulated to a constant value. 2) Throughout the duration of most of the cases that agreed with experiment, the stability factor $q(r)$ had its minimum off the magnetic axis $r = 0$.

Rapid thermal conduction ($\gamma_T \sim 10$) is probably responsible for the first feature, as well as for the absence of thermal instability[3].

The second feature suggests the possible presence of MHD instabilities of a type intermediate to the cases of localized flute modes and kink modes where the entire plasma column is shifted. The intermediate "non-local flutes" can occur when q has a minimum at $r \neq 0$, as will be discussed later.

Sample results of the simulation are shown in Fig. 4 for a case giving a reasonable fit to the data in Fig. 26 of Reference 6. The curves give the evolution of T_e, T_i, and τ_E and the history of the profiles $T_e(r)$, $j_T(r)$ and $q(r)$. For this case $\gamma_R = 4$ and $\gamma_T = 10$. Careful comparison of these curves with the data reveals discrepancy of small detail but reasonable overall agreement.

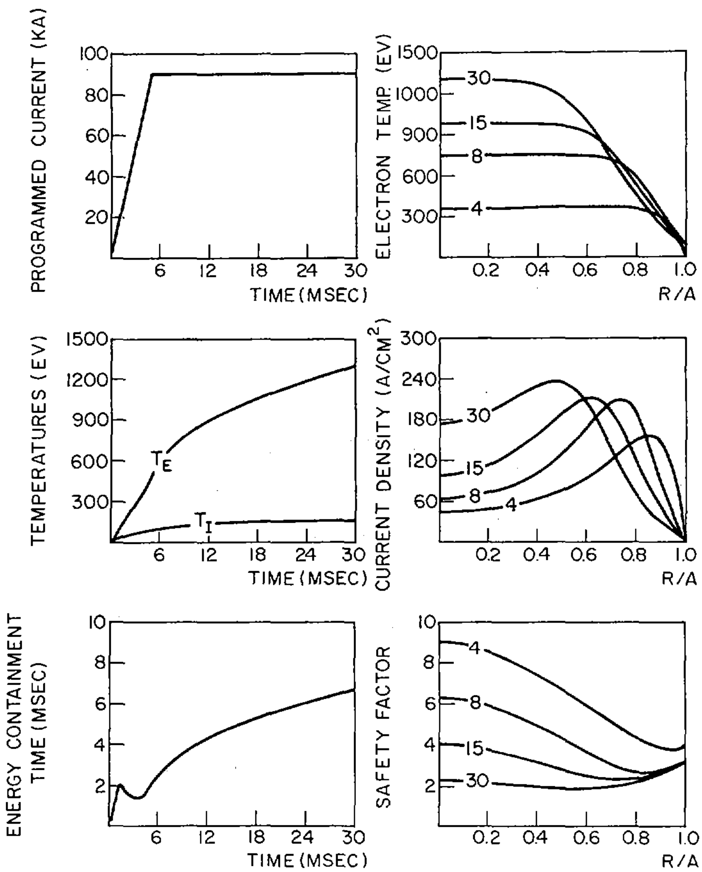

FIG.4. Results from simulation study of T-3 discharge. For this case B_T = 25 kG, n = 1.4 × 10^{13} cm^{-3}, R_0 = 100 cm, a = 15 cm, Y_R = 4 and Y_T = 10. Labels for profiles are time in milliseconds.

The curve displaying q(r) has off-axis minima throughout the course of the discharge. To estimate the severity of the non-local flute modes which arise from this, we use the technique described earlier[8] to calculate the plasma displacement $\xi_r(r)$ for a cylindrical equilibrium with $j_T \propto r^{\mu}(1 - r^{\nu})$. Preliminary results yield a growth rate as large as 0.3 times that for kink modes: $\gamma \sim B_P/a\sqrt{4\pi\rho}$ where ρ = plasma density, and we have taken $\mu = 2$, $\nu = 3$ and q(a) = m/n = 2.5. The mode is localized to the region where q < m/n, which can be nearly all the plasma as in Fig. 4.

Shafranov's arguments[9] on the importance of toroidal curvature effects for localized modes but not for kink modes suggests that a more inclusive study of the non-local flutes is needed. If the modes really exist in a torus, it should be possible to eliminate them by careful current programming to control the rate of current penetration and the q(r) profile.

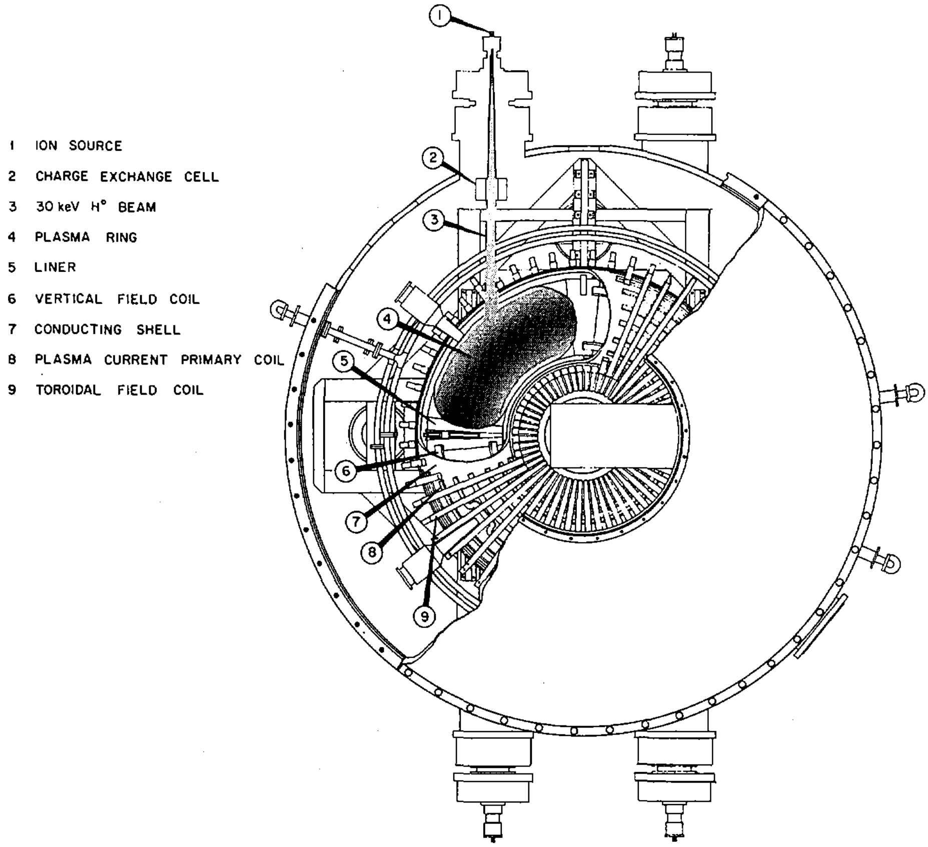

FIG. 5. ORMAK with injection heating.

4. HEATING BY ENERGETIC NEUTRAL INJECTION

With ohmic heating, ORMAK-I should produce a plasma with sufficient ion temperature to test the neo-classical theory well into the collisionless regime. As seen in the preceding section we can expect an ion temperature of about 600 eV at $n = 5 \times 10^{13}$ on the basis of neo-classical transport theory. At this density in ORMAK-I, the transition to the banana regime occurs at less than 200 eV. If the trapped particle instabilities predicted by Kadomtsev and Pogutse[2] occur their effects should be found in this parameter range. If they do not occur or are not found to be severely limiting, it will be desirable to go to higher temperatures to simulate a reactor plasma.

4.1. Injection Heating

To augment ohmic heating, we have investigated the technological feasibility of heating the plasma by injecting energetic neutrals[10] using the techniques developed in this laboratory. Sources now in existence (> 2 A at 30 keV) permit injection of sufficient energy to raise the plasma temperatures in ORMAK to > 2 keV if neo-classical theory is valid. Figure 5 illustrates the configuration of the injection experiment being considered for ORMAK.

A simple model has been used to calculate the time-dependent heating from energetic-particle injection. The model also provides rapid semi-quantitative prediction of performance with ohmic heating. It is based on neo-classical heat conductivity with anomalous electron losses, but differs from the calculations discussed in Section 3 by the simplifying assumption that density and temperature profiles are flat and that all plasmas have the same surface temperature gradient, adjusted to give the

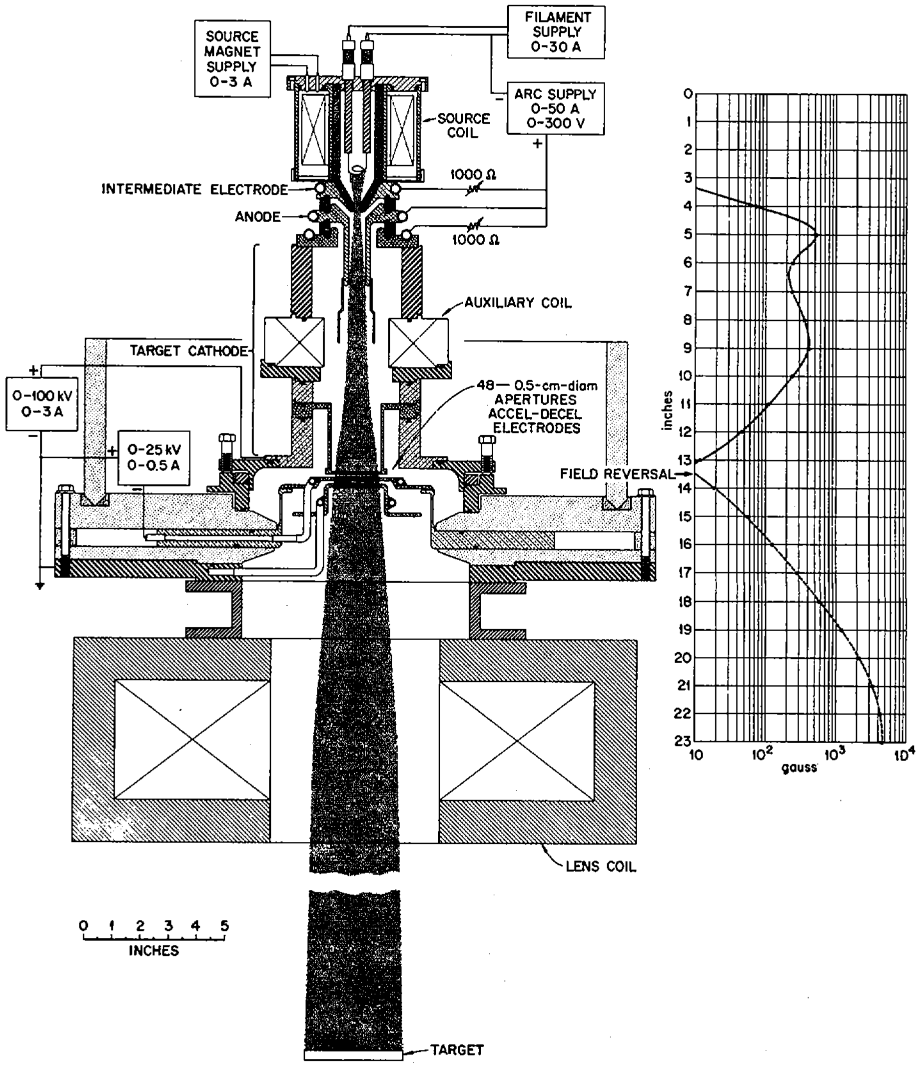

FIG. 6. High-current ion-heating system.

right answer for T-3. The history of each macro-particle is followed until it merges with the plasma thermal distribution. The proper energy transfer rates to ions and electrons are calculated at each step. The results indicate $T_e \approx T_i \approx 2.3$ keV at 200 msec. The spectrum of beam particles is approximately flat with a density of about 6×10^{-4} particles/keV/plasma ion from the group injected with the electric field. The density of the particles injected against the electric field is about 12% less than that of the other group.

Since injection heating will give us a means of controlling temperatures, it is important as a diagnostic tool to increase the range of plasma parameters. It can, for example, increase the beta of the plasma while keeping other parameters constant. It can also provide information on anomalous energy loss through the electrons by supplying a known energy feed to them. These injection experiments also will serve to demonstrate the usefulness of this method of heating the ions--with possible reactor application.

The most efficient method of heating the plasma ions is to use injected particles with an energy of only a few tens of keV. In this range the particles have several mean free paths for trapping in ORMAK, and there is a high percentage conversion of the ions to neutral particles in the charge exchange cell. Also a larger fraction of the energy of the injected particles is transferred directly to the plasma ions. These injection heaters must be capable of delivering tens of kilowatts of power for times of 0.1 to 0.2 sec if they are to contribute significantly to the ion heating. Our initial goal is to build injectors capable of delivering 60 kW; 2 Amps equivalent, at 30 keV, for times of 0.1 to 0.2 sec.

At present our injector can deliver 50 kW to the plasma and there appears to be no basic limitation at this level. This injector is shown in Fig. 6. It consists of an ion source (which we have called a duoPIGatron) with a 5-cm-diam multi-aperture electrode extraction system. The ion source presently produces 3.0 A of hydrogen ion beam at 30 to 35 keV for 0.1 sec pulses at a 10% duty cycle. Defining the useful beam as that obtained on a 9-cm-diam target located 1 meter from the magnetic lens, the injector delivers 1.8 A of $\approx$ 60% H_2^+ and 40% H^+ beam. These are 2.16 A of 17.5 keV particles from the H_2^+ ions yielding 1.8 A equivalent of 17.5 keV H^0 particles into the plasma. Also the 35 keV H^+ particles should produce $\approx$ 0.5 A equivalent of 35 keV H^0 particles into the plasma. This is a total power input of 50 kW. At the present time we are limited by our power supply. All of our results indicate that this injector can continue to be scaled to higher current. We anticipate scaling this system to a 10 A injector module when a power supply is available. The system is simple in design and operates reliably with greater than 50% gas efficiency and with no excessive erosion of components.

REFERENCES

[1] GALEEV, A. A., SAGDEEV, R. Z., "Transport Phenomena in a Collisionless Plasma in a Toroidal Magnetic System", Sov. Phys. - JETP 26 1 (1968) 233.

[2] KADOMTSEV, B. B., POGUTSE, O. P., Rev. of Plasma Phys. 5 (Consultants Bureau, New York 1970) 391.

[3] FURTH, H. P., ROSENBLUTH, M. N., RUTHERFORD, P. H., STODIEK, W., Phys. Fluids 13 (1970) 3020.

[4] MERCIER, C., SOUBBARAMAYER, Proc. Rome Conf. on Plasma Physics and Controlled Fusion, 16 (1970).
[5] DNESTROVSKII, Y. N., KOSTAMAROV, D. P., PAVLOVA, N. L., Proc. Rome Conf. on Plasma Physics and Controlled Fusion 17 (1970).
[6] FORREST, M. J., PEACOCK, N. J., ROBINSON, D. C., SANNIKOV, V. V., WILCOX, P. D., Culham Report CLM-R 107 (1970).
[7] HIROSE, A., ALEXEFF, I., JONES, W. D., KUSH, S. T., LONNGREN, K. E., Phys. Rev. Lett. 25 (1970) 1563; COPPI, B., MAZZUCATO, E., Phys. Fluids 14 (1971) 134.
[8] CLARKE, J. F., DORY, R. A., "Feedback and Dynamic Control of Plasmas", (CHU, T. K., HENDEL, H. W., Eds.) American Inst. of Phys., New York (1970) 68.
[9] SHAFRANOV, V. D., Technical Physics 15 (1970) 175.
[10] KELLEY, G. G., MORGAN, O. B., POSTMA, H., FORSEN, H. K., "Neutral Beam Ion Heating in ORMAK II", ORNL-TM-3076 (1970).

DISCUSSION

V.S. STRELKOV: The results you have obtained in the mathematical modelling of T-3 processes are very similar to those reported by Dnestrovsky and Kostomarov at the 1969 Dubna Conference. Could you say something more about the coefficients you introduce to allow for the deviation of thermal conductivity and diffusion from the values given by neoclassical theory?

G.G. KELLEY: Perhaps Mr. Dory would like to answer this question.

R.A. DORY: We first used the neoclassical coefficients summarized in Reference 3 of our paper. The model is then the same as that in Reference 5 and we compared our results with the Russian work as a check. More recently we used the scaling law suggested by Artsimovich and discussed by Yoshikawa in paper F-1 of this Conference. Adopting this pseudoclassical law, the comparison with experimental data was more satisfactory than with neoclassical laws plus anomaly factors, except that the pseudoclassical transport had to be enhanced by a factor γ(PC) $\sim$ 2.5 in order to fit the data. By making γ(PC) density-dependent, we were able to reproduce the observed variation of τ_E with n_e and I, and also to get good agreement with the T_e profiles.

B. COPPI: I should like to add here that, in view of the relatively low current density in the ORMAK experiment, a factor 4 for the resistivity anomaly is probably too large.

ЭКСПЕРИМЕНТЫ ПО РАВНОВЕСИЮ В ТОКАМАКЕ ТО-1 БЕЗ КОЖУХА С ПРИМЕНЕНИЕМ ОБРАТНЫХ СВЯЗЕЙ

Л.И.АРТЕМЕНКОВ, И.Н.ГОЛОВИН,
П.И.КОЗЛОВ, П.И.МЕЛИХОВ, Н.Н.ШВИНДТ
Институт атомной энергии им.И.В.Курчатова,
Москва,
В.К.БУТЕНКО, В.Ф.ГУБАРЕВ,
А.И.КУХТЕНКО, Ю.П.ЛАДИКОВ-РОЕВ,
Ю.И.САМОЙЛЕНКО
Институт кибернетики АН УССР, Киев,
Союз Советских Социалистических Республик

Доклад представлен В.Д.Шафрановым

Presented by V.D.Shafranov

Abstract — Аннотация

EXPERIMENTS ON EQUILIBRIUM IN THE UNCASED TO-1 TOKAMAK DEVICE BY MEANS OF A FEEDBACK SYSTEM.

The successful attempts to suppress flute instability in the Ogra-2 and Phoenix-2 devices by means of feedback systems have aroused interest in studying the possibility of suppressing other instabilities by the same method. It was decided to conduct experiments on the feedback stabilization of the large-scale modes of a helical instability in a Tokamak device. Study of the question has shown that, in addition to the traditional automatic control circuit, it is possible to construct systems in which the monitor and the control element are a single unit. It was decided to use such a system first of all in a simpler situation than that of a helical instability. The first step was to design a system for controlling automatically the equilibrium position of the plasma column in a Tokamak device without copper casing by means of an arrangement of spaced windings and regulators. The TO-1 Tokamak device was built for this study. Its main parameters are: major radius 60 cm; minor radius (diaphragm) 15 cm; maximum longitudinal magnetic field 20 kG; maximum plasma current 100 kA; maximum magnetic flux of the transformer for Joule heating 0.44 Vs. The single-wall vacuum chamber is made of 1 mm stainless steel with a ceramic insert. The chamber has four diagnostic tubes spaced uniformly around the torus. Between the solenoid of the longitudinal field and the vacuum chamber there is a system of spaced windings consisting of eight sections; four sections are above the equatorial plane of the torus and four below. The windings can be connected with one of three regulators depending on the distribution of the stray magnetic fields. The type of regulator adopted is for a maximum plasma current of 30 kA. When there is no plasma current, the system uses virtually no power. With this regulator system it is possible to reduce the displacement of the plasma column by comparison with the displacement which occurs when a superconducting casing is used.

ЭКСПЕРИМЕНТЫ ПО РАВНОВЕСИЮ В ТОКАМАКЕ ТО-1 БЕЗ КОЖУХА С ПРИМЕНЕНИЕМ ОБРАТНЫХ СВЯЗЕЙ.

Успешно осуществленные опыты по подавлению желобковой неустойчивости обратными связями на установках Огра-2 и Феникс-2 возбудили интерес к изучению возможности подавления и других неустойчивостей этим методом. Считалось целесообразным провести эксперименты по стабилизации обратными связями крупно-масштабных мод винтовой неустойчивости в токамаке. Изучение вопроса показывает, что кроме традиционной цепочки системы автоматического управления возможно построение систем, где датчик и исполнительный орган являются единым целым. Эту систему было решено применить сначала к более простой ситуации, чем случай винтовой неустойчивости. Таким первым шагом является создание автоматического регулирования положения плазменного шнура в токамаке без медного кожуха при помощи системы распределенных обмоток и регуляторов. Для этих исследований построен Токамак ТО-1. Основные параметры установки: большой радиус – 60 см, малый радиус (по диафрагме) – 15 см, продольное магнитное поле – до 20 кГс, ток плазмы – до 100 кА. Максимальная величина магнитного потока трансформатора для джоулева нагрева – 0,44 Всек. Вакуумная камера – одностенная, из нержавеющей стали толщиной 1 мм, с керамической вставкой. Камера имеет четыре диагностических патрубка, расположенных равномерно по тору. Между соленоидом продольного поля и вакуумной камерой располагается система распределенных обмоток, состоящая из 8 секций: четыре секции расположены выше экваториальной плоскости тора, четыре – ниже ее. В соответствии с распределением рассеянных магнитных полей обмотки включены на три регулятора. Принятый вариант регулятора рассчитан на ток в плазме до 30 кА. В отсутствие плазменного тока система потребляет практически нулевую мощность. Благодаря применению регулятора можно обеспечить меньшее смещение плазменного шнура, чем в случае применения сверхпроводящего кожуха.

ВВЕДЕНИЕ

Как известно, для обеспечения равновесия плазменного шнура в установках типа Токамак [1, 5] обычно применяется оболочка с высокой проводимостью (кожух). Время, в течение которого кожух эффективно работает, много меньше времени затухания индуцируемых в нем токов.

При заданных основных размерах установки это время может быть увеличено, если увеличить толщину или проводимость стенки кожуха. Однако увеличение толщины или применение глубокого охлаждения требует значительных материальных затрат и увеличивает вес установки.

Следует также отметить, что источником энергии, создающим индукционные токи в кожухе, является возмущенное магнитное поле разряда. В этом смысле кожух можно назвать пассивным элементом. В случае усиления индуцируемых токов равновесное смещение шнура стало бы меньше, что эквивалентно увеличению жесткости системы. Поэтому, несмотря на очевидные положительные качества (быстродействие, надежность, конструктивная простота кожуха), в последние годы были рассмотрены иные пути увеличения жесткости и времени удержания шнура в замкнутых ловушках. Они основаны на применении систем автоматического управления [2]. Примером успешного применения системы регулирования по принципу обратной связи для плазменных объектов явились опыты по подавлению желобковых неустойчивостей на установках Огра-2 и Феникс-2 [3, 4].

На Токамаке ТО-1 использована система автоматического уравновешивания плазменного шнура без кожуха. В данном докладе приведены предварительные результаты экспериментов с применением такой системы.

1. ПАРАМЕТРЫ УСТАНОВКИ И ИСПОЛЬЗУЕМАЯ ДИАГНОСТИКА

Схематический чертеж Токамака ТО-1 и его основные размеры даны на рис.1. Вакуумная камера – одностенная, из нержавеющей стали толщиной 1 мм. Камера имеет поперечный разрез с керамической вставкой и четыре диагностических патрубка. Диаметр диафрагмы – 28 см.

Для возбуждения вихревого электрического поля используется О-образный магнитопровод с максимальным магнитным потоком 0,4 Вб (при перемагничивании на обратное магнитное поле). Катушки первичной обмотки (всего 48 витков) располагаются вблизи каждого из четырех зазоров магнитопровода.

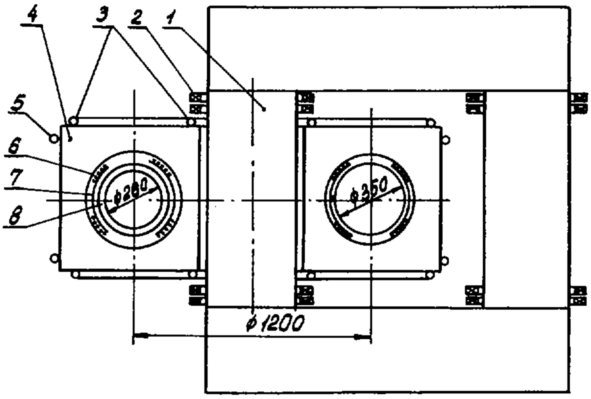

Рис.1. Схематический чертеж установки Токамак ТО-1:
1 – магнитопровод, 2 – вихревая обмотка, 3 – витки корректирующего вертикального магнитного поля, 4 – обмотка продольного магнитного поля, 5 – витки корректирующего горизонтального поля, 6 – управляющая обмотка, 7 – вакуумная камера, 8 – диафрагма.

Источником питания разряда служит схема, состоящая из конденсаторной батареи (энергия до 40 кДж), задающей фронт импульса тока, и магнитного накопителя. Максимальная энергия, запасаемая в накопителе, – 900 кДж. Схема обеспечивает в первичной обмотке трансформатора трапециевидный импульс тока заданной величины (0,2-3 кА) и длительности (до 0,1 сек).

Тороидальное магнитное поле создается 24 катушками, питаемыми от генераторов постоянного тока; проектная напряженность поля – до 20 кэ (в описываемых ниже экспериментах – 7,5 кэ).

Квазистационарные корректирующие магнитные поля создаются системой витков, питаемых от управляемых источников тока. Вертикальное поле может задаваться в пределах ±100 э (на оси камеры), горизонтальное ±10 э.

Управляющая обмотка, предназначенная для уравновешивания шнура, состоит из 4 секций. В каждой секции 48 витков (по 24 витка над и под экваториальной плоскостью тора). Витки W_y каждой секции соединены последовательно и подключены соответственно к 4 двухполюсникам (регуляторам). Постоянная времени закороченной секции – 16-18 мсек. Для сравнения заметим, что медный кожух толщиной 1,2 см имеет постоянную времени 70 мсек.

В описываемых опытах регистрировались следующие параметры: ток в плазме, сумма токов в плазме и в стенках камеры с помощью пояса Роговского, охватывающего камеру (для контроля отсутствия тока, шунтирующего керамическую вставку), напряжение разряда, токи в секциях управляющей обмотки, вертикальное и горизонтальное смещения шнура (по двум парам магнитных зондов, расположенным внутри камеры), плотность плазмы по отсечке сигнала СВЧ на длине волны 8 мм, интенсивность оптических линий Hα, С III, О IV, Mo I, Fe I и др. во времени, ширины и изменение во времени контуров линий С III и О IV.

2. СИСТЕМА АВТОМАТИЧЕСКОГО РЕГУЛИРОВАНИЯ ПОЛОЖЕНИЯ ПЛАЗМЕННОГО ШНУРА

В Токамаках, наряду с кожухом для уравновешивания плазменного шнура, обычно применяют дополнительные витки, создающие вертикальное магнитное поле определенной конфигурации. Ток в них может изменяться:

а) по заранее заданному временному закону (программное управление) или

б) в соответствии с изменением тока вихревой обмотки, когда дополнительная обмотка включается последовательно с вихревой (способ компенсации возмущений).

Очевидно, что при программном управлении не могут быть скомпенсированы ни газокинетическое давление, ни случайные возмущения, всегда имеющиеся в установке (флуктуации параметров плазмы, параметров электрических цепей и т.п.). В случае б) – еще меньшая свобода регулирования. Например, нельзя скомпенсировать газокинетическое давление шнура, увеличивающееся в процессе нагрева и приводящее к его расширению. В обоих случаях плазменный шнур автоматически уравновешивается без применения обратной связи.

На ТО-1 в настоящее время реализована система с обратной связью, без компенсации возмущений. Грубое воздействие на шнур осуществляется, как отмечалось выше, квазипостоянными вертикальным и горизонтальным магнитными полями, включаемыми до начала разряда.

Система автоматического регулирования положения плазменного шнура на ТО-1 представляет собой совокупность индуктивно связанных со шнуром контуров (рис.2), в цепи которых включены двухполюсники (регуляторы) с отрицательным импедансом. Такие двухполюсники являются аналогами известных в радиотехнике регенеративных схем и обеспечивают обратную связь. Активная и реактивная составляющие полного сопротивления двухполюсника могут изменяться в широких пределах: эквивалентное активное сопротивление цепи $R_э$ секции может быть уменьшено практически до нуля, а эквивалентная индуктивность $L_э$ снижена в несколько раз по сравнению с собственной индуктивностью секции.

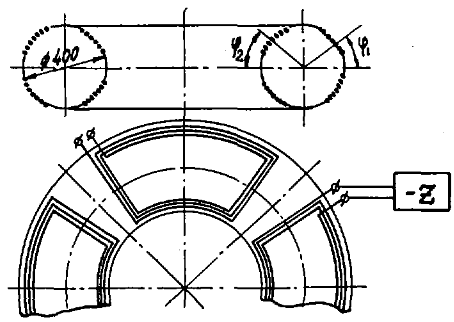

Рис.2. Схема управляющей обмотки, $\varphi_1 = 35°$, $\varphi_2 = 45°$, z – двухполюсник.

Описанная конструкция управляющей обмотки относительно перемещений шнура в экваториальной плоскости камеры является эквивалентом кожуха. Очевидно отличие состоит в распределении поверхностной плотности тока, закон распределения которой для кожуха близок к косинусоидальному (при небольших смещениях шнура). Для первых экспериментов на ТО-1 выбрана равномерная намотка секций, но может быть реализована и оптимальная (косинусоидальная) намотка. Оптимальная намотка имеет максимальный коэффициент жесткости (отношение силы, действующей на плазменный шнур, к перемещению, вызываемому этой силой). Меньшая жесткость приводит к увеличению равновесного смещения плазменного шнура.

Покажем, что, уменьшив эквивалентную индуктивность секций управляющей обмотки $L_э$, можно увеличить жесткость системы. Для процессов, длительность которых много меньше $\tau_э = L_э/R_э$, магнитный поток Φ_y, пронизывающий контур секции при малом смещении δ шнура от магнитной оси (магнитная ось – положение шнура, для которого $\Phi_y = 0$ при изменениях разрядного тока)

$$\Phi_y = \frac{L_э I_y}{W_y} = C_1 I_p \delta \qquad (1)$$

где I_y – ток секции управляющей обмотки, I_p – ток разряда, C_1 – коэффициент, зависящий от геометрических размеров установки.

Определяемый из (1) ток управляющей обмотки создает вертикальное магнитное поле, которое, взаимодействуя с током разряда, дает пондеромоторную уравновешивающую силу:

$$F = \frac{C_2}{L_э} I_p^2 \delta = G\delta \qquad (2)$$

где C_2 – коэффициент, зависящий от геометрических размеров, а $G = C_2 I_p^2/L_э$ – коэффициент жесткости системы, связанной с коэффициентом жесткости идеального (без разрезов, сверхпроводящего) кожуха G_0 соотношением:

$$G = G_0 \nu \cdot \frac{L_y}{L_э} \qquad (3)$$

(L_y – индуктивность секции управляющей обмотки, ν – коэффициент, зависящий от ее геометрических размеров).

Величину $K = L_y/L_э$ будем называть коэффициентом усиления системы регулирования. Для выбранных размеров управляющей обмотки в приближении сосредоточенного плазменного тока расчеты дают $\nu \simeq 0{,}8$. Из (3) следует, что при $K \geqslant 1{,}25$ получим $G \geqslant G_0$. Заметим, что коэффициент жесткости реального кожуха меньше G_0, так как из-за поперечных разрезов кожуха эффективно работает ~70% его длины по обходу тора.

Положение плазменного шнура определяется условием равенства силы, определяемой формулой (2), и суммой сил, состоящей из электродинамической силы растяжения шнура в вакууме F_1, силы его притяжения к магнитопроводу F_2, силы газокинетического давления плазмы $F_г$ и силы взаимодействия с корректирующим магнитным полем $F_\perp$. Оценочные расчеты дают $F_2 \simeq 0{,}6\ F_1$.

Из (2) и (3) находим смещение шнура относительно магнитной оси:

$$\delta = \frac{0{,}4\,F_l + F_r + F_\perp}{\nu \cdot K \cdot G_0} \tag{4}$$

Электродинамическую силу растяжения, в отличие от [1], здесь следует записать в виде:

$$F_l = \frac{\mu_0 I_p^2}{2}\left(\ln\frac{8R}{a} - \frac{3}{4}\right)$$

где $\mu_0 = 4\pi \cdot 10^{-7}$ гн/м, R – большой и a – малый радиусы шнура. Если же длительность импульса сравнима с $\tau_э$, то из-за затухания токов в управляющей обмотке положение равновесия шнура зависит от времени и в правую часть (4) добавляется множитель $(1 + t/\tau_э)$.

Связь между величинами токов разряда и в секции управляющей обмотки определяется соотношениями (1) и (4).

Использовались регуляторы с номинальным током до 100 А, диапазоном частот – $0 \div 10^4$ Гц. Постоянная времени секции при включении регулятора $\tau_э \sim 1$ сек. В этом случае максимальный ток разряда не превышает 20 кА. Для удержания в равновесии шнура с большим током следует оптимизировать геометрические параметры управляющей обмотки и применить более мощные регуляторы.

3. ЭКСПЕРИМЕНТАЛЬНЫЕ РЕЗУЛЬТАТЫ И ОБСУЖДЕНИЕ

Основная цель экспериментов состояла в проверке работоспособности импедансной системы регулирования равновесия шнура и в определении ее основных характеристик. Работоспособность системы оценивалась по изменению макроскопических характеристик разряда.

Эксперименты проводились при давлении водорода $\sim 1{,}8\ 10^{-4}$тор, который импульсно напускался в камеру перед разрядом. Вакуумная подготовка камеры осуществлялась ее "тренировкой" разрядами до такого состояния, когда давление в камере после импульса не превышало первоначального.

Ток разряда выбирался в диапазоне 10-15 кА для того, чтобы иметь достаточный запас устойчивости по q и чтобы токи в регуляторах не превышали допустимых значений (100 ампер).

Обычно эксперименты проводились при включенной схеме перемагничивания магнитопровода и оптимально подобранных корректирующих полях.

Настройка регуляторов перед началом серии импульсов состояла в доведении эквивалентной постоянной времени управляющей обмотки до 150-200 мсек и выборе коэффициента усиления r. Контроль настройки осуществлялся путем подачи прямоугольного импульса тока в витки вертикального корректирующего магнитного поля. На рис.3(а) изображена кривая тока I_y в секции управляющей обмотки при выключенном регуляторе (секция короткозамкнута), а на рис.3(б) – при включенном. Видно, что постоянная времени увеличилась от 16-18 до ~ 150 мсек, а коэффициент усиления $K \simeq 2{,}5$-3. Для сравнения укажем, что аналогичный опыт,

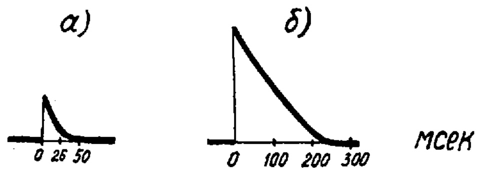

Рис.3. Осциллограммы тока в секции управляющей обмотки при подаче прямоугольного импульса тока в витки корректирующего вертикального магнитного поля: а) регулятор выключен, б) регулятор включен.

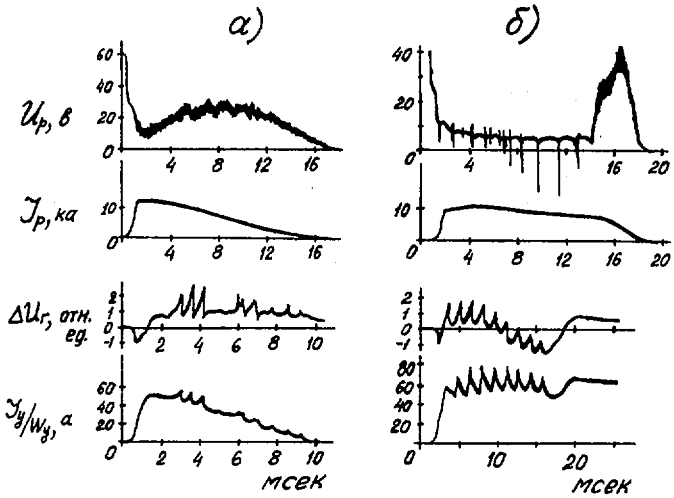

Рис.4. Осциллограммы напряжения на разряде (U_p), плазменного тока (I_p), разностного сигнала с горизонтальных магнитных зондов (ΔU_r) и тока в секции управляющей обмотки (I_y) в двух режимах: а) регулятор выключен, б) регулятор включен.

проведенный для медного кожуха толщиной 1,2 см, дал постоянную времени затухания индуцированных в нем токов (которые измерялись с помощью специального гибкого пояса Роговского) $\tau_{кож} \simeq 70$ мсек.

На рис.4 приведены типичные для двух режимов осциллограммы: а) при выключенных, б) при включенных регуляторах с коэффициентом усиления $\simeq 2,5-3$. Сравнение показывает, что в режиме б) существенно изменяется характер процессов.

Напряжение разряда U_p в средней части импульса уменьшается до ~ 5 В (в отдельных импульсах до 3 В), а высокочастотные колебания практически исчезают. Наблюдаются лишь отдельные острые пички, которые могут иметь отрицательную полярность. На спаде импульса тока напряжение разряда резко увеличивается. Магнитные зонды показывают, что в этот интервал времени шнур плазмы смещается по вертикали (несмотря на возрастание поля управляющей обмотки в вертикальном направлении в обе стороны от средней плоскости). Причина смещения шнура в этих экспериментах окончательно не установлена.

При включенных регуляторах форма импульса тока изменяется, рис.4(б), а его длительность (на уровне 0,5 $I_{p\,max}$) увеличивается в два раза.

Осциллограммы сигналов с магнитных зондов показывают, что разряд формируется всегда в нижней части камеры вблизи ее вертикального диаметра. Это объясняется тем, что в нижней части камеры расположен накаливаемый вольфрамовый катод, предназначенный для улучшения условий пробоя. Характерно, что в режиме с выключенными регуляторами большую часть времени шнур смещен к внешней стороне обхода камеры. В режиме б) во второй половине импульса шнур перемещается к внутренней стороне камеры.

Из осциллограмм следует, что в средней части импульса токи в секциях управляющей обмотки увеличиваются в ~ 1,5 раза. Наблюдаемые возмущения этих токов обычно появляются одновременно во всех секциях. В отдельных разрядах возмущения сдвинуты во времени. Это будет предметом дальнейшего изучения.

При работе с выключенными регуляторами характер осциллограмм разряда практически не зависит от изменения поперечных корректирующих магнитных полей. По-видимому, в этих условиях плазменный шнур плохо сформирован и в течение всего времени разряда сильно взаимодействует с диафрагмой. Область значений корректирующих полей, при которых шнур оторван от диафрагмы, отсутствует (либо очень узка).

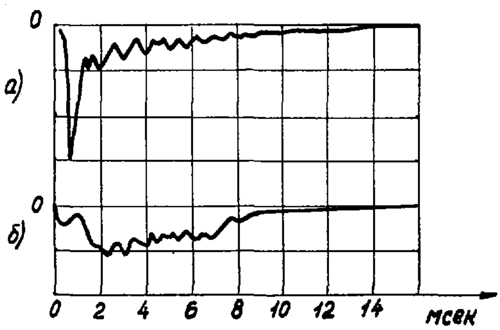

Рис.5. Осциллограммы интенсивности линий: а) $H\alpha$; б) OIV 5305 Å.

При работе с включенными регуляторами имеется область значений поперечных корректирующих полей, в которой характер осциллограмм существенно улучшается. В определенных условиях наблюдаются своеобразные нестационарные процессы с регулярными бросками токов в секциях управляющей обмотки. Возможно, это связано со следующим. В процессе нагрева плазмы увеличивается газокинетическое давление шнура, что увеличивает его смещение наружу. Вследствие взаимодействия с диафрагмой шнур охлаждается и возвращается в положение, близкое к исходному. Если при этом условия не изменились, то возникают релаксационные колебания на большинстве сигналов, регистрируемых за импульс. Однако в должной мере эти процессы нами еще не изучены.

На рис.5 приведены осциллограммы поведения интенсивности линий $H\alpha$ и O IV во времени. Как видно, кривые имеют типичный для экспериментов на Токамаках характер.

ЗАКЛЮЧЕНИЕ

В докладе представлены первые экспериментальные результаты по осуществлению равновесия по большому радиусу в Токамаке ТО-1 без медного кожуха с помощью управляющей обмотки, включенной на двухполюсники с отрицательными импедансами. Экспериментально подтверждена правильность предпосылок, используемых для расчетов такой системы, и показана ее работоспособность.

Включение регуляторов приводило к существенному изменению характеристик разряда. В этих условиях удалось получить шнур, существующий в течение 15-20 мсек, с напряжением на обходе 5-7 В при токе 12-15 кА. Температура электронов по проводимости составила 50-100 эВ. По ширине контура линии O IV температура ионов — 30-40 эВ.

Ограничение длительности импульса тока происходит из-за смещения шнура по вертикали (шнур охлаждается при сильном взаимодействии с нижними участками диафрагмы), причина которого пока не установлена.

Предполагается применить аналогичную систему для стабилизации некоторых мод винтовой неустойчивости.

Авторы выражают благодарность всему инженерно-техническому персоналу установки за четкую, слаженную работу, а также инженерам В.Ф.Богданову, П.А.Мухину, Л.Н.Папкову, А.П.Сабадашеву — за большую техническую помощь в проведении экспериментов.

Весьма полезными и плодотворными были обсуждения с В.В.Арсениным и В.Д.Шафрановым.

ЛИТЕРАТУРА

[1] АРЦИМОВИЧ, Л.А., Замкнутые плазменные конфигурации, изд-во "Наука", Москва, 1969.

[2] КУХТЕНКО, О.І., САМОЙЛЕНКО, Ю.І., Автоматичне керування плазмовими об'ектами, Вісник Академії наук Української РСР, 3, 1971.

[3] АРСЕНИН, В.В., ЖИЛЬЦОВ, В.А., ЧУЯНОВ, В.А., Труды Третьей международной конференции по физике плазмы и управляемому термоядерному синтезу, IAEA, VIENNA 2 1969, p.528.

[4] ЧУЯНОВ, В.А. и др., Доклад на Третьей европейской конференции по физике плазмы и управляемому синтезу, УТРЕХТ, 1969, стр.12.

[5] ШАФРАНОВ, В.Д., "Атомная энергия" 13 (1962) 521.

RADIAL TRANSPORT IN TOKAMAK DISCHARGES*

D.F. DÜCHS†, H.P. FURTH, P.H. RUTHERFORD,
Princeton University Plasma Physics Laboratory,
Princeton, New Jersey,
United States of America

Abstract

RADIAL TRANSPORT IN TOKAMAK DISCHARGES.

A multifluid numerical code is used to follow the evolution of radial profiles in the Tokamak discharge. Particle diffusion, electron and ion thermal diffusion, energy equilibration, and field diffusion are included in the model. The transport coefficients appropriate to the banana, plateau, and hydrodynamic regimes of classical theory for an axisymmetric torus (neoclassical theory) are employed, with recently calculated numerical coefficients exact to lowest order in aspect ratio. The authors report on two basic cases: a simplified three-regime neoclassical code, neglecting particle transport; and a banana-regime code that includes particle transport and the modification of the particle and electron thermal fluxes by the trapped-particle pinch effect. Pseudoclassical transport has also been studied, and various rules are examined for suppression of MHD-unstable skin-current layers. The relation of these results to present-day Tokamak experiments is discussed, and neoclassical and pseudoclassical extrapolations to higher temperature regimes are made. The code contains provision for the inclusion of high-Z impurities and cold and hot neutral atoms: these elements promise to be important to the simulation of present-day Tokamak experiments.

1. INTRODUCTION

Tokamak experiments [1, 2] have demonstrated energy confinement times roughly comparable to the times predicted by neoclassical theory [3]. Computer studies supporting this conclusion have been reported in [4]. Analytic results on a simplified neoclassical tokamak equilibrium model have been given in [5]. The present computer study has two principal objectives: (1) to follow the evolution in time of purely neoclassical tokamak discharges, with particular attention to such characteristic phenomena as thermal instability [5] and self-constriction of the current channel [6-8]; (2) to investigate what modifications of the neoclassical equations may be required in order to fit the details of the actual experimental observations.

A one-dimensional time-dependent code has been developed that treats four interacting fluid components: ions, electrons, cold neutrals, and hot neutrals. The ion and electron components are governed by the full set of neoclassical equations [9], with optional introduction of anomaly factors e.g., in the presence of MHD-unstable skin-current distributions.

The basic equations and the structure of the code are outlined in Section 2. The physical phenomena permitted by the full code are so complex that we have concentrated, in the initial phase of research, on

* This work was supported by USAEC Contract AT(30-1)-1238.

† Naval Research Laboratory, Washington, D.C.

the study of several more limited models. In Section 3, we treat a plasma with fixed density distribution and investigate the problems of thermal instability and skin effect. In Section 4, we use the full neoclassical transport equations, in the banana regime, to study the self-constriction of the current channel. The problems of advancing to higher-temperature tokamak regimes are discussed in Section 5. The effects of a realistic treatment of neutrals and impurities will be reported in a later publication.

2. TRANSPORT EQUATIONS

Computations have been made with two basic codes. The first, which we will call the simplified code, considers only thermal transport keeping the density fixed. The second, which we will call the neoclassical banana code, includes particle diffusion and the trapped particle pinch and associated bootstrap current effects; it also has the capability of treating atomic processes involving neutrals and the stripping of oxygen impurities. The simplified code normally uses ion and electron thermal conductivities taken from neoclassical theory, and selects locally at each time the banana, plateau, or classical regime as appropriate. The full neoclassical code employs recently formulated equations appropriate only to the banana regime [9] since the development of a similarly full formulation for the other regimes is as yet incomplete. We state below the equations used; the notation is standard.

2.1 Simplified code

Here, the equations are those of electron and ion thermal transport and poloidal field diffusion:

$$\frac{3}{2} n \frac{\partial T_e}{\partial t} = \frac{1}{r} \frac{\partial}{\partial r}\left(r \kappa_e \frac{\partial T_e}{\partial r}\right) - \frac{3m_e}{m_i} \frac{n}{\tau_e} (T_e - T_i) + \frac{\eta c^2}{(4\pi)^2} \left(\frac{1}{r} \frac{\partial (r B_\theta)}{\partial r}\right)^2 - P_{Br} \tag{1}$$

$$\frac{3}{2} n \frac{\partial T_i}{\partial t} = \frac{1}{r} \frac{\partial}{\partial r}\left(r \kappa_i \frac{\partial T_i}{\partial r}\right) + \frac{3m_e}{m_i} \frac{n}{\tau_e} (T_e - T_i) \tag{2}$$

$$\frac{\partial B_\theta}{\partial t} = \frac{c^2}{4\pi} \frac{\partial}{\partial r}\left(\frac{\eta}{r} \frac{\partial (r B_\theta)}{\partial r}\right) \tag{3}$$

where P_{Br} is the power loss through bremsstrahlung. The thermal conductivities for the various regimes are:

$$\kappa_e^b = 1.81\,\frac{n\rho_{e\theta}^2}{\tau_e}\left(\frac{r}{R}\right)^{1/2} \quad ; \quad \kappa_i^b = 0.68\,\frac{n\rho_{i\theta}^2}{\tau_i}\left(\frac{r}{R}\right)^{1/2} \qquad \text{(banana regime)}$$

$$\kappa_e^p = \frac{15(2\pi)^{1/2}}{8}\,\frac{n\,r\,T_e^{3/2} m_e^{1/2} c^2}{R^2 e^2 B B_\theta} \quad ; \quad \kappa_i^p = \frac{3(2\pi)^{1/2}}{2}\,\frac{n\,r\,T_i^{3/2} m_i^{1/2} c^2}{R^2 e^2 B B_\theta}$$

(plateau regime)

$$\kappa_e^c = 2.33\,\frac{n\rho_e^2}{\tau_e} A \quad ; \quad \kappa_i^c = \frac{n\rho_i^2}{\tau_i} A \qquad \text{(classical regime)}$$

$$\rho_{e,i} = \frac{c(2m_{e,i} T_{e,i})^{1/2}}{eB} \quad ; \quad \rho_{\theta e,i} = \frac{c(2m_{e,i} T_{e,i})^{1/2}}{eB_\theta}$$

$$\tau_e = \frac{3\,m_e^{1/2}\,T_e^{3/2}}{4(2\pi)^{1/2}\,n e^4 \ln \Lambda} \quad ; \quad \tau_i = \frac{3\,m_i^{1/2}\,T_i^{3/2}}{4\pi^{1/2}\,n e^4 \ln \Lambda}$$

$$A = 1 + 1.6\,\frac{r^2 B^2}{R^2 B_\theta^2}$$

this latter being the appropriate Pfirsch-Schlüter correction [10]. We adopt the rule

$$\kappa_e = \min\,[\kappa_e^b,\ \max\,(\kappa_e^p, \kappa_e^c)]; \quad \kappa_i = \min\,[\kappa_i^b,\ \max\,(\kappa_i^p, \kappa_i^c)] \ .$$

We find from the computations that, in most of the higher-temperature cases considered, the banana regime predominates. It is also of interest to consider various forms of anomalous electron thermal conductivity; in particular, we sometimes use

$$\kappa_e = 5\,\frac{n\rho_{e\theta}^2}{\tau_e} \qquad \text{(pseudoclassical)}$$

The code also allows for the effect of high-Z impurities; since these increase the momentum transfer collision frequency, we introduce an effective Z as a multiplier of the resistivity and of the electron and ion thermal conductivities in the banana, classical, and pseudoclassical regimes. (The quantity n is then the electron density.) A somewhat different case arises when we treat a $Z \neq 1$ plasma, rather than a hydrogen plasma with an effective $Z \neq 1$: the electron-ion energy transfer then must also be multiplied by Z (approximately).

2.2 Neoclassical banana code

Here, the equations are taken from a recent complete treatment of the banana regime [9].

$$\frac{\partial n}{\partial t} = -\frac{1}{r}\frac{\partial}{\partial r}(r n v) \tag{4}$$

$$v = \frac{\rho_{e\theta}^2}{\tau_e}\left(\frac{r}{R}\right)^{1/2}\left[-1.12\left(1+\frac{T_i}{T_e}\right)\frac{\partial \ln n}{\partial r} + 0.43\frac{\partial \ln T_e}{\partial r} + 0.19\frac{\partial \ln T_i}{\partial r}\right] - 2.44\,\frac{E_z}{B_\theta}\left(\frac{r}{R}\right)^{1/2} \tag{5}$$

$$\frac{3}{2}\frac{\partial (nT_e)}{\partial t} = -\frac{1}{r}\frac{\partial}{\partial r}\left[r\left(\frac{5}{2}n T_e v + q_e\right)\right] - v\left(T_i\frac{\partial n}{\partial r} - 0.17\, n\frac{\partial T_i}{\partial r}\right) + \frac{cE_z}{4\pi}\frac{1}{r}\frac{\partial (r B_\theta)}{\partial r} - \frac{3m_e}{m_i}\frac{n}{\tau_e}(T_e - T_i) \tag{6}$$

$$\frac{3}{2}\frac{\partial (nT_i)}{\partial t} = -\frac{1}{r}\frac{\partial}{\partial r}\left[r\left(\frac{5}{2}n T_i v + q_i\right)\right] + v\left(T_i\frac{\partial n}{\partial r} - 0.17\, n\frac{\partial T_i}{\partial r}\right) + \frac{3m_e}{m_i}\frac{n}{\tau_e}(T_e - T_i) \tag{7}$$

$$q_e = \frac{n T_e \rho_{e\theta}^2}{\tau_e}\left(\frac{r}{R}\right)^{1/2}\left[-1.81\frac{\partial \ln T_e}{\partial r} - 0.27\frac{\partial \ln T_i}{\partial r} + 1.53\left(1+\frac{T_i}{T_e}\right)\frac{\partial \ln n}{\partial r}\right] + 1.75\,\frac{n T_e E_z}{B_\theta}\left(\frac{r}{R}\right)^{1/2} \tag{8}$$

$$q_i = -0.68\,\frac{n\rho_{i\theta}^2}{\tau_i}\left(\frac{r}{R}\right)^{1/2}\frac{\partial T_i}{\partial r} \tag{9}$$

$$E_z = \frac{\eta_{\parallel}}{[1 - 1.9\,(r/R)^{1/2}]}\left\{\frac{c}{4\pi}\frac{1}{r}\frac{\partial (rB_\theta)}{\partial r} + \frac{c}{B_\theta}\left(\frac{r}{R}\right)^{1/2}\left[2.44\,(T_e + T_i)\frac{\partial n}{\partial r} + 0.69\, n\frac{\partial T_e}{\partial r} - 0.42\, n\frac{\partial T_i}{\partial r}\right]\right\} \tag{10}$$

$$\partial B_\theta/\partial t = c\,(\partial E_z/\partial r)$$

The code also includes ionization of neutral hydrogen atoms, treated (in a simplified model) as two populations: cold neutrals incident from outside and hot neutrals created by charge exchange. Ionization of stationary oxygen impurities through the ninth level and recombination into the lower levels can also be treated. Recombination of hydrogen has been neglected. The power losses due to ionization and charge exchange together with those due to bremsstrahlung and resonance line radiation [11] are included in the energy equations. Detailed computational results including these atomic processes must, however, be postponed until a later paper. Only initial results are reported in Section 4.

2.3 Numerical procedures

The above system of equations, together with proper boundary conditions, has been solved numerically with finite difference methods. The difference scheme is obtained by exact centering in time and space. Coefficients such as η, κ_e, κ_i, etc. have to be included in the centering. Nonlinear difference terms are linearized. These rules enforce an implicit method for solving the system of difference equations. Since this system mostly exhibits a series of tri-diagonal matrices, a generalized [12] Crank-Nicholson algorithm can be applied. Despite the many highly nonlinear terms in the system of equations the indicated method proves to be numerically stable so that errors are introduced only by truncation. The lack of time step restrictions necessary to ensure numerical stability allows a very economical utilization of the code. Since the equations for the densities of the oxygen impurities contain no spatial derivatives, these are computed by a Runge-Kutta technique which allows them to be handled on their own characteristic time scales (which are usually smaller than those for the thermal effects of interest here).

3. THERMAL DIFFUSION AND INSTABILITY

The dominant transport process in a neoclassical plasma is the ion heat diffusion κ_i. The electron heat diffusion κ_e and the particle diffusion D are smaller by the respective factors $3.5\,(m_e/m_i)^{1/2}$ and $4.4\,(m_e/m_i)^{1/2}$ in the banana regime, for equal T_e and T_i. To obtain a first impression of neoclassical energetics, it is appropriate to use a simplified model in which the plasma density profile remains fixed, while the temperature (and the current distribution) are allowed to evolve in time. This is the model to be studied in the present section; using the simplified code discussed in Section 2.1. Bremsstrahlung cooling is also included, but the effect will be significant only in some of the cases discussed in Section 5. We will use hydrogen and Z = 1 unless otherwise specified.

In [5] it was shown that a good fit to the equilibrium density and temperature profiles reported in [13] could be obtained analytically by assuming $n(r)/n_c = T_e(r)/T_c$, (where the subscript c refers to the value on axis). It was also found that, for fixed n(r), perturbations in $T_e(r)$ away from the equilibrium were unstable against exponential growth for a fairly wide range of parameters. The condition for such thermal instability was found to be roughly

$$Q_e \lesssim Q_i\; 0.15\left(2 - \frac{T_i}{T_e - T_i}\right) \qquad (11)$$

If the heat loss Q_e through the electron thermal conductivity is neglected entirely, the condition for instability becomes $T_e \gtrsim 1.5\, T_i$. Conversely, for $T_i \ll T_e$, the instability occurs for $Q_e \lesssim 0.3\, Q_i$.

The most important thermal instability corresponds to a peaking of T_e either on axis or near the edge of the plasma. In the linear theory these two perturbations, of course, differ only in sign and have the same growth rate ω. The lower limit on ω^{-1} is either the skin time or the plasma heat-up time, depending on which is greater. Nonlinearly one would expect thermal instability to grow more rapidly near the plasma edge, since the skin penetration time is lower and the heat-up time also becomes extremely short at the foot of the density profile.

3.1 Skin effect problems

When operating a neoclassical computer model of the tokamak discharge, one immediately encounters a serious problem: the skin effect during the current rise is very pronounced, and persists into the current plateau phase. This is illustrated in Fig. 1, where we treat a fixed parabolic density profile $n(r) = n_c\,[0.8\,(1 - r^2/a^2) + 0.2]$ with "20% pedestal," for $n_c = 10^{13}$ cm^{-3}, and a plasma current rising linearly from 2 kA during 5 msec to a 40 kA plateau. The initial temperature distribution—to which the results are not very sensitive—will be T_e constant at 40 eV and T_i constant at 20 eV. The boundary values are fixed at T_e = 40 eV and T_i = 20 eV. The purpose of a density pedestal is to keep T_e-excursions from becoming extreme at the plasma edge: The discharge behavior in the presence of a pedestal of only 10% is shown in Fig. 2. While the "pedestal models" for n(r) may appear somewhat artificial, they serve to simulate a physical process that will hold down T_e-excursions at the edge of a real plasma: namely, the influx of neutrals.

The range in r that has entered the banana regime, if any, is noted in Figs. 1 - 14: B_e for the electrons and B_i for the ions. In pseudoclassical cases, this marking is omitted. The maximum value of $\iota/2\pi = q^{-1}$ is listed on the figures: this is not necessarily equal to the value at the limiter .

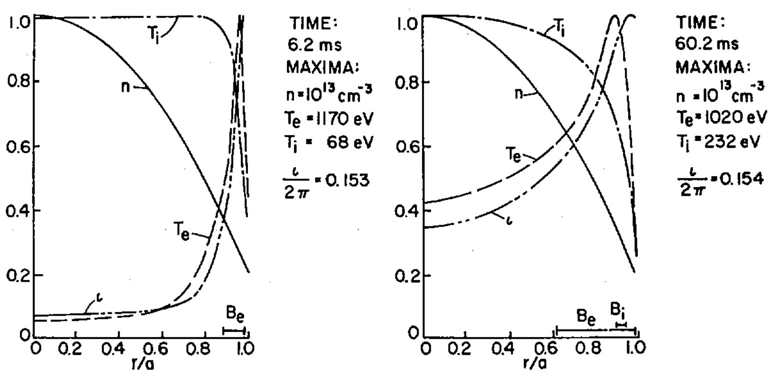

FIG.1. Neoclassical skin effect, $n_c = 10^{13}$ cm^{-3}, Z = 1. Current rises to 40 kA plateau in 5 ms.

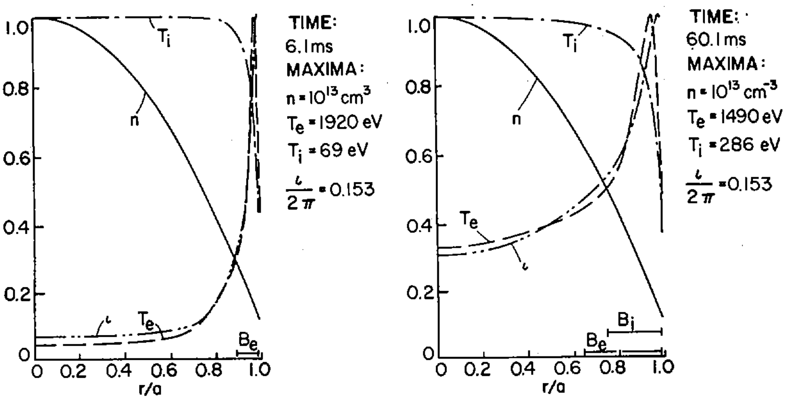

FIG.2. Neoclassical skin effect with small n (10%) at r = a. Otherwise like Fig.1.

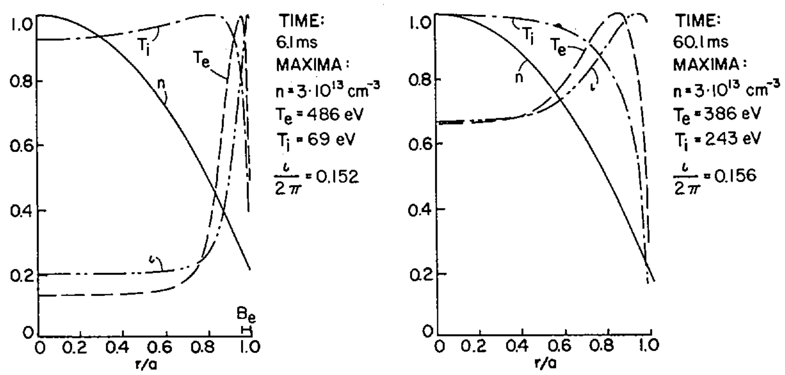

FIG.3. Neoclassical skin effect, $n_c = 3 \times 10^{13}$ cm^{-3}. Otherwise like Fig.1.

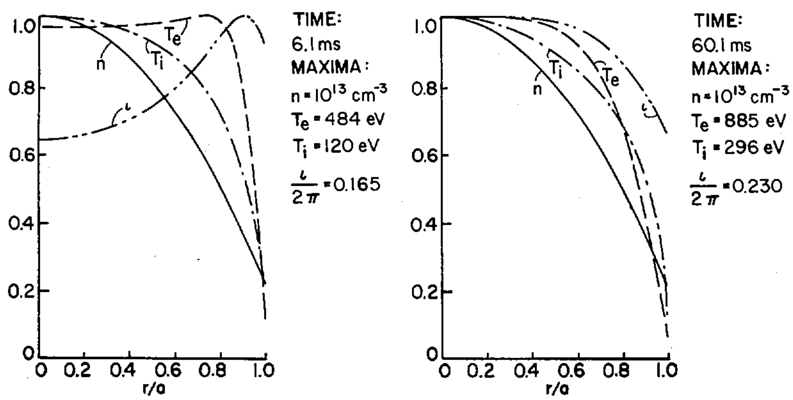

FIG.4. Pseudoclassical skin effect, $n_c = 10^{13}$ cm^{-3}, Z = 4. Current rises to 40 kA plateau in 5 ms.

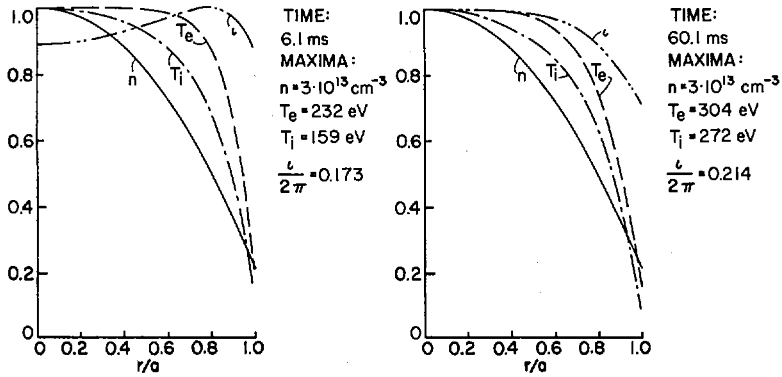

FIG.5. Pseudoclassical skin effect, $n_c = 3 \times 10^{13}$ cm^{-3}. Otherwise like Fig.4.

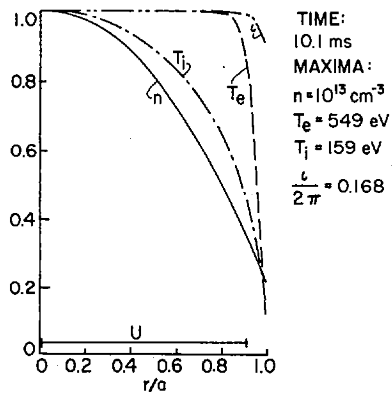

FIG.6. Pseudoclassical transport and "skin-limiter" rule (see text): κ_e-enhancement factor 100. Otherwise like Fig.4.

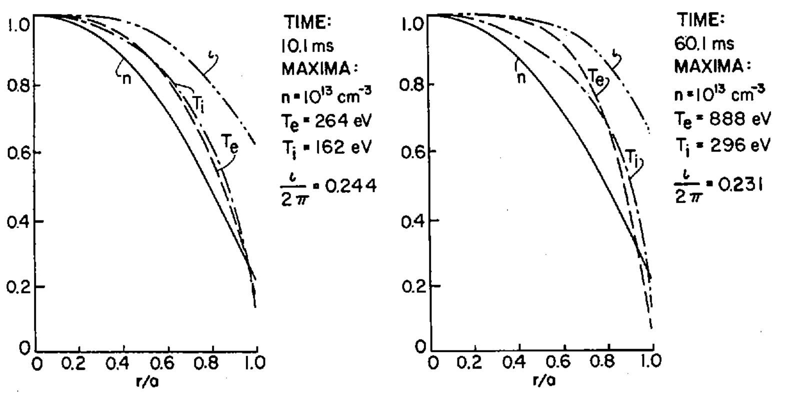

FIG.7. Pseudoclassical transport and "skin-limiter" rule: κ_e-enhancement factor 100 r^2/a^2. Otherwise like Fig.4.

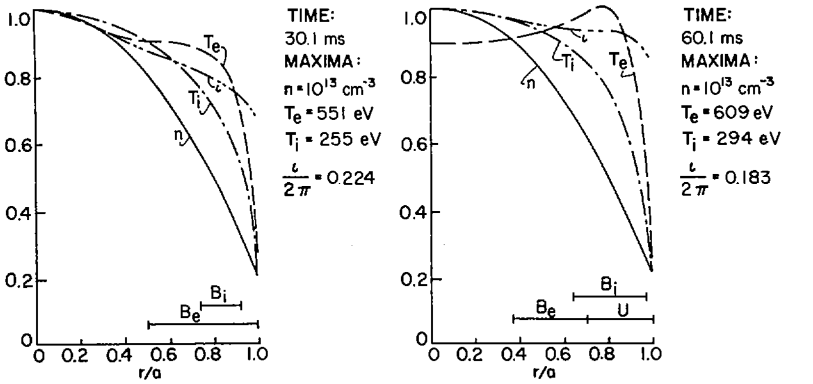

FIG. 8. Neoclassical transport and "skin-limiter" rule: κ_e-enhancement factor 1000 r^2/a^2. Otherwise like Fig. 1.

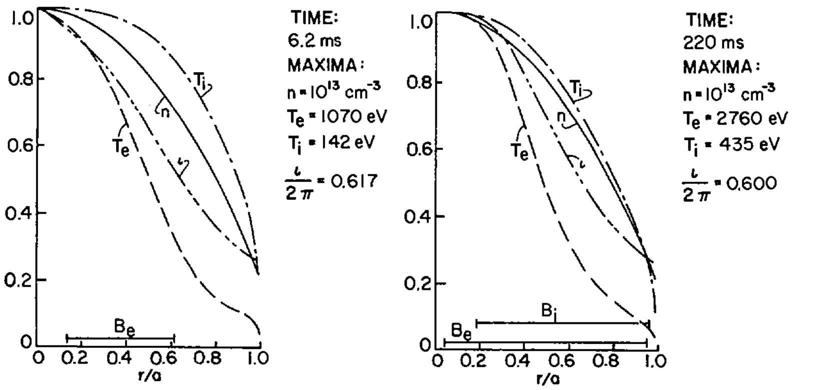

FIG. 9. Neoclassical constant-current phase. Initial J(r) peaked. $n_c = 10^{13}$ cm^{-3}, Z = 1.

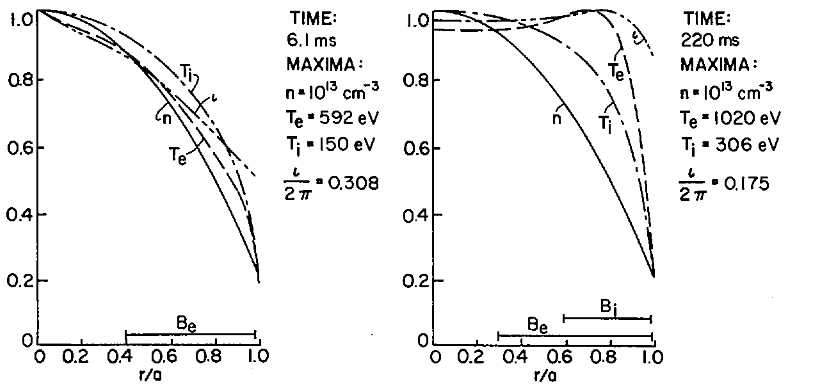

FIG. 10. Neoclassical constant-current phase. Initial J(r) parabolic. Otherwise like Fig. 9.

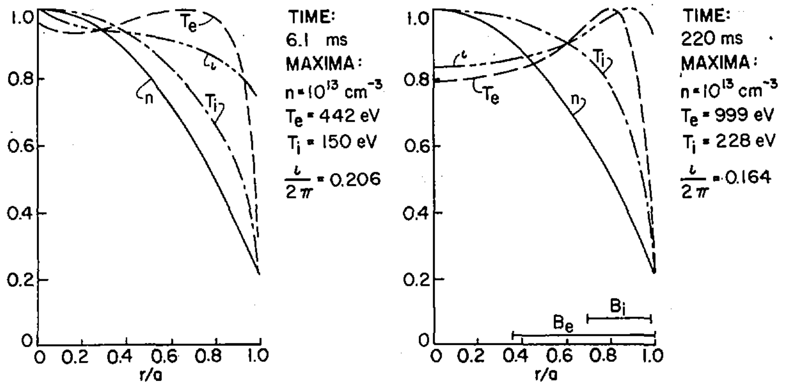

FIG. 11. Neoclassical constant-current phase. Initial J(r) flat. Otherwise like Fig. 9.

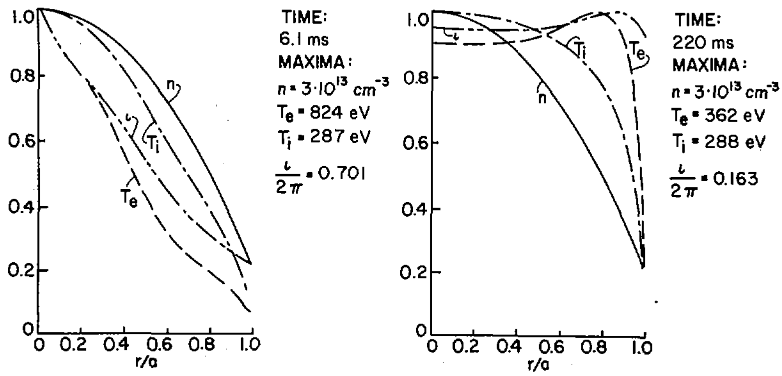

FIG. 12. Neoclassical constant-current phase. Initial J(r) peaked. $n_c = 3 \times 10^{13}$ cm^{-3}, Z = 1.

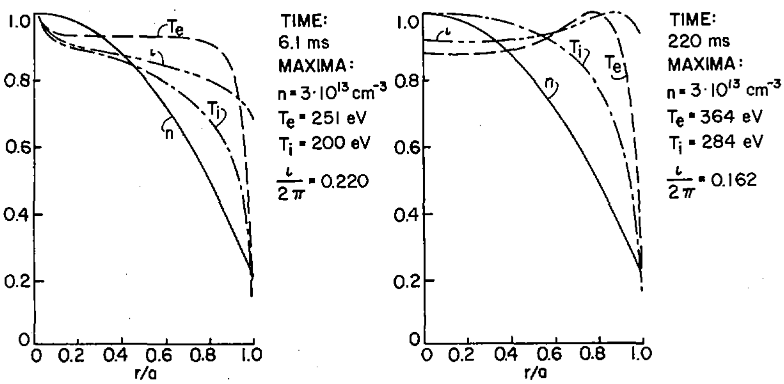

FIG. 13. Neoclassical constant-current phase. Initial J(r) flat. Otherwise like Fig. 12.

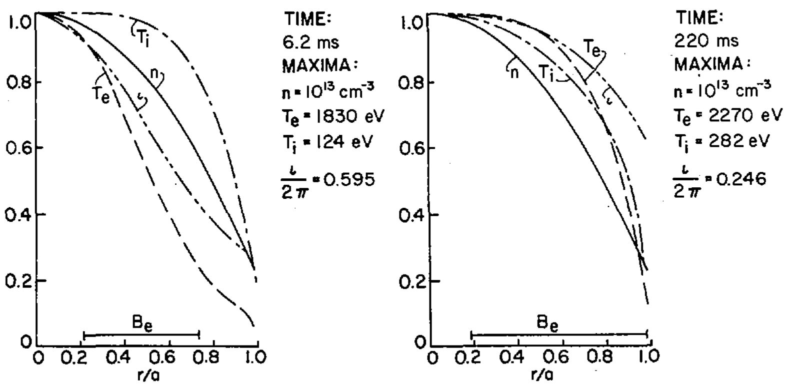

FIG. 14. Neoclassical constant-current phase. Initial J(r) peaked. $n_c = 10^{13}$ cm^{-3}, Z = 4.

The skin effect can be reduced appreciably by the two stabilizing features suggested by Eq. (11). If we raise the density to $n_c = 3 \cdot 10^{13}$ cm^{-3} so that T_e/T_i decreases, we obtain the results of Fig. 3. Likewise, if we enhance the electron thermal conductivity by a strong anomaly factor, the skin effect in T_e can be suppressed almost totally. In Fig. 4, we show a "realistic" model which differs from the case of Fig. 1 by using Z = 4 to enhance resistivity and thermal transport coefficients, and which furthermore uses the pseudoclassical electron thermal transport (i.e., $\kappa_e = 5 Z n \rho_{\theta e}^2 / \tau_e$). The result at all times is a rather flat T_e-profile, which agrees well with the measured experimental profiles in [13]—though not with those in [2]. The steady-state value of the electron β_θ is found to be ~ 0.5, as it should be, since the transport coefficient has been set up precisely for this purpose. Reduction of the density pedestal to 5%, in another computation, was found to reintroduce a strong skin effect in T_e during the current rise, but the T_e-profile still becomes flat after ~ 5 msec in the current plateau phase.

In the illustrations one notes that the skin effect is more persistent on the ι-distribution than on the T_e-distribution. It is clear, of course, that even the most effective measures taken against thermal instability will not allow arbitrarily rapid current penetration during the phase of linear current rise: in this respect the only effective remedies are to enhance the resistivity by introducing a Z-factor, or by depressing the electron temperature everywhere. A case of weak skin current is illustrated in Fig. 5, where we have used pseudoclassical transport, together with Z = 4 and $n_c = 3 \cdot 10^{13}$ cm^{-3}.

3.2 Limitation of the skin effect

There are two reasons why one wishes to eliminate strong skin effect from the computer tokamak studies: firstly, no such effect has been seen in the experiments [2,13] (at least not on the T_e-profiles, while J(r) remains to be studied); and secondly, the existence of such an effect is generally incompatible with MHD stability, so that one probably cannot ascribe any practical significance to computer results that exhibit strong skin currents.

The nature of the probable MHD instability in the skin layer deserves some comment. If the rotational transform ι does not decrease monotonically with radius, there will be a local null in shear, removing the usual constraint against flutelike modes. As Shafranov has shown, however, the flutelike modes of the tokamak have very small growth rates, lower by $(B_\theta/B_\phi)^2$ than those of the kink modes, and may indeed be stabilized altogether by toroidal effects [14]. The major MHD disturbances of the tokamak are probably due to the finite-resistivity kink, i.e., the tearing mode [15], which is much more strongly driven. In the presence of a skin current, the tearing mode becomes particularly unstable, even at high m-numbers. (For a nonmonotonic transform, the tearing mode can have two regions of singularity, at two different radii, with relatively large amplitude in the intermediate region.) It seems to us rather plausible that the magnetic disturbances and enhanced thermal transport observed during the skin phase of tokamaks are due primarily to the growth of the tearing mode, and the resultant destruction of magnetic surfaces.

It has also been suggested that the observed skin limitation in tokamaks is due to non-MHD phenomena: for example, an anomalous electron viscosity [16]. The idea that there could be strong microinstabilities is indeed supported by the observation on the computer experiments in this section that the ratio of electron drift velocity to sound velocity always becomes of order $v_d/v_s \gtrsim 5$ in the case of strong skin effect, though it remains typically of order $\lesssim 1$ in the case of flat temperature profiles. We note, however, that the first consequence of a weakly enhanced resistivity or electron viscosity in the skin layer will be to accelerate the growth of the tearing mode: much lower levels of microinstability are sufficient [17] in order to eliminate the skin by this micro-macroinstability collaboration than if the skin current were to be relaxed uniformly, by the microinstability mechanism alone.

In line with these ideas, we have provided an optional "skin-limiter" feature in our computer program, which enhances the electron thermal conductivity by some large factor whenever MHD instability is expected to be severe. (Affected regions are marked U in the figures.) The intention of such a feature is simply to allow the discharge to pass rapidly through the skin phase and then develop toward its natural equilibrium state. One soon discovers, however, that a "skin limiter" rule must be chosen with care: otherwise the plasma profile will settle down to marginal satisfaction of the rule, rather than evolving beyond the skin phase.

A pathological example is illustrated in Fig. 6. The basic case is the same as that in Fig. 4 (pseudoclassical, $Z = 4$, $n_c = 10^{13}$ cm^{-3}), but we use the skin-limiter rule that electron thermal transport is enhanced by a factor of 100 between any radius where $d\iota/dr \geq 0$ and an outer radius where ι has the same value. (When a point becomes "MHD-stable" again, the local enhancement of transport is allowed to decay with a time constant of 1 msec.) This rule is found to achieve the intended result of depressing

T_e and greatly increasing the resistivity in the skin region. After ~ 6 msec, the transform has become almost perfectly constant with radius, and a small MHD-stable region has formed near the outside. This profile turns out to be the steady state ! The discharge never finds its natural equilibrium, as in Fig. 4, and consequently remains at considerably lower temperature. In other cases with greater tendency toward thermal instability, such as the discharge in Fig. 1, the above skin-limiter rule leads to a permanent relaxation oscillation about $d\iota/dr = 0$. Unfortunately, these results may turn out to have physical significance in large, hot toruses, where the skin effect is strong: the instability of the skin layer is not necessarily self-healing.

A successful "skin limiter" rule is shown at work in Fig. 7. The case is the same as in Fig. 6, but we enhance the pseudoclassical transport by a factor $100\ r^2/a^2$ at all radii outward from any point where $d\iota/dr \geq 0$. The discharge then shows a much faster relaxation of the skin effect than the case of Fig. 4, and reaches the same end state.

In Fig. 8 the same rule, but with enhancement of electron thermal transport by $1000\ r^2/a^2$, is applied to a neoclassical case like that in Fig.1 ($Z = 1$, $n = 10^{13}\ cm^{-3}$), but has quite different consequences. After 30 msec, the discharge has become MHD stable; but by 60 msec the electron temperature has begun to peak significantly towards the outside, accompanied by a resurgence of skin current, which makes the profile MHD-unstable again. The electron temperature, which had reached a peak value of ~ 800 eV at 60 msec, then drops back to ~ 600 eV at 70 msec, MHD stability is recovered, and the whole cycle begins again.

3.3 Constant current models

We now turn to a more detailed study of thermal instability in the plateau phase of the current. The shape of the initial current distribution at the end of the rising-current phase can be controlled somewhat arbitrarily by the nature of the "skin-limiter" program that is employed; but it will be more convenient for the present study to operate with constant total current and to use various initial current distributions that are specified explicitly.

If is found that, depending on the choice of plasma parameters, the characteristic behavior of the discharge is either "thermally stable," in which case one arrives at the same final steady state, independent of initial profiles; or else the evolution—at least over extended periods of time—is sensitive to initial conditions, and we will call this behavior "thermally unstable." The critical feature for exciting various thermal excursions is the relative peakedness of the initial distributions of n(r) and J(r). The absolute shape of n(r) does not seem to matter as much (except near the foot of the profile); hence we will continue with the simple parabolic model (with pedestal) of Fig. 1. Whether a given thermal perturbation will damp out or grow, depends again on the ratios T_e/T_i and Q_e/Q_i, as suggested by Eq. (11).

In the following illustrations, the current is maintained steady at 40 kA, and J(r) is given various initial distributions: peaked, $(1 - r^2/a^2)^3$; parabolic, $1 - r^2/a^2$; or flat, $1 - r^6/a^6$. The initial T_e in all the following examples, unless otherwise specified, will be parabolic with $T_{ec} = 200$ eV and 20% pedestal; the initial T_i will be flat at 20 eV. The boundary conditions are still $T_e = 40$ eV, $T_i = 20$ eV.

For the case $n_c = 10^{13}$ cm^{-3}, Z = 1, the subsequent effect of the various initial J(r) profiles, is shown in Figs. 9 - 11. For peaked initial J(r), there is a very marked excursion of T_e near the axis (with T_e/T_i correspondingly very small). The excursion is found to grow rapidly during the first 50 msec, and then to remain essentially static for several 100 msec more. For parabolic or flat initial J(r), there results a mild outward peaking of T_e, which again is essentially static at late times. The outward peaking can be enhanced greatly by reducing the pedestal of n(r) below the standard 20%.

When the cases of Figs. 9 - 11 are repeated with $n_c = 3 \cdot 10^{13}$ cm^{-3}, the ratio T_e/T_i is reduced, and one would expect an approach to thermal stability. This is verified in Figs. 12 and 13, which show that peaked and flat initial J(r) give rise to substantially different transient behavior in the early stages, but after several 100 msec lead into the same end state.

When the cases of Figs. 9 - 11 are computed for $n_c = 10^{13}$ cm^{-3}, Z = 4, the time scale is effectively shortened (since Z enters linearly into both the resistivity and the transport coefficients). The electron-ion equilibration rate, however, is not increased (since we assume the "effective Z" to arise from a small percentage of high-Z ions). As a result, T_e/T_i is further increased; but a more important effect is that Q_e/Q_i is now forced to be greater, and so the overall effect of going to Z = 4 is stabilizing. These effects are shown in Fig. 14 where an initially peaked J(r) leads to a sharply peaked T_e-excursion, as in the case of Fig. 9, but the peak subsequently diminshes. For $n_c = 3 \cdot 10^{13}$ cm^{-3}, Z = 4, all three initial J(r)'s lead into the same final state (Fig. 15), which is characterized by a T_e-profile that is slightly peaked toward the outside.

Pseudoclassical transport and Z = 4 at $n_c = 10^{13}$ cm^{-3} gives another case that would be expected to be thermally stable, by virtue of large Q_e/Q_i. Figure 16 illustrates that initially peaked or flat J(r) does indeed lead into the same final state. This state is seen to be identical with that attained in Fig. 4, after termination of the skin current phase.

3.4 Relation to the experiments

Some characteristic discharge parameters of the illustrative cases of Figs. 1 - 16 are given in Table I for late times in each run. It is seen that the neoclassical cases with Z = 1 are generally characterized by $\beta_{\theta e}$-values and T_e/T_i—ratios that are remarkably close to the typical experimental results—especially if we consider that the neoclassical predictions are based on first principles, without benefit of any adjustable parameters. This general property was first noted in [4] and has served to stimulate interest in neoclassical calculations.

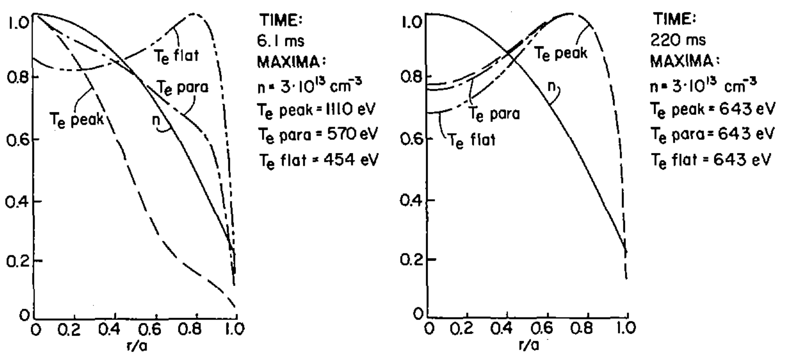

FIG.15. Neoclassical constant-current phase. Various initial J(r) profiles. $n_c = 3 \times 10^{13}$ cm^{-3}, Z = 4.

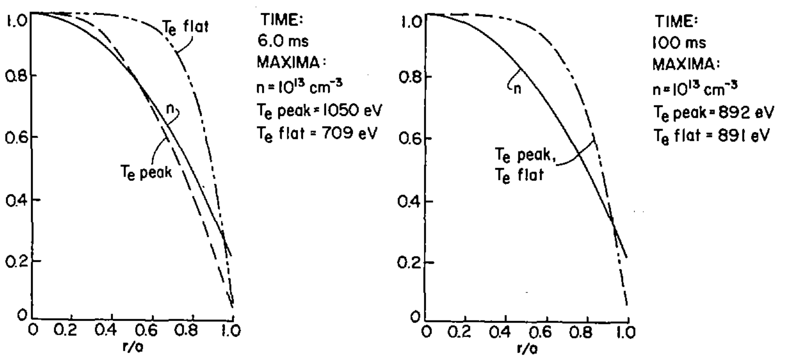

FIG.16. Pseudoclassical constant-current phase. Various initial J(r) profiles. $n_c = 10^{13}$ cm^{-3}, Z = 4.

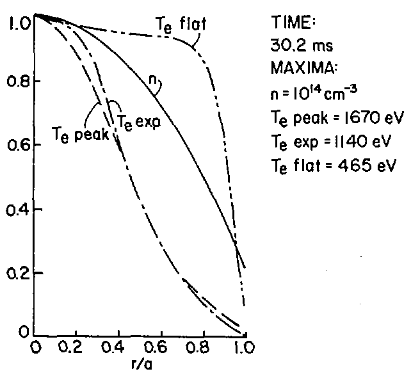

FIG.17. Neoclassical, $n_c = 10^{14}$ cm^{-3}, He, I = 55 kA (a = 12 cm). Initial J(r) flat, Z = 2; peaked, Z = 4; and experimental profile.

TABLE I. THERMAL DIFFUSION CASES: HYDROGEN, I = 40 kA, B = 30 kG, a = 14 cm, R = 109 cm. Definitions: W = total thermal energy per unit length, $\tau_E' = W/IE$. $\overline{Q}_e$, $\overline{Q}_i$ = cumulative electron and ion heat losses. T_{em}, T_{im} = maximum temperatures in T_e, T_i profiles.

Figure	κ_e	Z	$n_c \cdot 10^{-13}$, cm^{-3}	I	t, msec	$\beta_{\theta e}$	T_{em}, eV	T_{im}, eV	E, $mV\,cm^{-1}$	W, $J\,cm^{-1}$	τ_E', msec	$\overline{Q}_e/\overline{Q}_i$
1	Neo	1	1	Skin†	74	0.49	1009	240	0.39	0.79	50	0.65
2	Neo	1	1**	Skin	73	0.49	1446	308	0.32	0.84	66	0.63
3	Neo	1	3	Skin	75	0.69	379	255	1.12	1.43	32	0.43
4	Pseudo	4	1	Skin	77	0.53	888	296	1.59	0.85	13	7.8
5	Pseudo	4	3	Skin	79	0.57	304	272	6.42	1.25	5	6.7
6	Pseudo*	4	1	Skin	18	0.44	624	227	2.31	0.69	7	65
7	Pseudo*	4	1	Skin	79	0.53	889	297	1.58	0.85	13	14
8	Neo*	1	1	Skin	55	0.52	780	291	0.35	0.85	61	4.5
9	Neo	1	1	Peak††	233	0.86	2781	435	0.22	1.30	148	0.08
10	Neo	1	1	Para	235	0.68	1018	305	0.25	1.05	105	0.22
11	Neo	1	1	Flat	238	0.63	1000	288	0.28	0.99	89	0.27
12	Neo	1	3	Peak	233	0.73	363	287	1.04	1.54	37	0.09
13	Neo	1	3	Flat	238	0.73	364	284	1.04	1.53	37	0.13
14	Neo	4	1	Peak	230	1.3	2251	281	0.41	1.80	109	1.0
15a	Neo	4	3	Peak	231	1.3	643	348	1.95	2.30	29	0.21
b	Neo	4	3	Para	233	1.3	643	346	1.95	2.30	29	0.27
c	Neo	4	3	Flat	238	1.3	643	346	1.96	2.30	29	0.30
16a	Pseudo	4	1	Peak	113	0.53	891	297	1.58	0.86	14	6.9
b	Pseudo	4	1	Flat	113	0.53	891	297	1.58	0.86	14	7.2

*With "skin-limiter" rule.

**With 10% pedestal.

†Current rises linearly in 5 msec.

††Shape of initial current.

The most visible discrepancy relative to the experiments is that the measured torus voltages are typically considerably higher than those for the Z = 1 cases in Table I. This discrepancy can be alleviated within the neoclassical framework by ascribing it to the presence of high-Z ions, and using an "average Z factor" of about 4 to enhance the resistivity and the thermal conductivities in the computation. More than half this factor can, in fact, be documented directly in the experiments [2], mainly with reference to the presence of oxygen impurities.

Particularly good agreement with the ST experiment [2] has been found when using helium with $n_e = 10^{14}$. In Fig. 17 we show the computed results for a parabolic initial $J(r)$ with Z = 2 (which gives slightly too low and too flat a T_e-profile with 2.0 V IR-drop; and a peaked initial J(r) with Z = 4 (which gives slightly too high and peaked a T_e-profile with 2.5 V IR-drop). An experimental T_e profile kindly provided by the authors of [2] is shown for comparison. The measured IR-drop was ~ 2.9 V. The measured density profile was parabolic.

The variability of the temperature profile is a feature of the neoclassical model that is at least qualitatively in good agreement with the experimental pattern. As we have seen above, relatively small variations in the starting assumptions or edge conditions of the discharge can produce extremely different types of evolution for the same basic discharge parameters. This feature may help to explain the discrepancy between the T_e-profiles obtained in the T-3 [13] and ST [2] experiments, as well as the considerable variation of the ST profiles among themselves.

From Table I and the figures it is also clear that there are many points of marked disagreement between the neoclassical theory and the experiments. Generally the observed $\beta_{\theta e}$ is lower than predicted by a factor of 1.5 - 2, particularly for the low-density cases, where the observed peak T_e-values are not nearly as high as the ones computed for similar profiles. A related discrepancy is that the dominant energy loss in the experiments appears to be generally by way of the electrons, whereas in the neoclassical computations the ions generally carry off several times as large a heat flux. These discrepancies can be remedied by departing from the neoclassical theory and introducing an ad hoc anomalous electron thermal conductivity: the pseudoclassical thermal transport coefficient is designed for this role. A transport coefficient of the proper magnitude has been derived independently on the basis of plausible physical considerations [18].

As can be seen from Table I, the pseudoclassical cases always lead to moderate temperatures. We have also noted earlier that pseudoclassical temperature profiles are particularly stable. Precisely for this reason, however, one cannot hope to obtain the highly peaked T_e-profiles reported for the low-density regimes in ST. Various interesting alternatives suggestions have been made to account for the distinctive shape of these profiles. The possibility that the "trapped-particle pinch" effect of the full neoclassical equations may be responsible [6] is investigated in the next section.

4. PLASMA TRANSPORT AND PINCHING

We now depart from the approximation that the density profile is static, and use the full neoclassical banana code to study the evolution of discharges similar to those investigated in Section 3: namely, with $a = 14$ cm, $R = 109$ cm, $I = 40$ kA, and $B = 30$ kG. The initial density is parabolic with 20% pedestal, and there is now a boundary condition holding constant the edge density at its initial value. We again use a fixed plasma current, with various initial profiles. The initial T_e in Figs. 18 - 20 is parabolic with $T_{ec} = 200$ eV and there is a 40 eV boundary condition; the initial T_i is constant at 20 eV, and there is a 20 eV boundary condition. In one minor respect the present model is less complete than the one in Section 3: the transport is taken to be in the banana regime at all times and radii, irrespective of the actual local plasma parameters.

4.1 The trapped-particle pinch

In Fig. 18 we treat the same case as in Fig. 10 ($Z = 1$, $n_c = 10^{13}$ cm^{-3} at $t = 0$). We see that the density profile in Fig. 18 is pinched significantly at early times, and then relaxes somewhat. The T_e-profile is actually less peaked than in Fig. 10 (in fact, it shows a local minimum at $r = 0$), and reaches somewhat lower maximum values. This behavior is typical of all the cases we have studied. As can be seen directly from the equations of Section 2.2, the adiabatic pinching acts to raise n much more strongly than T_e, and the thermal-instability effect discussed in Section 3 then takes over and actually reduces T_e in the high-n region. In this sense, the simplified code of Section 3 is seen to be realistic: thermal transport is verified to be the dominant consideration in respect to the peakedness of the T_e-profile. On the other hand, the results of the present section verify the remarkable suggestion made by Ware [6] that the toroidal electric field in tokamaks might produce significant plasma density pinching on the same "fast" time-scale on which the thermal processes evolve.

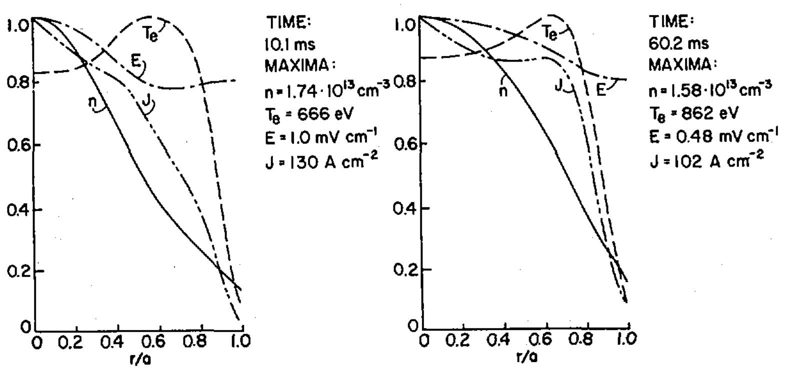

FIG. 18. Banana code. Initial J(r) parabolic, $n_c = 10^{13}$ cm^{-3}. Same case as Fig. 10, but n evolves in time.

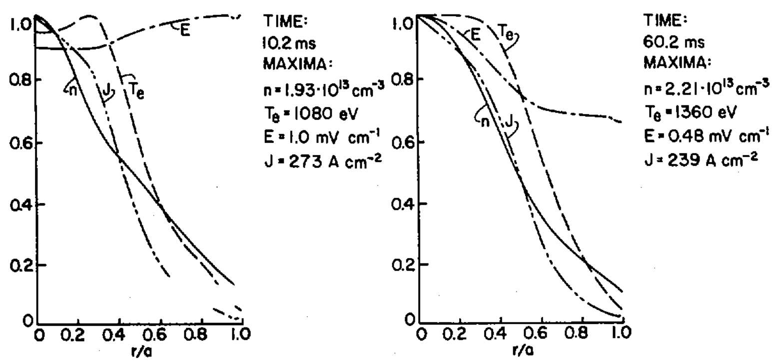

FIG.19. Banana code. Initial J(r) peaked, $n_c = 10^{13}$ cm^{-3}. Same case as Fig.9, but n evolves in time.

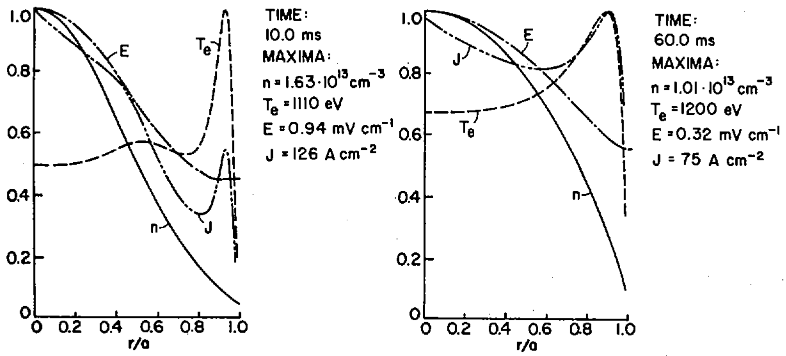

FIG.20. Banana code. Density pedestal reduced from 20% to 5%. Otherwise same as Fig.18.

In Fig. 19, we use a peaked initial current profile, as in the case of Fig. 9. We now find a pronounced central peak of T_e, though it is not as sharp in profile nor as large in magnitude as that seen in Fig. 9. The peaking of n is now considerably greater than in Fig. 18, and relaxes more slowly. As can be seen from Eq. (5), the sharp T_e-gradient due to the thermal instability is presumably responsible. Our conclusion is that, whereas the trapped-particle pinch effect does not enhance the T_e-peaking, the converse process does exist: the T_e-peaking due to the thermal instability enhances the density pinching.

The use of a boundary condition holding n fixed at 20% of the initial n_c leads to a substantial increase of total particles during the evolution of the discharge, since the radial flow velocity at the boundary is negative in the above examples. In the case of Fig. 20, we have reduced the density pedestal and boundary condition to 5%. (Otherwise the case is the same as for Fig. 18.) As was to be expected from the experiences of Section 3, the principal effect is the growth of a thermal instability, producing a sharp peak of T_e toward the outside. The central density pinching is reduced somewhat in the process, and the radial velocity at late times in the discharge is now mostly outward.

4.2 The bootstrap effect

One of the interesting consequences of the equations of Section 2.2 is the so-called bootstrap effect, whereby a plasma of sufficiently high $\beta_{\theta e}$ can maintain the tokamak current, even in the absence of applied electric field—or in the presence of a negative electric field. In the latter case, plasma thermal energy is converted into electrical energy, which flows into the external circuit. To attain such a regime, requires $\beta_{\theta e}$-values somewhat higher than those that can arise from Ohmic heating in the presence of neoclassical losses. In the examples of Figs. 21 and 22, we therefore begin with high initial density and temperature: $n_c = 5 \cdot 10^{13}$ cm^{-3}, $T_{ec} = 3000$ eV, $T_{ic} = 1500$ eV. (All initial profiles are parabolic, with pedestal.)

In Fig. 21, the boundary conditions are fixed at $n = 10^{13}$ cm^{-3}, $T_e = 100$ eV, $T_i = 50$ eV. At early times one finds that the plasma flow is now outward, and that the toroidal electric field is negative at all radii, except near the center. After about 30 msec, however, the temperature and density have dropped sufficiently so that E becomes everywhere positive again. The radial velocity at 30 msec shows "wavelike" alternate negative and positive regions; but after ~ 40 msec it has become everywhere negative. The plasma has not been able to find a thermal equilibrium that allows sufficient $\beta_{\theta e}$ to provide an electrical equilibrium with $E \approx 0$ (i.e., the bootstrap equilibrium).

In Fig. 22, we raise the temperature boundary conditions to $T_e = 2000$ eV, $T_i = 1000$ eV, thus avoiding the rapid cooling of the plasma encountered in the case of Fig. 21. We now find a much more persistent region of negative E, which gradually narrows from both the sides of small and large radii. After ~ 70 msec, enough plasma density has been lost so that E is again everywhere positive. The velocity, however,

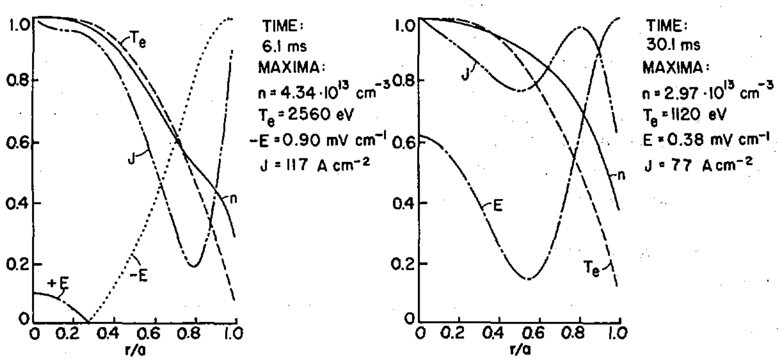

FIG. 21. Banana code. Bootstrap effect. Initial $n_c = 5 \times 10^{13}$ cm^{-3}, $T_{ec} = 3000$ eV, $T_{ic} = 1500$ eV. At $r = a$, $T_e = 100$ eV, $T_i = 50$ eV.

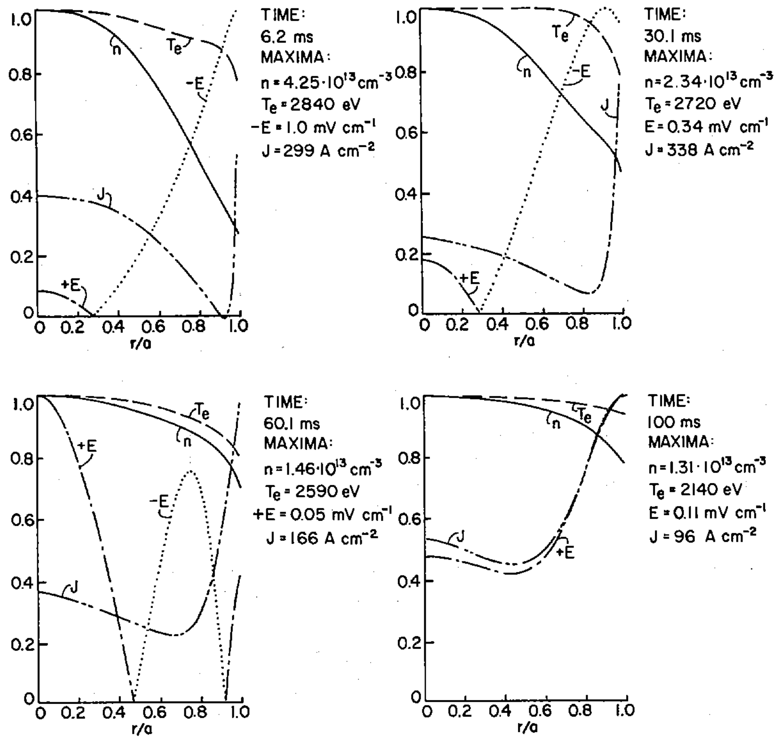

FIG.22. Banana code. Bootstrap effect. Same as Fig.21; but at r = a, T_e = 2000 eV, T_i = 1000 eV.

continues to be outward, except near the center, even after 100 msec. The current density J is depressed near the outside by the strong negative E-field, and even becomes slightly negative. At the very edge of the plasma, however, the strong temperature and density gradients produce a positive peak in J.

These examples serve to illustrate the general features of the bootstrap mechanism. In order to provide a true equilibrium, appropriate sources of plasma and of heat must be provided on the plasma interior. This problem will be pursued in a separate study.

4.3 The electron temperature peak in ST

It remains to find a plausible explanation for the sharp T_e-peaks observed in the ST tokamak. The thermal instability of the neoclassical low-density regime lends itself well to T_e-peaking, but it requires some physical starting mechanism. The pure neoclassical model also does not account for the observed magnitudes of electron heat loss and particle loss, particularly at low density.

We have therefore begun to investigate the possibility that the central peaking of the T_e-profile is triggered by the influx of cold neutrals from the outside. The power lost in heating the resultant cold plasma particles to the ambient temperature serves to depress T_e at large radii and encourages the current to channel nearer the center. Initial results supporting this picture are given in Fig. 23, which treats a case like that in Fig. 18, but with an initial n_c of $3 \cdot 10^{12}$ cm^{-3} with only 5% pedestal, and a wall density of cold neutrals of $5 \cdot 10^9$ cm^{-3} flowing in with a directed energy of 1 eV. The initial distribution of the cold neutrals was like r^4; the wall density was kept fixed. Ionization of the cold neutrals was, of course, included, as was charge exchange; but we neglected the interaction of the very low density of hot neutrals (produced by charge exchange) with the plasma. It is seen that T_e is now strongly peaked at the center, instead of having a minimum there, as in the case of Fig. 18. The density profile now becomes very flat, however, and even shows a central minimum at early times. The magnitude of the density also increases at a rapid rate. To obtain a realistic fit with the experimental data, it is evidently necessary to introduce an anomalous enhancement of the particle transport (especially at large radii), in order to remove the accumulating particle density. Initial studies show that the heat loss associated with enhanced particle transport of the pseudoclassical magnitude [18] also removes the peculiar T_e-spike on the plasma edge.

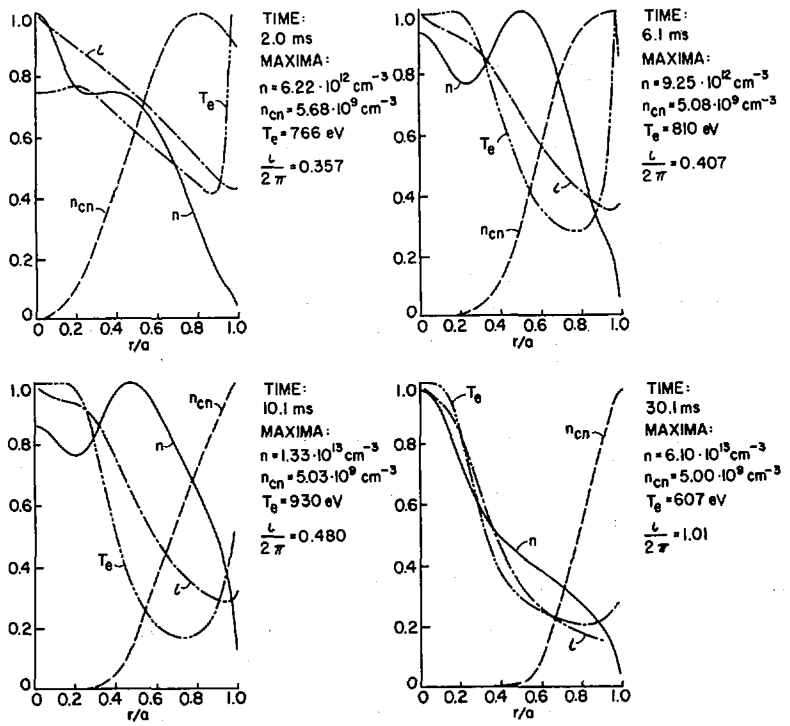

FIG. 23. Banana code and neutrals. Like Fig. 18, but initial $n_c = 3 \times 10^{12}$ cm^{-3} with 5% pedestal. At $r = a$, $n_{cn} = 5 \times 10^9$ cm^{-3}.

Among the many special physical processes of tokamaks not yet provided for in our code is the effect of runaway electrons, which can play an important role in driving thermal instability [5]. In the presence of an enhanced resistivity with effective Z = 4, runaway hydrogen ions can also maintain themselves in the energy range ~ $(m_i/m_e)^{1/3}\ T_e$ [17]. To the extent to which the tokamak magnetic field departs from axisymmetry—due to imperfect construction, or by experimental design—the ion thermal conductivity will have to be enhanced by superbanana corrections.

5. HIGHER-TEMPERATURE TOKAMAK EXPERIMENTS

Present-day tokamak experiments characteristically reach the condition $\beta_{\theta e} \sim 0.5$ in Ohmic-heated equilibrium. It follows that the electron energy confinement time must scale as $\tau_E \propto a^2/\eta$ (for fixed $\beta_{\theta e}$). Accordingly, any kind of basically classical transport theory (whether neoclassical or pseudoclassical, etc.) lends itself to fitting the present-day tokamak results. To what extent this type of scaling remains realistic outside the present parameter range is not established as yet.

At sufficiently low plasma currents (low T_e) the present scaling $\beta_{\theta e}$ ~ const. eventually becomes more pessimistic than Bohm scaling, and one suspects that Bohm diffusion will then limit the transport rate [18]. At large plasma currents (high T_e), the present scaling predicts extremely long τ_E—corresponding to extremely slow Ohmic heating. It seems likely that very weak loss mechanisms may then become dominant—for example, various trapped-particle modes. It is nonetheless of some interest to formulate the prescriptions of the neoclassical and pseudoclassical models in the high-temperature range, in order to indicate upper limits to possible tokamak performance. We will use the simplified code of Section 3.

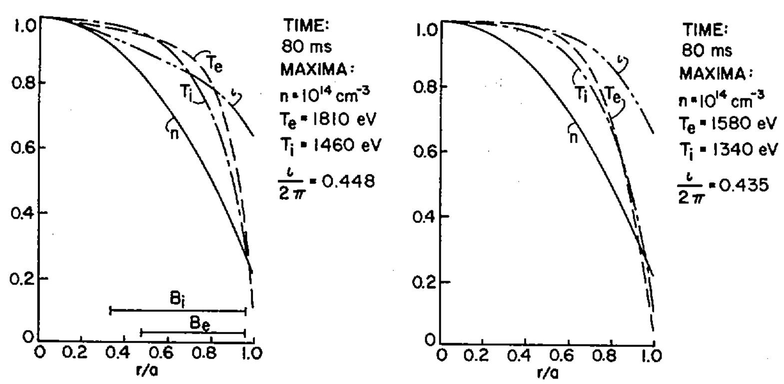

FIG.24. Neoclassical (left) and pseudoclassical (right), $n_c = 10^{14}\ cm^{-3}$, I = 200 kA, B = 80 kG (R = 109 cm, a = 14 cm).

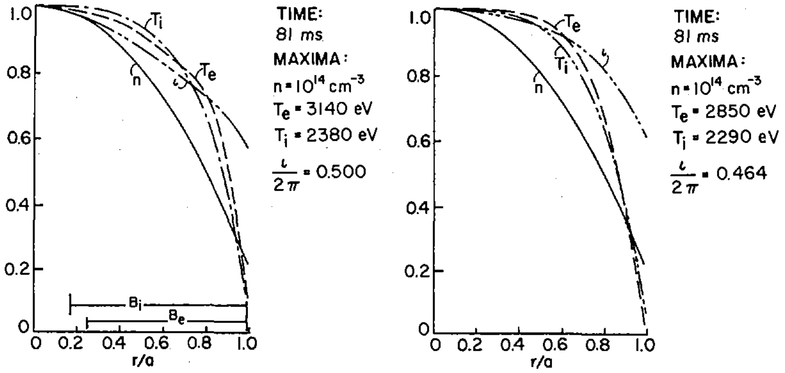

FIG. 25. Neoclassical (left) and pseudoclassical (right), $n_c = 10^{14}$ cm^{-3}, I = 300 kA, B = 120 kG (R = 109 cm, a = 14 cm).

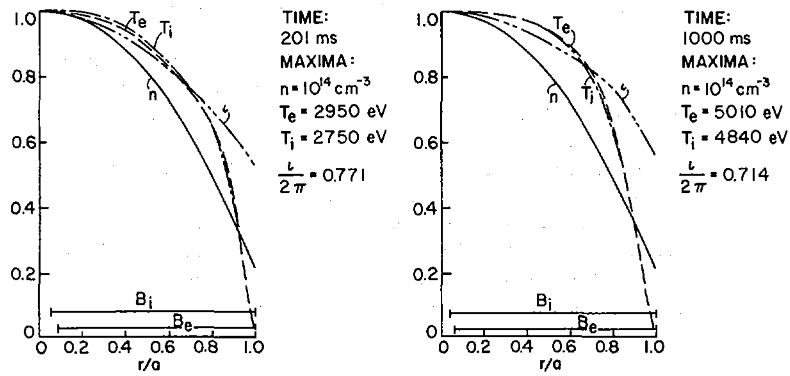

FIG. 26. Neoclassical, $n_c = 10^{14}$ cm^{-3}, I = 1.6 MA, B = 50 kG (R = 125 cm, a = 45 cm).

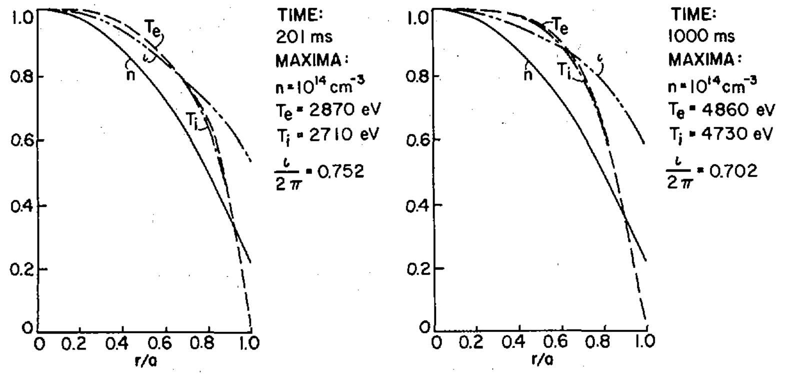

FIG. 27. Pseudoclassical (same parameters as Fig. 26).

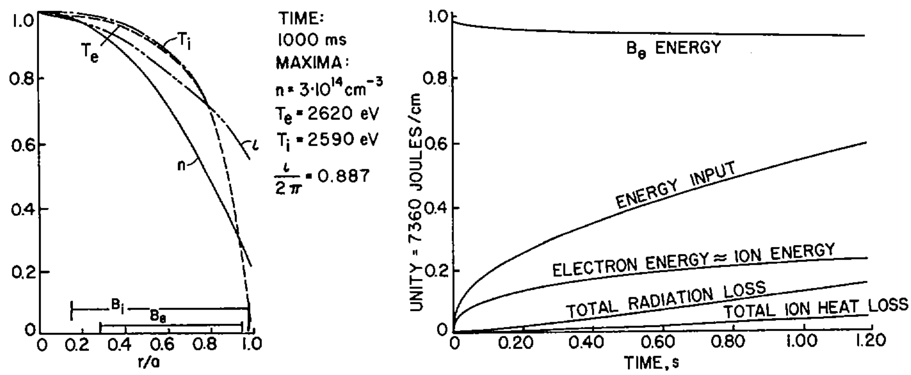

FIG.28. Neoclassical, $n_c = 3 \times 10^{14}\ cm^{-3}$, I = 4 MA, B = 75 kG (R = 250 cm, a = 75 cm).

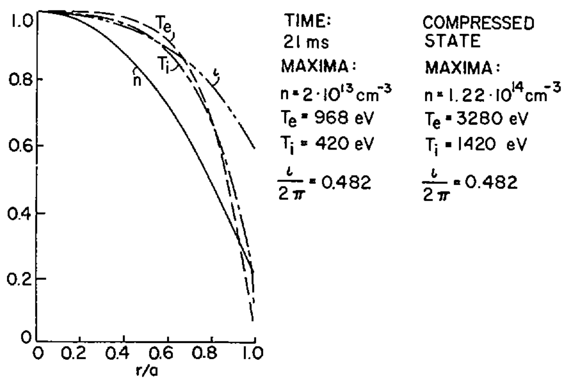

FIG.29. Pseudoclassical initial state, $n_c = 2 \times 10^{13}\ cm^{-3}$, I = 90 kA, B = 20 kG (R = 90 cm, a = 17 cm); compressed to R = 36 cm.

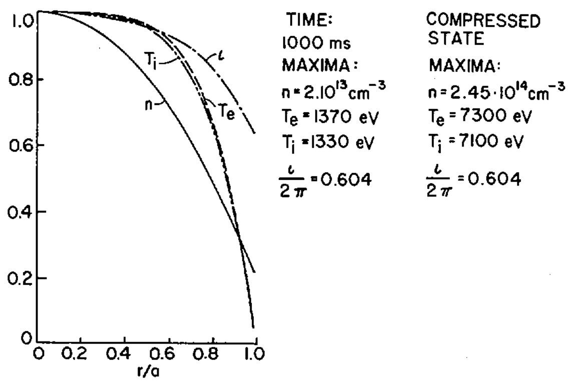

FIG.30. Pseudoclassical initial state, $n_c = 2 \times 10^{13}\ cm^{-3}$, I = 500 kA, B = 20 kG (R = 420 cm, a = 75 cm); compressed to R = 120 cm.

TABLE II. HIGH-TEMPERATURE TOKAMAK CASES: HYDROGEN, Z = 2, INITIAL CURRENT PARABOLIC

Figure	κ_e	$n_c \cdot 10^{-13}$, cm^{-3}	I, kA	B, kG	a, cm	R, cm	t, msec	$\beta_{\theta e}$	T_{em}, eV	T_{im}, eV	τ'_E, msec	$\overline{Q}_e/\overline{Q}_i$
24a	Neo	10	200	80	14	109	129	0.48	1841	1527	120	0.07
b	Pseudo	10	200	80	14	109	125	0.39	1620	1385	69	1.5
25a	Neo	10	300	120	14	109	120	0.37	3404	2668	180	0.07
b	Pseudo	10	300	120	14	109	125	0.33	3138	2577	140	1.5
26	Neo	10	1600	50	45	125	1083	0.19	5124	4964	1700	0.04
27	Pseudo	10	1600	50	45	125	1083	0.19	4972	4846	1600	0.35
28	Neo	30	4000	75	75	250	1182	0.14	2702	2672	1700	0.03**
29*	Pseudo	2	90	20	17	90	51	0.39	1100	520	45	1.3
30*	Pseudo	2	500	20	75	420	1088	0.30	1394	1354	1250	1.1

*Before compression.

**Ratio of cumulative Bremsstrahlung loss to $\overline{Q}_i$ is 3.2.

Present discharges in the ST tokamak have operated at rather high q-values at the limiter ($q = 2\pi/\iota \sim 7$), because of the peaked temperature profiles and apparently narrow current channels. In the following examples we will use a fixed total current, with parabolic initial distribution. As illustrated in Fig. 24, for the resultant flat T_e-distributions the value of q on axis can be kept greater than 2 even when q at the limiter is only slightly above 3. This would correspond to 100 kA at the present operating level of 40 kG, and to 200 or 300 kA, respectively, if 80 or 120 kG were available (Figs. 24 and 25). The neoclassical and pseudoclassical temperature predictions are seen to be roughly the same, though Table II shows that the energy loss channels are quite different. The ion temperatures of several keV that are indicated here would be an attractive experimental objective. A principal source of concern has to do with the neutral influx (see Section 4.3), which is quite important in small-sized systems. If the resultant discharge profile becomes as peaked as it is in the present ST data, the plasma current must be reduced by a factor of ~ 2, and the temperatures will drop accordingly. (The calculations in the present section are all for an effective Z of 2—corresponding to mild impurity content. The results are not sensitive to Z, except in respect to the time scale.)

An advance to larger tokamak dimensions is illustrated in Figs. 26 and 27, for I = 1.6 MA, B = 50 kG, a = 45 cm, and R = 125 cm. The neoclassical (Fig. 26) and pseudoclassical (Fig. 27) results are very similar, since thermal transport is now less important than the heat capacity of the plasma (see Table II). Bremsstrahlung cooling is beginning to account for a few percent of the losses. Temperature profiles are given at 200 msec and at a rather hopeful 1000 msec.

A regime where bremsstrahlung dominates the plasma heat loss is illustrated in Fig. 28. The general condition for Ohmic heating to be balanced by bremsstrahlung cooling is roughly $I \gtrsim 0.7/\beta_{\theta e}$ MA. In the example of Fig. 28, we use I = 4 MA, with B = 75 kA, a = 75 cm, R = 250 cm (corresponding to $q \gtrsim 1$ at the axis) and $n_c = 3 \cdot 10^{14}$ cm^{-3}. The evolution of the energetics as a function of time is also shown in the figure. At 1200 msec, a $\beta_{\theta e}$ of 0.14 has been reached.

One way to enhance the effectiveness of tokamak heating to high temperature is to compress an initial Ohmic-heated discharge adiabatically in major and minor radius [19]. Figure 29 illustrates how a T-3 type 90 kA discharge with B = 20 kG, a = 17 cm, R = 90 cm can be transformed to 2.5 times smaller R and $(2.5)^{1/2}$ times smaller a (by means of a pulsed vertical magnetic field). After compression, the current is 225 kA and the plasma is in a 50 kG region. The shape of the profiles remains the same, and $\iota(r)$ remains exactly the same. The compressional heating mechanism is applied on a much larger scale in Fig. 30, where a discharge of 500 kA with B = 20 kG, a = 75 cm, R = 420 cm is transformed to 3.5 times smaller R, with I = 1.75 MA. in a region of 80 kG.

As we have already noted from Table II, the large, high temperature devices considered here have relatively small thermal transport losses. It is important to recall, however, that the present calculations start after the completion of a hypothetical skin-relaxation phase. Unless the limiter radius is programmed as a function of time [20], the thermal losses incurred in passing through such a phase must necessarily be at least of the same order as the B_θ-field energy in the steady state. As Fig. 28 illustrates, in large tokamak experiments, this B_θ-field energy is typically a much larger quantity than the integrated heat loss from the plasma during a one-second current plateau phase.

ACKNOWLEDGMENTS

We are grateful to the authors of [2] for inclusion of some of their data and to the authors of [9] for use of their formulation of neoclassical theory, both in advance of publication. Most of the computational work was performed on the Princeton University IBM 360/91 facility supported in part by National Science Foundation Grant NSF-GP579; some was performed on the Naval Research Laboratory CDC 3800. Programming assistance at PPL was provided by L. G. DiMassa.

REFERENCES

[1] ARTSIMOVICH, L. A., et al., Nucl. Fusion, Special Suppl. (1969)p. 17.
[2] DIMOCK, D., ECKHARTT, D., EUBANK, H., HINNOV, E., JOHNSON, L. C., MESERVEY, E., TOLNAS, E., and GROVE, D. J., presented at the Fourth Conference on Plasma Physics and Controlled Nuclear Fusion Research, Madison, Wisconsin, June 1971, paper CN-28/C-9.
[3] GALEEV, A. A. and SAGDEEV, R. Z., Zh. Eksp. Teor. Fiz. 53 (1967) 348 [Sov. Phys. —JETP 26 (1968) 233].
[4] DNESTROVSKII, Y. N., KOSTOMAROV, D. P., and PAVLOVA, N. L., Fourth European Conference on Controlled Fusion and Plasma Physics, CNEN, Rome, 1970.
[5] FURTH, H. P., ROSENBLUTH, M. N., RUTHERFORD, P. H., and STODIEK, W., Phys. Fluids 13 (1970) 3020.
[6] WARE, A. A., Phys. Rev. Lett. 25 (1970) 916.
[7] GALEEV, A. A., Zh. Eksp. Teor. Fiz. 59 (1970) 1378.
[8] RUTHERFORD, P. H., ROSENBLUTH, M. N., KOVRIZHNIKH, L. M., and HINTON, F. L., Phys. Rev. Lett. 25 (1970) 1090.
[9] ROSENBLUTH, M. N., HAZELTINE, R., and HINTON, F. L., Phys. Fluids (to be published).
[10] SHAFRANOV, V. D., Atomnaye Energiya 19 (1965) 120 [J. Nucl. Energy Pt. C 8 (1966) 314].
[11] DÜCHS, D. and GRIEM, H. R., Phys. Fluids 9 (1966) 1099.
[12] DÜCHS, D. (to be published).
[13] PEACOCK, N. J., ROBINSON, D. C., FORREST, M. J., WILCOCK, P. D., and SANNIKOV, V. V., Nature 224 (1969) 488.
[14] SHAFRANOV, V. D., Zh. Tekh. Fiz. 40 (1970) 241 [Sov. Phys. — Tech. Phys. 15 (1970) 175].
[15] RUTHERFORD, P. H., FURTH, H. P., and ROSENBLUTH, M. N., presented at the Fourth Conference on Plasma Physics and Controlled Nuclear Fusion Research, Madison, Wisconsin, June 1971, paper CN-28/F-16.

[16] SCHMIDT, J. and YOSHIKAWA, S., Phys. Rev. Lett. 26 (1971) 753.
[17] FURTH, H. P. and RUTHERFORD, P. H. (to be published).
[18] YOSHIKAWA, S., Phys. Rev. Lett. 25 (1970) 353.
[19] FURTH, H. P. and YOSHIKAWA, S., Phys. Fluids 13 (1970) 2593.
[20] GOLOVIN, I. N., DNESTROVSKY, Yu. N., KOSTOMAROV, D. P., Proc. Nuclear Fusion Reactor Conference (Culham, 1969) p. 194. See especially p. 210.

DISCUSSION

A.A. WARE: I would like to make a comment regarding your work with the complete set of neoclassical equations. I do not think you have given these equations a fair chance of explaining the experimental results in the ST experiment. By incorrectly using the banana regime transport coefficients for all radii at all times, irrespective of the temperature, you have produced too much initial pinching, which leads to a more rapid peaking of the density than is observed experimentally. The off-axis maximum in T_e is a further consequence. If, instead, you were to use the correct plateau regime coefficients for the central part of the plasma at low temperatures, you would predict less initial pinching of the density. Ohmic heating, which raises T_e and not n, would be important for a longer time and I think density and temperature profiles closer to the ST results would then be obtained.

H.P. FURTH: Our computer studies on pinching in the banana regime were not aimed at getting a realistic fit with the ST-experiments. The objectives were to determine, (a), whether the set of banana transport equations used in papers C-4 and C-6 would lead to significant evolution of the density profile on the same time scale as for the evolution of the thermal profiles and, (b), whether the trapped particle pinch would result in a central peaking of the electron temperature profile. As regards the first of these points, our results lend support to your view that there would be a significant effect. It was found, however, that the banana equations produce a peaked density profile rather than a peaked electron-temperature profile. This feature can in fact be easily recognized from the set of equations.

We plan to study the plateau regime, for comparison with the ST-experiments. In this regime, the trapped-particle pinching becomes weak and, since the pinching appears to hinder rather than promote a central peaking of the T profile, its disappearance may indeed help the neutral influx and thermal instability to create T_e peaks like those observed in the experiments.

J.D. JUKES: I notice that your calculated variation of rotational transform $\iota(r)$ as a function of radius shows both maxima and minima in the plasma off-axis. One would therefore anticipate localized instabilities in these regions.

H.P. FURTH: The skin effect and the thermal instability of neoclassical Tokamaks tend to give rise to an outward peaking of the rotational transform. This configuration is unstable against various MHD-modes in and about the region for which the transform is double-valued. As stated in our paper, we believe that the most important resultant MHD-type instability is the tearing mode. In the presence of MHD instabilities, the transport coefficients are presumably enhanced, and the peaking of the transform is relaxed. Our code makes provision for such a mechanism.

B.D. FRIED: It appears that your models have sufficient freedom - anomaly factors, special "rules", inclusion of neutral gas and impurities etc - to fit a very large range of experimental results. However, an important application of such computations is in the prediction of Tokamak performance for new parameter regimes. In view of the flexibility of your models, and the fairly sensitive dependence of the calculated quantities on the choice of anomaly factors, effective atomic weight etc., how much reliability can be placed on the extrapolations to larger configurations?

H.P. FURTH: Our basic neoclassical model, on which I reported, has virtually no flexibility. The transport coefficients are derived from first principles. The experimental values of density etc., for which we calculate our profiles are accurately known, as are the actual experimental profiles with which we compare our results. The lack of flexibility of our code is shown by the fact that we cannot explain the T_e profiles of the ST-Tokamak unless we take into account the presence of neutral gas. In the latter case we introduce the measured value of the gas density at the plasma edge, and give the neutrals a velocity consistent with their observed depth of penetration into the plasma. In order to fit the observed levelling-off of plasma density at late times, we are then obliged to introduce an enhancement of the neoclassical particle diffusion. In our written paper we also experiment briefly with various other anomalous transport coefficients. As regards the extrapolation to high-temperature Tokamaks, our classical calculations are useful in setting an upper limit for performance, but new experimental evidence may well lead to anomalous transport coefficients - especially in the range of very low collision rates.

B.P. LEHNERT: I agree with Dr. Furth that it is essential to include the neutral gas interaction in the balance when dealing with Tokamak systems. The latter are permeable, as it were, and neutrals moving from the walls can penetrate into the centre of the discharge when the plasma density is less than about 10^{20} m^{-3} (10^{14} cm^{-3}). From measurements of the neutral gas density at the axis one can then estimate the rate of radial plasma diffusion. What values would you then get for the corresponding diffusion coefficients? How much larger are these coefficients than the classical and neoclassical ones?

H.P. FURTH: In recent calculations with neutrals, not reported in our written paper, we found that the neoclassical particle transport must be enhanced by about an order of magnitude in order to reach a state of equilibrium density in ST in the presence of the known neutral influx. Enhancement of the electron thermal conductivity, by a factor of roughly 3-10, is helpful in order to provide smoother T_e profiles, i.e. by reducing thermal instability.

ВЛИЯНИЕ ЭЛЕКТРИЧЕСКОГО ПОЛЯ НА ПРОЦЕССЫ ПЕРЕНОСА В АКСИАЛЬНО-СИММЕТРИЧНЫХ МАГНИТНЫХ ЛОВУШКАХ

Л.М.КОВРИЖНЫХ
Физический институт им.П.Н.Лебедева
Академии наук СССР, Москва,
Союз Советских Социалистических Республик

Abstract — Аннотация

EFFECT OF AN ELECTRIC FIELD ON TRANSFER PROCESSES IN AXIALLY SYMMETRIC MAGNETIC TRAPS.

By solving the kinetic equation in the drift approximation, expressions are derived for the particle flux and energy density across a strong magnetic field in axially symmetric systems of the Levitron or Tokamak type. In addition to the longitudinal accelerating electric field, which is responsible for creating the longitudinal current, account is taken of the presence of a quasistatic electric field directed along the minor radius and resulting from ambipolarity of dispersion. Both the case of very low collision frequencies (lower than the characteristic frequency of the azimuthal motion of the "blocked" particles) and that of intermediate and high collision frequencies are considered. It is shown that, if either the thermal velocity of the particles or the ratio of the poloidal magnetic field to the longitudinal magnetic field is fairly large (so that the mean longitudinal velocity of the toroidally "blocked" particles is much less than the azimuthal variations of their longitudinal velocity), then allowance for the radial electric field corresponds to allowance in the flux expressions for corrections of the next higher (i.e. fourth) order with respect to the smallness parameter used. In the opposite limiting case, allowance for the radial electric field becomes very important: in the region of very low and very high collision frequencies it leads to a substantial change in the functional dependence of the dispersion and heat conduction coefficients on the plasma and magnetic field parameters, while in the region of intermediate collision frequencies it leads to corrections proportional to the square of the ratio of the Larmor radius in the poloidal magnetic field to the characteristic dimension of the plasma inhomogeneity. In conclusion, the author discusses the question of determining a self-consistent radial electric field within the framework of a theory which takes into account only the lowest order with respect to the Larmor radius.

ВЛИЯНИЕ ЭЛЕКТРИЧЕСКОГО ПОЛЯ НА ПРОЦЕССЫ ПЕРЕНОСА В АКСИАЛЬНО-СИММЕТРИЧНЫХ МАГНИТНЫХ ЛОВУШКАХ.

Путем решения кинетического уравнения в дрейфовом приближении вычисляются выражения для плотности потоков частиц и энергии поперек сильного магнитного поля в случае аксиально-симметричных систем типа "Левитрона" или "Токамака". При этом, помимо продольного ускоряющего электрического поля, ответственного за создание продольного тока, учитывается также наличие квазистатического электрического поля, направленного по малому радиусу и возникающего вследствие амбиполярности диффузии. Рассмотрены как случай очень малых частот соударений, меньших характерной частоты азимутального движения запертых частиц, так и случай промежуточных и высоких частот соударений. Показано, что если величина тепловой скорости частиц, либо величина отношения полоидального магнитного поля к продольному достаточно велики, так,что средняя продольная скорость тороидально запертых частиц много меньше величины азимутальных вариаций продольной скорости, то учет радиального электрического поля соответствует учету в выражениях для потоков поправок следующего более высокого (а именно четвертого) порядка по используемому параметру малости. В обратном же предельном случае учет радиального электрического поля становится весьма существенным. Так, в области очень малых и очень больших частот соударений он приводит к существенному изменению функциональной зависимости коэффициентов диффузии и теплопроводности от параметров плазмы и магнитного поля, а в области промежуточных частот столкновений к поправкам, пропорциональным квадрату отношения ларморовского радиуса в полоидальном магнитном поле к характерному размеру неоднородности плазмы. В заключение обсуждается вопрос об определении самосогласованного радиального электрического поля в рамках теории, учитывающей лишь наинизший порядок по ларморовскому радиусу.

ВВЕДЕНИЕ

В последние годы появилось большое количество работ, посвященных исследованию различных вопросов теории процессов переноса поперек сильного магнитного поля в тороидальных системах. Однако в подавляющей части этих работ рассматривался случай, когда параметры системы таковы, что возникающее в квазистационарном режиме диффузии самосогласованное электрическое поле практически не оказывает влияния на характер движения отдельных частиц, а его эквипотенциали совпадают с магнитными поверхностями. Кроме того, до сих пор оставался открытым вопрос об определении самосогласованного радиального поля, возникающего в плазме, ибо для полностью ионизованной плазмы в наинизшем порядке по ларморовскому радиусу (то-есть по $1/B$) условие амбиполярности диффузии выполняется автоматически и, следовательно, не может служить уравнением для его определения.

Целью данной работы является восполнение указанных пробелов, т.е. получение выражения для потоков частиц и энергии с учетом как возможных отклонений эквипотенциалей от магнитных поверхностей, так и радиального электрического поля, а также выведение уравнения, позволяющего определить величину этого поля, ограничиваясь при решении кинетического уравнения первым приближением по тороидальности и ларморовскому радиусу. При этом мы ограничимся случаем аксиально-симметричных магнитных ловушек и достаточно малых частот соударений, когда уравнения гидродинамики становятся неприменимыми.

1. ПОСТАНОВКА ЗАДАЧИ И УРАВНЕНИЕ ДЛЯ ПРОДОЛЬНОЙ СКОРОСТИ

Итак, рассмотрим аксиально-симметричные магнитные ловушки, характеризуемые продольной $B_\zeta = B_0/1+(r/R)\cos\varphi$ и азимутальной (полоидальной) B_φ компонентами магнитного поля и предположим, что отношение $\theta = B_\varphi/B_\zeta$ много меньше единицы и не зависит от малого азимута φ[1]. Допустим далее, что в системе присутствует продольное вихревое электрическое поле $E_\zeta = E_0/(1+r/R\cos\varphi)$, вызывающее продольный ток и ответственное за создание стабилизирующего поля B_φ, и "собственное" электростатическое поле, созданное самой плазмой и характеризуемое потенциалом:

$$\Phi(r,\varphi) = \Phi_0(r) + \Phi_c(r)\cos\varphi + \Phi_s(r)\sin\varphi \tag{1}$$

который мы будем предполагать для определенности состоящим только из нулевой и первой $\Phi_{c,s}$ гармоник, причем амплитуду первой гармоники мы будем считать достаточно малой, так что отношение $|e_j\Phi_{c,s}|T_j \ll 1$ (T_j – температура частиц j-ого сорта).

Следует указать, что в рамках рассматриваемой здесь квазистационарной теории существуют два совершенно различных по своей природе механизма, приводящих к появлению азимутальных вариаций потенциала. Первый механизм связан с возникающим в результате тороидальности отклонением системы от симметрии по малому азимуту φ. Амплитуда

---

1 Для удобства мы будем использовать здесь точно те же обозначения, что и в предыдущих работах [1,2].

этих, так сказать, равновесных отклонений пропорциональна ларморовскому радиусу и величине тороидального отношения $\delta = r/R$ и может быть последовательно вычислена в рамках рассматриваемой здесь теории из условия квазинейтральности для поправок $\tilde{N}_j$ к плотности N_j : $\sum_j e_j \tilde{N}_j = 0$ (подробнее см. [1]). Вторая причина появления азимутальных вариаций потенциала – плазменные колебания. Высокочастотные колебания, частота (Ω) которых существенно превышает частоту столкновений, не могут непосредственно привести к увеличению диффузии или теплопроводности, хотя в случае турбулентности они и могут вызвать увеличение эффективных частот соударений. Однако достаточно низкочастотные колебания, частота которых много меньше как частот соударений, так и характерных частот азимутального движения запертых частиц, могут, очевидно, рассматриваться как квазистатические и, следовательно, могут быть достаточно последовательно учтены в рамках рассматриваемой теории [1,3] . При этом амплитуда вариаций потенциала рассматривается как заданная величина (определенная, например, из эксперимента).

Будем исходить из дрейфового кинетического уравнения:

$$\frac{\partial F_j}{\partial f} + \dot{r}\frac{\partial F_j}{\partial r} + \dot{\varphi}\frac{\partial F_j}{\partial \varphi} + \dot{u}\frac{\partial F_j}{\partial u} + \dot{w}\frac{\partial F_j}{\partial w} = St_j \tag{2}$$

где u и w – продольная и поперечная по отношению к магнитному полю компоненты скорости, St_j – интеграл столкновений, точка означает полную производную по времени, а индекс $j = e,i$ указывает, к какому сорту частиц (электронам или ионам) относится соответствующая величина. Умножая это уравнение на $h^2 u$, где $h = 1 + \delta\cos\varphi$, усредняя по φ и интегрируя по скоростям, легко находим[2]:

$$\begin{aligned}\frac{\partial \overline{h^2\langle uF_j\rangle}^{\varphi}}{\partial f} &= w_j\, \overline{\theta h\langle \dot{r}F_j\rangle}^{\varphi} + \overline{h^2\langle uSt_j\rangle}^{\varphi}\\ &+ \overline{\frac{e_j E_\zeta h^2}{m_j}\langle F_j\rangle}^{\varphi} - \frac{1}{r}\frac{\partial}{\partial r}\, \overline{rh^2\langle u\dot{r}F_j\rangle}^{\varphi}\end{aligned} \tag{3}$$

где угловые скобки означают операцию интегрирования в пространстве скоростей, так что, например, $\langle F_j\rangle$ есть плотность, $\langle uF_j\rangle$ – продольный, а $\langle \dot{r}F_j\rangle$ – радиальный потоки частиц и т.д., а черта с индексом φ – усреднение по азимуту φ. При получении (3) мы пренебрегли для простоты величинами порядка $\theta^2 \ll 1$ и электрическим дрейфом частиц $\theta E_\zeta/B_\zeta$, связанным с вихревым электрическим полем, по сравнению с тороидальным дрейфом, что соответствует, в частности, пренебрежению скоростью сжатия плазмы в результате обычного пинч-эффекта по сравнению со скоростью ее диффузионного движения.

Поскольку скорость радиального дрейфа $\dot{r}$ – величина первого порядка малости по тороидальности $\delta = r/R$ и по $1/B$ (то-есть ларморовскому радиусу), то для нахождения потоков частиц и энергии в первом неисчезающем приближении функцию распределения достаточно найти также лишь в первом порядке по δ и $1/B$. В соответствии с этим мы можем прене-

2 Впервые это соотношение было получено в работе [1], где оно было использовано для доказательства амбиполярности диффузии полностью ионизованной плазмы в наинизшем по ларморовскому радиусу приближении.

бречь в кинетическом уравнении зависимостью всех величин от времени и поправками к азимутальному движению, связанными с тороидальным дрейфом, а в уравнении для электронов – и поправками, связанными с электрическим дрейфом[3]. Если, кроме того, предположить, что вихревое поле E_ζ достаточно мало, так, что убегающие электроны отсутствуют, а энергия, приобретаемая в нем запертыми частицами, много меньше тепловой, то после перехода от переменных u и w к переменным $\mu = w^2/2B$ и $E = [(u^2 + w^2)/2] + [(e_j \Phi/m_j)]$ уравнение (2) можно записать в виде:

$$\frac{u}{rw_j}\frac{\partial hu}{\partial \varphi}\frac{\partial F_j}{\partial r} + (\theta u - v_E)\frac{1}{r}\frac{\partial F_j}{\partial \varphi} = \frac{e_j E_\zeta u}{T_j} F_j^M + St_j \tag{4}$$

где

$$w_j = \frac{e_j B_0}{m_j}; \qquad u = \sqrt{2E - \frac{2e_j\Phi}{m_j} - 2\mu B}; \qquad B \simeq B_\zeta$$

$$V_E = -\frac{1}{B_0}\frac{\partial \Phi_0}{\partial r}; \qquad F_j^M = \frac{N_j}{(2\pi v_j^2)^{3/2}} \exp - \frac{E - e_j\Phi/m_j}{v_j^2}$$

$v_j = \sqrt{T_j/m_j}$ – средняя тепловая скорость, а N_j – плотность частиц. При этом в уравнении для функции распределения электронов ($j = e$) мы будем пренебрегать также электрическим дрейфом V_E по сравнению с θu.

Это уравнение будет служить нам в качестве исходного для нахождения усредненных по магнитной поверхности радиальных потоков частиц S_j и энергии Π_j.

Нетрудно убедиться, что при $V_E \ll \theta v_j$ в наинизшем порядке по ларморовскому радиусу, т.е. в том же приближении, когда справедливо уравнение (4), соотношение (3) принимает вид:

$$w_j \theta S_j = -\overline{h^2\langle uSt_j\rangle}^{\varphi} - \overline{\frac{e_j E_\zeta h^2}{m_j} N_j}^{\varphi} \tag{5}$$

С другой стороны, поскольку интеграл столкновений St_j удовлетворяет закону сохранения импульса, т.е. в отсутствии нейтралов

$$\sum_j m_j \langle uSt_j\rangle \equiv 0 \tag{6}$$

то из (5) сразу же следует, что для полностью ионизированной плазмы в силу условия квазинейтральности $\sum_j e_j N_j = 0$ условие амбиполярности диффузии

$$\sum_j e_j S_j = 0 \tag{7}$$

выполняется тождественно. Иными словами, оно является непосредственным следствием исходного уравнения (4) и, следовательно, не может служить уравнением для определения радиального электрического поля $E_r = -\partial\Phi_0/\partial r$, возникающего в плазме.

Разрешение этой трудности можно искать в двух направлениях. Во-первых, можно было бы ожидать, что при переходе от рассматриваемо-

[3] Как правило, неравенство $\theta v_e \gg E_r/B_0$ выполняется всегда с большим запасом. Для ионов же это далеко не всегда так.

го нами первого приближения (по $1/B$) к более точному решению кинетического уравнения (2) возникает зависимость потоков от электрического поля, либо от его производных, и тогда условие квазинейтральности (7) приобретает более глубокое содержание, перестав быть тривиальным следствием исходного уравнения. Этот путь, однако, весьма сложен и требует, в частности, учета зависимости всех величин от времени, либо наложения дополнительных и, вообще говоря, искусственных условий стационарности [4].

Второй, и на наш взгляд более последовательный путь, ведущий к разрешению указанной трудности, заключается в использовании уравнения (3).

Действительно, умножая (3) на m_j, суммируя по j, используя условие амбиполярности (7) и пренебрегая малыми величинами порядка δ^2 и $(m_e/m_i)^{1/2}$, находим:

$$\frac{\partial N_i U_0}{\partial t} = - \nu_{i0} N_i U_0 - \frac{1}{r} \frac{\partial}{\partial r} r P \tag{8}$$

где $U_0 = \sum_j m_j \langle uF_j \rangle / \sum_j m_j \langle F_j \rangle$ – средняя "гидродинамическая" скорость плазмы,

$$P = \overline{h^2 \langle u\dot{r}F_j \rangle}^{\varphi} \tag{9}$$

а ν_{io} – частота столкновений ионов с нейтралами, которую в дальнейшем мы будем считать малой по сравнению с эффективной частотой ион-ионных столкновений[4].

Интересно отметить, что в рассматриваемом здесь случае слабосоударительной плазмы и не очень малых полоидальных полей, когда отношение $V_E / \theta v_j \ll 1$, величина P оказывается весьма просто связанной с диффузионным потоком ионов, а именно:

$$P = \frac{V_E}{\theta} S_i \tag{10}$$

Поскольку, как мы увидим ниже (см., впрочем, [2]), величина скорости U_0 оказывается однозначно связанной со скоростью азимутального электрического дрейфа V_E, то уравнение (8) можно рассматривать как недостающее нам уравнение для радиального электрического поля E_r.

При этом, поскольку $\dot{r}$ – величина первого порядка малости как по $1/B$, так и по тороидальности δ, то для вычисления входящей в уравнение (8) величины P функцию распределения достаточно определить также лишь в первом порядке по $1/B$ и тороидальности δ, т.е. как раз в том же приближении, что и для нахождения интересующих нас потоков S_j и Π_j[5]. Существенно, однако, что поскольку уравнение (8) справедливо в более высоком приближении, чем кинетическое уравнение (4), то даже в этом наинизшем приближении уравнение (8) будет нести в себе дополнительную информацию и, таким образом, позволит получить недостающее нам уравнение, не прибегая к более точному решению кинетического уравнения.

4 Для вывода же уравнения (8) этого условия, очевидно, не требуется.

5 Следует отметить, что, поскольку в силу амбиполярности обычно $S_i \ll \Pi_i T_i^{-1}$, то в ряде случаев к величине P, определенной согласно (10), следует добавить слагаемые более высокого порядка по тороидальности.

Физический смысл уравнения (8) весьма прост: оно выражает закон сохранения импульса плазмы при наличии диффузионных потерь частиц и указывает, в частности, на появление в процессе диффузии у всей плазмы компоненты скорости вдоль силовых линий магнитного поля. В режиме слабосоударительной плазмы наличие такого "ускорения" легко понять, если учесть, что основной вклад в диффузионные потери делают в этом случае "запертые" или "почти запертые" частицы, обладающие при наличии радиального электрического поля отличной от нуля средней продольной скоростью $U \sim V_E/\theta$ и, вследствие этого, непрерывно уносящие из плазмы определенный импульс; скорость такого "выноса" импульса из плазмы как раз и определяется последним слагаемым в правой части (8). Следует указать, что впервые на этот эффект было обращено внимание в работе [5] (см. также [6]), где были приведены экспериментальные данные, указывающие на наличие у плазмы продольной скорости, природа которой, по всей видимости, связана с рассмотренным выше механизмом "ускорения".

Обратимся теперь к нахождению потоков частиц S_j и энергии Π_j, радиального электрического поля E_r и продольной скорости плазмы U_0. При этом мы будем исходить из уравнения (4), интеграл столкновений St_j возьмем в форме, приведенной и использованной в работах [1,2], и ограничимся случаем сравнительно малых частот соударений, удовлетворяющих условиям:

$$r\nu_j^{eff} \ll \theta v_j \tag{11}$$

где

$$\nu_e^{eff} = \frac{4\sqrt{2\pi}}{3}\,\frac{e_e^2 e_i^2 N_i \lambda}{m_e^{1/2} T_e^{3/2}} \qquad \nu_i^{eff} = \frac{4\sqrt{\pi}}{3}\,\frac{e_i^4 N_i \lambda}{m_i^{1/2} T_i^{3/2}} \tag{12}$$

— эффективные частоты электрон-ионных и ион-ионных столкновений, используемые в обычной гидродинамике. Кроме того, мы будем считать, что отношение $m_e\nu_e^{eff}/m_i\nu_i^{eff} \ll 1$, а полоидальное поле B_φ не слишком мало, так что:

$$\left(\frac{r}{R}\right)^{1/2} \theta v_i \ll V_E \ll \left(\frac{r}{R}\right)^{1/2} \theta v_e \tag{13}$$

и в соответствии с этим будем пренебрегать в кинетическом уравнении (4) для электронов скоростью V_E по сравнению с θU.

Учитывая, что процедура решения уравнения (4) довольно стандартна (см., например, [1,2]), и не имея здесь возможности останавливаться на ней сколько-нибудь подробно, мы ограничимся ниже простым перечнем окончательных выражений, справедливых в тех или иных предельных случаях, и их кратким обсуждением.

2. ВЫРАЖЕНИЯ ДЛЯ ПОТОКОВ ЧАСТИЦ И ЭНЕРГИИ И УРАВНЕНИЕ ДЛЯ ЭЛЕКТРИЧЕСКОГО ПОЛЯ

А. Приведем вначале выражения для электронных потоков. Если отклонения эквипотенциалей от магнитных поверхностей достаточно малы, так что

$$V_e = |e_e|\,\frac{(\Phi_c^2 + \Phi_s^2)^{1/2}}{T_e} \ll \frac{r}{R} \tag{14}$$

и частота соударений удовлетворяет условию

$$r\nu_e^{eff} \ll \left(\frac{r}{R}\right)^{3/2} \theta v_e \tag{15}$$

то выражения для потоков имеют вид[6]:

$$S_e = -2{,}1 \cdot N_e\left(\frac{r}{R}\right)^{1/2} \frac{E_\zeta}{B_\varphi}$$

$$-2{,}1\,\nu_e^{eff} N_e\left(\frac{r}{R}\right)^{1/2} \frac{\rho_e^2}{\theta^2}\left\{\frac{\partial \ln N_e T_e^{-0{,}38}}{\partial r} + \frac{w_e\theta}{v_e^2}\left[U_0 - \frac{V_E}{\theta}\right]\right\} \tag{16}$$

$$\Pi_e = 1{,}1 \cdot S_e T_e - 2{,}1 N_e T_e\left(\frac{r}{R}\right)^{1/2} \frac{E_\zeta}{B_\varphi}$$

$$-2{,}4\,\nu_e^{eff} N_e T_e\left(\frac{r}{R}\right)^{1/2} \frac{\rho_e^2}{\theta^2} \frac{\partial \ln T_e}{\partial r} \tag{17}$$

где $\rho_j = v_j/w_j$ – ларморовский радиус частицы. В области промежуточных частот соударений, когда

$$\left(\frac{r}{R}\right)^{3/2} \theta v_e \ll r\nu_e^{eff} \ll \theta v_e \tag{18}$$

но условие (14) по-прежнему выполняется, находим:

$$S_e = -3{,}4 \cdot N_e\left(\frac{r}{R}\right)^2 \frac{|\theta| v_e}{r\,\nu_e^{eff}} \frac{E_\zeta}{B_\varphi}$$

$$-1{,}25\,\frac{|\theta| v_e}{r} N_e\left(\frac{r}{R}\right)^2 \frac{\rho_e^2}{\theta^2}\left\{\frac{\partial \ln N_e T_e^{1{,}5}}{\partial r} + \frac{w_e\theta}{v_e^2}\left[U_0 - \frac{V_E}{\theta}\right]\right\} \tag{19}$$

$$\Pi_e = 3 S_e T_e - 4{,}1 \cdot N_e T_e\left(\frac{r}{R}\right)^2 \frac{|\theta| v_e}{r\nu_e^{eff}} \frac{E_\zeta}{B_\varphi}$$

$$-3{,}75\,\frac{|\theta| v_e}{r} N_e T_e\left(\frac{r}{R}\right)^2 \frac{\rho_e^2}{\theta^2} \frac{\partial \ln T_e}{\partial r} \tag{20}$$

Если же вариации электростатического потенциала достаточно велики, т.е.:

$$V_e \gg \frac{r}{R} \tag{21}$$

то определяющую роль играет не тороидальный, а электрический дрейф и формулы (15)-(20) принимают вид:

$$S_e = -2{,}2 \cdot N_e V_e^{1/2} \frac{E_\zeta}{B_\varphi}$$

$$-3{,}8 \cdot \nu_e^{eff} N_e V_e^{1/2} \frac{\rho_e^2}{\theta^2}\left\{\frac{\partial \ln N_e T_e^{-0{,}9}}{\partial r} + \frac{w_e\theta}{v_e^2}\left[U_0 - \frac{V_E}{\theta}\right]\right\} \tag{22}$$

---

[6] Некоторое отличие приведенных здесь численных коэффициентов от соответствующих коэффициентов работы [2] связано с тем, что мы здесь использовали точные выражения для частот соударений, тогда как в работе [2] предполагалось, что $\nu_{jj} \sim 1/v^3$.

$$\Pi_e = 0{,}62 \cdot S_e T_e - N_e T_e V_e^{1/2} \frac{E_\zeta}{B_\varphi}$$

$$- 2{,}2 \cdot \nu_e^{eff} N_e T_e V_e^{1/2} \frac{\rho_e^2}{\theta^2} \frac{\partial \ln T_e}{\partial r} \qquad (23)$$

при $r\nu_e^{eff} \ll V_e^{3/2}\, \theta v_e$, и

$$S_e = - 0{,}62 N_e V_e^2 \frac{|\theta| v_e}{r\nu_e^{eff}} \frac{E_\zeta}{B_\varphi}$$

$$- 0{,}62 \frac{|\theta| v_e}{r} N_e V_e^2 \frac{\rho_e^2}{\theta^2} \left\{ \frac{\partial \ln N_e T_e^{-0{,}5}}{\partial r} + \frac{w_e \theta}{v_e^2} \left[U_0 - \frac{V_E}{\theta} \right] \right\} \qquad (24)$$

$$\Pi_e = 2 S_e T_e - 0{,}94\, N_e T_e V_e^2 \frac{|\theta| v_e}{r\nu_e^{eff}} \frac{E_\zeta}{B_\varphi}$$

$$- 1{,}25 \frac{|\theta| v_e}{r} N_e T_e V_e^2 \frac{\rho_e^2}{\theta^2} \frac{\partial \ln T_e}{\partial r} \qquad (25)$$

при $V_e^{3/2}\, \theta v_e \ll r\nu_e^{eff} \ll \theta v_e$.

Приведем, наконец, выражение для переменной по азимуту части плотности заряда $\tilde{q}_e$, связанной с электронами, которое понадобится нам для вычисления равновесных отклонений потенциала (то-есть не связанных с низкочастотными плазменными колебаниями). Оно оказывается единым для всех рассмотренных выше случаев:

$$\tilde{q}_e = - \frac{e_e^2 N_e}{T_e} \left[\Phi_c \cos\varphi + \Phi_s \sin\varphi \right] \qquad (26)$$

Условие же, при котором низкочастотные колебания с частотой Ω можно считать для электронов квазистатистическими, имеет вид:

$$\Omega \ll \nu_e^{eff} \qquad (27)$$

Б. Обратимся теперь к ионным потокам. Число предельных случаев здесь оказывается в два раза большим, поскольку отношение $V_E / \theta v_i$ может быть как много меньше, так и много больше единицы.

Остановимся вначале на наиболее практически интересном случае достаточно больших полоидальных полей, когда отношение:

$$V_E / \theta v_i \ll 1 \qquad (28)$$

При этом выражение для переменной части плотности заряда имеет вид, полностью аналогичный (26), а именно:

$$\tilde{q}_i = - \frac{e_i^2 N_i}{T_i} \left[\Phi_c \cos\varphi + \Phi_s \sin\varphi \right]$$

и из условия квазинейтральности $\tilde{q}_e + \tilde{q}_i = 0$ следует, что равновесные отклонения потенциала в рассматриваемом приближении равны нулю. Иначе говоря, в случае, когда выполняется условие (28), под V_j следует понимать вариации потенциала, связанные лишь с низкочастотными колебаниями. Для ионов их следует учитывать лишь при:

$$\Omega \ll \nu_i^{eff} \tag{29}$$

Если же частота колебаний $\Omega \gg \nu_e^{eff}$, то, как уже отмечалось выше, они не дают непосредственного вклада в потоки и можно считать, что $V_j = 0$. При $\nu_e^{eff} \gg \Omega \gg \nu_i^{eff}$ вариации потенциала следует учитывать лишь в выражениях для электронных потоков, а при $\Omega \ll \nu_i^{eff}$ – также и в выражениях для ионных потоков.

Пусть вариации потенциала достаточно малы, так что

$$V_i = e_i \frac{(\Phi_c^2 + \Phi_s^2)^{1/2}}{T_i} \ll \frac{r}{R} \tag{30}$$

Тогда в области малых частот соударений, когда

$$r\nu_i^{eff} \ll \left(\frac{r}{R}\right)^{3/2} \theta v_i \tag{31}$$

выражения для плотности потоков ионов S_i и из энергии Π_i имеют вид:

$$S_i = -0{,}17\,\nu_i^{eff}\Lambda N_i\left(\frac{r}{R}\right)^{1/2}\frac{\rho_i^2}{\theta^2}\left\{\frac{\partial \ln N_i T_i^{-0{,}15}}{\partial r} + \frac{w_i\theta}{v_i^2}\left[U_0 - \frac{V_E}{\theta}\right]\right\} \tag{32}$$

$$\Pi_i = -0{,}24\,\nu_i^{eff}\Lambda N_i T_i\left(\frac{r}{R}\right)^{1/2}\frac{\rho_i^2}{\theta^2}\left\{\frac{\partial \ln N_i T_i^{0{,}75}}{\partial r} + \frac{w_i\theta}{v_i^2}\left[U_0 - \frac{V_E}{\theta}\right]\right\} \tag{33}$$

где

$$\Lambda = \ln\left\{\frac{32|\theta|v_i}{r\nu_i^{eff}}\max\left[\left(\frac{r}{R}\right)^{3/2},\ V_i^{3/2}\right]\right\} \tag{34}$$

Если же в плазме присутствуют низкочастотные колебания, удовлетворяющие условию (29), причем амплитуда их настолько велика, что

$$V_i \gg \frac{r}{R} \tag{35}$$

то в области низких частот соударений

$$r\nu_i^{eff} \ll V_i^{3/2}\,\theta v_i \tag{36}$$

формулы для ионных потоков принимают вид:

$$S_i = -0{,}20\,\nu_i^{eff}\Lambda N_i V_i^{1/2}\frac{\rho_i^2}{\theta^2}\left\{\frac{\partial \ln N_i T_i^{-0{,}6}}{\partial r} + \frac{w_i\theta}{v_i^2}\left[U_0 - \frac{V_E}{\theta}\right]\right\} \tag{37}$$

$$\Pi_i = -0{,}34\,\nu_i^{eff}\Lambda N_i T_i V_i^{1/2}\frac{\rho_i^2}{\theta^2}\left\{\frac{\partial \ln N_i T_i^{0{,}3}}{\partial r} + \frac{w_i\theta}{v_i}\left[U_0 - \frac{V_E}{\theta}\right]\right\} \tag{38}$$

Если же полоидальное поле B_φ настолько велико, что $V_E \ll \left(\frac{r}{R}\right)^{1/2} \theta v_i$, т.е. и для ионов электрический дрейф не существенен, то коэффициенты $0{,}17\Lambda$; $0{,}24\Lambda$; $0{,}20\Lambda$ и $0{,}34\Lambda$ в формулах (32), (33), (37) и (38) надо заменить на 1; 1,4; 1,2; и 2, соответственно.

В области промежуточных частот соударений, когда

$$\left(\frac{r}{R}\right)^{3/2} \theta v_i \ll r\nu_i^{eff} \ll \theta v_i \quad \text{при} \quad r/R \gg V_i$$
$$V_i^{3/2} \; \theta v_i \ll r\nu_i^{eff} \ll \theta v_i \quad \text{при} \quad r/R \gg V_i \tag{39}$$

выражения для ионных потоков будут определяться формулами (19),(20) при $r/R > V_i$ и (24),(25) при $r/R < V_i$, в которых индекс "е" следует заменить на индекс "i". При этом в силу неравенства $m_e\nu_e^{eff} \ll m_i\nu_i^{eff}$ так же, как это было сделано при выводе формул (32)-(38), слагаемым, пропорциональным E_ζ/B_φ, описывающим сжатие под действием вихревого электрического поля, следует пренебречь по сравнению с остальными.

В. Обратимся теперь к выводу уравнения для электрического поля E_r. Как уже отмечалось, во всех рассмотренных выше случаях входящая в уравнение (8) величина P оказывается связанной с соответствующим потоком ионов соотношением (10).

Что же касается величины продольной скорости плазмы U_0 и, в частности, ее связи с радиальным электрическим полем, то она, в принципе, может быть найдена с помощью решения кинетического уравнения (4). Этот путь, однако, приводит к сложным и довольно громоздким вычислениям. Проще поступить иначе. Действительно, если вспомнить, что при $V_E/\theta \ll v_i$ равенство (5), а следовательно и амбиполярность диффузии, является непосредственным следствием уравнения (4), то связь между продольной скоростью U_0 и параметрами плазмы можно найти просто из условия амбиполярности (7) или, поскольку ионный коэффициент диффузии ионов, как правило, значительно превышает коэффициент диффузии электронов, из условия равенства нулю соответствующего ионного потока S_i. Подставляя теперь найденное для U_0 выражение в уравнение (8) и учитывая соотношение (10), получаем окончательно уравнение, определяющее изменение радиального электрического поля E_r (или V_E) со временем[7]. В качестве примера рассмотрим случай, когда эквипотенциали совпадают с магнитными поверхностями (то-есть $V_j \ll r/R$), а частоты столкновений ν_j^{eff} удовлетворяют условиям (15) и (31). Пренебрегая малыми величинами порядка $(m_e/m_i)^{1/2}$ по сравнению с единицей, из условия амбиполярности (7) находим:

$$U_0 = \frac{V_E}{\theta} - \frac{v_i^2}{w_i\theta}\,\frac{\partial \ln N_i T_i^{-0,15}}{\partial r} \tag{40}$$

С другой стороны, предполагая для простоты, что величина V_E/θ не зависит от радиуса r, и учитывая, что $S_e = S_i$, $a(\partial N_i/\partial t) = -(1/r)/(\partial/\partial r) r S_i$ из уравнения (8) находим:

$$\frac{\partial U_0}{\partial t} + \nu_{io} U_0 = \left[\frac{v_i^2}{\theta w_i}\,\frac{\partial \ln N_i T_i^{-0,15}}{\partial r}\right]\frac{\partial \ln N_i}{\partial t} \tag{41}$$

[7] Не следует, однако, забывать, что это уравнение будет справедливо лишь до тех пор, пока скорость $U_0 < v_i$. Это связано с тем, что использованная нами запись интеграла столкновений справедлива также лишь при $U_0 < v_i$.

Это уравнение и определяет нам искомую зависимость U_0, а следовательно, и E_r от времени и параметров плазмы. Из него, в частности, следует, что если $\frac{\partial \ln N_i T_i^{-0,15}}{\theta \partial r} \ll 0$, то скорость плазмы U_0 монотонно возрастает со временем, а радиальное электрическое поле вначале отрицательно (если при $t = 0$, $U_0 = 0$), а затем переходит через ноль и становится положительным.

Аналогичные уравнения могут быть получены и для других рассмотренных выше случаев.

Г. Рассмотрим, наконец, случай малых полоидальных полей B_φ, когда отношение:

$$z = V_E/\theta v_i \gg 1 \tag{41'}$$

В этом случае, как показывают расчеты, область параметров, где основной вклад дают "запертые" или "почти запертые" частицы, практически отсутствует, и потоки частиц и энергии целиком определяются пролетными частицами с продольными скоростями $U \lesssim v_i \ll V_E/\theta$.[8] При этом, как мы увидим ниже, величина $(1/r)/(\partial/\partial r) rP$ оказывается, вообще говоря, того же порядка малости, что и слагаемое $w_i \theta S_i$, а следовательно, условие амбиполярности (7) перестает быть следствием исходного кинетического уравнения (4) и, таким образом, позволяет нам определить радиальное электрическое поле $E_r = B_0 V_E$. В соответствии с этим в наинизшем по $\theta v_i/V_E$ приближении потоки оказываются не зависящими от продольной скорости; величина же этой скорости по-прежнему будет определяться уравнением (8).

Итак, при выполнении неравенства (41)' и произвольном соотношении между r/R и V_i находим для потоков частиц S_i и энергии Π_i следующие выражения[9]:

$$S_i = -0{,}2\nu_i^{eff} N_i \left(\frac{r}{R}\right)^2 \frac{v_i^2}{V_E^2} \rho_i^2 \left\{\frac{\partial \ln N_i T_i^{0,75}}{\partial r} - \frac{w_i V_E}{v_i^2}\right\} \tag{42}$$

$$\Pi_i = \frac{e_i \Phi_c R}{r} S_i - 0{,}45\nu_i^{eff} N_i T_i \left(\frac{r}{R}\right)^2 \frac{v_i}{V_E^2} \rho_i^2 \left\{\frac{\partial \ln N_i T_i^{1,4}}{\partial r} - \frac{w_i V_E}{v_i^2}\right\} \tag{43}$$

Переменная по азимуту φ часть плотности электрического заряда при этом имеет вид:

$$\begin{aligned} \tilde{q}_i &= \frac{2 r e_i N_i v_i^2}{R w_i V_E} \left[\frac{\partial \ln N_i T_i}{\partial r} - \frac{w_i V_E}{v_i^2}\right] \cos\varphi \\ &- \frac{e_i^2 N_i}{T_i} \frac{v_i^2}{w_i V_E} \frac{\partial \ln N_i}{\partial r} \left[\Phi_c \cos\varphi + \Phi_s \sin\varphi\right] \end{aligned} \tag{44}$$

[8] Так, например, в области, где выполняется условие (31), запертые частицы дают определяющий вклад лишь при значениях z, удовлетворяющих неравенству: $\delta^{3/2} z \ll \exp - z^2/2$ область же "плато" существует только, если $\delta z^4 \ll 1$.

[9] Заметим, между прочим, что формулы (42)-(44) справедливы во всей области частот соударений $r\nu_i^{eff} \ll V_E$.

а входящая в уравнение (8) величина P оказывается быстро убывающей функцией V_E и равна (при $V_i = 0$, $U_0 < v_i^2 \theta / V_E$)

$$P \simeq 3 \frac{\theta v_i^2}{V_E} \Pi_i T_i^{-1} \tag{45}$$

При не очень больших значениях $(V_E / \theta v_i)^2 \ll (m_i / m_e)^{1/2}$ из условия амбиполярности следует, что:

$$V_E = \frac{v_i^2}{w_i} \frac{\partial \ln N_i T_i^{0,75}}{\partial r} \tag{46}$$

и, следовательно, слагаемое $w_i \theta S_i$, входящее в уравнение (3), имеет тот же порядок, что и $(1/r)(\partial/\partial r) rP$.

Используя, наконец, формулы (26) и (44) и условие квазинейтральности $\tilde{q}_e + \tilde{q}_i = 0$, находим для амплитуд равновесных отклонений потенциала следующие выражения $\Phi_s = 0$:

$$e_i \Phi_c = -2 \frac{r}{R} \frac{e_i}{e_e} T_e \frac{1 - \dfrac{v_i^2}{w_i V_E} \dfrac{\partial \ln N_i T_i}{\partial r}}{1 - \dfrac{v_e^2}{w_e V_E} \dfrac{\partial \ln N_i}{\partial r}} \tag{47}$$

Отсюда следует, что в отсутствии градиента ионной температуры равновесные отклонения потенциала равны нулю. Они могут стать значительными лишь в окрестности точки, где:

$$\frac{T_i}{e_i} \frac{\partial \ln N_i T_i^{0,75}}{\partial r} = \frac{T_e}{e_e} \frac{\partial \ln N_i}{\partial r}$$

то-есть лишь в области, где $\partial \ln N_i / \partial \ln T_i < 0$. Такая ситуация, однако, представляется маловероятной.

ЛИТЕРАТУРА

[1] KOVRIZHNYKH, L.M., Transport Processes in Toroidal Magnetic Traps. Internal Report IC/70/86, IC/70/123, Trieste, 1970.

[2] KOVRIZHNYKH, L.M., Transport Processes in Toroidal Magnetic Traps. Internal Report IC/70/124, Trieste, 1970.

[3] КОВРИЖНЫХ, Л.М., Письма ЖЭТФ 13 9 (1971) 513.

[4] ROSENBLUTH, M.N., TAYLOR, I.B., KOVRIZHNYKH, L.M., Ambipolar Diffusion at Low Collision Frequencies. Internal Report IC/70/114, Trieste, 1970.

[5] БЕРЕЖЕЦКИЙ, М.С. и др., Труды IV Европейской конференции по управляемому синтезу, Рим, 1970, стр. 31.

[6] БЕРЕЖЕЦКИЙ, М.С. и др., Труды IV Международной конференции по физике плазмы и управляемому ядерному синтезу, Доклад IAEA-CN-28/H-4, (Мэдисон, США) 1971.

THE IMPORTANCE OF THE TRAPPED-PARTICLE PINCH EFFECT IN TOKAMAK PLASMAS*

A.A. WARE
The University of Texas at Austin, Austin, Texas,
United States of America

Abstract

THE IMPORTANCE OF THE TRAPPED-PARTICLE PINCH EFFECT IN TOKAMAK PLASMAS.

A recent discovery has shown that, in a Tokamak plasma, the conservation of canonical angular momentum requires that all trapped particles drift towards the magnetic axis with veolocity $-cE_\varphi/B_\theta$, which is a factor B_φ^2/B_θ^2 greater than the usual $\vec{E}\times\vec{B}/B^2$ drift. ($\theta$and φ are the angular co-ordinates in the poloidal and toroidal directions, respectively.) The importance of this drift has already been demonstrated in explaining both the good containment in stable Tokamaks and the relaxation oscillations which occur for low q or high density. In this paper, the effect is considered further in relation to the contraction and heating of the plasmas in the Tokamaks T-3 and ST, use being made of the new transport equations of Rosenbluth et al. The pulse length in these experiments is too short for a steady state to be attained and four different phases are distinguished in the heating and compression of the plasma. In particular, it is shown that when β_θ is of order unity, the dominant heating process is compressional heating caused by the trapped-particle pinch effect. An approximate calculation which balances ion thermal conduction with the compressional heating is shown to agree well with the final temperature profile in ST. The plasma in T-3 undergoes less contraction and compressional heating, the prime reason being that the driving force for the compression — the toroidal electric field — is maintained at sufficient strength for compression for a relatively shorter time. The new equations predict a more rapid current penetration, and a case is made that electrostatic trapping will be important in making this penetration even more rapid.

1. INTRODUCTION

The properties of the hot, well-contained plasma obtained in the Russian Tokamak experiment T-3 [1, 2] are now amongst the most widely known experimental results in plasma physics. The attempts [3-5] which were made to explain these properties in terms of the MHD-equations combined with the trapped-particle transport equations of Galeev and Sagdeev [6], although achieving some success, left unexplained several significant, though perhaps not glaring, discrepancies. Among these were the anomalous resistivity of the plasma, the lack of skin effect in the current, the slow contraction of the plasma in minor radius, and the observed equality for the gradients of ln T_e and ln n.

The relaxation oscillations [7] which occur for values of the stability parameter q less than about 3 or for plasma density above a critical value, and which lead to poor plasma containment, represent another discrepancy. These oscillations were mistakenly thought to be caused by the interaction of the plasma with the limiter. It was left to the workers on the Tokamak-type experiment at Canberra [8] to make a detailed study of these oscillations. Among their results [9] was the startling conclusion that the plasma was moving in the direction of the minor radius as if the toroidal component

* Work supported in part by the US Atomic Energy Commission.

of the magnetic field were absent. It was this glaring discrepancy which convinced the author that an MHD-model is a poor description of Tokamak plasmas and led him to the discovery of the trapped-particle pinch effect [10]. (The same effect was discovered independently by Galeev [11].)

The presence of the toroidal electric field (E_ϕ) causes the guiding-centre drifts of the trapped particles to have a non-zero average in the radial direction [10] so that all trapped particles drift towards the magnetic axis with velocity $-cE_\phi/B_\theta$. (The angular co-ordinates θ, ϕ are taken to be in the poloidal and toroidal directions, respectively.) This motion of some of the particles leads to a new term in the radial diffusion equation [11-13] which is an inward diffusion. This pinch effect is capable of balancing the normal outward diffusion driven by the density gradient and helps to explain the plasma contraction and the good particle containment in T-3. It was also shown that many of the detailed properties of the relaxation oscillations could be explained qualitatively in terms of the trapped-particle pinch effect [12].

In this paper this plasma contraction is considered further. Use is made of the new transport equations which have been obtained recently by Rosenbluth, Hazeltine and Hinton [14] (see section 2). It is first reported (section 3) that the steady-state solutions of these equations are a poor description of the plasmas in both T-3 and the more recent Tokamak experiment ST [15]. The reason is that the time constants of the pinching and heating effects are substantially longer than the current pulse in either experiment and a steady state is not attained experimentally.

A qualitative study of the time-dependent behaviour of these plasmas indicates that four heating phases can be distinguished in their evolution (section 4). The most notable feature is the dominance of compressional heating once β_θ becomes comparable with unity ($\beta_\theta = 8\pi p/B_\theta^2$). An approximate calculation balancing compressional heating with ion heat conduction is shown to be in good agreement with the constricted density and temperature profiles observed at the end of the pulse in ST. The smaller amount of contraction observed in T-3 can be explained by the different time dependence of the driving force for the compression, namely, the toroidal electric field.

2. TRANSPORT EQUATIONS

The equations which have been obtained by Rosenbluth, Hazeltine and Hinton [14] for the radial diffusion (Γ), the radial electron and ion heat fluxes (Q_e, Q_i) and the current parallel to $\vec{B}$ in a Tokamak-type plasma at low collision frequencies (banana regime) are

$$\Gamma \equiv \langle n v_r \rangle = n\left(\frac{r}{R}\right)^{\frac{1}{2}}\left\{\nu_e \rho_e^2 \left[-1{\cdot}12\left(\frac{T_e+T_i}{T_e}\right)\frac{n'}{n} + 0{\cdot}43\,\frac{T_e'}{T_e} + 0{\cdot}19\,\frac{T_i'}{T_e}\right] - 2{\cdot}44\,\frac{cE_\phi}{B_\theta}\right\} \tag{1}$$

$$Q_e = \frac{5}{2}T_e\Gamma + nT_e\left(\frac{r}{R}\right)^{\frac{1}{2}}\left\{\nu_e \rho_e^2\left[+1{\cdot}53\left(\frac{T_e+T_i}{T_e}\right)\frac{n'}{n} - 1{\cdot}81\,\frac{T_e'}{T_e} - 0{\cdot}27\,\frac{T_i'}{T_e}\right] + 1{\cdot}75\,\frac{cE_\phi}{B_\theta}\right\} \tag{2}$$

$$Q_i = \frac{5}{2} T_i \Gamma - 0.68\, n\, \nu_i\, \rho_i^2 \left(\frac{r}{R}\right)^{\frac{1}{2}} T_i' \tag{3}$$

$$\langle j_\| \rangle \simeq \langle j_\phi \rangle = \sigma E_\phi \left[1 - 1.95 \left(\frac{r}{R}\right)^{\frac{1}{2}}\right] + c\left(\frac{r}{R}\right)^{\frac{1}{2}} \left[\frac{-2.44(T_e+T_i)n' - 0.7nT_e' + 0.42n\, T_i'}{B_\theta}\right] \tag{4}$$

where ν_e, ν_i are the electron and ion collision frequencies for momentum transfer, ρ_e, ρ_i the Larmor radii of the electrons and ions in the poloidal field (B_θ), σ the normal parallel electrical conductivity in the absence of trapped-particle effects and r, R are the minor and major radii. The angular brackets $\langle\ \rangle$ denote values averaged with respect to θ. Boltzmann's constant is taken as unity.

2.1. Comments on the transport equations

The inward diffusion associated with the trapped-particle pinch effect is the term proportional to E_ϕ in Eq. (1). A minor criticism is made here of the interpretation of this term by Rutherford et al. [13]. These authors conclude that only a small fraction of this term (proportional to $[(r/R)^{3/2}]$ results directly from the trapped particles and that most of the term is caused by so-called boundary-layer particles. They arrive at this result because they define all particles with $\mu_j > \epsilon_j/B_{max}$ as trapped, where ϵ_j is the particle energy, omitting any potential energy due to E_ϕ. In this case, the part of f_0 associated with these particles makes zero contribution to the diffusion. In fact, because of E_ϕ, there are three groups of particles in this range of μ. Those particles with $\epsilon_{tj}/B_{max} > \mu > \epsilon_j/B_{max}$ and having $v_\|$ of the same sign as $e_j E_\phi$ are passing particles which, in the absence of collisions, undergo no reflections; those in the same range of μ but with opposite sign of $v_\|$ undergo a single reflection and become passing particles in the positive direction (hereafter termed "turning particles") and finally those with $\mu > \epsilon_{tj}/B_{max}$ are the truly trapping particles which undergo multiple reflections in the absence of collisions. ($\epsilon_{tj} = \epsilon - \int_{\pm\pi}^{\theta} e_j E_\phi B r d\theta / B_\theta$ with $\pi > \theta > -\pi$. The positive lower limit is for ions, the negative for electrons.) With the latter definition of trapped particles, the part of f_0 corresponding to trapped particles is now a function of θ and its contribution to the inward diffusion is equal to $-(2\sqrt{2}n[r/R]^{1/2}/\pi)cE_\phi/B_\theta$. This is a substantial fraction of the complete term. The "turning particles" contribute an equal and opposite outward diffusion.

This change in the interpretation of the inward diffusion term is important in considering the possibility of electrostatic particle trapping enhancing the magnetic trapping. The theory of Rosenbluth et al. considers only magnetic trapping, since it assumes that the ion (and electron) Larmor radii in the poloidal field are small and a case is made that this causes the variation of electrostatic potential on a magnetic surface to be small. In fact, the ion Larmor radius is not particularly small in Tokamak experiments. Secondly, the reduction in the effective conductivity of the plasma due to contraction can cause E_ϕ to be an order of magnitude larger than assumed in the ordering of the above theory (see section 4.2).

In the presence of a negative density gradient the inward motion of the trapped particles will create a reduction in their density ($-\delta n_t$) which will be counteracted by collisions creating more trapped particles. Balancing the two effects for ions gives

$$\delta n_{ti} \nu_i = - \frac{cE_\phi}{B_\theta} \left(\frac{2r}{R}\right)^{\frac{1}{2}} \frac{dn}{dr}$$

or $\delta n_{ti}/n \sim cE_\phi/\nu_i B_\theta L_n$. For the plasma in ST with $n = 5 \times 10^{12}$ cm^{-3}, T_e = 800 eV, $L_n \sim 3$ cm and since $cE_\phi/B_\theta \sim 10^3$ cm s^{-1}, the value of $\delta n_{ti}/n$ is of order unity. Since the trapped ions exist over only part of the magnetic surface, a variation in potential of order kT_e/e is required for quasi-neutrality. This in turn means strong electrostatic trapping. (The presence of appreciable electrostatic trapping justifies the use of ν_i in the above estimate of δn_{ti} rather than the scattering collision frequency $R\nu_i/r$.)

The effect of electrostatic trapping will be to increase the proportion of trapped particles and this will increase the numerical coefficients of the terms in the transport equations which contain the factor $(r/R)^{\frac{1}{2}}$. The equation for $j_{||}$ will be particularly sensitive to such an increase and this will be of special importance for the skin effect. A preliminary study of Eq.(4) shows that, for $\beta_\theta \sim 1$, E_ϕ should penetrate several times faster than given by the normal Spitzer conductivity. This factor will become much larger with a moderate increase in the number of trapped particles.

3. STEADY STATE SOLUTIONS

Using the fluxes Γ, Q_e, Q_i and the expression for the transfer of heat between electrons and ions, equations of change giving the time derivatives of n, T_e and T_i can be constructed [14]. Steady-state solutions have been obtained for the complete set of equations, the assumption being made that all the time derivatives are zero. (For time-dependent solutions it is necessary to correct these equations in the vicinity of r = 0, since the banana regime coefficients become infinite as $B_\theta \to 0$ and are not applicable. For steady-state solutions this correction is not important.) The detailed results will be published elsewhere [16]. The solutions show poor agreement with the experimental results of both T-3 and ST. For both systems the predicted electron temperatures are too high, the predicted electric fields are an order of magnitude too small and the temperature and density profiles are much flatter than those observed late in the pulse in ST.

This poor agreement is not too surprising. The time constants for the various processes in the equation for $\partial T_e/\partial t$ are of the order of $\pi\sigma a^2/c^2$. For an electron temperature of 500 eV, this is greater than 10^{-1}s and hence in both T-3 and ST the pulse length is too short for a steady state to be reached. As discussed in the next section, the plasmas in T-3 and ST are time-dependent and far from a steady state.

4. THE PLASMA HEATING IN PRESENT TOKOMAK EXPERIMENTS

4.1. The heating phases

To consider the importance of the different heating processes, the assumption will be made initially that the plasma density is sufficiently high such that $T_e \approx T_i = T$. (For the following order-of-magnitude considerations, the experimental observation showing $T_i \sim T_e/2$ is taken to be consistent with this assumption.) Adding the heat equations for ions and electrons then yields

$$3n\frac{dT}{dt} = -\frac{1}{r}\frac{\partial[r(q_e + q_i + 2T\Gamma)]}{\partial r} + jE \tag{5}$$

where $d/dt \equiv (\partial/\partial t) + (\langle v_r\rangle \partial/\partial r)$ and the heat fluxes have been written in the form $Q = q + 5/2\ T\Gamma$. Here and below, j and E refer to the components j_φ and E_φ.

With the aid of Eqs (1), (2) and (3), it can be shown that the terms in Eq.(5) which arise from the toroidal electric field E are proportional to β_θ, the terms arising from the gradients n', T' are proportional to β_θ^2, whereas the Ohmic heating term is independent of β_θ. From these and other considerations given below, the following four heating phases can be distinguished. (A stable plasma is assumed and heat losses due to radiation and ionizing impurities are neglected.)

PHASE I. $\beta_\theta << 1$, Ohmic heating.

At the beginning of the pulse, the dominant heating process will be Ohmic heating. This would be true even if Eq.(5) were valid since only this heating term is independent of β_θ, but due to T being low, trapped-particle effects will be unimportant and the other terms will be even smaller than given by Eq.(5). (The assumption $T_e \approx T_i$ will be a poor one for this phase because the collisional thermal transfer rate is proportional to β_θ and will be small compared with the Ohmic heating.)

PHASE II, plateau regime - Ohmic and compressional heating

When the temperature exceeds the value for the plateau trapped-particle regime, an extra heating mechanism will come into play involving the inward transport of heat due to the trapped-particle pinch effect. The heat transport equations obtained by Galeev [11] indicate that for temperatures well in the plateau regime the two heating mechanisms are comparable in magnitude.

PHASE III, banana regime and $\beta_\theta \sim 1$, compressional heating dominant

When the temperatures are sufficiently high for the banana regime (see phase IV, below), Eq.(5) will be valid and the following considerations show that when β_θ is comparable with unity, the dominant heating process is compressional heating. This heating comes from the terms proportional to E in $(q_e + q_i + 2T\Gamma)$, the main contribution comes from Γ (i.e., compressional heating), but there is a smaller contribution of opposite sign from q_e.

Considering firstly the central region of the plasma where n and T are close to their maxima and where the gradients are small, the compressional heating is given by

$$W_{\text{compressional}} = 2\pi r\ [3.2\ \frac{cnTE}{B_\theta}\ (r/R)^{\frac{1}{2}}] \tag{6}$$

Since the corresponding Ohmic heating term is $\pi r^2 jE$, the ratio of the two terms is

$$\frac{W_{\text{compressional}}}{W_{\text{Ohmic}}} = \frac{6.4\,nTc}{rj}\left(\frac{r}{R}\right)^{\frac{1}{2}} = 1.6\left(\frac{r}{R}\right)^{\frac{1}{2}}\left(\frac{a^2}{r^2}\right)\beta_{\theta o} \tag{7}$$

where $\beta_{\theta 0} = 8\pi nT/B_{\theta 0}^2$ and $B_{\theta 0}$ is the value that the poloidal field would have at radius a if j were constant over the whole radius. Assuming $\beta_{\theta 0} \sim 1$, the ratio in (7) is large compared with unity for $r \ll a$.

Over the outer regions of the plasma, the dominant part of the compressional heating term is $3.2\,(r/R)^{\frac{1}{2}}(cE/B_\theta)dp/dr$ and since for this region $|dp/dr| \gtrsim \beta_\theta B_\theta^2/8\pi a$ and $j \ll cB_\theta/2\pi a$, the compressional term again has larger magnitude than the Ohmic heating. (Because of the negative sign from dp/dr, the compressional term is a cooling effect for this region.)

From these considerations, it follows that the compressional heating (or cooling) will be the dominant term on the right-hand side of Eq. (5) when β is of order unity. Provided the density is sufficiently high for good energy exchange between ions and electrons (see discussion under phase IV), the main mechanism for energy loss will be ion heat conduction. The net transport of heat (Q) will be inwards for the electrons (the compressional heating term dominating the outward electron thermal conduction) and outwards for the ions.

PHASE IV, electron thermal runaway

The condition that there is good exchange of energy between electrons and ions requires the collisional exchange rate (W_{ei}) to be equal or greater than the electron heating rate. Applying this condition for the central part of the plasma and taking $T_i = T_e/2$ gives

$$\pi r^2\left(\frac{3nm\nu T_e}{2}\right)\sum\frac{n_i Z_i^2}{M_i} \gtrsim 2\pi r\left(0.75\,nT_e\left[\frac{r}{R}\right]^{\frac{1}{2}}\frac{cE}{B_\theta}\right) \qquad (8)$$

where allowance has been made for the presence of high-Z impurities in the plasma. This condition reduces to

$$\alpha^2 \gtrsim \frac{a^2}{r^2} \qquad (9)$$

where α^2 is given by

$$\alpha^2 = \left(\frac{a^2\omega_{pi}^2}{c^2}\right)\frac{\sum n_i Z_i^2\,\frac{M_p}{M_i}}{\sum n_i Z_i^2},$$

$\omega_{pi} = 4\pi n_0 e^2/M_p$, and M_p is the proton mass, n_0 the density at $r = 0$.

For the experiment ST, the value of α^2 is about 5 at the beginning of the pulse (no high-Z impurity) and decreases to between 1 and 2 as the increasing temperature multiply-ionizes the 10% oxygen impurity. Hence, at first sight it would appear that conditions (8) will always be violated for small radii. However, initially, this part of the plasma will not be in the banana regime and the compressional heating will be less than given by the right-hand side of Eq. (8). For T_e = 300 and 1000 eV, the minimum radii for the banana regime are 12 and 2.3 cm, respectively. Since a = 14 cm, condition (9) will be satisfied for $T_e \ll 1000$ eV, but as T_e approaches 1000 eV, condition (9) will be violated. That is, the electrons will be heated more rapidly in the centre than they can transfer heat to the ions. A marked increase in $\partial T_e/\partial t$ will occur for the central region since a large increase in $\partial T_e/\partial r$ is needed to make Q_e positive.

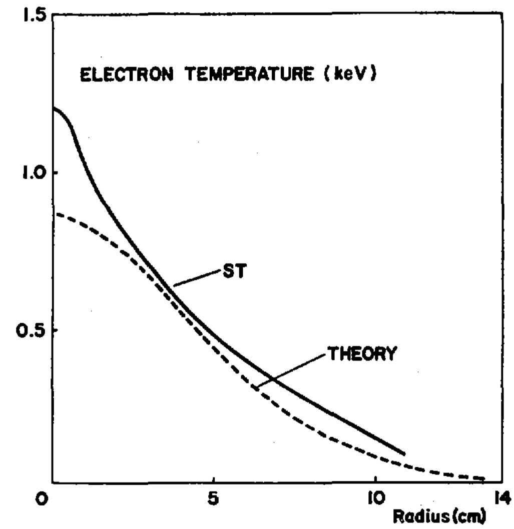

FIG. 1. Comparison between theory and experiment for the final electron temperature profile in ST. The theory balances compressional heating and ion heat conduction.

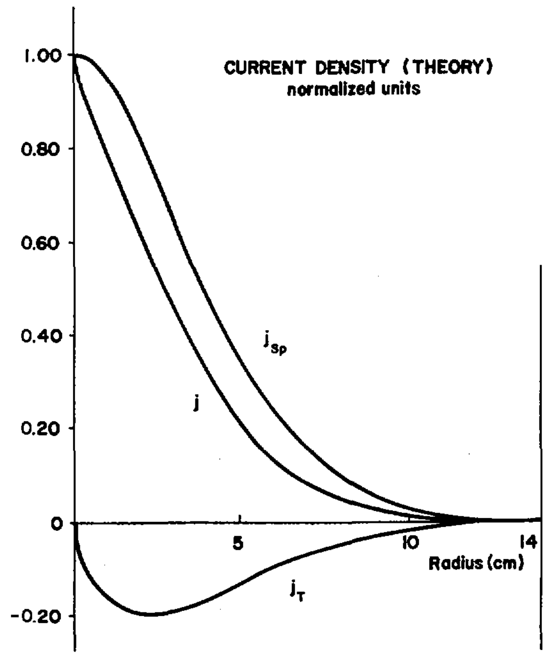

FIG. 2. Current density (j) profile predicted by theory. j_{sp} is the current density calculated from T_e using the Spitzer conductivity and $j_T = j - j_{sp}$.

4.2. Estimate of the maximum temperature in phase III

The correct procedure to compare the predictions of Eqs (1) to (4) with the experimental results is to solve the time-dependent equations. In the meantime, an approximate calculation is presented here which estimates the maximum temperature and the corresponding temperature, density and current profiles which would be caused by the compression in phase III. The following simplifying assumptions are made concerning the instant of maximum temperature:

1. 1. $T_e \simeq T_i = T$

2. $dT/dt = 0$ at all radii. This is an arbitrary assumption; it corresponds to $\partial T/\partial t = 0$ on the axis (maximum temperature) and at other radii the plasma is still moving in ($\Gamma < 0$) but remaining at constant temperatures as it moves.

3. $n'/n = T'/T$. This condition is observed experimentally for the results with T-3 and for the first part of the pulse with ST.

4. Boundary conditions $n = T = 0$ at $r = a$ with n and T finite and greater than zero at all smaller radii.

5. Ohmic heating can be neglected compared with compressional heating.

6. The inductive electric field due to the $\partial B_\theta/\partial t$ arising from the changing current distribution is assumed small compared with the applied electric field E. E is therefore taken constant with respect to radius. This assumption is checked later.

With the assumptions 2 and 5, Eq.(5) reduces to

$$q_e + q_i + 2T\Gamma = 0 \tag{10}$$

and substituting from Eqs (1), (2) and (3), using assumptions 1 and 3, this yields

$$\frac{T'}{T} = -0.19\,\frac{EB_\theta e^2}{\nu_e M\,T} \tag{11}$$

(The value of M/m for hydrogen has been used.)
After corresponding substitution, Eq.(4) for the current yields

$$\frac{c}{4\pi r}\,\frac{d(rB_\theta)}{dr} = j = \sigma E\left(1 - 1.7\left[\frac{r}{R}\right]^{\frac{1}{2}}\right) \tag{12}$$

(The "bootstrap current" is equal to $0.2\,\sigma E[r/R]^{\frac{1}{2}}$ and is small because the good ion thermal conductivity keeps the relative magnitude of the gradients n', T' small.)

If Eqs (11) and (12) are put in dimensionless form, then for fixed aspect ratio, there is a single solution satisfying the boundary conditions 5. Figures 1 and 2 show the solutions for T and j for the case R/a = 7. This solution is characterized by the relations

$$\beta_{\theta e} \equiv \frac{8\pi n_o T_o}{B^2_{\theta a}} = 1.7 \tag{13}$$

and

$$I = \frac{aB_{\theta a}}{2} = 0.082\ \pi a^2 \sigma_o E \tag{14}$$

The scaling for different values of a, E, n_0 or I, but the same aspect ratio, is given by these two equations. (A small change in R/a, for example to 7.8, changes the solutions by only a few percent.)

In Fig. 2, the current density predicted by the Spitzer conductivity (j_{sp}) is also plotted, together with the difference $j_T = j - j_{sp}$, which is the change in j caused by trapped particle effects.

To check assumption 6, a calculation was made using the time dependent transport equations to check the magnitude of the inductive electric field caused by the continuing compression ($\Gamma \neq 0$) at the time of peak temperature. Using the parameters for the ST-results (see section 4.3) it was found that the maximum reduction in E, which occurs at r = 0, was only about 10%. (It was necessary to use a correction factor to modify the transport coefficients near r = 0 because the trapped-particle effects are not in the banana regime there.)

4.3. Comparison with experiment

(a) Tokamak ST.

The electron-temperature profile observed towards the end of the pulse in ST (t = 16 ms) is shown by the solid line in Fig. 1. The broken line shows the solution of Eqs (11) and (12) which has been scaled to give the same current I with the same electric field E. The scaling equation (4) then gives T_0 and (13) yields n_0. This scaling and the values for T_0, n_0 and $\beta_{\theta e}$ are shown in Table I together with the experimental values. An average ion charge of 3 has been used in evaluating T_0 from σ_0.

The agreement theory and experiment is unjustifiably good, bearing in mind the crude approximations involved. Over most of the radius the agreement with T_e is very close. The fact that at small radii the experimental temperature exceeds theory is completely consistent with the plasma having entered heating phase IV. Because the compressional heating produces a temperature close to 1 keV, the heating rate for electrons will exceed the electron-ion transfer rate and the excess spike in T_e must occur. The theoretical density, although very close to experiment on axis, is about a factor 2 too small at larger radii. This order of discrepancy is more in keeping with the crude approximations.

A feature of the highly constricted current profile predicted by theory (Fig. 2) is that although q at r = a has been matched to the experimental value of 6.5, the value predicted for q at r = 0 is 0.54, which is a rotational transform of $\iota = 3.7\pi$. It may be significant that this is close to the value of 4π which was found by Liley et al. [9] to be the rotational transform at r = 0 for the onset of the expansion phase of the relaxation oscillations. A case can be made that this is the lowest rotational transform in such a plasma configuration at which the m = 1 MHD-instability will occur [17]. Such an instability could be the trigger for the expansion phase.

TABLE I. SCALING AND PARAMETER VALUES

Parameter	Experiment	Theory
I	37 kA	Taken as 37 kA
E	6.4×10^{-3} Vcm^{-1}	Taken as 6.4×10^{-3} Vcm^{-1}
T_{e0}	1.2 keV	0.86 keV
n_0	1.35×10^{13} cm^{-3}	1.28×10^{13} cm^{-3}
$\beta_{\theta e}$	2.4	1.7
q at r = a	6.5	6.5
q at r = 0	--	0.54

(b) Tokamak experiment T-3

The degree of plasma contraction which takes place in T-3 is less than in ST for the following two reasons. Firstly, the time constant for contraction ($\sim aB_\theta/cE$) is proportional to a^2 and hence the time constant is $(18/14)^2$ longer than for ST.

The second and more important reason is that the driving force for the compression – the toroidal electric field E – is applied with sufficient strength for only a fraction of the pulse length. In ST, the effect of the external circuit (a constant current source) is to maintain an approximately constant electric field after the initial transient. E changes only from 8.3×10^{-3} Vcm^{-1} at t = 4 ms to 6.3×10^{-3} Vcm^{-1} at 16 ms. In contrast to this, in T-3 the electric field, which is approximately the same after the initial transient, falls linearly with time and passes through zero substantially before the end of the pulse. For I = 70kA, E is 9×10^{-3} Vcm^{-1} at t = 20 ms falls linearly to zero at t = 50 ms [18]. (The current falls by about 50% during this time, but the average inductive electric field caused by the decreasing B_θ between the copper torus and the plasma surface is only about 10^{-3} V.) Since β_θ is comparable with unity, the outward diffusion term due to n' will make Γ positive well before t = 50 ms. Hence the time for the pinch effect to occur is substantially less than 30 ms. (The end of the transient is approximately where the plasma becomes hot enough for the trapped-particle effect to be important, and then only in the plateau region at first.) Also during this period, the average value of Γ will be substantially smaller than for ST because of the decreasing value of E. These effects combined with the longer time constant will cause a smaller contraction in T-3 than in ST.

ACKNOWLEDGEMENTS

The author wishes to thank Professors Rosenbluth and Hinton, and Dr. Hazeltine for permission to use their unpublished transport equations. He is particularly grateful to Professor Macmahon for the computer solution of Eqs (11) and (12),

REFERENCES

[1] ARTSIMOVICH, L.A. et al., in Plasma Physics and Controlled Nuclear Fusion Research (Proc. Conf. Novosibirsk, 1968), IAEA, 1 (Vienna, 1969) 157.
[2] PEACOCK, N.J., ROBINSON, D.C., FORREST, M.J., WILCOCK, P.D., SANNIKOV, V.V., Nature 224 (1969) 488.
[3] DNESTROVSKY, Y.N., KOSTOMAROV, D., International Symposium on Closed Confinement Systems (Dubna, 1969), to be published.
[4] FURTH, H.P., ROSENBLUTH, M.N., RUTHERFORD, P.H., STODIEK, W., Physics Fluids 13 (1970) 3020.
[5] ARTSIMOVICH, L., GLUKHOV, A.V., PETROV, M.P., Soviet Physics JETP Letts 11 (1970) 304.
[6] GALEEV, A.A., SAGDEEV, R.Z., Soviet Physics JETP, 26 (1968) 233.
[7] ARTSIMOVICH, L.A., MIRNOV, S.V., STRELKOV, V.S., Atomnaya Energiya, 17 (1964) 170. For the discovery of these relaxation oscillations, see also GORBUNOV, E.P., RAZUMOVA, K.A., Atomn. Énerg., 15 (1963) 363.
[8] GOLDBERG, R., LILEY, B.S., Vacuum 18 (1968) 631; LILEY, B.S., VANCE, C.F., SMITH, J.M., Proc. Inst. Rad. Electron. Engng (Australia) 29 (1968) 221.
[9] BOWERS, D.L., LILEY, B.S., MORTON, A.H., VANCE, C.F., to be published.
[10] WARE, A.A., Phys. Rev. Letts 25 (1970) 15.
[11] GALEEV, A.A., Zh. éksp teor. Fiz. (USSR) 59 (1970) 1378.
[12] WARE, A.A., Phys. Rev. Letts 25 (1970) 916.
[13] RUTHERFORD, P.H., KOVRIZHNIKH, L.M., ROSENBLUTH, M.N., HINTON, F.L., Phys. Rev. Letts 25 (1970) 1090.
[14] ROSENBLUTH, M.N., HAZELTINE, R., HINTON, F.L., to be published.
[15] GROVE, D.J., et al., Princeton University Report MATT-813, October, 1970.
[16] WARE, A.A., MACMAHON, A.B., to be published.
[17] WARE, A.A., to be published.
[18] MIRNOV, S.V., SEMENOV, I.B., Atomn. Énerg. 30 (1971) 14.

DISCUSSION

TO PAPERS IAEA-CN-28/C-5, C-6

A.A. WARE: I would like to summarize the conclusions of Paper C-6, which are essentially very simple. I conclude that Tokamak plasmas are pinch discharges. Admittedly, the pinching is in slow motion, the radial velocity being of the order of 10^3 cm sec^{-1}, but this slow contraction is large enough both to explain the good containment in Tokamaks and to make compressional heating the dominant heating mechanism once we have $\beta_\theta \sim 1$. If this compressional heating is balanced against the main loss mechanism, namely ion heat conduction, one can predict a temperature profile close to that observed in the Tokamak experiment ST. Lastly, the temperature profile in T-3 is less peaked because, after the plasma has become hot and pinching is important, the driving force for the pinching (E_ϕ) is maintained only a relatively short time at sufficient strength for compression.

G.O.J. von GIERKE: I should like to ask Mr. Ware a question on Paper C-6. The pinching effect is related to the number of trapped particles inside the Tokamak. Would there be any advantage in increasing the number of trapped particles? Would particles trapped in the toroidal field mirrors contribute to the pinching effects?

A.A. WARE: The trapped-particle pinch effect tends to balance the outward diffusion and therefore aids containment. However, increasing the trapped particle pinch effect is not necessarily a good thing: there is experimental evidence that if the pinch effect becomes too strong, it will generate too large a pressure gradient, which leads to an instability and causes a rapid expansion of the plasma. As regards your second question, I was not aware that the variations in the toroidal magnetic field in present experiments were large enough to be important, but such field variations will cause super bananas and hence some enhancement of the outward diffusion.

P.E.M. VANDENPLAS: I notice that Mr. Kovrizhnykh writes the Boltzmann equation for the distribution function in a form which is correct only in Cartesian co-ordinates. Of course, one can always do this in an abstract q_1, q_2, q_3...., Cartesian co-ordinate space, but the distribution function obtained in abstract space must then be transformed into the distribution function valid in curved physical space. If this was not done, some terms would be missing in the fluid equations used.

L.M. KOVRIZHNYKH: Yes. This was in fact done.

EVOLUTION SPATIO-TEMPORELLE D'UN PLASMA SOUMIS A UN COURANT DE DECHARGE

C. MERCIER, SOUBBARAMAYER
Association Euratom-CEA,
CEN, Fontenay-aux-Roses
et
J.P. BOUJOT
CEN, Saclay, France

Abstract — Résumé

THE SPATIAL-TIME EVOLUTION OF A PLASMA SUBMITTED TO A DISCHARGE CURRENT.

The spatial-time evolution of a plasma with a Tokamak-type discharge is described in terms of a two-fluid magnetodynamic model, including the Maxwell equations, mass continuity, equations of motion, and energy balance. The following causes of energy loss are taken into account: thermal conduction, ionization of neutrals and reheating of generated particles, charge exchange and radiations. A choice is allowed for the functional dependence and the amplitudes of the transport coefficients (diffusion, electric resistivity, thermal conductivity) to study the possible effects of impurities, anomalies and instabilities. This model is the subject of a numerical and theoretical study.

In the first part we present the numerical study, carried out on an IBM 360-91 computer and used for testing the possible interpretations of experimental results. Taking neoclassical forms for the transport coefficients, to which an adaptable numerical correction factor was applied, we compared all the measurements made on the Kurchatov T-3 and the Princeton ST with our model calculations. The results for confinement time and electron temperature profiles are discussed and the various mechanisms of energy loss analysed.

The second part is devoted to a theoretical study in a simple case. When the loss through electron thermal conduction is predominant - in the case of certain special functional forms of the coefficient - the stationary problem can be completely intregrated and may lead to zero, to one or to infinite solutions satisfying the particular conditions (given total current, zero temperature and current at the boundary). Numerical experiments performed with our model in these cases indicate the influence of the initial conditions, and of the path followed, on the state actually reached during time evolution.

EVOLUTION SPATIO-TEMPORELLE D'UN PLASMA SOUMIS A UN COURANT DE DECHARGE.

L'évolution spatio-temporelle d'un plasma lors d'une décharge du type Tokamak est décrite par un modèle magnétodynamique à deux fluides incluant les équations de Maxwell, la continuité de masse, les équations de quantité de mouvement et le bilan énergétique. Les causes suivantes de perte d'énergie sont prises en compte: conduction thermique, ionisation des neutres et réchauffement des particules générées, échange de charge et radiations. Un choix est laissé pour les dépendances fonctionnelles et les amplitudes des coefficients de transport (diffusion, résistivité électrique, conductivités thermiques) pour étudier les effets éventuels des impuretés, anomalies et instabilités. Ce modèle fait l'objet d'une double étude, numérique et théorique.

Dans une première partie nous présentons l'étude numérique, faite avec un ordinateur IBM 360-91, et appliquée à tester des interprétations possibles des résultats expérimentaux. En considérant des formes néo-classiques pour les coefficients de transport, affectées d'un coefficient correcteur numérique adaptable, nous avons confronté l'ensemble des mesures sur le T-3 de Kurchatov et sur le ST de Princeton avec les calculs de notre modèle. Les résultats sur le temps de confinement, les profils de température électronique et l'analyse des différents mécanismes de perte d'énergie sont discutés.

Dans une deuxième partie nous faisons une étude théorique dans un cas simple. Quant la perte par conduction thermique électronique est prédominante et pour certaines formes fonctionnelles particulières de ce coefficient, le problème stationnaire s'intègre complètement et peut conduire à zéro, une ou une infinité de solutions satisfaisant aux conditions voulues (courant total donné, température et courant nuls sur le bord). Des expériences numériques faites avec notre modèle dans ces cas montrent l'influence des conditions initiales et du chemin suivi sur l'état effectivement atteint au cours de l'évolution temporelle.

1 . INTRODUCTION.

Nous étudions l'évolution spatio-temporelle d'un plasma soumis à un courant électrique de décharge et stabilisé par un fort champ magnétique longitudinal. Les Tokamaks utilisant ce procédé pour confiner le plasma, notre modèle mathématique peut ainsi simuler les expériences sur ce type de machines et servir soit pour interpréter les expériences déjà faites soit pour faire des calculs d'extrapolation pour les machines futures. La base du modèle est l'ensemble des équations magnétodynamiques à deux fluides (électrons et ions) : équations de Maxwell , équations de continuité de masse, équations de la dynamique et équations de bilan énergétique. Pour une première étude simplifiée, cet ensemble a été ramené à un système de trois équations , en approximation cylindrique, décrivant les diffusions du courant électrique et des chaleurs électroniques et ioniques, sous l'effet des coefficients de transport (résistivité électrique, conductivités thermiques des électrons et des ions), et des sources et puits d'énergie (effet Joule, transfert d'énergie des électrons aux ions par collisions, pertes thermiques de surface etc...). Ce système est complet si l'on se donne les conditions initiales et aux limites ainsi que les trois fonctions coefficients de transport.

Nous avons choisi pour la résistivité électrique l'expression de Spitzer [1] corrigée éventuellement des effets d'impuretés et des électrons découplés et pour la conductivité thermique des ions l'expression néoclassique de Galeev-Sagdeev [2] des particules trappées. Quant à la conductivité thermique des électrons, de nombreux calculs confrontés avec les résultats expérimentaux nous ont amenés à proposer le modèle suivant : on définit deux régimes du plasma, l'un stable et l'autre instable (éventuellement séparés par un régime de transition), et la conductivité thermique des électrons prend <u>deux formes fonctionnelles</u> , que nous précisons, ces deux formes étant <u>différentes suivant le régime</u>. L'appartenance à un régime est déterminée par la valeur du shear du plasma, une forte valeur du shear étant un élément stabilisant.

Des applications de ce modèle sont traitées numériquement avec l'aide d'un ordinateur IBM 360-91. On montre que ce modèle peut expliquer qualitativement et quantitativement les principaux résultats obtenus à ce jour sur le T. 3 de Kurchatov et sur le S.T de Princeton. Une étude analytique approchée confirme l'importance de la dépendance fonctionnelle de la conductivité thermique des électrons.

2. MODELE MATHEMATIQUE

Les équations magnétodynamiques à deux fluides comportent les équations de Maxwell (voir [1] page 24), les équations de continuité de masse, les équations de la dynamique et les équations d'énergie (voir [3] page 214).
Nous ferons les approximations suivantes :

- a) Approximation cylindrique

- b) Les effets de la diffusion des particules sur le bilan d'énergie sont négligés. Cette hypothèse est justifiée par les résultats expérimentaux sur le T.3 montrant que le temps de vie des particules est très supérieur au temps de vie de l'énergie.

- c) La loi d'Ohm généralisée, qui est une combinaison linéaire des deux équations de la dynamique (voir [1] page 22) est simplifiée sous la forme

$$\vec{E} = \eta \vec{J}$$

où $\vec{E}$ est le champ électrique, $\vec{J}$ le courant électrique et η la résistivité.

-d) La source et les pertes d'énergie sont, pour les électrons, le chauffage Ohmique, la perte thermique due à la conductivité et l'énergie transférée aux ions par collisions, tandis que pour les ions elles sont respectivement l'énergie reçue des électrons et la perte thermique. Les autres termes de pertes (impuretés, radiations, ionisations, échange de charge avec les neutres etc...) sont pris en compte très grossièrement.

On est alors ramené à un système de trois équations :

$$(1) \quad \begin{cases} \dfrac{\partial J}{\partial t} - \dfrac{1}{4\pi}\dfrac{1}{\rho}\dfrac{\partial}{\partial \rho}\left[\rho \dfrac{\partial}{\partial \rho}(\eta J)\right] = 0 \\[2ex] \dfrac{3}{2} kn \dfrac{\partial T_e}{\partial T} - \dfrac{1}{\rho}\dfrac{\partial}{\partial \rho}\left(\rho k_e \dfrac{\partial T_e}{\partial \rho}\right) - \eta J^2 + \alpha (T_e - T_i) = 0 \\[2ex] \dfrac{3}{2} kn \dfrac{\partial T_i}{\partial t} - \dfrac{1}{\rho}\dfrac{\partial}{\partial \rho}\left(\rho k_i \dfrac{\partial T_i}{\partial \rho}\right) - \alpha (T_e - T_i) = 0 \end{cases}$$

Dans ce système la signification des notations est la suivante :

- ρ, t coordonnées radiale et temporelle
- J Densité du courant électrique
- T_e, T_i Températures électronique et ionique
- η Résistivité électrique
- k_e, k_i Conductivités thermiques électronique et ionique
- α Coefficient de transfert d'énergie des électrons aux ions par collisions.
- k Constante de Boltzmann.
- n Densité des électrons (égale à la densité des ions).
- ηJ^2 est le terme source Ohmique. Dans les calculs numériques du paragraphe suivant, nous considérerons $\eta J^2 (1-\lambda)$ avec $0<\lambda<1$, pour tenir compte grossièrement des autres termes de perte d'énergie.

Les conditions initiales et aux limites sont :

$$(2)\quad \begin{cases} t=0 & J, T_e, T_i \text{ donnés} \\ \rho=0 & \dfrac{\partial}{\partial\rho}=0 \\ \rho=a & T_e=T_i=0;\ \displaystyle\int_0^a 2\pi J\rho\, d\rho = I\,(t) \\ & \\ \multicolumn{2}{l}{a \text{ rayon du plasma (donné)}} \\ \multicolumn{2}{l}{I\,(t) \text{ profil du courant de décharge (donné)}} \end{cases}$$

Notre modèle de base est constitué par les équations (1) et (2), où il faut encore se donner les fonctions n, α, η, k_e et k_i . D'aprés l'approximation (b) nous ne tiendrons pas compte des variations de la densité électronique en fonction du temps et nous supposerons

$$n = n\ (\rho)$$

$n(\rho)$ étant une fonction donnée. Par exemple, on peut considérer pour $n(\rho)$ le profil mesuré. L'expression du coefficient α de transfert d'énergie électron-ion est classique (voir [3] page 217). Pour la résistivité électrique, nous considérons l'expression de Spitzer (voir [1] page 92) corrigée par un facteur γ_1 d'impureté et un facteur γ_2 d'électrons découplés.

$$(3)\qquad \eta = \eta_{SPITZER} \times \gamma_1 \times \gamma_2 \qquad \eta_{SPITZER} = \eta_0\, T_e^{-3/2}$$

on peut par exemple prendre pour γ_1 une constante et pour γ_2 le coefficient d'anomalie mesuré sur T. 3 [4]. La conductivité thermique des ions, d'après les résultats expérimentaux, est bien représentée par l'expression néo-classique de Galeev-Sagdeev [2]. Il reste donc à fixer la conductivité thermique K_e des électrons. On sait que les expressions classiques ou néo-classiques ne suffisent pas pour expliquer les résultats expérimentaux. De nombreux calculs nous amènent à proposer le modèle suivant :

Nous envisageons deux régimes de plasma, l'un stable et l'autre turbulent et nous supposons que la conductivité thermique K_e prend deux formes fonctionnelles K_1 et K_2 différentes suivant le régime. Soit θ le shear moyen de la région périphérique du plasma. On sait qu'une grande valeur du shear est un élément de stabilisation vis-à-vis de quelques types d'instabilités. Désignons par θ_{crit} une certaine valeur critique du shear et posons

$$(4)\qquad \begin{cases} k_e = k_1 & \text{pour} \quad \theta < \theta_{crit} \\ k_e = k_2 & \text{pour} \quad \theta \geqslant \theta_{crit} \end{cases}$$

Ce schéma revient à dire que la stabilité de tout le plasma, y compris la région près de l'axe, est conditionnée par la valeur du shear au bord du plasma c'est à dire par l'état du plasma au bord. Une justification de ce schéma serait la suivante. Il est probable que les instabilités qui dominent quand $\theta < \theta_{crit}$ sont liées au gradient de densité. Or le profil de densité dans les régimes stables est très plat. Dès que le critère n'est plus vérifié sur la périphérie, l'instabilité agit aussi sur le coefficient de diffusion des particules et la densité devient rapidement moins plate, ce qui entraine la propagation de la turbulence vers les régions centrales, le shear n'étant pas en général suffisant vers le milieu de la décharge pour stabiliser ces modes. Inversement quand une décharge turbulente atteint un régime où $\theta \gg \theta_{crit}$ sur la périphérie, la stabilisation locale améliore peu à peu le profil de densité et après un régime plus ou moins long de transition, la décharge se trouve entièrement dans le régime stable. L'ordre de grandeur du θ_{crit} nécessaire est en bon accord avec la formule théorique [5] que nous écrirons sous la forme :

$$\frac{\theta_{crit}}{\rho} = \left(\frac{m_e}{m_i} \frac{2\,\nu_{ei}}{a_i\, V_{thi}} \frac{\rho}{n} \frac{dn}{d\rho} \right)^{1/2} \tag{5}$$

Cette expression montre bien l'influence de la forme du profil de densité sur la stabilité. Si $n = n_0 (1 - \rho^p)$, on stabilise le centre du plasma avec $p \gg 4$ et on déstabilise pour $p < 4$

Le choix de K_1 et K_2 est plus délicat. Si nous écrivons la dépendance fonctionnelle de K vis à vis de la température sous la forme T^α, les nombreux essais numériques que nous avons faits montrent que

$\alpha < 0$ de l'ordre de $(-\frac{1}{2})$ pour K_1

$\alpha > 0$ de l'ordre de $(+\frac{3}{2})$ pour K_2, les expérience étant en général dans la zone 'plateau' de Galeev.

Nous avons donc choisi pour K_2 (et les expériences numériques que nous décrivons par la suite semblent confirmer ce choix)

$$K_2 = K_{2,0}\; K_{e,GS}$$

où $K_{2,0}$ est une constante et $K_{e,GS}$ est l'expression de Galeev-Sagdeev [2]. Il faut noter que J.C. ADAM et al. [6] donnent pour K_e, quand toutes les instabilités sensibles au shear sont stabilisées.

$$K_e \simeq \varepsilon^{-3/4}\; K_{e,GS} \tag{6}$$

où ε est le rapport d'aspect.

Pour K_1, région turbulente, nous avons choisi la forme la plus classique de Pfirsch et Schlüter [7] multipliée par un coefficient ajusté empiriquement (la dépendance en température de l'expression de Pfirsch et Schlüter est justement en $T^{-1/2}$).

$$K_1 = K_{1,0} \, K_{PS}$$

($K_{1,0}$ constante, K_{PS} expression de Pfirsch et Schlüter). L'expression (4) devient donc finalement :

$$(7) \quad \begin{cases} K_e = K_{1,0} \, (kn) \, \varepsilon^2 \, \nu_e \, r_\Phi^2 & \text{pour } \theta < \theta_{crit} \\ K_e = K_{2,0} \, K_{e,GS} & \text{pour } \theta \geq \theta_{crit} \end{cases}$$

où $\varepsilon = \frac{\rho}{R}$ est le rapport d'aspect local, ν_e la fréquence de collision des électrons, r_Φ le rayon de Larmor de l'électron dans le champ poloïdal B_Φ. Nous rappelons que $K_{1,0}$ et $K_{2,0}$ sont deux constantes ajustées empiriquement et que $K_{e,GS}$ est l'expression de Galeev-Sagdev.

3. APPLICATIONS NUMERIQUES

Le modèle ci-dessus exposé a été traité numériquement sur un ordinateur IBM 360-91 (voir appendice). Le début d'une décharge correspond en général à un shear faible donc à ce que nous avons défini comme régime instable. Par la suite quand le courant de décharge augmente, le courant pénétre, le plasma se chauffe et le shear croit. Trois cas peuvent alors se présenter.

PREMIER CAS : Décharge au cours de laquelle le shear dépasse la valeur critique.

Du régime instable, le plasma, après une éventuelle zone de transition, passe au régime stable. Ce cas correspond aux décharges classiques sur le T.3. Nous avons traité la décharge sur T.3 (voir [4, a]) correspondant à :

$$B_0 = 17 \text{ kG} \quad I = 60 \text{ kA} \quad \tilde{n} = 10^{13}$$

Nous avons ajusté les coefficients $K_{1,0}$ $K_{2,0}$ et θ_{crit} aux résultats des mesures et nous avons trouvé

$$(8) \quad K_{1,0} = 5000. \quad K_{2,0} = 30 \quad \theta_{crit} = 5 \times 10^{-2}$$

Il faut noter que l'ordre de grandeur de cette dernière valeur est en bon accord avec l'expression (5). Les résultats des calculs sont présentés sur la figure 1. La température électronique évolue vers un profil stationnaire plat du type donné par Robinson en $(1 - \rho^4)$. Ce dernier résultat qualitatif est valable pour toute décharge où le shear dépasse la valeur critique et où le plasma entre et reste en régime stable, indépendamment des valeurs numériques de $K_{1,0}$, $K_{2,0}$ et θ_{crit}. C'est un résultat dû essentiellement à la forme fonctionnelle de K_e pour $\theta \gtrsim \theta_{crit}$.

Les résultats stationnaires ne seront cependant physiquement atteints que si en période transitoire le plasma ne passe par aucun état prohibitif. Nous avons représenté sur la figure 2 les calculs de l'évolution de la self-inductance ℓ_i et du coefficient de stabilité q sur l'axe pour la décharge ci-dessus et pour la même décharge avec une densité du plasma dix fois plus forte($\tilde{n} = 10^{14}$). Si cette évolution ne présente aucune particularité pour la faible densité $\tilde{n} = 10^{13}$, il n'en est plus de même pour le cas de la densité forte. En effet dans ce cas ($\tilde{n} = 10^{14}$) un régime stationnaire du même type que

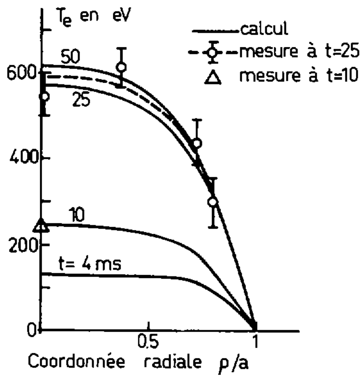

FIG.1. Calcul de l'évolution de la température électronique lors d'une décharge typique sur T.3.

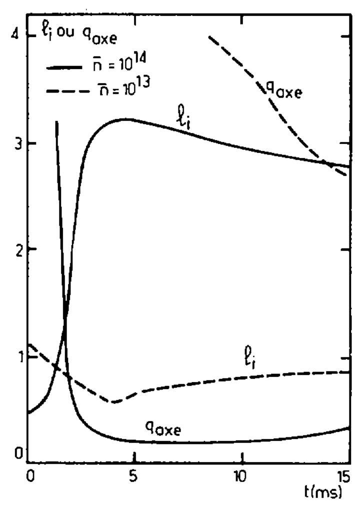

FIG.2. Calcul de l'évolution de ℓ_i et de q_{axe} lors d'une décharge sur T.3 pour deux valeurs de densité.

précédemment est bien atteint au bout de 120 millisecondes, mais dans les premières millisecondes la self-inductance passe par de fortes valeurs (de l'ordre de 3) et le coefficient q sur l'axe passe par des valeurs inférieures à 1 Ceci peut entrainer un déplacement important Δ du plasma vers la paroi, des instabilités M.H.D. (la limite de Kruskal n'étant plus respectée dans la région centrale du plasma), des instabilités d'électrons découplés etc.

Ce résultat peut expliquer la limitation en densité constatée expérimentalement dans les Tokamaks pour un champs magnétique et un courant donnés. Cette limitation serait alors due au régime transitoire conduisant à des états violemment anormaux qui empêchent l'évolution normale de la décharge. Notons que le seuil d'apparition des régimes de courant très piqués dépend de la densité d'une façon très critique.

DEUXIEME CAS : Décharge au cours de laquelle le shear ne dépasse pas la valeur critique.

Le plasma reste en régime instable tout au long de la décharge. Ce cas correspond aux décharges sur le Tokamak S.T de Princeton [8].
Nous avons traité ce cas

$$B_o = 27\,KG \qquad I = 35\,KA \qquad \tilde{n} = 10^{13}$$

avec les mêmes valeurs des coefficients $K_{1,0}$ $K_{2,0}$ et θ_{crit} que précédemment dans l'expression (8). Les résultats des calculs sont présentés sur la figure 3 . Le plasma reste effectivement constamment dans la région instable, le shear au bord ne dépassant jamais la valeur 5.10^{-2}.
La température électronique ne tend pas vers un état stationnaire et évolue en se piquant de plus en plus vers l'axe. Ce résultat est dû à la forme fonctionnelle de K_e pour $\theta < \theta_{crit}$
Il peut paraître surprenant a priori que le shear soit plus faible pour la décharge sur le S.T que sur le T.3. Une des raisons est que le rapport $\frac{\varepsilon}{q}$ (θ est en effet proportionnel à $\frac{\varepsilon}{q}$) pour la décharge S.T est environ deux fois plus faible.

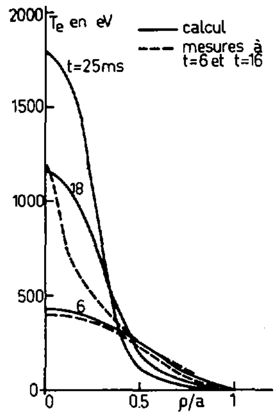

FIG.3. Calcul de l'évolution de la température électronique lors d'une décharge sur le S.T.

Nous avons traité un exemple numérique de décharge S.T. avec les mêmes valeurs que précédemment pour ε, I, $\tilde{n}$ mais $B_o \simeq 10$ kG et cette fois les calculs donnent bien des résultats pour T_e du même type que dans T.3. Ce résultat est cependant sujet à réserve du fait que nous n'avons pas tenu compte de la dépendance du θ_{crit} en fonction du champ B_o. Par ailleurs il reste encore à étudier l'influence de la forme du profil du courant de décharge sur la possibilité de stabiliser le plasma.

<u>TROISIEME CAS : Décharge au cours de laquelle le shear traverse plusieurs fois la valeur critique.</u>

C'est le cas de la décharge Mirnov [9] au cours de laquelle il y a successivement pour le courant une montée, un plateau, une descente, une deuxième montée et enfin une descente. Le plasma peut alors passer du régime instable au régime stable, se destabiliser de nouveau pour ensuite se restabiliser etc.

Mirnov a en effet constaté qu'au cours de la deuxième montée du courant, l'énergie du plasma décroissait d'un facteur important. Nous avons traité la décharge de Mirnov (correspondant à la figure 4 de [9]) et les résultats des calculs sont présentés sur la <u>figure 4</u>. On retrouve l'ordre de grandeur de la chute d'énergie et des valeurs de ℓ_i. Ce résultat a déjà été signalé dans [10] avec une théorie à un fluide.

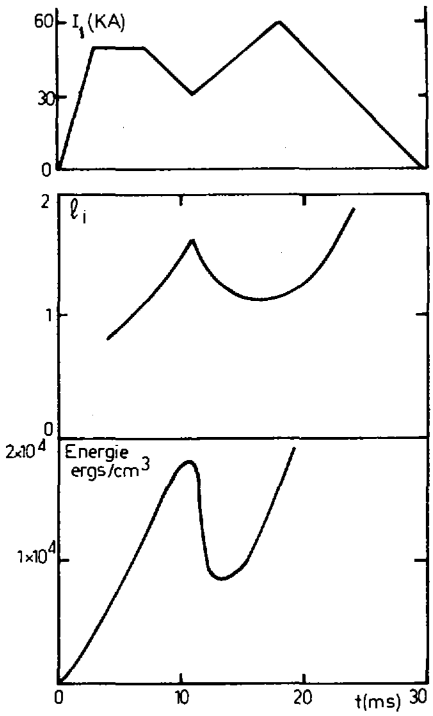

FIG.4. Calcul de l'évolution de l'énergie et de la self-inductance lors d'une décharge du type Mirnov.

EXTRAPOLATION POUR LE TOKAMAK DE FONTENAY

Avec notre modèle, nous avons fait les calculs d'extrapolation pour le Tokamak de Fontenay dont les caractéristiques sont :

Rayon du diaphragme : 20 cm
Rayon du tore : 98 cm
Champ magnétique : 60 kG
Intensité du courant de décharge : 400 kA
Durée maximum de décharge : 500 ms.

Deux valeurs de densité ont été considérées et on trouve les valeurs suivantesà t = 100 millisecondes.

	$\tilde{n} = 3,5 \cdot 10^{13}$	10^{14}
Température électronique moyenne	1600 eV	750 eV
Température ionique moyenne	900 eV	680 eV
β poloïdal	0,22	0,35
Temps de confinement τ_E	150 ms	75 ms
Self inductance ℓ_i	0,61	0,8

Les valeurs asymptotiques de ℓ_i (pour t $\sim$ 500ms) sont proches de 0,9 mais les autres grandeurs ne varient que légèrement.

4. ETUDE ANALYTIQUE DE L'INFLUENCE DES FORMES FONCTIONNELLES DES COEFFICIENTS DE TRANSPORT.

Nous avons constaté dans les résultats numériques la très forte influence de la forme fonctionnelle des coefficients de transport sur les régimes transitoires et asymptotiques des décharges de type Tokamak. Il est intéressant pour la suite du travail de comprendre analytiquement ces comportements variés du plasma.

Nous n'étudierons ici succinctement que l'état asymptotique de la décharge avec un modèle très simplifié mais qui a l'avantage de montrer simplement les complexités des résultats possibles.

Nous étudierons le système suivant, en supposant encore que $\tau_n >> \tau_E$

$$(9) \quad \begin{cases} -\dfrac{1}{\rho}\dfrac{\partial \rho}{\partial \rho}\rho K_e \dfrac{\partial}{\partial \rho} T_e = \eta j^2 - \alpha (T_e - T_i) \\ -\dfrac{1}{\rho}\dfrac{\partial}{\partial \rho}\rho K_i \dfrac{\partial}{\partial \rho} T_i = \alpha (T_e - T_i) \\ E_o = \eta j \end{cases}$$

Eo étant constant. Le rayon du plasma sera pris égal à l'unité,
Soit I le courant longitudinal

Posons $g = \frac{2\pi}{I}\int_0^\rho j\rho\, d\rho$ et $x = \rho^2$

Le système devient par intégration, en supposant $\rho\, K_{\substack{e\\i}} \frac{\partial}{\partial \rho} T_{\substack{e\\i}} \Big|_{\rho=0} = 0$

$$- \qquad 2x\, K_e \frac{\partial}{\partial x} T_e = \frac{E_o I}{2\pi}\, g - \frac{1}{2}\int_0^x \alpha\,(T_e - T_i)\, dx$$

$$- \qquad 2x\, K_i \frac{\partial}{\partial x} T_i = \frac{1}{2}\int_0^x \alpha\,(T_e - T_i)\, dx$$

$$E_o = \frac{I}{\pi}\,\eta\,\frac{dg}{dx}$$

Le terme $\int_0^x \alpha\,(T_e - T_i)\, dx$ représentant le terme de perte d'énergie des électrons par passage aux ions, étant en réalité faible devant la perte directe par diffusion, nous ferons les simplifications et hypothèses suivantes :

$$s = \frac{T_i}{T_e} = \text{constante}$$

$$\eta = \eta_o T_e^{-3/2}$$

$$\alpha = \alpha_o\, n^2\, T_e^{-3/2} = \alpha_o\, n_o^2\; T^{+1/2} \quad [\text{en supposant } n = n_o T]$$

D'où

$$\int_0^x \alpha\, T_e\, dx = \alpha_o\, n_o^2 \int_0^x T^{3/2}\, dx$$

$$g = \frac{2\ E_o}{I}\int_0^\rho \frac{\rho}{\eta}\, d\rho = \frac{n\, E_o}{I\,\eta_o}\int_0^\rho T^{3/2}\, dx = \frac{n\, E_o}{I\eta_o \alpha_o n_o^2}\int_0^x \alpha T_e\, dx$$

Le système à étudier devient :

$$K_e\, x\, \frac{dT_e}{dx} = -\frac{1}{4\pi}\left[E_o - (1-s)\,\frac{\eta_o\,\alpha_o\, n_o^2}{E_o}\right] I \cdot g$$

$$\frac{dg}{dx} = \frac{\pi E_o}{I\,\eta_o}\, T^n \qquad\qquad (n = \tfrac{3}{2}\ \text{classiquement})$$

Les diverses expressions données pour K sont du type (1): $K = f(x) T^{\alpha} g^{\beta}$ par exemple :

$K_{Spitzer} \sim n T^{-1/2}$

K (Pfirsch et Schlüter, Galeev-Sagdeev région particule trappée) $\sim x^2 n^2 T^{-1/2} g^{-2}$

K (Galeev-Sagdeev région plateau) $\sim x\, n\, T^{3/2} g^{-1}$

Ou plus généralement du type (2): $K = f(x)\, T^{\alpha} g^{\beta} \left(\frac{d}{dx}\left(\frac{g}{x}\right)\right)^{\gamma} \left(\frac{dT}{dx}\right)^{S}$

si on veut tenir compte du "shear" et du gradient de température (voir expression des coefficients K en turbulence).

f (x) peut dépendre de I et de B, champ magnétique principal.

La solution asymptotique que nous cherchons est pour un courant I appliqué donné. Cette solution doit vérifier les conditions suivantes :

Pour $x = 1$ – $g = 1$ $T_e = 0$

Pour $x = 0$ $g \sim x$ et T_e fini.

Pour la forme K de type (1) , le système s'écrit : $(\alpha + 1 \neq 0)$

$$\frac{d\mathcal{T}}{dx} = \mu(x)\, g^{p} \qquad \frac{dg}{dx} = \lambda\, \mathcal{T}^{q}$$

$$\mathcal{T} = T_e^{\alpha+1} \qquad p = 1 - \beta \qquad q = \frac{n}{1+\alpha}$$

$$\lambda = \frac{\pi E_o}{I\, \eta_o} \qquad \mu(x) = -\frac{1+\alpha}{4\pi}\, I \left[E_o - \frac{(1-S)\,\eta_o \alpha_o n_o^2}{E_o}\right] \frac{1}{x f(x)}$$

$$= \frac{-\mu_o(1+\alpha)}{x\, f(x)}$$

Ce système selon les paramètres et la forme de μ peut pour un I donné avoir :

Une solution (ou un nombre discret de solutions). A chaque I, correspond un (ou un nombre discret) de E_o.

Pas de solution.

Une infinité de solutions.

Dans ce cas, à un courant I donnée, correspond une infinité de profils de température $T(\rho)$, à chaque profil correspond un E_o. Nous dirons que nous avons affaire à un spectre continu. (E_o jouant le rôle de valeur propre dans ce problème non linéaire).

Donnons un exemple très simple $K = f(x)T^{\alpha} g$ avec (hypothèse physique) $x f(x) > 0$ et pouvant tendre vers 0 pour $x \longrightarrow 1$

Si $\boxed{\alpha + 1 > 0}$

$$\mathcal{T} = (1+\alpha)\,\mu_0 \int_x^1 \frac{dx}{x f(x)}$$

en supposant $\frac{1}{x f(x)}$ intégrable pour $x \to 1$

$$g = \lambda \int_0^1 \left[(1+\alpha)\,\mu_0 \int_x^1 \frac{dx}{x f(x)} \right]^q dx$$

La condition aux limites impose une condition

$$1 = \lambda \left[(1+\alpha)\,\mu_0 \right]^q \int_0^1 \left[\int_x^1 \frac{dx}{x f(x)} \right]^q dx$$

qui détermine une ou plusieurs valeurs de E_0 pour un I_0 donné -spectre discret

Si $\boxed{\alpha + 1 < 0}$

$$T_e = \left[\mathcal{T}_0 - \mu_0 (1+\alpha) \int_0^x \frac{dx}{x f(x)} \right]^{\frac{1}{1+\alpha}}$$

Il faut et il suffit pour satisfaire les conditions aux limites de T_e à $x = 1$ que $x\, f(x) \longrightarrow 0$ tel que $\int_0^x \frac{dx}{x f(x)} \longrightarrow +\infty$

La condition $g = 1$ à $x = 1$ déterminera $\mathcal{T}_0$ pour chaque I_0 et E_0 donné. Le spectre sera continu.

Si $\boxed{\alpha + 1 = 0}$ $\quad T_e = T_{e_0}\, e^{-\mu_0 \int_0^x \frac{dx}{x f(x)}}$

La condition $g = 1$ à $x = 1$ s'écrit :

$$1 = (\lambda T_{e_0}^n) \int_0^1 \exp\left[-n\,\mu_0 \int_0^x \frac{dx}{x f(x)} \right] dx$$

qui détermine Te_0 pour chaque I_0 et E_0 donnés. Spectre continu

L'étude du type 2 est plus complexe. Cependant si

$$k = k_0 \frac{T^{\alpha} (g/x)^{\beta} (dT/dx)^{\delta}}{\left(\frac{\partial}{\partial x} \frac{g}{x} \right)^{1+\delta}}$$

on obtient : si $\frac{\alpha}{\delta+1} + 1 \leq 0$ pas de solution

si $\frac{\alpha}{\delta+1} + 1 > 0$ la solution s'écrit :

$$T = \left[\frac{2+\alpha+\delta}{2-\beta+\delta} \left(-\frac{\mu_0}{K_0} \right)^{\frac{1}{\delta+1}} \left(v^{\frac{2-\beta+\delta}{1+\delta}} - 1 \right) \right]^{\frac{\delta+1}{\alpha+\delta+1}} = T(v)$$

$$\operatorname{Log} x = \int_1^v \frac{dv}{\lambda T^n(v) - v}$$

Le spectre est continu, En effet si pour un couple (E_o I_o) donné, on trouve une valeur υ_0 telle que :

$$\lambda T^n(\upsilon_0) - \upsilon_0 = 0$$

la condition pour x = 0 est vérifiée. Elle sera donc en général aussi vérifiée pour (I_o, $E_o + \delta E_o$) pour une valeur proche de υ_0.

Notons un cas particulièrement simple :

Si $k = \dfrac{k_0 T^{\alpha}\left(\frac{g}{x}\right)\left(\frac{dT}{dx}\right)^{\delta}}{\left(\frac{\partial}{\partial x}\ \frac{g}{x}\right)^{\alpha/n-1}}$ on trouve $\dfrac{j}{<j>} = \dfrac{1+\omega}{\omega}\left(1-\rho^{2\omega}\right)$

$I_o = \pi a^2 <j>$ et $\omega = \omega(E_o)$.

5. CONCLUSION

Le programme numérique élaboré pour le système (1) et (2) laisse une certaine souplesse pour les coefficients de transport. On peut introduire toute fonction donnée pour la résistivité électrique et les conductivités thermiques.

Nous avons montré ici que l'ensemble des résultats expérimentaux actuels peut s'expliquer avec un seul schéma simple de conductivité thermique, à savoir l'existence de deux régimes du plasma (un stable et un autre instable) liés au **shear**. Il faut noter que même quand le shear est élevé, la conductivité thermique est plus élevée d'un ordre de grandeur que les théories néoclassiques de Galeev- Sagdeev ne le prévoient. Il serait intéressant de vérifier la dépendance fonctionnelle de θ_{crit} et de K_1. Les résultats connus des expériences actuelles ne sont encore pas suffisants pour conclure.

Il faut enfin signaler que notre modèle est en cours d'amélioration pour tenir mieux compte des autres termes de perte, des effets d'impuretés, de la diffusion des particules et de l'évolution initiale du plasma.

RÉFÉRENCES

[1] SPITZER, L., Physique des gaz complètement ionisés, DUNOD - Paris (1959).

[2] GALEEV, A.A., SAGDEEV, R.Z. - Transport phenomena in a collisionless plasma in a toroidal magnetic system. Soviet Physics JETP 26 1 (1968) 233-240.

[3] BRAGINSKII, S.I., Transport process in a plasma, Reviews of plasma physics, Vol. 1, Consultants Bureau, New-York (1965).

[4] ROBINSON, D.C. and al.
- a) Measurements of the electron temperature by Thomson scattering in Tokamak T.3, Nature 224 Nov. (1969) 488-490.
- b) Measurements of the plasma parameters in Tokamak T.3 - A by Thomson scattering - CLM - R. 107 Culham (1970).

[5] LAVAL, G., PELLAT, R., COPPI, B. Convective modes driven by density gradients. Nuclear Fusion 6 (1966) 261-267.

[6] ADAM, J.C., LAVAL, G., PELLAT, R. - Modes de dérive dissipatifs dans les configurations du type TOKAMAK. (CN 28-F 15) - 4ème Conférence sur la Physique des plasmas et la fusion controlée. Madison, USA (1971).

[7] PFIRSCH, V.D., SCHLÜTER, A. - Report MPI/PA/7/62 - Max-Planck Institute für Physik und astrophysik - München (1962).

[8] GROVE, D.G. et al., Preliminary investigation of Ohmically Heated plasmas in the model ST. Tokamak. Fourth European Conference on Controlled fusion and plasma physics (Rome, 1970)

[9] MIRNOV, S.V. - Influence of the shape and magnitude of the discharge current pulse on plasma containment and heating in Tokamak 3. Nuclear Fusion 9. 1 (1969) 57-66.

[10] MERCIER, C., SOUBBARAMAYER - Space time evolution of a Tokamak type plasma - Fourth European Conference on Controlled Fusion and Plasma Physics (Rome, 1970).

APPENDICE

TRAITEMENT NUMERIQUE DU PROBLEME

Le but de notre étude est de simuler numériquement les expériences réalisées avec différentes machines du type Tokamak. Ceci a nécessité trois étapes :

- Choix du modèle mathématique : c'est le système MHD donné précédemment.

- Simplification du modèle pour traiter les équations par les méthodes numériques usuelles. Il est nécessaire de vérifier la qualité du modèle choisi.

- Obtention d'un programme dont le temps d'exécution est le moins onéreux possible et la fidélité la meilleure possible.

Ceci nous a conduit à concevoir le programme dans un mode conversationnel en utilisant les périphériques IBM-2250 (visualisation) du 360-91 de Saclay.

A - SIMPLIFICATION DU MODELE MHD.

Nous supposons que le tore a un diamètre suffisamment grand et que l'effet toroïdal est en première approximation négligeable : Nous écrivons les équations du système à deux fluides en géométrie cylindrique avec l'équation de la densité. La vitesse a été remplacée par $\frac{\mathcal{D}}{n}\,\overrightarrow{\text{grad}}\; n$ et dans le programme $\mathcal{D} = 0$ permet de traiter le problème posé au I.

Dans le système d'évolution considéré nous avons une seule variable d'espace ρ, variable radiale. Nous posons : $U = \log\, \theta_e$; $Z = \log\, \theta_i$; $W = \log\, n$ et pour les variables $\rho = a r$, $t = t_o \tau$ où a est le rayon du tore et t_o le temps réduit.

De plus, nous écrivons les fonctions inconnues sous la forme

$$g(\rho, t) = G_o\; G(r, \tau)$$

Le système d'évolution que nous traitons numériquement s'écrit :

$$\frac{\partial N}{\partial \tau} - A_1 \frac{1}{r} \frac{\partial}{\partial r}\left(r D \frac{\partial N}{\partial r}\right) = \text{Source de matière}$$

$$\frac{\partial J}{\partial \tau} - A_2 \frac{1}{r} \frac{\partial}{\partial r}\left(r \frac{\partial}{\partial r}(E J)\right) = 0.$$

$$\frac{\partial U}{\partial \tau} + A_1 D \frac{\partial U}{\partial r} \frac{\partial W}{\partial r} + A_3 \frac{1}{r} \frac{\partial}{\partial r}\left(r D \frac{\partial W}{\partial r}\right) - A_4 \frac{1}{N T_e} \cdot \frac{1}{r} \frac{\partial}{\partial r}\left(r K_e T_e \cdot \frac{\partial U}{\partial r}\right) =$$

$$A_5 \frac{J^2 . E}{N T_e} - A_6 \frac{\alpha}{N T_e} (T_e - T_i)$$

$$\frac{\partial Z}{\partial \tau} + A_1 D \frac{\partial Z}{\partial r} \cdot \frac{\partial W}{\partial r} + A_3 \frac{1}{r} \frac{\partial}{\partial r}\left(r D \frac{\partial W}{\partial r}\right) - A_7 \frac{1}{N T_i} \frac{\partial}{\partial r} \frac{\partial}{\partial r}\left(r K_i T_i \frac{\partial Z}{\partial r}\right) =$$

$$A_6 \frac{\alpha}{N . T_i} (T_e - T_i) - \text{Source et puits d'énergie}$$

où A_i, $i = 1 \ldots 8$ sont des nombres adimensionnels.

Conditions aux limites

$$T_e(1, \tau) = T_i(1, \tau) = \tau \quad ; \quad N(1, \tau) = f(\tau) ; \frac{\partial}{\partial r}(E J) = g(\tau)$$

Conditions initiales : Elles sont données.

Nous supposons que le problème défini par le système les conditions initiales et aux limites est un problème bien posé.

B - TRAITEMENT NUMERIQUE PROGRAMME.

La méthode numérique utilisée est une méthode de décomposition liée aux techniques de pas fractionnaires. On peut consulter [1-2]. Si l'on note $\vec{G}$ le vecteur de composantes N, J, $\mathcal{U}$, Z, le système s'écrit :

$$\frac{d\vec{G}}{d\tau} + \mathcal{A}\,\vec{G} = \vec{\mathcal{F}}$$

où $\mathcal{A}$ est une matrice dont les éléments sont des opérateurs différentiels non linéaires.
Les coefficient K_e, K_i, E, D intervenant dans les coefficients de la matrice peuvent être modifiés comme on le désire.

Le programme est conversationnel. Toutes les constantes physiques du problème apparaissent à l'écran du 2250 - IBM et peuvent être modifiées après sélection au light pen. Il est ainsi possible de changer les conductivités thermiques et la diffusion particulaire. Il est aussi possible de choisir comme conditions initiales d'un cas physique, l'état d'un cas précédent arrêté à un instant fixé par l'utilisateur, par exemple lorsque le critère de shear cesse de jouer.

Sur l'écran, à chaque temps t choisi par l'utilisateur apparaissent les courbes représentatives des fonctions N, J, T_e, T_i ainsi que les quantités annexes : Température électronique moyenne, température ionique moyenne, β poloïdal, température électronique maximale. Il apparaît aussi le calcul de $\frac{\partial \eta J}{\partial r}$ au point r = 1 et la valeur imposée par la condition aux limites du problème. La comparaison de ces deux valeurs, l'allure générale des courbes et leur régularité, permet de décider, à cet instant t_i, si l'on peut continuer à intégrer le système I ou si l'on doit revenir à un temps $t_j < t_i$ afin d'intégrer à nouveau le système avec un pas de temps plus petit.

Les résultats numériques sont imprimés sur listing ainsi que les quantités auxiliaires telles que les quantités moyennes, le β poloïdal, le temps de confinement, l'inductance, les invariants intégraux de l'équation de la température électronique, les valeurs des coefficients de diffusion électroniques et ioniques et les zones de Galeev-Sagdeev où ils sont calculés.

On a aussi la possibilité à chaque instant d'imprimer sur microfilm tout ce qui se trouve à l'écran du 2250 IBM par simple pression sur une touche présélectée du clavier.

L'enchainement des cas permet d'effectuer toute étude paramétrique d'une façon dynamique, c'est à dire en utilisant immédiatement les résultats de l'étude antérieure.

RÉFÉRENCES

[1] TEMAM, R. - Sur la stabilité et la convergence de la méthode des pas fractionnaires. Annali di Math. (1968)

[2] YANENKO, N.N. - Méthode des pas fractionnaires, Novosibirsk (1966) Armand Colin (1970)

DISCUSSION

F.G. WAELBROECK: Your numerical calculations seem to agree well with the results of widely different experiments. How many empirical constants have to be fitted to get this agreement?

SOUBBARAMAYER: Three coefficients - $K_{1,0}$, $K_{2,0}$ and θ critical - have to be fitted with experimental results. To do this, account is taken of all the measurements, corresponding to different moments of the discharge.

C. OBERMAN: What is the value of υ_D/υ_{TE} for 400 kA? Does it correspond to the current inhibition regime i.e. $\upsilon_D/\upsilon_{TE} \sim 1/3$?

SOUBBARAMAYER: The code computes the value of υ_D/υ_{TE} at each moment of the discharge and at each point of the plasma. This quantity is needed for the anomalous factor of electrical resistivity, which we have based on the experimental curve given by Robinson. In the two cases of the Fontenay Tokamak presented in this paper, the quantity υ_D/υ_{TE} is much less than 1/10 so that it never enters the regime you mention. All the physical parameters needed for the computations are given in the paper.

ИССЛЕДОВАНИЯ УДЕРЖАНИЯ И НАГРЕВА ПЛАЗМЫ В УСТАНОВКЕ ТОКАМАК-4

Л.А.АРЦИМОВИЧ, В.А.ВЕРШКОВ, А.В.ГЛУХОВ,
Е.П.ГОРБУНОВ, В.С.ЗАВЕРЯЕВ, С.Е.ЛЫСЕНКО,
С.В.МИРНОВ, И.Б.СЕМЕНОВ, В.С.СТРЕЛКОВ
Институт атомной энергии им.И.В.Курчатова,
Москва,
Союз Советских Социалистических Республик

Abstract — Аннотация

INVESTIGATIONS OF PLASMA CONFINEMENT AND HEATING IN THE TOKAMAK T-4 DEVICE.

The authors present experimental results obtained with the Tokamak T-4 device, which differs from the Tokamak T-3a mainly in that it has a stronger stabilizing magnetic field (50 kOe). Plasma energy balance and electron and ion heating experiments are described. The electron temperature was determined by measuring the absorption of soft X-rays and the ion temperature by measuring the intensity of neutron emission. The total energy in the plasma column was found by measuring the diamagnetic effect. As the main results are for relatively high plasma concentrations ($n_e \geqslant 3 \times 10^{13}$ cm^{-3}), the transfer of energy from the electrons to the ions is assumed to be caused principally by pair Coulomb collisions. On the basis of this assumption, the ion energy lifetime τ_{Ei} is determined from the steady-state ion temperature. The ion temperatures found experimentally are compared with temperature values calculated on the basis of the neoclassical Galeev-Sagdeev theory.

ИССЛЕДОВАНИЯ УДЕРЖАНИЯ И НАГРЕВА ПЛАЗМЫ В УСТАНОВКЕ ТОКАМАК-4.

В работе приводятся экспериментальные результаты исследований на установке Токамак-4, в основном отличающейся от установки Токамак-3а большей величиной стабилизирующего магнитного поля (50 кэ). Описываются эксперименты по энергобалансу плазмы и нагреву электронов и ионов. Температура электронов измерялась по поглощению мягкого рентгеновского излучения, а температура ионов – по интенсивности нейтронного излучения. Полный запас энергии в плазменном шнуре определялся по диамагнитному эффекту. Поскольку основные результаты получены при относительно высокой концентрации плазмы ($n_e \geqslant 3 \cdot 10^{13}$ см$^{-3}$), предполагается, что передача энергии от электронов к ионам происходит, в основном, за счет парных кулоновских столкновений. В рамках этого предположения по установившемуся значению ионной температуры определяется энергетическое время жизни ионов τ_{Ei}. Полученные экспериментальные значения температуры ионов сравниваются с рассчитанными по неоклассической теории Галеева-Сагдеева.

1. ВВЕДЕНИЕ

Установка Токамак-4 (Т-4) представляет собой дальнейшую модификацию установки Токамак-3а (Т-3а) и имеет следующие параметры:

радиус сечения лайнера	$a_л = 20$ см
радиус отверстия диафрагмы	$a_д = 17$ см
радиус медного кожуха	$в = 23$ см
максимальная величина стабилизирующего магнитного поля	50 кэ
максимальное значение тока в плазме, допускаемое размерами центрального магнитопровода	300 кА

Следует отметить, что конструкция диафрагмы в установке Т-4 несколько изменена с целью уменьшения удельного энерговыделения на ее поверхности.

2. МЕТОДЫ ИЗМЕРЕНИЙ

Осциллографировались напряжение на обходе тора и ток в плазме. Величина смещения плазменного шнура и структура возмущений вблизи его поверхности определялись по сигналам магнитных зондов. Для измерения концентрации плазмы использовался радиоинтерферометр двухмиллиметрового диапазона. Температура электронов измерялась по поглощению мягкого рентгеновского излучения, а температура ионов – по интенсивности нейтронного излучения, возникающего в результате d-d-реакции. Величина энергии в плазменном витке определялась по измерению диамагнетизма плазмы.

3. РЕЗУЛЬТАТЫ

Корреляционные измерения сигналов магнитных зондов на установке Т-3а показали, что по мере роста тока при приближении запаса устойчивости $q(a_д)$ к трем происходит развитие резонансных возмущений третьей моды [1]. Эта неустойчивость обычно ограничивала величину тока в плазме на уровне, определяемом условием $q(a_д) \geqslant 3$. Однако программирование тока позволило получить устойчивые режимы также и при $2 < q(a_д) < 3$.

На установке Т-4 значениям $q(a_д) = 2$ при магнитном поле 25 кэ соответствует сила тока около 200 кА.

На рис.1 приведены осциллограммы тока, напряжения и концентрации для двух режимов разряда. В случае (a) плазменный виток устойчив, в режиме (b) наблюдается ярко выраженная неустойчивость, развивающаяся вблизи значения тока, соответствующего $q(a_д) = 2$. В первом случае амплитуда тока достигает 180 кА, напряженность электрического поля в момент максимума разрядного тока составляет $6 \cdot 10^{-3}$ В/см. Электропроводность плазмы, усредненная по площади отверстия диафрагмы в этот момент времени, равна $3{,}3 \cdot 10^{16}$ CGSE. Концентрация плазмы в центральной части шнура достигает $4 \cdot 10^{13}$ см$^{-3}$.

Все описанные ниже результаты относятся к устойчивым режимам.

На рис.2 приведена типичная зависимость внутренней энергии плазмы от времени, полученная в результате обработки диамагнитного сигнала. Схема измерений в нашем случае отличилась от принятой ранее способом компенсации влияния продольного магнитного поля, что позволило избежать трудностей, связанных с большой длительностью процесса и несохранением магнитного потока. Поперечная энергия плазмы достигает значений 6 Дж/см. С учетом точности измерений в этот момент времени величина $\beta_J = 0{,}35 \pm 0{,}1$.

Электронная температура определялась по жесткости рентгеновского излучения в области $1 \div 10$ Å. Анализ его осуществлялся обычным методом по поглощению в фольгах (Al – 20,40,60 мк). В качестве приемника излучения использовался ФЭУ с пластическим сцинтиллятором. Результаты этих измерений согласуются с предположением о максвелловском

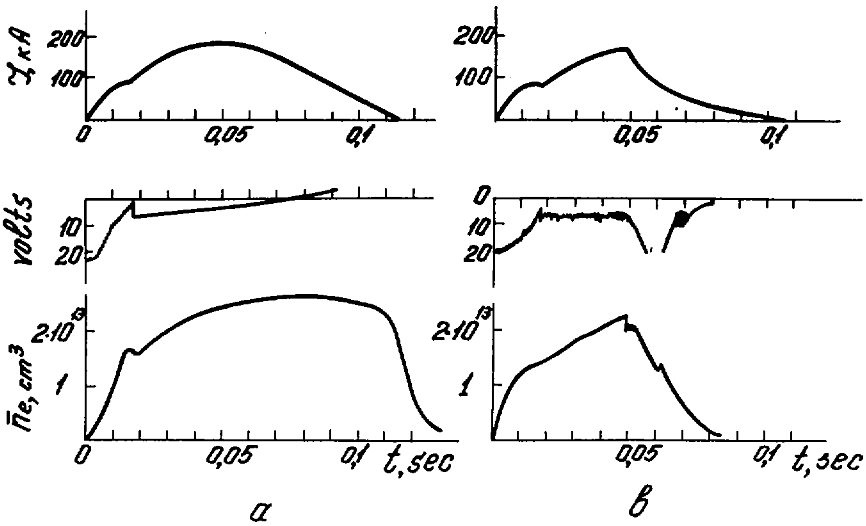

Рис.1. Изменение тока, напряжения и средней концентрации плазмы во время разряда: а) устойчивый режим; b) неустойчивый режим.

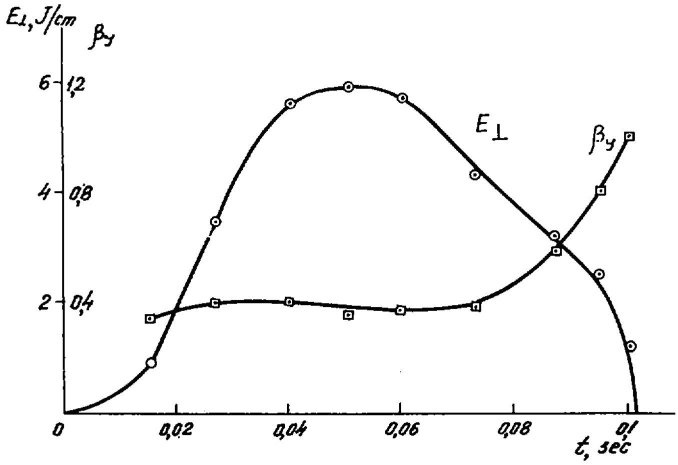

Рис.2. Временная зависимость поперечной компоненты энергии плазмы и величины β_J .

характере распределения электронов по энергиям. Этот метод достаточно прост и позволяет получать ход электронной температуры во времени на протяжении каждого разрядного импульса. Величина температуры T_e , определенная таким способом при использовании фильтров достаточно большой толщины, должна быть близка к максимальной температуре электронов в сечении плазменного шнура.

Значения T_e в различных экспериментах изменялись в пределах от 800 до 2400 эВ в зависимости от величины разрядного тока и концентрации плазмы.

На рис.3 приведена одна из типичных осциллограмм мягкого рентгеновского излучения, прошедшего через фильтр Al (20 мк).

На рис.4. показаны зависимости электронной температуры $T_e(0)$, величины β_J, электропроводности σ и энергетического времени жизни τ_E от концентрации плазмы в средней части разряда при сохранении постоянной амплитуды тока (110 кА). Для сравнения на том же рис.4 приведена температура электронов в сходных режимах на установке Т-3а, определенная по лазерному рассеянию [2]. Видно, что значения электронной температуры, найденные разными методами, оказываются достаточно близкими, а зависимости других величин от концентрации аналогичны полученным ранее [3].

На рис.5 приведена временная зависимость электронной температуры в центральной части шнура, найденная из рентгеновских измерений.

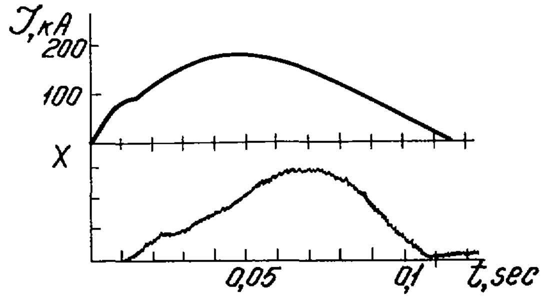

Рис.3. Осциллограммы тока и мягкого рентгеновского излучения.

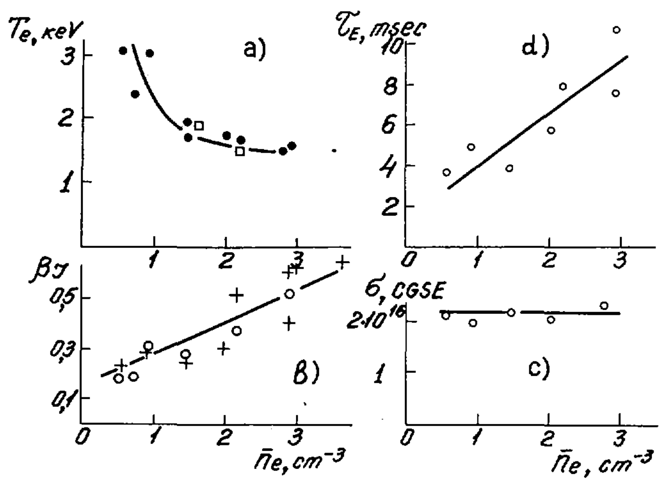

Рис.4. Зависимости от концентрации:
a) электронной температуры по рентгеновским измерениям (•) и по лазерным данным (□);
b) величины β_J по диамагнитным измерениям (+) и по рентгеновским и микроволновым данным (o);
c) электропроводности плазмы;
d) энергетического времени жизни плазмы.

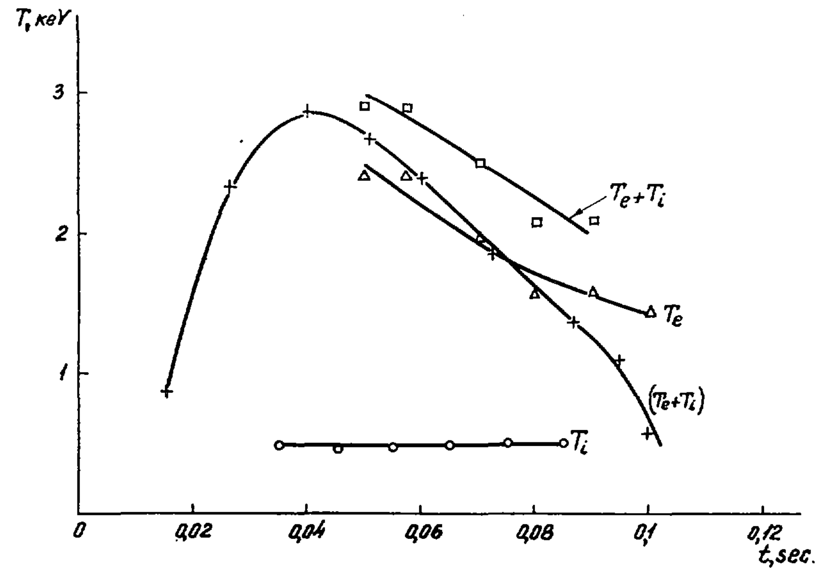

Рис.5. Сравнение температуры в центре плазменного шнура по рентгеновским измерениям (△), по нейтронному выходу (о), их суммы (□) с температурой, определенной по диамагнетизму плазмы.

На установке Т-3а было показано, что абсолютная величина интенсивности нейтронного излучения соответствует температуре ионов, измеренной по спектру атомов перезарядки [4]. В экспериментах на установке Т-4 интенсивность нейтронного излучения была выше и достигала $5\cdot10^6$ нейтронов за импульс. Анализатор позволял регистрировать интенсивность излучения в различные моменты времени. На рис.5 приведена температура дейтронов в центре плазменного шнура, определенная по интенсивности нейтронного потока.

На том же рис.5 приведена зависимость от времени суммы электронной и ионной температур, вычисленной на основании диамагнитных и микроволновых измерений. При этих вычислениях, а также при нахождении температуры ионов предполагалось, что $T_{e,i}(r) = T_{e,i}(0)\,[\,1-(r/a_д)^4\,]^2$ и $n_e(r) = n_e(0)\,(1-r^2/a_1^2\,)$.

Зависимости такого вида для $T_e(r)$ и $n_e(r)$ были найдены в предыдущих экспериментах [2].

4. ОБСУЖДЕНИЕ РЕЗУЛЬТАТОВ

Первая серия экспериментов, проведенных на установке Т-4, показала, что в определенных условиях (в режиме со вторичным нарастанием тока) может быть получен устойчивый плазменный шнур при $q < 3$. При приближении к $q = 2$ начинается развитие второй моды, которое, вероятно, приводит к срыву тока.

Следует заметить, что при росте амплитуды программированного тока первоначально происходит увеличение электронной температуры; однако при приближении к значениям, соответствующим $q(a_д)$, близким к 2, рост электронной температуры прекращался или она несколько падала, в то время как нейтронный выход продолжал возрастать. Такое поведение электронной температуры может быть связано с увеличением электронной теплопроводности при возникновении вблизи поверхности плазменного шнура резонансных возмущений с $m = 2$.

Зависимость энергетического времени τ_E от тока согласуется с эмпирическим выражением $\tau_E \sim a^2 H_J$, полученным в работе [3].

Совокупность диамагнитных, рентгеновских, нейтронных и микроволновых измерений дает достаточную информацию для вычисления одной и той же величины различными методами. На рис.4 приведено сравнение величины β_J, найденной двумя способами, в зависимости от концентрации плазмы. На рис.5 изображена зависимость от времени суммы температур $(T_e + T_i)(0)$, вычисленной по диамагнетизму плазмы, с суммой электронной и ионной температур, определенных независимыми методами. Видно, что эти величины достаточно хорошо совпадают.

Как видно из рис.4, начиная с 30 мсек, температура ионов практически постоянна. В работе [5] найдены стационарные значения температуры ионов в предположении, что теплопередача от электронов к ионам обусловлена парными столкновениями, электронная температура значительно выше ионной, а потери энергии из ионной компоненты соответствуют теории Галеева-Сагдеева [6]. На рис.6, взятом из работы [5], прямые линии соответствуют расчету при разных предположениях о характере распределения концентрации плазмы и плотности тока по сечению плазменного шнура. Результаты экспериментов на установке Т-4 показаны на том же рис.6 наряду с данными, полученными на установках Т-3а и ТМ-3. Эти результаты хорошо согласуются с зависимостью температуры ионов от параметров, следующей из неоклассической теории.

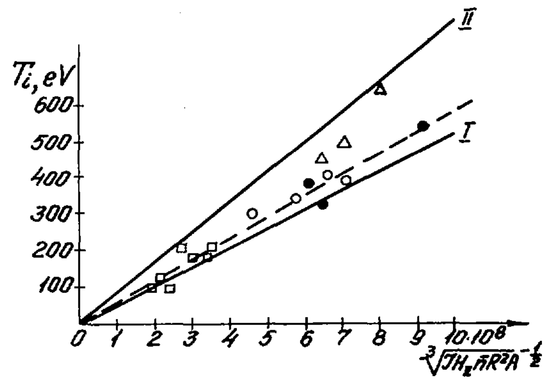

Рис.6. Зависимость ионной температуры от параметров плазмы:
▪ – установка ТМ-3, о,● – установка Т-3а, △ – установка Т-4. Прямая I вычислена при $n_e(r) = \text{const.}$, плотности тока $j(r) = \text{const}$. Прямая II вычислена при $n_e(r) = n_e(0)(1 - r^2/a^2)$, $j(r) = j(0)(1 - r^2/a^2)$.

Таким образом, эксперименты на установке Т-4 не противоречат предположению об определяющей роли классических механизмов в энергетическом балансе плазмы. В рамках этого предположения при стационарном значении ионной температуры можно определить время удержания энергии в ионной компоненте, которое в исследованных режимах достигает 17 мсек.

В заключение авторы выражают благодарность техническому персоналу установки Т-4, обеспечившему пуск и эксплуатацию установки; особенно необходимо отметить Н.В.Краснова, В.П.Вербова, А.И.Никонорова, Ю.И.Данилова и В.Г.Шеина, а также М.М.Свирину. Численные расчеты были выполнены Л.Г.Исаенко.

ЛИТЕРАТУРА

[1] МИРНОВ, С.В., СЕМЕНОВ, И.Б., Атомная энергия 30 (1971) 20.
[2] АНАШИН, А.М. и др., ЖЭТФ 60 (1971) 2095.
[3] ГОРБУНОВ, Е.П., МИРНОВ, С.В., СТРЕЛКОВ, В.С., Nucl. Fusion 10 (1970) 43.
[4] АРЦИМОВИЧ, Л.А. и др., Письма в ЖЭТФ 10 (1969) 130.
[5] АРЦИМОВИЧ, Л.А., ГЛУХОВ, А.В., ПЕТРОВ, М.П., Письма в ЖЭТФ 11 (1970) 449.
[6] ГАЛЕЕВ, А.А., САГДЕЕВ, Р.З., ЖЭТФ 53 (1967) 348.

DISCUSSION

B. COPPI: What is your general opinion regarding the effects of the copper shell on the stability of T-3 and T-4 plasmas?

V.S. STRELKOV: Experiments carried out on T-3 and T-4 show that the stability is improved by the closeness of the conducting shell.

B. COPPI: Have you made any progress in understanding the nature of the density limitation observed with T-3 plasmas?

V.S. STRELKOV: This limitation is probably due to an increased influx of neutral atoms into the plasma column, which accompanies the growth in concentration and the stronger cooling of the outer regions.

H. DREICER: Has the role of the metallic limiter or diaphragm in Tokamak operation been the subject of an experimental study? In particular, is it known whether or not the emission of neutral atoms from the limiter has an important influence on Tokamak plasma behaviour?

V.S. STRELKOV: In the vicinity of the limiter the flux of hydrogen atoms and impurities is several times greater than in other parts of the column. The amount of impurities and hydrogen ions increases sharply the moment an instability develops.

B.P. LEHNERT: In regard to Mr. Dreicer's question, I should like to point out that the limiters in Tokamaks may have a stabilizing effect on flute disturbances in the plasma as a result of line-tying, which fixes the electric potential of the outermost plasma boundary layers at the potential of the limiters. Do you agree with this?

V.S. STRELKOV: The conducting liner may have some stabilizing effect but the influence of the limiter itself is smaller. If there are transverse currents through the limiter the equilibrium conditions may be changed.

G.J. YEVICK: You stated that without the limiter your plasma would burn a hole in the liner. In this case, how much damage has been done to the limiter?

V.S. STRELKOV: The damage to the limiter varies with the different regimes, and one can observe only the integral effect, when the chamber is dismantled. The edge of the limiter is fused.

G.J. YEVICK: Did you measure the absolute amounts of impurities in the plasma, in particular the amount of tungsten?

V.S. STRELKOV: No absolute measurements were made.

J.P. GIRARD: With these long times the shell does not fulfil its function of keeping the plasma centred. In view of this, how is the vertical field programmed?

V.S. STRELKOV: A transverse magnetic field set up by the currents in control windings increases with time, as the shell field is weakened through damping of the reflected currents.

A. GIBSON: Your earlier measurements on T-3 showed that an anomalous electron thermal conductivity was necessary to explain the observed energy replacement times. Is a similar anomalous loss required to explain the observations in T-4, which now extend to higher values of electron temperature than were attained in T-3?

V.S. STRELKOV: Yes. The coefficient of electron thermal conductivity is higher than the value given by neoclassical theory.

J.L. TUCK: From your very interesting paper, it appears that Tokamaks are continuing to advance and T-4 is appreciably better than T-3. How is this improvement reflected in the energy and particle confinement times? At 0.1 sec, near the end of the confinement period, what would be the value of the gross energy quotient of the plasma, i.e. the ratio $\frac{\text{total particle energy}}{\text{total energy input}}$?

V.S. STRELKOV: In stable Tokamak regimes the energy stored in the plasma per unit time is 30-40% of the Joule heating power.

R. PELLAT: Why is the energy confinement time only 10 milliseconds? The magnetic field is stronger than in the T-3 installation and the electron and ion temperatures are higher, so that a longer confinement time might be expected.

V.S. STRELKOV: The value τ_E = 10 ms corresponds to the empirical formula $\tau_E \sim a^2 H_I$ for the discharge parameters adopted in experiments on T-4.

J.C. HOSEA: Is it not true that, like Mirnov and Semenov, you also obtained stable q = 2 operation before the onset of the disruptive instability (critically) in T-3, indicating that the smaller copper radius did not substantially change the critical q.

V.S. STRELKOV: On the contrary, even though the radius of the copper shell in T-4 is only slightly different from its value in T-3, 23 cm as compared with 25 cm, stable regimes with a q of about 2 were obtained more easily in T-4.

PARTICLE AND ENERGY BALANCE IN THE ST TOKAMAK

D. DIMOCK, D. ECKHARTT,* H. EUBANK, E. HINNOV,
L.C. JOHNSON, E. MESERVEY, E. TOLNAS, D.J. GROVE**
Princeton University, Plasma Physics Laboratory,
Princeton, New Jersey, United States of America

Abstract

PARTICLE AND ENERGY BALANCE IN THE ST TOKAMAK.

Plasma energy content and particle and energy confinement times have been measured in the ST Tokamak device. Initial filling pressure is varied from 3×10^{-5} to 3×10^{-4} Torr in hydrogen or helium, ohmic heating current I_φ from 2 to 60 kA, and limiter diameter from 8 to 28 cm. Electron temperatures T_e and densities n_e at the centre of the plasma range from 30 to 1500 eV and from 5×10^{12} to 1×10^{14} cm^{-3}, respectively. Particle confinement times range from 1 to 20 ms and are equal to corresponding energy confinement times to within a factor of two.

Radial profiles of electron temperature and density are measured by Thomson scattering of a ruby-laser pulse. For typical plasma conditions, T_e is 800-1200 eV at the centre. Late in the discharge, the T_e profiles are much more strongly peaked than those reported for T3-A, although the total plasma energy content for comparable values of I_ϕ is approximately the same. Proton temperatures in hydrogen plasmas, measured by charge-exchanged neutrals, reach peak values of 400-500 eV. Ion temperatures, obtained from Doppler broadening of OVII (λ 1623) and CIV (λ 1548) lines, are in good agreement with proton temperatures.

The measured plasma resistance is not significantly different from that calculated from the Spitzer formula using the measured content of impurity ions (primarily oxygen), and assuming that the electric field $\vec{E}_\phi$ is independent of the minor radius.

Plasma confinement improves rapidly with increasing I_ϕ. Over a range of two orders of magnitude the plasma energy content varies approximately as I_ϕ^2; at constant I_ϕ, there is a weaker increase with n_e for the conditions studied.

In comparison with available T3-A results, substantial agreement on directly observable data is found, with the exception of radial temperature and density profiles, but there are significant differences in interpretation. Our results do not indicate substantial anomalies in resistivity or in electron energy loss distinct from anomalous loss of particles.

1. INTRODUCTION

Preliminary reports have been made on the operation of the ST tokamak [1, 2]. In this paper we report recent experimental results on plasma energy content and particle and energy confinement times. The range of externally variable parameters is: the filling pressure p_o (0.3 - 3×10^{-4} Torr) in helium and hydrogen, toroidal ohmic heating current I_ϕ(2 - 60 kA), the aperture limiter radius a (4 - 14 cm), and the toroidal confining field B_ϕ(11 - 44 kG). It appears that for a given current and electron density the behavior of hydrogen and helium plasmas does not differ appreciably after the initial plasma formation stage, so that for plasma confinement studies H and He discharges may be used interchangeably. Helium has several practical advantages: it allows an independent check on ionization rate determinations which are crucial to the measurement of particle

* Permanent address: Max-Planck-Institut für Plasmaphysik, Garching bei München.

** On loan from Westinghouse Research Laboratories, Pittsburgh, Pa.

confinement times (section 2); the higher value of ionic charge makes the role of impurities less important; finally, it appears that for a given ultimate electron density, the initial filling pressure required is less, thus making easier the initial breakdown and early development of discharges which have high electron density.

Figure 1 presents a plan view of the ST tokamak with its dimensions and the locations of the various diagnostics: the ohmic heating current (from a Rogowski coil) and loop voltage (measured across a ceramic break in the vacuum vessel); the ruby laser Thomson scattering device for measurement of the distribution of electron temperature and density along a major radius; 4 mm and 2 mm microwave interferometers for independent determination of electron line densities; a neutral hydrogen energy analyzer for determination of the energy spectrum of the H^+ ions via resonant charge exchange processes in the discharge; a high-resolution grating spectrometer with LiF optics for measurement of Doppler profiles of various ion lines in the Schumann region, particularly λ1623Å of OVII, λ1548 of CIV, and λ1640 of HeII; a grazing incidence vacuum monochromator for the determination of ultraviolet radiation intensities and concentrations of impurity ions; several

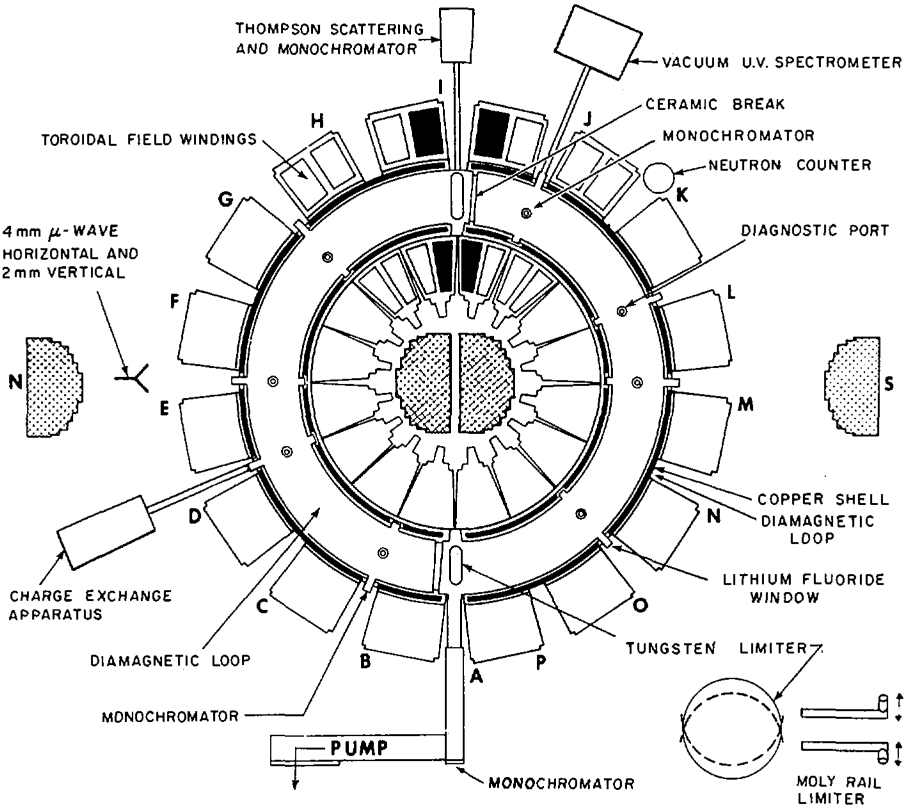

FIG. 1. Plan view of ST Tokamak showing location of various diagnostics. Major radius = 109 cm; minor (limiter) radius variable (4-14 cm); stainless steel vacuum vessel radius = 16 cm, thickness = 3 mm; copper shell thickness = 3 cm.

calibrated monochromators for the determination of the absolute intensities of the lines of the working gas (H or He) in the visible, including their axial and radial distributions; and an assortment of diamagnetic loops, B_θ pickup coils, and x-ray monitors. The plasma aperture can be limited by a two-piece tungsten iris limiter, or at top and bottom by a pair of movable molybdenum rails. Both limiters are located at the pumping port A.

2. GENERAL CONSIDERATIONS

The mean particle confinement time τ_p is defined from

$$\frac{N_e}{\tau_p} \equiv \sum \text{ionization rates} - \frac{dN_e}{dt} \tag{1}$$

where N_e is the total number of electrons in the plasma. Similarly, the "energy confinement" time $\tau_E(e)$ for the electrons is defined by

$$\frac{W_e}{\tau_E(e)} \equiv P_{in} - \frac{dW_e}{dt} - P_{e-i} - P_r \tag{2}$$

where W_e is the total electron kinetic energy in the plasma, P_{in} is the power input by ohmic heating, P_{e-i} is the net power transferred from electrons to the ions by Coulomb collisions, and P_r is the power lost by radiation (which includes the ionization potentials, usually a minor contribution). The physical meaning of the right side of Eq. (2) is the power required to heat the electrons produced by ionization to the prevailing electemperature and to provide power for any electron energy loss not explicitly mentioned. This definition of $\tau_E(e)$ allows an easy comparison with τ_p. Thus $\tau_E < \tau_p$ implies that on the average the electron energy is lost faster than 1.5 kT_{eav} times the particle loss rate.

Because of the considerable amount of data required to evaluate $\tau_E(e)$ according to Eq. (2), we also employ a related quantity

$$\tau'_E(e) \equiv W_e/P_{in} \tag{3}$$

as a parameter describing a discharge. Although $\tau'_E(e)$ is not so directly comparable with τ_p, larger values of τ'_E generally indicate better plasma confinement.

Before presenting the experimental data, we briefly discuss two topics essential for the determination of particle confinement times - the impurity concentrations in the discharges, and the method of deducing ionization rates from observed line intensities.

The major impurity whose concentration can be absolutely determined in these discharges is oxygen. Oxygen is present very early in the pulse, and the total amount of oxygen does not seem to vary appreciably during the pulse. After the discharge is fully established, the oxygen ions are fully stripped in the center of the discharge. The hot center is surrounded radially by shells of oxygen ions in various states of ionization, the thickness of the shells being determined by the electron temperature and density profiles, and the speed of the radial motion of the ions. In particular, the radiation of the OVI ions appears to originate at a radius where the electron temperature, T_e, is typically 80-100 eV, and that of the OVII ions at a radius where $T_e \approx 300$ - 400 eV. The total oxygen concentration varies somewhat with discharge parameters; in addition, there has been a slow decrease from about 7-10% at the start of operation a year ago to about 2-4% at present. Carbon and sometimes nitrogen ions are also present, but at concentrations that make these ions negligible in comparison with oxygen.

The main effect of these oxygen concentrations is to increase the plasma resistivity above the values that a pure hydrogen plasma would have at a given electron temperature. The effective value of the ionic charge $\bar{Z}$ is typically 2-3 near the center of the plasma, and drops slowly toward the periphery. In addition, the oxygen ionization affects noticeably the total ionization rate, and hence deduced particle confinement times, in hydrogen plasma; the radiation by the oxygen ions may amount to a small but not negligible fraction (10-20%) of the power input. In helium plasmas all these effects are relatively less, and in some cases almost negligible.

Neutral Fe, Cr, and Ni lines have also been observed; their intensity increases considerably, if the discharge is allowed to "lean" outward along the major radius. Ionization rate estimates for these ions yield an average density of the order of 10^{10} cm^{-3}, but these estimates are unreliable.

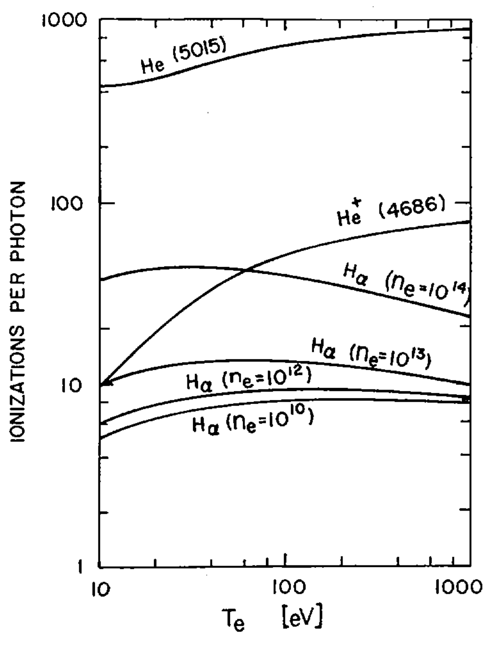

FIG.2. The ratio of the rate of ionization of H, He^0, and He^+ atoms to the rate of photon emission of Hα, λ 5015 and λ 4686 lines, respectively, in plasmas of electron temperature T_e(eV), density n_e(cm^{-3}). Only low-density values are shown in the case of helium, for which substantial deviations are not expected for $n_e < 10^{14}$ cm^{-3}.

Presumably there are also ions of tungsten and molybdenum in unknown amounts. These heavy ions have qualitatively the same effect as oxygen.

The dominating ionization rate is that of the working gas, hydrogen or helium. In order to determine this rate, we measure as a function of time the total photon flux of a suitable line of this element, including as far as possible its axial and radial distribution. The relative rate coefficients for ionization and for excitation of this line in a plasma (in general a function of electron density and temperature) may be calculated with adequate accuracy from experimentally or theoretically established cross sections. The ratios of these rate coefficients, or the number of ionization events per emitted photon in the temperature and density range of interest for the H_α line, and for neutral and singly-ionized helium lines, are shown in Fig. 2. A previous calculation of ionizations per H_α photon (Abramov et al. [3]), which seems to have been used to determine ionization rates in the TM3 and T3-A tokamaks [4, 5] gives incorrect results, especially for low electron densities. Apparently this is due to a factor of 10 error in the radiative transition probabilities used; in the density range of interest this results in an underestimate of about a factor 3 in the hydrogen ionization rate with a corresponding increase in derived values of particle confinement time.

The helium ionization to excitation ratios in Fig. 2 are given only in the low electron density limit, because the short radiation lifetimes involved result in a negligible density dependence in our density range. Since most helium atoms entering the plasma become doubly ionized, the measurement of both λ 5015 and λ 4686 line intensities evidently gives two simultaneous independent determinations of the total ionization rate of helium.

3. RESULTS

3.1 Hydrogen discharges

The time behavior of various parameters in a hydrogen discharge (terminated at about 20 msec because of ohmic heating system limitations), is shown in Fig. 3. The electron temperatures before 8 msec were deduced from observed excitation and ionization rates of oxygen and carbon ions, those after 8 msec from Thomson scattering. The ion temperatures are determined from the energy spectrum of the charge exchanged neutral atoms (which presumably give the peak temperature because of selective detection efficiencies) and of the Doppler widths of OVII and CIV ion lines, which originate at different distances from the center of the discharge. Figure 4 shows the Thomson scattering radial profiles of the electron temperature and density at t = 16 msec (symmetrized about the peak of the T_e profile, which was about 1 cm toward the outside of the vacuum vessel center at this time), and a reconstruction of a probable T_i profile. The radial locations of the OVII and CIV light, as well as the probable radial profile of the effective ionic charge $\overline{Z}$, were deduced assuming that these ions diffuse radially inward with a velocity a/τ_p. (The results are insensitive to the value of this velocity.)

In the particle confinement times shown in Fig. 3, hydrogen contributes about 2/3 of the total ionization rates, oxygen most of the rest.

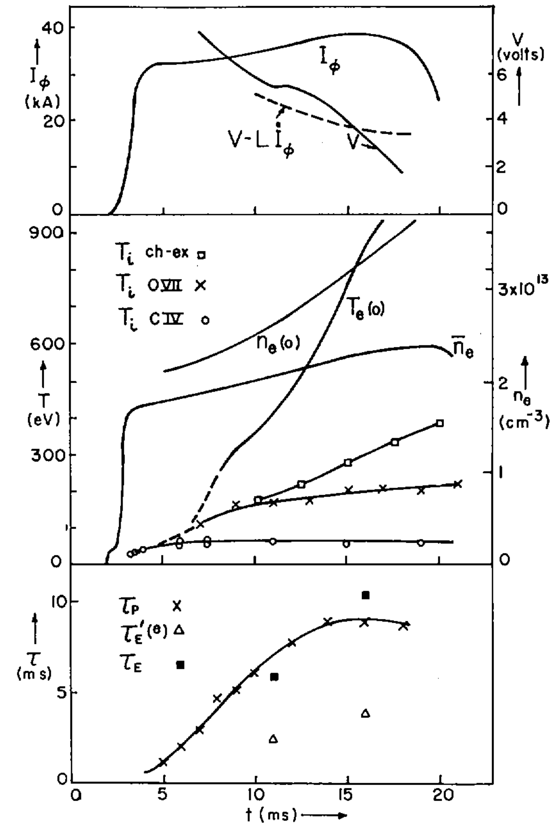

FIG. 3. Time behaviour of a 20 msec discharge in hydrogen with $p_0 = 3.4 \times 10^{-4}$ Torr, $B_\phi = 27$ kG, limiter radius 13 cm, no vertical B-field. Upper figure: Ohmic heating current and loop voltage, including corrections for dI_ϕ/dt. Central figure: peak and average electron densities; peak temperatures; ion temperatures measured by energy distributions of charge-exchanged atoms (□), from Doppler profiles of the λ 1623 line of OVII(X), and λ 1548 line of CIV(O). Lower figure: particle (X) and electron energy confinement times (■), and τ_E' from Eq.(3) (△).

Roughly half of the total ionization occurs in the immediate vicinity of the limiter, with a half-intensity distance about 12-15 cm along the major circumference (ϕ-direction).

For the data of Fig. 3 at 16 msec the various terms in Eq. (2) have the values $W_e = 0.37$ kJ, $P_{in} = 97$ kW, $dW_e/dt = 18$ kW, $P_{e-i} = 25$ kW, and $P_r = 19$ kW yielding $\tau_E(e) = 10$ msec. The relative numbers for the various power terms are fairly typical for hydrogen discharges studied so far, and so is the relationship between $\tau_E(e)$ and $\tau_E'(e)$ shown in Fig. 3.

The most important uncertainty in Eq. (2) is, somewhat surprisingly, the power input term, P_{in}. In a steady state discharge P_{in} can be set equal to VI where V is the loop voltage measured at the vacuum vessel ceramic break. In the present case (Fig. 3) the discharge parameters are varying

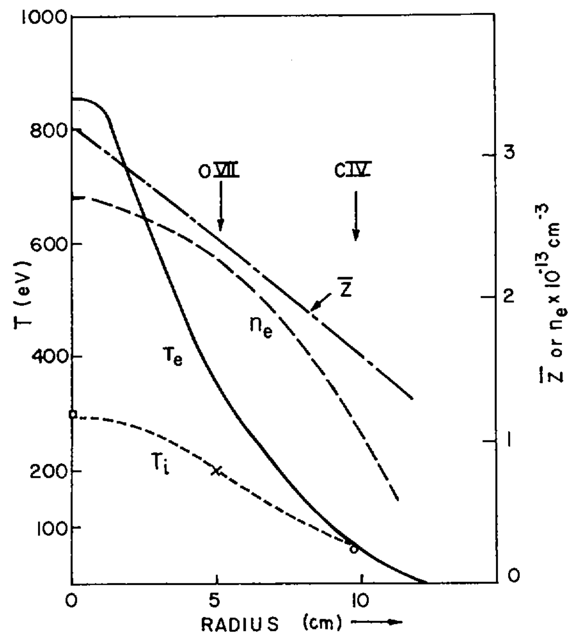

FIG.4. Radial profiles of plasma parameters for the discharge depicted in Fig.3 at t = 16 ms. T_e and n_e are from laser Thomson scattering measurements. The location of OVII and CIV light, and the probable distribution of T_i and $\bar{Z}$ are calculated from assumptions stated in the text. Ion temperatures are from charge-exchanged H energy spectra, (□), and from the Doppler profiles of OVII λ 1623 (X), and CIV λ 1548 (O), respectively.

with time, and corrections must be made for inductive effects; i.e., $P_{in} = V_R I$, where $V_R = V - (d/dt)(LI)$ and L is the leakage inductance between the current channel and the wall. dI/dt is measured, but L and dL/dt can be obtained accurately only from the distribution of current density, J, which has not been measured. In order to calculate V_R from the available data [$T_e(r)$ and $\bar{Z}(r)$], we assume (1) that J(r) is proportional to the local electrical conductivity $\eta(r)^{-1}$; i.e., that the time lag in the current distribution due to skin effect is negligible, and (2) that the resistivity $\eta(r)$ is the Spitzer resistivity. This allows both the calculation of V_R directly (yielding $V_R = 2.6$ volts, $P_{in} = 97$ kW) and the determination of L and dL/dt, for the correction of the observed loop voltage. The latter procedure, because of remaining uncertainties in dL/dt, gives a range of $1.8 < V_R < 3.9$ volts.

3.2 Helium discharges

Figures 5 and 6 show the time behavior of a helium discharge of a considerably longer duration. (The helium data were taken after improvements in the Ohmic heating system allowed longer pulses and higher currents than for most of the hydrogen data.) Clearly, after about 30 msec the discharge has settled to a relatively steady state that is terminated only by the Ohmic heating current capability. In this discharge the oxygen concentration was almost negligible, and, aside from the possible presence of

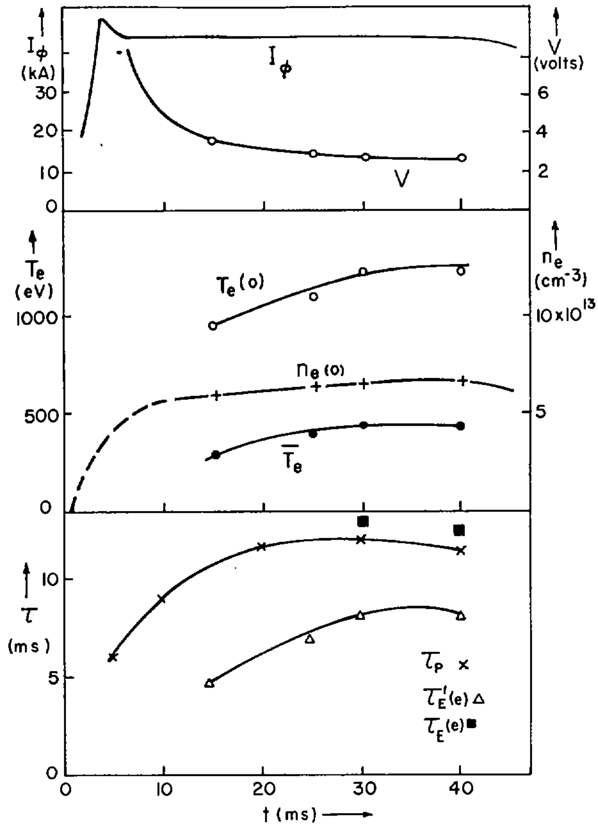

FIG. 5. Time behaviour of a 50 msec discharge in helium, with $p_0 = 2.0 \times 10^{-4}$ Torr, $B_\varphi = 44$ kG, limiter radius 12 cm, applied vertical field = 37 G. Upper figure: Ohmic heating current and loop voltage. Central figure: peak electron densities (+), and peak (O) and average (●) temperatures. Lower figure: particle confinement times (X) and energy confinement times, τ_E' (e) (△) and τ_E (e) (■).

ions of tungsten or from stainless steel, the mean ion charge is only slightly above $\overline{Z} = 2$. The particle confinement times deduced from the λ 5015 light of HeI and the λ 4686 light of HeII agree to within better than 20%. Roughly 3/4 of the total ionization occurred near the limiter in this case, with a half-intensity distance from the limiter in the ϕ direction about 10 cm for He^o and 25 cm for He^+.

In the power balance equation, [Eq. (2)], W_e is the same (.93 kJ) at both 30 and 40 msec, so that the dW_e/dt term (after 30 msec) is small. The P_r term is about 20 kW. Unfortunately, the central ion temperatures could not be measured in this discharge, but P_{e-i} is still estimated to be about 20-30 kW. In this case the current distribution is presumably in a steady state, and therefore P_{in} (= 116 kW at 30-40 msec) is found from the measured loop voltage. This gives $\tau_E'(e)$ = 8 msec and $\tau_E(e)$ = 13 msec $\cong \tau_p$.

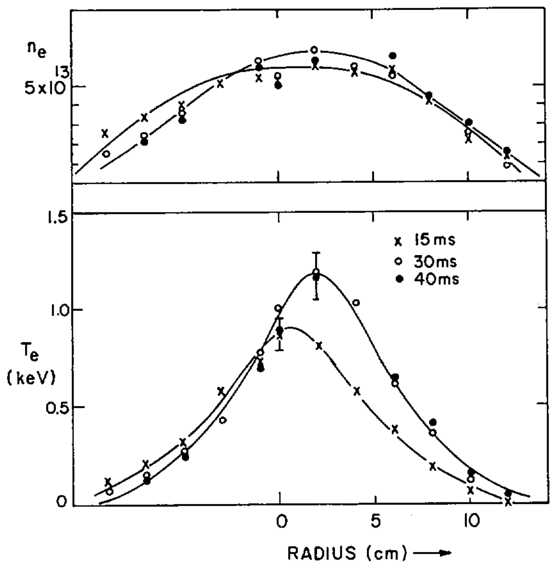

FIG.6. Radial distribution of n_e (upper traces) and T_e (lower traces) at 15 (X), 30 (O), and 40 (•) ms in the discharge described in Fig.5. The points shown give actual Thomson scattering data; the error bars indicate repeatability of measurements at a single point. Symmetrized curves through the points centre at +0.7 cm (15 msec) and +2.0 cm (30 and 40 ms). Vacuum vessel centre is at 0. Rail limiter at 12 cm top and bottom. Profiles taken along major radius. + = outward.

If we again evaluate the plasma resistance from the Thomson scattering T_e with the assumptions stated above, we calculate a loop voltage of 1.9 volts, compared to an observed value of 2.7 volts. Part of this difference (~ 20%) must be due to the toroidal field effects (trapped particles in "banana" orbits), and another part to the presence of heavy ion impurities. Both effects must have been present also in the earlier case, although heavy ion impurities may be relatively more important in the longer current pulses and in discharges with smaller oxygen concentrations. It may be noted that in the present case a concentration of 2 - 3 $\times 10^{10}$ cm^{-3}, or about 0.1% of the average electron density, would account for the discrepancy in the resistivity. The heavy atoms would be roughly 30 times ionized. Such an amount of heavy impurities would contribute only a few per cent to the total ionization rate, and the radiated power (almost entirely line radiation rather than Bremsstrahlung) would not exceed one kW. Thus the quoted values of τ_p and τ_E would not be appreciably affected.

3.3 Experimental data for various discharge parameters

In this section, we present some experimental data obtained by changing the externally variable discharge parameters. In order to get discharges with good pulse to pulse reproducibility for the Thomson scattering profile measurements, only those conditions were used in which the traces

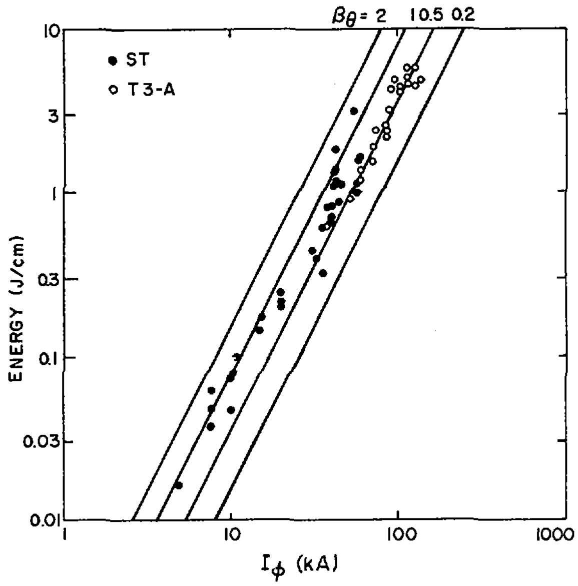

FIG.7. The total plasma energy (electron + ion) per cm axial length as a function of the ohmic heating current for a variety of conditions. Open circles are T3-A data reported in Ref.[5]. The straight lines indicate the values of $\beta_\theta = 8\pi \overline{nkT}/B_\theta^2(a)$.

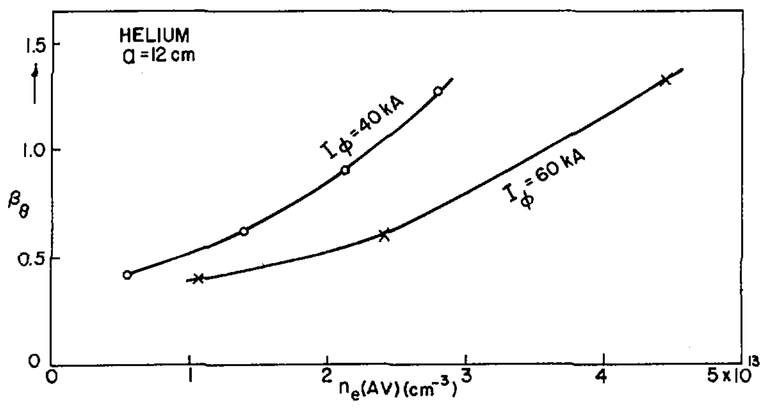

FIG.8. A detail of the data of Fig.7: β_θ versus average density at fixed aperture (a = 12 cm) and two different fixed currents: 40 kA (O) and 60 kA (X). Values of β_θ are from Thomson scattering electron profiles with 30% added for estimated ion energy.

TABLE I. VALUES OF PARTICLE CONFINEMENT TIME, τ_p AND THE TIME PARAMETER, τ_E' EQ. (3), FOR VARIOUS DISCHARGE CONDITIONS ARRANGED IN ORDER OF DECREASING τ_p.
B_ϕ = toroidal field; p_0 = gas filling pressure; a = radius determined by limiter setting and plasma displacement; I_ϕ = toroidal Ohmic heating current; $2\pi/q$ = rotational transform; P_{in} = Ohmic heating input power to electrons; R = plasma resistance from measured current and voltage corrected for inductive effects; $n_{eav} \equiv (2/a^2)\int n_e r dr$; $T_{eav} \equiv \int T_e n_e r dr / \int n_e r dr$; $\bar{v}_{de}$ = average electron drift velocity $(I/\pi a^2 e\, n_{eav})$; $\bar{v}_{th,e} = (2kT_{eav}/m_e)^{\frac{1}{2}}$.

B_ϕ (kG)	Gas	p_o (mTorr)	a (cm)	I_ϕ (kA)	q	P_{in} (kW)	R (mohm)	n_{eo} ($10^{13}/cm^3$)	n_{eav} ($10^{13}/cm^3$)	T_{eo} (eV)	T_{eav} (eV)	$\bar{v}_{de}/\bar{v}_{th,e}$	τ_E' (msec)	τ_p (msec)
44	He	0.28	12	56	5.2	163	0.052	9.2	4.5	1140	493	0.013	10.1	22
44	He	0.12	12	60	4.8	202	0.056	5.3	2.5	1080	468	0.026	4.3	15
35	He	0.11	12	40	5.8	123	0.077	3.9	1.5	1300	372	0.035	3.4	12
44	He	0.20	12	43	6.8	150	0.081	5.7	3.1	950	297	0.016	4.6	12
44	H_2	0.20	10	42	4.8	132	0.075	4.0	1.9	1450	470	0.036	3.4	13
27	H_2	0.34	12	39	4.6	98	0.064	3.4	2.2	870	247	0.026	3.7	9
35	H_2	0.32	11	45	4.3	196	0.097	2.8	1.5	1300	430	0.042	2.0	7.5
44	He	0.12	8	31	4.2	111	0.115	3.4	1.2	1050	447	0.067	2.1	8
44	He	0.12	8	15	8.6	63	0.280	1.6	0.8	440	190	0.069	1.2	5
22	He	0.12	8	15	4.3	56	0.25	2.1	0.6	690	289	0.076	1.7	4.5
44	He	0.12	8	7.7	16.8	39	0.660	1.0	0.53	235	107	0.073	0.49	2.1
12	He	0.12	8	7.8	4.5	34	0.560	0.80	0.32	350	197	0.092	0.69	1.3
12	He	0.12	8	4.1	8.6	34	2.0	0.75	0.37	76	44	0.088	0.24	1
12	He	0.12	8	1.7	20.7	~10	3.5	--	~0.25	--	17	0.087	0.14	1
27	H_2	0.11	6	10	4.5	37	0.37	1.1	0.8	450	140	0.099	0.51	1

(loop voltage in particular) were relatively free of oscillations. In general, this restricted the value of q ($\equiv aB_\phi/RB_\theta$) calculated at the limiter to be $\gtrsim$ 4.

Figure 7 shows the total plasma energy per cm axial length, as a function of the Chmic heating current. These data contain both hydrogen and helium discharges, with various limiter radii and toroidal fields. The estimated ion energy contribution has been included by multiplying the electron energies by 1.5 in the case of hydrogen and by 1.3 in the case of helium discharges. The open circles at the top are the T3-A data from Ref. 5. The data points at the lower end are not very different from the C stellarator results at comparable currents and radii.

These data clearly show that the particle energy depends strongly on the Ohmic heating current, approximately as I_ϕ^2. The vertical spread of the data points is not primarily statistical variation. For example, Fig. 8 clearly shows that the variation of the energy at constant current (or $\beta_\theta \equiv 8\pi\, \overline{nkT}/B_\theta^2 \propto W/I_\phi^2$) has a functional dependence on average electron density. Similar results were reported by Artsimovich et al. [6] for a somewhat different density range.

Values of τ_p and the associated τ_E' are given in Table I for various discharge conditions. It is clear that the confinement becomes better at higher values of toroidal current. Other parametric dependences do not emerge uniquely from these data in the restricted range so far studied.

4. CONCLUSIONS

To summarize the principal results, we find that (1) the particles and energy are lost from the plasma at substantially the same rate, (2) the plasma electrical resistivity is nearly equal to the Spitzer resistivity; the discrepancy of typically a factor about 1.5 is probably largely due to small amounts of heavy impurities from the limiter and vacuum walls, (3) typically only 20-25% of the power input is lost through the ions, (4) the plasma confinement improves rapidly with increasing ohmic heating current, and (5) over a range of more than 2 orders of magnitude the energy deposited in the plasma varies approximately as I^2; β_θ ($\propto W/I^2$) at a given current is, however, not constant, but shows a distinct increase with increasing density.

Comparing our results with available T3-A data, we find that with the sole exception of the radial temperature and density profiles there is a substantial agreement on all more or less directly observable data, but there are some significant differences in the interpretation. In particular, to explain our results, there appears to be no need to invoke anomalous resistivity or anomalous heat conductivity distinct from the anomalous particle loss [7].

ACKNOWLEDGMENT

Our particular thanks are due to Mr. Philip A. Thompson for his constant and invaluable assistance in on-line data analysis with the IBM 1800 computer. We are grateful to Dr. M. B. Gottlieb for his support and encouragement. We also acknowledge interesting discussions with Dr. H. P. Furth and other members of the Plasma Physics Laboratory staff. Many thanks go to the tokamak operating crew under Mr. J. M. Perron.

This work was supported by USAEC Contract AT(30-1)-1238. Use was made of computer facilities supported in part by National Science Foundation Grant NSF-GP579.

REFERENCES

[1] GROVE, D. J., DIMOCK, D. L., HINNOV, E., HOSEA, J. C., JOHNSON, L. C., MESERVEY, E. B., TOLNAS, E. L., IV. European Conference on Controlled Fusion and Plasma Physics, Rome (1970). Princeton University, Plasma Physics Laboratory MATT-813 (1970).

[2] MESERVEY, E. B., DIMOCK, D. L., HOSEA, J. C., JOHNSON, L. C., TOLNAS, E. L., HINNOV, E., Bull. American Physical Society II, 15 (1970) p. 1417.

[3] ABRAMOV, V. A., KUZNETSOV, E. I., KOGAN, V. I., Atomnaya Energiya, 26 (1969), p. 516, (trans.: Soviet Atomic Energy 26, 599 (1969).

[4] ARTSIMOVICH, L. A., BOBROVSKY, G. A., GORBUNOV, E. P., IVANOV, D. P., KIRILOV, V. D., KUZNETSOV, E. I., MIRNOV, S. V., PETROV, M. P., RAZUMOVA, K. A., STRELKOV, V.S., SHCHEGLOV, D. A., Plasma Physics and Controlled Nuclear Fusion Research (Proc. Novosibirsk Conf.). Nuclear Fusion Special Supplement 1969, p. 17.

[5] FORREST, M. J., PEACOCK, N. J., ROBINSON, D. C., SANNIKOV, V. V., WILCOCK, P. D., Culham Laboratory Report R 107 (1970).

[6] ARTSIMOVICH, L. A., BOBROVSKII, G. A., MIRNOV, C. B., RAZUMOVA, K. A., STRELKOV, B. C., Atomnaya Energiya 22 (1967), p. 259. Princeton University Plasma Physics Laboratory MATT-TRANS-35.

[7] ARTSIMOVICH, L. A., ZH. E. T. F. Pis. Red. 13, 101 (1971) (trans.: JETP Letters, 13, 70 (1971).

EFFECT OF NON-AXISYMMETRIC CONFINING FIELDS ON TOKAMAK DISCHARGES

W. STODIEK, K. BOL, H. EUBANK, S. VON GOELER, D.J. GROVE*
Princeton University Plasma Physics Laboratory,
Princeton, New Jersey, United States of America

Abstract

EFFECT OF NON-AXISYMMETRIC CONFINING FIELDS ON TOKAMAK DISCHARGES.

To test the importance of axisymmetry on confinement, the Princeton ST Tokamak facility can provide a local toroidal field inhomogeneity up to ± 30%, approximately equal to the radial variation of the toroidal field strength across the aperture. We have compared discharge characteristics of the "symmetric" and asymmetric cases, respectively, ($\Delta B/B$ = 1.5% and +30%), with the following results: a decrease in energy confinement time of 30% is observed for the asymmetric case, resulting from larger power input due to increased plasma resistivity, and to a lesser extent from a reduction of the amount of stored energy. The confinement time always remains longer than that obtained from C stellarator data assuming Bohm scaling. The plasma resistance increase and the depletion of the energetic tail of the ion distribution, observed for the asymmetric case, are discussed on the basis of single-particle trapping.

1. INTRODUCTION

In this paper we report experimental results obtained on the Princeton ST tokamak [1] concerning the dependence of the energy confinement and single particle trapping effects on the toroidal field symmetry. To test the effect of nonaxisymmetry, the ST tokamak facility can provide a local toroidal field inhomogeneity of up to 30% which is approximately equal to the radial variation of the toroidal field strength across the aperture. This arrangement is also intended to simulate systems such as the C stellarator with straight sections. It was considered important to provide a local increase in field (magnetic mountain) rather than a decrease (valley) because with the former the trapping volume extends over most of the torus. A similar experiment with a magnetic valley on the T3-A tokamak, in which one of the magnetic field coils was shorted, showed little effect on confinement [2].

2. MAGNETIC FIELD CONFIGURATION

The magnetic field inhomogeneity is produced by over or under-powering a set of confining field coils up to ± 60% in current. The resulting large forces restrict the main confining field to 35 kG. In Fig. 1 the variation of field strength on the minor axis is shown as a function of the azimuth angle of the torus. The scale length of this inhomogeneity is about 4 times greater than that of the transition between straight and curved sections of the C stellarator. The magnetic mountain leads to a shift of the field lines toward a smaller major radius at the mountain location. For a 30% field inhomogeneity this shift is about 1.5 cm at the vessel center and 3.0 cm at

* On loan from Westinghouse Research Laboratories, Pittsburgh, Pa.

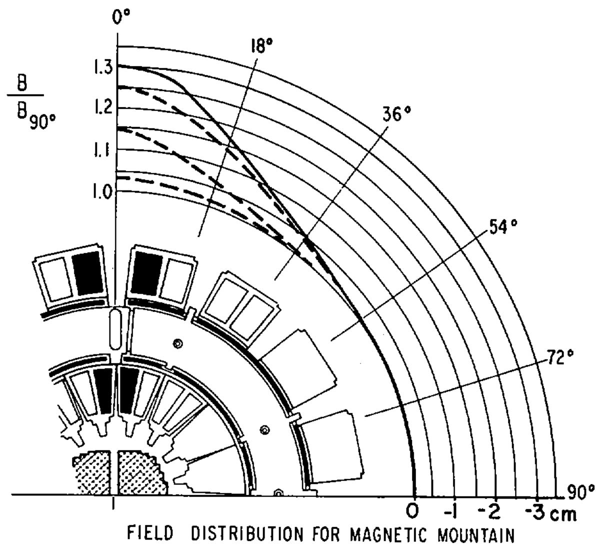

FIG. 1. ST device, location of confining coils and pattern of magnetic field strength varying along the circumference of the machine with the magnetic mountain operative. Dashed curves indicate the shift of the magnetic lines in the midplane of the torus for 97 cm, 109 cm, and 121 cm radius.

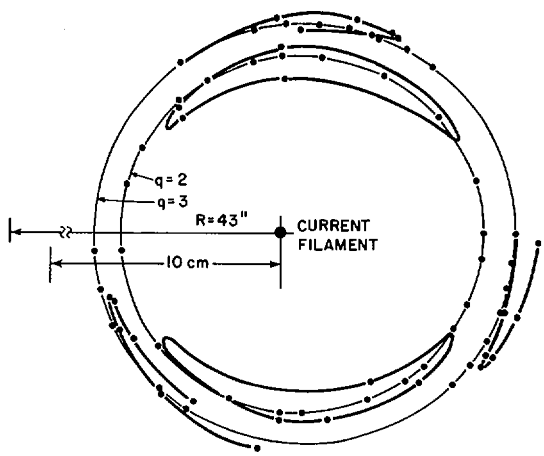

FIG. 2. Cross-section through the magnetic surfaces obtained by combining the actual toroidal field with a simulated plasma current consisting of a filament current located at the "vessel centre". The cross-section is in the unperturbed field section opposite the magnetic mountain. The pattern shown is for 30% magnetic mountain. The smooth surfaces are obtained if the current filament follows the line of force; the island surfaces if the current filament is placed everywhere at a radius of 109 cm. The same smooth surfaces can be obtained by moving the mountain-producing confining field coils outward if the current filament is located at 109 cm radius, so that the current again follows the lines of force.

the plasma edge. Because the current, in first approximation continues to flow along the field lines, this shift spoils the axisymmetric location of the plasma current channel in the copper casing and causes the induction of additional vertical fields [3]. The column as a whole will therefore seek a new equilibrium position which is given by the condition that the average vertical field seen by the plasma is the same as the one seen for the flat field. Since the induced fields are closely proportional to corresponding column shifts, it follows that the displacement of the current channel from the former equilibrium position, averaged around the machine, must also vanish. For a 30% mountain, the new equilibrium in the uniform field region occurs at a major radius about 1 mm greater than for the flat field case. This horizontal displacement requires the current to flow at a slight angle to the field in the vertical plane, but the maximum departure of the column vertically from the midplane is only about 0.5 mm. Measurements of the transverse fields are in rough agreement with these conclusions.

A second problem related to the nonaxisymmetry is the question of the existence of magnetic surfaces free of islands [4]. We have obtained an insight into this problem by computing the surfaces for two cases. In the first, we simulate the plasma current by a filament that follows the line of force which is the vessel axis in the unperturbed region. In this case no island structure was observed for surfaces corresponding to $q = 2$ and $q = 3$. For the second case we require the current filament to follow a true circular path so that in the 30% mountain case the filament deviates from the line of force by 1.5 cm. This case produces the islands shown in Fig. 2; the first case results are also shown for comparison. Since, as noted in the previous section, we expect deviations of the current from the field lines to be less than 1 mm, we have assumed that island formation can be neglected in the interpretation of the experimental results.

3. DISCHARGE CONDITIONS

The discharges investigated are essentially of the same type as described in greater detail in Ref. [5]. It was planned originally to compare the homogeneous field configuration with both the local magnetic mountain and the local magnetic valley configurations, but in the latter case the plasma is very close to the vacuum vessel wall and produces a large influx of neutral gas thus changing the plasma density. Therefore in most of our experiments the homogeneous case was compared with the magnetic mountain case only. The plasma is limited to 12 cm radius by a rail type limiter which allows it to move horizontally without changing its radius as its equilibrium position changes with time. A steady vertical field of less than equilibrium strength (25 G) is used to reduce the plasma shift resulting from the finite conductivity of the copper shell. The confining field was 35 kG and the plasma current 40 to 60 kA. The measurements were carried out late in the discharge when the electron density decay has slowed down and the density and temperature profiles and most other parameters are stationary. At this time the highest electron and ion temperatures are observed and the energy confinement time is the longest. The discharge parameters that were measured are current and voltage; electron density (relative values from Thomson scattering were standarized with microwave interferometer measurements); electron temperature (Thomson scattering); total electron and ion energy (diamagnetic effect);and ion velocity distribution (charge exchange spectrometer).

4. EXPERIMENTAL RESULTS

Experimental results of a high density discharge in deuterium and a low density discharge in hydrogen are summarized in Table I. Deuterium was used in the high density discharge in order to have the neutron production rate as a measure of the high energy tail of the ion velocity distribution. This problem will be discussed in Section 4.3. The density and temperature profiles and the charge exchange temperature measurements are shown in Figs. 3a, 3b, 4a, 5 and 6. Each data point represents a discharge. Although the discharges are very reproducible from shot to shot in all macroscopic respects, the laser scattering data showed a large spread. There is also a systematic asymmetry in the density profile which may have to do with laser window transmission problems. We have, therefore, averaged the left and right side of the temperature and density profiles. The curves drawn through the data points also take into account the relative reliability of the points.

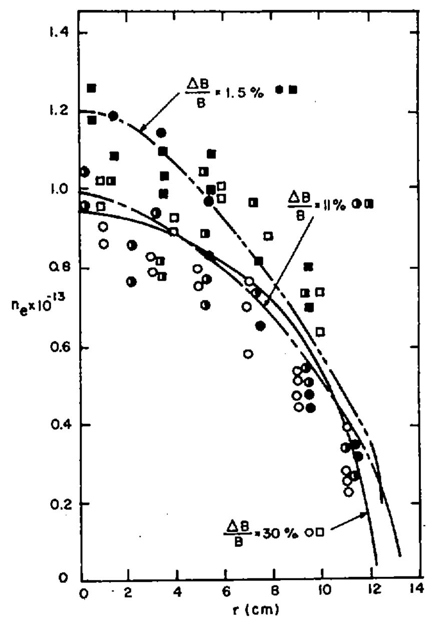

FIG.3a. Density profile for H_2 discharge of 1.0×10^{-4} Torr filling pressure for different field strengths of magnetic mountain: $\Delta B/B = 1.5\%, 11\%, 30\%$. The profiles have been folded over the centre, the circles indicate the half toward larger major radius. We observe that the scattering is of about the same order as the deviation of the different profiles. Time is 40 ms after start of the discharge. The relative density profile is absolutely calibrated by 4 mm microwave interferometer. Confining field 35 kG, plasma current 43 kA, plasma radius 12 cm (rail limiter).

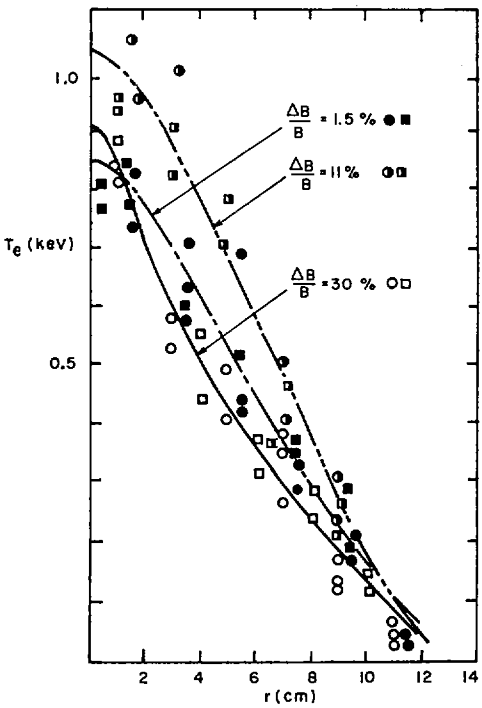

FIG.3b. The corresponding electron temperature profile. The legend of the curves is the same as in Fig.3a.

4.1 Energy confinement

The quantity most pertinent to this experiment is the energy confinement time, defined as $\tau'_E = W/P_{in}$, where W is the kinetic energy stored in the plasma and P_{in} the input power determined from voltage and current. The energy W is determined from measurements of plasma diamagnetism and independently by taking the sum of the ion energy as obtained from charge exchange and the electron energy as found from the Thomson scattering measurements. Comparison of the corresponding values of β_θ (Table I, lines 18 and 19), shows that the two results are in fair agreement.

It is evident from Table I that for a 10% inhomogeneity in field there is no deterioration of discharge conditions. For the larger 30% mountain there is a systematic drop - about 30% - in energy confinement time, the drop coming mostly from a somewhat larger power input and to a lesser extent from a decrease in stored energy. The observed drop in confinement - although quite systematic and probably real - is not larger than the variations observed for different runs under nominally the same conditions.

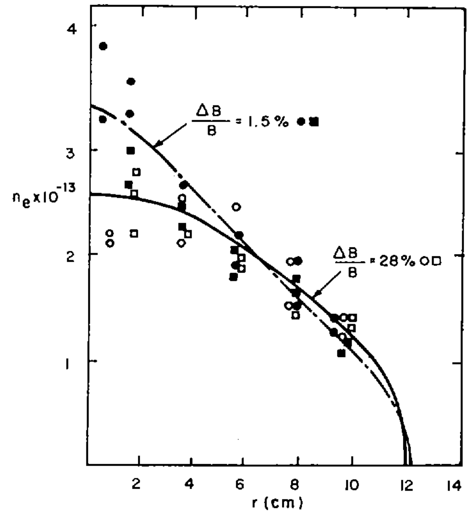

FIG.4a. Density profile for D_2 discharge of 1.4×10^{-4} Torr filling pressure for different field strengths of magnetic mountain: $\Delta B/B$ = 1.5%, 28%. Nomenclature same as in Fig.3a; time 30 ms after start of discharge; absolute calibration with 2 and 4 mm interferometer. Confining field 35 kG; plasma current 56 kA; plasma radius 12 cm (rail limiter).

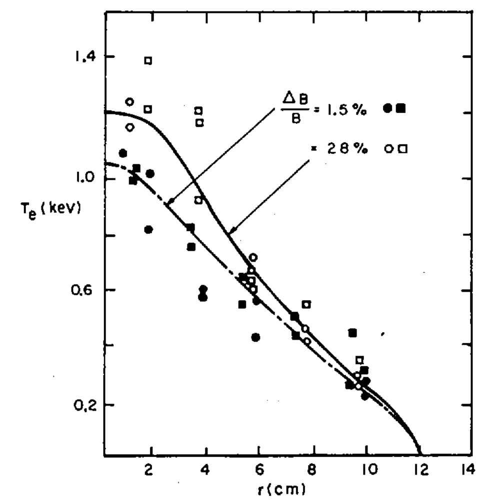

FIG.4b. The corresponding electron temperature profile. The legend of the curves is the same as in Fig.4a.

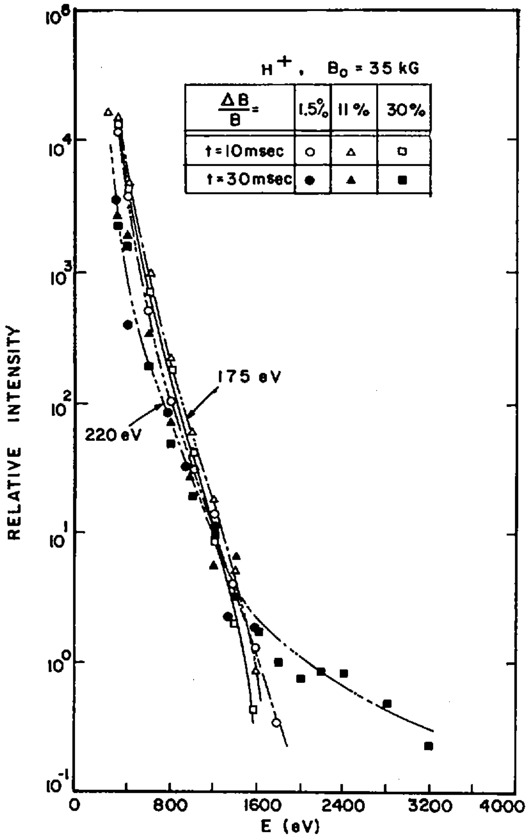

FIG.5. Energy distribution from charge-exchange spectrometer for hydrogen discharge of 1.0×10^{-4} Torr filling pressure: for field strength of magnetic mountain: $\Delta B/B$ = 1.5%, 11%, 30%. Time 10 ms and 30 ms after start of discharge. Confining field 35 kG; plasma current 43 kA; plasma radius 12 cm (rail limiter).

A direct comparison between tokamak and stellarator confinement cannot be made at present, because there exist no stellarator measurements with plasma current and minor radius equal to T-3 or ST. Values of energy confinement time, obtained by extrapolation of the data from Model C to the radius and temperature of ST, using Bohm scaling, are compared with the confinement time in ST in line 21 of Table I. The small effect of asymmetry in the ST makes it unlikely that confinement in stellarators is limited by their inherent field asymmetries. While it is clear that a high degree of symmetry is by no means essential for the attainment of the discharge parameters typical of the ST tokamak, it is also clear that it would be rash to extrapolate this conclusion to other, perhaps less collisional devices, where particle trapping effects, as described in the following sections, play a more dominant role in the confinement.

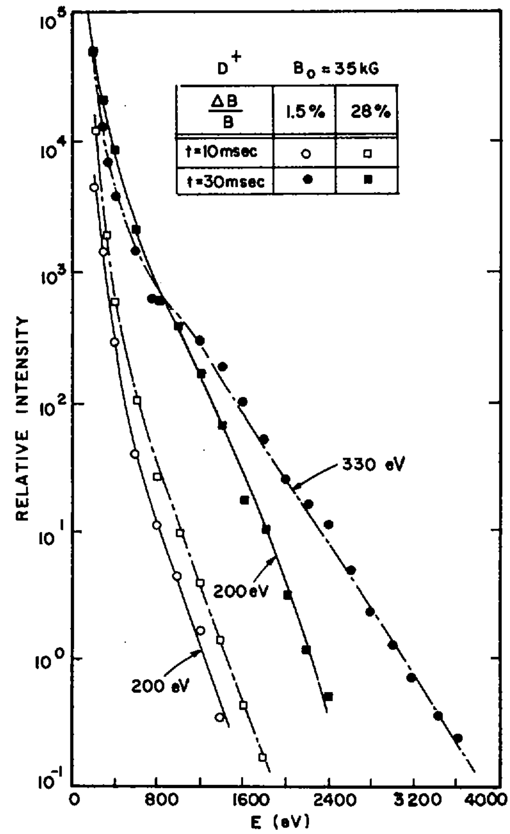

FIG. 6. Energy distribution from charge-exchange spectrometer for 1.4 × 10^{-4} Torr deuterium filling pressure; for different field strength of magnetic mountain: $\Delta B/B$ = 1.5%, 28%. Time 10 ms and 30 ms after start of discharge. Confining field 35 kG; plasma current 56 kA; plasma radius 12 cm (rail limiter).

4.2 Plasma resistivity

Mirror trapping of electrons should cause an increase of the usual Spitzer resistivity value by a factor of approximately $[1 - 1.05(\Delta B/B)^{1/2}]^{-1}$, in the limit of small inhomogeneity $\Delta B/B$, long mean free path, and weak electric field [6]. For the 11% mountain the factor is about 1.5, and for the 30% mountain (for which the approximation is not valid) it is 2 or 3. Trapping in the axisymmetric field leads to a factor 1.2 so that the increases expected would be about 1.2 for the 11% mountain and a doubling for the 30% mountain. Experimentally, increases in resistance are in fact observed, particularly for the high pressure case, as shown in Table I (line 12). The most inconsistent value is for the case with 30% mountain and low pressure. Discharge conditions may of course have been somewhat different in respect to impurity content (effective Z) and plasma noise (anomalous resistance), two aspects that were not investigated. Bremsstrahlung spectra

TABLE I. COMPARISON OF PLASMA PARAMETERS

		HYDROGEN 1×10^{-4} Torr			DEUTERIUM 1.4×10^{-4} Torr	
1.	$\Delta B/B$ [%]	1.5	11.0	30.0	1.5	28
2.	t [msec]	40	40	40	35	35
3.	V_L [V]	2.6	3.0	3.3	3.2	5.0
4.	I_{pl} [kA]	43.8	43.4	42.8	56.6	56.0
5.	P_{in} [kW]	113	130	141	181	280
6.	n_{eo} [10^{13}]	1.2	1.2	1.06	3.5	2.55
7.	$n_{e\,av}$ [10^{13}]	0.65	0.68	0.71	1.53	1.52
8.	T_{eo} [eV]	870	1060	930	1040	1240
9.	$T_{e\,av}$ [eV]	368	444	312	500	550
10.	T_{io} [eV]	200	200	200	330	200
11.	$T_{e\,cond}$ [eV]	393	480	320	413	496
12.	η_{obs}/η_{calc}	3.8	5.8	3.8	4.0	8.5
13.	ℓ_i	1.08	1.12	1.22	1.25	1.25
14.	q at 10.5 cm	4.4	4.4	4.5	4.0	4.0
15.	q at 0.0 cm	1.36	1.35	1.0	1.0	1.0
16.	Δ [cm]	0.88	1.05	1.29	1.1	1.2
17.	Λ	1.46	1.56	1.81	1.35	1.5
18.	β_θ Diamagn	0.31	0.32	0.31	0.43	0.40
19.	$\beta_{\theta\, e+i}$	0.25	0.30	0.21	0.42	0.43
20.	τ'_E [msec]	2.6	2.5	2.0	4.15	2.7
21.	τ'_E/τ_{EC}	11.7	13.5	7.7	25.4	18.2

NOTES:

1. $\Delta B/B$ = ratio of increment in magnetic field at mountain location to unperturbed field.

2. t = time after start of discharge.

3. V_L = loop voltage

4. I_{pl} = plasma current

5. P_{in} = product of voltage and current at constant current.

6. n_{eo} = electron density at plasma axis.

7. $n_{e\,av}$ = average electron density = $\dfrac{\int n_e(r) r\,dr}{\int r dr}$; n_e from Thomson scattering normalized by 4 mm microwave interferometer.

8. T_{eo} = electron temperature on plasma axis; Thomson scattering.

9. $T_{e\,av}$ = average electron temperature = $\dfrac{\int T_e n_e r\,dr}{\int n_e r\,dr}$ from Thomson scattering.

10. T_{io} = ion temperature from charge exchange, assumed to be on axis.

11. $T_{e\,cond} = \left[\dfrac{\int T_e^{3/2} r\,dr}{\int r\,dr}\right]^{2/3}$

12. η_{obs}/η_{calc} = ratio of observed resistivity to resistivity computed from $T_{e\,cond}$.

13. ℓ_i = internal inductance per length, assuming conductivity proportional to $T_e^{3/2}$.

14, 15 $q(r) = \dfrac{r}{R}\,\dfrac{B_o}{B_\theta(r)}$; $B_\theta(r)$ computed assuming conductivity $\sim T_e^{3/2}$.

16. Δ = plasma shift from vessel axis, from measurements of B_θ. [3]

17. $\Lambda = \beta_\theta + \left(\beta_{\|} - \dfrac{\beta_\theta}{2}\right) + \dfrac{\ell_i}{2}$. [3]

18. $\beta_{\theta\,Diamgn} = \dfrac{\phi_{Diamgn}}{\phi_{Paramagn}} = \dfrac{16\pi}{a^2}\,\dfrac{\int_o nk(T_e + T_i) r\,dr}{B_\theta^2(a)}$; from diamagnetic loop.

19. $\beta_{\theta e+i} = \left(1 + \frac{T_{io}}{T_{eo}}\right) \frac{16\pi}{a^2} \frac{\int_o^a n(r)kT_e(r)r\,dr}{B_\theta^2(a)}$, computed from

Thomson scattering profiles of n and T_e. $T_i(r)$ assumed proportional to $T_e(r)$.

20. τ_E' = energy confinement time = stored kinetic energy of ions and electrons/P_{in}. Stored energy computed from average of $\beta_{\theta\ \mathrm{Diamagn}}$ and $\beta_{\theta\ e+i}$.

21. τ'_E/τ_{EC} = energy confinement relative to "Bohm" time.
$\tau_{EC} \equiv .016 \frac{B_o a^2}{T_{e\,av}}$ ms. One half of the so-called Bishop-Hinnov value was used to compute τ_{EC} because energy - and not particle - confinement times are compared.

were measured, however, and with increasing mountain strength these showed for the low pressure case a strong increase in the number of electrons at some tens of kilovolts of energy. At higher pressure the number of such electrons is in general less. Although the data are still somewhat preliminary in that the impurity question needs further work, it appears likely that the rise in resistivity seen at high pressure is the result of trapping, but that in the low pressure, 30% mountain case sufficient current is carried by superthermal electrons to mask the trapping effect and in fact to cause a reduction in relative resistance from the 11% mountain case.

As noted in [5], the factor of 4 difference observed between the resistivity in the axisymmetric field and the Spitzer value computed for Z = 1, can be accounted for by substituting the effective Z of about 3 which is found spectroscopically, and applying the 1.2 trapping factor, obviating the need for an anomaly factor in the axisymmetric case. This may be considered additional justification for attributing increases in resistivity resulting from applying the mountain, to electron trapping effects.

4.3 Effect of ion trapping

Introducing the magnetic mountain should - according to "superbanana" theory - cause a preferential loss of energetic ions if radial electric fields are small. [7] We measure the ion distribution with a charge exchange spectrometer which is aligned perpendicular to the toroidal field. The acceptance angle is 0.2 degree so that only trapped ions are detected. The energy spectra which are shown in Figs. 5 and 6 corresponds to the conditions of Table I. As in the T-3 [8] we observe a low and a high

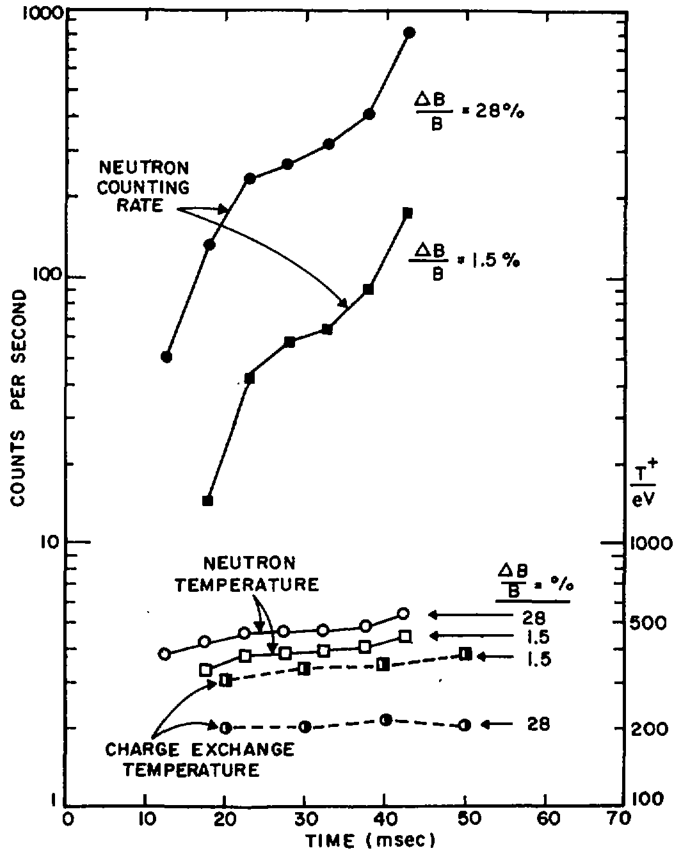

FIG. 7. Neutron counting rates and ion temperatures versus time for the high-density deuterium discharges of Table I for different magnetic field strength of mountain $\Delta B/B = 1.5\%, 28\%$. Filling pressure 1.4×10^{-4} Torr, confining field 35 kG, plasma current 56 kA, plasma radius 12 cm (rail limiter).

temperature component; presumably the low temperature component originates in the outer region of the plasma and is enhanced by the larger neutral concentration there, while the hot component comes from the central region. It is not certain that under the energy loss and heating conditions that exist in these discharges a Maxwellian distribution can be established out to 5-10 times the average energy, where the measurements are made; however, if the slope of the distribution between 1-3 keV is interpreted as a temperature, then we have the following results for the axisymmetric case: in the low density discharge a stationary distribution is already established at 10 ms with an apparent temperature of 175-200 eV; in the high density discharge the temperature continues to increase beyond its value of 200 eV at 10 msec to a final value of 330 eV, measured at 30 msec.

Superbanana losses caused by the introduction of the magnetic mountain should increase the slope of the energy spectra at high energy by partially depleting the distribution tail, which might appear as a lower temperature. Experimentally, just this effect is seen when the mountain is introduced, but only in the high density discharge; there the apparent ion temperature is lowered from about 300 to 200 eV. At low density we observe a low intensity high energy tail in the ion distribution. These discharges show in general a very noisy loop voltage and a large flux of energetic electrons. This high energy ion tail may be similar in origin to the one observed in low density TM-3 discharges, and could be due to runaway ions or ions accelerated in some instability processes. [9] Preliminary measurements of the neutron production show that the neutron flux is higher for the case with 30% mountain than for the flat field case (Fig. 7). The ion temperature deduced from the neutron measurement, assuming that the neutrons are of thermonuclear origin is in fair agreement with the charge exchange temperature for the flat field, but disagrees by a large factor for the mountain. We have begun a detailed investigation which will be reported elsewhere, but we do not expect the main conclusions of this paragraph to be changed.

To the accuracy to which we know the plasma conditions (such as the average Z) the results of the charge exchange measurement are described fairly well by a simple model in which ions with collision times longer than the grad B drift times are not confined at all. This accounts for the absence of an effect by the mountain on the lower temperature distributions, within the accessible energy range, as well as for the presence of a depletion effect on the high density 330 eV temperature distribution. The truncation of the tail will also result in a small reduction of the bulk ion temperature, but the main effect remains the truncation of the tail if we use an effective Z of 3 for estimating the electron-ion as well as the ion-ion collision frequencies.

Even if the bulk of the ions cooled appreciably, the effect of this cooling on the energy confinement time would still be small because the total energy flow from electrons to ions assuming $\bar{Z} = 3$ is only 30 kW or about 15% of the total power input, and the energy stored in the ions is only 30% of the total.

We conclude that for existing ion temperatures the effect of asymmetry on the ion distribution is rather small, but that it can be expected to increase significantly at higher temperatures. A particle detector is now installed to establish more directly that the observed effects are indeed the result of superbanana diffusion, by measuring the flux of energetic ions directly at the top or bottom of the torus depending on the direction of the confining field.

5. SUMMARY

Introducing a magnetic mountain of up to 30% $\Delta B/B$ in the toroidal confining field of the ST tokamak shows qualitatively the expected effects of enhanced electron trapping on the resistivity, and of ion trapping on the tail of the ion velocity distribution. The important result is that the energy confinement time for such a large field deviation from axisymmetry is only slightly reduced for our still rather collisional plasma conditions.

ACKNOWLEDGMENT

We are very much indebted to Mr. G. Sheffield for computing and analyzing the island pattern of Fig. 2 and Drs. Dimock, L. Johnson, and E. Tolnas for carrying out the laser scattering measurements. We are grateful to Dr. H. P. Furth and Dr. M. B. Gottlieb for their support and encouragement. Many thanks go to the tokamak operating crew under Mr. J. M. Perron.

This work was supported by USAEC Contract AT(30-1)-1238. Use was made of computer facilities supported in part by National Science Foundation Grant NSF-GP579.

REFERENCES

[1] GROVE, D. J., DIMOCK, D. L., HINNOV, E., HOSEA J. C. JOHNSON, L. C., MESERVEY, E. B., TOLNAS, E. L. Fourth European Conference on Controlled Fusion and Plasma Physics, Rome (1970). Princeton University, Plasma Physics Laboratory MATT-813 (1970).

[2] KURCHATOV TOKAMAK GROUP, private communication.

[3] SHAFRANOV, V. D., Plasma Physics (Journal of Nuclear Energy Part C) 5, 251 (1963), Atomna Energya 13, 521 (1962), Nuclear Fusion 4, 114 (1964).

[4] MOROZOV, A. J., SOLOV'EV, L. S., JEPT 18, 660 (1960). KERST, D. W., Journal Nuclear Energy Part C, 4, 253 (1962).

[5] DIMOCK, D. et al., Proceedings Fourth Conference on Plasma-physics and Controlled Nuclear Fusion, Madison, 1971, CN 28/C-9.

[6] HINTON, F. R., OBERMAN, C., Nuclear Fusion 9, 319 (1969). ROSENBLUTH, M., HAZELTINE, R., HINTON, F., to be published in Phys. Fluids.

[7] GALEEV, A. A., SAGDEEV, R. Z., JEPT 26, 233 (1968), RUTHERFORD, P. H., Phys. Fluids 13, 482 (1970). FURTH, H. P. AND ROSENBLUTH, M. N., Plasma Physics and Controlled Nuclear Fusion Research (Proc. Novosibirsk Conf.), (Int. Atomic Energy Agency, Vienna, 1969), Vol. I, p. 821.

[8] ARTSIMOVICH, L. A., BOBROVSKY, G. A., GORBUNOV, E. P. IVANOV, D. P., KIRILOV, V. D., KUZNETSOV, E. I., MIRNOV S. V., PETROV, M. P., RAZUMOVA, K. A., STRELKOV, V. S. SHCHEGLOV, D. A., Plasma Physics and Controlled Nuclear Fusion Research (Proc. Novosibirsk Conf.) Nuclear Fusion Special Supplement 1969, p. 17.

[9] BOBROVSKII et al., JEPT 50, 1103 (1970).

DISCUSSION

TO PAPERS IAEA-CN-28/C-9, C-10

L.M. KOVRIZHNYKH: Could you comment on the differences existing between US and Soviet confinement times - density and energy?

E. MESERVEY: I think the main difference between our results and the Soviet results is not in the basic data but in their interpretation for calculating particle containment times. The value we use for the number of ionization events per H_α photon emitted is about 3 or 4 times greater than that which you use. Consequently, we get much shorter particle containment times. I have made a relatively uninformed estimate of this number and have come out with a value of about 20. Hinnor and Johnson have made careful calculations and find values varying between 10 and 20, depending on conditions of temperature and density.

V.S. STRELKOV: In this connection I should like to point out that for comparison of the results obtained with ST and T-3A one must use the same definition of energy confinement time. If τ_E used for ST is the same as that for T-3A then τ_E and τ_p for ST will differ by a factor of 2 and will not correspond. Moreover, if higher ionization coefficients are used for T-3A, i.e. the same as those for ST, there will still be a difference between τ_E and τ_P.

E. MESERVEY: The reason for using τ_E as we define it is that $\tau_P = \tau_E$ can then be easily interpreted and this means that there is no need for anomalous electron heat conductivity on the average. τ_E ($\equiv$ We/P_{in}, i.e. contained electron energy divided by input power) is indeed less by a factor which may vary from 1.5 to 5. As regards particle containment time, τ_P, our main difference is in the value used for ionization events per H_α photon emitted. I think you have used a value 3 or 4 times smaller than ours and you have therefore obtained correspondingly larger values of τ_P. To make a more direct comparison of the ST and T-3A results, we would have to know more about the axial variations of light emission in T-3A, at the limiter and away from the limiter.

L.M. KOVRIZHNYKH: What range of collision frequency was used in determining the effect of asymmetry on lifetime?

E. MESERVEY: For most of our data, the collision frequency falls in the plateau region of neoclassical theory if we use average values of temperature and density and the proper effective ion charge, Z, from impurity concentrations.

V.S. STRELKOV: In the experiments with additional corrugation of the magnetic field there was no observed effect of this corrugation on the ion spectrum. This is not very significant since use was made of a spectrum of ions perpendicular to the direction of the toroidal field. These ions may be trapped in the mirror plugs through the natural corrugation of the field and the additional corrugation may change in the ion spectrum only slightly. It would be interesting to consider the spectrum of ions parallel to the magnetic field.

E. MESERVEY: A very good point. It would be of great interest. We are going to look more parallel to the field, but this is difficult because access to the plasma is limited.

J.L. TUCK: There have been past conferences where everything was referred to Bohm - so many times better or worse than Bohm, how to build reactors with Bohm diffusion, etc. Now, we see from your last diagram that the Tokamak knows nothing of Bohm, and this from Princeton, the laboratory which has done most to promote the concept. Other physicists, besides myself, have felt very doubtful as to whether the concept of Bohm diffusion is physical. Not even Bohm himself founded it with a physical background. May we hope that we shall never hear of Bohm diffusion again?

D. MESERVEY: In the regimes in which we operated the C-stellarator we found a definite B/T_e particle loss rate, which coincided with Bohm's formula over a wide range of conditions. We were at least as sorry as you. If we are operating Tokamaks under conditions that produce different parameter dependences, we should find out from the data what those dependences are. At present I don't think there is firm evidence to support any particular theory.

B. COPPI: Your attainment of a density $n = 10^{14}$ represents an important step. Could you give more data about this experiment?

E. MESERVEY: The electron density of 10^{14} cm^{-3} was obtained at the centre of a helium discharge, where the temperature was about 1 keV; the measured average particle containment time is 20 ms. Applying this 20 msec to the central region, we get $n\tau = 2 \times 10^{12}$ s/cm^3 for electrons, or 1×10^{12} s/cm^3 for the doubly-ionized helium, a very good result.

B. COPPI: In regard to your electrical resistivity measurements I think that, given the large temperature gradient existing in the model ST plasmas, the absence of resistivity anomaly shows satisfactory consistency with existing theories.

D.W. KERST: You refer to the inhomogeneity of the longitudinal magnetic field. If there is a gap in the copper shell, there will be a transverse field effect. Have you considered the influence of local transverse fields?

E. MESERVEY: We have not studied the effect of local transverse fields. We are trying to design coils to put at one of the gaps to make time-varying local fields, but mechanical space problems make this difficult.

ТЕОРИЯ УДЕРЖАНИЯ ПЛАЗМЫ В ТОКАМАКЕ ПРИ БОЛЬШИХ ТЕМПЕРАТУРАХ

А. А. ГАЛЕЕВ, Р. З. САГДЕЕВ
Институт высоких температур
Академии наук СССР, Москва,
Союз Советских Социалистических Республик

Abstract — Аннотация

THE THEORY OF PLASMA CONFINEMENT IN A TOKAMAK AT HIGH TEMPERATURES.

The dynamics of the plasma in a Tokamak are examined in cases where the path lengths are so long that the particles can justifiably be divided into "blocked" and "in-transit" categories. The paper consists of two parts, in the first of which the kinetic equilibrium of the plasma in a Tokamak is considered. In the determination of the equilibrium configuration of the magnetic field account is taken of the "banana" currents of blocked and in-transit particles, which are similar to the Larmor current in a homogeneous magnetic field. Expressions are derived for the values of the diamagnetic signal and the displacement of the column measured during Tokamak experiments. The dynamics of the plasma column are calculated on the basis of equations for the heat balance and particles with neo-classical transfer coefficients. A value is found for the limiting pressure of the plasma in a Tokamak $\beta < (a/R)^{3/2} q^{-2}$ ($\beta = 8\pi p/B_0^2$, where p is the plasma pressure, B_0 is the toroidal magnetic field and q the factor of assurance calculated at the boundary of the plasma column). The limiting pressure is determined from the Kruskal-Shafranov condition for the supplementary current occurring during entrainment of in-transit particles by blocked particles drifting through them. The second part of the paper analyses the remaining difference between the neoclassical and experimental values of the transfer coefficients in dilute plasma. Models are discussed of the anomalous transfer due to low-frequency turbulence of the in-transit and blocked particles.

ТЕОРИЯ УДЕРЖАНИЯ ПЛАЗМЫ В ТОКАМАКЕ ПРИ БОЛЬШИХ ТЕМПЕРАТУРАХ.

Рассматривается динамика плазмы в Токамаке при столь больших длинах пробега, что справедливо разделение частиц на "запертые" и "пролетные". Работа состоит из двух частей. В первой части изучается кинетическое равновесие плазмы в Токамаке. При определении равновесной конфигурации магнитного поля учитываются "банановые" токи запертых и пролетных частиц, аналогичные "ларморовскому" току в однородном магнитном поле. Получены выражения для величин диамагнитного сигнала и смещения шнура, измеряемых в экспериментах на Токамаке. Динамика плазменного шнура рассчитывается на основе уравнений баланса тепла и частиц с неоклассическими коэффициентами переноса. Найдено значение для предельного давления плазмы в Токамаке $\beta < (a/R)^{3/2} q^{-2}$ ($\beta = 8\pi p/B_0^2$, p – давление плазмы, B_0 – тороидальное магнитное поле, q – коэффициент запаса, вычисленный на краю плазменного шнура). Предельное давление определяется из условия Крускала-Шафранова для дополнительного тока, возникающего при увлечении пролетных частиц дрейфующими сквозь них запертыми частицами. Во второй части работы анализируется остающееся различие между "неоклассическими" и экспериментальными значениями коэффициентов переноса в разреженной плазме. Обсуждаются модели аномального переноса из-за низкочастотной турбулентности пролетных и запертых частиц.

ВВЕДЕНИЕ

Неоклассическая теория процессов переноса помогла объяснить потери энергии в плазме, происходящие в Токамаке по ионному каналу [1,2]. Однако электронный поток тепла существенно превышает оценки, дававшиеся неоклассическими формулами. Если это расхождение окажется неустранимым, потребуется построить новую теоретическую модель процессов переноса в Токамаке. Эта модель, очевидно, должна быть гибридом неоклассической ионной и аномальной электронной теорий. Первые попытки найти подходящие для этой цели неустойчивости, приводящие к турбулентным переносам по электронному каналу, показали, что в типичном диапазоне параметров современных Токамаков это сделать не так просто.

В то же время сопротивление плазмы в Токамаке также в несколько раз превышает классическое сопротивление. Поскольку ионно-звуковая неустойчивость для типичных режимов в Токамаке может считаться абсолютно исключенной, в настоящее время трудно найти иные объяснения этой аномалии, кроме предположения о том, что ν_{eff} повышается из-за столкновений электронов с многозарядными ионами примесей.

Учитывая все изложенное выше, нам представляется важным построить такую теоретическую модель переносов в Токамаке, в которой все аномалии связаны с наличием примесей. В разделе 1 показано, как видоизменяются неоклассические формулы коэффициентов переноса при учете столкновений с примесями. Ионный поток тепла в условиях Токамака практически не меняется, так как ионная теплопроводность должна соответствовать так называемому режиму "плато", в котором исчезает зависимость от частоты столкновений. Однако электроны, температура которых достаточно высока, оказываются в "банановом" режиме неоклассической теории. Электронный поток тепла оказывается пропорциональным ν_{eff}. Эффективный коэффициент электронной температуропроводности дается выражением:

$$\chi_e \approx 5\epsilon^{1/2}\nu_{eff}\, r_{e\theta}^2$$

(Л.А. Арцимович из анализа экспериментальных данных дает эмпирическую зависимость [3]: $\chi_e \cong 5\nu_{eff}\, r_{e\theta}^2$).

Предельное значение отношения давления плазмы к давлению тороидального магнитного поля $\beta_J = 8\pi p/B_\theta^2$ оказывается порядка $\epsilon^{-1/4}$ ($\epsilon = r/R$) и не зависит от ν_{eff} (так как при джоулевом нагреве выделение тепла и теплоотвод одинаково пропорциональны ν_{eff}). В современных Токамаках, использующих джоулев нагрев, этот потолок практически уже достигнут.

В разделе 2 обсуждается вопрос об абсолютном верхнем пределе β в неоклассическом Токамаке, который нельзя превзойти при любом методе нагрева. Этот предел связан с существованием в "банановом" режиме дополнительного электрического тока.

В разделе 3 обсуждаются низкочастотные неустойчивости неоклассического Токамака, связанные с наличием примесей.

1. НЕОКЛАССИЧЕСКИЙ ТОКАМАК С ПРИМЕСЯМИ

Неоклассические коэффициенты переноса были рассчитаны нами для случая двухкомпонентной плазмы, состоящей из электронов и однозарядных ионов [2]. Поэтому полученные коэффициенты нельзя сравнивать с коэффициентами, полученными при проведении эксперимента на установках Токамак, плазма которых содержит довольно значительный процент многозарядных примесных ионов [1]. Хотя в экспериментальных условиях частоты соударений электронов с ионами плазмы и ионами примесей оказываются сравнимыми, мы, чтобы сделать приведенные формулы более обозримыми, будем пренебрегать соударениями с ионами плазмы.

Следует различать "банановый" режим и режим "плато" в процессах переноса. Коэффициенты переноса в "банановом" режиме уменьшаются с уменьшением частоты соударений, а в режиме "плато" – совсем не содержат соударений. Причем оказывается, что численные коэффициенты в выражении для диффузии частиц, вместе с тем и для полного потока тепла электронов, зависят от того, в каком режиме находятся ионы. В дальнейшем мы сравним наши численные коэффициенты с эмпирическими, полученными на установке Т-3. Поэтому в выборе режимов мы будем ориентироваться на параметры плазмы в установке Т-3. В частности, можно считать, что в использованном на этой установке интервале изменения параметров плазмы ионы всегда находятся в режиме "плато", тогда как электроны можно отнести к "банановому" режиму. Интерполяционные формулы для коэффициентов температуропроводности ионов и электронов удобно записать так, чтобы знаменатель в условиях эксперимента лишь незначительно подправлял их значения соответственно в режиме "плато" и в "банановом" режиме:

$$\chi_i \approx \frac{1{,}3qr_i^2 v_{Ti}/R}{1+1{,}9v_{Ti}\,\nu_{i+}^{-1}\,\epsilon^{3/2}/qR} \tag{1}$$

$$\chi_e \approx \frac{3{,}1\,\epsilon^{1/2}\nu_{eff}r_{e\theta}^2(1+5/3\tau)}{1+0{,}68\,\dfrac{1+5/3\tau}{1+5/7\tau}\,\dfrac{qR}{v_{Te}\nu_{eff}^{-1}}\,\epsilon^{-3/2}} \tag{2}$$

где $\epsilon^{-1} = R/r$ – тороидальное отношение (см. рис. 1),

$q = B_{0z}\,r/B_{0\theta}R$ – коэффициент запаса устойчивости,

$\tau = T_{0e}/T_{0i}$, $v_{Tj} = \sqrt{2T_j/m_j}$ – тепловая скорость частиц сорта j,

r_j – ларморовский радиус в тороидальном магнитном поле B_{0z},

$r_{j\theta} = q\epsilon^{-1}r_j$ – то же в поле собственного тока $B_{0\theta}$,

$\nu_{j+} = 16\,\pi^{1/2}n_+e^4Z^2\ln\Lambda/3m_j^2v_{Tj}^3$ – частота соударений частиц с примесями.

Эффективная частота соударений электронов с примесями определена таким образом, чтобы проводимость плазмы выражалась через нее без дополнительных коэффициентов:

$$\sigma = \frac{ne^2}{m_e\nu_{eff}} \qquad \nu_{eff} = 0{,}29\nu_{e+} \tag{3}$$

В поток тепла электронов дают вклад как диффузия, так и электронная теплопроводность. При суммировании вкладов был использован экспериментально обнаруженный факт подобия профилей плотности и температур частиц [4]. Кроме того, мы считали, что коэффициент теплопроводности ионов численно больше коэффициента диффузии электронов[1]. В соответствии с этим предположением условие баланса импульса ионов и электронов в режиме стационарной диффузии определяет следующую связь между величиной радиального электрического поля $\Phi_0(r)$ и макроскопической скоростью ионов вдоль тора $U_\parallel^i$ [5]:

$$\frac{c}{B_{0\theta}}\frac{d\Phi_0}{dr} = U_{*i} - U_\parallel^i \qquad U_{*i} = \frac{cT_i}{eB_\theta}\left[\frac{d\ln n}{dr} + \frac{3}{2}\frac{d\ln T_i}{dr}\right] \tag{4}$$

[1] В неизотермической плазме поток тепла электронов при этом может оказаться больше, чем поток тепла ионов.

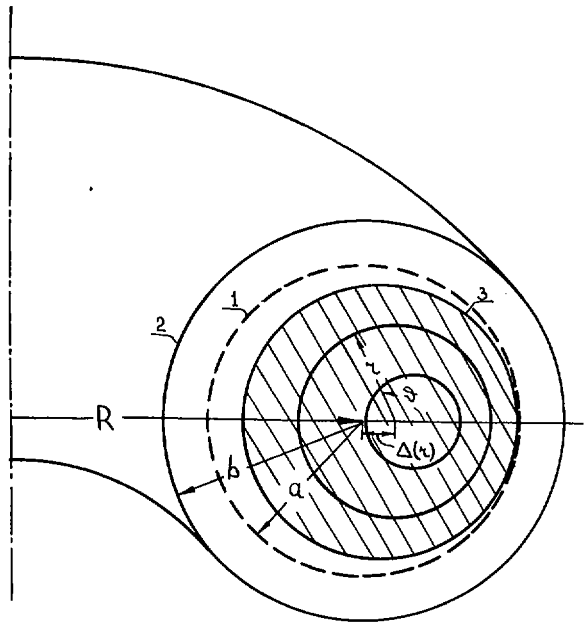

Рис. 1. Сечение тороидальной камеры Токамак:
1 — диафрагма, 2 — внешняя камера, 3 — магнитная поверхность, ограничивающая плазменный шнур.

Полученное соотношение, вообще говоря, не определяет однозначно величину электрического поля, что соответствует факту амбиполярности стационарной диффузии, независимо от этой величины. В тех случаях, когда ловушка заполняется покоящейся плазмой, мы можем допустить макроскопическую скорость ионов равной нулю и найти электрическое поле из соотношения (4). Однако диффузия плазмы является амбиполярной лишь приближенно, и поэтому в дальнейшем величина электрического поля будет медленно меняться из-за потери момента вращения плазмы вследствие вязкости, трения о нейтралы или эффектов конечного ларморовского радиуса, рассмотренных Т. Стрингером [6].

Помимо переноса тепла за счет диффузии и теплопроводности в плазменном шнуре с собственным током имеется перенос тепла вследствие пинчевания "запертых" частиц [7,8]. Поток тепла из-за этого эффекта направлен внутрь:

$$q_e = -\frac{1{,}75\epsilon^{1/2}\,\nu_{\mathrm{eff}}\,r_{e\theta}^{2}}{1+2{,}2\,\dfrac{qR}{v_{Te}\,\nu_{\mathrm{eff}}^{-1}}\,\epsilon^{-3/2}}\,\frac{B_{0\theta}}{8\pi r}\,\frac{d}{dr}\,rB_{0\theta} \qquad (5)$$

Если ориентироваться на условия в установке Т-3, то пинчеванием можно пренебречь.

Найдем, далее, предельное значение давления плазмы, достижимое в Токамаке с джоулевым нагревом. Рассмотрим сначала случай, когда теплоотвод происходит главным образом через электронный канал, и поэтому неустойчивости перегревного типа оказываются застабилизированными [9]. Уравнения теплового баланса по формуле совпадают с исследованными в работе [9], и поэтому мы можем воспользоваться полученными там результатами. В "банановом" режиме для электронов отношение введенных в этой работе параметров λ_b, μ_b выражается только через отношение давления плазмы к давлению магнитного поля:

$$\frac{\mu_b}{\lambda_b} = \frac{16\pi^2 \sigma \chi_e n_0 T_{0e}}{c^2 B_{\theta a}^2} \approx 1{,}6 \, \frac{\epsilon_a^{1/2} \beta_J^2}{(1+1/\tau)^2} (1+5/3\tau) \tag{6}$$

Подставляя сюда численные значения коэффициентов $\mu_b = 3$, $\lambda_b = 0{,}7$ и полагая, кроме того, $\tau \gg 1$, получаем для предельного значения:

$$\beta_J = \frac{8\pi p(0)}{B_\theta^2(a)} \approx 1{,}6 \left(\frac{R}{a}\right)^{1/4} \tag{7}$$

Величина предельного давления уменьшается, если часть потерь происходит по ионному каналу.

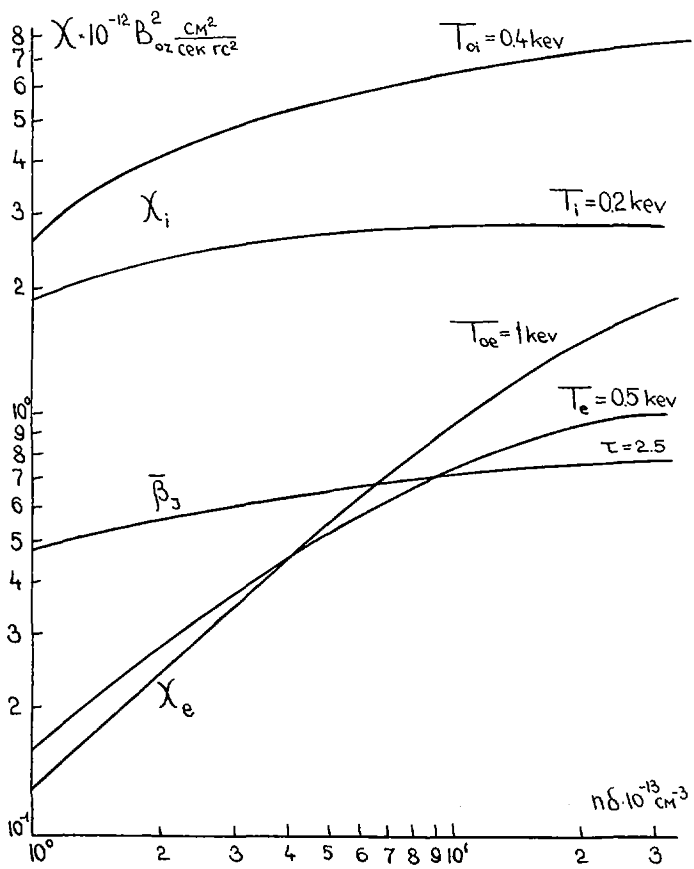

Рис. 2. Неоклассические коэффициенты переноса и предельное давление.

Теоретические значения коэффициентов переноса неоднократно сравнивались с экспериментом на различных установках. Плазма в Токамаке Т-3 лучше всего поддается неоклассическому описанию. Так, нагрев ионов в установке Т-3 может быть обеспечен за счет передачи энергии от электронов при кулоновских соударениях [10], а потери энергии могут быть объяснены неоклассической формулой для ионной теплопроводности, вычисленной на "плато" [11]. Теоретическое значение коэффициента электронной температуропроводности отличается от эмпирической формулы работы [3] лишь на корень из тороидального отношения. Далее, мы предположим, что "аномальное" сопротивление целиком обязано соударениям электронов с примесями, и в соответствии с этим введем коэффициент аномальности сопротивления:

$$\delta = \sigma_{sp}/\sigma_{eff} = 0{,}57 n_+ Z^2/n \tag{8}$$

При значениях $\delta \sim 3 \div 5$ уход тепла по электронному каналу в условиях установки Т-3 может достигать 30% от полных потерь (см. рис. 2, где изображена зависимость коэффициентов температуропроводности от плотности частиц для различных значений их температуры). Величина равновесного значения давления плазмы при этом оказывается зависящей от распределения потерь между электронным и ионным каналом. Численные значения этой величины рассчитаны для нескольких значений параметра τ и приведены на рис. 2.

2. РАВНОВЕСИЕ РАЗРЕЖЕННОГО ПЛАЗМЕННОГО ШНУРА В ТОКАМАКЕ И ПРЕДЕЛЬНОЕ ДАВЛЕНИЕ ПЛАЗМЫ

Равновесие плазменного шнура в Токамаке в модели идеальной магнитной гидродинамики (МГД) к настоящему времени изучено довольно детально, а результаты исследований изложены в ряде обзоров [12,13]. В области высоких температур плазмы, где становится существенным разделение частиц на "запертые" и "пролетные", МГД не работает. Поэтому мы лишь напомним хорошо известные результаты МГД-теории, а более подробно остановимся на тех изменениях, которые вносит учет "запертых" частиц.

Следуя В. Д. Шафранову, мы будем пользоваться системой координат, изображенной на рис. 1. При большом тороидальном отношении магнитное поле с точностью до малых, порядка $\epsilon = r/R$, равно:

$$B_z = B_{0z}(1 - \epsilon \cos\theta) \qquad B_\theta = B_{0\theta}(1 - \Lambda(r)\cos\theta) \tag{9}$$

Параметр $\Lambda(r)$, учитывающий искажение магнитного поля токами в проводящей оболочке, нетрудно выразить через распределение давления плазмы и плотности тока, если воспользоваться уравнением Максвелла:

$$\mathrm{rot}\,\vec{B} = \frac{4\pi}{c}\,\vec{I}\,(\nabla p) \tag{10}$$

Функциональная зависимость тока в плазме от градиентов давления считается известной. В идеальной магнитной гидродинамике последняя определяется уравнением баланса сил:

$$\nabla p = \frac{1}{c}\,\vec{I} \times \vec{B} \tag{11}$$

Пренебрегая сначала тороидальностью системы, из (10)-(11) получаем уравнение равновесия плазменного шнура по малому радиусу:

$$\frac{1}{c}\, I_{0\theta}(r) B_{0z} = \frac{dp}{dr} + \frac{B_{0\theta}}{4\pi r}\,\frac{d}{dr}\, r B_{0\theta} \tag{12}$$

где ларморовский ток $I_{0\theta}(r)$ зависит только от магнитной поверхности. В экспериментах на Токамаке с помощью этого уравнения связывают измеряемую величину изменения магнитного потока продольного поля $\delta\Phi$ при возникновении разряда со средним давлением плазмы $\bar{p}$, полным током J и токовым радиусом шнура a:

$$\delta\Phi = \frac{2\pi}{B_{0z}}\left(\frac{J^2}{c^2} - 2\pi a^2 p\right) \tag{13}$$

Для вычисления ротора магнитного поля с точностью до величины порядка ϵ следует воспользоваться значениями метрического тензора, приведенного в обзоре [13]. В этом приближении уравнение Максвелла можно записать в виде:

$$-\left[\frac{1}{rB_{0\theta}}\,\frac{\partial}{\partial r}\, r B_{0\theta}^2(\Lambda(r) - \epsilon) + \frac{B_{0\theta}}{R}\right]\operatorname{Cos}\theta = \frac{4\pi}{c}\, I_{\sim}(r,\theta) \tag{14}$$

Если подставить в правую часть ток Пфирша-Шлютера, необходимый для замыкания тороидального дрейфа частиц,

$$I_{ps} = -\frac{2c}{B_{0\theta}}\,\epsilon\frac{dp}{dr}\,\operatorname{Cos}\theta \tag{15}$$

то уравнение (14) совпадает с уравнением, полученным В. Д. Шафрановым. Величина смещения плазменного шнура $\Delta(r)$ связана с параметром Λ следующим соотношением:

$$\Delta(r) = -\int_r^b \left[\Lambda(r) - \frac{r}{R}\right] dr \tag{16}$$

где: b — радиус внешней камеры.

В разреженной плазме, кроме ларморовского тока, появляется "банановый" ток. В отличие от ларморовского тока, текущего строго поперек магнитного поля, "банановый" ток направлен вдоль силовых линий. Величина тока собственно запертых частиц равна произведению разности числа частиц, охватываемых соседними траекториями частиц, $(d\delta n_t/dr)\,\Delta r_t$ и скорости $\Delta v_{\parallel} \sim \epsilon^{1/2} v_T$ (см. рис. 3). Воспользовавшись для смещения запертых частиц от магнитной поверхности известной оценкой $\Delta r_t \sim r_\theta \epsilon^{1/2}$, получаем:

$$I_{bt} \approx -\epsilon^{3/2}\,\frac{c}{B_{0\theta}}\,\frac{dp}{dr}$$

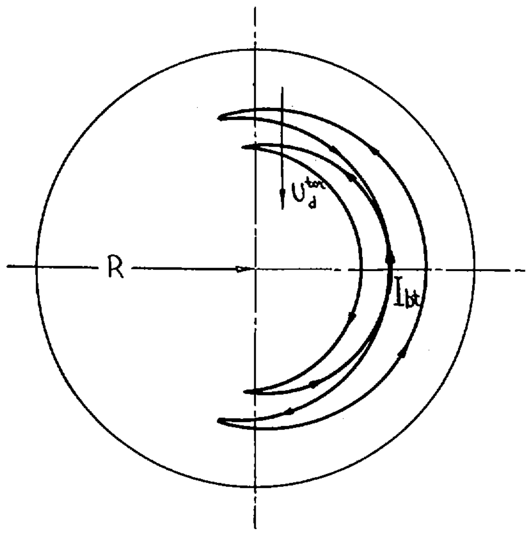

Рис. 3. Соседние траектории "запертых" частиц в плоскости (r, θ).

Видим, что эта величина меньше, чем ток Пфирша-Шлютера. Однако ввиду большой частоты соударений запертых электронов с пролетными, сила трения между ними настолько велика, что запертые электроны увлекают за собой огромную массу пролетных электронов и создают гораздо больший ток. Величину последнего находим из баланса сил трения, действующих на пролетные электроны со стороны запертых электронов и всех ионов:

$$\nu_{ei}\, m_e\, I_b \approx \frac{\nu_{ee}}{\epsilon}\, m_e I_{bt}$$

где ν_{ei} и ν_{ee} – частоты электрон-ионных и электрон-электронных соударений, соответственно. Эта оценка хорошо согласуется с точными расчетами [5,7]. Если принять во внимание экспериментально обнаруженный закон подобия профилей плотности и температур [4] и, кроме того, считать плазму изотермической, то дополнительный ток может быть выражен через градиент полного давления:

$$I_b = 0{,}33\,\epsilon^{1/2} \frac{c}{B_{0\theta}}\, \frac{dp}{dr} \tag{17}$$

Из рассмотрения рис. 3 может создаться впечатление, что "банановый" ток имеет переменную по магнитной поверхности составляющую вследствие явной асимметрии внешнего и внутреннего обвода тора для запертых частиц. Однако, хотя сам по себе "банановый" ток запертых частиц действительно имеет максимум на внешней поверхности тора, тем не менее, при учете тока "медленнопролетных" частиц переменная составляющая полного тока отличается от тока Пфирша-Шлютера лишь на величину порядка ϵ (а не $\epsilon^{1/2}$, как это было бы, если бы "банановый" ток запертых частиц не сокращался с током медленнопролетных частиц). Имеющаяся неоднородность силы трения пролетных частиц о запертые частицы в горячей плазме также не приводит к неоднородному по магнитной поверхности току электронов, а компенсируется за счет свободного перетекания пролетных электронов вдоль силовых линий магнитного поля и установления Больцмановского распределения в эффективном "потенциале".

Составляющие дополнительного тока по малому и большому азимутам следует рассматривать раздельно, так как они входят в существенно различные условия удержания плазмы в Токамаке. Составляющая "бананового" тока по малому азимуту соответствует парамагнитному увеличению магнитного потока и вычитается из диамагнитного тока частиц. В результате несколько изменяется выражение для $\delta\Phi$ (ср. с (13)):

$$\delta\Phi = \frac{2\pi}{B_{0z}}\left(\frac{J^2}{c^2} - 2\pi a^2\bar{p}\,[1-0{,}33\,\epsilon^{1/2}]\right) \tag{18}$$

Использование соотношения (13), таким образом, приводит к систематической ошибке порядка десяти-двадцати процентов при экспериментальном определении параметров плазмы и величины смещения шнура. Более существенным наличие дополнительного тока оказывается для Токамака без омического тока. Прежде всего, в отсутствие омического тока в горячей плазме обнаруженный нами дополнительный ток обеспечивает вращательное преобразование магнитного поля и, следовательно, равновесие плазмы. Поэтому кажется, что если воспользоваться подходящим методом нагрева (напр., адиабатическим сжатием плазмы по малому и большому радиусу, как это было предложено Л. А. Арцимовичем), то можно достичь значений β_J более высоких, чем в Токамаке с джоулевым нагревом. На самом деле, выигрыш в величине β_J получается небольшим, так как увеличение давления плазмы и вместе с этим дополнительного тока приводит к нарушению критерия Крускала-Шафранова:

$$q = \frac{B_{0z}\,r}{B_{0\theta}\,R} \tag{19}$$

где магнитное поле $B_{0\theta}$ теперь вычисляется по величине дополнительного тока I_b. Численное значение величины β, получающееся из подстановки в этот критерий, зависит от деталей распределения давления плазмы по сечению шнура [14]. В случае изотермической плазмы с подобными профилями плотности и температур, а также с однородным по сечению шнура током уравнение Максвелла (10) дает следующий профиль давления плазмы, совместимый с наложенными условиями:

$$2\pi p(r)\left(\frac{a}{R}\right)^{1/2} \approx B_{\theta a}^2\left[1-\left(\frac{r}{a}\right)^{3/2}\right] \qquad B_{0\theta} = B_{\theta a}\cdot\frac{r}{a} \tag{20}$$

Предельное давление плазмы при этом есть

$$\beta = \frac{8\pi p(0)}{B_{0z}^2} \approx 4\left(\frac{a}{R}\right)^{3/2} q^{-2} \tag{21}$$

Интересно отдельно рассмотреть также случай почти однородной плотности по сечению шнура. Он может реализоваться в установках, где плазма касается стенок или диафрагмы и вылетающие из стенок ионы охлаждают края плазмы, не уменьшая сильно плотности частиц. В этом случае дополнительный ток направлен в противоположную сторону омическому току и предел на давление плазмы накладывает не критерий устойчивости, а условие наличия равновесия. Ограничиваясь опять-таки случаем равномерного рапределения тока по сечению шнура, находим, что предельное давление вдвое меньше значения [21].

3. ВОЗМОЖНЫЕ АНОМАЛИИ В ПОВЕДЕНИИ ПЛАЗМЫ В ТОКАМАКЕ

Плазму в установках Токамак только весьма приближенно можно рассматривать как термодинамически равновесную. Так, обнаруженное на установке ТМ-3 большое аномальное сопротивление не может быть объяснено наличием примесей и, вероятнее всего, связано с развитием мелкомасштабной турбулентности [15]. Естественно, что наличие в плазме турбулентного движения сказывается как на величине коэффициентов переноса, так и на величине равновесного давления плазмы.

Ионно-звуковая турбулентность разреженной плазмы увеличивает эффективную частоту соударений электронов с ионами. Для оценки коэффициентов переноса достаточно подставить вместо кулоновской частоты соударений эффективную. В случае частых соударений с турбулентными пульсациями теплопроводность электронов переходит в режим "плато" и перестает расти с дальнейшим увеличением сопротивления. В то же время джоулев нагрев непрерывно увеличивается. Это приводит к тому, что турбулентный перенос тепла достаточен для теплоотвода лишь при значениях давления, больших ранее найденного в разделе 1. Поэтому при использовании в Токамаке турбулентного нагрева величина равновесного давления оказывается выше:

$$\beta_J \sim \left(\frac{R}{a}\right)^{1/4} \left[qR\epsilon^{-3/2}/v_{Te}\nu_{eff}^{-1}\right]^{1/2} \tag{22}$$

В заключение мы хотели бы обратить внимание на явление потери равновесия при касании шнура загрязненной диафрагмы, которое в экспериментальных условиях проявляется в виде самопроизвольных выбросов шнура на стенки камеры [16].

Физика этого явления такова. Горячий плазменный шнур смещается к внешнему обводу тора и касается диафрагмы. Ионы плазмы бомбардируют поверхность диафрагмы и распыляют адсорбированные на ней атомы примесей. Последние летят в плазму и ионизируются под действием соударений с электронами. Ионизованные холодные примеси увлекаются затем "банановым" током запертых ионов плазмы, что приводит к появлению дополнительного примесного тока. Смещение шнура продолжает расти, если этот ток больше тока, наводимого в стенках внешней камеры, из-за приближения шнура с током к стенке.

Описанное явление может быть названо примесной неустойчивостью шнура. Для его расчета можно использовать приведенное в разделе 2 уравнение для величины смещения шнура (14), линеаризованное относительно бесконечно малой величины смещения:

$$-\frac{1}{rB_{0\theta}}\frac{\partial}{\partial r}rB_{0\theta}^{2}\frac{\partial\Delta_1}{\partial r}\,\mathrm{Cos}\,\theta=\frac{4\pi}{c}\left(j_{\parallel e}+j_{\parallel +}\right)_{\sim} \tag{23}$$

$$\left.\frac{d\Delta_1}{\partial r}\right|_{r=0}=0 \qquad \Delta_1(b)=0$$

Здесь $j_{\parallel +}$ — ток примесей, а $j_{\parallel e}$ — электронный ток, наводимый в плазме при появлении тока примесей. Эффект скинирования примесного тока электронами учитывается путем включения в рассмотрение индукционного электрического поля $E_{\parallel\sim}$:

$$\left[\frac{1}{r}\frac{\partial}{\partial r}r\frac{\partial}{\partial r}+\frac{1}{r^2}\frac{\partial^2}{\partial\theta^2}\right]E_{\parallel\sim}=\frac{4\pi}{c^2}\frac{\partial}{\partial t}\left(j_{\parallel e}+j_{\parallel +}\right)_{\sim} \tag{24}$$

$$j_{\parallel e\sim}=\sigma E_{\parallel\sim}$$

$$E_{\parallel\sim}\big|_{r=0}=E_{\parallel\sim}\big|_{r=b}=0 \tag{25}$$

Для вычисления тока примесей нам нужно найти относительную скорость примесей и ионов, а также плотность примесей. Если примеси впрыскиваются в первоначально чистый разряд, то их можно рассматривать как пробные частицы. Относительная скорость примесей и ионов в этом случае определяется из баланса сил трения примесей о пролетные и запертые ионы [2] :

$$0=-\alpha_E^{+}m_i\nu_{+i}w_{\parallel\sim}+\alpha_{+i}\epsilon^{1/2}m_i\nu_{+i}(\gamma-1)\frac{c}{eB_\theta}\nabla T_i\,\mathrm{Cos}\,\theta \tag{26}$$

где численные коэффициенты α_E^{+}, α_{+i} и γ вычисляются в работах [2,17]:

$$\alpha_E^{+}=0{,}29 \qquad \alpha_{+i}=0{,}70 \qquad \gamma=1{,}33$$

При вычислении плотности распыленных примесей следует иметь в виду, что длина свободного пробега атомов примеси относительно ионизации электронами плазмы значительно меньше радиуса плазменного шнура. Поэтому примеси занимают лишь тонкий слой вблизи диафрагмы, а их число связано с количеством бомбардирующих диафрагму ионов плазмы простым соотношением:

$$n_{1+}(r,t)=S(T_{ia})\,n_a\,\delta(r-a)\Delta_{1a}(t) \tag{27}$$

Здесь индекс (а) указывает на то, что значения соответствующих величин вычислены на радиусе $r=a$; $S(T_{ia})$ — коэффициент распыления атомов примесей, адсорбированных на поверхности и захваченных в кристаллическую решетку вещества диафрагмы.

[2] Сила трения примесей о запертые ионы может быть оценена по величине "бананового" тока запертых ионов. Вклад от градиентов давления ионов в "банановый" ток оказывается малым при установлении баланса импульса ионов и электронов [5], и поэтому градиент давления не входит в силу трения.

Примесный ток связан с величиной относительной скорости простым соотношением:

$$j_{\parallel+\sim} = m_+ n_{1+}\left(\frac{e_+}{m_+} - \frac{e_i}{m_i}\right) w_{\parallel\sim} \tag{28}$$

В случае равномерного распределения тока по сечению шнура система линеаризованных уравнений решается в терминах функций Бесселя. Соответствующее дисперсионное уравнение для инкремента нарастания возмущений ω имеет вид:

$$1 = -\frac{4\pi a n_a \nabla T_{ia}}{B_{\theta a}^2}\frac{\alpha_{+i}(\gamma-1)}{\alpha_E^+}\epsilon^{1/2}\sum_{(+)} S_+(T_{ia})\frac{m_+}{m_i}\left(2\frac{b^2}{a^2}-1\right)$$

$$\times I_1(\sqrt{\omega\tau_s})\left[K_1(\sqrt{\omega\tau_s}) - \frac{K_1\left(\frac{b}{a}\sqrt{\omega\tau_s}\right)}{I_1\left(\frac{b}{a}\sqrt{\omega\tau_s}\right)} I_1(\sqrt{\omega\tau_s})\right] \tag{29}$$

Здесь $\tau_s = 4\pi\sigma a^2/c^2$ – время скинирования тока,

$I_1(x)$, $K_1(x)$ – модифицированные функции Бесселя.

Кроме того, в дисперсионном уравнении проведено суммирование по всем сортам примесей. В рассмотренном анализе мы пренебрегли стабилизирующим влиянием сброса части горячей плазмы на диафрагму, в результате которого происходит облегчение плазменного шнура и он стремится всплыть в эффективном поле тяжести внутрь камеры. Чтобы количественно учесть этот эффект, в уравнениях Максвелла к возмущению примесного тока следует прибавить возмущение тока Пфирша-Шлютера из-за сброса плазмы на диафрагму. В случае подобных профилей плотности и температуры это приводит к изменению правой части уравнения (29) на множитель:

$$1 + j_{ps}^{(1)}/j_{\parallel+}^{(1)} \approx 1 - \frac{1,25\epsilon^{1/2}}{S_+\frac{m_+}{m_i}}\left(1 + \frac{T_{ea}}{T_{ia}}\right) \tag{30}$$

который существенен для определения порогового значения коэффициента распыления. Ограничиваясь для конкретности геометрическими параметрами установки ТМ-3 ($\epsilon = 0,2$; $b/a = 3/2$) и воспользовавшись при вычислениях найденным нами в разделе 1 профилем давления горячей плазмы в случае однородного тока, из уравнения (29) с учетом высказанного выше замечания находим пороговое значение величины S_+ :

$$S_+(T_{ia}) > 2,9\frac{m_i}{m_+} \tag{31}$$

Экспериментальные данные по коэффициентам распыления поверхностей металла легкими ионами весьма немногочисленны. Тем не менее, можно утверждать, что уже сам вес распыленного материала диафрагмы при энергиях ионов дейтерия порядка 1 кэв может превышать указанный выше предел (напр., для серебра $S_+ = 0,1$ [18]). Если же поверхность металла загрязнена чужеродными атомами, как это имеет место в экспериментах, то распыление происходит еще интенсивнее.

Таким образом, при плохих условиях разряда (касание загрязненной диафрагмы) количество распыляемых примесей может оказаться намного больше допустимого. В этом случае критерий устойчивости накладывает сильное ограничение на давление плазмы, устойчиво удерживаемой в Токамаке. При нарушении критерия устойчивости плазменный шнур выбрасывается на стенки камеры за скиновое время.

ЛИТЕРАТУРА

[1] АРЦИМОВИЧ, Л.А., "Замкнутые плазменные конфигурации". Наука, М., 1969.
[2] ГАЛЕЕВ, А.А., САГДЕЕВ, Р.З., ЖЭТФ 53 2 (1967) 348.
[3] АРЦИМОВИЧ, Л.А., Письма в ЖЭТФ 13 2 (1971) 103.
[4] PEACOCK, N.J., ROBINSON, D.C., FORREST, M.J., WILCOCK, P.D., SANNIKOV, V.V., Nature 224 (1969) 488.
[5] ГАЛЕЕВ, А.А., САГДЕЕВ, Р.З., Доклады АН СССР 189 6 (1969) 1204.
[6] STRINGER, T., Phys.Rev.Lett. 22 (1970) 770.
[7] ГАЛЕЕВ, А.А., ЖЭТФ 59 10 (1970) 1378.
[8] WARE, A.A., Phys.Rev.Lett. 25 (1970) 15.
[9] FURTH, H.P., ROSENBLUTH, M.N., RUTHERFORD, P.H., STODIEK, W., Physics of Fluids 14 1 (1971).
[10] АРЦИМОВИЧ, Л.А., АНАШИН, А.М., ГОРБУНОВ, Е.П., ИВАНОВ, Д.П., ПЕТРОВ, М.П., СТРЕЛКОВ, В.С., Письма в ЖЭТФ 10 (1969) 130.
[11] АРЦИМОВИЧ, Л.А., ГЛУХОВ, А.В., ПЕТРОВ, М.П., Письма в ЖЭТФ 11 (1970) 449.
[12] ШАФРАНОВ, В.Д., в сб. "Вопросы теории плазмы". Под ред. М.А.Леонтовича. Вып.2, Госатомиздат, М., 1963, стр.111.
[13] КАДОМЦЕВ, Б.Б., ПОГУЦЕ, О.П., там же. Вып.5, Госатомиздат, М., 1967, стр.209.
[14] ГАЛЕЕВ, А.А., САГДЕЕВ, Р.З., Письма в ЖЭТФ 13 3 (1971) 162.
[15] БОБРОВСКИЙ, Г.А., КУЗНЕЦОВ, Э.И., РАЗУМОВА, К.А., ЖЭТФ 59 10 (1970) 1103.
[16] BOBROVSKII, G.A., RASUMOVA, K.A., SHCHEGLOV, D.A., Plasma Phys. 10 2 (1968) 436.
[17] БРАГИНСКИЙ, С.И., в сб. "Вопросы теории плазмы". Под ред. М.А.Леонтовича, Вып.1, Госатомиздат, М., 1963, стр.183.
[18] КАМИНСКИЙ, М., Атомные и ионные столкновения на поверхности металла. МИР, М., 1967.

DISCUSSION

R. PELLAT: I do not agree that the dissipative trapped particle electron mode found by Kadomtsev and Pogutse is stabilized by shear. The reason can be found in our paper F-15.

A.A. GALEEV: We considered the stabilization only of those "trapped particle" modes which, up to the time of this Conference, had been regarded as dangerous and we found that they are stabilized. The question of new instabilities must be considered separately.

NEOCLASSICAL EFFECTS ON PLASMA EQUILIBRIA AND ROTATION

M.N. ROSENBLUTH, P.H. RUTHERFORD, J.B. TAYLOR,
E.A. FRIEMAN, L.M. KOVRIZHNIKH
International Centre for Theoretical Physics, Trieste, Italy,
Institute for Advanced Study and
Plasma Physics Laboratory, Princeton, New Jersey,
United States of America

Abstract

NEOCLASSICAL EFFECTS ON PLASMA EQUILIBRIA AND ROTATION.

Since the original investigations of Galeev and Sagdeev collisional plasma diffusion in an axisymmetric torus has been extensively studied. To determine the evolution of the radial electric field and the plasma rotation, it is necessary to carry out a calculation of fourth order in the gyro-radius; it is the purpose of this paper to study this problem in particular in the low-collision-frequency ("banana") regime.

1. INTRODUCTION

Since the original investigations of Galeev and Sagdeev [1] collisional diffusion of plasma in an axisymmetric torus has been extensively studied [2, 3]. To lowest order in the gyro-radius, conservation of angular momentum is always sufficient to ensure that the diffusion be ambipolar, irrespective of the strength of the radial electric field. Consequently it is necessary to go to fourth order in the gyro-radius to determine the evolution of the radial electric field and the plasma rotation. It is our purpose to study this question particularly in the low collision frequency ("banana") regime.

For simplicity we consider an axisymmetric configuration with concentric circular flux surfaces: $B_\varphi = B_o/h$, $B_\theta = B_{\theta_o}/h = B_o\Theta/h$; $h = 1 + (r/R)\cos\theta$, with r, θ, φ the usual toroidal coordinates. We assume $\Theta \ll 1$, and will also treat $r/R \ll 1$ in the final evaluation. Let us first briefly review the situation with respect to rotation as it exists in the short mean free path (fluid) regime.

At this point we must distinguish between two types of rotation. Thus in ideal MHD theory $\vec{V} = \vec{\mathcal{E}} \times \vec{B}/B^2 + (V_\parallel/B)\vec{B}$ and 2 arbitrary constants (the radial electric field and a free flow along field lines) are available for divergence free rotation. Hence even if the total angular momentum (p_φ) on a magnetic surface is specified, one degree of freedom remains. When transport processes are introduced into the fluid theory, they affect the two types of rotation very differently. Diffusion of angular momentum between surfaces is fairly slow, being proportional to gyro-radius squared, while rapid readjustments of rotation within the surface are possible, so that on a fairly short time scale this extra degree of freedom is removed. As

Stringer [4] and others have shown, in certain transport regimes instabilities of this readjustment may result and shocks may even be formed [5]. However, as the mean free path becomes fairly long, the dominant transport process is ion parallel viscosity, and the velocity within the surface is governed by an equation of the form $\partial V_{\parallel}/\partial t = (\lambda v_{th}/3)\vec{n}\cdot\nabla(\vec{n}\cdot\vec{n}\cdot\nabla\vec{V})$ (with with $\vec{n}$ a unit vector along $\vec{B}$), so that on a short time scale $(1/\tau \approx \lambda v_{th} \times (B_\theta/B)^2 (1/r^2))$ the rotation reaches a steady state with respect to parallel viscosity in which $V_{\parallel} \approx -\phi'/B_\theta$. Thus on this fast time scale the radial electric field adjusts itself to a value consistent with the amount of conserved angular momentum on the surface. Subsequently, on a slow time scale, characterized by the time necessary for classical perpendicular viscosity to transport angular momentum between surfaces, the electrostatic potential adjusts itself so that $ne\nabla\phi = -\nabla p_i$. Note that the fast rate is proportional to ν. Of course the fluid analysis becomes inapplicable when the mean free path becomes longer than the connection length rB/B_θ, and we must turn to the kinetic equation for this discussion.

2. DEVELOPMENT OF THE FORMALISM

As velocity space coordinates we use the energy, $\varepsilon = V^2/2 + e\Phi/m$, and magnetic moment $\mu = V_\perp^2/2B$, in terms of which the parallel velocity $q = [2(\varepsilon - \mu B - e\Phi/m)]^{\frac{1}{2}}$ and the velocity space element $d^3\vec{v} = 2\pi B d\mu d\varepsilon/|q|$. Φ is the electrostatic potential. For our axisymmetric situation, the kinetic equation for $f(r,\theta,\varepsilon,\mu,t)$ in the guiding center approximation in which the gyro-radius in the toroidal field vanishes ($\Theta \ll 1$) may be written [2, 3]:

$$\frac{\partial f}{\partial t} + \frac{e}{m}\frac{\partial \Phi}{\partial t}\frac{\partial f}{\partial \varepsilon} + q\Theta\frac{1}{r}\frac{\partial f}{\partial \theta} + \frac{m}{er}\left[q\frac{\partial}{\partial \theta}\left(\frac{q}{B}\right)\frac{\partial f}{\partial r} - q\frac{\partial}{\partial r}\left(\frac{q}{B}\right)\frac{\partial f}{\partial \theta}\right] = Cf \qquad (1)$$

where Cf is the collision operator. Eq. (1) may be derived from the usual equations for guiding center drifts; it also follows simply from conservation of canonical angular momentum. A non-radial electric field is included in the analysis but can be shown not to modify the results essentially provided that the primary trapping remains magnetic, i.e. $e\partial\Phi/\partial\theta < Tr/R$, which will be true in the small gyro-radius limit. Hence for simplicity we consider only $\Phi(r)$.

Note that the radial drift velocity is given by

$$V_{dr} = \frac{m}{er}\, q\, \frac{\partial}{\partial \theta}\left(\frac{q}{B}\right) \qquad (2)$$

Since we intend to solve equation (1) to high-order in the gyro-radius, it is perhaps worth commenting on why it is adequate to use this lowest order drift equation. If we were to write down higher order corrections in the gyro-radius to equation (1) itself, then these would of course be small in the gyro-radius in the main toroidal field. Since simple symmetry arguments (e.g. conservation of angular momentum) show that the desired transport fluxes must be of the same order in m/e as we calculate here, it follows that any corrections resulting from higher order terms in equation (1) must be of order Θ compared to those we retain.

The first step in our calculation is to express the radial particle flux in terms of moments of the collision operator:

$$S_n = r < \int (qh)^n V_{dr} f d^3\vec{v} > = \frac{m}{eB_o} < \int q(qh)^n \frac{\partial(qh)}{\partial\theta} f d^3\vec{v} >$$

where V_{dr} is the radial drift as given in Eq. (2), and the brackets denote a surface average $< A > = (2\pi)^{-1} \int hA d\theta$. Taking moments of equation (1) we obtain a hierarchy of equations for the quantities S_n, namely

$$n\, S_{n-1} - \frac{m}{eB_o\Theta} \frac{\partial S_n}{\partial r} = - T_n \qquad (3)$$

where

$$T_n = \frac{mr}{eB_o\Theta} < \int (qh)^n \left[Cf - \frac{\partial f}{\partial t} - \frac{e}{m}\frac{\partial\Phi}{\partial t}\frac{\partial f}{\partial\varepsilon} \right] d^3\vec{v} > \qquad (4)$$

An iterative solution yields the particle flux Γ:

$$r\Gamma = S_o = -T_1 + \frac{m}{e\Theta B_o} \frac{\partial S_1}{\partial r}$$

$$= - T_1 - \frac{1}{2!} \frac{m}{eB_o\Theta} \frac{\partial T_2}{\partial r} - \frac{1}{3!} \left(\frac{m}{eB_o}\right)^2 \frac{1}{\Theta} \frac{\partial}{\partial r} \frac{1}{\Theta} \frac{\partial T_3}{\partial r} \cdots \qquad (5)$$

From the conservation of momentum in collisions it is immediately clear that the collisional term in T_1 always gives ambipolar diffusion (with no contribution from like particle collisions). The other terms in Eq. (5) are clearly much larger for ions than electrons, and only ion-ion collisions are significant. Requiring that these terms vanish to insure ambipolarity yields:

$$r \frac{\partial}{\partial t} m < \int qhfd^3\vec{v} > = - \frac{\partial}{\partial r} m S_1$$

$$= \frac{\partial}{\partial r} \left[m \frac{T_2}{2!} + \frac{m^2}{3!\, eB_o\Theta} \frac{\partial T_3}{\partial r} + \cdots \right. \qquad (6)$$

an equation of conservation of angular momentum, p_φ. The ambipolar condition implies no net radial current, and hence no torque, so that angular momentum must diffuse between surfaces as shown by the character of Eq. (6).

To proceed further, it is of course necessary to expand the solution to equation (1) in a power-series in m/e; $f = f_o + f_1 + f_2 \ldots$. Since we wish to identify the terms in Eq. (1) which contain m/e explicitly as being in fact small in that order we must require that $\partial/\partial r(q/B)$, $\partial/\partial\theta(q/B)$ not be too large. In particular the radial electric field ϕ' must be restricted so that $\phi'/B_\theta < q$. As we will find potentials typically of the order of T/e, the validity of our approximation scheme requires that the radius be many gyro-radii in the <u>poloidal</u> magnetic field, making it marginal for many present devices. Further it should be noted that, while we keep terms of second order in m/e, we only retain terms linear in collision frequency. However, it is easy to show that terms of second-order in ν have the wrong symmetry to contribute to the flux, thus justifying our neglect.

However, it is necessary on occasion to retain first-order terms in collision frequency. Thus a double expansion is indicated

$$f = f_o^{\,o} + f_o^{\,1} + f_1^{\,o} + f_1^{\,1} + f_2^{\,o} + f_2^{\,1} \tag{7}$$

where the subscript refers to order in gyro-radius, the superscript to order in collision frequency, ν. As we will rarely need to deal with f^1, we will usually suppress the superscript on f^o. For example, since the expressions for T_n (see Eq. (4)) are explicitly proportional to ν we need only employ f^o therein.

To lowest order in collision frequency f_1 and Cf_1 will be found to be odd in q so that $T_2(f_1)$ will vanish. Thus the lowest order contributions will arise from $T_2(f_2^1)$ and $T_3(f_1)$. We consider the term $\partial f_o/\partial t$ to be proportional to ν and gyro-radius squared as it will be from diffusion processes. Processes involving electron-ion collisions (such as particle diffusion) may be neglected as small in $(m_e/m_i)^{\frac{1}{2}}$, with the exception that if $T_i \neq T_e$ an interchange of energy takes place which is small in $(m_e/m_i)^{\frac{1}{2}}$ but does not involve the gyro-radius. For maximal ordering we assume that ion-electron energy exchange is of the same order as $\partial T/\partial t$.

Let us now consider the zeroth order terms in Eq. (1):

$$\frac{\partial f_o}{\partial t} + \frac{e}{m}\frac{\partial \Phi}{\partial t}\frac{\partial f_o}{\partial \varepsilon} + \frac{q}{r}\frac{B_\theta}{B}\frac{\partial f_o}{\partial \theta} = C(f_o) \tag{8}$$

[Note that as discussed earlier $e\phi \approx \mathcal{O}(1)$.] It is at this level that the fast time-scale relaxation of rotation within the surface occurs. As in the fluid limit this relaxation does not involve the gyro-radius or radial dependence.

Evidently an arbitrary initial distribution will relax to a Maxwellian:

$$f_o = \frac{n}{T}\, e^{-(\varepsilon - e\phi)/T} \tag{9}$$

with n, T, and Φ functions of radius, on a time-scale characteristic of Landau damping $(1/\tau = v_{th}/R)$ for θ dependent perturbations, or of collision frequency, ν, for θ independent perturbations. Such relaxation will occur for arbitrary perturbations, including as a special class those corresponding to nonequilibrium rotations. Henceforth we choose f_o to be given by equation (9), noting that $f_o^{\,1} \equiv 0$, and thus are dealing with the slow time scale for rotation relaxation.

We may now write down the dominant terms for the determination of the non-ambipolar flux:

$$T_2 = \frac{mr}{eB_o\Theta} < \int (qh)^2 \left[Cf_2 + \frac{f_o}{T}\frac{\partial T}{\partial t}\left(\frac{3}{2} - \frac{m\varepsilon - e\Phi}{T}\right) + C_{ie}(f_o)\right] d^3\vec{v} > \quad (10)$$

$$T_3 = \frac{mr}{eB_o\Theta} < \int (qh)^3 Cf_1 d^3\vec{v} > \quad (11)$$

where Cf is bilinear, i.e. $Cf_o = 0$; $Cf_1 = C(f_o, f_1) + C(f_1, f_o)$; $Cf_2 = C(f_o, f_2) + C(f_2, f_o) + C(f_1, f_1)$.

We are now ready to proceed with the solution of Eq. (1) in the usual low collision frequency (banana) limit, treating the convective term $q(B_\theta/Br)\partial f/\partial\theta$ in Eq. (1) as the large one. That is to say we are in the "banana" regime where the effective collision frequency for trapped particles is less than their bounce frequency, i.e.

$$\nu_{ii}\frac{R}{r} < v_{th}\sqrt{\frac{r}{R}}\frac{\Theta}{r}$$

This leads to the solution

$$f_1^{\,o} = -\left(\frac{mq}{eB_\theta}\right)\frac{\partial f_o}{\partial r} + g_1(\varepsilon, \mu, r) \quad (12)$$

with a solubility condition (for $f_1^{\,1}$), $\int Cf_1^{\,o}(d\theta/q) = 0$, in order to determine g_1. If $T' = 0$, we see from Eq. (9) that the first term in f_1 is simply proportional to q so that $f_o + f_1$ is a displaced Maxwellian for which $C(f_o, f_1)$ evidently vanishes, and $g_1 \equiv 0$. If $T' \neq 0$ we may use the result for f_1 previously obtained in the study of ion thermal conductivity [3]. With the Fokker-Planck collision operator we have:

$$f_1 = \frac{m}{T} qhf_o \left[U + \frac{T'}{eB_{\theta_o}}\left(\frac{3}{2} - \frac{m\varepsilon - e\phi}{T} - 0.17\right)\right] + g_1(\varepsilon, \mu, r) \quad (13)$$

$$U = -\frac{T}{eB_{\theta_o}}\left[\frac{n'}{n} + \frac{e\phi'}{T} - 0.17\frac{T'}{T}\right] \quad (14)$$

$$g_1 = -\frac{mf_o}{eB_{\theta_o}}\frac{T'}{T}\int_\mu^{\mu_m}\frac{B_o d\mu}{<q>}\left[\frac{3}{2} - \frac{m\varepsilon}{T} - 0.17\right] \quad (15)$$

where $\mu_m = \varepsilon - e\Phi/B_{max}$ represents the boundary between trapped and untrapped particles. g_1 vanishes for trapped particles $\mu > \mu_m$. Note that except for trapped or nearly trapped particles ($q \sim V(r/R)^{\frac{1}{2}}$), f_1 is simply a Maxwellian displaced by U, which is the effective macroscopic rotation velocity, i.e. $U \equiv V_\parallel \equiv V_\varphi$. Note that the only θ dependence of f_1 is in terms $qh \approx B_o(q/B)$.

Using Eq. (13) for f_1 we must now solve Eq. (1) for f_2. As before we make the low collision frequency assumption treating $q(B_\theta/B)(\partial f_2/\partial\theta)$ as the large term. This yields:

$$f_2 = -\frac{m}{e}\frac{B_o}{B_{\theta_o}}\left\{\left(\frac{q}{B}\right)^2\frac{1}{2}\frac{\partial}{\partial r}\left[\frac{mB_o f_o}{T}\left(U - \frac{T'}{eB_{\theta_0}}\left(\frac{3}{2} - \frac{\varepsilon - e\phi}{T} - .17\right)\right)\right] + \right.$$
$$\left. + \frac{q}{B}\frac{\partial g_1}{\partial r}\right\} + g_2(\varepsilon,\mu,r) \tag{16}$$

In addition there remains the solubility condition for $f_2^{\,1}$. This yields

$$\oint\frac{d\theta}{q}\left[Cf_2 + \frac{f_o}{T}\frac{\partial T}{\partial t}\left(\frac{3}{2} - \frac{m\varepsilon - e\Phi}{T}\right) + C_{ie}(f_o)\right] + \frac{m}{er}\frac{\partial}{\partial r}\frac{r}{\Theta B_o}\oint h\,d\theta\, Cf_1 = 0 \tag{17}$$

where the last term arises from the terms in $f_1^{\,1}$ which contribute to the equation for $f_2^{\,1}$. We have used the fact that $(q\Theta/r)\,\partial f_1/\partial\theta = Cf_1^{\,o}$, as seen in equation (1).

It is interesting to consider the solubility of equation (17). In particular we know that collisions conserve mass, momentum, and energy. Hence the appropriate moments of Cf_2 must vanish. The first two moment equations are trivially satisfied. However, it is of interest to multiply equation (17) by $\varepsilon q/|q|$ and integrate $d\varepsilon d\mu$. This gives

$$< \int d^3\vec{v}\varepsilon\left[Cf_2 + \frac{f_o}{T}\frac{\partial T}{\partial t}\left(\frac{3}{2} - \frac{m\varepsilon - e\Phi}{T}\right) + C_{ie}\right] >$$
$$+ \frac{m}{er}\frac{\partial}{\partial r}\frac{r}{\Theta}\int\frac{d\theta\, d\varepsilon}{B}\,d\mu\,\frac{\varepsilon q}{|q|}\,Cf_1 = 0$$

Using $Cf_1 = (q\Theta/r)\,\partial f_1'/\partial\theta$, and equation (2), the last term becomes, after integration by parts on θ,

$$-\frac{1}{r}\frac{\partial}{\partial r} r < \int d^3\vec{v}\varepsilon v_{dr} f_1^{\,1} >$$

Hence, carrying out the integrals, the solubility condition for equation (17) becomes simply the ion heat balance equation:

$$\frac{3}{2}\, n\,\frac{\partial T}{\partial t} = Q_{e,i} - \nabla\cdot Q_i \tag{18}$$

with Q_i the ion thermal flux, and $Q_{e,i}$ the heat deposition by electrons.

We may note that the first term in equation (17) is very similar to our expression Eq. (10) for T_2. To see the implications of this let us first consider the case $T' = 0$ for which $g_1 \equiv Cf_1 \equiv 0$.

3. CASE OF ZERO TEMPERATURE GRADIENT

We note first that Eq. (16) may be written in the form (carrying out the differentiation):

$$f_2 = + \frac{m^2}{T^2} \frac{(qh)^2}{2} U^2 f_o - \frac{m^2}{eB_o T} \frac{(qh)^2}{2\Theta} f_o \frac{\partial U}{\partial r} + g_2(\varepsilon, \mu, r)$$

We see that the first term here merely represents the second order expansion of the displaced Maxwellian given by equation (13). Since the collision operator vanishes to all orders when applied to a Maxwellian, it follows that

$$C(f_2, f_o) + C(f_o, f_2) + C(f_1, f_1) = C(\hat{f}_2, f_o) + C(f_o, \hat{f}_2) \equiv \tilde{C}(\hat{f}_2)$$

with

$$\hat{f}_2 = - A \frac{(qh)^2}{2} f_o + g_2(\varepsilon, \mu, r) \tag{19}$$

$$A = \frac{m^2}{eB_o \Theta T} \frac{\partial U}{\partial r} \tag{20}$$

The terms arising from $\partial T/\partial t$ and C_{ie} occur in the same combination in Eqs. (10) and (17). Moreover they are functions only of ε. Hence, we may eliminate them by looking for a solution of $\tilde{C}\hat{g}_2 = \partial T/\partial t + \ldots$, where $\hat{g}_2$ may then be absorbed into the arbitrary function $g_2(\varepsilon, \mu)$ in Eq. (19). We have seen earlier that the ion heat balance equation shows that we can indeed solve for $\hat{g}_2(\varepsilon)$.

Thus our problem reduces to the following. We must evaluate:

$$T_2 = - \frac{mr2}{eB_o \Theta A} < \int d^3\vec{v} \left[-A \frac{(qh)^2}{2} \right] \tilde{C} \left[-A \frac{(qh)^2}{2} f_o + g_2 \right] >$$

$$T_2 = - \frac{mr2}{e\Theta A} \int d\theta \, d\varepsilon d\mu \frac{1}{|q|} \left[-A \frac{(qh)^2}{2} + \frac{g_2}{f_o} \right] \tilde{C} \left[-A \frac{(qh)^2}{2} f_o + g_2 \right] \tag{21}$$

subject to the constraint condition

$$\int \frac{d\theta}{q} \tilde{C} \left[- A \frac{(qh)^2}{2} f_o + g_2 \right] = 0 \tag{22}$$

We now use the well-known self-adjointness property of the linearized collision operator $\tilde{C}(f_2)$ (related to the Boltzmann H theorem) that $\int d^3\vec{v} \hat{f} \tilde{C}(\hat{g} f_o) = \int d^3\vec{v} \hat{g} \tilde{C}(\hat{f} f_o)$ for arbitrary $\hat{f}, \hat{g}$. This enables us to see trivially that equation (21) for T_2 is variational, i.e. that the $g_2(\varepsilon, \mu)$ which minimizes T_2 will be a solution of Eq. (22). We see further that only the θ dependence of (qh) prevents a choice of $g_2, (\mu, \varepsilon)$ which would cause T_2 to vanish. It is clear then that the minimizing g_2 will be that which cancels $(qh)^2/2$ on the average, i.e.

$$g_2 = Af_o(\varepsilon - \mu B_o) = Af_o\left\{\frac{q^2}{2} - \left(\varepsilon - \frac{q^2}{2}\right)\frac{r}{R}\cos\theta\right\} \tag{23}$$

Due to the variational nature of equation (21) this approximation for g_2 should be adequate.

Finally it is necessary to introduce the explicit form for the ion Fokker-Planck collision operator [6].

$$C = -\frac{2\pi e^4 \ln\Lambda}{m^2}\frac{\partial}{\partial v_k}\int d^3\vec{v}'\left\{f(\vec{v})\frac{\partial f(\vec{v}')}{\partial v_\ell'} - f(\vec{v}')\frac{\partial f(\vec{v})}{\partial v_\ell}\right\}U_{k\ell} \tag{24}$$

with

$$U_{k\ell} = \frac{|\vec{v}-\vec{v}'|^2\delta_{k\ell} - (v_k - v_k')(v_\ell - v_\ell')}{|\vec{v}-\vec{v}'|^3}$$

from which we may easily derive the desired quadratic form:

$$K = \int d^3\vec{v}\,\hat{f}\,\tilde{C}(\hat{f}f_o) = \Gamma\int d^3\vec{v}\int d^3\vec{v}' f_o(\vec{v})f_o(\vec{v}')\left(\frac{\partial\hat{f}}{\partial v_k} - \frac{\partial\hat{f}}{\partial v'_k}\right)\left(\frac{\partial\hat{f}}{\partial v_\ell} - \frac{\partial\hat{f}}{\partial v'_\ell}\right)$$
$$\times\ \frac{(v_k - v_k')(v_\ell - v_\ell') - |\vec{v}-\vec{v}'|^2\delta_{k\ell}}{|\vec{v}-\vec{v}'|^3}$$

with $\Gamma = \pi e^4 \ln\Lambda/m^2$ and $\hat{f} = -A(r/R)\cos\theta\,[(q^2/2)+\varepsilon]$ to lowest order in r/R. From the symmetry of the operator it is evident that the term in ε will not contribute and we find:

$$K = A^2\left(\frac{r}{R}\cos\theta\right)^2\Gamma\int d^3\vec{v}\int d^3\vec{v}' f_o(\vec{v})f_o(\vec{v}')\frac{(q-q')^4 - (q-q')^2|\vec{v}-\vec{v}'|^2}{|\vec{v}-\vec{v}'|^3}$$

Introducing the standard variables $\vec{v}+\vec{v}'$, $\vec{v}-\vec{v}'$ the integrals are done readily to yield

$$K = -A^2\left(\frac{r}{R}\cos\theta\right)^2\Gamma\frac{8}{15\sqrt{\pi}}\left(\frac{T}{m}\right)^{\frac{1}{2}}n^2$$

Finally we substitute into Eq. (21) to find

$$T_2 = \frac{8}{15}\frac{r}{e^2(B_o\Theta)^2}n^2\sqrt{\pi}\,e^4\ln\Lambda\left(\frac{r}{R}\right)^2\left(\frac{m}{T}\right)^{\frac{1}{2}}\frac{\partial U}{\partial r}$$

and substituting into Eq. (13) and (6) we obtain the desired result for the rate of change of rotation for the case $T' = 0$ (noting that $T_3(f_1) \equiv 0$);

$$n\frac{\partial U}{\partial t} = \frac{1}{r}\frac{\partial}{\partial r}rn\chi\frac{\partial U}{\partial r} \tag{25}$$

Here, the effective viscosity

$$\chi = \frac{1}{10}\left(\frac{1}{\iota}\right)^2 \rho_i^{\,2}\nu_{ii} \tag{26}$$

where we have introduced the conventional definitions for ion gyro-radius, $\rho_i = (2mT)^{\frac{1}{2}}/eB_o$, collision frequency, $\nu_{ii} = 4\pi^{\frac{1}{2}}ne^4\ln\Lambda/3m^{\frac{1}{2}}T^{3/2}$, and rotational transform $\iota = \Theta(R/r)$. We note that Eq. (25) describes a relaxation towards solid rotation. If boundary conditions at the wall are $U = 0$, then we see from Eq. (14) that $e\phi' = -\nabla p_i$ as might be expected.

We note that our expression for the viscosity χ is rather surprising in that none of the usual banana regime trapped particle effects occur. Thus the ion thermal conductivity, κ, [3] differs from χ, aside from a numerical factor, by a large factor $(R/r)^{3/2}$. By comparison χ differs from classical viscosity in a straight magnetic field [6] only by a factor $2/3(1/\iota)^2$, essentially the Pfirsch-Schlüter factor. In the absence of such trapped-particle enhancement it seems clear that Eq. (26) will continue to apply in the "plateau" region as well, since our solution of the drift equation only requires $\nu < v_{th}/R$ in this case. Moreover, while to the best of our knowledge toroidal viscosity in the fluid (short mean-free path) regime has not been calculated, the form of equation (26) is consistent with what is known about other transport coefficients in this regime.

4. THE CASE $T' \neq 0$

There remains now consideration of the case $T' \neq 0$. Again we must return to our basic equations (10) and (17). Now $Cf_1 \neq 0$ and the final term in Eq. (17) will prevent the near cancellation which led to the factor $(r/R)^2$ in the previous case. We also note that as the equations for g_2 and T_2 are linear we may without loss of generality keep in our equations only $\bar{g}_2(\varepsilon,\mu,\nu)$, that portion of f_2 proportional to the final term in equation (17). From equation (10) we have:

$$T_2 = \frac{2mr}{e\Theta}\int \frac{d\theta d\varepsilon d\mu}{|q|}\left[(\varepsilon-\mu B_o) + \frac{2r}{R}\cos\theta\,\varepsilon - \frac{r}{R}\cos\theta\,\mu B_o + \mathcal{O}\left(\frac{r}{R}\right)^2\right]\approx{C}(\bar{g}_2)$$

Here by the notation $\approx{C}(\bar{g}_2)$ we mean $\tilde{C}(\bar{g}_2) + \frac{\partial T}{\partial t}\ldots$.
Using collisional conservation of energy $\int d^3\vec{v}\varepsilon C = 0$, this becomes

$$T_2 = \frac{2mr}{e\Theta}\int \frac{d\theta d\varepsilon d\mu}{|q|}\left[(\varepsilon-\mu B_o) + \frac{r}{R}\cos\theta\,\frac{q^2}{2} + \mathcal{O}\left(\frac{r}{R}\right)^2\right]\approx{C}(\bar{g}_2)$$

The second term is the original integral multiplied by an explicitly small factor r/R in addition to a harmonically varying factor and may clearly be neglected. Interchanging the integration order and using Eq. (17) we now have

$$T_2 = -\frac{2m^2}{e^2\Theta}\frac{\partial}{\partial r}\frac{r}{\Theta B_o}\int d\theta d\varepsilon d\mu\,\frac{q}{|q|}\,h(\varepsilon-\mu B_o)\tilde{C}f_1 \tag{27}$$

At this point it is again necessary to introduce the explicit collision operator. Here however we note from Eq. (13) that f_1 is, apart from a displaced Maxwellian, highly localized to the region of trapped and nearly trapped particles. We therefore do not need to use here the full Fokker-Planck operator but only that part which describes pitch-angle scattering--i. e. the appropriate Lorentz operator acting on the localized part of f_1 given by [2]:

$$Cf = \frac{\nu(\varepsilon)}{B} q \frac{\partial}{\partial\mu} q\mu \frac{\partial f}{\partial\mu} \tag{28}$$

with

$$\nu(\varepsilon) = \frac{\sqrt{2}\,\pi e^4 n \ln\Lambda}{m^{1/2} T^{3/2}} F(\varepsilon/T) \tag{29}$$

and

$$F(x) = \frac{2}{\sqrt{\pi}} \frac{1}{x^{3/2}} \left[(1 - \frac{1}{2x}) \int_0^{\sqrt{x}} e^{-x^2} dx + \frac{1}{2\sqrt{x}} e^{-x} \right] \tag{30}$$

Using equations (13) and (15) we then find to lowest order in r/R (noting that $h \equiv 1$, but q^2 itself is of order r/R):

$$T_2 = - \frac{m^3}{e^3 \Theta} \frac{\partial}{\partial r} \frac{T'}{T} \frac{r}{\Theta^2 B_o^3} \int d\varepsilon f_o \nu(\varepsilon) [\frac{3}{2} - \frac{m\varepsilon}{T} - 0.17] H(\varepsilon) \tag{31}$$

with

$$H(\varepsilon) = \int d\theta d\mu (q^2 - 2\mu B_o \frac{r}{R} \cos\theta) q \frac{\partial}{\partial\mu} q\mu \frac{\partial}{\partial\mu} \left[q - \int_{\mu}^{\mu_{Max}} \frac{B_o d\mu}{<q>} \right] \tag{32}$$

Integrating by parts and noting that $\partial q/\partial\mu = - B/q$ we have

$$H(\varepsilon) = + \int d\theta d\mu B_o^2 \left(3q - \frac{2\mu B_o (r/R) \cos\theta}{q} \right) \mu [\frac{q}{<q>} - 1] \frac{q}{|q|} \tag{33}$$

neglecting terms of order $q^2/\mu B_o$. As before, the first term in the square brackets is to be taken only for untrapped particles. We now note that the terms proportional to $\cos\theta$ vanish on integration to higher order in r/R. This is obvious for the first term in square brackets, while for the second we note that $\int d\varepsilon d\mu/|q| \to \int d^3\vec{v}$ so that when we replace μB_o by $v_\perp^2/2$, correct to order r/R, we are left with $\int d\theta \cos\theta \int d^3\vec{v} g(\vec{v}) = 0$.

At this point we note that the integrals appearing in the definition of T_3, equation (11), differ from those in equation (27) only in the replacement of $(\varepsilon - \mu B_o)$ by $(\varepsilon - \mu B)$. The difference is precisely those factors in $\cos\theta$ which we have just seen to vanish. We conclude therefore

$$T_2 = - \frac{m}{B_o \Theta} \frac{\partial T_3}{\partial r} \tag{34}$$

We now return to evaluation of $H(\varepsilon)$ as given in Eq. (33). Putting $\lambda = \mu B_o/\varepsilon$ we find

$$H(\varepsilon) = 3\sqrt{2}\,\varepsilon^{5/2} \int d\lambda \left\{ \frac{1-\lambda}{\frac{1}{2\pi}\int_0^{2\pi} d\theta \sqrt{1-\lambda+\lambda(r/R)\cos\theta}} - \frac{1}{2\pi} \oint d\theta \sqrt{1-\lambda+\lambda(r/R)\cos\theta} \right\}$$

The θ integrals may be expressed in terms of complete elliptic integrals, and we find to leading order in r/R,

$$H(\varepsilon) = 6\varepsilon^{5/2}\left(\frac{r}{R}\right)^{3/2} \left\{ \int_0^1 \frac{dk^2(2-k^2)}{k^5}\left[\frac{\pi}{2E(k^2)} - 1 - \frac{k^2}{4}\right] + \frac{1}{6} \right\}$$

This may be evaluated using a power series expansion for E to yield $H(\varepsilon) = 3.8\,\varepsilon^{5/2}(r/R)^{3/2}$. The energy integral in Eq. (31) may now be performed analytically yielding finally for T_2,

$$T_2 = 2.0\,\frac{1}{e\Theta B_o}\,\frac{\partial}{\partial r}\,r\left(\frac{r}{R}\right)^{3/2}\,\frac{nmT}{e^2\Theta^2 B_o^{\,2}}\,\nu_{ii}\,\frac{\partial T}{\partial r} \qquad (36)$$

Combining Eqs. (6), (34), (36) and (25) we may now write down the final equation for the change of rotation

$$n\frac{\partial U}{\partial t} = \frac{1}{r}\frac{\partial}{\partial r}\left[rn\chi\frac{\partial U}{\partial r} + \frac{3.5}{\Theta}\frac{\partial}{\partial r}\,r\left(\frac{R}{r}\right)^{\frac{1}{2}}\frac{n\chi}{eB_o}\frac{\partial T}{\partial r}\right] \qquad (37)$$

with $\chi = .1(\iota)^{-2}\rho_i^{\,2}\nu_{ii}$.

Before discussing this result we may now justify several earlier approximations in the spirit of the aspect ratio expansion. Thus we see from equation (13) that in the presence of a temperature gradient the mean plasma rotation $\int qfd^3\vec{v}$ is not simply nU but contains an additional small term proportional to $nT'/eB_o\Theta(r/R)^{3/2}$ whose time derivative we have neglected. Similarly in the approximations leading to equation (27) we have neglected terms proportional to $(r/R)^2\,\nabla\cdot Q_i$, the terms we have kept in equation (37) being seen to be of order $(r/R)\nabla\cdot Q_i$.

5. DISCUSSION

The most surprising feature of our result is of course the large coupling between rotation and temperature gradients. Thus it is seen from Eq. (37) that in steady state

$$U \sim \mathcal{O}\left[\left(\frac{R}{r}\right)^{\frac{1}{2}}\frac{T'}{eB_o\Theta}\right]$$

which implies large electrostatic potentials. It should be stressed again, however, that the time necessary to establish a rotational steady state is very long, of order $(R/r)^{3/2}$ times the neo-classical ion thermal equilibration times.

As a particular example consider a steady state with a uniform energy source, with a fixed rotational transform, i.e. $\Theta = \iota r$, and plasma boundary at $r = a$.

Treating density and viscosity as independent of radius, and taking only the dominant $(R/r)^{3/2}$ effect in the thermal conductivity, we see from the heat balance equation

$$\frac{1}{r}\frac{\partial}{\partial r} r\left(\frac{R}{r}\right)^{3/2} \frac{\partial T}{\partial r} = -S$$

that $T \approx T_o[1 - (r/a)^{7/2}]$. Then in steady state Eq. (37) yields

$$U = \frac{37}{\iota}\frac{R^{3/2}}{a^{7/2}}\frac{T_o}{eB_o}(r-a) = \frac{25}{\iota}\left(\frac{R}{a}\right)^{3/2}\left(\frac{r}{a} - 1\right)\frac{\rho_i}{a}\sqrt{\frac{T_o}{M}} \tag{38}$$

This is of course a very high rotation speed, although still well below thermal velocity in reactor size.

Finally we may calculate the electrostatic potential from Eq. (14) ($U = -e\phi'/eB_o\Theta$) to find

$$e\phi = -6T_o\left(\frac{R}{a}\right)^{\frac{1}{2}}\left[1 - 3\left(\frac{r}{a}\right)^2 + 2\left(\frac{r}{a}\right)^3\right]$$

We see then that a large negative potential is established under rotational equilibrium.

Finally we close with a few brief remarks on the extension of these results to the "plateau" regime where the collision frequency is intermediate between the bounce time for trapped particles and average particles; i.e.

$$1 > \frac{\nu_{ii} r}{\Theta v_{th}} > \left(\frac{r}{R}\right)^{3/2}$$

We will not attempt a formal calculation, but merely indicate the qualitative features of the result. As we have mentioned earlier, the calculation of the true viscosity, the first term in Eq. (37), did not involve the trapped particles in any special way, hence might be expected to remain valid also in the plateau regime. As for the second term, the temperature gradient effect, we see from Eq. (27) or Eq. (11) that it is proportional to the same integrals which occur in the usual transport coefficients, e.g. thermal conductivity, except for an extra factor q^2/ε. In the banana regime q^2/ε is that characteristic of trapped particles, i.e. r/R. Hence our factor of

$(R/r)^{\frac{1}{2}}$ instead of $(R/r)^{3/2}$ as in thermal conductivity. In the plateau regime, however, q is that for which the effective collision frequency equals the bounce frequency, i.e.

$$q \approx \left[\frac{r\nu_{ii}v_{th}^2}{\Theta}\right]^{1/3}$$

Thus in the plateau regime we would expect the second term in Eq. (37) to go like the thermal conductivity, ν^{o}, times q^2 or like $\nu^{2/3}$, while the first term continues proportional to ν. Hence the ratio goes like $\nu^{-1/3}$, and by the time ν has increased to the edge of the fluid regime the factor $(R/r)^{\frac{1}{2}}$ in equation (37) will have disappeared and we will have $e\phi \sim T$.

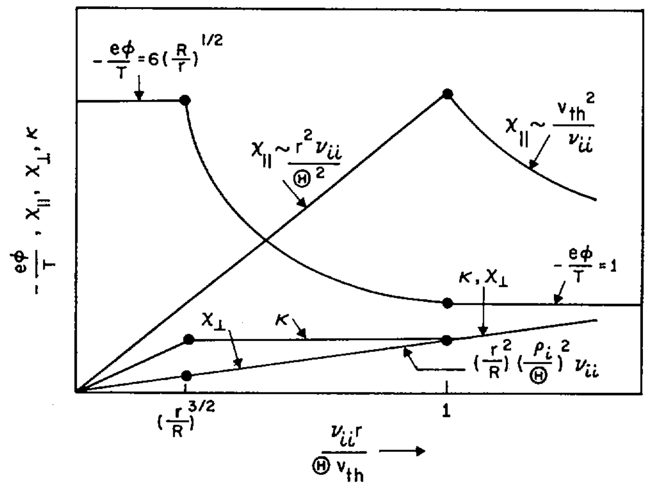

FIG. 1. Dependence of potential φ, parallel viscosity, $\chi_{\parallel}$, perpendicular viscosity, $\chi_{\perp}$, and ion thermal conductivity, κ, on collision frequency, ν_{ii}.

We summarize these various effects in Fig. 1, indicating how thermal conductivity (κ), fast rotation relaxation (parallel viscosity $\chi_{\parallel}$), slow rotation relaxation (perpendicular viscosity $\chi_{\perp}$), and plasma potential, $e\phi/T$, vary with collision frequency.

We acknowledge the hospitality of the International Center for Theoretical Physics in Trieste, where much of this work was performed, and the support of the U.S. Atomic Energy Commision.

REFERENCES

[1] GALEEV, A. A. and SAGDEEV, R. Z., Zh. Eksp. Teor. Fiz. 53 (1967) 348 [Sov. Phys.—JETP 26 (1968) 233].

[2] RUTHERFORD, P. H., Phys. Fluids 13 (1970) 482.

[3] ROSENBLUTH, M., HAZELTINE, R., and HINTON, F., Phys. Fluids (to be published).

[4] STRINGER, T. E., Phys. Rev. Letters 22 (1969) 770.
[5] ROSENBLUTH, M. N., HAZELTINE, R., and LEE, E., Phys. Fluids 14 (1971) 36.
[6] BRAGINSKII, S. I., Reviews of Plasma Physics (Consultants Bureau, New York, 1965) Vol. 1.

PLASMA FOCUS
LASER- AND ELECTRON-BEAM-PRODUCED PLASMAS

(Session D)

Chairman: B. BRUNELLI

Papers D-1 and D-2 were presented by
C. MAISONNIER as Rapporteur

Papers D-3 to D-5 were presented by
N. J. PEACOCK as Rapporteur

Papers D-6 and D-7 were presented by
E. P. VELIKHOV as Rapporteur

Papers D-8 and D-9 were presented by
D. E. POTTER as Rapporteur

STRUCTURE OF THE DENSE PLASMA FOCUS, PART I: NUMERICAL CALCULATIONS, X-RAY AND OPTICAL MEASUREMENTS

P. GRATREAU, G. LUZZI*, CH. MAISONNIER,
F. PECORELLA, J.P. RAGER†, B.V. ROBOUCH,
M. SAMUELLI
Laboratori Gas Ionizzati, Associazione EURATOM-CNEN,
Frascati, Rome, Italy

Abstract

STRUCTURE OF THE DENSE PLASMA FOCUS: PART I: NUMERICAL CALCULATIONS, X-RAY AND OPTICAL MEASUREMENTS.

Preliminary results of numerical calculations are presented. They are based upon the application of Potter's code to our particular DPF-geometry. The implosion phase, the radial oscillations of plasma, and the axial drift of constant-density profiles in the plasma column are studied.

The electronic temperature is determined by detecting simultaneously the continuum X-ray radiation passing through different filters.

By using a new diagnostic tool, which has recently been developed in Frascati, and consists of a channel-multiplier array associated with a conventional image-converter camera, X-ray framing pictures with 10-ns exposure time are obtained. They allow an evaluation of the location and dimensions of the hot plasma.

Correlations between neutron and X-ray emissions are discussed.

The optical emission during the compression phases is recorded by an image-converter streak camera observing the axial region through a 100 μ slit parallel to the axis. In this way, the radial oscillations and the axial motion of the plasma are studied.

A new diagnostic method is proposed. It allows simultaneous determination of both the electronic temperature and density by using time-resolved, relative, spectroscopic measurements on suitably chosen impurity lines. . The characteristics of this method are described in this paper.

INTRODUCTION

Investigations of the structure of a dense plasma focus (DPF) have been carried out using an experimental facility of the Filippov geometry (fast condenser bank of 120 KJ, 40 KV) / 1 /.

In this paper, are reported:

a) preliminary results of the MHD numerical calculations, based on the application to our particular geometry of a modified Potter's Code / 2 /;
b) results on soft x-ray measurements: T_e from conventional filter techniques, high speed photography using channel--plate intensifiers;
c) streak pictures of the axial region during the compression phases;

---

* CNEN Contracts Nos 1823, 2073, 3911.

† EURATOM postgraduate fellow.

d) theoretical considerations on a proposed spectrographic method for the determination of n_e and T_e requiring only relative measurements.

Neutron measurements, as well as the tentative conclusions which can be drawn from all the results, are presented in a second paper.

a) <u>COMPUTER RESULTS</u>

A numerical simulation of the Frascati DPF experiment is being studied. It aims at helping the interpretation of experimental results, checking and, eventually, extrapolating the scaling laws, and optimising the parameters of the facility. The programme is largely inspired by the code of D. Potter / 2 / kindly placed at our disposal. At the time of the writing, the programme is still being refined, and the coarseness of the mesh, imposed by computation time considerations, does not allow, as yet, a thorough discussion of the final stage of the collapse. The following phenomena were, however, observed:

1) The general progression of the plasma sheath (visualized through its density) in its implosion towards the axis, illustrated in Fig. 1.
2) Upon arrival at the axis, the plasma forms an axial, irregular, fluctuating column with the following characteristics:
   - The mean particle density within the axial mesh element increases, about , 200 fold; for the typical

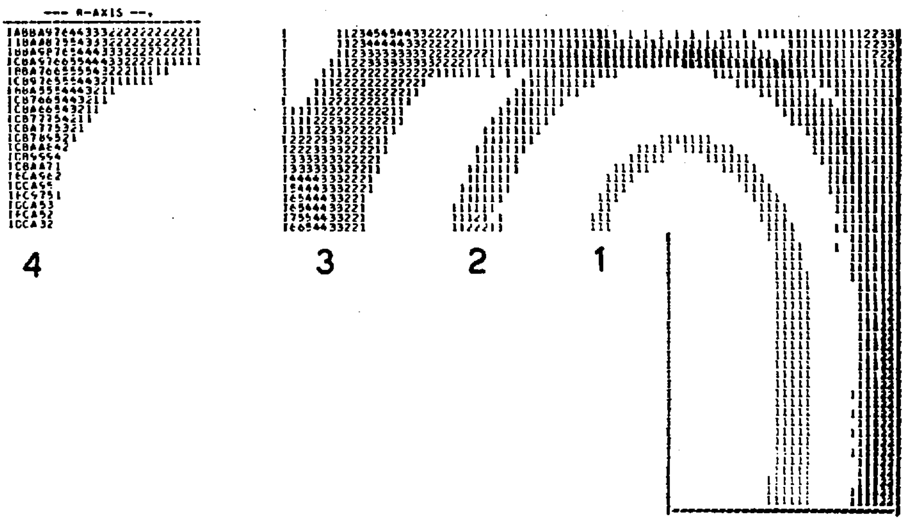

FIG. 1. General aspect of the progression of the plasma sheath (visualized through its density) in its implosion to the axis: 1), 2) Two successive, early stages of the collapse; 3) The sheath reaches the axis, and the focus starts forming; 4) A compressed state of the pinch.

case considered (32 kV, 144 μF, 1.275 torr initial D_2 pressure) this corresponds to a final average density of $1.8.10^{19}$ cm^{-3}. If a Bennett distribution of density is fit to the results, the maximum density on the axis turns out to be 3.6 10^{19} cm^{-3}, $[n/n_o \simeq 400]$.

- During the compression period, the plasma in the column flows axially with a steady speed of the order of 10 cm/μs.
- The profiles of equal density propagate along the axis at about twice the speed of the plasma.
- In collapsing onto the axis, the sheath overcompresses the plasma it gathers. The plasma starts oscillating, and a travelling radial compression-rarefaction-compression-rarefaction sequence propagates along the z-axis, as witnessed by the successive radial mass velocity reversals. The period of these oscillations is of $\sim$0.1 μs.

b) SOFT X-RAY MEASUREMENTS

The soft x-ray emission of the DPF, as recorded with a Li drifted Si solid state detector (100 μ depletion depth, rise time $<$ 10 ns), exhibits two or three successive bursts, the first of which (or first and second in the case of three bursts) is shown later to be representative of the minimum radius of the plasma column, while the last one corresponds to more diffuse recompression of the plasma.

1) The simultaneous use of five aluminium filters of different thicknesses coupled to solid state detectors has given a time resolved temperature determination on single shots / 3 /.
   Results reported in Fig. 2 give a best fit for T_e=6 keV at the maximum of the first x-ray burst. This temperature appears to be rather constant in the vicinity of the peak of the emission.
   During the last burst, a significant measurement of T_e has not yet been performed.

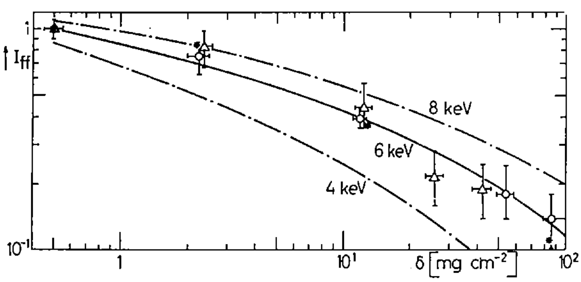

FIG. 2. Relative free-free emission, I_{ff} (arbitrary units) versus Al-filter thickness, δ.
O: shot 57 at peak emission (t = 0 ns);
*: shot 57 at t = -25 ns;
Δ: shot 51 at peak emission.

2) An x-ray image intensifier / 4 / based upon the use of channel electron multiplier arrays has been recently developed in Frascati. Associated, presently, with a normal image converter for time resolution purposes, it has been possible to obtain a few 10ns-picture framings of the discharge using a 200 μ pinhole for imagery.
A sketch of the channel array mounting is given in Fig. 3. Static tests on space resolution, performed with a ^{55}Fe soft x-ray source (main emission at the 5.9 keV MnK α and 6.5 keV MnK β) of 5 mCi (10^7 ph.s^{-1}. cm^{-2}) with proximity focusing of the object are given in Fig. 4a. The object is a stainless steel grid 300 μ thick, with a pitch of 2 mm. The use of 10,000 ASA Polaroid film as the final recorder allows the detection of 10^6 incoming x-ray photons cm^{-2} per shot. Space resolution performed in a real situation (on the DPF experimental facility) is shown in Fig. 4b.
A recently developed two-stage intensifier has shown a static gain 250 times that of the single-stage one. As channel plates possess inherently a good time resolution ($\sim$ 1 ns), shorter exposure framings are expected in the near future.
Results are given in Fig. 5.
The main result obtained has been the identification of a maximum plasma compression with the first burst of x-rays (the first two in the case of three), Figs. 5a and 5b; the plasma diameter is about 2 mm. The last burst does not present on the pictures any fine structure as do the preceding ones (Fig. 5c) but seems to

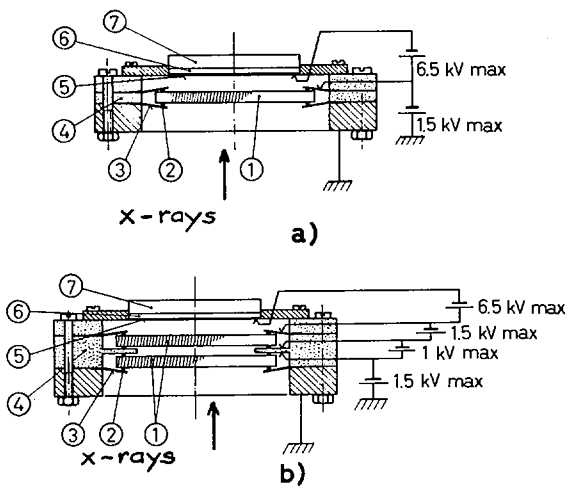

FIG. 3. Single (a) and two-stage (b) X-ray image intensifiers: 1) channel plate array; 2) indium ring; 3) flexible washer; 4) insulator; 5) Al-deposit 400-Å thick; 6) plastic scintillator 10 μ thick; 7) quartz window.

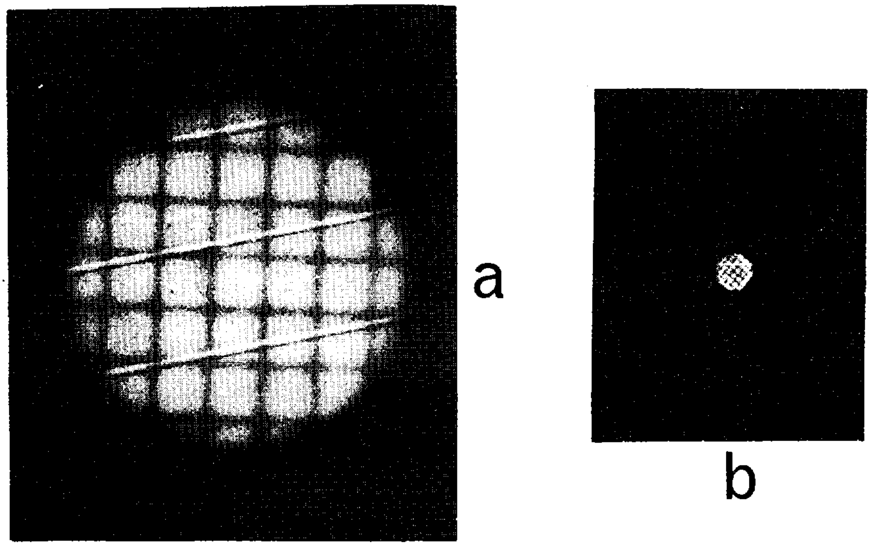

FIG. 4. X-ray image-intensifier static tests; X-ray source 1/2 inch.
a) Large image size for space-resolution test;
b) optics chain as in case of the DPF-experiment.

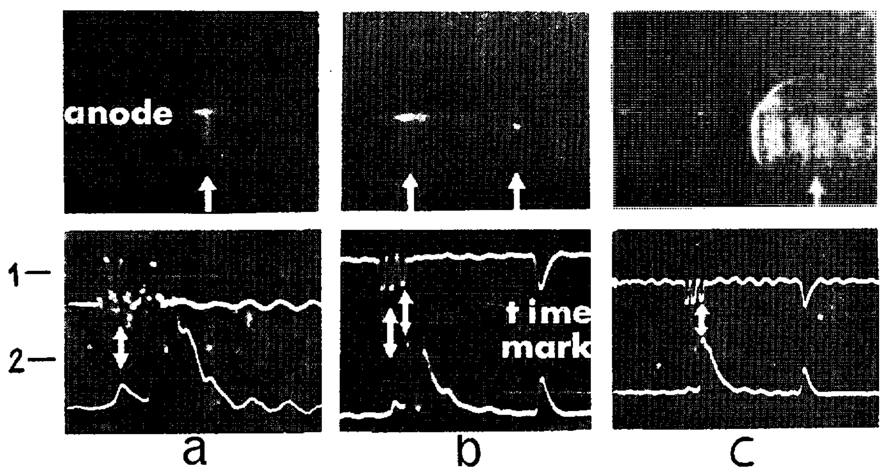

FIG. 5. X-ray framing of the discharge: a) 10 ns; b) 20 ns; c) 20 ns - 1: image converter monitor, 2: X-ray emission.

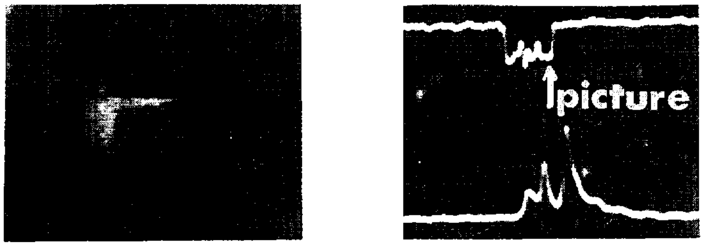

FIG. 6. 50-ns framing X-ray picture of the discharge.

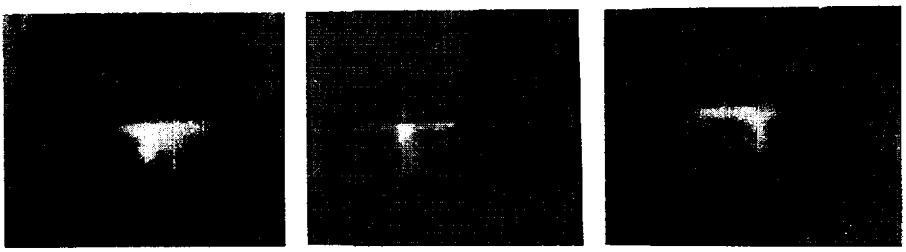

FIG. 7. Integrated pictures of the discharge.

be associated with a diffused cloud of plasma. When pictures are taken with a poor time resolution, the small bright image of the first compression can be superimposed on the dimmer, more diffuse image of the second burst: Fig. 6 is a 50 ns exposure frame including the maximum of the first compression superimposed onto the beginning of the second burst.
Integrated pictures give evidence of a displacement of the focus (typically $\sim$ 1 cm) from shot to shot (Fig.7).

3) From the systematic plotting of global neutron outputs and peak x-ray emissions, emerges a correlation between the maximum amplitude of the last burst and the total number of neutrons; conversely any correlation with the maximum amplitude of the first burst can be discarded (Fig. 8).
This conclusion holds whatever be the filters (Al or Be).

4) Two kinds of anodes are currently in use: one is flat, the other has a central hole 10 mm deep, 20 mm in diameter. Both give the same neutron output, under identical conditions; however, in contrast to the flat one, it has been impossible to record any x-ray picture, even integrated in time, above the plane of the drilled electrode.

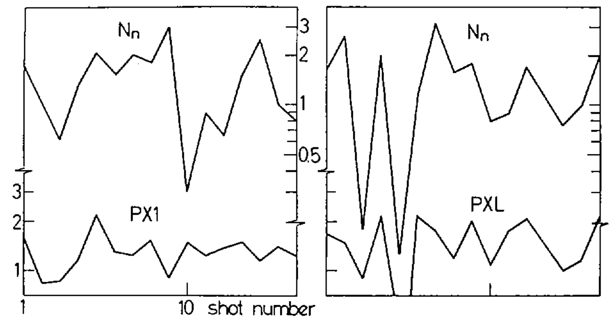

FIG. 8. Correlation between the total neutron yield (N_n) and the intensity of the first (PX1) and last (PXL) X-ray peaks (arbitrary units).

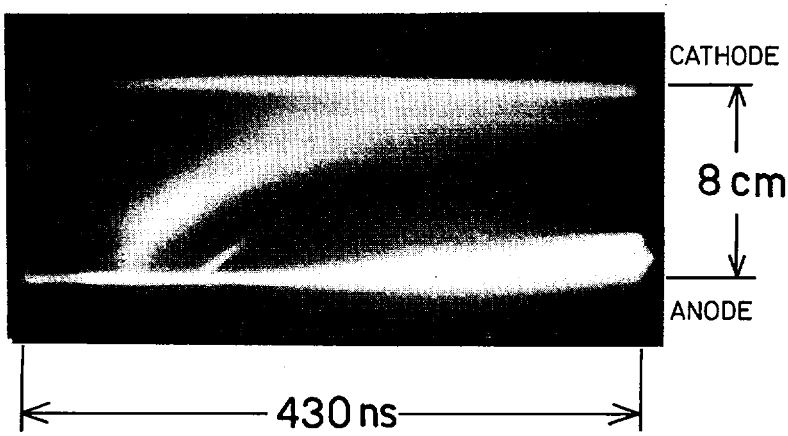

FIG. 9. Streak picture of the axial zone of the discharge.

c) STREAK PICTURES

Streak pictures of the axial region of the discharge chamber are taken using an STL image converter camera; a 100 μ slit parallel to the axis is used / 5 /. An Hβ filter is mounted on the image converter optics. Fig. 9 shows a typical record. In the vicinity of the electrode, we observe successively an initial, intense, light pulse, a dark period of about 100 ns, and a second, bright, light spot that recedes from the anode at a velocity of about 30 cm/μs. The time correlation between these streak signals and the two neutron bursts detected by plastic scintillators coupled to photomultipliers (Fig. 5, Part 2) shows that the beginning of the two pulses of light is synchronous with the two neutron emissions. The total number of neutrons (N_n) emitted per shot is plotted versus the time gap between the two

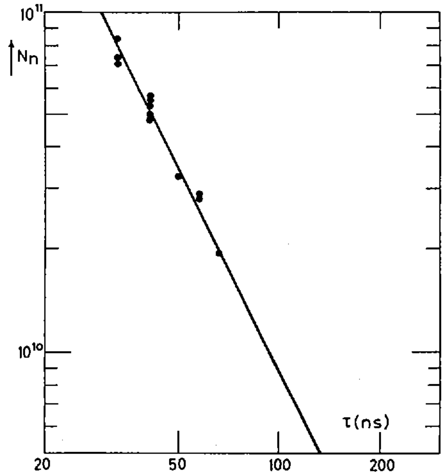

FIG. 10. Plot of the time delay between the two successive light signals (τ) versus the total neutron yield (N_n). (32 kV, p = 1.85 torr).

light pulses (τ), for identical, initial, experimental conditions (Fig. 10). One can observe that the variation can be represented by the following relation: $N_n \tau^2 =$ cost.

d) THEORETICAL CONSIDERATIONS ON A SPECTROGRAPHIC MEASUREMENT OF n_e and T_e

The present work deals with the determination of both the electronic temperature (T_e) and density (n_e) from purely relative intensity measurements.
We consider the spectroscopic determination ($\lambda < 20$ Å) of T_e and n_e in a DPF seeded with a suitable impurity. The relative density of impurities is assumed to remain constant (snow-plough model). The relative intensities of the H and He like resonances are observed in the region of the maximum of T_e (i.e. $T_e \sim$ constant). If n_e varies rapidly, a high temporal resolution of the diagnostic devices ($\sim$ 5 ns) may allow the determination of both T_e and n_e.
To measure temperatures in the 1-10keV region, Al to A elements should be used for seeding; in fact, by the end of the measurement, the impurity ought to be totally ionized. In practice, SiH_4 can be used for T_e<3 keV, and Argon for T_e>3 keV.
The method described is based on a precise knowledge of the different coefficients of ionization, S, and of recombination, α / 6 /. From the latest theoretical and experimental results, the following precisions were obtained: 5% for S_H (H like ion); 20% for S_{He} (He like ion); 1% for α_i (totally ionized ion to H like ion) and 20% for α_H (H like ion to He like ion, with due account for the dielectronic recombination).

The continuum spectrum, corresponding to the ionization equilibrium, can be calculated, in terms of the above coefficients; this is necessary in measuring T_e in the presence of impurities by the standard methods (filter techniques and spectrometry).
Spectra are determined with due account for the recombinations to all levels (Li like ions are negligible) using the full expressions for the Gaunt factors.
The interpretation of spectra under transient conditions, in particular the variation of the intensity of the resonance lines, is greatly simplified as the ionization energy for Li like ions is smaller than that of He like ions (about 1/4).
The system is thus defined by the last two stages of ionization. If $T_e \simeq$ constant, letting $d\varphi = n_e dt$, $\varphi(t=0) = 0$, and $t = \int_0^{\varphi} d\varphi / n_e(\varphi)$, the phenomenon is described by the following two equations, with constant coefficients:

$$n''_H + \Sigma \cdot n'_H + \Delta \cdot n_H \sim p \cdot S_{He} (\alpha_i n_e + n'_e)$$

$$n''_{He} + \Sigma \cdot n'_{He} + \Delta \cdot n_{He} \sim p \cdot [\alpha_i \alpha_H n_e + (\alpha_i + \alpha_H + S_H) n'_e + n''_e]$$

where: $n' = dn/d\varphi$, and n_H, n_{He} are the densities of the ions of H and the He types respectively, and p = the impurity content ($\sim$1% in number density) and:

$$\Sigma \simeq \alpha_i + S_H + \alpha_H + S_{He}$$

$$\Delta \simeq S_{He} (S_H + \alpha_i) + \alpha_i \alpha_H$$

The relative line intensities i_H and i_{He} are, hence:

$$i_H \propto n_e n_H \quad ; \quad i_{He} \propto n_e n_{He}$$

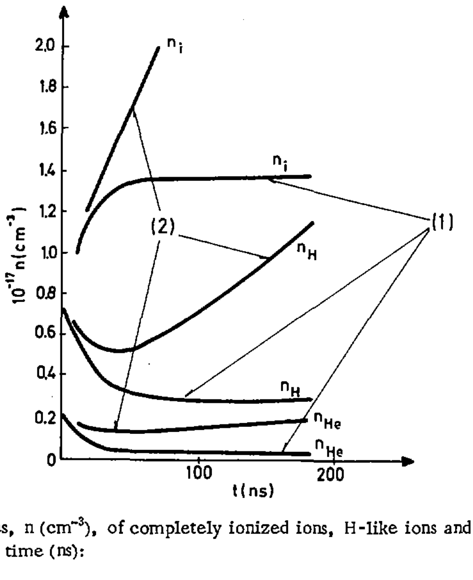

FIG. 11. Absolute densities, n (cm^{-3}), of completely ionized ions, H-like ions and He-like ions (T_e = 6 keV; argon impurity: 1%) versus time (ns):
(1) $n_e = 2 \times 10^{19}\ cm^{-3}$
(2) $n_e = 2 \times 10^{19}\ e^{0.007t}\ cm^{-3}$.

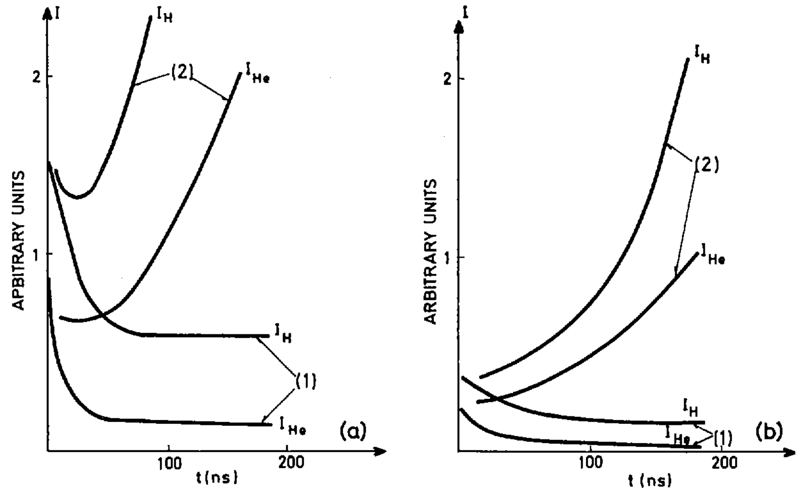

FIG. 12. Relative intensities, i (in arbitrary units), of argon resonance lines of H-and He-like ions versus time (T_e = 6 keV, χ_{He}/χ_H = 2):
a) $n_e^0 = 2 \times 10^{19}$
b) $n_e = 10^{19}$
Curves (1) correspond to $n_e = n_e^0$;
Curves (2) correspond to $n_e = n_e^0 e^{0.007t}$.

In the linear approximation ($n_e = n_e^\circ + \lambda\varphi = n_e^\circ.\exp(\lambda t)$) the system depends upon three variables (T_e , n_e° , λ) and three constants (a constant of proportionality of the relative intensity measurements, assumed to be common to both lines, and two constants of integration describing the past history of the plasma). It requires, hence, six relative intensity measurements while T_e is constant: three successive measurements are sufficient if both lines are observed simultaneously and if the ratio of their excitation coefficients (χ_{He}/χ_H) is known. Such measurements seem quite feasible on DPF experiments, and an experimental effort in this direction has been initiated. Numerical results of such a treatment are reported graphically (for T_e = 6 keV, Argon impurity: 1%, χ_{He}/χ_H = 2) : Fig.11 gives the absolute densities n_i, n_H, n_{He} while Fig. 12a gives the corresponding relative intensities i_H and i_{He} for $n_e^o = 2.10^{19}$ cm^{-3}; Fig. 12b corresponds to n_e^o = 10^{19}cm^{-3}. The method can be extended to four successive, simultaneous measurements, in the case of a non-exponential variation of n_e, and can lead to the value of (χ_{He}/χ_H) at the temperature under investigation. The case of a variable temperature can also be treated.

REFERENCES

/ 1 / MAISONNIER, Ch., SAMUELLI, M., LINHART, J.G., GOURLAN, C.: Proc. 3rd Int. Conf. on Plasma Physics and Controlled Nuclear Fusion, Novosibirsk (1968), 2, p. 77.

/ 2 / ROBERTS, K.V., and POTTER, D.E.: Methods in Computational Physics, 9 Academic Press, London (1970) p. 339.

/ 3 / ELTON, R.C.: NRL-Report 6738 (Dec. 1968).

/ 4 / BETTINALI, L., PECORELLA, F., RAGER, J.P.: Soft x-Ray Image Intensifier with High Space and Time Resolution Note submitted to: Rev. Sci. Instr.

/ 5 / KOLESNIKOV, Yu.A., FILIPPOV, N.V., FILIPPOVA, T.I.: Proc. 7th International Conference on Phenomena in Ionized Gases, Belgrad (1965) 2, p. 833.

/ 6 / GRATREAU, P., ROBOUCH, B.V.: Radiative Recombination of Hydrogenic Ions in High Temperature Plasmas Submitted to: Astrophs. J.

STRUCTURE OF THE DENSE PLASMA FOCUS, PART II: NEUTRON MEASUREMENTS AND PHENOMENOLOGICAL DESCRIPTION

CH. MAISONNIER, C. GOURLAN, G. LUZZI*, L. PAPAGNO†
F. PECORELLA, J.P. RAGER**, B.V. ROBOUCH, M. SAMUELLI
Laboratori Gas Ionizzati, Associazione EURATOM-CNEN,
Frascati, Rome, Italy

Abstract

STRUCTURE OF THE DENSE PLASMA FOCUS: PART II: NEUTRON MEASUREMENTS AND PHENOMENOLOGICAL DESCRIPTION.

In this paper the results of neutron measurements carried out on the DPF facility at Frascati are presented. These measurements are done using nuclear emulsions, activated counters, and scintillators coupled to photomultipliers.

The neutron-flux anisotropies are measured with a precision better than 2%, and the reported energy spectra correspond to neutrons emitted in a single discharge. The results obtained exclude the applicability of simple models in interpreting the DPF, but are consistent with a phenomenological model proposed in this paper which consists of a combination of a moving boiler with a beam-target.

The set of the experimental results, presented in this and the preceding paper of these Proceedings and which refers to X-ray, optical and neutron measurements, as well as to the preliminary results of numerical computations, is discussed and the evaluation of certain plasma parameters is given.

INTRODUCTION

The results obtained from numerical calculations, from soft x-ray measurements and from streak pictures, relative to a dense plasma focus (DPF) of the Filippov type, have been presented in the preceding article. The present article contains:

a) the results of neutron measurements made with: activation counters (showing the anisotropy of the emission and the scaling laws of DPF), nuclear emulsions (giving the energy spectra in various directions), and plastic scintillators (allowing time correlations with other observations);
b) a discussion of a phenomenological model proposed for the structure of the DPF;
c) an evaluation of some parameters of the plasma in the focus.

a) NEUTRON MEASUREMENTS:

The following measurements have been carried out:

- Activation counters

The neutron fluxes are measured with the help of 3 silver-activated Geiger counters placed respectively at 0° (axially, cathode side), 90° (laterally), and 180° (axially, anode

* CNEN Contracts Nos 1823, 2073, 2911.
† University of Rome.
** EURATOM postgraduate fellow.

side). The system was carefully calibrated "in situ" / 1 / with the help of a Po/B radioactive source, having a neutron energy spectrum similar to that of a DD Plasma Focus. The scattering, due to the masses around the DPF, necessitates a calibration precise to within 1% if relative intensity measurements are to be made with a precision of 2%.
The ratios of the fluxes, relative to the (0°,180°) and (0°,90°) directions, are given as a function of the total neutron yield (see Fig. 1). These ratios are nearly constant, at about 1.08 and 1.18, respectively, and do not depend upon the voltage of the bank. With a suitable calibration of the diagnostic system, absolute values of the neutron fluxes are measured. Previously obtained scaling laws, / 2 /, are given in Fig. 2.

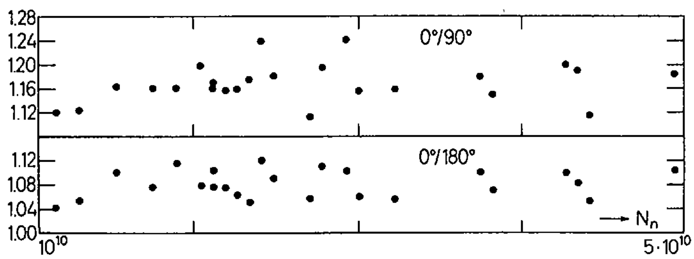

FIG. 1. Calibration-corrected ratios of the neutron fluxes in the different directions as a function of the total DPF neutron yield, N_n. (32 kV; 1.3 torr D_2); Fast valve: 9-15 bar).

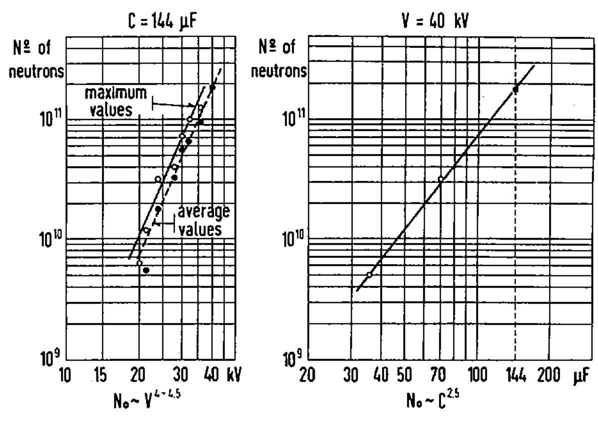

FIG. 2. Scaling laws (experimental).

- Nuclear emulsions

The energy spectra of the neutrons emitted in the 3 directions are measured using Ilford K2 200 μ nuclear emulsions. Fig. 3,4 give the histograms obtained by overimpressing 15 successive shots, as well as those corresponding to a single shot impression. About 400 tracks were recorded per emulsion; only tracks making an angle $\theta < 30°$ with the direction DPF--emulsion were observed. A smaller number of tracks was also recorded at $\theta < 10°$: the position of the maximum, as well as the shape of the high energy part of the histograms, are not modified, which shows that scattering should not introduce a large perturbation. The 90° histogram is centered at

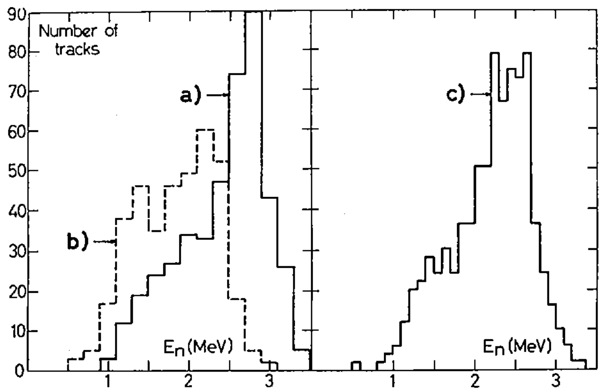

FIG. 3. Neutron-energy spectrum, E_n, as from nuclear emulsions exposed to 15 successive shots (30 kV) and placed at: a) 0°; b) 180°; c) 90°.

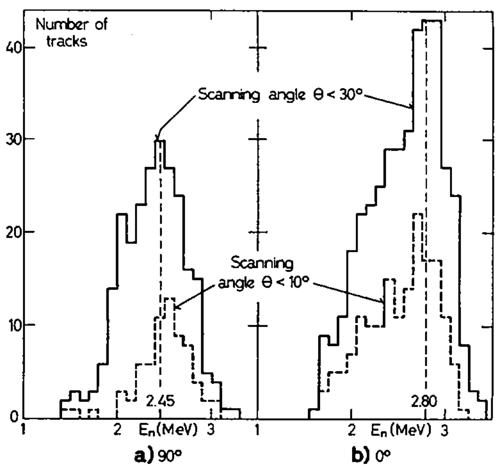

FIG. 4. Neutron energy spectrum, E_n, as from nuclear emulsions exposed to a single shot (36 kV; 1.2 torr D_2; Fast valve: 14 bar). Directions:
a) 90°; b) 0°.

2.45 MeV, while the 0° and 180° histograms are displaced by about 350 keV towards higher and lower energies, respectively. The width at half-amplitude on the energetic front of the spectrum of the 90° histogram (to minimize the scattering effect) gives $T_i \lesssim 22$ keV / 3, 4 /.

- Plastic scintillators

Time resolved neutron measurements have been carried out using plastic scintillators coupled to Philips 56 AVP photomultipliers (PM). The scintillators are placed along the two directions 0° and 90°, at 6.2 m and 7.0 m, respectively, from the center of the experimental chamber; a time-of-flight resolution of the γ pulse (attributed to ($n\,\gamma$) reactions with the iron of the electrodes) and of the neutron pulse is then possible. A precise timing of the electronic devices (delays along cables, PM cathode-anode transit time, transit time of γ rays) permits a measure of the time correlation between the signals of both PM's, of the X-ray signals from solid-state detectors, and of the image converter. A typical oscillogram is given in Fig. 5. All oscillograms display two neutron pulses (and two γ-ray pulses) separated by a variable time delay of about 100 ns. Under identical, initial, experimental conditions, the delay (τ) depends on the total number of neutrons (N_n) emitted by the DPF: $N_n \tau^2$ = constant (Fig. 6).

Time-of-flight results show that the neutrons emitted at 0° and 90° have an average energy of 2.8 MeV and 2.5 MeV, respectively, in agreement with the nuclear emulsion results.

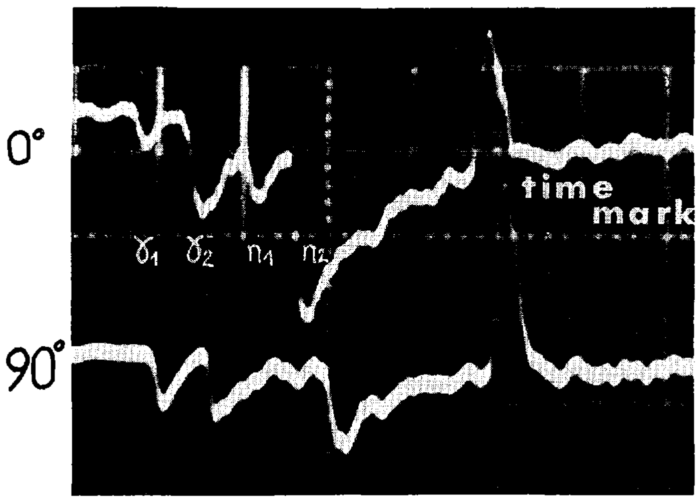

FIG. 5. PM signals: two γ-peaks and two neutron peaks can be seen. Initial conditions: 32 kV, 1.4 torr D_2 (no fast valve).

- Relative timing

  A typical timing of the streak pictures, neutron and x-ray signals is given in Fig. 7. It should be noted that the starts of the two streak traces coincide with those of the respective two neutron pulses (half width ≃ 60 ns) while the x-ray pulses are delayed by 25 ns and 50 ns, respectively.

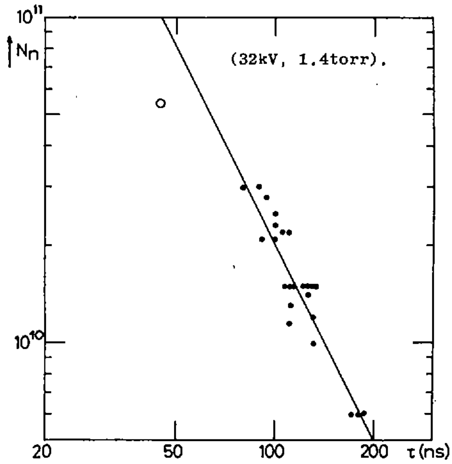

FIG. 6. A plot of the time delay, τ, between the two successive neutron signals versus the total neutron yield, N_n (32 kV, 1.4 torr).
[O = 1.85 torr, for comparison with Fig. 10, Part I].

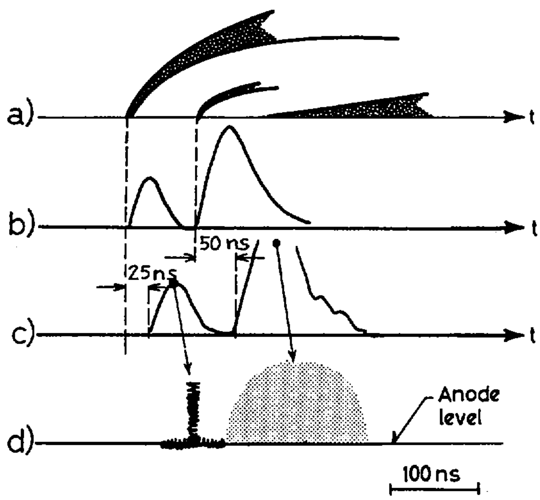

FIG. 7. Typical timing: a) streak picture; b) neutron pulses, c) X-ray pulses; d) X-ray framings.

TABLE I. NEUTRON FLUX RATIOS

	Static boiler	Moving boiler	Axial beam-target	Conical beam-target 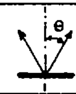	Composed beam-target + boiler model
$\left.\frac{0°}{180°}\right)$	1	$\frac{1+2a_2}{1-2a_2}$	$\frac{1+2a_1}{1-2a_1}$	$\frac{1+2a_1 \cdot \cos\theta}{1-2a_1 \cdot \cos\theta}$	$\frac{\alpha(1+A)(1+2a_1)+(1-\alpha)(1+2a_2)}{\alpha(1+A)(1-2a_1)+(1-\alpha)(1-2a_2)}$
$\left.\frac{0°}{90°}\right)$	1	$1+2a_2$	$(1+A)(1+2a_1)$	$\frac{(1+A\cos^2\theta)(1+2a_1\cos\theta)}{1+\frac{1}{2}A\sin^2\theta}$	$\alpha(1+A)(1+2a_1)+(1-\alpha)(1+2a_2)$

Energy shift between the neutron spectra corresponding to 0° and 180° $\Delta E_n = E_n^* \, 4\, a \cos\theta$

Definition of the symbols

α = percentage of the neutrons due to the beam-target

$\left.\begin{matrix} a_1 \\ a_2 \end{matrix}\right\} = \frac{\text{center of mass velocity}}{2.2.10^9} \left\{\begin{matrix} \text{beam-target} \\ \text{boiler} \end{matrix}\right.$

$\frac{d\sigma}{d\omega} = 1 + A\cos^2\beta + \ldots..$ (DD reaction)

$E_n^* = \left\{\begin{matrix} \text{energy of the neu-} \\ \text{tron in the center} \\ \text{of mass system} \\ \text{(2.45 MeV)} \end{matrix}\right.$

b) AN EMPIRICAL MODEL FOR THE DPF

An attempt is made here to find a rather simple, phenomenological model capable of fitting all our experimental results. A physical interpretation of this model is still to be elaborated.

Neutron measurements serve to value a given DPF model. The neutron fluxes in the three directions (0°, 90°, 180°) are proportional to certain expressions that depend on the values of "a" (center of mass velocity of the colliding deuterons/velocity of 2.45 MeV neutrons) and of "A" (coefficient of anisotropy of the d(d, He^3)n cross-section); these expressions depend on the considered DPF model.

All proposed simple DPF models (moving boiler, beam-target, conical beam-target) were checked to be incompatible with the experimental results / 5 /, in particular with regards to the value of "a" as obtained from both nuclear emulsion and time-of-flight measurements, and, that from flux anisotropy measurements. Moreover, in the case of the moving boiler ("A" = 0) and of the axial beam-target ($A \neq 0$), it is impossible to find an agreement even between the values of "a" and "A" as obtained from flux anisotropy measurements (a and A are known functions of the particle energies).

A model, consisting of a mixture of "beam-target+moving boiler", is able to explain the experimental results; four parameters have to be determined (α, a_1, a_2, A; where α is the fraction of neutrons due to the beam-target) (see Table I) from four available relations: the two flux rations: 0°/180° and 0°/90°, the relation between "a" and "A" (as given in the literature / 1 /), the value of "a" (as determined from nuclear emulsions and from time-of-flight measurements). The solution is: $\alpha = 0.2$; $A = 1.0$; $a_1 = 0.07$; $a_2 = 0.008$.

The analysis of the shape of the nuclear emulsion histograms, obtained in the light of such a model, provides an independent check of the model itself and more precise evaluation of the parameters; the shape of the single shot 0°-histogram (Fig. 4b), obtained with an emulsion placed very close to the DPF ($\simeq$ 10 cm), allowing the assumption that the contribution of the scattered neutrons is negligible or at least uniform, can in fact be interpreted as follows:

If the "boiler" and "beam-target" neutrons are centered around 2.50 MeV ($a_2 = 0.008$) and 2.80 MeV ($a_1 = 0.07$), respectively, the part of the histogram at the left of 2.50 MeV will be due practically to the "boiler" (exactly, if the "beam" is monoenergetic). Assuming a symmetrical distribution of the "boiler" neutrons around 2.50 MeV, the histogram of the "beam" neutrons can be easily obtained (Fig. 8) giving a more accurate determination of the energy of the "beam" and an independent value for the fraction of the neutrons corresponding to the "beam". As can be seen (Fig. 8), the

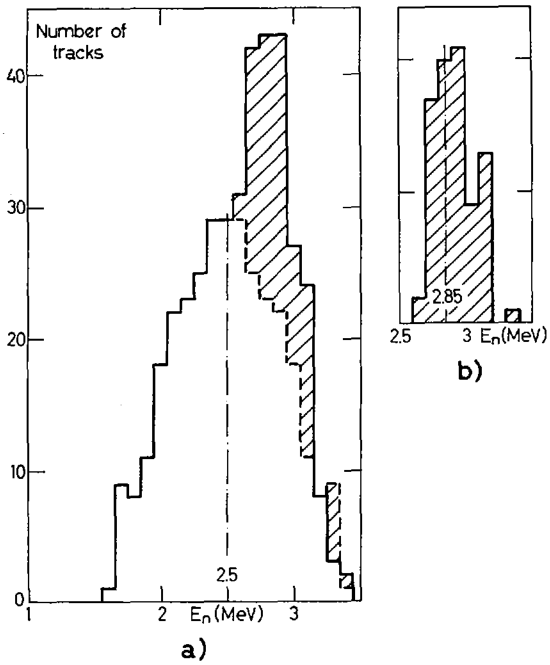

FIG. 8. Retrieval of the histogram of the "beam" neutrons:
a) Overall histogram; symmetric (around 2.50 MeV) "boiler" spectrum; in shaded area: remaining "beam" neutrons.
b) Resulting "beam" neutron histogram.

"beam" contributes about 20% of the neutrons, with an energy centered at 2.85 MeV, in good agreement with the previous 2.80 MeV; one thus gets, for a typical discharge at 36 kV: 20% from a beam of 105 keV, and 80% from a boiler moving at a velocity of 15 cm/µs.

c) EVALUATION OF THE PARAMETERS (for a typical 32kV, 77 KJ discharge).

- The ion drift velocity of 15 cm/µs obtained from the neutron measurements is in good agreement with the preliminary numerical results (macroscopic velocity $\simeq$ 10 cm/us). If the "streak" records the region of maximum density, the experimental value of the velocity of this maximum ($\sim$ 30 cm/us) is also in agreement with the numerical results which give a value of about twice the macroscopic velocity.
- The time-resolved x-ray pictures give directly for the region of high T_e a diameter of $\simeq$ 2 mm and a height of $\simeq$ 1 cm during the first compression, and a much larger diameter during the second compression. T_e is 6 KeV at the maximum of the first compression.

From the neutron spectra, $T_i \leq$ 22 KeV during the second contraction.

- The streak pictures and the neutron emission oscillograms are interpreted as witnessing two successive plasma contractions, in agreement with the conclusions obtained from the numerical calculations.

  Numerical calculations, based upon a simplified theory of adiabatic oscillations of the plasma column / 6 /, show that for identical initial conditions the neutron production $\mathcal{N}$ should vary as τ^{-2} (τ is the delay between the two successive contractions), which is effectively observed on streak pictures and time-resolved neutron measurements. Physically, this can be understood as follows: for the same initial conditions, the most important jitter is on the thickness of the plasma layer and, hence, on the radius r of the focus; for the same line density and temperature, $\mathcal{N}$ varies as r^{-2}, and τ is proportional to r as seen from dimensional considerations. The $\mathcal{N}\tau^{2}$= const relation has been derived on the assumption of purely dynamical heating; one can take its experimental verification as an argument against the importance of turbulent heating, which would be largely a function of current density and then of plasma diameter. The numerical calculations give a relationship between focus radius, density and temperature.

- Another relation between these three parameters is provided by the number of neutrons emitted from the boiler, assuming a Maxwellian ion temperature (not always legitimate).

  Two possible sets of values, satisfying these two relations, are given below as examples:

  a) r = 0.5 mm $\quad n \simeq 10^{20} \quad$ T = 3 KeV

  b) r = 2.0 mm $\quad n \simeq 6.10^{18} \quad$ T = 6 KeV

  (here already the ions are no more Maxwellian).

- The delay between the neutron and x-ray pulses being about equal to the half-width of the neutron pulses, the equipartition time ($t_{ie} \propto T_e^{3/2}.n^{-1}$) is definitely longer than the pulse duration. The measurement of T_e (first burst) gives then an upper limit to the density: $n \ll 5.10^{20}$ during the first compression. On the other hand, T_i should be larger than T_e.

- It seems then that the main neutron burst (second compression) could originate from a plasmoid which would be definitely hotter ($T_i \simeq$ 10 KeV,?), bigger (r = a few mm) and less dense (n = a few times 10^{18}) than previously accepted.

- The current carried by the run-away ions can be calculated from the energy of the beam (100 KeV): $I \simeq 10^{24}/n$ (A) (n is the density of the target supposed to be 1 cm thick), while $I_{total} \simeq$ 1 MA. The conduction current carried by

the ions is proportional to (N . ν_{boiler}). Substituting an approximate value of N obtained from the Bennett relation, and assuming $T_e \simeq T_i \simeq 6$ KeV, it turns out that an appreciable part of the current is carried by the ions.
– The physical implications of these results are not yet clear.

REFERENCES

/ 1 / LUZZI, G., SAMUELLI, M.: Internal Report LGI No. 70/17/E

/ 2 / MAISONNIER, CH., SAMUELLI, M., ROBOUCH, B.V., PECORELLA, G.: "IV European Conference on Controlled Fusion and Plasma Physics", Rome (1970) p. 177.

/ 3 / CIPOLLA, F.: Internal Report LGI No. 68/23.

/ 4 / LEHNER, G., POHL, F.: Z. Physik 207,(1967) 83.

/ 5 / SAMUELLI, M., LUZZI, G., MAISONNIER, CH.: APS Bulletin Nov. 1970, p. 1463, and Internal Report LGI No. 71/3/E.

/ 6 / SAMUELLI, M., MAISONNIER Ch., ROBOUCH, B.V., Internal Report LGI (to be published).

DISCUSSION

TO PAPERS IAEA-CN-28/D-1, D-2

M.J. BERNSTEIN: The neutron energy spectra for our device are similar to those presented by Mr. Maisonnier and we can explain these results by a sophisticated beam-target model. The acceleration model is illustrated in Fig. A. We assume rapid diffusion of the azimuthal magnetic field corresponding to the constricting distribution of current density. As a result of this changing magnetic field, an axial electric field is generated. A small fraction of the ions can be accelerated to high energies in these crossed fields following trajectories such as shown on the right side of the figure. Similar trajectories will be discussed in Paper D-8. There are two important aspects to these trajectories. First, the velocity vectors for fusion collisions with stationary target ions have a wide range of angles with respect to the axis. Second, ions with higher energies move more parallel to the axis. Using reasonable ion-energy and angular distributions, we have computed neutron-energy spectra and relative fluences in good agreement with those presented for the device at Frascatti. Our results are shown in Fig. B. Measured spectra at 0° and 180° are shown in the upper right. The assumed energy and angular distributions are shown on the left and the computed results are displayed on the lower right.

Except for the low-energy scattered neutrons in the measured results, one sees good agreement with regard to the widths of the spectra and the average energy shift. The computed spectra at 90° also match the results reported in Paper D-2. Neutron energy and flux measurements on several discharges give results that can be explained by the crossed-field acceleration of deuterons, which then collide with stationary ions. But there are some experimental results that can only be explained by the collison of energetic ions with ions of comparable energies.

J.P.F. CONRADS: I might mention that at Jülich we also have evidence of two different distributions of the ions producing the neutrons. One of these distributions is predominantly one-dimensional (axis of the electrodes) with an average energy of about 300 keV. This high energy has been confirmed, along with other measurements, by the appearance of the two neutron lines of the ^{7}Li (d, n) ^{8}Be reaction with energies of 10.8 MeV and 13.3 MeV, respectively. The neutron yield from these lines is at least as high as the yield of the d, d-reaction with a neutron line close to 2.5 MeV.

I also have a question. Figure 5 of Paper D-2 shows two PM-signals from X-rays and two for neutrons, for both 0° and 90° observation directions. The ratio of your X-ray-signals γ_1/γ_2 is different for the two directions of observation. Have you any explanation for this?

C. MAISONNIER: The second signal, γ_2, is due mainly to (n, γ) reactions in iron ($\simeq$ 900 keV), as mentioned, so that the ratio of the amplitudes of γ_2 and n_2 should be (and is effectively) the same at 0° and 90°: the 900 keV γ-rays and the neutrons cross the various obstacles without appreciable attenuation. On the other hand, the first pulse, γ_1 is a mixture of γ-rays from (n, γ) reactions and hard X-rays (up to 100 keV) emitted by the discharge during maximum compression; these X-rays suffer different attenuations along the 0° and 90° directions. Moreover, these X-rays could be emitted anisotropically.

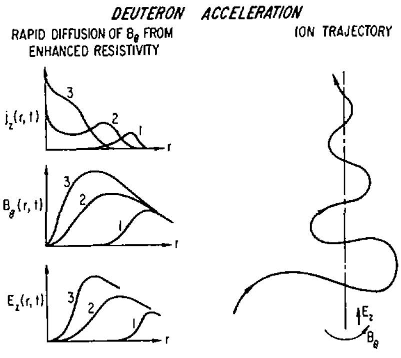

FIG. A. Acceleration model.

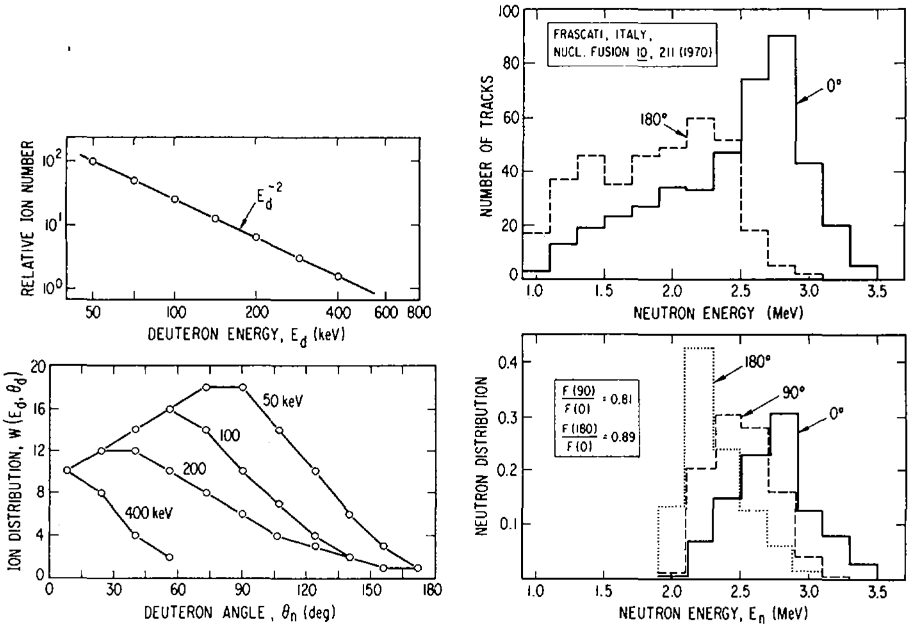

FIG. B. Measured and calculated results on ion and neutron distributions.

J.H. LEE: Your last slide showed temporal correlations of various measurements; the X-ray onset is seen to be delayed after the start of the neutron pulse, which coincides with the plasma focus formation observed optically. However, in axial streak pictures similar to yours, which I made with a Mather-type device, I found that the onset of X-rays always coincided with the optically recorded focus formation. Is the time of flight in your experiments compensated for the neutron pulse which comes from the detector located some distance away? And, have you any explanation for the delayed X-ray emission?

C. MAISONNIER: The time correlation between the various signals is a true one: appropriate corrections have been applied for the various time-of-flight and transit times.

Since the electrons are probably heated by the ions, and the electron-ion collision time is much longer than the duration of compression, it was to be expected that the maximum X-ray emission would occur during the decay of neutron emission.

W.H. BOSTICK: I should like briefly to refer to our own work. Image-converter photographs (5 ns) of the plasma focus with a hollow centre electrode along the electrode axis show the visible "pinch", 4 mm in diameter, at the moment of maximum compression. No neutrons are detected at this time; the neutrons begin about 30 ns later and reach their peak after about 150 ns when there is no longer a visible pinch on the axis. During neutron production the photos show bright regions, where vortex filaments are combining in pairs, in an extended volume in the crown of the "umbrella". These photos were taken with the apparatus operating at the threshold of neutron production, where usually only one neutron pulse is observed. When operating at higher voltages, usually two neutron pulses are observed, one coincident with the filament annihilation in the "shaft" of the umbrella, the other coincident with annihilation in the crown of the umbrella. Even at the moment of maximum compression of the "pinch", the visible 4 mm diameter area contains bright spots about 0.2 mm in diameter, which we interpret also as filaments, end-on, at the commencement of annihilation. We ascribe the observed neutrons and X-rays to the magnetic energy which is released locally with annihilation of the plasma vortex filaments. This is basically the solar flare phenomenon.

MEASUREMENTS OF THE PLASMA CONFINEMENT AND ION ENERGY IN THE DENSE PLASMA FOCUS

N.J. PEACOCK
UKAEA Culham Laboratory, Culham, Abingdon, Berks
M.G. HOBBY
University of Leicester
P.D. MORGAN
Royal Holloway College, London
United Kingdom

Abstract

MEASUREMENTS OF THE PLASMA CONFINEMENT AND ION ENERGY IN THE DENSE PLASMA FOCUS.

The structure and velocity of the plasma boundary during the implosion phase of the dense plasma focus has been studied using repetitively-pulsed, 1 nanosecond exposure, transmission photography with spatial resolution of 100 microns. Both acceleration and deceleration of the plasma boundary are observed by shadowgram and schlieren photography. Long-wavelength, Rayleigh-Taylor instabilities grow on the boundary during its acceleration. On subsequent deceleration, a singularly-steep density gradient is observed transiently on the axis of symmetry and has dimensions smaller than any other plasma parameter except the collision-free skin depth. The density distribution, which is approximately parabolic with a maximum on the axis of symmetry when the pinch is well developed, is derived directly from interferograms. Local break-up of the pinch takes place, of ten due to m = 0 and, less commonly, m = 1 instabilities. The sustainment time of the pinched plasma is not more than 50 nanoseconds and corresponds directly with the initial burst of thermal X-rays.

No correlation of the refractive index gradients could be found with the later, double and triple pulses of soft X-rays (and neutrons), which in some instances are emitted 200 nanoseconds after the first pulse, and this implies the existence of a more tenuous plasma ($n_e < 8 \times 10^{18}$ cm^{-3}) at this time.

The ion energy distributions, transverse to the axis of symmetry, of several ion species of argon and neon have been measured using high resolution, X-ray spectroscopic techniques. The ions have a thermal energy distribution with a mean energy of about 9 keV. These results, in addition to the deuterium ion temperature estimated from the neutron emission, are interpreted as giving a scaling law for the transverse energy $E_{Z/M} = T_0 (1 + Z^2/M)$, where T_0 results from compression and resistive heating and the remainder may be due to weak turbulence.

Dielectronic recombination is responsible for the Li-like ion satellites and has to be taken into account to explain the intensity and the time of appearance of the line emission.

1. INTRODUCTION

In contrast to much of the research on the dense Plasma Focus which is aimed at providing an explanation for the characteristics of the intense neutron emission [1,2], the authors' programme attempts to relate the particle heating and confinement to the observed dynamics and structure in the collapse phase. An important feature of this programme has been the development of a 2-dimensional (r,z,t), 2-fluid MHD numerical code to describe the Focus, [3], and its comparison with the experimental observations, [4].

The present paper extends the experimental observations on the dynamics and structure of the focus [5, hereinafter referred to as Paper 1] using improved time and spatial resolution, and examines the role of instabilities in the plasma. The object of the experiments is to derive a more detailed description of the plasma dynamics and of the electron density distribution which then may be compared with the code. The dimensions of the electrodes and the discharge chamber and the parameters of the electrical circuit are identical to those described previously, [Paper 1,6].

In addition, the spectroscopic study of the ion energies and the ion confinement reported in the earlier Paper 1 has been extended. Profiles of line emission from heavy gases seeded into the deuterium and viewed transverse to the axis of symmetry give information on the mean transverse ion energy as a function of mass and charge of the ion, and enable us to propose a mechanism for the ion heating.

Since any comprehensive model of the neutron emission [2] is likely to involve anisotropic ion energies in the directions transverse and parallel to the axis of symmetry (i.e. $E_r \neq E_z$), it is clearly desirable to measure both components. The present paper discusses only the transverse energy.

2. DYNAMICS OF THE FOCUS

2.1 Experimental Arrangement - Nanosecond Transmission Photography

Measurements of the plasma refractive index and its gradients across the plasma boundary are conveniently made by interferometric, shadowgraph and schlieren photography using a pulsed ruby laser as an external light source. In order to study the fine structure (< 0·1 mm) in the focus a time resolution of 1 nanosecond is required. This is achieved by clipping the output from the conventionally Q-switched laser with an extra-cavity, electro-optic shutter, [7].

In the shadowgraph and schlieren photography, a time-sequence of typically three exposures is obtained by splitting the laser pulse and illuminating the same discharge at variable time intervals using optical-delay techniques, [8]. In the schlieren technique a spherical obstacle is used to record density gradients in the plasma in all directions in the plane orthogonal to the incident laser beam. By varying the obstacle diameter it has been ascertained that deviations of the laser light of up to ~ 30 milliradians are introduced by plasma refraction. This sets a lower limit to the maximum density and its gradient.

The density itself is measured by fringe-shift interferometry using a parallel-plate Mach-Zehnder, arranged so that single-plate control is possible, [9].

2.2 Results of Shadowgraph and Schlieren Photography - Motion of the Plasma Boundary, Dimensions of the Plasma and Fine Structure

Figure 1 shows a sequence of shadowgrams taken during the implosion of the current sheath, the time between exposures, Δt, being in this case 15 nanoseconds. Figure 2 shows a sequence, later in time, during the dense pinch phase where $\Delta t = 6{\cdot}5$ nanoseconds, and it is evident that there is considerable change in the boundary and structure of the focus even on this rapid time scale. From these and similar records, values of the velocity and acceleration of the boundary can be derived particularly since instabilities at the boundary serve as local identification tags. The change in the refractive gradient at the boundary is quite sharp $\delta\left(\frac{\partial ne}{\partial r}\right) \lesssim 1$ mm and does not change appreciably during the implosion. The non-cylindrical nature of the plasma compression is thus readily followed. The velocity of the boundary is initially greatest close to the anode where, due to the cusped shape, figure 3, the plasma pressure is highest. As pressure balance is

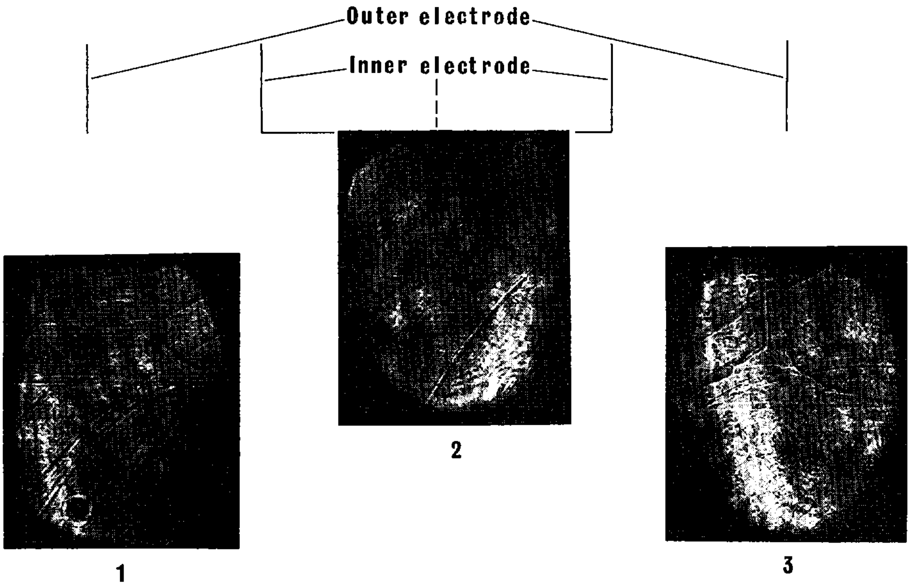

FIG. 1. Shadowgram sequence during run-down and pinch stages; time interval between frames = 15 ns. Inner electrode diameter = 5 cm; V = 30 kV; p_0 = 2.5 torr (D_2 + 4% Ar).

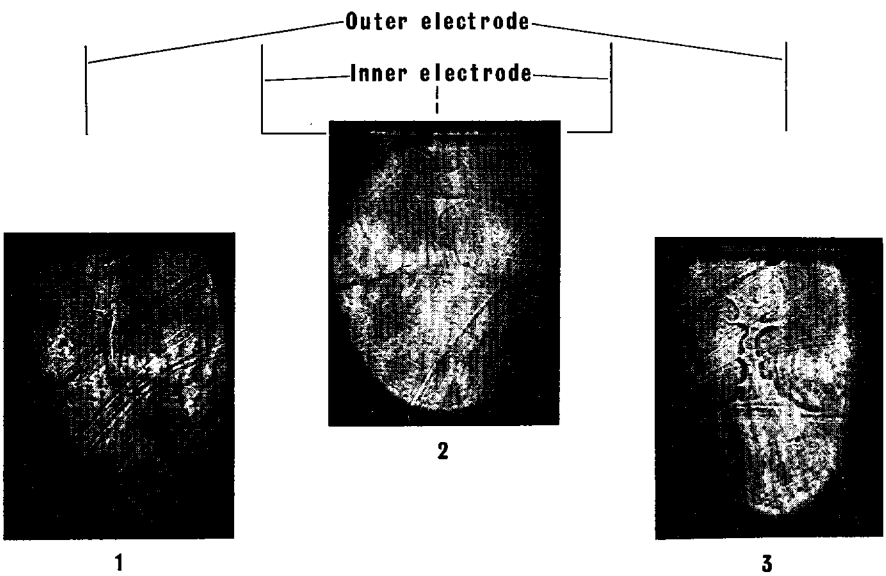

FIG. 2. Shadowgram sequence during dense-pinch stage; time interval between frames = 6.5 ns. Inner electrode diameter = 5 cm; V = 30 kV; p_0 = 2.5 torr (D_2 + 4% Ar).

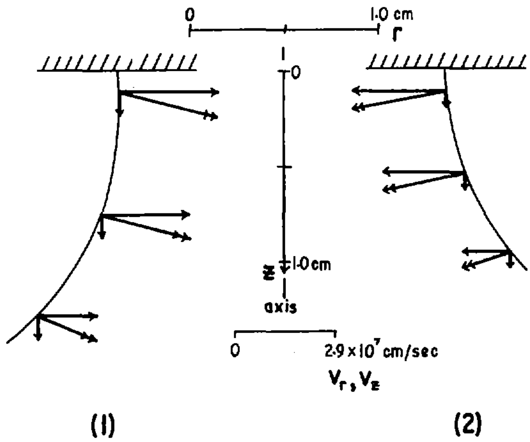

FIG. 3. Variation of radial and axial velocity of the imploding sheath with distance from electrode surface; (1) V = 28.3 kV; (2) V = 24.3 kV; p_0 = 2.5 torr (D_2 + 4% Ar).

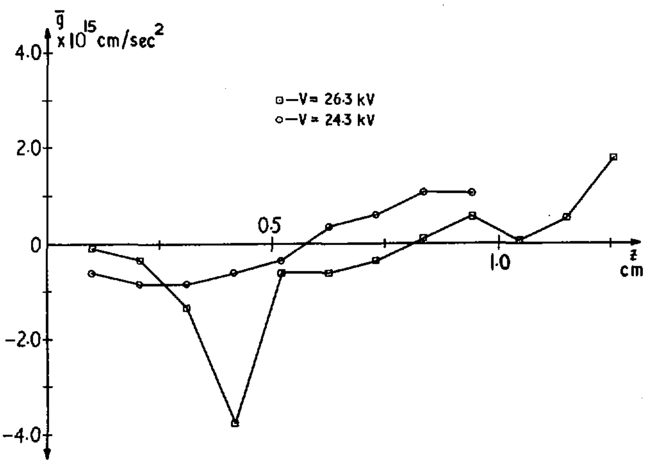

FIG. 4. Variation of radial acceleration of the imploding sheath with distance from electrode surface, for two different charging voltages. Initial pinch diameters ~1.7 cm at z = 0.1 cm. p_0 = 2.5 torr (D_2 + 4% Ar).

approached the boundary close to the anode decelerates as illustrated in figure 4. Boundary velocities up to a maximum of 4×10^7 cm sec^{-1} have been measured, corresponding to the highest voltages (30 kV) and with filling pressures of 3 torr D_2. A few percent of argon added to even lower deuterium pressures is sufficient to slow down the implosion. All of the subsequent analysis pertains to 2·5 torr D_2 + 4% Ar doping. At the time the plasma has reached a maximum compression the boundary is fluted (figure 2) due to the Rayleigh-Taylor instabilities, which have grown earlier during the implosion phase (figure 1). However local break up of the pinch then proceeds through the growth of m = 0 and, less often, m = 1 instabilities (figure 2). Over a field of view (z × 2r) of 3·8 cm × 2·7 cm covered by the transmission photography, the total duration of the quasi-cylindrical implosion, of the formation of the dense pinch and its break-up is no greater than 100 nanoseconds.

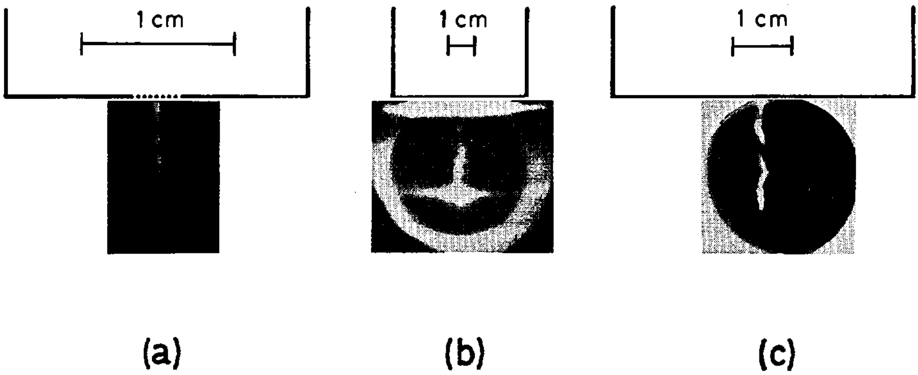

FIG. 5. (a) Schlieren, (b) image-converter camera and (c) time-integrated soft X-ray photographs of dense-pinch stage. V = 30 kV; p_0 = 2.5 torr (D_2 + 4% Ar).

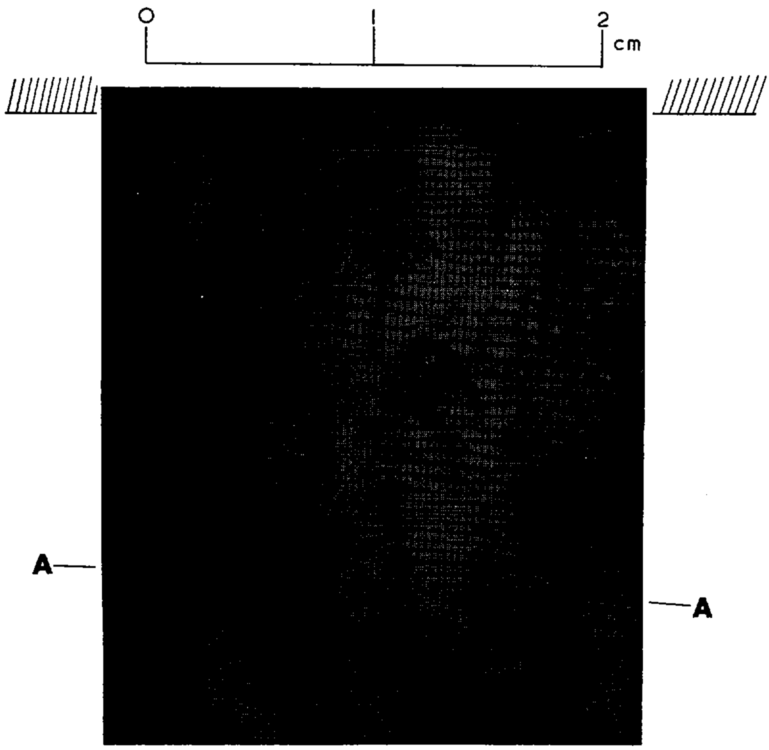

FIG. 6. Mach-Zehnder interferogram of dense-pinch stage. V = 30 kV; p_0 = 2.5 torr (D_2 + 4% Ar). [AA is section along which the fringe shifts have been analysed - see Fig. 7].

After this time no features are observed with $\hat{n}_e > 8 \times 10^{18}$ cm^{-3} (see also section 2.4).

At a distance z below the anode where locally the boundary decelerates to almost zero velocity, there appears transiently, along the axis of symmetry, a singularity in the density gradient (see figures 2,6). The dimension of $\delta\left(\frac{\partial ne}{\partial r}\right) \lesssim 100$ microns and is smaller than all characteristic plasma dimensions except the collisionless skin depth c/ω_{pe}. This may be interpreted as damping of a collision-free shock arriving on the axis of symmetry.

The regions of the plasma, with refractive index n, which result in maximum laser beam refraction $2\int_{\ell=0}^{r} \frac{1}{n}\frac{\partial n}{\partial r}\,d\ell$, are readily determined by inserting a large obstacle in the schlieren optics and resorting to a long (unclipped) Q-spoiled laser pulse of width about equal to the duration of the dense-pinch phase. A schlieren photograph, figure 5, shows the region of the steepest density gradients and highest density to be on the axis. The fine structure occurs within an envelope 1 mm in diameter. This region also corresponds, figure 5, to the locality of intense line emission due to collisions of thermal (2 keV) electrons with ions, [Paper 1]. A lower limit for the peak density in this region can be derived from the refraction and is $7{\cdot}5 \times 10^{19}$ cm^{-3}. The average density across the plasma is however less, (section 2.4 and also Paper 1) by at least a factor of two.

2.3 Instability Growth Rates

During the acceleration phase, Rayleigh-Taylor instabilities (R.T) develop in the plasma boundary. Direct measurements of ω, the growth rate, g, the acceleration and k, the wave number are taken from the shadowgrams (figure 1). Dissipative processes such as viscosity ν and resistivity (σ^{-1}) will damp out the fastest growing (large k) disturbances, and there will be some value of ω (i.e. ω_m) where the inertial forces are just balanced by the rate of energy dissipation, [10]. The corresponding wave-length k_m^{-1} will then dominate the instability spectrum.

Assuming resistive damping as the dominant mechanism, the observed R.T. wavelength could be explained by a resistivity which is anomalously higher than the zero-field value by a factor approaching 100 or, as is more likely, by the effects of a few percent Li-like argon ions in the plasma. If, on the other hand, viscous damping was dominant, a consideration of the figures in Table I shows that the observed wavelength can be accounted for provided $\omega_{ci}\tau_{ii} \approx 2$, an entirely reasonable situation. For either damping mechanisms (e.g. Table 1) ω (observed) $< \omega_m$ (calculated). A plane boundary approximation has however been used in these preliminary calculations.

TABLE I. COMPARISON OF PARAMETERS

ω (observed)	λ (observed)	$\sqrt{gk}$	λ_m	$\sqrt{gk_m/2}$
3.3×10^7 s^{-1}	3.2 mm	2×10^8 s^{-1}	3.2 mm	1.3×10^8 s^{-1}

Rayleigh-Taylor growth for mean plasma radius $r_p = 9$ mm, $g = 2.1 \times 10^{15}$ cm s^{-2}, $V_b = 26.3$ kV, $p_0 = 2.5$ torr (D_2+ 4% Ar), $T_e = 100$ eV and $T_i = 250$ eV (from the computations [3]), $n_e = 2 \times 10^{18}$ cm^{-3} (from interferometry, section 2.4), $\omega_{ci}\tau_{ii} \approx 2$

In the pinch phase local break-up of the compressed plasma is due to m = 0 instabilities as seen in figure 2. The growth time and wavelength are derived and the former is in reasonable agreement with that estimated from $r_p/\sqrt{\gamma p/\rho}$ ($\approx$ 10 nsecs), where the square root factor is the sound speed. Kink (m = 1) instabilities are less commonly observed with much slower growth rates and these are less important in the break-up of the pinch.

2.4 Interferometry - Radial Density Distribution

The interferogram at peak compression in figure 6 shows well-developed m = 0 instabilities and an early-stage of an m = 1 instability. The fringe shifts along the section A A (figure 6) are plotted in figure 7 as a function of position r/a orthogonal to the axis of symmetry, where a is the radius of the column. An average value of density $\bar{n}_e(r/a)$, at position r/a, may be obtained by dividing $\int_0^\ell n_e dl$ at that position by the chord of length $2(a^2 - r^2)^{\frac{1}{2}}$. In figure 7, $\bar{n}_e(r/a)$ is plotted versus r/a and is in approximate agreement with the parabolic function $\bar{n}_{em}(1 - (r/a)^2)$, where $\bar{n}_{em}$ is the maximum value of $\bar{n}_e(r/a)$. Thus it is also reasonable to propose a parabolic distribution for the actual density, $n_e(r/a)$, and thus obtain an estimate of the peak density on the axis, $\hat{n}_e$. For the section A A, a value of 8×10^{18} cm^{-3} is obtained for $\hat{n}_e$. Values of $\hat{n}_e$ up to 4×10^{19} cm^{-3} have been evaluated at other axial positions, closer to the anode, and are in good general agreement with those evaluated from the schlieren measurements (section 2.2) and from the soft X-ray intensity [Paper 1]. Relaxation of the sharp density front, observed during the implosion, to the parabolic distribution implies considerable penetration of the current finally into the pinch. Taking

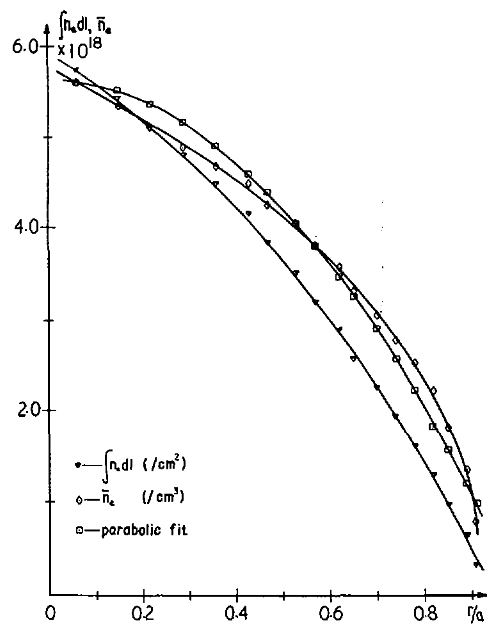

FIG. 7. Variation of $\int_0^\ell n_e d\ell$ and $\bar{n}_e(r/a)$ with axial distance. Analysis has been made along section AA of Fig. 6. A parabolic function $\bar{n}_{em}(1-(r/a)^2)$ is also shown. V = 30 kV; p_0 = 2.5 torr (D_2 + 4% Ar).

into account the effect of the impurities, the electrical conductivity temperature must be anomalously low by at least a factor of 10 to explain the field diffusion.

3.1 Line Emission Profiles in the X-ray Region

Line radiation between 3 and 14 Å from optical and inner-shell transitions in argon and neon seeded into the focus are observed from the pinched plasma, [Paper 1].

Doppler broadening of the lines due to thermal motion is,

$$\Delta\lambda_D = \lambda \cdot 2{\cdot}44 \times 10^{-3} \cdot \left(\frac{T}{M}\right)^{\frac{1}{2}} \text{(T in keV, M in a.m.u)} \quad (1)$$

For a complete profile analysis a resolution $\frac{\lambda}{\Delta\lambda_{inst}} > 10^3$ is required at temperatures of the order of 1 keV, and this was achieved using a focussing mica spectrometer [11] with an aperture W, of a few cms. Spectra from several discharges of the Plasma Focus (viewed orthogonal to the axis of symmetry and in 2·5 torr, D_2 + 4% Ar, Ne) were recorded in several orders on photographic emulsion placed round the Rowland circle. The Ar XVII lines shown in a microphotometer trace, figure 8, are considerably broadened relative to the characteristic X-ray lines of the anode material, e.g. $W_L\beta_1$.

The measured line profiles are subject to several instrumental broadening effects which must be removed before a true analysis can proceed. As well as the intrinsic broadening due to the dispersive crystal diffraction window there is an aperture-dependent geometrical aberration inherent in semi-focussing optics of the Johann type. There is also the broadening introduced by the finite emulsion thickness at oblique incidence. Overall corrections to the intensity profiles due to these effects are typically quite small, being 8% of FWHM for $W_L\beta_1$ in figure 8 and 3% of FWHM for the $^1S_0$ - $^1P_1$ Ar XVII line.

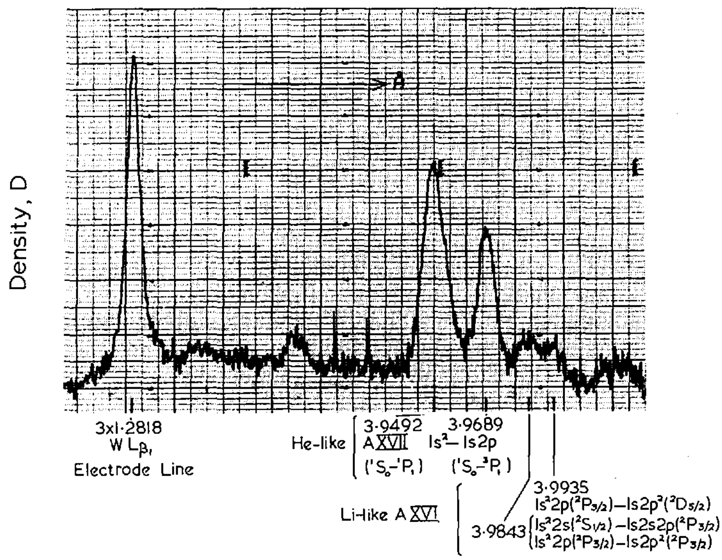

FIG. 8. Concave curved mica spectrum of a plasma focus discharge; V = 28 kV, p_0 = 2.5 torr (D_2 + 4% Ar).

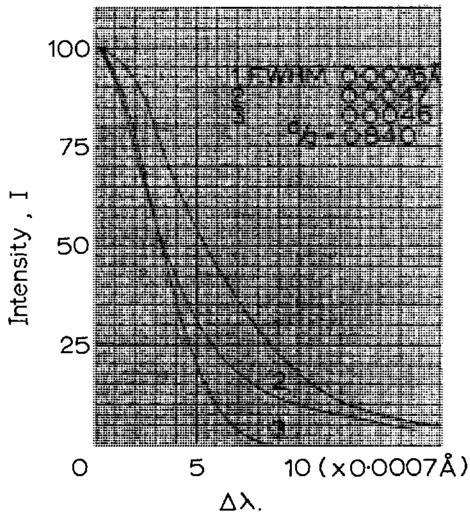

FIG. 9. Measured Ar XVII profile 1 (Voigt), compared with instrumental 2 (dispersive), and true 3 (Gaussian) profiles.

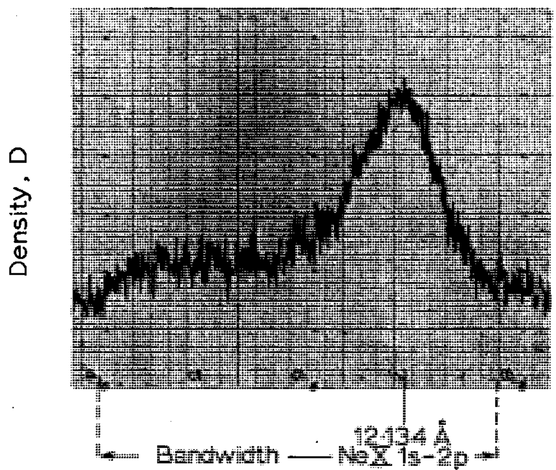

FIG. 10. Concave curved mica spectrum of a plasma focus discharge showing the effect of limited bandwidth; V = 28 kV, p_0 = 2.5 torr (D_2 + 6% Ne).

The corrected profiles e.g.,figure 9, are found to be a good fit to a Voigt function. The dispersive component of the profiles can be accounted for in all orders and at all wavelengths by the crystal diffraction pattern and the remaining Gaussian component is the true source function.

3.2 Results

Figure 10 shows the component profiles of the Ar XVII 3·9492 Å line. The Gaussian component of 0·0046 ± 0·0006 Å, if interpreted as a thermal width, corresponds to an ion temperature of 9 ± 3 keV. A similar analysis for the same argon line in third order yields an equivalent ion temperature of 10 ± 1 keV, and for the Ne X line in first order 9 ± 1 keV. The results are shown in Table II. The deuterium ion temperature has not been measured in this work but laser-beam scattering experiments in a similar apparatus [13], the neutron emission assuming a moving thermal source [12] and numerical calculations [3], all indicate an ion temperature of about 1 keV or slightly more. There remains only the problem of explaining the Gaussian source function and in particular its scaling with ion charge, Z, and atomic mass, M.

TABLE II. RESULTS OF LINE ANALYSIS

Ion	Transition	λ (Å)	Order n	$\Delta\lambda_{1/2}$ (Gaussian)	T_i(equiv)	Z	M
Ar XVII	$1s^2\ {}^1S_0 - 1s2p\,{}^1P_1$	3·9492	1st	0·0046	9 ± 3 keV	16	40
Ar XVII	$1s^2\ {}^1S_0 - 1s2p\,{}^1P_1$	3·9492	3rd	0·0048	10 ± 1 keV	16	40
Ar XVII	${}^1S_0 - {}^3P_1$	3·9689	1st	0·0047	9·4 ± 1 keV	16	40
Ne X	1s − 2p	12·134	1st	0·0203	9 ± 1 keV	9	20
DII					~1° → 2 keV* <5 keV+	1	2

°[13], *[3], +[12]

3.3 Interpretation of source function of lines

In summary, the spectroscopic results are (a) the source function $I_\lambda(d\lambda)$ is Gaussian, (b) $\frac{\lambda}{\Delta\lambda_{1/2}} \propto \sqrt{M}$, and (c) $\frac{\lambda}{\Delta\lambda_{1/2}} \sim 500$ to 1000 for the Neon and Argon lines. Resonance absorption broadening can be discounted on the grounds that the oscillator strength of the intercombination line is 10^5 times smaller than that of the allowed line of Ar XVII while the broadening of both lines is similar. Stark broadening at densities of $\sim 10^{19}\ cm^{-3}$ is also small relative to Doppler effects at these short wavelengths. For the Ne X Lyman series, the quasi-static effect is

$$\Delta\lambda_{stark(cm)} \simeq 0{\cdot}064\ \lambda^2\ n^2\ E\ (E \text{ in kV/cm})$$

which is $\sim 8 \times 10^{-4}$ Å at approximately 10 Å for Lyα. This is likely to be an upper limit to Stark broadening for the spectral lines under consideration. Wavelength shifts corresponding to the observed plasma velocity (section 2.2) of $\leqslant 4 \times 10^7$ cm sec^{-1} can quantitatively account for the observed line broadening, $\Delta\lambda_{1/2}$. However, the source function $I(d\lambda)$ is strictly Gaussian and this requires the ion velocities to have, or imitate, a thermal distribution.

The spectroscopic data is consistent with an ion temperature $T_i \sim 9$ keV, common to all the ions in the plasma. In this case, however, the neutron emission from thermonuclear reactions would exceed the observed emission while the plasma kinetic energy would also exceed that predicted by pressure balance. It is more reasonable to propose that the deuterium ion temperature is closer to that observed by laser scattering [13] and is between 1 and 2 keV as predicted by the 2-dimensional MHD code [3]. It is, therefore, probable that each separate ion species has a characteristic ion temperature. This could arise for example when there are electric fields in the plasma due to current-driven ion acoustic waves [14] with characteristic frequency $< \omega_{ip} = 1 \cdot 5 \times 10^2\, n_e^{1/2}$ c/s, (i.e. $< 7 \cdot 5 \times 10^{11}$ c/s). These waves will be damped by coulomb collisions, $\nu_{ei} \simeq 10^{11}$ c/s.

An estimate of the electric field, $\xi_0 e^{i\omega t}$ due to these waves can be derived from the average particle energy, E,

$$E = \frac{e^2 \xi_0^2}{4(\omega_{ip}^2 + \nu_{ei}^2)} \; \frac{Z^2}{M} \tag{2}$$

$\xi_0 \simeq 5 \times 10^4$ V/cm, and this is still smaller than the interionic Stark field in the plasma.

It is clear that if one includes an estimated value for T_i, for deuterium, Table 2, the ion energies do not scale either with M or Z alone. However, a scaling with Z^2/M gives as a best fit to the results.

$$E_{Z/M} = T_0(1 + Z^2/M) \tag{3}$$

with T_0 the true thermal component equal to $1 \cdot 4$ keV. Since the ion-ion relaxation time is of the order of a few nanoseconds, it is somewhat difficult to explain the existence of a separate energy for the different ions. However, a similar situation is known to exist in the orthogonal pinch, [15].

We now consider whether current-driven turbulence could play a role in heating the ions. Certainly the critical field for run-away electrons

$$E_C = 2 \times 10^{12}\ n\, Z^2/Te \qquad \text{V/cm}$$

can be exceeded in a magnetic field-free region by the inductive $\left(\frac{V \times B}{10^8}\right)$ V/cm field in the plasma column. The flux of hard (> 100 keV) X-rays are evidence that much higher electric fields can be generated during the plasma column break-up. However, the condition for relatively weak ion-acoustic turbulence, namely that the electron drift velocity should exceed the ion sound speed, is not satisfied unless a substantial fraction of the total current is confined to dimensions of the order of the filamentary structure observed with the nanosecond transmission photography and with the space resolved Ar XVII emission (see sections 2.2 and 3.4).

It has been pointed out recently [16 ,17] that a two-component ion distribution with a non-thermal component accelerated along the axis of symmetry could suitably modify the moving thermal plasma concept proposed in [1] and [18] to explain the puzzling features of the neutron emission (the latter are the large equivalent centre of mass velocity of the ions, > 10^8 cm sec^{-1}, and the nearly isotropic neutron emission). The spectroscopic analysis in this paper is concerned only with the thermal component since the plasma is viewed orthogonal to the axis of symmetry and the results in no way discount the existence of two-component ion-energy distribution.

3.4 Source-Crystal Aspect (and Evidence for Fine Structure)

Also emerging from the study of line profiles obtained with various source-spectrometer configurations is the vital importance of geometrical matching of the source to the crystal and its plane of curvature for maximum use of the source-radiation. The bandwidth of the instrument is entirely determined by the angular width of the source. The effect of this is demonstrated in figure 10 where the limited bandwidth of $\sim$ 0·1 Å imposed by a source 1 cm long, 130 cms from the crystal truncates the Ne X 1s - 2p line. Deliberately mismatching the source and crystal so that the bandwidth would be severely restricted for a very narrow source has, in fact, indicated the presence of thin, mobile filamentary structures in the pinch. Figure 11 shows the spectral intensity of the Ar XVII resonance line in third order when such a mismatch was effected. The 'structure' is consistent with emitting regions of the order of 100 μm in diameter. Filaments of the same dimensions are also evident in interferometric and shadowgram studies of the discharge, section 2.2.

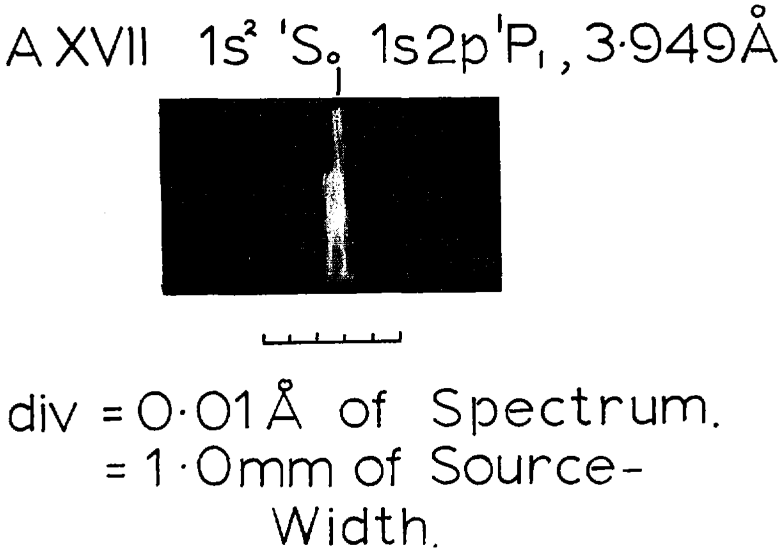

FIG. 11. Concave curved mica spectrum of a plasma focus discharge showing the effect of source fine-structure and motion when the bandwidth is deliberately set less than the line-width; V = 28 kV, p_0 = 2.5 torr (D_2 + 4% Ar).

3.5 Time-Resolution of Line Emission and Evidence for Dielectronic Recombination

In Paper 1, calculations of the ion confinement, estimated from the appearance time and relative intensities of the H and He-like argon ions, depended on the rate coefficients for ionisation and recombination. Following this, it is important to consider modifications to those rates due to dielectronic recombination, autoionisation and collisional step-wise excitation [19].

At most it would seem that the ionisation rates could be enhanced by a factor of 2 or 3 due to step-wise effects. Dielectronic recombination, on the other hand, could account for most of the recombination for highly-stripped ions. A consideration of the expression derived by Burgess, [20], indicates that for Ar XVII with $n_e = 2 \times 10^{19}$ cm^{-3} and Te = 2 keV, dielectronic recombination could be a factor of ten higher than collisional-radiative recombination, assumed in Paper 1.

The effect of the low thermal limit ($n^* = 10$ for Ar XVII) which decreases the dielectronic recombination has been taken into account in this estimate.

The structure of the Li-like satellites ($1s^2 2s - 1s2s2p, 1s2p^2$) to the He-like resonance line ($1s^2\ ^1S_0 - 1s2p\ ^1P_1$), shown in figure 8 for the Ar XVII ion, provides direct confirmation that dielectronic recombination is the dominant process for this ion. In the case where dielectronic recombination populates the upper levels of the satellite lines there will be typically two satellites, of equal intensity; this according to [21] should be ~ 20% of the resonance line intensity.

In the focus the two Li-like satellites, figure 8, have been identified previously, [6], and have an intensity which is 20% of the He-like resonance line intensity for neon, and 15% for argon. In the alternative case that the $1s2s2p, 1s2p^2$ levels are populated directly from the Li-like ion, only one component, that arising from the $1s2p^2\ ^2P^e$ level, would be in evidence. The other levels would lead preferentially to autoionization.

The effect of the enhanced recombination is to lower the degree of ionization which would exist in the steady-state at a given temperature. The intensity of H-like relative to He-like argon then indicates a closer approach to a steady state than in Paper 1.

In the analysis of ion energies it has been demonstrated [22] that it is important to compare ions which appear at the same time. Figure 12 shows typical time-histories of the inner-shell Li-like lines and the He-like resonance lines of argon measured with p-n junction surface barrier detectors [Paper 1]. These are compared with the neutron emission and the electrical waveforms. For all the plasma lines considered in this paper the time of emission was similar, though this result may be in error, since, except for the $1s^2 - 1s2p$ transitions a relatively large continuum contribution was admitted with the line.

It is of interest to note that when the plasma meets the axis of symmetry (dI/dt (Minimum)) the peak of the soft X-rays follows some 20 nsecs or so later, and after a similar time interval the peak of the neutron emission follows. In many instances double and even

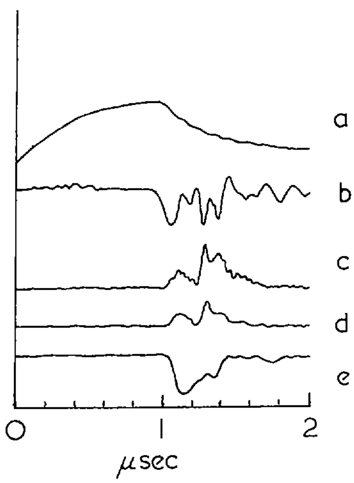

FIG. 12. Electrical, soft X-ray and neutron diagnostic time sequences of a plasma focus discharge; V = 28 kV, p_0 = 2.5 torr (D_2 + 4% Ar). (a) I, (b) dI/dt, (c) soft X-rays, Ar XVII He-like wavelength, (d) soft X-rays, Ar XVI Li-like wavelength and continuum, (e) neutrons (corrected for time of flight).

triple, soft X-ray pulses have been seen, separated by 100 nsec or more. Corresponding multiple neutron pulses are also seen, with the later ones of low intensity. These later pulses of soft X-rays were synchronized with the laser pulse used in the optical studies but no refraction or shift of the background fringe pattern could be discerned.

4. CONCLUSIONS AND DISCUSSION

The nanosecond-exposure transmission photography confirms the following features of the plasma dynamics which are predicted by the 2-D two fluid code, [3]: (a) The cusped topology of the plasma boundary during the implosion phase results in a continuous axial flow of plasma from the compression volume so that only a small fraction (~ 5% is measured by the interferograms) of the original gas exists in the final pinch. (b) The width of the plasma boundary is $\lesssim 1$ mm during the implosion, but at peak compression the density distribution relaxes to a parabolic form typical of a diffuse pinch.

Rayleigh-Taylor instabilities cause fluted distortions of the imploding sheath but since the boundary decelerates before maximum compression they do not contribute greatly to plasma loss. The most highly compressed region of the pinch, initially close to the anode, suffers break-up through $m = 0$ and, less often, $m = 1$ instabilities, the former having a growth time of 10 nanoseconds.

One feature not predicted by the fluid code is the fine (< 100 microns) filamentary structure within the envelope of the compressed plasma. This has been observed both in the optical study and in the X-ray spectroscopy.

The emission line profile analysis indicates a thermal energy distribution for each ion species, the transverse energy in each scaling as Z^2/M. The component of the ion energy along the axis has not been investigated. The importance of dielectronic recombination for these ions has been indicated.

Average values of the measured pinch parameters e.g. the deuterium ion temperature, the electron density and the electron temperature measured previously, [5], are in agreement within a factor of two with those predicted by the fluid code.

The scaling of temperature with Z^2/M suggests a method for transferring some of the directed energy in the implosion into thermal energy, namely the addition of a small percentage of heavy gas (less than that which would cause radiative cooling i.e., $\lesssim 5\%$ argon). Finally the X-ray and neutron pulses which occur up to 200 nanoseconds later than the first pulses cannot be identified with any optical features of a dense focus. This is unlikely to be simply a field of view limitation, since this was extended to 6 cm below the centre electrode. It is more likely that the source of the later emission is a much more tenuous plasma with $\hat{n}_e \ll 8 \times 10^{18}$ cm^{-3}.

REFERENCES

[1] BOTTOMS, P.J., CARPENTER, J.P., MATHER, J.W., WARE, K.D. and WILLIAMS, A.H. Paper CN-24/G-5, Proc. of IAEA 3rd Conf. on Plasma Physics and Controlled Nuclear Fusion Research, Novosibirsk, (1968).

[2] POTTER, D.E. and HAINES, M.G. Proc. of IAEA 4th Conf. on Plasma Physics and Controlled Nuclear Fusion Research, Wisconsin, (1971).

[3] POTTER, D.E. Ph.D Thesis, University of London, (1970).

[4] MORGAN, P.D., PEACOCK, N.J. and POTTER, D.E. Proc. of 3rd European Conf. on Controlled Fusion and Plasma Physics, p.118, (1969).

[5] PEACOCK, N.J., WILCOCK, P.D., SPEER, R.J. and MORGAN, P.D. Paper CN-24/G-4, Proc. of IAEA 3rd Conf. on Plasma Physics and Controlled Nuclear Fusion Research, Novosibirsk, (1968).

[6] PEACOCK, N.J., SPEER, R.J. and HOBBY, M.G. J. Phys. B, 2, p.798-810, (1969).

[7] MORGAN, P.D. and PEACOCK, N.J. To be published, (1971).

[8] BASOV, N.G., KROKHIN, O.N. and SKLIZKOV, G.V. Appl. Opt., 6, p.1814-1817, (1967).

[9] KINDER, W. Optik, 1, p.413-448, (1946).

[10] GREEN, T.S. and NIBLETT, G.B.F. Nuclear Fusion, 1, p.42-46, (1960).

[11] JOHANN, H.H. Z. Phys., 69, p.185-206, (1931).

[12] PATOU, C. Journal de Physique, 31, p.339-349, (1970).

[13] BERNARD, A., CESARI, G., COUDEVILLE, A., JOLAS, A., de MASCUREAU, J. and WATTEAU, J.P. Proc. of IAEA 4th Conf. on Plasma Physics and Controlled Nuclear Fusion Research, Wisconsin, (1971).

[14] HAMBERGER, S.M. and JANCARIK, J. Phys. Rev. Lett., 25, p.999-1002, (1970).

[15] SAWYER, G.A., BEARDEN, A.J., HENINS, I., JAHODA, F.C. and RIBE, F.L. Phys. Rev., 131, p.1891-1897, (1963).

[16] POTTER, D.E. Proc. of 4th European Conf. on Controlled Fusion and Plasma Physics, p.116, (1970).

[17] BERNSTEIN, M.J. Phys. Fluids, 13, p.2858-2866, (1970).

[18] AGAFONOV, V.I., GOLUB, G.V., GOLUBCHIKOV, L.G., DYACHENKO, V.F., IVANOV, V.D., IMSHENNIK, V.S., KOLESNIKOV, Yu.A., SVIRSKY, E.B., FILIPPOV, N.V. and FILIPPOVA, T.I. Paper CN-24/G-2, Proc. of IAEA 3rd Conf. on Plasma Physics and Controlled Nuclear Fusion Research, Novosibirsk, (1968).

[19] JORDAN, C. Mon.Not. Roy. Astr. Soc., 142, p.501-521, (1969).

[20] BURGESS, A. Astrophys. J., 141, p.1588-1590, (1965).

[21] GABRIEL, A.H. and JORDAN, C. Case Studies in Atomic Collision Physics, vol.2, Editors McDowell and McDaniel, North Holland Press, (1971).

[22] JONES, B.B. and WILSON, R. Nucl. Fusion Supplement, pt.3, p.889-893, (1962).

ETUDE DU PLASMA FOCUS PAR DIFFUSION THOMSON ET ANISOTROPIE DES NEUTRONS PENDANT L'EMISSION NEUTRONIQUE

A. BERNARD, G. CESARI, A. COUDEVILLE, A. JOLAS,
J. de MASCUREAU, J.P. WATTEAU
CEA, Centre d'études de Limeil,
Villeneuve-Saint-Georges, France

Abstract — Résumé

A STUDY OF PLASMA FOCUS BY THOMSON SCATTERING AND NEUTRON ANISOTROPY DURING NEUTRON EMISSION.

The spectrum of light scattered through 90° during 50 ns can be analysed before neutron emission. The 90°-scattering cannot be ovserved during this emission. This is attributed to a broadening of the spectrum which reduces the signal-to-noise ratio; the broadening is due to a rapid increase of T_e/n_e making $\alpha < 1$ and the electron component of the spectrum dominant over the ion component. To keep $\alpha > 1$ during neutron emission use is made of a 7° observation device which has actually given scattering signals before and during neutron emission. These are resolved for wave-length by a Fabry-Pérot spectrometer and twelve photomultipliers. The first results obtained 15 ns after the start of the neutron emission show that the deuteron temperature is less than 1.5 keV.

The number of neutrons per unit solid angle is measured at 0° and 90° particularly for the régime 40 kV, 72 kJ, 1.5 MA with a large variation in pressure (7-25 Torr). Various operating régimes are shown; this corresponds to the Potter calculations.

The average number of neutrons measured with a "squirrel-cage" external electrode at 90° is between 1.5×10^9 and 3×10^{10} for 3-20 Torr, 18-40 kV, 15-70 kJ, 0.5-1.5 MA. These different conditions are obtained with good coupling between the energy bank and the plasma discharge: neutron emission then takes place when the current is a maximum and the formation of an arc is avoided upstream of the plasma sheet. Such arcs cause a considerable part of the current to drift and prevent focusing.

ETUDE DU PLASMA FOCUS PAR DIFFUSION THOMSON ET ANISOTROPIE DES NEUTRONS PENDANT L'EMISSION NEUTRONIQUE.

On sait analyser le spectre de la lumière diffusée à 90° pendant 50 ns avant l'émission neutronique. La diffusion à 90° n'est pas observable pendant cette émission. On attribue ceci à un élargissement du spectre qui réduit le rapport signal sur bruit; l'élargissement résulte d'une élévation rapide de T_e/n_e qui rend $\alpha < 1$ et la composante électronique du spectre prépondérante devant la composante ionique. Pour conserver $\alpha > 1$ pendant l'émission neutronique, on utilise un montage d'observation à 7° qui a donné effectivement des signaux de diffusion avant et pendant cette émission. Ceux-ci sont résolus en longueur d'onde par un Pérot-Fabry et douze photomultiplicateurs. Les premiers résultats obtenus 15 ns après le début de l'émission neutronique montrent que la température des deutérons est inférieure à 1,5 keV.

Le nombre de neutrons par unité d'angle solide est mesuré à 0° et 90° particulièrement pour le régime 40 kV, 72 kJ, 1,5 MA avec und grande variation de pression (7 à 25 Torr). On met en évidence plusieurs régimes de fonctionnement ce qui est à rapprocher des calculs de Potter.

Un nombre moyen de neutrons, mesuré à 90°, de $1,5 \times 10^9$ à 3×10^{10}, est obtenu avec une électrode extérieure en «cage d'écureuil», dans la plage 3-20 Torr, 18 - 40 kV, 15 - 70 kJ, 0,5 - 1,5 MA. Ces fonctionnements aussi variés sont réalisés en gardant un bon couplage entre le banc d'énergie et la décharge de plasma: d'une part, l'émission neutronique se produit quand le courant est maximum; d'autre part, on évite la formation d'un arc en amont de la nappe de plasma. De tels arcs sont connus pour dériver une partie importante du courant et empêcher la focalisation.

Pour parvenir à une meilleure compréhension des phénomènes intervenant dans l'expérience Focus, nous avons concentré nos efforts d'une part sur la mesure de la température des deutérons par diffusion Thomson, d'autre part sur les problèmes à résoudre pour créer le plasma quand on utilise des bancs de condensateurs d'énergie de plus en plus grande. Lors de cette deuxième étude, l'utilisation d'une géométrie en «cage d'écureuil» a permis de mettre en évidence que le mécanisme d'émission neutronique n'est pas unique.

1. MESURE DE LA TEMPERATURE IONIQUE

La mesure de la température ionique T_i par diffusion Thomson est effectuée sur un canon coaxial du type Mather décrit dans la référence [1]. Les conditions expérimentales sont les suivantes:
- pression de remplissage: 2,7 Torr de deutérium,
- caractéristiques du banc de condensateurs: 15 kJ - 18 kV,
- courant maximal: 500 kA,
- nombre moyen de neutrons émis par décharge: $1,5 \cdot 10^9$.

Pour mesurer la température ionique du plasma, nous devons conserver une diffusion collective, c'est-à-dire un paramètre α de Salpeter supérieur ou égal à 1.

Nous avons:

$$\alpha = \frac{\lambda_0}{4\pi\ \lambda_D \sin(\varphi/2)}$$

où λ_0 est la longueur d'onde laser,

$\lambda_D = (\epsilon_0 k T_e/n_e e^2)^{\frac{1}{2}}$ est la longueur de Debye, et

φ est l'angle de la direction d'observation et de l'onde incidente.

La diffusion a d'abord été observée à $\varphi = 90°$ [2] où il est plus facile de réduire la lumière parasite due au laser. Les spectres obtenus ont été comparés aux spectres théoriques de Salpeter par une méthode de moindres carrés. Nous prenons comme origine des temps de début de l'émission neutronique et la précision des mesures est à 10 ns près. Nous avons obtenu au temps t = -10 ns les valeurs suivantes:

$$T_i = 370 \pm 50 \text{ eV}$$

$$\beta = \left[\frac{T_e}{T_i} \cdot \frac{\alpha^2}{1+\alpha^2}\right]^{\frac{1}{2}} = 0,7$$

L'ensemble du spectre est décalé en fréquence vers les hautes longueurs d'onde, ce qui signifie que le plasma est animé d'une vitesse d'ensemble qui l'éloigne de l'électrode et dont la composante suivant l'axe est au maximum $v = 2 \cdot 10^7$ cm/s. Par diffusion Rayleigh nous pouvons estimer la densité électronique $n_e > 4 \cdot 10^{18}$ cm^{-3} et le paramètre $\alpha \geqslant 1,25$, d'où une température électronique 180 eV < T_e < 300 eV [2]. Nous trouvons donc une température ionique supérieure à la température électronique.

L'absence de signaux diffusés à $\varphi = 90°$ pendant l'émission neutronique est interprétée comme résultant d'une diminution du paramètre $\alpha \sim [1/\sin(\varphi/2)]\,(n_e/T_e)^{\frac{1}{2}}$, qui devient inférieur à l'unité.

Le signal diffusé se réduit alors à sa «composante électronique» dont le spectre est beaucoup trop large pour être observé avec un bon rapport signal sur bruit. Pour conserver une diffusion collective pendant l'émission, nous compensons l'augmentation de $(T_e/n_e)^{\frac{1}{2}}$ en diminuant l'angle d'observation φ. Nous choisissons $\varphi = 7°$ qui permet toutes choses égales par ailleurs, d'élever la valeur de α d'un facteur 10.

Pour vérifier cette hypothèse, nous avons monté une expérience dans laquelle nous observons simultanément les signaux diffusés à 90° et à 7° sans les analyser en longueur d'onde. Le volume observé a un diamètre de 1 mm et une longueur de 6 mm suivant l'axe des électrodes et est centré à 10 mm devant l'électrode intérieure. Un dispositif mécanique composé de diaphragmes annulaires sélectionne rigoureusement la lumière diffusée entre 6° 30' et 7° 30'. Le premier diaphragme se trouve à 150 mm des électrodes. Les oscillogrammes de la figure 1 montrent les résultats obtenus pour deux décharges, A et B, qui ont donné respectivement $1,7 \cdot 10^9$ et $1,3 \cdot 10^9$ neutrons. Pour chaque décharge nous enregistrons a) la dérivée de l'émission neutronique dN/dt, b) la dérivée du courant dI/dt, c) l'impulsion laser et les signaux d) à 7° et e) à 90°. Dans le tir A le laser est déclenché à t = 0 ns, les signaux diffusés à 7° et à 90° apparaissent. Dans le tir B à t = +40 ns, seul le signal diffusé à 7° demeure.

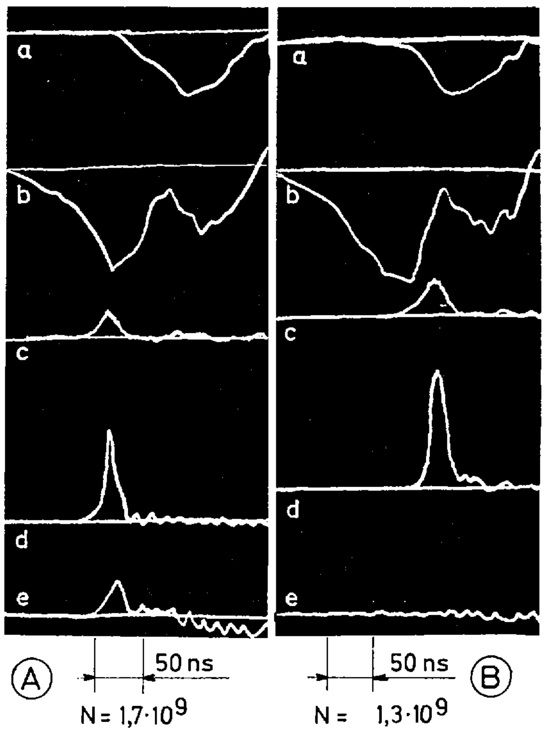

FIG. 1. Résultats obtenus pour deux décharges, A et B.

Les photomultiplicateurs sont efficacement protégés contre le rayonnement X dur de la décharge par un blindage en plomb. Les signaux diffusés à 7° pendant l'émission neutronique ont une amplitude variable et semblent d'autant plus probables que le laser est synchronisé avec le début de l'émission neutronique. D'autre part, le maximum du signal diffusé ne coïncide pas toujours avec le maximum de l'impulsion laser. Nous attribuons ce phénomène à une localisation non reproductible du filament de plasma par rapport au volume observé.

Nous avons ensuite analysé le spectre diffusé à 7°.

Le montage se compose d'un filtre interférentiel de 9 Å de large, d'un étalon interférentiel de Fabry-Pérot dont l'intervalle spectral libre est de 8 Å, de 12 photomultiplicateurs interceptant chacun 0,65 Å. Un dispositif du type «Fafnir» [3] composé de 12 miroirs annulaires, concentriques, décalés angulairement, réfléchit l'interférogramme fourni par le Fabry-Pérot sur les photomultiplicateurs.

L'étalonnage relatif des différents canaux est effectué à l'aide d'un laser à gaz He-Ne (6328 Å) de 20 mW découpé en impulsions de 10 μs par un secteur tournant. Les canaux sont balayés un par un en faisant varier la pression du gaz dans la chambre contenant le Fabry-Pérot. La largeur instrumentale du système est inférieure à un canal et la lumière parasite laser est 10 à 100 fois inférieure à la lumière diffusée sur le canal correspondant à la longueur d'onde incidente.

La figure 2 montre un spectre de lumière diffusée au temps t = +15 ns pour un tir ayant donné $2,7 \cdot 10^9$ neutrons. Il se répartit sur six canaux et n'est pas incompatible avec un spectre gaussien dont la largeur à mi-hauteur est voisine de 2 Å. Compte tenu du faible angle de diffusion et par suite de la valeur vraisemblablement élevée de α, nous supposons $\alpha^2/(1 + \alpha^2) \simeq 1$ et $\beta \simeq (T_e/T_i)^{\frac{1}{2}}$. D'autre part, le profil du spectre implique

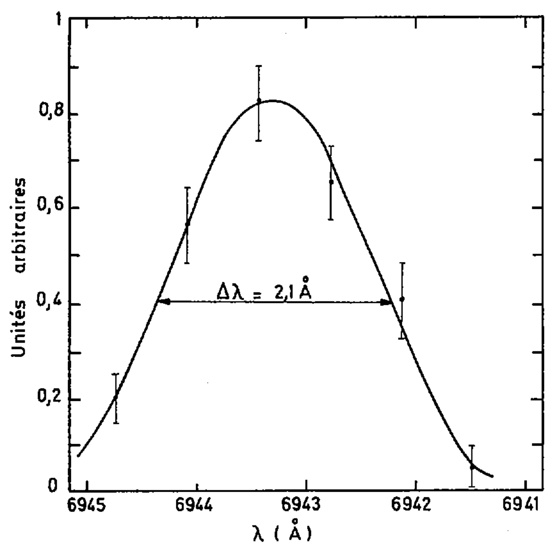

FIG.2. Spectre de lumière diffusée au temps 15 ns pour un tir ayant donné $2,7 \cdot 10^9$ neutrons.

que $\beta \lesssim 1$. De la largeur à mi-hauteur de 2 Å, on déduit suivant la valeur de β choisie:

$$\beta = 1, \quad T_i = T_e = 580 \text{ eV}$$

$$\beta = 0,5, \quad T_i = 4\, T_e = 1100 \text{ eV}$$

Cette évaluation est préliminaire car les résultats sont très récents. Comme à 90°, nous comparerons par une méthode de moindres carrés les spectres expérimentaux et théoriques pour déterminer β et T_i.

2. ANISOTROPIE DE L'EMISSION NEUTRONIQUE

Parallèlement à ce premier diagnostic, on a mesuré l'anisotropie du nombre de neutrons émis par unité d'angle solide en fonction de la pression initiale de deutérium. Les résultats présentés ont été obtenus avec des plasmas différents, créés par des bancs de condensateurs variés, ce qui permet de penser que le phénomène mis en évidence est général. A titre d'exemple, on présente trois diagrammes (fig. 3) pris dans les mêmes conditions électriques et géométriques: tension 40 kV, énergie 72 kJ, longueur des électrodes 160 mm, diamètres 100 et 150 mm. Le seul paramètre qui diffère est la pression de remplissage, soit 7 Torr, 10 Torr et 25 Torr de deutérium; la trentaine de points de chaque diagramme correspond donc à la dispersion obtenue expérimentalement, toutes les conditions initiales étant identiques. On porte en ordonnées $\Phi_{0°}/\Phi_{90°}$ où $\Phi_{0°}$ et $\Phi_{90°}$ sont des nombres de neutrons par unité d'angle solide, mesurés respectivement sur l'axe en avant des électrodes et dans une direction perpendiculaire à l'axe. On porte en abscisses le nombre de neutrons émis dans les 4π (ce nombre est déduit après étalonnage du compteur de neutrons à 90° en supposant l'émission isotrope).

Le changement de régime de fonctionnement est nettement mis en évidence quand on modifie la pression initiale. On note, en comparant 3 a et 3 c, que malgré la dispersion des mesures, $\Phi_{0°}/\Phi_{90°}$ pour une décharge de 3 a est toujours supérieur à la valeur de ce rapport pour une décharge de 3 c. D'autres diagrammes obtenus à 13 Torr et 20 Torr (non représentés) montrent que le changement de régime est progressif. La même étude a été refaite pour des conditions électriques et géométriques différentes: tension 30 kV, énergie 27 kJ, longueur des électrodes 200 mm, diamètres 50 mm et 100 mm. On obtient, en faisant varier la pression, le même changement dans l'anisotropie des neutrons. Les pressions extrêmes étudiées dans ce deuxième cas sont 3 Torr et 9 Torr. Pour d'autres cas des mesures en nombre plus limité ont montré une même variation en fonction de la pression. Le fonctionnement du même montage dans une plage de variation de la pression aussi importante a été rendu possible par l'utilisation d'une électrode extérieure en «cage d'écureuil» constituée par des barreaux parallèles à l'axe.

Les électrodes et l'environnement modifiant l'anisotropie de l'émission du plasma Focus, il est nécessaire de faire un étalonnage. On utilise pour cela un radioélément de dimensions faibles (20 mm de diamètre,

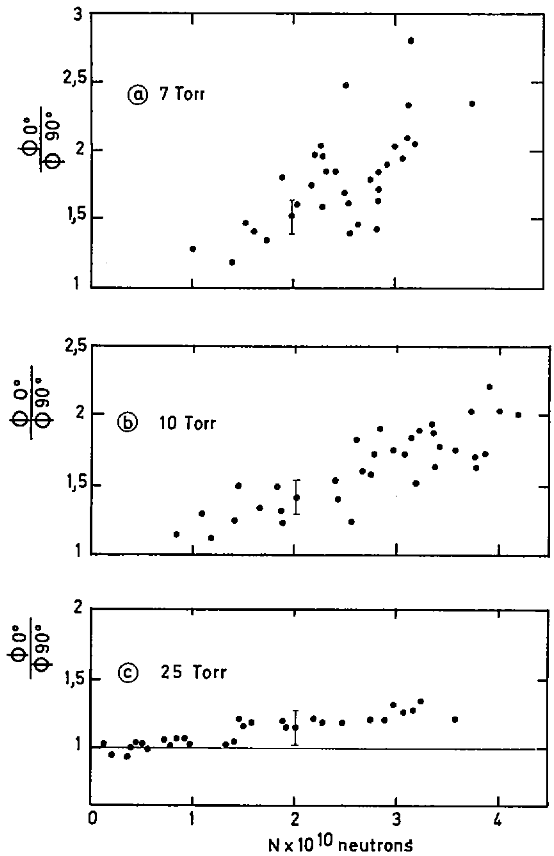

FIG.3. Anisotropie de l'émission neutronique.
a) pression de remplissage 7 Torr
b) pression de remplissage 10 Torr
c) pression de remplissage 25 Torr.

30 mm de haut) que l'on place sur l'axe des électrodes sans rien changer au montage. Il s'agit d'une source Am-Be dont le spectre de neutrons est centré sur 3 MeV, valeur très voisine de 2,45 MeV, énergie des neutrons de la réaction D-D. Le radioélément seul a un rayonnement isotrope, et placé sur l'axe des électrodes à 1 cm en avant de l'électrode centrale, le rapport des flux mesurés est de $0,81 \pm 0,06$ (il varie très peu quand on change la position du radioélément sur l'axe). On a obtenu cette valeur par la moyenne des mesures de trois types de compteurs: ceux à activation d'argent qui comptent les flux de neutrons du plasma Focus (après correction pour tenir compte des γ émis par le radioélément), des compteurs à BF_3 et des compteurs à activation d'indium (ces deux types ne sont pas sensibles aux γ). Cette valeur de 0,81 indique que la part des neutrons diffusés n'est pas prépondérante et l'on admettra réciproquement qu'à un rapport de 0,81 sur une décharge Focus correspond une émission isotrope.

L'interprétation des résultats obtenus est simple si l'on accepte, comme l'a proposé Potter, que l'émission neutronique est due à deux mécanismes [4]. Le premier est la quasi-thermalisation du plasma focalisé donnant une émission isotrope. En fait, d'après nos résultats expérimentaux de diffusion Thomson et les calculs de Potter [5], ce plasma s'éloigne de l'axe à une vitesse de quelques 10^7 cm/s qui n'est pas suffisante pour produire une anisotropie en flux observable. Le deuxième mécanisme est l'accélération à de grandes énergies d'un nombre faible de deutérons qui bombardent la masse du plasma et produisent une émission neutronique très anisotrope. Sur le diagramme 3 c les décharges ayant produit moins de $1,5 \cdot 10^{10}$ neutrons ont une émission isotrope indiquant une contribution négligeable du deuxième mécanisme. Les tirs produisant le plus de neutrons sont ceux où il y a superposition des deux mécanismes et l'anisotropie globale atteint 1,3. La reproductibilité des phénomènes n'est pas bonne, mais on remarque néanmoins que pour les décharges où le mécanisme thermique est dominant (diagramme 3 c) la dispersion de $\Phi_{0°}/\Phi_{90°}$ est très faible. Le découplage des deutérons rapides étant d'autant mieux réalisé que la pression est plus faible, il est normal que les valeurs de $\Phi_{0°}/\Phi_{90°}$ soient beaucoup plus importantes dans les diagrammes 3 a et 3 b; on atteint des valeurs de l'ordre de 3.

3. ADAPTATION A HAUTE ENERGIE

Pour étudier le problème de l'adaptation de l'expérience Focus à des bancs d'énergie élevée, plusieurs expériences ont été réalisées à des tensions comprises entre 18 et 45 kV et à des énergies comprises entre 15 et 72 kJ. La géométrie adoptée pour les premiers essais à 500 kA [1] (utilisée encore sur l'expérience de diffusion Thomson) a une longueur ajustée pour que le courant atteigne son maximum lorsque la nappe de plasma se trouve à l'extrémité du canon, ce qui assure la

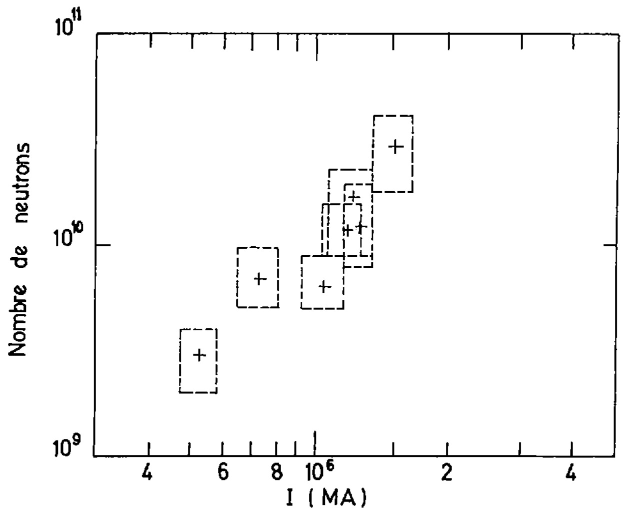

FIG. 4. Nombre de neutrons en fonction de l'intensité du courant.

compression radiale au courant maximal. Nous avons montré qu'une telle géométrie ne peut pas être employée pour des intensités supérieures à 0,75 MA: on observe au-delà un claquage parasite derrière la feuille de plasma [6]. Ce phénomène se produit lorsque la tension aux bornes du canon V = d(LI)/dt dépasse une valeur critique qui dépend de la géométrie, des conditions derrière le piston magnétique, ainsi que de la rapidité du banc d'énergie. Pour éviter ce claquage, il faut compenser l'augmentation du courant I par une diminution de l'inductance L du canon. Nous n'avons pas modifié la longueur des électrodes afin de conserver une compression à courant maximal, mais nous avons choisi de réduire le rapport R_2/R_1 de 2 à 1,5 (R_2 = 75 mm, rayon de l'électrode extérieure; R_1 = 50 mm, rayon de l'électrode intérieure). Ceci a conduit à un fonctionnement stable de l'expérience Focus entre 0,75 et 1,5 MA.

Les divers essais ayant été effectués dans des conditions électriques et géométriques différentes, nous avons préféré étudier, en fonction de l'intensité du courant, la variation du nombre de neutrons. Un compteur à activation d'argent, placé à 90° de l'axe des électrodes, permet de mesurer le nombre de neutrons avec une précision de 15%. Le nombre moyen est déterminé à partir d'un histogramme portant sur une centaine de tirs. Le carré d'erreur représenté sur la figure 4 comprend 80% des tirs. Sans vouloir indiquer une loi d'extrapolation, on remarque qu'en passant de 0,5 à 1,5 MA le nombre de neutrons est augmenté d'un facteur 10.

CONCLUSION

La température des deutérons du plasma focalisé a été mesurée expérimentalement pour la première fois. L'étude se poursuit de façon à connaître l'évolution de la température en fonction du temps. Jusqu'à présent, aucun tir n'a révélé de valeur supérieure à 1,5 keV, ce qui est en accord avec le modèle MHD de Potter [5]. Une fois le diagnostic de diffusion Thomson bien au point, l'étude simultanée par ce diagnostic et par les mesures neutroniques sera particulièrement fructueuse. Elle devrait permettre de mieux faire la part des différents mécanismes de production de neutrons. Et par l'utilisation ultérieure sur un montage à haute énergie, on peut espérer dégager une loi d'extrapolation expérimentale.

REFERENCES

[1] PATOU, C., SIMONNET, A., WATTEAU, J.P., J. Phys. 29 (1968) 973.

[2] BACONNET, J.P., CESARI, G., COUDEVILLE, A., WATTEAU, J.P., Ionic temperature measurements by 90° cooperative scattering on a plasma Focus, Ninth Int. Conf. on Phenomena in Ionized Gases (Proc. Conf. Bucharest, 1969) I, Editura Academiei Republicci Socialiste România, Bucharest (1969) 643.

[3] HIRSCHBERG, J.G., BRETON, C., CHABBAL, R., Method of application of the multichannel Fabry-Pérot interferometer to spectral lines, Third Symp. on Engineering Problems in Thermonuclear Research, (Proc. Conf. Munich, 1964) II, Institut für Plasmaphysik (1965) 383.

[4] POTTER, D.E., Neutron production mechanisms in the plasma Focus, Fourth European Conf. on Controlled Fusion and Plasma Physics (Proc. Conf. Rome, 1970) I, C.N.E.N., Rome (1970) 116. Neutron production mechanisms in the plasma Focus, même Congrès, communication orale.

[5] POTTER, D.E., Thesis, Ph.D., University of London, 1970.

[6] BERNARD, A., COUDEVILLE, A., WATTEAU, J.P., Neutron yield of a Focus discharge in various experiments, Phys. Lett. 33A 8 (1970) 477.

RECENT STUDIES OF DENSE PLASMA FOCUS*

J.W. MATHER, P.J. BOTTOMS, J.P. CARPENTER,
K.D. WARE, A.H. WILLIAMS,
Los Alamos Scientific Laboratory,
University of California,
Los Alamos, N. Mex.,
United States of America

Abstract

RECENT STUDIES OF DENSE PLASMA FOCUS.

Empirical solutions to the problems of restrike or subsidiary break-down in the breech of the plasma focus accelerator have been found for 50-kV operating voltages. Restrike during the acceleration phase has plagued focus experiments because its occurrence actually short-circuits the capacitor energy from the current sheath. Quality control of the Pyrex insulator, electric flux control at the centre electrode surface, and lower electric fields across the inter-electrode space are effective measures reducing restrike. The transition from the inverse pinch to the axial rundown phase as well as the fraction of time taken up by the inverse stage relative to the quarter period is of concern. These and other dynamical aspects will be discussed. There seems to be no single or simple plasma mechanism that can account entirely for the rapid heating of ions and electrons in the plasma focus. Neutron production continues, on the average, to scale as I^4, and the neutron flux ratios at 0°/90° vary from 1.1 to 1.7 under high-voltage operation. Peak D-D neutron yields of $\sim 3 \times 10^{11}$/discharge have been achieved at 50 kV, 120 kJ. X-ray absorption measurements previously made with DPF III (25 kV, 100 kJ) suggest, by and large, a thermal kT spectrum with electron temperatures of 3 to 4 keV; the precise contribution of line radiation is not known; however, the total photon energy above 40 keV is < 5%. X-ray spectra, obtained on a single discharge with multiple K-absorption vacuum diodes (variable-Z cathodes), and selective filters will be discussed. The relevance of impedance considerations to good plasma focusing cannot be overemphasized. In this respect, high-voltage operation and high capacitor bank impedance, relative to the plasma focus impedance, are necessary conditions for large discharge currents per joule stored energy. The application of the swinging Marx circuit in the plasma focus system, DPF VI (50 kV, 214 kJ), shows a convenient and practical method of obtaining power sources at least up to 100 kV.

1. INTRODUCTION

Efforts to increase the capacitor bank energy, and hence the energy of the dense plasma focus, by increasing the capacitance (C) or voltage (V) have led to careful examination of the complete electrical discharge circuit. Increased capacitance for a limited range of plasma-focus machine parameters can be shown to decrease the efficiency of delivered current per joule of stored energy. Because neutron production varies as the 4th power of current, I, the decrease in current efficiency with increased capacitance seriously limits higher-energy Focus operation. On the other hand, current is a linear function of voltage. However, this means that high-voltage break-down and current-sheath propagation problems in the discharge tube become quite formidable. Whether the plasma focus accelerator geometry [1] as presently used in the United States and Europe can operate at voltages

---

* Work performed under the auspices of the US Atomic Energy Commission and the Defense Atomic Support Agency.

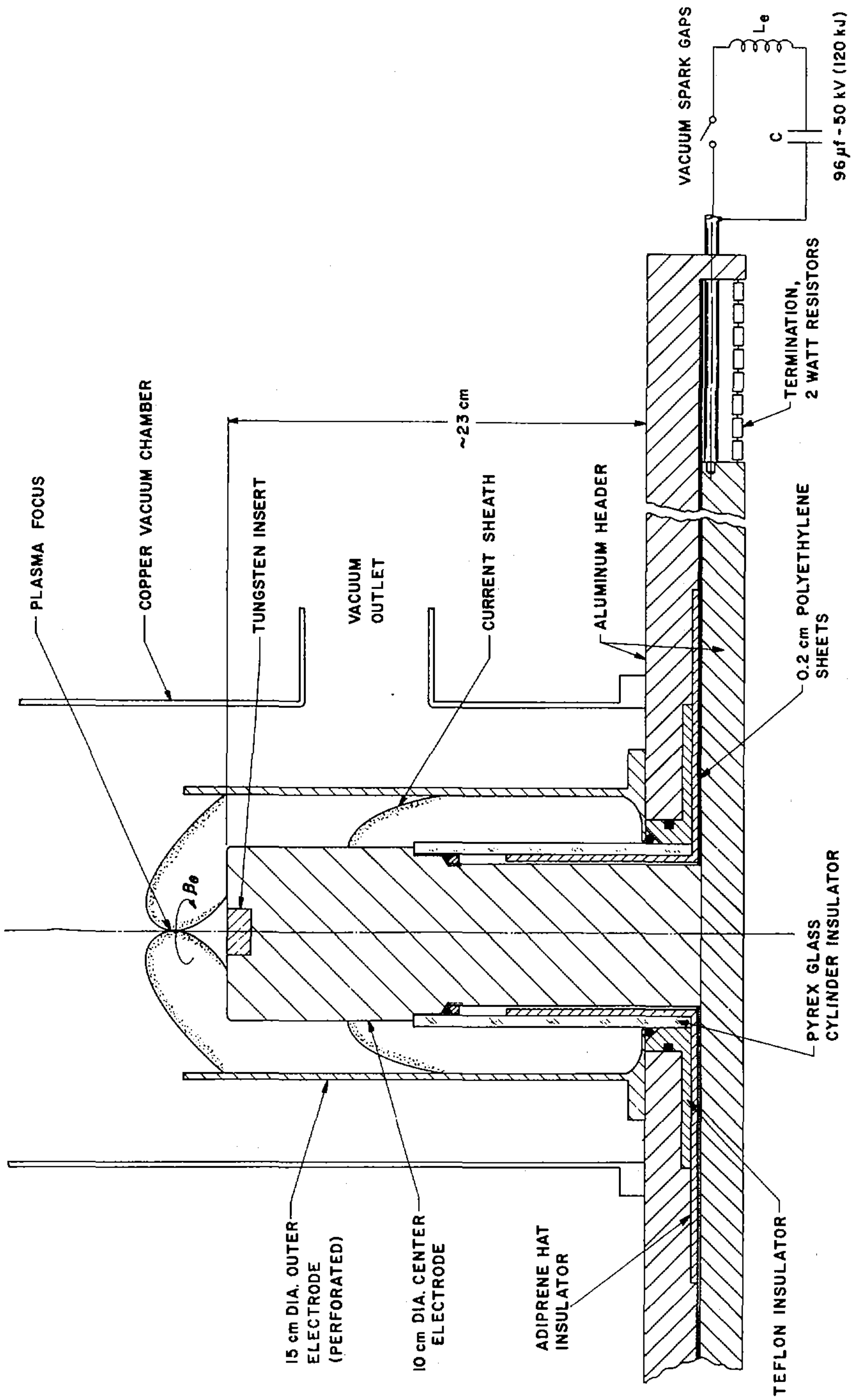

FIG.1. Schematic representation of DPF V1.

>50 kV remains for the experimentalist to answer. Operation at higher voltage would, indeed, circumvent most of the subtle impedance problems [2] associated with high-energy, high-capacitance networks. Some of the problems associated with dense plasma focus (DPF V) operation at 50 kV and some empirical solutions to subsidiary voltage breakdown will be discussed.

Another area of extreme interest is the dynamics of the current-sheath collapse and the heating mechanisms that lead to formation of a highly compressed hot plasma. Many diagnostic investigations [3, 4] of neutron and X-ray production, from which the plasma properties, particle distributions, and flow dynamics of the plasma column can be delineated, are being made throughout the world. The results or interpretations of such measurements are not always universal because, basically, density, temperature, volume, and duration of the plasma are not controllable, and small variations in these properties grossly affect, for example, neutron and X-ray production from which deductions about other plasma properties are initially made. This paper discusses a multichannel X-ray diagnostic technique used to determine the X-ray spectral distribution from the Focus plasma.

2. HIGH-VOLTAGE OPERATION – DPF V

DPF V, a 120-kJ, 50-kV, plasma-focus machine, is shown schematically in Fig. 1. DPF V parameters include 15-cm-i.d. and 20-cm-o.d. electrodes, a 10-cm-long Pyrex insulator, a 10-cm-long exposed center electrode, a 6-Torr D_2 operating pressure, and ≤ 52-kV voltage. A maximum neutron production of 3×10^{11} neutrons per discharge at 52 kV has been obtained with a dependence upon current, I^4. In the early phases, DPF V appeared limited in voltage to ~35 kV, i.e., a voltage limit defined where the neutron production fourth-power law began to fail. Now, through optimization, operation at 50 kV is achieved. The basic problem was axial breakdown (restrikes) along the Pyrex insulator and radial restrikes across the interelectrode space. Restrikes occurred most often when the interelectrode voltage exceeded 12 kV. These effects were photographed by an image-converter camera. Examples are shown in Fig. 2 with a timing pulse and machine current waveform. A restrike early in time always leads to a poor current waveform. Although many photographs show axial and radial restrikes occurring ~0.5 μsec after the termination of the inverse pinch phase, none show restrikes during the inverse phase. The axial restrike has been eliminated by longer insulators. This has permitted 50-kV operation. However, reduction of radial restrikes is more difficult. Changes in interelectrode spacing, Δr; reduction of discharge voltage by addition of external inductance, L_0; elimination of sharp metal boundaries; changes in operating pressure, and, hence, center electrode lengths; and changes in the shape of the insulator and outer electrode to reduce the impact of the inverse-current sheath at the outer electrode, are altogether effective in reducing radial restrike. It should be recognized that these parameter changes are subtly interconnected and difficult to separate. However, it is expected that changes in insulator shape will be beneficial in reducing the violent shock and current interaction with the outer electrode surface and should permit operation of the coaxial accelerator at still higher voltages.

Figure 3 shows several soft X-ray, time-integrated pinhole photographs with and without a B_z stabilizing magnetic field [5] at 47 kV. When very small B_z, or none, is used, radial perturbations appear in the Focus column, but B_z fields ≥ 100 gauss give definite spatial stability. Although this stabilizing technique reduces the heating and compression, it does produce a plasma configuration that is useful for studying the interaction of intense lasers and electron beams with a dense plasma.

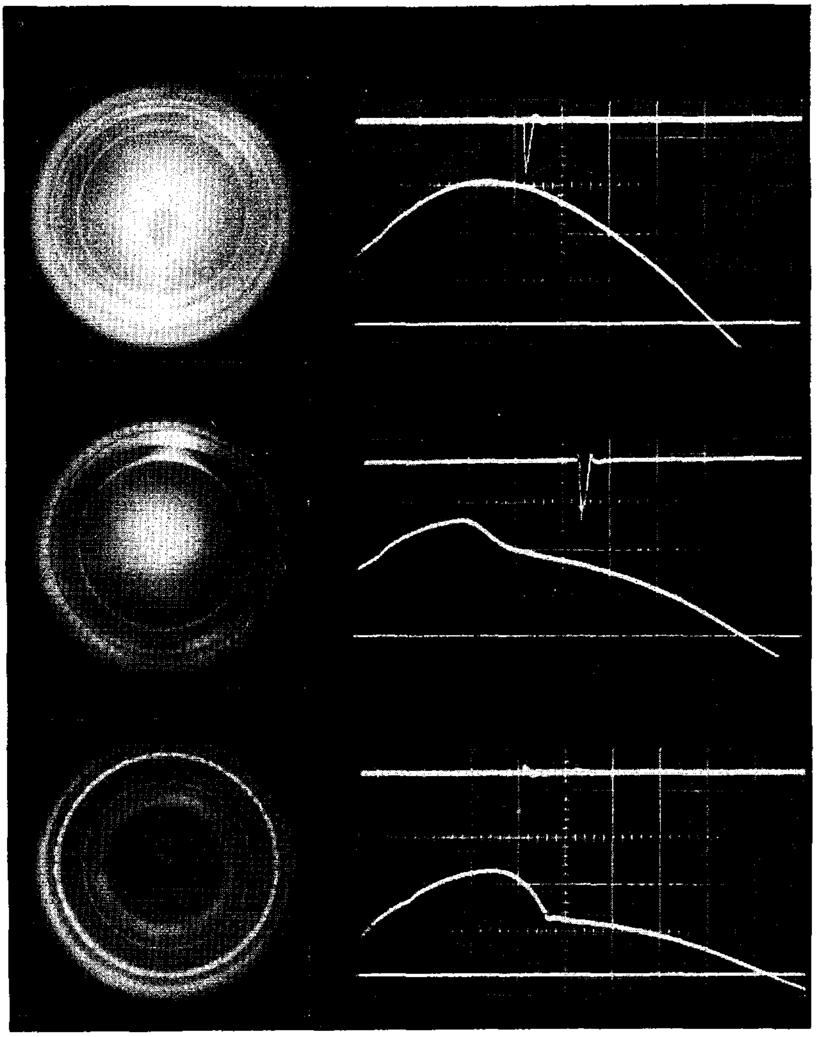

FIG. 2. Image-converter photographs (axial view) (5-ns exposition) with timing pulse and current waveform.

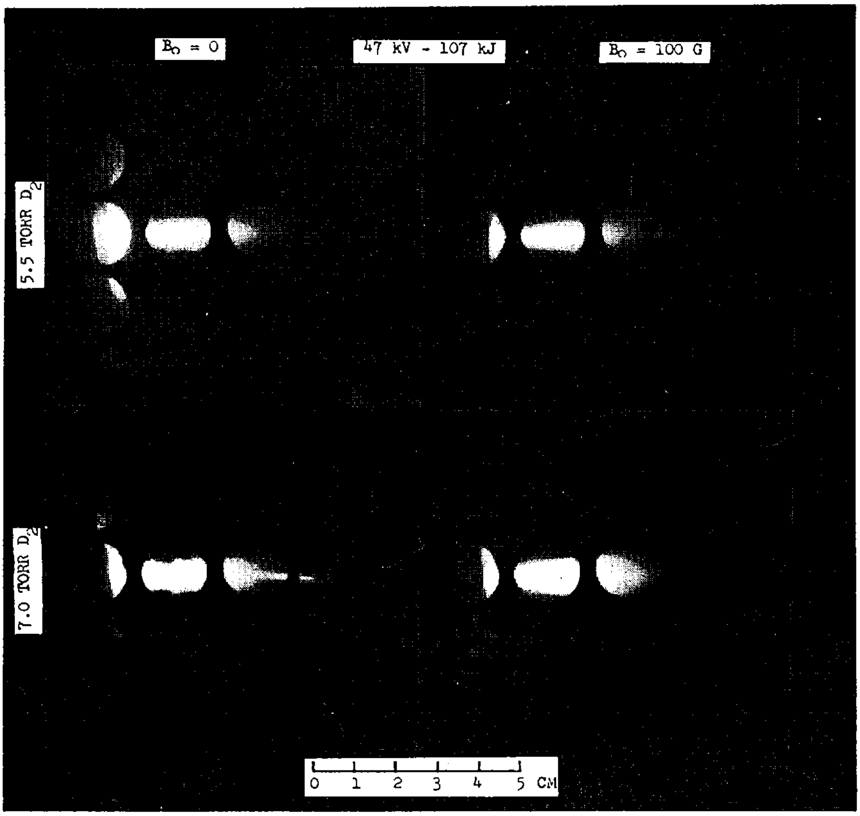

FIG.3. Time-integrated, X-ray, 0.3-mm-diam. pinhole photographs with and without stabilizing B_z field. Centre electrodes at left.

3. VOLTAGE RESTRIKE IN COAXIAL GEOMETRY

In addition to the problem of impedance matching, there is a still more basic problem, namely, how to sustain the driving voltage (V) for a given time (t) across the interelectrode space of the coaxial plasma accelerator. Tentative measurements, different from those mentioned earlier, show that the azimuthal magnetic field (B_θ); the residual plasma density (ρ) behind the moving sheath (result of incomplete snowplow); and the applied voltage influence the time of subsidiary voltage breakdown. In the range of a few tens of mTorr of D_2 used to simulate the residual density and over a limited range of applied voltage (5 to 15 kV) for a fixed inter-electrode space, voltage breakdown occurs within microseconds. Sufficient information has been obtained to show the effect of B_θ, V, ρ, and the geometrical aspect ratio, r_0/r, upon t, but it is not enough at present for derivation of an empirical law for voltage holdoff. There has been considerable controversy about the role of a limiting dI/dt in the plasma-focus acceleration. This study will attack the problem of internal breakdown in terms of the driving voltage associated with sustaining plasma motion, i.e., d/dt (LI) for a given coaxial geometry with different physical boundary conditions.

4. X-RAY SPECTRAL ANALYSIS OF DPF VI

4.1. X-ray detector arrangement

In previous work [6], the X-ray spectral distribution from the DPF III machine (100 kJ) was determined by the well-known filtration technique using fast, lithium-diffused silicon, soft X-ray detectors (250-μ thick). Deductions from such data showed that the X-ray emission consisted of plasma bremsstrahlung (T_e = 3 to 4 keV) and some fraction corresponding to copper K_α and K_β, and tungsten L-line radiation. More recently, with the DPF VI machine (214 kJ), a different diagnostic technique that utilizes K-edge vacuum diode detectors has been employed. For a spectral determination, the diode seems superior to the silicon detector in that one can take advantage of the K edges of various Z cathodes, in addition to selective filters ahead of the diode, to define narrow energy channels. It is possible to obtain K-edge diodes over the atomic range Z = 13 to 82, and further, one can group a selection of diodes to more specifically define a given energy range in the total spectrum.

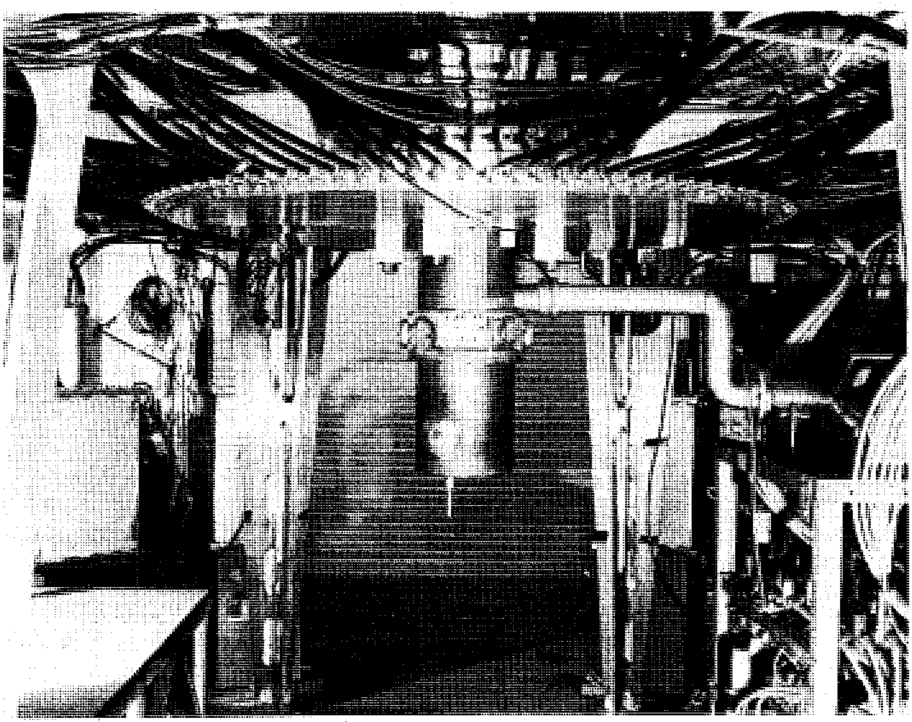

FIG.4. Lower view of DPF-VI machine showing collimating X-ray channels.

In the DPF VI experiment, 10 X-ray channels in a plane at 90° from the Focus axis and equally spaced azimuthally are provided as shown in Fig. 4. Two of the 10 channels are reserved for a time-integrated, X-ray pinhole camera and a 3-mm-thick germanium detector, the latter for total energy measurement up to ~100-keV energy. The other eight channels are fitted with a selection of diodes. Each detector and output lead is doubly shielded with iron pipe to reduce low-frequency noise pickup to a negligible value. An array of 546 Tektronix oscilloscopes with 150-Mc bandpasses is used to record the outputs of the detectors simultaneously. Timing pulses and sweep calibrations are used on each oscilloscope.

4.2. DPF VI apparatus

The machine, DPF VI, used for the spectral measurement consists of a 720-μF, 25-kV capacitor bank connected to the plasma-focus machine through a two-stage, swinging Marx circuit [7]. This electrical circuit differs from DPF V in that the two-stage Marx circuit initially charged to 25 kV is erected in 80 μsec through a reversal switch in the lower stage. Each of the 12 two-stage Marx modules has an inductance of ~48 nH with a combined value, including the cable header, of ~14 nH. The effective capacitance is 180 μF at 50 kV with a maximum current of ~4.5 MA. For the spectral measurements, the operating voltage is ≤ 40 kV. The discharge geometry consists of center and outer electrodes of 10- and 15-cm diam., respectively, and a 10-cm-long Pyrex glass insulator similar to that shown in Fig. 1. The centre electrode has a hemispherical end, through which a 1-cm-diam. tungsten rod protrudes ~1 cm. Although the rod deteriorates very rapidly in high discharge currents and has to be adjusted frequently, it tends to localize the plasma. The 10-channel collimators are arranged to view the plasma.

4.3. Spectral results

A typical plasma produced at the end of the tungsten rod is shown in Fig. 5. This is a time-integrated 0.3-mm-diam., pinhole-camera photograph (magnification 1 : 1). Using the diode-filter arrangements, Al + no filter, Ca + Ti, Ti + Fe, Cr + Ni, Fe + Zn, Cu + Zr, Zr + Mo, and Ag + Sn, and filter thicknesses of one mean free path for energies at the filter K-absorption edge, provides selected narrow energy bands from ~1.6 to 30 keV. Thus, on a single discharge, the time-dependent X-ray emissions are simultaneously recorded. The X-ray pulse data are then tabulated on IBM cards, and using the known response function for each detector, the information is reduced by a computer code. The charge produced by each detector can be expressed as

$$Q = \int_{E_1}^{E_2} K(E)\, R(E)\, \frac{dP(E)}{dE}\, dE \tag{1}$$

where K(E) is the transmission function for various windows, filters, etc., R(E) is the response function of the K-edge diode, and dP(E)/dE is the differential power per energy-interval unit of the X-ray source. The code

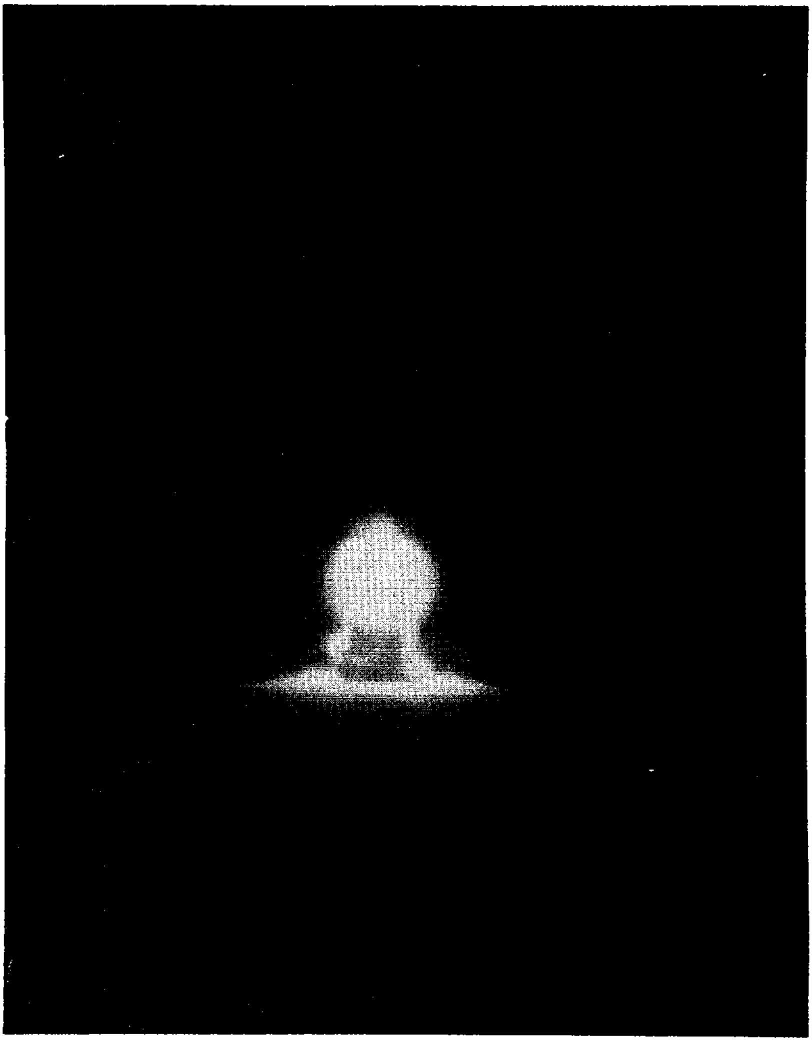

FIG.5. Time-integrated, X-ray pinhole photograph. Note hemispherical centre electrode and protruding 1-cm-diam. tungsten rod.

acts upon Eq. (1) by assuming a particular form of dP(E)/dE and calculates, by many iterations, until the Q_{calc} converges to the experimental Q value within a given accuracy. The simplest form of dP/dE = constant is taken as the first trial, although other forms have been used. The end result, in any case, is that the code adjusts the final spectrum to the experimental Q values by the iterative process.

A particular energy spectrum plotted in semilog coordinates is shown in Fig. 6. The primary features in the spectrum are as follows. (1) The low-energy portion of dP/dE is exponential. (2) There is a peak in dP/dE

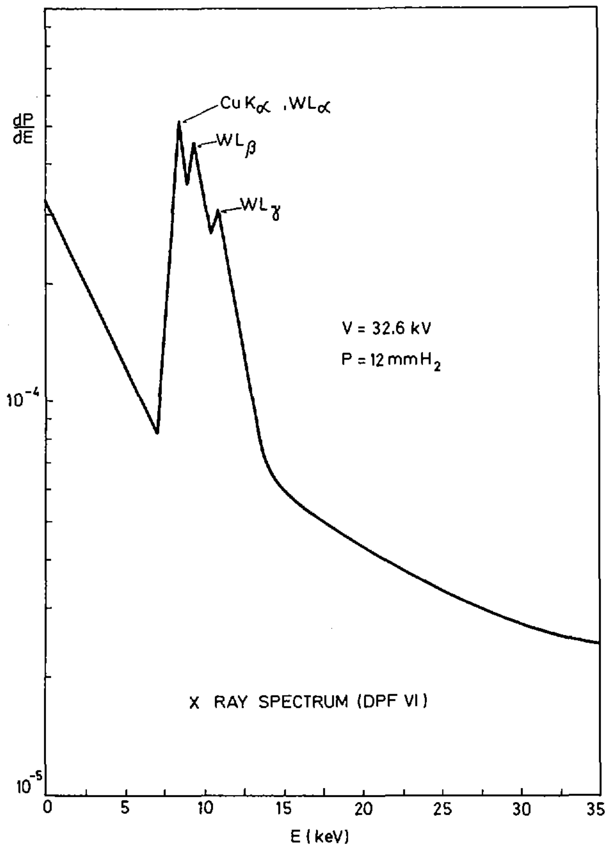

FIG.6. A typical X-ray spectral distribution, dP(E)/dE versus E.

near 9 keV. (3) There is a higher-energy portion above 30 keV. Because of the 0.5-keV energy resolution of the code, the spectrum width near 9 keV is not necessarily real. In fact, this portion is made up of line radiation from copper and tungsten.

The most important feature of Fig. 6 is the exponential energy dependence at low energy. This dependence suggests that this part of the Focus emission is primarily bremsstrahlung radiation due to a Maxwellian electron distribution. The shapes of many dP/dE spectrums under different operating conditions show that electron temperatures range from 2 to 7 keV. In Fig. 6, $T_e \sim 3$ keV. Were it not for the line contribution around 9 keV, the exponential dependence would be more extensive.

The appearance of line radiation at ≈ 9 keV is primarily due to the high-Z material of the centre rod, but other evidence shows that some high-Z material is entrained in the current sheath from other areas of the discharge. Changing the electrode material affects the position of the line contribution. In fact, the sensitivity of the code has been tested in this manner.

The form of dP/dE for E > 30 keV has not been specifically investigated. With the limited number of detectors on DPF VI, it is not possible to examine the complete spectrum. It is necessary to group detectors in a limited energy range for accuracy. Thus, the portion of the spectrum above 30 keV in Fig. 6 is not significantly defined. However, there are data that show that Focus X-ray emission extends to at least 100 keV.

5. SUMMARY

Effort has been directed toward understanding the development and collapse stages of plasma focus. Optimized launching of the current sheath and sustaining the driving voltage subject to boundary conditions are basic considerations in the production of high-density, high-temperature plasmas. Efforts to develop a unique X-ray diagnostic technique for studying the plasma focus seem necessary if the time-dependent processes of heating and confinement are to be understood.

REFERENCES

[1] MATHER, J.W., Phys. Fluids 8 2 (1965) 366.

[2] CARPENTER, J.P., WARE, K.D., BOTTOMS, P.J., WILLIAMS, A.H., MATHER, J.W., Symposium on Engineering Problems of Fusion Research (Proc. 1969) Los Alamos Scientific Laboratory Rep. LA-4250, E5.

[3] BOTTOMS, P.J., CARPENTER, J.P., MATHER, J.W., WARE, K.D., WILLIAMS, A.H., Plasma Physics and Controlled Nuclear Fusion Research, IAEA, Vol.II (1969) 67.

[4] See references this meeting.

[5] MATHER, J.W., BOTTOMS, P.J., CARPENTER, J.P., WILLIAMS, A.H., WARE, K.D., Phys. Fluids 12 11 (1969) 2343.

[6] BOTTOMS, P.J., MATHER, J.W., CARPENTER, J.P., WARE, K.D., WILLIAMS, A.H., Abst. Bull. Am. Phys. Soc. 15 4 (1970) 642.

[7] BOTTOMS, P.J., MATHER, J.W., CARPENTER, J.P., WARE, K.D., WILLIAMS, A.H., Abst. Bull. Am. Phys. Soc. 15 11 (1970) 1463.

DISCUSSION

TO PAPERS IAEA-CN-28/D-3, D-4, D-5

G.J. YEVICK: In the work just reported by Mr. Maisonnier, there appears to be a uniform plasma focus without marked radial constrictions, whereas a number of investigators, including yourself, have shown two, three, or even four "hot spots" in the dense plasma focus. Could you comment on this?

N.J. PEACOCK: The relatively uniform, diffuse plasma results from the self-destruction of the dense focus and occurs later. It appears that neutrons are being emitted from this diffuse plasma. The "hot spots" are associated with one or sometimes two earlier dense pinches.

V. NARDI: Your data, in particular on the long-lasting neutron production (even during a late focus stage of relatively low plasma density), seem to confirm the idea that neutrons are related more closely to the decay of a magnetic structure than to the compression shock. Do you consider your data consistent with this point of view?

N.J. PEACOCK: Yes.

V. NARDI: In your view, Rayleigh-Taylor instabilities seem to determine the fluted configuration of the current sheath boundary in the axial region. Does this mean that you consider negligible shear or no shear at all in the magnetic field, i.e. that you assume it to be a purely azimuthal field? Have you made magnetic field measurements on the current sheath?

N.J. PEACOCK: We have made no direct measurements of the magnetic-field distribution within the plasma. This is a difficult task. Perhaps I could turn the question around and inquire why interchange instabilities should not take place at the plasma boundary? Several damping mechanisms could explain the observed growth rates. If the boundary breaks up completely into isolated filaments, I certainly expect to see axial components of the field.

V. NARDI: Magnetic probe data from the Stevens Institute of Technology (Proc. I.A.U. Symp. No. 43, Paris 1970, pp. 443-456) show that, at least before focus formation, there is a strong component of the magnetic field orthogonal to the azimuthal component, i.e. in the direction of observed plasma filaments. One should not overlook the fact that these filaments can play a major role in neutron and X-ray production at the focus stage, when their magnetic structure is decaying. Do you disagree on this point?

N.J. PEACOCK: The magnetic energy in the compression region is considerably higher than the plasma kinetic energy in the pinch. After the break-up of the pinch into a turbulent, convective diffuse plasma, some of the magnetic energy will be dissipated and thus may provide the mechanism for the later neutron emission.

W.J. PRIOR: Would you please explain how you clipped your laser pulse?

N.J. PEACOCK: It was essentially a pulsed transmission mode laser, which was clipped with an electro-optic shutter.

B.D. FRIED: Can you give a few more details concerning the degree and duration of the field penetration near the time of maximum compression.

N.J. PEACOCK: We know from the interferogram sequence that the radial density distribution changes abruptly, within about 20 ns from a step function just before maximum compression to a distribution which is almost parabolic. Even taking into account the effect of impurities, the conductivity temperature has to be at least an order of magnitude lower than the measured value to explain this field diffusion.

R.L. MORSE: With regard to micro-instabilities that can cause anomalous resistivity and diffusion in the plasma focus, I would like to point out that recent stability analysis has shown that the ion-acoustic instability does not occur for the parameters of interest here, with the current flowing perpendicular to the magnetic field. However, another instability, the electron cyclotron drift instability, can occur when the drift velocity is much less than the electron thermal velocity and it is almost independent of the electron to ion temperature ratio. This instability is almost certainly present in most plasma focus experiments. Details of this instability and the way in which it causes anomalous resistance and diffusion will be discussed in Paper E-18.

N.J. PEACOCK: It is true that the electron drift speed cannot easily exceed the ion sound speed in the focus unless an appreciable fraction of the current is carried as runaways. The results of the Kurchatov focus, presented at Novosibirsk, suggest that this may be the case. The mechanism you suggest for microinstabilities is interesting and may indeed predominate but would'nt the temperature of the electrons then greatly exceed that of the ions?

M.J. BERNSTEIN: I wish to comment first on Mr. Nardi's question regarding the duration of neutron emission. On several devices it has been observed that the highest neutron yields are generated with pulse widths of less than 100 ns. Generally, when the neutrons are emitted in several pulses over 200-300 ns, the total neutron output is not as high.

I also want to discuss the different time correlations between neutron, X-ray and visible-light emissions. It is important to recognize that the various investigators are not consistent with each other in referring to radiation as soft or hard. We have made time-resolved and spectrally-resolved measurements of the X-radiation from our device and we found that only the very soft emission, in the 1-2 keV range, was coincident with compression of the plasma column, as observed from streak photographs. The radiation above 4 keV photon energy was mostly non-thermal and was delayed by 10 ns or more with respect to the very soft radiation. Spectral measurements of the radiation below 3 keV corresponded to a temperature less than 1 keV, in agreement with the ion temperature reported from Limeil, France. The neutron emission coincided only with hard emission above 30 keV.

B. BRUNELLI (Chairman): The dependence of the neutron yield on the energy of the capacitor bank reported here by the Limeil group seems to fit a parabola with an exponent roughly equal to 1.7. This is only a rough evaluation, and I may well be mistaken because a lower value of about 1 was quoted by the Limeil people in a previous discussion.

ЭКСПЕРИМЕНТАЛЬНОЕ И ТЕОРЕТИЧЕСКОЕ ИССЛЕДОВАНИЕ ПИНЧЕВОГО РАЗРЯДА ТИПА "ПЛАЗМЕННЫЙ ФОКУС"

Н. В. ФИЛИППОВ, В. И. АГАФОНОВ, И. Ф. БЕЛЯЕВА, В. В. ВИХРЕВ, В. А. ГРИБКОВ, Л. Г. ГОЛУБЧИКОВ, В. Ф. ДЬЯЧЕНКО, В. С. ИМШЕННИК, В. Д. ИВАНОВ, О. Н. КРОХИН, М. П. МОИСЕЕВА, Г. В. СКЛИЗКОВ, Т. И. ФИЛИППОВА
Институт атомной энергии им. И. В. Курчатова,
Москва,
Союз Советских Социалистических Республик

Доклад представлен Е.П.Велиховым

Presented by E.P.Velikhov

Abstract — Аннотация

EXPERIMENTAL AND THEORETICAL INVESTIGATION OF A GAS DISCHARGE OF THE "PLASMA FOCUS" TYPE.

The authors continue theoretical and experimental investigations of the development of the high-current gas discharge (of the "plasma focus" type) accompanying the non-cylindrical compression of the Z pinch. In addition to the usual operating regimes, with uniform filling of the chamber with deuterium, variants involving a complex gas density profile are tried. Considerable attention is paid to the influence of impurities in the form of heavy atoms on the progress of the discharge. The principles underlying the increase in neutron yield as a function of capacitor bank energy and working gas composition are determined. The authors perform simplified machine calculations of the motion of the plasma sheath when there are wide variations in the initial conditions and the electrotechnical characteristics of the discharge circuit. They also continue their investigations of X-ray emission from a plasma focus and obtain frame-by-frame photographs of the pinch through a thin aluminium filter with an exposure of about 30 ns. The emission spectra of strongly ionized impurity atoms deliberately introduced into the plasma focus are studied theoretically and experimentally. On the basis of an analysis of the spatial distribution of the charged products of (d, d) interactions and a comparison of this distribution with theoretical predictions, the authors consider various models of the structure of a plasma focus at the moment of neutron emission. In the same investigations they determine the maximum magnetic field at the boundary of the pinch and (for separate cases) the proton and neutron energy spectra. In view of the need for a fuller theoretical description of the final stage of compression (plasma focus), the authors undertake a new series of calculations of a two-dimensional magnetohydrodynamic model of the pinch effect with allowance for finite electric conductivity, viscosity and heat conductance, together with the time dependence of the total current. The plasma dispersion coefficients are assumed to be Coulombic and isotropic. The problem is solved by the free-point method, the initial conditions and electrotechnical parameters of the device being the same as in the earlier calculations (i.e. for W = 50 kJ). While the parameters of the first compression virtually coincide with the results of the preceding calculations, results similar to those observed in the experiments were obtained for the second, more powerful compression (which had previously taken place without interruption). The second compression begins approximately 200 ns after the first and has the following parameters: $T_{max} \approx 1.5$ keV; density $\rho_{max} = n/n_0 \approx 500$; $r_{min} \approx 1$ mm; $\Delta Z \approx 5$ mm. The authors discuss questions connected with the stability of plasma sheath motion.

ЭКСПЕРИМЕНТАЛЬНОЕ И ТЕОРЕТИЧЕСКОЕ ИССЛЕДОВАНИЕ ПИНЧЕВОГО РАЗРЯДА ТИПА "ПЛАЗМЕННЫЙ ФОКУС".

Продолжались теоретические и экспериментальные исследования характера развития сильноточного пинчевого разряда при нецилиндрическом сжатии z-пинча (типа "плазменный фокус"). Кроме обычных режимов работы при равномерном заполнении камеры дейтерием, опробованы также варианты сложного профиля плотности рабочего газа. Большое внимание обращено на изучение влияния примесей тяжелых атомов на характер протекания разряда. Определены закономерности увеличения нейтронного выхода в зависимости от энергии батареи конденсаторов и состава рабочего газа. Проведены упрощенные машинные расчеты движения плазменной оболочки при широком варьировании начальных условий и электротехнических характеристик разрядного контура. Продолжены исследования рентгеновского излучения плазменного фокуса (ПФ) и получены покадровые фотографии пинча через тонкий Al-фильтр с экспозицией около 30 нсек. Теоретически и экспериментально исследовались спектры излучения высокоионизированных атомов примесей, специально вводившихся в ПФ. С помощью анализа пространственного распределения заряженных продуктов (dd)-реакций и сравнения его с теоретическими предсказаниями рассматриваются различные модели структуры ПФ в момент эмиссни нейтронов. В этих же исследованиях определяется значение максимального магнитного поля на границе пинча и для отдельных случаев – энергетические спектры протонов и нейтронов. В связи с необходимостью более полного теоретического описания конечной стадии сжатия (ПФ) была предпринята новая серия расчетов двумерной магнитогидродинамической модели пинч-эффекта с учетом конечной электропроводности, вязкости и теплопроводности одновременно с зависимостью полного тока от времени. Коэффициенты диссипации плазмы считались кулоновскими и изотропными. Задача решалась по методу свободных точек, начальные условия и электротехнические параметры установки были теми же, что и в предыдущих расчетах, т.е. для $W = 50$ кДж. Если параметры первого сжатия практически совпали с результатами предыдущего расчета, то для второго, более мощного сжатия, которое раньше происходило безостановочным образом, получились результаты, близкие к наблюдаемым в экспериментах. Второе сжатие наступает приблизительно через 200 нсек после первого и имеет следующие параметры: $T_{max} \simeq 1{,}5$ кэВ, плотность $\rho_{max} = n/n_0 \simeq 500$, $r_{min} \simeq 1$ мм, $\Delta z \simeq 5$ мм. В работе обсуждены вопросы, связанные с устойчивостью движения плазменной оболочки.

ВВЕДЕНИЕ

В данной работе продолжено изучение импульсного пинчевого разряда, при нецилиндрическом сжатии которого образуется плотный плазменный фокус (ПФ) [1-3]. Эти исследования были направлены на углубление понимания причин образования и динамики развития ПФ. Успех в подобных исследованиях мог бы дать возможность реально оценить перспективность этого принципа нагрева и удержания плазмы для развития будущей термоядерной энергетики и создания в настоящее время интенсивных нейтронных источников для физических исследований.

1. ОПИСАНИЕ УСТАНОВКИ

Основные эксперименты выполнены на установке, состоящей из конденсаторной батареи емкостью 576 мкФ, разрядной камеры, аналогичной [3], и кольцевого вакуумного включателя. Разрядная камера (рис. 1) имеет анод (1) в виде медного диска диаметром 66 см, изолированного от катода (2) цилиндрическим фарфоровым изолятором (3). Вакуумный корпус (15) камеры, диаметр которого 100 см, изготовлен из нержавеющей стали. Внутри камеры установлен металлический лайнер (5), ограничивающий движение плазменной оболочки и позволяющий менять начальное распределение тока в рабочем объеме. (Лайнер может быть изолирован от корпуса камеры). Непосредственно под камерой укреплен тороидальный разрядник (7), соединенный с анодом камеры гибкими проводниками (10), позволяющими менять начальную индуктивность контура. Напряжение на камере измерялось емкостным делителем, а ток, протекающий через камеру, – поясом Роговского (11).

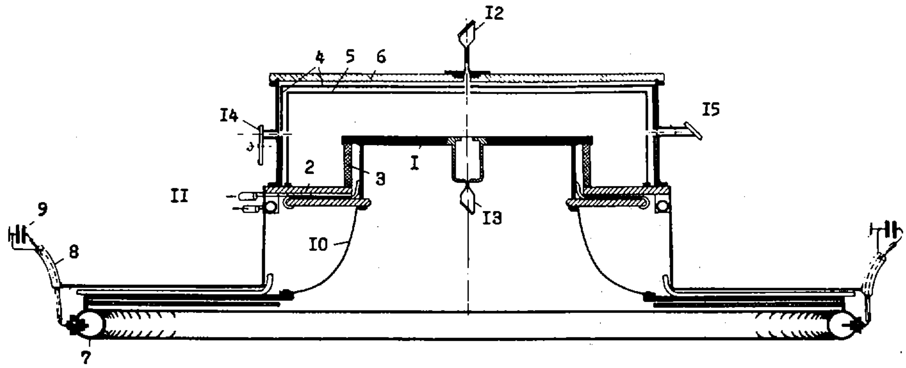

Рис. 1. Схема разрядной камеры:
1 — анод, 2 — катод, 3 — фарфоровый изолятор, 4 — изоляция лайнера, 5 — лайнер, 6 — верхняя крышка камеры, 7 — вакуумный кольцевой разрядник, 8 — кабельная ошиновка, 9 — конденсаторная батарея (C = 576 мкФ), 10 — переменная индуктивность — L_c, 11 — емкостной делитель и пояс Роговского, 12,13 — "протонные" камеры-обскуры, 14 — камера-обскура для мягкого рентгена и УФ, 15 — щель и кассета для регистрации протонов.

В ходе экспериментов, направленных на поиски способов увеличения эффективности и стабильности работы установки, проводилось большое количество конструктивных изменений, касающихся формы и материала лайнера, катода и анода камеры при одном и том же основном изоляторе. При этом для оценки влияния сделанного изменения на параметры ПФ подавляющая часть экспериментов проводилась при типичном режиме — 1 тор D_2, 18 кВ, 93 кДж. Такой мягкий режим работы высоковольтной конденсаторной батареи позволил провести более 10^4 разрядов без существенных неполадок в работе установки. Известно, что установка даже без внесения каких-либо изменений в камере, а лишь после перерыва в работе, и тем более после развакуумирования камеры, требует проведения серии тренировочных разрядов. В нашем случае тренировка считалась оконченной, когда при типичном режиме для W = 93 кДж нейтронный выход достигал $2{\cdot}10^{10}$ н/имп, либо давление газа в камере после такого разряда практически не менялось.

2. ИССЛЕДОВАНИЕ ЗАВИСИМОСТИ НЕЙТРОННОГО ВЫХОДА ОТ РАЗЛИЧНЫХ ПАРАМЕТРОВ УСТАНОВКИ

Камера установки откачивалась до давления $\sim 2{\cdot}10^{-6}$ тор с вымораживанием паров масла жидким азотом. Особенностью установок с ПФ является сравнительно высокое начальное давление дейтерия в камере и возможность проводить серию в 10 и более разрядов без смены рабочего газа. Это не означает, что чистота дейтерия, количество и состав примесей не сказываются на работе установки. Ранее отмечалось, но никогда не исследовалось детально, что на ход развития разряда существенно влияют специальные добавки N_2, Xe и других газов. Контроль за составом газа в камере проводился с помощью измерителя парциальных давлений ИПДО-1, масс-спектрометра на циклотронном резонансе. Прибор может работать в двух режимах — в режиме развертки по массам всех сор-

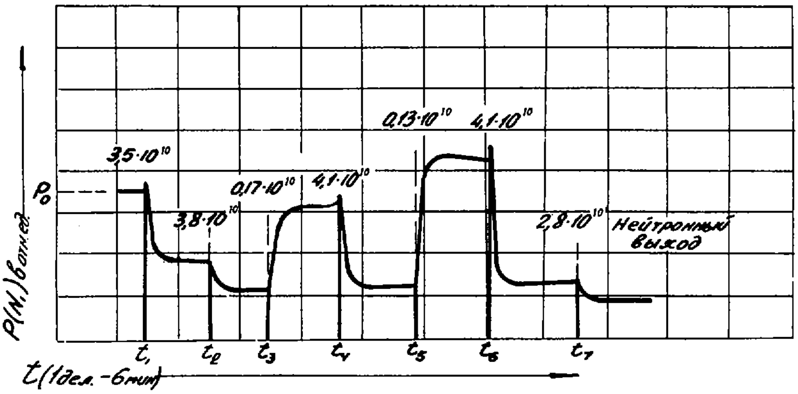

Рис. 2. Временной ход концентрации азота для серии последовательных разрядов.

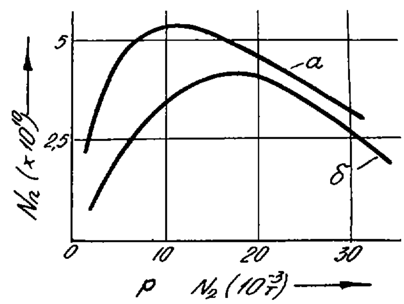

Рис. 3. Зависимость нейтронного выхода от добавки N_2:
а) $U_0 = 20$ кВ, $P_0 = 1,5$ тор D_2
б) $U_0 = 18$ кВ, $P_0 = 1$ тор D_2

тов молекул анализируемого газа и в режиме регистрации временного хода концентрации молекул выбранной массы. Измерения показали, что при отсутствии специальных добавок суммарное количество примесей в дейтерии не превосходит $10^{-4} \div 10^{-3}$. На рис. 2 приведена типичная запись временного хода концентрации азота в камере для серии последовательных разрядов. Оказалось, что для данной конструкции анодной вставки (медная труба с отверстием 2,5 см) азот поглощается из рабочей смеси после разрядов с большими нейтронными выходами и выделяется при "неудачных" разрядах.

Влияние добавки азота и ксенона на эффективность работы камеры показана на рис. 3.

Нейтронный выход существенно зависит от содержания примеси в рабочей смеси, хотя роль добавки N_2 уменьшается с увеличением начального давления дейтерия. В противоположность азоту, ксенон не сорбировался.

Впервые увеличение нейтронного выхода было обнаружено при добавках к дейтерию воздуха. Впоследствии оказалось, что роль основных ком-

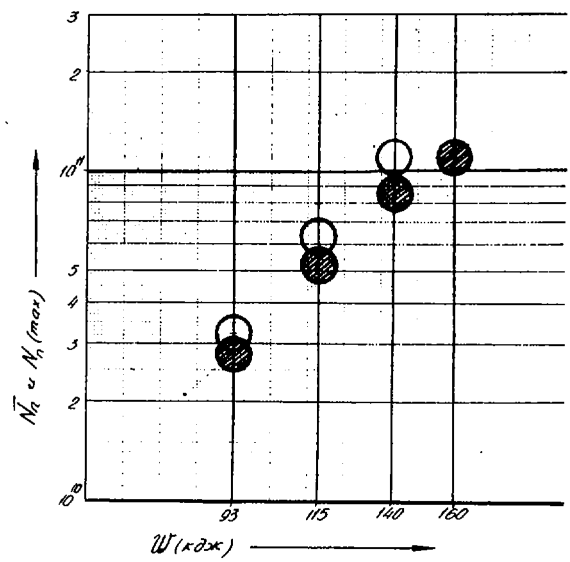

Рис. 4. Зависимость нейтронного выхода от $CU^2/2$ ($Lg\,N_n$ в зависимости от $Lg\,W$).

понентов воздуха N_2 и O_2 противоположна, т. е. кислород уменьшает нейтронный выход. Будучи электроотрицательным газом с большим сродством к электрону, кислород задерживает нарастание ионизации, тем самым удлиняя начальную стадию разряда и задерживая процесс скинирования. Примесь азота увеличивает коэффициент размножения электронов по сравнению с чистым дейтерием, что, по-видимому, облегчает скинирование и, кроме того, уменьшает величину остаточных токов в центральной части камеры, случайный характер распределения которых не способствует хорошей симметрии плазменной оболочки. Исследовалась также закономерность роста нейтронного выхода с ростом энергии установки при увеличении начального напряжения на конденсаторной батарее.

При начальных давлениях 1,4 тор D_2 с добавкой 0,6% N_2 производилась серия разрядов. Наибольший нейтронный выход достигался при первом разряде в серии. Существенно было, чтобы последний разряд серии перед откачкой камеры был с минимальным нейтронным выходом (за счет сорбции азота серией из $4 \div 6$ разрядов), но с симметричной начальной стадией, что устанавливалось по форме осциллограммы напряжения. При такой последовательности работы камеры разброс в величине нейтронного выхода от разряда к разряду был невелик и построение искомой зависимости не требовало большой статистики.

Заметим, что при исследовании влияния какого-либо параметра на нейтронный выход целесообразно выбирать лишь разряды с максимальным значением последнего. Этот прием позволяет уменьшить влияние остальных случайных факторов, как правило нарушающих "идеальную" схему протекания процесса. На рис. 4 приведена зависимость нейтронного выхода от $CU^2/2$ для $C = 576$ мкФ, которая может быть представлена степенным законом с показателем $K = 2,3 \div 2,5$:

$$N_n = N_{on}\left(\frac{W_n}{W_o}\right)^K \qquad (1)$$

Перспективность установок с ПФ для решения проблемы управляемого термоядерного синтеза практически полностью определяется величиной К, так как указанная зависимость означает, что ядерный к. п. д. системы растет как W^{K-1}. Предстоит проверить экспериментально значение коэффициента К при увеличении энергии в $10^2 \div 10^3$ раз. Естественно, что увеличение используемого запаса энергии должно сопровождаться изменением размеров камеры для обеспечения эффективного вклада энергии в ПФ.

3. СОГЛАСОВАНИЕ РАЗРЯДНОГО КОНТУРА С ДВИЖЕНИЕМ ТОКОВОЙ ОБОЛОЧКИ

Для выяснения условий согласования разрядного контура с движением оболочки были проведены модельные расчеты упрощенного двумерного "snow-plough" по схеме, изложенной в работах [4,5]. Применимость этого метода проверялась путем сравнения рассчитанных положений плазменной оболочки с полученными экспериментально из обработки щелевых фоторазверток. В подобных расчетах трудно учесть движение вещества вдоль оболочки. Поэтому кривизна внутренней, сходящейся к оси, части оболочки получилась меньше действительной. Это приводило к завышению расчетной индуктивности оболочки и уменьшению скорости радиального сжатия.

Однако в этих расчетах хорошо проявлялась степень согласованности контура с плазменной нагрузкой, т. е. доля вложенной энергии в сходящуюся часть оболочки. В качестве критерия согласованности бралась энергия, приходящаяся на единицу высоты пинча в зоне фокуса при сжатии его до радиуса $r_K = 0{,}1$ см. Выбор такого критерия определялся тем, что энергия на единицу высоты пинча слабо зависит от процесса вытекания массы вдоль оболочки. Оптимум в этом случае мало зависит от выбранной величины r_K.

На рис. 5(а) представлена зависимость энергии на единицу высоты плазменного фокуса от начального давления (P_0) дейтерия в камере для типичного режима работы установки ($U_0 = 18$ кВ, $W = 93$ кДж, $L_0 = 30$ нгн). Видно, что для исследуемого варианта камеры (рис. 1) установка будет работать в согласованном режиме при $P_0 = 1{,}5$ тор D_2. Этот результат близок к экспериментальному (наибольший нейтронный выход получался при 1,3 тор D_2). На рис. 5(б) показано соотношение энергии магнитного поля, энергии плазмы (кинетической и тепловой) и энергии в конденсаторной батарее в момент сжатия. В согласованном режиме энергия в конденсаторной батарее в момент кумуляции не превышает 1% от первоначально запасенной.

Подобный оптимум имеется и при выборе начальной индуктивности контура L_0. Оказалось, что для согласования контура с движением плазменной оболочки необходимо, чтобы начальная индуктивность контура L_0 составляла около половины индуктивности оболочки в сжатом состоянии, т. е. около одной трети от полной индуктивности. При соблюдении этого условия магнитная энергия пинча в момент кумуляции составляет около 40% от полной.

Вследствие того что в районе оптимума зависимость энергии на единицу высоты пинча от L_0 и P_0 слабая, выгоднее работать при несколько меньших индуктивностях контура L_0, чем оптимальная (это уменьшает

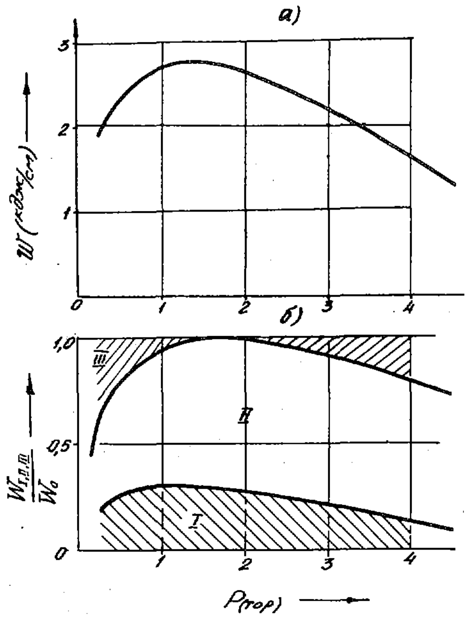

Рис. 5. (а) Зависимость энергии на единицу длины пинча от P_C (U_0 = 18 кВ, W_0 = 93 кДж, L_0 = 30 нгн)

(б) Соотношение между отдельными видами энергии в момент кумуляции на оси: I – магнитная энергия, II – энергия в плазме, III – энергия в конденсаторах.

напряжение на камере в момент сжатия), и при меньших давлениях P_0, что дает несколько большую скорость схождения оболочки, чем в согласованном режиме.

В расчетах, проведенных для камеры с высотой изолятора 12 см и расстоянием между анодом и крышкой камеры 14 см, согласованный режим в дейтерии осуществляется при радиусе камеры:

$$R = (0{,}072\ CU_0P_C^{-1/2})^{0,53} \tag{2}$$

где R выражено в см, C – в мкФ, U_0 – в кВ, P_0 – в тор. Изменение в разумных пределах высоты изолятора и расстояния между электродами слабо влияет на согласованность. Из (2) следует, например, что в установке с энергией батареи 10 МДж и напряжением 50 кВ для согласования при давлении 1 тор D_2 необходимо, чтобы радиус камеры был равен 2,5 м.

4. ДВУМЕРНЫЙ МАГНИТОГИДРОДИНАМИЧЕСКИЙ РАСЧЕТ ПИНЧ-ЭФФЕКТА

Решение двумерных уравнений магнитной гидродинамики без учета диссипаций в задаче об образовании ПФ имеет целый ряд качественных свойств, подробно обсуждавшихся в [3,6]. Образование перетяжки непос-

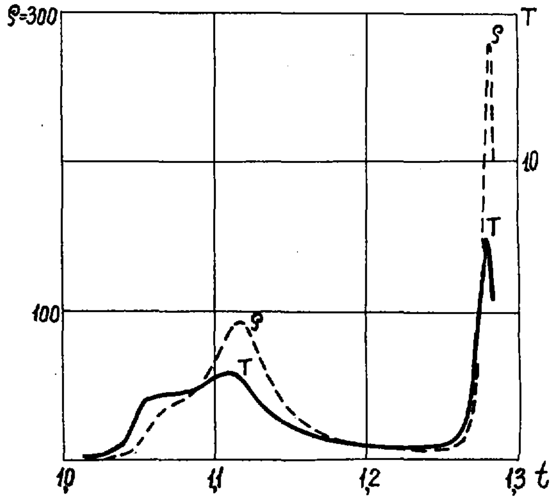

Рис. 6. Изменение во времени температуры и плотности в двух последовательных сжатиях.

редственно над анодом сопровождалось истечением плазмы в верхнюю часть объема, причем в приосевой области формировалась узкая плазменная струя со скоростью $\sim 7 \cdot 10^7$ см/сек. Сжатие плазмы в месте наименьшего расстояния от токовой оболочки до оси происходило в два этапа, через промежуток времени ~ 20 нсек. Второе сжатие характеризовалось более высокой температурой. Однако, в приближении идеальной магнитной гидродинамики, наиболее интересное второе сжатие протекало, по-видимому, безостановочным образом, приводя к разрыву плазмы на оси и прекращению счета. Оценки, сделанные в [6], показали, что диссипативные эффекты могут препятствовать безостановочному сжатию плазмы. Важность учета диссипаций вытекает также непосредственно из экспериментальных результатов. В самом деле, параметры плазмы в фокусе заставляют придти к выводу, что радиус фокуса и длина свободного пробега близки по величине – ситуация, аналогичная структуре фронта ударной волны, где диссипации играют определяющую роль. При решении уточненной задачи нецилиндрического сжатия Z-пинча естественно было включить в расчет электротехническое уравнение полного тока для описания индуктивного сопротивления ПФ. Относительная роль различных диссипативных процессов заранее не была ясна, так что при расчетах были учтены электропроводность, вязкость и теплопроводность полностью ионизованной дейтериевой плазмы. Для упрощения в расчетах предполагалось равенство электронной и ионной температур, а теплопроводность считалась ионной. Тем самым средняя температура в фокусе, вероятно, получилась несколько завышенной, а сдерживающая роль джоулева нагрева при сжатии плазмы, отмеченная в [6], – заниженной. В физической постановке задачи с учетом диссипаций были сделаны еще два существенных предположения:

1) граничные условия на электродах не были изменены по сравнению с предыдущей задачей – теперь они получили смысл условий симметрии;

2) из уравнений исключены эффекты Холла, старшие члены которых исчезают в рассматриваемом аксиально-симметричном случае.

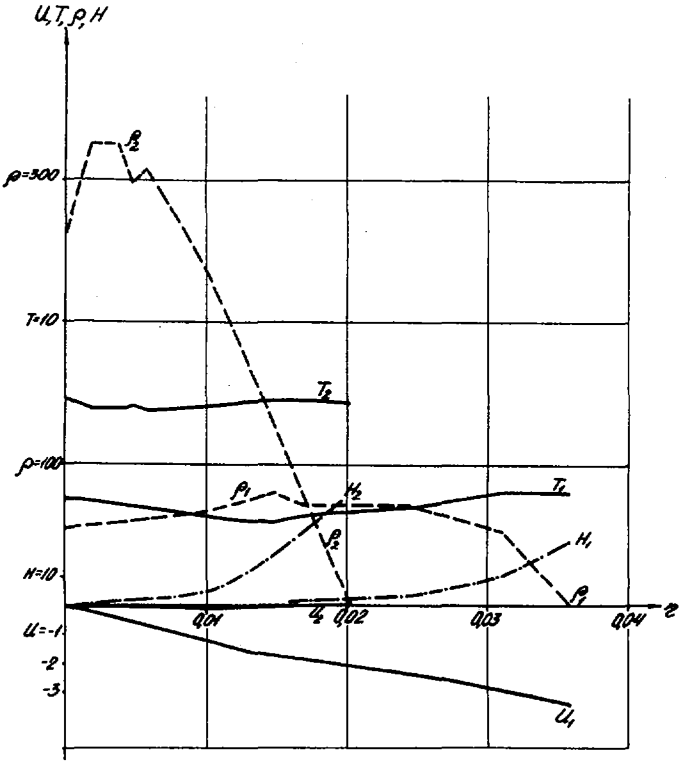

Рис. 7. Структура плазменного фокуса во втором сжатии для двух моментов времени: а) $t_1 = 1{,}273$, б) $t_2 = 1{,}281$

Первое предположение исключает сложную, да и физически не обоснованную задачу определения пограничного слоя, поскольку взаимодействие плазмы с металлической поверхностью включает еще и много других трудноучитываемых процессов. Второе предположение тоже имеет смысл поддержания некоторого разумного уровня строгости: учет остающихся младших членов эффекта Холла на данном этапе исследований был бы неоправданным усложнением задачи.

С учетом сделанных предположений решалась система одножидкостных уравнений магнитной гидродинамики в нестационарном аксиально-симметричном случае. Тензор вязкости взят в полном виде, а начальные условия – те же, что и в предыдущей задаче. Цель расчета – установление параметров второго сжатия плазмы, во время которого испускается основная доля нейтронов.

На рис. 6 представлено изменение во времени плотности и температуры в двух последовательных сжатиях. Эти величины взяты на оси в такой точке Z, где достигаются наивысшие параметры плазмы. Первое сжатие соответствует $Z = 0{,}15$, второе $Z = 0{,}18$, т. е. фокус смещается вверх по оси Z. (Единицы измерения в данном расчете были следующими: $R_0 = 13$ см, $t_0 = 1{,}47 \cdot 10^{-6}$ сек, $\rho_0 = 2{,}4 \cdot 10^{-7}$ г/см^3, $T_0 = 82$ эВ, $v_0 = 8{,}86 \cdot 10^6$ см/сек, $H_0 = 1{,}54 \cdot 10^4$ Гс).

Структура плазменного фокуса во втором сжатии для двух моментов времени изображена на рис. 7. Второй момент времени (t_2) взят еще до максимального сжатия плазмы (ср. с рис. 6). Радиус плазмы по максимуму плотности (t_2) составляет около 2 мм, но скорость еще довольно велика, так что окончательный радиус оказывается меньше 1 мм. Скинирование магнитного поля можно считать умеренным: толщина скин-слоя несколько меньше половины радиуса. Трубчатая структура фокуса по мере достижения максимального сжатия уменьшается или вовсе исчезает. Интересно отметить, что величина плотности во втором сжатии оказалась порядка плотности в первом, и что учет диссипативных эффектов привел к заметному возрастанию времени между сжатиями по сравнению с предыдущим расчетом. Вместо 20 нсек этот промежуток времени стал порядка 200 нсек.

Важной характеристикой двумерных расчетов является истечение плазмы из области ПФ в осевом направлении. К моменту первого сжатия в сечении фокуса ($Z = 0{,}06$) остается около 10% массы. К моменту второго сжатия эта величина уменьшается еще приблизительно вдвое. На рис. 6 видно, что скорость v невелика, но разрезы вдоль Z свидетельствуют, что в окрестности ПФ градиент скорости весьма значителен. Любопытно отметить, что на всех этапах процесса истечение вещества происходит внутри разреженного слоя плазмы, примыкающего к внешней границе токовой оболочки, а не в более плотных слоях, начинающихся от внутренней границы скин-слоя и простирающихся вплоть до оси системы.

Проведенные расчеты создают впечатление, что временные характеристики второго сжатия (его длительность и запаздывание по сравнению с первым сжатием), как впрочем и расположение фокуса по оси Z, очень чувствительны к деталям всего процесса, т. е. к ним нужно относиться с некоторой осторожностью.

При учете диссипаций несколько ослабла плазменная струя в осевом направлении, максимальная скорость ее оказалась порядка $(4 \div 5) \cdot 10^7$ см/сек. Однако в этом вопросе также уместны оговорки, относящиеся к пространственно-временным характеристикам второго сжатия. Рис. 8 представляет интегральные характеристики разряда в зависимости от времени: N_n – нейтронный выход; E_k, E_T и E_H – соответственно кинетическая, тепловая и магнитная энергия всей плазмы, I – полный ток. Нейтронный выход во втором сжатии во много раз превосходит их выход в первом сжатии.

На рис. 9 изображена конфигурация оболочки в окрестности плазменного фокуса в некоторые характерные моменты времени. Хорошо видно, что первое сжатие имеет более правильный цилиндрический характер, чем второе сжатие, хотя в обоих случаях продольный размер по оси Z превышает размер по радиусу r. Важным физическим вопросом является вопрос о факторах, определяющих форму токовой оболочки. Не вызывает сомнения, что ее нерегулярная форма обусловлена развитием неустойчивостей, которые свойственны пинч-эффекту.

В данной постановке задачи могут развиваться неустойчивости типа перетяжек или неустойчивости нулевой моды по азимутальному углу φ. В нецилиндрическом Z-пинче трудно говорить о применимости известной линейной теории, поскольку в начальных условиях уже содержится возмущение очень большой амплитуды – радиус токовой оболочки в начальный момент времени возрастает от анода к катоду на 30% (рис. 9). Такая начальная форма оболочки, конечно, и определяет явление плазменного фо-

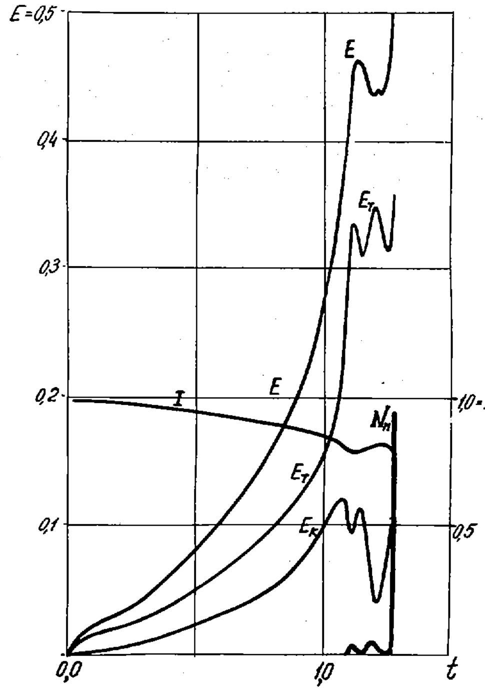

Рис. 8. Интегральные характеристики разряда в зависимости от времени.

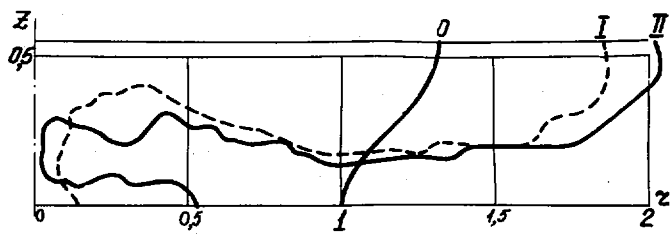

Рис. 9. Конфигурация плазменной оболочки в окрестности ПФ в некоторые моменты времени.

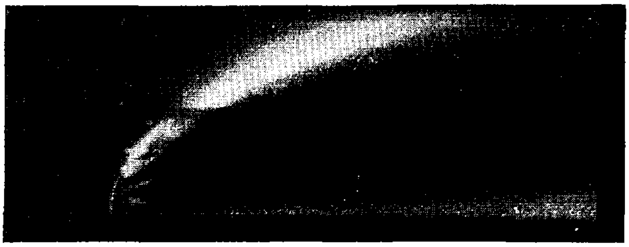

Рис. 10. Фоторазвертка свечения разряда, полученная через щель, параллельную оси камеры.

куса, являющегося следствием прорыва нижней части оболочки к оси. На это начальное возмущение формы оболочки, несомненно, накладываются более коротковолновые, развивающиеся в процессе сжатия [3,6], и связанные с ускоренным движением границы плазмы поперек магнитного поля. Для неустойчивости, развивающейся в плоскости (r, Z), применима теория Релей-Тейлора. С учетом вязкости эта теория изложена в [7]. Максимальная величина инкремента роста возмущений $\gamma_{max} = 0{,}4\,(g^2/\nu)^{1/3}$, а соответствующее волновое число $k_{max} = 0{,}5\,(g/\nu^2)^{1/3}$, где g – ускорение плазмы (только в сторону оси), ν – кинематическая вязкость. Оценка λ_{max} для двух моментов времени (для начального и для непосредственно предшествующего второму сжатию) показывает, что λ_{max} не очень сильно изменяются в процессе разряда и равны $0{,}4 \div 0{,}1$, а соответствующий безразмерный инкремент γ_{max} получается порядка 10. Можно сделать качественный вывод, что изображенная на рис. 9 токовая оболочка приобретает волнообразную форму в результате развития неустойчивости типа Релея-Тейлора. Длинные волны, по-видимому, не возрастают с теоретическими инкрементами $\gamma \sim \sqrt{k}$, поскольку для них играет большую роль неоднородность плазмы. Короткие волны, для которых $\gamma \sim k^{-1}$, тоже подавляются в расчетах, когда их длина сравнивается с пространственным шагом задачи. Если есть преимущественные условия возбуждения какой-либо характерной длины волны, тогда k_{max} с максимальным инкрементом γ_{max} потеряет свое доминирующее значение. Видимо, такой случай имеет место для разрядов в смеси дейтерия с ксеноном, когда на фотографиях пинча в мягком рентгене появляется характерная, периодическая по Z структура в виде "четок" (рис. 16). На соответствующих фоторазвертках (рис. 10) через вертикальную щель видна та же периодическая модуляция формы токовой оболочки. Длина волны неустойчивости определяется здесь, по-видимому, ионизационными явлениями в смеси газов.

Естественно встает вопрос, каким образом можно объяснить при наличии ускоренного движения плазмы к оси высокую степень симметрии по азимуту. Подчеркнем, что выход нейтронов крайне чувствителен к этой симметрии, хотя может оставаться достаточно высоким при смещении оси фокусировки плазмы от геометрической оси системы. Регулярное начальное возмущение по азимуту, создаваемое специальными периодическими "насечками" на аноде также не развивается, а наоборот, практически исчезает к моменту возникновения ударного фронта (примерно на половине радиуса электрода). Была сделана попытка оценить устойчивость нецилиндрического пинча по азимуту на основе линейной теории Релея-Тейлора. Возмущение всех величин в плазме пропорционально

ТАБЛИЦА I. ИЗМЕРЕННОЕ УСКОРЕНИЕ ОБОЛОЧКИ И КРИТИЧЕСКОЕ УСКОРЕНИЕ

t мксек	2,6	3,0	3,4	3,8	4,0	4,2
$g_{эксп}$, см/сек^2	$2\cdot10^{12}$	$2,5\cdot10^{12}$	$3,5\cdot10^{12}$	$4,5\cdot10^{12}$	$5\cdot10^{12}$	$6\cdot10^{12}$
$g_{крит}$ $(\rho=\rho_0)$	$6\cdot10^{12}$	$8,6\cdot10^{12}$	$13,6\cdot10^{12}$	$32\cdot10^{12}$	$42\cdot10^{12}$	$82\cdot10^{12}$
$g_{крит}$ $(\rho=4\rho_0)$	$1,5\cdot10^{12}$	$2,2\cdot10^{12}$	$3,4\cdot10^{12}$	$8\cdot10^{12}$	$10\cdot10^{12}$	$20\cdot10^{12}$

$\exp\,(ik_\varphi R_\varphi + |k_\varphi|(r-R) + \omega t)$, где k_φ – волновой вектор в азимутальном направлении, R – радиус поверхности плазмы. Внутрь плазмы возмущения экспоненциально убывают. Согласно [8], инкремент равен:

$$\omega^2 = \frac{1}{4\pi\rho}(Hk_\varphi)^2 - gk_\varphi \qquad (k_\varphi > 0) \tag{3}$$

H – азимутальная компонента магнитного поля на поверхности плазмы. Постоянство величин H, ρ, g и пренебрежение кривизной поверхности плазмы, конечно, предполагаются в линейной теории, так что, строго говоря, в применении к нашему случаю $k_\varphi > k_0$, некоторой величины, характеризующей обратный линейный размер (скажем, $k_0 = R^{-1}$ и т. п.). В приведенной формуле (3) магнитное поле внутри плазмы положено равным нулю, т. е. имеется ввиду ограничение рассматриваемых k_φ также и с другой стороны – $k_\varphi < k_0'$, где $k_0' = d^{-1}$ (d – толщина скин-слоя). Можно показать, что учет вязкости плазмы приведет к уменьшению ω, но не изменит границу неустойчивости со стороны коротких волн:

$$k_{\varphi\max} = \frac{4\pi g\rho}{H}$$

Из условия периодичности по углу g вытекает, что может осуществляться возбуждение дискретного спектра возмущений: $k_n = n/R$. Достаточное условие устойчивости, которое является вариантом условия Крускала-Шафранова, тогда должно иметь вид:

$$k_{\varphi\max} < k_2 = 2/R\text{, т. е.}$$

$$g \leqslant \frac{H^2}{2\pi\rho R} = \frac{2\,10^{-2}\cdot I^2}{\pi\rho\cdot R^3} = g_{крит} \tag{4}$$

Это условие означает, что длина волны наиболее опасной для симметрии второй (n = 2) гармоники возмущения оказывается меньше, чем критическая длина волны $\lambda_{\varphi\max} = 2\pi k_{\varphi\max}^{-1}$. На всем протяжении процесса схлопывания токовой оболочки к оси можно сравнить $g_{эксп}$ с критическим ускорением $g_{крит}$ из (4), проверив тем самым выполнимость критерия устойчивости. К сожалению, фоторазвертка дает величину R(t), а g(t) находится лишь при двойном дифференцировании экспериментального графика. Точность определения $g_{крит}$ в основном зависит от принятого значения ρ, так как R(t) и I(t) находятся достаточно просто из тех же фоторазверток и осциллограмм тока. Для временного интервала 2,6 ÷ 4,2 мксек построена табл. I. Критическое ускорение вычислено для двух значений ρ, соответствующих начальной плотности ($\rho_0 = 2{,}4 \cdot 10^{-7}$ г/см^3) и сжатию в 4раза за фронтом ударной волны. В это время радиус оболочки меняется от R_0 до $R_0/3$.

Чем меньше радиус токовой оболочки, тем больше запас устойчивости, т.е. тем лучше выпоняется условие: $g_{эксп} < g_{крит}$ (даже для $\rho = 4\rho_0$).

5. АНАЛИЗ ПРОСТРАНСТВЕННОГО РАСПРЕДЕЛЕНИЯ ЗАРЯЖЕННЫХ ЧАСТИЦ DD-РЕАКЦИИ

По сравнению с нейтронным излучением поток заряженных частиц несет дополнительную информацию о величине, направлении и распределении магнитного поля.

Заряженные продукты DD-реакций, проходя через собственное магнитное поле пинча, отклоняются в нем. Это сказывается на характере угловых и пространственных распределений частиц. Указанные распределения были получены для протонов DD-реакций, протекающих в ПФ, и результаты интерпретированы путем сравнения экспериментальных распределений с распределениями, рассчитанными на ЭВМ в следующих модельных представлениях.

Предполагалось, что частицы излучаются изотропно из точечного источника и токовая оболочка не меняется в процессе эмиссии протонов.

На основании скоростной фотосъемки форма оболочки определялась как поверхность вращения, задаваемая уравнением:

$$Z^2 = \alpha \cdot (r - r_0)$$

где Z – ось вращения, r_0 – минимальный радиус фокуса пинча, α – параметр, характеризующий кривизну оболочки (рис. 11). Предполагалось, что весь ток (~1 МА) течет по бесконечно тонкой оболочке. Поэтому поле внутри токовой оболочки равно нулю, а вне – спадает как $1/r$.

Предположение точечности источника не вносило существенных искажений в конечные результаты, если учесть малость размеров пинча ($h \sim 2 \div 3$ см и $r_0 \ll 1$ см) по сравнению с расстояниями до детекторов протонов.

В расчетах не учитывалось рассеяние частиц в плазме, так как длина свободного пробега протонов с энергией 3 мэВ при средней плотности дейтерия в камере 10^{17} см$^{-3}$ составляет $2 \cdot 10^4$ см, что существенно больше длины их траекторий в плазме.

На рис. 11 вместе с продольным сечением токовой оболочки с параметрами $\alpha = 10$ и $r_0 = 0{,}05$ см представлены траектории протонов, вылетающих из точечного источника под углами θ, равными 20°, 90° и 170°. Как видно из рис. 11, большинство частиц, неоднократно отражаясь от магнитного поля, движется вверх. Анода достигнут лишь те частицы, которые вышли вниз в очень узком конусе, зависящем от выбранных параметров α, r_0. Эта доля невелика, что подтверждается отсутствием сколько-нибудь заметного числа протонов на ядерных пластинах, неоднократно помещавшихся со стороны анода.

На рис. 12 представлены рассчитанные при разных значениях α, r_0 угловые распределения частиц, попавшие на небольшой участок крышки по оси разрядной камеры. Здесь плотность частиц в относительных единицах является функцией углов, под которыми протоны попадают на крышку камеры. Полученные распределения оказались чувствительными к изменению параметров α, r_0.

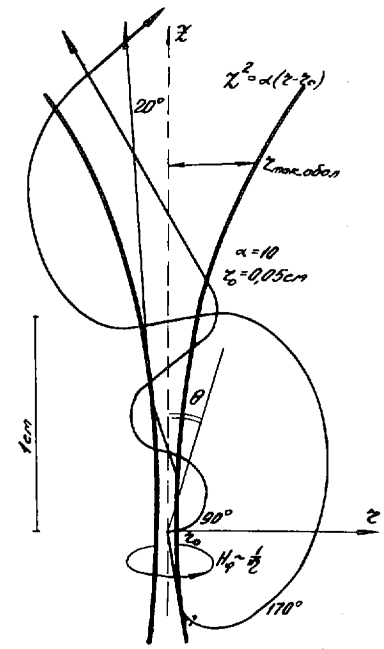

Рис. 11. Сечение токовой оболочки с параметрами $\alpha = 10$, $r_0 = 0{,}05$ и траектории протонов, вылетающих из точечного источника под углами $\theta = 20°, 90°, 170°$.

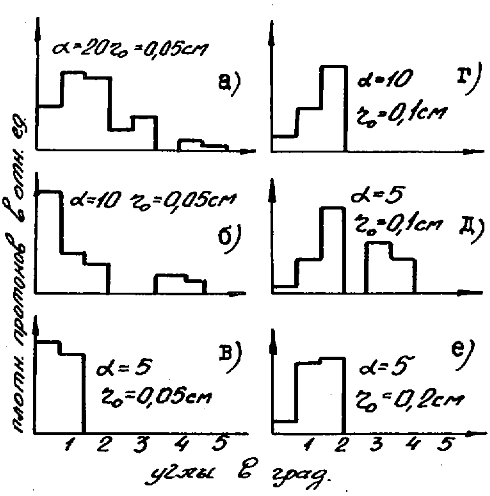

Рис. 12. Угловое распределение протонов для разных α и r_0 (расчет).

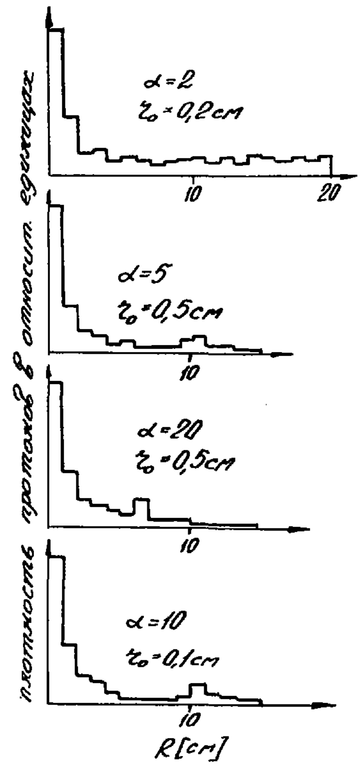

Рис. 13. Пространственные распределения протонов для разных α и r_0 (расчет).

На рис. 13 приведены пространственные распределения протонов, рассчитанные для различных параметров α, r_0. По координатным осям отложены расстояния по крышке камеры от геометрической оси разряда и плотность частиц в относительных единицах. Влияние собственного магнитного поля таково, что даже при широких и низких пинчах (большое r_0 и малое α), когда поле наиболее слабое, распределения практически кончаются на расстоянии 20 см. Это составляет примерно 45° по отношению к оси разряда. Следовательно, при углах, больших 45°, протоны не должны наблюдаться.

Экспериментально угловые распределения протонов были получены при помощи камер-обскур. Детектором служили пластины с ядерной эмульсией типа Н-3 НИКФИ, толщиной 100 мк, которая дает хорошее разрешение для протонов до 5 мэВ и мало чувствительна к рентгеновскому излучению ПФ. Диаметр отверстия обскур, удаленных от анода на 19 см, был равен 0,17 мм, угол зрения менялся во время опыта (8° и 23°). Труба со стороны анода делает условия экспонирования верхней и нижней пластин примерно одинаковыми, рис. 1(12,13).

Для получения пространственных распределений частиц дополнительно к обскурам на боковой стенке камеры на уровне анода под углом 90° к оси

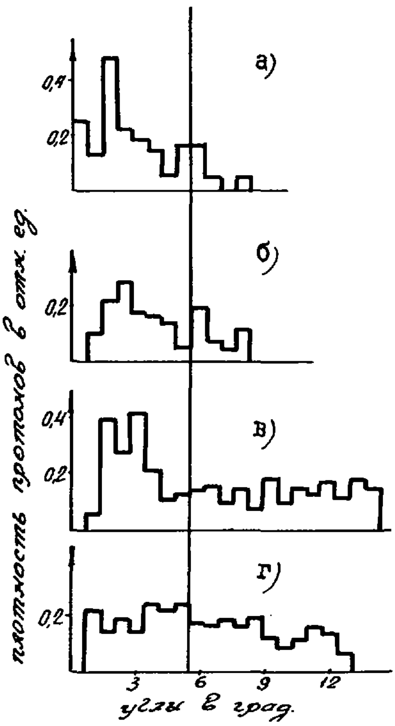

Рис. 14. Экспериментально полученные угловые распределения протонов:
а),б) – угол зрения системы 8°
в),г) – угол зрения системы 23°.

разряда располагалась щель высотой 17 мм и шириной 0,1 мм. Расстояние до центра анода составляло 55 см. За щелью помещалась пластина с ядерной эмульсией.

Все пластины располагались под углом 45° к геометрической оси разрядной камеры. Применение камеры-обскуры сбоку не имело смысла из-за малой плотности частиц на боковой стенке камеры, рис. 1 (15).

Регистрация заряженных частиц эмульсией происходит с эффективностью 100%, причем все треки начинаются на поверхности эмульсии (свободный пробег протонов с энергией 3 мэВ в эмульсии не превышает $2 \cdot 10^{-6}$ мм). Фон от нейтронов, создающих протоны отдачи во всем объеме эмульсии, легко учитывался по глубине залегания следов, их длине и углам отклонения.

На рис. 14 представлены угловые распределения протонов, полученные по пластинам, экспонированным сверху. Угловые распределения протонов со стороны анода не были получены из-за недостатка треков на пластинах. Этот факт полностью согласуется с результатами расчетов, как уже упоминалось. Разная ширина нормированных распределений на рис.14 объясняется разными коллимирующими свойствами регистрирующих систем. Распределения рис. 14 (а,б) получены с углом зрения системы 8°,

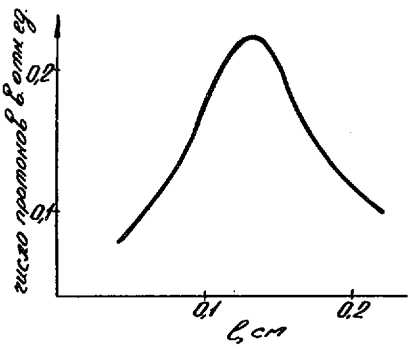

Рис. 15. Распределение протонов, полученное через боковую щель, см. рис. 1 (15).

а рис. 14(в,г) — с углом зрения 23°. Кроме того, график на рис. 14(а) представляет собой среднее распределение протонов для четырех разрядов, зарегистрированных одной и той же пластиной. Остальные распределения получены в результате однократного облучения пластин.

На рис. 15 показано распределение протонов, полученное с боковой щелью, за один разряд. По осям отложены расстояния по пластине и число протонов в относительных единицах. В приведенном случае зарегистрировано ощутимое количество протонов ($\sim$100 на щель). Это на два порядка ниже ожидаемого количества в случае изотропного распределения, но выше рассчитанного.

Оценка величины магнитного поля в момент кумуляции была сделана путем сравнения экспериментальных (рис. 14) и теоретических (рис. 12) угловых распределений протонов.

В пределах углов $4° \div 5°$ экспериментальные распределения по форме достаточно четко согласуются с некоторыми теоретическими распределениями (ср. рис. 14(а) и рис. 12(а), рис. 14(б, в) и рис. 12(г, д), рис. 14(г) и рис. 12(е). При больших углах распределения не согласуются. Экспериментальные распределения много шире, причем увеличение угла зрения обскуры не вызывает изменения формы центральной части распределения (опять-таки в пределах углов $4° \div 5°$), а лишь удлиняет почти равномерный хвост. Никакая комбинация параметров α, r_0, а также перемещение точечного источника, сжатого собственным магнитным полем, на 2-3 см вдоль геометрической оси разрядной камеры не объясняют такой большой ширины угловых распределений.

Своеобразие полученных экспериментально угловых распределений, а также наличие протонов на боковой пластине позволило нам следующим образом интерпретировать результаты.

Прежде всего, было принято, что в центральную часть экспериментальных угловых распределений в пределах 5° основной вклад вносят протоны, образующиеся в плазменном фокусе и движущиеся в магнитном поле согласно модели. Путем подбора теоретических распределений, наиболее близких к экспериментальным, найдено, что радиус фокуса для разных вариантов разряда лежит в интервале от 0,5 до 2 мм. Величина магнитного поля пинча в этих случаях оценивается как $(1 \div 4) \cdot 10^6$ Э.

Объяснить присутствие протонов на боковой пластине и большую ширину экспериментальных угловых распределений по сравнению с теоретическими можно, если предположить, что некоторая доля протонов излучается из области, расположенной вблизи верхней крышки разрядной камеры. Вероятнее всего, эта область является частью источника, распределенного вдоль оси, что согласуется с результатами нейтронных измерений [3,15]. Благоприятные условия для регистрации боковой пластиной протонов из этой части источника создаются за счет того, что протоны встречаются с магнитным полем на достаточно большом радиусе. Более того, само поле к моменту излучения этой группы частиц может ослабевать из-за уменьшения протекающего по оси камеры разрядного тока [3] [1].

По плотности частиц на боковой пластине и по плотности протонов в хвосте соответствующего экспериментального углового распределения, рис. 14(в), количество излучаемых частиц было определено $\sim 10^8$ за разряд при общей мощности источника $2{,}5 \cdot 10^{10}$ за разряд.

6. НАБЛЮДЕНИЯ В МЯГКОМ РЕНТГЕНЕ И УЛЬТРАФИОЛЕТЕ

Было продолжено исследование структуры ПФ в мягком рентгене.

Изображение пинча в рентгеновских лучах в масштабе 1 : 10 получено при помощи двух многодырочных камер-обскур, ориентированных по радиусу разрядной камеры в двух взаимно перпендикулярных направлениях. Каждая из камер-обскур имела восемь отверстий диаметром от 4 до 44 мк. Расстояние от обскуры до пленки, определяющее масштаб изображения, равнялось 50 мм. Изображение ПФ регистрировалось на пленочном диске, аналогичном описанному в [1]. Для регистрации использовалась пленка с безжелатинной эмульсией УФ-αТ, разработанной в НИКФИ. От видимого света эмульсия обычно защищалась алюминиевым фильтром толщиной 6 мк. В камере-обскуре поддерживалось давление порядка 10^{-2} тор. Применение многодырочных камер-обскур было обусловлено следующими причинами. Каждая точка объекта в обскуре изображается кружком, диаметр которого примерно равен диаметру отверстия камеры-обскуры. (Дифракционными эффектами при выбранном расстоянии от отверстия до пленки можно было пренебречь). Поэтому выгоднее для улучшения разрешающей способности брать диаметр отверстия возможно меньшим.

С другой стороны, при уменьшении диаметра отверстия падает освещенность фотопленки и для изображения менее ярко светящихся деталей может нехватить экспозиции. Применение камер-обскур с рядом отверстий разных диаметров позволило получить сразу изображения наиболее ярких деталей пинча с большим разрешением и менее ярких деталей с меньшим разрешением.

Фотографии, полученные при помощи двух обскур через отверстия одинакового размера, давали парные изображения пинча, которые позволяли судить о пространственной структуре плазменного фокуса. Кроме того, удалось оценить диаметр наиболее ярко светящейся области пинча, размеры которой в некоторых случаях оказываются не больше 0,1 мм. Набор объективов разных диаметров позволил экстраполировать результаты измерений на отверстие "нулевого" диаметра, т.е. осуществить своеобразный учет аппаратной функции обскуры.

---

[1] В [3] на рис. 7(а,б) и рис. 9 вместо времени 0,2 мксек, указанного на масштабе, следует читать 1 мксек.

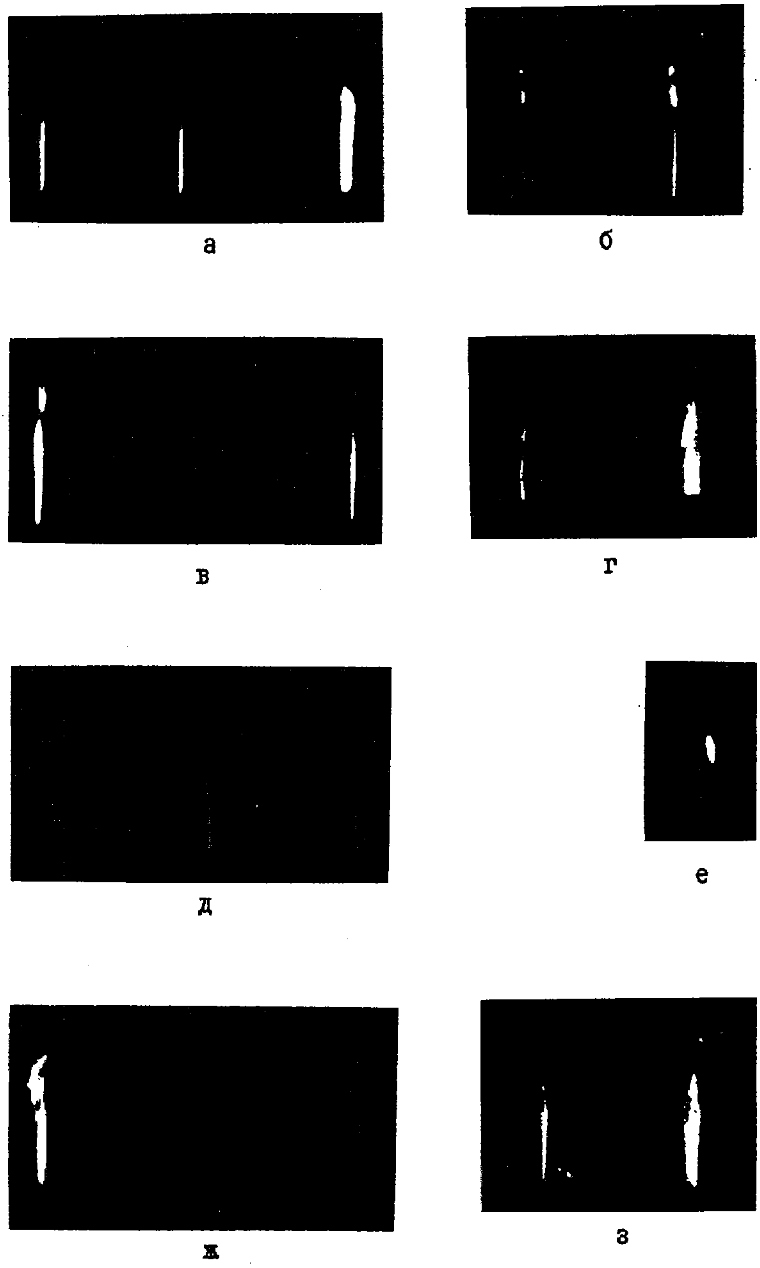

Рис. 16. Обскурограммы плазменного фокуса в масштабе 1 : 1 (Условия экспонирования приведены в табл. II).

ТАБЛИЦА II. ПАРАМЕТРЫ ПЛАЗМЕННОГО ФОКУСА ДЛЯ ОБСКУРОГРАММ РИС.16

Рис.№№	Давление дейтерия, тор	Примесь	U_0, кВ	Нейтронный выход	Диаметр отверстий, мк
16(а)	1,5	Xe	20	$3{,}6\cdot10^{10}$	15; 12; 44
(б)	1,5	Xe	20	$2{,}5\cdot10^{10}$	17; 32
(в)	1,0	Xe	18	$2{,}6\cdot10^{10}$	32; 7; 15
(г)	1,5	Xe	18	$1{,}5\cdot10^{10}$	12; 44
(д)	1,5	N_2	18	$3{,}5\cdot10^{10}$	27; 34; 25
(е)	1,0	Xe	18	$2{,}2\cdot10^{10}$	44
(ж)	1,0	Xe	18	$2{,}7\cdot10^{10}$	32; 7; 15
(з)	1,5	Xe	20	$2{,}9\cdot10^{10}$	32; 23
17(а)	1,5	N_2	20	$1{,}9\cdot10^{10}$	3[a]
(б)	1,5	N_2	20	$1{,}9\cdot10^{10}$	44
(в)	1,5	N_2	20	$2{,}8\cdot10^{10}$	3[a]
(г)	1,5	N_2	20	$2{,}8\cdot10^{10}$	44
(д)	1,5	Xe	18	$1{,}4\cdot10^{10}$	3[a]
(е)	1,5	Xe	18	$1{,}4\cdot10^{10}$	44
(ж)	1,0	N_2	18	$2{,}8\cdot10^{10}$	3[a]
(з)	1,0	Xe	16	$1{,}2\cdot10^{10}$	3[a]

[a] Без фильтра.

Как уже отмечалось выше, конечная стадия разряда характеризуется двумя последовательными сжатиями; при этом максимальная температура достигается во втором сжатии, ответственном за генерацию основного количества нейтронов.

Практически на всех обскурограммах, приведенных в натуральном масштабе на рис. 16, заметны две таких стадии ПФ. Мы предполагаем, что прямой длинный стержень отвечает первому сжатию, а короткий след, зачастую обладающий сложной формой и находящийся обычно выше первого, соответствует второму сжатию.

Небольшое "размазывание" изображения на ряде снимков показывает, что за время своего существования пинч иногда испытывает небольшие радиальные перемещения. Такими перемещениями ($\sim$2 мм) можно объяснить, например, структуру отдельных снимков на рис. 16(г,з). Начальные условия эксперимента приведены в табл. II. Разрядам со сложной структурой обычно соответствуют меньшие нейтронные выходы, что связано с недостаточной симметрией последней стадии кумуляции.

В результате анализа большого числа парных фотографий не удалось показать существования трубчатой структуры пинча, как это предсказывали расчеты в [6]. Наоборот, правильнее утверждать, что плотность вблизи оси – максимальна.

Одновременно с получением изображений пинча в мягком рентгене осуществлялось фотографирование зоны фокуса камерой-обскурой с отверстием 3 мк, не закрытым фильтром. Видимый свет разряда рассеи-

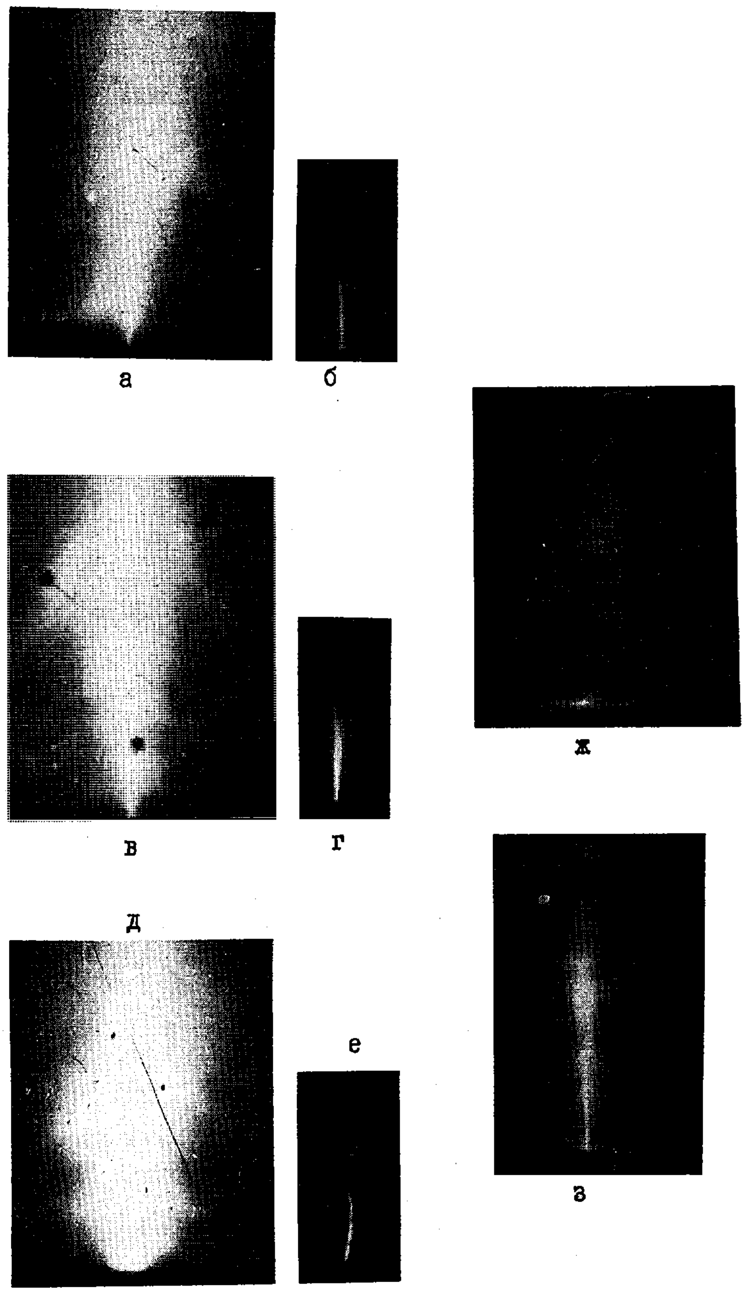

Рис. 17. Обскурограммы плазменного фокуса в масштабе 1 : 1 (Условия экспонирования приведены в табл. II).

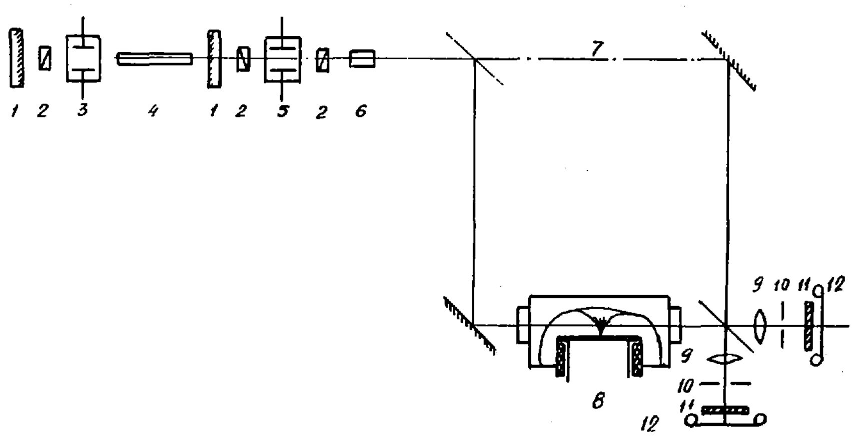

Рис. 18. Оптическая схема эксперимента:
1 – зеркала, 2 – поляризаторы, 3 – ячейка Керра, 4 – кристалл рубина, 5 – обостряющая ячейка Керра, 6 – кристалл KDP, 7 – интерферометр Маха-Цандера, 8 – разрядная камера, 9 – объективы, 10 – диафрагмы, 11 – фильтры, 12 – фотопленка.

вался за счет дифракции, а ультрафиолетовое и длинноволновое рентгеновское излучение пинча регистрировалось эмульсией. На рис. 17 приведен ряд таких обскурограмм плазменного фокуса (см, табл. II). Для отдельных случаев рядом помещены фотографии того же разряда через алюминиевый фильтр толщиной 6 мк.

Заметные на рис. 17(в,д)"усы", вероятно, отвечают ряду последовательных, наложенных друг на друга изображений движущегося вверх слоя паров материала электрода. Возникающая "стробоскопичность" связана с временной последовательностью излучения наиболее ярких спектральных линий, появляющихся в процессе нагрева и возбуждения атомов металла.

7. ЛАЗЕРНАЯ ДИАГНОСТИКА ПЛАЗМЕННОГО ФОКУСА

На более высоком техническом уровне была возобновлена лазерная диагностика плазменного фокуса [14]. Применялись три методики оптической диагностики:

1) теневое фотографирование – для осуществления синхронизации импульса лазера с разрядом,

2) шлирен-фотографирование – для выявления градиентов плотности в плазменном фокусе и установления степени симметричности и

3) интерферометрия в двух длинах волн – для установления распределения плотности плазмы в фокусе.

Оптическая схема эксперимента изображена на рис. 18.

В связи с тем, что скорость схлопывания оболочки порядка $3{\cdot}10^7$ см/сек [3], для получения достаточного временного разрешения был применен лазер, аналогичный использованному в работе [9] с длительностью импульса $\sim$1 нсек. При этом пространственное разрешение на фотографиях ударной волны составляет величину порядка 0,3 мм. В области кумуляции это разрешение выше, так как здесь изменение электронной

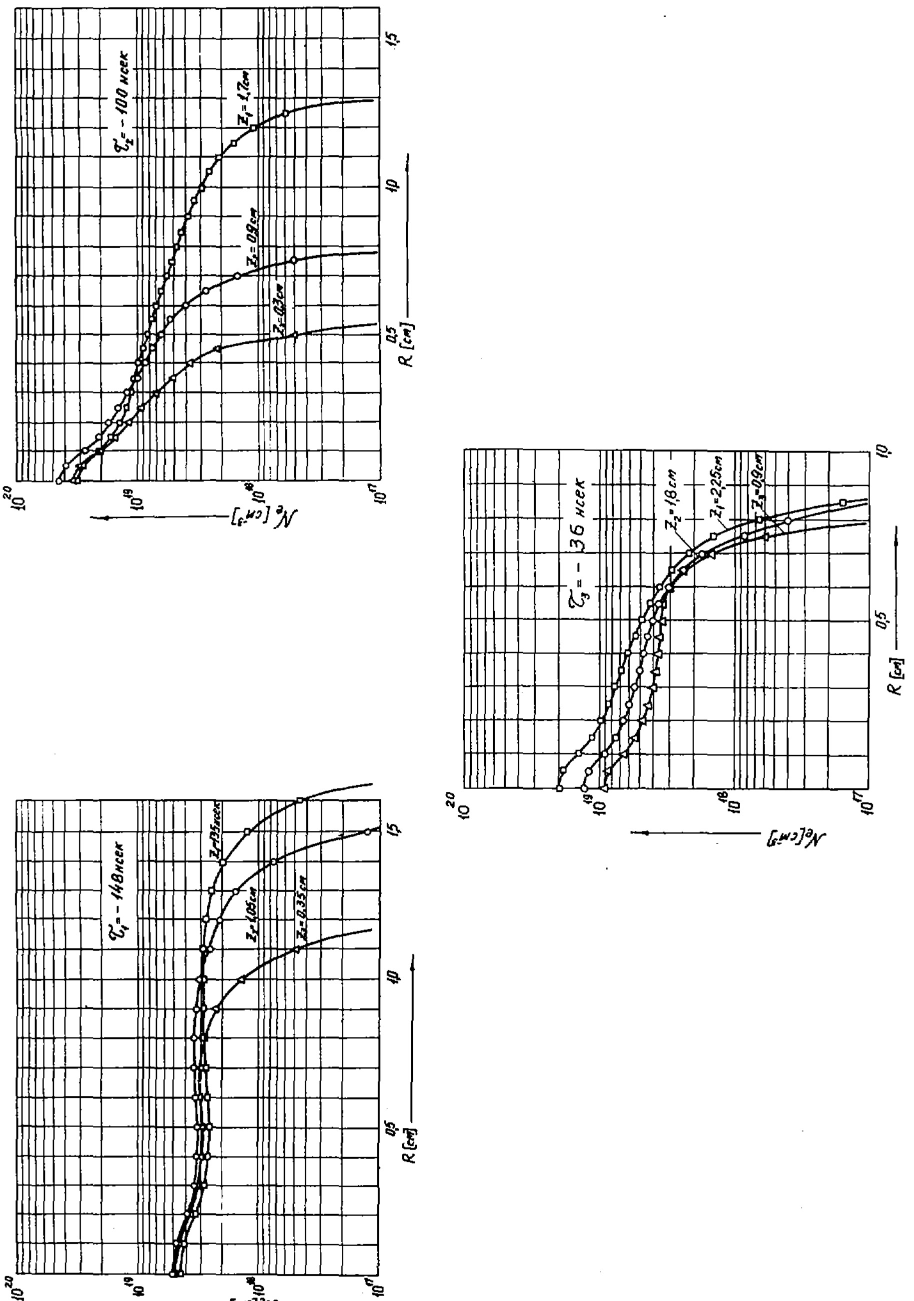
τ₂ = − 100 нсек
Z₁ = 1,7 см
Z₂ = 0,9 см
Z₃ = 0,3 см
τ₁ = − 148 нсек
Z₁ = 1,35 см
Z₂ = 1,05 см
Z₃ = 0,35 см
τ₃ = − 36 нсек
Z₂ = 1,8 см
Z₁ = 2,25 см
Z₃ = 0,9 см
R [см]
Nₑ [см⁻³]

(a)

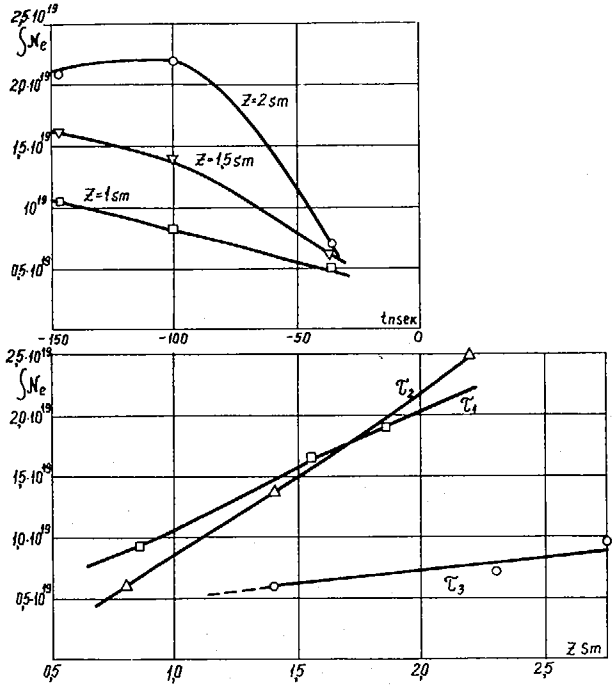

(б)

Рис. 19. а) Распределение электронной плотности по радиусу пинча в различные моменты времени для трех сечений, соответствующих высотам – z_1, z_2, z_3 над анодом. Экспозиция – 2 нсек, время τ отсчитывается от максимума рентгеновского импульса. (Максимум рентгеновского импульса отстоит от максимума нейтронного импульса на ~20 нсек); б) Полное число частиц в сечении на единицу высоты пинча (1 см) в зависимости от времени и от расстояния до анода.

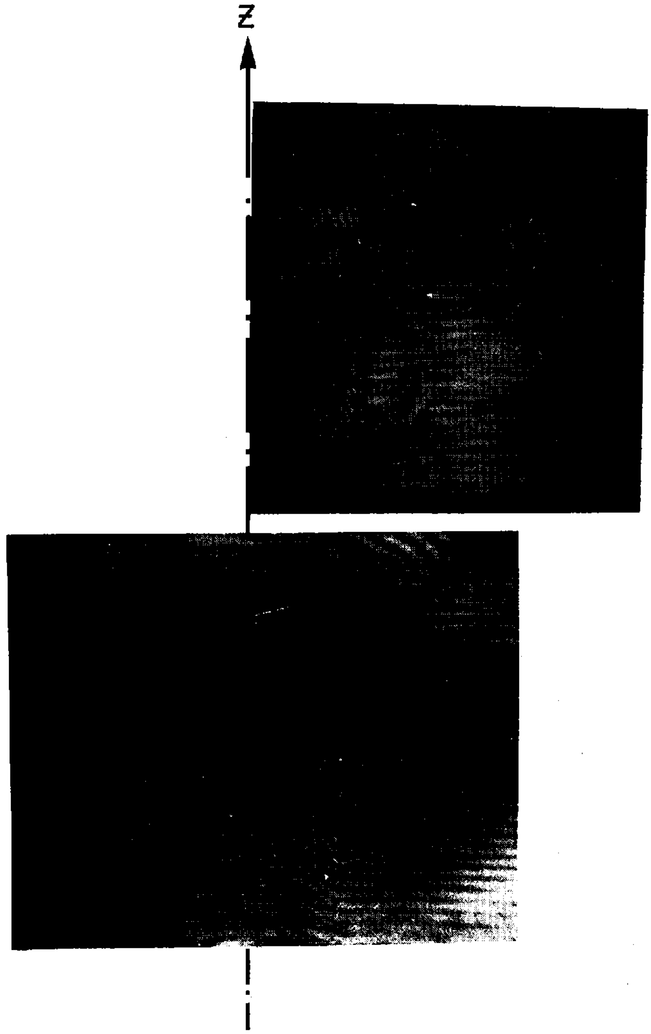

Рис.20. Типичные интерферограммы разряда. Экспозиция – 2 нсек.

плотности во времени в момент сжатия значительно медленнее. Определяется оно рисующей оптикой и составляет на длине волны рубина $\lambda = 0{,}694$ мк величину $\sim 10^{-3}$ см, а на длине волны второй гармоники $\lambda = 0{,}347$ мк – порядка $3 \cdot 10^{-3}$ см. Для улучшения когерентных свойств излучения короткий импульс вырезался из передней части длинного импульса лазера с модулированной добротностью.

Так как в эксперименте дейтерий применялся в смеси с азотом или ксеноном, то необходимо было проведение интерферометрии плазмы в двух длинах волн для исключения вклада ионов в плазменный показатель преломления [10]. Для этого применялась вторая гармоника рубинового лазера. По таблицам [11] было проверено отсутствие линий излучения примесей с длинами волн, совпадающими с длиной волны просвечивающего излучения. В фокусе нет также интенсивных линий с длиной волны, бóльшей длины волны лазера.

В связи с тем, что плазменный фокус обладает резкими градиентами плотности и одновременно большим абсолютным значением ее, возникает вопрос о влиянии рефракции на интерференционную картину. Формулу для угла, под которым просвечивающий луч выходит из плазмы, получаем из уравнения эйконала [12]:

$$\operatorname{tg}\alpha \simeq \operatorname{grad} \ln \nu \, dx$$

где ν – показатель преломления плазмы.

Из сдвига полос на интерферограмме за счет рефракции [13], определяемого по формуле

$$\delta \approx \frac{\alpha^2 x}{12\lambda}$$

нетрудно получить, что при обработке интерферограммы с точностью до 1/10 полосы и длине пути в плазме ~ 1 мм искажения интерферограммы за счет рефракции лежат в пределах точности измерений. При этом отображающая оптика собирает лучи с углами отклонения, меньшими 2^0. Геометрия нашего эксперимента удовлетворяла поставленному условию. Диафрагмы, помещенные в фокусах отображающих объективов, избавляли от излучения плазмы. Электронная компонента фазового показателя преломления плазмы определяется формулой:

$$\nu_{\text{эл}} = 1 - \frac{f_p^2}{2f^2}$$

где $f_p = \sqrt{(N_e \cdot e^2)/(\pi m_e)}$ – электронная плазменная частота, а f – частота просвечивающего излучения.

В данном случае формула справедлива для $\lambda = 0{,}694$ мк и тем более для $\lambda = 0{,}347$ мк, несмотря на высокие значения плотности ($\sim 10^{20}$ см$^{-3}$), температуры (~ 1 кэВ) плазмы и величины магнитного поля ($\sim 10^6$ Гс), так как при этих значениях $f_c/f = (n\,\sigma\,v)/f \simeq 2 \cdot 10^{-2} \ll 1$ и $f_H/f = eB/(2\pi m_e cf) \simeq 6 \cdot 10^{-3} \ll 1$, где f_c – частота столкновений электронов с ионами, а f_H – электронная циклотронная частота.

Для обработки отбирались интерферограммы с наилучшей цилиндрической симметрией.

Расчет распределения электронной плотности в фокусе проводился на ЭВМ по методу параболической аппроксимации с выбором оптимального числа зон, который дает более высокую точность по сравнению с ранее применявшимися методами, при одновременном сокращении вычислительной работы.

Типичные фотографии и результаты представлены на рис. 19 и 20.

В заключение авторы выражают искреннюю признательность Л.А. Арцимовичу и Н.Г. Басову за их интерес к данной работе, ценные дискуссии и поддержку. Авторы благодарят своих товарищей по работе за помощь в проведении экспериментов.

ЛИТЕРАТУРА

[1] ФИЛИППОВ, Н.В., ФИЛИППОВА, Т.И., ВИНОГРАДОВ, В.П., Nuclear Fusion, 1962 Supplement, part 2, p.577.

[2] ФИЛИППОВ, Н.В., ФИЛИППОВА, Т.И., Plasma Phys. and Contr. Nucl. Fusion Research, IAEA 2 1966, p.405.

[3] АГАФОНОВ, В.И. и др., Plasma Phys. and Contr. Nucl. Fusion Research, IAEA 2 1969, p.21.

[4] BASQUE, D., JOLAS, A., WATTEAU, J.P., Phys. Fluids 11 (1968) 1384.

[5] ROBUOCH, B.V., DI COLA, G., "A one-dimensional model of a two-dimensional snow-plough Mirapi-focus discharge". Laboratori Gas Ionizzati, Frascati, LGI 70/5/E (1970).

[6] ДЬЯЧЕНКО, В.Ф., ИМШЕННИК, В.С., ЖЭТФ 56 (1969) 1766-1777.

[7] CHANDRASEKHAR, S., "Hydrodynamic and hydromagnetic stability", Oxford, Clarendon Press, 1961.

[8] СТИКС, Т., "Волны в плазме", ИИЛ, 1966.

[9] БАСОВ, Н.Г. и др., ЖЭТФ 54 4 (1968).

[10] ALPHER, R.A., WHITE, D.R., Phys. Fluids 2 (1959) 162.

[11] Atomic Transition Probabilities 1, National Standard Reference Date Series, National Bureau of Standards, Washington.

[12] БОРН, М., ВОЛЬФ, Э., "Основы оптики", Наука, 1970.

[13] JAHODA, F.G. et al., Journal of Appl. Phys. 35 (1964) 8.

[14] ВИНОГРАДОВ, В.П., ГОЛУБЧИКОВ, Л.Г., ФИЛИППОВ, Н.В., ФИЛИППОВА, Т.И., ТВТ 5 (1967) 343-348.

[15] BERNSTEIN, M.J., MESKAN, D.A., VAN PASSEN, H.L., Phys. Fluids 12 (1969) 2193-2202.

МЕХАНИЗМ ФОРМИРОВАНИЯ ПЛАЗМЕННОГО ФОКУСА КОАКСИАЛЬНОГО ИНЖЕКТОРА

И. Н. БУРДОНСКИЙ, Р. П. ВАСИЛЬЕВА,
М. И. ПЕРГАМЕНТ, А. И. ЯРОСЛАВСКИЙ
Институт атомной энергии им. И. В. Курчатова,
Москва,
Союз Советских Социалистических Республик

Доклад представлен Е.П.Велиховым

Presented by E.P.Velikhov

Abstract — Аннотация

MECHANISM OF PLASMA FOCUS FORMATION IN A COAXIAL INJECTOR.

In an earlier paper, the authors established that most of the fast component of a plasmoid is generated in the "plasma focus" – i.e. the region in front of the end of the injector, where the plasma density and temperature are orders of magnitude higher than in the surrounding space. The present paper deals with the mechanisms involved in the formation of a focus and the heating of the plasma therein. It is established that almost the entire current shorts through the fairly thin moving current layer only in the first, relatively short stage of the process. In the second stage, the current is at first distributed comparatively uniformly through the entire plasma volume; it then shorts at the rear end of the plasma gun, forming a current eddy. In the longitudinal sectional view of the electrode gap, the eddy current lines look like nested ovals extending along the electrodes and projecting in the forward part beyond the electrode system. With time, the rear boundary of the current eddy shifts – together with the plasma – in the direction of acceleration, while the forward boundary of the current distribution remains stationary. The radial equilibrium of the current eddy depends on the fact that the forces $\vec{j} \times \vec{H}$ acting in that part of the current loop in which the current lines are almost parallel to the electrode system are balanced by the pressure gradient. The latter is due to the non-uniformity of Joule heating of the plasma in the current loop, as the current density is zero at the centre of the electrode gap and rises sharply as the electrodes are approached. The topography of the magnetic and current fields at the end of the electrode system is such that the forces $\vec{j} \times \vec{H}$ acting in the thick current distribution layer focus a significant part of the plasma flowing through the electrode gap at the axis of the system in front of the central electrode. These same forces accelerate the plasma from (5×10^6)-(1×10^7) cm/s in the electrode gap to $(2\text{-}3) \times 10^7$ cm/s in the zone adjacent to the focus. The process is quasi-stationary in the sense that the characteristic times of variations in the compression zone parameters are substantially greater than the time of plasma renewal in the compression zone. In the focus zone $nk\,(T_e + T_i) \gg H^2/8\pi$; in other words, compression is the result of inertial motion of the plasma fluxes formed in the electrode gap. On the basis of magnetic field, density field and temperature measurements, the authors carry out a numerical integration along the trajectories and establish the configurations of the plasma fluxes. There is a discussion of the conditions in the electrode gap under which the described mechanism is transformed into a mechanism whereby a focus is formed by the thin current layer which collects the gas.

МЕХАНИЗМ ФОРМИРОВАНИЯ ПЛАЗМЕННОГО ФОКУСА КОАКСИАЛЬНОГО ИНЖЕКТОРА.

В предыдущей работе авторов было установлено, что основная часть быстрой компоненты плазменного сгустка генерируется в "плазменном фокусе" – области перед торцом инжектора, где плотность плазмы и ее температура на порядки величин выше, чем в окружающем пространстве. Данная работа посвящена исследованию механизмов формирования фокуса и нагрева в нем плазмы. Установлено, что только в первой относительно короткой стадии процесса почти весь ток замыкается через достаточно узкий движущийся токовый слой. Во второй стадии ток сначала сравнительно равномерно распределяется по всему объему плазмы, а затем замыкается у заднего торца пушки, образуя токовый вихрь. В продольном разрезе межэлектродного зазора линии тока вихря выглядят как вытянутые вдоль электродов, вложенные друг в друга овалы, в передней части вынесенные за электродную систему. Во времени задняя граница токового вихря вместе с плазмой перемещается по направлению ускорения, в то время как передняя граница токового распределения остается неподвижной. Радиальное равновесие токового вихря определяется тем, что силы $\vec{j} \times \vec{H}$, действующие в той части токовой петли, в которой линии тока почти параллельны электродной системе, уравновешиваются градиентом давления. Последний возникает из-за неравномерности джоулева нагрева плазмы в токовой петле, поскольку плотность тока равна нулю в центре межэлектродного зазора и резко растет к электродам. Топография магнитных и токовых полей на торце электродной системы такова, что силы $\vec{j} \times \vec{H}$, действующие в широком слое токового распределения, фокусируют значительную часть плазменного потока, текущего в межэлектродном зазоре, на ось системы перед центральным электродом. Эти же силы ускоряют плазму от $5 \cdot 10^6 \div 1 \cdot 10^7$ см/сек в межэлектродном зазоре до $2 \div 3 \cdot 10^7$ см/сек в зоне, прилегающей к фокусу. Процесс – квазистационарен в том смысле, что характерные времена изменения параметров в зоне сжатия существенно больше времени обновления плазмы в ней. В зоне фокуса $nk(T_e + T_i) \gg H^2/8\pi$, другими словами, сжатие – результат инерциального движения плазменных потоков, сформированных в межэлектродном зазоре. В работе на основании экспериментально измеренных магнитных полей, полей плотности и температуры проведено численное интегрирование вдоль траекторий и установлены конфигурации плазменных потоков. Обсуждаются условия в межэлектродном зазоре, при которых описанный механизм трансформируется в механизм формирования фокуса тонким токовым слоем, сгребающим газ.

1. ВВЕДЕНИЕ

В предыдущей работе [1] было установлено, что основная часть быстрой компоненты плазменного сгустка генерируется в "плазменном фокусе" – области перед торцом инжектора, где плотность плазмы и ее температура на порядки величин выше, чем в окружающем пространстве.

Данная работа посвящена исследованию механизмов формирования фокуса и нагрева в нем плазмы. Эксперименты проводились на "типичном" коаксиальном инжекторе: диаметры электродов – 3,2 и 7 см, их длина – 31 см, впрыск газа на середине длины электродной системы, конденсаторная батарея – 32 мкФ, напряжение – 7,5 кВ. Подробные данные об установке и применяемых на ней диагностических методах приведены в работах [1,2]. В угоду хорошей повторяемости был выбран режим, далекий от предельного – температура в фокусе не превышала $40 \div 50$ эВ, а плотность – $2 \div 3 \cdot 10^{17}$ см$^{-3}$.

2. НАЧАЛЬНЫЕ СТАДИИ ПРОЦЕССА

Старт процесса подробно изучен в работе [2], где показано, что сразу же после пробоя разряд локализуется в 12 каналах, соответствующих напускным отверстиям во внутреннем электроде. Вплоть до максимума ток остается привязанным к плотным газовым струям, что хорошо фиксируют как оптические, так и магнитные измерения. Все это время устойчиво сохраняется азимутальная симметрия разряда, несмотря на то что плазменные каналы, ускоряясь вперед, расширяются по азимуту, сливаясь друг с другом. В этот период времени движение плазмы хорошо соответствует модели "токовой перемычки", предложенной в работе [3]. Однако уже на второй микросекунде разряда токовый слой отрывается от плотной тыловой зоны и с резким ускорением уходит вперед.

Его движение, как это следует из сигналов магнитных зондов, полностью соответствует картине, полученной в работе [4]. Другими словами, в этой стадии процесса реализуется модель "проницаемого токового слоя". Как известно, в представлениях этой модели проницаемый токовый слой движется сквозь начальное газовое распределение, не сгребая газ, но оставляя за собой плазму, вмороженную в магнитное поле. Ионы образующейся плазмы приобретают продольную энергию в аксиальном электрическом поле токового слоя. Как показывают расчеты, в типичных режимах работы инжектора длина пробега нейтрального атома до ионизации — порядка половины длины токового слоя. Поэтому дейтоны рождаются по всей глубине токового слоя и проходят различную разность потенциалов, приобретая целый спектр скоростей. Лишь малая доля дейтонов, рожденная на фронте слоя, приобретает его скорость. Этим, собственно, и определяются физические причины прозрачности токового слоя. Сгребание же нейтрального газа при таких режимах ничтожно из-за малого сечения перезарядки дейтонов стоэлектронвольтных энергий на молекулярном дейтерии. При большей плотности газа в межэлектродном зазоре и большем энерговкладе токовый слой рождает ударную волну и сгребает практически весь газ, что приводит к процессу, в корне отличному от процессов ускорения в коаксиальных инжекторах [5]. Так, к примеру, излом на осциллограмме тока — так называемая "особенность" — и соответствующий ей выброс напряжения обусловлены в нашем случае не пинчеванием вынесенных токов, а началом резкого ускорения токового слоя

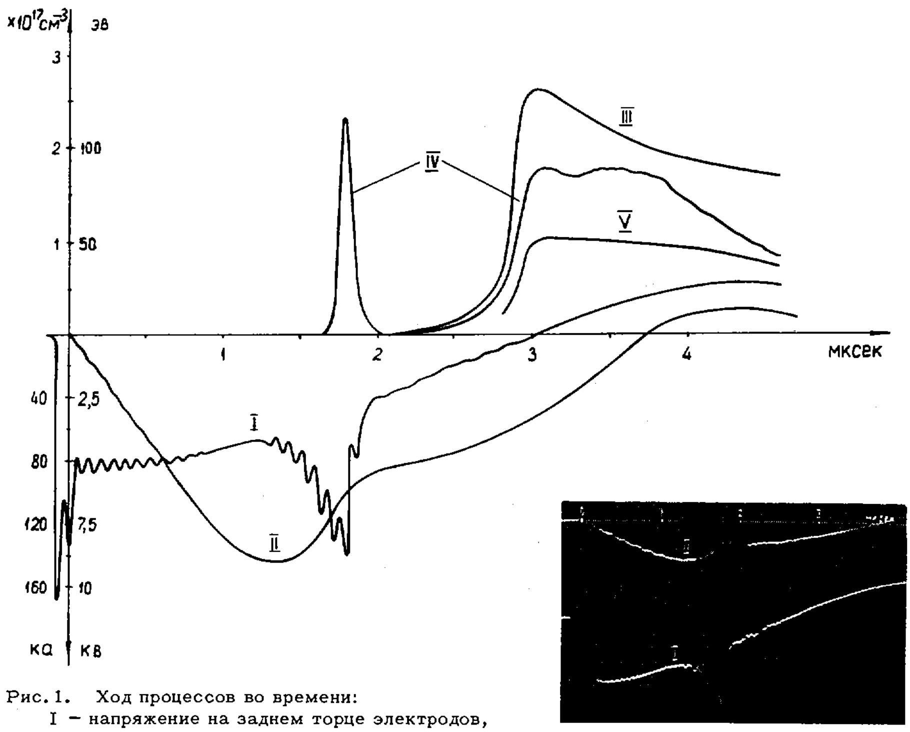

Рис. 1. Ход процессов во времени:
I — напряжение на заднем торце электродов,
II — ток в наружной цепи инжектора,
III — плотность в зоне плазменного фокуса,
IV — сигнал датчика мягкого рентгеновского излучения,
V — температура в зоне плазменного фокуса.

и возникающим в результате противополем. $\vec{E}_r = \vec{V} \times \vec{H}_\varphi$. Момент начала особенности совпадает с отрывом токового слоя от плотной зоны, а конец – с моментом прекращения движения переднего фронта токового распределения. Как следует из экспериментальных данных [4,6], только в первой относительно короткой стадии этого процесса почти весь ток замыкается через достаточно узкий движущийся токовый слой. Во второй стадии ток сначала сравнительно равномерно распределяется по всему объему плазмы, а затем замыкается в районе напускных отверстий, образовывая токовый вихрь. Момент замыкания вихря соответствует выходу фронта токового распределения на торец электродной системы и характерен всплеском мягкого рентгеновского излучения и импульсной эмиссией сверхэнергичных частиц из межэлектродного зазора. Ход процессов удобно проследить по рис. 1, на котором нанесены соответствующие кривые. Там же помещены реальные осциллограммы тока и напряжения. Замыканием тока в вихрь на 2-ой микросекунде разряда заканчиваются начальные стадии процесса. К этому моменту времени $10 \div 20\%$ энергии, запасенной в конденсаторной батарее, переходит в плазму, причем основная ее часть оказывается сосредоточенной во вмороженном в плазму магнитном поле. Трансформация энергии вмороженного в плазму магнитного поля в кинетическую энергию ионов происходит в заключительной стадии во время существования токового вихря.

3. ЗАКЛЮЧИТЕЛЬНАЯ СТАДИЯ ПРОЦЕССА

В продольном разрезе межэлектродного зазора линии тока вихря выглядят как вытянутые вдоль электродов, вложенные друг в друга овалы в передней части, вынесенные за электродную систему. Их вид показан на рис. 2. Во времени задняя граница токового вихря вместе с плазмой пе-

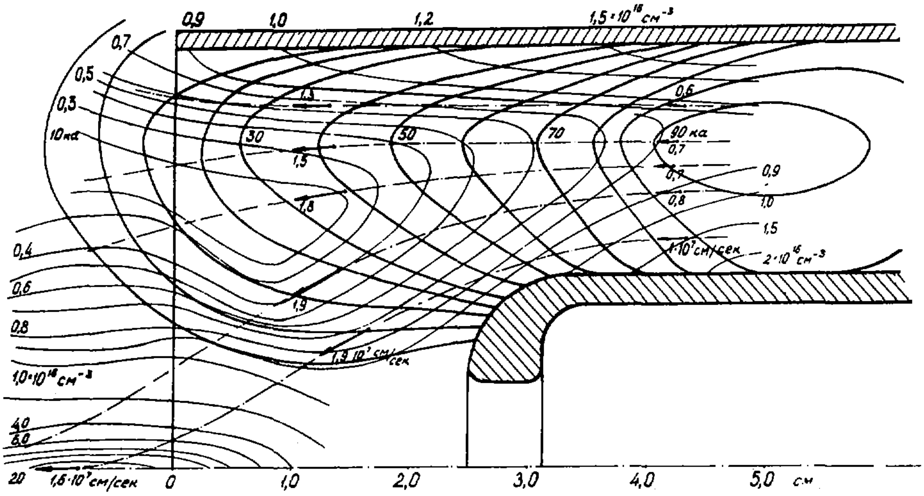

Рис. 2. Топограмма токовых полей и полей плотности. Штрихпунктирными линиями нанесены линии тока вещества.

ремещается по направлению ускорения, в то время как передняя граница токового распределения остается неподвижной. Перемещение задней границы обусловлено, с одной стороны, кинетическим давлением $\rho V^2/2$ плотной хвостовой части и, с другой стороны, давлением магнитного поля, сосредоточенного в пространстве между задней границей токового вихря и изолятором. (Напомним, что токовая петля замыкается в тот момент времени, когда ток в наружной цепи составляет ~100 кА).

Топограмма магнитного поля понятна из рис. 2, на котором отложены линии тока через каждые 10 кА. Как видно из рис. 2, радиальные составляющие силы $(\vec{j}\times\vec{H})/C$, действующие в той части токовой петли, в которой линии тока почти параллельны электродной системе, стремятся прижать плазму к электродам, что собственно и происходит в момент образования токовой петли. Однако образующийся затем градиент давления обеспечивает радиальное равновесие плазмы в токовом вихре. Градиент давления обусловлен радиальным нарастанием плотности и температуры плазмы в обе стороны от центра межэлектродного зазора. Повышение температуры плазмы по направлению от центра межэлектродного зазора, во-первых, связано со сжатием плазмы магнитным полем в первые моменты существования токового вихря и, во-вторых, с неравномерностью джоулева нагрева плазмы в токовой петле, поскольку плотность тока равна нулю в центре межэлектродного зазора и резко растет к электродам. На рис. 3 представлены радиальные составляющие сил $(\vec{j}\times\vec{H})/C$ и ∇p, вычисленные на основании интерферометрических и магнитных измерений.

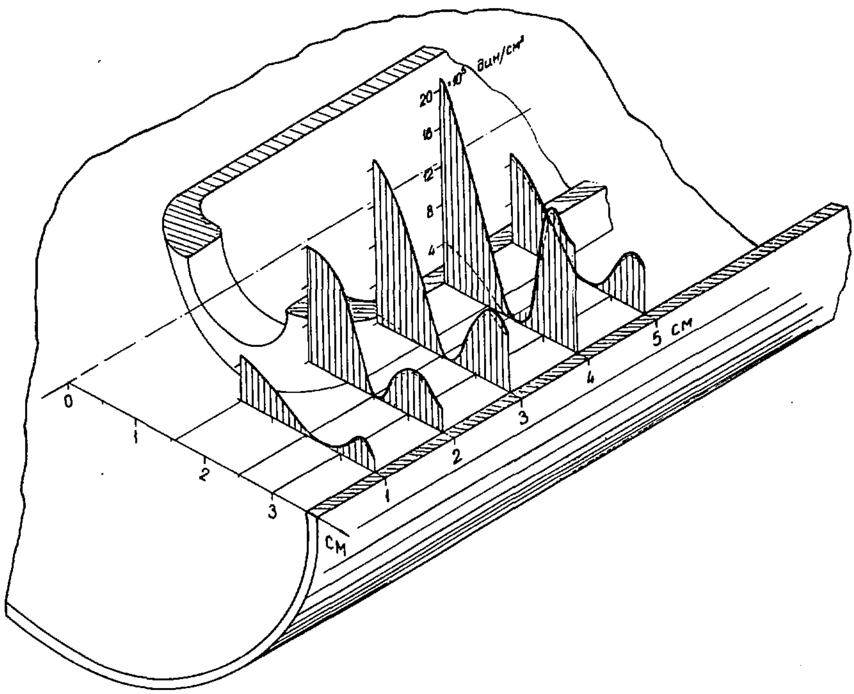

Рис. 3. Модули радиальных составляющих сил $(\vec{j}\times\vec{H})/C$ (сплошные линии) и ∇p (прерывистые линии).

При расчете температурных полей учитывались оба названных выше эффекта. Сжатие предполагалось адиабатическим, потери за счет электронной теплопроводности поперек поля достаточно малыми. Как видно из рис. 3, в глубине зазора силы $[(\vec{j}\times\vec{H})/C]_r$ и $\partial p/\partial r$ практически уравновешены. Не так обстоит дело с приближением к торцу электродной системы. Топография магнитных и токовых полей здесь такова, что силы $(\vec{j}\times\vec{H})/C$, действующие в широком слое токового распределения, фокусируют значительную часть потока, текущего в межэлектродном зазоре, на ось системы перед центральным электродом. Эти же силы ускоряют плазму от $6\cdot10^6 \div 10^7$ см/сек в межэлектродном зазоре до $\sim 2\div3\cdot10^7$ см/сек в зоне, прилегающей к фокусу. Следует заметить, что распределения токов и плотностей, показанные на рис. 2, равно как и значения сил, представленных на рис. 3, квазистационарны в том смысле, что характерные времена их изменения существенно больше времен пролета этой области ионами плазмы. Это позволяет, численно интегрируя вдоль траекторий уравнение

$$\rho V = -\nabla p + \frac{\vec{j}\times\vec{H}}{C}$$

найти линии тока вещества. В расчеты закладывались значения магнитных полей и полей плотности, полученные из интерферометрических и магнитных измерений и представленные на рис. 2, а также "начальные" скорости, оцененные на основании измерения E_r, в предположении $\vec{E}_r = \vec{V}_z\times\vec{H}_\varphi$ (метод расчета температурных полей указан выше).

Трубки тока вещества, полученные таким образом, показаны на рис. 2. Точность измерения полей плотности и магнитных полей, также как и корректность расчетов, проверялась по уравнению непрерывности вдоль линий тока вещества. Разброс значений $n\cdot V\cdot r\cdot f$ не превышал $\pm30\%$. Вдоль линий тока вещества выполняется и условие Бернулли:

$$i(p) + \frac{V^2}{2} + \frac{H^2}{4\pi\rho} = \text{const}$$

Здесь $i(p) = \int\frac{dp}{\rho} = \frac{\kappa}{M}\cdot\frac{\gamma}{\gamma-1}\cdot T$.

(В зоне фокуса, где кинетическая энергия ионов тратится также на нагрев электронной компоненты, $i(p) = \frac{2\kappa}{M}\cdot\frac{\gamma}{\gamma-1}\cdot T$).

В потоках, формирующих плазменный фокус, энергия трансформируется дважды. В середине межэлектродного зазора $H^2/4\pi\rho \gg V^2/2 \gg i(p)$ и энергия вмороженного магнитного поля переходит в кинетическую энергию ионов. За счет действия сил $(\vec{j}\times\vec{H})/C$ в широком слое токового распределения этот процесс весьма эффективен. Вблизи фокуса уже $V^2/2 \gg H^2/4\pi\rho \gg i(p)$. И, наконец, в области фокуса значительная доля кинетической энергии трансформируется в тепло.

В зоне фокуса $nk(T_i + T_e) \gg H^2/8\pi$. Другими словами, сжатие, а значит и нагрев, есть результат инерциального движения плазменных потоков, сформированных в межэлектродном зазоре. Значения температуры, вычисленные из уравнения Бернулли и замеренные по рентгеновскому излучению фокуса, удовлетворительно совпадают и составляют для режима, представленного на рис. 2, 40 ÷ 50 эВ. В ряде режимов электронная температура фокуса поднималась до 100-500 эВ. Примерно той же величины было и значение температуры, расчитанное из энергетического распределения ионов, вылетающих из области фокуса. Это понятно, поскольку времени пролета плазмой зоны фокуса достаточно для выравнивания температур между компонентами.

Рассматриваемое явление — сжатие к оси за счет сил, действующих в "размазанном" токовом слое, нагрев и последующее ускорение, по-видимому, достаточно распространено. За счет такого механизма происходит нагрев и ускорение плазмы в магнито-плазменном компрессоре [7]. По-видимому, точно такой же механизм действует и в каскадных ускорителях плазмы [8].

4. ВЫВОДЫ

1) Развитие процессов в плазменном инжекторе носит характер последовательных стадий. В силу этого к различным стадиям ускорения или к разным зонам течения следует применять разные модели.

2) При импульсном напуске газа и небольших задержках включения конденсаторной батареи старт плазменного образования достаточно хорошо описывается моделью жесткой "токовой перемычки" с постоянной массой.

3) Заполнение плазмой межэлектродного зазора соответствует модели "проницаемого токового слоя". При этом ток первое время замыкается через узкий, движущийся сквозь нейтральный газ токовый слой; затем сравнительно равномерно распределяется по всему объему плазмы и, наконец, замыкается в токовый вихрь.

4) Радиальное равновесие плазмы в токовом вихре обеспечивается градиентом давления. Во вмороженном в плазму магнитном поле вихря сосредоточена подавляющая часть энергии, перешедшей в плазму от накопителя.

5) Магнитные и токовые поля вихря, действующие в широком слое токового распределения, фокусируют значительную часть плазменного потока на ось системы перед центральным электродом. Этот процесс квазистационарен в том смысле, что характерные времена изменения параметров течения больше времени обновления плазмы в трубках тока вещества.

6) Сжатие и нагрев плазмы в области фокуса — результат инерциального движения плазменных потоков, сформированных в межэлектродном зазоре. Процессы формирования фокуса хорошо описываются уравнениями магнитной гидродинамики.

7) Механизм генерации сверхэнергичных частиц, рождающихся в межэлектродном зазоре в момент замыкания токовой петли, не ясен. Имеющиеся экспериментальные данные не противоречат ряду предложенных механизмов, в том числе и предложенному в работе [9].

В заключение авторы выражают свою признательность непременным участникам всех экспериментов — П. Т. Шевцову и Ю. М. Жевлакову и благодарят А. И. Морозова, Ю. В. Скворцова и А. А. Калмыкова за плодотворные обсуждения.

ЛИТЕРАТУРА

[1] ВАСИЛЬЕВА, Р.П., ПЕРГАМЕНТ, М.И., ЯРОСЛАВСКИЙ, А.И., Plasma Physics and Controlled Nuclear Fusion Research, Vienna 2 1969, pp.39-50.
[2] АРЕТОВ, Г.Н., ПЕРГАМЕНТ, М.И., СТЕПАНЕНКО, М.М., ЯРОСЛАВСКИЙ, А.И., Proc. 7-th Intern. Conf. on Phenomena in Ionized Gases, Beograde 3 1965, pp.289-294.
[3] АРЦИМОВИЧ, Л.А., ЛУКЬЯНОВ, С.Ю., ПОДГОРНЫЙ, И.М., ЧУВАТИН, С.А., ЖЭТФ 33 1 (7) (1957) 3-8.
[4] BURKHARD, L.C., LOVBERG, R.H., Phys. Fluids 5 3 (1962) 341-347.
[5] BOTTOMS, P.J., CARPENTER, J.P., MATHER, J.W., WARE, K.D., WILLIAMS, A.H., Plasma Physics and Controlled Nuclear Fusion Research, Vienna, 2 1969, pp.67-75.
[6] ВАЛЬКОВ, Ю.А., ЗБРАИЛОВА, Н.Л., СКВОРЦОВ, Ю.В., ЖТФ XL 4 (1970) 772-780.
[7] МОРОЗОВ, А.И., Вестник АН СССР 6 (1969) 28-36.
[8] АЗИЗОВ, Э.А., КОМЕЛЬКОВ, В.С., Сб. Физика плазмы, Госатомиздат, М., (1967) 36-50.
[9] ХИЖНЯК, Н.А., КАЛМЫКОВ, А.А., ЖТФ XXXYI 9 (1966) 1608-1621.

DISCUSSION

TO PAPERS IAEA-CN-28/D-6, D-7

P.K. KAW: Are any experiments being performed in the Soviet Union on the use of an intense laser pulse for plasma focus heating?

E.P. VELIKHOV: No.

NON-ADIABATIC IONS IN THE DISTRIBUTION FUNCTION FROM SELF-CONSISTENT CALCULATIONS OF THE PLASMA FOCUS

D. E. POTTER, M. G. HAINES,
Imperial College, London
United Kingdom

Abstract

NON-ADIABATIC IONS IN THE DISTRIBUTION FUNCTION FROM SELF-CONSISTENT CALCULATIONS OF THE PLASMA FOCUS.

A three-dimensional simulation in phase space of the ions in the plasma focus has demonstrated that in some modes of operation of the experiment, the ion distribution function has two components. Most of the ions are in a quasi-thermal equilibrium, but a small component of the distribution function is accelerated to high energies in agreement with experimental results to be reported at this conference by Hobby, Morgan, Peacock. The interaction of this high energy component with the background ions yields a high neutron emission and, in particular, gives rise to an anisotropy in the energies of the neutron emission.

Previous two-dimensional magnetohydrodynamic simulations of the dense plasma focus have in many respects agreed quantitatively with experiment. The MHD-simulations, however, while describing a thermonuclear neutron emission, have not been able to account for the experimentally observed anisotropic neutron emission. The numerical experiments of a "magnetohydrodynamic focus" have shown that, at high bank energies and lower densities, the ions become collisionless in the plasma focus. This paper therefore reports the simulation of 20 000 ion particles, which interact in the self-consistent electromagnetic field of an electron fluid. The particles have co-ordinates of radius, radial velocity, and axial velocity. The singular ions are produced by non-adiabatic motion of ions with large Larmor radius about the fieldfree axis of the pinch.

While these ions produce an anisotropic neutron emission, they effectively remove the high-energy tail of a Maxwellian distribution, and thereby limit a larger thermonuclear emission from the dense plasma focus. To minimize this effect, the escape of high-energy singular ions must be halted by ion-ion collisions. Hence, as the bank energy of the plasma focus is increased, the density of the plasma focus must necessarily be increased further. Thus on the basis of the simulations reported in this paper, scaling laws of the optimized neutron yield for the plasma focus to bank energies of a megajoule have been determined.

Further applications of these computer simulations of non-adiabatic self-consistent ion motions include studies of the tail of the magnetosphere and reversed fields in the theta-pinch.

I. INTRODUCTION

The dense plasma formed axisymmetrically at the end of a fast coaxial electrode system has proved to be a rich source of physical phenomena (1,2). Very high kinetic energies, high neutron yields and the emission of both soft and hard X-rays, have led to a conflict of ideas on whether the plasma may be described as a fluid, and hence analysed in terms of fluid equations, or whether the phenomena arise from microscopic particle effects.

Extensive two-dimensional fluid calculations (3, 4, 5) have demonstrated the formation of a shock between coaxial electrodes, and the resultant two-dimensional formation of a hot dense plasma pinch (the plasma focus) at the end of the centre electrode. These fluid calculations have provided good agreement with experiment in describing quantitatively the formation stages of the focus, the heating mechanisms in the focus, and the parameters of density, electron temperature, and dimensions of the hot pinch region (4).

The parameters determined by the calculations suggest that a thermonuclear emission with a yield in agreement with experiment would be produced. On the other hand violation of the Dreicer condition (4), suggests the possibility of runaway electrons which leads to the emission of hard X-rays.

However one clear discrepancy in particular was found in the comparison with experiment. Experiment has shown that certainly under some conditions, the neutron emission occurs from a plasma moving with a centre of mass velocity of 2×10^8 cm.sec^{-1} (7). The fluid calculations clearly showed that the centre of mass velocity of the hot pinch region typically had an axial centre of mass velocity of 3×10^7 cm.sec^{-1}(4), and a fluid model could not describe such a large anisotropy as that demonstrated by experiment.

Particularly at low densities in the fluid calculations, the ion temperature in the focus hot pinch becomes so large, that the ion-ion collision time becomes large compared to the ion cyclotron time, and at small radii the ion stress tensor is not well defined. This is because near the axis of the pinch, ion motion becomes non-adiabatic, and the possibility exists therefore of a singular class of ions which though small in number can gain large energies and may have a radical effect on the plasma properties (8).

Bernstein (9) suggested the possibility of such a mechanism on the basis of trajectories of single particles, and on experimental analyses of the nature of the neutron emission. In this paper, a self-consistent ion particle model is described, and its application in determining the structure of the ion distribution function in the hot dense plasma focus is discussed. The physical model and the assumptions made in obtaining a finite mathematical model are described in Section 2, while the difference method is described in Section 3. The results of the application of this particle model are presented in Section 4. We demonstrate that at low densities when the plasma is collisionless the distribution function becomes radically anisotropic in axial velocity space, and in Section 5, the contribution of such an effect to the neutron yield is discussed.

2. THE ION PARTICLE MODEL.

Both experiment and fluid computations (10, 4) have shown that once the coaxial shock has collapsed to the axis a long small radius pinch is formed. Variables in the pinch are a strong function of radius, but only slowly varying in the axial direction. We therefore describe the focus pinch by an ion plasma in three dimensional phase space (radius r, and axial and radial velocity co-ordinates w_z, w_r). It is the purpose of this model to describe phenomena associated with the ion cyclotron frequency (Ω_{ci}) and ion larmor radius (a_i) (typically 10^9secs and 10^{-2} cms respectively in the plasma focus (4). The plasma is therefore described by K ions ($K \sim 10^3 - 2 \times 10^4$) each of which move in the (r-z) plane in cylindrical coordinates

<u>k = 1, K</u>

$$\frac{mi}{e} \frac{d\vec{w}}{dt} k = \vec{E} + \vec{w}_k \times \vec{B} \tag{1}$$

$$\frac{dr}{dt} k = w_{r_k} \tag{2}$$

where mi and e are the ion mass and ion charge respectively, r_k is the radius of the kth ion, and $\vec{w}_k$ is the velocity of the kth ion. $\vec{E}$ and $\vec{B}$

are the local self consistent electric and magnetic fields experienced by the ion,

$$\vec{E} = \vec{E}\,(r, t), \quad \vec{B} = (0, B_\theta, 0) = \vec{B}\,(r, t) \tag{3}$$

Azimuthal symmetry is assumed and only an azimuthal component of magnetic field is permitted. The electric field may have components in the axial and radial directions. From the distribution function (f) of the ions, obtained from the ion equations of motions (Eqs. 1, 2), the local ion density n_i, and ion centre of mass velocity $\vec{v}(r, t)$ may be obtained:

$$n_i(r, t) = \int f\, d\vec{w}$$

$$n_i\, \vec{v} = \int f\, \vec{w}\, d\vec{w} \tag{4}$$

Ideally to obtain a complete description of the plasma, it would be satisfying to describe the total electron distribution function, and consequently to determine the electromagnetic fields resulting from the charge and current densities of the ion-electron assembly. However since we are interested in scale lengths (the ion Larmor radius a_i) and scale times (the ion cyclotron time) much larger than the Debye length and the electron electron collision time respectively, quasineutrality is assumed and an electron fluid model is applied. Since the electron Larmor radius is small compared to the ion Larmor radius the electrons are assumed to be adiabatic and moment equations are applied:

$$n_e = n_i \tag{5}$$

$$\vec{E} + \vec{v}_e \times \vec{B} = \eta\, \vec{j} \tag{6}$$

η is the resistivity, n_e is the electron density and $\vec{v}_e$ is the electron centre of mass velocity,

$$\vec{v}_e = \vec{v} - \frac{\vec{j}}{n_e} \tag{7}$$

where $\underline{j}$ is the current density as defined by Ampere's Law. The second term in this equation (7) is of the order $\frac{\Omega_{ci}}{L} \cdot \lambda_s^2$

where λ_s is the collisionless skin depth ($\lambda_s = \frac{c}{w_{pi}}$) and w_{pi} is the ion plasma frequency. Given the form of the magnetic field (Eq. 3), the current flows only in the axial direction.

Finally using the electric field as determined by electron motion (Eq. 6), the self consistent magnetic field in the pinch which acts on the ions is determined by Faraday's Law,

$$\frac{\partial \vec{B}}{\partial t} + \nabla \times \vec{E} = 0 \tag{8}$$

A self-consistent model describing the ion distribution function in the focus where non-adiabatic particle motion occurs, is thus obtained. The program IONCYCL solves these equations in difference form.

3. THE DIFFERENCE ION PARTICLE MODEL.

The trajectories of each of the K ions are followed by integrating the particle equations (Eqs. 1, 2) implicitly over small timesteps Δt.

Normalising the equations with respect to the ion mass and charge and using complex variable notation,

$$w = w_r + iw_z, \quad E = E_r + iE_z$$

the equations (1, 2) reduce to

$$\frac{dw_k}{dt} = E + i\, w_k\, \Omega \tag{9}$$

The equations are integrated over the timestep n to n+1 with

$\phi = \frac{\Omega\, \Delta t}{2}$, (ϕ is half the change in the cyclotron phase angle of the particle in the timestep Δt),

$$w_k^{n+1} - w_k^n = E\, \Delta t + i\, \phi (w_k^{n+1} + w_k^n) \tag{10}$$

and solving,

$$w_k^{n+1} = E\, \Delta t \frac{(1+i\phi)}{1+\phi^2} + w_k^n \frac{(1+\phi^2+2i\phi)}{1+\phi^2} \tag{11}$$

the two components of each particle velocity at each time level n+1 are obtained. It is easily shown that such a particle difference scheme is unconditionally stable, second-order accurate in the timestep, reversible and energy conserving to high-order in Δt. The new particle radii may then be found at each timestep:

$$r_k^{n+1} = r_k^n + \tfrac{1}{2}(w_{r_k}^{n+1} + w_{r_k}^n)\Delta t \tag{12}$$

At the end of each timestep, having integrated the particle co-ordinates, the plasma density and velocity fields are determined locally on a radial Eulerian mesh with step Δ.
At cell j,

$$n_j = \sum_{k=1}^{K} \delta\left(\frac{r_k}{\Delta} - j\right) \tag{13}$$

$$n_j \vec{v}_j = \sum_{k=1}^{K} \delta\left(\frac{r_k}{\Delta} - j\right) \vec{w}_k \tag{14}$$

These parameters may now be used to establish a Lagrangian mesh on which Faraday's Equation (8) is differenced to determine the new electromagnetic fields. The time loop is then complete, and particle trajectories may again be integrated using the new electromagnetic fields.

4. APPLICATION TO THE PLASMA FOCUS.

The calculations are initiated by applying a step function magnetic field at large radii, and the particles are initially distributed uniformly over all radii with a Maxwellian distribution of velocities. Initially the temperature of the Maxwellian is small (the initial plasma pressure is small compared to the magnetic pressure). A shock develops the implosion of which produces a steady pinch over small radii.

In the examples illustrated the resistivity is taken as a constant and finite (typically the magnetic Reynolds number R_n is of the order unity). Two interesting cases are isolated and contrasted. For the radial equilibrium of the pinch, in order to balance magnetic and thermal pressure the ion larmor radius is equal to the collisionless skin depth ($a_i = \lambda_s$).

Consequently it is found that when the ion larmor radius is of the order of the radius of the pinch, the electric field produced by the electron drift current is dominantly large. This electric field is the containing negative radial electric field

$$E_r = - \frac{j_z B_\theta}{ne} \tag{15}$$

and large negative axial drifts are imparted to the ions (Fig. 1). Particle motion is then dominated by this electric field.

In the contrary case, where the ion larmor radius (and skin depth) is smaller than the radius of the pinch, the ions are 'magnetically' confined, and the effect of the electron current does not dominate the electric field. Under these conditions it is found that if a small axial electric field is applied, the ion distribution function rapidly obtains a singular component. The orbit of a particle contributing to the high energy tail of the distribution is illustrated in Fig. (2b). Such an orbit occurs since on the axis of the pinch, a "neutral line" in the magnetic field exists. As a particle crosses the axis (r=0), its direction of cyclotron orbiting reverses, and it therefore may be freely accelerated to very high energies by even a small axial electric field.

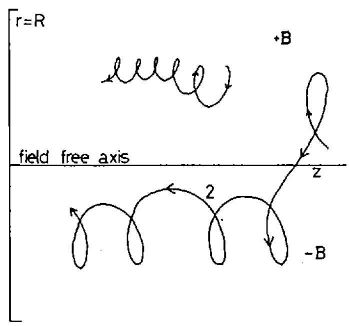

FIG. 1. Characteristic particle orbits for the case where runaway ions do not occur. The collisionless skin depth $\lambda_s = c/w_{pi}$ is of the order of the radius of the pinch, and particles are electrostatically confined by a large negative radial electric field. Particles drift in the negative axial direction with a large E/B drift. The orbit (2) illustrates a particle which crosses the field-free axis of the pinch.

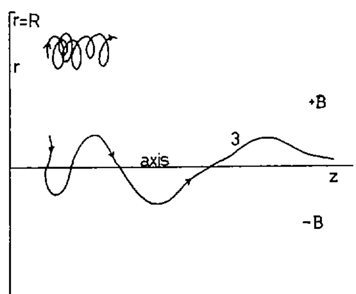

FIG. 2. Characteristic computed particle orbits for the case where runaway ions do occur. The collisionless skin depth is smaller than the radius of the pinch. The trajectory (3) illustrates the computed motion of a singular ion which is not trapped by the magnetic field and is rapidly accelerated to high energies as it crosses and recrosses the field free axis of the pinch.

Figures (3) and (4) illustrate the distribution of particles in w_z-r phase space for the non-singular and singular particle cases respectively. In the former case the distribution is dominated by the negative axial E/B drift which is at a maximum at small radii, and which therefore produces a shear velocity. In contrast however for the singular particle case, runaway ions at small radii rapidly achieve large axial velocities.

The radial distributions of magnetic field and density for the case of singular particles are illustrated in Fig. 5. In Fig. 6 the ion distribution function in the axial velocity w_z, is shown for the case where

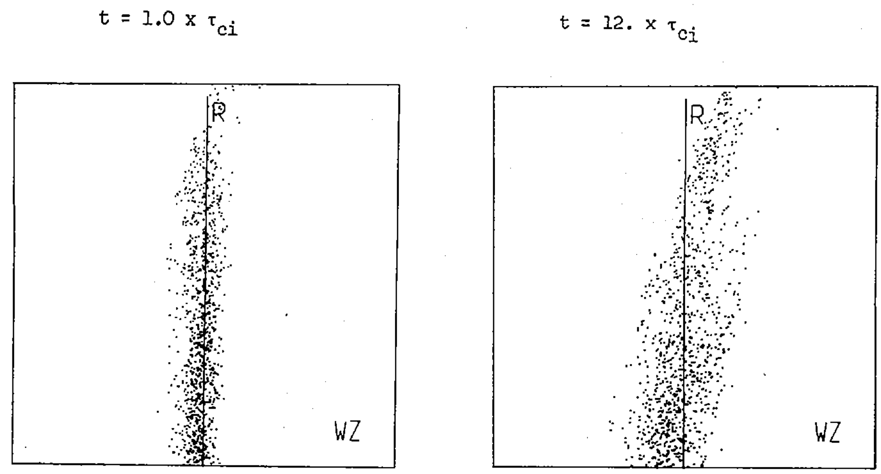

FIG. 3. The distribution of a representative set (1000) of particles in (r-w_z) phase space for the case where singular ions do not occur (the collisionless skin depth is of the order of the radius). A large negative radial electric field induces particle drifts particularly at small radii in the negative axial direction. A shear of the particles in phase space results.

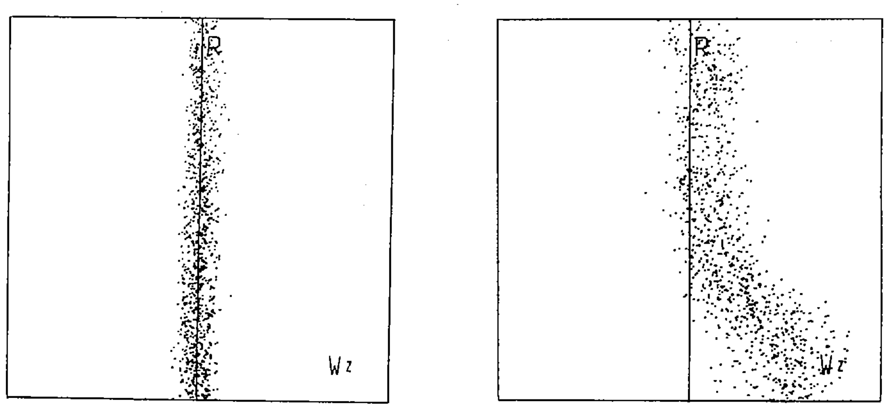

FIG. 4. The distribution of a representative set (1000) of particles in (r-w_z) phase space for the case where singular ions do occur (see Fig. 2). Non-adiabatic particles near the axis of the pinch are not trapped and are freely accelerated to high energies by a positive axial electric field.

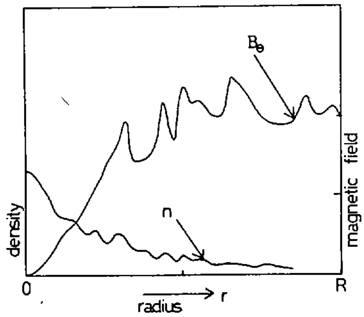

FIG. 5. The radial structure of the magnetic field and density of a contained pinch in the case where singular runaway ions occur near the axis of the pinch. The fluctuations in the magnetic field and density are due to the radial propagation of Alfvén waves on the Lagrangian mesh.

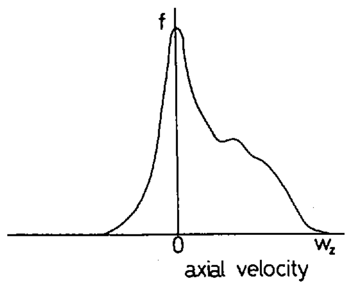

FIG. 6. The computed anisotropic ion distribution function which results from the runaway ion mechanism. At later times the anisotropy is enhanced further. The magnification of the distribution function in the positive w_z dimension yields a significant anisotropic neutron emission.

singular particles occur. Such a distribution occurs when the mean ion Larmor radius is

$$a_i = 0.15 \times R$$

and R is the radius of the pinch. The magnitude of the applied electric field E_o compared to the thermal "electric·field" $\overline{w}B(R)$, is

$$E_o = 0.05 \times \overline{w}B(R)$$

It must be stressed that the use of the small axial electric field E_o is non-physical, since in the case of a model with variables independent of the axial z-dimension, the electric field as defined by ohm's law (Eq. 6) does not admit such an axial field. Our results have shown that if the electrons are assumed to be adiabatic (Eq. 6) no enhanced tail occurs in the ion-distribution function. On the other hand the adiabatic approximation for the electrons is probably not justified since according to the parameters of the focus pinch from both experiment and fluid models (4), the Dreicer condition for runaway electrons is certainly violated. Again according to experiment a large axial electric field of the order of 100 keV exists along the pinch during the focus stage. We may therefore expect non-adiabatic electrons to occur. Consequently an axial electric field may be supported in the plasma, which leads in turn to a singular ion component in the ion distribution function.

5. APPLICATION TO NEUTRON EMISSION MECHANISMS IN THE PLASMA FOCUS.

On the basis of these results it is clear that two mechanisms for the emission of neutrons exist. Fluid calculations (4) certainly describe a plasma in the focus pinch which gives a thermonuclear yield of neutrons (ν_1) comparable with experiment,

$$\nu_1 \doteq \pi R^2 n^2 \ell \tau \left(\frac{2.3 \times 10^{-14}}{T^{3/2}} \exp - \frac{18.76}{T^{1/2}} \right) \tag{16}$$

where n is the density, T is the ion temperature in kilovolts, ℓ is the length of the pinch and τ is the duration of the pinch. The results of fluid calculations for the case of a bank energy, U, corresponding to 32 kilojoules suggest an emission,

$$\nu_1 = 5 \times 10^9 \text{ neutrons} \tag{17}$$

In contrast however, the particle model reported in this paper demonstrates the existence of singular particles which achieve high energies in the focus pinch and contribute to the neutron emission by interacting with the background thermal ions in the pinch. If n_1 is the density of singular ions, n_o is the background density of thermal ions and v is the ultimate velocity of singular ions, the neutron yield (ν_2) of such an emission may be estimated,

$$\nu_2 = \pi \lambda^2 n_o v \sigma (v) n_1 \tau \tag{18}$$

σ is the deuterium-deuterium cross-section for fusion reactions and λ is the radius over which the singular particles oscillate around the field free axis of the pinch. The computations have shown that the oscillation width λ may be equated with the ion collisionless skin depth $\lambda_s = \frac{c}{wp_i}$.

Using the results of the fluid computations (4) to provide values for the parameters of the dense focus pinch, and with the results of Section 4,

$$n_o = 10^{19} \text{ cm}^{-3}$$
$$n_1 = 10^{19} \text{ cm}^{-3}$$
$$\lambda_s = 10^{-2} \text{ cm}$$
$$\tau = 5 \times 10^{-8} \text{ sec}$$
$$v = 2.3 \times 10^8 \text{ cm.sec}^{-1}$$

The assumed velocity v of a singular ion corresponds to an energy of 100 keV in agreement with an electric field down the pinch suggested by the hard X-ray component. Then,

$$\nu_2 = 4 \times 10^9 \text{ neutrons} \tag{19}$$

which as an order of magnitude calculation is certainly comparable with experiment (for the bank energy U = 32 kilojoules), and of the same order as the thermonuclear yield (ν_1). Such an emission would exhibit properties in agreement with experiment. In particular the emission occurs continually from the hot dense pinch region of the plasma focus while the neutrons would appear to be emitted, from a source moving with a centre of mass axial velocity of half the singular ion energy = $\frac{1}{2}v = 1.2 \times 10^8$ cm.sec^{-1}.

Rather than differentiating between the two mechanisms it is probable that both the thermonuclear emission and the singular particle emission contribute to the neutron yield in the plasma focus. For radial equilibrium in the pinch, the Bennett relation is satisfied (4)

$$NT \propto I^2 \qquad (20)$$

where I is the total current in the pinch. For a given energy therefore, clearly to optimise the thermonuclear yield (ν_1), the temperature in the pinch for a given current (bank energy) may be maximised subject to the Bennett condition (20). On the other hand as the ion temperature is maximised, the density is diminished, the ions become collisionless ($\Omega_{ci}\ \tau_{ii} > 1$), and the singular particle emission becomes dominant. It follows that at high densities (low temperature) the dominant mechanism is thermonuclear while at low densities (high temperature) singular particles occur and the emission becomes anisotropic. It is clear that at a given energy the optimum neutron yield will occur for that density and temperature such that $\Omega_{ci}\ \tau_{ii} \sim 1$.

6. DISCUSSION.

The ion particle model reported in this paper has demonstrated that a singular component of the ion distribution function in the plasma focus can occur, due to the crossing and recrossing of ions across the magnetic field free axis of the pinch. The conditions for such a component are that the ions are collisionless $\Omega_{ci}\ \tau_{ii} > 1$; that the ion larmor radius and consequently the skin depth λ_s, are smaller than the radius of the pinch $\lambda_s < R$; and that all the electrons are not adiabatic. Under experimental conditions of low density and high temperature, these conditions are fulfilled. The singular component of the deuterium ion distribution function may obtain high axial velocities and give rise to a significant anisotropic neutron emission from the dense pinch region of the focus. The competing mechanisms of thermonuclear and singular particle yields suggest an optimum working density and temperature for a given bank energy.

The particle model used however is not fully self-consistent, since electron inertia should be included, and non-adiabatic electron motion described. While an electron-ion mass ratio $\frac{m_e}{m_i} = 3700$, in such a particle model is not conceivable with present day computers, computations with a reduced mass ratio would nevertheless provide interesting results.

REFERENCES

(1) MATHER, J.W., Second IAEA Conf. on Plasma Physics and Controlled Nuclear Fusion Research, Culham (1965), Vol.2, p.389.

(2) FILIPPOV, N.V., FILIPPOVA, T.I., and VINOGRADOV, V.P. (1962). Nucl. Fusion Suppl. 2, 571.

(3) ROBERTS, K.V. and POTTER, D.E., "Magnetohydrodynamic Calculations" in Methods of Computational Physics, Vol. 9 (Eds. ALDER, FERNBACH, ROTENBERG), Academic Press, New York (1970).

(4) POTTER, D.E. (1971). To be published in Phys. Fluids, August, 1971.

(5) POTTER, D.E., Ph.D. Thesis, University of London (1970).

(6) DYACHENKO, V.F., and IMSHENNIK, V.S., Zh. Eksp. Teor. Fiz. 56 (5), 1766 (1969). Culham Laboratory Translation CTO/639.

(7) BOTTOMS, P.J., CARPENTER, J.P., MATHER, J.W., WARE, K.D., and WILLIAMS, A.H., Third IAEA Conf. on Plasma Physics and Controlled Nuclear Fusion Research, Novosibirsk (1968). Paper CN-24/G-5.

(8) POTTER, D.E., Fourth European Conference on Controlled Fusion Research and Plasma Physics, Rome (1970). C.N.E.N. p.116.

(9) BERNSTEIN, M.J., Phys. Rev. Letters 24, 724 (1970).

(10) MORGAN, P.D., PEACOCK, N.J. and POTTER, D.E., Third European Conf. on Plasma Physics and Controlled Fusion, Utrecht (1969) p.118 (Wolters-Noordhoff).

NUMERICAL AND LABORATORY EXPERIMENTS IN THE POLYTRON CONFIGURATION

M.L. WATKINS, D.E. POTTER, J.D. KILKENNY,
M.G. HAINES, A.E. DANGOR
Physics Department, Imperial College, London,
United Kingdom

Abstract

NUMERICAL AND LABORATORY EXPERIMENTS IN THE POLYTRON CONFIGURATION.

A two-dimensional MHD two-fluid numerical model has been constructed to simulate the plasma behaviour in the r-z plane of a linear Polytron - a multi-cusped pinch device in which the plasma flows through the cusps. Of importance in this code compared to the earlier "Focus" code (a two-dimensional MHD code developed by Potter) is the inclusion of the other two components of magnetic field B_r, B_z and azimuthal velocity. With the dominance of the Hall effect, it is found that the characteristic velocity determining the mesh time-step is the whistler-wave velocity rather than the Alfvén speed. Present results show that the collapse of an axial current sheet to the axis is modified by the cusp field to give several interesting phenomena: firstly, Hall acceleration of the ions in the axial and azimuthal direction; secondly, asymmetric ion compressional heating and electron Ohmic heating; thirdly, due to the existence of a radial component of the current density locally, there can be reversal of Hall acceleration in certain regions leading to the circulation of plasma; fourthly, there is qualitative agreement with a single-particle model so that a central core of plasma appears well defined and detached from the walls.

Laser scattering diagnostics are being employed on the laboratory toroidal experiment in order to measure the electron temperature and density enabling direct comparison with the numerical model. Magnetic-probe measurements in the ring-cusp plane show that the axial current-density component is confined to the magnetic axis. From the line intensity of argon-IV radiation an axial asymmetry about the ring cusp has been found and confirmed by the numerical model. Toroidal effects have also been observed, namely the preferential outward drift of the plasma in the later stages of the discharge and the associated vertical shift of the plasma which is periodic with the radial magnetic field.

1. GENERAL INTRODUCTION

1.1. Basic Polytron Concept

The Polytron experiment is designed to study the containment and stability properties of a plasma that is moving rapidly through a series of cusp-shaped magnetic fields around the minor axis of a torus. The cusp fields have very favourable stabilising properties for plasma containment, and it is proposed that the convective motion of the plasma through the cusp fields should considerably reduce losses of plasma through the ring cusps. The axial motion of the plasma is achieved by inducing an electric field in this direction, and employing the Hall acceleration mechanism to attain an axial ion current (1).

1.2. Analytical Theory

1.2.1. Conditions for Hall Acceleration

A one dimensional MHD model of Hall acceleration of ions of mass m_i in the direction of an applied electric field E_z in the presence of a spatially periodic transverse magnetic field $B_{ro}\sin kz$ yields the condition for Hall acceleration of the ions (1)

$$\frac{m_i c}{eB_{ro}/\sqrt{2}} \cdot k \cdot \frac{cE_z}{B_{ro}/\sqrt{2}} > 0.8 \qquad (1)$$

valid for a wide range of the Hall parameter, $\alpha = \frac{\sigma B_{ro}}{\sqrt{2}\, nec}$. The characteristic time τ_a for acceleration of the ions to a terminal velocity $\sigma E_z/ne$ is given by

$$\tau_a = \frac{1 + \alpha^2}{\alpha \Omega_i} \qquad (2)$$

where $\Omega_i = \frac{e B_{ro}}{m_i c\sqrt{2}}$ is the mean ion gyro frequency. When the perturbation of the applied magnetic fields by the induced Hall currents is included in the model, a second condition is found, which essentially states that the azimuthal Hall currents should not be large enough to destroy the applied cusp fields (2). That is,

$$\frac{4\pi ne\, c\, E_z}{c\, B_{ro}/\sqrt{2}} \quad \frac{1}{k\, B_{ro}/\sqrt{2}} < 1 \qquad (3)$$

If this condition is violated, an axial electron current flows and the ion acceleration time becomes much longer. Conditions (1) and (3) can be simultaneously satisfied only if

$$\frac{m_i\, c^2\, k^2}{4\pi\, ne^2} = \frac{c^2\, k^2}{w_{pi}^2} >> 1 \qquad (4)$$

This condition places great problems in the numerical simulation discussed in this paper.

1.2.2. Conditions for containment

When the acceleration process is complete, containment will be possible if the ion centre of mass velocity is much greater than the ion thermal velocity, i.e. there are negligible ions at rest in the laboratory,

$$v_z >> \sqrt{(\frac{2kT}{m_i})} \qquad (5)$$

In order that electrostatic instablities do not arise, the ion centre of mass velocity however should be much less than the electron velocity, i.e.

$$v_z << \sqrt{(\frac{2kT}{m_e})} \qquad (6)$$

These last two conditions can easily be satisfied since $m_e << m_i$. If we choose $v_z^2 \simeq \frac{2kT}{\sqrt{(m_e\, m_i)}}$, the ions, constituting a current $I = Nev_z$ where N is the line density, can satisfy the self-focussing relations of Bennett

$$I^2 = 4NkTc^2 \qquad (7)$$

if the operating line density is

$$N \simeq \frac{2\sqrt{(m_e\, m_i)}c^2}{e^2} = 4.3\text{x}10^{14}\text{cm}^{-1} \qquad (8)$$

Further theoretical work has been carried out on particle trajectories and on the stability of the configuration, but will not concern us in this paper.

1.3. Earlier Experimental Work

The Hall acceleration mechanism was investigated experimentally first in a straight configuration (3) and the magnetic stress tensor was measured, demonstrating an axial force of about 13 kgm.wt. Similar forces have been measured in the toroidal experiment in which 36 cusp coils have been energised. At Novosibirsk (4) measurements of the radial distribution of azimuthal Hall currents were presented, and an ion axial motion of 10^6 cm/sec was deduced from the Doppler shift of an argon IV line. About 2 kA of ion current was achieved, but not satisfying condition (5) above - the centre of mass velocity was only about sonic. In part this might be due to the fact that preionisation was limited to rather higher densities so that the line density was about 20 times that indicated by eq. (8). At Utrecht (5) it was shown that as the plasma density was increased the axial current switched over from being an ion current to a much larger electron current, in keeping, quantitatively, with condition (3). In all cases plasma losses through the ring cusp occurred after about 1 μsec. Calculated single particle trajectories showed that these losses could be due to that plasma which originated near the walls, and that the remainder of the plasma could be accelerated and contained indefinitely (6). In the experiment the losses are probably also caused by an insufficiently large axial ion velocity, thus violating condition (5). The experimental time was also limited to times less than τ_a.

1.4. Present Research

1.4.1. Computational Model

The analytic work is limited either to a linear approximation or to a quasi-one-dimensional approach that precludes the theoretical study simultaneously of radial plasma compression with axial Hall acceleration, magnetic field distortion, radial losses, instabilities, etc. A single particle computational model gives an insight into the possible trajectories that can occur in the complex field configuration, but the most powerful theoretical model with which all these phenomena can be studied is a numerical simulation using magnetohydrodynamic equations for a two-fluid plasma. A computer code (GEMINI) has been set up to obtain axisymmetric solutions in the r-z plane of a straight cylinder (7). Several production runs have been made. GEMINI is a generalisation of the Plasma FOCUS CODE (8) which has been most successful in describing experimental phenomena. All three magnetic field components are present in GEMINI and this introduces new computational problems associated with the whistler wave. This will be discussed below.

1.4.2. Experiment

The present experimental work is devoted to more detailed measurements of electron density and temperature using laser scattering techniques. Also the problem of preionisation at lower densities is being studied in order that conditions (4) and (8) can be satisfied.

2. THE TWO-DIMENSIONAL MHD CODE, GEMINI

2.1. The MHD Equations

The numerical model employs a rectangular Eulerian mesh mapped on the r-z plane of a cylindrical infinitely long polytron configuration.

Periodic boundary conditions are applied in the axial direction, there being one complete cusp length in the domain. On the mesh points the following plasma and magnetic field parameters, ρ, B_θ, A_θ, v_z, v_r, v_θ, T_e and T_i, are found and followed in time using the equations below.

$$\frac{\partial \rho}{\partial t} + \nabla.(\rho\vec{v}) = 0$$

$$\frac{\partial(\rho\vec{v})}{\partial t} + \nabla.(\rho\vec{v}\,\vec{v}) = \vec{J} \times \vec{B} - \nabla(p_i + p_e) + \rho\,\vec{g}$$

$$\frac{\partial p_e}{\partial t} + \nabla.(p_e\vec{v}_e) = (\gamma-1)\ (\eta J^2 - p_e\nabla.\vec{v}_e - \text{EQUIP}\ (T_e - T_i) - \text{RAD})$$

$$\frac{\partial p_i}{\partial t} + \nabla.(p_i\vec{v}) = -(\gamma-1)\ (p_i\nabla.\vec{v} + \text{EQUIP}\ (T_i - T_e)) \qquad (9)$$

$$\frac{\partial A_\theta}{\partial t} - \eta\nabla^2 A - (\vec{v}_e \times \vec{B})_\theta = 0$$

$$\frac{\partial \xi_\theta}{\partial t} + (\nabla\times(\vec{\xi}\times\vec{v}))_\theta = -(\nabla\times(\eta\nabla\times\vec{\Omega}_\theta))_\theta - (\nabla\frac{1}{\rho}\times\nabla p_i)_\theta$$

where $p_e = \rho T_e$, $p_i = \rho T_i$, $\vec{v} = (v_r, v_\theta, v_z)$, $\vec{B} = (B_\perp, B_\theta)$, $B_\perp = \nabla\times\vec{A}_\theta$, $J_\perp = \nabla\times\vec{B}_\theta$

$J_\theta = -\nabla^2 A_\theta$, $\xi_\theta = \Omega_\theta + (\nabla\times\vec{v})_\theta$, $\Omega_\theta = eB_\theta/m_i$, $\vec{\xi} = \vec{\Omega} + \nabla\times v_\theta$, $\vec{\Omega} = e\vec{B}/m_i$, $\vec{v}_e = \vec{v} - m_i\vec{J}/\rho e$, $\underset{\sim}{\vec{g}} = \vec{r}v_\theta^2/r^2$

EQUIP equipartition term (included implicitly), RAD bremsstrahlung radiation term (included explicitly to second order).

At present thermal conduction and viscous terms have not been included. These present additional difficulties because of the strong anisotropy of the transport coefficients in a large magnetic field, the direction and magnitude of which vary in time and space.

2.2. The Time-step for the Calculation

The equations (9) above may be studied analytically, allowing perturbations from an initial steady state in order to obtain the linearised dispersion relation for all possible mode frequencies w, the highest of which will determine the maximum time-step for proceeding with an explicit calculation.

It is found that the highest frequency present in the parameter range of interest is that of the whistler mode. Because this restricts the calculations to very small time steps, the possibility of damping or removing this wave by resistivity, viscosity and finite Larmor radius effects was investigated. For a uniform plasma immersed in a straight uniform magnetic field, the fastest mode is transverse with wave number $\underline{k}$ parallel to the magnetic field. The dispersion relation is a quartic which factorises into two quadratics.

$$0 = (w - iw_R)^2 \pm (1+\beta)s(w - iw_R) - i(w_\nu - w_R)(w - iw_R)$$
$$-1 \mp i(w_\nu - w_R)s + \beta s^2 \qquad (10)$$

where the mode frequency w is normalised to the Alfven frequency kv_A, and the other parameters, in c.g.s. units, are

$$s^2 = \frac{m_i k^2 c^2}{4\pi n e^2} = \frac{k^2c^2}{w^2_{pi}} \tag{11}$$

and $$w_R = \frac{\eta k c^2}{4\pi v_A}\ ,\quad w_\nu = \frac{\mu k}{\rho_o v_A}\ ,\quad \beta = \frac{4\pi p_i}{B_o^2} \tag{12}$$

η and μ being the resistivity and viscosity respectively.
We note that the finite Larmor radius effects enter through the β of the plasma.

In absence of resistivity, viscosity and finite Larmor radius effects, w has the 4 values $\pm\{\sqrt{(\frac{1}{4}s^2 + 1)} \mp \frac{1}{2}s\}$.

From a comparison of equations (4) and (11) it is clear that for the polytron conditions where k is the wavenumber of the cusp fields we require $s \gg 1$. The highest frequency is then approximately $skv_A = \frac{k^2 v_A c}{w_{pi}}$ $\sec^{-1}$.

Because of the dispersive nature of this whistler mode, in its application to a finite difference scheme with mesh points separated by k_m^{-1}, the required timestep Δt_m of the mesh is given by

$$\Delta t_m = \frac{w_{pi}}{k_m^2\ v_A\ c} \tag{13}$$

In contrast, when the magnetic field is normal to the plane of the calculation (as in the plasma focus code), the time step is $(k_m v_A)^{-1}$ for $v_A \gg$ sound speed, corresponding to the fast magnetosonic wave. Thus, like the diffusion problem, doubling the number of mesh points quadruples the number of required time steps. We can estimate the number of time steps necessary to reach the characteristic acceleration time τ_a given by eq. (2) by taking the ratio of eqns (2) and (13), and using $v_A w_{pi} = \Omega_i c$, viz.,

$$\text{Number of time steps} = \frac{\tau_a}{\Delta t_m} = \frac{1+\alpha^2}{\alpha}\ .\ (\frac{kc}{w_{pi}})^2\ .\ (\frac{k_m}{k})^2 \tag{14}$$

Each of the factors in equation (14) is much larger than one, the factor k_m/k being the number of linear mesh points in the cusp period. In order to satisfy condition (4) and also have a fine mesh, the number of time steps is very large. It is well known that when the Lundquist number is smaller than one viscosity or resistivity removes the Alfven modes. Therefore methods of removing the short wavelength whistler modes, were investigated: eq. (10) describes the effect of viscous and resistive damping on these modes.

2.2.1. Resistive damping of the whistler mode

In figure 1(a) the real and imaginary parts of the normalised frequency w are plotted for different values of the parameter s. In each constant s curve, increasing w_R results in evolution along the curve in the direction of decreasing $|w_r|$ where $w = w_r + iw_i$ and k is real. The curves for s=0 indicate that for sufficiently small Lundquist number the Alfven wave is completely damped. However for finite s, whilst resistivity increases the damping and reduces w_r in all cases, for large s the reduction is small for two of the four modes. (Two modes are illustrated in figure 1, the other two modes simply correspond to $w = -w_r + iw_i$).

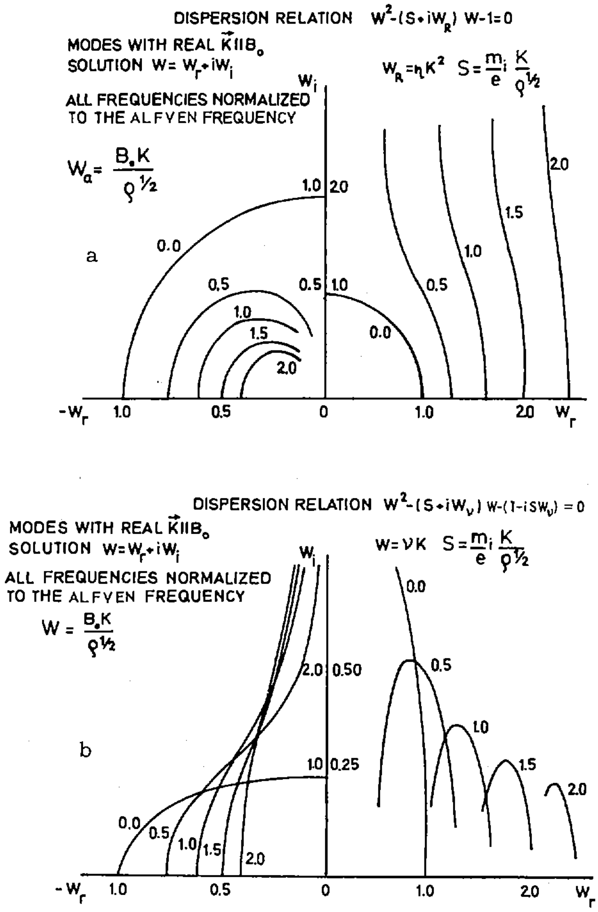

FIG. 1. Dispersion curves showing resistive (a) and viscous damping (b) of whistler modes.

2.2.2. Viscous Damping of the Whistler Mode

With w_ν non-zero but w_R and β zero in eq. (10) we can examine the effect of viscous damping which, for non-zero s, is different to resistive damping. In figure 1(b) the real and imaginary parts of the normalised frequency are similarly plotted for the indicated values of s. For large s, increasing values of w_ν do not result in much reduction of w_r.

2.2.3. Finite Larmor radius effects

In absence of viscosity and resistivity, we retain the parameter β in eq. (10) which arose in the analysis through the inclusion of collisionless viscosity. w is real and has the values $\pm\ \{\sqrt{(\frac{1}{4}s^2(1-\beta)^2+1)} \mp \frac{1}{2}s(1+\beta)\}$. For large s, instead of two of the roots cutting off at the ion gyrofrequency, they now have a group velocity β times that of the other two modes.

2.3. Numerical Scheme for GEMINI

To simulate the differential equations (9) on a finite-difference-mesh, the set of equations are solved either implicitly - a most difficult, if not impossible, task due to the mixture of hyperbolic (essentially time-evolution) equations and elliptic (essentially boundary-value) equations - or explicitly. The latter was chosen, but is severely limited in the problem at hand due to the necessity of restricting the timestep of the calculation to such a value that the mode with the shortest timescale or fastest group velocity may be followed. If this timestep criterion is not satisfied, numerical instabilities will develop immediately. Although the equations solved are non-linear, the numerical stability criterion deduced from linear stability theory applies very well to assess the stability of small timesteps. The non-linearity will result in isolated regions of parameter space having much higher frequencies than those associated with the rest of the parameter space. The stability criterion reduces the error in most regions of parameter space due to taking a finite difference solution. (This error is of order $(w\Delta t)^n$ where n is the order of the scheme used and w is the fastest mode frequency.)

Clearly, from eq. (14), it is difficult to simulate for reasonable times the behaviour of the plasma in a polytron regime, i.e. with Hall acceleration and conditions (1), (3) and (4) holding. Alternatively, borderline cases can be followed for reasonable times or strongly satisfied cases for very short times. Whilst viscosity and resistivity dampen the fast whistler mode a little, no obvious solution to the problem of removing the whistler wave whilst retaining the Hall terms in the equations has been found.

The code GEMINI (7) has been developed for the numerical simulation of an axisymmetric plasma in a general magnetic field configuration. Equations (9) are written in a differenced form to apply to an Eulerian mesh, and solved using the second-order accurate explicit Lax-Wendroff method (9). All equations, with the exception of that for A_θ are solved this way, only initial values being strictly necessary for their solution; but due to the discrete mesh pseudo-boundary values have also to be applied. The equation for A_θ (determining B_r and B_z) is treated as a boundary value problem, using the method of Successive over relaxation (10) to solve implicitly at the end of each half- and full-timestep of the explicit calculation.

2.3.1. Boundary Conditions

In the polytron simulation, periodic boundary conditions are applied at z=0 and $z=\lambda=10$cm. For A_θ are imposed additionally the boundary conditions that at the axis (r=0) it is zero, whilst at the insulating boundary ($r=r_o$ =4cm) it has a sinusoidal form, representing the cusp-shaped magnetic field lines. In the laboratory experiment A_θ is generated by energising coils external to the region of the calculation. To minimise the computing to only that which is important A_θ is not calculated outside the region bounded at $r=r_o$. This is equivalent to having a perfectly conducting region immediately outside the insulating boundary.

In the toroidal laboratory experiment the axial current is induced by changing the magnetic flux threading through the torus. In the straight cylindrical simulation it is not possible to employ the same physical method because $\frac{\partial A_z}{\partial t}$ is a measure of the change of B_θ flux within a radius r rather than the change of flux in some external region. In the numerical code an electrostatic electric field is applied and a simple external circuit for the total axial current I is considered. I is governed by the equations

$$I = -\frac{dQ}{dt} \quad \text{and} \quad \frac{Q}{C} = \frac{d}{dt} \iint B_\theta drdz + L\frac{dI}{dt} \qquad (15)$$

The resulting value of the current is used to set B_θ on the insulator boundary for the next timestep.

3. COMPUTATIONAL RESULTS

The results of two numerical experiments are presented in this paper. Experiment 1 explores the polytron regime whilst in experiment 2 the Hall terms are virtually suppressed for comparison. This latter case illustrates the pinch dynamics in a cusp configuration including at later times the radial loss of plasma through the ring cusp region.

The initial conditions for each of the numerical experiments are as follows:

Initial velocity = 0
Initial filling density of deuterium = 4.5×10^{14} cm^{-3}
Initial electron and ion temperatures = 2 eV
Capacitance C = 20 μF
Charge on capacitance Q = 20 mC
Current I = 1 kA
Maximum B_r = 8 kG

A vacuum A_θ is set in the region by solving $\nabla^2 A_\theta = 0$, subject to the given boundary conditions.

3.1. Numerical Experiment 1

This experiment illustrates the asymmetry introduced into the problem by the inclusion of the Hall term $j_\theta B_\perp$, with the resultant Hall acceleration of the ions competing with the other dynamic effects of pinching and cusp-loss. In figure 2(a) the density, (b) B_θ, (c) the electron temperature are shown at the early time of 0.3 μsec, and then figure 2(d) (e) and (f) are the corresponding parameters at the later time of 0.7 μsec. In figure 3(a) contours of rA_θ illustrate the shape of the magnetic field lines at 0.3 μsec and 0.7 μsec; in 3(b) and (c) contours of rB_θ show the current flow pattern in the r-z plane at 0.3 μsec and 0.7 μsec respectively. The ion temperature and the velocity vectors in the r-z plane are shown in figure 3(d) and (e) respectively at 0.7 μsec.

Several phenomena are of interest, in particular, the growing asymmetric distortion of the cusp fields, and the tendency for the r-z current to follow the cusp shape field except at the ring cusp itself. In this region we note the axial plasma velocity ($\sim 3\times10^6$ cm sec^{-1}) resulting from the azimuthal Hall current. The axial component of the magnetic field also interacts with the azimuthal Hall current to set up a radial velocity component. In fact we expect $v_z/v_r \sim B_r/B_z$ i.e. motion normal to the cusp fields, which in the polytron act as a magnetic lens. In addition the $j_z B_\theta$ pinch forces are acting on the plasma and give a large compression of the plasma on the axis under the coils where the axial current is more concentrated. Nearer the walls the plasma density builds up in the ring cusp region, consistent with the single particle trajectory calculations (6), due to the flow of the plasma along the field lines. The ion temperature has maxima ($\sim$ 8eV) on the axis downstream of each coil due to compressional heating, whilst the electron temperature ($\sim$ 70eV) is also affected considerably by Ohmic heating. The ion temperature also rises downstream of the plane of the ring cusps due to axially accelerated ions compressing the downstream stationary plasma.

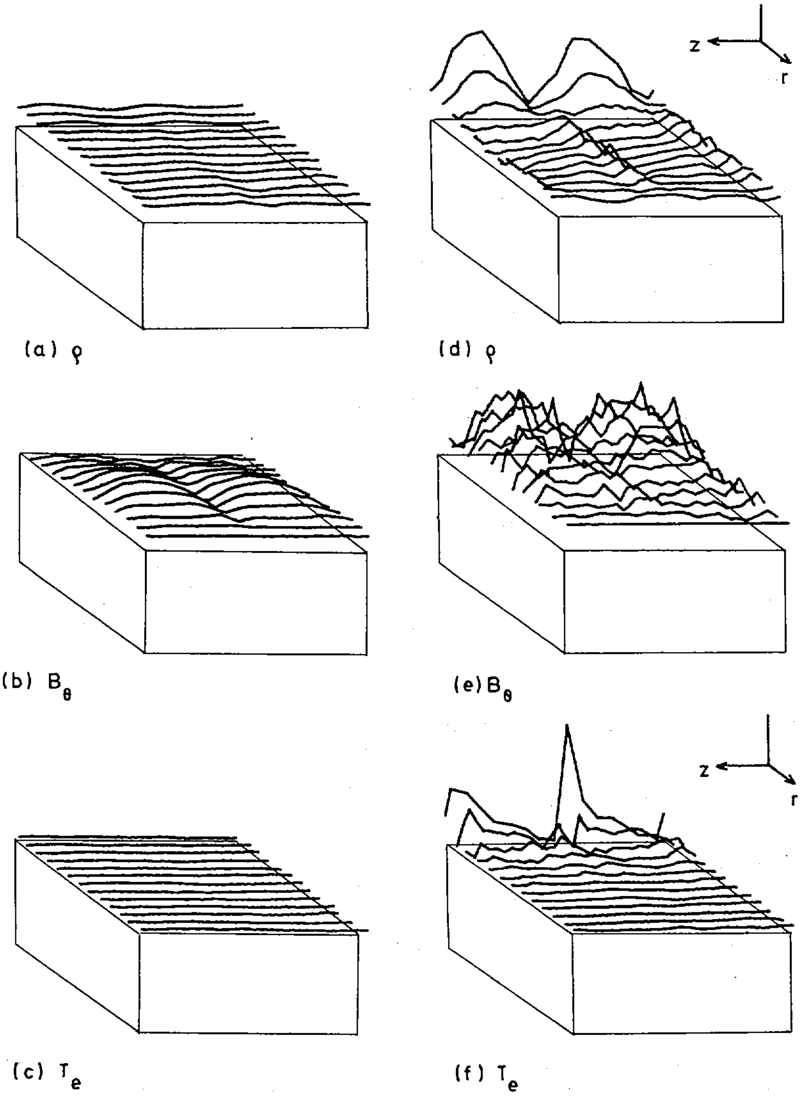

FIG. 2. Experiment 1 (Hall terms included).

Unfortunately this plasma at later times begins to be lost through the ring cusps, as indicated by the velocity diagram (fig. 3(e)). A set of parameters more in keeping with the conditions outlined in section 1 are required so that larger axial velocities occur before too many particles are lost.

As the plasma is compressed to the axis it leaves behind a plasma of low density. Within this region spurious closed loops of current develop in the r-z plane, which in turn induce azimuthal Hall currents of alternate sign. In figure 3(a) the 50% contour is thus distorted outwards at the later 0.7 μsec time. If the density of the plasma becomes less than

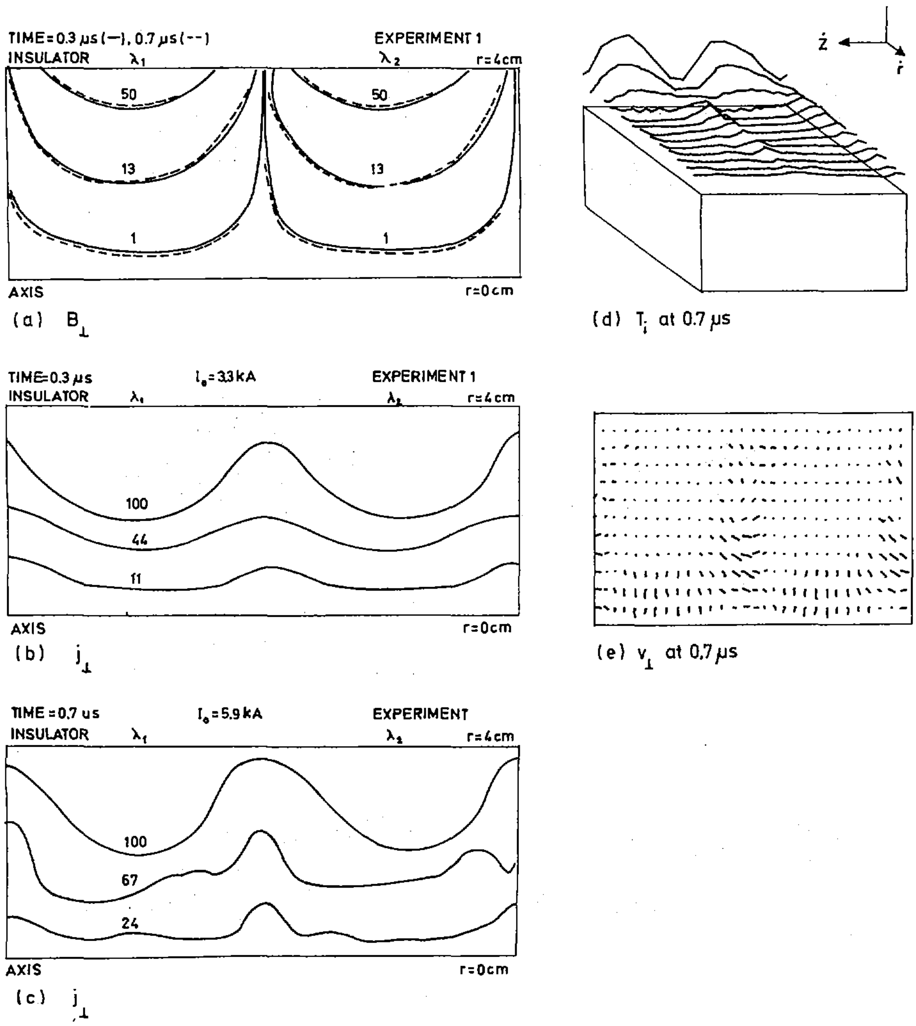

FIG. 3. Experiment 1. The magnetic field coils are positioned at λ_1 and λ_2 in (a), (b) and (c) and the contours are in terms of flux of $B_\perp$ or $j_\perp$ enclosed between the given contour and the axis.

a given (arbitrary) value, vacuum conditions of infinite resistivity, zero currents are imposed.

In figure 2(e) the growth of short wavelength modes on B_θ by 0.7 μsec shows the numerical problems that arise through the physical presence of such modes.

3.2. Numerical Experiment 2

In this experiment the Hall terms have been virtually removed, and symmetric behaviour each side of the ring cusp plane is expected.

Figure 4(a) shows rA_θ contour plots at 0.5 μsec and 1.0 μsec and figures 4(b) and (c) show the current flow patterns at these times. The effect of the inward diffusing B_θ on the vacuum cusp fields is to compress the field lines, thus generating an azimuthal current which causes a $j_\theta B_z$ force to oppose the $j_z B_\theta$ compression force. Figure 4(d) shows the azimuthal magnetic field at 1.0 μsec which has short wavelength Alfven wave structure superimposed on its profile.

A core of compressed plasma, compressed by a factor of 6, is formed on the axis (fig. 4(f)) but at 1.5 μsec it is being squeezed along the field lines into the ring cusps. Figure 4(e) shows the velocity vectors at each mesh point at 1.50 μsec, and the radial flow to the walls is dominant.

In comparison with experiment 1 we note that the current flow patterns follow more closely the cusp shaped vacuum fields, that there is no unidirectional axial motion, and that there is a much greater radial loss. All this is due to the suppression of the Hall effect.

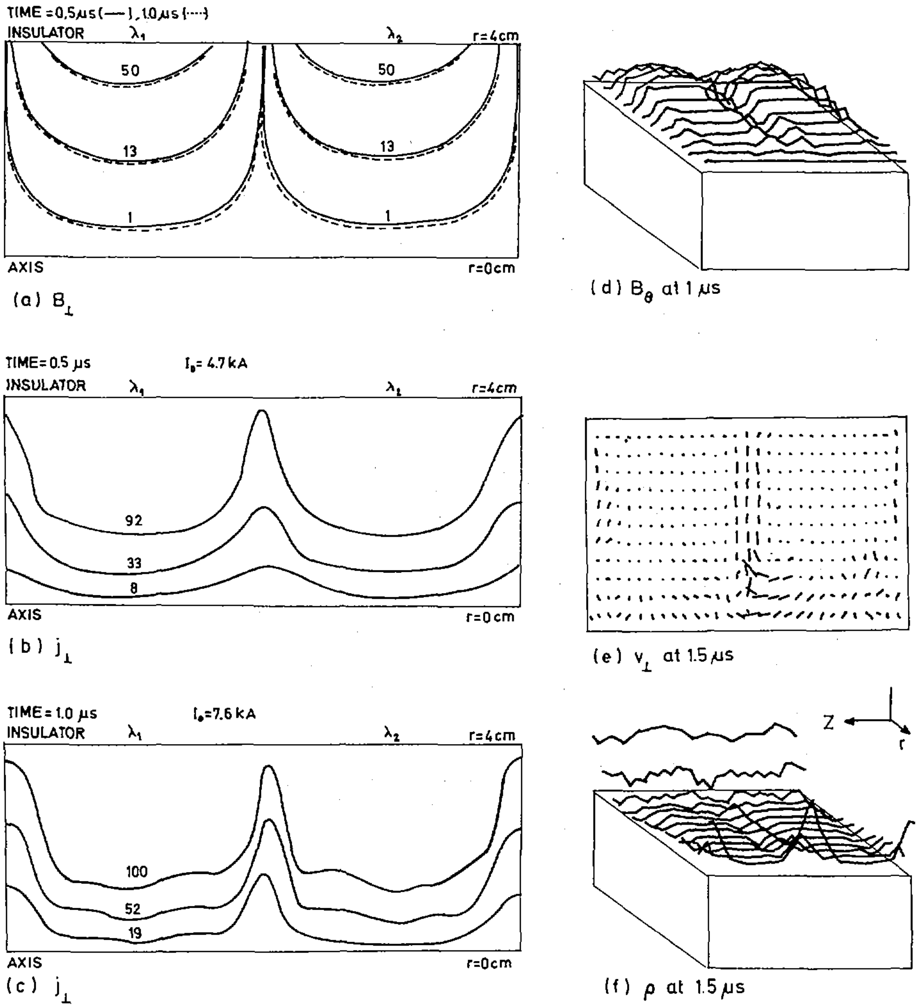

FIG. 4. Experiment 2. Hall term suppressed. a, b, c are as in Fig. 3.

4. RECENT EXPERIMENTAL RESULTS

At early times (∿ 1 μsec in argon) image convertor photographs show a bright plasma well confined on the tube axis with a radius of about 1.5 cm expanding to 2 cm. The axial current profile in the plane of the ring cusp at this time is bell-shaped with a half width of 1.5 cm. From the time history of the appearance and disappearance of argon II, III and IV line radiation the temperature of this hot plasma is estimated to be 20 to 30 eV. Axial velocities of 1.1 x 10^6 cm/sec have previously been reported (4).

At about 1.5 μsec, the temperature falls rapidly to a few eV. Axial scans of argon IV and III line intensities in the neighbourhood of the ring cusp show that the cooling is more rapid downstream of the ring cusp plane. A narrow bright ring located at the wall in the ring cusp plane is obtained in photographs at this time. This ring shifts axially downstream.

These results are in qualitative agreement with the computational model.

5. SUMMARY

A two-dimensional MHD code for a general magnetic field configuration has been constructed and successfully run. An important problem, namely the limitation of the timestep for the calculation by the fast whistler mode, has been identified. The solution of this problem by resistive, viscous and finite Larmor radius damping is being studied.

The computational model shows qualitative agreement with experiment, and vindicates the predictions of Hall acceleration and ion focussing from earlier analytic theory. Further optimisation of parameters is required to reduce the radial plasma loss to an acceptable amount.

REFERENCES

(1) HAINES, M.G., Nuclear Fusion 1962 Supp. Pt 3 1122 (Abstract only). See also 6th Int. Conf. Ionization Phenomena in Gases, Paris (1963) 4, 477.
(2) DUNNETT, R.M., Nuclear Fusion 8 (1968) 4.
(3) ETHERINGTON, R.J. and HAINES, M.G., Phys. Rev. Lett., 14 (1965) 1019.
(4) DANGOR, A.E. et.al., Plasma Physics and Controlled Nuclear Fusion Research (1968) vol.1 (1969) 255.
(5) DANGOR, A.E. et.al., Third European Conf. on Plasma Physics and Controlled Fusion Research, Utrecht (1969) 83 (Wolters-Noordhoff).
(6) KILKENNY, J.D. and DANGOR, A.E., Fourth European Conf. on Plasma Physics and Controlled Fusion Research, Rome (1970).
(7) WATKINS, M.L., Second Conf. on Computational Physics, London (1970), 92 (I.P.P.S.).
(8) POTTER, D.E., Ph.D. Thesis, University of London (1970).
(9) LAX, P.D., WENDROFF, B., Comm. Pure and Appl. Math., 13 (1960) 217.
(10) ROBERTS, K.V., POTTER, D.E., "Magnetohydrodynamic Calculations", Vol.9, Methods of Computational Physics (ALDER, FERNBACH, ROTENBERG, Eds.), Academic Press, New York (1969).

DISCUSSION

TO PAPERS IAEA-CN-28/D-8, D-9

B.D. FRIED: Could you briefly describe the polytron experiment to which your simulation calculations apply?

D.E. POTTER: Perhaps Mr. Haines will answer this question.

M.G. HAINES: Briefly, the polytron experiment consists of a quartz torus surrounded by 36 single-turn cusp coils, co-linear with the minor axis and with currents in alternating directions. A toroidal electric field is induced and, through the Hall acceleration effect (Ref. 1 of paper D-9), an ion current is formed in the toroidal direction. If this ion-flow velocity is greater than the ion thermal speed, then only few ions are at rest in the laboratory frame and ring cusp leakage should be greatly reduced. Experimentally, we have achieved 2 kA of toroidal ion current and have measured the Hall currents and the corresponding mechanical reactions on the coils. The ring cusp losses have not been suppressed, however, and this can be attributed to two factors - first, the ion-flow velocity is only of the order of the ion thermal speed and, second, a three-dimensional single-particle calculation of ion trajectories indicates that particles originating near the wall are lost to the ring cusps in the first transit time. However, the rest are contained indefinitely (Ref. 6 of paper D-9).

B.D. FRIED: What are the major and minor radii of your torus? What did you mean by the statement that the paraxial ions are contained "indefinitely"?

M.G. HAINES: The major radius of the torus is 25 cm and the minor radius is 3.6 cm.

The cusp field magnitude is typically 4 kG and the voltage induced around the torus varies from 10 kV to 25 kV. The single-particle calculations show that those ions that are accelerated through the cusps and attain a terminal velocity, fixed by resistivity and lying between two limits determined by magnetic lens considerations (Ref. 6), are not lost after many toroidal transits.

M.J. BERNSTEIN: You apparently now share my own view that at least a large fraction of the neutron production results from a mechanism associated with rapid diffusion of the azimuthal magnetic field. There is a lot of experimental evidence showing that a few percent of impurity gas (0.1-4%) sometimes enhances the neutron output, as reported by the Fillipov group in Paper D-6. In other devices, a small amount of impurity greatly diminishes the neutron output. Since you have now treated the plasma focus using both fluid and particle models, would you offer an explanation for the different impurity effects?

D.E. POTTER: In reply to your first comment, the model described in this paper is a quasi-steady-state model, and does not rely on the time-dependent rapid diffusion of the magnetic field. It does, of necessity, require the magnetic field to be diffused through the plasma, but as a steady state. For this, we require a resistivity enhanced over classical.

To answer your question on small percentage impurities in the plasma, I have not included such an effect in either the fluid or particle calculations. I could suggest however that, at the densities of the hot pinch ($n_e \gtrsim 10^{19}$ cm^{-3}), enhanced radiation cooling from impurities of high atomic number (cf.

deuterium) will tend to stabilize the pinch and hence enhance the neutron yield. Too large a heavy-atom component on the other hand will have the effect of slowing down the imploding shock before pinch, and thus reduce the deuterium temperature in the pinch.

ОЦЕНКИ ВОЗМОЖНОСТЕЙ ПРИМЕНЕНИЯ МОЩНОГО ПУЧКА РЕЛЯТИВИСТСКИХ ЭЛЕКТРОНОВ ДЛЯ ТЕРМОЯДЕРНОГО СИНТЕЗА

М.В.БАБЫКИН, Е.К.ЗАВОЙСКИЙ,
А.А.ИВАНОВ, Л.И.РУДАКОВ
Институт атомной энергии им. И.В.Курчатова,
Москва,
Союз Советских Социалистических Республик

Abstract — Аннотация

EVALUATION OF THE POSSIBILITIES OF USING A POWERFUL BEAM OF RELATIVISTIC ELECTRONS FOR THERMONUCLEAR FUSION.

The paper discusses the possibility of heating plasma with the density of a solid deuterium-tritium mixture to thermonuclear temperature with the help of a powerful beam of relativistic electrons. A proposal to this effect was put forward by E.K. Zavoisky in 1968. The use of electron beams may be more promising than that of a laser, since the efficiency of transmission of electrical energy to an electron beam attains 35%, as compared with 0.1% in the case of lasers operating in the nanosecond range. For reducing the amount of energy and the beam strength required to initiate a thermonuclear reaction it is proposed to heat the plasma in a shell of heavy material hindering rapid expansion, as a result of which the critical energy can be reduced to 10^5 J and the critical power to 10^{14} W. Contrary to what applies in the case of the laser method of heating, this is possible thanks to the fairly high penetrating power of relativistic electrons and the low thermal conductivity of the heated plasma at the wall due to the presence of the magnetic field created by the beam. For focusing of the beam it is proposed to make use of the magnetic field of the beam formed as a result of the partial dissipation of the reverse current in the plasma. As it is frozen in the plasma, the magnetic field confers macroscopic stability on the beam. Calculations show that plasma having the density of a solid deuterium-tritium mixture can be heated by means of the ohmic dissipation of the reverse current to a temperature of 0.5-1 keV. Heating of the plasma to thermonuclear temperature by the beam can be accomplished by means of the co-operative effects. Theoretical analysis of the instability of the relativistic electron beam yields the following expression for the linear stopping power: $L = \lambda_c(\epsilon)\bar{\theta}^2(\epsilon/mc^2)(T_e/mc^2)^2$, where $\lambda_c(\epsilon)$ is the Coulomb path length of a relativistic electron of energy ϵ, $\bar{\theta}$ is the mean thermal angular scatter of the beam particle velocities, and T_e is the plasma temperature.

ОЦЕНКИ ВОЗМОЖНОСТЕЙ ПРИМЕНЕНИЯ МОЩНОГО ПУЧКА РЕЛЯТИВИСТСКИХ ЭЛЕКТРОНОВ ДЛЯ ТЕРМОЯДЕРНОГО СИНТЕЗА.

В докладе обсуждается возможность нагрева плазмы с плотностью твердой ДТ-смеси до термоядерной температуры с помощью мощного пучка релятивистских электронов. Такое предложение было сделано Е.К.Завойским в 1968 г. Использование электронных пучков может оказаться более перспективным методом по сравнению с использованием лазера, так как эффективность передачи электрической энергии в электронный пучок достигает 35% по сравнению с 0,1% для лазеров, работающих в наносекундном диапазоне. Для снижения величин энергии и мощности пучка, требуемых для инициирования термоядерной реакции, предлагается нагревать плазму в оболочке из тяжелого вещества, препятствующего быстрому расширению, благодаря чему критическая энергия может быть понижена до 10^5 Дж, а критическая мощность – до 10^{14} Вт. В отличие от лазерного способа нагрева, это возможно благодаря достаточно большой проникающей способности релятивистских электронов и малой теплопроводности нагретой плазмы на стенке из-за наличия магнитного поля, создаваемого пучком. Для фокусировки пучка предлагается использовать собственное магнитное поле пучка, образующегося вследствие частичной диссипации обратного тока в плазме. Будучи вмороженным в плазму, магнитное поле придает пучку макроскопическую устойчивость. Расчеты показывают, что плазма с плотностью твердой ДТ-смеси может быть нагрета за счет омической диссипации обратного тока до температуры 0,5÷1 кэВ. Нагрев плазмы пучком до термоядерной температуры может быть осуществлен вследствие коллективных эффектов. Теоретический анализ неустойчивости пучка релятивистских электронов дает следующее выражение для длины торможения: $L = \lambda_c(\epsilon)\,\bar{\theta}^2(\epsilon/mc^2)(T_e/mc^2)^2$, где $\lambda_c(\epsilon)$ – кулоновская длина пробега релятивистского электрона с энергией ϵ, $\bar{\theta}$ – средний тепловой разброс скоростей частиц пучка по углам, T_e – температура плазмы.

ВВЕДЕНИЕ

Возможность применения мощного пучка электронов для быстрого нагрева небольшого объема конденсированной ДТ-смеси появилась в связи с развитием техники получения мегаамперных пучков релятивистских электронов [1-3]. Предложение об использовании сильноточного пучка электронов для турбулентного нагрева сверхплотной плазмы за счет коллективного торможения пучка было сделано в 1968 году Е. К. Завойским, а также независимо — Ф. Винтербергом [6].

Как показал Харрисон [4], для получения положительного выхода энергии при быстром нагреве и разлете мишени необходимо, чтобы нагреваемый объем был больше некоторой критической величины, т. е. необходимо затратить энергию, превышающую определенное пороговое значение, составляющее по разным оценкам $10^7 - 10^8$ Дж [4-6]. Эта энергия должна быть вложена в критический объем за время, меньшее времени расширения $\sim 10^{-9}$ сек, т. е. мощность источника также должна превышать пороговую величину порядка 10^{16} Вт.

Использование электронного пучка для нагрева конденсированной смеси может оказаться более перспективным по сравнению с пучком света от лазера, так как эффективность передачи электрической энергии в электронный пучок достигает $20 \div 30\%$ по сравнению с 0,1% для лазеров, работающих в наносекундном диапазоне. Полная энергия в импульсе, достигнутая к настоящему времени в электронном пучке, превышает 100 кДж [2], что также примерно на два порядка величины превышает полную энергию в лазерном импульсе сравнимой длительности. Максимальная мощность электронного пучка в настоящее время достигает $2 \cdot 10^{12}$ Вт при длительности пучка ~ 80 нсек [2], в то время как в лазерах мощность 10^{12} Вт достигается пока что только в пикосекундных импульсах с полной энергией в импульсе порядка 1 Дж.

Основным эффектом, приводящим к охлаждению нагреваемого объема и определяющим величину критической энергии, является быстрое расширение нагретой области, поэтому естественно попытаться замедлить расширение, окружив нагреваемый объем оболочкой из тяжелого вещества. Это позволило бы существенно уменьшить критическую энергию. Однако с уменьшением размеров критической области включается механизм потерь за счет электронной теплопроводности. При использовании электронного пучка эта трудность снимается, так как пучок электронов всегда создает магнитное поле, которое уменьшает теплопроводность. С другой стороны, электроны релятивистского пучка обладают значительной проникающей способностью и, чтобы использовать их энергию в малом объеме, необходимо вводить предположение о развитии мелкомасштабной неустойчивости и коллективного торможения пучка.

Однако большая проникающая способность электронов с энергией $\sim 10^7$ эВ позволяет надеяться нагреть плазму внутри полностью замкнутой оболочки из тяжелого вещества. Такая возможность связана с тем, что пучок с плотностью энергии, достаточной для получения эффекта коллективного торможения в плазме из легких элементов, не может вызвать коллективных эффектов в плазме, образованной из вещества с большим Z, и будет проходить через него с относительно небольшими потерями, определяемыми обычными кулоновскими взаимодействиями. Поэтому нет надобности делать отверстие для ввода электронов, как это совершенно необходимо в случае использования пучка лазерного света. Использование замкнутой тяжелой оболочки позволило бы уменьшить критический размер в $\sqrt{\rho_1/\rho_0}$ раз, что при $\rho_1/\rho_0 = 100$ дает уменьшение критического диаметра в 10 раз (до $0{,}4 \div 1$ мм) и критической энергии в 10^3 раз, т.е. до $10^4 - 10^5$ Дж. При этом теплопроводность будет снижена за счет магнитного поля пучка, а охлаждение плазмы за счет передачи тепла равновесному излучению не успеет произойти, так как температура излучения в этих условиях определяется относительно холодными стенками, число фотонов относительно мало́ и время передачи энергии электронами в излучение за счет обратного комптон-эффекта оказывается больше времени расширения.

Малый коэффициент использования энергии лазерами приводит к тому, что для получения положительного выхода энергии при лазерном способе нагрева всегда необходимо работать в режиме "вспышки" или детонации, а это означает, что нужно превысить критическую энергию для инициирования детонации, которая на два-три порядка величины больше критического значения для получения положительного выхода энергии.

С применением пучка электронов можно получить положительный выход энергии при меньших значениях критической энергии, особенно при использовании оболочки из тяжелого вещества. Стремление получить высокий коэффициент воспроизводства энергии приводит к увеличению критической энергии, и при некотором значении этого коэффициента критическая энергия сравнивается с порогом детонации. Тем не менее, и микровзрывы с низким коэффициентом воспроизводства энергии (т.е. с наименьшей критической энергией) представляют интерес как источник нейтронов в бридерах, производящих делящиеся изотопы для атомных станций.

При сравнении электронного и лазерного нагрева нельзя не отметить, что световой пучок обладает существенным преимуществом при фокусировке и проводке до мишени, однако и для мощного электронного пучка проблема проводки и фокусировки на мишень, по-видимому, может быть решена.

ФОКУСИРОВКА И ПРОВОДКА МОЩНОГО ПУЧКА РЕЛЯТИВИСТСКИХ ЭЛЕКТРОНОВ

Использование пучка для нагрева твердой мишени размером менее 0,1 см^3 до термоядерных температур возможно, если ток I в пучке в практическом интервале значений энергии электронов $1 \div 10$ мэВ, превышает $10^8 \div 10^7$ А. Это на несколько порядков величины больше критического тока:

$$I_A = \frac{mc^3}{e}\beta\gamma = 1{,}7 \cdot 10^4\, \beta\, \gamma \quad \text{(ампер)}$$

но при таких токах плотность магнитной энергии превышает плотность кинетической энергии в I/I_A раз. В соответствующее число раз уменьшается полезная мощность пучка.

Индуктивность пучка можно уменьшить до допустимого значения, если пропускать его через плазму, концентрация которой превышает концентрацию частиц в пучке. Если характерное время нарастания тока пучка много меньше, чем скиновое $(4\pi\sigma r^2)/c^2$ (σ – проводимость плазмы, r – радиус пучка), то в плазме возникает обратный ток, по величине почти равный в каждой точке току пучка. Экспериментальные данные, подтверждающие существование обратного тока, получены в работе Беннета и Робертса [7]. В рамках обсуждаемой проблемы, где время инжекции пучка должно быть меньше, чем 10^{-8} сек, условие скинирования плазмой магнитного поля пучка практически всегда будет выполнено.

Естественно, что в плотной плазме отсутствуют электрические радиальные поля и вызываемое ими расталкивание пучка. Но вместе с тем из-за обратного тока исчезает и стягивающее пучок магнитное поле. Поэтому в случае бесконечной проводимости пучок разлетался бы с радиальными тепловыми скоростями. Однако из-за конечной проводимости плазмы обратный ток будет частично диссипироваться и появится фокусирующее магнитное поле, хотя и малое в сравнении с полем, рассчитанным по полному току пучка.

Пусть начальный радиус релятивистского пучка, входящего в плазму, есть R, а средний разброс поперечных скоростей $\langle\theta\rangle^2 = \langle(\theta - \bar{\theta})^2\rangle$ ($\bar{\theta}$ — угол расхождения пучка). Ток пучка нарастает по закону $I = I(t)$. Если учесть, что за время, много меньшее $(4\pi\sigma r^2)/c^2$, для плотностей тока пучка j' и плазмы j справедливо неравенство $|j' - j| \ll j'$, то уравнение, определяющее рост магнитного поля во времени, будет иметь следующий простой вид:

$$\frac{\partial H_\varphi}{\partial t} = - c\cdot\frac{\partial}{\partial r}\cdot\frac{j'}{\partial(r,t)} \tag{1}$$

В этом процессе выделяется джоулево тепло и проводимость плазмы быстро увеличивается.

Возникающее магнитное поле будет вморожено в плазму. Таким образом, для электронов пучка ранее пролетевшими частицами будет образован магнитный канал.

Используя уравнения движения для релятивистского пучка и плазмы, можно получить оценку для длины фокусировки и равновесного радиуса пучка, когда сила сжатия уравновесится силой давления [8]:

$$\ell \simeq R\left(\frac{\sigma_0 p_0}{j_0'^2 t}\right)^{1/5}\left(\frac{n_0' m' c^2}{p_0}\right)^{1/2} \sim I^{1/10}\, t^{-1/5}\, n^{-3/10}\, R^{4/5} \tag{2}$$

где j', R, $\langle\theta_0\rangle$ — начальные плотности тока, радиус и угловой разброс в пучке,

p_0 — начальное давление плазмы,

n', n — плотность пучка и плазмы,

t — время инжекции.

На этой длине пучок сожмется до радиуса:

$$r = \ell\,\langle\theta_0\rangle \tag{3}$$

Последний результат получен в предположении, что показатель адиабаты равен 2 (двумерное сжатие, $\langle\theta\rangle = \langle\theta_0\rangle R/r$, давление пучка $p' = n'm'c^2\langle\theta\rangle^2$). Магнитное поле, обеспечивающее такую фокусировку, равно:

$$H_\varphi \simeq \frac{I_A}{cr}\,\langle\theta\rangle^2 \tag{4}$$

Чем дольше пропускается по плазме пучок, чем больше плотность плазмы, тем сильнее диссипируется обратный ток. Поэтому, в принципе, можно конструировать нужную форму магнитного канала или "магнитной линзы" и обеспечить необходимую фокусировку пучка.

Степень сжатия пучка может быть увеличина, если создать условия, когда проводимость плазмы аномально низка. Так, при условии $n'/n > (T_e/Mc^2)^{1/2}$ обратный ток может оказаться неустойчивым относительно раскачки ионного звука в плазме, что приведет к сильному увеличению частоты рассеяния электронов.

Вследствие нагрева плазмы в магнитном канале за счет омической диссипации обратного тока и действия силы $(-1/c)(jH_\varphi)$ плазма с вмороженным магнитным полем начинает разлетаться. Давление плазмы в канале примерно равно поперечному давлению частиц пучка:

$$nT \simeq n'm' c^2 \langle\theta\rangle^2 \qquad m' = \gamma m \tag{5}$$

Поэтому относительно простая картина фокусировки может иметь место только при времени инжекции пучка, меньшем времени разлета:

$$t < \frac{r}{c}\left(\frac{Mn}{m'n'}\right)^{1/2} \tag{6}$$

Практически это условие может быть выполнено.

Наиболее опасными с точки зрения проводки пучка являются возмущения, приводящие к поперечному смещению пучка как целого, т.е. к неустойчивости возмущений вида плоских змеек или винта. Имеется физическая причина для таких неустойчивостей. Она связана с тем, что на поток частиц пучка, двигающихся по искривленной траектории, действует центробежная сила. Но поток релятивистских электронов может двигаться только по магнитному каналу, и для того чтобы сместить пучок электронов, нужно сместить магнитный канал. Однако двигаться он может только вместе с плазмой, в которую "вморожен". Инкремент такой "шланговой" неустойчивости зависит от массы плазмы, захваченной движением:

$$\mathrm{Im}\,\omega = \left(\frac{n'm'}{nM}\right)^{1/2} \cdot \frac{c}{r}\langle\theta\rangle \tag{7}$$

Формула (7) справедлива пока скорость поперечного смещения мала в сравнении со скоростью звука. Однако при сверхзвуковом движении резко возрастают потери энергии, и неустойчивость должна стабилизироваться. Поэтому при выполнении условия (6) шланговая неустойчивость не опасна.

Другой макроскопической неустойчивостью релятивистского пучка в относительно редкой плазме $n'/n > \langle\theta\rangle^2$ является неустойчивость, приводящая к расслоению прямого и обратного тока и возникновению неоднородной структуры. Ее можно сравнить с проводником, набранным из большого числа тонких перевитых проволочек, по которым течет ток I_A в разных направлениях, но суммарный ток при этом не превышает I_A. Такая неустойчивость может привести к увеличению $\langle\theta\rangle$ и, следовательно, радиуса пучка r.

В заключение этого раздела подчеркнем, что согласно формуле (3) возможность предельно сильной фокусировки определяется, главным образом, начальным угловым разбросом частиц пучка $\langle\theta_0\rangle$. Это — следствие того, что в интересующих нас процессах малой длительности радиальное сжатие пучка будет протекать адиабатически, и поэтому поперечное давление $n'm'c^2\langle\theta\rangle^2$ быстро растет с уменьшением радиуса $\langle\theta\rangle \sim 1/r$.

Если бы удалось получить из ускорителя пучок электронов с очень малым угловым разбросом, то благодаря магнитной самофокусировке можно, в принципе, получить удивительный физический объект: сгусток релятивистских электронов в виде тонкой иголки с плотностью частиц, сравнимой с плотностью твердого тела. Плотность энергии в таком сгустке электронов была бы порядка 10^{11} джоулей/см^3(!). Несомненно, что изучение газо- и электродинамики такого релятивистского образования чрезвычайно интересно и могло бы дать неожиданные результаты.

В проекте использования электронных пучков для инициирования термоядерной реакции предполагается окружать мишень тяжелой оболочкой и тем самым уменьшать скорость разлета горючего. Однако при этом необходимо, чтобы плазма не успевала охлаждаться за счет контакта с тяжелым веществом стенок. Этому может помочь вымороженное магнитное поле. Действительно, в мишени при $T_e = 10^4$ эВ и $n = 5\cdot 10^{22}$ частота кулоновского рассеяния электронов равна $\nu_{ei} = 10^{12}$ сек$^{-1}$ и меньше, чем значение $\omega_H = eH/mc$, оцененное по формуле (4). Поэтому мишень не успеет охладиться из-за теплопроводности за характерное время разлета, если:

$$\frac{T_e}{m\omega_H^2}\cdot\frac{\nu_{ei}}{r^2} < \frac{c_s}{r} \qquad \text{или} \qquad \gamma^2\langle\theta\rangle^4 > \frac{2T_e}{mc^2}\cdot\frac{\nu_{ei}r}{c_s} \tag{8}$$

Здесь c_s определяется температурой мишени и массой оболочки. При $T_e = 10$ кэВ, $r = 2\cdot 10^{-2}$ см, $c_s = 2\cdot 10^7$ см/сек это неравенство численно таково: $\gamma^2\langle\theta\rangle^4 > 40$. При столь сильной фокусировке величина $\langle\theta\rangle$ будет близка к единице, так что условие малости потерь тепла из-за теплопроводности может быть выполнено.

НАГРЕВ ПЛАЗМЕННОЙ МИШЕНИ

Диссипация обратного тока может обеспечить предварительный нагрев плазмы твердой ДТ-мишени до температуры порядка 1 кэВ, см. формулу (5). При этой температуре плазма уже идеальная. Дальнейший нагрев возможен только за счет коллективных эффектов.

Для нерелятивистских относительно слабых пучков ($I = 10^{-3} \div 10$ А) коллективное торможение, связанное с пучковой неустойчивостью, хорошо изучено теоретически и экспериментально и является фундаментальным явлением физики плазмы.

Коллективное торможение релятивистских пучков теоретически изучалось в работах [9-11]. Ниже приводятся основные результаты работы [10].

Пучок, входящий в мишень, должен быть сфокусированным, и поэтому разброс частиц пучка по углам будет велик. При большом разбросе, $\langle\theta\rangle < (n'/n)^{1/6}\gamma^{-1/2}$, коллективное торможение пучка – следствие индуцированного эффекта Черенкова, приводящего к генерации ленгмюровских колебаний. Этому препятствуют три эффекта.

Во-первых, поглощение колебаний из-за кулоновских столкновений электронов с ионами. В плотной плазме мишени этот механизм накладывает существенное ограничение на ее температуру. Условие неустойчивости:

$$\nu_{ei} < 2\delta \qquad \delta \simeq \frac{n'}{n}\omega_p/\gamma\,\langle\theta\rangle^2 \tag{9}$$

Практически, неустойчивость пучка с параметрами, необходимыми для осуществления термоядерной реакции, возможна только при температуре мишени около 1 кэВ и выше.

Во-вторых, в неоднородной плазме возможен срыв неустойчивости из-за расстройки фазового резонанса между электронами пучка и ленгмюровскими колебаниями, так как их фазовая скорость меняется при распространении по плазме с переменной плотностью. Этот эффект изучался Д.Д.Рютовым и Б.Н.Брейзманом [11]. По нашим представлениям он несущественен, если:

$$\frac{1}{n}\cdot\frac{dn}{dz} < \frac{\omega_p}{c}\cdot\frac{n'}{n\gamma} \tag{10}$$

Отсюда следует, что при одной и той же мощности пучка, пропорциональной величине $n'\gamma$, правая часть неравенства (10) пропорциональна γ^{-2}. Поэтому можно, уменьшая γ и увеличивая соответственно ток пучка, усиливать неравенство (10).

В третьих, ограничение уровня возбуждаемой пучком турбулентности и срыв неустойчивости возможен из-за нелинейных эффектов трансформации волн (нелинейного рассеяния на частицах плазмы). Этот эффект также приводит к нарушению фазового резонанса. Впервые его влияние на неустойчивость пучков было изучено В.Н.Цытовичем и В.Д.Шапиро. Для релятивистских пучков этот эффект практически всегда важен.

Все эти эффекты были учтены в работе [10]. Приведем здесь из [10] интерполяционную формулу для длины коллективного торможения пучка релятивистских электронов, со средним импульсом P, для значений $\langle\theta\rangle$, удовлетворяющих условию $\left[\frac{(mc^2)}{(Mv_{Te}^2)}\right]^{1/4} > \langle\theta\rangle > 1/\gamma$:

$$L(p) = \lambda_c(p)\,\gamma\langle\theta\rangle^2\left(\frac{T}{mc^2}\right)^2\cdot\left(1 - \frac{\nu_{ei}}{2\omega_p}\cdot\frac{n\gamma}{n'}\langle\theta\rangle^2 - \frac{c\gamma}{\omega_p n'}\cdot\frac{dn}{dz}\right)^{-1} \tag{11}$$

где λ_c — длина пробега релятивистского электрона в плазме мишени относительно кулоновских столкновений.

Специфика коллективного торможения релятивистского пучка заключается в том, что за время торможения почти не увеличивается $\langle\theta\rangle$. Поэтому в (11) надо подставлять угловой разброс,получающийся в процессе фокусировки.

Оценки L(p) по формуле (11) показывают, что длина торможения пучка может быть уменьшена в сравнении с $\lambda_c(p)$ на несколько порядков величины. $L(p) \sim n$ и удовлетворяет необходимому условию: в разреженной плазме магнитного канала плазмопровода длина коллективного торможения должна быть велика и потери малы.

Численный анализ условий инициирования термоядерной реакции в ДТ-мишени пучком релятивистских электронов на основе приведенных здесь формул показывает, что они не противоречивы и осуществимы, хотя и без большого запаса, для пучка электронов с энергией $10^7 \div 10^6$ эВ и током для пучка $10^7 \div 10^8$ А, сфокусированного до радиуса $(2 \div 5)\,10^{-2}$ см.

ЗАКЛЮЧЕНИЕ

Для осуществления идеи нагрева плазмы с плотностью твердого тела мощным электронным пучком необходимо решить ряд физических и технических проблем. К основным физическим проблемам относятся фокусировка пучка и коллективное торможение в мишени. Проблема фокусировки может быть изучена при токах пучка, меньших, чем необходимые для нагрева твердой мишени. Чтобы ответить на вопрос о существовании коллективного торможения в твердой мишени, нужно, как уже отмечалось, нагреть плазму до температуры порядка 1 кэВ, т. е. для этого нужен очень мощный и хорошо сфокусированный пучок.

Для создания пучков требуемой мощности нужно решить ряд технических проблем. Мощность, требуемая для инициирования термоядерной реакции, должна быть порядка 10^{14} - 10^{16} Вт, а скорость нарастания мощности – порядка 10^{23} - 10^{25} Вт/сек. Это значит, что основными техническими проблемами являются создание источника энергии большой мощности и быстрая коммутация этой мощности.

Предельный поток мощности, протекающий через 1 см^2 сечения линии, а также через единицу поверхности согласованной нагрузки, дается формулой Пойнтинга, если в нее подставить предельное электрическое поле, допустимое для данного диэлектрика:

$$w = c\sqrt{\epsilon}\cdot\frac{[\bar{E}\times\bar{H}]}{4\pi}$$

В бегущей волне E = H, следовательно:

$$w = c\sqrt{\epsilon}\cdot\frac{E^2}{4\pi}$$

Так как поток мощности ограничен прочностью диэлектрика, то это означает, что для получения мощности W площадь сечения линии и площадь поверхности нагрузки не могут быть ниже некоторой величины: $S > W/w$.

Это может означать, что для получения мощностей порядка 10^{14} Вт и более при использовании линий придется работать с полыми электронными пучками с диаметром порядка 1 м.

В общем случае поток мощности зависит от произведения $[\bar{E}\times\bar{H}]$ и может быть увеличен при том же E, если $H > E$. Так может быть, если линия согласована по сопротивлению, но нагрузка имеет меньший радиус, чем линия и, следовательно, имеет паразитную индуктивность. Это, конечно, приведет к удлинению фронта импульса, но если удлинение не выходит из допустимых пределов, то это позволит повысить мощность на единицу поверхности нагрузки.

Другим путем повышения потока мощности при $H > E$ может быть использование магнитных накопителей с обрывом тока. Однако для этого должны быть изучены возможности более быстрого обрыва тока, чем полученные до сих пор ($\sim 10^{-7}$ сек).

Для обеспечения требуемой скорости нарастания мощности необходимо решить проблему быстрой коммутации. Одиночный сосредоточенный коммутатор не подходит для этой цели. В данном случае нужно применять распределенный или многоканальный коммутатор. Отсюда следует, что важными проблемами является управление распределенным коммутатором или синхронизация большого количества коммутаторов с точностью менее 1 нсек. Большие возможности могут быть скрыты в электронных способах коммутации, поэтому необходимо развивать и это направление.

Итак, приведенные выше результаты теоретического анализа нагрева ДТ-смеси с плотностью твердого водорода до термоядерных температур $\sim 10^4$ эВ показывают, что поставленная задача, в принципе, осуществима. Ее практическое решение зависит, во-первых, от успехов в развитии техники генерирования сверхмощных пучков и, во-вторых, от результатов исследования фундаментальных физических свойств сильноточных релятивистских пучков. Основные данные о свойствах мощных релятивистских пучков могут быть получены на установках значительно меньшей мощности, чем требуется для достижения окончательной цели. Строительство таких установок при существующем уровне развития техники вполне возможно.

ЛИТЕРАТУРА

[1] DENHOLM, A.S., IEEE Trans. Nucl. Sci. NS-12 3 (1965) 780.
[2] MARTIN, T.H., IEEE Trans. Nucl. Sci. NS-16 3 (1968) 59.
[3] OLIPHANT, W.F., VITKOVITSKY, I.M., Bull. Am. Phys. Soc. Ser. II 15 11 (1970) 1401.
[4] HARRISON, E.R., Phys. Rev. Lett. 11 (1963) 535.
[5] MAISONNIER, Ch., Nuovo Cimento 62B (1966) 332.
[6] WINTERBERG, F., Phys. Rev. 174 (1968) 212.
[7] BENNETT, W.H., ROBERTS, T.G., Plasma Phys. 10 (1968) 381.
[8] ИВАНОВ, А.А., РУДАКОВ, Л.И., ЖЭТФ 58 (1970) 1332.
[9] ФАЙНБЕРГ, Я.Б., ШАПИРО, В.Д., ШЕВЧЕНКО, В.И., ЖЭТФ 57 (1969) 966.
[10] РУДАКОВ, Л.И., ЖЭТФ 59 (1970) 2091.
[11] БРЕЙЗМАН, Б.Н., РЮТОВ, Д.Д., Письма в ЖЭТФ 11 (1970) 606.

DISCUSSION

R.N. SUDAN: It is not clear to me how these high-current electron beams can be focussed when propagating in a plasma. Their self-magnetic field is cancelled by the plasma return current and, by the time this current has decayed sufficiently to give a sizeable self-magnetic field for focussing, most of the energy in the beam has been transferred to the plasma.

L.I. RUDAKOV: There are two aspects of the focussing problem. The relativistic beam with a current greater than the critical value is self-pinched in the plasma without return current, which has an undesirable effect. However, in a very dense plasma where the return current almost completely balances the forward current, the magnetic field is only weak and there is no self-focussing. It is thus necessary to find the optimal conditions, under which there is adequate focussing whilst the return current is strong enough to prevent self-focussing.

INVESTIGATION OF LASER-PRODUCED PLASMAS IN THE keV TEMPERATURE RANGE

K. BÜCHL, K. EIDMANN, P. MULSER,
H. SALZMANN, R. SIGEL, S. WITKOWSKI
Max-Planck-Institut für Plasmaphysik, Garching, Munich,
Federal Republic of Germany

Abstract

INVESTIGATION OF LASER-PRODUCED PLASMAS IN THE keV TEMPERATURE RANGE.

Experimental and theoretical investigations of the problems associated with plasma production by laser radiation of very high intensity are reported. In the experiment, nanosecond and picosecond laser pulses were focused onto plane targets of solid hydrogen and deuterium. Reflection measurements of the laser light were performed. The electron temperature of the plasma was determined from soft X-ray continuum intensity measurements. The spatial distribution of the ions in the expanding plasma, their kinetic energy and their total number were determined by a set of charge-collecting probes. Neutron production in the plasma was measured with two fast scintillation detectors. The experimental results are compared with numerical calculations, which describe the gasdynamic behaviour of laser-heated solid deuterium with allowance for $T_e \neq T_i$ and including the effect of heat conduction.

1. SCOPE OF THE INVESTIGATIONS

With the improvement of high-power lasers it has become posssible to produce plasmas with densities and temperatures which are of interest for thermonuclear research. Recently, substantial neutron emission from such plasmas has been reported [1]. To project into the future the possibilities for this field of plasma physics, detailed understanding of the properties of these plasmas is necessary. In this paper, we report results which we have obtained by using a variety of diagnostic techniques applied to plasmas produced within a wide range of laser power. Results of new theoreticl investigations are also reported.

2. EXPERIMENTAL SET-UP

The laser is a multi-stage neodymium glass laser constructed in our laboratory. Two oscillators, one in the nanosecond range and one in the picosecond range can be used alternatively with a linear amplifier chain. The nanosecond oscillator is Q-switched by a Pockels cell. A pulse-shaping system consisting of a laser-triggered spark gap, a Kerr cell, and two crossed polarizers produces rectangular laser pulses of 10 ns duration with a rise time less than 2 ns. At present, these pulses can be amplified up to 20 J energy, corresponding to a power of 2 GW. The picosecond oscillator is mode-locked by a bleachable dye (Kodak 9740) and is set up to avoid any axial mode selection. Single pulses are selected from the train of picosecond pulses by a device similar to the pulse-shaping system mentioned above. Before entering the linear amplifier chain they are pre-amplified by passing twice through a short amplifier chain. Their pulse duration is measured by using the conventional two-photon fluorescence technique. The pulse duration is less than 10 ps. After passing the main amplifier chain energies up to 3 J have been obtained. With both oscillators, after amplification a beam divergence of about 1 mrad has been achieved. The laser pulses are focused onto targets of solid hydrogen and deuterium [2]. Performance of the laser system without damage to the optical components was possible only by inserting two optical isolators (Faraday rotators together with polarizers). Thereby the light reflected from the target into the amplifier chain is attenuated by more than 10^4. The different diagnostic methods which are partly described in a previous paper [3] are shown schematically in Fig. 1. They will be commented upon in the following.

3. EXPERIMENTAL RESULTS WITH NANOSECOND PULSES

3.1. Streak photography

Streak photographs of the expanding plasma were taken by using an image-converter camera with a time resolution of 1 ns. A time mark generated by the incident laser light allowed the light emission of the plasma to be exactly pinpointed in time relative to the laser pulse. These pictures show that the plasma is created at the laser-irradiation side of the solid deuterium disc and expands with a velocity of 10^7 cm/s towards the focusing lens. The onset of plasma production coincides with the onset of the laser pulse, thus no plasma is produced by a forerunner.

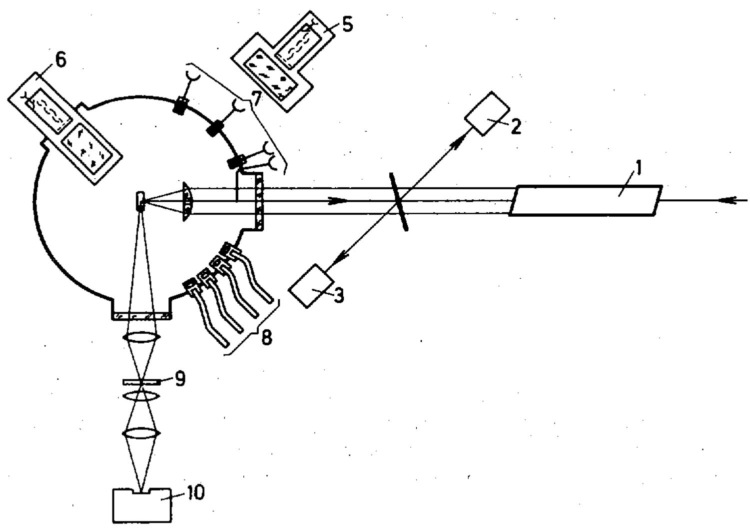

FIG. 1. Scheme of the diagnostics: 1) last amplifier rod, 2, 3) photodiodes, 5, 6) neutron counters, 7) probes, 8) X-ray diagnostics (beryllium foils, scintillators, light pipes), 9) streak slit, 10) image-converter streak camera.

3.2. Time-resolved reflection measurements

A considerable fraction of the incident laser-pulse energy has been observed to be reflected at the target. The pulse shape of the incident at the target. The pulse shape of the incident and the reflected laser light was recorded by using calibrated vacuum photodiodes. The pulse shape and the intensity of the reflected light depend on the light flux at the target. The higest degree of reflection and the best reproducible time behaviour of the reflected laser light were observed at the highest light flux using an f = 5 cm aspherical lens. The pulse shapes of the incident and the reflected laser light are shown in Fig. 2 for this case. In some shots the reflectance reaches values of up to 30%.

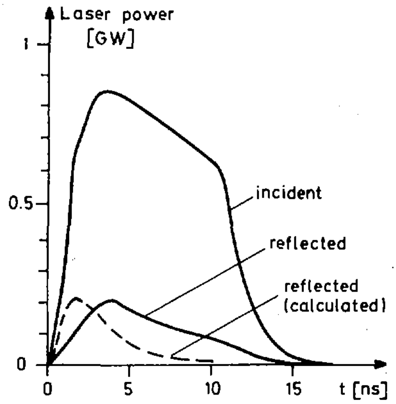

FIG. 2. Intensity of incident and reflected laser light versus time.

3.3. Electron temperature measurements

The electron temperature was determined from the bremsstrahlung continuum using the well-known absorber method. The X-ray radiation from the plasma was transmitted through four different thick beryllium windows, then converted into visible light by plastic scintillators and fed by light pipes to four photomultipliers with a time resolution of ~10 ns [4]. Extensive tests of this method were made with a carbon target under a wide range of conditions (pulse duration, laser energy, focal spot diameter). Curve (a) in Fig. 3 was obtained with such a target. The slope of the intensity of the X-ray signals versus cut-off frequency (expressed in keV) of the different absorber foils is as expected for the bremsstrahlung continuum of a thermal plasma and corresponds to an electron temperature of 400 eV, in this case. However, such unequivocal results were never obtained with solid-deuterium and solid-hydrogen targets. Curve (b) in Fig. 3 was obtained with solid deuterium. As can be seen, enhanced X-ray emission from the plasma is observed at the high-energy end of the measured range. If the laser energy is lowered then this non-thermal radiation dominates the whole measuring range and simulates temperatures of the order of several keV. In addition, a strong correlation between the X-ray intensity and the intensity of the reflected light has been observed.

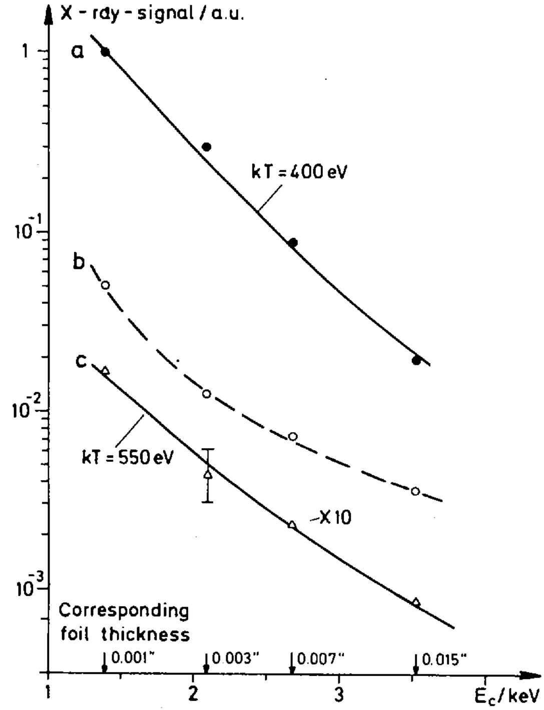

FIG. 3. Electron-temperature measurement.
Curve a: Test of the method with a carbon-target, 10-ns-laser pulse.
Curve b: Solid deuterium target, 10 ns, 10 J.
Curve c: Solid deuterium target, 10 ps laser pulse, 1 J.
The drawn-out curves are calculated. The relative X-ray intensities in the different cases are as shown in the figure; however, the values of curve (c) have been multiplied by a factor 10.

This observation is especially striking at low laser energies when the intensity and pulse shape of the reflected light varies strongly from shot to shot. For the highest power densities achieved when kT_e is expected to become comparable with the cut-off energy E_c of the thinnest foils, the slope of the curves at the low-energy end of the measured range may be representative for the temperature of the main part of the electrons. We thus determine tentatively a temperature of about 500 eV from the curve (b) in Fig. 3.

3.4. Time-of-flight and charge collection measurements

Up to six ion-collecting probes under different angles to the laser axis (the 0° probe looking through a hole in the focusing lens) were used to measure the angular distribution of ion flux and ion kinetic energy. From these measurements an energy balance can be established by integration over the half-space. We find that about 80% of the incident laser energy is contained in the plasma. Taking into account the measured energy loss due to reflection of laser light and the amount of energy transferred into a shock wave entering the solid deuterium ice [5] the whole incident laser energy is recovered.

For our typical experimental conditions (10-20 J, 10 ns, focused with an f = 5 cm aspherical lens) the mean kinetic energy of the ions averaged over all directions is 1.5 ... 2.0 keV, the mean kinetic energy measured by the 0° probe is 2.5 ... 3.5 keV. However, fast ions with energies up to 20 keV are also observed. Though the origin of these fast ions is not understood at present, our measurements indicate that the neutron yield of the plasma increases with the appearance of these groups.

3.5. Neutron diagnostics

Two scintillation detectors (time resolution 5-10 ns, distance 4 cm and 34 cm from the target respectively shielded by 5 mm lead) were used to monitor neutron emission from the plasma. Calibration was performed by positioning a Pu-Be-neutron source at the place of the target. With both counters, signals obviously due to neutrons from D-D-fusion reactions were obtained. This was confirmed by the following tests:

(a) If solid hydrogen instead of solid deuterium was used as target material the signals disappeared under otherwise identical conditions.

(b) One of the counters was positioned at a larger distance from the target (1 m). The delay of the signals observed corresponded to the time of flight of 2.45 MeV neutrons.

The threshold of neutron emission was as low as 5 J for the f = 5 cm aspherical lens and 10 J per shot for a simple f = 15 cm lens.

With laser energies of 15-20 J and the f = 5 cm lens neutron emission was observed in more than 80% of the shots. The average neutron yield as a function of time is shown in Fig. 4. According to Fig. 4, about 15 neutrons are emitted during the 10 ns laser pulse. The total number of neutrons observed is of the order of a few hundred per shot. It is, however, not yet clear if the rather long period of neutron emission can be explained by scattering in the apparatus alone or if there is indeed neutron emission after the end of the pulse.

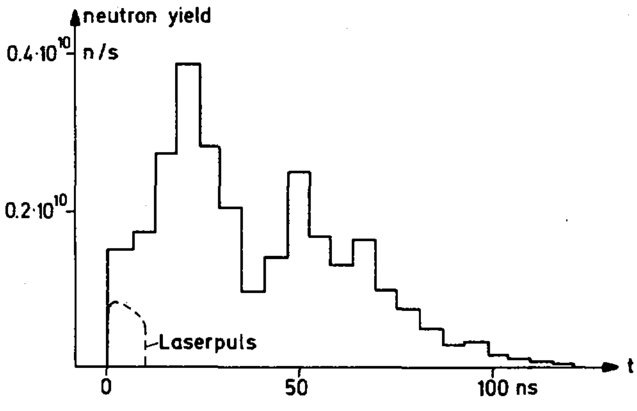

FIG. 4. Neutron yield as a function of time (time-of-flight subtracted). Average 52 shots. Mean laser energy 15 J. Aspherical lens f = 5 cm.

4. RESULTS OF NUMERICAL COMPUTATIONS

Parallel to the described experiments, numerical computations were performed in order to study the plasma formation, heating and expansion for the case of laser-irradiated solid deuterium. The gasdynamic equations were solved in a one-dimensional geometry for different laser intensities Φ. Gas heating was assumed to be due to local absorption of laser light by inverse bremsstrahlung. In addition to previous ones [5] these calculations allow for $T_e \neq T_i$ and include the effects of electron heat conduction. Figure 5 shows numerical results obtained for an intensity of $\Phi = 10^3$ W/cm^2 in a plane geometry.

As can be seen in Fig. 5, the electron temperature is considerably higher than the ion temperature. This is due to the effect that the laser light is absorbed by the electrons and then transferred by collisions to the ions. In the vicinity of the critical electron density n_{crit}, where the electron plasma frequency equals the laser frequency, the light intensity steeply descends to zero. The effect of heat conduction can clearly be seen in the overdense region ($n > n_{crit}$), where the matter is heated by heat conduction alone. For the laser intensity of Fig. 5 the neutron production rate reaches its maximum in the region $n < n_{crit}$ near the maximum of the ion temperature. However, for higher laser intensities the maximum

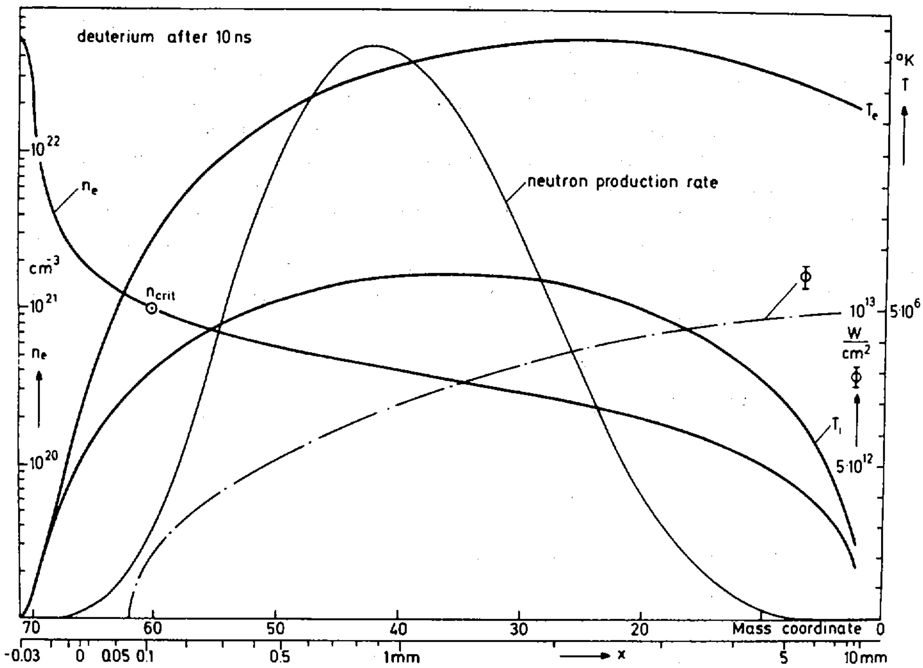

FIG. 5. Profiles of electron density n_e, electron temperature T_e, ion temperature T_i, light flux Φ and neutron production rate (in arbitrary units) from numerical calculations. Laser light incident from the right. Laser pulse is a step function, beginning at t = 0. The incompressible solid fills the halfspace x < 0 for t = 0 (plane geometry). The curves are drawn for a solid deuterium target after 10 ns for a light flux of $\Phi_0 = 10^{13}$ W/cm^2.

TABLE I. MAXIMUM ION AND ELECTRON TEMPERATURE $kT_{i,max}$ AND $kT_{e,max}$, MEAN ION EXPANSION ENERGY $\bar{E}_i$, TOTAL NUMBER OF IONS N_i AND NEUTRONS N_n (ASSUMED FOCAL SPOT 10^{-4} cm^2, PULSE DURATION 10 ns)

Φ [W/cm^2]	$kT_{i,max}$ [keV]	$kT_{e,max}$ [keV]	$\bar{E}_i$ [keV]	N_i	N_n	
3.33×10^{12}	0.32	0.45	2.2	0.95×10^{16}	41	theory
10^{13}	0.48	0.80	3.6	1.7×10^{16}	2.6×10^{3}	theory
3.33×10^{13}	0.7	1.5	6.0	3.5×10^{16}	1.2×10^{5}	theory
10^{14}	1.3	2.6	9.2	6.8×10^{16}	4.4×10^{6}	theory
$\sim 10^{13}$	-	0.5	1.6 (0°-probe: 3.1)	4×10^{16}	10-10^2	experiment

of the neutron production rate shifts well into the overdense region. Maximum electron and ion temperature, the asymptotic ion kinetic energy and the number of ions and neutrons produced are given for different laser intensities in Table I.

5. EXPERIMENTAL RESULTS WITH PICOSECOND PULSES

Selected single laser pulses from the above described mode-locked oscillator were focused onto the surface of solid deuterium targets. Energy densities in the range of 10^3-3×10^4 J/cm^2 corresponding to power densities of 10^{14} to 3×10^{15} W/cm^2 were obtained.

5.1. Reflection measurements

The intensity of the incident as well as of the reflected laser light were measured with a time resolution of 0.5 ns. This allowed us to control whether really a single pulse or, owing to incomplete mode-locking, a pulse of a complex time structure within the 7 ns gate of the pulse selection system was incident on the target. With clean, single pulses less than 10% of the incident laser energy was back-scattered into the solid angle of the lens (0.08 sterad). In the measured range no dependence of the reflectance on the pulse energy was observed.

5.2. Electron-temperature measurements

The spectral distribution of the X-rays emitted by the plasma were found to depend critically on the shape of the incident laser pulse. Pulses with a complex structure on a nanosecond time scale showed an X-ray intensity distribution like the one obtained with nanosecond pulses (curve (b) in Fig. 3) with an enhanced intensity of hard X-rays. However, with clean single pulses striking the target X-ray signals as expected from a thermal plasma with a Maxwellian electron distribution function were obtained in the measured range from 1 to 4 keV. Curve (c) in Fig. 3 shows the averaged X-ray signal from twelve shots. From the slope an electron temperature of 550 eV is determined.

5.3. Time-of-flight and charge collection measurements

Figures 6a and 6b show the mean expansion energy E_i and the total number N_i of the ions obtained by integrating over the halfspace as a function of the energy density ϵ at the target surface. On the average, 60% of the energy of the incident laser energy has been recovered as kinetic energy of the expanding plasma. The rest may be attributed to the shock wave and to additional scattering of the incident light into angles larger than those covered by the focusing lens. The angular distribution of ion flux and ion kinetic energy do not considerably differ from the nanosecond case.

It has been stated [6] that plasma heating in the case of picosecond pulses occurs by an electron thermal wave. For a plane geometry the dependence of the mean ion expansion energy E_i, their total number N_i and the electron temperature T_e from the energy density ϵ ($E_i \sim \epsilon^{1/3}$, $N_i \sim \epsilon^{2/3}$) resulting from this model have been drawn in absolute units in

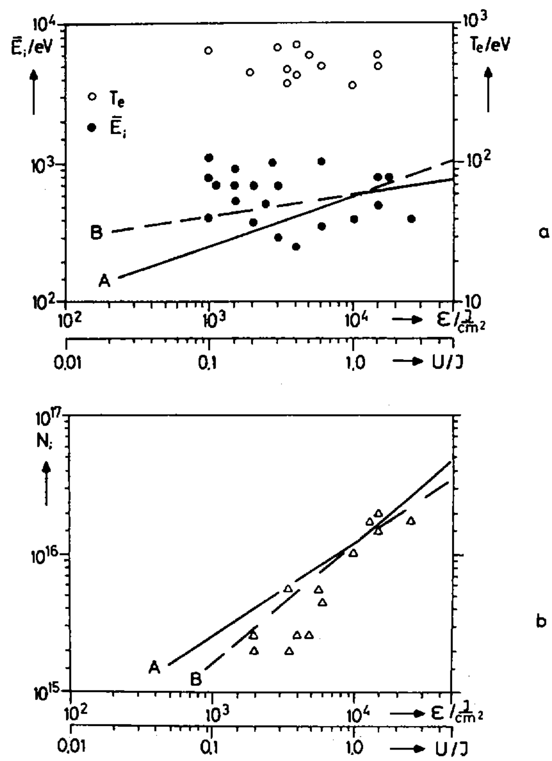

FIG. 6. a) Electron temperature T_e and mean ion expansion energy E_i versus energy density ϵ and laser energy u (picosecond pulses). b) Total number of ions N_i versus energy density ϵ and laser energy u (picosecond pulses).

curve A in Fig. 6a. Our measurements do not show a perceptible variation of the electron temperature and of the ion expansion energy on the energy density ϵ of the laser light which is varied by a factor 10. This might be due to the fact that in the experiment a plane geometry is not realized. Curve B in Figs 6a and 6b give the dependences mentioned for the case of plasma with an instantaneous point source. In this case, the ion energy and electron temperature vary even less with the laser energy than for a plane geometry and fit better the experimental data.

6. DISCUSSION OF THE RESULTS

In Table I the experimental results obtained with nanosecond pulses are opposed to those from the numerical calculations. The experimental data seem to be consistent with those calculated for $3.3 \times 10^{12} < \Phi < 10^{13}$ W/cm^2. Remaining differences may be attributed to the fact that in the calculations a plane geometry was assumed whereas in the experiment a lateral expansion takes place.[1]

However, there are, on the other hand, indications that the model underlying the calculations does not cover all processes occurring in the plasma. First, in the experiments with solid hydrogen and deuterium always energetic X-rays with an intensity much higher than expected for a thermal plasma were observed. In addition, fast ions with energies well over kT_i are ejected from the plasma. As the neutron yield is correlated with the appearance of these ions we can by no means be sure that in our experiments all the neutrons are born in a thermal plasma. We remember, in this connection, also the fact that in our experiment neutron emission does not seem to be restricted to the duration of the laser pulse but lasts for several tenths of nanoseconds where the initially hot and dense plasma is already in a state of rapid expansion. It should be kept in mind, however, that in our experiment the laser intensity has just reached the threshold for neutron production and is lower than in Ref. [7], in which such an excess of neutrons at late times has not been reported.

The irradiation of the target with picosecond pulses turned out to be an extremely difficult and scarcely practical way for the achievement of very high power densities. This is due to the lack of reproducibility in the mode-locking of the oscillator, self-excitement of the high gain amplifier chain and formation of filaments in the laser glass. However, single clean pulses could in some shots be obtained. Only such pulses were evaluated for obtaining Figs 6a and 6b.

One of the most remarkable features results from a comparison of the mean kinetic energy E_i of the expanding ions and the thermal energy $(3/2)kT_e$ of the electrons in the hot plasma. Whereas with ns pulses, E_i was found to be greater than $(3/2)kT_e$ by at least a factor 2 ... 3, thus indicating that the plasma is set into motion during heating, in the case of psec pulses E_i equals $(3/2)kT_e$ corresponding to a plasma at rest during heating. Thus, as our measurements show, the abovementioned heat wave model seems to be an appropriate description of plasma formation with picosecond pulses.

---

[1] Comparison of the experimental data with recent numerical results obtained for a spherical geometry which probably approaches better the experimental conditions show an even better agreement for $\Phi \approx 10^{13}$ W/cm^2.

One of the most important problems is that of absorption and reflection of the laser light. The numerical calculations are based on absorption due to inverse bremsstrahlung in the optical approximation. Assuming that the laser light is totally reflected at the point where $n = n_{crit}$ is reached, a time-dependent reflection coefficient can be obtained from these calculations. The dashed curve in Fig. 2, which shows the calculated intensity of reflected light, was obtained by multiplying the intensity of the incident light with this reflection coefficient. Though exact agreement between the calculated and the measured curve cannot be expected as neither geometry nor pulse shape in the experiment are exactly those of the calculations, the intensity and pulse shape of the measured reflected light are in rough agreement with the calculated curve. Thus the classical absorption mechanism assumed seems to be consistent with the experimental data. It should be mentioned, however, that the experimentally determined reflection coefficient is significantly lower than the calculated one if such a comparison is made with the numerical results obtained in a spherical geometry. With pico-second pulses almost complete reflection of the laser light should be expected assuming collisional absorption. This was not observed experimentally. Thus other absorption mechanisms might have to be considered at these high intensities.

REFERENCES

[1] FLOUX, F., COGNARD, D., DENOEUD, L.G., PIAR, G., PARISOT, D., BOBIN, J.L., DELOBEAU, F., FAUQUIGNON, C., Phys. Rev. 1 3 (1970) 821.

[2] SIGEL, R., KRAUSE, H., WITKOWSKI, S., J. Phys. E: scient. Instrum. 2 2 (1969) 187.

[3] SIGEL, R., Z. Naturforsch. 25a 4 (1970) 488.

[4] SIGEL, R., WITKOWSKI, S., BAUMHACKER, H., BÜCHL, K., EIDMANN, K., HORA, H., MENNICKE, H., MULSER, P., PFIRSCH, D., SALZMANN, H., MPI für Plasmaphysik, Garching, Report IPP IV/9 (1971).

[5] MULSER, P., Z. Naturforsch. 25a 2 (1970) 282.

[6] CARUSO, A., GRATTON, R., Plasma Phys. 11 10 (1969) 839.

DISCUSSION

G. J. YEVICK: What was the diameter of your focal spot, and what size pellet did you use?

R. SIGEL: The diameter of the focal spot was about 100 microns. Its size is determined mainly by the angular divergence of the laser beam; the solid deuterium ice was in the form of round discs with a diameter of 2 mm and a thickness of 1 mm.

G. J. YEVICK: What is the physics behind such a large focal spot?

R. SIGEL: The laser beam was focussed on the centre of the disc i. e. on a plane surface.

E. H. BECKNER: Have you attempted to find the most efficient position in the target for focussing the laser?

R. SIGEL: The intensity of the X-rays and of the reflected laser light, and also the neutron yield, depend critically on the distance of the focussing lens from the target. At the beginning of each series of shots we looked for the optimum lens position by observing the intensity of these quantities.

Moving the lens more than 100 microns relative to the target reduces the signals considerably. For various reasons the absolute position of the focal plane is very difficult to determine.

E.H. BECKNER: Have you irradiated any materials other than D_2 ice, for example CD_2 or LiD?

R. SIGEL: Solid deuterium is the only fusionable material which has been used.

K. PAPADOPOULOS: Magnetic fields spontaneously created near the focus, as a result of thermoelectric currents or pressure gradients, could alter the dynamics of the expansion. Such fields, of the order of 1 kG, have been observed in the laser experiment at N.R.L. Did you measure any such fields in your experiment? Effects of this kind in the exponsion dynamics might account for the discrepancy between the computations and the experimental data.

R. SIGEL: Thank you for bringing this to our attention. We have not tried to measure magnetic fields in the plasma, so we do not know whether such fields exist.

R.L. MORSE: Do you have any absorption measurements for pulses less than one nanosecond?

R. SIGEL: Reflection measurements with picosecond pulses have been made. These are discussed in the printed paper.

F.R. SCHWIRZKE: In curve b of Fig. 3 enhanced X-ray emission is observed at higher energies. Is this observation due to the limited time resolution of the detector? In other words, does the plasma start to expand during the time of observation while the temperature decreases? Or do you assume that the observation indicates a deviation from a Maxwellian velocity distribution and possibly the occurrence of laser-induced instability?

R. SIGEL: The X-ray spectrum obtained certainly seems to indicate a deviation from a Maxwellian electron velocity distribution. The slope at the high-energy end of the measured range can hardly be interpreted as a transient temperature. A temperature of 2 keV, or even more in some series, is incompatible with the other experimental data as well as with the results of the numerical calculations. This is not affected by the time resolution of the detectors. The curve you mentioned was determined from the maxima of the X-ray signals, which occur at the same time. Time resolution was 5-10 ns and the time correlation between the four photomultipliers used simultaneously at each shot was even better. A maximum temperature of 500 eV or even somewhat lower, as derived from the slope of the curve at the low-energy end of the measured range, seems to be quite consistent with the other data. Of course the temperature will start from zero, reach its maximum value and then decay after the end of the pulse. This is difficult to evaluate however as the laser pulse duration is of the same order as the time resolution of the X-ray detectors. Note also that measurements with a carbon target, where no hard X-rays are observed, demonstrate the reliability of the apparatus. An example of these measurements is given in the printed paper.

APPLICATION A LA FUSION CONTROLEE DES PLASMAS DENSES CREES PAR LASER

J.-L. BOBIN, F. FLOUX, G. TONON
CEA, Centre d' etudes de Limeil,
Villeneuve-Saint-Georges, France

Abstract — Résumé

THE APPLICATION OF LASER-PRODUCED DENSE PLASMAS TO CONTROLLED FUSION.

Having recalled the main results obtained from the interaction of a powerful laser beam with a target the authors describe the thermal models permitting their interpretation. The good agreement of experiment and theory allows the calculation of the conditions prerequisite for fusion. If they cannot all be realized in an immediate future it should nevertheless be noted that it is within the range of present technology to obtain temperatures of the order of 10^{8}° K in the course of interaction with a deuterium target.

APPLICATION A LA FUSION CONTROLEE DES PLASMAS DENSES CREES PAR LASER.

Après avoir rappelé les principaux résultats obtenus dans l' interaction d' un puissant faisceau laser avec une cible, les auteurs décrivent les modèles thermiques qui permettent de les interpréter. Le bon accord entre l' expérience et la théorie permet à calculer à partir de là les conditions à réunir pour la fusion. Si elles ne peuvent être toutes réalisées dans un avenir immédiat, on doit cependant remarquer qu' il paraît à la portée des techniques actuelles d' obtenir des températures de l' ordre de 10^{8}°K au cours de l' interaction avec une cible en deutérium.

1. INTRODUCTION

Rappelons les conditions bien connues pour un réacteur à fusion [1] utilisant la réaction DT, soit:

$$T > 10^{8}\,°K$$

$$n\,\tau > 10^{14}\ s/cm^{3} \qquad (1)$$

La première est la plus restrictive, la seconde autorisant une grande variété de dispositifs. C'est ainsi que parallèlement aux études sur les configurations à basse densité et confinement aussi long que possible, des recherches sont menées depuis longtemps sur des plasmas plus transitoires dont la haute densité compense la brève durée de vie. La comparaison des différentes voies peut se faire sur un diagramme où sont portées: en ordonnée les densités d'énergie atteintes dans le combustible thermonucléaire et en abscisse les durées de vie du plasma (fig. 1). Les conditions de Lawson apparaissent comme une sorte de pente (-1) au-dessus de laquelle les points représentatifs des conditions d'un réacteur thermonucléaire doivent obligatoirement se trouver. Il est remarquable de constater que les points représentatifs des machines à plasmas que l'on pense pouvoir extrapoler jusqu'aux conditions de fusion, s'alignent sensiblement sur une parallèle à la droite de Lawson. Les chiffres pour les machines lentes sont tirés d'un article de Pease [2]. Ceux concernant les plasmas produits par laser au néodyme se refèrent aux expériences de l'Institut Lebedev à

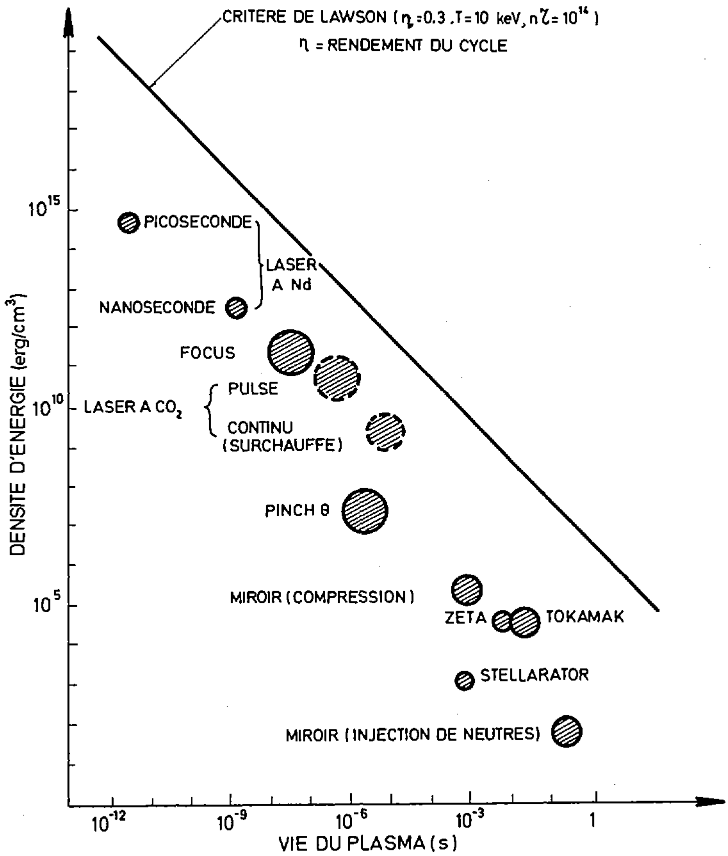

FIG. 1. Plasmologie comparée au critère de Lawson.

Moscou [3] pour les picosecondes et aux expériences de Limeil [4]. Ceux pour les lasers à CO_2 résultent de calculs développés à Princeton pour les systèmes continus [5], à Limeil pour les systèmes pulsés. L'écart avec les conditions de fusion est de 2 à 3 ordres de grandeur. Les plasmas créés par laser apparaissent bien placés dans ce diagramme. Il convient cependant de tempérer cet élément favorable en raison des remarques suivantes:

- le diagramme ne rend pas compte de l'écart technologique entre les expériences de laboratoire de 1971 et ce que pourraît être un véritable réacteur à fusion;
- l'énergie minimale nécessaire dépend, comme on le verra, de la qualité du confinement. Or, un champ de 3 mégagauss qui constitue la limite supérieure de ce que l'on sait faire à l'heure actuelle au laboratoire correspond à une densité d'énergie d'environ $5 \cdot 10^{11}$ erg/cm^3 (β = 1) déjà nettement «explosive». C'est ainsi que la décharge Focus où des conditions voisines sont approchées dans la phase intéressante, a un

comportement remarquablement transitoire. De même, il apparaît que le laser à verre au néodyme conduit à des plasmas que l'on n'arrivera pas à confiner.

Ainsi, contrairement aux machines à basses densité pour lesquelles le problème principal est le temps de confinement, il s'agit essentiellement de chauffer un milieu et de lui communiquer une énergie d'autant plus grande que le confinement sera plus mauvais ou absent.

2. GENERALITES SUR LES EXPERIENCES POURSUIVIES A LIMEIL

Commencées en 1964 avec des expériences de claquage des gaz, ces études ont rapidement évolué vers les plasmas créés en irradiant une cible solide. Ceux-ci sont beaucoup plus intéressants du point de vue du chauffage: en effet, la densité de coupure correspondant à la fréquence de l'onde laser (10^{21} électrons cm^{-3} pour le verre au néodyme $\lambda = 1,06\ \mu m$, 10^{19} électrons cm^{-3} pour le CO_2 $\lambda = 10\ \mu m$) est très inférieure à la densité du solide et sera donc nécessairement atteinte dans le mouvement de détente du plasma qui reçoit le flux. Or, il est bien connu [6] que la température d'un plasma chauffé par une absorption linéaire du rayonnement (formule de Kramers) est une fonction croissante de la densité.

Nous utilisons deux sortes de cible: des surfaces métalliques lorsque nous attendons de l'interaction qu'elle produise des ions lourds multichargés; (nous avons observé par exemple du fer 20 fois ionisé [7]); lorsqu'il s'agit au contraire de chauffer au maximum un milieu léger, la cible est soit du polyéthylène, soit du deutérium solide sous la forme de bâtonnets à la température de 10°K.

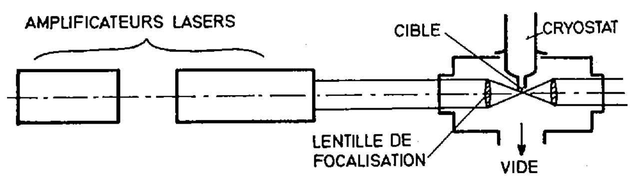

FIG.2. Schéma d'une expérience d'interaction.

Pour obtenir, à puissance laser donnée, un flux maximal sur la cible, le faisceau est focalisé au moyen de lentilles plan-asphériques de grande ouverture, spécialement calculées et taillées pour cet usage [8]. L'ensemble cible + objectif de focalisation est placé sous vide (fig. 2). Dans l'un de nos montages, il est possible de produire le plasma dans un champ magnétique de plusieurs centaines de kilogauss. Ce champ est obtenu au centre d'un enroulement à un tour, secondaire d'une transformation d'intensité. On peut lui donner aisément une configuration à miroirs (deux spires alimentées en parallèle). Il n'est limité que par la tenue mécanique des matériaux constituant la ou les spires.

Les mesures concernent: le faisceau laser lui-même, les températures électroniques T_e et ioniques T_i, la densité et la vitesse du plasma dans l'écoulement, les neutrons émis lors d'éventuelles réactions nucléaires. T_e est mesuré par la classique méthode des absorbants; une

TABLEAU I. EXPERIENCES AVEC DIVERS LASERS A NEODYME

Energie incidente (J)	Largeur d'impulsion (ns)	Front de montée	Flux maximum atteint (W/cm²)	Cible	Température électronique	Neutrons
100	40	$\times 10$ en 30 ns	$5 \cdot 10^{12}$	deutérium	500 eV	-
3	30	$\times 10$ en 30 ns	10^{12}	fer	200 eV	-
40	40	$\times 10$ en 30 ns	10^{12}	polyéthylène	200 eV	-
30	7	$\times 10^3$ en 3 ns	10^{13}	deutérium	> 700 eV	$2,5 \cdot 10^3$
70	4	$\times 10^5$ en 1,5 ns	$5 \cdot 10^{13}$	deutérium	> 1 keV	$3 \cdot 10^4$

évolution de T_i résulte de l'examen des spectres de particules chargées émises par le plasma. Pour les densités, nous utilisons les méthodes interférométriques (Jamin ou holographie), et une évaluation des vitesses est déduite des clichés pris au moyen d'une caméra à fente. Les neutrons sont détectés soit par des scintillateurs de grandes dimensions lorsqu'il s'agit d'en connaître l'énergie au moyen d'une mesure de temps de vol, soit par des compteurs à BF_3 lorsqu'on veut connaître leur nombre. Les dimensions et la sensibilité de ces détecteurs sont adaptés aux faibles flux que nous avons obtenus jusqu'à présent.

Le tableau I rassemble les principaux résultats obtenus avec différents lasers à verre au néodyme. Il met en évidence l'importance du flux sur la cible et du temps de montée de l'impulsion. Celle-ci est mise en forme au moyen de cellules de Pockels. La dynamique de 10^6 en $1,5 \cdot 10^{-9}$ s résulte du passage de l'impulsion à travers deux cellules à ouverture rapide commandées par le faisceau laser lui-même (fig. 3).

Les expériences avec le laser moléculaire à CO_2 ne font que commencer. Elles sont très intéressantes pour l'application à la fusion comme nous le verrons plus loin.

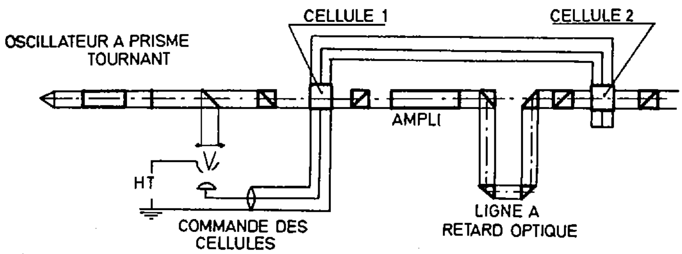

FIG. 3. Dispositif de découpage de l'impulsion laser (front de montée rapide).

3. RESULTATS EXPERIMENTAUX

Au moyen des différentes mesures mises en place autour de l'expérience, nous recueillons un ensemble d'informations qui bien qu'incomplètes nous permettent d'avoir une certaine idée des caractéristiques du plasma et de son évolution.

L'énergie laser reçue par la cible se répartit entre une énergie réfléchie ou diffusée, de l'énergie thermique et de l'énergie cinétique communiquées au matériau de la cible. Aussi convient-il d'abord de connaître l'énergie effectivement absorbée. Nous avons pu vérifier que la part diffusée ou transmise était négligeable (moins de 1%). Par contre, une part importante est réfléchie, comme le montre la figure 4. Si l'on connaît le profil de densité, cette mesure permet de remonter indirectement à la température du plasma. La réflexion est importante surtout dans le cas d'un laser très puissant et à front de montée raide. Elle est d'autant plus grande que la focalisation est meilleure (flux maximal sur la cible) et l'on a trouvé expérimentalement entre l'énergie réfléchie ϵ_r et incidente ϵ_i la relation

$$\epsilon_r \propto \epsilon_i^{7/6} \qquad (2)$$

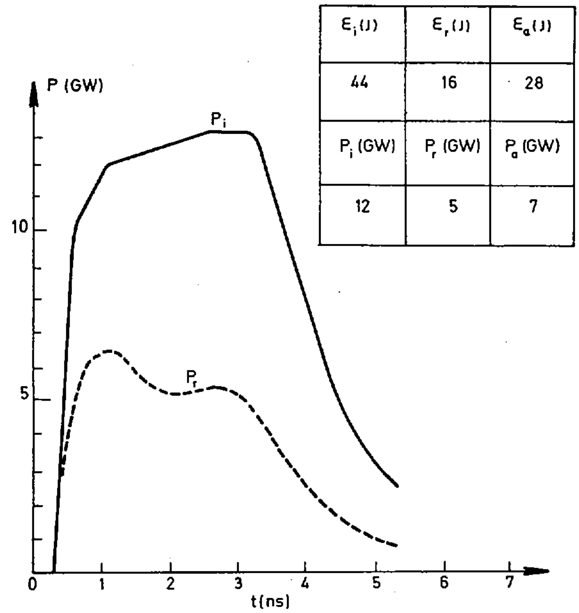

$\mathcal{E}_i$(J)	$\mathcal{E}_r$(J)	$\mathcal{E}_a$(J)
44	16	28
P_i (GW)	P_r (GW)	P_a (GW)
12	5	7

FIG. 4. Impulsions laser incidente et réfléchie (cible de deutérium solide).

La réflexion diminue en fin d'impulsion. Outre la perte de rendement, ce phénomène est dangereux pour la vie du laser dont la chaîne d'amplificateurs doit être spécialement protégée par des rotateurs de Faraday et des cellules de Pockels, contre l'amplification en retour de la lumière réfléchie. Des impulsions plus longues à puissance égale nous semblent devoir conduire d'autre part à une meilleure utilisation de l'énergie.

Les profils de densité électronique ont été déterminés à l'aide d'un interféromètre de Jamin éclairé par de la lumière prélevée sur le faisceau d'interaction. Le détecteur est la photocathode d'un convertisseur d'images dont le temps de pose est de 1 ns. L'impulsion laser a une puissance d'environ 1 GW pour une largeur à mi-hauteur de 30 à 40 ns. La cible est du polyéthylène. La figure 5 montre les profils de densités obtenus en dépouillant les interférogrammes avec et sans champ magnétique. Dans ce dernier cas la densité maximale obtenue dans le bourrelet est proportionnelle au carré de l'induction. Une mesure de température électronique par la méthode des absorbants n'a pas révélé d'influence détectable du champ sur la température. Il n'en serait pas de même avec un laser moléculaire à CO_2 car alors à champ égal, on aurait une absorption plus forte du rayonnement. En l'absence de champ des ions sont recueillis par un analyseur électrostatique placé assez loin de la cible. On trouve une distribution en énergie gaussienne et la largeur du spectre donne une même température pour les différentes espèces (fig. 6). Cette température, relative à une phase de l'évolution dans laquelle les distributions sont gelées, ne peut être comparée sans précaution aux températures électroniques mesurées à l'instant même où elles existaient.

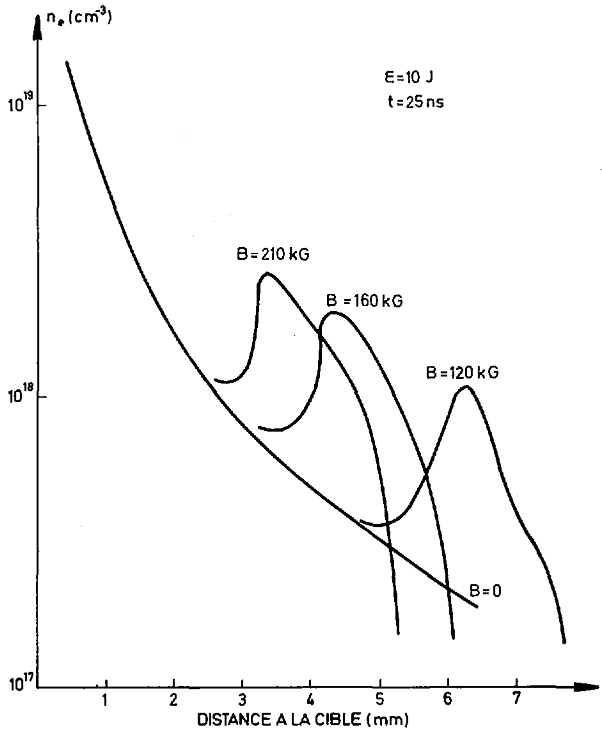

FIG. 5. Profils de densités en fonction du champ magnétique. Les lignes de force sont parallèles à la cible donc perpendiculaires au sens de l'écoulement. L'instant de prise de vue est repéré par rapport au sommet de l'impulsion laser.

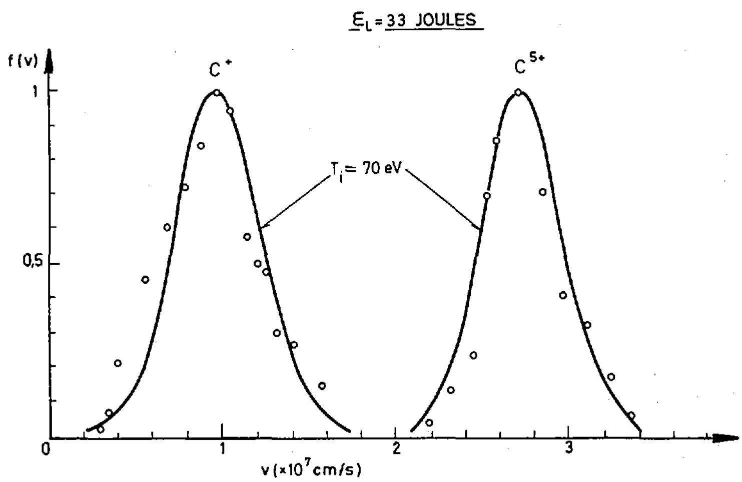

FIG. 6. Détermination d'une température ionique à partir du spectre des ions de deux états de charge différents.

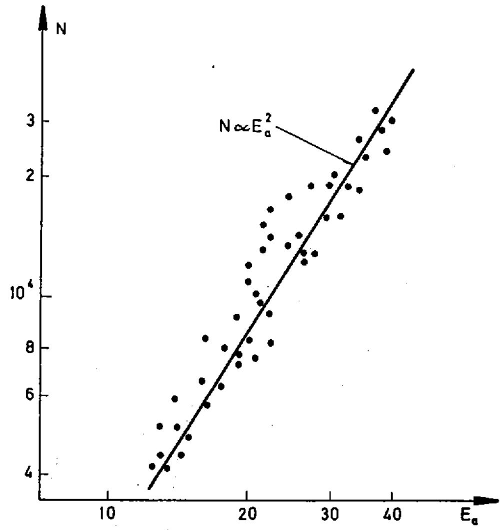

FIG. 7. Nombre de neutrons par tir en fonction de l' énergie absorbée. La mesure est faite avec un compteur au BF_3.

Dans le cas des cibles lourdes, c'est l'état de charge le plus élevé recueilli par l'analyseur qui peut être relié à la température règnant dans le plasma. C'est ainsi que nous avons pu faire une comparaison entre un laser à neodyme et un laser à CO_2. Les mêmes ions (F_e^{12+}) ont été obtenues dans le deuxième cas avec un flux incident 100 fois plus faible.

Contrairement aux méthodes précédentes, la détection des neutrons ne nous permet pas encore de caractériser le plasma. Les émissions que nous avons obtenues jusqu'ici en irradiant du deutérium solide sont, en effect, beaucoup trop faibles. Par contre, il nous a été possible, au moyen du plus puissant laser que nous exploitons, de déterminer la variation du nombre N de neutrons produits en fonction de l'énergie E_a effectivement absorbée par la cible. Les résultats montrent (fig. 7) que dans la gamma explorée

$$\langle N \rangle \propto E_a^2 \tag{3}$$

Nous avons vérifié sur une base de temps de vol de 1, 50 m que les neutrons provenaient bien de l'une des branches de la réaction DD. Nous avons trouvé, en effet, une énergie de 2, 45 ± 0, 37 MeV. Nous avons essayé d'autre part de mettre en évidence une éventuelle anisotropie en flux, en disposant des compteurs à 45° et à 135° de l'axe du faisceau laser. Les différences observées n'ont jamais dépassé l'erreur que l'on doit attendre de nos mesures (environ 20%).

4. THEORIES DE L'INTERACTION AVEC UNE CIBLE ET COMPARAISON AVEC L'EXPERIENCE

Les études théoriques menées parallèlement à l'expérimentation peuvent concerner aussi bien les mécanismes par lesquelles l'énergie laser est transférée au matériau, que l'évolution de l'écoulement du plasma couplée à l'absorption de la lumière. Nous nous sommes surtout intéressés à ce deuxième aspect plus proche de nos expériences. Ainsi avons nous exploré deux sujets: l'écoulement de plasma couplé à l'absorption de photons, et l'interaction d'un tel plasma avec un champ magnétique élevé.

Les écoulements de plasmas sont décrits convenablement dans leurs grandes lignes par le modèle de la déflagration radiative [9] dans lequel le milieu froid non perturbé est séparé du plasma chaud par une zone dont la densité est supérieure à celle du solide mais dont la température reste relativement basse. Les frontières entre ces milieux sont des discontinuités de densité et de pression: front de choc entre milieu non perturbé et son intermédiaire, front de déflagration entre milieu intermédiaire et plasma chaud. Les fronts se déplacent vers l'intérieur de la cible tandis que la matière est éjectée en sens inverse. En fait, le front de déflagration a une structure complexe, il comprend une zone d'interaction de densité inférieure à la coupure ρ_c dans laquelle les photons laser sont absorbés, et une zone de conduction de densité supérieure à la coupure dont le profil dépend de la conduction thermique électronique. Si l'écoulement est monodimensionnel plan, et si le flux demeure constant, on peut trouver des structures stationnaires [10] calculables analytiquement. C'est ainsi que l'on trouve entre le flux absorbé et la température la relation suivante:

$$T_{°K} = 8 \cdot 10^{-9} \left(\frac{\phi}{\rho_c}\right)^{2/3} \quad \text{(cgs)} \tag{4}$$

Cette relation est assez bien vérifiée par l'expérience [11] dans le cas d'un milieu léger (deutérium) à des températures supérieures à 100 eV. Pour l'épaisseur de la zone de conduction il vient (m_i masse des ions, γ coefficient adiabatique, $AT^{5/2}$ conductivité électronique non linéaire):

$$X = \frac{4}{5}\ \frac{\gamma - 1}{5\gamma - 1} \left(\frac{m_i}{k}\right)^{3/2} A\ T^2/\rho_c \tag{5}$$

Ces formules établies dans le cas d'un fluide unique doivent être modifiées pour les hautes températures où l'on doit s'attendre à un découplage entre ions et électrons. Toutefois, dans les cas stationnaires l'écart en température ne dépasse pas 20%.

Bien évidemment, les situations calculables analytiquement sont fort éloignées de la réalité expérimentale. D'abord, le flux sur la cible est constamment variable. Ensuite, on observe une forte détente latérale du plasma chaud; ainsi l'écoulement n'est certainement pas monodimensionnel plan. De plus, il faut tenir compte du découplage électrons ions particulièrement important dans les cas instationnaires lorsque le flux a une croissance très rapide. Enfin, aux très haut flux, l'absorption de la lumière par les électrons du plasma peut se faire suivant d'autres mécanismes que le Bremsstrahlung inverse linéaire. En ce qui concerne ce dernier point, la physique de l'interaction est loin d'être complètement élucidée et fait l'objet de nombreuses études théoriques aussi bien qu'expérimentales qui n'en sont qu'à leurs débuts.

Si donc on veut établir une théorie qui puisse prendre en compte le problème de l'interaction avec une cible dans toute sa complexité, il convient de revenir à un code numérique. La mise au point d'un tel code ne peut se faire que par étapes. Dans un premier temps le fluide n'a qu'une seule composante, la lumière est absorbée mais non réfléchie à la coupure (un seul sens de propagation) et l'écoulement est pseudo-bidimensionnel: le faisceau focalisé est assimilé à un cône dont l'ouverture est celle de la lentille, sauf au voisinage du foyer où on le confond avec un cylindre dont le rayon est celui de la tache focale. L'écoulement est confiné à l'intérieur de la caustique ainsi idéalisée: à l'intérieur du cylindre il est monodimensionnel plan, dans la partie conique il est monodimensionnel sphérique. L'impulsion laser a une évolution temporelle aussi semblable que possible à la réalité. La figure 8 reproduit à un instant donné, proche du sommet de l'impulsion, les profils de température, densité et flux fournis par le code. L'épaisseur de la zone de conduction déterminée ainsi est assez proche du résultat d'un traitement analytique approché reposant, il est vrai, sur les mêmes équations de conservation.

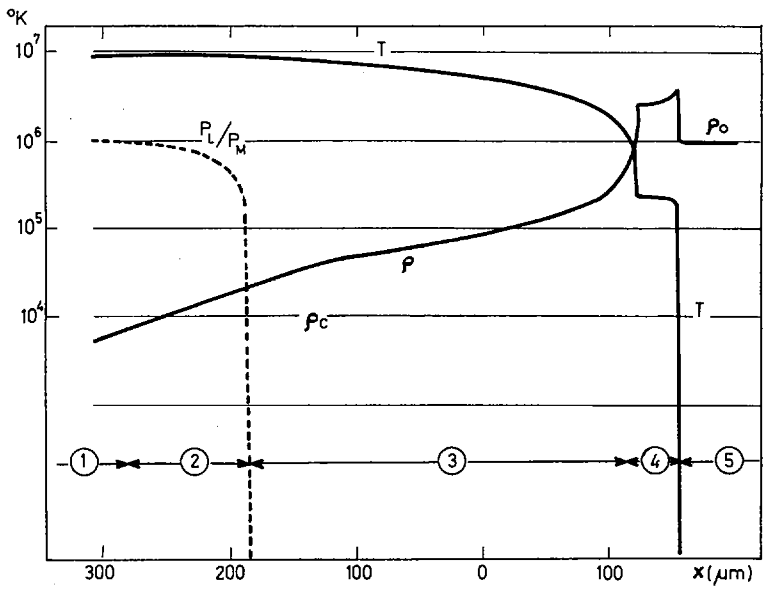

FIG. 8. Profils de densité, température et flux laser à un instant donné. La cible est du deutérium initialement à 10°K:

1 - détente
2 - zone d' interaction
3 - zone de conduction
4 - zone de choc
5 - solide non perturbé.

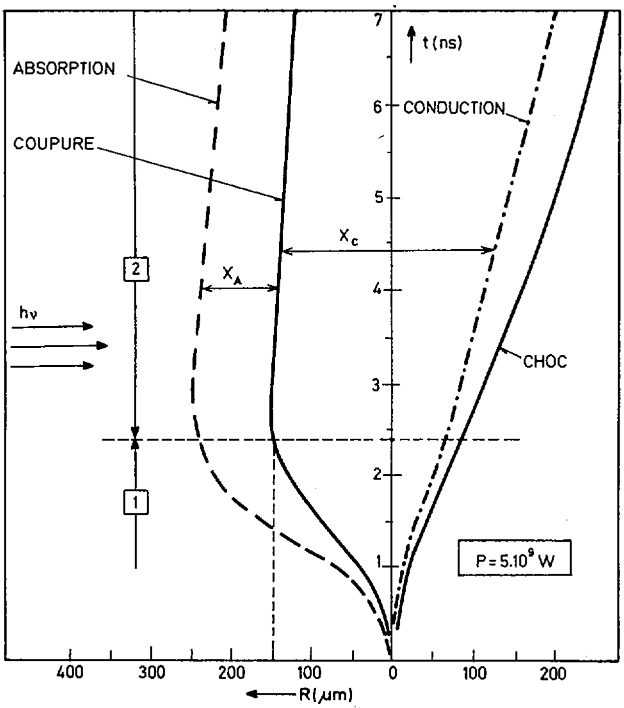

FIG. 9. Diagramme (R, t) de l'écoulement pour une puissance laser de 5 GW.

La figure 9 décrit le mouvement des différents fronts dans le cas d'une impulsion du plus puissant laser à neodyme dont nous disposons tombant sur du deutérium initialement à l'état solide. Sur les clichés de caméra à fente, le plasma ejecté est limité par un front lumineux diffus correspondant à une densité inférieure à la coupure pour laquelle le rayonnement est juste suffisant pour impressionner le détecteur et dont le mouvement suit assez bien celui prédit par le code pour la zone à la densité de coupure ρ_c [12]; l'ordre de grandeur des températures prédites par le code s'accorde également aux prévisions des modèles analytiques et aux mesures de température électroniques. Les mesures de densité par interférométrie n'ont jusqu'ici donné de résultats que loin de la cible là où la densité est basse. Les profils obtenus correspondent à une détente sensiblement isotherme ainsi que le prévoit le code.

Les étapes ultérieures de la mise au point sont d'abord l'introduction de la réflexion de la lumière à la fois sur le gradient de densité et à la coupure, puis le passage à un fluide à deux composantes ions et électrons. Enfin, suivant les progrès de la physique de l'interaction, on sera conduit à modifier la loi d'absorption de la lumière par le plasma.

Dans le cas d'une cible à Z élevé, la complexité du milieu est un sérieux défi même aux méthodes numériques. Aussi n'a-t-on jusqu'ici procédé qu'à des évaluations de paramètres caractéristiques au moyen de théories très simples. En particulier, l'état d'ionisation des différentes espèces doit être déterminé à partir d'un modèle coronal. Une grandeur intéressante est le temps τ_i nécessaire à l'apparition d'un état de charge donné Z_i. Appelant S_{ci} et α_{ri} respectivement les coefficients d'ionisation par collision et de recombinaison radiative, le modèle coronal donne

$$\frac{1}{n_e \tau_i} = S_{ci}(Z_i, T_e) - \alpha_{ri}(Z_i, T_e) \tag{6}$$

ce qui permet de tracer $n\tau$ en fonction de T_e pour les différents états de charge comme nous l'avons fait sur la figure 10 pour le fer. Pendant l'interaction, les ions traversent une zone à haute température dont l'épaisseur est de l'ordre de X en un temps X/v ($v \propto T_i^{1/2}$). Il en résulte que l'on a

$$n_e \tau_i \propto \frac{T^{3/2}}{Z} \left(n_e \sim \frac{\rho_c}{m_i} \right) \tag{7}$$

ce qui détermine sur chaque courbe de la figure 10, le point de fonctionnement et par suite la température minimale qu'il convient d'atteindre pour obtenir un état de charge donné. Le recoupement avec les mesures de températures électroniques pour la méthode des absorbants est satisfaisant.

Le dernier type d'étude théorique que nous avons menée, l'interaction du plasma produit avec un champ magnétique élevé, est aussi examinée avec un code numérique. Les calculs mettent en évidence, pendant la détente, un bourrelet de densité très analogue, en rapport de compression et en épaisseur, à celui qui a été observé par interférométrie (fig. 5).

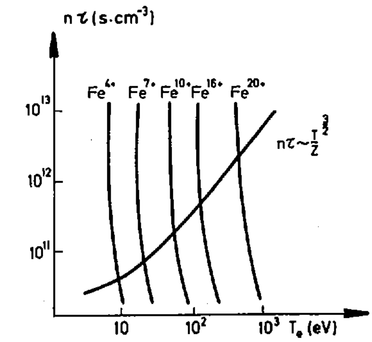

FIG. 10. Détermination de la température de formation d'un état d'ionisation donné.

5. APPLICATION A LA FUSION CONTROLEE

Les premières évaluations des plasmas créés par laser quant à la fusion contrôlée [13, 14] ont été faites avant que l'on connaisse dans le détail les mécanismes d'interaction. La possibilité d'obtenir de très hautes températures a été reconnue tout de suite et confirmée par de nombreuses expériences. Le problème porte ainsi essentiellement sur la manière de satisfaire à la deuxième condition de Lawson, $n\tau > 10^{14}$, et en particulier sur l'énergie minimale nécessaire pour y arriver.

Les résultats de nos diverses expériences avec des lasers à néodyme à impulsion nanoseconde montrent que le produit $n\tau$ y est de l'ordre de 10^{12} s/cm^3. D'autre part, la comparaison des modèles théoriques aux résultats expérimentaux ayant montré un accord satisfaisant, il nous est loisible de procéder à quelques extrapolations. La relation (4) nous permet de définir le flux sur la cible nécessaire à obtenir la température de 10^8°K. On trouve pour une cible en DT:

$$\begin{cases} \phi = 5 \cdot 10^{14}\ \mathrm{W/cm^2} \text{ avec un laser à néodyme} \\ \phi = 5 \cdot 10^{12}\ \mathrm{W/cm^2} \text{ avec un laser à } CO_2 \end{cases} \tag{8}$$

Ces valeurs ne sont pas très éloignées de ce que nous savons faire à l'heure actuelle avec des impulsions nanosecondes. Il est donc raisonnable de penser que dans un avenir proche, des températures dites thermonucléaires seront effectivement atteintes.

D'autre part, connaissant la structure de déflagration radiative en fonction du flux sur la cible (ou ce qui revient au même en fonction de la température maximale), il nous est relativement aisé de calculer le nombre de réactions thermonucléaires qui peuvent s'y produire. Reprenons alors le raisonnement de Lawson. Soient η le rendement de conversion de tout le cycle énergétique (énergie laser $\rightarrow$ énergie thermonucléaire $\rightarrow$ énergie thermique $\rightarrow$ énergie électrique $\rightarrow$ énergie laser) et R le rendement du réacteur. Dans le cas de la déflagration radiative:

$$R = \frac{\text{énergie libérée par les réactions nucléaires}}{\text{énergie rayonnée + énergie (thermique + cinétique) du plasma}} \tag{9}$$

La condition à remplir est

$$\eta\,(R + 1) > 1 \tag{10}$$

Or, le calcul de R dans le modèle de la déflagration montre qu'il dépend de la température et du temps suivant les courbes de la figure 11. Les temps correspondent au laser à verre au néodyme; ils seraient 100 fois plus long dans le cas du laser moléculaire à CO_2. A chaque valeur de η correspondent des conditions sur le temps et la température. L'énergie minimale par cm^2 correspond au cas où η = 0, 3, T $\sim$ 10^8°K ($\phi = 5 \cdot 10^{14}$ W/cm^2). Alors on doit avoir:

$$\begin{aligned} \tau &> 2 \cdot 10^{-7} \text{ s pour le verre au néodyme} \\ \tau &> 2 \cdot 10^{-5} \text{ s pour le } CO_2 \end{aligned} \tag{11}$$

Et il faut fournir au moins 10^8 J/cm^2 de cible [15].

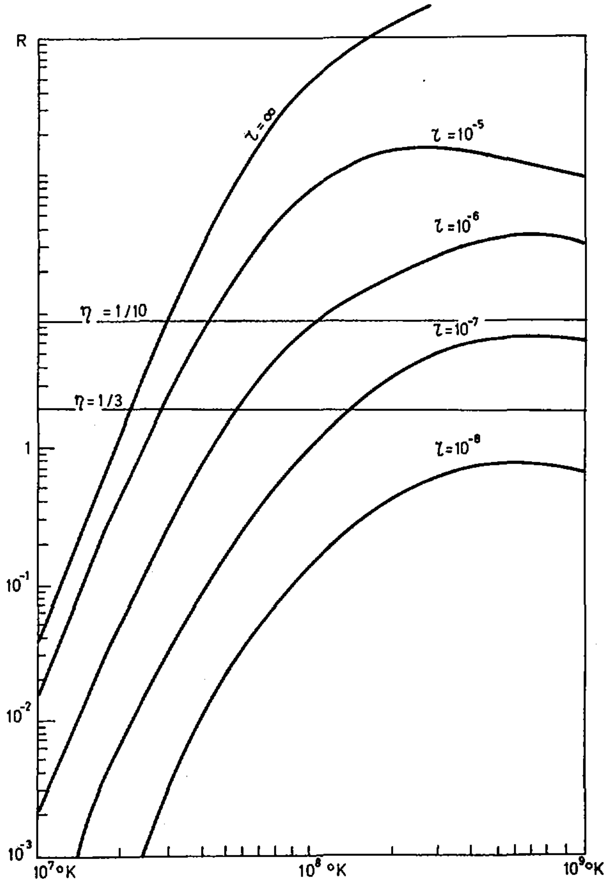

FIG. 11. Détermination des conditions de bilan d' énergie positif pour une déflagration radiative entretenue par un laser à verre au néodyme.

Ces résultats correspondent à un écoulement monodimensionnel plan. Celui-ci ne peut être maintenu que par un confinement inertiel ou magnétique. Dans ce dernier cas, les valeurs de champ à appliquer sont de 30 MG ($n \sim 10^{21}/cm^3$) pour le néodyme et seulement 3 MG ($n \sim 10^{19}/cm^3$) pour le CO_2. La première de ces valeurs paraît définitivement être hors d'atteinte. L'application du modèle monodimensionnel plan de la déflagration radiative à la fusion apparaît ainsi limitée au CO_2 en présence d'un fort confinement magnétique. Si la surface de cible à irradier est limitée uniquement par des considérations d'optique, l'énergie minimale à fournir est alors de $1,5 \cdot 10^7$ J.

Cette valeur se situe à la limite inférieure des évaluations qui ont pu être faites pour divers processus d'interaction laser matière. La moyenne se situe aux environs de 10^9. Situant, sur l'échelle des énergies, le réacteur à des valeurs supérieures à $1,5 \cdot 10^7$ J, la zone des expériences significatives peut se trouver à partir de 10^4 J pour l'impulsion laser.

Cette énergie, à fournir en plusieurs nanosecondes, est de deux ordres de grandeur supérieure aux meilleures réalisations actuelles.

Un autre point doit être signalé. Le facteur η comprend évidemment le rendement du laser. Or, le laser à néodyme a un très mauvais rendement: 2‰. Par contre, le laser à CO_2 même pulsé atteint facilement 10% et peut encore être augmenté. Cette propriété et la plus grande facilité de confinement font du laser à CO_2 un outil particulièrement adapté à des recherches sur la fusion.

6. CONCLUSION

Les études tant expérimentales que théoriques effectuées à Limeil confirment l'intérêt des plasmas denses créés par laser pour la fusion.

La réalisation de la deuxième condition de Lawson est cependant très incertaine. Elle exige des énergies sans commune mesure avec l'état actuel de la technique. Une solution verra peut-être le jour avec de très puissants lasers moléculaires pompés par des réactions chimiques, donc à bon compte.

Par contre, il apparaît que des températures de l'ordre de 10^8 °K peuvent dans un proche avenir être atteintes dans les expériences d'interaction d'un faisceau laser avec une cible. Il s'agit là d'une possibilité réellement intéressante pour l'étude des plasmas aux températures requises par les conditions de fusion.

REMERCIEMENTS

Les auteurs tiennent à remercier MM.D. Cognard, A. Saleres, J.F. Benard, J. de Metz, D. Colombant, A. Billebize, D. Schirmann, M. Rabeau, C. Faure, A. Perez pour leur contribution aux recherches dont il est rendu compte dans cette communication.

REFERENCES

[1] LAWSON, J.D., Proc. phys. Soc. 70B (1957) 6.
[2] PEASE, R.S., The growth points of physics, Europ. phys. Soc. (1970) 184.
[3] BASOV, N.G. et al., Soviet Phys. JETP Letts 8 (1968) 14, Journ. of Quantum Electronics QE4 (1968) 864.
[4] FLOUX, F. et al., Phys. Rev. 1A (1970) 821.
[5] DAWSON, J.M., Princeton University Report, MATT 786 (1970).
[6] Perspectives on Controlled Thermonuclear Research, TID 24804 (1968) 40.
[7] TONON, G., FAURE, C., PEREZ, A., C. r. Acad. Sci. (à paraître).
[8] MARIOGE, J.P., de METZ, J., MILLET, F., MAKE, C., Optics technology 2 (1970) 27.
[9] FAUQUIGNON, C., FLOUX, F., Phys. Fluids 13 (1970) 386.
[10] BOBIN, J.L., Bull. Am. Phys. Soc. 15 (1970).
[11] BOBIN, J.L. et al., Nucl. Fusion 9 (1969) 115.
[12] FLOUX, F., COGNARD, D., SALERES, A., BENARD, J.F., C. r. Acad. Sci (à paraître).
[13] BASOV, N.G., KROKIN, O.N., Troisième conférence d'électronique quantique, Paris (1963).
[14] DAWSON, J., Phys. Fluids 7 (1964) 981.
[15] BOBIN, J.L., COLOMBANT, D., TOTON, G., (à paraître dans Nuclear Fusion).

DISCUSSION

P.K. KAW: I think it is rather dangerous to make quantitative predictions for a fusion reaction using lasers by extrapolating present experiments. These experiments seem to indicate that there is a large tail on the ion-velocity distribution; one cannot otherwise explain the observed neutron emission since, in particular, the two-dimensional calculations show that the ions would be too cold. In the absence of any additional knowledge of the ion-velocity distribution, therefore, various questions regarding power requirements, etc., remain unsettled.

J.L. BOBIN: It is true that we don't know the origin of neutron emission. However, the yield is consistent with ion temperature ($\neq T_e$) calculations. The $(E_\Delta)^2$ law might be due to three-dimensional flow or to differences in ion and electron temperatures. Both might contribute. As far as extrapolating to fusion conditions is concerned, the important question is whether the physics will be the same at the required fluxes? We now have evidence of non-linear laser-plasma interactions. Second harmonic generation has been observed with fluxes of the order 10^2-10^{13} W/cm^2 (see M. DECROISETTE, B. MEYER, G. PIAR. To appear in the proceedings of the Tenth Conference on Ionization Phenomena in Gases - Oxford 1971).

T.P. WRIGHT: Have you studied the dependence of neutron production on laser-pulse width?

J.L. BOBIN: Not yet, but we intend to do so in the nanosecond range – 3 to 10 ns, for instance.

T.P. WRIGHT: What is your focal spot size?

J.L. BOBIN: In vacuo the focal spot can be made as small as 10 μ in diameter (half energy). In the presence of a target, owing to refraction effects, the focal spot size is estimated at 100 μ (100 wavelengths), but we have no accurate measurements for the latter case.

W.H. BOSTICK: It is likely, as Schwirzke has shown, that magnetic fields are generated around the laser-produced plasma jet. As the plasma attempts to expand against these fields, one can expect the production of strong turbulence in the form of plasma vortex filaments and, when these vortex filaments combine, one can expect X-rays and neutrons, as are produced in the plasma focus. The vortex filament annihilation is basically the solar flare process.

J.L. BOBIN: Strong turbulence may exist in laser-produced plasma. The most puzzling problem is high-energy ion generation. So far, we have no satisfactory explanation which would account for such a phenomenon.

D.E. POTTER: If Mr. Bobin will excuse me, I would like to remark briefly on the last comment by Mr. Bostick. The filamental structures which Mr. Bostick observes in the coaxial gun, and which he describes as vortices, have not been observed by other authors (for example at this conference Peacock et al. D-3; Maisonnier et al. D-2; and Mather et al. D-5). This may be due to the fact that their experiments are operated at higher energies and densities. Heating in the plasma focus has been described adequately through viscous shock heating in the two-dimensional fluid calculations of Potter (Phys. Fluids, August 1971).

LONG-WAVELENGTH, HIGH-POWERED LASERS FOR CONTROLLED THERMONUCLEAR FUSION

J.M. DAWSON, A. HERTZBERG †, R.E. KIDDER ‡,
G.C. VLASSES†, H.G. AHLSTROM†, L.C. STEINHAUER†
Plasma Physics Laboratory, Princeton University,
Princeton, New Jersey,
United States of America

Abstract

LONG-WAVELENGTH, HIGH-POWERED LASERS FOR CONTROLLED THERMONUCLEAR FUSION.

This paper discusses the possibilities of applying relatively long-wavelength lasers to the problems of obtaining controlled thermonuclear reactions. In particular, the very attractive possibilities opened up by the recent development of high-powered, high-efficiency 10.6-μm N_2-CO_2 lasers are examined. These lasers can effectively heat plasmas in the density range of 10^{17}-10^{19} particles/cm^3 to thermonuclear temperatures. Absorption lengths for 10-μm radiation range from a few tens of centrimetres to a few kilometres, depending on density and temperature; calculations show that the laser beam will be self-focusing and thus confined to the plasma. Such plasmas can be confined by available magnetic fields; for the lower densities, fields of 200-300 kG are required, while at the higher densities fields of 2-3 MG are needed. A number of reactor possibilities are considered. The simplest is a straight device operated in a pulse mode, similar to the θ-pinch configurations considered by Ribe. However, the laser method has the advantage that the magnetic field is not used to produce and heat the plasma. The coils can thus be designed for optimum production of the field with respect to field strength, magnetic energy required, and energy dissipation in the coils. The size of such a device depends on the strength of the magnetic field that can be used and on one's ability to inhibit plasma and heat loss from the ends. For fields of 300 kG, it appears that a working reactor of roughly 500 m is possible; for higher fields shorter devices will suffice, with the length scaling like $1/B^2$. Calculations of the parameters for such devices will be given. Small experiments, using available pulsed hi h-field magnetics and CO_2 lasers, should be able to answer many of the questions related to building such a device. They should also be able to provide hot plasma in a number of different confinement configurations for conducting important experiments. These might include wave propagation, instability, and plasma confinement studies in finite, but adjustable-β, plasmas.

1. INTRODUCTION

Recently, 10.6-μ, high-power, high-efficiency N_2-CO_2 lasers have been developed. Continuous wave power levels of 60 kW have been reported, [1] while the energy per pulse of pulsed devices has risen from millijoules to 130 joules [2] in the last three years. The electrical conversion efficiency can be quite high; over 30% has been achieved in practice. This may be compared to the efficiency of a fraction of 1% for the 1-μ neodymium glass laser.

For the production and heating of plasmas 10-μ radiation has some distinct advantages over 1-μ radiation. Foremost of these is its ability to heat plasmas at relatively low densities, which can be confined by available

† University of Washington, Seattle, Wash., USA.

‡ Lawrence Radiation Laboratory, Livermore, Calif., USA.

magnetic fields. Ten-μ radiation can effectively heat plasmas at densities of 10^{17} to 10^{19} electrons/cm^3, whereas 1-μ radiation becomes ineffective for densities below 10^{19-20}. For a temperature of 10 keV and plasma densities of 10^{17}, 10^{18}, and 10^{19} particles/cm^3 the required confining fields are 2.8×10^5, 9×10^5, and 2.8×10^6 G respectively. The first of these is within the capabilities of steady magnetic field technology and the second within the technology of pulsed fields. The confinement times required to meet the Lawson condition ($n\tau \approx 10^{14}$) are in the range of 10 to 1000 microseconds which fall within the operating ranges of high-powered pulsed CO_2 lasers.

If the laser is used to heat a plasma in a pulsed thermonuclear reactor then the fact that one must obtain more usable fusion energy than is required by the laser places a very high value on efficiency. While the presently obtained electrical conversion efficiency of more than 30% for electrical discharge CO_2 lasers is good it can probably be improved upon. The quantum efficiency is 40% and it has been shown by Nighan [3] that the fractional power transfer of electron energy to upper level vibrational energy can approach 90%. Since the gas, after lasing, is left at a high temperature (about 700° K) an appreciable fraction of its energy could be recovered by a thermal cycle. One can imagine overall efficiencies of 40% to 50%. Finally, it has been shown that in principle (and a specific model system presented which uses gas-dynamic techniques) that heat is convertible to laser energy with thermo-dynamic efficiencies [4].

It is the purpose of this paper to present some of the basic considerations connected with the production and heating of plasmas by means of long-wavelength laser radiation. Some possible thermonuclear reactor configurations are considered. It is also possible to use long-wavelength laser radiation to produce plasmas for experiments. They offer a unique, highly controllable, and quiescent method for producing a hot plasma in almost arbitrary magnetic geometry, independent of the method of producing the field. Such hot plasmas might be produced under conditions that are difficult or impossible to achieve by other methods (for example, inside a cold gas or cold plasma blanket).

The calculations which are presented are intended to be exploratory in nature; no effort has been made to make highly accurate numerical estimates. The transport formulae used are those obtained from arguments based on mean free paths and mean free times between collisions.

2. ABSORPTION OF LASER RADIATION

2.1 Inverse Bremsstrahlung

Central to the problem of heating a plasma by means of lasers is the absorption of radiation. The simplest absorption process is that of inverse bremsstrahlung or resistive absorption due to electron-ion collisions. This absorption process gives an absorption length of

$$\ell_{ab} = \frac{5 \times 10^{27}\, T_e^{3/2}}{n_e^2 Z \lambda^2} \left(1 - \frac{\lambda^2}{\lambda_p^2}\right)^{1/2} \qquad (1)$$

Here λ is the wavelength in cm, λ_p is the wavelength of radiation at the plasma frequency

$$\lambda_p = \frac{2\pi c}{\omega_p} \quad , \qquad \omega_p^2 = \frac{4\pi ne^2}{m_e} \tag{2}$$

T_e is the electron temperature in eV, n_e is the electron density in cm^{-3}, and Z is the ionic charge. The laser radiation penetrates the plasma only if

$$n_e \lambda^2 < 10^{13} \tag{3}$$

If $\lambda/\lambda_p < 1$ then $(1-\lambda^2/\lambda_p^2)^{1/2} \approx 1$. In this case the absorption length varies as n^{-2} and λ^{-2} for fixed T_e. The optimum conditions for absorption occur when the maximum plasma density is near the critical density for the wavelength used. It may not be possible to confine a plasma at this optimum density, in which case the best absorption is achieved by operating at the longest wavelength which is practical.

2.2 Inverse Synchrotron Absorption

A second absorption process which applies for a plasma in a magnetic field is inverse synchrotron absorption [5]. The absorption length due to this process depends on the polarization and upon the angle of propagation with respect to the magnetic field. It is strongest for propagation perpendicular to B and becomes rather inefficient if the angle to the perpendicular is greater than v_T/c (v_T is the thermal velocity). For a Maxwellian distribution and propagation perpendicular to B (or within the angle v_T/c of $\perp$) this absorption length is roughly given by

$$\ell = \frac{7.6 \times 10^8 B}{n} \left(\frac{m_o c^2}{kT_e}\right)^{j-3/2} \frac{1}{j^{j-3}} \tag{4}$$

where j is the harmonic number, $j = \lambda_c/\lambda$, $\lambda_c = 2\pi c/\omega_c$.

$$\lambda_c = 10^4/B \text{ cm} . \tag{5}$$

Equation (4) applies for j = 1, 2, 3, 4, ... but starts to fail for $(j^2 kT)/mc^2 \approx 1$.

The absorption length is a very strong function of j and kT_e/mc^2. For keV temperatures this mechanism is ineffective for harmonics above 5 or 6. A magnetic field of 10^7 G gives λ_c equal 10 μ. Thus for 10-μ radiation it will be difficult to make use of the inverse synchrotron absorption for fields less than about 2 MG. Longer wavelengths, say 100 μ, could be effectively absorbed by plasma in fields of a few hundred kilogauss. This process might be used to heat lower density plasmas to very high temperatures since the absorption length varies as $n_o^{-1} T_e^{3/2-j}$ in contrast to $n_o^{-2} T_e^{3/2}$ for inverse bremsstrahlung.

2.3 Anomalous Absorption

If radiation of sufficient intensity falls on a plasma it can create instabilities which lead to enhanced absorption of the radiation [6, 7]. Such processes can be very efficient if the laser radiation is near the plasma frequency or twice the plasma frequency, leading to absorption in a few wavelengths.

Sufficient powers for this mechanism to operate have been achieved with CO_2 lasers. However, it is difficult to magnetically confine a plasma at the high densities required for these mechanisms to be effective (megagauss fields are required). If lower frequency lasers are developed, this mechanism might be important.

There has been some investigation of the possibilities of anomalous absorption for frequencies well above the plasma frequency [8]. However, these processes have not been investigated as thoroughly as those near ω_p and $2\omega_p$ and it appears that they will not be so efficient at converting radiation energy to plasma energy.

3. THE LAWSON CONDITION

In order to have a successful pulsed thermonuclear reactor the reaction must produce enough energy to initiate a new pulse. If we need α times as much energy as is required to heat the plasma (where α is determined by overall efficiency, η) then we must confine the plasma for a time τ such that

$$n_o n_\tau \langle \sigma v \rangle Q\tau = \alpha \frac{3}{2} kT (n_D + n_T + n_e) \tag{6}$$

where σ is the cross section for reactions between deuterium and tritium, $\langle \sigma v \rangle$ is the average over a Maxwellian, Q is the energy released in the reaction. This equation neglects the bremsstrahlung emission, which is permissible for the conditions considered. We shall take Q to be 22.2 MeV, including the 17.6 MeV obtained directly from the D-T reaction plus 4.6 MeV from breeding tritium from lithium 6. If we assume we have the optimum mixture with n_D equal n_T equal $n_e/2$ equals $n/2$

$$n\tau = \frac{\alpha\, 12\, kT}{\langle \sigma v \rangle Q} \tag{7}$$

A plot of $n\tau/\alpha$ versus T is shown in Fig. 1.

For a steady or quasi-steady state reactor where the reaction supplies the energy to heat incoming fuel and maintain the plasma temperature, the energy confinement must satisfy (7) with α at least equal 6 since one sixth of the reaction energy (3.5 MeV) is carried by charged (He) reaction products which can deposit their energy in the plasma. However, in order for these products to maintain the temperature they must be stopped in the plasma. The stopping is mainly by collisions with electrons, and the stopping time is given by

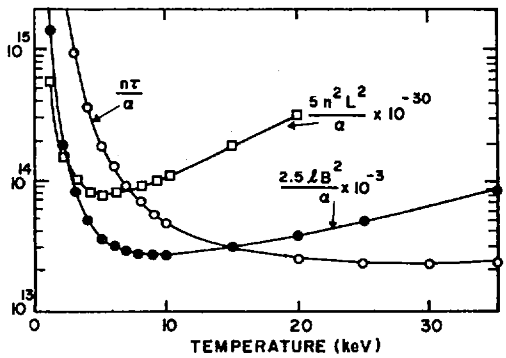

FIG. 1. Plots of $n\tau/\alpha$, n^2L^2/α, and $\ell B^2/\alpha$ versus T.

$$\tau_s = \frac{4.5 \times 10^7 \, T_e^{3/2}}{n_e} \tag{8}$$

with the velocity given by $v = v_o \exp(-t/\tau_s)$. The stopping distance is

$$\ell_s = v_o \tau_s = \frac{4.5 \times 10^{16} \, T_e^{3/2}}{n_e} \tag{9}$$

The fraction of the energy which the particle deposits in traveling the distance x is given by

$$f = \left(1 - \frac{v(x)^2}{v_o^2}\right) = \frac{x}{\ell_s}\left(2 - \frac{x}{\ell_s}\right) \tag{10}$$

Thus, in a distance of $0.3\,\ell_s$, 50% of the reaction products energy is deposited.

4. THE PLASMA IN A LONG STRAIGHT SYSTEM

4.1 General Remarks

One of the simplest configurations for laser heating a magnetically confined plasma consists of a long straight solenoid producing an axial field into which a laser beam propagates along the axis. The plasma is assumed to stream freely out the end; methods for inhibiting the end losses are discussed in Section 5.

This configuration is similar to that produced by θ pinches [9], but here an arbitrary portion of the plasma energy can be supplied by the laser rather than by fast magnetic compression. This method, immediately leads to two major advantages over a conventional pinch. First, it makes possible simultaneous achievement of thermonuclear temperatures and very high densities (10^{17} - 10^{19}) that cannot be produced by pinches operating at practical capacitor voltages; there results a corresponding reduction in reactor length. The maximum density is limited primarily by magnet structural considerations. Secondly, with a laser augmented pinch it is possible to produce dense, thermonuclear plasmas in such a way that the plasma occupies a large fraction of the coil volume. The confining field annulus needs only be large enough to prevent significant cross-field diffusion in a Lawson time. Therefore, the ratio of magnetic energy to plasma energy can be of order one or less. By way of contrast, in a conventional θ pinch this ratio is typically of order 10^2. Thus the laser augmented pinch would appear to be roughly 10^2 times more efficient in this sense.

The addition of laser energy and of magnetic field energy to the plasma-field system within the coil could be programmed in a number of ways. For example, after a slight initial pinch to get the plasma off the wall, the laser energy and field energy could be added simultaneously at a rate such that the plasma pressure $p = (n_e + n_i)kT$ at all times equals the magnetic pressure $B^2/8\pi$. In this case the filling density would be approximately equal to the final density and all the plasma energy is supplied by the laser while the capacitor bank provides field energy. Another case is obtained by strongly pinching the plasma to a thin column in quasi-equilibrium in the conventional manner. Laser energy is then added to the column causing it to expand and increase in temperature, until it again occupies most of the coil volume. A quantitative thermodynamic analysis [10] shows that for a θ pinch about 70% of the laser energy goes into plasma heating and the balance into magnetic field energy. The first of these schemes would probably be preferable for a long (reactor length) device in order to match absorption length to column length; in the second the laser energy absorption occurs at higher densities which is advantageous for smaller scale devices.

Laser augmentation could of course be applied to a Z pinch as well. This has the advantage of providing a somewhat reduced magnetic pressure on the coil, but at the cost of a decrease in stability. As the stability is increased by addition of a bias field, and by moving the coil wall closer to the plasma boundary, the reduced coil pressure benefit diminishes.

The ideal situation is one in which the solenoid is superconducting and the capacitor bank is not required. The laser would heat cold gas, causing it to expand and increase the field by flux conservation. The feasibility of this approach depends on advances in superconducting magnet technology as well as on answers as to the influence of the cold plasma blanket surrounding the hot core; an alternative is to fill only the central region with a beam of neutrals.

4.2 Scaling Laws

The field required to confine a $\beta = 1$ plasma is

$$B = 6.3\times 10^{-6}\,[\,(n_e + n_i)\,T\,]^{1/2} \tag{11}$$

For uninhibited flow out the end the confinement time is roughly given by

$$\tau = \frac{\ell}{2\,v_T} \tag{12}$$

where ℓ is the coil length and v_T the ion thermal velocity. The Lawson condition, Eq. (7), can thus be written

$$n\,\ell = \frac{24\times 10^6\,\alpha\,k\,T^{3/2}}{\langle\sigma v\rangle\,Q} \tag{13}$$

(Use of a more accurate similarity solution [11] for plasma loss gives similar results.) Since equilibrium requires a balance between magnetic and plasma pressure, Eq. (13) can be written as

$$\ell = \frac{(1.9\times 10^{-3})\,k\,T^{5/2}}{\langle\sigma v\rangle\,Q}\cdot\frac{\alpha}{B^2} = f(T)\,\frac{\alpha}{B^2} \tag{14}$$

A plot of $f(T) = \ell B^2/\alpha$ vs. T is shown in Fig. 1; f(T) has a shallow minimum for T = 10 keV. The length for this temparature is thus

$$\ell_c = 0.8\times 10^{16}\,\frac{\alpha}{B^2}\ \text{cm} \tag{15}$$

which gives the minimum reactor length as a function of α and B.

The absorption length must be of the order of the reactor length at the final temperature for efficient absorption of laser radiation. For a $\beta = 1$ plasma and a density not too near the critical density, Eq. (1) becomes

$$\ell_{ab} = \frac{3.5\times 10^7\,T_e^{7/2}}{B^4\,\lambda^2} \tag{16}$$

At 10 keV, therefore,

$$\frac{\ell_{ab}}{\ell_c} = \frac{7.07\times 10^5}{\alpha(B\lambda)^2} \tag{17}$$

For $\alpha = 3$ ($\eta = 1/4$), $\lambda = 10.6$, and B = 500 kg (which corresponds to a density of 3×10^{17}), the reactor length becomes $\ell_c = 10^3$ meters and $\ell_{ab} = 0.71\,\ell_c$.

4.3 Details of the absorption process

One of the properties of inverse-bremsstrahlung absorption is a significant increase in the absorption length as the plasma is heated. The result is the propagation of an absorption or bleaching "wave" into the plasma at a hole-burning velocity as successive opaque layers are heated and rendered more transparent. This occurs for both static heating and when radial expansion is allowed and has been studied in detail in Refs. [12] and [13].

With rapid addition of laser energy to the plasma the electron temperature exceeds that of the ions. However, the equilibration time (τ_{eq}) based on classical calculations [14] is roughly 1/3 of the required confinement time as given by Eq. (7) so that sufficient equilibration should occur. Thermal conduction will easily give a uniform temperature in the long plasma column within the confinement time.

Figure 2 shows the region in which the Lawson criterion is exceeded ($n\tau \geq 10^{14}$, $T_i \geq 10$ keV). The abscissa represents the total energy in the laser pulse divided by the cross-sectional area of the plasma column.

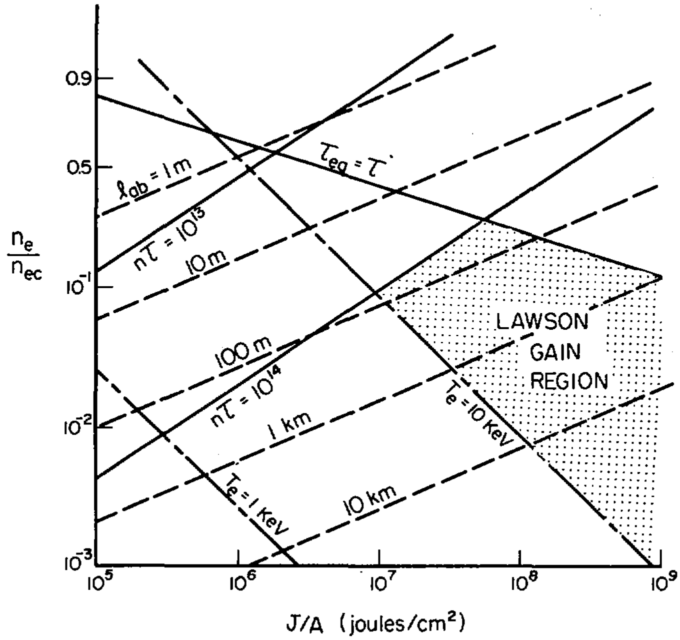

FIG. 2. Region of interest for laser heated plasma in the n_e/n_{ec} (electron density/critical electron density), joules/cm^2 plane.

The ordinate is the ratio of the electron density to the critical electron density. It is assumed that the reactor length equals the absorption length of the 10 keV plasma. The results have been calculated assuming that quantities vary in the axial direction only. This is not strictly true but gives a reasonable approximation for the case where the laser beam is trapped (Sec. 4.4).

4.4 Refraction of the Beam and Self-Focusing

It has been assumed in previous discussions that the laser beam is directed along the axis of the plasma column and is not refracted out of the plasma before being absorbed. Light rays traversing a highly ionized plasma are deflected toward the region of lower density. It is clear that the electron density must have a minimum on axis and increase in the radial direction before decreasing at the plasma-field boundary. The required depth of the density minimum is very small; it needs only be sufficient to overcome the diffraction spreading of the laser beam.

To illustrate some salient features, consider a TEM_{00} beam propagating along a plasma column with a parabolic (unfavorable) density distribution. A ray optics calculation [15] shows that the distance the beam will travel before one half its energy has been refracted out of the column is given by

$$\frac{x}{a} = 1.14 \frac{1-(1-\gamma/2)\zeta_m}{\gamma\zeta_m} \tag{18}$$

where a is the plasma radius, γ is the ratio of the laser beam radius to the plasma radius, and ζ_m is the ratio of the electron density along the axis to the critical density. For $\zeta_m = 0.5$ and $\gamma = 1$, $x/a = 1.39$. However, the absorption length at 10 keV is given by

$$L = 79 \frac{\sqrt{1-\zeta}}{\zeta^2} \text{ cm} \tag{19}$$

so for $\zeta = 0.5$, $L = 220$. Even if we make $\gamma \ll 1$, say $\gamma = 10^{-2}$, $x/a = 12.3$ which is still not sufficient for a reasonable value of $a = 1$ cm.

On the other hand, it is shown in Ref. [13] that a parallel beam is always trapped in a minimum region of the plasma density. Solutions for the phase propagation have been worked out for one density distribution and from this case it was shown that the effective absorption length can also easily be reduced by a factor of two.

There are at least three simple approaches to obtaining a favorable density distribution to guarantee the confinement and absorption of the laser beam. If the density distribution has a minimum initially, the laser energy addition will be straightforward and refraction effects will be favorable. Such a distribution exists early in the dynamic phase of a θ pinch; trapping of 337-μ radiation in this case has been observed experimentally [16].

If the initial density distribution is unfavorable then one could use a short-wavelength laser (1.06 μ) which reduces ζ_m to 5×10^{-3}, with $r = 10^{-2}$ to add a small amount of energy near the axis of the plasma. In this case $x/a = 2000$, i.e., refraction of the 1.06-μ pulse is negligible. Because of the temperature increase near the axis, the plasma will expand in the center and compress toward the outside, thus creating a density minimum. Then the long-wavelength laser can be used to heat the plasma to the required 10 keV.

If sufficient control of the laser pulse shape is available then a dynamic process using only the long-wavelength laser is possible. The laser pulse would be programmed so that as it propagates into the plasma column, it creates the required density minimum. Most of the energy of the pulse would be at the end of the pulse so that even though some energy is lost due to refraction while creating the favorable density distribution it will still be a small percentage.

Self-focusing may occur in a plasma due to the ponderomotive force [17]. This effect, if it is significant for conditions of interest, will enhance the self-focusing due to density gradients.

5. STRAIGHT SYSTEM WITH INHIBITED END LOSSES

Even with optimistic assumptions concerning the size of the magnetic field and the efficiency factor α, it appears that a simple straight device of this type would have to be on the order of 1 km long to work. There are, however, a number of relatively simple possibilities for reducing this length.

First, we might confine the plasma in the axial direction by means of material walls. These walls will have to be shielded from the plasma by high-pressure cold gas since otherwise the energy flux to them will far exceed their ability to conduct heat away.

For such a situation we must overcome the heat conduction to the cold gas at the ends. The time it takes for heat to diffuse a distance ℓ is given by

$$t = \frac{(Z+1)\, n_e \ell^2}{2 \times 10^{19}\, T_e^{5/2}} \tag{20}$$

If the plasma is confined, then the reaction will maintain the temperature provided the energy confinement time satisfies Eq. (7) with $\alpha = 6$. Thus we find for the length (taking $L = 2\ell$)

$$L^2 = \frac{9.60 \times 10^{20}\, T_e^{7/2}}{\langle \sigma v \rangle (1+Z)\, n_e^2\, Q} \tag{21}$$

A plot of $n^2 \ell^2/\alpha$ vs. T is shown if Fig. 1 for an effective Z of 1. For a density of 6×10^{17} and a temperature of 5×10^3 eV we find L equals 7×10^3 cm per unit $\sqrt{\alpha}$.

This length is too short to stop the reaction products by about a factor of 4 [Eq. (9)]. Taking the mean path length through the plasma to be $L\sqrt{3}/2$; $\sqrt{3}$ because they spiral about the magnetic field, and 1/2 because on the average they will transit only half the system. By Eq. (10) they will deposit roughly half of their energy in the plasma. We will thus have to make the plasma slightly longer than this to achieve energy balance. Nevertheless this does not seem like an unreasonable length for a working device.

A second possibility for reducing loss out the ends of a straight system is to apply mirrors along the length of the system. If the mirrors are spaced about a mean free path apart, then the particles will perform a random walk from one mirror to another, and the loss out the end will be a diffusion. A second way to look at it is the following: As the plasma flows along the field it sees a modulated field, and so it appears to be magnetically pumped. This dissipates energy which must come from the flow. The flow is rather dissipative and is of the nature of diffusion. If the mean free path of a particle is less than or about equal to the distance between mirrors then the magnetic pumping arguments give for the diffusion coefficient [18]

$$D \approx \frac{15\nu}{k^2 M^2}$$

where k is the wave number associated with the mirrors, ν is the ion-ion collision frequency, and M is the modulation in the magnetic field, $M = \Delta B/\overline{B}$; $\overline{B}$ is the mean magnetic field, and ΔB is the maximum deviation from the mean.

As A specific example we will consider the case of B = 300 kG with mirror fields of 500 kG (M = 0.3) one mean free path apart. We take the plasma to have a density of 2×10^{17} and a temperature of 5 keV. The mean free path is 120 cm which we set equal to $2\pi k^{-1}$. The diffusion coefficient is then found to be

$$D = 3 \times 10^{10}\ \mathrm{cm^2/sec}$$

In order to have an $n\tau$ of 10^{15} , the half length of the system must be 1.3×10^4 cm.

This length is shorter than the stopping distance for the reaction products. However, here the mirrors offer a large advantage since they trap most of these (70% for this case) so that their energy is delivered to the plasma. An appreciable fraction of the energy of the untrapped reaction products (20%) will also be deposited in the plasma.

Simple mirror configurations are well known to be unstable. The system could be made stable in the minimum average B sense through the use of the periodic multipole configuration of Furth and Rosenbluth [19]. However, even for the case of simple mirrors estimates of the minimum disruption time appears to be within a factor of ten of that required to meet the Lawson criterion. Stabilization or reduction of instability growth rates by a number of mechanisms such as by a surrounding cold dense plasma might suffice.

The plasma radius required for these long straight plasmas is determined by the requirement that the radial loss of plasma and energy not exceed the axial loss, as this has already been chosen to be just tolerable. We find the following values for the required radii and energies under the assumptions given ; B = 300 kG.

(a) r = 0.3 cm, $E = 5 \times 10^5$ J — classical diffusion, no heat loss perpendicular to B (plasma surrounded by vacuum);

(b)	$r = 2$ cm $E = 2.5 \times 10^7$ J	classical ionic heat conduction perpendicular to B to a cold plasma surrounding the thermonuclear plasma;
(c)	$r = 52$ cm $E = 2 \times 10^{10}$ J	Bohm diffusion of either plasma or heat.

6. OTHER GEOMETRIES

Laser radiation can be used to create and heat plasmas in other geometries. Hot plasmas created by vaporizing pellets with the high-powered, short-pulse lasers, have been used as a plasma source in a number of devices. This method can be used with CO_2 lasers if pulse lengths of one to ten nanoseconds are available.

With magnetic confinement we can use relatively long laser pulses to heat plasmas slowly and quiescently. Almost any magnetic geometry can be used. However, if we wish to achieve thermonuclear conditions then limitations on magnetic field strengths and plasma densities in some of these limit the usefulness of 10-μ lasers.

One popular geometry is the toroidal geometry of stellarators and tokamaks. To heat the plasma in such devices to thermonuclear temperatures with 10-μ radiation appears difficult for a number of reasons. First, it appears that in toroidal devices the maximum β will be about 0.1. The corresponding lower density greatly reduces the absorption. Second, if superconductors are used, there is a maximum field at which they will operate and this is determined by the maximum field seen by any point of the coil. The proportion of the coil toward the center of the torus sees a considerable larger field than the plasma since one to two meters of neutron shielding is required. This reduces the density and hence the absorption that can be achieved even further.

For a toroidal field of 300 kG, a density of 2×10^{16} at 5 keV ($\beta = 0.1$) the absorption length of 10-μ radiation is 4.5×10^6 cm and extremely many passes of the beam through the plasma would be required for effective heating.

If efficient lasers in the 100-μ wavelengths range were to become available this situation would be greatly altered. Such lasers might make use of inverse synchrotron absorption or anomalous absorption.

The situation is also not so bad for experimental devices where thermonuclear conditions are not achieved. It appears that it should be possible to obtain 500 eV plasmas in the 10^{17} density range by using 10-μ laser radiation in a torus.

7. CONCLUSIONS

The advent of the high-efficiency, high-powered, 10-μ CO_2 laser opens up the possibility of producing thermonuclear plasmas in the density range $10^{17} \sim 10^{19}$. It is possible to confine these plasmas with available magnetic fields in the $10^5 \sim 10^6$ G range. If such lasers were used to heat a plasma in a long straight solenoid with free flow of the plasma out the ends it appears that a working reactor would be of the order of 10^5 cm long (using realistic B fields and laser efficiencies). If some steps are taken to inhibit flow out the ends of the device reactors of several hundred meter length should be possible.

ACKNOWLEDGMENTS

One of the authors, J.M.D., would like to acknowledge many stimulating discussions with Dr. W. M. Hooke. He is also indebted to Dr. H. Dreicer for the suggestion of using inverse synchrotron absorption.

This work was supported jointly by U. S. Atomic Energy Commission Contract AT(30-1)-1238; and by the National Science Foundation Grant GK 28562

REFERENCES

[1] GERRY, E.T., IEEE Spectrum 7 (1970) 51.
[2] DUMANCHIN, R., et al., IEEE Quantum Electronics Conference, Tokyo, September (1970).
[3] NIGHAN, W., Phys. Rev. A2 (1970) 1989.
[4] HERTZBERG, A., JOHNSTON, E.W., and AHLSTROM, H.G., AIAA 9th Aerospace Sciences Meeting, New York, N.Y. (1971), paper no. 71-106.
[5] TRUBNIKOV, B.A. and BAZHANOVA, A.E., Plasma Physics and the Problem of Controlled Thermonuclear Reactions, Pergamon Press, London, Vol. III (1959) 141.
[6] KAW, P. and DAWSON, J.M., Phys. Fluids 12 (1969) 2586.
[7] KRUER, W.L., KAW, P.K., DAWSON, J.M., and OBERMAN, C., Phys. Rev. Letters 24 (1970) 987.
[8] SILIN, V.P., Zh. Eksp. Teor. Fiz. 57 (1969) 183; [Sov. Phys. JETP 30 (1970) 105].
[9] RIBE, F.L., OLIPHANT, Jr., T.A.O., and QUINN, W.E., Los Alamos Scientific Lab., Report LA-3294-MS (1965).
BELL, G.I., BORKENHAGEN, W.H., and RIBE, F.L., Nuclear Fusion Reactors Conference, London, British Nuclear Energy Society (1969) 242.
[10] VLASSES, G.C., Phys. Fluids 14 (to be published, 1971).
[11] DAWSON, J.M., KAW, P., and GREEN, B., Phys. Fluids 12, (1969) 875.
[12] STEINHAUER, L. and AHLSTROM, H.G., Phys. Fluids 14, (1971) 81.
[13] STEINHAUER, L., Ph.D. Thesis, University of Washington (1970).
[14] SPITZER, L., Physics of Fully Ionized Gases, 2nd ed., Interscience, New York (1962) 135.
[15] STEINHAUER, L. and AHLSTROM, H.G., Phys. Fluids 14 (to be published, 1971).
[16] TURNER, R. and POEHLER, T.O., Phys. Fluids 13 (1970) 1072.

[17] HORA, H., Opto-Electronics 2 (1971) 201.
[18] DAWSON, J.M., WINSOR, N.K., BOWERS, E.C., and JOHNSON, J.L., Proc. of the IV European Conf. on Controlled Fusion and Plasma Physics, Rome, Italy, C.N.E.N. (1970) 9.

DISCUSSION

F.F. CHEN: Before any laser energy can be absorbed, a plasma of density above 10^{17} cm^{-3} must be created. Do you envisage for this purpose a series of theta-pinches, whose efficiency you have not calculated, or are you considering some sort of avalanche requiring a long pulse?

J.M. DAWSON: I think there is no difficulty there. The intense laser beam will cause breakdown if only a few free electrons are present. Remember that the laser intensity is of the order of $10^9 \sim 10^{10}$ watt/cm^2.

Low temperatures of the order of a few eV and densities of 10^{16} give full absorption in a few metres and breakdown will occur even at much lower density. The initial ionization, if required, can be provided in various ways. One method would be to use a weak theta-pinch, a second would be to use a very intense laser pulse (perhaps from a glass laser) which gives breakdown more easily, a third way would be to use a weak electron beam, and a fourth would be to use a flash of ultraviolet or X-rays. Details of the initiation of the plasma are given in Refs [12] and [13] of the paper.

P.H. REBUT: I have done similar work (unpublished) to yours and in general I obtained the same orders of magnitude; however, the end losses, due to electron thermal conductivity, are the main losses and they determine the minimum length of the reactor. It is, therefore, hard to believe that successive mirrors migth have a decisive effect on these losses.

J.M. DAWSON: If the plasma is in contact with cold material at the ends, then electron heat conduction to the ends is very important. One can reduce the electron heat conduction by adding a small amount of high-Z material. This increases the radiation loss but, since the plasma is generating much more energy than it is radiating (50 times as much at 10 keV; 10 times as much in charged particles), we can stand some high-Z. One should probably balance radiation and heat conduction losses. I do not believe that the mirrors will reduce the electron heat conduction much although they have some effect.

P.H. REBUT: My second remark relates to the plasma production. Instead of an N_2-CO_2 laser I thought it preferable to use a beam of electrons, whose energy can be adjusted according to the interactions involved (minimum energy of 400 keV). The beam is used, in particular for initial production of the plasma, which is then maintained by reabsorption of α particles.

J.W. DAWSON: One could use an electron beam. However, the stopping of the beam may be a problem. If low-energy electrons are used and they are stopped by Coulomb collisions, very large currents are needed. There may be trouble with instabilities generated by the beam. For energetic beams the instabilities excited by the beam will have to stop it. It is not sure what other effects these instabilities will have. However, electron beams might work very well and I think this possibility is worthy of investigation.

A. J. LICHTENBERG: With your plasma density and size one would expect an output power of twenty to thirty thousand megawatts. Since this is rather large, I wonder whether it is possible to reduce the plasma radius and, if so, what are the restrictions on this reduction?

J. W. DAWSON: The radius is limited by the condition that radial plasma and heat losses should not be excessive. This requires radii greater than one or two centimetres. I can imagine the device operated on a pulse basis, which would limit the average power output to values the walls can withstand.

A. J. LICHTENBERG: How did you calculate the reduction in the plasma length needed to achieve power balance in the presence of multiple mirrors?

J. W. DAWSON: For the multiple-mirror calcuation the energy dissipated by the plasma as it flowed through the mirrors was calculated from magnetic pumping calculations, which are referenced in the paper. The pressure drop needed to maintain the flow was then computed and the diffusion coefficient was obtained from the relation

$$nV = D\,\frac{\partial n}{\partial x}$$

M. KRISTIANSEN: Work carried out in our laboratory indicates that the CO_2 laser absorption in weakly absorbing materials can be increased at least ten-fold if the absorbing material is placed in a coupled or intra-resonator arrangement. Have you considered this method and what do you think about it in connection with your proposed laser heating arrangement?

J. M. DAWSON: Yes this is possible; the beam can be passed back and forth through the plasma many times. For this reason one can consider absorption lengths as long as a few times 10^5 cm for devices of the size of a few times 10^4 cm.

CHAIRMEN OF SESSIONS

Session A	M. GOTTLIEB	USA
Session B	C.M. BRAAMS	Netherlands
Session C	B.B. KADOMTSEV	USSR
Session D	B. BRUNELLI	Italy
Session E	J.B. TAYLOR	UK
Session F	B. LEHNERT	Sweden
Session G	M. TROCHERIS	France
Session H	G. VON GIERKE	Federal Republic of Germany
Session J	C.N. WATSON-MUNRO	Australia
Session K	E.P. VELIKHOV	USSR
Session L	K. HUSIMI	Japan
Session M	H. POSTMA	United States of America

SECRETARIAT

Scientific Secretary:	H.S.T. DRIVER	Division of Research and Laboratories, IAEA
Administrative Secretary:	C. DE MOL VAN OTTERLOO	Division of Scientific and Technical Information, IAEA
Editors:	R. SCHENIN J.W. WEIL	Division of Publications, IAEA
Records Officer:	D.J. MITCHELL	Division of Languages, IAEA

HOW TO ORDER IAEA PUBLICATIONS

Exclusive sales agents for IAEA publications, to whom all orders and inquiries should be addressed, have been appointed in the following countries:

UNITED KINGDOM	Her Majesty's Stationery Office, P.O. Box 569, London S.E.1
UNITED STATES OF AMERICA	UNIPUB, Inc., P.O. Box 433, New York, N.Y. 10016

In the following countries IAEA publications may be purchased from the sales agents or bocksellers listed or through your major local booksellers. Payment can be made in local currency or with UNESCO coupons.

ARGENTINA	Comisión Nacional de Energía Atómica, Avenida del Libertador 8250, Buenos Aires
AUSTRALIA	Hunter Publications, 23 McKillop Street, Melbourne, C.1
BELGIUM	Office International de Librairie, 30, avenue Marnix, Brussels 5
CANADA	Information Canada, Ottawa
C.S.S.R.	S.N.T.L., Spálená 51, Prague 1 Alfa, Publishers, Hurbanovo námestie 6, Bratislava
FRANCE	Office International de Documentation et Librairie, 48, rue Gay-Lussac, F-75 Paris 5e
HUNGARY	Kultura, Hungarian Trading Company for Books and Newspapers, P.O. Box 149, Budapest 62
INDIA	Oxford Book and Stationery Comp., 17, Park Street, Calcutta 16
ISRAEL	Heiliger and Co., 3, Nathan Strauss Str., Jerusalem
ITALY	Agenzia Editoriale Commissionaria, A.E.I.O.U., Via Meravigli 16, I-20123 Milan
JAPAN	Maruzen Company, Ltd., P.O. Box 5050, 100-31 Tokyo International
NETHERLANDS	Martinus Nijhoff N.V., Lange Voorhout 9—11, P.O. Box 269, The Hague
PAKISTAN	Mirza Book Agency, 65, The Mall, P.O.Box 729, Lahore-3
POLAND	Ars Polona, Centrala Handlu Zagranicznego, Krakowskie Przedmiescie 7, Warsaw
ROMANIA	Cartimex, 3-5 13 Decembrie Street, P.O. Box 134-135, Bucarest
SPAIN	Librería Bosch, Ronda Universidad 11, Barcelona-7
SWEDEN	C.E. Fritzes Kungl. Hovbokhandel, Fredsgatan 2, Stockholm 16
SWITZERLAND	Librairie Payot, rue Grenus 6, CH-1211 Geneva 11
U.S.S.R.	Mezhdunarodnaya Kniga, Smolenskaya-Sennaya 32-34, Moscow G-200
YUGOSLAVIA	Jugoslovenska Knjiga, Terazije 27, Belgrade

Orders from countries where sales agents have not yet been appointed and requests for information should be addressed directly to:

Publishing Section,
International Atomic Energy Agency,
Kärntner Ring 11, P.O.Box 590, A-1011 Vienna, Austria

INTERNATIONAL
ATOMIC ENERGY AGENCY
VIENNA, 1971

PRICE: US $ 20.00
Austrian Schillings 482,-
(£8.08; F.Fr.110,40 DM 66,40)

SUBJECT GROUP: III
Physics/Plasma Physics, Fusion